DECHEMA

VDI

BOOK OF FULL PAPERS

14 – 17 September 2014
Friedrichshafen · Germany

10th International Conference on DISTILLATION & ABSORPTION 2014

www.da2014.de

© Bayer AG

PROCESSNET
EINE INITIATIVE VON DECHEMA UND VDI-GVC

EUROPEAN FEDERATION OF CHEMICAL ENGINEERING
EFCE
Event No. 705

ORGANISER & CONTACT

DA2014 CONFERENCE OFFICE AND ORGANISER

DECHEMA e.V.

Nina Weingärtner and Christopher Diaz Maceo

Theodor-Heuss-Allee 25

60486 Frankfurt am Main, Germany

Phone: +49 - (0)69 - 7564-125 or -243

SPONSORS

The organisers convey their sincere thanks for supporting the 10th International Conference on Distillation & Absortption 2014 to the following companies:

BASF SE
Ludwigshafen/D

Bayer Technologies Services GmbH
Leverkusen/D

Elsevier Ltd.
Amsterdam/NL

ENVIMAC Engineering GmbH
Oberhausen/D

Evonik Industries AG
Hanau/D

GEA 2H Water Technologies GmbH
Wettringen/D

INEOS Phenol GmbH
Gladbeck/D

KOCH-GLITSCH
Fenton/UK

Linde AG
Pullach/D

Maleta cyclic distillation LLC
Tallin/EST

ProSim SA
Labege/FR

Process Systems Enterprise
London/GB

RASCHIG GmbH
Ludwigshafen/D

RVT Process Equipment GmbH
Steinweisen/D

Siemens AG
Frankfurt at the Main/D

Shell Global Solutions International B.V.
Amsterdam/NL

Sulzer Chemtech Ltd
Winterthur/CH

Tracerco
Zellik/BE

Vereinigte-Füllkörper-Fabriken GmbH & Co. KG
Ransbach-Baumbach/D

EXHIBITORS

Bayer Technologies Services GmbH
Leverkusen/D

Elsevier Ltd.
Amsterdam/NL

ENVIMAC Engineering GmbH
Oberhausen/D

GEA 2H Water Technologies GmbH
Wettringen/D

Maleta cyclic distillation LLC
Tallin/EST

ProSim SA
Labege/FR

RVT Process Equipment GmbH
Steinweisen/D

Tracerco
Zellik/BE

TABLE OF CONTENT

LECTURE PROGRAMME

	MODELINGS & SIMULATION — Tuesday, 16 September 2014	Page
09:15	**Comprehensive investigation and comparison of refinery distillation technologies** A. Szoke-Kis, Budapest University of Technology and Economics/H; C.I. Farkas, MOL Plc., Százhalombatta/H; P. Mizsey, Budapest University of Technology and Economics/H	167
09:40	**Distillation in special chemistry** C. Hiller, R. Meier, Evonik Industries AG, Marl/D; G. Niggemann, Evonik Industries AG, Hanau/D; A. Rix, Evonik Industries AG, Marl/D	173
10:05	**Enrichment of light components at gas-liquid interfaces by density gradient theory and molecular simulation** K. Langenbach, S. Werth, M. Horsch, H. Hasse, TU Kaiserslautern/D	179
10:30	**From concept to design: the use of membrane residue curve maps to characterize and design membrane processes** M. Peters, University of South Africa, Johannesburg/ZA; N. Seedat, University of the Witwatersrand, Johannesburg/ZA; D. Hildebrandt, D. Glasser, University of South Africa, Johannesburg/ZA	186
11:20	**Evaluation of equilibrium and non-equilibrium models for simulation of distillation** J. Holtbruegge, TU Dortmund/D; E. Sorensen, University College London/UK; A. Górak, P. Lutze, TU Dortmund/D	192
11:45	**Analysis of a gas flow in structured packed bed columns using CFD** N. Jäntti, J. Vaittinen, T. Keskitalo, K. Keskinen, Neste Jacobs Oy, Porvoo/FIN; T. Siikonen, Aalto University, Espoo/FIN	198
12:10	**A study of the liquid viscosity impact on separation efficiency of structured packings using a modelling approach based on X-ray tomography** A. Janzen, J. Steube, University of Paderborn/D; M. Crine, P. Marchot, D. Toye, University of Liège/B; E.Y. Kenig, University of Paderborn/D	204

	MEGA EQUIPMENT — Tuesday, 16 September 2014	Page
09:15	**Columns subject to motion: maldistribution sensitivity and susceptibility** M. Duss, M. Roza, Sulzer Chemtech Ltd., Winterthur/CH	211
09:40	**CO_2 capture from coal flue gas: measurement of gas stream impurities and their effect on process operation and design** C. Satterley, E.ON New Build & Technology, Nottingham/UK; B. Schallert, W. Albrecht, S. Neuhaus, H. Rode, E.ON New Build & Technology, Gelsenkirchen/D; S. Reddy, Fluor Corporation, Irvine, CA/USA	218
10:05	**Large diameter experimental evidence on liquid (mal)distribution properties of structured packings** Z. Olujic, Delft University of Technology/NL; H. Jansen, Julius Montz GmbH, Hilden/D	224
10:30	**Mega tower design considerations** D. Summers, M. Pilling, D. Wiesman, Sulzer Chemtech, Tulsa, OK/USA	230
	BIOBASED PROCESSES — Tuesday, 16 September 2014	
11:20	**Dividing wall column for industrial multi-purpose use** D. Staak, T. Gruetzner, B. Schwegler, D. Roederer, Lonza Ltd., Visp/CH	236
11:45	**Process intensification of the production process of biojet fuel** C. Gutiérrez-Antonio, Universidad Autónoma de Querétaro/MEX; F.I. Gómez-Castro, J.G. Segovia-Hernández, Universidad de Guanajuato/MEX; A. Briones-Ramírez, Exxerpro Solutions, Querétaro/MEX	242
12:10	**Biocatalysts for enhanced CO_2 post-combustion capture efficiency in absorption columns** A. Kunze, V. Penner, TU Dortmund/D; M.T. Gundersen, J.M. Woodley, Technical University of Denmark, Lyngby/DK; A. Górak, P. Lutze, TU Dortmund/D	248
14:20	**Biocatalytic reactive distillation: fundamentals and experimental investigations** R. Heils, TU Hamburg-Harburg/D; M. Wierschem, TU Dortmund/D; L. Hilterhaus, A. Liese, TU Hamburg-Harburg/D; P. Lutze, TU Dortmund/D; I. Smirnova, TU Hamburg-Harburg/D	254

POSTER PROGRAMME

POSTER PROGRAMME

POSTER PROGRAMME

Lecture Programme

Mathematical gnostics, a powerful method of evaluating experimental heat capacity data

Z. Wagner, A. Andresová, M. Bendová, K. Machanová, J. Rotrekl
Institute of Chemical Process Fundamentals ASCR, v. v. i.,
Rozvojová 135/1, 165 02 Prague 6 - Lysolaje, Czech Republic

Abstract
The work demonstrates a powerful method of data analysis based on algorithms of mathematical gnostics and shows its application for evaluation of experimental heat capacity data. The method was first used during the initial setup and testing the functionality of a newly bought calorimeter. The stability of the calorimeter was examined and the optimum heating rate was determined. The optimum is chosen in order to maximize the signal to noise ratio. It is estimated as a temperature rate where the values of heat capacities obtained in repeated measurement have narrowest tolerance interval and narrowest interval of typical data. Heat capacities of three ionic liquids were further measured in the temperature range of 20–75 °C and repeatability analyzed by algorithms of mathematical gnostics. The width of the interval of typical data is less than 0.25 % in all cases.

Keywords
Mathematical gnostics, critical evaluation, heat capacity.

1. Introduction

In any experimental work, data analysis is equally important as data acquisition. Experimentalists do their best to prevent systematic errors and improve the procedure in order to obtain high quality data. However, no mater how careful the experimental work is, for various reasons the data may not fulfill assumption of frequently used statistical procedures, especially the distribution of experimental errors may not be normal. This is the case of measurement very low concentration or in techniques where the signal to noise ratio is low. The problems are thus caused by the physical nature of the experimental method. Similar problems arise if data come from several data sets, for instance if data measured by two or more authors have to be compared and critically evaluated. In such cases we have to assume that the data set consisting of all available data is not homogeneous and the distribution may have several modes. We need a tool that can reliably prove or reject this hypothesis.

Statistics offers several robust algorithms. However, they were derived using a prior assumption on the distribution of inliers and outliers. This is the reason why the problems are not completely solved. These methods often provide useful results but may unpredictably fail. Such failure was already demonstrated in one of the previous works [1].

A good candidate for such applications is mathematical gnostics [2] mainly because it does not make any assumption on the distribution of experimental errors. Their distribution function is estimated during data analysis adopting the paradigm: “Let the data speak for themselves.” Mathematical gnostics is based upon two axioms. The first axiom says that the process of measurement is influenced by uncertainty the nature of which is unknown. The measured value can be expressed as a sum

$$A = A_0 + S\Phi \tag{1}$$

where A is the measured value, A_0 is the ideal value meaning the true value that we wish to obtain. Symbol Φ denotes normalized uncertainty and S is a scale factor. Equation (1) can be reformulated into a multiplicative model

$$Z^{1/S} = Z_0^{1/S} e^{\Phi} \tag{2}$$

using the following mappings

$$Z = e^{A}, \quad Z_0 = e^{A_0} \tag{3}$$

The second axiom defines the composition law that that is used to estimate properties of the data sample from the properties of each individual measurement. The composition law provides us also with tools for estimating the optimum value of the scale parameter. The composition law enables us to define four kinds of gnostic distribution function from which only two are important for our application. Derivation of the expressions can be found in the above mentioned book [2].

The estimating global distribution function is per definition unimodal and serves for description of a homogeneous data sample. Composition is not additive and the value of the scale parameter is found by minimizing the difference between the estimating global distribution function and the empirical distribution function of the experimental data. Due to nonadditivity the resulting function may not fulfill properties required by statistics which means that the estimating global distribution function of the particular data sample does not exist and the hypothesis of homogeneity must be rejected.

On the contrary, the estimating local distribution function may be multimodal. If the distribution function is unimodal, the local estimate of location (position of the mode) has an interesting property described in book [2]. The estimate is robust which means that the local estimate of location is insensitive to outliers. Given a data sample we can test the influence of an added datum to the value of the local estimate of location Z_0. If the added datum is equal to the value of the local estimate of location. If the value is continuously decreased, first the value of the local estimate of location will also decrease till the added datum reaches a particular value Z_L where the value of the local estimate of location will approach a local minimum Z_{0L}. If the added datum is decreased further, it will be considered as an outlier, its influence will be gradually weaker and finally the value of the local estimate of location will return to Z_0. The behaviour in case of an added datum greater than Z_0 is analogical. We can therefore determine five values: $Z_L < Z_{0L} < Z_0 < Z_{0U} < Z_U$. Values Z_{0L} and Z_{0U} bound the *tolerance interval* because the value of the local estimate of location can never move outside it. Values Z_L and Z_U bound the *interval of typical data* where the dependence of the value of the local estimate of location on the added datum is increasing. This unique property can be used to estimate the precision of measurement even in case of small data samples as well as to test agreement of two or more data samples. The detailed description of the procedure can be found in the above mentioned book [2]. It was applied in several previous works, for instance for evaluation of literature data of high-pressure vapour-liquid equilibrium in systems of carbon dioxide with ionic liquids [3]. It is routinely used by automatic analysis of

particle size distribution of atmospheric aerosols [4] and found numerous applications included but not limited to medical research [5].

2. Results and discussion

The algorithms of mathematical gnostics were used during the setup of the newly bought Setaram μDSC III evo microcalorimeter. First the optimum heating rate for the continuous method was estimated and the stability was checked. Further the heat capacities of three ionic liquids were measured and repeatability verified.

2.1 Estimation of optimum rate of heating rate

Theoretically,continuous method of heat capacity measurement should be possible both during heating and cooling. The first tast was therefore estimation of the optimum rate and verification whether results obtained during heating and cooling provide the same results. There seems to be a software problem. If heat capacities are measured during heating, the values are reported at integer values of temperature (in degrees Centigrade) but this is not the case of the results obtained during cooling. Moreover, the heat capacity obtained during cooling exhibit high and irregular scatter. These results were therefore disregarded and only the results obtained during heating were further analyzed.

We assume that high heating rate may cause temperature gradient and thus incorrect values. Moreover such temperature gradient may be irreproducible. On the other hand, if the rate is too low, the signal to noise ratio will also be low which will result in increased scatter. We should therefore examine the dependence of the data scatter on the heating rate. In the terminology of statistics, we have to estimate data variance. The minimum sample size $n_{\min}$ required for this statistical procedure can be calculated from expression

$$n_{\min} = \frac{g_2(x) - 1}{4\delta^2(s)} + 1 \tag{4}$$

where δ is the required relative error of variance estimation and kurtosis g_2 is defined by

$$g_2 = \frac{E[(X - \mu)^4]}{(E[(X - \mu)^2])^2} \tag{5}$$

where X is the vector of experimental values, μ is the mean value and E is the operator of the arithmetic mean. The $n_{\min}$ values for several statistical distributions are given in Table 1.

Distribution	Kurtosis	$n_{\min}$
Uniform	1.8	21
Normal	3.0	51
Exponential	6.0	126
Laplace	9.0	201
Lognormal	15.0	351

Table 1: Minimum sample size for for determination of data variance with 10% error, i. e. the value of $\delta = 0.1$.

The estimators of mathematical gnostics are derived by composition of properties of each individual measurement, therefore the results are valid even for small sample sizes. Four values are often sufficient to obtain useful results. In order to perform gnostic analysis, heat capacity of water was measured at four distinct heating rates and each measurement was carried our four times. It was verified that the data sample for each distinct temperature and heating rate is homogeneous. Afterwards the tolerance intervals and intervals of typical data were calculated. The results are graphically summarized in Figure 1. For better clarity the intervals and to values of the local estimate of location are connected by lines although only the points make sense.

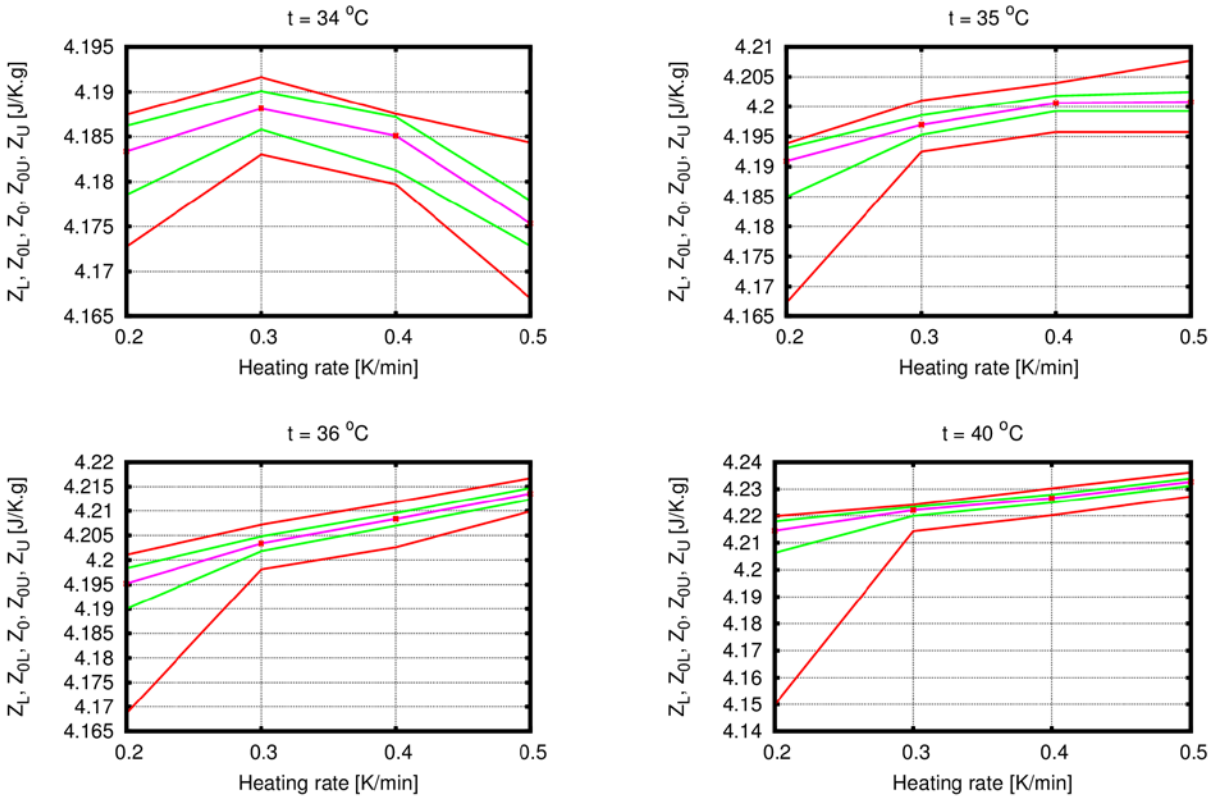

Figure 1: Dependence of tolerance intervals and intervals of typical data on heating rate

The results show that the results do not depend much on the heating rate and the trend is not unique. However, we can see that in most cases the interval of typical data at the rate of 0.2 K/min is considerably larger most probably due to low signal to noise ratio. Similar behaviour although not that pronounced can be observed at the rate of 0.5 K/min. Therefore the choice of the heating rate is not critical but the optimum value is 0.3 K/min. It is important to stress that this value need not be universal for all instruments.

2.2 Verification of long term stability

The measurement of the heat capacity of water as described in the preceding section was used to test the correct function of the calorimeter. Values measured at heating rate of 0.3 K/min were used to evaluate the local estimate of location and the tolerance interval and the interval of typical data at each temperatures. The results together with the literature data [6] are shown in Figure 2.

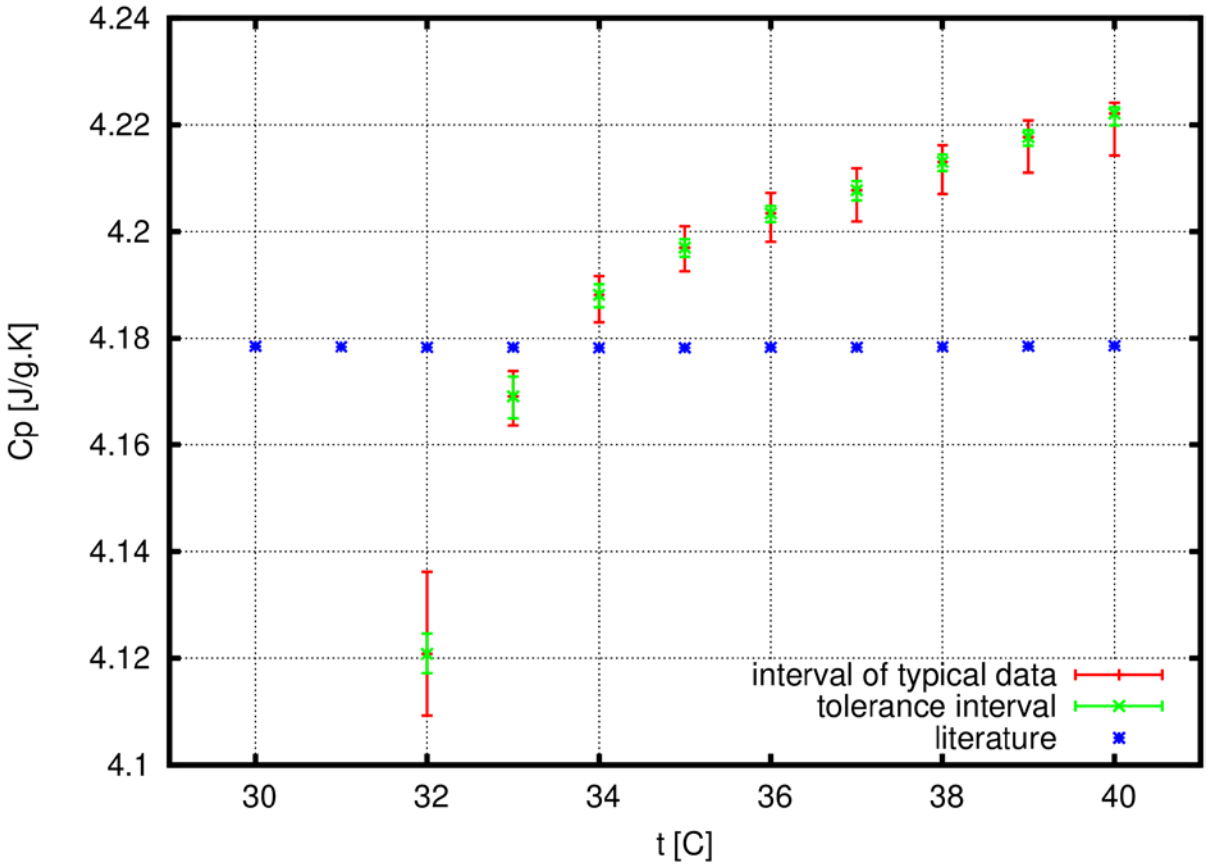

Figure 2: Test measurement of heat capacity of water, comparison with literature data.

The value measured at 32 °C is close to the beginning of the operation interval. According to information from the manufacturer this value should be disregarded. Indeed, the interval of typical data is much wider that the intervals of typical data at higher temperatures. It is also evident that our data do not agree with literature. Measurement of sapphire showed the source of the problem. In February 2012 the measured value was 0.8114 J/K.g with tolerance interval (0.8111, 0.8115) and interval of typical data (0.8103, 0.8117) while the measurement repeated in November 2012 provided value 0.8210 J/K.g with tolerance interval (0.8205, 0.8214) and interval of typical data (0.8192, 0.8218). After Joule effect recalibration our measurement agreed with the literature data.

2.3 Measurement of heat capacities of ionic liquids

Heat capacities of three imidazolium based ionic liquids were measured in temperature range of 20–75 °C. The ionic liquids differ in the substituent on the imidazolium ring, aliphatic, branched an cyclic, namely $[C_4C_5IM][NTF_2]$, $[C_4iC_5IM][NTF_2]$, $[C_4cC_5IM][NTF_2]$, respectively. Heating rate was 0.2 K/min. The results were analyzed by the algorithms of mathematical gnostics and the estimating global distribution function detected many cases where the values obtained at a particular temperature did not form a homogeneous sample. At most one value has to be removed in order to achieve sample homogeneity. Afterwards the tolerance intervals and intervals of typical data were calculated. The width of the interval of typical data is less than 0.25 % of the measured value in all cases.

3. Conclusions

During intial instrument setup and testing heat capacities of water were repeatedly measured and analyzed by algorithms of mathematical gnostics. The analysis allowed us to detect the necessity of Joule effect recalibration as well as to find the optimum heating rate. The experience shows that calibration should periodically be checked. Analysis by mathematical gnostics may help to find problems early and thus detect the need for Joule effect recalibration.

Subsequent measurement of heat capacities showed that after removing outliers detected by the estimation global distribution function the width of interval of typical data is below 0.25 %. The existence of outliers proves our finding that heating rate of 0.2 K/min is too low.

Acknowledgements

The authors would like to acknowledge partial support by MEYS INGO II grant No. LG12032.

References

1. Wagner Z., Morávková L., Linek J.: Comparison of Statistical and Gnostic Methods for V^E Correlation. (Eng) 12th International Conference on Physical Chemistry Romphyschem-12, Abstract Book, p. 236, Bucharest, Romania, 06–08 September 2006.
2. Kovanic P. and Humber M. B.: The economics of information — mathematical gnostics for data analysis, September 24, 2013. URL http://www.math-gnostics.com. Available only online, cit. 2014-01-26.
3. Sedláková Z., Wagner Z.: High-Pressure Phase Equilibria in Systems Containing CO_2 and Ionic Liquid of the $[C_n mim][Tf_2N]$ Type. (Eng) Chem. Biochem. Eng. Q 26(1), 55–60 (2012).
4. Wagner Z., Fridrich M., Schwarz J., Ždímal V., Váňa M.: Measurement and Analysis of Near Real Time Data on Particle Size Distribution in Atmospheric Aerosol. (Eng) 36th International Invention Show (gold medal awarded), Katalog, p. 130, Zagreb, Croatia, 09–12 November 2011.
5. Prochazka V., Klosova H., Stetinsky J., Gumulec J., Vitkova K., Salounova D., Dvorackova J., Bielnikova H., Klement P., Levakova V., Ocelka T., Pavliska L., Kovanic P., Klement G. L.: Addition of platelet concentrate to Dermo-Epidermal Skin Graft in deep burn trauma reduces scarring and need for revision surgeries. Biomed Pap Med Fac Univ Palacky Olomouc Czech Repub. 2013; 157.
6. Osborne, Stimson, and Ginnings, B. of S. Jour. Res., 23, 238 (1939) in Handbook of Chemistry and Physics, 53rd ed., Cleveland, Ohio, D128 (1972–1973).

On the Responses of Azeotropes to Pressure Variations

Abildskov J.[1], *O'Connell J.P.*[2]
[1]*CAPEC-PROCESS, Dept. Chem. Biochem. Eng., DTU, Kgs. Lyngby, Denmark;*
[2]*Dept. Chem. Eng., Univ. Virginia, Charlottesville, Virginia, U.S.A.*

Abstract
Systems with azeotropes cannot be separated by simple distillation since the vapor and liquid compositions are the same. Variation of the applied pressure can shift the azeotropic composition out of the range of purification of a single column or may allow pressure swing operation of two columns. Because of the sensitivity of column size to accurate estimates of the relative volatility, it is important to use reliable phase equilibrium thermodynamics when exploring the possibility of varying pressure to avoid an azeotrope. Based on an analysis of the pressure sensitivity of azeotropic compositions, we show examples of the impact of different modeling strategies for binary and multicomponent mixtures.

Keywords
Azeotropy, distillation, pressure sensitivity.

1. Introduction

Distillation has been the separation method of choice for systems that have coexisting vapor and liquid within the allowable temperature range, because of its simplicity of equipment, robustness of operation, and ease of maintenance. The process is viable as long as the phases have different compositions at equilibrium. Many combinations of substances will form azeotropes in which the vapor and liquid have the same composition, a phenomenon that has been known for at least one and a half centuries [i]. There are two fundamental approaches to eliminating azeotropes: One is to add another component, in extractive and azeotropic distillation, to shift the separability of the components to obtain one stream of desired composition followed by removal and recycle of the added component in another column also producing the other desired product. This can be very effective, but requires addition and separation of a solvent that can have undesirable contamination and cost effects. An alternative is to change the pressure of the distillation column either to conditions for which there is no azeotrope over the range of compositions, or to use two columns at different pressures (pressure swing) where azeotropes of different compositions from the columns are recycled while they also produce streams of the desired products. However, there are limits to the effectiveness of pressure variations because the effect on composition may not be large enough to achieve the desired effect. Important elements of decisions about conceptual process design are commonly based on estimates of properties from thermodynamic models. With azeotropes there is high sensitivity of equipment size and operating costs to the separability of components. Here we analyze and show examples of the responses of azeotrope composition and temperature to variations of pressure that should provide reliable screening about the feasibility of using this approach for overcoming azeotropes. In particular, we address the impact of models and parameter regressions on pressure sensitivity of homogeneous azeotropes of binary and multicomponent mixtures.

2. Results and discussion

2.1 Theory

The thermodynamics of phase equilibrium shows that for P phases to exist in a system of C components with only PV work, the number of independent intensive variables, F, is given by the Gibbs Phase Rule

$$F = C - P + 2 - S \tag{2.1}$$

Here S is the number of special constraints on the system. For an azeotrope, the value of S is C - 1 for equality of vapor and liquid mole fractions of each of the components. Thus, setting the pressure for an azeotrope sets all phase mole fractions and the temperature, a total of C variables. To find the values of these variables, C phase equilibrium relations are solved. Commonly these set the fugacity of a component, *i,* in the vapor equal to its fugacity in the liquid. Equation (2.2) shows the general form for a system below the critical temperatures of the pure components using the Lewis/Randall standard state:

$$\begin{aligned} & f_i^V\left(T,P,[y]\right) = f_i^L\left(T,P,[x]\right) \\ & y_i\varphi_i(T,P,[y])P = x_i\gamma_i\left(T,[x]\right)\varphi_i^S(T)P_i^S(T)\exp\left[\int_{P^S}^{P}\frac{\overline{V}_i\left(T,p,[x]\right)}{RT}dp\right] \end{aligned} \tag{2.2}$$

Here, φ_i is the vapor fugacity coefficient, a function of system temperature, pressure and vapor composition, and is obtained with a selected equation of state model. Also, γ_i is the liquid activity coefficient, a function of system temperature and liquid composition, and is obtained from a selected excess Gibbs energy model. Further, $\varphi_i^S P_i^S$ is the product of the fugacity coefficient and pressure of the pure saturated vapor, functions only of system temperature. Finally, $\overline{V}_i\left(T,p,[x]\right)$ is the partial molar volume of the component in the liquid [iii]. In the treatment below, we assume the pressure is low enough that the fugacity coefficients effectively cancel and the exponential term is unity. Then for an azeotrope at mole fraction, *z*

$$P = \gamma_i\left(T,[\mathrm{z}]\right)P_i^S(T) \tag{2.3}$$

The analysis of Rowlinson and Swinton [ii] for the pressure derivatives of temperature and composition, directly shows the pressure sensitivity of the temperature and the azeotropic composition, z_1, in a binary mixture:

$$\frac{dT}{dP} = \sum_{j=1}^{2} z_j\Delta\overline{V}_j \Big/ \sum_{j=1}^{2} z_j\Delta\overline{S}_j\,, \quad \frac{dz_1}{dP} = \frac{\Delta\overline{V}_1\Delta\overline{S}_2 - \Delta\overline{V}_2\Delta\overline{S}_1}{(\partial^2\Delta g/\partial z_1^2)\sum_{j=1}^{2} z_j\Delta\overline{S}_j} \tag{2.4}$$

Here, Δ denotes the property difference between the vapor and the liquid phases. Note that the properties in Eq. (2.4) are derivatives of the property models. For the 10 systems we have examined here, the range of dz_1/dP is from -0.08 to 0.2. Consistent with the approximations of Eq. (2.3), the pressure derivative of the composition can also be expressed

$$\frac{dz_1}{dP} = -\frac{1}{P}\frac{1}{Det(\boldsymbol{J}_{\mathrm{P}})}\left[\left(\overline{H}_1^E - \overline{H}_2^E\right) + \left(\Delta h_1^{lv} - \Delta h_2^{lv}\right)\right]$$
$$Det(\boldsymbol{J}_{\mathrm{P}}) = \frac{1}{1-z_1}\frac{\partial \ln \gamma_1}{\partial z_1}\bigg|_T \times\left[z_1\overline{H}_1^E + (1-z_1)\overline{H}_2^E + z_1\Delta h_1^{lv} + (1-z_1)\Delta h_2^{lv}\right] \quad (2.5)$$

This is the binary result of a general multicomponent mathematical development. The ternary azeotrope relation for the same approximations is

$$\frac{dz_1}{dP} = \frac{1}{P\cdot \det(J_P)}\left\{\begin{array}{l}\left[\left(\overline{H}_1^E - \overline{H}_2^E\right) + \left(\Delta h_1^{lv} - \Delta h_2^{lv}\right)\right]\dfrac{\partial \ln \gamma_3}{\partial z_2}\bigg|_{T,z_1} + \left[\left(\overline{H}_2^E - \overline{H}_3^E\right) + \left(\Delta h_2^{lv} - \Delta h_3^{lv}\right)\right]\dfrac{\partial \ln \gamma_1}{\partial z_2}\bigg|_{T,z_1} \\ + \left[\left(\overline{H}_3^E - \overline{H}_1^E\right) + \left(\Delta h_3^{lv} - \Delta h_1^{lv}\right)\right]\dfrac{\partial \ln \gamma_2}{\partial z_2}\bigg|_{T,z_1}\end{array}\right\} \quad (2.6)$$

Here

$$\mathrm{Det}(J_P) = \frac{1}{z_3}\left[\frac{\partial \ln \gamma_1}{\partial z_1}\bigg|_{T,z_2}\frac{\partial \ln \gamma_2}{\partial z_2}\bigg|_{T,z_1} - \frac{\partial \ln \gamma_1}{\partial z_2}\bigg|_{T,z_1}\frac{\partial \ln \gamma_2}{\partial z_1}\bigg|_{T,z_2}\right]$$
$$\times\left[z_1\left(\overline{H}_1^E + \Delta h_1^{lv}\right) + z_2\left(\overline{H}_2^E + \Delta h_2^{lv}\right) + z_3\left(\overline{H}_3^E + \Delta h_3^{lv}\right)\right] \quad (2.7)$$

Thus, for both binary and multicomponent systems, the principal effect on pressure sensitivity of the azeotropic composition is a difference of non-ideality terms plus a difference of pure component enthalpies of vaporization. Enthalpies of vaporization are much greater than the non-ideality terms, but often similar in magnitude. For example, Trouton's rule gives a universal value at the normal boiling point, T_b, of $\Delta h^{lv} / RT_b = 10$. Table 1 shows some substances without hydrogen bonding within the range from 10.2 to 10.6; those with hydrogen bonding range from 12.5 to 13.2. Out of the 220 substances tabulated by Poling et al. [iii], boiling between 300 and 460 K, less than ¼ deviate from the average over 10%. Table 1 also shows the liquid molar volumes and Antoine vapor pressure model parameters used in calculations below. As we will show, the term for the non-ideality difference can be greater than the term for the pure component difference in Eqs. (2.5) and (2.6). Thus, the reliability of computed pressure sensitivity may in some cases be determined by the reliability of the temperature dependence of the selected excess Gibbs energy model.

2.2 Method of analysis

To illustrate the effects of different systems and excess Gibbs energy models, we choose binary systems for which ternary azeotrope pressure data exist. We show that there can be an impact of non-ideality from fitting the model parameters to only vapor-liquid equilibrium data or to a combination of VLE data for activity coefficients and heats of mixing data for h^E as well as when the parameters are considered temperature independent as well as linearly dependent. An indication of the non-ideality term will be the excess Gibbs energy at equimolar composition, while an indication of the pure component vaporization enthalpy difference is found from the last column of Table 1. We also compare the resulting pressure dependencies with results from smoothing the azeotrope composition variation with pressure with polynomial fitting of azeotropic data [iv] directly.

Table 1. Pure Component Properties [iii]							
Substance	V, m^3 kmol^{-1}	T_b, K	A^*	B^*	C^*	Δh^{lv}, kJ mol^{-1}	$\Delta h^{lv}/RT_b$
acetone	0.0738	329.22	4.42448	1312.253	-32.445	29.1	10.6
chloroform	0.0805	334.33	4.56992	1486.455	-8.612	29.2	10.5
n-hexane	0.131	341.88	4.00266	1171.530	-48.784	28.9	10.2
methanol	0.0406	337.69	5.20409	1581.341	-33.500	35.2	12.5
ethanol	0.0586	351.80	5.24677	1598.673	-46.424	38.6	13.2
water	0.0181	373.15	4.65430	1435.264	-64.848	40.7	13.1

*A,B,C: Antoine Constants for the form: $\log_{10}(P^S) = A - (B / (T + C))$; P^S, bar; T, K

2.3 Results

2.3.1 Binary Systems

The Wilson model parameters have been fitted to VLE data only and VLE plus heats of mixing data [v] for several binary systems.

$$\ln \gamma_i = 1 - \ln e_i - \sum_k \Lambda_{ki} \frac{x_k}{e_k} \quad , \quad e_i = \sum_k x_k \Lambda_{ik} \quad , \quad \Lambda_{mn} = \frac{V_n}{V_m} e^{-\frac{A_{mn} + B_{mn}(T - T_0)}{T}} \tag{2.8}$$

Here T_0 = 273.15 K [vi]. We have used the liquid volumes and Antoine constants in Table 1. We have treated ternary systems with the NRTL model, in addition (see below). Table 2 lists the excess Gibbs energy at midpoint composition, to indicate the non-ideality of the system, and the derivative, dz_1/dP, evaluated at 1 atmosphere for ethanol(1)/water(2) from the Wilson model with constant (all B_{ij} = 0) and linearly dependent parameters ($B_{ij} \neq 0$). Also given is a "Smoothed" result from differentiation of a function which described well, measured (z_1,P) data [iv]. Scatter in the data limits the number of reliable significant figures, but the signs and orders of magnitude should be reliable. Because the $\Delta h^{lv}/RT_b$ values are very similar for water and ethanol, the pure component terms are comparable to the non-ideality terms. Depending upon the data included, we find pressure sensitivities can even differ in sign, so temperature dependence of the parameters makes significant difference. Consistent with this, Gmehling and Kolbe [vii] concluded that the Wilson model (only fitted to VLE data) produces erroneous pressure dependence of the azeotropic composition for this system. Addition of heats of mixing improves the predicted pressure sensitivity, however.

Table 2. Ethanol (1) + Water (2) with the Wilson Équation.						
Data Included	A_{12}	A_{21}	B_{12}	B_{21}	g^E/RT (x_1 = 0.5)	dz_1/dP (bar^{-1})
VLE [viii]	289.6	471.9	0	0	0.32 (352.5 K)	0.04
VLE [viii]+h^E [v]	-7.33	424.7	3.0	0.76	0.32 (352.5 K)	-0.01
					Smoothed [iv]:	-0.03

Table 3. Chloroform (1) + Ethanol (2) with the Wilson Equation.						
Data Included	A_{12}	A_{21}	B_{12}	B_{21}	g^E/RT (x_1 = 0.5)	dz_1/dP (bar^{-1})
VLE [ix]	-164.0	763.2	0	0	0.24 (335 K)	-0.08
VLE [ix]+ h^E [x]	-206.5	964.4	0.94	-4.2	0.24 (335 K)	-0.08
					Smoothed [iv]:	-0.05

Table 3 shows results for chloroform(1)/ethanol(2) with VLE and VLE plus h^E data fitted to the Wilson model. In Table 3, however, the same pressure sensitivity is

found regardless of the data and temperature dependence of the parameters because the pure component difference term is much larger than the non-ideality difference. Table 4 shows results resembling the ethanol/water system for chloroform(1)/n-hexane(2). Meanwhile, Table 5 shows that although n-hexane/ethanol is much more non-ideal than chloroform/ethanol, the pure component vaporization enthalpies differ substantially, and so their azeotropic pressure sensitivities are independent of liquid non-ideality. In a similar fashion NRTL (α = 0.3 in all cases) parameters have been determined from regressing binary data for the three pairs of the and acetone(1)/chloroform(2)/n-hexane(3) systems [xi], using *VLE* with and without h^E data. For brevity we do not give the equation and parameters; they can be obtained from the authors upon request. Table 6 gives the pressure sensitivities. The pressure sensitivities chloroform/hexane are very similar, but not exactly the same as those from the Wilson model given in Tables 4-5.

Table 4. Chloroform (1) + n-Hexane (2) with the Wilson Equation.

Data Included	A_{12}	A_{21}	B_{12}	B_{21}	g^E/RT (x_1 = 0.5)	dz_1/dP (bar^{-1})
VLE [xii]	112.9	66.8	0	0	0.10 (334.5 K)	0.001
VLE [xii] +h^E [xiii]	116.6	77.5	0.40	-0.86	0.10 (334.6 K)	0.01
					Smoothed [iv]:	0.03

Table 5. n-Hexane (1) + Ethanol (2) with the Wilson Equation.

Data Included	A_{12}	A_{21}	B_{12}	B_{21}	g^E/RT (x_1 = 0.5)	dz_1/dP (bar^{-1})
VLE [xiv]	149.4	1082.1	0	0	0.53 (332.0 K)	-0.08
VLE [xiv] + h^E [xv]	181.9	1140.2	-0.41	-1.3	0.53 (332.0 K)	-0.08
					Smoothed [iv]:	-0.07

Table 6. dz_1/dP (bar^{-1}) (using linearly dependent parameters).

	Acetone	Chloroform	n-hexane
Acetone		-0.07(-0.03)*	0.006(0.01)*
Chloroform	-0.04(-0.03)$^+$		-0.01(0.03)*
n-hexane	0.018(0.01)$^+$	0.012(0.03)$^+$	

*Temperature independent parameters (all B_{ij} = 0) (Smoothed Value [iv])
$^+$Linearly dependent on T ($B_{ij} \neq 0$) (Smoothed Value [iv])

2.3.2 Ternary Systems

We now examine ternary systems composed of the substances considered above: ethanol(1)/chloroform(2)/n-hexane(3) [iv] {System I}, and acetone(1)/chloroform(2)/n-hexane(3) [iv] {System II}. We want to test whether the binary parameters can describe the ternary azeotrope compositions and their variation with pressure as well as whether the apparent pattern of sensitivity to the parameter dependence on temperature and data regressed would be maintained. Table 7 shows the variations for System I where there are 3 data points over the pressure range from 0.53 to 1.01 bar, while Table 8 shows results for System II where there are 6 data for pressures from 0.27 to 1.01 bar. First it can be seen that the calculated azeotrope compositions are close to experiment for System I and for System II (though less), with little difference between the parameter sets. Second, both constant and linearly dependent parameters describe the azeotrope composition dependence on pressure of System I, as well as for its binaries. The linearly dependent parameter set describes the pressure sensitivity of System II somewhat better. This is consistent

with the pattern described above for binaries because the components of System II all have similar Δh^{lv} values whereas those of System I are significantly different.

Table 7. Ternary Azeotrope of Ethanol (1)/Chloroform (2)/n-Hexane(3) [iv]				
Parameters	Ethanol (1)		Chloroform (2)	
	z_1	dz_1/dP	z_2	dz_2/dP
Constant	0.42 (0.44)	-0.2 (-0.2)	0.370 (0.358)	0.066 (0.08)
Linear in T	0.42 (0.44)	-0.2 (-0.2)	0.367 (0.358)	0.068 (0.08)

Table 8. Ternary Azeotrope of Acetone (1)/Chloroform (2)/n-Hexane(3) [iv]				
Parameters	Acetone (1)		Chloroform (2)	
	z_1	dz_1/dP	z_2	dz_2/dP
Constant	0.0358(0.065)	-0.014 (-0.01)	0.695 (0.60)	0.054(0.1)
Linear in T	0.0347(0.065)	-0.003 (-0.01)	0.688 (0.60)	0.066(0.1)

3. Conclusions

In determining the variation of azeotropic composition with pressure, we have shown that if enthalpies of vaporization of the components forming a binary or ternary azeotrope are similar, e.g., all hydrogen-bonding, care must be taken in regressing the parameters of the applied excess Gibbs energy model since the calculated pressure sensitivity of these cases depends on the accuracy of predicting the temperature dependence of activity coefficients. In particular, heat of mixing data should be included and temperature-dependent parameters should be used in these cases. However, if one or more of the components in a binary or ternary azeotropic system have significantly different enthalpy of vaporization, e.g., nonpolar with hydrogen bonding, the sensitivity of the estimate to the g^E model is much less, and prediction of composition dependence is adequate, regardless of the g^E model and parameterization. Though the testing of these conclusions as presented here is limited, we believe they are correct for all systems.

4. References

[i] a) J.P. Knapp, M.F. Doherty, 1992. Ind. Eng. Chem. Res., 31: 346-357; b) W.K. Lewis, Dehydrating Alcohol and the Like. US. Patent 1,676,700, July 10, 1928.

[ii] Rowlinson J.S., Swinton F., 1982. Liquids and Liquid Mixtures, 3rd edn., Butterworths, London.

[iii] B.E. Poling, J.M. Prausnitz, J.P. O'Connell, The Properties of Gases and Liquids, The McGraw-Hill Companies, Inc., 2000.

[iv] Gmehling J., Menke J., Krafczyk J., Fischer K., 1994. "Azeotropic Data". VCH, Weinheim..

[v] Larkin J.A., 1975. J. Chem. Thermodyn, 7: 137.

[vi] a) Nagata I., Yamada T., 1972. "Correlation and Prediction of Heats of Mixing of Liquid Mixtures", Ind. Eng. Chem. Proc. Des. Dev., 11(4): 574; b) Nagata I., Yamada T., 1973. "Prediction of Excess Heat Capacities of Alcohol-Hydrocarbon Mixtures", J. Chem. Eng. Data, 18(1): 87.

[vii] Gmehling J., Kolbe B., 1983. Fluid Phase Equilibria, 13: 227.

[viii] Orchillés A.V. et al., 2010. J. Chem. Eng. Data, 55: 1669–1674.

[ix] Morachevsky A.G. et al., 1959. Zh. Prikl. Khim., 32: 458.

[x] Shatas J.P. et al., 1975. J. Chem. Eng. Data, 20: 406.

[xi] a) Fordyce C.R., Simonsen D.R., 1949. Ind. Eng. Chem., 41: 104; b) Kudryavtseva L.S., Susarev M.P., 1963. Zh. Prikl. Khim., 36: 1231; c) Schnelle K.B., Canjar L.N., 1962. Chem. Eng. Sci., 17: 189; d) Morris J.W., Mulvey P.J., Abbott M.M., Van Ness H.C., 1975. J. Chem. Eng. Data, 20: 403; e) Kudryavtseva L.S., Susarev M.P., 1963. Zh.Prikl.Khim., 36: 1471; f) Schaefer K., Rohr F.J., 1960. Z. Phys. Chem.(Frankfurt Am Main), 24: 130.

[xii] Kudryavtseva L.S., Susarev M.P., 1963. Zh. Prikl. Khim., 36: 1231.

[xiii] Sharma B.R., Pundeer G.S., Singh P.P., 1975. Thermochim. Acta, 11: 105.

[xiv] Kudryavtseva L.S., Susarev M.P., 1963. Zh. Prikl. Khim., 36: 1471.

[xv] Brown I. et al., 1964. Aust. J. Chem., 17: 1106.

Direct spatiotemporally resolved fluorescence investigations of gas transfer in liquid film flows

V. Kapoustina[1], *M. Rädle*[1], *J.-U. Repke*[2]
[1]*Institute for Process Control and Innovative Energy Conversion, Mannheim University of Applied Sciences, Mannheim, Germany;*
[2]*Institute of Thermal, Environmental and Natural Products Process Engineering, Freiberg University of Mining and Technology, Freiberg, Germany*

Abstract
The characterization of mass transfer and transport phenomena in liquid film flows is crucial in multi-phase unit operations as e.g. distillation and absorption processes. On the other hand experimental methods for the direct measurement of local transfer parameters (e.g. diffusion coefficients, local mass transfer coefficients) are still limited. These, however, are needed for the optimal design of the complex equipment. In an attempt to overcome these challenges, a measuring technique is needed that is able to collect data with the actual conditions encountered. Therefore a non-invasive optical measuring technique based on planar Laser-induced fluorescence (PLIF) was developed, which enables the quantitative determination of the local mass transport in liquid flows.
The fluorescence quenching technique is used for concentration analysis of a gas absorbed in a liquid film. The absorption and desorption process is visualized using oxygen in ethanol. A Ruthenium complex with high quantum efficiency is used as fluorescence indicator. The fluorescence is induced by illuminating the region of interest inside the indicator solution with a blue laser. It is strongly reduced by the presence of molecular oxygen as a result of dynamic quenching. The decrease in intensity is detected and interpreted by image analysis. The image analysis provides a spatiotemporal value for fluorescence intensity and therefore enables the direct characterization of local transport phenomena in the liquid film flow of ethanol.

Keywords
Planar Laser-induced fluorescence, mass transfer, diffusion, liquid flow, absorption, desorption

1. Introduction

In multi-phase unit operations the liquid phase often occurs as a film (d ≈ 0.5-1mm). Mass transfer correlations in the gas or liquid phase are important for the apparatus-design. However, they are not well understood, as the measurements inside thin liquid films are complex. Kohrt et al (2011) measured the integral mass transfer in order to analyze the impact on different packing material textures to liquid-side controlled mass transfer. In order to understand the effect of e.g. surface textures the knowledge of the local mass transfer characteristic is essential. For this purpose, a spatiotemporally resolved non-invasive technique is needed that does not disturb the film flow and the transport process of interest.

The Laser Doppler Anemometry (LDA) and the Particle Image Velocimetry (PIV) are well-established technologies that are applied to investigate the velocity field inside a moving liquid. For concentration field measurement, (planar) Laser-induced fluorescence techniques ((P)LIF) were developed: Münsterer and Jähne (1998) described the oxygen transfer across the aqueous mass boundary layer at a free water surface. Mass transfer observations across liquid-phase boundaries were described by Mühlfriedel and Baumann (2000). Roy and Duke (2004) analyzed concentration gradients at bubble surfaces in water. The interaction between oxygen absorption into water as a function of shear-induced turbulence was investigated by Herlina and Jirka (2004). Schagen and Modigell (2005) applied LIF for the simultaneous measurement of oxygen concentration inside a liquid film and the local film thickness. Charogiannis and Beyrau (2013) investigated evaporating liquid flows, introducing the Laser-induced phosphorescence (LIP) imaging.

The optical measuring technique, presented in this work, enables the investigation and quantification of mass transport inside a thin liquid film with high spatiotemporal resolution. This enables the direct measurement and determination of the influence of various structures on the flow characteristic and mass transport. The results could be used to provide data for optimal apparatus-design and for the validation of CFD simulations.

2. Results and discussion

The optical measurement system is designed for the direct (time and locally resolved) investigation of the diffusion process of gas (oxygen) into a stagnant liquid (ethanol) as well as the mass transfer process inside a moving film. In the first case, the oxygen saturation along a thin slot is determined (→1D). The second case is realized by adding a second observation dimension (→ 2D), so that a defined area can be illuminated and interpreted.

Tris(4,7-diphenyl-1,10-phenanthroline)-rutheniumhexafluorophosphate $Ru(dpp)_3(PF_6)_2$, an orange powder with a molecular weight of 1388.19 kg/kmol, is used as fluorescence dye ($\lambda_{fluoro,max}$ = 612 nm). Because of the dye's high quantum efficiency its concentration in ethanol is low (c_{dye} = 20 mg/l). The fluorescence is induced by illuminating the region of interest inside the indicator solution with a blue laser ($\lambda_{em,max}$ = 405 nm).

The (P)LIF technique makes use of the fact that oxygen is a strong quencher, when coming into contact with the Ruthenium-dye. The decrease in intensity occurs instantly, so that abrupt changes in concentration distribution are registered.

2.1 LIF technique for measurement of oxygen diffusion into ethanol

For the observation of oxygen diffusion into ethanol, the oxygen concentration profile along a thin slot is measured. Therefore, a measuring chamber was designed and built that is equipped with fittings for gases and liquids. A thin plate is placed in the centre of the measuring room. Three cover glasses with defined thickness that are glued on the front side of the plate form a slot. The chamber is made of polymethyl methacrylate (PMMA). Figure 1 shows the flow sheet of the experimental set-up.

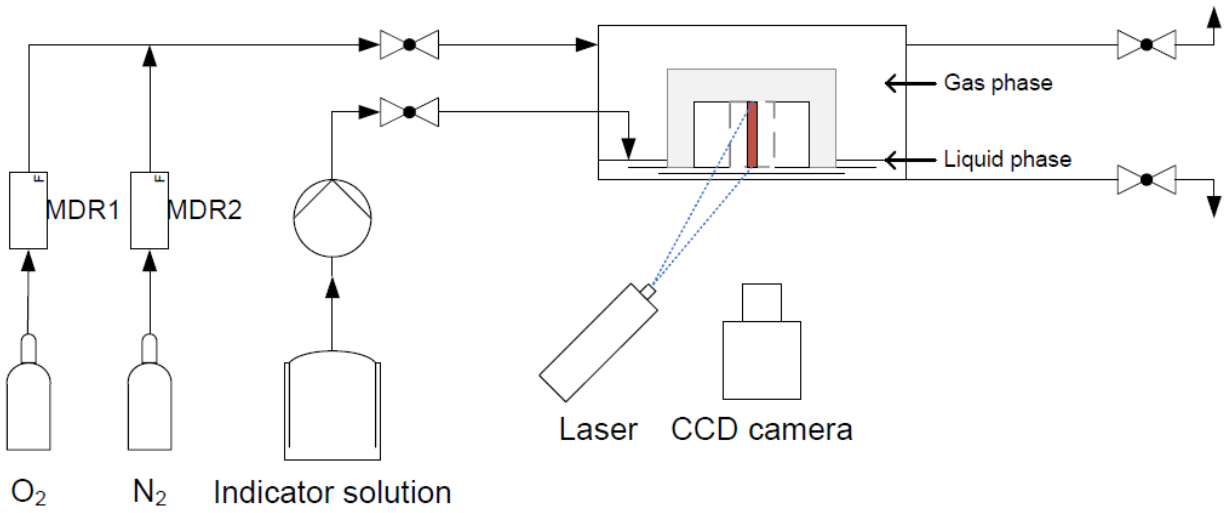

Figure 1: Experimental set-up for the measurement of oxygen diffusion into ethanol: flow sheet. The slot (marked in red) is filled with indicator solution and illuminated by laser light.

The laser and the camera are positioned to the polished front side of the measuring chamber. Before the experiment starts, the chamber is purged with nitrogen in order to set the initial condition (oxygen-free atmosphere). After that, the measuring room is filled with indicator solution, until the liquid reservoir stands about 1 mm high. The liquid enters the slot from the bottom and rises inside the slot through capillary forces. The high surface tension forces prohibit convective transport inside the slot, so that only diffusion should occur.
The chamber can be inclined and equipped with different basic structures as well as packing material textures.

The measurement of the fully oxygen saturated liquid is taken as reference. Figure 2 shows the intermediate status of the diffusion experiment. Here, the oxygen saturation of the liquid is plotted as a function of the slot height y (y = 0 mm is located near the surface) at different times of measurement.

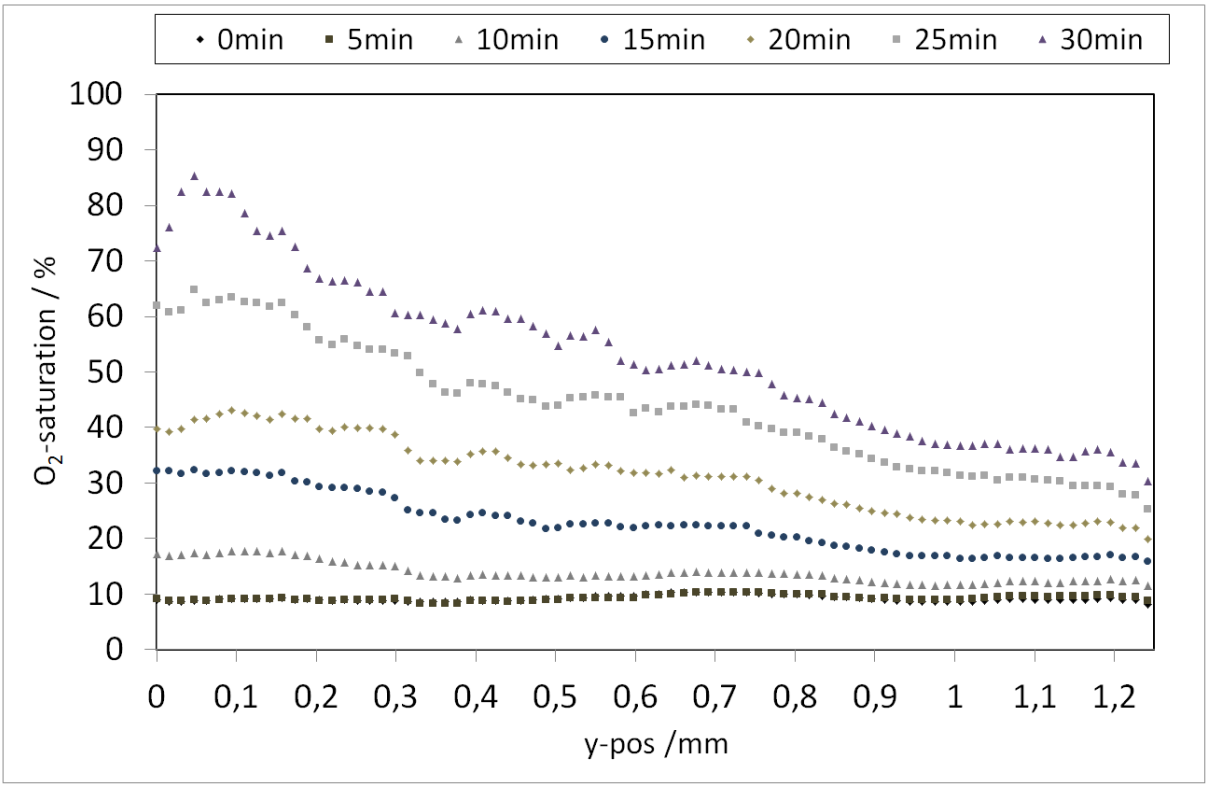

Figure 2: Progress of oxygen penetration into ethanol

An offset of 10% oxygen saturation at the beginning of the measurement (t = 0 min) indicates, that the solution was not completely oxygen-free. The enrichment of the near-surface area with oxygen can be registered after about ten minutes. According to Fick's Law, the oxygen concentration decreases towards the deoxygenated near-bottom area.
The experiment was aborted after 30 minutes. The advance towards an even saturation level is clearly evident.

2.2 PLIF technique for measurement of mass transport in liquid film flows
The enhancement of the LIF technique by adding a second observation dimension leads to planar LIF (PLIF). A blue laser ($\lambda_{em,max}$ = 405 nm) that is positioned perpendicular to the camera generates a light sheet (15 x 5 mm) inside a liquid flow. The camera is positioned to the front side of the measuring chamber. In this way, the change in oxygen concentration can be measured along the film thickness as well as in flow direction in dependence on time. The first measurements are realized on a plane surface. The measuring chamber is purged by nitrogen. The liquid flow is air-saturated, when entering the chamber. For the first experiments that are shown here the chosen film thickness is higher as it is normally found in liquid films. It will be reduced to a height of about 1 mm in the next step.
The oxygen concentration distribution as a function of time and space is shown in Figure 3.

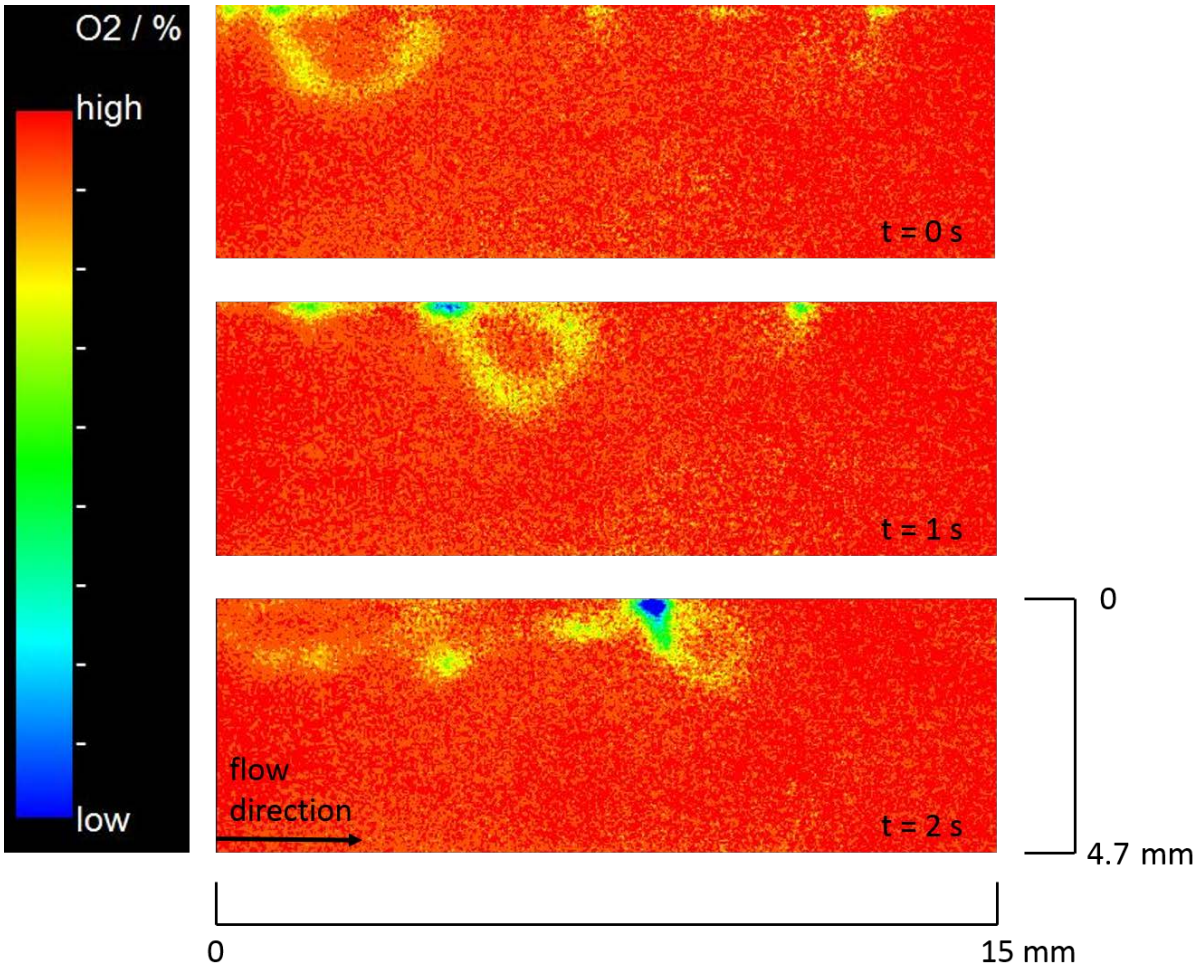

Figure 3: Gas transport into a moving liquid (u_{liquid} = 0.3 cm/s). The oxygen saturation of the liquid is shown as a function of time and space.

Figure 3 exemplarily shows the oxygen saturation of a moving liquid as a function of the flow direction and of the liquid height at three times of measurement (Δt = 1s). The deoxygenation on the surface as a consequence of the penetrating nitrogen can be monitored. It reaches deeper regions inside the liquid with advancing distance in flow direction.

The developed measuring system demonstrates that the gas penetration inside a liquid can be efficiently monitored by using the PLIF technique. In the next step, the film thickness will be reduced to 1 mm, as the measuring system is designed for observation of liquid film flows under real operating conditions. With a camera frame rate of t_{fr} = 15 s^{-1} the penetration characteristic of a gas into and inside a moving liquid will be analyzed with high time resolution.

Furthermore, the influence of different packing surface structures and of counter current gas flow on the mass transfer will be investigated, as these measures are both expected to intensify the mass transfer. This will be discussion in the presentation.

3. Conclusions

For the investigation of gas transport into a liquid, the material system oxygen/ethanol with a Ruthenium complex as fluorescence indicator was found to be suitable. A measuring technique based on (planar) Laser-induced fluorescence was developed and could be demonstrated successfully. The time-dependent oxygen concentration distribution is shown inside a stagnant liquid as well as inside a liquid film flow.

In the next step, the experimental data will enable the determination of a mass transfer correlation in liquid film flows and its interpretation for absorption and desorption processes on different surface textures.

References

Charogiannis A., Beyrau F. (2013) Laser induced phosphorescence imaging for the investigation of evaporating liquid flows. Exp Fluids 54:1518

Herlina, Jirka G.H. (2004) Application of LIF to investigate gas transfer near the air-water interface in a grid-stirred tank. Exp Fluids 37:341-349

Kohrt M., Ausner I., Wozny G., Repke J.-U. (2011) Texture influence on liquid-side mass transfer. Chem. Eng. Res. Des. 89:1405-1413

Mühlfriedel K., Baumann K.-H. (2000) Concentration measurements during mass transfer across liquid-phase boundaries using planar laser induced fluorescence (PLIF). Exp Fluids 28:279-281

Münsterer T., Jähne B. (1998) LIF measurements of concentration profiles in the aqueous mass boundary layer. Exp Fluids 25:190-196

Roy S., Duke S.R. (2004) Visualization of oxygen concentration fields and measurement of concentration gradients at bubble surfaces in surfactant-contaminated water. Exp Fluids 36:654-662

Schagen A., Modigell M. (2005) Luminescence technique for the measurement of local concentration distribution in thin liquid films. Exp Fluids 38:174-184

Phase processes and critical states in reactive systems with liquid phase splitting: phase diagrams and thermodynamic peculiarities

Alexander Toikka, Artemiy Samarov
Saint-Petersburg State University, Department of Chemical Thermodynamics and Kinetics, Saint-Petersburg, Russia

Abstract
Peculiarities concerning phase diagrams and thermodynamic singularities of reacting systems with liquid phase splitting are considered. The main attention is given to the use of affinity for the complex thermodynamic and kinetic consideration of processes and equilibria in the systems with immiscibility area. The opportunities and advisability of the use chemical affinity for the analysis of separation and coupled processes in reacting media are considered. The inclusion in the analysis additional topological elements – stoichiometric lines, chemical equilibrium and iso-affinity curves, surfaces or hyper surfaces – leads to results that are useful for more precise characteristics of diagrams of heterogeneous reacting systems. The critical states in multicomponent reactive systems are discussed.

Keywords
Phase processes, phase diagrams, liquid phase splitting, critical states, thermodynamic peculiarities.

1. Introduction

Liquid phase splitting in reactive systems may significantly influence on the run of chemical engineering processes. On the one hand the splitting of the reacting mixture leads to the unfavorable changes in reaction kinetics and hydrodynamic conditions in chemical reactor. On the other hand the reactions in heterogeneous media may be useful for the design of coupled processes “reaction + separation” such as reactive extraction, reactive distillation or extractive distillation. In comparison with non-reactive mixtures the diagrams of heterogeneous reacting systems include some additional singularities: stoichiometric lines, chemical equilibrium and iso-affinity manifolds, i.e. curves or surfaces (hyper surfaces) of constant affinity. The special case is the presence of critical points of liquid – liquid (LLE) and vapor – liquid (VLE) equilibria. In our work we consider some singularities of such systems that are important for the design of coupled reactive and separation processes.

2. Results and discussion

2.1 Some thermodynamic peculiarities of reacting systems in the case of the splitting of reaction mixture

The shifting of the composition of initial homogeneous system in the run of nonequilibrium chemical reaction or in coupled reaction – mass-transfer process may be accompanied by splitting of solution. In other words, the stoichiometric lines may cross or fall into immiscibility gap. Such case could be undesirable for the process design: one should take into account the multiphase flow and peculiarities of heterogeneous kinetics. The data on the topological structure of phase diagrams including the disposition of critical points would help to choose the initial

compositions of the mixture to avoid the ingress in heterogeneous area. In symposium lecture we present various diagrams of multicomponent reactive systems with immiscibility gap. Now we will consider peculiarities that concerns additional thermodynamic regularities of phase diagrams caused by chemical reactions.

The thermodynamic description and analysis of phase diagrams singularities may be discussed in the terms of affinity. The change of the affinity on binodal curves is determined by the run of chemical equilibrium curve, tie-lines and stoichiometric lines dispositions in composition triangle. The correct thermodynamic analysis should be carried out on the base of conditions of stability and phase equilibrium.

The concept of affinity was introduced by De Donde and was developed by Prigogine and co-workers[1]. In general affinity (A) should be determined by uncompensated heat (Q') of arbitrary process

$$Q' = Ad\xi \geq 0 ,$$

where ξ is internal parameter which characterized the run of the process[1]. In the case of chemical reaction the affinity could be presented by algebraic sum of products $\nu_i \mu_i$

$$\mathrm{A} = -\sum_i \nu_i \mu_i ,$$

where μ_i and ν_i are chemical potential and stoichiometric number of specie i respectively; ν_i are positive for reaction products and negative for initial reagents; for chemical reaction ξ is reaction extent. The affinity is useful for the analysis of thermodynamic peculiarities of the systems with chemical interactions: the affinity is also the parameter of chemical kinetics and is connected with reaction rate V as following:

$$AV \geq 0 .$$

Thus the affinity has the same sign as reaction rate. When affinity is equal to zero the rate also takes null value, i.e. the system would be in chemical equilibrium. Unfortunately the application of affinity for the design of reacting systems separation is very limited in spite some useful relationships related to LLE and VLE. For example in the point of extremum of pressure on stoichiometric line in VLE reacting system the following condition holds: tie-line touches iso-affinity curve. It also could be ordinary azeotrope or the point where concentration derivative of affinity has a zero value (rare case)[2]. Some additional aspects concerning the significance of affinity in VLE consideration would be discussed in symposium lecture. Now we will consider the special cases of extremum of the affinity at the curves of LLE. In LLE (reactive or non-reactive) the following condition for chemical potential of any component are valid:

$$\mu_i^{(1)} = \mu_i^{(2)} ,$$

where superscript is the index of phase. Respectively the affinity also has the equal value in phases

$$A^{(1)} = A^{(2)}. \qquad (1)$$

In general the dependence of affinity on composition is given by stability conditions. At constant temperature both for homogeneous and heterogeneous condensed systems the necessary stability conditions could be presented in following form:

$$d\mu_1 dm_1 + d\mu_2 dm_2 + ... + d\mu_n dm_n > 0 .$$

where m_i is number of moles of specie *i*; the influence of the pressure on chemical potentials of components in condensed phases may be neglected. Because all species are reagents or products of reaction the change of them could be presented by mean of reaction extent ξ:

$$\frac{dm_i}{\nu_i} = \frac{dm_1}{\nu_1} = \frac{dm_2}{\nu_2} = ... = \frac{dm_n}{\nu_n} = d\xi^{(r)},$$

therefore for stability condition the following equations hold:

$$-dAd\xi > 0, \quad \frac{dA}{d\xi} < 0 . \qquad (2)$$

The last inequalities has the well-known form[1] but now we consirder not only homogeneous but also heterogeneous (splitted) solutions. In paper[3], for the sake of simplicity, futher considerations concerned only ternary systems. For example one of possible cases of mutual disposition of stoichiometric lines, tie-lines, binodal and CE curves is presented in Figure 1 for the fragment of composition triangle.

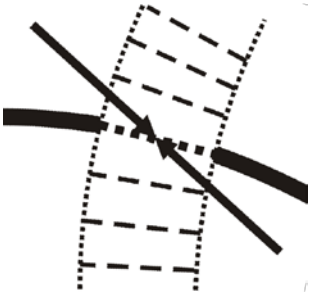

Figure 1. Stoichiometric lines (→) for direct and reverse reactions, binodal (····), tie-lines (----) and CE curve (▬): fragment of diagram of ternary LL system; ▪▪▪▪ – the unique reactive tie-line.

One of tie-lines on Figure 1 belongs to CE curve; it is so-called unique reactive tie-line[4]. The affinity on unique reactive tie-line because it corresponds to CE is of zero value. According to Eq. (2) the affinity for direct and reverse reactions in the vicinity of CE along the stoichiometric lines should decrease. Because of it the shifting along the branches of binodal to the unique reactive tie-line (i.e. CE curve) should be also

accompanied by the decreasing of affinity.

Other examples for ternary systems are presented in Figure 2. Arrows indicate the direction of stoichiometric lines, i.e. the run of reaction. In assumption of validity of Eq. (2) the affinity diminishes in this direction. According to Eqns. (1) and (2) the affinity on tie-line "*c*" (Figure 2a) has a greater value in comparison with tie-line "*a*" and "*b*". Therefore on binodal branches the affinity falls in the process of transfer from tie-line "*c*" to "*a*"[3].

The second example for ternary system corresponds to the extremum of affinity on binodal curves (Figure 2b); it is also a special case of unique reactive tie-line. The type of extremum is determined by a slope of neighboring tie-lines relatively to considered stoichiometric line: the case of Figure 2b corresponds to the minimum of affinity on binodal.

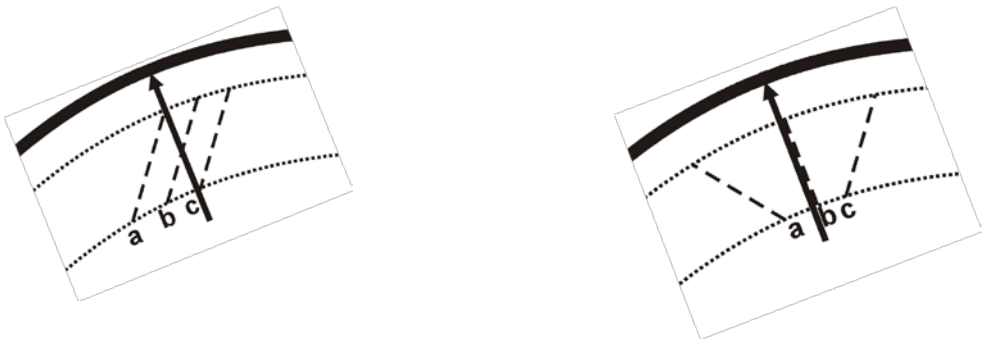

a b

Figure 2. Two cases of disposition of tie-lines, binodals, chemical equilibrium curves and stoichiometric lines: fragment of diagrams of ternary LL system. The notation for lines and curves is the same as in Figure 1. The description of cases "a" and "b" is given in the text.

These and other similar conclusions (see paper[3]) could be generalized for the systems with arbitrary numbers of components – quaternary and other multicomponent systems. The general conclusions for reacting systems with immiscibility area are following:

- the change of the affinity on binodal is determined by the slope angle between tie-lines and stoichiometric lines,
- the concordance of tie-line with the run of stoichiometric line corresponds to extreme value of affinity on binodal (or inflection point).

Now we considered particular case of iso-affinity manifolds, i.e. CE. More detailed conclusions follow from consideration of the general case of iso-affinity curves, surfaces or hypersurfaces. Any case presented examples show that the inclusion in the analysis of diagrams of reactive systems such elements as stoichiometric lines, CE and isoaffinity manifolds gives opportunity to set an additional thermodynamic conditions and specify the topological structure of diagrams. From our point of view it may be also usufull for the design of separation or coupled processes.

2.2 Critical states of LLE in quaternary reacting systems

The experimental data on critical states in reacting systems could be considered on the base of our recent data on the systems with ester synthesis reactions (e.g.

papers[3, 5-10]). The experimental data sets on quaternary systems at few temperatures gave the opportunity to construct the polythermal critical surface (the case of propyl acetate synthesis reaction). The disposition of critical curves (at given temperature) or critical surface (for poly-thermal conditions) gives the opportunity to take into account the borders of immiscibility area in composition tetrahedron. Combined with LLE data one can determine the possibility of reacting system to fall into heterogeneous region in the run of chemical reaction. The last case could be undesirable due to the hydrodynamic conditions in reactor and kinetic problems (the difference of reaction rate in different phases). The illustrations will be given in symposium lecture. There are some other features concerning the critical states in multicomponent reacting systems. For example the diagrams of systems with ethyl acetate and *n*-propyl acetate synthesis reactions are slightly differ. In the system with *n*-propyl acetate synthesis reaction CE is realized both in homogeneous and heterogeneous area (in the region of reaction solution splitting). Accordingly there are critical phases of LLE which are in simultaneous CE. The system with ethyl acetate synthesis reaction reaches CE states in homogeneous area only. Of course these conclusions are limited by conditions of our experiments (293.15 – 313.15 K).

Some other experimental examples of our studies on phase diagrams and thermodynamic singularities of reacting systems with liquid phase splitting could also be found in our recent papers[11,12].

3. Conclusions

Some thermodynamic peculiarities concerning phase diagrams and separation processes in reacting systems are considered. The opportunities and advisability of the use chemical affinity for separation design in reactive systems is considered. The analysis of state diagrams of heterogeneous reacting systems should include additional elements, such as stoichiometric lines, chemical equilibrium and iso-affinity curves or surfaces (hyper surfaces). The critical states of phase equilibrium including polythermal critical surfaces are also discussed. The knowledge of peculiarities considered would be useful for optimization of the design of separation in the reactive systems including coupled processes.

Acknowledgement

This research was supported by Russian Foundation for Basic Research (grants 12-03-00522a and 13-03-00985a). Authors are also grateful to Maria Toikka and Maya Trofimova for experimental research and fruitful discussions.

References

1. Prigogine I., Defay R., *Chemical Thermodynamics*, Longmans, Green and Co., London, New York, Toronto (1954).
2. Toikka A.M., *Vestnik St Petersburg Univ., Phys., Chem.* Issue 4 (2004) 63-70.
3. Toikka M.A., Toikka A.M., *Pure Appl. Chem.*, 85 (2013) 277-288
4. Ung S., Doherty M., *Chem Eng. Sci.*, 50 (1995) 3201-3216.
5. Toikka A.M., Toikka M.A., Trofimova M.A., *Russ. Chem. Bul.*, 61 (2012) 741-751.
6. Toikka A.M., Toikka M.A., *Pure Appl. Chem.*, 81 (2009) 1591-1602.
7. Trofimova M., Toikka M., Toikka A., *Fluid Phase Equilib.*, 313 (2012) 46-51.
8. Toikka A.M., Trofimova M.A., Toikka M.A., *Russ. Chem. Bull.*, 61 (2012) 659-661.
9. Toikka M.A., Gorovits B.I., Toikka A.M., *Russ. J. Appl. Chem.*, 81 (2008) 223-230.
10. Toikka M.A., Tsvetov N.S., Toikka A.M., *Theor. Found. Chem. Eng.*, 45 (2011) 454-460.
11. Toikka M., Samarov A., Golikova A., Trofimova M., Tsvetov N.S., Toikka A., *Fluid Phase Equilib.*, 373 (2014) 72-79.
12. Toikka M., Samarov A., Toikka A., *Fluid Phase Equilib.*, 375 (2014) 66-72.

The Effects of Fluid Physical Properties and Tray Geometry on Entrainment and Weeping in Sieve Tray Columns

R.K. Moses, A.J Burger and J.H. Knoetze[1]
[1]*Department of Process Engineering, Stellenbosch University*
Private Bag X1, Matieland, 7602, South Africa

Abstract
This study endeavoured to improve the current understanding of the effects of different fluid physical properties on weeping and entrainment in a sieve tray column with varying fractional hole area and sieve tray hole diameter. Fluid properties, such as viscosity, surface tension and density were shown to have a significant effect on the entrainment rate, but entrainment was also strongly influenced by the dispersion characteristics above the tray. As observed by previous researchers (Bennet et al., 1995; Kister, 1992; Lockett, 1986), hole diameter had a prominent effect on the entrainment. Entrainment increased with increasing hole diameter (between 3.2 mm and 12.7 mm) and decreasing fractional hole area at liquid flow rates below 20 m^3/(h.m) and above 60 m^3/(h.m). However, hole diameter and fractional hole area had a minimal effect on entrainment at intermediate flow rates around 25 m^3/(h.m) to 50 m^3/(h.m). The weeping rate as a function of liquid flow rate showed a parabolic dependence on liquid flow rate. Important distillation parameter (e.g. entrainment, weeping, etc) could be correlated as a function of well-known hydrodynamic dimensionless numbers as basis, such as the Weber number (We), Froude number (Fr) and Reynolds number (Re).

Keywords
Sieve tray, distillation hydrodynamics, entrainment, weeping, fluid properties

1. Introduction

Distillation is widely used in the chemical process industry for the large-scale fractionation of liquid mixtures. Despite the fact that it is a mature and well-established technology, the continuous improvement and optimization of related designs are still necessary to ensure future cost effective operation of distillation units. In order to characterise and predict the performance and capacity limits of a distillation column, the thermodynamics, hydrodynamics and the mass transfer phenomena inside the column need to be understood clearly.

In this study, the hydrodynamic effects inside a sieve tray column were investigated at zero mass transfer, *i.e.* passing pure liquids and gases with different physical properties in counter-current fashion to characterise phenomena such as entrainment and weeping with different sieve tray configurations.

The objectives of the investigation were:

- to characterise the effect of liquid properties on entrainment and weeping by changing the surface tension, viscosity and density of the liquid;
- to characterise the effect of gas properties on entrainment and weeping by changing the viscosity and density of the gas;
- to establish a rudimentary understanding of the effect of changing sieve tray hole diameter and fractional hole area on entrainment and weeping while varying the physical properties of the fluids.

2. Experimental setup

The pilot distillation column – as used for related experiments - was rectangular in shape with internal dimensions (width x length) of 175 mm by 635 mm (Uys et al., 2012). A chimney tray was used to capture the weeping liquid at the bottom and a de-entrainment tray combined with a mist eliminator pad captured the entrained liquid at the top. The up-flowing gas flowed out through the top of the column and back into a surge tank, which also absorbed potential pressure fluctuation of the gas, before being recycled to the column.

The fractional hole areas of the different sieve trays were 7%, 11% and 15%, while hole diameters were either ⅛, ¼, or ½ inches (3.2, 6.4, or 12.7 mm). Butanol, ethylene glycol, water and silicone oil were used as liquids, and the gases were air and carbon dioxide (CO_2).

3. Results and discussion

3.1 Effects of Column Configuration and Fluid Physical Properties

The dispersion behaviour inside the sieve tray column could be categorised into two typical regimes, *i.e.* the spray regime [Q_L < 25 m^3/(h.m)] and froth regime [Q_L > 25 m^3/(h.m)], where Q_L is the liquid flow rate per weir length. One could also observe the two typical dispersed liquid layers above the sieve tray, *i.e.* the froth layer (liquid bottom layer) and the spray layer (top droplet layer). At low liquid flow rates the dispersion was unstable and sloshed in random fashion, whereas at high liquid flow rates the dispersion appeared to be more uniform and stable across the tray.

Entrainment was shown to be far more sensitive to the sieve tray fractional hole area at low liquid flow rates [typically < 25 m^3/(h.m)] than at moderate flow rates [between 25 and 60 m^3/(h.m)]. An example is shown in Figure 1, where entrainment – depicted by L'/D – is notably more prominent at smaller fractional hole areas of 7.3% and low liquid flow rates. At higher liquid flow rates [above 60 m^3/(h.m)] the entrainment rate increased again with decreasing fractional hole area.

Figure 2 provides an example of the interaction between weeping rate and sieve tray hole diameter at varying liquid flow rates. The weeping rate approaches zero as the flow rate increases. The trends are less obvious, and there is little to choose between the 3.2 mm and 6.4 mm hole sizes. However, the 12.7 mm hole size caused notably less weeping than the other two at higher liquid flow rates, reaching a zero weeping rate at a lower liquid flow rate as the flow rate increases for all fluid combinations.

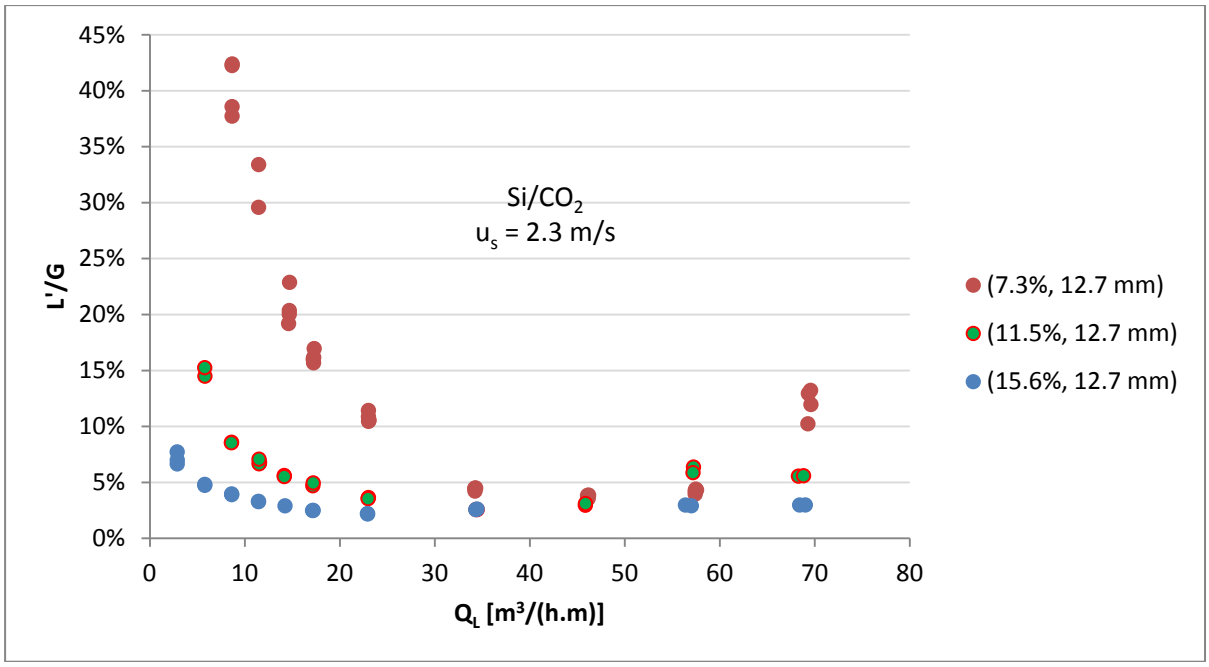

Figure 1: Effect of fractional hole area on entrainment (L'/G) for silicone-oil/CO_2 with a 12.7 mm hole diameter and a superficial gas velocity (u_s) of 2.3 m/s.

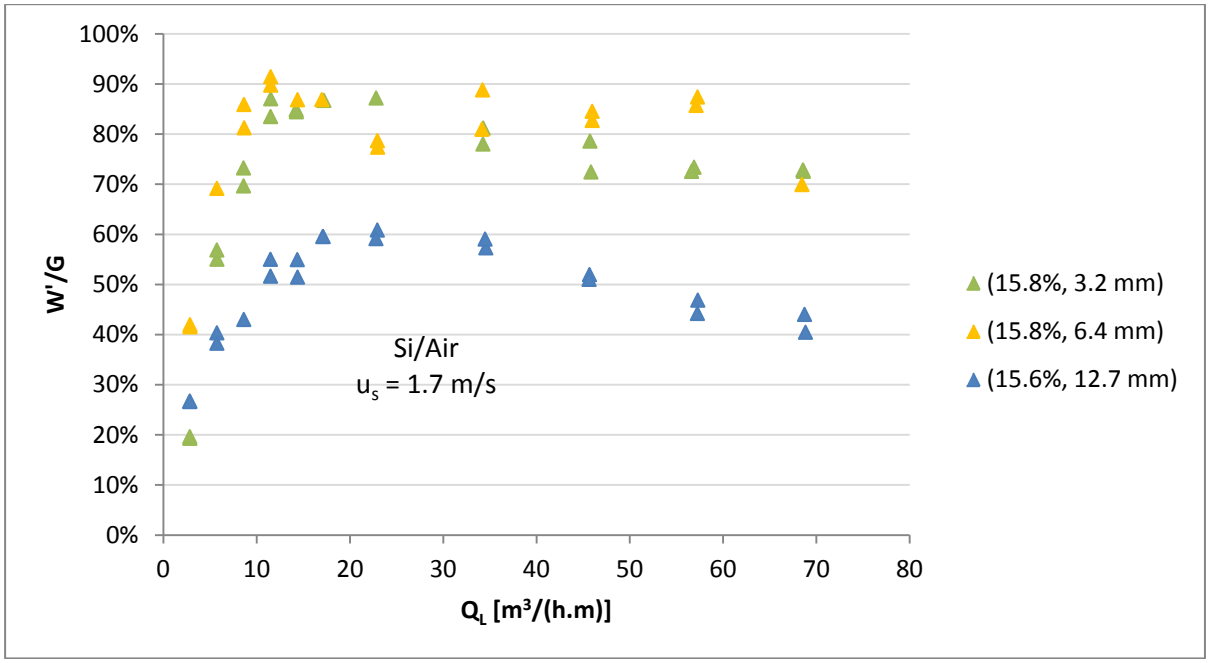

Figure 2: Effect of hole diameter on weeping (W'/G) for silicone-oil/air with a 15% fractional hole area and a superficial gas velocity of 1.7 m/s.

Figure 3 shows typical liquid dispersion profiles observed on distillation trays, as proposed by (Uys et al., 2012). These are now used to describe the trends observed for entrainment and weeping. Note that a low liquid fraction is believed to be present at the tray floor in zones with high dispersion peaks. In these zones, the liquid flow trajectory corresponds best with the upward gas flow trajectory (i.e. the liquid 'jumps' over tray holes). Subsequently, as this dispersed liquid drops down to the plate, a localized high-pressure zone is formed (i.e. the liquid predominantly follows a

downward trajectory onto the plate, thus countering the upward movement of the gas). Such high pressure zones could correspond with higher levels of weeping, while the dispersion peaks could correspond with higher levels of entrainment. A high pressure zone is also believed to occur as the liquid enters the tray and before the first dispersion surge.

At both high gas flow rates and high liquid flow rates, the dispersion peaks are higher and more extended dispersion layers are formed, thus covering larger flow path lengths. Subsequent high pressure zones (where the dispersion layers collapse and more weeping is believed to occur) thus develop at longer flow path lengths closer to the overflow weir. Profiles 1 to 5 represent the systematic change in dispersion patterns observed above the sieve tray as the liquid flow rate is increased. Profile 1 represents the dispersion in the so-called spray regime, where the first dispersion peak occurs at a relatively short flow path length, so that another dispersion peak can develop fully before the liquid reaches the overflow weir. This oscillatory behaviour (allowing two unstable dispersion peaks and pressure zones to form) indirectly increases the dependence of entrainment rate on the plate hole characteristics.

As the liquid flow rate increases, the dispersion profile changes from profile 1 to 2 and then to 3, where profiles 2 and 3 show typical dispersion trends for intermediate liquid flow rates around 25 m^3/(h.m) to 50 m^3/(h.m). At these flow rates, the dispersion becomes stable; less dependent on the upward gas force and more dependent on the horizontal liquid force. As the liquid flow rate increases further, the dispersion profile changes from 3 to 4. At this point, the dispersion becomes highly dependent on the gas velocity, where high gas velocities lead to entrainment flooding. When the liquid flow rate increases further, the high liquid cross flow causes the liquid to 'jump' over the entire flow path length, which results in a close to zero weeping rate.

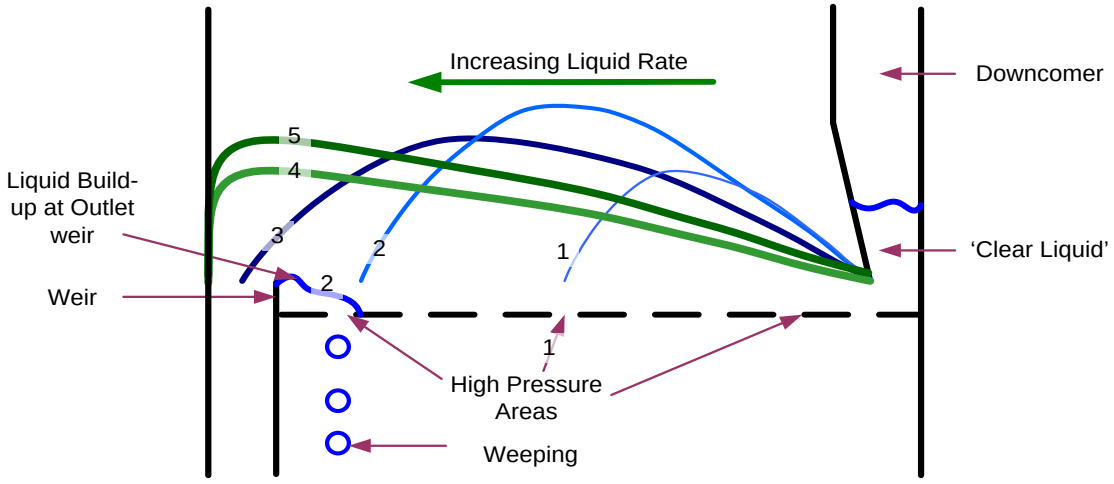

Figure 3: Liquid dispersion trends. Adapted with permission from Uys et al. (2012).

3.2 Dimensionless Numbers Predictive Models Trends

The experimentally measured entrainment and weeping rate data were correlated against selected dimensionless numbers, such as the Froude and construction numbers, in order to identify potential prominent trends. The Froude number defines

the ratio of the inertial forces to the gravitational forces acting on the fluid, where the form of the modified flow Froude number (Fr^+) in equation 3.2.1 is taken from (Uys, 2012). The effect of tray geometry on the entrainment rate (L'/G) is evaluated using the construction number (*Co*) in equation 3.2.2 which is a dimensionless number identified by (Kozoil & Mackowaik, 1990). The construction number is shown by equation 3.2.2, which relates the fractional hole area (A_f), tray spacing (S), column diameter (D_c) and hole diameter (d_H) to one another.

$$Fr^+ = \frac{3600u_s^3}{gQ_L}\left(\frac{\rho_g}{\rho_l - \rho_g}\right)^n \quad \rightarrow \quad \text{Modified flow Froude number} \quad [3.2.1]$$

$$Co = \left(\frac{A_f S}{\left(\frac{D_c d_H}{1000}\right)^{\frac{1}{2}}}\right) \quad \rightarrow \quad \text{Construction number} \quad [3.2.2]$$

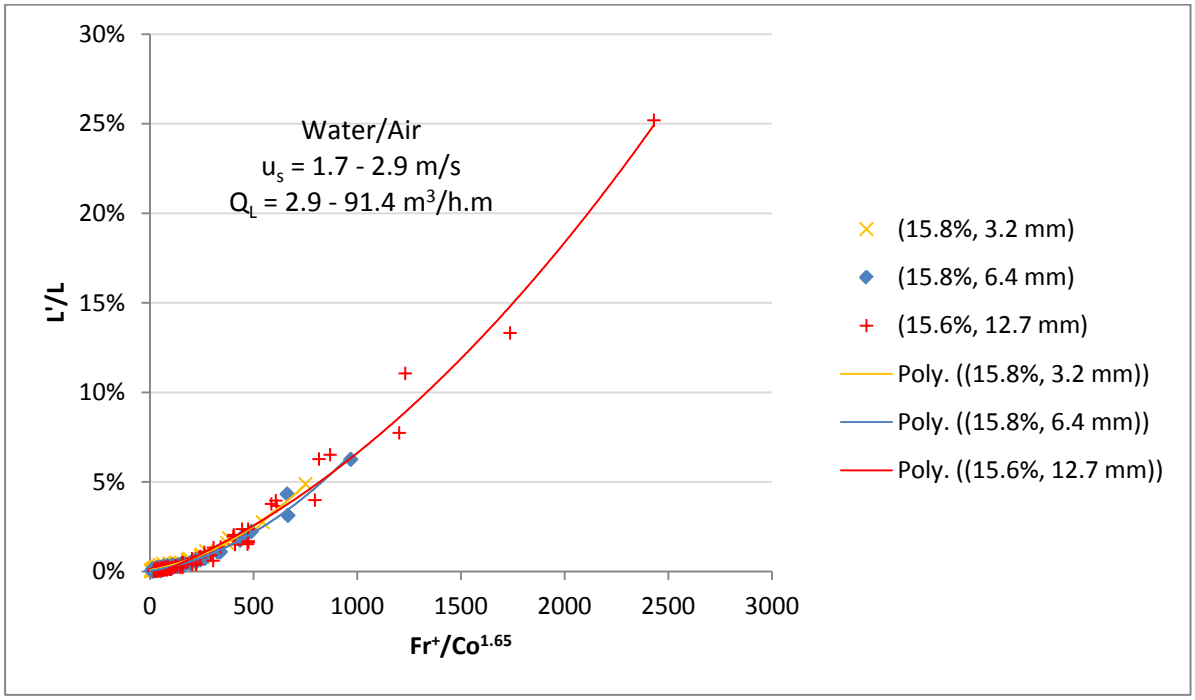

Figure 4: Entrainment (L'/L) changing with the modified flow Froude number (Fr^+) to construction number (Co) ratio for water/air at a fractional hole area of 15% and at different hole diameters.

The entrainment rate (L'/L) is plotted against the ratio of the modified flow Froude number (Fr^+) and construction number (*Co*) for a water/air system (Figure 4) and at different sieve tray hole diameters, where n is taken as 0 in equation 3.2.1, since a single system is analyzed in Figure 4. The modified flow Froude number is shown to be one of the most significant dimensionless numbers since it has a monotonic relationship with the entrainment rate for a particular system and tray configuration. The construction number is shown to be a useful dimensionless number that could be used to describe the effect of tray geometry on the entrainment rate. The Froude and construction number ratio in Figure 4 describes the effect of tray hole diameter on the entrainment rate when the construction number is plotted to the power of 1.65. In a similar plot, the effect of fractional hole area on the entrainment rate can be described when the construction number is plotted to the power of 1.6.

3. Conclusions

At intermediate liquid flow rates [between 25 m^3/(h.m) to 50 m^3/(h.m)] the entrainment rate is not strongly dependent on the sieve tray hole diameter and fractional hole area. However, at liquid flow rates above and below this range, entrainment increases with increasing sieve tray hole diameter and decreasing fractional hole area.

In the evaluation of the effect of the sieve tray hole diameter on the weeping rate, it was shown that the trends differed notably with changing fluid combinations. Furthermore, the 12.7 mm hole size caused notably less weeping than the 3.2 mm and 6.4 mm trays at higher liquid flow rates. At low liquid flow rates the dispersion peaks occurred at a low flow path length. Consequently, more than one dispersion peak and localised pressure zone could develop before the liquid reached the overflow weir. This amplified the dependence of the entrainment rate on the fractional hole area in the specific test rig. It is believed that weeping occurred preferentially at so-called localised high pressure zones on the sieve tray. At high gas and liquid flow rates, the resultant extended dispersion layer allowed minimal intimate contact between the plate and the liquid (minimising such localized high-pressure zones). In effect, the liquid 'jumped' over the entire flow path length in the test rig, thus resulting in low weeping rates at high gas and liquid rates.

A fundamental dimensionless number analysis confirmed that well-known dimension-less numbers could be used to develop entrainment and weeping rate correlation. The modified flow Froude number was shown to be the most useful dimensionless number, since it displayed a monotonic relationship with the entrainment rate for a particular system and tray configuration. The construction number was shown to be a useful dimensionless number that could be used to describe the effect of tray geometry on the entrainment rate.

Acknowledgements

This work is based on the research supported in part by the National Research Foundation of South Africa (Grant specific unique reference number UID 83966) and Sasol Technology (Pty) Ltd. The authors acknowledge that opinions, findings and conclusions or recommendations expressed in any publication generated by the supported research are that of the authors, and that the sponsors accept no liability whatsoever in this regard.

References

1. BENNET, D.L., A.S. KAO, and L.W. WONG. 1995. A Mechanistic Analysis of Seive Tray Froth Height and Entrainment. AIChE Journal. 41(9), pp.2067-2081.
2. KISTER, H.Z. 1992. Distillation Design. McGraw-Hill.
3. KOZOIL, A. and J. MACKOWAIK. 1990. Liquid Entrainment in Tray Columns with Downcomers. Chemical Engineering and Processing: Process Intensification. 27, pp.145-153.
4. LOCKETT, M.J. 1986. Distillation tray fundamentals. New York: Cambridge University Press.
5. UYS, E.C. 2012. The influence of gas and liquid physical properties on entrainment inside a sieve tray column. Stellenbosch.
6. UYS, E.C., C. E. SCHWARZ, A.J. BURGER, and J.H. KNOETZE. 2012. New Froth Behaviour Observation and Comparison of Experimental Sieve Tray Entrainment Data with Existing Correlations. Chemical Engineering Research and Design. 90(12), pp.2072-2085.

Higher Energy Saving with New Heat Integration Arrangement in Heat Integrated Distillation Column (HIDiC)

Toshihiro Wakabayashi[1], *Shinji Hasebe*[2]
[1]*Toyo Engineering Corporation, Narashino, Japan*
[2]*Kyoto University, Kyoto, Japan*

Abstract

In conventional heat integrated distillation columns (HIDiC), the internal heat exchange is executed between the pressurized rectifying section and the stripping section which are located at the same elevation. In such a structure, the amount of heat exchanged between two sections depends on the temperature profile of both sections. This suggests that more energy saving may be achieved by providing appropriate arrangement of heat exchanges between sections.

We extended the graphical design method of the heat exchange structure in HIDiC, which was proposed in a previous paper, to a multi-component system by adopting the idea of a quasi-binary system. Also, we developed a new HIDiC structure that can realize the outcomes of the proposed design method. The economics of the proposed structure was precisely evaluated through a case study of a commercial scale column.

Keywords

Energy conservation, HIDiC, Multi-component, H-xy diagram

1. Introduction

In view of energy conservation of distillation columns, the reversible distillation provides the ultimate figure. The heat integrated distillation column (HIDiC) attracts great attention since its concept is to realize a similar enthalpy profile inside of a column as that in reversible distillation (Nakaiwa *et al*.,2003). Usually, as a hardware structure, heat exchange between the stripping and rectifying sections at same elevation has been discussed since HIDiC was first proposed by Mah *et al*. (1977). With such pairing of heat exchange, the heat duty at each internal heat exchanger is merely the consequence of temperature difference of the sections involved in the heat exchange. Accordingly, the heat duty largely depends on the temperature profile of the column, and is fairly different from that of the reversible distillation column.

Wakabayashi and Hasebe (2013) proposed a completely new approach to design of the HIDiC by providing the side heat exchange arrangement appropriately. In the proposed design method, the condenser and the reboiler are regarded as candidates of heat exchange stages in addition to the internal stages in the rectifying and stripping sections. Then, i) composition/stage to provide an optimal side heat exchange arrangement, ii) heat duty to each side heat exchanger, and iii) pairing of side heat exchangers, are derived. These values are derived so that the enthalpy profile in the column becomes close to that with the reversible distillation.

In this paper, we extend the design methodology developed by us for a binary system applied to a multi-component system. Moreover, a new HIDiC structure

realizing the outcomes of the proposed design methodology is presented. The economics is also evaluated on the newly proposed HIDiC system.

2. Design methodology for multi-component system

Here, the design methodology developed for binary system is generalized so as to be applied to multi-component system. The method takes a graphical approach, in which the Ponchon-Savarit *H-xy* diagram is largely modified. Due to space limitations, and as the procedure is similar to that for a binary system, only the outline is explained.

2.1 Set the target energy saving by HIDiC to conventional distillation system

The unique feature of the proposed methodology is that the target energy saving with HIDiC to the conventional distillation column is determined in advance, and then the side heat exchange arrangement to satisfy it is investigated. When a distillation problem is given, the number of theoretical stages, $N_{\text{T-conv}}$ and the reboiler duty of a conventional distillation column, $Q_{\text{r-conv}}$, are first calculated, taking the fixed and operation costs into account. In referring to $Q_{\text{r-conv}}$ and $N_{\text{T-conv}}$, the reboiler duty, Q_{r}, the compressor power, Ws, and the number of theoretical stages, N_{T}, are decided by design engineers. The operating pressure at the stripping section, P_{S}, in HIDiC is set at this stage. In this research, it is assumed that the heat exchange is not executed at every stage. Thus, the number of heat exchange stages, N_{E}, is also decided.

2.2 Calculation of artificial vapor-liquid equilibrium condition and enthalpies

For a binary system, once the liquid concentration of one component is given, the composition and the enthalpy of the vapor at the saturated condition can be identified uniquely. Subsequently, the enthalpy curves at saturated conditions can be drawn on an *H-xy* diagram. However, in the multi-component system the composition and the enthalpy are not determined by the concentration of single component. Also, in the multi-component system, the possible composition range in a column depends on the feed and product compositions. By taking this fact into account, the multi-component system is approximated to a quasi-binary system.

First, a rigorous simulation that satisfies the product specification is executed for conventional distillation column with N_{T} stages. The obtained components are divided into two groups based on the key components of the separation. The light key component and lighters are regarded as the light component, whereas the heavy key components and heaviers are regarded as the heavy component in the system. Then, for the quasi-binary system, the artificial vapor-liquid equilibrium condition and the enthalpies of the vapor and liquid are defined. This makes it possible to treat the multi-component system as a quasi-binary system.

2.3 Provide the ideal side heat exchange arrangement in the stripping section

In the reversible distillation condition, the stripping section has an infinite number of stages, and the equilibrium line and the operating line are overlapped. Heat is added to each stage to satisfy the enthalpy change of the reversible distillation. The distillation curve on *H-xy* diagram for such ideal condition is hereafter called the *reversible distillation curve*, RDC. To draw RDC on an *H-xy* diagram, the equilibrium line of arbitrary composition, *e.g.* $x_{\text{S},j}$, is extended until it comes across $x = x_{\text{B}}$. The enthalpy at $x = x_{\text{B}}$, *i.e.*$h^{\infty}_{\text{S},j}$ on **Figure 1**, is the enthalpy of bottoms at hypothetical state corresponding to $x_{\text{S},j}$.

2.4 Determine the side heat exchange arrangement in the stripping section

The relationship between the liquid composition of the light component in quasi-binary system and the corresponding hypothetical enthalpy is termed the *operating locus* in the stripping section. First, the ideal operating locus is drawn by shifting RDC downward. This curve is the *shifted reversible distillation curve*, S-RDC. The distance between RDC and S-RDC is determined so that the number of theoretical stages becomes the pre-specified value when the composition and enthalpy change are given in accordance with that S-RDC (See **Figure 2**). Once the location of S-RDC is determined, the operating locus is provided so as to be overlapped with S-RDC. As the number of side heat exchangers is given, the operating locus becomes a piecewise flat line. The composition and the amount of enthalpy change, q_k, are adjusted so that the obtained number of stages agrees with the pre-specified value. The determination of the operating locus in the stripping section means that the heat exchange stage and its composition and the heat duty for each side heat exchangers are decided.

2.5 Provide the ideal side heat exchange arrangement in the rectifying section

Similar to the stripping section, RDC can be provided for the rectifying section on *H-xy* diagram. First, from the reboiler duty, compressor power and the total heat duties of side heat exchanges which are calculated in section *2.4*, the pressure at the rectifying section, P_{R}, is calculated. Once P_{R} is decided, the artificial vapor-liquid equilibrium condition and the enthalpies of the vapor and liquid are defined by the procedure explained in section *2.2*. By using the obtained data, the enthalpy curve of saturated liquid and vapor at P_{R} can be drawn. Then, RDC in the rectifying section is provided in the similar manner of the stripping section (See **Figure 3**).

2.6 Determine the side heat exchange arrangement in the rectifying section

The overall heat balance of HIDiC including the total heat duties of side heat exchanges can be shown as the straight line across (x_{B}, $\hat{h}_{\mathrm{B}}^{0}$), (z_{F}, $h_{\mathrm{F}} + Ws/F$) and (x_{D}, $\hat{h}_{\mathrm{D}}^{0}$) (See Figure 3). Note that $\hat{h}_{\mathrm{B}}^{0}$ represents $h_{\mathrm{B}} - Q_{\mathrm{r}}/B - \sum q_k /B$, and $\hat{h}_{\mathrm{D}}^{0}$ represents $h_{\mathrm{D}} + Q_{\mathrm{c}}/D + \sum q_k /D$. Since $\sum q_k$ is already determined through the study in the stripping section, (x_{B}, $\hat{h}_{\mathrm{B}}^{0}$) is known. (z_{F}, $h_{\mathrm{F}} + Ws/F$) is also known since Ws is given as

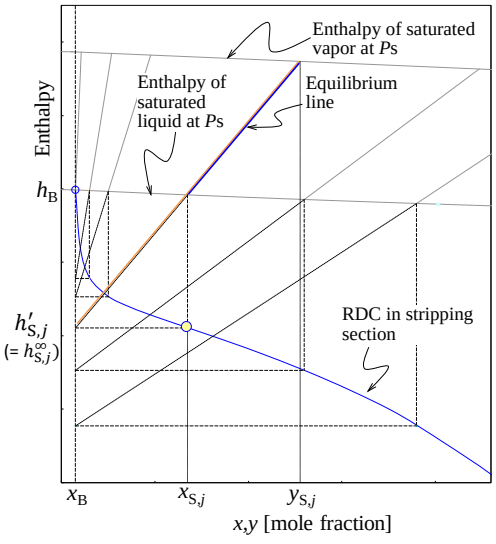

Figure 1 RDC on *H-xy* diagram

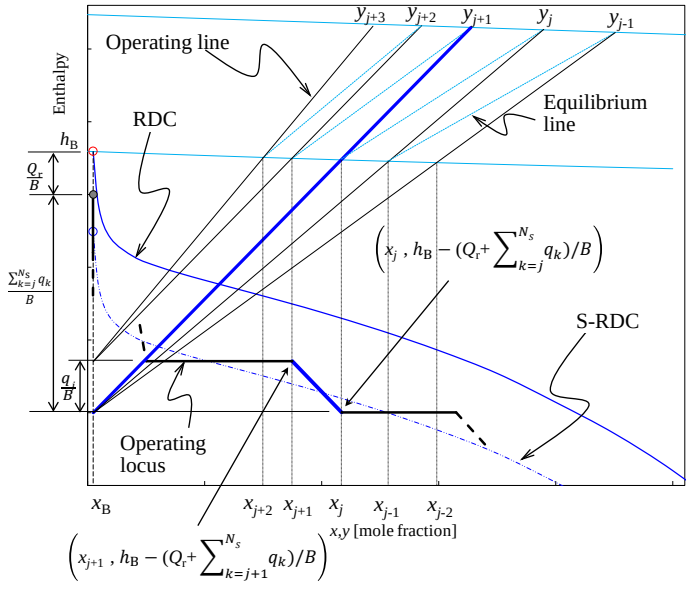

Figure 2 S-RDC and ope. locus on *H-xy* diagram

a premise. Therefore, (x_D, $\hat{h}_D^0$) can be uniquely identified. Here, S-RDC in the rectifying section is provided so as to pass through (y_F, $\hat{h}_D^0$). Thus, the position of S-RDC can be uniquely determined. Besides, each q_k has been already decided in the stripping section. So, the operating locus starting from point (x_D, h_D^0) changes its enthalpy step-wise according to the values of q_k. The operating locus should be given so as to overlap with S-RDC. The location of composition change is determined so that the number of theoretical stages meets the pre-specified value.

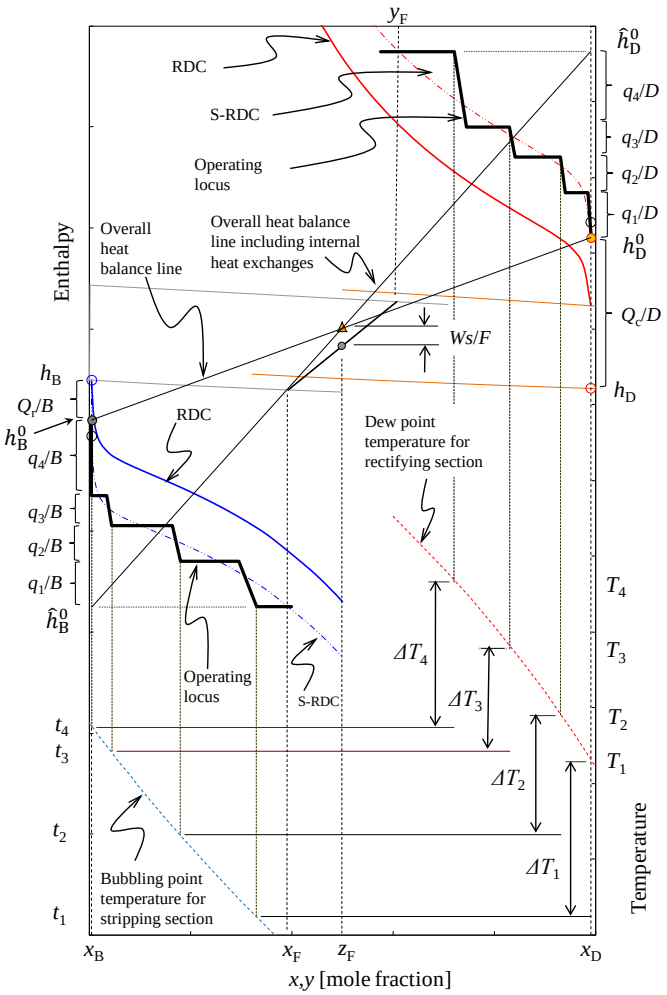

Figure 3 Overview of design methodology on *H-xy* & *T-xy* diagram

2.7 Confirmation of temperature difference of each side heat exchangers

To get the temperature information, the *T-xy* diagram is integrated with the *H-xy* diagram (Figure 3). When the enthalpy curves were provided by using simulation results, the temperature has been also available. Since the composition for the enthalpy change to occur has been known, the temperature corresponding to the composition can be readily taken from the dew/bubbling point temperature curves.

Finally, by using the rigorous process simulation, the conditions obtained through the graphical method are verified.

3. Novel HIDiC structure to realize outcomes of design methodology

The side heat exchange structure obtained by the design method in Chapter 2 is quite different from that of the conventional HIDiC structure. The limited number of side heat exchangers is used and the heat exchange is not executed between the stages at the same elevation. These characteristics suggest departing from the concentric structure.

To realize the concept, a novel HIDiC structure depicted in **Figure 4** was developed (Japan Pat. 4803470, 2011). This new structure consists of well-utilized equipment in industries. For instance, the normal tray/packing are used as column internals, and side heat exchanges are executed by stabbed-in type heat exchangers. What is different from a conventional distillation column is that the low pressure stripping section is installed above the high pressure rectifying section. With such structure, the following advantages can be enjoyed:

- Side heat exchangers can be installed at the stage/composition where the design method suggests.
- Side heat exchangers can be paired in line with the design results. Such pairing

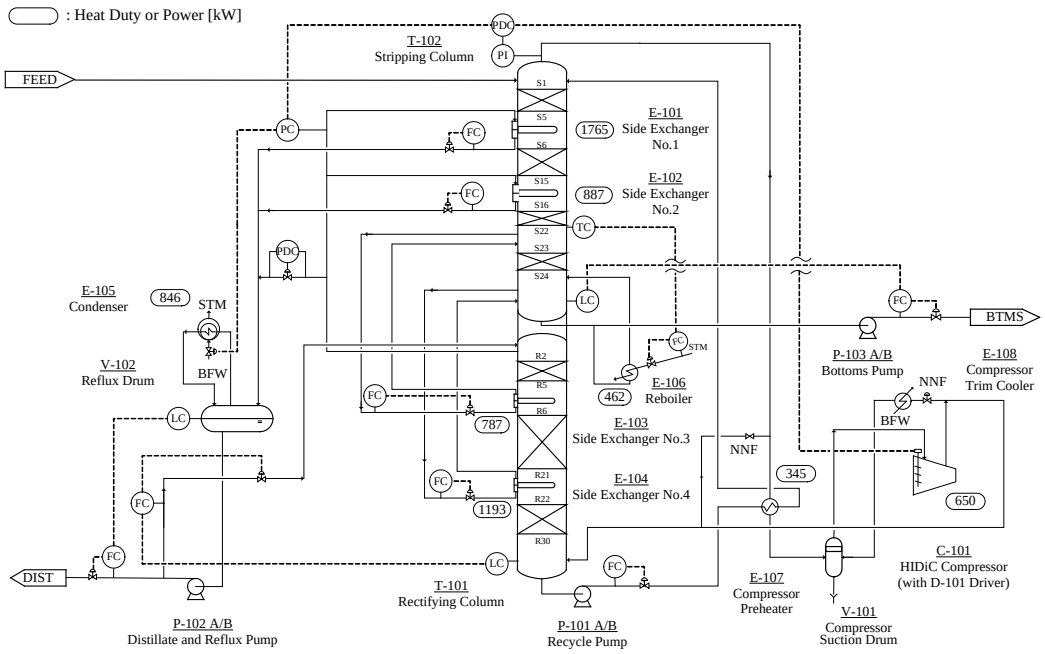

Fig.4 Process flow diagram based on results of case study for new HIDiC structure

is achievable by installing the stabbed-in type heat exchanger at a decided stage in either the rectifying or stripping section and by connecting the piping externally from the counter stage to the tube side of the heat exchanger. Since the stripping section is located above the rectifying section, the heat exchange can be accomplished by thermo-siphon effect or gravity.

- Heat duty of side exchanger can be given in line with the design results. This is because the heat transfer area of the stabbed-in heat exchanger can be changed so as to meet the required duty. Thus, the heat duty is not merely dependent on the temperature difference of the paired stages.

Accordingly, the proposed novel structure can have an optimized enthalpy profile inside of the column in keeping a sufficient temperature difference at side exchanger.

4. Economics of the proposed HIDiC structure

The economics of the proposed HIDiC was evaluated through a case study of a commercial scale xylene column separating C8 aromatics from C9 heaviers (See **Table 1**). The reboiler duty, $Q_{\text{r-conv}}$, of the conventional distillation column operating at a reflux ratio that is 1.15 times larger than the minimum reflux ratio is 4.78 MW at operating pressure of 106.3 kPa. The target energy conservation was given as 50%. Here, Q_{r} was assumed as 478 kW, which corresponds to 10% of $Q_{\text{r-conv}}$, and subsequent Ws was set as 700 kW with the power generation efficiency of 36.6%. N_{T} in HIDiC was set as identical to that in the conventional distillation. And N_{E} was set as four. We used the steady state equilibrium model simulator of Pro/II and Soave-Redlich-Kwong equation for properties prediction model.

The side heat exchange arrangement, inlet temperature difference, and heat transfer area obtained by the design are summarized in **Table 2**, together with Q_{r}, Ws and P_{R}. The obtained Q_{r} and Ws were 462 kW and 650 kW, which is quite similar to the set values. With the appropriate overall heat transfer coefficient, the heat transfer area is good enough to be installed in the column diameter decided based on vapor and liquid traffic inside of column. The subsequent energy saving was 53% for the conventional distillation. The new HIDiC structure to realize the design results was

already given in Figure 4. To evaluate the economics, the total investment cost (TIC) for the new HIDiC system and the conventional distillation system was calculated. With the obtained material/heat balance, the equipment size was calculated for both systems. TIC for each system was calculated as per the procedure described by Turton *et al.*,2012. Note that the TIC here corresponds to a grassroots cost in the referenced literature. Under the utility cost of 13K steam as USD 30/ton and the electricity as USD 0.12/kWh, the operating costs (OC) for both systems were calculated as in **Table 3**.

The differences of these values between the conventional column and the new HIDiC are expressed by ΔTIC and ΔOC, respectively. From ΔTIC and ΔOC, the payout period was calculated for evaluation. The operating time per year was assumed as 8000 h/y. ΔTIC and ΔOC were USD 3.46 x 10^6 and USD 1.28 x 10^6, respectively. Subsequent ΔTIC/ΔOC was 2.7 years. Such a payout period is well within the criterion in industry of three years.

5. Conclusions

The graphical design methodology which had been proposed in a binary system was extended and applied to a multi-component system. It was confirmed that the side heat exchange arrangement in a multi-component system can be determined as similar to that in a binary system. Furthermore, a new HIDiC structure was developed by which the side heat exchange arrangement obtained by the proposed method can be realized. It was demonstrated that the new structure shows attractive economics.

References

Japanese Pat, No.4803470, (2011), U.S. Pat, No.8440056 (2012)

Mah, R.S.H., J.J.Nicholas, Jr. and R.B.Wodnik, "Distillation with Secondary Reflux and Vaporization: A Comparative Evaluation," *AIChE J.*, **23**, 651-658 (1977

Nakaiwa, M., K.Huang, A. Endo, T. Ohmori, T. Akiya and T. Takamatsu ; "Internally Heat-Integrated Distillation Columns: A Review," *Chem. Eng. Res. Des.*, **81**, 162－177 (2003)

Turton, R., R.C. Bailie, W.B. Whiting, J.A. , "Analysis, Synthesis, and Design of Chemical Processes 4thed," Prentice-Hall, NJ (2012)

Wakabayashi, T. and S. Hasebe , "Design of heat integrated distillation column by using *H-xy* and *T-xy* diagrams," *Computers and Chemical Engineering*, **56**, 174-183 (2013)

Table 1 Process condition for case study

Feed rate	[kmol/s]	1/18
Feed composition	[mol %]	
Toluene / Ethylbenzene		0.5 / 10.0
p/m/o-Xylene		11.0 / 25.0 / 14.5
Cumene / n-propylbenzene		1.0 / 2.2
m-Ethyltoluene / 1,2,3-trimethylbenzene		15.8 / 20.0
Liquid molar fraction in feed	[-]	1
Separation specifications		
C9 aromatics in distillate	[mol %]	0.7
C8 aromatics in bottoms	[mol %]	1.5
NTS at rect. section & strip. section	[- / -]	30 / 25
HETP of column packing	[m]	0.35
Overall heat transfer coefficient		
Tube bundle in vapor space	[kW/(m^{2}K)]	0.60
Tube bundle in liquid pool	[kW/(m^{2}K)]	0.85
Pressure drop		
Theoretical stages	[kPa/stage]	0.22
Condenser / Reboiler	[kPa / kPa]	50.0 / 0.05
Pressure in strip. section	[kPa]	106.3

Table 2 Results of case study

Reboiler duty, Q_r			[kW]	462
Compressor power, *Ws*			[kW]	650
Ope. press. in rect. section at top/bottom			[kPa]	245.9 / 252.1
Side exchanger conditions				
	Combination	Duty, q_k	Inlet delta-T	Heat trans.area
	[—]	[kW]	[K]	[m^2]
No.1	S5-R1	1765	24.0	151
No.2	S15-R1	887	14.6	164
No.3	S22-R6	787	10.8	182
No.4	S25-R22	1193	11.9	250

Table 3 OC of new HIDiC and conv. distillation system

		New HIDiC	Conv. dist.
Reboiler duty	[MW]	0.462	4.78
Steam consumption	[kg/h]	848	8787
Shaft power			
Compressor/Pumps	[kW]	650 / 15	- / 12
Cost for steam	[k USD/y]	204	2109
Cost for electricity	[k USD/y]	638	12
Total utility cost	[k USD/y]	842	2120

Enlarged Operation Ranges for Thermosiphon Reboilers Using Thermoplates

Robert Goedecke, Stephan Scholl
Technische Universität Braunschweig, Institute for Chemical and Thermal Process Engineering, Braunschweig, Germany

Abstract
Thermosiphon reboilers are widely used as reboilers in distillation columns and as evaporators in the chemical and petrochemical industry. The main reasons are the low investment and operating costs. Additionally high heat transfer and low fouling tendency are characteristic for this apparatus. The heat transfer and the fluid dynamics are strongly linked in thermosiphon reboilers. Because of this reason the operation range of these evaporators is limited.
Thermoplates offer a very good heat transfer with a low pressure drop. Therefore great potential is expected for their use in thermosiphon reboilers. Evaporation experiments with a thermosiphon reboiler consisting of three thermoplates with a heat transfer area of 0.7 m² were carried out with water and a water-glycerol mixture. The total pressure, the static liquid head and the temperature difference between heating and evaporation side were varied. The circulation rate and heat transfer were measured. Stable self circulation was seen over a wide range of influence parameters. Even at low total pressures and at low static liquid heads the self circulation was stable. For water, even at an overall temperature difference of 5 K, a stable self circulation was obtained.
Compared to literature data for tubular thermosiphon reboilers the operating limits for thermoplate thermosiphon reboilers can be increased, especially at low total pressures, low static liquid heads and low temperature differences. The measured heat transfer is increased compared to tubular stainless steel thermosiphon reboilers.

Keywords
Thermoplate, thermosiphon reboiler, stability, operation range

1. Introduction

Of all reboilers types, thermosiphon reboilers are most widely used in chemical industry [1]. They show very good heat transfer and a low fouling tendency. This apparatus is characterized by a simple setting and low investment and operation costs since no circulation pump is required. Furthermore the shear stress on the product is comparatively low.
The self circulation in the evaporator is caused by pressure differences between the column and the evaporator tube due to the density difference of the liquid in the column and the vapor-liquid mixture in the evaporator. Inside the evaporator a characteristic temperature profile over the height of the evaporator can be observed. At the inlet of the evaporator the liquid enters subcooled, mainly caused by the hydrostatic pressure. First the temperature of the liquid increases in the heating zone due to single phase heat transfer. When nucleate boiling in the bulk flow can be

observed, the temperature decreases according to boiling temperature, because the hydrostatic pressure is decreasing. This is the evaporation zone [2].
The static liquid head h_s* is defined as the ratio of liquid height in the column h_s to the height of the heat transferring area L. For a thermoplate heat exchanger L is the height of the thermoplates.
Disadvantages of thermosiphon reboilers are the very complex design as fluid dynamics and heat transfer are strongly connected. The operation range is limited due to this reason. An evaporation pressure of $p_{abs} \geq 200$ mbar and a temperature difference between heating side and evaporation side of $\Delta T_{ov} \geq 12.5$ K should be applied to guarantee a stable operation [3].
Generally thermoplates are used in the food industry for vessels or in the chemical industry as condensers in columns [4]. Due to manufacturing, thermoplates have pillow structures which can increase the heat transfer associated with low pressure drop. The geometry of the thermoplates can be varied over a wide range of parameters, such as pillow size, welding point size and, weld point distance, the plate size and the distance of plates to each other. The main advantages of thermoplate apparatuses are the compact and light design and good heat transfer properties. Therefore thermoplates are promising for the use as thermosiphon reboilers. In this work the applicability and the operation range of thermoplates for the use as a thermosiphon reboiler were investigated

2. Results and discussion

2.1 Experimental setup
The experiments were carried out with the thermoplate apparatus E1 which consists of three thermoplates with the geometry of 800 x 1.5 x 220 mm (height x wall thickness x width) and an overall heat transfer area of A = 0.7 m². The flow diagram of the experimental setup is shown in Figure 1.
The circulating mass flow was determined using a coriolis flow meter and the temperature profiles within the apparatus were measured. In vessel V1 the vapor-liquid mixture is separated. The hydrostatic pressure in thermoplate evaporator H1 can be altered by varying the liquid head in V1. The vapor is condensed in heat exchanger E2 and the condensate can be weight in V2. Heat exchanger E3 heats up the condensate before reentering in V1. On the heating side saturated steam is used. The steam condensate was weight in vessel V3. As testing media water and a water-glycerin mixture with $x_{Water} = 0.71$ mol_{Water}/mol_{ov} were used. The evaporation pressures were $p = 200, 800, 1000$ mbar with overall temperature differences of $\Delta T_{ov} = 5 \ldots 20$ K. The transferred heat flux can be calculated by three energy balances:
1. Cooling water energy balances
2. Measurement of steam condensate
3. Measurement of the product condensate.
The arithmetic average value of these three energy balances was used as transferred heat flux.

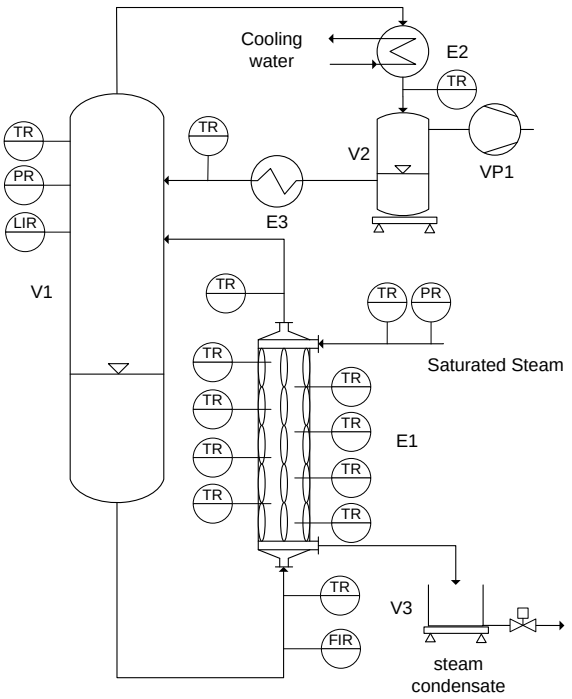

Figure 1: Flow diagram of experimental setup

2.2 Fluiddynamic

The experimental results for the circulating flow for water and the water-glycerol mixture at an evaporation pressure of 200 mbar and 1000 mbar are shown in Figure 2.

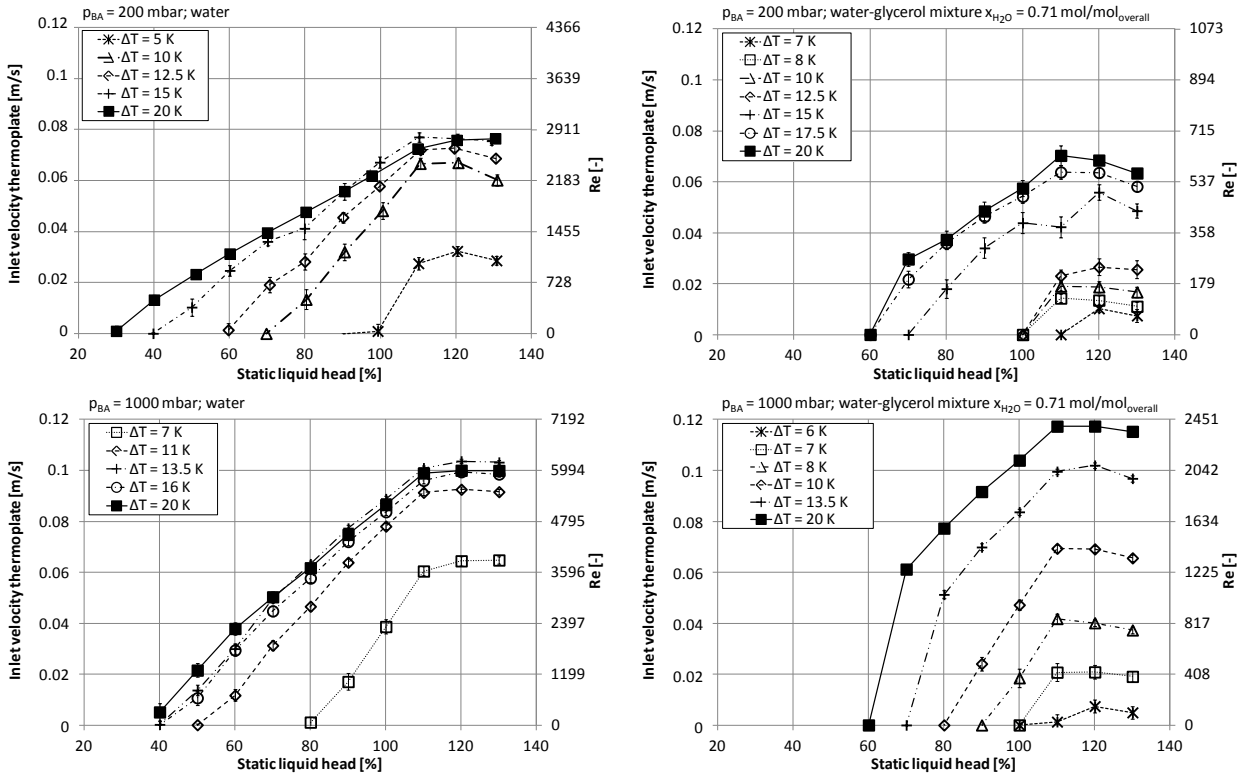

Figure 2: Dependency of inlet velocity from static liquid head for water (left) and water-glycerol mixture (right); for p_{BA} = 200 mbar (top) and p_{BA} = 1000 mbar (down)

The inlet velocity increases with increasing static liquid head, until the static liquid head reaches a value of 110 %. Afterwards an almost constant value of the velocity could be observed. This can be explained with the increased hydrostatic pressure which leads to an increasing driving force for the circulation. Between the static liquid heads of 109.5 % and 115.5 % the vapor outlet tube is flooded. Under flooded conditions the increase of the circulation stops.
For the observed experimental conditions the inlet velocity increases with increasing driving temperature difference. Higher temperature differences lead to an increased evaporation, therefore the density differences between the evaporator and the liquid in vessel V1 is higher. For this reason the driving force for the circulation is increased. The increase caused by the temperature difference decreases for water at $\Delta T_{ov} > 10$ K. Apparently the higher pressure drop caused by the increased amount of vapor stops a further increase of the velocity. For the experiments with water it is obvious that higher temperature differences enlarge the range of static liquid head to lower values where a self circulation could be observed. The operation range enlarges up to a static liquid head of 40 % for a $\Delta T_{ov} = 20$ K. Even at a low temperature difference of 5 K a self circulation could be observed up to a static liquid head of 110 %.
In comparison to these results for the water-glycerol mixture a decreased inlet velocity at the entrance of the thermoplate apparatus at 200 mbar was observed. The operation range in respect to the static liquid head is decreased compared to the water results. At $\Delta T_{ov} = 20$ K and above a static liquid head of 70 % a self circulation was observed. At lower static liquids heads the circulation was decreased until the mixture in the evaporator was not mixed well enough. The concentration of the glycerol increased until the boiling temperature of the local mixture was higher than the heating steam temperature. Under these conditions evaporation stopped.
Until a minimum temperature difference of 7 K self circulation was possible. The ratio of evaporated water-glycerol mixture and mass flow in the circulation was about 1 %.
At a pressure of 1000 mbar higher inlet velocities were measured. Compared to 200 mbar the vapor density at 1000 mbar is higher. Therefore the vapor-liquid mixture in the evaporator and the vapor pipe causes a lower pressure drop, which explains the increased velocities. The highest velocities were measured for the water-glycerol mixture. Obviously the decreased heat transfer leads to less vapor and therefore to a lower pressure drop compared to the water experiments which will be explained later. At 1000 mbar experiments for water were carried out down to $\Delta T_{ov} = 7$ K. The high velocities and the observed operation range of a minimal static liquid head of 90 % indicate, that at lower temperature differences a self circulation could be possible. The water-glycerol mixture showed at a pressure of 1000 mbar a self circulation until a temperature difference of 6 K. The error bars shown in Figure 2 are the standard deviations of the measured inlet velocities. As indicated by the small error bars a very stable circulation could be measured over all examined experimental conditions. At 200 mbar the standard deviation increases and bigger fluctuations in the self circulation were seen, but these fluctuations are still very small compared to other findings [5].

2.3 Heat transfer

The results for the overall area-averaged heat transfer coefficient for both media are shown in Figure 3. The dependency of the heat transfer of the overall temperature difference can be seen. The heat transfer increases with increasing temperature difference. This can be explained by two mechanisms. First the length of the heating

zone decreases with increasing heat transfer. Therefore the length of the evaporation zone is increased. Given that the single phase heat transfer is lower than the heat transfer in the evaporation zone, the integral heat transfer increases. Second the nucleate boiling in the evaporation zone increases at higher temperature differences. These two effects mainly determine the overall heat transfer.

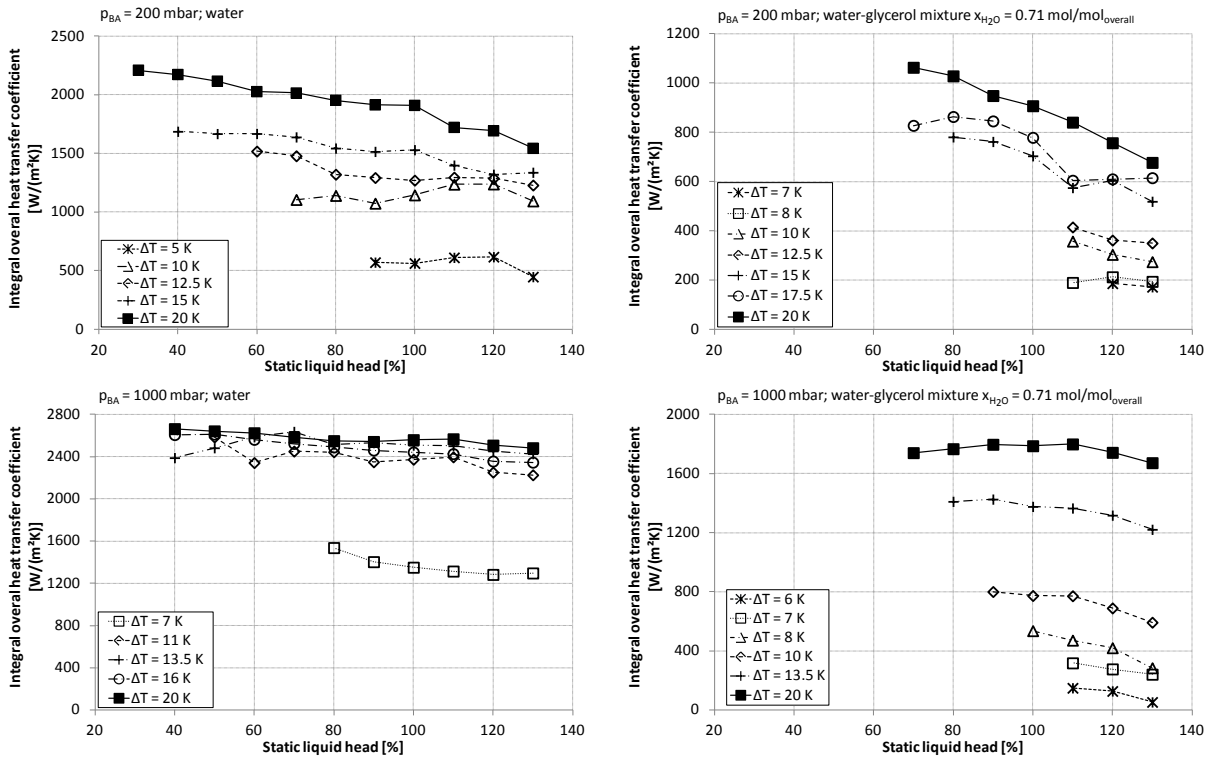

Figure 3: Dependency of the integral overall heat transfer coefficient from static liquid head for water (left) and water-glycerol mixture (right); for p_{BA} = 200 mbar (top) and p_{BA} = 1000 mbar (down)

For 200 mbar and temperature differences of $\Delta T_{ov} \geq 12.5$ K for water and $\Delta T_{ov} \geq 10$ K for the water-glycerol mixture, the heat transfer decreases with increasing static liquid head. The reason is the increased hydrostatic pressure in the evaporator which leads to an increased subcooling of the inlet fluid. Therefore the length of the heating zone is increased and the length of the evaporation zone is decreased.

The heat transfer for water is much higher compared to water-glycerol. Mainly the increased viscosity of the water-glycerol mixture decreases the heat transfer. At 200 mbar the dynamic viscosity of water-glycerol was about 2.23 mPas compared to 0.47 mPas for water. The high viscosity leads to a decreased heat transfer in the heating zone which leads to an increased length of the heating zone.

The heat transfer values for 1000 mbar were significantly above those observed for 200 mbar. The two main reasons here are the decreased viscosity which promotes the single phase heat transfer and the decreased subcooling of the liquid at the inlet of the evaporator.

The shown integral overall heat transfer coefficients show large values. A thermoplate thermosiphon reboiler shows an increased heat transfer compared to smooth tubes [1; 3]. Advantages of this apparatus are the stable circulation and the

good heat transfer over a wide range of the static liquid head. The good results even for 200 mbar show further potential at even lower pressures which should be investigated in further studies.

3. Conclusions

A thermoplate heat exchanger consisting of three thermoplates was investigated for use as a thermosiphon reboiler. Measurements with water and a water-glycerol mixture were carried out under atmospheric pressure, vacuum and temperature differences of 5 … 20 K. The static liquid head was varied between 30 … 130 %.
Down to a minimal temperature difference of 5 K for water and 7 K for the water-glycerol mixture stable self circulation and evaporation was investigated. These are lower values as in the literature are recommended for a stable circulation. The circulation was very stable. Very small standard deviations were observed and pulsation or other disturbance of the flow did not occur. The flow velocities with water were higher compared to the results of the water-glycerol mixture. The apparatus showed a stable circulation over a wide range of the static liquid head. The minimal liquid head where self circulation could be seen, increases with higher temperature differences.
The heat transfer increases with enhanced pressure and global temperature difference. The heat transfer with water-glycerol was much smaller compared to the results with water. This is caused by the higher viscosity.
The thermoplate apparatus showed good results as a thermosiphon reboiler. Very stable self circulation with a good heat transfer were observed even at low temperature differences and at a pressure of 200 mbar, which is the minimum limit proposed by the literature. The compact design of this apparatus should also be highlighted.

Acknowledgements

Financial support by the “Bundesministerium für Bildung und Forschung” within the collaborative research project “Innovative equipment and plant concepts to increase efficiency of production processes – InnovA²” (033RC1013A) is gratefully acknowledged.

References

[1] S. Arneth, J. Stichlmair, Int. J. Therm. Sci., 2001, 40, 385-391

[2] K. Dialer, Dissertation, ETH Zürich, 1983

[3] S. Scholl, Chem. Ing. Tech., 2012, No. 11, 1939-1947

[4] J. Mitrovic, R. Peterson, Chem. Eng. Technol. 2007, 30 (7), 907-919

[5] J. Hammerschmidt, Dissertation, TU Braunschweig, 2013

Batch Distillation with Heat Pump Applying Different Working Fluids

Gabor Modla, Peter Lang
Budapest University of Technology and Economics,
Department of Building Service and Process Engineering, Budapest, Hungary

Abstract
Application of a heat pump system is a possibility for decreasing the high energy demand of distillation. The use of different working fluids (WF-s) for a vapour compression system for batch distillation is investigated. WF-s are classified as “wet” and “dry” based on their behaviour during the compression. The separation of a low relative volatility mixture (n-heptane – toluene) is investigated by rigorous simulation performed with a professional flow-sheet simulator. Standard reactor-reboiler is applied and simulated in a rigorous way (including the conditions of heat transfer). The basic criteria for the selection of the possible WF-s are determined. Based on these criteria n-hexane, n-pentane, ethanol and iso-propanol are studied as WF-s. The effectiveness of different WF-s is compared. The effect of the main operational parameters on the length of the payback period is investigated. The minimal payback time is determined for the different working fluids. The best results are obtained for n-hexane.

Keywords batch distillation, vapour compression, working fluids

1. Introduction

Application of a heat pump system (HP) is a possibility for decreasing the energy demand of distillation. The working fluid (WF) of HP can be the top vapour itself (vapour recompression, VRC) or a material different from the components to be separated (vapour compression, VC). Recently Jana and his team published several papers about the application of the VRC for batch distillation (BD) (e.g. Jana and Maiti, 2013). Modla and Lang (2013) studied the BD separation of a close boiling hydrocarbon mixture by rigorous dynamic simulation. They studied BD-VRC and BD-VRC with the application of an external heat exchanger and BD-VC systems (with n-pentane as WF). The most favourable results were obtained for the BD-VRC-E and BD-VC systems. In this paper the vapour compression system is studied by applying different working fluids. The goals of this paper:

-to study the process of batch distillation with vapour compression by rigorous dynamic simulation with a professional flow-sheet simulator,
-to study its economic feasibility by cost calculations,
-to compare the effectiveness of different working fluids by the payback time.

The mixture studied is n-heptane – toluene. The working fluids studied are n-hexane, n-pentane, ethanol and iso-propanol. The influence of the main operational parameters of the HP on the payback time is studied for the WFs of two different types then their optimal values providing the minimal pay-back time are determined.

2. Batch distillation with vapour compression

In batch distillation with vapour compression (VC, Figure 1) the working fluid (WF) is independent of the mixture to be separated. The basic parts of a VC cycle are as

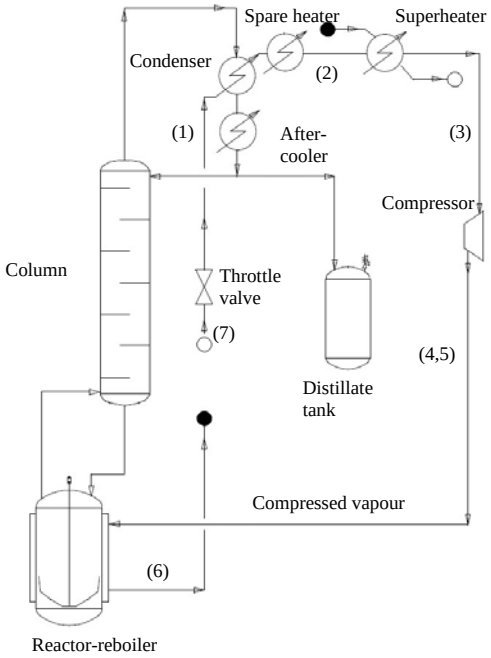

Figure 1. Scheme of batch distillation with vapour compression

follows (Figure 2). The WF is evaporated at the condenser (between 1 and 2), compressed to a higher pressure with higher saturation temperature (3→4), condensed in the reboiler (5→6), and cooled down by expansion over a throttle valve (7→1) to a (saturation) temperature below the condenser temperature. The optional parts of the cycle depending among others on the thermodynamic properties of the WF are: superheating of the WF (2→3, if necessary in order to prevent the (partial) condensation of WF in the compressor) and cooling down of WF in the reboiler to its dew point (4→5, if it leaves the compressor as superheated vapour), sub-cooling of the condensed WF before expansion (6→7). The compressor (the heat pump system) can be already operated during the heating-up of the column. The spare heater must be operated in the heating-up while there is no top vapour in sufficient quantity.

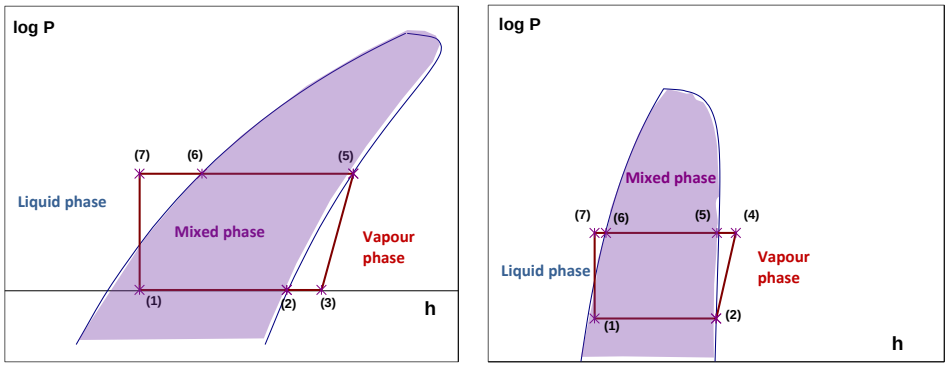

a. Wet WF b. Dry WF

Figure 2. Thermodynamic cycles of VC for different types of WFs

3. Properties of working fluids

3.1 Criteria for selecting working fluids

The basic criteria for the selection were as follows:

1. The boiling point of the WF at 1.01 bar must be less at least by 15 °C than the lowest temperature of the top vapour (in our case the bubble point of the light component (n-heptane) at 1.01 bar, 98.4-15=83.4 °C).
2. The critical temperature of the WF must be higher than the maximal temperature at the utility side of the reboiler (in our case the temperature of the water steam of 4 bar: 143.7 °C).
On the basis of the above criteria the following WF-s were selected: n-pentane, n-hexane, iso-propanol and ethanol. Table 1 shows the relevant thermodynamic data of substances studied. For the different WF-s for the temperatures of utility side of the reboiler (126.0 and 143.7 °C) the vapour pressures (p^0_{rel}) and latent heats (λ_{rel}) are divided with their values at the temperature of utility side of the condenser (83.4 °C).

	NBP [°C]	p° [bar]	$p°_{rel}$	$p°_{rel}$	λ [kJ/mol]	λ_{rel}	λ_{rel}	T_{cr} [°C]
		83.4 °C	126.0 °C	143.7 °C	83.4 °C	126.0 °C	143.7 °C	
n-pentane	36.07	3.99	2.57	3.57	22.65	0.827	0.737	196.5
n-hexane	68.73	1.53	2.92	4.23	28.07	0.874	0.814	234.2
ethanol	78.29	1.21	4.21	6.86	38.27	0.899	0.849	240.8
i-propanol	82.26	1.03	4.32	7.07	39.79	0.871	0.809	235.2
water	100.0	0.53	4.51	7.55	41.58	0.949	0.927	374.2
n-heptane	98.43	NR	NR	NR	NR	NR	NR	NR
toluene	110.56	NR	NR	NR	NR	NR	NR	NR

NR: not relevant

Table 1. Thermodynamic data of the substances studied

3.2 Behaviour of different working fluids during the compression
Behaviour of the different WF-s during compression was investigated. From this point of view we divided the working fluids into two different types. If the WF of saturated vapour partially condensates during compression, then it is called “wet” (Figure 2a) otherwise “dry” (Figure 2b) fluid. The wet WF-s (n-pentane and n-hexane) must be superheated before the compressor in order to protect the compressor from the liquid break. The dry WF-s (ethanol and iso-propanol) from saturated vapour state become superheated during compression.

4. Simulation results

In this section first the BD then the BD-VC process by applying different working fluids are investigated. The BD-VC processes are compared with the basic, optimized batch distillation process (without any heat pump system). For the calculation we used the ChemCad professional flow-sheet simulator.
The mixture is n-heptane – toluene. The charge (800 dm^3) contains 50 mol% n-heptane. The specified product purity is 98 mol% n-heptane. The number of theoretical stages for each case is 50 (excluding the total condenser and the reboiler). The pressure drop of the column is 0.1 bar. The reactor-reboiler is DIN AE-1000 type. In the BD process the heating medium is water-steam of 4 bar.
At the beginning of the process the column is empty (“dry start-up”). During the start-up step (heating-up of the column) total reflux is applied. In the production step the reflux ratio (R) is 12 and this step is finished when the n-hexane concentration falls below 98 mol% in the product tank.

4.1 Results for the BD process

The influence of the duration of start-up (Δt_{st}) on the recovery of n-heptane (η) and on the (total) heat demand of the whole process (SQ) is investigated. Limits of Δt_{st}:
-its minimum is 93 min, which is necessary for that the top vapour reaches the product purity prescribed (98 mol%),
-its maximum is 278 min, since by then the purity of top vapour practically reaches its maximum (99.78 mol%), which can be produced with the given column under R=∞.

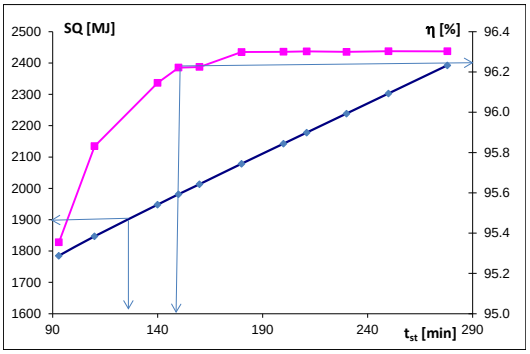

Figure 3. Influence of start-up duration on the yield and the total heat demand

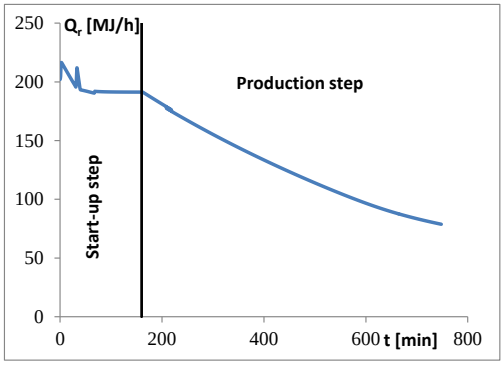

Figure 4. Evolution of the heat transfer rate in the reboiler

Figure 3 shows that there is an optimal duration. Until the optimum time ($t_{st,opt}$) the recovery sharply increases, after that it increases only slightly, it remains almost constant. The optimal duration is 160 min for which the recovery is 92%, the total heat demand is 1770 MJ and the batch operation time (BOT) is 748 min.
In the production step the heat transfer rate in the reboiler (Q_r) is decreasing (Figure 4) since the active surface area and the driving force for the heat transfer are diminishing. The HP must be operated with a higher load in the start-up period and with a lower, continuously decreasing load during the production step when the increase of the vapour fraction (above 0.05) in the WF leaving the reboiler is prevented with a PI controller modifying flow rate of the WF.

4.2 Investigation of the BD-VC process for different working fluids

The aim is to obtain the minimal payback period of the compressor (heat pump system) investment. First operational variables of the process are investigated:
Compressor inlet pressure (P_{in})
It is an independent variable, but it has both a lower (atmospheric pressure) and an upper bound. In our former work (Modla and Lang, 2013) we stated that P_{in} has small effect on the payback period. In this work always its maximal value (upper limit) is specified (determined from the bubble point of the more volatile component at the condenser pressure - temperature difference of the heat transfer in the condenser).
Pre-superheating of the working fluid (ΔT_S)
It is an independent variable. It has a lower limit for the wet working fluids (in order to prevent the condensation in the compressor). It has also an upper limit (in our case 50 °C), since the heat for superheating is ensured by the condensed WF leaving the reboiler. Between these streams a minimal temperature difference is needed.
Compressor outlet pressure (P_{out})
It is an independent variable, but it has a lower limit ($P_{out,min}$), which is determined from the minimal condensation temperature at the utility side of the reboiler (bubble

point of the less volatile component at the reboiler pressure + temperature difference of the heat transfer in the reboiler, in our case 111 +15=126 °C).

Start-up duration (Δt_{st})

In order to compare the results with those of BD it must be unchanged (Δt_{st}=160 min).

Flow rate of the working fluid (V_{wf})

Since Δt_{st} is fixed values of P_{out} and ΔT_s determine its value in the start-up ($V_{wf,max}$).

Batch operation time (BOT)

Since the duration of the start-up equals to that of the BD ($\Delta t_{st,BD}=\Delta t_{st,BD\_VC}$) the batch operation time also equals to that of the BD ($BOT_{BD}=BOT_{BD-VC}$).

Hence the independent variables of the optimization are P_{out} and ΔT_s. Their values are varied between their limits and the value of $V_{wf,max}$ is calculated for the given values of P_{out} and ΔT_s. In order to find the minimal payback period (PBP) the following principle is applied. The optimum is at the minimal electrical energy demand of the start-up, since the investment and operational costs of the compressor are proportional to the electrical energy demand and the operational cost of the production step is proportional to that of the start-up step.

First the effect of the compressor outlet pressure (P_{out}, Figure 5a) then that of the extent of pre-superheating (Figure 5b) on the electrical energy demand of the start-up step (SMP_{st}) are investigated

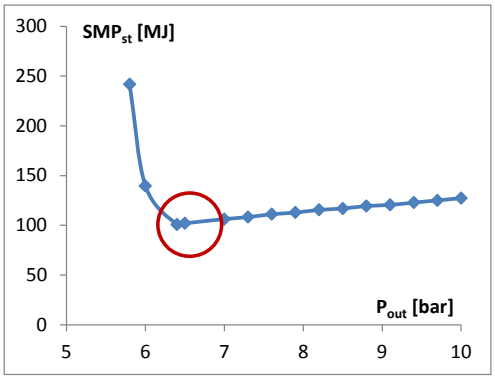

Figure 5a. Effect of P_{out} on the electrical energy demand (n-hexane, ΔT_s=40 C)

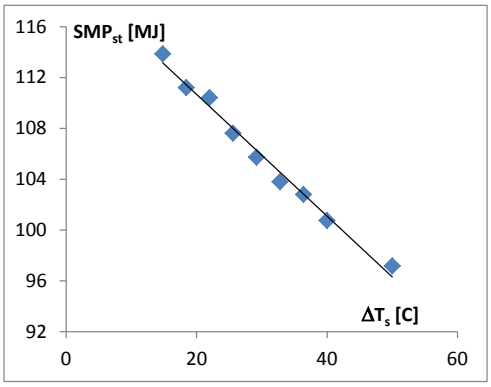

Figure 5b. Effect of pre-superheating on the electrical energy demand (n-hexane,P_{out}=6.4 bar)

For all WF-s we found that, there is a P_{out} value where SMP_{st} has minimum (Figure 5a). On the increase of ΔT_s SMP_{st} decreased in a monotone way.

From the results two data series are presented. In the first case not optimised (Table 4a) P_{out} is determined for each WF for the temperature of the water steam of 4 bar (143.7 °C). ΔT_s is specified for its minimal value (lower limit). In the second case (Table 4b) the maximal ΔT_s (50 °C) is applied and the optimal value of P_{out} is determined by seeking the minimal PBP.

Comparing the results without and with optimization (Table 4) it can be seen that the value of P_{out} only slightly while that of V_{wf} considerably changed. Moreover the results show that for the wet fluids the total electrical energy demand (SMP) considerably decreased by the optimization. The outlet temperature is much higher for dry WF-s, which can cause several problems (application of special construction materials, distillation of heat sensitive materials).

Comparing the payback periods (Figure 6) calculated for two different durations of operation we stated that due to the optimisation for the wet WF-s PBP considerably, for the dry WF-s only slightly decreased.

WF	P_{in} [bar]	ΔT_s [°C]	P_{out} [bar]	T_{out} [°C]	$V_{wf,max}$ [kg/h]	SMP [MJ]
n-pentane	4.00	19	14.23	143.7	775	453
n-hexane	1.53	24.4	6.47	143.7	687	397
ethanol	1.21	0	8.3	178.3	250	363
i-propanol	1.03	0	7.28	149.6	346	382

a.

WF	P_{in} [bar]	ΔT_s [°C]	P_{out} [bar]	T_{out} [°C]	$V_{wf,max}$ [kg/h]	SMP [MJ]
n-pentane	4.00	50	14.0	174	612.5	375
n-hexane	1.53	50	6.425	169	575.0	346
ethanol	1.21	50	8.3	231	219.5	358
i-propanol	1.03	50	7.2	199	298.0	363

b.

Table 2. Values of main operational parameters without (a) and with optimisation (b).

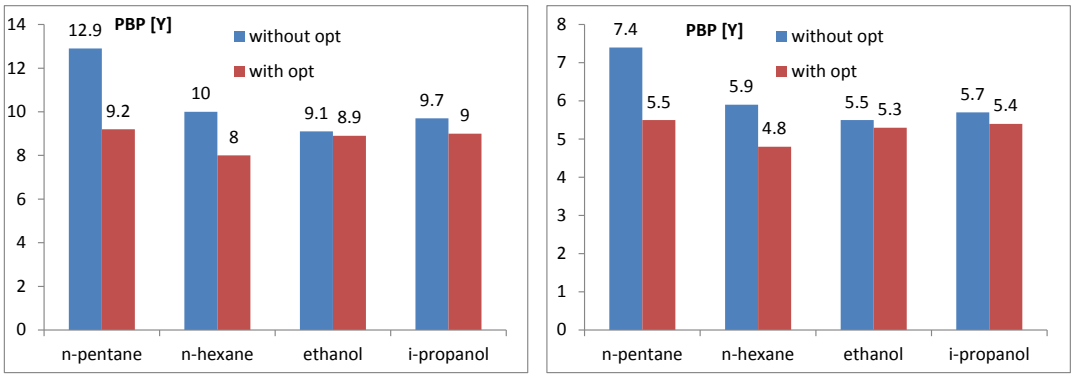

Figure 6. Payback periods (PBP) for the different working fluids
a. 4000 working hours per year b. 6000 working hours per year

The best results (lowest PBP-s) were obtained for n-hexane. On the increase of the duration of yearly operation, as it was expected, PBP considerably decreased.

5. Conclusions

The purpose of the current study was to investigate different working fluids for vapour compression systems integrated to real, batch distillation columns. Working fluids were classified as “wet” and “dry” based on their behaviour during the compression. The separation of a low relative volatility mixture (n-heptane – toluene) was investigated by rigorous dynamic simulation. The basic criteria for the selection of the possible working fluids were determined. Based on these criteria n-hexane, n-pentane, ethanol and iso-propanol were studied as working fluids. The effectiveness of the working fluids was compared. The minimal payback time was determined. The best results (lowest PBP-s) were obtained for n-hexane.

Acknowledgements

This work was supported by the Hungarian Research Funds (OTKA, No.: K-106268).

References

A. K. Jana, D. Maiti, 2013, Assessment of the implementation of vapour recompression technique in batch distillation, Separation and Purification Technology, 107, 1-10.
G. Modla, P. Lang, 2013, HP systems with mechanical compression for batch distillation, Energy, 62, 403-417.

New, useful dividing wall columns for sustainable distillation

Gautham Madenoor Ramapriya[1], Mohit Tawarmalani[2], Rakesh Agrawal[1]
[1]School of Chemical Engineering, Purdue University, West Lafayette, USA;
[2]Krannert School of Management, Purdue University, West Lafayette, USA

Abstract
Industrial application of the dividing wall column (DWC) derived from the three-component Fully Thermally Coupled (FTC) column is on the rise because of its low heat duty requirements and reduced capital costs. To obtain maximum heat duty benefits and achieve high purity in the product streams from the DWC, it should be operated close to optimality. But, close-to-optimal operation of the DWC is challenging because the split of vapor at the bottom of its vertical partition cannot be independently regulated externally from the column. Based on our previous work, where a thermal coupling link is converted to a liquid-only transfer stream,[1] we propose new, more operable DWCs for ternary distillation. These new DWCs allow regulating the vapor split across the two parallel zones on either side of the vertical partition. Further, we show that each of these new, more operable DWCs is equivalent to the FTC configuration. Based on the findings, we extend our framework to four components and obtain DWCs from the corresponding FTC configuration which can be beneficially operated. We believe that the proposed DWCs will enable the successful industrial implementation and optimal operation of the 4-component FTC configuration in a single distillation column shell.

Keywords
Dividing wall column; Fully Thermally Coupled Configuration; Operability; Energy Savings; Equivalent Configurations

1. Introduction

The three-component Fully Thermally Coupled (FTC) configuration shown in Figure 1a is popular among distillation researchers and engineers because of its low heat demand.[2,3] The configuration is called so, because it has thermal coupling links for all possible submixtures, i.e., at AB and BC. In this paper, A, B, C, and D denote pure components, whose volatilities decrease in the same order. Further, filled and unfilled circles in all figures of the paper respectively denote condensers and reboilers. We consider only zeotropic separations in this paper.

The configuration shown in Figure 1a is generally difficult to operate because the vapor flows at the top and bottom of column 1 are in opposite directions, and therefore cannot be easily accomplished by regulating constant pressure in each column. Multiple solutions have been suggested to overcome this operational difficulty, without compromising on its heat duty requirement.[1,4] One such solution is shown in Figure 1d.[4] To obtain this configuration from the configuration of Figure 1a, the section 2a at the top of column 2 is shifted to the top of column 1, resulting in the section 1a of Figure 1d. Such a rearrangement of the section ensures that the vapor flows between columns 1 and 2 are in the same direction.

An alternate solution is shown in Figure 1b where the thermal coupling at submixture BC is replaced by a liquid-only transfer stream, and an extra section 1d is created.[1] This eliminates the vapor transfer between columns associated with the thermal coupling, and hence simplifies operation. The configuration in Figure 1b is derived from the one in Figure 1a in the following manner. In Figure 1a, the vapor that enters column 1 at the bottom is generated in the reboiler of the second column. To make up for this vapor flow from column 2 to column 1 at submixture BC, and still have a net mass flow from column 1 to 2, a liquid feed is provided to column 2 from column 1. So, the net mass feed to column 2 at submixture BC is liquid. To obtain the configuration in Figure 1b from Figure 1a, an additional section and reboiler are added to the bottom of column 1 below the withdrawal location for submixture BC. In this reboiler, the exact same amount of vapor is generated that was conveyed in Figure 1a from column 2 to column 1 at submixture BC. Such an arrangement obviates the need to have a thermal coupling at submixture BC. Only a liquid stream is used to provide the feed to column 2 from column 1 as was also the case with Figure 1a according to the preceding discussion. The reboiler of the second column of Figure 1b generates just enough vapor so that the vapor flow in section 2c of Figures 1a and 1b is maintained the same. The sections 1d and 2d of Figure 1b have the same L/V ratio as the section 2d in Figure 1a. While all of the B is distilled in Figure 1a from the bottom of column 2, it is divided between the two equivalent sections 1d and 2d in Figure 1b. Thus, the two configurations in Figures 1a and 1b are only different topologically, but are equivalent in all other aspects.

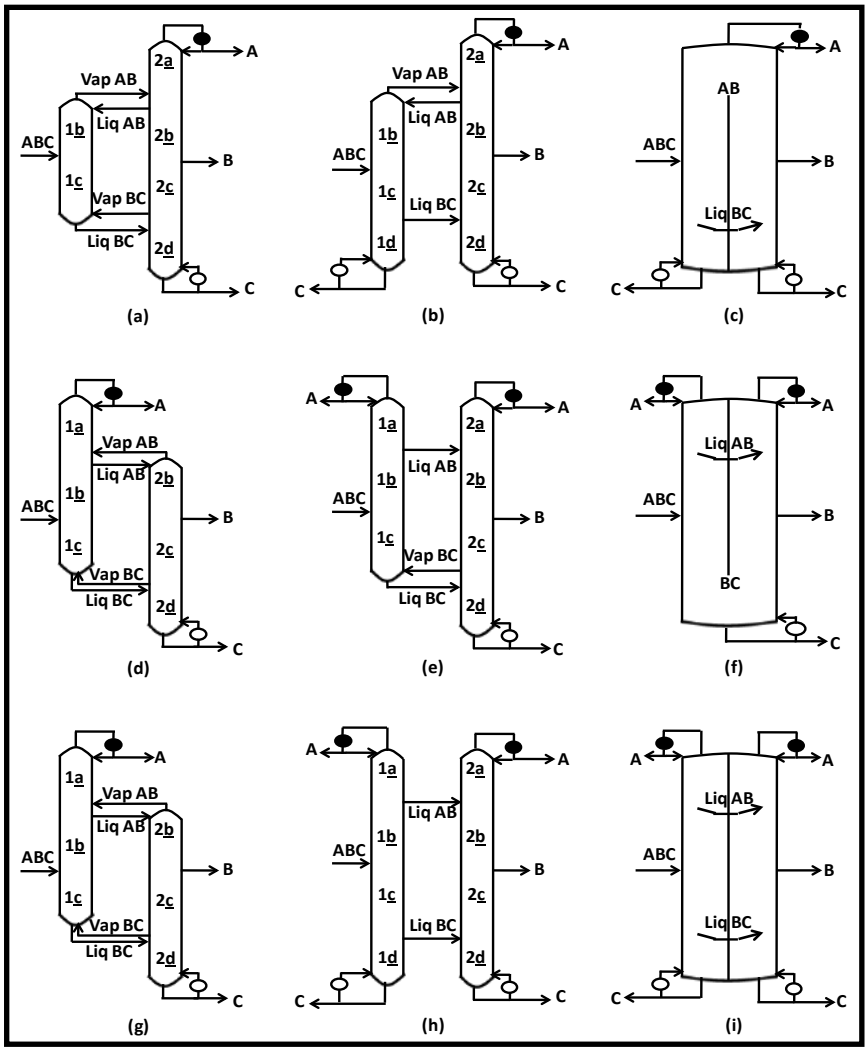

Figure 1. (a),(d),(g) 3-component FTC configurations; **(b),(e),(h)** FTC-equivalent configurations obtained by converting thermal couplings to liquid-only transfer streams; **(c),(f),(i)** DWC implementations of (b),(e),(h)

A similar derivation of the configuration in Figure 1e can be made from the configuration in Figure 1d. In this case, the thermal coupling at submixture AB is converted to a liquid-only transfer stream. Prior to understanding this conversion, it is worth noting that, in Figure 1d, the liquid AB stream fed to column 2 from column 1 makes up for both the vapor AB stream that is returned from column 2 to 1, and the net mass that is fed to column 2 at submixture AB. To obtain Figure 1e from Figure 1d, the section 2a is newly added. This section retains the exact same quantity of vapor flow that is diverted in Figure 1d from the top of column 2 to 1. Thus, in Figure 1e, the vapor connection at AB between the two columns is eliminated, and only a liquid stream that accounts for the mass feed from column 1 to 2 is retained. The sections 1a and 2a of Figure 1e have the same L/V ratio as that of section 1a in Figure 1d. Thus, the two configurations in Figures 1d and 1e differ only topologically, but are equivalent in all other aspects. By combining the strategies just discussed, both thermal couplings of Figure 1g can be eliminated to obtain another equivalent configuration depicted in Figure 1h.

2. New DWCs of FTC configurations

Using the groundwork established in the introduction, we now present novel three-and-four-component DWCs, and discuss their benefits. Since this is a continuation of our prior work,[5] we refer the reader to our earlier article for aspects that are only briefly covered here.

2.1 Three-component FTC DWCs

In Figures 1c, 1f, and 1i, we respectively show the DWCs that are obtained when the two columns of the configurations in Figures 1b, 1e and 1h are incorporated into a single shell with a vertical partition. Since these DWCs are derived from Figures 1b, 1e, and 1h, they have the same heat duty requirement as the FTC configuration.

The vertical partition in each of these DWCs starts at one of the ends of the column and is continuous. The liquid transfer that is shown is made around the vertical partition. A unique feature about these DWCs is that the vapor flows in both parallel zones, one on each side of the vertical partition, can be regulated using the heat exchangers at the top and bottom of the DWC. While the DWC in Figure 1f has one vapor split at the bottom of its vertical partition which can be controlled by the condensers at A, the ones in Figures 1c and 1i have none. The desired vapor flow in each parallel zone on either side of the vertical partition of the DWCs in Figures 1c and 1i can be maintained by generating the respective quantity of vapor in the reboilers of the column. Alternatively, one could use valves at appropriate locations in the vapor lines to control the vapor flow in each zone adjacent to the vertical partition. This feature of being able to establish the desired quantity of vapor flow during operation in each parallel zone is absent in the conventional DWC,[6] shown in Figure 2, which can be derived from the configurations in Figures 1a and 1d by incorporating their columns into a single shell. In this DWC, during operation, there is no

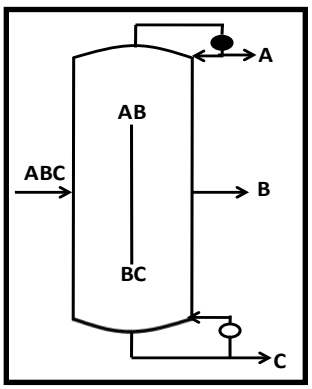

Figure 2. Conventional 3-component FTC DWC

external independent control on the split of vapor at the bottom of the vertical partition, and hence, the vapor flows in the parallel zones on either side of the vertical partition are unregulated. On-site implementation of such a DWC may thus often lead to suboptimal operation, unlike the ones proposed here. Thus, we expect the three options in Figures 1c, 1f and 1i to be more operable than the one shown in Figure 2.

2.2 Four-component FTC DWCs

The 4-component FTC DWC is shown in Figure 3. According to the available literature,[7] there has not been a single industrial implementation of this DWC. One important reason for this is the inability to independently control the vapor split during operation at the bottom of its three vertical partitions. Even if this DWC is implemented in future, we believe it is unlikely that its benefits will be fully realized because of these operational difficulties. To circumvent these operational complications, we look towards equivalent FTC configurations and consider their dividing wall implementations.

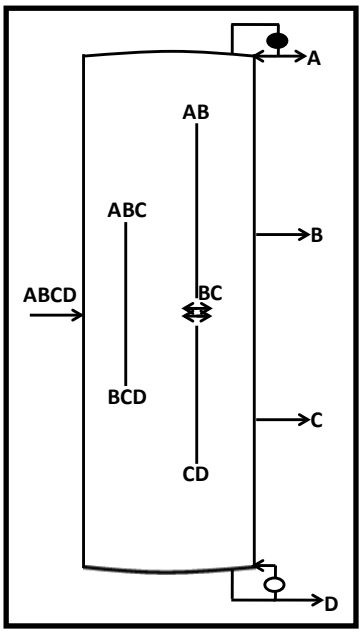

Figure 3. Conventional 4-component FTC DWC

Interestingly, all the thermodynamically equivalent FTC configurations obtained by moving sections around columns[8] result in the same DWC, which is shown in Figure 3. Alternate FTC-equivalent DWCs have hitherto been unknown to verify their operability. However, based on the discussions in the previous section, there is hope of deriving novel FTC-equivalent DWCs by converting thermal coupling links to liquid-only transfer streams, and identifying the more operable ones out of these. We provide one demonstration of this conversion for four component mixtures in Figure 4, where the thermal coupling at submixture ABC is converted to a liquid-only transfer stream. Apart from the DWC in Figure 3, there are 35 FTC-equivalent DWCs with three vertical partitions, including the one in Figure 4b. Among these, we have identified 5 DWCs in which the vapor flow in every parallel zone alongside every vertical partition can be regulated during operation either by the use of heat exchangers or other associated equipment like valves at the top and bottom of the column. The five DWCs are shown in Figure 5. We believe that these DWCs will enable the successful industrial

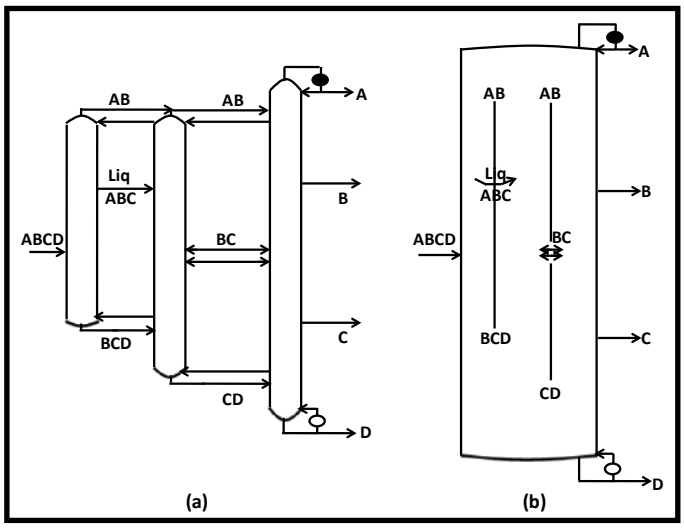

Figure 4. (a) A 4-component FTC-equivalent configuration; **(b)** Novel DWC implementation of (a)

implementation and optimal operation of the 4-component FTC configuration.

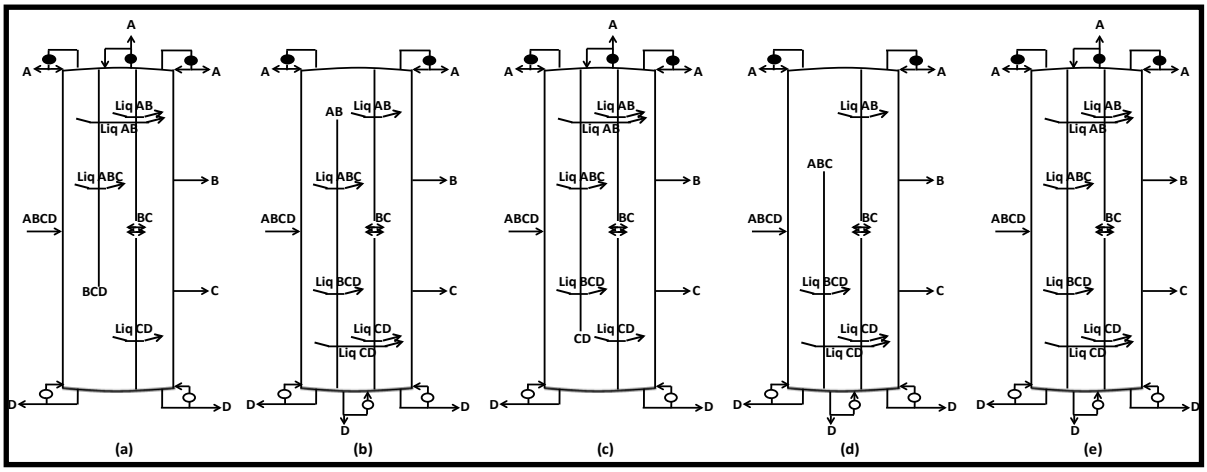

Figure 5. More operable 4-component FTC-equivalent DWCs

While there are only 5 more operable 4-component FTC-equivalent DWCs, this number significantly increases if we make a small modification to the FTC configuration. In the FTC configuration, to simplify operation, the back-and-forth liquid-vapor communication associated with submixture BC can be replaced by a simple liquid one-way communication. With this modification, we expect the resulting configuration, though not equivalent to the FTC configuration, to have a heat duty demand for most applications to be comparable to that of the FTC configuration. Such a modification eliminates the need to transfer vapor stream in the middle of the dividing wall (location BC), and therefore, eliminates discontinuity in this dividing wall. This results in only two vertical partitions in the dividing wall implementation. With fewer vertical partitions, the number of vapor splits is fewer, and hence, we can expect a larger number of *modified-FTC*-equivalent DWCs that are more operable. In all, there are 36 *modified-FTC*-equivalent DWCs. Of these, we have identified 15 DWCs in which the vapor flows in all parallel zones adjacent to all the vertical partitions can be regulated during operation. To demonstrate that constructing DWCs based on *modified-FTC*-equivalent configurations can yield significantly larger number of more operable options than FTC-

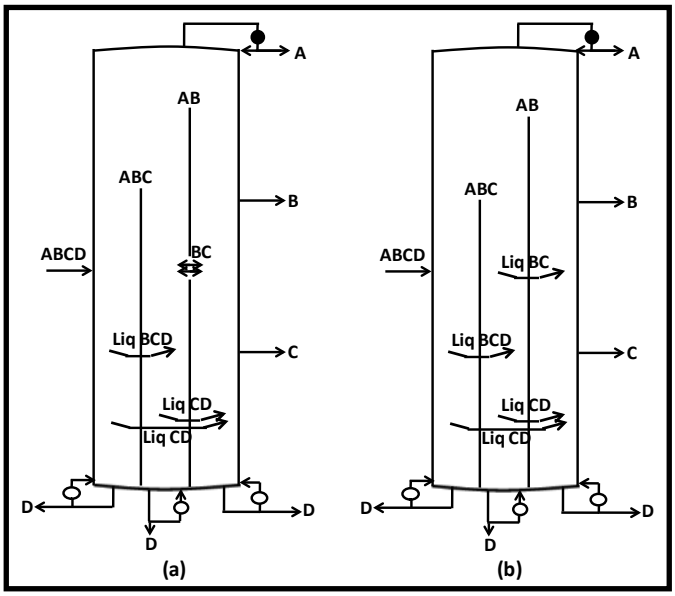

Figure 6. (a) A 4-component FTC-equivalent DWC; **(b)** A 4-component *modified-FTC*-equivalent DWC

equivalent configurations, we use the DWCs shown in Figures 6a and 6b as examples. The difference between the two DWCs is only the nature of mass exchange associated with submixture BC. While the vapor split at submixture BC in the FTC-equivalent DWC of Figure 6a cannot be independently regulated during onsite operation, the vapor flow in each parallel zone of the *modified-FTC*-equivalent DWC in Figure 6b can be externally controlled during operation.

3. Conclusions

The DWCs derived from the conventional FTC configuration has certain operational complications associated with it. The 3-component FTC DWC has an unregulated vapor split at the bottom of its vertical partition during operation. Due to this, the benefits that a 3-component FTC DWC offers are often lost because the operating conditions are suboptimal. This problem is further compounded as the number of components in the feed increases due to an increase in the number of unregulated vapor splits in the corresponding FTC DWC. This is perhaps one reason why an FTC DWC of four components or higher has never been built and operated.

In this work, we introduce new DWCs by laying out a framework to convert FTC configurations to FTC-equivalent configurations with liquid-only transfer streams, which are then implemented into new DWCs. For three components, all three FTC-equivalent DWCs that are proposed here are found to be more operable than the conventional FTC DWC because the vapor flow in each parallel zone alongside the vertical partition can be independently regulated during operation. Hence, these DWCs can be operated closer to optimality.

For four components, thirty five FTC-equivalent DWCs with three vertical partitions are identified. However, among these, only five have the ability to independently manipulate the vapor flows during operation in all the parallel zones adjacent to the vertical partitions. If one modifies slightly the 4-component FTC configuration, fifteen other *modified-FTC*-equivalent DWCs with similar operability features and comparable heat duty demand can be constructed. We believe that these twenty DWCs provide options that can be successfully implemented in an industrial setting allowing for the first time to reap the full benefits of a 4-component FTC configuration.

References

1) Agrawal R, *AIChE Journal*, 46(2000) 2198-2210
2) Petlyuk FB, Platonov VM and Slavinskii DM, *International Chemical Engineering,* 5(1965) 555-561
3) Fidkowski ZT and Krolikowski L, *AIChE Journal*, 32(1986) 537–546
4) Agrawal R and Fidkowski ZT, *AIChE Journal*, 44(1998) 2565-2568
5) Madenoor Ramapriya G, Tawarmalani M and Agrawal R, *AIChE Journal*, submitted
6) Wright RO, (1949). US Patent 2,471,134.
7) Dejanovic I, Matijasevic L and Olujic Z, *Chemical Engineering and Processing: Process Intensification,* 49(2010) 559-580
8) Agrawal R, *Chemical Engineering Research and Design*, 77(1999) 543-553

Energy and economic trade-off in partially adiabatic distillation columns

J. Rafael Alcántara-Avila, Ken-Ichiro Sotowa, Toshihide Horikawa

Department of Chemical Science and Technology, The University of Tokushima, Tokushima 770-8506, Japan

Abstract
The trays in conventional distillation columns are adiabatic since heat is neither supplied to nor removed from them because heat exchange only exists at the reboiler and condenser. However, diabatic distillation columns (DDC) can realize heat integration at each tray along the distillation column. DCC have been researched from the exergy point of view and have shown that they can attain the minimum entropy production rate for the separation of a multicomponent mixture into two product streams (Hirata, 2009). However, DCC might be unfavorable from the economic point because a heat exchanger is requested at each tray along the column, which results in a large number of side heat exchangers, thus an increase in the equipment cost. Therefore, this increase might take over the operating cost savings resulted from energy reduction. In this research, the trade-off between energy consumption and the total annual cost in partially diabatic columns is assessed through process simulations and optimization techniques based on mathematical programming where the location, number of heat exchangers and the amount of heat exchanged are the optimization variables.

Keywords
Process design, Heat integration, Diabatic distillation column, Optimization

1. Introduction

Distillation is a separation technology that repetitively boils liquid streams and condensates vapor streams from the bottom at high temperature the top of the column at low pressure. Although distillation columns are energy-intensive units with low thermodynamic efficiency, they are widely used in the Chemical industry.

In addition, the energy is supplied at the bottom of the column, which is at the highest temperature, while the energy is removed at the top of the column, which is at the lowest temperature. If energy can be supplied at temperature lower than that at the reboiler and removed at temperature higher than that at the condenser, economic and energy savings can be attained as well as the thermodynamic efficiency can be improved.

Conventional distillation can be regarded as adiabatic distillation because the is not heat exchange in the trays in the column. If heat can be exchanged in the stages of the column, the distillation column can be regarded as diabatic distillation.

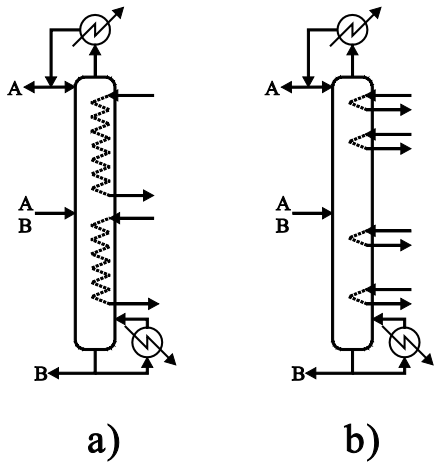

Figure 1: Totally and partially diabatic distillation column

In this work diabatic distillation is divided in two types: 1) totally diabatic distillation column (TDDC) in which all the stages are heat-integrated, and 2) partially diabatic distillation column (PDDC) in which only few stages are heat-integrated. Hirata (2009) studied the TDDC and compared it with the heat integrated distillation column (HIDiC) and vapor recompression column (VRC). His results showed that TDDC was better than VRC and HIDiC in terms of entropy production. In the other hand, PDDC was addressed by Chen et al. (2013) for the separation of a binary mixture and by Alcántara–Avila et al. (2013) for the separation of a ternary mixture. In both works, the optimal solution with the minimum cost realized heat integration in locations other than condensers and reboilers. Figure 1a shows the PDDC while Figure 1b shows a TDDC.

In Figure 1, A is the light component and B is the heavy component. The dotted lines represent heat exchange in the column. The presented TDDC has two diabatic stages in the rectifying section and two in the stripping section.

The aim of this work is to assess the PDDC and several optimal TDDC in terms of energy consumption and total annual cost (*TAC*) for the separation of a binary mixture. It also aims to explicitly evaluate the trade-off between the number of optimal intermediate heat exchangers and the amount of energy allocated at each intermediate heat exchanger. The synthesis procedure combines rigorous simulations and the solution of a mixed integer linear programming (MILP) problem.

2. Design of diabatic and adiabatic distillation columns

2.1 Simulation of the conventional column

Given the feed flow rate, composition and operating pressure, a distillation column can be designed by manipulating the reflux ratio and reboiler duty to attain the specification of the products leaving the column. In this research, Aspen Plus 8.0 was used to simulate a conventional distillation column, which is the starting point to design TDDC and PDDC. The *TAC* of the conventional column was minimized according to Equation 1

$$TAC = FC/PT + OC \cdot OT \tag{1}$$

where *FC* and *OC* are the fixed cost and operation cost. *PT* is the payback time, and *OT* is the annual operation time. *FC* is a function of the diameter and number of trays

in each column, reboiler and condenser heat duty and transfer areas while *OC* is the product of the utility costs by heat duties. This research adopts the Guthrie method proposed by Seider et al. (2009) to calculate the fixed cost.
For the conventional column sequence, the reflux ratio and the reboiler heat duty are used to adjust the product composition. Thus, the variables which can be used for optimization are: 1) The number of stages, and 2) Feed stage.

2.2 Optimization of TDDC and PDDC

Optimal TDDC and PDDC are obtained by minimizing Equation 1 through the solution of an MILP problem. Since the optimization of TDDC and PDDC is more complex than conventional distillation, additional optimization variables are needed. Thus, the variables which can be used for optimization are: 1) number diabatic stages, 2) location of diabatic stages, and 3) heat exchanged at each diabatic stage. The solved MILP problem was adopted from one of our previous works by doing minor modifications (Alcántara–Avila et al. 2013).

3. Results and discussion

The benzene/toluene separation was taken up to find optimal the TDDC and several PDDC and compare them with the conventional column. Table 1 summarizes the parameters used to solve the optimization procedure shown in section 2. Additionally, the assumed *PT* was set at 3 years while *OT* was 8000 hours. The heat transfer coefficients for condensers and reboilers were 0.7 and 1 kW/m^{2}K. The utility cost of cooling water was 0.86 $/MWh, and that for steam was 11.06 $/MWh. These parameters were taken from Seider et al. (2009).

Table 1: Parameters used in the optimization algorithms

Feed	flow rate [kmol/h]	: 100
	composition (benzene/toluene) [mol%]	: (50/50)
Benzene product	composition [mol%]	: 99.5
Toluene product	composition [mol%]	: 99.5
Operating pressure [bar]		: 1.0
Diabatic stages	(lower bound, upperbound) [-]	: (0, 25)
Heat exchanged at diabatic and adiabatic stages		
	(lower bound, upperbound) [kW]	: (0, 1200)

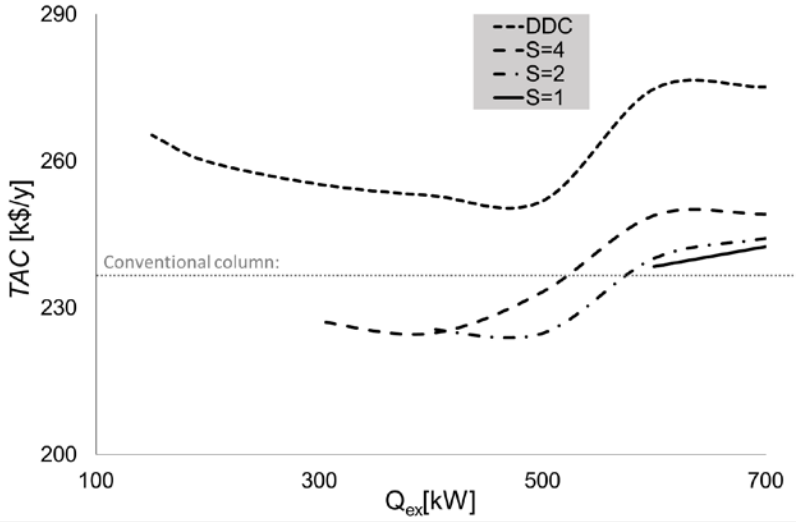

Figure 2: Relation between *TAC* and the possible number of diabatic stages

Figure 2 shows the optimization results of *TAC* minimization for the conventional, TDDC and PDDC. In the figure, S denotes the maximum number of possible diabatic stages. In the figure, the *TAC* of optimal TDCC and PDCC are represented by solid and dotted black lines while the dotted gray line represents the values of the conventional column which was 237.29 k$/y. The structures below this gray line implies that economic savings are possible in PDCC when the number of diabatic stages is between 2 and 4 at the rectifying and stripping sections. Also, economic savings are possible when the heat exchanged in diabatic and adiabatic stages is below 550 kW.

As for the TDDC, economic savings were not attained regardless the values of the maximum amount of energy exchanged at diabatic and adiabatic stages. This is because a large number of heat exchangers must be installed, which results in high *TAC*. In addition, three types of heat exchangers were considered. If the heat transfer area was higher than 200 ft, floating head and kettle reboiler where used at the condenser and reboiler, respectively. If the heat transfer area was lower than 200 ft, double pipe heat exchangers were used. Therefore, economic savings were attain when the floating head and kettle reboiler were used at the adiabatic stage and double pipe exchangers at diabatic stages.

Figure 3 shows the PDDC with the minimum *TAC* (224.7 k$/y) which has 4 diabatic stages while Figure 4 shows the PDDC with the minimum *TAC* (224.8 k$/y) which has 2 diabatic stages. In both cases most of the energy is removed at diabatic stages close to the adiabatic stages (i.e., condenser and reboiler).

In Figure 3, 400 kW are supplied to stage 2, 308 kW to stage 3, 6 kW to stage 15, and 6 kW to stage 16, respectively. In addition, 8 kW are supplied to stage 28, 9 kW to stage 29, 324 to stage 31, and 400 kW to stage 32, respectively in diabatic stages. In Figure 4, 500 kW are supplied to stage 2 and 116 kW to stage 3, respectively. In addition, 137 kW are supplied to stage 31 and 500 kW to stage 32, respectively in diabatic stages.

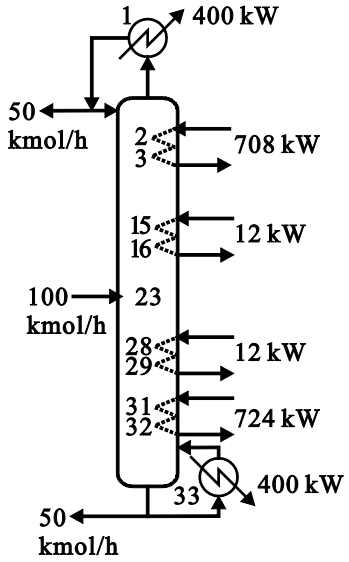

Figure 3: Optimal PDDC with 4 diabatic stages

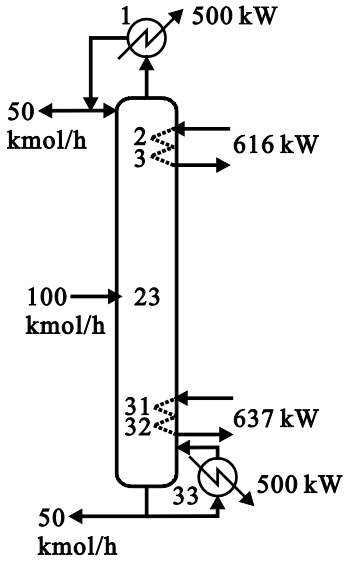

Figure 4: Optimal PDDC with 2 diabatic stages

4. Conclusions

Totally and partially diabatic distillation columns were obtained through combining rigorous simulations and optimization techniques based on mathematical programming. The objective function was to minimize the total annual cost. The totally diabatic distillation column did not attain economic savings because cost of the side heat exchangers, thus the fixed cost was larger than that in conventional distillation, however, partially diabatic distillation columns attained economic savings around 5 % when several types of heat exchangers are considered. Energy savings can be larger if more expensive utilities are used at adiabatic stages.

The optimal location of diabatic stages was close to the location of adiabatic stages, and the amount of energy exchanged at each diabatic location was large for stages near the top or bottom of the column while it was low for stages near to the feed.

Partially diabatic distillation columns proven to be more appealing than the totally diabatic distillation column in terms of economic savings. From the control viewpoint partially diabatic distillation columns because they are less integrated than totally diabatic distillation columns.

References

J. R. Alcántara–Avila, M. Kano, S. Hasebe. New synthesis procedure to find the optimal distillation sequence with internal and external heat integrations. *Ind. Eng. Chem. Res.*, 2013, 52, 4851–4862.
D. Chen, X. Yuan, L. Xu, K. T. Yu. Comparison between different configurations of internally and externally heat-integrated distillation by numerical simulation. *Ind. Eng. Chem. Res.*, 2013, 52, 5781–5790.
K. Hirata. Heat integration of distillation column. *Chem. Eng. Trans.*, 2009, 18, 39–44.
W. D. Seider, J. D. Seader, D. R. Lewin, S. Widagdo. Product and Process Design Principles. Asia: John Wiley & Sons, Inc. 2010.

Retrofit of distillation columns together with their heat transfer devices

Mohammed Awwal Suleiman, Megan Jobson
School of Chemical Engineering and Analytical Science
The University of Manchester, Sackville Street, Manchester, M13 9PL, Manchester, United Kingdom

Distillation columns are integral to most chemical processes. Increasing the throughput of an existing column can create significant economic benefits. However, capacity limits (or bottlenecks) of the column must be considered when throughput is increased. Retrofit options for distillation processes include minor modifications, such as feed conditioning, intermediate heat exchange and adjusting operating conditions. Hydraulic analysis tools have been developed to screen for effective retrofit modifications based on column hydraulic performance. However, the effects of these modifications on the performance of heat transfer devices associated with the column have not been investigated. This research considers bottlenecks in the reboiler, condenser, feed preheater, etc. if the feed to the column is increased.

A systematic approach for retrofit is proposed using process simulation, hydraulic analysis and heat transfer models. These models capture interactions between the column and associated heat transfer devices. For example, increasing feed preheating may avoid heat transfer and hydraulic constraints in the reboiler but might create a bottleneck in the rectifying section or preheater.

The new methodology complements existing column retrofit methodologies by systematically generating and evaluating options to overcome bottleneck in the reboiler when column throughput is increased. Case studies illustrate the approach.

Wastewater Ammonia Stripping with Closed Air Loop System

Peter Faessler, Sulzer Chemtech, Process Technology, Allschwil, Switzerland

Abstract

Wastewater from biological fermentation processes often comes with a significant content of ammonia. Being a strong biocide, free ammonia has to be removed to acceptable ppm levels before entering further biological treatment.
A multinational company, with a plant located in Thailand, produces a wastewater stream with a free ammonia content up to 3,000 ppm, that has to be treated to reach a maximum ammonia content of 100 ppm. The flow rate is 40 m^3/hr.
The solution provided consists of an ammonia stripper, operated at atmospheric pressure, using a closed air loop, conveyed by a standard type ventilator, and sulphuric acid in a chemisorption unit to neutralise the stripped free ammonia.
In-line pH control for fresh sulphuric acid dosing, as well as a density control, ensure that an ammonium sulphate solution of 40 wt% can be produced. This may then be directly sprayed as fertilizer on the local pineapple fields.
The plant concept, combining heat integration and the use of structured packings with minimized overall pressure drop, ensures very low operating costs in view of energy consumption.
Robust long term operation and flexibility regarding feed, ammonia content and capacity are additional advantages.

Keywords
Wastewater, ammonia stripping, closed air loop

1. Introduction

Wastewaters containing ammonia exceeding a certain limit (typically around hundred ppm) cannot be treated in biological treatment units as ammonia acts as a biocide. Physical steam or air stripping is a common praxis to lower the ammonia content to acceptable concentration levels. Shifting the ammonia from the liquid into the vapor phase can, however, often create another, environmental issue and therefore nowadays is no longer a way to solve the task. In case the stripped ammonia cannot be reused or recycled, it must be treated additionally in such a way that no emissions into the atmosphere will occur.

2. The closed air loop system

The closed air loop system consists of a **s**ingle „ALL-IN-ONE“ column set-up, integrating the stripper and chemisorption section into one column shell.

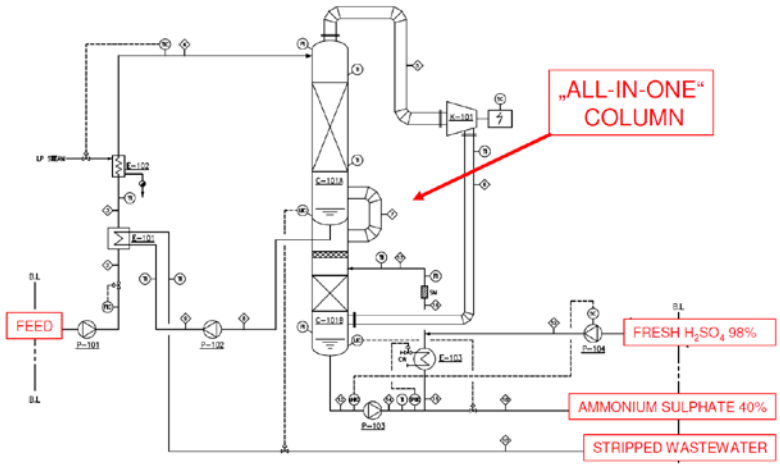

Figure 1 Flow diagram

The system consists mainly of:

- Ammonia stripper and chemisorption section, designed as pumparound and combined in a single column
- Heat integration with simultaneous heating of raw and cooling of stripped wastewater
- Additional cooler and heater to meet specific conditioning of the relevant streams
- Ventilator
- Sulfuric acid dosing system
- Pumps
- Control system

Features:

- The use of high performance packing provides a high stripping and absorption efficiency with a compact design and a minimum air circulation rate. Typically MellapakPlus™ 252Y, in stainless steel for the stripper and in polypropylene for the chemisorber, are used.

Figure 2 MellapakPlus™ in PP and stainless steel

- A low pressure drop over the packing and vapor piping, as well as an integrated economizer plate heat exchanger in connection with the closed air loop (with the need of only marginal additional heating and cooling), result in low operating cost.
- The column shell and main piping can be made of stainless steel, Glass Fiber reinforced Plastic (GFP) and/or carbon steel with rubber lining.
- An ammonium sulfate solution with a concentration of up to 40 wt% can be achieved, which can be directly used as fertilizer.
- The use of undiluted sulfuric acid is possible.

Purpose of the heat exchangers:

- Economizer: Heats and cools the feed to achieve an optimum stripping temperature.
- Heater: Balances the remaining temperature gap from the economizer and compensates heat losses in the circuit due to ammonia stripping out of the liquid phase.
- Cooler: Removes reaction heat from the ammonia neutralization with sulphuric acid. It also controls condensation of water vapor from the saturated air loop.

In this way the ammonium sulphate solution concentration is controlled.

Density of aqueous ammonia sulfate solutions

%	0°C	20°C	40°C	80°C	100°C
1	1.0061	1.0041	0.9980	0.9777	0.9644
2	1.0124	1.0101	1.0039	.9836	.9705
4	1.0248	1.0220	1.0155	.9953	.9826
8	1.0495	1.0456	1.0387	1.0187	1.0066
12	1.0740	1.0691	1.0619	1.0421	1.0303
16	1.0980	1.0924	1.0849	1.0653	1.0539
20	1.1215	1.1154	1.1077	1.0883	1.0772
24	1.1448	1.1383	1.1304	1.1111	1.1003
28	1.1677	1.1609	1.1529	1.1338	1.1232
35	1.2072	1.2800	1.1919	1.1731	1.1629
40	1.2350	1.2277	1.2196	1.2011	1.1910
50	1.2899	1.2825	1.2745	1.2568	1.2466

Table 1 Densities of aqueous ammoniumsulfate solution [1)]

2.1 Typical example

A wastewater stream out of a fermentation process containing 2,000 wt ppm free ammonia needs to be treated to reach a final concentration of no more than 100 ppm to make it fit for further biological treatment. Gaseous emissions are to be avoided.

The stripped ammonia in the vapor phase shall be converted into an ammoniumsulfate solution with a concentration of 40 wt% to be directly used subsequently as liquid fertilizer.

Low operating costs, operational flexibility to cater for fluctuations in the ammonia concentration and the flowrate of the feed, as well as a robust performance are additional requirements.

Feed and Products					
Stream Description		FEED	STRIPPED WATER	FRESH H2SO4	AMMONIUMSULPHATE SOLUTION
Temperature	C	30.000	31.000	30.000	58.465
Total Molecular Weight		18.015	18.017	90.068	27.707
Total Enthalpy	M*WATT	1.395	1.426	-0.012	-0.044
Total Sp. Enthalpy	KJ/KG	125.573	129.971	-197.545	-217.126
Total Actual Density	KG/M3	992.802	993.690	1797.874	1215.823
Total Mass Rate	KG/HR	40000.000	39494.941	223.500	728.618
Total Weight Comp. Percents					
AMMONIA		0.200	0.010	0.000	0.000
H2O		99.780	99.970	2.000	59.495
HEAVIES		0.020	0.020	0.000	0.010
AIR		0.000	0.000	0.000	0.000
SULFURIC ACID		0.000	0.000	98.000	0.004
AMMONIUM SULFATE		0.000	0.000	0.000	40.492

Figure 3 Feed and products

Beside the stripping efficiency, one of the other key points for an economical operation of the plant is the overall pressure drop of the entire air loop system, which includes packings for both a stripper and an absorber, and adjacent piping. This has a direct impact to the ventilator design and operating cost. Figure 4 shows the plant's overall pressure drop depending on plant capacity.

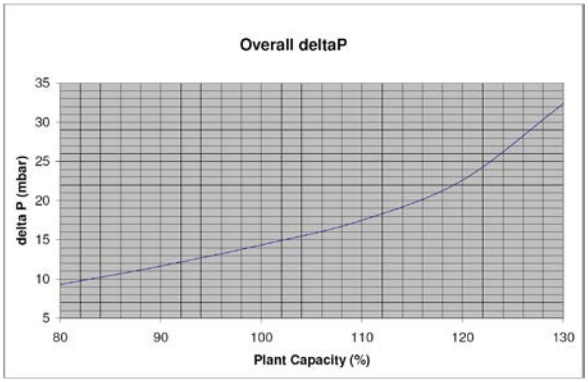

Figure 4 Overall plant pressure drop at different capacities

At fixed operating conditions, the required air circulation rate is almost linearly in line with the plant operating capacity.

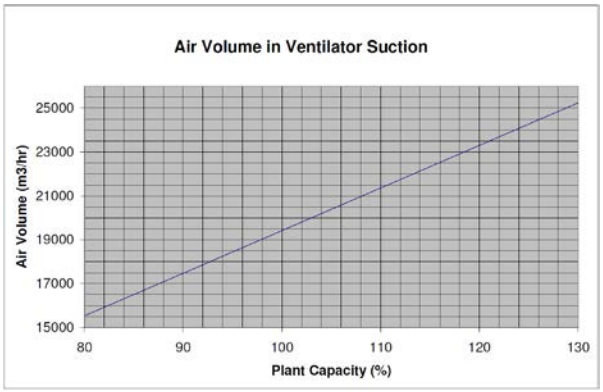

Figure 5 Required air circulating volume at different capacities

The heating and cooling utility requirements are, respectively 180 kW for steam and 150 kW for cooling water.

The economizer (internal heater and cooler) has a duty of approximately 1,315 kW.

The compression ratio (P_{out}/P_{in}) is typically in the range of 1.03 - 1.07, depending on the plant capacity.

The electrical energy consumption depends on the ammonia concentration in the feed and product stream, as well as on the selected ventilator type and manufacturer. Standard ventilators can be used for this purpose. For the current example it equals approximately 3-5 kWhr/m³ wastewater.

Figure 6 Example of Ventilator

2.2 Operational flexibility

The plant design is flexible enough to process ammonia feed concentrations within a specified range. The main operating parameter to be adapted is the operating temperature.

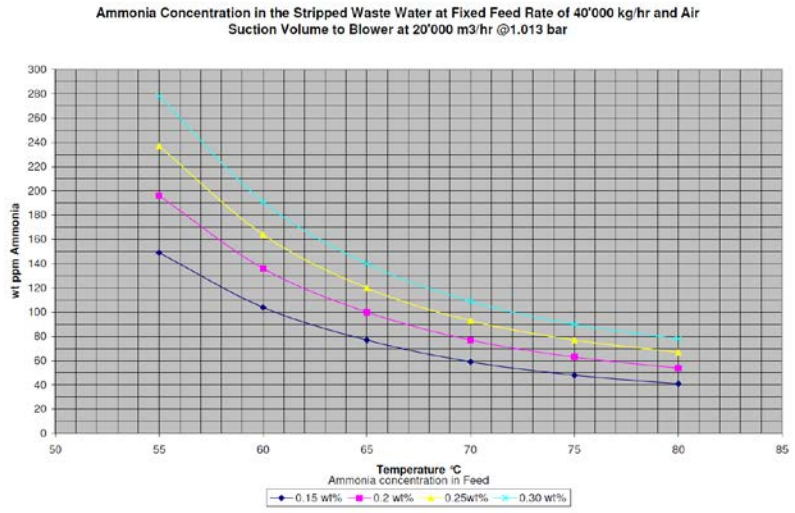

Figure 7 Operational flexibility at different ammonia concentrations in feed

2.3 Additional design considerations

The decade long experience available, ensures a reliable, but also compact, thus economic design.

➢ Stripping Section

Fluid Data:	Top	Btm
Gas:		
Mult. Vapor Rate [kg/h]:	19050.7	18843.3
Density [kg/m³]:	0.977	1.004
Viscosity [cP]:	0.0183	0.0183
QV [m³/s]:	5.42	5.21
Liquid:		
Mult. Liquid Rate [kg/h]:	40000.0	39792.6
Density [kg/m³]:	980.00	981.94
Surface Tension [mN/m]:	66.06	66.56
Viscosity [cP]:	0.447	0.467
QL [m³/h]:	40.82	40.52
System Factor:	1.00	1.00
Calculated Output:		
Capacity [%]:	63.0	61.7
F-Factor [Pa0.5]:	2.36	2.30
Spec. liquid load [m³/m²/h]:	17.98	17.85
Pressure drop [mbar/m]:	1.80	1.72
Flow Parameter:	0.066	0.068
Liquid Holdup [%]:	5.2	
Bed pressure drop [mbar]:	13.50	

➢ Absorption Section

Fluid Data:	Top	Btm
Gas:		
Mult. Vapor Rate [kg/h]:	19050.0	18843.2
Density [kg/m³]:	1.050	1.013
Viscosity [cP]:	0.0184	0.0183
QV [m³/s]:	5.04	5.17
Liquid:		
Mult. Liquid Rate [kg/h]:	54084.1	54292.3
Density [kg/m³]:	1196.46	1193.79
Surface Tension [mN/m]:	67.00	66.50
Viscosity [cP]:	3.000	3.000
QL [m³/h]:	45.20	45.48
System Factor:	1.00	1.00
Calculated Output:		
Capacity [%]:	61.9	62.4
F-Factor [Pa0.5]:	2.28	2.29
Spec. liquid load [m³/m²/h]:	19.92	20.04
Pressure drop [mbar/m]:	1.30	1.33
Flow Parameter:	0.084	0.084
Liquid Holdup [%]:	6.5	
Bed pressure drop [mbar]:	1.97	

Figure 8 Ammonia stripper and chemisorber design

For the chemisorption section it is essential to avoid any carry-over of liquid droplets into the absorber to avoid potential corrosion issues. For this purpose an additional high efficiency Mellachevron™ demister, made in polypropylene (PP), is installed on top of the liquid distributor.

Figure 9 Mellachevron™ demister and liquid distributor in PP

However, the selected packing height in the absorber is on purpose selected small enough, so to allow a certain slippage of non-absorbed ammonia to pass through, neutralizing sulfuric acid droplets on their way to the absorber.

2.4 Operating experience

The plant mentioned as example has been in operation since autumn 2012 to the full satisfaction of the end client, with proven easy, reliable and robust operation.

3. Conclusions

The combination of compact column designs, the use of high efficiency packings with very low overall pressure drop, advanced heat integration and reliable, simple plant control leads to an economic attractive solution for both investment and operating costs. The absence of any exhausts and the possibility of direct use of the stripped ammonia in the form of ammoniumsulfate as fertilizer is a very environmental-friendly solution.

[1)] Perry's Chemical Engineers Handbook 7th edition. McGraw-Hill 1999

Optimization of an Industrial Batch Extractive Distillation Process

Laszlo Hegely, Peter Lang
Budapest University of Technology and Economics, Department of Building Services and Process Engineering, Budapest, Hungary

Abstract
The recovery of methanol by batch distillation (BD) and batch extractive distillation (BED) from a multicomponent azeotropic waste solvent mixture (acetone-methanol-THF-water-toluene) is studied. The organic impurities are removed in two fore-cuts. Water as solvent is able to remove methanol from beside these impurities, thus reducing methanol loss in the fore-cuts, therefore increasing the recovery of methanol. The optimization of both processes is performed by a genetic algorithm (GA) coupled with a professional flow-sheet simulator performing the dynamic simulation. The optimization variables are the reflux ratios of all operation steps, the termination criteria of the two fore-cuts, the location, flow rate and duration of solvent (water) feeding. The objective function to be maximized is the profit for one batch. The optimized BD and BED processes are compared with the one currently applied in the plant.

Keywords
batch distillation, extractive distillation, optimization, genetic algorithm

1. Introduction

For the separation of pharmaceutical waste solvent mixtures, batch distillation (BD) is frequently applied method. These (usually multicomponent) mixtures often contain several components forming azeotropes with each other, rendering the recovery of the main component by conventional batch distillation more difficult, or even infeasible. In these cases, a special (e.g. extractive) distillation method must be applied. In batch extractive distillation (BED, Yatim et al, 1993), a solvent (entrainer, S) is fed continuously into the column, changing the relative volatilities favourably.

BED is usually applied to extract pollutants of moderate concentration from the main component to be recovered. However, if S reduces the volatility of the main component, it can be then extracted from beside the pollutants of low concentration forming minimum azeotropes with it. These pollutants can be removed in fore-cuts, which, nevertheless, cause a loss of the main component, since they contain it in considerable amount. It is possible to reduce the loss of the main component with the fore-cuts by BED. However, the high amount of S fed renders the separation of the main component from it more difficult and the application of BED can be even uneconomical.

S-feeding can be started after the start-up of the column, or during the heating-up, as early as the vapour reaches the location of the feed, as suggested by Lang et al. (2006). A new BED policy, where S-feeding is applied only during the heating-up, was studied by Hegely et al. (2013) for the separation of a waste solvent mixture of a pharmaceutical plant containing methanol (B), THF (C), water (D) and toluene (E), from which methanol must be recovered in a purity of 99.5 mass%. The solvent was water. The new BED policy was compared with BD and the traditional policy of BED by laboratory and industrial-size experiments. The best results were obtained by the new BED policy. In this study neither the BD nor the BED policies were optimized.

Barreto et al. (2011a) optimized the heterogeneous BED of the chloroform-methanol azeotropic mixture by a GA coupled with a simplified model. The pollutant methanol was extracted with water. Barreto et al. (2011b) studied the same process, but by using a flow-sheet simulator and multiple objectives.
The aim of this paper is to optimize both the BD and BED separation of the mixture studied by Hegely et al. (2013). Optimization variables are the reflux ratios of all operation steps, the termination criteria of the taking of the first and second fore-cut and the parameters of water feeding (feed plate, flow rate, duration). The optimization was executed by a GA with ChemCAD performing the dynamic simulation. The objective function to be maximized is the profit for one batch.

2. Vapour-liquid equilibrium conditions

The charge contains 0.07 mass% A (acetone), 37.14 % B, 4.89 % C, 56.34 % D and 1.56 % E. The boiling points of these components and their azeotropes, together with the azeotropic compositions are given in Table 1. For VLE calculations UNIQUAC model is applied. The recovery of B is disturbed by the azeotropes B–C and B–E. (The low amount of A is removed without a significant loss of B). The addition of a moderate amount of water moves both relative volatilities away from 1.0 considerably (Hegely et al., 2013), that is, BED using water as solvent is suitable for the removal of C and E in the fore-cuts more efficiently and with lower loss of B than BD.

Component	T_{bp} (°C)	Composition (mass%)				
		A	B	C	D	E
A - B	55.3	86.6	13.4	-	-	-
A	56.3	100	-	-	-	-
B - C	59.5	-	30.0	70.0	-	-
B - E	63.6	-	71.5	-	-	28.5
C - D	63.9	-	-	94.3	5.7	-
B	64.7	-	100	-	-	-
C	66.0	-	-	100	-	-
D - E	84.4	-	-	-	19.7	80.3
D	100.0	-	-	-	100	-
E	110.6	-	-	-	-	100

Table1. Boiling points and compositions of the azeotropes

3. Separation methods

The BD separation of one batch consists of the following separation steps (Hegely et al., 2013):

- Step 0: heating-up of the column under total reflux. At the end of heating-up, the condensate is rich in B and C, compositions and temperatures start to stabilize.
- Step 1: taking the first fore-cut, which contains a high amount of C and E in addition to B. The first fore-cut is incinerated.
- Step 2: taking the second fore-cut, which contains more B and less pollutant than the first fore-cut. The aim of both fore-cuts is the removal of organic pollutants. The second fore-cut is recycled to the next batch in order to decrease the loss of B.
- Step 3: taking the main-cut that is the product B in high purity.
- Step 4: taking the after-cut, which is aqueous B. The aim of this step is to remove B from the still residue, so that the residue can be sent to biological purification. As the after-cut contains a considerable amount of B, it is recycled to the next batch.

In the BED process, the steps are the same as presented above, except Step 0, which can be divided into two parts:

- Step 0a: heating-up without water feeding. The step ends as the vapour reaches the top of the column.
- Step 0b: heating-up with water feeding. Water is fed continuously to the column causing a decrease in $x_{D,B}$ and an increase in $x_{D,C}$.

Water feeding can be stopped at the end of Step 0b or it can be still continued during Steps 1 and 2, as well. In the later case, the loss of B in the fore-cuts can be further reduced, but this dilutes the mixture from which B is to be recovered and can also increase the amount of the fore-cuts increasing the cost of incineration and energy.

4. Calculation method

The objective function (OF) to be maximized is the profit of the processing of one batch. It is defined as:

$$OF = p_B m_{MC} - c_{inc} m_{FC1} - c_{st} \frac{\dot{Q}_{st}}{r_{st}} t - c_{cw} \frac{Q_{cond}}{cp_{cw} \Delta T_{cw}} - c_{bio} m_{SR} \quad (1)$$

where m_{MC} is the mass of the main-cut, m_{FC1} is that of the first-fore-cut, m_{SR} is that of the still residue. p_B is the price of methanol (0.46 \$/kg), c_{inc} is the cost of incineration (0.21 \$/kg), c_{st} is cost of heating steam of 3 bar (57.6 \$/t), r_{st} is its heat of condensation (2263.5 MJ/t), $\dot{Q}_{st}$ is the heat duty (1800 MJ/h) and t is the duration of the whole process. Q_{cond} is total heat withdrawn by the cooling water, cp_{cw} is the specific heat of the cooling water and ΔT_{cw} is the increase in its temperature. c_{cw} is the cost of cooling water and c_{bio} is the cost of biological purification, which are neglected. (These are not debited to the solvent recovery plant). Therefore, operation cost is the term related to the heating steam.

The optimization is performed by a real-coded elitist GA written in VBA under Excel. GA was chosen as OF can only be evaluated by simulation, that is, with a black box approach. The parameters of the GA: mutation probability: 5 %, population size: 30, crossover probability: 70 %. OF is evaluated by dynamic simulation using different modules of the flowsheet simulator ChemCAD. The failure to reach the specified purity of B (99.5 mass%), is penalized by changing the value of OF to -10,000 \$.

The mass of charge is 22,675 kg. The column has 25 theoretical plates (excluding the condenser and reboiler). The top pressure of the column is atmospheric, the pressure drop: 0.25 bar. The hold-up of the condenser: 0.45 m^3, that of the column: 0.05 m^3/plate. The termination criteria for Steps 1 and 2 are optimization variables (Cr_1 and Cr_2), while the criterion for Step 4 is based on industrial experiences:

- Step 1: $x_{D,C} < Cr_1$ (mass fraction of C in the distillate)
- Step 2: $x_{D,C} < Cr_2$
- Step 3: $x_{MC,A} < 99.52$ mass%
- Step 4: $x_{SR,B} < 0.25$ mass% (mass fraction of B in the still residue)

4.1. Batch distillation

The optimization variables were the reflux ratios of the steps: R_1 (1st fore-cut), R_2 (2nd fore-cut), R_3 (main-cut), R_4 (after-cut), and the termination criteria of Steps 1 and 2 (Cr_1 and Cr_2). The lower and upper bounds for all reflux ratios were 0.6 and 15. The lower bound of both termination criteria was 0.05 mass%, the upper bounds were 40 % (Step 1) and 10 % (Step 2), respectively. However, the value of Cr_1 also acted as an upper bound for Cr_2. Another constraint is added in order to ensure the recyclability of the second fore-cut to the next batch: the B/C and B/E ratios in the

second fore-cut cannot exceed those of the policy applied in the plant (basic BD). Step 0 lasted 360 min. The results were compared with the basic BD, where $R_1=R_2=R_4=6$, $R_3=2$, $Cr_1=20$ % and $Cr_2=2$ %.

4.2. Batch extractive distillation

The duration of Step 0a was 160 min, after which water feeding (of 15 °C) was started. Step 0b was 200 min long. Nine variables were optimized: the 4 reflux ratios, Cr_1, Cr_2 and 3 new variables connected to water feeding. These new variables and their ranges were: feed plate (integer variable, counted from the top of the column with plate 1 being the condenser): $1 \leq f \leq 13$; flow rate: $0 \leq F_{water} \leq 3000$ kg/h; duration (even integer): $0 \leq t_F \leq 1000$ min. (Water feeding was always stopped at the end of Step 2, even if t_F had been longer.)

5. Optimization results

The results for basic BD (Table 2) will serve as a basis for comparison. The optimum results (after 100 generations) for BD (Table 3) show a significant increase (59 %) in profit compared to basic BD. The income increased by 8.3 % and the incineration cost decreased by 4.9 %. The duration of the processes was virtually the same.

	First fore-cut	Second fore-cut	Main-cut	After-cut	Income ($)	2397
R	6	6	2	6	Incineration cost	469
Duration (min)	404	342	590	446		
Mass (kg)	2232	1487	5211	1225	Operation cost	1635
A (mass%)	0.6	0.2	0.0	0.0		
B	46.8	81.4	99.5	67.3	*Profit*	*293*
C	43.4	8.7	0.2	0.0		
D	0.0	0.0	0.3	32.7		
E	9.1	9.8	0.1	0.0		

Table 2. Reflux ratios and results for the basic BD process.

	First fore-cut	Second fore-cut	Main-cut	After-cut	Income ($)	2597
R	6.22	3.07	3.05	5.41	Incineration cost	492
Cr	17.5	2.62	-	-	Operation cost	1638
Duration (min)	438	172	856	320	*Profit*	*467*
Mass (kg)	2341	1267	5646	880		
A (mass%)	0.6	0.1	0.0	0.0		
B	47.4	82.3	99.5	57.1		
C	42.4	7.8	0.3	0.0		
D	0.0	0.0	0.1	42.9		
E	9.6	9.8	0.1	0.0		

Table 3. Results for the optimized BD process.

R_1 is practically the same as in basic BD, but slightly greater amount of first fore-cut is taken, as Cr_1 us lower. The lower R_2 and higher Cr_2 result in a lower amount of fore-cut, and a lower loss of B (even if the B content is higher, Figure 1), and at the same time the shorter Step 2 enables a longer Step 3 without increased process duration. The increase of R_3 has a very significant effect, as a much higher amount

of main-cut can be obtained. Figure 1 clearly shows how much longer Step 3 became. Both the duration of Step 4 and the amount of the after-cut is lower, because B was already removed to a greater extent from the still during Step 3.

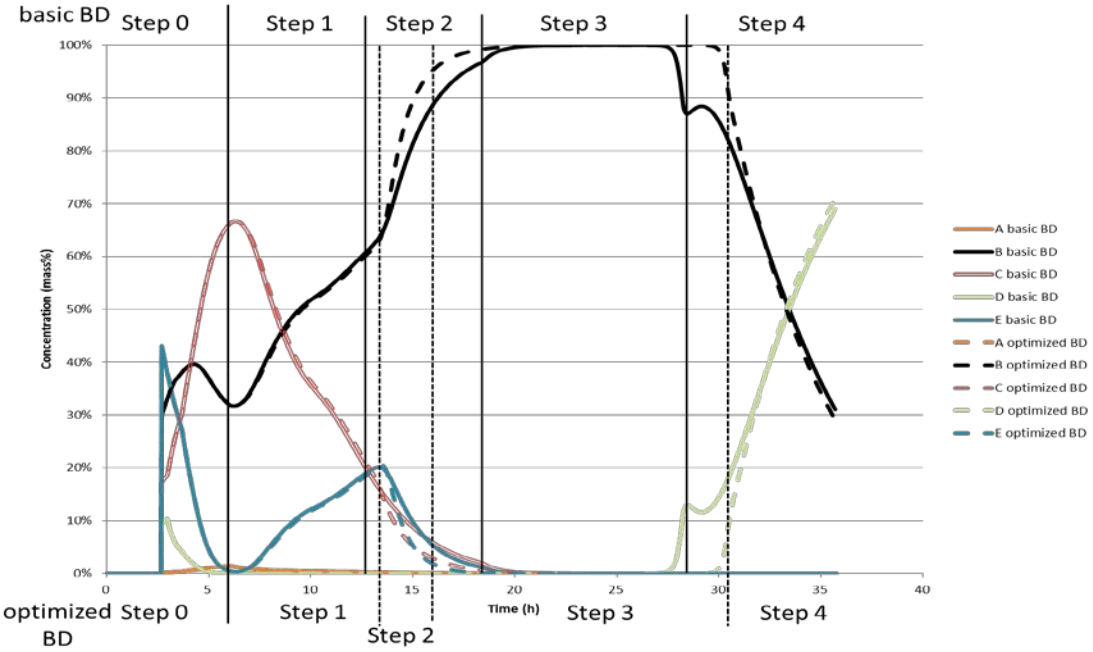

Figure 1. Evolution of condensate composition for the basic and optimized BD processes.

Comparing the results of BED (Table 4, Figure 2) and the optimized BD process, a further increase in profit (by 69.8 %) can be observed. Though process duration and thus operation cost increased, this was offset by a strong increase in income and decrease in incineration cost. Water feeding had important favourable effects. Although R_1 was slightly higher, the mass of the first fore-cut (and the duration of Step 1) was lower. The B content of the first fore-cut was much lower, which means a much lower loss of B, finally resulting in higher recovery by 15.6 % and higher profit. R_2 and R_3 are slightly higher, while R_4 is slightly lower. The optimal feeding location is the top plate of the column. Water feeding is still continued for 386 min during Step 1, as well. Its optimal flow rate is moderate, and therefore the liquid volume in the still never exceeds its value when the charge begins to boil.

	First fore-cut	Second fore-cut	Main-cut	After-cut	Income ($)	3003
R	7.74	3.41	3.48	4.72	Incineration cost	390
Cr	18.7	3.83	-	-	Operation cost	1820
Duration (min)	408	136	1092	388	*Profit*	*793*
Mass (kg)	1855	896	6529	1157		
A (mass%)	0.7	0.2	0.0	0.0		
B	22.9	85.2	99.5	52.3		
C	54.1	9.1	0.4	0.0	f	2
D	6.0	0.5	0.0	47.7	F_{water} (kg/h)	283
E	16.3	5.1	0.1	0.0	t_F (min)	574

Table 4. Results for the optimized BED process.

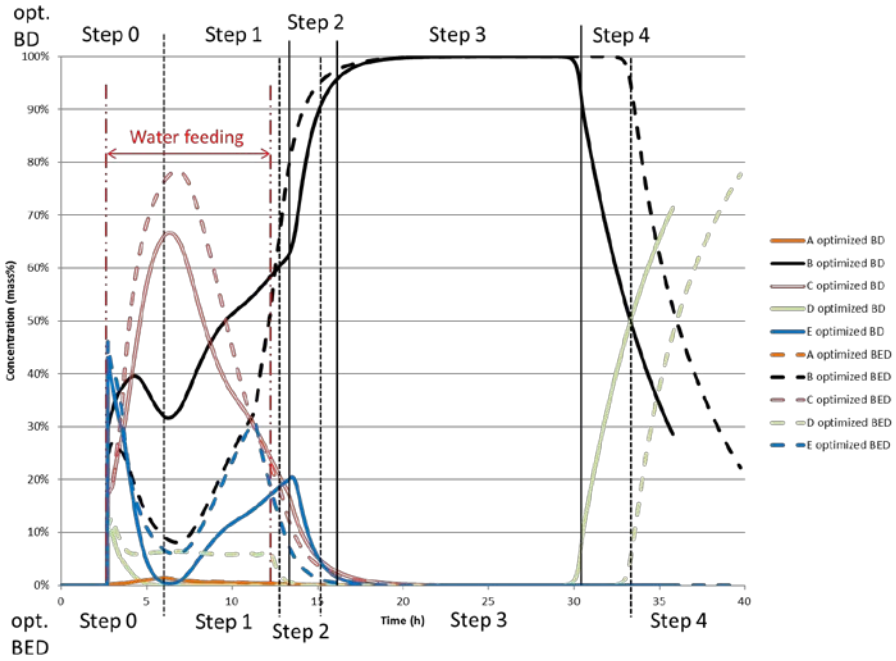

Figure 2. Evolution of condensate composition for optimized BD and BED.

6. Conclusions

The recovery of methanol from a multicomponent azeotropic waste solvent mixture was studied by dynamic simulation and optimization. The components of the mixture (acetone-methanol-THF-water-toluene) form several minimum azeotropes limiting the recovery of methanol by traditional batch distillation (BD). By batch extractive distillation (BED) using water as solvent (entrainer) the separation process can be made more profitable. The optimization of both BD and BED processes was performed by a genetic algorithm coupled with the ChemCAD professional simulator performing the dynamic simulation. The objective was to maximize the profit for one batch. The optimization variables were the reflux ratios of all operation steps, the termination criteria of the two fore-cuts, location, flow rate and duration of solvent feeding. The appropriate composition of the fore-cut to be recycled was ensured with additional constraints. Both optimized BD and BED processes provided much higher profit than the original BD process. The highest profit was reached by the optimized BED process.

Acknowledgements

The authors thank Gábor Modla for his help in the optimization. This work was supported by OTKA K-106286 and TÁMOP-4.2.2.B-10/1-2010-0009.

References

A. A. Barreto, I. Rodriguez-Donis, V. Gerbaud, X. Joulia, 2011a, Optimization of Heterogeneous Batch Extractive Distillation, Ind. Eng. Chem. Res, 50, 5204–5217.

A. A. Barreto, I. Rodriguez-Donis, V. Gerbaud, X. Joulia, 2011b, Multi-objective optimization of three-phase batch extractive distillation, Computer Aided Chemical Engineering, 29, 562–566.

L. Hegely, P. Lang, G. Kovacs, 2013, A New Batch Extractive Distillation Operational Policy for Methanol Recovery, Chemical Engineering Transactions, 35, 949-954.

P. Lang, G. Kovacs G., B. Kotai, J. Gaal-Szilagyi, G. Modla, 2006, Industrial application of a new batch extractive distillation operational policy, IChemE Symposium Series, 152, 830-839.

H. Yatim, P. Moszkowicz, M. Otterbein, P. Lang, 1993, Dynamic Simulation of a Batch Extractive Distillation Process, Comput. Chem. Eng., 17, S57-62.

Novel Developments in Tray Mechanical Design

Nicola Morotti, Greg Spencer, Neil Sandford
[1] *Koch-Glitsch Italia, Aprilia, Italy;*
[2] *Koch-Glitsch, Stoke-on-Trent, UK;*
[3] *Koch-Glitsch, LP, Wichita, KS, USA*

Abstract
Early distillation trays used very heavy construction techniques, often being built from plate materials welded directly to the pressure vessel shell. In the 1930s Glitsch introduced a lighter construction method using sheet metal components. The limitations of this construction method are mainly in maximum span length of the deck panels – beyond approximately 3 m [10 ft] in length the panels require additional beams for support.

As the size of new olefins and aromatics plants has steadily increased to benefit from economies of scale, we are seeing the need for structural beams more frequently. Structural beams must provide the structural support for the trays, respecting maintenance and operational loads while meeting required limits for deflection. At the same time it is important the structural beams do not interfere with the flow of liquid and vapour across and through the trays. The widely used method of trusses for tray support is effective in meeting these needs, but is very labour intensive in the field, often requiring the beams to be constructed from individual members that must be welded together inside the tower.

New mechanical design construction techniques using Sectionalized Beams and Ported Downcomers will be presented. These novel design improvements reduce material use and involve greater utilization of shop fabrication, reducing field installation time. The improved efficiencies of these designs result in significant time and cost savings. The new designs also allow improvements in resistance to the potential for damage caused by process upsets or harmonic vibration.

Keywords
Distillation, Tray, Mechanical, Construction, Beam

1. Introduction

The distillation equipment of a century ago used construction techniques that would today be considered excessive in terms of material thickness and weight. Tray deck panels were either fabricated separately from their supporting members or welded directly inside the pressure vessel. Glitsch introduced a more efficient lightweight construction method[1] in the late 1930s using support flanges that are formed integral to the active deck panels. Later developments included the introduction of finger joints that improved process performance by reducing the distance across tray joints while eliminating a major portion of the bolted connections required for installation. In the early 2000s FLEXILOCK™ tray construction[2] further improved on the finger joints by providing a positive locking connection between adjacent deck panels. This

significantly reduced tray installation time in the vessel shop or in the field and provided improved resistance to panels shifting due to upsets or vibration. One remaining area of high cost is the use of heavy and complex structural beams. We present some novel, recent developments in the mechanical design of trays and tower internals that aim to provide improvements in this area.

1.1 Traditional Tray Support Beam Designs

Current designs for distillation trays allow them to be self supporting up to a diameter of approximately 3 m [10 ft] depending on the applicable requirements for deflection and mechanical loading. Even for large diameter towers, if there is a sufficient quantity of downcomers, the downcomer may still be used to support the tray, though this may not always provide the most efficient use of materials. If the span of the horizontal, active decks between the downcomers exceeds 3 m (10 ft), major support beams will usually be required. These beams may be provided in a variety of configurations: 'C' channels; forged 'I' beams or; 'I' beams made using back-to back C channels. Depending on the required span of the beam, mechanical loading, and allowed deflection criteria, the beam thickness and depth may need to be increased. Ultimately the beam depth has to be limited to avoid unwanted interaction with the hydraulic and mass transfer operation of the tray. A common way to achieve the aims of support and deflection is by using trusses (Figure 1 – sometimes referred to as "lattice beams" – but, more correctly, this is a "Pratt" truss). The truss is a structural support constructed of an interconnected web of structural members. A single level of trusses is used to support two or more levels of trays. In rare cases the trusses may be shop fabricated and installed in the vessel – either during the initial construction phase before the vessel heads have been welded in place or via a larger than typical manhole access. Installation in the vessel shop requires careful coordination between the tray manufacturer (who will design the beams) and the vessel fabricator (who will install them). More typically the trusses are installed in the field. In cases of tower revamps when the beams require replacement or modification, field work is generally unavoidable.

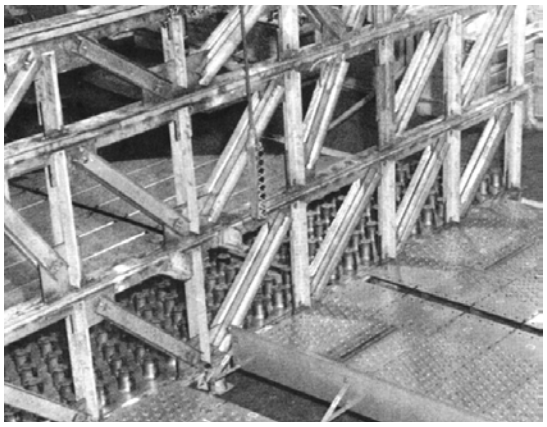

Figure 1 (from reference 8)

2. Improved Support Beam Designs

2.1 Sectionalized Beam

A recent development that is replacing the use of trusses and deep solid beams is the Sectionalized Beam[3] (Figure 2). The main concept of Sectionalized Beams is to provide a design that maximizes the use of shop fabrication and minimizes field work, particularly welding, to greatly speed up the

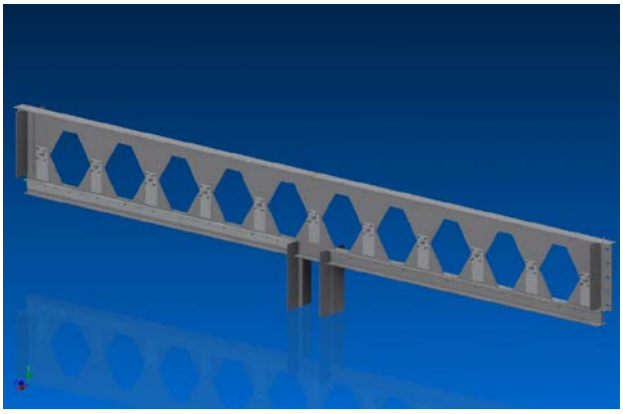

Figure 2

installation process. Sectionalized Beams, as with trusses, can be used to support multiple levels of trays. The beam is split into two sections longitudinally. In its simplest application where one beam is used to support two levels of trays, the two halves of the beam are only slightly more than one half of the nominal tray spacing in height, and so are capable of passing through a typical vessel manhole.

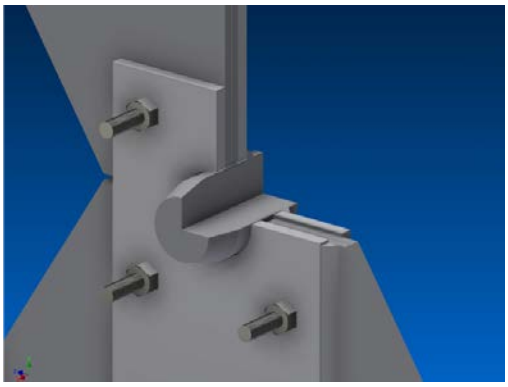

Figure 3

The lower half of the beam is installed first and levelled, using optional shims, on beam seats, one at each end of the beam. The upper half is then brought into the tower and connected to the lower section via locating holes surrounding a series of pins (Figure 3) that transfer the load from the upper beam segment to the lower. These load transferring pins and associated connectors also serve to stiffen the joint and resist lateral deflection. Openings in the beam provide necessary passages for communication of the froth and vapour space above the tray deck. Additional openings may be provided in the beam web as deemed necessary. Material utilization is extremely efficient since the two halves of the beam are cut from the same piece of raw material with minimal scrap.

Maintaining the effective levelness of the tray deck panels has been demonstrated to be important to ensure optimal mass transfer efficiency[4]. The two-part beam can readily be fabricated with an upwards camber to compensate for deflection, reducing the required thickness and weight of the beam. After adding the dead load of the tray deck panels and operating process fluids, the beam and tray assembly becomes level within the defined tolerance.

Weight savings compared to traditional trusses will vary depending on the tray spacing. In the example shown in Figure 4, an 8-pass high performance SUPERFRAC™ tray was supported using two Sectionalized Beams per each pair of trays. In this case the tray spacing was low enough that the complete beam was able to pass through the tower manhole. To further improve the speed of installation, the two halves of the beam were welded together in the Koch-Glitsch shop and supplied as a completed unit.

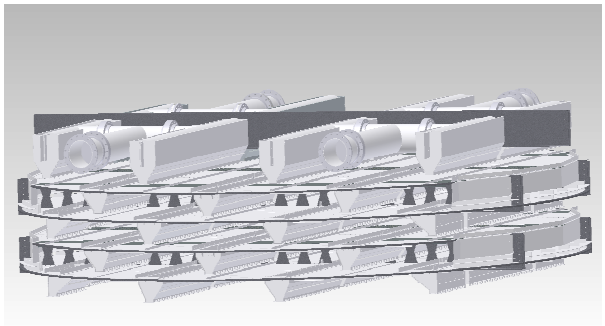

Figure 4

Compared to a traditional truss, the use of Sectionalized Beams allowed a weight savings of nearly 20%. At the time of writing, all fabrication is complete, but the trays have not yet been installed. Estimates are that the Sectionalized Beams will save at least eight hours per tray for the field installation time. This is especially significant considering that this olefins splitter tower has over 150 trays.

The beams in this ~10 m [~33 ft] diameter tower are fabricated with an upwards camber and on installation they will be level within a 6 mm [.236 in] tolerance.

2.1.1 Other Applications of Sectionalized Beams

The use of Sectionalized Beams is not limited to distillation trays – they have also found use to support other types of column internals, such as collector trays and the support grids for random and structured packed beds. In one such example, a ~9.5 m [31 ft] diameter refinery vacuum column required the emergency replacement of several large wash bed support beams that were severely corroded. Normally in such situations to avoid delays the original equipment is re-supplied exactly as originally made. In this case additional constraints included no welding allowed inside the tower and the beams to be removable through a 600 mm [24 in] nominal manhole size. The original trusses were replaced by new Sectionalized Beams.

2.2 Ported Downcomer Beam

Commonly, for trays that have downcomers, the downcomer is made in two pieces with only the upper section of downcomer used to support the horizontal deck of the tray. Frequently this requires that the upper downcomer be fabricated from a much thicker material gauge to provide the necessary support. The “Ported Downcomer” (Figure 5) is a new concept that was recently introduced and has now been applied in approximately 20 commercial designs. The Ported Downcomer uses the entire downcomer height as a beam, extending slightly through the tray below. The downcomer clearance, by which liquid exits from the downcomer, is in this case provided by a series of rectangular windows or ports – from which the device gets its name.

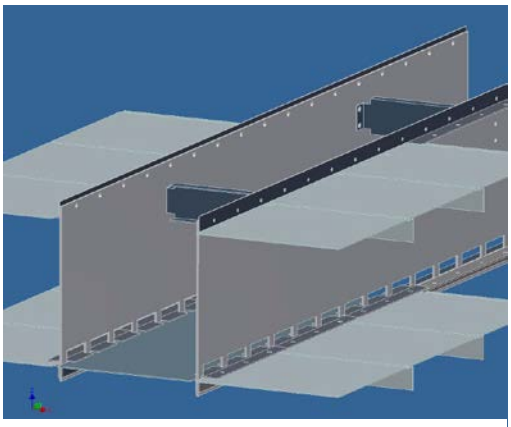

Figure 5 Patent Pending

The structural webs between the ports restrict the downcomer escape area to a small extent – in some cases this is desirable if the liquid rate is very low or if required to control the flows from off-centre downcomers of multi-pass trays. For a given required downcomer escape area, the use of ports will require a slight increase in the downcomer clearance. A common design practice for many years has been to make the outlet weir of the tray slightly taller than the downcomer clearance. In extreme cases with high liquid rates the increased ported clearances may result in a perceived loss of this static downcomer seal. In most situations the liquid rate is high enough that the downcomer remains dynamically sealed. The sealing mechanism for dynamically sealed downcomers is quite well understood[5], having been used with high performance trays, such as SUPERFRAC™ trays, for more than 20 years.

Ported Downcomers provide improved stiffness and reliability compared to traditional downcomer beam supported trays. The absence of major beams within the mass transfer zone of the tray results in improved hydraulic performance. Savings are also passed on to the vessel fabricator who has to weld in fewer beam seats. End reactions of the Ported Downcomer beam are transferred to the vessel wall through the downcomer bolting bars. Overall installation time in the vessel shop or in the field is reduced due to the reduced quantity of tray parts and reduced weight of major structural components. The two trays above and below the Ported Downcomer are

more positively coupled together, greatly reinforcing the entire tray structure. Additional reinforcing struts and shear clips can readily be applied if necessary for added resistance to uplift or vibration effects.

3. Tray Vibration

A number of studies have been made into the causes of tray vibration. Winter[6] notes that the auto-pulsation frequency increases with increasing tower diameter. Improvements in computer power have made techniques such as finite element analysis (FEA) much more readily available to engineers. Using such techniques we can now more efficiently evaluate the potential of large diameter tray designs for vibration issues.

3.1 Vibration Case Study

A new 4 m [14 ft] diameter distillation tower was to be constructed containing 2-pass trays. The client had a history of problems related to vibration-induced tray damage in a similar reference tower. Key targets for improvement in the new design were increased rigidity and higher fundamental resonance for improved resistance to flow-induced vibration. The reference design (Figure 6) used a network of shallow interconnected support beams. Multiple beams restrict tray accessibility and can impact tray performance. In particular, beams perpendicular to the liquid flow direction have been observed[7] to result in as much as 10% loss of tray capacity, depending on the beam depth and tray spacing.

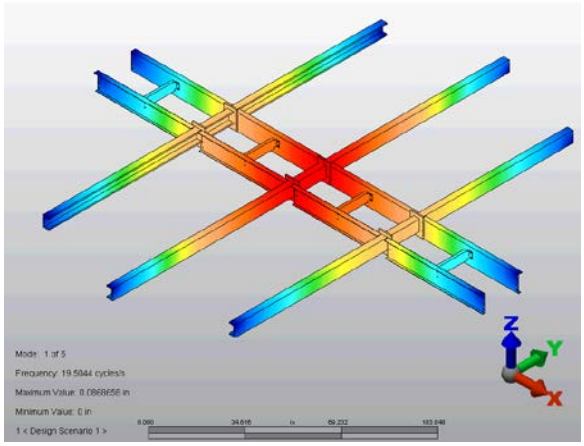

Figure 6

Two designs were evaluated: the first using Sectionalized Beams and the second using Ported Downcomers combined with integrated supports. The effectiveness of the proposed designs was evaluated using FEA (Figures 6-9) to determine the fundamental resonant frequency and compared with the reference design that was known to suffer from vibration-induced tray damage. The fundamental resonance predicted for the major support structure of the reference design was relatively low at approximately 19 Hz, and within a range that is commonly believed to be susceptible to excitement by flow-induced vibration within tray towers

3.11 Design Using a Sectionalized Beam

The first option used a single sectionalized major beam on the tower centreline, running parallel to liquid flow (Figure 7). This design showed a significant increase in the moment of inertia of the major support members which increased the fundamental resonance of the support structure from 19 Hz to 51 Hz. In addition

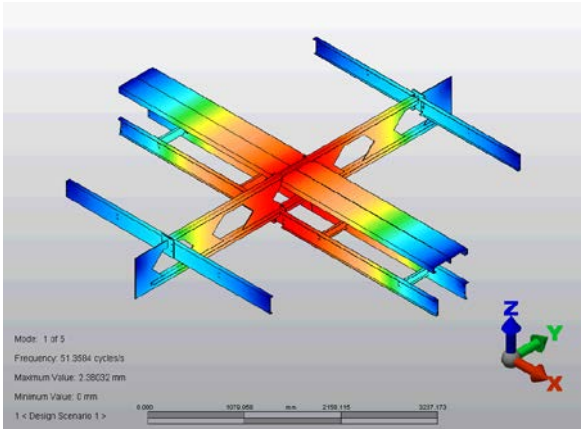

Figure 7

to the mechanical design improvements, there were additional benefits of improved access for maintenance.

3.1.2 Design Using Ported Downcomers

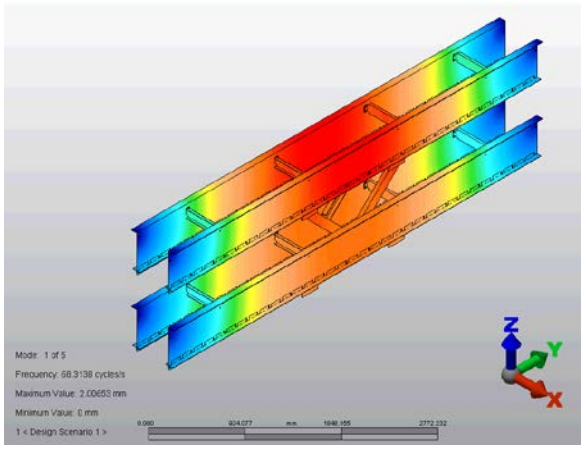

Figure 8

A second option used ported side and centre downcomer beams without any major beams (Figures 8 and 9). Additional reinforcement strutting was provided between tandem tray assemblies to interconnect all of the trays. This design increased rigidity and increased the fundamental resonance of the support structure to 68 Hz, yielding increased resistance to flow-induced vibration. Interconnecting the trays allowed the design to better accommodate any variations in the exciting frequencies in different sections of the tower.

Both designs eliminated the network of shallow beams, resulting in less segregation within the tray space for increased access during installation and maintenance of the trays. The improved access meant that fewer tray manways were required; resulting in fewer bolted connections and improved reliability. The new design also required simpler tower attachments to be welded to the vessel shell due to the need for fewer beam seats. A reduced overall quantity of tray parts also shortened the installation time.

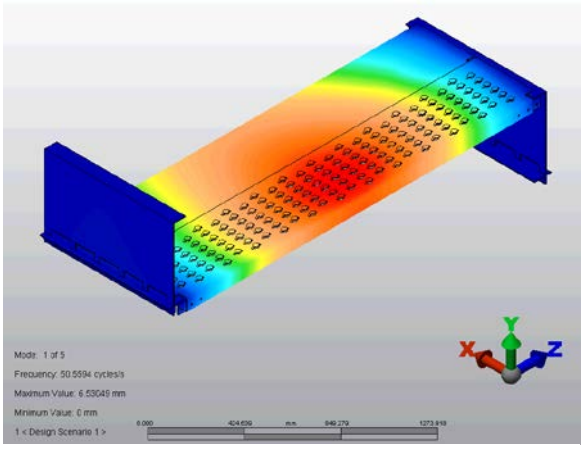

Figure 9

4. Conclusions

The alternate designs presented in this paper achieve significant improvements in the predicted natural frequency of the major support structure. Elevation of the natural frequency of the major support structure reduces the risk of excitement by flow-induced vibration within the system, as well as the risk of creating multiples that could support excitement by vibration in the active area of the tray.

While the Sectionalized Beam yields a necessary improvement in rigidity and represents a more effective design for installation, the Ported Downcomer beam provides the most optimal design in terms of rigidity, reliability, installation and access.

When evaluating the cost of a new large-diameter fractionation vessel, it is important to consider the method of structural support of the mass transfer internals as this can significantly impact the total installed cost. Alternatively, when revamping towers where structural beams require replacement, consider the time savings possible using new beam designs compared to traditional designs that may require significant amounts of welding inside the tower.

Acknowledgements
The authors wish to acknowledge the contributions of Darran Headley, Billy Unruh and Dave Ewy, all of Koch-Glitsch, LP, Wichita, KS, USA.

References
1. United States Patent Number 2,341,091 – Bubble Tray
2. United States Patent Number 6,592,106 – Locking Hinged Joint for Vapor-Liquid Contact Trays
3. United States Patent Number 8,485,504 – Apparatus for Supporting Internals Within a Mass Transfer Column and Process Involving Same
4. “The Evaluation of Out-of-Level Trays for the Improvement of Industry Guidelines“, Chemical Engineering Research & Design [Transactions - IChemE Part A] (Print 0263-8762; Electronic 1744-3563), Remesat, D., Chuang, K., Svfcek, W.
5. “High Capacity Nye trays”, International Conference Distillation & Absorption 1992, De Bruyn, G., Gangriwala, H.A., Nye, J.O.
6. “Avoid vibration damage to distillation trays“, Winter J.R., AIChE - American Institute of Chemical Engineers, May 1993, p 42-47.
7. “Hydraulic investigations to increase the capacity of trays in distillation columns“, AIChE Annual Meeting 2007, Friese, T., Joedecke, M., Schuch, G.
8. Ballast Tray Design Manual - Bulletin 4900 Sixth Edition, 100 year Anniversary Reprint 2013, Koch-Glitsch LP., Wichita, KS

A High Capacity Retray that Wasn't - A Practical Lesson in Counter-Intuitive Thinking

Sean Hennigan- Separations and Heat Transfer Advisor
BP Chemicals Ltd, Hull, United Kingdom

Abstract
This paper presents a column limitation problem that was diagnosed and solved by applying "technical troubleshooting" techniques. Powerful analyses from basic plant data can be employed to pin down where and why column limitations have been reached; these can be derived just from plant data and spreadsheets without a great deal of complex simulation. The problem diagnosed by this technique is also offered as a clear lesson on the need to follow through all the implications of changes to column design (and in this case changes to those changes) that often involve several iterations. A key and somewhat counter-intuitive point is that installing a high capacity device may not always make things immediately better, in this example the retray appeared to reduce capacity.

Keywords
Distillation, retray, troubleshooting, capacity, flooding.

1. Introduction

The following system as shown in Figure 1 was subject to debottlenecking. It is a medium sized, simple column that separates light component A from a set of heavier components characterised by a key component B for the purpose of this analysis. Component A is an impurity to be removed but has the potential to be a high value product in its own right , so there is economic incentive to keep the system steady and to keep overhead stream of this column as rich as possible in A.

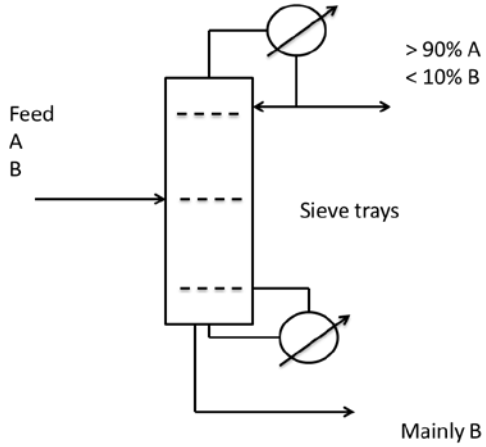

Figure 1

Lack of separation was noted as reduction in the absolute recovery of A overhead - analysis of tray performance both in-house and with the vendor suggested that the sieve trays in place were close to flooding, particularly in the column base and a plan was developed to preheat the feed to this tower to reduce internal loads below the

feed , (effectively keeping the same internal loads above the feed point through a fixed reflux ratio) and also retraying the tower throughout with higher capacity fixed valve trays. These new trays are based on the same active area as the existing trays so any increase in capacity should be modest (5-10%), but the open area was effectively doubled, which has a major effect on pressure drop.
Due to several issues with project scheduling a decision was taken to install the preheater at a later phase, and to go ahead with the retray only.
Upon restart it was immediately clear that pressure drop and stability of the column was worse than pre-retray conditions as was the recovery of A, all indicative of some kind of hydraulic problem within the column.
A detailed "*triple check*" analysis of flooding potential was employed to analysis this problem. If carried-out correctly this can provide a very powerful argument for the existence of a jet flood point and can pin down the loading at which this occurs to a very precise region. This analysis requires a set of real time plant data from a plant historian or similar software that can be easily transferred to spreadsheet format. The following calculation procedure was used..

- Determine the latent heat λ (kJ/kg), and liquid densities ρ_L (kg/m3) at bottom of the column. These properties are assumed not to change over the operating envelope.
- Develop a relationship between system pressure P_s (bara) and vapour density ρ_V (kg/m3) - this is easily obtained from physical property databases or approximating a function of density to system pressure and temperature. For the following analyses the density was approximated from the basic ideal gas equation ($P_sV = nRT_s$) taking the pressure and temperature from plant data and adjusting the molecular weight to match the predicted vapour density.
- Details of tray active area A_b (m2) are obtained from the tray data sheet.
- Gather plant historian data on column DP, measured reboiler duty and base, temperatures, process these data to give the following inferred parameters.

N.B. subscripts $_T$, $_B$ refer to column top and column bottom respectively.

Very simply, knowing the reboiler duty Q (kW) we can infer the vapour velocity (v_B m/s) on the tray active area at the lowest tray as follows..

$$v_B = \frac{Q}{\rho_{vB}.\lambda_B.A_{bB}} \quad ms^{-1}$$

Equation 1

The C factor (a simple measure of entrainment potential) can then be simply calculated at the bottom of the tower

$$C = v\sqrt{\frac{\rho_v}{(\rho_l - \rho_v)}} \quad ms^{-1}$$

Equation 2

According to Kister's rules of thumb (Ref 1) a typical limiting C factor around the threshold for jet flood for typical tray spacings of 18 -24 inches is 0.07 - 0.1 m/s for sieve trays and 0.09 - 0.12 m/s for valve trays.

A similar view is obtained from Branan (Ref 2) for trays with an F -factor of 0.1-0.2 which is in the region of operation of these trays.
Another rule of thumb derived from Lieberman (Ref 3) for the same kind of tray spacing and liquid specific gravity in the range of these components suggests that a measured tray pressure drop as high as 8-12 mbar/tray is likely to be an indicator of the start of entrainment.
A third guideline from several texts notably Kister (Ref 4) leads us to expect that if we plot some measure of column internal load, be it reflux + overhead flow or steam to the reboiler against column pressure drop we should expect a discontinuity in the curve when the column is near the flooding point .
The "*triple -check*" method incorporates all three of these rules into one picture, plotting the heat balance derived C factor along the abscissa and the pressure drop per tray (simply total pressure over number of trays) up the ordinate. If we see a change in gradient around C = 0.1 m/s and DP/tray of 10 mbar/tray then we will have located the column flooding limit by 3 independent measures.

2. Results and discussion

An analysis of the internal loads was carried out in this way based on the reboiler steam flow as a measure of the column internal loads - the vendor and internal simulations all suggested that the base of the column would be the highest load, even with feed preheat, so focussing in on flooding behaviour around the column base should give the clearest picture.

2.1 Analysis of column performance pre-retray and immediately post-retray

Figure 2 below shows the "*triple-check*" plot for both pre-retray and immediately post-retray data. For pre-retray there is an increase in the slope of the pressure drop vs C-factor data around 0.09 m/s and at a pressure drop of 11mbar/tray. All three of these criteria point to a column flooding condition for sieve trays.
For the post retray data the C-factor is around 10% higher than the pre-retray case even though the steam to the column is kept the same, plus the pressure drop per tray is generally higher, not lower as expected.
At face value the high capacity trays have delivered a worse performance than the old trays, which opened up several debates about tray quality, installation etc.
However because this "*triple-check*" method gives a much bigger picture of the column limitation this analysis was able to conclude a more subtle and counter-intuitive explanation and short term fix.

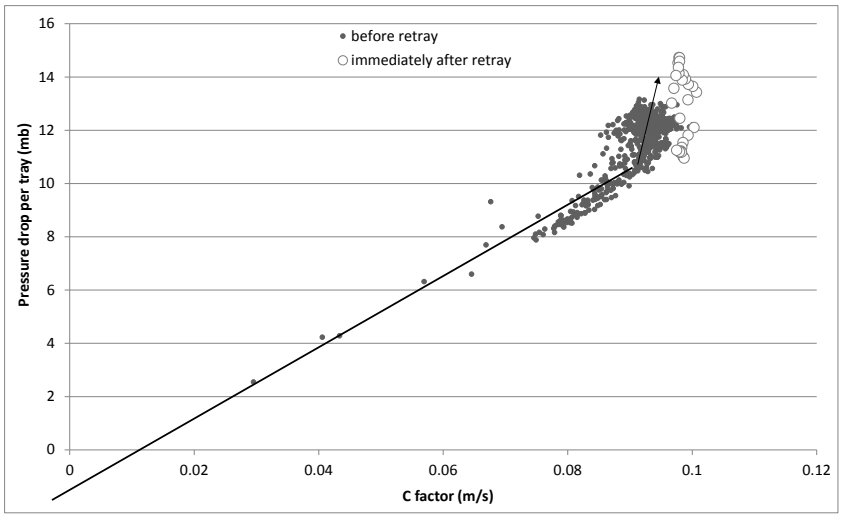

Figure 2

2.2 Analysis of column performance with increasing system pressure

A simple way to move a column away from jet flooding (particularly columns at low pressure) is to increase the system pressure. This was carried out in several stages and the curves below in Figure 3 show the effect of this (white circles were base case, diamonds were moderate pressure increases, crosses were the highest pressure). The plots show a tentative location for the new flood point for these new trays as there is a change in gradient at the highest pressures. More significantly the overall pressure drop of the system halved, the column became more stable and signs of improved recovery of A overhead was seen.

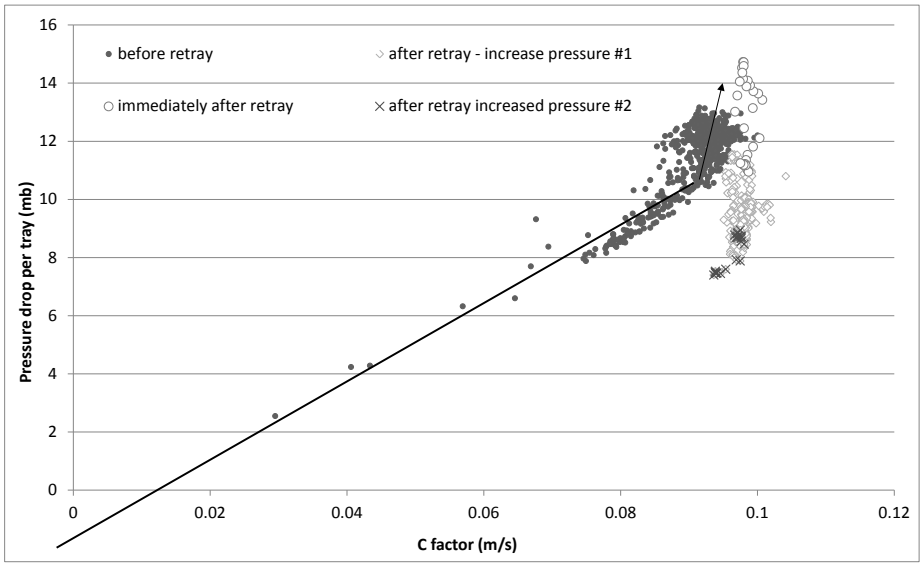

Figure 3

Figure 4 below shows the longer term performance of the system after continued effort to optimise head pressure. From this it can be clearly seen that the C-factor at flood is around 5-10% larger for the post retray case; a reasonable expectation for a sieves to valves revamp of the same active area. Without accounting for the effects of pressure the trays misleadingly appeared to have a lower capacity.

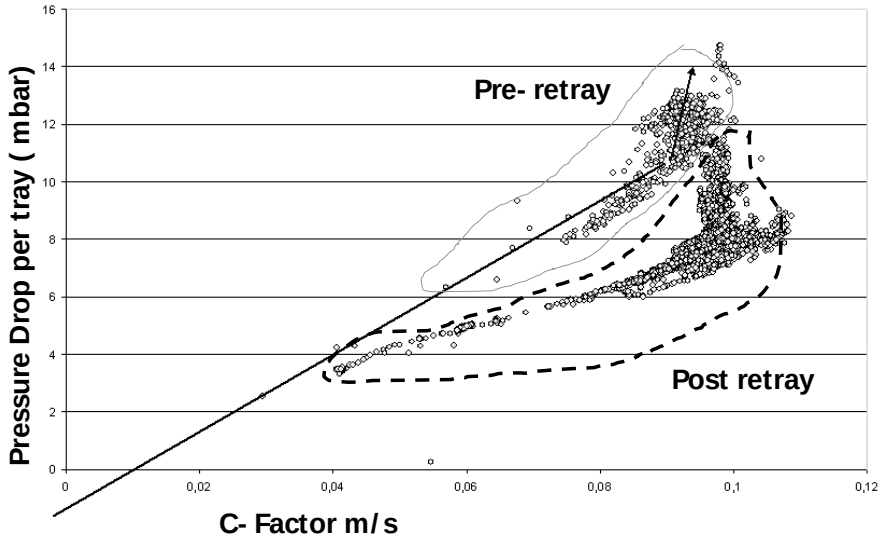

Figure 4

A flooding calculation was carried-out and summarised in figure 5 below. For this analysis the "Glitsch Equation 13" method (Ref 5) was used for the new valve trays and the FRI sieve tray model (Ref 6) for the old sieves. An 85% flood limit is a usual design guideline and clearly for the sieve tray case this was exceeded.
The yellow points show the pre-retray predictions for the sieve trays, the blue points show the same data based on the Glitsch Equation 13 calculation as a simple comparison of the potential benefit in going to valve trays with the same active area. The purple points show the calculated Glitsch Equation 13 flood on new data immediately after the retray. It is noteworthy that this is a very low surface tension system, so misses out on the crediting effect that surface tension can have on jet flood. Glitsch Equation 13 similarly does not credit for surface tension so it is perhaps not too surprising for a system like this to see real signs of flooding when the prediction is 85-90%.

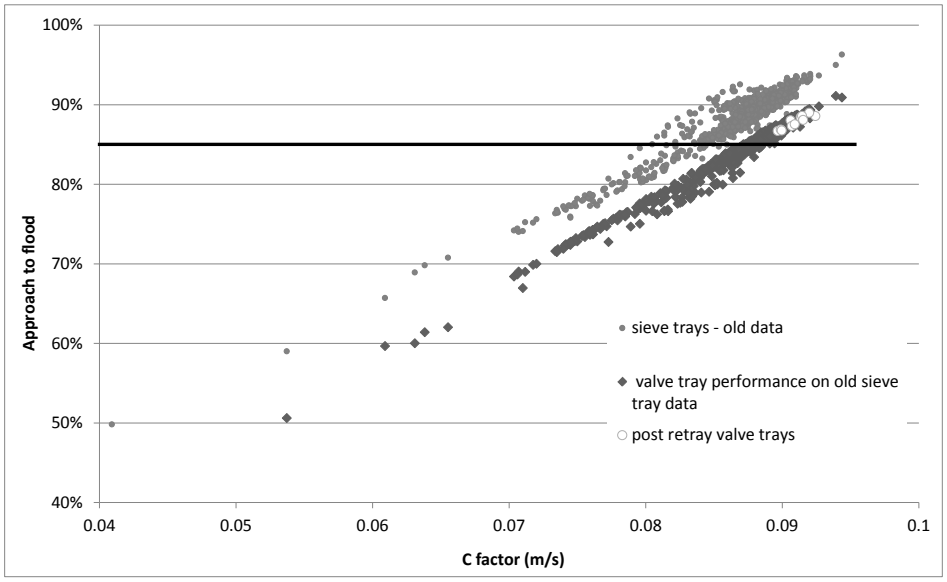

Figure 5

3. Conclusions

The key result from all of these analyses is the fact that the *C-factor at the base was higher* after the revamp. The process of installing the high capacity trays above the feed actually required the trays in the column base to do more capacity than they had gained. A lower pressure and therefore a lower vapour density and high vapour velocity was effectively being transmitted to the base trays, so without installation of feed preheat the real loading on the base trays is significantly higher than before. The new base trays have in theory a modestly higher capacity (recall that the active area is the same so one would not expect too much capacity increase), but were being loaded beyond this improved capacity due to the dramatic reduction in pressure drop (and hence pressure) above the lowest trays. For the full potential of the column to be realised, it needed both the feed pre-heat and the retray.
A moral from this experience can be simply stated: for low pressure systems avoid debottlenecking a tower by putting low pressure drop devices above the flooding pinch point unless you have fully accounted for the change in vapour densities. The low pressure drop transmits the low column top pressure to the bottom - even for the same mass loadings, the vapour velocities, C-factors and hence approaches to jet flood all increase in the column base. Carefully consider pressure drop implications and if necessary always iterate these changed pressure drops back into the sizing. This situation is particularly acute for packings over trays where the pressure drop can be an order of magnitude lower than the equivalent trayed system. Shortly after this experience in another part of the company a proposal to debottleneck the top of a column by going from trays to packing was swiftly re-appraised and rejected after applying these lessons.

Acknowledgements
The author acknowledges the invaluable contributions from the plant technical support engineers in gathering the all-important data (without which this paper would be just theory not evidence), engaging with and supporting the conclusions presented here enough to make the plant work better.

References
1 Kister HZ, Practical Distillation Course Notes 2006, IChemE
2 Branan CR, Rules of Thumb for Chemical Engineers p.90 1998, Gulf Publishing
3 Lieberman NP, Lieberman ET, A Working Guide to Process Equipment, p.12 1997, McGraw Hill
4 Kister HZ , Distillation Operation, p. 382 1990, McGraw Hill.
5 Ballast Tray Design Manual Bulletin 4900 6th Edition, p.26 - Glitsch Publication
6 F.R.I. Design manual p.4 -8, 2004. F.R.I. Publication

Influence of tray geometry and hydraulic conditions on vibration induced damages of sieve and valve trays

Christian Geipel[1], *Andreas Wolgast*[1]
[1]*RVT Process Equipment GmbH, Steinwiesen, Germany*

Abstract
The present paper is a summary of observations on failures of trays in various industrial applications. The affected trays include fixed valve trays (type SVG and SRV), movable valve trays (V1-valves and A3-cage valves) as well as sieve trays.
Different incidents are investigated to derive general indications that promote vibrations and – as a consequence – failures of the trays. The failures are analyzed with regard to valve types, special design features as well as operating conditions that lead to the failure. The basis is operating data and pictures of the damaged trays.
Also the failure modes of the trays are investigated in detail to derive the destruction mechanism. Where possible video sequences through a sight glass were taken in operating columns to visualize gas and liquid flow as well as vibrations. These findings were compared to experimental results in a pilot plant with a transparent column.
General design features that promote vibrations in combination with special operating conditions like low liquid load could be identified.
The position of all operating points in the operating range has to be carefully investigated with respect to parameters that influence tray vibrations.
Based on these findings, guidelines for potentially critical trays were derived. These include mechanical design criteria as well as process and hydraulic design guidelines.

Keywords
Tray vibration, mechanical failure, design guidelines

1. Introduction

Vibration induced tray damage is a known phenomenon since long time. First approaches to predict when harmful vibrations will occur date back to the 1970s[1] or even earlier. However, reliable theoretical models that predict vibration are still scarce. Rigorous guidelines that could be used during design of trays are still not publically available.
The present paper gives an overview on some reasons for vibration induced damages.
A phenomenon that is not further discussed here is heavy pressure fluctuations in the column. These could be caused by high liquid level in the bottom of the column flooding the bottom trays, steam hammering, vacuum collapses or e.g. free water flashes. Often one single incident already leads to destruction of one or several trays.

Other vibration phenomena mentioned in literature are caused by the gas-liquid interaction on the tray. Different root causes for vibration induced tray damage are distinguished:

- One reason is so called “liquid swashing”[3,4]. Under certain circumstances a standing wave across the column diameter can built up. The wave is perpendicular to the liquid flow, pulsating at low frequency. Typical frequencies are below 5Hz.
- Another type of vibrations occurs when the pulsations created by the gas-liquid interaction excite the resonance frequency of the tray. The excitation is created by the forces resulting from bubble formation or jet flow pulses at the valves or orifices[2,5]. This phenomenon is the most investigated among the listed effects, also because it often leads to tray damage within very short time. Several authors agree that resonance occurs at low liquid and gas loads. Therefore it can lead to tray damage already during turndown operation of the column at startup. Typical frequency of the tray vibration is in the range of approx. 15 – 40 (60) Hz.

Several authors have shown that only the gas load that was present during vibration did not lead to vibration on a dry tray.

2. Results and discussion

Subject of the present article is a summary of failures of operating trays in various industrial applications, including sieve, fixed valve and movable valve trays.
The following types of trays were affected by vibration cracking:

- Valve trays with big fixed valves: SVG and SRV
- Valve trays with movable valves: V1 and A3
- Failures for sieve and dual flow trays have also been observed

2.1 Characteristics of the affected trays

Mainly tray diameters in the range of 1800 - 3000mm with only one pass and resulting long weir lengths and sometimes huge enveloped downcomers were affected. It was observed that often designs with long tray segments were used. For bigger tray diameters >3200mm mainly two pass trays were affected.
All types of trays had integrated support beams (bent panel edges) and no lugs or support brackets below the downcomer.
Often the trays were designed for low Δp of < 20mmWC (dry) respectively gas hole velocities of <11m/s at 100% load.
The failures happened at operating points with low liquid load combined with low gas load and therefore at unit references below 100%.
In the following, the effects occurring will be explained exemplarily for trays equipped with V1 valves.

2.2 Investigation of tray failures of V1-valves

Figure 1 and 2 show operating points that lead to tray damage in production columns.

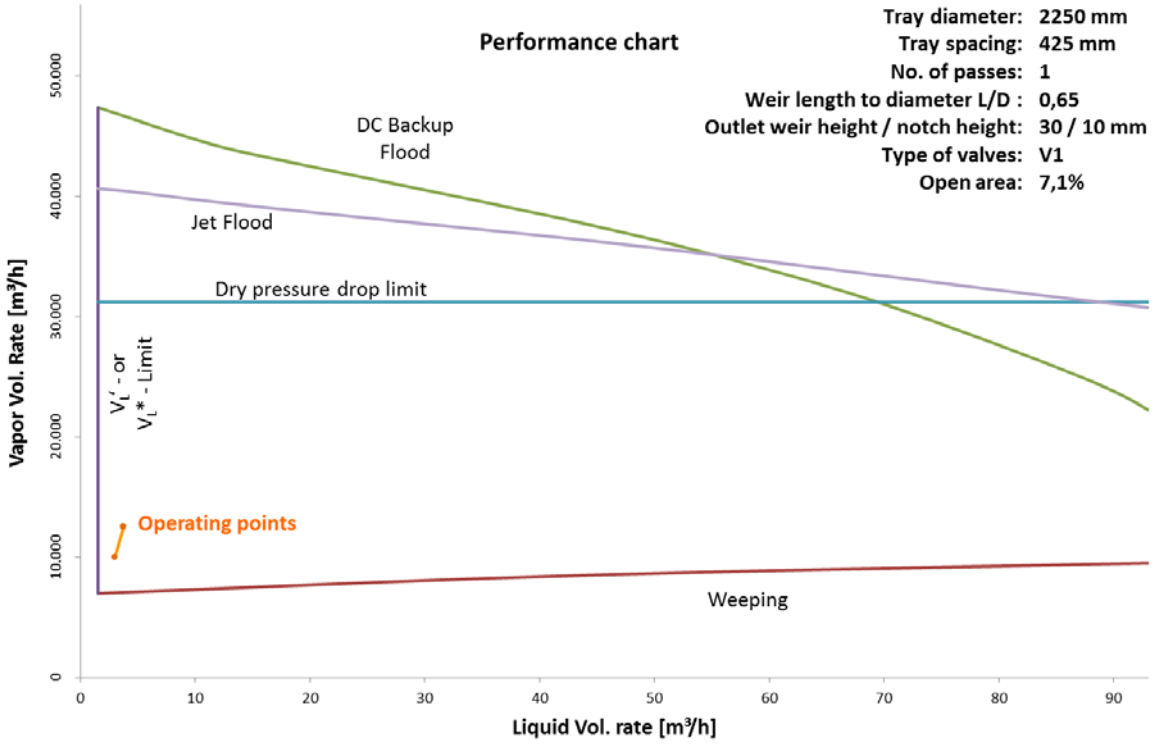

Figure 1: Operating points leading to damage, V1-valves, one pass

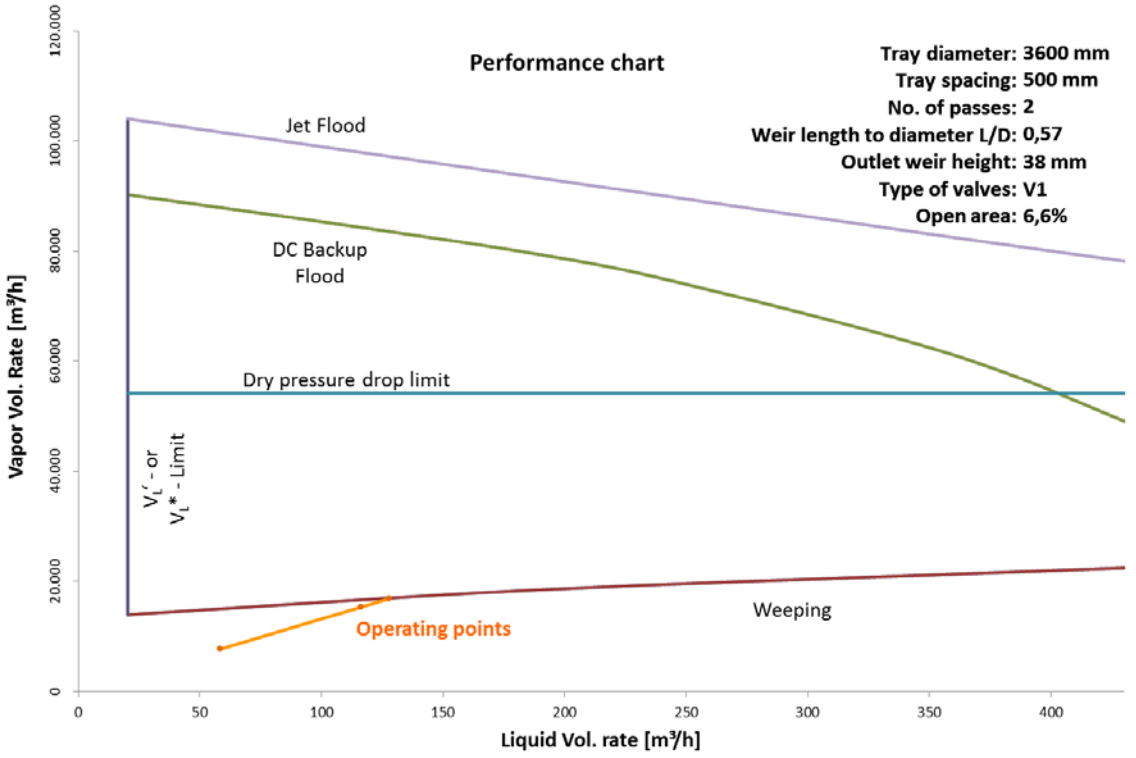

Figure 2: Operating points leading to damage, V1-valves, two passes

The failures in the two cases were quite similar to other cases examined: Vibration crackings in tray segments starting from the corner of the bent part through the next opening (screw or valve hole) and then in a zigzag pattern through the next valve or sieve holes (see Figure 3). Often pieces up to the size of a hand palm break out of the tray.

Figure 3: Typical failure patterns of V1-valve trays

Furthermore, whole tray segments were torn out of their bolting. The destruction is often more pronounced at the inlet side of the tray. It was observed that about 30-40% of the V1 valves were dislocated and traces of turning and scratching were observed on the top and bottom side of the tray (see Figure 3, right). This happened regardless of the valves being equipped with an anti-rotation device or not. From the valves that were found on the tray always one leg was broken off.
Cracks at the downcomer formed in parallel with the screw line at the small brackets fixing the downcomer wall. Also these brackets themselves often break (see Figure 4).

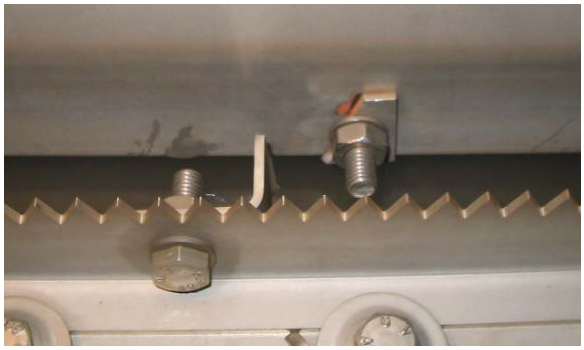

Figure 4: Broken downcomer bracket

The mechanisms leading to the failure were examined in several steps:

- First movies were taken through the sight glass of the affected columns. Even though the destruction had already happened, the trays were still vibrating at low frequency of < 5Hz with amplitude of approx. 20mm. *(-> movie will be shown during presentation)*
- In a second step pilot plant experiments in a transparent 1.5m column were carried out. The gas factor was varied in ranges close to those in the real column. It could be shown that in a certain range the valves started knocking synchronously. This already can be considered as one source of vibration, although the liquid will also have an influence on the forces on the tray. *(-> movie)*

- When the liquid load was added, heavy weeping was observed. Also, the height of the liquid level on the tray started pulsating. Consequently, also the flow over the weir pulsated heavily and there is an intermittent gas bypass flow through the downcomer. These pulsations lead to heavy vibration of the trays. In the pilot plant column we reached a condition where the trays were ruptured out of their boltings within seconds. *(-> movie)*

With these experiments the failure mode became much clearer. Similar experiments and theoretical investigations were also done for other valve types. The following general observations could be derived.

2.4 General observations for different valve types

Observations in pilot plant and industrial size columns showed that:

- Generally low gas loads – often combined with low liquid loads – can cause vibration of tray segments und thus damage of the tray
- If V1-valves are not fully open, they tend to knock in the same frequency
- If A3-cage valves are not fully open, they can show strong vibration and beat or clash
- A11-cage valves can show very strong vibration before they are fully open
- Already deflection of the tray segments in the range of ≥2mm can lead to gas/liquid maldistribution. In critical operation regions this maldistribution can lead to vibration. Also inclination of the trays and long flow paths favor vibration.
- The visible amplitude of the integrated support beams is often >20mm (at variable frequency)

3. Conclusions

The analysis of the above mentioned phenomena leads to the following guidelines for tray design if the tray is operated in regions where vibration is considered is to be possible:

- Avoid integrated beams and use separate beams with gusset plates, lugs etc.
- Use more, narrow segments instead of bigger ones
- Use thicker tray decks, e.g. 3mm instead of 2mm. The effect on Δp respectively weeping has to be considered!
- Where possible, use more robust caged valves instead of V1-valves
- Use reasonable turndown rates. Allow sufficient gas velocities resp. pressure drop, especially for crossflow trays
- Block weir length at low liquid load (no notches) and increase weir height (if possible)
- Use a combination of light and heavy valves if possible
- Use inlet weirs with liquid seals ≥15mm at low liquid loads
- For trays that operate in a regime that could favor vibration inclinations or deflections have to be strictly avoided!
- Also the operating range of the column should be defined carefully. Especially huge operating ranges combined with strict pressure drop requirements favor vibration in low load regions.

The above investigations have pointed out indications of proneness to vibrations of trays. The desired load points have to be checked carefully concerning their location in the tray performance chart. All operating points including startup, turndown etc.

have to be considered. If a risk of vibration is identified for a tray, the design criteria listed above should be considered.

Acknowledgements

We would like to thank all companies that were involved in our investigations on tray vibrations. The basis of the investigations was data from several plants and results could only be derived in valuable discussions with the plant and design engineers who shared their experience with us.

References

[1] Summers, D.R., “Bad vibrations”, Hydrocarbon Engineering, March 2005, pp. 51-54
[2] Summers, D.R., “Harmonic vibrations cause tray damage”, AIChE Annual Meeting 2003
[3] Winter, J. R., “Avoid vibration Damage to Distillation Trays”, Chemical Engineering Progress, May 1993, pp. 42-47
[4] Priestman, G.H.; Brown, D.J., “Flow-induced Vibration and Damage in Sieve-tray Columns”, Chem. Eng. Comm, 1988, vol 63, pp. 181-192
[5] Zeitsch, K., “Eine neue Theorie der Schwingungserregung an Kolonnenböden”, Chem. Techn. Heft 10, Oct. 1984, pp. 415-418

Separation of cyclohexene/ cyclohexane mixtures by a reactive dividing-wall distillation column with two reactive sections

Haiyang Zhang, Kejin Huang, Xinhui Yao, Chunying Xia
[1]Haiyang Zhang, Beijing, People's Republic of China;
[2]Kejin Huang, Beijing, People's Republic of China;
[3]Xinhui Yao, Beijing, People's Republic of China;
[4]Chunying Xia, Beijing, People's Republic of China

Abstract
A novel reactive dividing-wall distillation column with two reactive sections (RDWDC-TRS) was proposed for the separation of cyclohexene/cyclohexane mixtures, based on both a coupled process consisting of two reactive distillation columns and a dividing-wall column. The synthesis and design of the RDWDC-TRS were studied and the optimum process designs of the RDWDC-TRS and the coupled process were derived in terms of the minimization of total annual cost (TAC). Detailed comparisons were then conducted with the coupled reactive distillation columns in steady-state performance. It was found that the RDWDC-TRS was effective to separate the binary mixtures of cyclohexene and cyclohexane and achieve almost complete separation of the two components. In comparison with the coupled reactive distillation columns, the RDWDC-TRS featured a relatively high degree of reduction in capital investment and space. To the best of our knowledge, the structure of the RDWDC-TRS is firstly proposed for the separation of the binary mixtures of cyclohexene and cyclohexane.

Keywords
Reactive distillation; Integration; The coupled process; Dividing-wall column; Design

1. Introduction

Cyclohexene is widely used in industry as raw material for the synthesis of cyclohexanol, which can be manufactured from cyclohexene via one-step hydration in the "Asahi Process" [1]. However, under industrial conditions, the cyclohexene feed as hydrocarbon will usually contain cyclohexane playing a role of an inert component, which will inevitably make an unfavorable effect on the production of cyclohexanol. Therefore, it is desirable to separate the cyclohexene/cyclohexane mixtures by using a separation process. Thus, Steyer et al [2] designed a feasible coupled process to reactively separate cyclohexene and cyclohexane leading to quite high purities, which cannot be easily achieved by conventional distillation due to the very close boiling temperatures of cyclohexene and cyclohexane. Although the coupled process was feasible to gain a high degree of separation, the employment of multiple reboilers and cyclic streams between the reactive distillation columns reminded us of the possibility of further enhancing its process design through the further reinforcement of internal mass integration and internal energy integration. In this paper, based on the principle of an innovative dividing-wall column by Schultz M A and O'Brien D E [3], a new reactive dividing-wall distillation column with two reactive sections (RDWDC-TRS) is proposed to reactively separate the cyclohexene/cyclohexane mixtures. Optimal flowsheets of the coupled structure and

the RDWDC-TRS will be obtained by minimizing total annual cost (TAC). Furthermore, the detailed comparison of the two designing schemes will be made.

2. Results and discussion

2.1 Kinetic and thermodynamic models

2.1.1 Kinetic model

This system only consists of one-step hydration reaction. The hydration reaction is shown in the following:

$$C_6H_{10} + H_2O \Leftrightarrow C_6H_{11}OH \tag{1}$$

The kinetic expression of this system with Langmuir-Hinshelwood form can be obtained from Steyer and Sundmacher [4]:

$$r = \left(m_{cat} k_{het} \frac{K_{ads}^{ene} K_{ads}^{H_2O}}{(1 + a_{ene} K_{ads}^{ene} + a_{H_2O} K_{ads}^{H_2O} + a_{nol} K_{ads}^{nol})^2} \right) \left(a_{ene} a_{H_2O} - \frac{a_{nol}}{K_{eq}} \right) \tag{2}$$

The reaction equilibrium constant K_{eq} and reaction rate constant k_{het} are given as follows:

$$K_{eq} = 4.29 \times \exp\left[3390 \times \left(\frac{1}{T} - \frac{1}{298} \right) \right] \tag{3}$$

$$k_{het} = 7.71 \times 10^{12} \times \exp\left(\frac{-93687}{RT} \right) \tag{4}$$

Where R is gas constant [J mol^{-1} K^{-1}], T is the temperature [K]. And in eq. (2) the adsorption constant (K_{ads}) for water (H_2O), cyclohexene (ene) and cyclohexanol (nol) are equal to 19.989, 0.056839 and 0.77324, respectively.

2.1.2 Thermodynamic model

In this studied system, there are four components: cyclohexene (ENE), water (H_2O), cyclohexanol (NOL) and cyclohexane (ANE) as an impurity. In this paper, the NRTL model is chosen for the description of the vapor-liquid and liquid-liquid equilibrium behavior in the system. The model parameters of this system can be found in Steyer and Sundmacher [5] with two pairs (cyclohexene-cyclohexanol, cyclohexane-cyclohexanol) re-fitted via using regression by Hao-Yeh Lee et al [6] and readjusted by this paper from the experiment data. The boiling point temperature of the components in this system is 80.78 ℃ (ANE), 82.88 ℃ (ENE), 100.02 ℃ (H2O) and 160.84 ℃ (NOL), respectively. And the azeotropic point temperature is 69.41 ℃ (water-cyclohexane), 70.71 ℃ (water-cyclohexene) and 98.33 ℃ (water-cyclohexanol), respectively.

2.2 Design flowsheet

In this section, the total annual cost (TAC) based on Douglas [7] was used to find optimal design variables. The TAC includes the operating cost and the annualized capital cost. The operating cost includes steam for the reboilers, cooling water for the condenser, and catalyst cost. The capital cost includes the column shell, internal trays, reboilers, and condenser. A capital charge factor of 3 years is assumed in the calculation.

2.2.1 The coupled process

The coupled structure (Figure 1A) is made up of two reactive distillation columns. The first reactive distillation column (C1), where the hydration reaction takes place, is designed to obtain the impurity cyclohexane. The second reactive distillation column (C2) is a cyclohexanol splitting column for producing cyclohexene. The operating pressure of this system is selected at atmospheric pressure.

For the two columns, the design variables includes: number of stage of the rectifying section, the reactive section, the stripping section; the feed locations; the location of the aqueous or organic phase recycle stream. In addition, the cyclohexane composition ($x_{ane,RDC}$) at the bottom of C1 is designed as the main variable of this coupled process due to the increase for C1 and the reduction for C2 of energy consumption as the $x_{ane,RDC}$ going up.

In the simulation of the system, vapor-liquid-liquid equilibrium is allowed in each tray. The water feed flow rate is set to be 80 kmol/h and the feed flow rate of the mixtures is assumed to be 100 kmol/h with cyclohexene of 80 kmol/h and cyclohexane of 20 kmol/h. The cyclohexane product purity is set at 99.5 mol% by varying Distillate rate and $x_{ane,RDC}$ is controlled by varying Reboilers duty. After the optimal design of the first column at each value of $x_{ane,RDC}$ is obtained by using a sequential iterative optimization procedure, the optimization of the second column can easily be done at each value of $x_{ane,RDC}$ with the cyclohexene purity specifications set at 99.5 mol%.

The optimal design of this process is found at $x_{ane,RDC}$ of 0.06 mol%, which can be seen from Figure 2A. The optimal design variables of this coupled structure are shown in Table 1.

Table 1 Optimal design variables of the coupled process

Column configuration	C1	C2
Total number of trays	20	23
Number of trays in rectifying section	0	6
Number of trays in reactive section	19	17
Number of trays in stripping section	1	0
Water feed tray	2	
The mixtures feed tray	19	
The feed tray of C2		23

2.2.2 The proposed RDWDC-TRS

The RDWDC-TRS (Figure 1B) is designed for reinforcement of the coupled structure by merging the two reactive distillation columns into one. The cyclohexene/cyclohexane mixtures and water is fed into the left section of the RDWDC-TRS. The left-top vapor (almost water-cyclohexane azeotrope) of the column after cooling down to 40 ℃ directly goes into a decanter. The aqueous phase of the decanter is completely recycled back to the column while the organic phase partially recycled back to the column. The right-top vapor (nearly water- cyclohexene azeotrope), after condensation, is partially refluxed back to this column. The overhead product is fed into a decanter operating at 40 ℃ with the organic phase partially recycled back to the column and the aqueous phase completely introduced into the left section.

Although the separation mechanism of the proposed flowsheet is the same with that of the coupled process, its design variables are changed. Its design variables include:

number of trays in the non-dividing section; number of trays in the dividing section; location of the two reactive sections relative to the bottom of the dividing section; number of trays in the two reactive sections; location of the feeds. Moreover, the cyclohexane composition ($x_{ane,RDWC}$) of the bottom in the left-dividing section is selected as the main variable to get the minimum TAC, and the optimal design is attained (as shown in Figure 2B). Notice that operating pressure, the feed rates and the two product purities are equal to these of the coupled process. And the vapor-liquid-liquid equilibrium is also allowed in each tray. The two product specifications are set by varying the product flow rate of the top and the reflux ratio of the right-dividing section, respectively. $x_{ane,RDWC}$ is designed by varying the vapor flow rate of entering into the left-dividing section. The optimal design variables are shown in Table 2.

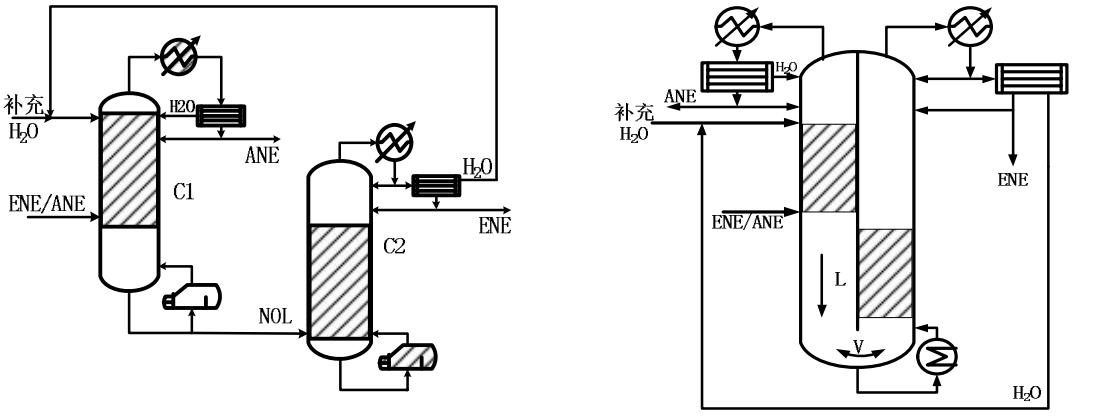

A B

Figure 1 The design flowsheet of the coupled process (A) and RDWDC-TRS (B).

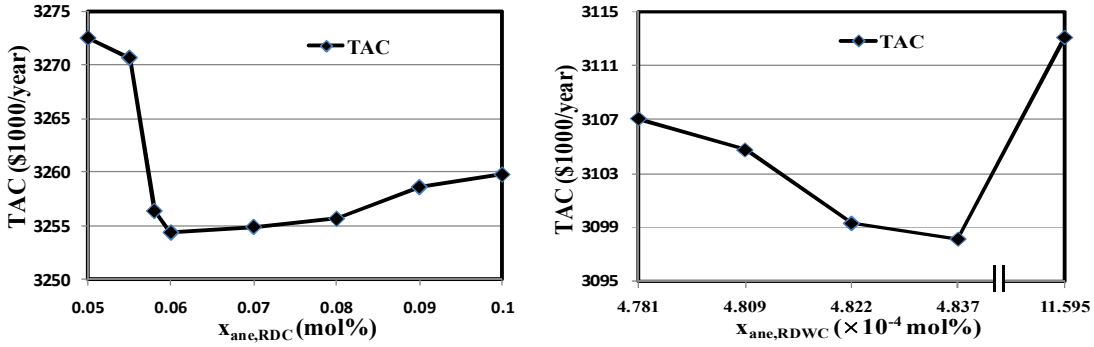

A B

Figure 2 Effects of $x_{ane,RDC}$ (A) and $x_{ane,RDWC}$ (B) on the TAC.

Table 2 Optimal design variables of the RDWDC-TRS.

Column Configuration	Optimum	*Column Configuration*	Optimum
Total number of trays	23	$x_{ane,RDWC}$ ($\times 10^{-4}$ mol%)	4.837
Number of trays in non-dividing section	1	*Number of trays in left-reactive section*	20
Number of trays in dividing section	22	*Number of trays in right-reactive section*	17
Location of the water		*Location of the left-reactive*	

feed	2	*section*	2-21
Location of the mixtures feed	19	*Location of the right-reactive section*	6-22

2.2.3 Comparison of the two optimal structures

It is obvious that $x_{ane,RDWC}$ is less than $x_{ane,RDC}$ when the optimal designs of the two structures are achieved. This is because of the wider high temperature section of left-area of the RDWDC-TRS than that of C1 (as can be seen in Figure 3) due to the effect of thermal coupling, which results in that its high cyclohexanol composition section is also bigger (shown in Figure 4), and because of the fact that the number of trays in the left-section of RDWDC-TRS is larger than that of C1. The information of TAC for two optimal structures is listed in Table 3, and the total quantity of catalyst of the RDWDC-TRS is set to be the same with that of the coupled process.

Table 3 Details of the TAC for the two optimal designs.

Configuration ($1000/year)	Coupled structure	RDWDC-TRS
Total capital cost	1051.94	894.57
Total operating cost	2202.41	2203.56
Total annual cost (TAC)	3254.35	3098.13

It can be observed that only the capital cost of the RDWDC-TRS attains a reduction by 14.96% due to the decrease of the heat exchangers and the integration of two columns into one. However, the operating cost is almost unchanged as compared with that of the coupled structure because of the almost same Reboilers duty which can be detected from the nearly same bottom vapor flow rates (513 kmol/h and 1640 kmol/h for RDWDC-TRS, 526 kmol/h and 1617 kmol/h for the coupled process).

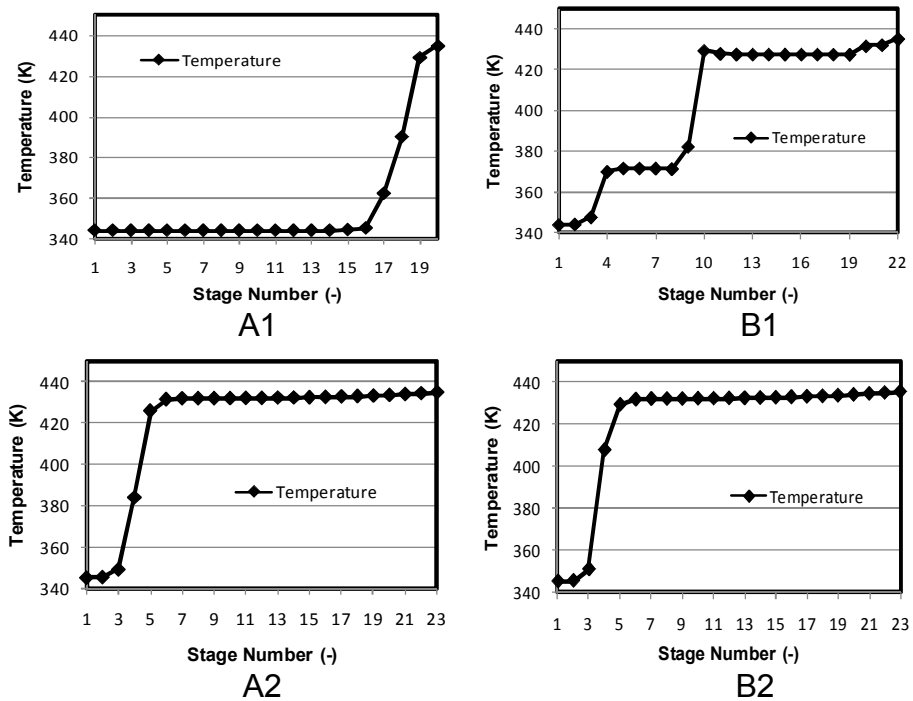

Figure 3 Temperature profiles of the first column (A1) and second column (A2) of the optimal coupled process, the left section (B1) and right section (B2) of the optimal proposed RDWDC-TRS.

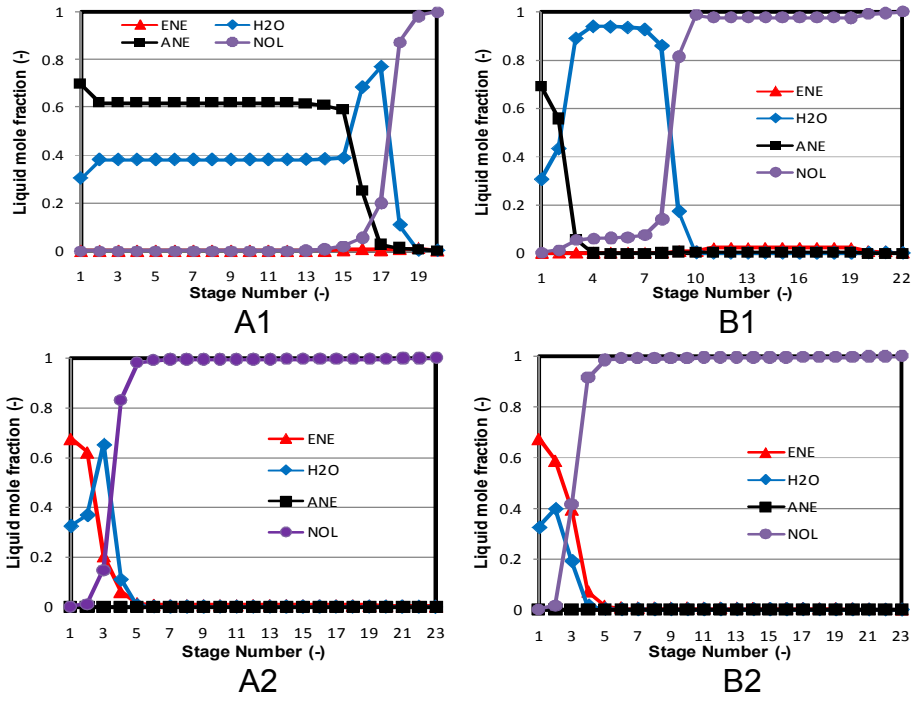

Figure 4 Liquid composition profiles of the first column (A1) and second column (A2) of the optimal coupled process, the left section (B1) and right section (B2) of the optimal proposed RDWDC-TRS.

3. Conclusions

In this paper, an innovative reactive dividing-wall distillation column with two reactive sections (RDWDC-TRS) is reported to separate the cyclohexene/cyclohexane mixtures. This new structure is an attempt of intensifying a coupled process consisting of two reactive distillation columns with the aim to reduce its capital investment and operating cost. The simulations of the RDWDC-TRS and the coupled structure are carried out in order to identify the optimal designs and operating parameters via minimizing the total annual cost (TAC), respectively.

The results show that using the proposed RDWDC-TRS, almost complete separation of cyclohexene and cyclohexane can be achieved. Compared with the coupled scheme, the RDWDC-TRS including only one column reduces the TAC by 4.80% and the capital investment by 14.96% with a nearly unaltered operating cost. Therefore, not only can the firstly presented RDWDC-TRS be provided with the beneficial performance of separating the cyclohexene/cyclohexane mixtures, but it is also equipped with relatively favorable superiority of capital saving and space-saving.

References

[1] Y. Takamatsu and T. Kaneshima, *US* Patent 6,552,235, April 22, 2003.
[2] F. Steyer, Z. W. Qi and K. Sundmacher, *Chem. Eng. Sci.*, 57 (2002), 1511-1520.
[3] M. A. Schultz et al., *16th European Symposium of Computer Aided Chemical Engineering*, Elsevier. Garmisch-Partenkirchen, Germany (2006), 695-700.
[4] F. Steyer and K. Sundmacher, *Ind. Eng. Chem. Res.*, 46 (2007), 1099-1104.
[5] F. Steyer and K. Sundmacher, *J. Chem. Eng. Data*, 49 (2004), 1675-1681.
[6] Hao-Yeh Lee et al., *4th International Symposium on Advanced Control of Industrial Processes*, Hangzhou, China (2011), 78-83.
[7] J. M. Douglas, *Conceptual Design of Chemical Processes*. New York: McGraw-Hill, 1988.

Performance characteristics of an intermediate area high performance structured packing

Žarko Olujić[1], Thomas Rietfort[2], Helmut Jansen[2], Egon Zich[2]

[1]Delft University of Technology, Delft, the Netherlands
[2]Julius MONTZ GmbH, Hilden, Germany

Abstract

Results are presented of total reflux distillation experiments carried out with Montz-Pak B1-350MN in a 1.22 m internal diameter column at Fractionation Research Inc. using two tests systems at two operating pressures, i.e. cyclohexane/n-heptane, at 0.31 and 1.62 bar, and paraxylene/orthoxylene at 0.1 and 1 bar, respectively. In all cases an impressive packing efficiency was achieved, ranging from five stages- at low to four stages per unit bed height at high vapour loads (F-factor). Comparison with data obtained earlier with B1-250MN under similar conditions indicates a relatively higher maximum useful capacity of B1-350MN, while the relative efficiency and pressure drop are close to the ratio of installed specific geometric areas. The Delft model captures observed packing geometry related effects quite well qualitatively. Quantitatively, the efficiency and pressure drop predictions are on the safe side.

Keywords
Distillation, Packed columns, Structured packings, High performance packings

1. Introduction

Prototypes of Montz high performance corrugated sheet structured packings (B1-MN series) with specific geometric area of 250, 350 and 500 m^2/m^3 have undergone total reflux distillation tests in a 0.59 m internal diameter column at Bayer Technology Services (BTS) in Leverkusen, Germany, using chlorobenzene/ethylbenzene (CB/EB) as test system at 0.1 bar [1]. All packings performed accordingly, and thereupon decision was made to start with manufacturing and delivery of these highly efficient packings. Since then, these packings have found numerous applications and have proven to be a cost-effective choice in both new designs and retrofits.

Regarding their favourable performance characteristics, an industrial scale confirmation came recently, from a series of total reflux distillation tests performed in 2011 with B1-250MN at Fractionation Research Inc. (FRI), using 1.22 m internal diameter column in conjunction with standard tests systems cyclohexane/n-heptane at 0.31 and 1.62 bar, and paraxylene/orthoxylene at 0.1 bar [2]. Even more, the obtained efficiencies appeared to be highest one measured so far with a 250 m^2/m^3 packing in a FRI test. Such a result has impressed and motivated FRI membership to choose B1-350MN for a category 1 test in 2012. This paper provides a summarised overview of, again, impressive results obtained during the tests with this intermediate area structured packing.

Interesting to mention here is that efficiency curves for B1-250MN measured at BTS and FRI overlapped each other, i.e. this packing with two close boiling systems exhibited same efficiency and same maximum useful capacity [2]. However the difference in measured pressure drop was rather large, well above that that could be attributed to the difference in column diameters employed in these tests. So, a question was raised whether B1-350MN will behave similarly in this respect.
As it will be shown later, the Delft model, which accounts for corrugation geometry features (short smooth bend at the bottom of corrugations and a corrugation inclination angle below 45^o) of B1-MN series packings, appeared to be capable of reproducing observed trends and approaching measured efficiencies and pressure drop from the safe side.

2. Experimental section

Total reflux distillation tests with Montz-Pak B1-350MN have been conducted in 2012 using facilities available at Fractionation Research Inc. (FRI) in Stillwater, OK, USA. Detailed description of experimental set-up and procedure can be found in a paper describing similar tests carried out in 2011 with Montz-Pak B1-250MN [2]. A difference was that in addition to tests performed with cyclohexane/n-heptane (C6/C7) system at 0.31 and 1.62 bar, and paraxylene/orthoxylene (px/ox) at 0.1 bar also a test has been performed with the latter at 1 bar.
The specific geometric area of the B1-350MN packing is around 350 m^2/m^3. Figure 1 shows a photograph of a side segment of B1-350MN packing on a layer assembled of four segments of this packing, illustrating the build-up of a packed bed with subsequent layers rotated to each other by 90^o. To avoid achieving too high purities of overheads the total bed height was limited to 2.6 m, while in the case of B1-250MN it was 3 m.
Figure 2 shows a photograph of the high turndown, narrow trough Type-R Montz liquid distributor (143 pour or drip points per m^2 cross sectional area) with integrated predistributor, used in this as well as in a previous test with Montz-Pak B1-250MN [2].

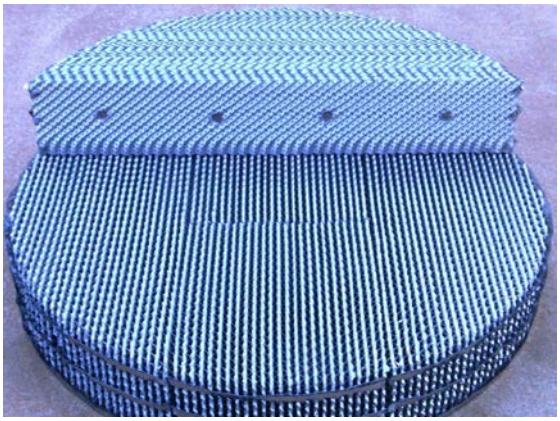

Figure 1 Layout of a layer of B1-350MN with a segment indicating corrugated sheet design (Courtesy of Dr. S. Chambers of FRI).

Figure 2 High turndown narrow trough Type-R Montz liquid distributor. (Courtesy of Dr. S. Chambers of FRI).

Another difference with respect to earlier tests was that condensers of high- and low-pressure installations were coupled in parallel (a necessary arrangement during a preceding summer time test). This resulted in case of px/ox at 1 bar in excessive subcooling of reflux, which however has not influenced the results of the test.

Final results of a total reflux distillation test are measured packing efficiency, i.e. the number of equilibrium stages or theoretical plates per unit bed height or depth, which is in the present study expressed as the height equivalent to a theoretical plate, *HETP* (m), and the pressure drop per unit height, *dp/dz* (mbar/m), both shown here as a function of the vapour load (*F-factor*).
One should note that FRI in their reports and publications usually expresses *HETP* and *dp/dz* as a function of the vapour capacity factor, c_G (m/s), which is related to F-factor via following relation: $c_G = F_G/(\rho_L-\rho_G)^{0.5}$, where F_G (m/s(kg/m^3)$^{0.5}$ = Pa$^{0.5}$) is *F-factor* or the vapour load, and ρ_L (kg/m^3) and ρ_G (kg/m^3) are liquid and vapour densities. One should keep in mind that in a total reflux distillation test the liquid load increases proportionally to the vapour load. Unlike all other properties and parameters, which are based on an average of top and bottom of the bed values, the *F-factor* corresponds to the bottom of the bed conditions. All data were taken twice at a time interval, and the *F-factor*, *HETP* and *dp/dz* values shown in this paper are arithmetic averages of two, mainly nearly identical values (except at vapour loads close to the flooding point).

3. Results and discussion

Measured efficiencies and pressure drops for px/ox system, at 0.1 and 1 bar, and C6/C7 system, at 0.31 and 1.62 bar, are shown in Figures 3 and 4, respectively, as a function of F-factor.

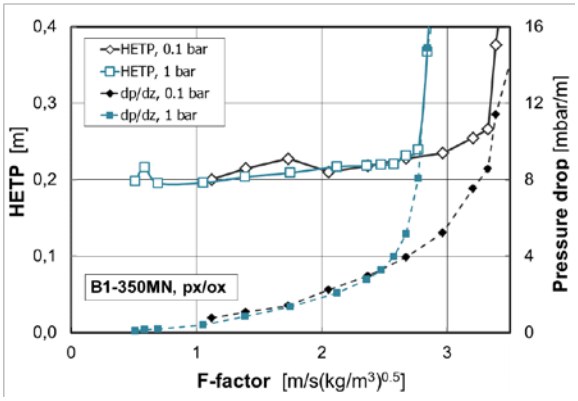

Figure 3 Measured efficiency and pressure drop as a function of vapour load for px/ox system at 0.1 and 1.0 bar.

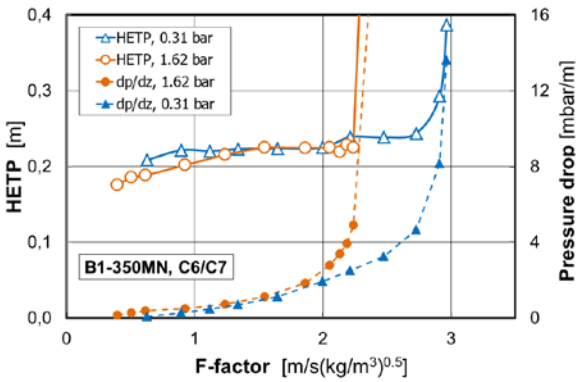

Figure 4 Measured efficiency and pressure drop as a function of vapour load for C6/C7 system at 0.31 and 1.62 bar.

Interestingly, in both cases the efficiency is not affected by operating pressure and the efficiencies obtained with px/ox system are similar to those obtained with C6/C7 system. Also in both cases the best efficiencies are obtained at low end of the *F-factor*, but, as shown later, the slope of efficiency curve is less pronounced than in the case of B1-250MN packing. The fact that in all cases more than four theoretical plates per unit bed height were realized over the whole range of vapour loads indicates a rather high efficiency of this packing. Sudden departure of efficiency at *F-factors* close to flooding point indicates the maximum useful or efficient capacity for given system and pressure. The flooding limit shifts with increasing pressure to lower vapour load, depending on the system. One should note that in case of px/ox system the ratio of two operating pressures is 10, while for C6/C7 system it is about 5. Since vapour density is strongly affected by a change in pressure, the specific liquid loads change accordingly.

Table 1 shows for two systems at given pressures the specific liquid loads corresponding to given values of the F-factor. The specific liquid load for px/ox system is factor 3.1 larger at 1 than at 0.1 bar, while in the case of C6/C7 it is factor 2.1 larger at 1.62 than at 0.31 bar. The fact that highest efficiencies were obtained at lowest vapour load confirms that both, the packing tested and the liquid distributor used in this study perform exceptionally well at very low specific liquid loads (distributor minimum design specific liquid load is 2.65 m^3/m^2h).

Specific liquid load (m^3/m^2h)				
F-factor ($Pa^{0.5}$)	px/ox 0,1 bar	px/ox 1 bar	C6/C7 0,31 bar	C6/C7 1,62 bar
0,5	1,39	4,28	2,78	5,9
1	2,79	8,57	5,55	11,8
1,5	4,18	12,9	8,33	17,7
2	5,57	17,1	11,1	23,6
2,5	6,97	21,4	13,9	29,5
3	8,36	25,7	16,7	-
3,5	9,76	-	-	-

Table 1 Specific liquid loads corresponding to given F-factors for test sytems and pressures employed in this study.

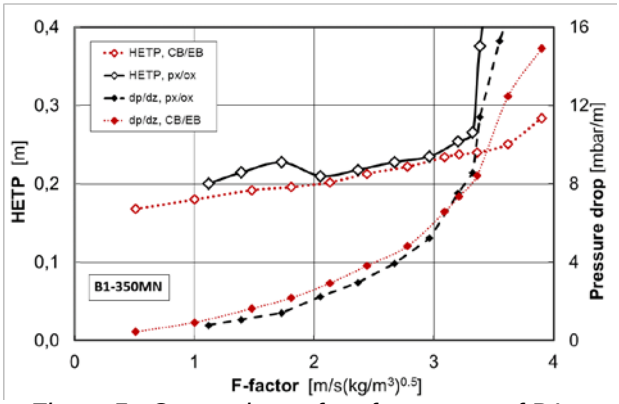

Figure 5 Comparison of performances of B1-350MN measured at 0.1 bar with px/ox system at FRI and with CB/EB system at BTS.

Figure 5 shows a comparison between efficiency and pressure drop measured at FRI and at BTS (internal column diameter = 0.59 m) with two different close boiling test systems. Similar to the previous test with B1-250MN [2], measured efficiencies agree very well, however in FRI test the maximum (useful) efficient capacity seems to be somewhat lower than that measured at BTS. On the other hand, the pressure drop measured at BTS is somewhat larger, but this discrepancy is not as pronounced as it was found in case of B1-250MN [2]. Exception are vapour loads close to flood limit, where FRI pressure drop curve crosses that of the BTS test and the point of sudden increase in pressure drop coincides with the point of sudden departure in efficiency. In BTS tests, with both, B1-250MN and B1-350MN, the transition from the point of maximum useful (efficient) capacity to flooding is not so pronounced.

Figure 6, 7 and 8 show a comparison of efficiencies and pressure drops of B1-350MN and B1-250MN measured with px/ox system at 0.1 bar, and C6/C7 system at 0.31 and 1.62 bar, respectively. The B1-250MN was not tested at 1 bar. The specific geometric area of B1-350MN is 1.4 times larger than that of B1-250MN. If we take an F-factor of 2 $m/s(kg/m^3)^{0.5}$ as reference point, then it appears that in case of px/ox system the efficiency ratio is nearly equal to that of installed areas, while in the case of C6/C7 system, at both pressures it is somewhat larger, indicating in latter case a better utilisation of installed area. For px/ox system B1-350MN generates more pressure drop than expected, while relatively less pressure drop is experienced with C6/C7 system at 0.31 bar and, more pronouncedly, at 1.62 bar.

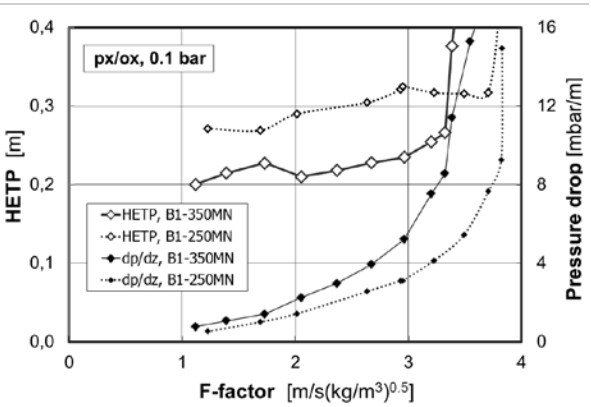

Figure 6 B1-350MN vs. B1-250MN (px/ox at 0.1 bar).

The pressure drop per theoretical plate is at chosen reference point very low, depending on the distance to flood point. It is below 0.5 mbar/theoretical plate for two test systems under vacuum, with vapour loads between 50 and 70 % of the flood. It is somewhat larger for C6/C7 at 1.62 bar, i.e. 0.56 for B1-350 and 0.67 mbar/theoretical plate for B1-250MN, at vapour loads of 89 % and 83 % of the flood, respectively. Most distinctive difference in behaviour of this two well performing packings is observed within the loading region, where the efficiency of B1-250MN packing tends to stabilize and even improve close to flooding point, while that of B1-350MN shows a gradually increasing trend (px/ox) or remains stable (C6/C7) until flooding point.
From Figures 7 and 8, it can be seen that the capacity of B1-350MN approaches closely that of B1-250MN (less than 10% difference at both pressures) while in case of the px/ox system (Figure 6) the difference is nearly 12 %.

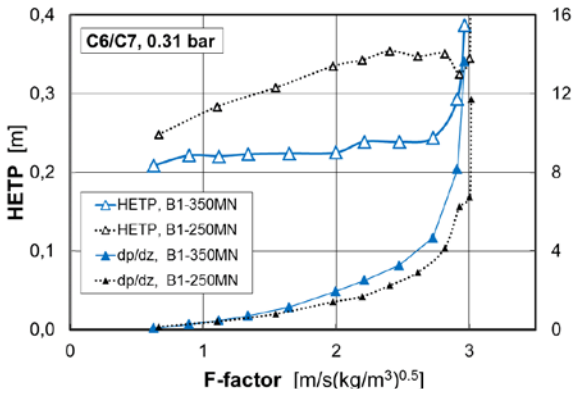

Figure 7 B1-350MN vs. B1-250MN (C6/C7 at 0.31 bar).

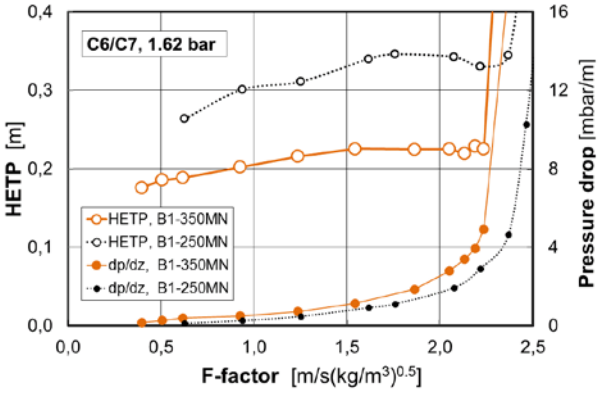

Figure 8 B1-350MN vs. B1-250MN (C6/C7 at 1.62 bar).

Figures 7 and 8 show clearly that with decreasing vapour load the efficiency of B1-250MN tends to improve at faster pace than that of B1-350MN. Although this cannot be stated for px/ox system, similar, even more pronounced relative improvement in efficiency has been observed at the same pressure (0.1 bar) with CB/EB system [1].
Figures 9 and 10 show a comparison of measured efficiencies and pressure drops (larger symbols) and those estimated (smaller symbols) for the same conditions

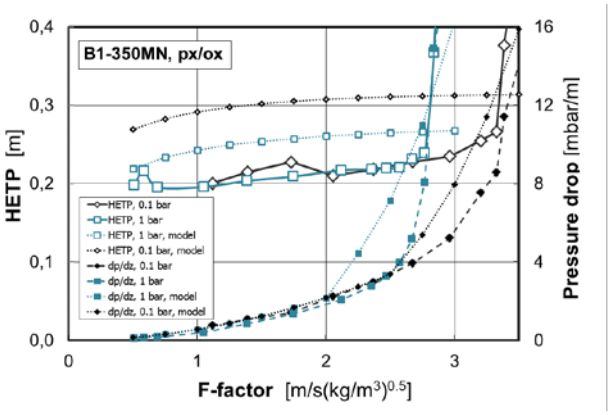

Figure 9 Predicted vs. measured (px/ox at 0.1 and 1.0 bar.

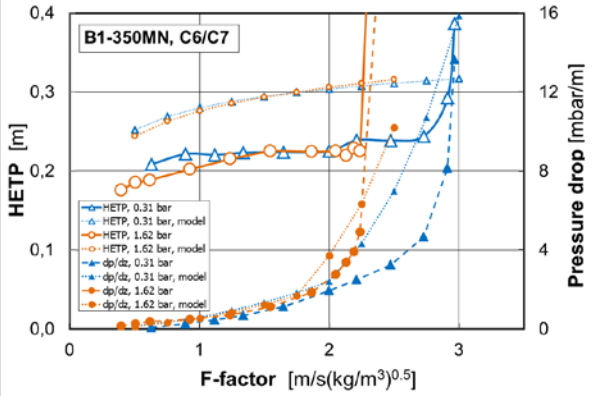

Figure 10 Predicted vs. measured (C6/C7 at 0.31 bar and 1.62 bar).

using modified Delft Model [1]. One should note that this model accounts for corrugation geometry features as encountered in B1-MN series of packings and does not require any adjustable empirical parameter. The physical properties for px/ox at 1

bar are shown in Table 2, while those for px/ox system at 0.1 bar and C6/C7 at 0.31 and 1.62 bar can be found elsewhere [2]. Estimated HETP values are consistently larger, and closer in fact to those considered safe for design purposes than to measured ones. Interestingly, in case of C6/C7 there is no pressure effect, while in case of px/ox system the model predicts higher efficiency for 1 bar than for 0.1 bar. This could be attributed to an increased effective interfacial area due to a factor three larger specific liquid loads. On pressure drop side, for both systems and test pressures the predictions agree well with measurement in preloading range, while a pronounced over-prediction is evident within the loading range. This is mainly due to the fact that the predicted point of onset of loading is in all cases significantly lower than the observed one.

Property / Test system	px/ox (1 bar)
Temperature (°C)	140
Liquid composition (-)	0.51
Liquid density (kg/m^3)	761
Liquid viscosity (Pa s)	2.47 x 10^{-4}
Liquid diffusivity (m/s^2)	6.87 x 10^{-9}
Vapour density (kg/m^3)	3.1
Vapour viscosity (Pa s)	9.1 x 10^{-6}
Vapour diffusivity (m/s^2)	7.6 x 10^{-6}
Schmidt number, vapour (-)	0.77
Surface tension (N/m)	0.017
Relative volatility (-)	1.165
Equilibrium line slope (-)	0.99
Specific liquid load (m^3/m^{2}h) at F-factor = 2 Pa$^{0.5}$	17.1

Table 2 Representative values of physical properties of px/ox system at 1 bar.

Owing to its rather low pressure drop per stage proven in many industrial applications, B1-350MN appears to be a versatile and cost-effective packing, considered presently as first choice for design of dividing wall columns.

4. Conclusions

In line with expectations based on performance of B1-250MN, B1-350MN also performed very well in total reflux distillation tests conducted at FRI, using two well established tests systems at two operating pressures. B1-350MN efficiencies appeared to be unaffected by pressure and were in the range from five to four theoretical plates per unit bed height/depth. Similar to previous tests with B1-250MN, best efficiencies were obtained at low F-factors.

The efficiencies measured with px/ox system agree well with those measured at BTS at the same pressure (0.1 bar), and the discrepancy in measured pressure drop is less pronounced than in case of B1-250MN. The latter outperformed B1-350MN at low F-factors, while, around the design point, the efficiency ratio was close to that of installed specific surface areas.

Delft model captures observed effects quite well qualitatively. Quantitatively the efficiency and pressure drop predictions as well as that of the point of onset of loading are on the safe side. However, this is more pronounced than in case of B1-250MN [2]. Since the trends are similar, only one adjustable parameter is needed to ensure perfect match.

Acknowledgements

Dr. Simon Chambers for his professional zest and personal devotion during execution of the tests and the FRI operations team for performing accordingly.

References

[1] Olujić, Ž., Rietfort, T., Jansen, H., Kaibel, B., Zich, E., Frey, G., Ruffert, G., Zielke Torsten, Experimental characterisation and modelling of high performance structured packings, Ind. Eng. Chem. Res. 51 (2012) 4414-4423.

[2] Olujić, Ž., Kaibel, B., Jansen, H., Rietfort, T., Zich, E., Fractionation Research Inc. test data and modelling of a high performance structured packing, Ind. Eng. Chem. Res. 52 (2013) 4888-4894.

The tool box for distillation column revamps focussed on capacity and efficiency improvement

P.M.Wilkinson, E.J. Vos, Shell Global Solutions International B.V., Amsterdam/The Netherlands; M. Roza, Sulzer Chemtech ltd, Winterthur/Switzerland;

Abstract

In this paper recent experimental results for HiFi™ Plus trays (tested at FRI) are presented which were tested at tray spacings of 305 and 610 mm. These results are used to illustrate the capacity (and or efficiency) gains that can be achieved by changing from a conventional tray to a high capacity tray.

HiFi '3 bucket' design for FRI testing.

Shell HiFi Trays are high capacity multidowncomer trays which were first developed in Shell over 20 years ago. Since 2000 Sulzer Chemtech Ltd is the world-wide licensee for Shell Global Solutions' high capacity tray and phase separation technology and the alliance also covers joint development of new or improved technology. Also the HiFi tray has been improved since the alliance started which has lead to the HiFi Plus tray as tested at FRI. The FRI high pressure test column (D=1.22m) is relatively small for a multi downcomer tray such as the Shell HiFi Plus tray. Typically for this scale the Shell design tools for HiFi trays would recommend a single path HiFi tray for a tray spacing of 610mm (24inch). However, in order to demonstrate that a multi downcomer tray can be applied on this small scale to achieve high capacities while still giving good tray efficiencies despite the short flow-path length, so-called '3-bucket' HiFi trays (Figure 1) have been designed for testing at FRI. In total 4 different designs were tested with the iC4/nC4 system.

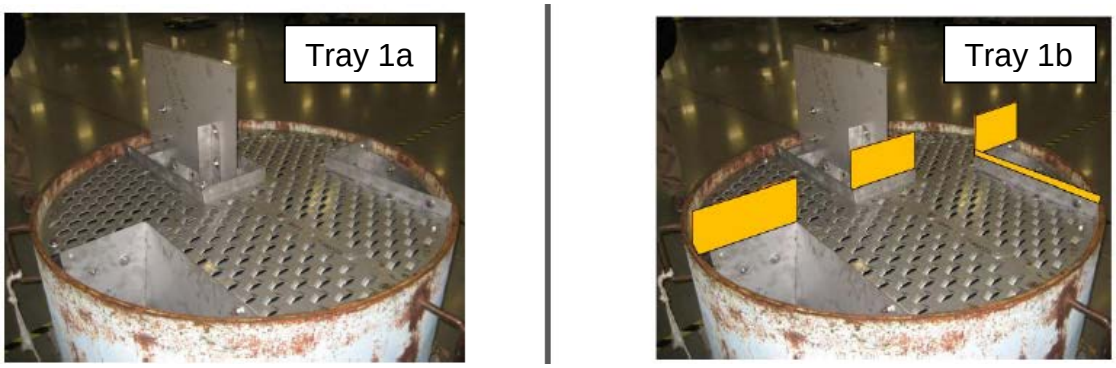

Figure 1. '3-bucket' HiFi™ Plus configuration, for details see Table 1 below.

The data collected from these tests cover a wide range of physical properties (due to testing at 11.4, 20.7 and 27.6 bara) and a wide range of flow rates, because total reflux as well as circulation runs for L/V < 1 and L/V > 1 were conducted (where L and V are representing Liquid and Vapour mass flows). Previously FRI has also collected data for similar conditions using conventional tray layouts. A selection of these results is used to assess the capacity gain that can be achieved by changing a column equipped with conventional trays to a high capacity tray.

The overview in Table 1 shows that many items have been selected from the distillation tray design 'tool box' focussed on capacity enhancements, for example:

- Bubbling area is maximised by sloping and truncating the downcomers.
- Small fixed directional valves (MVG). Note that alternative high capacity valves such as the 'UFM' [1] were not available at the time the tests were conducted.
- Anti splash baffle in the downcomer.
- Bubbling area fully interconnected for a uniform froth distribution.
- Very long weir length due to multi downcomer design to minimize froth expansion.
- High open area to reduce downcomer back-up for the low tray spacing design.

Table 1. HiFi Plus details of the trays tested at FRI.

	Tray 1a	Tray 1b	Tray 2a	Tray 2b
Tray spacing (m)	0.61		0.305	
Weir length (m)	2.74	2.02(1)	2.64	2.0(1)
Weir height (mm)	50.8	76.2	50.8	
Weir height short side (mm)	50.8	203.2	50.8	152.4
Downcomer area (%)	24		20	
Downcomer design	Truncated, sloped and with anti splash baffle			
Perforations	MVG (fixed valves)			
Open area (%column area)	11.5		10	
Flow path length (mm)	≈305		≈335	
Test pressures (bara)	11.4, 20.7, 27.6	11.4	11.4, 20.7, 27.6	11.4

(1) 'Effective weir length' reduction relative to Tray 1a is due to heightening of short sides of the downcomers (Figure 1).

That these choices have indeed led to very high capacities can be seen in Figure 2 below which contains the maximum capacities achieved with the HiFi Plus tray combined with data which were selected for developing a system limit correlation [2].

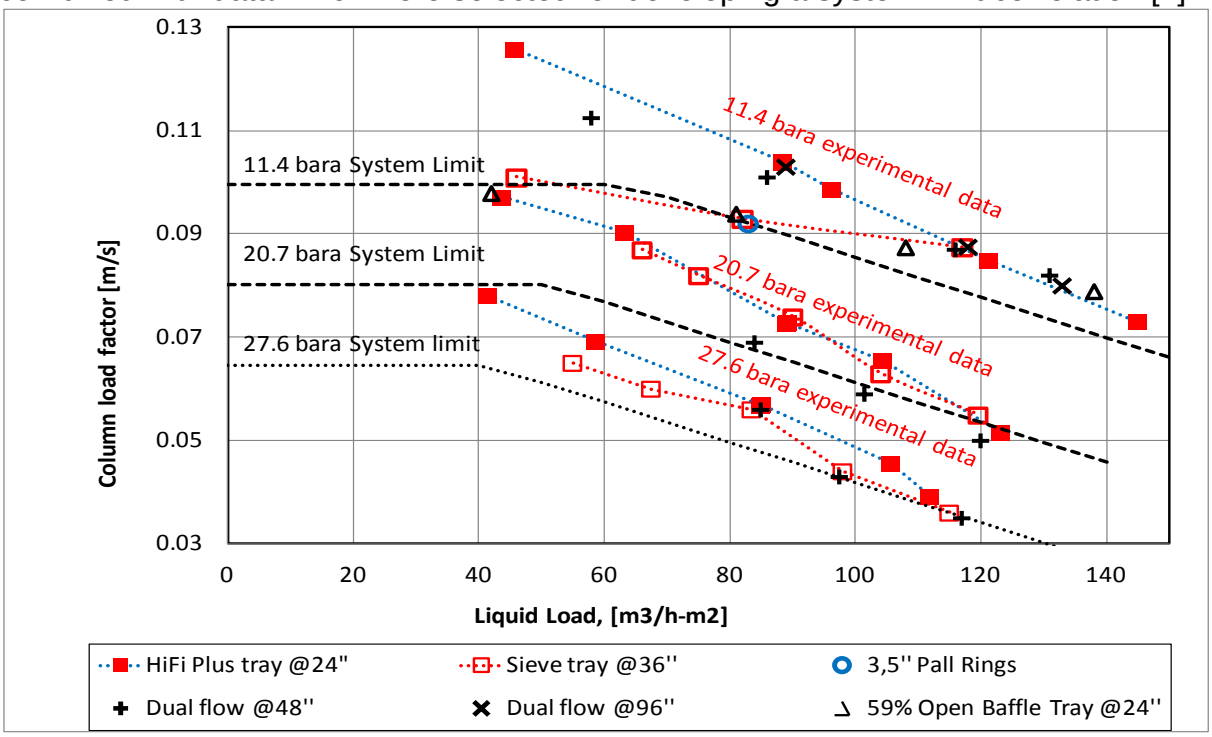

Figure 2. Comparison of maximum capacities achieved for different internals combined with the system limit prediction [2].

This comparison shows that the HiFi Plus tray capacities are always equal or higher than the capacity achieved with the other internals with very high capacity. In fact all HiFi Plus data points exceed the capacity predicted by the system limit correlation [2]. However, other devices also (partly) exceed the system limit line which suggest that this correlation is somewhat under predicting the system limit for the iC4/nC4 system. When focusing on the comparison with the 36" tray spacing conventional tray it appears that the results are similar for 20.7 and 27.6 bara, while for the 11.4 bara conditions the HiFi Plus tray (with just 24" tray spacing) gives significantly more capacity at the lower liquid loads. For the HiFi Plus tray with lower tray spacing (305 mm, 12") comparisons have also been made to iC4/nC4 total reflux data for conventional tray as tested at FRI (Figure 3).

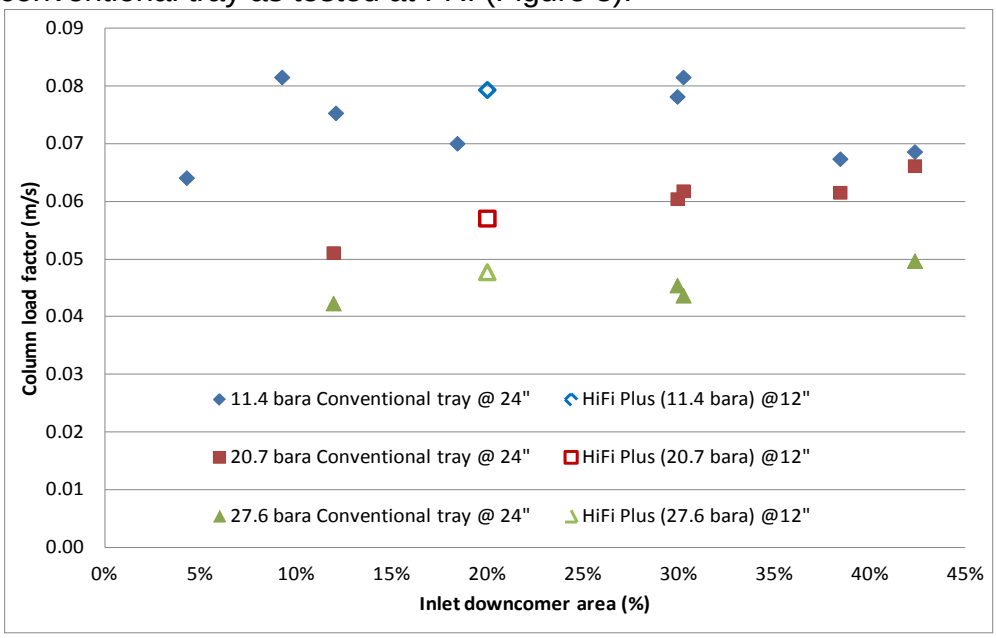

Figure 3. Capacity comparisons between 305 mm Tray spacing HiFi^{TM} Plus and conventional trays with 610 mm Tray spacing at 3 pressures for the iC4/nC4 system.

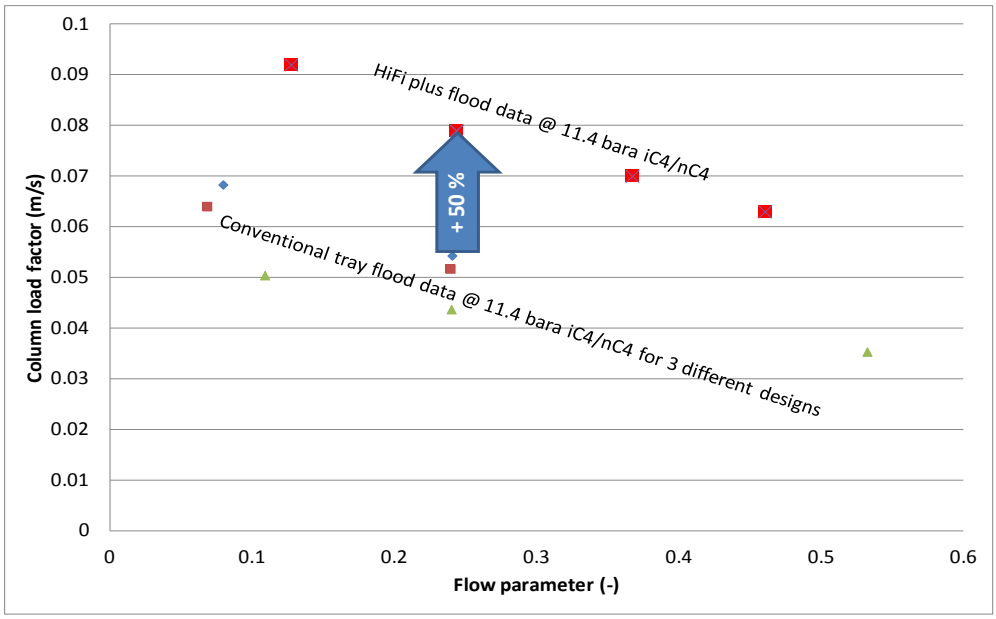

Figure 4. Capacity comparisons between 305 mm Tray spacing HiFi^{TM} Plus and conventional trays with 305 mm Tray spacing.

These comparisons show that the capacity of the HiFi tray with 305 mm tray spacing is approximately equal to the capacity of a conventional tray with 610 mm tray spacing, while it has about 50% more capacity than a conventional tray with same tray spacing (Figure 4).

Efficiency results

The test results for the tray efficiencies of the HiFi Plus trays show (Figure 5) many similarities with results previously found at FRI for conventional trays (with iC4/nC4 system). For example:

- The efficiency was not a strong function of pressure for the entire range of pressure tested (11-27.6 bara).
- The tray spacing does not have much impact on tray efficiency.

Other findings were:

- The tray efficiency can still be above 100% for a tray design with a very short flow path (≈300 mm).
- 'Blocking' the short side of the downcomers (by raising the weir) increases the efficiency by some 5% (Table 1: tray 2b relative to tray 2a design).
- 'Blocking' the short side of the downcomers *and* raising the weir height by 25 mm (Figure 1) increases the efficiency by some 5-10% as shown in Figure 5.

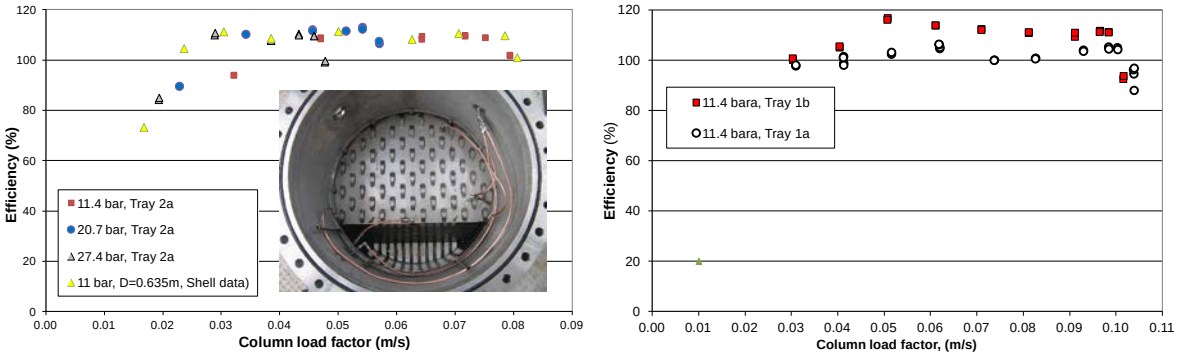

Figure 5. Efficiency (based on reflux & bottom samples) as a function of weir modification, pressure and tray spacing (on the left 305 mm tray spacing data and on the right 610 mm tray spacing data is shown). Note that the 'photo' shows a 'single path' HiFi^{TM} tray tested at Shell (referred to as 'Shell' data).

The changes to the weir were made to illustrate that there is a 'tool box' available to tailor the performance of a tray depending on the requirements. For example if a higher efficiency is required the flow path length and/or the weir height may be increased. Typically such changes may lead to some capacity reduction. However for the HiFi Plus tray it was seen that the capacity reduction due to the changes made was very limited. By using the 'Francis weir crest' equation it is possible to make a rough estimate of the clear liquid height increase due to the reduction in weir length (see Table 1: tray 1a ➔1 b: 26% weir length reduction, 2a ➔ 2b 24% weir length reduction). This order of magnitude calculation shows that the clear liquid height increase on the trays due to the weir length reduction is expected to be small < 10 mm (Figure 6) and hence it is also not surprising that the capacity reduction due to these changes is also very small (but slightly increases towards higher liquid loads).

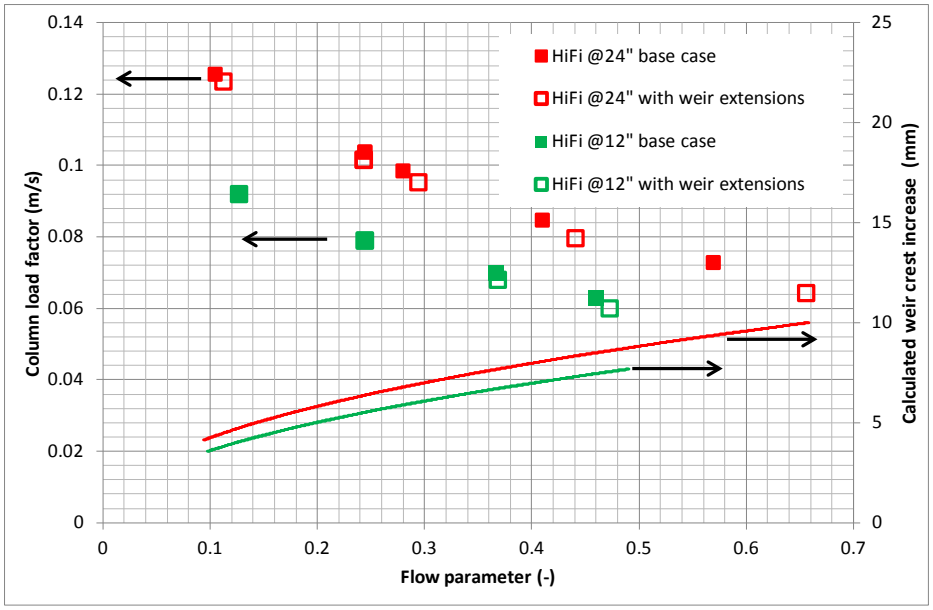

Figure 6. Capacity impact of weir extensions (for details see Table 1) combined with 'crest over weir increase' resulting from weir extensions based on Francis weir correlation.

Efficiency improvement options for revamps

The results in this paper have shown that there are several options in the 'tool box' to increase capacity when revamping a conventional tray by a high capacity tray such as the HiFi Plus tray. In some column revamps [3] increasing capacity but not efficiency will lead to utility constraints (e.g. reboiler/condenser). Then it can be very beneficial to increase both capacity and efficiency. This can be achieved by replacing conventional trays by high capacity trays while at the same time increasing the tray count (e.g. by doing a 3 for 2 or 4 for 3 replacement). The results presented in this paper were used to correlate the capacity of the HiFi Plus tray and a conventional tray as a function of tray spacing in order to estimate the impact on capacity when increasing the tray count to increase the number of stages.

Table 2. Calculated attainable capacity increase for revamping conventional trays with a high capacity tray, while increasing tray count.

Tray replacement:	1:1	5:4	4:3	3:2	2:1
Tray Count Increase:	**0%**	**25%**	**33%**	**50%**	**100%**
Tray spacing (mm)[1]	**Capacity increase[3]**				
600	32%	21%	18%	13%	0%
500	35%	23%	20%	15%	
450	37%	26%	22%	17%	
400	40%	28%	25%		
350	44%				
300	47%				

Tray spacing < 300 mm[2]

(1) Tray spacing of conventional tray (pre-revamp condition).
(2) Typically the tray spacing is not reduced < 300 mm in revamps with HiFi trays.
(3) Correlations used for this evaluation are shown below:

$$\frac{Cs_{HiFi.TS}}{Cs_{HiFi.305mm}} = \left(\frac{TS_{HiFi}}{305}\right)^{0.4}, \quad \frac{Cs_{Conventional.TS}}{Cs_{Conventioal.610mm}} = \left(\frac{TS_{Conventional}}{610}\right)^{0.6}, \quad \frac{Cs_{Conventional.610mm}}{Cs_{HiFi.305mm}} = 1$$

$$\rightarrow \frac{Cs_{HiFi.TS}}{Cs_{Conventional.TS}} = \left(\frac{TS_{HiFi}}{305}\right)^{0.4} * \left(\frac{610}{TS_{Conventional}}\right)^{0.6}$$

(Cs= Maximum column load factor, TS=Tray Spacing)

Conclusions

Test results with the iC4/nC4 system covering a wide range of high pressures for conventional trays and high capacity Shell HiFi Plus trays have been used to estimate the typical capacity increase that can be achieved in revamping conventional trays by a multi downcomer tray. The results show that for a 1 to 1 tray replacement capacity increases in the order of 50% are possible at low tray spacing (305mm), while at higher tray spacing the capacity increase is still substantial but less (≈32% at 610 mm tray spacing). The data has also been used to show (and quantify) that it is often possible to increase both capacity *and* efficiency by increasing the number of trays installed (but at a lower tray spacing). Obviously the numbers shown should *not* be considered as hard upper limits for capacity increases in revamps where the existing column shell is to be retained as there are more extreme solutions possible, for example the ConSep™ tray [3,4,5].

References

[1] AIChE Kister Symposium 2013, UFM Valve: An Advanced Mini-Valve to Boost the Performances of the Fractionation Trays, Mosca, G., Pilling, M. W., Hirsch S., Sulzer Chemtech.
[2] Stupin, W.J. and Kister, H.Z.; "System limit: The ultimate capacity of fractionators"; Trans IChemE, Vol 81, Part A, pg. 136-146 (January 2003).
[3] De Villiers, W.E., Bravo, J.L., Wilkinson, P.M., Summers, D.R., 'Further advances in light hydrocarbon fractionation', PTQ Summer 2004
[4] Wilkinson, P.M., De Villiers, W.E., Mosca, G., Tonon, L., 'Achieve Challenging Targets in Propylene Yield using Ultra System Fractionation Trays', ERTC 2006.
[5] Majumder, K., Mosca, G., Mahon, K., Application of Ultra High Capacity Shell ConSep Tray For De-Bottlenecking of a Crude Distillation Unit. AIChE 2012 Spring Meeting.

(*) Shell HiFi is a Shell trademark
(**) Shell ConSep is a Shell trademark

Practical evaluation of efficiency measurement of structured packings in alcohol-water system

Oleg Pajalic, Perstorp Group, 28480 Perstorp, Sweden

Abstract

To be able to design gas-liquid separation equipment, the efficiency of separation units is necessary to collect. Packings efficiency is a critical parameter because not only the equipment capital cost are limited but even production cost can increase and plant capacity decrease in the case of poor design. The efficiency depends on: packings geometry and type, relative volatility, vapor and liquid load, physical properties (density, viscosity, surface tension and diffusivity), water occurrence in the system, liquid distribution and column diameter.

Several tests with Neopentyl glycol (NPG) – Water binary mixture have been performed in two different pilot distillation columns filled with Sulzer BX gauze stainless steel structured packing. For the efficiency calculations, commercial software Chemcad has been used. In Chemcad, the theoretical models used for HETP evaluation are: Bravo, Rocha and Fair and Billet and Schultes. System NPG– Water is a non-ideal and UNIFAC has been chosen in calculation of VLE and then compared with NRTL with modified binary parameters. Reported deviations, in literature, in prediction of mass transfer efficiency for HETP models used in this work are ± 50% which could give uncertainty in column up-scaling. In this work, NRTL parameters have been modified in order to minimize predicted components concentrations at the top and bottom of the column. A good consistency with experimental values has been shown using Bravo, Rocha and Fair model. That approach has been applied in an existing plant column filled by Sulzer MELLAPAK 250Y packings showing rather good predicted results in comparison with collected samples for the given conditions. ody text – Arial 12 pt., left-justified - margins: 4 cm

Keywords

Distillation, structured packings, mass transfer model, activity

1. Introduction

To design a distillation and absorption column is an issue in industrial applications. Often, there is no experimental data for efficiency for a specific separation system. Only available efficiency data are regarding's ideal binary system measured under total reflux conditions. Those data are not of big use especially in the specialty chemicals business where most of the separation systems are non-ideal. There is often no any experimental data available for Vapour-Liquid Equilibrium (VLE) for such systems. Normal approach is to gather equilibrium data experimentally, but that is either time demanding or laboratory resources and analyses competences are missing. In this work are NRTL parameters adjusted in order to fit experimental data gathered for efficiency calculation.

Experimental values of VLE of Water-NPG binary are missing. UNIFAC is used initially to predict VLE. UNIFAC based model shows that NPG and water behave quite ideally at low concentration and at the higher concentration NPG start to behave non-ideally as it is shown on Figure 1.

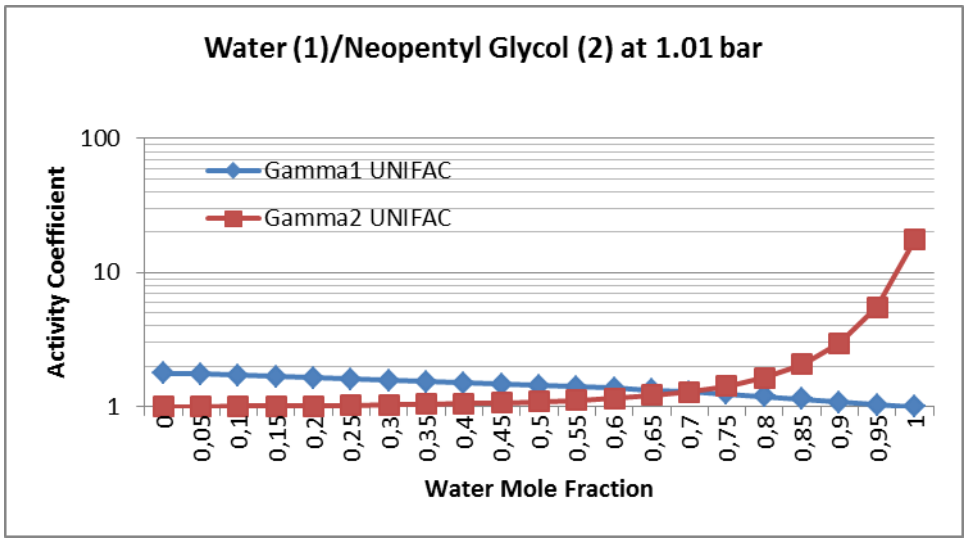

Figure 1. Activity coefficients of NPG and water as predicted by UNIFAC

Chemcad has been used for NRTL parameters fitting and for efficiency calculations. Two different mass transfer models are available for structured packing in Chemcad[3]:

-Bravo, Rocha and Fair[1] for structured packing

-Billet and Schultes[2] for random and structured packing

The Bravo, Rocha and Fair model is used in Chemcad.

2. Experimental

Two test sets with different column arrangements have been performed in order to evaluate packing efficiency. For each experiment number of data is collected such as: column total pressure, temperature, reflux and distillate flow, NPG mass fraction at the top and bottom of the column.

The F-factor is calculated and is defined as the square root of the kinetic energy of the vapour $u_V \sqrt{\rho_V}$, where u_V is superficial the gas velocity and ρ is density.

Following specifications were specified: low pressure drop and reflux ratio due to energy saving demand, high separation efficiency and low content of alcohol in distillate, capacity and relatively high pressure in the system, 1 to 2,5 bar, considering use of gauze packings.

In both column arrangements the distillation columns were filled with structured packings type Sulzer BX. The first setup included the column with inner diameter of 0.07m and packings height 1 m and with no distributor. The tests were performed batch-wise in both experimental setups. The pressure in the column was set on 2.5 bar. The experimental results are shown in Table 1.

TEST Number	Liquid Load	Reflux flow (top)	Distillate	F-Factor	Gas Flow (top)	Gas Inlet Flow	Bottom flow	NPG fraction inlet	Water	Reflux	NPG fraction bottom	NPG fraction top
	m^3/m^2h	kg/h	kg/h	Pa^0,5	kg/h	kg/h	kg/h	Weight %	Weight %		Weight %	Weight %
1	0,9	3,24	0	0,2	3,22	3,24	3,24	0,36	99,64	total	0,36	0,01
2	0,89	3,21	0	0,2	3,22	3,21	3,21	0,79	99,21	total	0,79	0,02
3	0,19	0,68	2,74	0,21	3,38	3,42	0,68	0,1	99,9	0,25	0,44	0,02
4	0,18	0,65	2,59	0,2	3,22	3,24	0,65	0,13	99,87	0,25	0,55	0,02
5	0,1	0,34	2,74	0,19	3,06	3,08	0,34	0,09	99,91	0,13	0,5	0,04
6	0,1	0,34	2,74	0,19	3,06	3,08	0,34	0,11	99,89	0,13	0,63	0,05
7	0,16	0,58	2,32	0,18	2,82	2,9	0,58	0,23	99,77	0,25	1	0,04
8	0,16	0,58	2,32	0,18	2,82	2,9	0,58	0,28	99,72	0,25	1,21	0,04
9	0,16	0,58	2,31	0,18	2,82	2,88	0,58	0,33	99,67	0,25	1,51	0,04
10	0,16	0,58	2,31	0,18	2,82	2,88	0,58	0,4	99,6	0,25	1,83	0,04
11	0,1	0,36	2,88	0,2	3,22	3,24	0,36	0,26	99,74	0,13	1,57	0,1

Table 1. Distillation set-up 1 with 0.07 m column diameter

Second test was performed in a bigger column 0.5 m in diameter with 2 beds of 2 m each with possibilities to choose either one or both beds in the distillation tests. The pressure in the column was set on 1 bar. The experimental results are shown in Table 2.

TEST Number	Liquid Load	Reflux flow (top)	Distillate	F-Factor	Gas Flow (top)	Gas Inlet Flow	Bottom flow	Reflux Ratio	NEO fraction inlet	Watten Halt	Height	NEO fraction bottom	NEO fraction top
	m^3/m^2h	kg/h	kg/h	Pa^0,5	kg/h	kg/h	kg/h		%	%	m	%	%
12	0,16	30,1	120,41	0,28	150,82	150,51	30,1	0,25	9,47	90,53	2	47,37	0
13	0,09	16,56	132,45	0,28	149,21	149,01	16,56	0,13	5,38	94,62	2	48,16	0,03
14	0,07	13,92	139,22	0,28	152,44	153,15	13,93	0,1	4,47	95,53	2	48,53	0,06
15	0,09	16,56	132,45	0,28	150,82	149,01	16,56	0,13	5,35	94,65	4	48,09	0,01
16	0,07	12,51	125,11	0,27	142,74	137,63	12,52	0,1	4,39	95,61	4	47,94	0,03

Table 2. Distillation set-up 2 with 0.5 m column diameter

All measurement has been performed at very low liquid load and F-factor in order to resemble to the plant data. Pressure drop has not been measured but is assumed to be very low because of low gas load and relatively high pressure.

3. Results and discussion

Simulations were first carried out using the experimental results collected from two different pilot setups. The aim of the simulations was to fit the experimental data to mass transfer model by varying the binary interaction parameters used in NRTL activity coefficient model. First test set was performed at low inlet Neo fractions and is used to predict the behaviour of the NPG-Water solution for low NPG concentration while the second test is used for predicting VLE for high concentrations of Neo in the inlet flow of gas.

The NRTL BIPs are adjusted accordingly. Adjusted Activity coefficients are shown in the Figure 2.

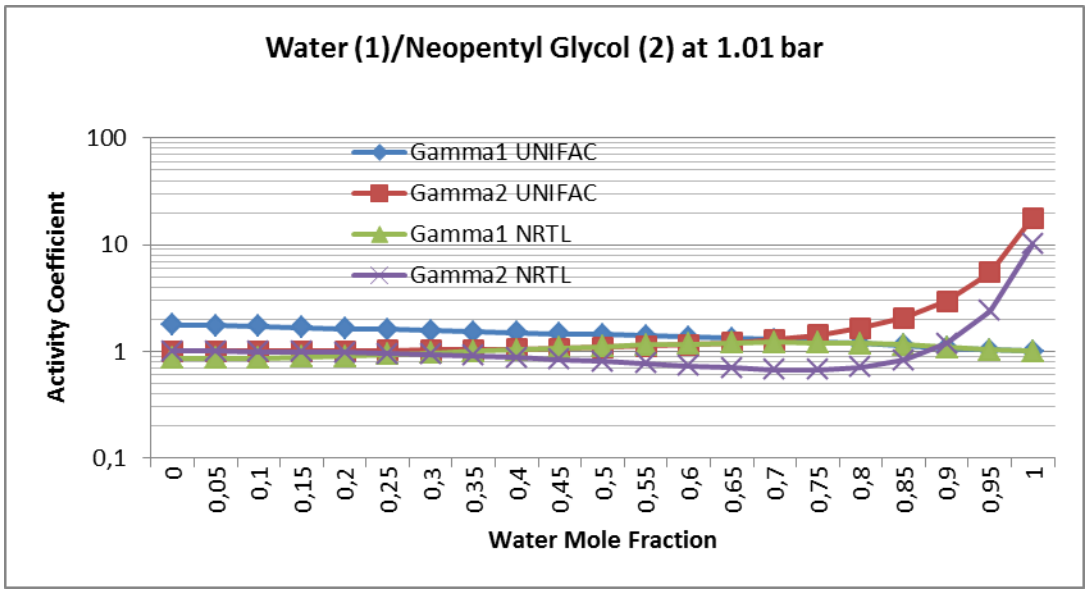

Figure 2. Activity coefficients of NPG and water as predicted by NRTL

BIPs for low NPG mass fractions, which are derived from first test setup, are: Bij=1907, Bji=-600 (i=1. j=2), α =0,28, and the BIPs obtained in the second test setup are the following: Bij =1907, Bji =-622, α =0,31.

Simulation results show good consistency with experimental results after fittings of the NRTL parameters as shown in Figure 3 and 4. HETP values is calculated from first setup 0.085 m for concentration range of 0.01 to 1.5 mass % of NPG and 0.21 m for concentration range of 0.01 to 49 mass % of NPG from second setup.

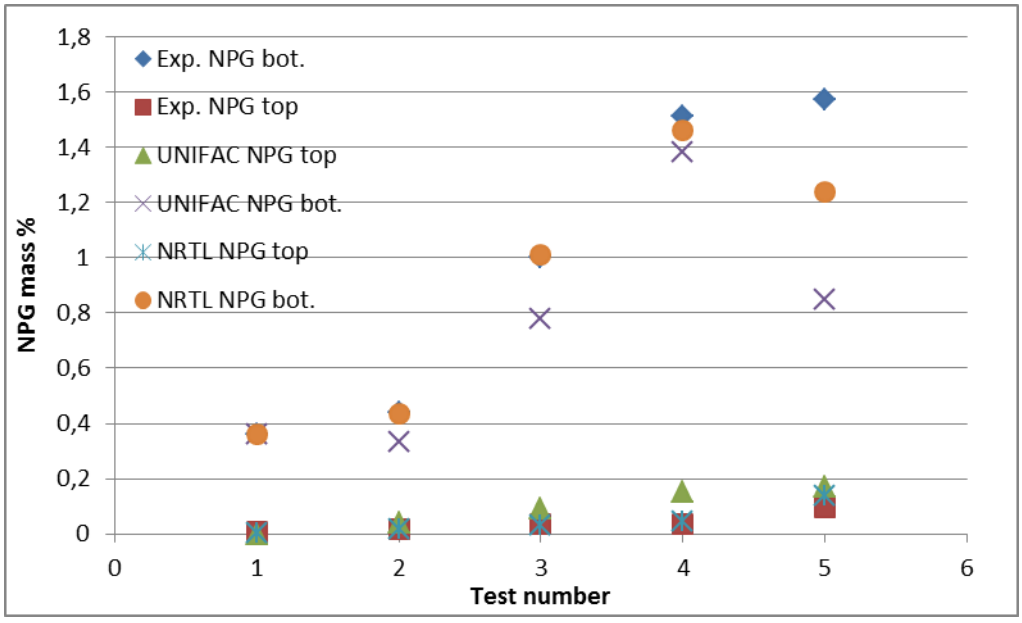

Figure 3. Neo mass fractions at the top and bottom of the column in first test setup

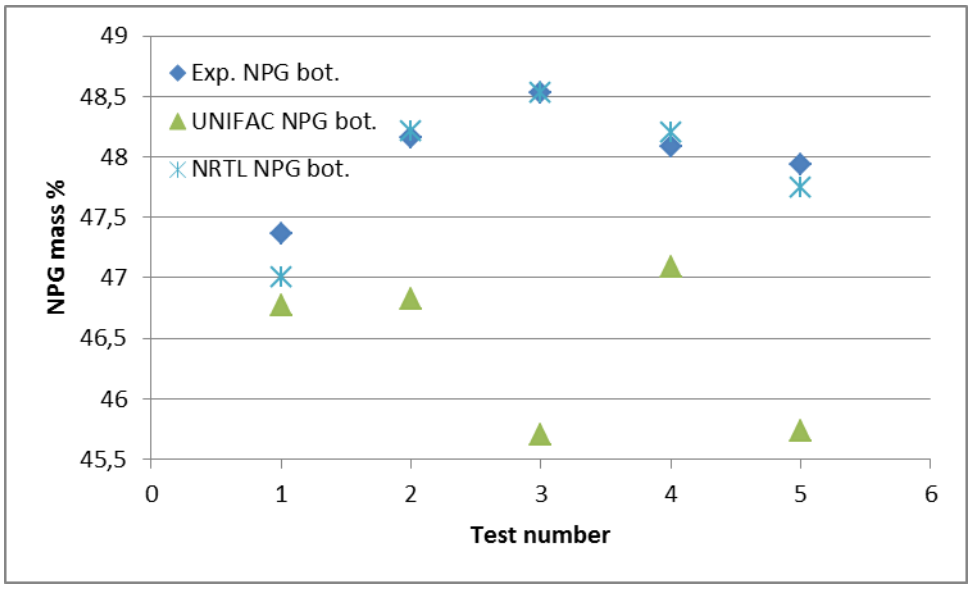

Figure 4. Neo mass fractions at the top and bottom of the column in second test setup

The method is further verified in production plant column. Plant column with 1.6 m in diameter was filled with 7m Mellapak 250Y packing and has. Using the BIPs sets derived from the experiments above, a comparison of experimental and calculated NEO mass fractions was made. The result is shown in Table 3.

Experimental -Plant data		2 BIPs set: Pilot second set-up BIP at the bottom – first set-up BIP at top		
NPG bottom %	NPG top %	NPG bottom %	NPG top %	HETP m
39,53	0,158	39,31	0,19	0,7

Table 3. Plant column results text – Arial 12 pt., left- justified- margins: 2,5 cm

3. Conclusions (Subheading – Arial 12 pt. bold, left-aligned)

The method applied in this paper is based on two steps: first step is to fit NRTL BIPs and the second one is to calculate mass transfer model using Bravo, Rocha and Fair method. Calculation is done in Chemcad. This procedure has been applied on non-ideal system of Neopentyl Glycol-Water. The experimental data for fittings of BIPs parameters has been collected from two different column arrangements: 0.07 m column and 0.5 m diameter column filled with Sulzer BX packings. The method has been verified on production plant column filled with 250 MELLAPAK Sulzer packings showing good simulations prediction.

Litterature

1. Kister, H. Z. *Distillation Design*. New York: McGraw-Hill (1991). p528-532.
2. Billet, R., Schultes, M. *Prediction of the Mass Transfer columns with Dumped and Arranged packings*, Chem. Eng. Res. Des. 77, (1999) 498-504.
3. Nor-Par a.s, *CHEMCAD Mass Transfer Distillation Manual*
http://www.norpar.com/mtr_manl.html
4. R. H. Chávez at all, Effect of the Structured Packing on Column Diameter, Pressure Drop and Height in a Mass Transfer Unit. Int. J. Thermodynamics, ISSN 1301-9724 Vol. 7, (No. 3), (2004) 141-148,
5. Olujic, Z., *Standardization of Structured Packing Efficiency Measurements*,
http://www.tkk.fi/Units/ChemEng/efce/2008/presentations/Olujic-document.pdf (2008)
6. A. E. Orlando Jr., L. C. Medina, M. F. Mendes, E. M. A. Nicolaiewsky, *HETP evaluation of structured packing distillation column*, Braz. J. Chem. Eng. Vol.26 no.3,(2009)

Integrated Workflow for Modeling, Simulation and Experiments of Distillation Processes

Regina Benfer[1], Tobias Keller[1], Norbert Asprion[1], Sergej Blagov[1], Roger Böttcher[1], Michael Bortz[2], Richard Welke[2], Jakob Burger[3], Erik von Harbou[3], Karl-Heinz Küfer[2], Hans Hasse[3]

[1]BASF SE Chemical and Process Engineering, Ludwigshafen, Germany;
[2]Fraunhofer Institute for Industrial Mathematics ITWM, Kaiserslautern, Germany;
[3]Laboratory of Engineering Thermodynamics, University of Kaiserslautern, Germany

Abstract

Design of pilot plant experiments, data evaluation, model validation and adjustment are essential tasks in developing chemical processes. These tasks are often not well supported by the working environment of process engineers, which is usually focused on the process simulations and pilot plant experiments. Therefore, in the present work, an integrated framework was developed which provides an interactive tool for model-based design of pilot plant experiments, evaluation of the pilot plant data and their use for improving the model.

One central feature of that framework is sensitivity analysis based on steady state process simulations. The goal of sensitivity analysis is to identify the impact of input parameters on the simulation model. It is also used for quantifying the impact of uncertainties in input parameters on the output. The input parameter space is typically large and contains parameters of different types, like state variables, parameters of fluid property models or stage numbers. Suitable measures for the sensitivity have to be defined and efficient algorithms are needed for the simulation-based sensitivity analysis in that large parameter space, in which a brute force enumeration is prohibitive, not only because it is tedious but also as it would drown the design engineer in a flood of information. Further challenges arise from the fact that results of the analysis depend on the operating point and hence not only one point but an operating window has to be covered. The results of the sensitivity analysis need to be visualized interactively and will support the process designer in the tasks of model adjustment, design of experiments and optimization.

These issues are addressed and solved in the interactive process design tool INES (INterface between Experiment and Simulation) which was developed in the present work. Examples are discussed which illustrate its application in distillation process design based on pilot plant experiments.

Keywords

Sensitivity analysis, model adjustment, data validation, design of experiments, uncertainties.

1. Introduction

Process development is usually based on experiments which often include the operation of the process or at least the essential parts of it, in a pilot- or miniplant. Process models are generated to describe and to optimize the concept. Distillation processes are usually modeled based on the equilibrium stage concept using detailed thermodynamic models. These models contain a large number of parameters which are either estimated or adjusted to experimental data by minimizing a distance measure between the model results and the data. Examples are the parameters of the thermodynamic model, the tray efficiency or HETP, respectively, but also prices which are used in cost functions.
We focus on continuous distillation here, which is ideally in steady state.

The cycle of data evaluation, model adjustment and use of the adjusted model to find optimal operating conditions, where new data are recorded, is in practice often only poorly supported and still requires a lot of handwork by the process engineers. Thus, data are recorded but not systematically analyzed, models are not optimally adjusted to the process under consideration and, as a result, optimization potential is not fully exploited in the process development. In this contribution, we present the framework INES (INterface between Experiment and Simulation) which offers an integrated solution for the data evaluation and selection process, the model adjustment and the optimization including optimal experimental design (OED) within one software environment. Special emphasis is given here to the sensitivity analysis, which plays a key role for identifying optimal experimental designs, choosing the most influential parameters for the optimization and for quantifying the impact of uncertainties in the model parameters on output functions.

2. Framework description

The INES framework supports the three essential steps in data-supported model-based process design, see Figure 1:

- Data validation: Data can be imported via different interfaces and their reliability can be assessed using different assistance functions.
- Model adjustment: Model parameters can be adjusted to data taken at various operation conditions.
- Model sensitivity analysis and OED: A sensitivity analysis to measure the impact of changes in model parameters on output functions can be performed for various operating points. This leads to the identification of optimal experimental designs as well as the choice of promising parameters for further optimization /Bortz et al. 2013/.

One of the essential features of INES is the use of interactive decision support functions which help the engineer to arrive at solutions that have the highest practical relevance under the given conditions. In the following, we will comment on the three aspects mentioned above.

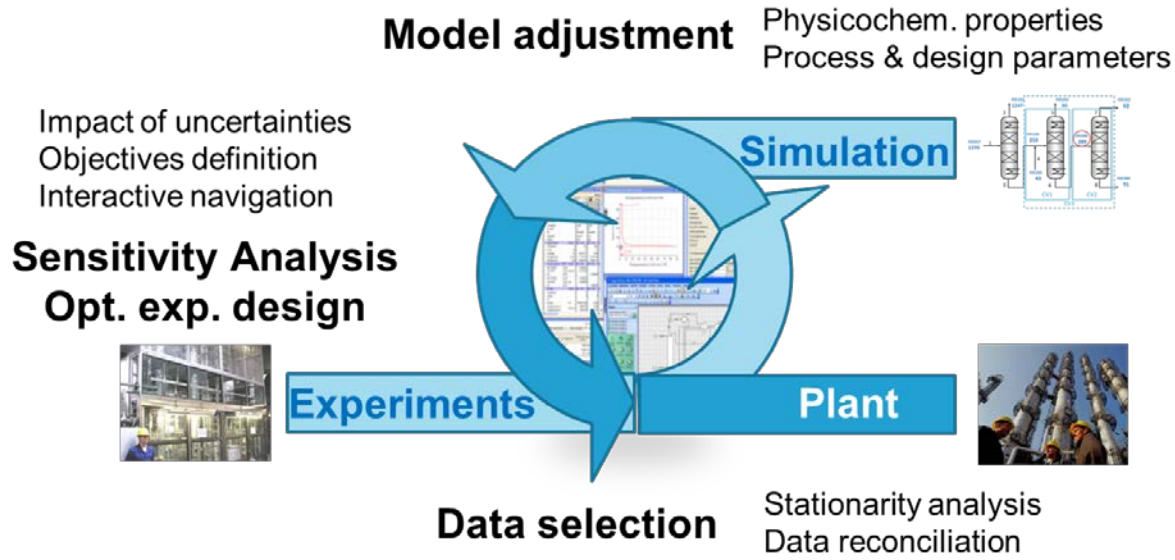

Figure 1: Cycle of data selection, model adjustment and sensitivity analysis with OED supported within the INES framework.

2.1 Data selection

In modern chemical plants a lot of experimental data is available which is impossible to analyze comprehensively - often not only confusing in terms of the number of the data but also in terms of the scattering. Random and gross errors, changing trends and fluctuations make it difficult to use the data directly for the adjustment of process models. Therefore in a first step a systematic procedure for data selection and evaluation is necessary. This needs a reliable identification of the change points which separate time-stationary intervals. The data are readout from process information management systems (PIMS) using for example IP 21 (Aspen) or PI (OSIsoft) for production plants. For experiments in lab or miniplant scale or analytical measurements still sometimes Excel is used for data storage. So, the tool provided for data selection offers an interface to these different software systems.

The analysis of different time series is facilitated by visualizing operation data in plots of measured data vs. time. Interesting periods can be selected and are subsequently analyzed to identify stationary time intervals. Different segmentation algorithms taken from literature e.g. /Fukuda et al. 2004/ are implemented and may be chosen. To simplify the selection procedure, an interactive scaling of the data to remove outliers is offered. For different selected periods averaged data and the variance of mean are calculated and interactive stationary tests can be performed. Usually, different sets of data are available for the period of interest. The subset of this data that is used of the stationarity analysis is selected by the user. The remaining sets are not used in the analysis, but an indication of stationarity level is given. Averaged data and their standard deviation are used for further calculations.

In the following step, the experimental data can be reconciled. For that reconciliation, a model is needed that correlates the data from the different types of measurements. Only the most simple correlations are taken into account in the present approach, namely overall and component mass balances and the summation equation for the mass fractions. Furthermore, chemical reactions may occur so that stoichiometric

constraints have to be accounted for. The procedure has to be able to handle cases in which the full set of possible chemical reactions is not known. For balancing, also the connectivity of the different streams has to be known. That information is taken from the flowsheet. Furthermore, mass balances refer to certain control volumes, and there are always different options to choose their boundaries, so that a selection is needed. In the present work CHEMASIM, the flowsheet simulator by BASF is used. The topology of the flowsheet is taken from CHEMASIM.

This data reconciliation is implemented such that it is possible to choose control volumes in order to obtain information about redundancy and (non-) observability of unmeasured streams by graph-theoretical concepts /Narasimhan 1999/. Reconciled data may be gained for example by minimizing the weighed sum-of-squares residuals between measured and calculated values /Manenti et al 2011/. The result of the data reconciliation, combined with statistical tests, allows obtaining information on the reliability of measured quantities, i.e. it helps to detect erroneous measurements or leakage streams.

2.2 Model adjustment

A flowsheet simulation model contains usually several types of input parameters: physicochemical properties like activity coefficients or NRTL parameters, reaction parameters like equilibrium constants or rate constants, process operating parameters like pressures and temperatures, design parameters like the feed heights or number of theoretical stages. Additionally there are output parameters like flow rates, concentrations, cost or energy consumption. The sensitivity analysis of the different adjustable parameters is an essential procedure when working with process models. It supports the identification of the essential parameters for an adjustment of the model to different operating points previously chosen by use of the data selection framework as will be described in the following.

2.3 Sensitivity analysis and optimal experimental design (OED)

The goal of sensitivity analysis is to identify the impact of input parameters on the output of the model. In the case of model validation uncertainties of physico-chemical, reaction or process parameters have to be analyzed. Uncertainties are quantified as uncertainties of directly measurable experimental data, and not as uncertainties in model parameters. I.e. for a pure component vapor pressure, not the uncertainties of the parameters of an Antoine equation are given but rather the uncertainty of the vapor pressure itself. The resulting confidence intervals are visualized as well as the parameters on sliders which make it possible to navigate in the corresponding model space. This enables an interactive investigation of the input and output parameters and helps finding the most important parameters for model adjustment. It also helps answering the question where uncertainties have to be reduced, see Figure 2.
OED aims for obtaining a reliable process simulation by adjusting uncertain parameters to a limited number of experiments. These experiments shall be conducted such that the measured quantity is as sensitive as possible to the parameters to be adjusted. In literature (see, for example, /Franceschini 2008/, different measures for local sensitivity have been proposed in the context of OED.

Unfortunately, it is by no means clear which is the most suitable of these measures. Furthermore, in practice, it turns out that OED is not a single-objective, but rather a multicriteria optimization problem: For example, a laboratory reactor is supposed to be operated to obtain a certain yield corresponding to that of the industrial process, but at the same time to be highly sensitive in order to determine reaction constants accurately in an experiment. Both objectives are usually contradictory.

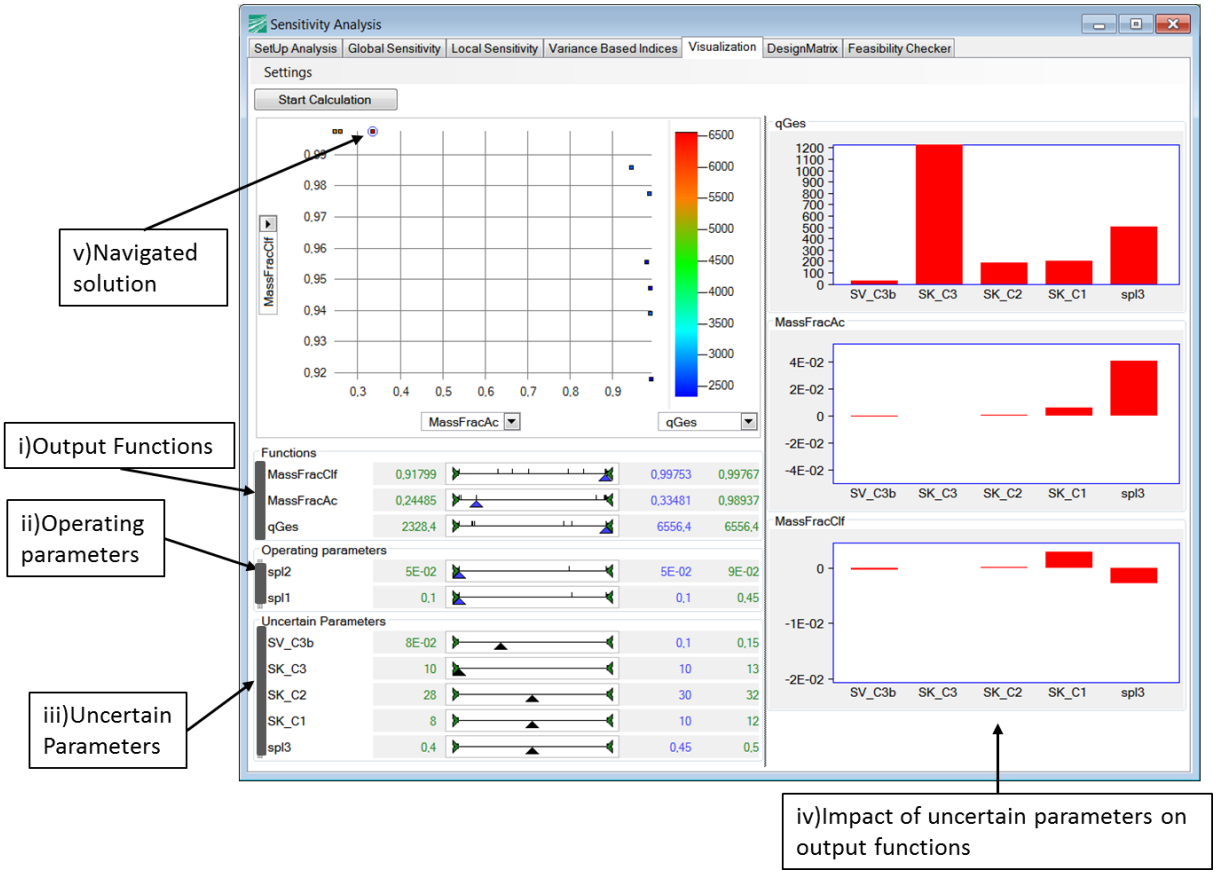

Figure 2: Screenshot of software prototype to perform an interactive sensitivity analysis. Each precomputed operating point with its operating parameters and output function values corresponds to one tick on the sliders i) and ii). The bars iv) are an estimate of how a change in each of the uncertain parameters in the range indicated by the sliders iii) affects the value of each output function. By navigating on the precomputed solutions, the user can compare these both with respect to the output function values and to the uncertainty measures.

Since optimizing local uncertainty measures as one of the objectives in OED is numerically unstable and of limited practical use, in INES we pursue a different strategy. Operating points from a promising region of operating parameters are enumerated. For each of these operating points, different sensitivity measures are calculated. Then, the trade-off between the objectives and the sensitivities can be explored interactively by the user as shown in Figure 2. The sensitivities can be measured both locally and globally: Local sensitivity matrices can be determined as well as averaged differential quotients stemming from a fractional factorial design and variance-based indices /Saltelli 2008/. The variance-based indices are obtained by using Sobol-sequences to sample the space of the uncertain parameters, which makes it easy for the user to obtain higher-precision values by adding further points.

The computationally relatively cheap averaged differential quotients based on an adequate fractional factorial design serves as a first guideline to the user which are

the most influential quantities. In a second step, a more refined analysis for these quantities can be undertaken by calculating the variance-based indices to obtain full quantitative insight into how the output functions are affected.

3. Conclusions

In process development, experimental investigations and simulation model development are often executed in parallel. Only the connection between both methods leads to a deeper understanding of the process which then speeds-up and enhances the process development. This is achieved by the interactive process design tool INES which is developed in this project and supports interfacing experimental studies with modeling and simulation. The focus of INES on the experimental side is in miniplant experiments, but also various types of accompanying experiments like measurements of physico-chemical data are supported in a consistent way. On the simulation side, the focus is on steady state process simulation. Different methods for data reconciliation, sensitivity analysis and optimal experimental design are supported and combined for that purpose. Typical applications include the development of distillation and absorption processes. The INES framework is incorporated in the process design toolbox ProcessNet of BASF.

Acknowledgements

Thanks will be given Oliver Hirth, Stefan Höser, Jako Niewoudt, Michael Rieger (all BASF SE), Martin Kaul (University of Kaiserslautern), Jan Schwientek, Maksym Berezhnyi (both Fraunhofer ITWM) for their contributions to INES.

References

Asprion N., Blagov S., Ryll O., Welke R., Winterfeld A., Dittel A., Bortz M., Küfer K.-H., Burger J., Scheithauer A., Hasse H., 2011, Pareto-Navigation in Chemical Engineering, Computer-Aided Chemical Engineering 29A, pp 422-426.

Bortz M., Burger J., Asprion N., Blagov S., Böttcher R., Nowak U., Scheithauer A., Welke R., Küfer K.-H., Hasse H., 2013, Multicriteria optimization in chemical process design and decision support by navigation on Pareto sets, Computers and Chemical Engineering, pp

Buzzi-Ferraris G., Manenti F., 2011, Outlier detection in large data sets, Computers and Chemical Engineering 35, 388–390.

Franceschini G., Macchietto, S., 2008, Model based design of experiments for parameter decision: State of the art, Chemical Engineering Science 63, pp 4846-4872

Fukuda K., Stanley H.E., Amral L.A.N., 2004, Heuristic segmentation of a nonstationary time series, Physical Review E, 69 (2), 021108.

Gani R., Cameron I., Lucia A., Sin G., Georgiadis M., 2012, Process Systems Engineering, 2. Modeling and Simulation, Ullmann's Enc. of Ind. Chemistry, Electr. Release, Wiley-VCH, Weinheim.

Klatt K.-U., Marquardt W., 2009, Perspectives for process systems engineering—Personal views from academia and industry, Computers and Chemical Engineering 33, 536–550.

Kwiatkowski D., Phillips P.C.B., Schmidt P., Shin Y., 1992, Testing the null hypothesis of stationarity against the alternative of a unit root: How sure are we that economic time series have a unit root?, Journal of Econometrics, 54 (1–3), 159-178.

Manenti F., Grottoli M.G., Pierucci S., 2011, Online Data Reconciliation with Poor Redundancy Systems, Ind. Eng. Chem. Res., 50, 14105–14114.

Narasimhan S., Jordache S., 1999, Data Reconciliation & Gross Error Detection, An intelligent use of process data, Gulf-Publishing.

Saltelli A., Ratto M., Andres T., Campolongo F., Cariboni J., Gatelli D., Saisana M., Tarantola S., 2008, Global Sensitivity Analysis, The Primer, John Wiley & Sons.

Reliable and efficient calculation of azeotropes and pinch points in homogeneous and heterogeneous multicomponent distillation

Mirko Skiborowski[1], Jürgen Bausa[2], Wolfgang Marquardt[1]
[1]Aachener Verfahrenstechnik – Process Systems Engineering, RWTH Aachen University, Aachen, Germany
[2]Bayer Technology Services GmbH, 51368 Leverkusen, Germany

Abstract
The reliable calculation of azeotropes and pinch points are essential requirements in synthesis and conceptual design of distillation processes. It is complicated by the strong nonlinearity stemming from thermodynamic equilibrium relations, the a-priori unknown number of solutions, and the necessary consideration of potential phase splitting. To overcome the high computational effort of reliable (global) algorithms, efficient continuation methods have been proposed for azeotrope and pinch calculation. However, they utilize different formulations. In this paper we show by means of an equivalency between certain pinch branches and univolatility curves, that continuation applied to the pinch equation system with an integrated phase stability test provides a unifying means for azeotrope and pinch point calculation in homogeneous and heterogeneous mixtures.

Keywords
azeotropes, pinch points, univolatility curves

1. Introduction

The calculation of azeotropes is an essential step for topological synthesis methods, as well as shortcut methods, which require the definition of feasible product compositions. However, this task is especially challenging, as it requires the calculation of all solutions of a strongly nonlinear set of algebraic equations. In case of heterogeneous mixtures, phase stability needs also to be accounted for. Consequently, a tremendous effort has been directed towards the development of reliable algorithms for the calculation of azeotropes. Global optimization guarantees the detection of all azeotropes in homogeneous [1] and heterogeneous mixtures [2], but is computationally expensive, especially for mixtures with a large number of components. The same applies for methods based on interval analysis [3]. Beside continuation methods, based on a homotopy from the ideal to the non-ideal equilibrium relationship, have been suggested as an efficient means to determine all azeotropes in homogeneous [4] and heterogeneous mixtures [5]-[7].
Continuation is also used for the determination of pinch points, another important task in conceptual design of distillation-based processes. Pinch points are fixed points of the equation system describing the composition profile in a column section. These are of special importance for the determination of feasible products and minimum energy demand calculations (e.g. [8]-[10]). Pinch branches, i.e. the locus of all pinch points for varying reflux ratios, can be calculated based on a continuation starting from pure components and azeotropes. Recently, Felbab [10] proposed a variant of such an algorithm for homogeneous mixtures and suggested to use the same continuation algorithm to determine the location of azeotropes. However,

Felbab [10] did not work out the promising idea. In this paper, we first introduce a continuation approach for the pinch equation system, which includes a phase stability test to detect changes in the number of valid phases and is therefore applicable to homogeneous and heterogeneous mixtures. We further motivate and demonstrate the calculation of azeotropes by the same continuation approach using an equivalence of the solutions of the pinch equation system for pure component products and univolatility curves, which comprise all points with equal K-values.

2. Calculation of pinch branches by means of continuation

The continuation approach is based on a discrete model describing the tray-by-tray profile in a general column section (cf. Figure 1).

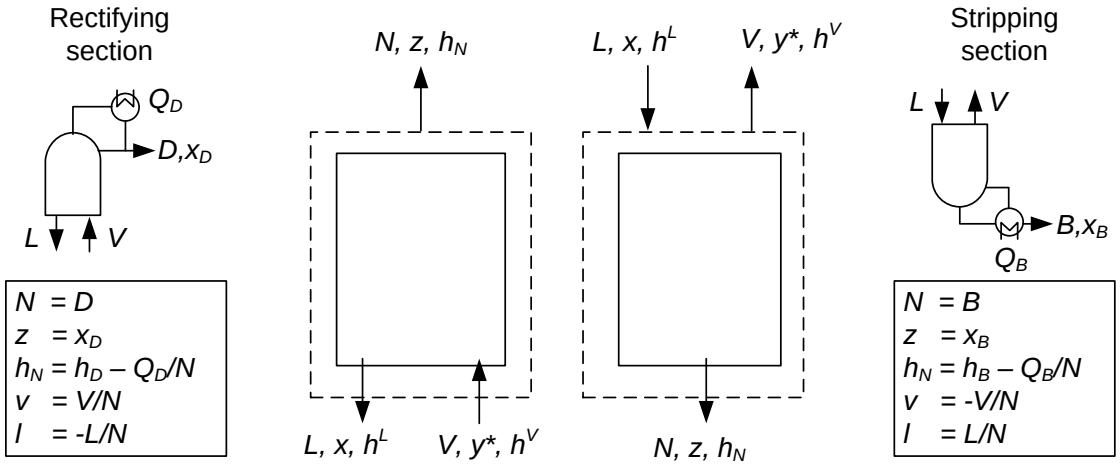

Figure 1: General column section and relation to rectifying and stripping section

The pinch equation system consists of mass and energy balances, summation constraints and equilibrium conditions:

$$0 = v \cdot y_i^* - l \cdot x_i - z_i \quad , i = 1, \dots, n_C, \tag{1}$$
$$0 = v \cdot h^V(y^*, T, p) - l \cdot h^L(x, T, p) - h_N, \tag{2}$$
$$0 = \sum_{i=1}^{n_c} x_i - 1, \tag{3}$$
$$0 = \sum_{i=1}^{n_c} y_i^* - 1, \tag{4}$$
$$0 = y_i^* - K_i(x, y^*, T, p) \cdot x_i \quad , i = 1, \dots, n_C. \tag{5}$$

Here, v and l represent normalized liquid and vapor flow rates, based on the liquid, vapor and net flow rates L, V and N (cf. Figure 1). The vapor phase compositions y_i^*, $i = 1..n_C$, are considered to be in equilibrium with the liquid phase compositions x_i, $i = 1..n_C$. The K-values K_i are the distribution coefficients of the components in vapor-liquid equilibrium (VLE). As the net enthalpy h_N only occurs in the energy balance, the system of equations can be split and only eq. (1) and (3)-(5) need to be solved in order to calculate the solution set. In a subsequent step the net enthalpy can be calculated as the solution to eq. (2).

Pure components and azeotropes, i.e. the singular points of the system, are always solutions of the pinch equation system. However, the normalized vapor flow rate v tends to infinity at these points. While Felbab [10] avoids the singular points, starting the integration at pinch points at high reflux in their vicinity we utilize a reformulation of the pinch equation system to overcome the numerical difficulties at the singular

points. Introducing an additional parameter α to multiply the mass balance with eq. (1) is replaced by the following two equations:

$$0 = \bar{v} \cdot y_i^* - \bar{l} \cdot x_i - \alpha \cdot z_i \ , i = 1, \dots, n_C, \quad (6)$$
$$0 = \alpha^2 - \bar{v}^2 - 1. \quad (7)$$

The reformulated pinch equation system, eq. (3)-(7), with the reformulated flow rates $\bar{v} = \alpha \cdot v$ and $\bar{l} = \alpha \cdot l$ can be solved everywhere, including the singular points.
In case of a heterogeneous system, phase splitting needs to be accounted for. Assuming a maximum of two liquid phases, the equilibrium relationship (eq. (5)) needs to be exchanged by VLE equations for the two liquid and the vapor phase, to account for vapor-liquid-liquid equilibrium (VLLE):

$$0 = x_i - (1 - \phi) \cdot x_i^I - \phi \cdot x^{II} \ , i = 1, \dots, n_C, \quad (8)$$
$$0 = y_i^* - K_i(x^I, y^*, T, p) \cdot x_i^I \ , i = 1, \dots, n_C \quad (9)$$
$$0 = y_i^* - K_i(x^{II}, y^*, T, p) \cdot x_i^{II} \ , i = 1, \dots, n_C. \quad (10)$$

Here x_i^I and x_i^{II} are the phase compositions of the two liquid phases and ϕ describes the liquid phase ratio. However, determining the equilibrium solution for a given overall liquid composition and pressure by means of a separate routine, including a phase-stability test [11], the continuation can still be performed for eq. (3)-(7), if the K-values are calculated as a pseudo-homogeneous K-values by

$$0 = K_{p,i}(x, y^*, T, p) - \frac{K_i(x^{II}, y^*, T, p) \cdot K_i(x^I, y^*, T, p)}{(1-\phi) \cdot K_i(x^{II}, y^*, T, p) + \phi \cdot K_i(x^I, y^*, T, p)} \ , i = 1, \dots, n_C. \quad (11)$$

Note, that in case of a heterogeneous solution, the calculation of the net enthalpy the needs to account for liquid phase splitting too:

$$0 = h_p^L(x, T, p) - (1 - \phi) \cdot h^L(x^I, T, p) - \phi \cdot h^L(x^{II}, T, p). \quad (12)$$

With the integrated phase-stability test the solution of the under-determined equation system (eq. (3)-(7)) in form of $g(u) = 0$, with $u = \{x^T, y^{*T}, T, \alpha, \bar{v}, \bar{l}\}$, is valid in homogeneous and heterogeneous regions and has one degree of freedom. As the solution set is one-dimensional and can be parameterized (e.g. by $\bar{v}$) it can be solved by means of continuation starting from solutions which are a-priori known. As all singular points are also solutions to the pinch equation system, all pure components and azeotropes are valid initial solutions [8,9].
A pseudo-arc-length algorithm is used to calculate the pinch branch, starting from the singular points. The determinant of the Jacobian $\frac{\partial g}{\partial u}$ is monitored in every step of the method to detect bifurcations along the pinch branch, which relate to additional branches. The direction of these branches results directly from an analysis of the kernel of the Jacobian. The calculation of the eigenvalues and eigenvectors of the Jacobian provides also important information, including the number of unstable eigenvalues to allow for a classification of the stability of the actual solution. This is of special importance for the utilization of pinch points in pinch-based shortcut methods and the determination of thermodynamical consistency in case of singular points. For an elaborate description of the algorithm and the implementation, we refer to [12].

3. Calculation of azeotropes

The relative volatility is a measure of the differences in volatility between two

components and indicates how easy or difficult a particular separation by means of distillation will be. It is defined by the ratio of the K-values of two components i and j

$$\alpha_{ij} = \frac{y_i/y_j}{x_i/x_j} = \frac{K_i}{Kj}\,. \tag{13}$$

For a relative volitility of one (univolitility), the K-values as well as the volatility of both components are equal [$K_i = K_j$]. Azeotropes represent a special case of univolatility, as the K-values of the present components are not only equal, but also equal unity. It is well known that the existence of azeotropes directly entail the existence of univolatility curves/surfaces connecting the azeotrope with the boundaries of the subspaces [13,14]. Westerberg and Wahnschafft [15] already proposed to utilize univolatility curves for determining homogeneous azeotropes and present a profound discussion of the theory. Thus, continuation along univolitility curves is an option for determining all azeotropes of a mixture. However, the previously described continuation of the pinch branches can be used for exactly this purpose by an appropriate choice of the net product composition z.

In the special case of a pure component (w.l.o.g. we choose component 1), the mass balance for the pinch equation system, presented by eq. (1), results in

$$0 = v \cdot \begin{bmatrix} y_1 \\ y_2 \\ \vdots \\ y_{n_c} \end{bmatrix} - l \cdot \begin{bmatrix} x_1 \\ x_2 \\ \vdots \\ x_{n_c} \end{bmatrix} - \begin{bmatrix} 1 \\ 0 \\ \vdots \\ 0 \end{bmatrix}. \tag{14}$$

Therefore, for all components $\boldsymbol{i \neq 1}$ the following equation holds:

$$0 = v \cdot y_i - l \cdot x_i \;, i = 2, \dots, n_C. \tag{15}$$

This means, that either the compositions of a component $\boldsymbol{i}$ are zero ($\boldsymbol{x_i = 0}$ and $\boldsymbol{y_i = 0}$), or

$$\frac{l}{v} = \frac{L}{V} = \frac{y_i}{x_i} = K_i \;, \forall (i \in \{1, .., n_C\} \mid x_i > 0) \tag{16}$$

holds. Therefore, in case of a pure component product, all components present at a pinch point have equal K-values and accordingly the pinch branches either correspond to a binary edge or a univolatility curve. Thus, the continuation of the pinch branches is equivalent to a continuation along univolatility curves. This is the basis for the determination of the azeotropes.

Figure 2 presents an exemplary illustration of the pinch lines for the ternary mixture of acetone, ethanol and water (AEW) at an elevated pressure of 10 atm and a quaternary mixture of acetone, chloroform, methanol and benzene (ACMB) at 1 atm. For both systems, which exhibit multiple azeotropes, a continuation starting from only one pure component product suffices to detect all azeotropes. The azeotropes are found by means of a simple search along the pinch branches (binary edges and univolatility curves). Higher-order azeotropes (e.g. Az(ACMB) in Figure 2 (right)) are located on higher-order univolatility curves ($\boldsymbol{K_A = K_C = K_M}$), which bifurcate from lower-order univolatility curves ($\boldsymbol{K_C = K_M}$). The stability of each azeotrope is derived from the information on the eigenvalues and eigenvectors and is in accordance with

the stability information of the pinch branch. Based on this information, topological consistency [16] can easily be checked, too. Note, while all azeotropes are located, not all univolatility curves are computed, performing the calculation for just one pure component product. The calculated univolatility curves are the specific curves, connected to the specific subspace. E.g., there exists a complete univolatility surface ($\boldsymbol{K_A = K_M}$) in the quaternary reigon in the ACMB mixture, but only the univolatility curve connected to the AC-edge is calculated for the pure benzene product.

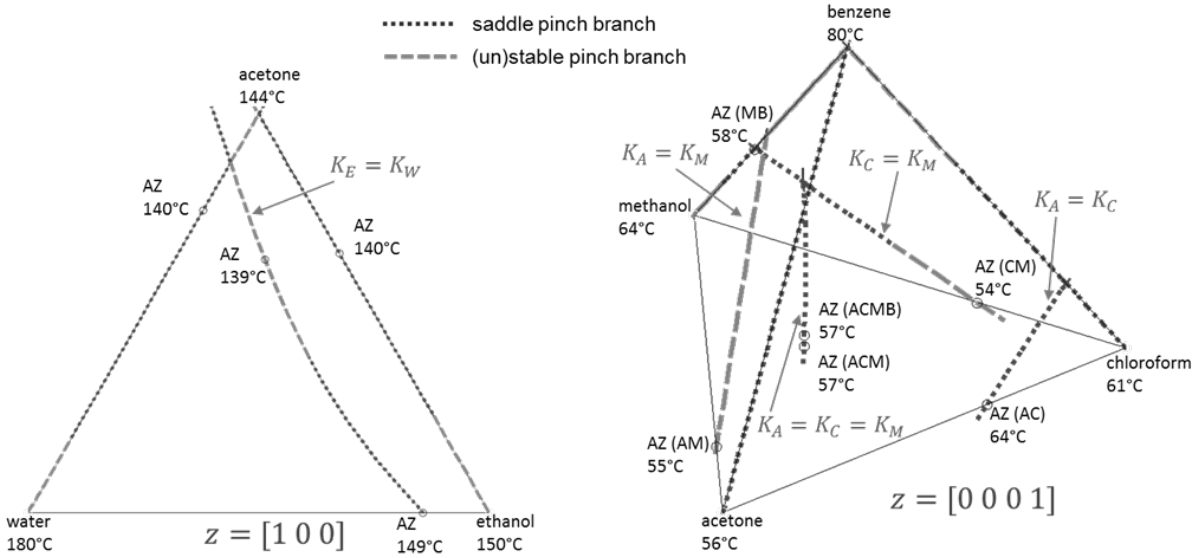

Figure 2: Pinch branches for AEW system at 10atm and ACMB system at 1 atm and pure component product z

The equivalance can also be extended to heterogeneous mixtures considering the pseudo-homogeneous K-value, defined by eq. (11). For a solution of the pinch equation system the composition of a component i, different from the pure component product, is again either zero ($x_i = 0$ and $y_i = 0$), or

$$\frac{L}{V} = \frac{y_i}{x_i} = K_{p,i}\ ,\ \forall(i \in \{1,..,n_C\} \mid x_i > 0). \tag{17}$$

Thus, for a pure component product all pinch branches correspond to either a binary edge or a univolatility curve also inside a miscibility gap. Outside of the miscibility gap(s) the pseudo-homogeneous K-values are equal to the standard K-values for the homogeneous system.

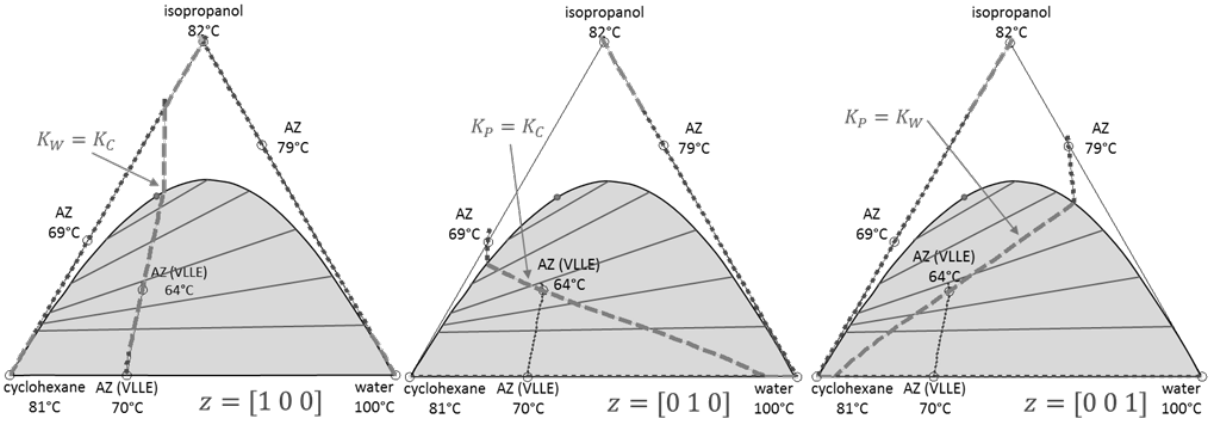

Figure 3: Pinch branches for pure comp. products of the PWC mixture at 1 atm.

Figure 3 presents an exemplary illustration of the pinch lines for the heterogeneous ternary system of isopropanol, water and cyclohexane (PWC) at 1 atm. The system exhibits three binary and one ternary azeotrope. The ternary and the binary water-cyclohexane azeotropes are located inside the miscibility gap and are therefore labeled as VLLE. All four azeotropes are determined correctly independent of the choice of the pure component product.
The quaternary mixture of ethanol, water, cyclohexane and benzene is the most complex heterogeneous reference mixture, used as case study for previous methods [2,5]. Even within the current not-optimized prototype implementation the presented method determines all 11 azeotropes and their stability within ~ 1 sec, using the NRTL model to describe the non-ideality of the liquid phase(s). Application to multicomponent mixtures are therefore feasible.

4. Conclusions

The continuation approach with the integrated phase stability test and the illustrated equivalence provide an efficient mean for the calculation of univolatility curves, azeotropes and pinch points in a unifying manner. Thereby, it presents a general tool which provides nearly all the information required, for the application of topological synthesis methods, feasibility analysis and pinch-based shortcut methods for the determination of the minimum energy demand. Note, although continuation along the univolatility curves should facilitate the determination of all azeotropes, a proof is still missing. Investigation of such proof and the extension to reactive mixtures, which require only minor changes to the pinch equation system [12], are subject to future research.

Acknowledgements

Financial support by the German Research Foundation (DFG) under contract MA 1188/26-2 is gratefully acknowledged.

References

[1] S.T. Harding et al., Ind. Eng. Chem. Res. 36 (1), (1997), 160–178.
[2] S.T. Harding et al., Ind. Eng. Chem. Res. 39 (6), (2000), 1576–1595.
[3] R.W. Maier et al., AIChE J. 44 (8), (1998), 1745–1755.
[4] Z.T. Fidkowski et al., Comp. Chem. Eng. 17 (12), (1993),1141–1155.
[5] S.K. Wasylkiewicz et al., Ind. Eng. Chem. Res. 38 (12), (1999), 4901–4912.
[6] J.E. Tolsma and P.I. Barton, Chem. Eng. Sci. 55 (18), (2000), 3817–3834.
[7] J.E. Tolsma and P.I. Barton, Chem. Eng. Sci. 55 (18), (2000), 3835–3853.
[8] Z.T. Fidkowski et al., AIChE J. 37 (12), (1991), 1761–1779.
[9] P. Pöllmann and E. Blass, Gas.Sep. Purif. 8 (4), (1994), 194–229.
[10] N. Felbab, Ind. Eng. Chem. Res. 51 (20), (2012), 7035–7055.
[11] J. Bausa and W. Marquardt, Comp. Chem. Eng. 24, (2000), 2247–2456.
[12] J. Bausa, Fortschritt-Berichte VDI, 3, 692, VDI Verlag (2001)
[13] V.N. Kiva et al., Chem. Eng. Sci. 58 (10), (2003), 1903–1953.
[14] F.B. Petlyuk, Distillation theory and its application to optimal design of separation units. Cambridge, Cambridge University Press. (2004)
[15] A.W. Westerberg and O.M. Wahnschafft, Adv. Chem. Eng. 23, (1996) 63–170.
[16] V.T. Zharov, Russ. J. Phys. Chem. 43 (11), (1969), 2784–2791.

The influence of mass transfer parameters in acid-gas treating and non-reactive processes using rate based models.

Richard Arendsen[1], Patrick Huttenhuis[1] and Geert Versteeg[2]
[1] PROCEDE Gas Treating, P.O. Box. 328, 7500 AH Enschede, The Netherlands;
[2] RuG, Nijenborgh 4, 9747 AG Groningen, The Netherlands;

Abstract
The growing importance of chemically based separation processes, such as the use of alkanolamines for gas processing and now carbon capture underline the importance of proper modeling of coupled mass transfer and chemical kinetics in multiphase systems. Details related to the construction of empirically determined mass transfer parameters are important since the interactions between their different governing equations and equation parameters are not always intuitive and sound understanding of what they are. For example, in physical separation processes only the product of mass transfer coefficient and specific area for the gas and liquid phases is required, while for chemically reactive mass transfer limited separation processes the individual values of mass transfer coefficients and specific areas are required for the gas and liquid phases. Therefore, how they affect the simulation results is an important part of the learning process required by a process engineer to become proficient in using simulators incorporating these features and consequently benefit from these more sophisticated rate based models. The quality and experimental information on these parameters is very scarce and a discussion on how this type of data should be collected and incorporated into a simulation model will be presented in this paper. Examples are given, on how correct values of mass transfer parameters and specific areas are not enough to provide meaningful estimates for process performance or for process design.

Keywords
mass transfer, acid-gas treating, non-reactive processes, rate based models.

1. Introduction

For steady-state simulation of acid gas treating processes the Procede Process Simulator (PPS) is developed as a new flowsheeting tool [1]. The models combine all issues relevant for the design, optimization and analysis of acid gas treating processes, including post-combustion and pre-combustion carbon dioxide capture. The simulator consists of a user-friendly graphical user interface and a very powerful numerical solver that handles rigorous modeling of thermodynamics, kinetics and rate-based mass transfer. Moreover, it supports all unit operations relevant for gas treating plants (absorbers, strippers, flash drums, heaters, pumps, compressors, mixers and splitters, etc.). The Procede Process Simulator has been used for several carbon capture research projects [2,3,4].

The program includes an extensive database of thermodynamic parameters, interaction coefficients, kinetics, etc. that have been optimized to accurately predict the vapor liquid equilibriums (VLE), thermodynamic and physical properties and the kinetically enhanced mass transfer (both analytical and rigorous) of amine based capturing processes. The thermodynamic model combines an excess Gibbs model for the liquid phase with a cubic equation of state model for the gas phase. For the optimal prediction of column performances, the program includes a database of various tray types, as well as a large collection of both dumped and structured packing respectively. Several mass transfer and hydrodynamic models have been implemented that benefit from accurate physical property models (density, viscosity, surface tension, diffusivity, conductivity) specifically selected for acid gas treating applications. The tool is able to describe complete acid gas treating processes, including complex processes with multiple (mixed or hybrid) solvent loops, and is able to significantly improve the understanding of the performance of potential new solvents.

The most important mass transfer parameters for gas treating applications are the liquid and gas side mass transfer coefficient (k_L and k_G) and the effective interfacial area for mass transfer (a_e). A significant amount of experimental studies related to predict these mass transfer parameters in absorption columns have been carried out. From these studies several empirical or semi-empirical correlations are derived by regression of the correlations with the experimental (pilot) data or correlations are derived from theoretical hydraulic models. In general overall or volumetric mass transfer coefficients are determined from these experiments; however, a distinction between mass transfer coefficient (k_L and k_G) and effective interfacial area (a_e) is basically not possible. For non-reactive processes, however, the distinction between these two parameters is not very relevant, because the product of these parameters determines the overall absorption rate. Contrary to gas-treating processes, where chemical solvents are used, both parameters must be known individually as will be shown in this paper.

For gas absorption the most important parameter is the effective interfacial area (a_e). There are several definitions on the area in packed columns (geometrical area, wetted area, effective area). If for example part of the liquid is not renewed on the packing material, the packing is wetted, but the area is not effective for mass transfer. On the other hand Bravo and Fair [5] investigated that the effective area is not only determined by the wetted area, but also mist, gas bubbles, ripples and the column wall can contribute to the overall mass transfer rate. All these effects are dependent on the packing material and process conditions and will influence the column performance. Therefore, they should be determined as accurate as possible. However, this is only possible experimentally.

The first attempts to determine correlations for the calculation of effective area, were based on studies to liquid flow profiles and distribution. One of these models is developed by Shetty and Cerro [6]. They studied flow patterns and velocity profiles of thin, viscous liquid over surfaces at different angles and derived liquid hold-up and wetted area from this. The penetration theory was used to derive the mass transfer correlations. The individual contributions of k_L and a_e are derived form an overall k_La_e and therefore a function of the approach used by Shetty and Cerro [6].

Bravo et al. [7] measured the mass transfer in finely woven gauze packing material for systems like o/p xylene and ethyl benzene/styrene desorption from water. However, from these experiments only the volumetric mass transfer coefficients, k_La_e and k_Ga_e, can be measured. Therefore the correlations they derived to determine the

gas and liquid side mass transfer correlations, a_e, k_L and k_G respectively, are dependent on how Bravo et al. [7] attributed the contributions to the individual parameters. It must be noted that these correlations are still used by many process engineers at the moment. Bravo et al. [7] assumed that the gauze packing was completely wetted during the experiments and therefore the effective area was set equal to the geometric area. In later work of these authors introduced correction to account for lower values of a_e for the various packing material.
Billet and Schultes [8] derived a theoretical expression to calculate the liquid hold-up. By incorporating the penetration theory both gas and liquid side mass transfer coefficients were calculated theoretically from this expression. The interfacial area was determined from experimental studies using 70 different packing elements, different packing material and 30 different chemical systems. From these studies the volumetric mass transfer coefficients were determined and with the already determined k_L and k_G from the liquid hold-up, the effective interfacial area was calculated.It must be noted that all the experiments mentioned above were carried out for systems without chemical reaction.
Another commonly used model, i.e. the Delft model, was developed by Olujic et al. [9] for corrugated packing's. In this model the liquid flow is considered as a thin liquid film of uniform thickness, while the gas flow is traveling in a zigzag profile through the packing. The k_G is calculated from Sherwood numbers, while k_L is calculated via the penetration theory. For the calculation of the effective interfacial area, it is assumed that the liquid is completely distributed.
A systematic comparison between non-reactive and reactive processes will now be presented using the removal of CO_2 from high-CO_2 natural gas streams with aqueous MDEA. The conditions are given in Table 1 and 2. Under these conditions the k_L and a_e are varied two-dimensionally and the capture for non-reactive and reactive absorption is calculated. The non-reactive absorption is simulated via physical absorption at identical process conditions as for the reactive absorption. The value of k_G is set at 0.01 m/s for all simulations. For all the process conditions studied the gas phase resistance had hardly any influence. Neither packing type, nor correlations are selected because a_e, k_L and k_G are set at specific values.

Table 1: Gas and liquid input parameters

	Gas	**Liquid**
Pressure	70 bara	70 bara
Temperature	40 °C	40 °C
Flow rate	200,000 Nm^3/hr	3,960 m^3/hr
CO_2	15 vol%	0.02 mole CO_2 / mole MDEA
CH_4	85 vol%	-
H_2O	100 %Saturation	50 wt%
MDEA		50 wt%

Table 2: Absorber input parameters

Packing Depth	30 m
Column Diameter	4 m
k_G	0.01 m/s

2. Results and discussion

Figure 1a and 1b show the results of the calculated capture for non-reactive and reactive absorption in contour plots, respectively. The lines represent constant

capture conversions in the k_L and a_e surface. The k_L is varied from 10^{-5} to 10^{-3} m/s and a_e is varied from 1 to 250 m^{-1}.

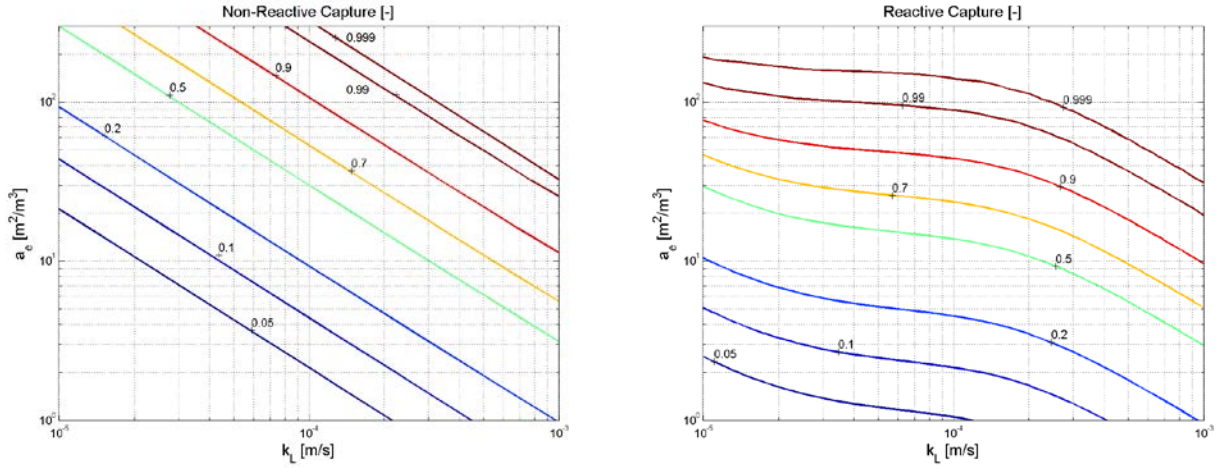

Figure 1a and 1b: Contour plots of calculated capture for non-reactive and reactive absorption in the k_L and a_e surface.

The non-reactive, physical absorption lines of constant capture are straight diagonal lines. This clearly shows that the capture is only a function k_La_e and is independent of the individual values of k_L and a_e, as long as the product k_La_e remains constant. Also it can be concluded that it is not possible to determine the separate values for k_L and a_e based on physical ab- or desorption experiments only. All combinations of k_L and a_e constant value for k_La_e result in the same process performance. However, for non-reactive absorption processes it is not necessary to know k_L and a_e separately. This conclusion also holds for distillation processes.

The reactive absorption lines of constant capture rates are much more curved. Above a k_L of $3{\cdot}10^{-4}$ m/s the constant conversion lines show exactly the same straight diagonal lines at the same values for reactive and non-reactive absorption. This means that at these values no enhancement by the chemical reaction is achieved, the absorption fluxes for non-reactive and reactive absorption are the same. At lower k_L the lines show a more horizontal trend. At these conditions the effect of k_L on the capture becomes less pronounced. It must be noted however, that values for k_L of $3{\cdot}10^{-4}$ m/s for a 50 w% MDEA solution can be considered as extremely high. This effect is clearer at higher captures rates, c.q. a_e's. Below a k_L of $3{\cdot}10^{-5}$ m/s the lines bend back to horizontal diagonal lines. Of course, it is also not possible to determine the separate values for k_L and a_e values based on a measured capture for reactive absorption. In this case, combinations of k_L and a_e that give the same product will even result in different captures. In a range of one decade for k_L, from $3{\cdot}10^{-5}$ and $3{\cdot}10^{-4}$ m/s, especially at high capture rates the sensitivity of the capture for k_L is much less than for a_e. These are typical values for full scale packed beds and tray columns. Therefore in this range the determination of a_e on capture measurements is more reliable. On the other hand, for reactive absorption processes it is absolutely necessary to know the individual values of k_L and a_e to calculate the capture. This clearly shows that mass transfer correlations that are based on non-reactive validations cannot be used for reactive absorption.The effects shown in Figure 1 will be explained in the following. The volumetric flux (N) in moles / (time * volume) depends on the effective interfacial area, the overall mass transfer coefficient and the driving force, according to:

$$N = k_{ov} \cdot a_e \cdot \left(C_G - \frac{C_L}{m} \right) = \frac{a_e}{\frac{1}{k_G} + \frac{1}{m \cdot k_L \cdot E_A}} \cdot \left(C_G - \frac{C_L}{m} \right)$$

The driving force is defined as the concentration difference between the gas (C_G) and liquid (C_L) phase, m is the distribution coefficient based on concentrations. E_A is the enhancement factor, which is the ratio of the flux with reaction and the flux without reaction at identical driving forces. For non-reactive systems the enhancement factor is by definition equal to one. Figure 2 shows an illustration of E_A as a function of k_L for two different conditions in these simulations. Above a k_L of $3 \cdot 10^{-4}$ m/s E_A approaches the value of one, indicating that the mass transfer rate is fast compared to the chemical reaction. For these conditions the flux with reaction is equal to the flux without reaction. Below a k_L of $3 \cdot 10^{-4}$ m/s the flux is enhanced by the chemical reaction. The maximum possible enhancement, E_A^{∞}, depends on the diffusion of the amine towards the interface. At (very) low k_L and high partial pressures of the gas phase reactant the amine diffusion can become rate limiting.

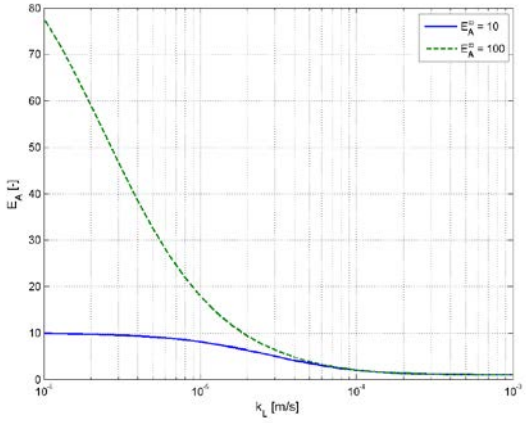

Figure 2: E_A as a function of k_L.

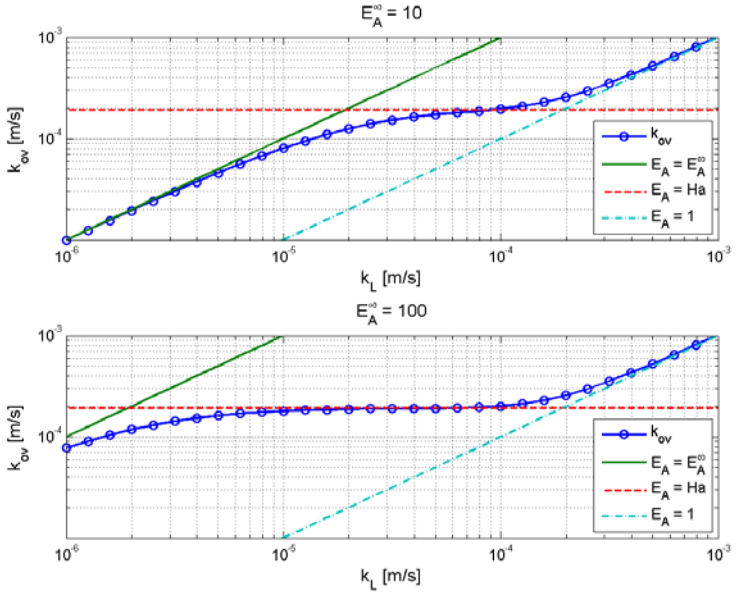

Figure 3: k_{ov} as a function of k_L for E_A^{∞} is 10 and 100.

Figure 3 shows an illustration of k_{ov} as a function of k_L for two different E_A^{∞}'s. Above a k_L of $3 \cdot 10^{-4}$ m/s the dotted line for k_{ov} approaches the E_A=1 line. These lines correspond to the straight diagonals in figure 1 for reactive and non-reactive absorption. Below a k_L of $3 \cdot 10^{-4}$ m/s k_{ov} approaches the E_A=Ha line. In this case k_{ov} becomes almost independent of k_L, because nearly all CO_2 is converted near the interface. These lines correspond to the almost horizontal lines in figure 1b. Because at higher captures E_A^{∞} increases the horizontal lines at high a_e's are more pronounced. At low k_L's k_{ov} approaches the $E_A=E_A^{\infty}$ line and the contour lines in figure 1 bend back to diagonals again.

3. Conclusions

A systematic comparison between non-reactive and reactive processes is presented using the removal of CO_2 from high-CO_2 natural gas streams with aqueous MDEA. For non-reactive absorption processes it is only necessary to know the product of k_L and a_e, all combinations of k_L and a_e that give the same product for k_L and a_e result in the same capture. For reactive absorption processes it is absolutely necessary to know the individual values of k_L and a_e to calculate the capture. It is shown that mass transfer correlations that are based on non-reactive validations cannot be used for reactive absorption.

References

1. E.P. van Elk, A.R.J. Arendsen, G.F. Versteeg, A new flowsheeting tool for flue gas treating, Energy Procedia 1, 1481–1488, 2009.
2. E.S. Hamborg, P.W.J. Derks, E.P. van Elk, G.F. Versteeg, Carbon dioxide removal by alkanolamines in aqueous organic solvents. A method for enhancing the desorption process, Energy Procedia 4, 187-194, 2011.
3. J.C. Meerman, E.S. Hamborg, T. van Keulen, A. Ramírez, W.C. Turkenburg and A.P.C. Faaij, Techno-economic assessment of CO2 capture at steam methane reforming units using commercially available technology, To be published, 2012.
4. A.R.J. Arendsen, E. van Elk, P. Huttenhuis, G. Versteeg, F. Vitse, Validation of a post combustion CO2 capture pilot using aqueous amines with a rate base simulator, SOGAT, 6th International CO2 Forum Proceedings, Abu Dhabi, UAE, 2012.
5. Bravo, J. L.; Fair, J. R. Generalized Correlation for Mass Transfer in Packed Distillation Columns. Ind. Eng. Chem. Process Des. Dev. 1982, 21, 162.
6. Shetty, S.; Cerro, R. L. Fundamental Liquid Flow Correlations for the Computation of Design Parameters for Ordered Packings. Ind. Eng. Chem. Res. 1997, 36, 771
7. Bravo, J. L.; Rocha, J. A.; Fair, J. R. Mass Transfer in Gauze Packings. Hydrocarbon Process. 1985, 64, 91.
8. Billet, R.; Schultes,M. PredictingMass Transfer in Packed Columns. Chem. Eng. Technol. 1993, 16, 1.
9. Olujic, Z. Development of a Complete Simulation Model for Predicting the Hydraulic and Separation Performance of Distillation Columns Equipped with Structured Packings. Chem. Biochem. Eng. Q. 1997, 11, 31.

Progress in Design of Random Packing for Gas-Liquid Systems

J. Maćkowiak

Prof. Dr.-Ing. Jerzy Maćkowiak, ENVIMAC Engineering GmbH, Im Erlengrund 27, 46149 Oberhausen, Germany, e-mail: j.mackowiak@envimac.de

Abstract

The following work presents a generally applicable model for the prediction of the separation efficiency of random non-perforated and lattice-type packing with size between 8 and 90 mm for gas-liquid systems in the entire operating range up to the flooding point. The new model was derived on the basis of the droplet flow model and that mass transfer in the gas phase occurs from continuous gas phase into the swarm of droplets. The presented correlations do not require empirical, individual packing specific constants.

About 4150 experimental distillation, absorption and desorption data of ENVIMAC data bank (EDB) were validated with the new model in a very wide range of changing operational and constructive parameters; from low top pressure of 13 mbar up to 2 bar. Good consistency was found between experimental values of the separation efficiency for about 115 different types of random packings and calculated values based on the new model.

Keywords:

random packing, lattice-type packing, separation efficiency, mass transfer in the gas and liquid phase, distillation, absorption

1. Introduction

During the last 5 decades, a lot of random packings have been developed, which can be divided into 4 generations, from classical spheres to new modern random lattice type packings of 3rd and 4th generation. Random packings are widely and successfully used not only in the distillation, absorption and stripping processes but also in environmental protection processes like waste gas and wastewater treatment. Their form has changed significantly during that time and the field and range of applications compared to the first generation packings significantly increased. A big progress in the available design methods was observed during that period of time, especially in the modelling of fluid dynamics, which is presented in the literature [1,2].

One of the first models for the design of random packing of 1st and 2nd generation was the model of Onda et al. (1968) [4], followed by the improved Monsanto Model of Bolles & Fair (1979) [5], the model of Zuiderweg (1978) [6] and models presented by Zech & Mersmann (1978) [7]. The first model for the design of distillation columns not only for classical random packings but also for lattice type packings of the 3rd generation was the model developed by Billet & Maćkowiak (1984) [8] which has been modified by Maćkowiak (1991) [9]. This model was developed for more than 60 different packings for systems with the main mass transfer resistance located in the vapour phase. Based on the assumption of film formation in the packed bed, Billet & Schultes (1993,1999) [2,10] derived new correlations for determining the effective interfacial area per unit volume a_e and mass transfer coefficients in the gas and liquid phase for 55 different classical and lattice-type packings.

The main aim of this work is to develop a generally applicable method for determining the volumetric mass transfer coefficient in the gas phase and the separation efficiency n_t/H or HTU_{OV} not limited to certain packing types for distillation and absorption systems.

2. Mass transfer in the liquid phase

For predicting the efficiency of random packing acc. to the static n_t/H-model or the kinetic HTU_{OV} x NTU_{OV} model of Chilton and Colburn (1935), the knowledge of the liquid phase and gas phase volumetric mass transfer coefficients $\beta_L \cdot a_e$ and $\beta_V \cdot a_e$ is required. A new, generally valid model for the calculation of $\beta_L \cdot a_e$-values has been presented by Maćkowiak (2011) [11]. Based on observations and measurements of droplet proportions in packed beds with different packing carried out by Bornhütter & Mersmann [12], the new method [11] was developed on the assumption of droplet flow in the packed bed. Thus interfacial area per unit volume a_e can be determined for gas-liquid systems with the fundamental Eqn. (1) [1], valid for disperse systems. According to the model, mass transfer is interrupted during the formation of rivulets and only recommences when new droplets are formed. The

process is therefore non-stationary, as has been described by the well-known model of Higbie [13], Eqn. (2):

$$a_e = 6 \cdot \frac{h_L}{d_T} \left[m^2 / m^3 \right], \qquad (1) \qquad \beta_L = \frac{2}{\sqrt{\pi}} \sqrt{\frac{D_L}{\tau}} \quad [m/s]. \qquad (2)$$

The contact time τ in eqn. (2) is described by the time that a droplet needs to cover the distance *l* between two contact points within the packing. Hence:

$$\tau = \frac{l}{\overline{u}_L} \Rightarrow \frac{l \cdot h_L}{u_L} \quad for \quad \overline{u}_L = \frac{u_L}{h_L} \quad [s] \qquad (3)$$

Acc. to [1], the liquid hold-up h_L in random packings for turbulent liquid flow $Re_L \geq 2$ in the range below the loading point $F_V \leq 0.65\ F_{V,Fl}$ can be described by Eqn. (4a) or (4b) [1]:

$$h_L = 2.2 \cdot B_L^{1/2} \left[m^3 / m^3 \right] \quad (4a) \qquad \text{or} \qquad h_L = 0.57 \cdot Fr_L^{1/3} \left[m^3 / m^3 \right]. \qquad (4b)$$

Correlations for the range above the loading line are presented in the literature [1].The contact paths *l* in eqn. (3) for the random packing was determined on the basis of the following correlation [11]:

$$l = 0.115 \cdot (1 - \varphi_P)^{2/3} \cdot d_h^{1/2} \quad [m], \qquad (5)$$

where φ_P is a form factor as geometrical parameter related to the characteristic structure of a packing element and d_h is the hydraulic diameter of packed beds [1].

Substitution of the relations of Eqn. (3) into Eqn. (2) and of Eqn. (4b) into Eqn.(1) leads to the Eqn. (6) for the prediction of the volumetric mass transfer coefficient $\beta_L \cdot a_e$ in columns with random packing in the operating range below the loading line $F_V \leq 0.65\ F_{V,Fl}$ and for turbulent liquid flow $Re_L \geq 2$ [11]:

$$\beta_L \cdot a_e = \frac{15.1}{(1 - \varphi_P)^{1/3} \cdot d_h^{1/4}} \cdot \left(\frac{D_L \cdot \Delta\rho \cdot g}{\sigma_L} \right)^{1/2} \cdot \left(\frac{a}{g} \right)^{1/6} \cdot u_L^{5/6} \left[1/s \right] \qquad (6)$$

For the operating range above the loading line $F_V > 0.65\ F_{V,Fl}$ the following Eqn. (7) is valid [12]:

$$(\beta_L \cdot a_e)_S = \frac{15.1}{(1 - \varphi_P)^{1/3} \cdot d_h^{1/4}} \cdot \left(\frac{D_L \cdot \Delta\rho \cdot g}{\sigma_L} \right)^{1/2} \cdot \left(\frac{a}{g} \right)^{1/6} \cdot \left(0.35 + \frac{F_V}{F_{V,Fl}} \right)_{u_L = const} \cdot u_L^{5/6} \left[1/s \right] \qquad (7)$$

Eqns. (6) and (7) allow to predict the volumetric mass transfer coefficient in the liquid phase $\beta_L \cdot a_e$ in random packings containing packing elements of different types and sizes, enabling the prediction of $\beta_L \cdot a_e$ values for any of the studied types of modern and classic packing with d=0.012-0.090 m accurate enough for practical applications with a mean error of ± 15 % in the range below the flooding line [11].

3. Mass transfer in the gas phase

The new model is based on the assumption, that mass transfer is takes place from the continuous gas or vapour phase into the individual droplets falling down in packed bed acc. to Eqn. (8) of Hugmark & Frössling (1967) [14].

$$\underset{h_L \to 0}{Sh_{V,T}} = 2 + C_V \cdot Re_T^n \cdot Sc_V^{1/3} = 2 + C_V \cdot \left(\frac{u_R \cdot d_T}{\nu_V} \right)^n \cdot \left(\frac{\nu_V}{D_V} \right)^{1/3} \qquad (8)$$

For a falling swarm of droplet in random packings, the mass transfer coefficient can be described with the following relation Eqn. (9):

$$\beta_{V,h_L>0} = \beta_{V,T\,h_L \to 0} \cdot \left(1 - \frac{h_L}{\varepsilon} \right)^m \qquad [m/s] \qquad (9)$$

and the volumetric mass transfer coefficient in the vapour phase $\beta_V \cdot a_e$ will be estimated acc. to Eqn. (10)

$$(\beta_V \cdot a_e) == \beta_{V,h_L>0} \cdot a_e = \frac{D_V}{d_T} \cdot \left(2 + C_V \cdot Re_T^n \cdot Sc_V^{1/3} \right) \cdot \left(1 - \frac{h_L}{\varepsilon} \right)^m \cdot 6 \cdot \frac{h_L}{d_T} \qquad [1/s] \qquad (10)$$

as the product of Eqn.(1) and Eqn.(9), in which the constants C_V and exponents “n” and “m” must be evaluated from the experimental data.

4. Model validation

The ENVIMAC data bank (EDB) was used to check the model presented here for 23 different test systems, 115 packing types of 1st – 4th generation with size of d= 8 to 100 mm made of metal, ceramic and plastic. The total number of experimental data evaluated within this work was about 1050 for distillation systems and 3100 data points for absorption systems.
Evaluation of the experimental data of the data bank (EDB) leads to following correlation, Eqn. (11):

$$\left(\beta_V \cdot a_e\right) = 6 \cdot \frac{h_L}{d_T^2} \cdot D_V \cdot \left(2 + 0.0285 \cdot \frac{u_R \cdot d_T}{\nu_V} \cdot \left(\frac{\nu_V}{D_V}\right)^{1/3}\right) \cdot \left(1 - \frac{h_L}{\varepsilon}\right)^6 \qquad \left[1/s\right] \tag{11}$$

The relative mean error for evaluated volumetric mass transfer coefficient $\beta_V \cdot a_e$ in the gas phase for absorption systems was found to be 17.3% for the operating range below the loading line and 18.9% for the entire range up to about 90% of the flooding point.

Figure 1 presents, as an example, the comparison between the experimentally determined theoretical separation efficiency n_t/H calculated acc. to model presented above and experimental data of Billet [15] in the operating range up to 90-95% of flooding point for 50 mm metallic Pall rings, valid for different distillation systems and in *Figure 2* for 25 and 50 mm metallic Pall rings, valid for absorption systems.

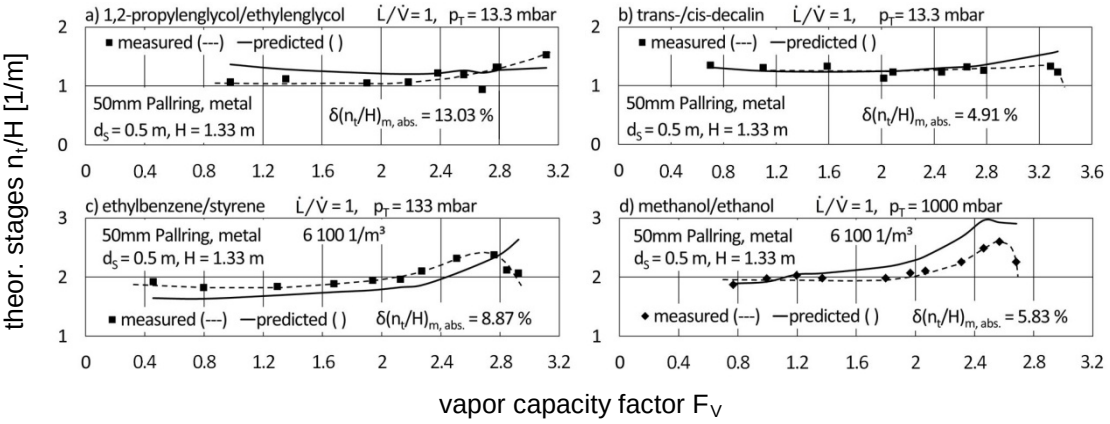

Figure 1: Experimental verification of the model for distillation for 50 mm metallic Pall rings.

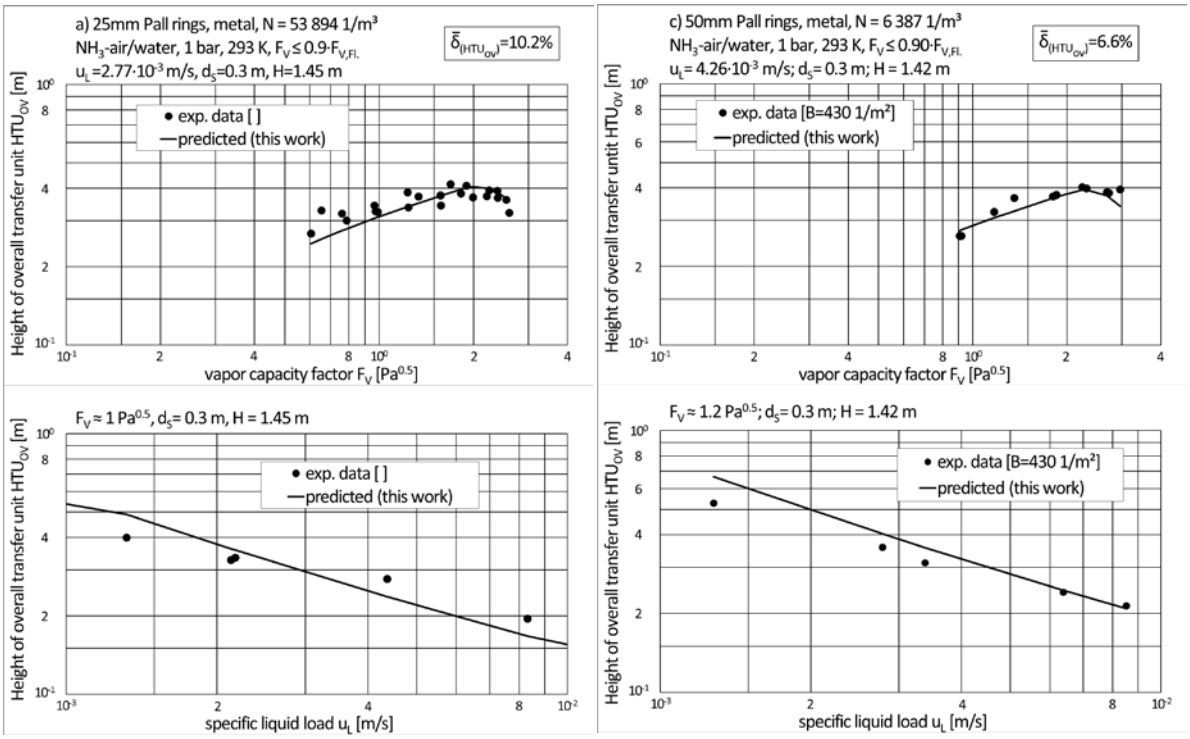

Figure 2: Experimental verification of the model for gas-liquid systems for metallic Pall rings.

Figures 3 and 4 show the parity plots for different packing types of 1st, 2nd, 3rd and 4th generation for experimental distillation data in the operating range up to 90-95% of the flooding point.
The estimated mean relative error of all data evaluated for packings of 2-4th generation is in the range between 3.15% and 15.5% and for different packing of 1st generation between 11.2% to 27.5%.

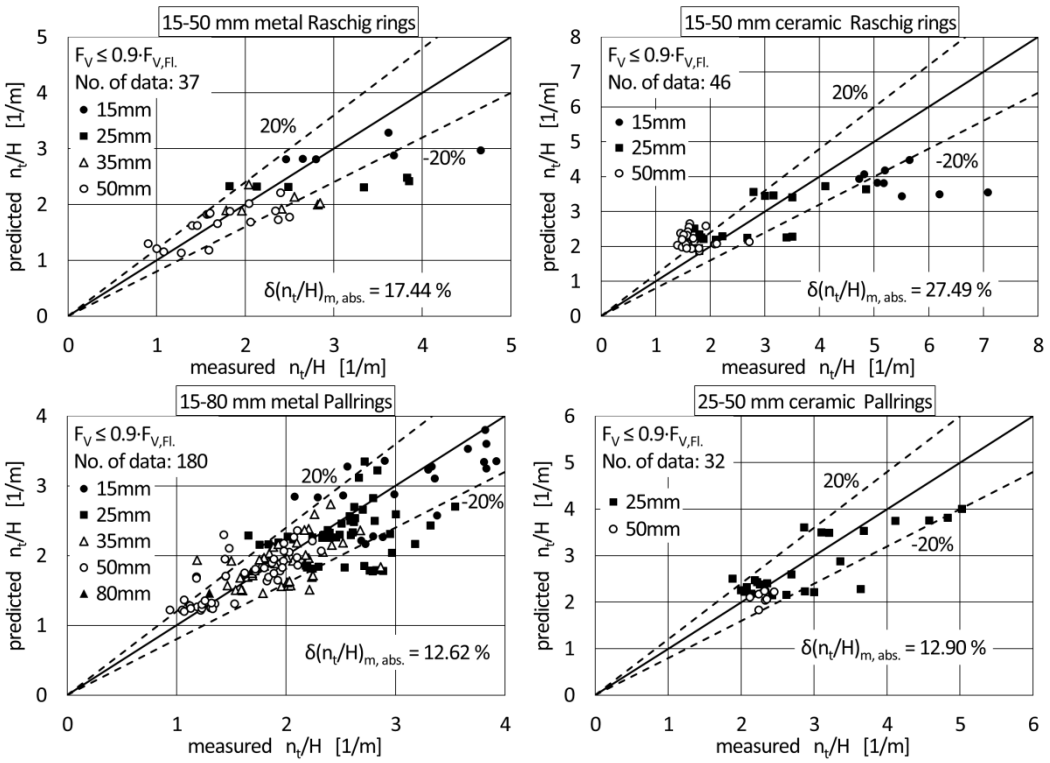

Figure 3: Experimental verification of the model for distillation for packings 1st and 2nd generation.

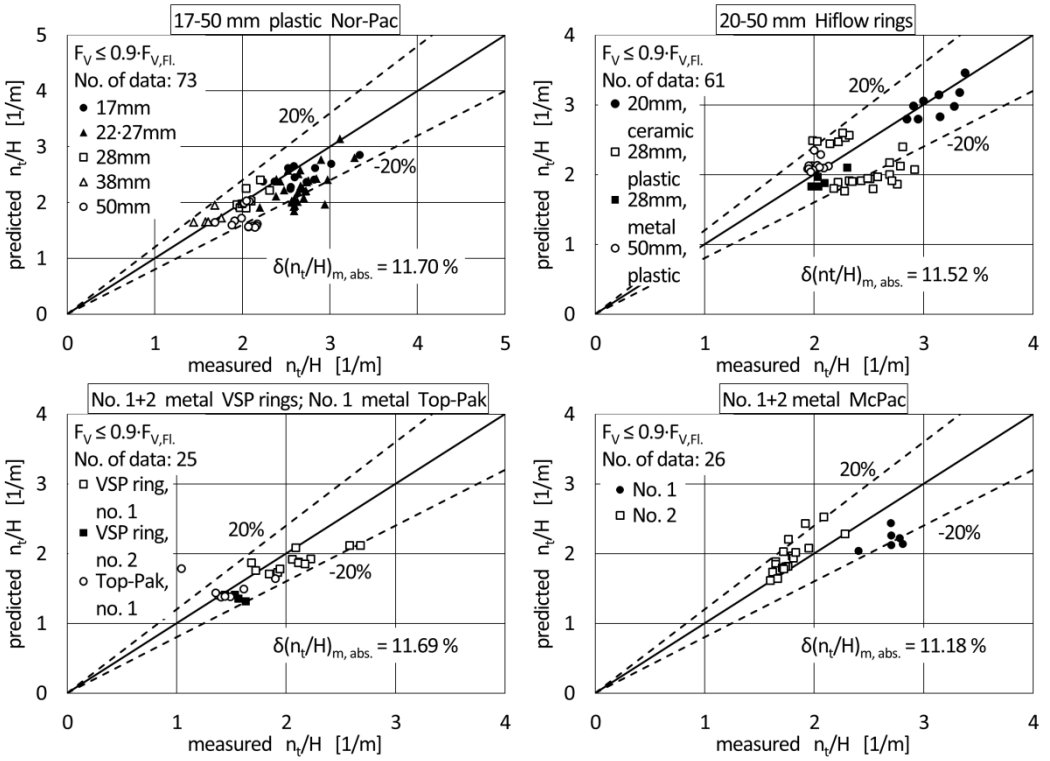

Figure 4: Experimental verification of the model for distillation for packings 3rd and 4th generation.

5. Comparison of the presented model with correlations from literature

The results of the evaluation of the absorption and desorption data from the EDB-data bank for gas-liquid systems with different correlations from literature is shown in *Table 1*.

Table 1: Results of exp. data evaluation for gas/liquid systems – comparison with correlation from literature

Author	Onda et al. [4] (1968)		Zuiderweg [6] (1978)		Zech & Mersmann [7] (1978)		Billet & Schultes [2,10] (1993/1999)		this work	
	No. of exp. data	δ $(HTU_{OV})_m$ [%]	No. of exp. data	δ $(HTU_{OV})_m$ [%]	No. of exp. data	δ $(HTU_{OV})_m$ [%]	No. of exp. data	δ $(HTU_{OV})_m$ [%]	No. of exp. data	δ $(HTU_{OV})_m$ [%]
total	973	69.9	2084	30.84	2084	23.44	1203	15.26	2084	14.73
loading range $F_V < 0.65 \cdot F_{V,Fl}$	759	67.11	1684	26.42	1684	21.63	977	14.34	1684	14.80
below flooding $0.65 \le F_V/F_{V,Fl} < 1$	214	78.8	400	49.45	400	31.06	226	19.24	400	14.33

The model presented in this work allows predicting the separation efficiency HTU_{OV} below the loading line with similar accuracy to the model of Billet & Schultes (1993/1999), but with a higher accuracy above the loading line and for more different packing types and systems. A generally better prediction of the separation efficiency is achieved compared to classical correlations like that of Onda et al. (1968) [4], Zuiderweg (1978) [6] and Zech & Mersmann (1978) [7], which were developed for classical packings of 1st and 2nd generation only. This can be confirmed by the data listed in *Table 2* which shows a comparison of calculated separation efficiencies to experimental distillation data of Billet [15]. It becomes apparent that all correlations are useful for calculation of separation efficiency for classical packings, but correlation presented in this work leads to best accuracy.

Table 2: Comparison of the model prediction with literature correlations with experimental data of Billet [15] for 15-50 mm metallic Pall rings, d_S=0.5 m;
System: ethylbenzene/styrene, p_T = 133 mbar, $\dot{L}/\dot{V}=1$

	Exp. data [15]		Onda et al. [4] (1968)		Zuiderweg [6] (1978)		Zech & Mersmann [7] (1978)		Maćkowiak [9] (1990)		Billet & Schultes [2,10] (1993/1999)		this work	
Pall rings:	F_V [$Pa^{0.5}$]	n_t/H [1/m]	n_t/H [1/m]	δ(n_t/H) [%]	n_t/H [1/m]	δ(n_t/H) [%]	n_t/H [1/m]	δ(n_t/H) [%]	n_t/H [1/m]	δ(n_t/H) [%]	n_t/H [1/m]	δ(n_t/H) [%]	n_t/H [1/m]	δ(n_t/H) [%]
50 mm	1.93	1.95	1.68	-13.7	1.64	-16.1	2.66	36.6	1.66	-14.8	2.73	40.1	1.82	-6.8
35 mm	1.77	2.15	2.53	17.8	1.83	-14.7	2.73	27.0	1.97	-8.3	2.44	13.5	2.05	-4.7
25 mm	1.7	2.4	3.54	47.4	2.07	-13.6	2.73	13.9	2.32	-3.4	2.79	16.2	2.32	-3.5
15 mm	1.7	3.36	2.65	-21.2	2.63	-21.9	2.86	-14.8	3.22	-4.2	3.32	-1.1	3.02	-10.2
$\bar{\delta}(n_t/H)$	–		25.0		16.6		23.1		7.7		17.7		6.3	

6. Final remarks

6.1 The presented model, which is based on the droplet flow model in packed column filled with random packing, allows the prediction of the separation efficiency for all investigated types of packings of 1st – 4th generation in the entire operation range up to 90-95% of flooding point with a satisfactory accuracy for practical applications. For the determination of volumetric mass transfer coefficients in both liquid and vapour phase only the physical properties of the systems and packing characteristic data related to the geometrical shape of the packing such as the specific packing area "a", packing void fraction "ε" and packing form factor "φ_P" are required. These data are also needed to determine the fluid dynamics of random packings [1]. The characteristic data of about 150 different types and size of random packing are listed in literature [1].

6.2 The use of individual packing specific constants for mass transfer prediction is not necessary in the presented model, what distinguishes the presented model from other models in literature.

6.3 *Table 3* shows the validity range for the investigated systems.

Table 3: Validity range of presented model

d	=	0.008 – 0.090 m	ρ_V	=	0.076 – 5 kg/m³	$F_V/F_{V,Fl}$	≤	0.90 – 0.95
a	=	54.2 – 550 m^2/m^3	ρ_L		641 – 1100 kg/m³	p_T	=	0.013 – 2 bar
ε	=	0.696 – 0.987 m^3/m^3	σ_L	=	17.2 – 72.7 mN/m	$Re_L \in \langle 0-150 \rangle$		
d_S	=	0.10 – 1.4 m	Sc_L	=	45 – 10000			
d_S/d	≥	6	Sc_V	=	0.4 – 1.25	$Re_V \in \langle 400-17500 \rangle$		
H	=	0.8 – 4 m						

References

[1] J. Maćkowiak, *Fluid Dynamic of Packed Columns,* Springer,Heidelberg/New York (2010)

[2] R. Billet, M. Schultes, *Chem. Eng. Technol.* 16 (1993) p. 1
[3] R. Billet, J. Maćkowiak, Chem-Techn. (Heidelberg) 9 (1980), p. 219 - 226
[4] K. Onda, H. Takeuchi,Y. Okumoto, *J.of Chem.Eng*, 1 (1968),p.56-62
[5] W.L. Bolles,J.R. Fair, Proceedings -3rd Int. Symp. on Distillation (1979), London, p.3.3/35-89 and *Chem.Engineering*, 12 (1982) p.109-116
[6] F.J. Zuiderweg, *vt Verfahrenstechnik* 12 (1978), p. 674-677
[7] J.B. Zech, A. Mersmann, *Chem.-Ing.-Techn.* 50 (1978), no. 7 MS 604/78
[8] R.Billet, J. Maćkowiak, *Fette,Seifen,Anstrichmittel*,86 (1984)p.349-358
[9] J. Maćkowiak, *Paper presented on AICHE-Meeting*, Chicago (1990), 16. Nov.
[10] R. Billet, M. Schultes, *Trans IChemE* ,77 (1999) p.498-504
[11] J. Maćkowiak, *Chem. Eng. Research & Design*, 89 (2011), p. 1308-1320
[12] K. Bornhütter, A. Mersmann, *Chem. Eng. Technol.* 16 (1993), p. 46-57
[13] R. Higbie, R., *AIChE Journal* (1935), p. 365-389
[14] G.A. Hughmark, *I&EC Fundamentals,* 6 (1967) p.408-413
[15] R. Billet, *Distillation Engineering*, Chem. Publishing Company, New York (1979)

Symbols

a	[m²/m³]	geometric surface area of packing per unit volume
a_e	[m²/m³]	interfacial area per unit volume
B_L	[–]	dimensionless specific liquid load acc. to [1]
C_V	[–]	constant, eqn. (8) and (10)
d	[m]	packing diameter
d_h	[m]	hydraulic diameter; $d_h = 4 \cdot \varepsilon / a$
d_P	[m]	particle diameter; $d_P = 6 \cdot (1-\varepsilon) / a$
d_S	[m]	column diameter
d_T	[m]	mean droplet diameter acc. to Sauter, $d_T = C_T \sqrt{\sigma_L / \Delta\rho \cdot g}$ with $C_T = 1$
D_V, D_L	[m²/s]	diffusion coefficient in the gas or liquid phase
F_V	[Pa$^{0.5}$]	gas load factor in relation to full column cross section, $F_V = u_V \cdot \sqrt{\rho_V}$
g	[m/s²]	acceleration of gravity
h_L	[m²/m³]	liquid hold-up in relation to total packing volume V_S, $h_L = V_L / V_S$
HTU_{OV}	[m]	height of an overall transfer unit related to vapour phase
H	[m]	height of packed bed
K	[–]	wall factor, acc. to [1]
l	[m]	mean contact path
$\dot{L}$	[kmol/h]	molar flow of liquid
n_t/H	[1/m]	number of theoretical stages per 1 m packing height
NTU_{OV}	[–]	number of overall transfer units, related to vapour phase
p_T	[mbar, bar]	operating pressure
u_L	[m/s]	specific liquid load in relation to full column cross section
u_R	[m/s]	relative phase velocity $u_R = \frac{u_V}{\varepsilon - h_L} + \frac{u_L}{h_L}$
u_V	[m/s]	linear gas velocity in relation to full column cross section
V_L	[m³]	liquid volume
V_S	[m³]	packing volume, $V_S = H \cdot \pi \cdot d_S^2 / 4$
$\dot{V}$	[kmol/h]	molar flow of gas or vapour

Greek symbols

β	[m/s]	mass transfer coefficient
$\beta \cdot a_e$	[1/s]	volumetric mass transfer coefficient
$\delta_i(\ldots)$, $\bar{\delta}(\ldots)$	[%]	relative error, middle value of relative error
φ_P	[-]	packing form factor acc. to [1]
τ	[s]	contact time
ρ, Δρ	[kg/m³]	density, density difference $\Delta\rho = \rho_L - \rho_V$
σ_L	[N/m]	surface tension
ν	[m²/s]	kinematic viscosity

Indices

L	relating to liquid
Fl	relating to operating point at flooding point
S	relating to operating point at loading point; $F_V = 0.65 \cdot F_{V,Fl}$
V	relating to gas or vapour

Dimensionless numbers

$Fr_L = \frac{u_L^2 \cdot a}{g}$ Froude number of liquid

$Sc = \frac{\nu}{D}$, Schmidt number

$Re_L = \frac{u_L}{a \cdot \nu_L}$ Reynolds number of liquid

$Re_V = \frac{u_V \cdot d_p}{(1-\varepsilon) \cdot \nu_V} \cdot K$ Reynolds number of gas / vapour

$Re_T = \frac{u_R \cdot d_T}{\nu_V}$ Reynolds number of droplet

$Sh_{V,T} = \frac{\beta_{V,T} \cdot d_T}{D_V}$ Sherwood number of droplet

$B_L = \left[\frac{\eta_L}{\rho_L \cdot g^2} \right]^{1/3} \cdot \frac{u_L}{\varepsilon} \cdot \frac{1-\varepsilon}{\varepsilon \cdot d_P}$ dimensionless liquid load

Comprehensive investigation and comparison of refinery distillation technologies

Anita Szőke-Kis [1,], Csaba I. Farkas[3], Péter Mizsey[1,2]*
[1] Budapest University of Technology and Economics, Department of Chemical and Environmental Process Engineering, P.O. Box 1521, H-1111, Budapest, Budafoki Street 8., Hungary;
[2] University of Pannonia, Research Institute of Chemical and Process Engineering, P. O. Box 125, H-8200, Veszprem, Egyetem Street 10., Hungary
[3]MOL Plc. DS Development 2440, Százhalombatta Olajmunkás u. 2. Hungary
**Corresponding author, e-mail: szokeancsa@gmail.com*

Abstract

In spite of its significant energy consumption, the distillation is still an important and widely applied separation. One of its major application areas is the crude oil refining. There are many incentives to reduce the distillation's energy consumption. In the crude oil refining a so called progressive distillation (PD) is an alternative of the conventional crude oil fractionation, atmospheric and vacuum distillation (AV). This alternative solution is investigated and compared with the AV plant.

For the sake of the comparison, simulation models of the two different distillation technologies are built in professional flowsheeting environment. The different technologies are processing the same quality and quantity crude oil, and producing the same petroleum fractions. As a result of the calculations, the progressive distillation proves to be an appropriate and competitive method for producing crude oil fraction with proper quality.

Keywords

refinery technologies, progressive distillation

1. Introduction

Crude oil plays a significant role in the worlds power supply. The first step of crude oil refining after desalting the crude is the crude oil distillation, which enables the fractionation of the crude oil into petroleum fractions. The conventional method for crude oil distillation is the atmospheric and vacuum distillation technology, referred as AV plant or AV unit.

The AV unit is chosen as a base case for the comparison of the technologies. The flowsheet of an AV plant with a prefractionator is shown in Figure 1. The preheated crude oil enters the prefractionator column, C1, where the light ends and light naphta are recovered as top products. This mixture is fed to the naphta stabilizing column, C2, where the gases are separated from the naphta fraction. The bottom product of the column C1 is fed to the atmospheric column C10 after preheating in the atmospheric furnace. Applying a prefractionator decreases the energy required in the furnace. [Parkash, 2003]

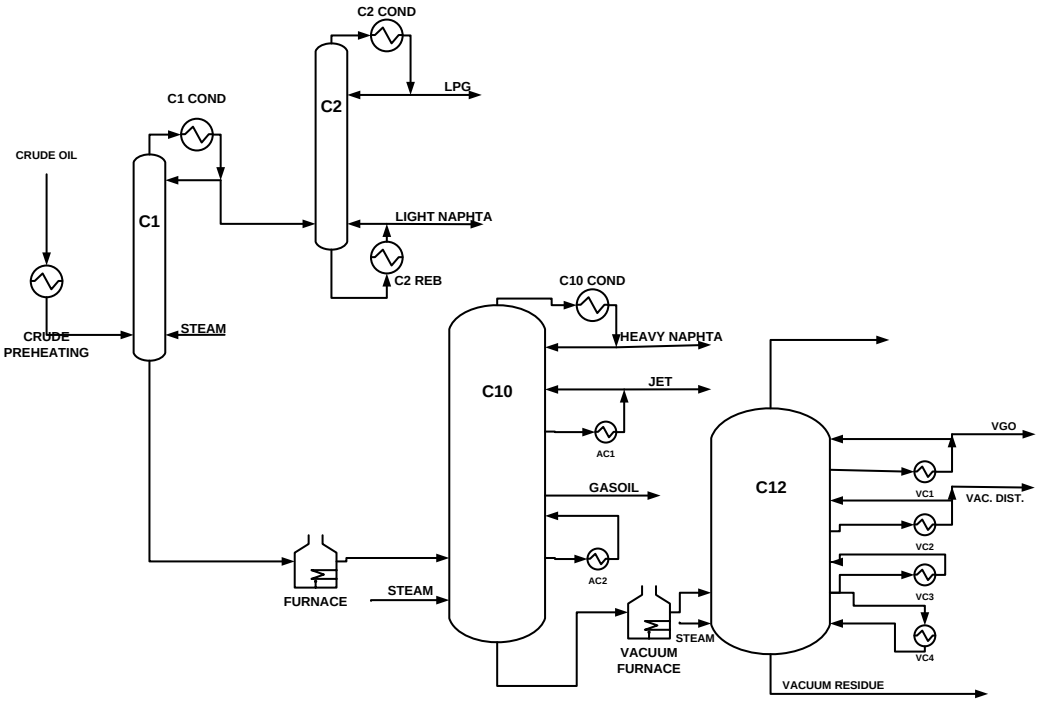

1. Figure

The atmospheric column separates the heavy naphta, jet fuel and gasoil fractions. The jet fuel and the gasoil fraction are withdrawn as side products, and may contain compounds from adjacent fractions, which are stripped with steam in the side stripper columns. To improve the energy efficiency of the tower, pump-around streams are used: liquid is withdrawn from the tower, cooled in the heat exchanger network, then returned to the column at a higher plate, generating reflux inside the column. [GARY *et al.* 2007]

The bottom produced in column C10, the atmospheric residue is processed in the vacuum tower, C12. The stream is preheated in the vacuum furnace before entering the tower. The operating pressure is 80-110 Hgmm, which enables the fractionation of the heavier fraction without thermal degradation, thus vacuum gas oil and vacuum distillate are produced as side products. The bottom product of the vacuum distillation is the vacuum residue.

The columns C1, C10 and C12 are stripped with high pressure steam, while the column C2 has a reboiler. The vapor phases of the top products are condensated in the head condensers producing liquid product and the required refluxes [Kister, 1990]. In case of the vacuum tower, the vacuum is provided at the top of the tower.

Since the energy consumption of the distillation unit, the operating costs and the emissions are enormous, there is a need to develop and investigate alternative distillation technologies. As an alternative technology the progressive crude oil distillation is examined. The potential of the technology is the reduced energy consumption with a more effective utilization of recovery heat. [DEVOS *et al.* 1987] The flowsheet of the technology is shown in Figure 2. The technology consists of two series of distillation columns and the total number of distillation columns is more than that of the conventional AV units.

The columns in the first series are connected in the direct sequence, in each column the most volatile fractions are separated from the residue. The columns of the first series are the columns C1, C2, C3 and C10, and are operating at atmospheric or higher pressure. The crude oil is fed to the first column of the first series, which is

separating the light gases and a part of the light naphta from the residue. The second column of the first series is separating the remained light naphta components and a part of the heavy naphta, and lastly the third column is separating the remained heavy naphta from the residue.

The last column of the first series is the atmospheric column, C10, which is operating similarly to the atmospheric column of the conventional design. The top product of the column contains the heavy naphta and the jet fuel. One side product is withdrawn, gasoil, the quality of the product is ensured with operating a stripper side column. Two atmospheric pump-around are operating to ensure reflux and energy efficiency. The feeds of the atmospheric columns require preheating in both cases, which are carried out in furnaces.

The columns of the first series are heated with steam, added at the bottom of the columns, below the feed plate; expect column C1 which is operating with a reboiler. The required amounts of reflux in the different towers are ensured with operating head condensers.

Since the separation in the columns of the first series is not sharp, and small amounts are removed as head products, the energy consumption of the columns in the first series is lower. The produced top products are fed individually into a column of the second series, where a sharp separation of the petroleum fractions is carried out. The columns of the second series are the columns C7, C4 and C5.

The first column of the second series, fed by the column C1, is a naphta stabilizing column, removing the LPG fraction. The column is operating similarly then the naphta stabilizing column in the AV plant. The bottom product of the column is then mixed with the top product of the column C2, and the mixture is feeding the second column of the second series, the column C4 which is a naphta fractionating column. In the column the light naphta is separated and withdrawn as the top product. The last column of the second series is fed with the mixture of the top product of the column C3 and C10, and is separating the heavy naphta from the jet fuel. The top product, mixed with the bottom product of the column C4 is the heavy naphta fraction, and the bottom product is the jet fuel.

Since the cuts between the fractions are sharp, the towers have a higher theoretical number of trays then the column in the first series. The columns of the second series are operating with head condensers and with reboilers.

The last column of the unit, column C12 is a vacuum column processing the atmospheric residue. The composition of the residue is identical regardless of the technology since after vaporizing the non-degradable fraction at atmospheric pressure the same molecules are retained in the residue, thus the vacuum column of the progressive distillation plant operates the same manner as the vacuum column in the atmospheric and vacuum distillation plant.

The described technology is considered as a combination of the direct and indirect sequences [DOBESH *et al.*]. The energy saved in the first series can be utilized in the second series, which results lower energy consumption in the whole technology. [BRUNETTI *et al.*]. This implies that using progressively located columns of larger number and smaller volume results in a better heat recovery/utilization, while the

produced fractions are the same quantity and quality when produced using conventional distillation technology and the flexibility of the progressive distillation process enables producing different product with rearranging the columns.

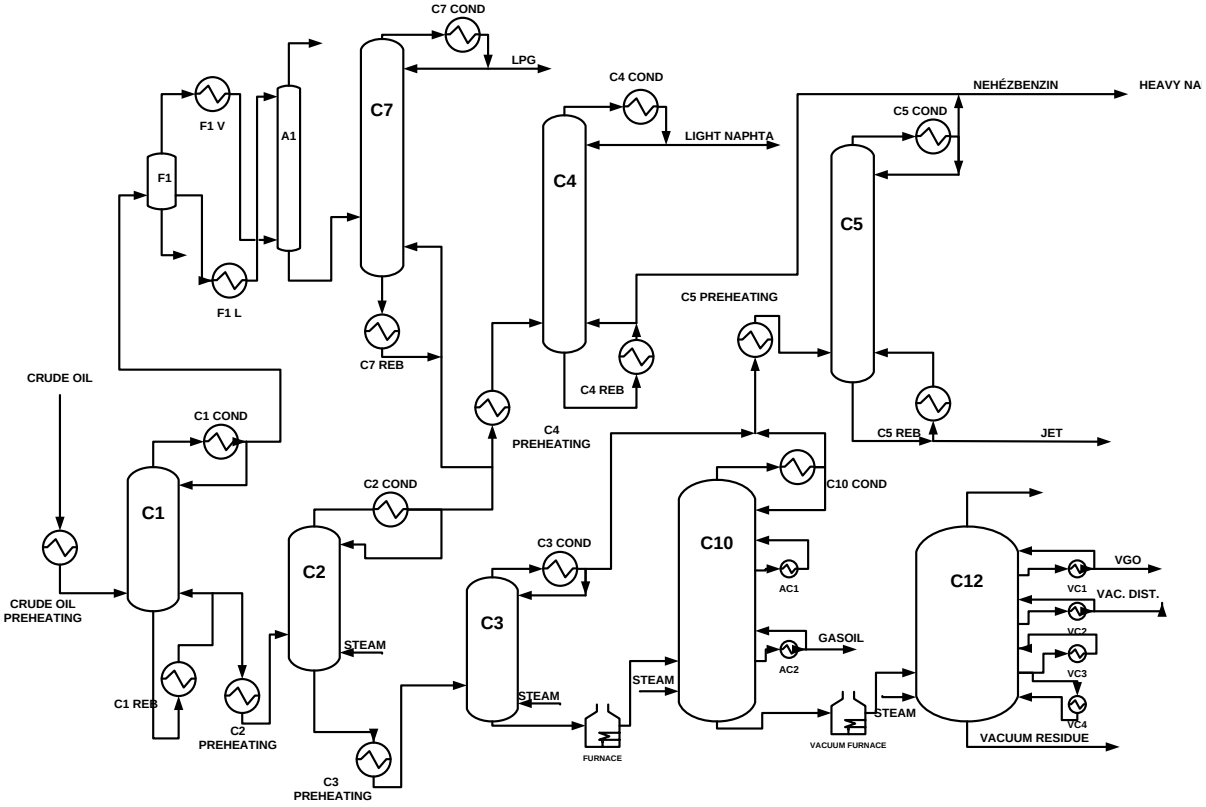

2. Figure

2. Results and discussion

To determine whether the progressive distillation is adequate for producing petroleum fractions, computer models are built for both refinery plants in professional flowsheeting software environment for industrial scale [Smith, 2005]. The two refinery plants are tested for a selected crude oil. The simulations are built based on the shown flowsheets. For modeling the thermodynamic equilibrium, the Soawe-Redlich Kwong equition of state is used. [Soave, 1972]

The crude oil chosen as the sample raw material is an existing, widely used one available on the stock market. Same amount of crude oil is processed in both plants, and the operational circumstances are selected so that both plants produce the same products in the same quantity and quality. These products are LPG, light and heavy naphta, JET, gasoil, vacuum gas oil and vacuum distillate [SCHOBERT, 1990].

The quality requirements of the fractions are given based on their distillation curves, true boiling curves (TBP curves) are used to give specifications and monitor qualities. The initial boiling point (IBP) and final boiling point (FBP) values [RIAZI, 2005] are given in specifications, which are chosen to ensure that they are in the desired temperature interval. The identical curve characteristic of the same product produced in different plant is checked with representing the true boiling point curves in one diagram, shown in Figure 3. The curves belonging to the same products

overlap, and the IBP and FBP temperatures meet the specifications. This means that the products produced with different technologies have the same quality; this implies that the progressive distillation plant is applicable for fractionating crude oil.

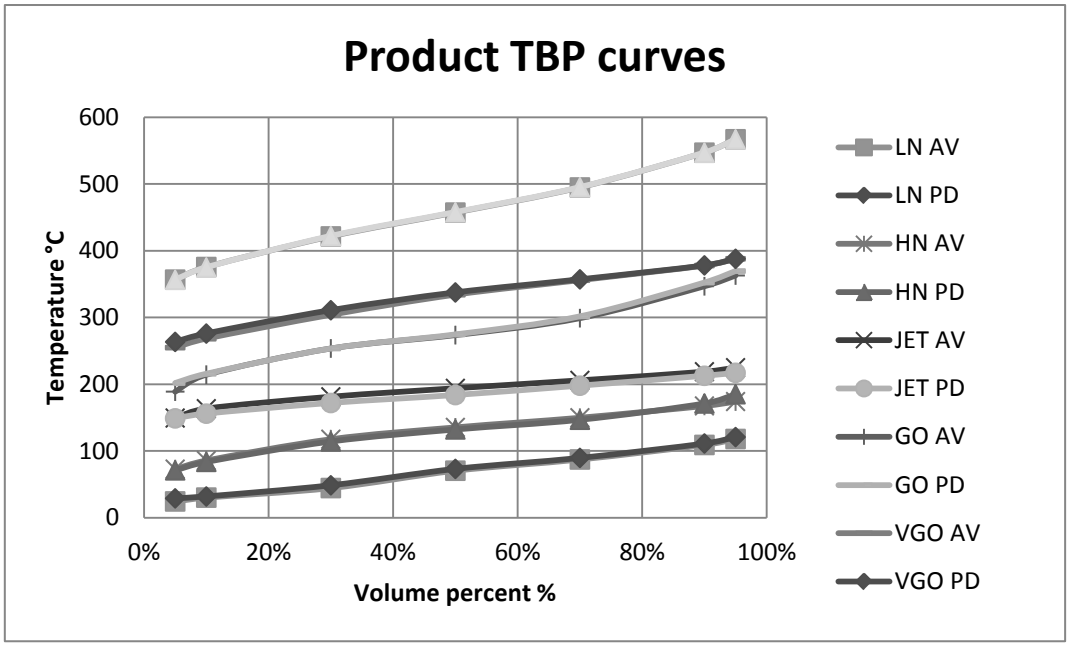

3. Figure

The heat balance of the plants is calculated based on simulation data, without heat integration and is shown in Table 1. Heat is added in two different ways, superheated steam and fuel gas are used as utilities in the furnaces. Steam is added as a stripping component to the columns below the last tray, it is also heating the feeds before entering towers, and heating reboilers. Fuel gas is burned in the furnaces to preheat feeds to higher temperatures.

AV plant	GJ/h	PD plant	GJ/h
C1 steam	4,4	C2 steam	0,5
		C3 steam	6,0
C10 steam	4,5	C10 steam	7,8
C12 steam	6,8	C12 steam	6,8
Crude preheating	203,9	Crude preheating	135,0
C2 reboiler	31,6	Reboilers	98,3
		Columns preheatings	91,2
C10 furnace	**147,1**	C10 furnace	**98,3**
C12 furnace	**110,9**	C12 furnace	**105,5**
Total	509,2		549,4

1. Table

Although the total energy consumption of the progressive distillation plant is slightly higher, than the consumption of the AV plant but this does not mean that the progressive distillation is a worse technology in the term of energy use. The total duty required in the furnaces is lower in the case of the PD plant. The vacuum furnaces

have approximately the same duties since the quality and quantity of the atmospheric residue and the operating condition of the vacuum towers are the same; the difference is caused by the lower consumption in the atmospheric furnace.

Usually, a furnace cannot be replaced with heat integration because of its high temperature, but heat integration in the lower temperature areas may be feasible. As it is stated, in the PD the heat integration among the distillation columns is feasible resulting in much lower energy consumption than shown in Table 1. The simulation shows that the distillation columns of the progressive distillation plant work at lower temperature values than those of the atmospheric and vacuum plant. Since the number of the streams in the progressive distillation plant is also higher, a well-executed heat integration could terminate the difference in energy consumption. The results of the calculations are encouraging and predict good results with the further investigation of the progressive distillation technology.

3. Conclusions

At the first glance, the results of the investigation (Table 1) show a negative picture for the progressive distillation plant since its total energy consumption without any energy integration is higher than that of the atmospheric and vacuum plant. But if we make a detailed review of the numbers we can see that the furnaces of the PD plant consume less energy than those of the AV plant. This predicts that the energy supply of the PD plant takes place at lower temperature level that in the case of the AV plant and this means cheaper energy sources, more possibilities for energy integration and a more efficient operation with lower emission.

References

BRUNETTI, S., HOWARD, B., BAGAJEWITZ, M. An Evaluation of a Progressive Crude Oil Distillation Scheme (The University of Oklahoma)

DEVOS, A., GOURLIA, J. P., PARADOWSKI, H. 1987. Process for Distillation of Petroleum by Progressive Separations (United States Patent 4,664,785)

DOBESH, D., SANDLIN, J., BAGAJEWITZ, M. 2008. Evaluation of the Energy Savings Claims of Progressive Distillation (The University of Oklahoma)

GARY, H. J. HANDWERK, G. E., KAISER, M. J. 2007 Petroleum Refining (New York, CRC Press)

PARKASH, S. 2003 Refining Process Handbook (USA, Elsevier)

Riazi, M. R. 2005 Characterisation and Properties of Petroleum Fractions (Philadelphia, ASTM)

SCHOBERT, H. H. 1990 The Chemistry of Hydrocarbon Fuels (Butterworths, Cornwall)

KISTER, H. Z. 1990 Distillation Operation (McGraw-Hill, Inc. New York)

SMITH, R. 2005. Chemical Process Design and Integration (John Wiley and Sons Ltd., Southern Gate, Chichester)

SOAVE, G. 1972 Equilibrium constants from a modified Redlich-Kwong equation of state (Chemical Engineering Science, 27 (6) 1197-1203)

Distillation in Special Chemistry

C. Hiller[1], R. Meier[1], G. Niggemann[2], A. Rix[1]
[1]Evonik Industries, Marl, Germany;
[2]Evonik Industries, Hanau, Germany

Abstract
Most specialty chemicals are multifunctional molecules of high reactivity and are produced in multi-step synthesis. Formation of by-products and product loss in waste streams are major cost-drivers. The characteristics of specialty chemicals frequently lead to column operating conditions outside proven limits of accepted design correlations and require particularly careful internals design.
An example is operation in deep vacuum in order to minimize thermal degradation. Enlarging column diameter to meet an allowable pressure drop specification instead of a certain flooding factor entails designs with low liquid loads well below the limits given in literature. Tailor-made distributor designs are required to ensure acceptable efficiency.
A second example is reactive distillation, a powerful tool to increase conversion or selectivity. However, process intensification reduces the number of degrees of freedom and additional interactions between process and internals design arise. On trays for homogenous reactions, the load dependence of liquid holdup and other variables needs to be considered in process design. In heterogeneous catalysis, plant designs must allow to increase pressure to counteract catalyst deactivation.

Keywords
Distillation at low liquid load, distributor design, distillation hydraulics, reactive distillation, special chemistry

1. Introduction

Special chemistry products are typically designed and produced for very specialized markets and applications. In the final product, they often are a minor ingredient by volume, but are essential for its performance and function. Production rates range from several 100 t/y in fine chemicals like pharma intermediates up to some 100.000 t/y in large volume specialties like specialty monomers, co-monomers and polymers. Product specifications often require high purity and tight control of contaminants or by-products down to the part per million or part per billion level. Secondary qualities like viscosity, color number, flavor or (absence of) odor may also be specified.
Most specialty chemicals are multifunctional molecules with low vapor pressure and limited thermal stability. Their high reactivity often calls for rather gentle operating conditions in process equipment and may require the use of stabilizers also for storage and transport. They are produced in complex multi-step synthesis. Therefore purity and recovery are the most important design objectives for separation process. Product life cycle may be rather short and time to market may be the deciding parameter in process development. Separations often have to be designed based on scale-up from laboratory experiments, experience from similar processes and common sense before accurate or even preliminary phase equilibrium and physical property data is available. Internals cannot always be selected solely from hydraulic considerations: Often a close match to the pilot plant setup is desired or existing equipment is to be reused to save investment or time to market. Other important

factors influencing selection and design of internals are resistance against foaming or fouling and easy access for cleaning.
To allow for fast reaction to changes in demand, specialty chemicals processes are often designed for high flexibility, i.e. e. high turndown ratios and fast product changeover. Continuous processes are favored because of their lower residence times and higher recovery of products. Operating pressures range from 5 mbar to 40 bar, column diameters from 60 mm to more than 7 m. Internals cover the whole range from dual flow trays, high capacity fixed-valve trays to random and structured packing.

2. Distillation in specialty chemicals

2.1 Distillation at low liquid load

Many specialty chemicals are temperature-sensitive multifunctional molecules with low vapor pressure and high reactivity. Deep vacuum operation is preferred to achieve gentle operating conditions in order to reduce thermal degradation, fouling or polymerization. Allowable pressure drops of 0.5 mbar / stage or less can only be achieved by increasing diameter. Column designs with very low liquid load result. The obvious selection of gauze packing is discouraged in systems with even slight fouling tendency.

2.1.1 Minimum liquid load for structured packing

The operating points of several industrial columns successfully separating both organic and aqueous temperature-sensitive mixtures are shown as symbols in **Figure 1**. Most of these columns are designed for low flooding factors of 50% or less to limit total pressure drop. Some liquid loads are well below 1 m³/m³h.
It is obvious, that packing separation efficiency will be impaired below a minimum liquid load. As a rule of thumb, minimum liquid loads of 2 and 10 m³/m²h for organic and aqueous systems are recommended [1]. Based on extensive experimental data for metal and ceramic Raschig and Pall Rings, Schmidt [2] derives a correlation for the minimum liquid load $u_{L,min}$ (in m/s):

$$u_{L,\min} = 1.25 \cdot 10^{-4} \frac{C_L^{2/9}(1-\cos(\Theta))^{2/3}}{(1-F/F_{\max})^{1/2}} \cdot \left(\frac{g}{a_P}\right)^{1/2}, \quad C_L = \frac{\rho_L \sigma^3}{\mu_L g} \qquad (1).$$

C_L is the capillary or falling film number, F/F_{max} the flooding factor, Θ the liquid-solid contact angle and a_P the specific surface. A second correlation of similar structure neglects the contact angle. It coincides with Equation (1) for Θ=10.3°. The influence of the contact angle is outstanding. For aqueous systems a minimum liquid load of about 15 m³/m²h is predicted, while it is zero for perfect wetting.
It is difficult to measure contact angles in systems with very good wetting and it is recommended by [3] to use no values less than 25°. Results obtained from Equation (1) for different contact angles (25° and 10.3°) and packing sizes (250, 350 and 500 m²/m³) are shown in **Figure 1**.
Minimum liquid load decreases with larger packing surface area. This is counter-intuitive and in contradiction to wetting models for falling-film evaporators. In distillation, however, complete wetting is not essential, as long *enough* wetted area is provided for mass transfer. The thick solid line shows the result for the correlation neglecting the influence of the contact angle. A minimum liquid load of ~1 m³/m²h is predicted.
Equation (1) is very useful to identify critical applications requiring special care in distributor design. However, most of the industrial example columns shown run outside of the predicted operating range. It is not really surprising, that the model fails

to predict these examples, since it is derived on 1st and 2nd generation random packing data. Recent investigations show, however, that structured packing surface microstructure reduces the contact angle and not only improves liquid spreading, but liquid-side mass transfer as well [4, 5].

The well-known hysteresis effect for wetting and de-wetting is reflected in the industrial practice of starting up columns with the highest liquid rate possible to improve conditions for initial liquid wetting.

The phenomena of de-wetting of modern packing would surely be worthy of renewed investigation. In **Figure 1**, the line marked "TR" shows the operating line of total reflux experiments in the o-/p-xylen system at 100 mbar. Either deeper vacuum or a non-total reflux data in reasonably sized columns for modern structured and random packing with high-performance distributors would be greatly appreciated by designers.

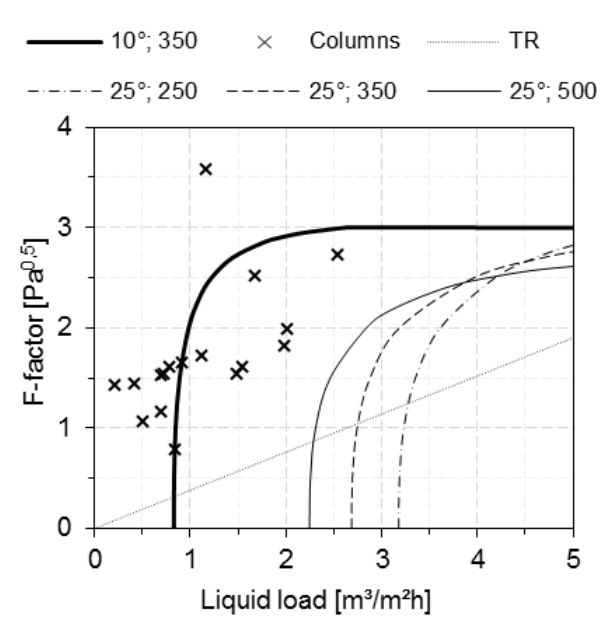

Figure 1: Influence of contact angle and specific surface on minimum liquid load.
Symbols: Industrial columns.
TR: HETP experiments @ total reflux.

2.1.2 Distributor design

In liquid distributors, metering orifices in the bottom or side wall of troughs are evenly distributed across the column section. The flow from the orifices is driven by gravity according to Torricelli's equation [6]:

$$u_L = N \frac{\pi}{4} D^2 C_O \sqrt{2 g H} \qquad (2),$$

where u_L is the liquid load in m/s. **Figure 2** shows results from Eq. (2) for different drip point densities N as a function of liquid load. A constant overflow height H=75 mm and a minimum orifice diameter D=2.5 mm are chosen to ensure distribution quality in spite of imperfect distributor leveling to provide resistance against fouling and to allow for turndown. Clearly, a reasonable compromise is required.

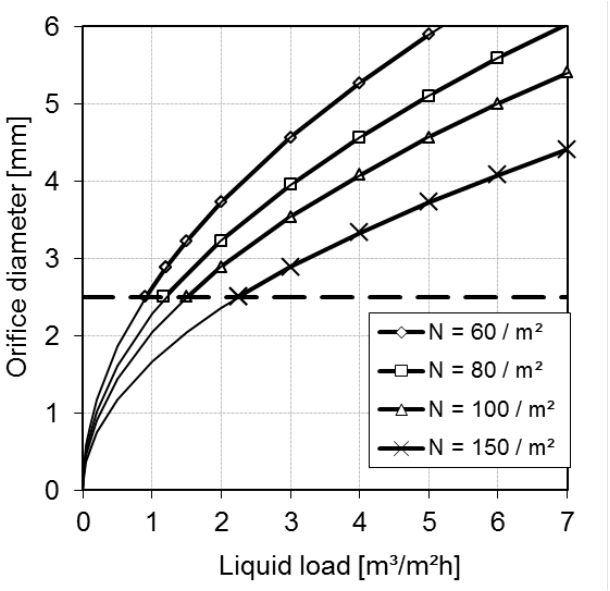

Figure 2: Diameter of distributor metering orifice for 75 mm liquid head and different drip point densities (C_0=*0.7*).

The first option is the reduction of the number of primary drip points and use of flow multiplying devices. Several proprietary devices are available on the market. A second option is the use of line distributors [7], where metering orifices in the side walls of the troughs discharge against a baffle on which the individual liquid jets spread and discharge a continuous liquid film to the packing.

Furthermore, the minimum overflow height can be reduced. Highest manufacturing standards concerning diameter, position and exact form of the metering orifices is required. Designs must allow for lateral mixing by communicating channels between the distributor troughs or in the parting box and for leveling of individual troughs. Installation by an experienced team and tight quality control are essential. There is positive industrial experience with distributors with flow deviations of less than 5% at overflow heights of only 25 mm. Every single distributor should be water-tested, even if several distributors are of the same design.

2.1.3 Tray operation in the spray regime

At low liquid load, trays often operate in the spray regime, which is prone to low efficiency and can be avoided using picket fence weirs [8].

2.2 Reactive distillation

Many processes in specialty chemicals rely on reactive distillation to increase conversion or selectivity. The combination of reaction and separation in one vessel reduces the investment entailing a loss of degrees of freedom. Because parameters like holdup (i.e. residence time) are load dependent, a close interaction of internals and process design results. Excellent VLE data is required to precisely predict all composition profiles relevant for reaction kinetics.

2.2.1 Heterogeneous catalysis

In heterogeneously catalyzed systems, both amount and position of catalyst are fixed. Design relies on experimental data and scale-up is complicated by the fact, that laboratory-size differs from industrial-size packing in catalyst holdup, efficiency and capacity. Pilot plant data is often required. In order to compensate for catalyst deactivation and load effects, large variations in column pressure must be foreseen in design. Protection of catalyst from poisons is of outmost importance, since catalyst replacement requires a complete packing exchange.

2.2.2 Homogeneous catalysis

While reactive packing is among the most expensive column internals on the market, homogenous catalysis implies running costs for fresh catalyst, its separation and waste. Reaction trays with high weirs are often used to provide the holdup required for slower reactions. Conversion and selectivity can be controlled by manipulating catalyst concentration in the column. The location of the reaction zone can be changed by providing multiple catalyst feed nozzles.

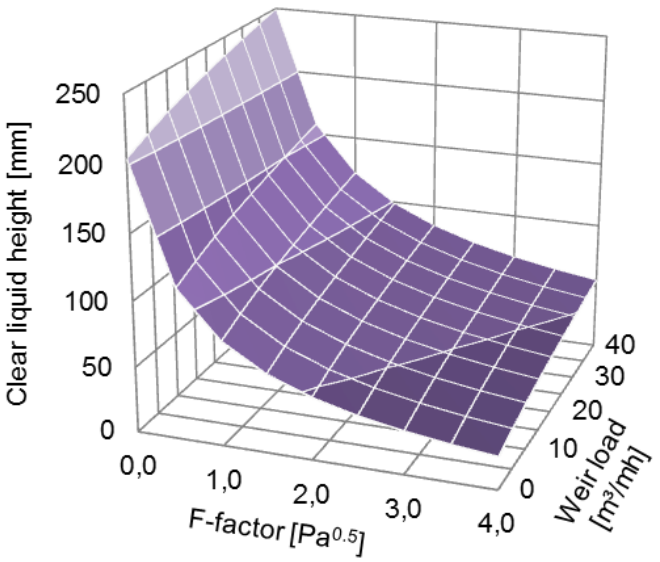

Figure 3: Clear liquid height of a reaction tray as a function of liquid and vapor load.

However, internals design should be already considered in detail during process design, because vapor load increasing with production rate will adversely affect clear liquid height and residence time on the tray. As an example, the well-known methyl acetate system is studied [9, 10]. Acetic acid and methanol are fed to opposite ends of the reaction zone at a rate of 100 kmol/h.

10 non-reacting stages are provided above and below the reaction zone comprising 60 trays. In the reaction zone, trays with 200 mm weir height and 1.9 m diameter are assumed. Temperature on tray 53 is controlled by distillate flow rate.

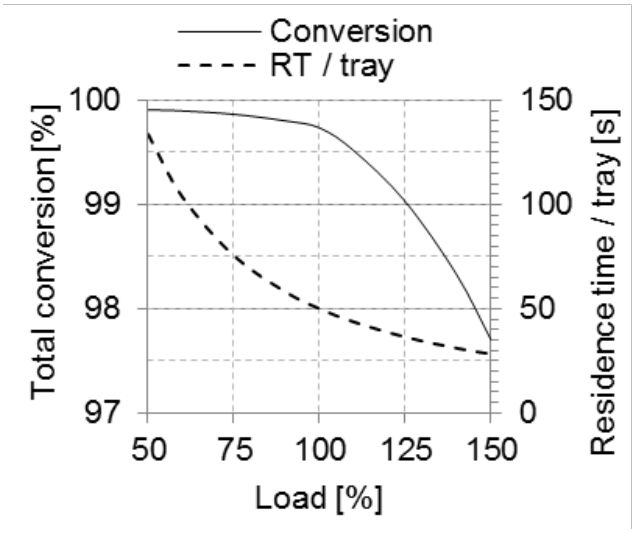

Figure 4: Conversion and residence time as a function of load.

Figure 3 shows the clear liquid height on the tray as a function of liquid and vapor load computed from the Colwell model [11]. Although the model is extrapolated, we consider it useful for large weir heights, because it is based on a Froude-number with clear liquid height as the characteristic length. The effect of liquid load on holdup is only very small, while the tray is literally blown dry with rising vapor load.

The effect of vapor load on conversion and residence time is shown in **Figure 4**. At 50% load, residence time is almost tripled and conversion increases accordingly. On the other hand, byproduct formation can be expected to rise, unless catalyst concentration is reduced. Increasing the load has small impact on residence time, but conversion decreases rapidly. Residence time on the tray decreases over-proportionally with load.

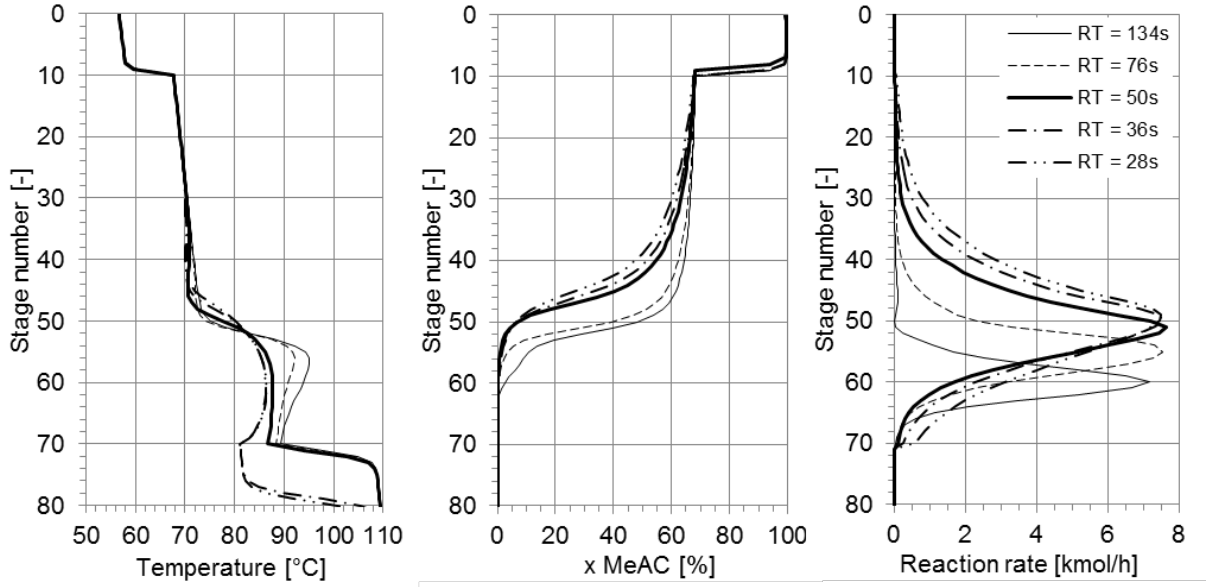

Figure 5: Temperature, concentration and reaction rate profiles for different residence times corresponding to loads of 50, 75, 100, 125 and 150%.

Reactive distillation often allows much higher conversion or even the breaking of azeotropes by quantitatively reacting away one of its components. This implies simplified product separation and further investment and energy savings. However, disturbances and load changes may affect reactive distillation processes more severely, than conventional ones. With the conversion loss shown in **Figure 4**, the methanol concentration in the distillate rises by a factor of 2.5, water concentration is almost doubled. Great care has to be taken to ensure, that these concentrations do not overload the distillate purification system. Here, a major drawback of reactive

distillation becomes apparent: The loss of degrees of freedom may cause a disturbance in a single unit to propagate further in the process.
The profiles of temperature, methyl acetate concentration and reaction rate are shown in **Figure 5**. Although temperature is controlled on tray 53, all profiles undergo large deviations for the load range of 50 to 150% investigated. At low load, most of the conversion takes place in the lower part of the reaction section. As residence time decreases, more and more of the reaction volume is utilized. The increased breakthrough of reactants to the distillate for residence times lower than 50s can only be seen in the bottoms temperature profile. In order to successfully operate a process involving reactive distillation, plant-wide control, excellent quality of instruments and even on-line analytics are recommended. Validation of plant data from reactive distillation processes is notoriously difficult.

3. Conclusions

Two distillation topics important in specialty chemistry are investigated.
In temperature-sensitive systems, column designs with very low liquid load result. Operating points of several successful applications, running well below the limits given in literature, are shown in a load diagram. Distributor design needs to find a sensible compromise between drip point density, orifice size and overflow height. Tight quality control during manufacture, testing and installation will pay out. New experimental data for modern structured packing at very low liquid load utilizing modern, high open-area distributors would be very helpful for designers.
In reactive distillation, large investment savings are possible. Breaking of azeotropes or near-total conversion of reactants may considerably reduce investment. On the other hand, the loss of degrees of freedom is a possible pitfall. Internals design must be considered already in early process design stages. Important variables like holdup or catalyst activity depend on either load or runtime. Reactive distillation processes are therefore more susceptible to disturbances, which may propagate further downstream, e.g. if design assumptions like near-total conversion of a reactant no longer hold.
Large changes in operating range frequently occur in specialty chemicals production and must be anticipated and considered in both conceptual process and hydraulic internals design.

References

[1] J. G. Stichlmair, J.R. Fair. “Distillation. Principles and Practice”. Wiley-VCH, New York, 1998
[2] Schmidt, R.: The lower capacity limit of packed columns, Inst. Chem. Eng. Symp. Series 56 (1979), Vol. 2, pp. 3.1/1-14
[3] M.G. Shi, A. Mersmann. Effective Interfacial Area in Packed Columns, Ger. Chem. Eng. 8 (1985), 87-96
[4] P. Valluri, O.K. Matar, G. F. Hewitt, M. A. Mendes. Thin film flow over packings at moderate Reynolds numbers, Chem. Eng. Sci. 60 (2005), 1965-1975
[5] M. Kohrt, I. Ausner, G. Wozny, J.-U. Repke. Texture influence on liquid-side mass-transfer, Chem. Eng. Res. Des. 89 (2011), 1405-1413
[6] Schultes, M., Grosshans, W., Müller, S. and M. Rink: All the Mod Cons Part 1, Hydrocarbon Engineering, January 2009,
[7] Spiegel, L.: A new Method to Assess Liquid Distributor Quality, Chemical Engineering Processing 45 (2006), pp. 1011-1017
[8] Summers, D. R. and A. W. Sloley: Tray Design at Low Liquid Load Conditions, AIChE Spring Meeting, April 23rd, 2006, Orlando Florida
[9] V. H. Agreda, L. R. Partin, W. H. Heise: High-purity Methyl Acetate via reactive distillation. Chem. Eng. Prog. 86 (1990), No. 2, pp. 40-46
[10] V. H. Agreda, L. R. Partin, U. S. Patent 4,435,595, (Mar 1984)
[11] Colwell, C. J.: Clear liquid height and froth density on sieve trays. *Industrial & Engineering Chemistry Process Design and Development*, *20*(2) (1981), 298-307.

Enrichment of Light Components at Gas-Liquid Interfaces by Density Gradient Theory and Molecular Simulation

Kai Langenbach, Stephan Werth, Martin Horsch, Hans Hasse
Laboratory of Engineering Thermodynamics, University of Kaiserslautern, Kaiserslautern, Germany

Abstract

In separation processes, bulk thermodynamic properties always play a crucial role. However, if the mixture of interest separates into two or more phases, also interfacial effects occur and the apparent resistances to heat and mass transport may attain unexpected values. This effect has been attributed to the enrichment of one component at the interface. Unfortunately, such effects are presently not directly experimentally accessible. Therefore, theoretical methods are needed with which they can be studied and which, thereby, contribute to the understanding of unusual values of the transport coefficients. These effects are investigated here by two independent methods, namely density gradient theory, based on equations of state, and molecular simulation based on force field models. Both methods are shown to give consistent results.

From a molecular point of view, there exists no sharp interface. *E.g.*, in vapor-liquid equilibrium, the density changes smoothly from its liquid bulk to its gas bulk value. For mixtures, however, unexpected effects are observed in that transition region. This holds especially for wide boiling systems, which are common in absorption. While the mixture density decreases monotonously from the bulk liquid to the bulk gas, this is not true for the components' molarities. In many cases, maxima of the molarity of the light boiling component are observed in the interfacial region, where it can reach values several times larger than the bulk values.

The present work concerns systems with significant super-elevations of the molarity of the absorbed component at the interface. The force field models for molecular simulation are taken from previous own work and the results from density gradient theory are based on equations of state from the literature. Both approaches and their results are compared. The study strongly indicates that important surface effects occur and that they should be explicitly included in process models of absorption.

Keywords
surface enrichment, binary mixture, molecular simulation, density gradient theory, equation of state, carbon capture

1. Introduction

In separation technology, the transport between two phases is one of the limiting factors for apparatus design. This transport is typically accounted for by models like the two-film theory, assuming transport resistance in the interface is negligible. If, however, light components like inert gases are present in the mixture, the

experimentally achieved transport rates are often smaller than theoretically predicted [*e.g.* 1]. This is mostly attributed to an enrichment of such components at the interface [*e.g.* 1,2,3].
Such adsorption at the interface is not directly experimentally accessible and therefore usually theoretical models are employed, in order to study it. Two of the methods used to this end are molecular simulation techniques [*e.g.* 4,5,6,*7*,8,9] and the density functional theory of inhomogeneous systems [*e.g.* 10,*11*,12,13,14]. Some authors have compared both methods for simple models such as Lennard-Jones mixtures [*e.g.* 15,16], but for real fluids there exists no comparison, at least to the best of the authors' knowledge.
The present contribution addresses the issue of adsorption at fluid interfaces, comparing molecular simulation and density gradient theory results for real fluids using molecular potentials from our group [17,18] and the Perturbed-Chain Statistical Associating Fluid Theory (PC-SAFT) equation of state [19,20]. Both methodologies indicate the need to explicitly account for the interface in transport theories for applications with more than one phase.

2. Results and discussion

2.1 Molecular Simulation

Molecular simulation of vapor-liquid equilibria can be performed in numerically very efficient manner with methods like the Grand Equilibrium [21], *NpT* plus test particle [22] or Gibbs ensemble [23]. These methods sample the vapor and the liquid phase separately and provide access to bulk properties along the saturation curve. Due to this methodology the interface and its relevant properties are not sampled. In order to compute the surface tension and adsorption processes at fluid interfaces with molecular simulation techniques, the interfacial region has to be sampled directly. Figure 1 shows one molecular simulation snapshot of the mixture containing carbon dioxide + water. The enrichment of carbon dioxide at the interface is clearly visible.

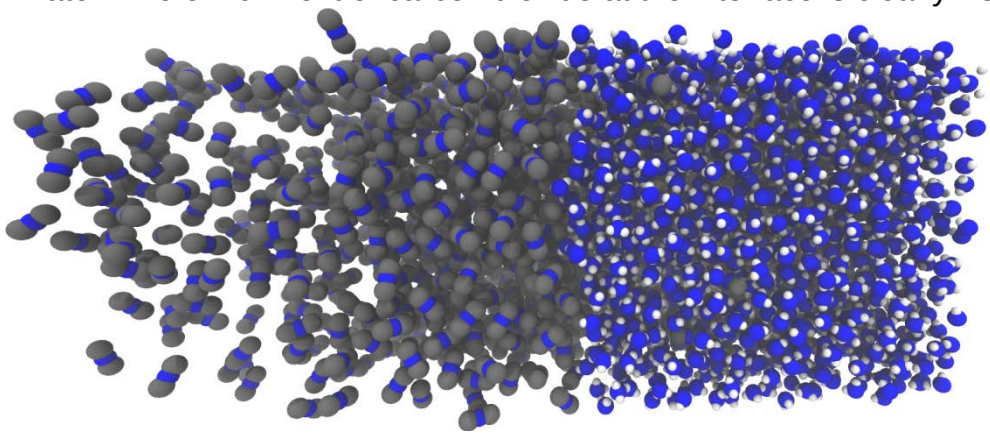

Figure 1: Molecular simulation snapshot of the carbon dioxide (gray) + water (blue) mixture at T = 300 K and p = 6 MPa.

In this contribution molecular simulations of mixtures containing carbon dioxide + methanol are conducted. The molecular models are taken from previous work of our group [17, 18]. The molecular model of methanol is taken from Schnabel *et al.* [17], and consists of two Lennard-Jones sites, representing the CH_3- and OH- groups and three point charges representing the polarity and hydrogen bonding capabilities of methanol. The molecular model of carbon dioxide by Vrabec *et al.* [18] contains two

identical Lennard-Jones [24,25] sites and one superimposed point quadrupole in the center of mass.
Unlike electrostatic interactions, *e.g.* between charges and quadrupoles, are treated in a physically straightforward way, using the laws of electrostatics. In case of the interaction between unlike Lennard-Jones sites, the modified Lorentz-Berthelot combining rules are used [26,27]

$$\sigma_{ijab} = \frac{\sigma_{iiaa} + \sigma_{jjbb}}{2} \tag{1}$$

$$\varepsilon_{ijab} = \xi\sqrt{\varepsilon_{iiaa}\varepsilon_{jjbb}} \tag{2}$$

The binary interaction parameter ξ is usually adjusted to one single experimental vapor pressure [28]. The parameter $\xi = 1.01$ [17] is used in this work.
The molecular simulations were performed with the *ls1* MarDyn molecular dynamics code [29] in the canonical ensemble with a total particle number of N = 16 000. The equations of motion were solved by a leapfrog integrator [30] with a time step of Δt = 1 fs. A cutoff radius of 17.5 Å was used throughout with an additional slab based long range correction [31]. The simulations were conducted for 3 000 000 time steps to ensure fully equilibrated systems. The simulations were started with a liquid phase in the center of the simulation volume surrounded by vapor phases on both sides. The carbon dioxide particles were placed randomly in the simulation volume. The temperature was kept constant with velocity rescaling at T = 298.15 K. The total mole fraction in the simulation volume was varied between x_{CO_2} = 0.01 and x_{CO_2} = 0.5.
Figures 2 shows an exemplaric snapshot of a molecular simulation of the mixture containing carbon dioxide + methanol at *p* = 4.1 MPa. The enrichment of CO_2 at the interface results in roughly the double value of partial density compared to the liquid phase.

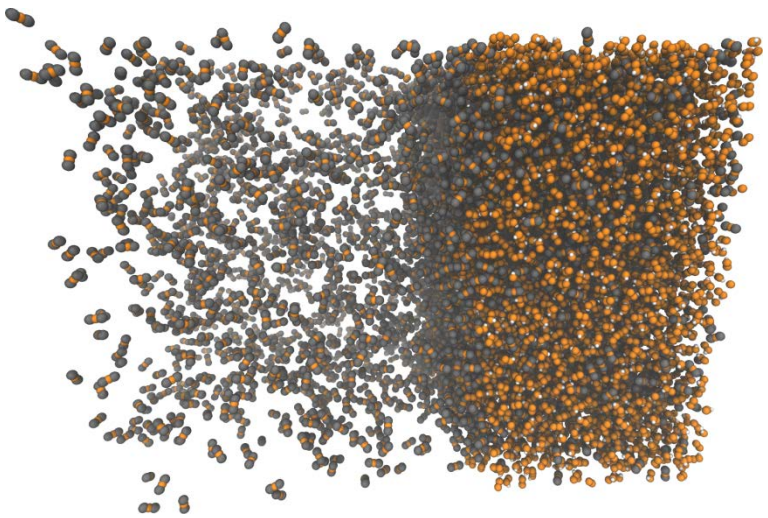

Figure 2: Molecular simulation snapshot of the mixture containing carbon dioxide (gray) + methanol (orange) at *p* = 4.1 MPa and *T* = 298.15 K.

2.2 Density Gradient Theory

While molecular simulation resolves thermodynamic properties on the scale of atoms and molecules, density gradient theory takes on a mesoscopic perspective. It was first introduced by van der Waals [32] and then rediscovered by Cahn and Hilliard [33] for pure compounds. Later on it was generalized to mixtures by Poser and Sanchez [10]. The basic idea is the development of the free energy of a non-uniform

system around the equilibrium state in the density gradient and higher spatial derivatives of the density.
Using isotropy arguments and truncating the series after the square gradient term, the resulting expression for the free energy expressed as a functional of the partial density profiles $\rho_i(z)$ is [10]

$$A\left[\rho(z)\right] = S\int_{-\infty}^{\infty}\left[a_o\left(\rho_i(z)\right) + \frac{1}{2}\sum_i\sum_j \kappa_{ij}\left(\frac{\mathrm{d}\rho_i}{\mathrm{dz}}\right)\left(\frac{\mathrm{d}\rho_i}{\mathrm{dz}}\right)\right]\mathrm{dz} \tag{3}$$

for an inhomogeneous system with a planar interface. Here S is the expansion of the surface perpendicular to the z direction, a_0 is the local free energy density per volume and ρ_i is the partial density of component i. The κ_{ij} are the so-called influence parameters. They are mostly fit to single experimental points of the surface tension for pure compounds [*e.g.* 34] calculable via density gradient theory, while often a geometric mixing rule is applied for mixtures

$$\kappa_{ij} = \beta_{ij}\sqrt{\kappa_{ii}\kappa_{jj}} \tag{4}$$

where β_{ij} is a correction factor according for deviations from the geometric mixing rule. Minimization of the free energy of equation (3) yields the Euler-Lagrange equations for the multi-component case [35]

$$\sum_j \kappa_{ij}\frac{\mathrm{d}^2\rho_j}{\mathrm{dz}^2} = \Delta\mu_i \tag{5}$$

where $\Delta\mu_i = \mu_i^0\left(\rho_k\right) - \mu_i^{bulk}$ is the difference between the local chemical potential and the bulk value. This system of n differential equations, where n is the number of components, simplifies further to a system of $n-1$ algebraic equations [35], if $\beta_{ij} = 1$ is valid.

$$\sqrt{\kappa_{ii}}\Delta\mu_{ref} = \sqrt{\kappa_{ref,ref}}\Delta\mu_i \tag{6}$$

The missing n^{th} equation is then replaced by choosing a reference density ρ_{ref} and the interfacial profiles are obtained by computing the position z via [35]

$$\mathrm{dz} = \sqrt{\Delta\Omega^{-1}\left(\rho_k\right)\sum_i\sum_j\frac{1}{2}\kappa_{ij}\frac{\mathrm{d}\rho_i}{\mathrm{d}\rho_{ref}}\frac{\mathrm{d}\rho_j}{\mathrm{d}\rho_{ref}}}\mathrm{d}\rho_{ref} \tag{7}$$

where $\Delta\Omega = a_0 - \sum_i \rho_i\mu_i^{bulk} + P$ is the grand thermodynamic potential.

Since density gradient theory is a gradient expansion, an expression for the free energy of the homogeneous systems, *i.e.* an equation of state, is needed in order to complete the above expressions. An example of such an equation of state is the Perturbed-Chain Statistical Associating Fluid Theory (PC-SAFT), the details of which are described elsewhere [19,20]. The pure component parameters for PC-SAFT, used for the density gradient calculations in this contribution, are taken from Gross and Sadowski [19,20] and the parameter for the unlike interaction energy, k_{ij}, is taken from Román-Ramírez *et al.* [36]. The influence parameters κ_{ii} are taken from Fu *et al.* [37] and the β_{ij} are assumed to have the value one.

2.3 Numerical Results

Test calculations are carried out for a temperature of 298.15 K for the system CO_2 + Methanol at two different mole fractions. The results are shown in Figure 3 and Figure 4.

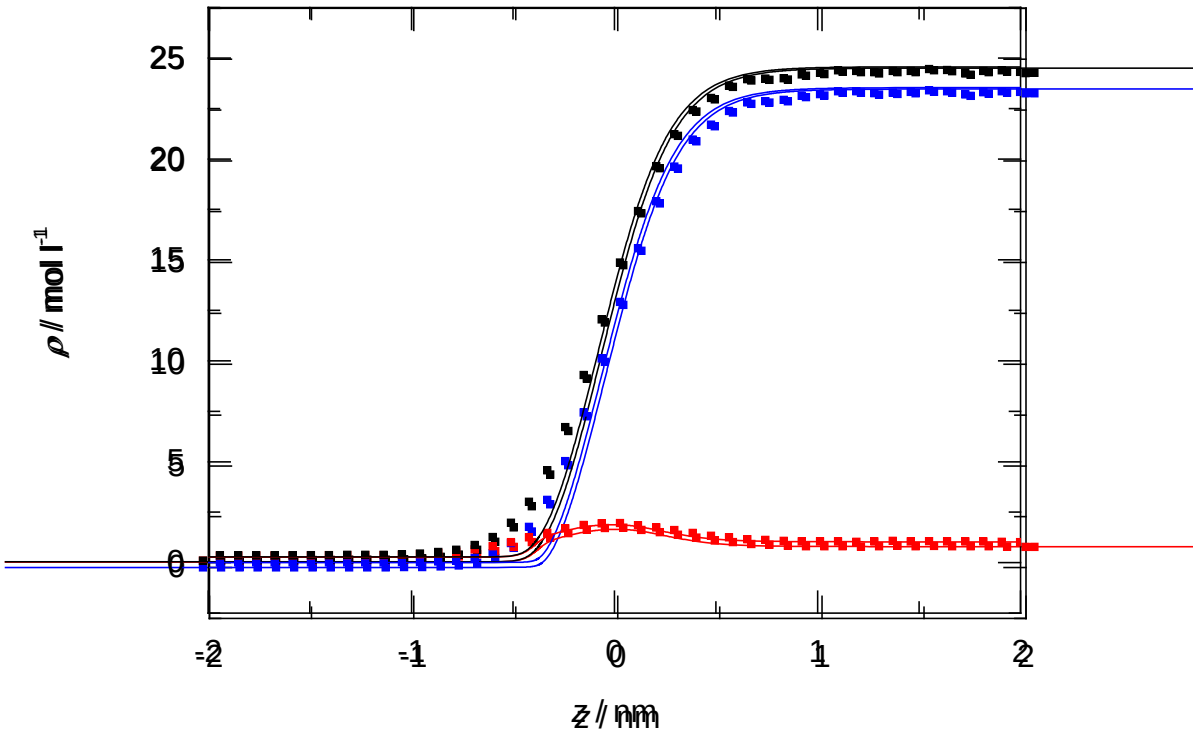

Figure 3: Partial density of methanol (blue), carbon dioxide (red) and the total density (black) over the coordinate normal to the interface calculated from molecular simulation (dots) and density gradient theory (lines) at a temperature of T = 298.15 K and a carbon dioxide concentration of x_{CO_2} = 0.042.

Figure 3 shows the partial density profiles of methanol and carbon dioxide, as well as the total density over the coordinate normal to the interface calculated from both methods, as indicated by the caption at a liquid mole fraction of CO2 of 0.042. The density profiles indicated that carbon dioxide adsorbs at the interface. The increase of partial density of carbon dioxide reaches roughly double the partial density in the liquid phase. Figure 4 shows the corresponding calculated density profiles for a liquid CO2 mole fraction of 0.132. Again the maximum in partial density of CO2 is roughly the double value of its liquid partial density for both methods. For both test cases the maximum in partial density agrees remarkably well between both methods. However, the width of the interface in case of the DGT is in both cases smaller than the corresponding interfacial width from molecular simulation. This may result from two effects, namely the molecular simulation with slab-wise evaluation of density profiles introduces a softening of the profiles due to the finite slab thickness, whereas no long ranged potentials were used in the modeling of CO_2 and methanol using PC-SAFT. The first of these effects would enlarge the interfacial region for the molecular simulation, while the second one would narrow it for calculations with DGT. The combination of these effects may result in the difference in interfacial thickness from both methods.

The computing times of both methods vary significantly, while calculations using the density gradient theory require minutes, molecular simulations run for several days using high performance computers. In turn, the usage of density gradient theory requires one parameter to be fit to one surface tension, while molecular simulation does not require an additional parameter.

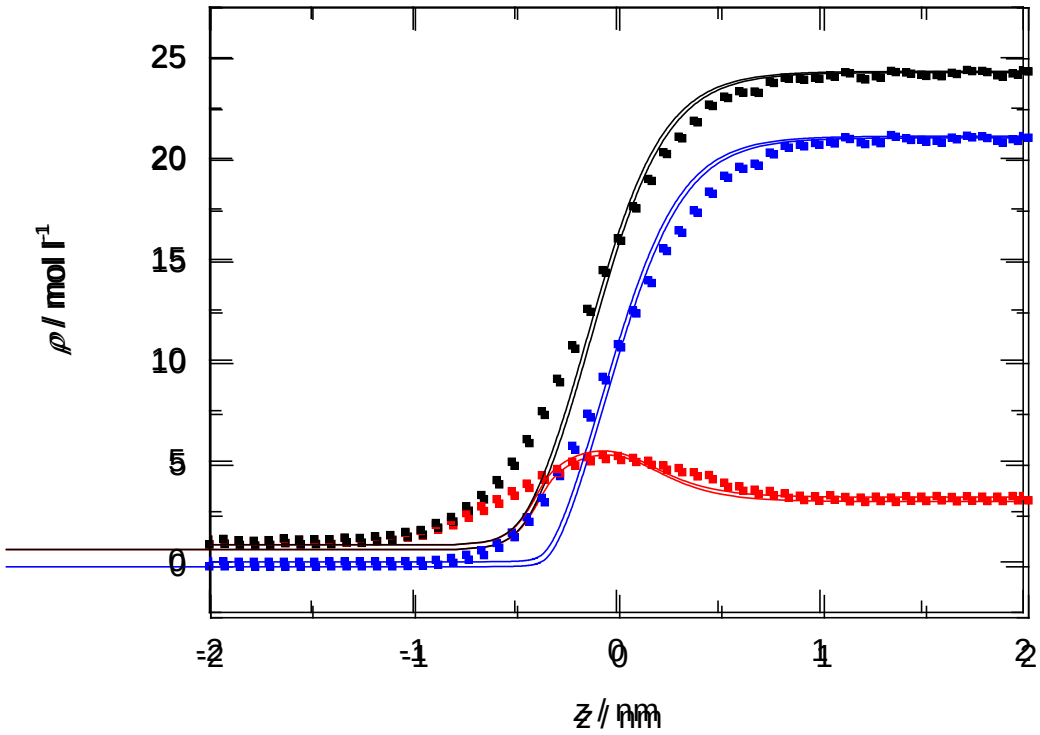

Figure 4: Partial density of methanol (blue), carbon dioxide (red) and the total density (black) over the coordinate normal to the interface calculated from molecular simulation (dots) and density gradient theory (lines) at a temperature of T = 298.15 K and a carbon dioxide concentration of x_{CO_2} = 0.132.

3. Conclusions

Using two independent methods, namely molecular simulation and density gradient theory, it is shown that surface adsorption in the strongly non-ideal mixture CO_2 + methanol occurs. The predicted enrichment at the interface agrees well for both methods. The results suggest that interfacial adsorption may indeed be the reason for unexplained slow transport processes across interfaces in mixtures where light components are present and that the interface should be accounted for explicitly. In light of the complex behavior of real mixtures, further investigations should systematically explain the mechanisms underlying the aggregation behavior.

References

[1] S.K. Park, M.H. Kim, K.J. Yoo, Int. J. Multiphase Flow 22 (1996) 893.
[2] F. Goodridge, I.D. Robb, Ind. Eng. Chem. Fund. 4 (1965) 49.
[3] R.P. Borwankar, D.T. Wasan, Ind. Eng. Chem. Fund. 25 (1986) 662.
[4] D.J. Lee, M.M. Telo da Gama, K.E. Gubbins, Mol. Phys. 53 (1984) 1113.

[5] D.J. Lee, M.M. Telo da Gama, K.E. Gubbins, J. Chem. Phys. 89 (1985) 1514.
[6] E. Salomons, M. Mareschal, J. Phys. Cond. Matt. 3 (1991) 9215.
[7] V.G. Baidakov , S.P. Protsenko, J. Phys. Chem. C 112 (2008) 17231.
[8] M. Mecke, J. Winkelmann, J. Chem. Phys. 110 (1999) 1188.
[9] M. Horsch, M. Heitzig, T. Merker, T. Schnabel, Y.-L. Huang, H. Hasse, J. Vrabec, in W.E. Nagel, D.B. Kröner, M.M. Resch: High Performance Computing in Science and Engineering '09, Springer, Berlin Heidelberg, 2010.
[10] C.I. Poser, I.C. Sanchez, Macromol. 14 (1981) 361.
[11] S. Enders, K. Quitzsch, Langmuir 14 (1998) 4606.
[12] H. Kahl, S. Enders, Phys. Chem. Chem. Phys. 4 (2002) 931.
[13] O.G. Nino-Amezquita, S. Enders, P.T. Jaeger, R. Eggers, Ind. Eng. Chem. Res. 49 (2010) 592.
[14] E. Schäfer, G. Sadowski, S. Enders, Fluid Phase Equilibr. 362 (2014) 151.
[15] J. Winkelmann, J. Phys. Cond. Matt. 13 (2001) 4739.
[16] A. Mejía, J.C. Pàmies, D. Duque, H. Segura, L.F. Vega, J. Chem. Phys. 123 (2005) 034505.
[17] T. Schnabel, A. Srivastava, J. Vrabec and H. Hasse, J. Phys. Chem. B 111 (2007) 9871.
[18] J. Vrabec, J. Stoll and H. Hasse, J. Phys. Chem. B 105 (2001) 12126.
[19] J. Gross, G. Sadowski, Ind. Eng. Chem. Res. 40 (2001) 1244.
[20] J. Gross, G. Sadowski, Ind. Eng. Chem. Res. 41 (2002) 5510.
[21] J. Vrabec and H. Hasse, Mol. Phys. 100 (2002) 3375.
[22] D. Möller and J. Fischer, Mol. Phys. 69 (1990) 463.
[23] A. Z. Panagiotopoulos, Mol. Phys. 61 (1987) 813.
[24] J.E. Jones, Proc. Roy. Soc. 106A (1924), 441.
[25] J.E. Jones, Proc. Roy. Soc. 106A (1924), 463.
[26] H. A. Lorentz, Ann. Phys. 12 (1881) 127.
[27] D. Berthelot, Compt. Rend. Ac. Sc. 126 (1898) 1703.
[28] T. Schnabel, J. Vrabec, H. Hasse, J. Mol. Liq. 135 (2007) 170.
[29] M. Buchholz, H.-J. Bungartz and J. Vrabec, J. Comput. Sci. 2 (2011) 124.
[30] D. Fincham, Mol. Phys. 8 (1992) 165.
[31] S. Werth, G. Rutkai, J. Vrabec, M. Horsch and H. Hasse, Mol. Phys. (2014) in press.
[32] J.D. van der Waals, PhD thesis, University of Leiden, 1873.
[33] J.W. Cahn, J.E. Hilliard, J. Chem. Phys 28 (1958) 258.
[34] G. Niño-Amézquita, D. van Putten, S. Enders, Fluid Phase Equilibr. 332 (2012) 40.
[35] C. Miqueu, B. Mendiboure, A. Graciaa, J. Lachaise, Ind. Eng. Chem. Res. 44 (2005) 3321.
[36] L.A. Román-Ramírez, F. García-Sánchez, C.H. Ortiz-Estrada, D.N. Justo-García, Ind. Eng. Chem. Res. 49 (2010) 12276.
[37] D. Fu, XY. Hua, YF. Xu, J. Phys. Chem. C 115 (2011) 3340.

From Concept to Design: The use of Membrane Residue Curve Maps to characterize and design membrane processes

Mark Peters[2], Naadhira Seedat[1], Diane Hildebrandt[2], David Glasser[2]
[1]School of Chemical and Metallurgical Engineering, University of the Witwatersrand, Private Bag 3, WITS 2050, Johannesburg, South Africa
[2]Materials and Process Synthesis: A Research Unit at UNISA, Private Bag X6, Florida 1710, Johannesburg, South Africa

Abstract
During a concept design, engineers are tasked with evaluating and comparing a vast array of different processing options by looking at their respective technical capabilities, economics, as well environmental impacts, amongst others. In a very limited time, and with a very limited budget, they are required to make highly informed decisions about the feasibility of design – decisions that have far-reaching effects on the outcome of a process. With so many alternative and novel technologies emerging, the need to equip design engineers with the tools to quickly and cheaply compare process options has become imperative. As an example, we explore the development of a particular design tool, namely Membrane Residue Curve Maps, from their theoretical background, the experimental validation, and finally their use in concept design for quickly evaluating different membrane types, and being able to glean important information in a simple yet effective manner. Using this, and other related methods, allows for a designer to confidently make important decisions.

Keywords
Concept Design; Feasibility Study; Design Techniques; Membrane Residue Curve Maps; Separations.

1. Introduction

1.1 The Nature of Concept Designs

In the early stages of a design of either a new chemical process, or modification thereof, a design team is often tasked with screening a wide range of various (sometimes competing) technologies. A technology is primarily considered from its technical ability to produce the desired product/output needed for the overall process. If this is the case, the cost, both capital and operating, of the particular technology are then established and thereafter other factors are considered too, such as environmental impacts and legal regulations. The various applicable methods or technologies are then compared with each other and assessed for their strengths and weaknesses in each regard. The aim of a Concept Design (or Feasibility Study) is to evaluate if a project exhibits the necessary aspects to warrant pursuing it further, and possibly even to completion. Thus, a vast amount of information (technical or otherwise) needs to be obtained, evaluated and assessed in order to make informed decisions.

To add to matters, this very often needs to be done in a short period of time, with a limited budget. However, because of the impact that the findings of the feasibility

have on the outcome of a projects lifetime, the decisions taken in this beginning phase have lasting effects that ultimately affect the way forward for the entire project. It then goes without say that it is of vital importance that one can be able to assess a wide range of options quickly and cheaply, allowing for crucial informed decisions to made confidently.

While many innovative technologies and processes have recently emerged as favourable alternatives over the more conventional or traditionally used techniques, these may not become the chosen process to be implemented. This is often due to the lack of availability of data and simple, yet effective, methods for the design of such alternative processes. Thus the inclusion or rejection of an alternative process is not based on ineffective technical ability, but rather a limitation in the access to information about the technology.

1.2 The Concept of Separations

As a case and point, consider the above-discussion by looking at the field of separations. In the realm of industrial separations, membrane permeation is a relatively new method when compared to distillation processes, which has a well-established track-record. While the physical operating mechanisms of the two processes are very different from each other, the overall aim of each is to achieve a certain separation, resulting in either one being a possible candidate for a separation step in a process design. The design techniques of distillation systems are (for the most part) publically available, with numerous texts providing the necessary details and many mainstream software programs containing built-in sub-routines for the design of both the process as well as equipment. When compared to distillation, the concept design methods of membrane systems are very limited, and are often regarded as protected information. It is therefore desirable to have available a method that can be used to design a process using membrane separation rapidly and inexpensively, but more importantly be able to compare it to traditional processes. In order to compare these two processes, one would like to have available *similar* design techniques for each.

In order to address the need for comparing membrane systems from the same standpoint as distillation, Membrane Residue Curve Maps (M-RCMs) were developed and applied as a tool for the design and synthesis of such processes[1-3]. This graphical design method has previously proven its value in the conceptual stages of a distillation process[4,5], and by developing the same method for membrane systems allows for ease of comparison of the two.

So as to validate the existence and usefulness of M-RCMs, a simple batch experiment was designed and built[6]. The apparatus was designed in such a way that, for a particular membrane, the properties and operation of the membrane can be quickly assessed. Thereafter, the measured data can be easily used to generate M-RCMs and this can be incorporated in the concept design.

The development of this novel graphical tool for membrane systems, not only allows one to compare membranes with distillation, but also to compare different membranes with each other: Some membranes are highly selective to what they permeate, and undergo extensive research and testing, thus come at a substantial cost. On the other hand, there exist cheaper, more robust membranes that are non-

selective in nature, but yet can still achieve the same separation as the selective membrane. Using the M-RCM approach not allows one to only design the membrane process, but also consider its feasibility for use in an overall design.

1.3 Example: Syngas clean-up

To demonstrate this, we considered an example of a syngas (H_2 and CO) stream contaminated with undesirable levels of CO_2. The aim is to reduce the CO_2 levels as far as possible. The aim of both the selective and non-selective membrane is to separate CO_2 from syngas for various applications such as Fischer Tropsch processes, as well as in refineries to recover the CO_2 which is bought by gas companies that sell CO_2 to beverage and other companies that require CO_2.
While a selective membrane could be used, these are relatively expensive when compared to more robust non-selective membranes. For this, a readily-available and easily-accessible polyethylene membrane was investigated. The batch experiment was operated generating M-RCMs, which were then used to design a continuously-operated process for the effective removal of CO_2 from syngas.

2. Theory of M-RCMs

2.1 Derivation of M-RCMs

Consider a simple batch apparatus where a fluid mixture is enclosed by a suitable membrane. Permeation of material through the membrane can be brought about by a difference in pressure across the membrane (typical for gas separations). Dynamic material balances around the batch system result in the residue curve equation:

$$\frac{dx_i}{d\tau} = (x_i - y_i)\,, i = 1,2 \ldots n-1 \qquad (1)$$

where x_i and y_i are the mole fractions of component *i* in the retentate (non-permeate) and permeate phases, respectively, *n* is the number of components present, and τ is dimensionless time determined by *–ln(Ro/Rt)* where *Ro* and *Rt* refers to the retentate initially and at time *t* respectively. A full derivation of equation (1) can be found in Peters et al.[1,3]. This equation mathematically describes the change in retentate composition over time during batch permeation. It is applicable for all types of membranes, and thus knowledge regarding permeation flux for a chosen membrane is needed to solve it.

In order to solve the set of differential equations in equation (1) a relationship between the retentate and permeate compositions needs to be defined. For the purposes of this discussion, a simple gas separation model can be used[1,3,7]:

$$\frac{y_i}{y_j} = \alpha_{ij}{}^{M} \frac{x_i}{x_j} \qquad (2)$$

where $\alpha_{ij}{}^{M}$ is the constant relative permeability of component *i* with respect to *j*. The value of $\alpha_{ij}{}^{M}$ depends on the interaction of the respective species with the membrane material.

It is worth noting that, although equation (1) is derived for a batch process, it has previously been shown to be directly applicable to single-stage continuously-operated membrane modules[2,3].

2.2 Non-selective membranes

A non-selective membrane is one in which all species present permeate through the membrane, but at varying rates. For the example, the gas composes of three components, namely Hydrogen (A), Carbon Monoxide (B) and Carbon Dioxide (C). The constant relative permeabilities at 25°C of these components relative to the carbon monoxide flux rate can represented as ${\alpha_{AB}}^{M} = 31$ and ${\alpha_{BC}}^{M} = 60$. These relative permeabilities are based on mass transfer through a natural rubber membrane and have been adapted[7,8]. Figure 1(a) depicts the theoretical M-RCM plot for the system and a non-selective polyethylene membrane using the theory stated above.

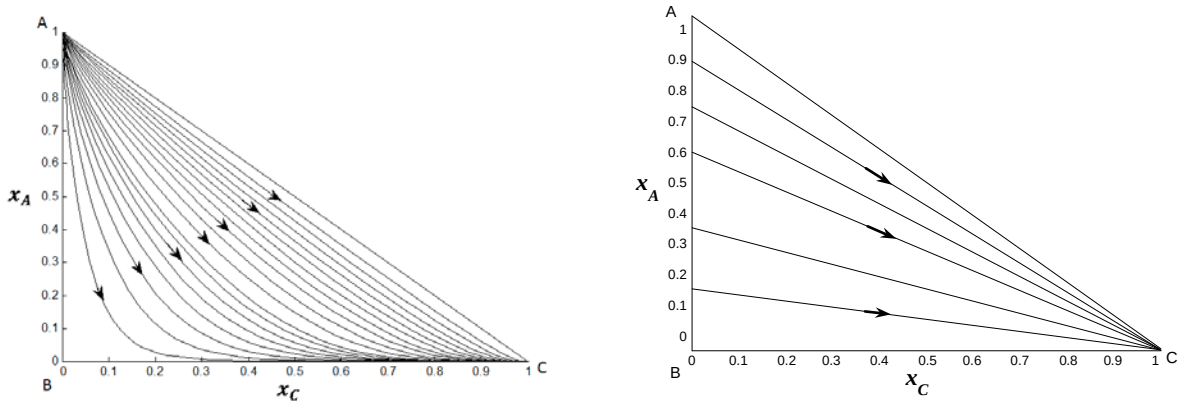

(a) **(b)**

Figure 1: M-RCM of the hydrogen (A), carbon monoxide (B) and carbon dioxide (C) system using a (a) non-selective membrane (polyethylene)[6], and (b) selective membrane.

2.3 Selective membranes

Selective membranes, on the other hand, are designed to preferentially separate one component from a mixture. These membranes are usually specially researched and designed to perform a certain separation, thus knowledge of their flux rates are not usually made available in the public domain. For this reason, we need to use hypothetical values for the relative permeabilities: ${\alpha_{AB}}^{M} = 1$ and ${\alpha_{CB}}^{M} = 0.01$. From this, it can deduced that the membrane selectively holds back carbon dioxide (C) while the syngas is selectively permeated. Figure 1(b) depicts the theoretical M-RCM plot for the system and a hypothetical selective membrane using the theory and relative permeabilities stated above.

3. Measurement of M-RCMs

3.1 Apparatus

Seedat et al.[6] designed a simple batch experimental apparatus to generate data to validate and measure membrane residue curves, and their associated data. The apparatus was designed using the basis of the theory laid out in section 2.1.The apparatus is cheap and easy to operate, allowing for reliable results in a short space of time. The results can then be used in the process design. Since the aim of this paper is show the reader the usefulness of the M-RCM design tool, rather than detail the methods of experimentation, the reader is referred to Seedat et al.[6] for more information in the regard.

3.2 Results of experimentation

The system of gases, namely H_2, CO and CO_2, were permeated through a non-selective polyethylene membrane using the above-mentioned apparatus. Figure 2

depicts the results obtained from Seedat et al.[6]. It can be seen that the experimental and theoretical data correlate and move towards CO_2 (C) which is the slowest permeating component, H_2 (A) is the fastest permeating component and CO (B) is the intermediate permeating component. The results also depict that the correct relative permeabilities were used as the trends are predicted correctly.

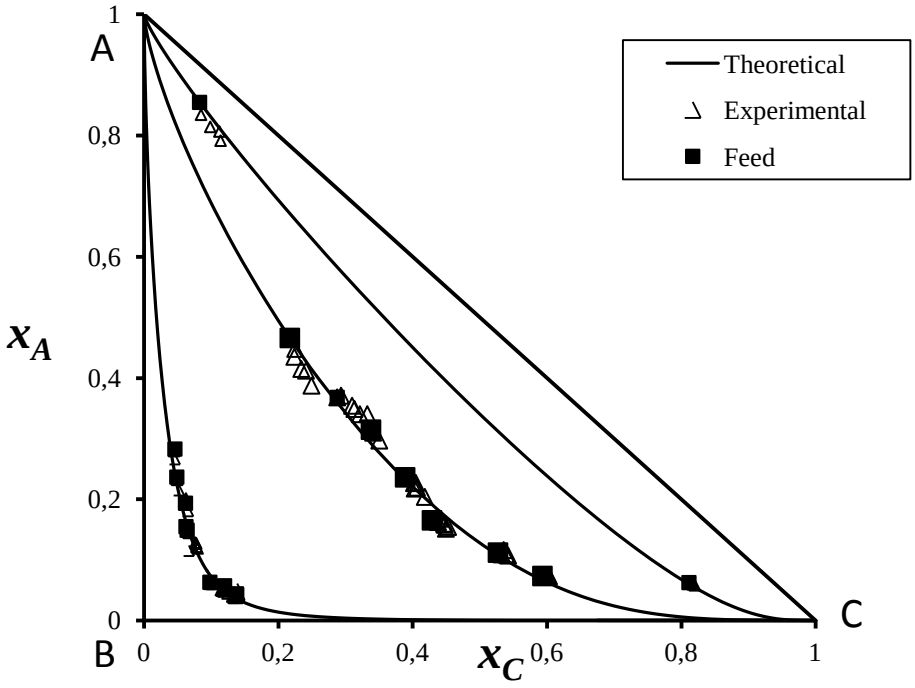

Figure 2: Residue curve map depicting the theoretical and experimental data for the CO_2 and synags system using a non-selective membrane[6].

The results of a single profile took the order of a few (4-6) hours to generate, using a minimal amount of gas, thus providing a simple yet effective way of validating and verifying the design models for the membrane, without the need for having to pilot. This information is very valuable when conducting the concept study.

Because of the versatility of the experiment, similar experiments can be done using any other suitable membrane (i.e. a selective membrane) on the same apparatus.

4. Process Design

With the theory, as well as data validation in place, we are now able to confidently design a process that removes CO_2 from syngas using either membrane type. With this, further informed decisions about their respective applicability to the process can then be made.

4.1 Selective membrane

Firstly, consider the selective membrane, whose behaviour is depicted by the profiles in Figure 1(b). The data associated with these profiles is such that the syngas (both H_2 and CO) move through the membrane at a rate 100 times that of CO_2, resulting in CO_2 not permeating rapidly. The retentate thus becomes increasingly richer in CO_2, while the permeate is an almost-pure syngas stream. From a technical operation perspective, this is a very simple and easy way to achieve the desired separation, since a single membrane module, with a relatively small area is required. However, the capital costs of purchasing a selective membrane is very high as these

membranes have specifically been designed for the purpose of removing CO_2 from syngas and are normally IP-protected in one form or another, resulting in them being very expensive. Furthermore, replacing these membranes is very costly too: since they are protected, replacements can only be bought via the vendor that developed it. This has both direct and indirect cost-impacts.

4.2 Non-selective membrane

If the non-selective polyethylene membrane is used, reference to the profiles in Figure 1(a) reveals that there is no selectivity to any component. The curves start at the fastest permeating species, H_2, and quickly move toward the next fastest permeating species, CO. CO_2 is the slowest permeating, and is thus "held back" by the membrane, with the retentate becoming richer in CO_2 as permeation progresses. It can further be seen that pure CO_2 can be reached but it will be take a series of membranes (i.e. a relatively large area), and possibly a recycle stream in order to obtain a high recovery of syngas. Although a number of membrane modules would be required, the capital costs may very well still be cheaper when compared to the selective membrane as non-selective membranes are readily and easily available and are inexpensive. The same can be said for replacement costs.

5. Concluding Remarks

The aim of this paper was to introduce to the reader to ideas and simple methods for evaluating and comparing different technologies in a quick and efficient manner. It was never the intention to promote one separation method over another, nor one membrane over another. The aim is not to identify which type of separation is better – that decision depends on the process requirements. The aim was to better-equip the design engineer with the necessary tools to make confident and informed decisions early on in a design without wasting unnecessary time and funds. It was further intended to plant the seeds for more creative and novel design techniques to be explored and formulated. While M-RCMs have shown their worth for membrane and related separation processes, similar approaches need to be taken (in future) for other process equipment.

References

1. Peters, M., Kauchali, S., Hildebrandt, D. & Glasser D. Derivation and Properties of Membrane Residue Curve Mas*. Ind. Eng. Chem. Res*. **2006**, 45, 9080-9087.
2. Peters, M., Kauchali, S., Hildebrandt, D. & Glasser D. Application of Membrane Residue Curve Maps to Batch and Continuous Processes*. Ind. Eng. Chem. Res.* **2008**. 47, 2361-2376.
3. Peters, M., Glasser, D., Hildebrandt, D. & Kauchali, S. *Membrane Process Design Using Residue Curve Maps*; John Wiley & Sons: New York, 2011
4. Doherty, M. F. & Malone, M. F. *Conceptual Design of Distillation Systems*; McGraw-Hill: New York, 2001.
5. Fien, G. A. F. & Liu, Y. A. Heuristic Synthesis and Shortcut Design of Separation Processes Using Residue Curve Maps: A Review. *Ind. Eng. Chem. Res.* **1994**, *33*, 2505-2522.
6. Seedat, N., Parag, P., Govender, D., Peters, M., Hildebrandt, D., Glasser, D. Experimental Measurement of Membrane Residue Curve Maps. *Ind. Eng. Chem. Res.*, **2013**, *52* (32), 11142–11150
7. Wijmans, J. G. & Baker, R. W. The solution-diffusion model: a review. *J. Membr. Sci.* **1995**, 107, 1-21.
8. Geankoplis, C.J., 1993. *Transport Processes and Unit Operations*. 3rd ed. New Jersey, Prentice-Hall, Inc. pp. 760
9. Michaels, A.S. & Bixler, H.J., Flow of Gases Through Polyethylene. *Journal of Polymer Science.* **1961**. L, 413-439.

Evaluation of equilibrium and non-equilibrium models for simulation of distillation

Johannes Holtbruegge[1], Eva Sorensen[2], Andrzej Górak[1], Philip Lutze[1]
[1]Laboratory of Fluid Separations, TU Dortmund University, Dortmund, Germany
[2]Department of Chemical Engineering, University College London, London, UK

Abstract
This study compares equilibrium and non-equilibrium approaches for simulation of distillation implemented in Aspen Plus®. Insights are used to identify simulation tasks for which the predictions using the two approaches deviate, and guidelines are recommended for how to select the best-suited model approach for the simulation of a given separation task by investigating the influence of different chemical systems and structural and operational degrees of freedom on the simulation results. To successfully run the non-equilibrium approach, a guideline for its initialization, especially in terms of discretization of the bed height for packed columns, was developed. The subsequent analysis of the approaches showed a strong dependence of the simulation accuracy on the applied internals. The guidelines were validated against experimental results.

Keywords
Distillation, model discrimination, rate-based model, Aspen Plus®

1. Introduction

Distillation is the most commonly applied thermal separation technique in the process industries. The design of distillation columns is constantly improving due to the development of sophisticated modeling and design tools, leading to a reduced need for over-sizing due to safety concerns and with that, an operation close to the most economical point. However, the use of an inaccurate model during the design stage can still result in an incorrect design and thus increased energy demand, products that are off-specifications, as well as potential operational difficulties.

The most common modeling approaches used for simulation of distillation columns are i) the equilibrium stage approach (EQ), which assumes phase equilibrium between the streams leaving a stage, and ii) the non-equilibrium stage approach (NEQ), which considers actual heat- and mass-transfer rates between the phases and assumes phase equilibrium to be existent only at the phase interface. The solution of the NEQ has been found to be highly accurate, although requiring a higher computational effort than solution of the EQ [1]. The higher computational effort of the NEQ may be critical, especially in simulation and optimization of distillation sequences consisting of multiple steps. Thus, if possible, the use of EQ in such cases can potentially reduce the time to market for new products.

The aim of this study was to evaluate the performance of both modeling approaches (EQ and NEQ) for different zeotropic and azeotropic chemical systems by developing and applying a systematic procedure, and to identify deviations between them as a function of the physicochemical and thermodynamic properties of the chemical system as well as structural and operational degrees of freedom of the distillation column. Based on this, guidelines have been developed to suggest when which model, and with which model parameters, needs to be used for a given simulation task. The theoretical findings have also been compared to experimental results underlining the capabilities of the proposed procedure.

2. Results and discussion

We have developed a systematic procedure for comparing the performance of the two modeling approaches under the same conditions (Section 2.1). At the start, different degrees of freedom of the simulation task are introduced before simulation results using both modeling approaches are presented. In this context, a base-case distillation column design including fixed values for the different degrees of freedom was generated (Section 2.2). Then, initialization of the NEQ, especially a proper discretization of the bed height for packed columns, is discussed (Section 2.3). The results obtained with the appropriately initialized NEQ are then compared to those obtained using the EQ for various separation tasks (Section 2.4), and used to identify simulation tasks for which the use of the EQ gives sufficiently accurate results. Finally, an experimental study is used to validate the results.

2.1 Systematic procedure for comparison of modeling approaches

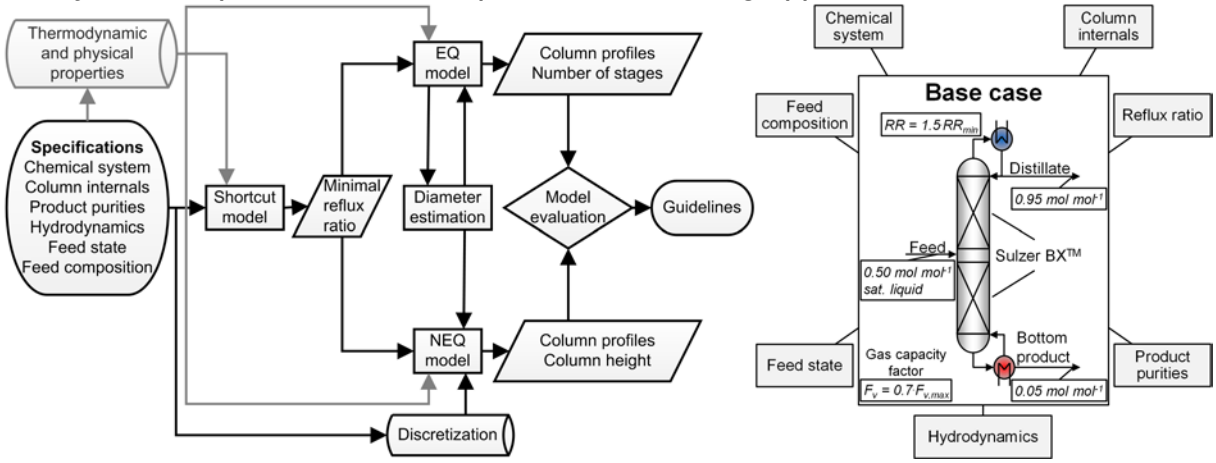

Figure 1: (left) Systematic procedure to compare EQ and NEQ modelling approaches for distillation and (right) degrees of freedom considered within the simulation studies of the column used for model evaluation. In *italic*, values for the base-case design are given.

Figure 1 (left) introduces the systematic procedure that was developed within this contribution. In the “specifications” step, the simulation is specified by fixing the different degrees of freedom. To study the influence of physicochemical and thermodynamic properties on the modelling approaches, the chemical system is treated as degree of freedom. Furthermore, structural (e.g., column internals and feed position) and operational (e.g., reflux ratio, feed composition and state and product purities) degrees of freedom have to be fixed. Figure 1 (right) summarizes the degrees of freedom of the distillation column which were considered in this study. The values for the degrees of freedom are entered in a physicochemical and thermodynamic database which is used to compute the properties necessary to properly describe the chemical system. In the calculations, the Aspen Plus® database APV7.2 PURE24 was applied with the UNIQUAC g^E-model [2] to describe the thermodynamic interactions between the components. Physicochemical and thermodynamic properties and the predefined specifications were used to initialize Aspen Plus® simulations using both approaches. The DSTWU (Winn-Underwood) model is used to calculate the minimal reflux ratio for the simulation task and is passed to the EQ and the NEQ implemented in the Aspen Plus® RadFrac model. Both approaches were specified with the same values for the degrees of freedom. The EQ is used to calculate the number of equilibrium stages that are necessary to fulfil the given purity specifications. The NEQ is then used to calculate the packed bed height that is necessary to reach the desired purity of an equivalent column. As

the NEQ uses rate equations based on the two-film theory to calculate the heat and mass-transfer rates along the packed bed height, a proper discretization of this height is necessary to guarantee sufficiently accurate results (Section 2.3) [3].

2.2 Base-case design of the distillation column

The large number of degrees of freedom considered leads to a large simulation effort to capture all their influences on the model accuracy. To minimize the effort for model comparison, a base-case design of the distillation column was established. Figure 1 (right) summarizes the values for the degrees of freedom based on which the studies were performed. The reflux ratio (RR) was dependent on the chemical system and was fixed to 1.5 times the minimal RR. A total of 29 different binary zeotropic and azeotropic chemical systems, with different boiling point differences, enthalpies of vaporization and activity coefficients in infinite dilution (thermodynamic interactions), were studied, however, only some of these binary systems will be discussed here.

2.3 Initialization of the non-equilibrium approach

The influence of the segment height (discretization) used to run the NEQ was investigated for the base-case design with a thermodynamically ideal binary system with a boiling point difference of 10 K for different column internals. From the class of structured packings, Sulzer Mellapak 250.X/Y, BX^{TM} and CY^{TM} were tested, whereas Intalox Saddles and Raschig Super Rings were considered as random packings. To evaluate the influence of the segment height on the simulation accuracy, the so-called discretization accuracy parameter Ψ is introduced as follows:

$$\Psi = \sum_{k=1}^{n_{seg}} \dot{N}_{lb,k} \Big/ \sum_{k=1}^{n_{seg}^{\infty}} \dot{N}_{lb,k} \tag{1}$$

To calculate this parameter, the mass-transfer rate of the low-boiling component $\dot{N}_{lb}$ is summed up for a finite number of segments n_{seg} and divided by the same sum for an infinite number of segments n_{seg}^{∞}. The accuracy parameter can therefore vary between 0 and 1 with higher values representing more accurate simulation results due to smaller segment heights (and more segments). However, a too large number of segments increases the computational effort without significantly improving the simulation results. Thus, an accuracy parameter of 0.99 was found to be required to achieve a suitable trade-off between simulation accuracy and computational effort.

Figure 2 (left) shows the influence of the distillate and bottom product purities on the allowable inverse segment height for the different packings. The maximal allowable segment height is reached when the discretization accuracy parameter equals 0.99. The inverse segment height decreases with increasing product purities; thus, higher segments are allowable when reaching high purities. The trend is the same for all packings considered but there are significant deviations between their absolute values. Note that reaching the same accuracy parameter as assumed in this work with the Aspen Plus® recommendation (inverse segment height of 10 m^{-1}) is only advisable for high distillate purities [4]. We will argue that the recommendation by Aspen Plus® should be replaced with a recommendation based on the *discretization factor ζ* which considers the height equivalent to a theoretical plate ($HETP_{lit}$). The $HETP_{lit}$ for a given packing is available in the literature and accounts for the separation performance of the packing within the discretization:

$$\zeta = HETP_{lit} / dz \tag{2}$$

Figure 2 (right) shows the proposed recommendation for discretization. Based on the discretization factor, the trends of all packings move closer together and a unique guideline for discretization can be developed, and is indicated with grey steps in this diagram. The guideline shows high discretization factors for low product purities, and vice versa and can be used to properly discretize the NEQ for description of distillation for the studied combinations of packings and chemical systems.

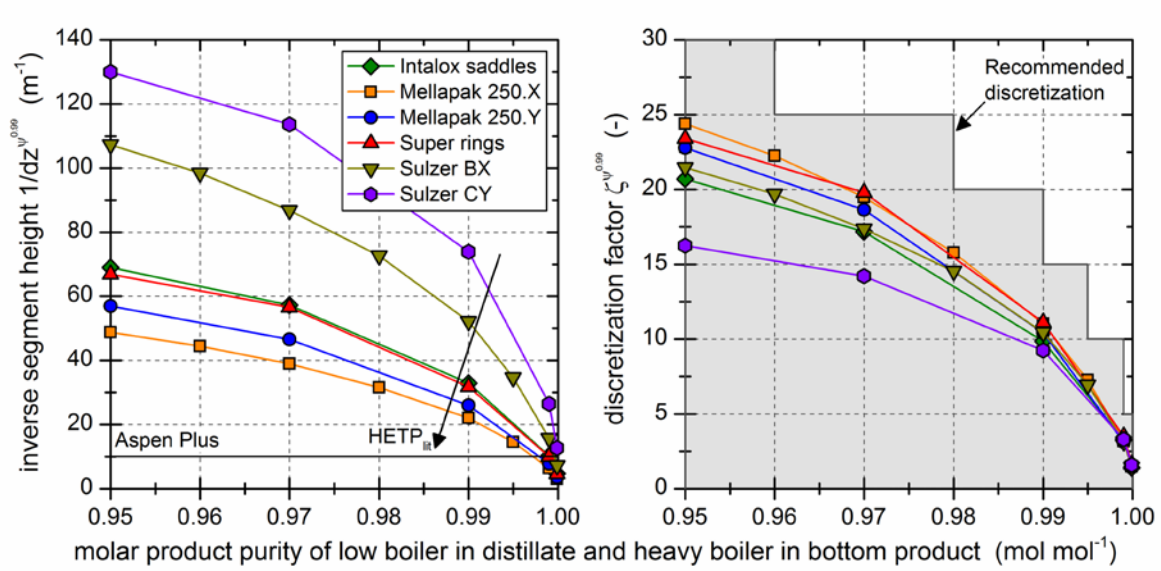

Figure 2: Influence of product purities on (left) the inverse segment height and (right) the discretization factor necessary to obtain accurate simulation results with the NEQ. The black horizontal line in the left diagram indicates the segment height recommended by Aspen [4], whereas the guideline developed here is indicated with grey steps in the right diagram.

2.4 Model evaluation

The guideline for discretization presented above was used to initialize the NEQ within the model evaluation, thus allowing a fairer comparison of its results with those calculated with the EQ. To compare the simulation results of both approaches, the so-called $HETP_{calc}$ is introduced which determines the ratio between the packed bed height $h_{col,NEQ}$ calculated with the NEQ, and the number of equilibrium stages $n_{th,EQ}$, calculated with the EQ, i.e. a calculated HETP:

$$HETP_{calc} = h_{col,NEQ} / n_{th,EQ} \quad (3)$$

To transfer equilibrium stages calculated with the EQ into a real apparatus, HETPs are necessary. These values are listed in literature for various packings ($HETP_{lit}$) and its comparison to the $HETP_{calc}$ can give insights on the appropriateness of using the EQ combined with the $HETP_{lit}$ for a given simulation task. If the $HETP_{calc}$ equals the $HETP_{lit}$, then the results of both approaches are the same when using the $HETP_{lit}$ to transfer the number of equilibrium stages to a corresponding bed height. For $HETP_{calc}$ higher than the $HETP_{lit}$, the column designed with the EQ would be too small to achieve the specifications. $HETP_{calc}$ values smaller than the $HETP_{lit}$ would lead to an over-sized column if designed with the EQ, although this is not an operational issue as the product specifications can still be reached. Hence, the task of this section is to identify simulation tasks for which the $HETP_{calc}$ is higher than the $HETP_{lit}$, and where therefore the NEQ approach must be used. Figure 3 (left) compares the normalized HETP values which are calculated from the $HETP_{calc}$ for the base-case design and the $HETP_{lit}$ for the six packings considered. The packings do not behave the same way; some of the normalized HETP values are almost one

whereas some are significantly smaller, thus representing a conservative estimate of their separation characteristics. The different values of the normalized HETP value clearly show that the model evaluation and selection depends on the used packings characteristics in combination with the given $HETP_{lit}$. Hence, this section will present results of the model evaluation for the Sulzer BX™ structured packing.

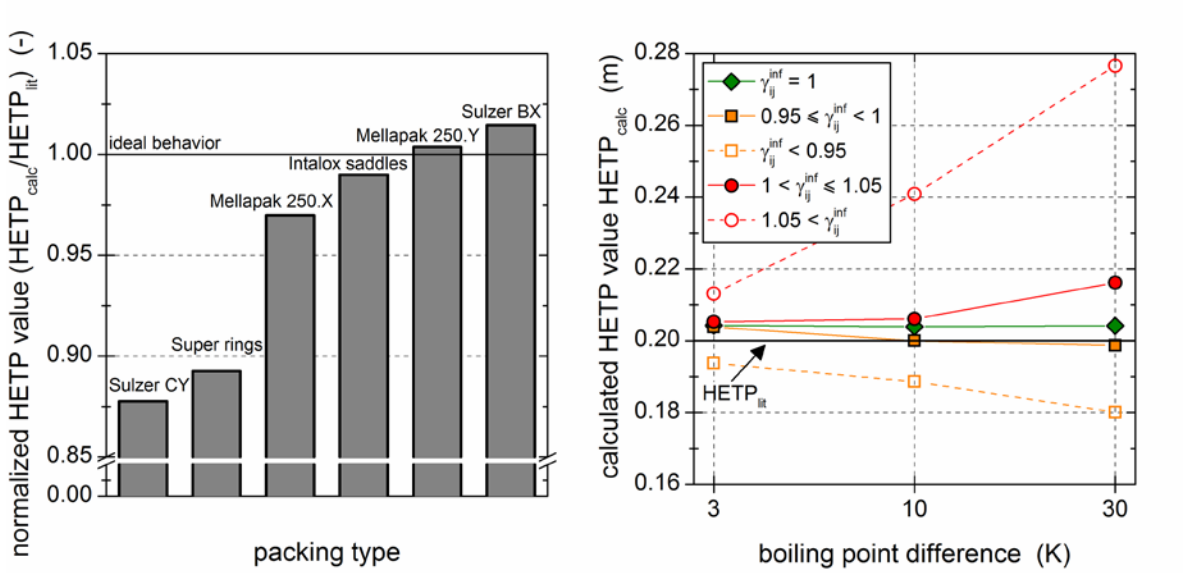

Figure 3: (left) Normalized HETP value calculated for the packings investigated under base-case conditions and (right) influence of the boiling point difference on the $HETP_{calc}$. The influence is shown for ideal systems ($\gamma_{ij}^{inf} = 1$), systems with maximum ($\gamma_{ij}^{inf} < 1$) and minimum ($\gamma_{ij}^{inf} > 1$) pinch and maximum ($\gamma_{ij}^{inf} << 1$) and minimum ($\gamma_{ij}^{inf} >> 1$) azeotropes.

Figure 3 (right) captures the influence of the degrees of freedom on the deviation between both approaches by showing the influence of the boiling point difference, for chemical systems with different activity coefficients in infinite dilution, on the $HETP_{calc}$ and compares it to the $HETP_{lit}$ (0.2 m) to evaluate the difference between the modeling approaches. It can be seen that for systems with activity coefficients around one ($0.95 \leq \gamma_{ij}^{inf} \leq 1.05$) influences of the other degrees of freedom have to be studied to allow a final evaluation. On the other hand, systems with minimum azeotropes ($\gamma_{ij}^{inf} > 1.05$) should always be simulated using the NEQ approach. The influence of all other degrees of freedom was also studied, although considered beyond the scope of this contribution. The obtained insights were used to develop a detailed guideline based on a system analysis that helps to identify simulation tasks for which the EQ can be used with confidence and for when the NEQ must be used.

3 Practical application and experimental validation

The guidelines to properly initialize the NEQ and to evaluate the accuracy of the EQ were validated using experimental results. For the simulations, only physicochemical and thermodynamic system information, product purities and yields, feed state and composition and targeted column load were necessary. All validation comparisons showed high accuracy of the predicted product compositions also for multicomponent systems. An example is considered for the separation of a quaternary mixture consisting of dimethyl carbonate (DMC), methanol (MeOH), propylene carbonate (PC) and propylene glycol (PG). Figure 4 introduces the set-up of a DN50 pilot-scale column equipped with Sulzer BX™ packings (left) and shows the experimental and the corresponding simulated (EQ and NEQ) concentration profiles of one experiment (right) [5]. Both simulated concentration profiles fit the experimental data very well.

This was expected as the discretization guideline predicted a discretization factor of 30 to end up with sufficiently accurate results of the NEQ for the given distillate and bottom product purities. However, use of the complex NEQ is not necessary as the model evaluation guideline recommended the simpler EQ using the corresponding $HETP_{lit}$ to have a sufficient accuracy of the simulation.

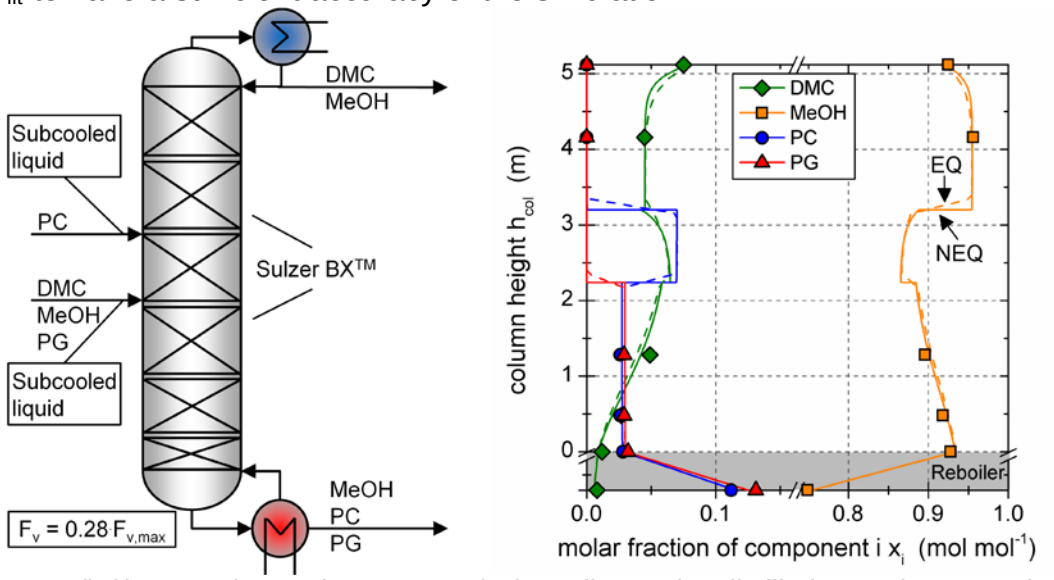

Figure 4: (left) Experimental set up of the pilot-scale distillation column and (right) corresponding concentration profile. Symbols represent experimental results [5]; continuous lines denote simulations using the NEQ and dashed lines using the EQ.

3. Conclusions

A systematic procedure that helps to select an appropriate modeling approach, either an equilibrium stage approach (EQ) or a non-equilibrium stage approach (NEQ), to describe a given distillation task was developed. The sensitivity of the EQ and NEQ towards the simulation task, established by specifying the type of chemical system together with structural and operational degrees of freedom, was studied. The simulations performed with the Aspen Plus® RadFrac model showed major impact on the predictions based on the number of segments chosen for the NEQ and a guideline for the choice of segments was established. Next, both approaches were compared and simulation tasks for which the EQ predictions deviate from the NEQ predictions were identified. The gained insights were used to predict that the accuracy of the EQ is sufficient to describe the separation of a non-ideal quaternary mixture, and this was experimentally verified.

Acknowledgements

This work is part of the Collaborative Research Centre on “Integrated Chemical Processes in Liquid Multiphase Systems”. The authors gratefully acknowledge the Deutsche Forschungsgemeinschaft (DFG) for providing financial support. Furthermore, financial support of the German Federal Ministry of Education and Research (Project number: 01 RC1008H) is acknowledged.

References

[1] A. Górak et al., 1987, *Chem. Ing. Tech.*, 59, 2, 95–106.
[2] D.S. Abrams et al., 1975, *AIChE J.*, 21, 1, 116–128.
[3] H. Mori et al., 1996, *J. Chem. Eng. Jpn.*, 29, 2, 307–314.
[4] Aspen Technology, 2010, Aspen Plus V7.2 Help, Patent, Cambridge.
[5] J. Holtbruegge et al., 2013, *Chem. Eng. J.*, 234, 448–463.

Analysis of a gas flow in structured packed bed columns using CFD

Niina Jäntti[1], Johanna Vaittinen[1], Tuomo Keskitalo[1], Kari Keskinen[1,2], Timo Siikonen[2], [1]Neste Jacobs Oy, Porvoo Finland; [2]Aalto University, Espoo, Finland

Abstract

Post-combustion carbon capture is one of the most important technologies for CO_2 recovery from the flue gases of power plants. The vast flue gas amounts to be treated lead to large column dimensions, where the flow-field control may be problematic and maldistribution of the phases may appear. This decreases the mass transfer efficiency of the column. In this study, a flow field and a gas-phase distribution in a structured packed bed consisting of Sulzer's Mellapak 250Y packing is studied by computational fluid dynamics (CFD). The study concentrates on modelling the gas flow in the bed and describing the bed as an anisotropic porous media.

Keywords

CFD, gas flow, maldistribution, porous medium, structured packing

1. Introduction

Fossil fuels are a common energy resource in many countries. The power plants using fossil fuels produce large amounts of CO_2 emissions that induce global warming. One solution to decrease CO_2 emissions is by recovery of the CO_2 from the flue gases, for example with post-combustion CO_2 capture. The post-combustion carbon dioxide capture is typically conducted in absorption columns that have a large diameter due to the vast amount of flue gases to be treated at nearly atmospheric pressure. Structured packings are commonly used in various heat and mass transfer applications. They are also often applied in absorption columns due to their lower pressure drop per mass transfer efficiency in comparison to random packing. The structured packings have the preferential flow direction in the direction of the channels formed by the corrugated sheet structure of the packing. This leads to good radial spreading, but can also cause maldistribution of the phases, which lowers the mass transfer efficiency of the column.

A CFD model for engineering purposes for a structured packed bed is validated according to the experimental results from literature. The model is applied to the large-scale CO_2 absorption column to investigate a gas maldistribution. In this work it is hypothesized, that the gas maldistribution is indicative of the liquid maldistribution, as well. Therefore, the analysis of the gas phase distribution might also provide an indication of the liquid maldistribution.

2. Modelling methods

The structured packed bed is modelled as an anisotropic porous media and only the gas flow in the bed is studied. Anisotropy means that the resistance induced by the packing to the flow is different in different directions. One alternative could be to model the exact geometry of the packing, but this option is not feasible because of the large size of the column and the small length scales of the packing flow channels. The approach to study only the gas flow is justified by the fact that the multiphase CFD calculations are computationally expensive and also more complicated as well as unstable.

A fluid dynamics solver *porousSimpleFoam* implemented in OpenFOAM 2.1.1 [1] is used to conduct the calculations. The fluid flow is assumed incompressible, since the pressure changes are not large and the flow velocities are low compared to the speed of sound. Also the temperature is assumed to be constant. The porous media option in OpenFOAM is modelled with the aid of the Darcy-Forchheimer equation, which is principally a source term in momentum equations

$$\frac{\partial(\rho u_i)}{\partial t} + \frac{\partial(\rho u_i u_j)}{\partial x_j} + \frac{\partial p}{\partial x_i} = \frac{\partial \tau_{ij}}{\partial x_j} + \rho g_i + S_i \quad (1)$$

$$S_i = -\left(\mu d_i + \frac{1}{2}\rho|u_i f_i|\right) u_i \quad (2)$$

where S_i is the Darcy-Forchheimer equation. In OpenFOAM, there are two ways for the porosity treatment, explicit and implicit alternatives, of which the implicit porosity treatment is applied. The solver is described in more detail in [2].

The packed bed is effectively modelled as an additional resistance to the flow and there is no real solid obstacle modelled in the geometry of the bed. Thus there is no solid medium that could have an effect on the turbulence model either, which may lead to difficulties, since the effect of the real solid structure is not taken into account. A flow aligned to Mellapak 250Y channels in the packing has a lower resistance than in the directions perpendicular to the metal packing sheets. In OpenFOAM, this can be taken into account by the porous model coefficients in Equation (2) in the corresponding directions. The inclination angle of a corrugated sheet in the Mellapak 250Y structured packing is 45°, so the local co-ordinates are defined to be inclined at 45° compared to the global co-ordinates.

3. Results and discussion

The model parameters for anisotropic porous media were adjusted against the experimental results of Owens [3]. Olujic [4] has conducted experiments on the gas maldistribution and these results were also used for validation of the model.

3.1 Pressure-drop parameter determination

The study of Owens provides experimental pressure-loss data to define values for the coefficients for the porous media model in Equation (1). The packed bed in the

column of Owens consisted of Mellapak 250Y structured packing and it was modelled as an anisotropic porous media. The packed bed of this column consists of two packing layers, where the upper one is rotated horizontally 90° with respect to the lower layer. Each packing layer is 305 mm of its height. Figure 1 presents the slices of the column with the simulated velocity distribution and the packed bed position as grey slices. In Table 1 the different cases for different model set-up are presented. Different cases were examined to decide which set-up corresponds to experimental results. In Figure 2 the experimental results and simulation cases *c* and *d,* which correspond well to experimental results, are presented.

Table 1: Cases in a parameter determination for the pressure-drop.

Calculated cases in pressure drop parameter determination	
a	Turbulent case with a bulk flow inlet. The SST k-ω turbulence model applied.
b	Turbulent case with fully developed inlet flow. The SST k-ω turbulence model is applied
c	Turbulence case with fully developed inlet flow, the modified SST k-ω turbulence model is applied.
d	Laminar case with a fully developed inlet flow.

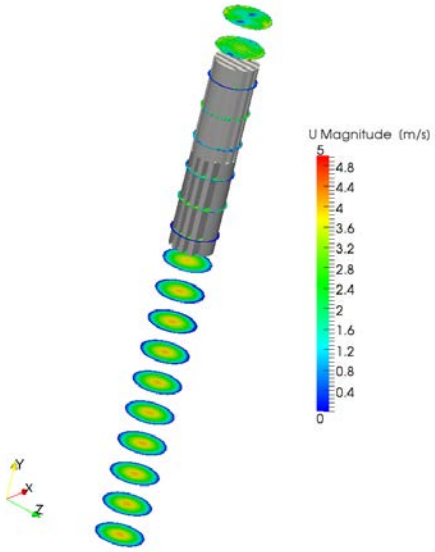

Figure 1: Slices from the column used in pressure drop simulations.

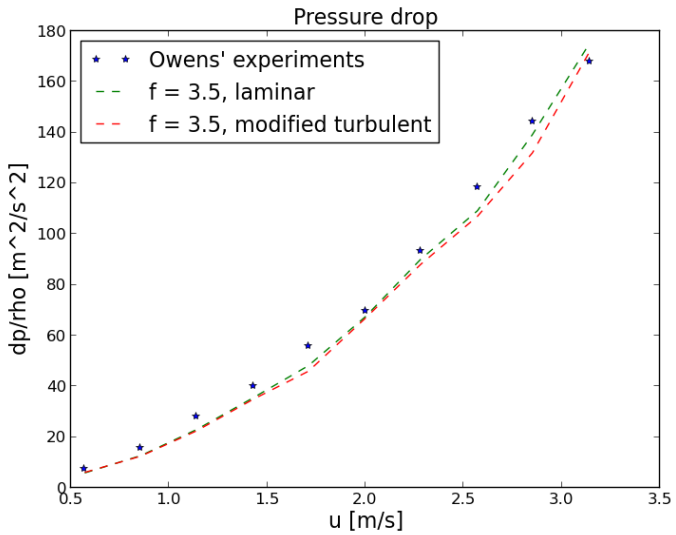

Figure 2: Pressure drop as a function of the mean inlet velocity.

The viscous term dominates the flow through the porous medium when $Re < 100$ according to [5]. In this study, the flow Reynolds numbers according to the hydraulic diameter of the packing are in the range of $Re = 562-3096$: thus it can be deduced that the inertial term dominates the flow through the porous media. The parabolic shape of the curve in Figure 2 also indicates that the second-order term, i.e. the inertial loss term could predict the pressure drop across the packed bed in relation to the gas flow velocity. This also holds with the results shown later. Therefore, only the inertial term is taken into account from the Darcy-Forchheimer equation 2. In the simulations, the physical properties were set according to the experiment conditions: the mean inlet velocity was in the range $u = 0.56$ - 3.14 m/s, the gauge pressure $p = 0$ Pa at the inlet and the kinematic viscosity $v = 1.56 \cdot 10^{-5}$ m^2/s.

In Figure 2 the pressure drop as a function of the mean inlet velocity is presented. Coefficient *f* is the inertial term coefficient in Equation (2). The two simulation cases, laminar (*d)* and modified turbulent (*c*), are compared to the experimental results [3].

The best correlation with the simulations is obtained with the coefficient value $\boldsymbol{f_2}$ = 3.5 for Equation (2), where the subscript *2* means the local co-ordinate direction of the packing flow channels. In other directions, the coefficient value is set to $\boldsymbol{f_1}$ = $\boldsymbol{f_3}$ =1000. In Figure 3, the vertical cross-sections of the column are presented for two cases, for the conventional SST k-ω turbulence model and for the modified SST k-ω model. It can be seen that, in the fully turbulent case the turbulence is produced in the bed area, even if it should be a laminar zone according to the *Re*-number. In the modified turbulence model case little turbulence is produced mainly after the bed and the velocity is not damped as much as in the turbulent bed.

In Figure 4, it can be seen that the turbulent cases (a) and (b) have a much higher pressure loss compared to case (c) and to the modified SST k-ω model case (d). Because of the anisotropic porous model presenting the structured packing, the flow turns towards a lower resistance in the porous media. Therefore, there are very large velocity gradients in the packing, and thus the turbulence production term increases. Consequently, turbulence viscosity v_t increases and this increases the pressure losses in cases where the bed is modelled as turbulent. The results presented here show that the SST k-ω model applied cannot predict the turbulence in the packed bed realistically in its basic formulation. Therefore, the modified turbulence model was created in OpenFOAM using the SST k-ω turbulence model as a base, and where the porous medium representing the packed bed is assumed to be a laminar zone by setting turbulence production to zero in the porous media.

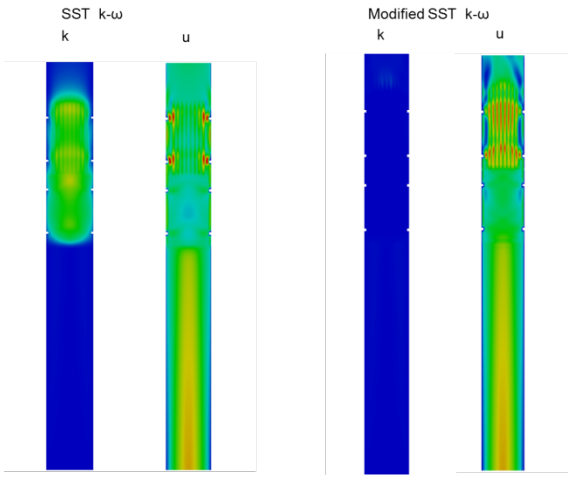

Figure 3:Turbulence kinetic energy velocity in the column in cases b and c.

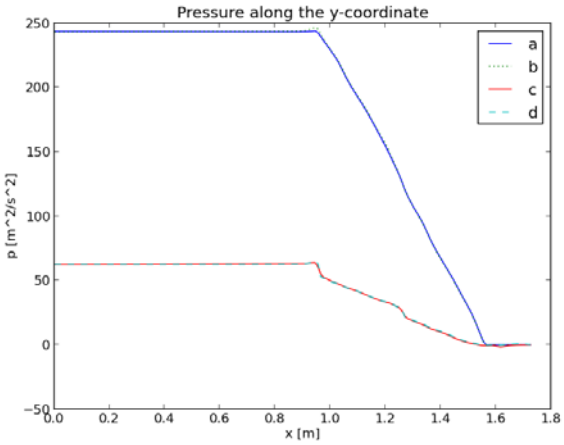

Figure 4: Pressure per density profile and along the column height.

3.2 Pilot scale model validation

After obtaining the porous model coefficient according to Owens' experimental results, the model was applied against the experimental results obtained by Olujic in order to test whether the model captures the maldistribution in the structured packed bed. Olujic conducted gas maldistribution experiments in a 1.4 m diameter column [4]. Initial maldistribution was obtained with the aid of a plate below the bed. Simulations are performed here for a similar column to the one used in the experiments and the simulation results are compared to the experimental results. The inlet velocity to the

bed was u = 3.7 m/s and the gauge pressure p = 0 Pa. The density was ρ = 1.2 kg/m^3 and the kinematic viscosity $v = 1.56 \cdot 10^{-5}$ m^2/s.

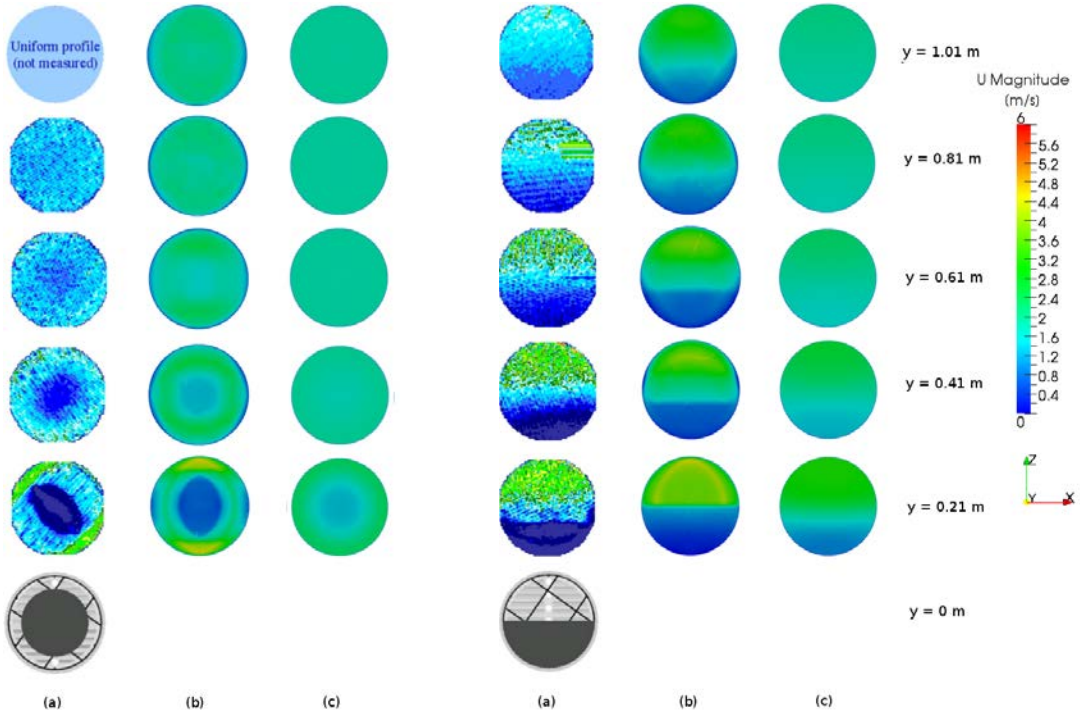

Figure 5: Central blockage case on the left and chordal blockage case on the right.

The two cases studied here are chordal and centre blockage cases (Figure 5). In both cases, (a) refers to Olujic's experimental results at different heights in the column, (b) refers to the anisotropic porous model validated according to Owens' experiments, and (c) is the isotropic porous model. From Figure 5 it can be seen that the anisotropic porous model captures the maldistribution of the gas flow better than the isotropic porous model. If the isotropic model is used, the velocity variations smooth out too fast.

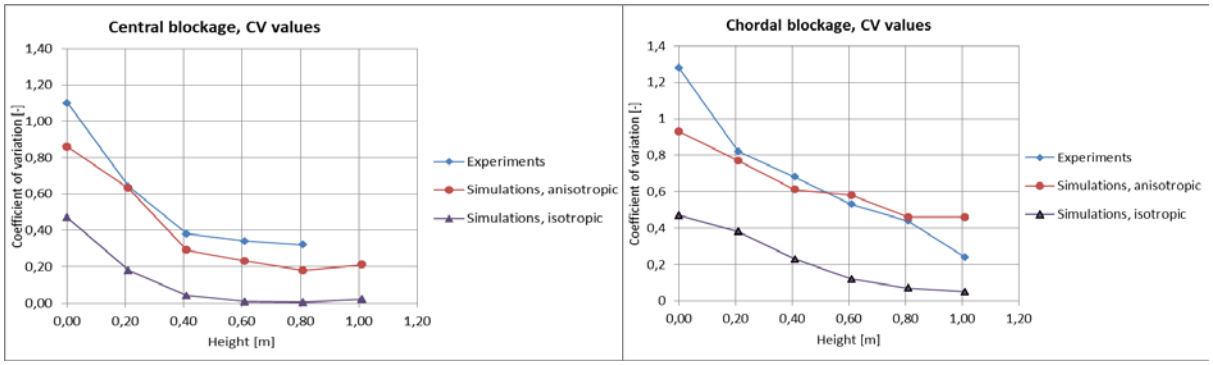

Figure 6: Comparison of the coefficient of variation (CV) between experiments and simulation in the central and chordal blockage cases.

In Figure 6, the coefficient of variation (CV) values are calculated from the velocity values in different layers of the bed as a measure of the maldistribution. If the CV approaches zero, the flow is a uniform bulk flow. It can be seen that the simulation cases for chordal blockage and central blockage referring to the anisotropic bed

modelling produce similar CV values to the experiments. Conversely, the CV values with the isotropic bed modelling are not in line with the experiments.

4. Conclusions

The final outcome of this work is a validated anisotropic porous model. The anisotropic porous model for a structured packed bed seems to work within the accuracy needed on an industrial-scale column design to investigate the gas maldistribution in pilot-scale columns. Therefore, the model can be applied to model industrial CO_2 capture columns. The results provide input data for the modelling tools that predict, e.g. the mass transfer in columns. These tools can be used to predict the influence of a distorted gas distribution on the final efficiency of CO_2 capture. The advantage of the model is that it is effective for the large industrial-scale column design as well, since the geometry is simplified with the porous model.

It should be noted that the simulations are conducted with a gas phase only, but in reality, liquid flows down on to the packing walls. In this work, it was assumed that the gas maldistribution would also be indicative of the liquid maldistribution. The effect of the liquid and gas interaction should still be investigated, as has already been done, for example, by Raynal and Royon-Lebeaud [6]. The turbulence significantly affects the flow in the packing, and also the pressure drop. In this study turbulence was ignored in the packing due to the low Reynolds number, but in reality some turbulence is probably produced. The effects of the turbulence and correct turbulence modelling should be further studied.

References

1. Weller H.G., Tabor G., Jasak H., Fureby C. A tensorial approach to computational continuum mechanics using object-oriented techniques. American Institute of Physics, 1998. S0894-1866(98)01906-3

2. Jäntti, N. Analysis of a gas flow in structured packed bed columns using computational fluid dynamics. Aalto University, Espoo, Finland, 2013.

3. Owens, S.A. Advanced Analysis of Structured Packing Using Computational Fluid Dynamics. The University of Texas at Austin, 2010.

4. Olujic, Z. Effect of the initial gas maldistribution on the pressure drop of structured packings. Chemical Engineering and Processing., 2004, Vol. 43.

5. Pietarinen, K. Fluid Flow and Dispersion Predictions in Porous Media by Utilizing Advanced Numerical Methods. Lappeenranta University, Lappeenranta, Finland, 2005.

6. Raynal, L., Royon-Lebeaud, A. A Multi-Scale Approach For CFD Calculations Of Gas-Liquid Flow Within Large Size Column Equipped With Structured Packing. Chemical Engineering Science, 2007, Vol. 62.

A study of the liquid viscosity impact on separation efficiency of structured packings using a modelling approach based on X-ray tomography

A. Janzen[1], M. Crine[2], P. Marchot[2], D. Toye[2], E. Y. Kenig[1]
[1]Chair of Fluid Process Engineering, University of Paderborn, Germany;
[2]Laboratory of Chemical Engineering, University of Liège, Belgium

Abstract

The objectives of this work are the investigation of liquid flow morphology inside a structured packing using X-ray tomography and the development of a modelling approach based on hydrodynamic analogy between the real complex flow patterns and simplified fluid-dynamic elements. To study the influence of viscosity, water and mixtures of water and glycerine with varying glycerine fraction are used as working liquids.
X-ray tomography is applied to determine the spatial distribution of liquid in the cross-section of a column filled with MellapakPlus 752.Y packing elements. The resulting images are used to evaluate liquid hold-up, gas-liquid interfacial area and to analyse liquid morphology. Liquid flow patterns (film flow, contact-point liquid, flooded regions) are identified, and the fraction of liquid within each flow pattern depending on flow rate and liquid viscosity is determined.
The results of the liquid flow morphology analysis are used to develop a hydrodynamic analogy model. To implement the gas-liquid contact area and the flooded regions into this model, the packing is represented as a bundle of dry, filled and irrigated cylindrical channels, while the ratio between different type channels is determined from the analysis of tomographic images. This simplified hydrodynamic description allows a direct application of rigorous partial differential transport equations, and their solution yields local concentration fields which are used for the evaluation of the separation efficiency.
The new modelling approach is validated by comparison with separation efficiency data obtained from experiments with CO_2 desorption from saturated water-glycerine mixtures into air. The presented modelling approach is capable of predicting the influence of viscosity on separation efficiency of columns filled with structured packings.

Keywords
structured packing, liquid viscosity, X-ray tomography, liquid morphology, flow pattern, hydrodynamic analogy model

1. Introduction

It is known that both capacity and separation efficiency of packed bed columns decrease with rising liquid-phase viscosity [1,2]. Nevertheless, most of the available modelling approaches for the prediction of fluid dynamics and separation efficiency of packed columns are based on experimental data for low viscosity test systems. Moreover, they usually employ the assumption of uniform liquid distribution and film flow over the column cross-section and height. However, the gas-liquid flow patterns prevailing in structured packings are more complex, and a deeper understanding of the multiphase flow phenomena is required for the improvement of performance models for packing columns.

X-ray computer tomography (XCT) has been shown to be an efficient, non-invasive method to adequately display liquid distribution in packed columns [3-8]. Usually, water and air were used as working liquids in XCT studies, whereas the influence of viscosity on liquid distribution was analysed in just few works [9,10]. Sidi-Boumedine and Raynal [9] investigated the influence of liquid viscosity in the range of 1 to 20 mPas, in a co-current gas-liquid flow in trickle bed reactors. In a previous work, Janzen et al. [10] used high-energy and high-resolution X-ray tomographic measurements to study the influence of viscosity on liquid flow inside structured packing by a novel image analysis method.

This work is dedicated to the investigation of the impact of liquid viscosity on separation efficiency and on the development of a modelling approach based on hydrodynamic analogy between the real liquid flow and simplified flow patterns. The latter is possible by using the results of the tomographic image analysis.

2. Model development

Modelling of the separation efficiency of structured packing is usually linked with the modelling of fluid dynamics. Tomographic measurement techniques offer an insight into the real liquid-flow morphology inside structured packing. Thus, it is possible to identify physically-based assumptions for the characterization of fluid dynamics.

In the context of this work, the results of the tomographic image analysis published by Janzen et al. [10] are used to develop a modelling approach for the prediction of the separation efficiency of structured packing. In order to describe the model development, a short summary of the main results is given. Based on these results, conclusions on mass transfer behaviour are made which are further used to develop corresponding hydrodynamic analogies. The latter build a basis of the presented modelling approach.

2.1 Tomographic image analysis results

To study the influence of viscosity, water and mixtures of water and glycerine with varying glycerine fraction are used as working liquids. Tomographic images of the irrigated packing are taken for several cross-sections along the column height, within a 100 mm diameter and 1 m high packed column filled with four MellapakPlus 752.Y packing elements. The result of these experiments is a set of cross-sectional images which are used to evaluate the axial distribution of liquid holdup and the gas-liquid interfacial area.

Furthermore, the tomographic images are employed to analyse liquid flow patterns. The analysis reveal that film flow over the packing layers represents the predominantly flow pattern. Moreover, it can be observed, that liquid originating from two facing sheets retains at the contact points between them, due to adhesive forces and surface tension. We call this flow pattern “contact-point liquid” (C-P liquid).

Where high local liquid loads appear, the entire space between two packing sheets is filled with liquid. These “flooded regions” represent the third flow pattern.
An image analysis method is developed to obtain quantitative information about the contribution of each of the three identified flow pattern to the overall liquid hold-up, as a function of both operating conditions and liquid properties. Liquid flow structures are analysed on the basis of their size and shape. Thus, it is possible to quantify the fraction of liquid flow within each flow pattern. In order to investigate the global impact of liquid load and viscosity on flow morphology inside the packing column, average values of each flow pattern hold-up fraction over the total packing height are calculated.

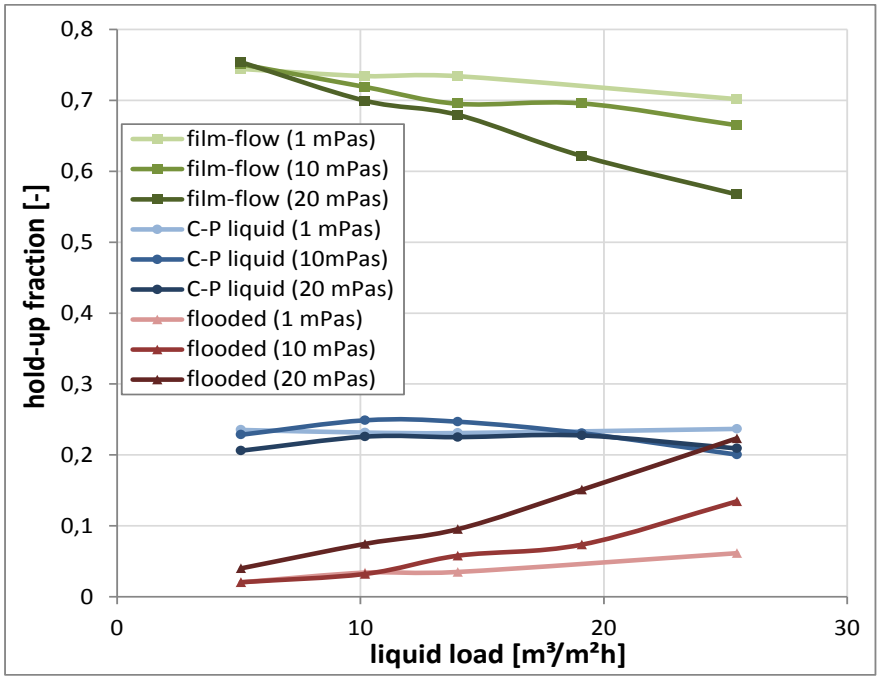

Figure 1: Influence of liquid load and viscosity on average values of each flow pattern fraction: green squares - film flow; blue circles - C-P liquid; red triangles - flooded regions [10].

Figure 1 shows the influence of the liquid load on the relative contributions of the different flow patterns to the total liquid hold-up at different viscosities. The relative contribution of the film-flow pattern decreases with both the liquid load and liquid viscosity, while the ratio of flooded regions increases correspondingly. The fraction of the C-P liquid is independent of the parameters varied in this study.
Further details about the tomographic measurements and the image analysis can be found in Janzen et al. [10].

2.2 Conclusions on mass transfer behaviour in structured packing
The results of the image analysis confirm film flow to be the dominating flow pattern. Thus, the usual assumption for modelling of liquid flow in structured packing is largely correct. Nevertheless, the results show also that there are regions inside the packing where only one phase is present. On the one hand, some part of the packing surface is dry. On the other hand, there are flooded regions between the packing sheets. Obviously, no mass transfer can occur in the regions in which only gas or liquid phase are present.
Concerning C-P liquid, it is not clear whether it contributes as a static part to the liquid hold-up or whether it is renewed by the liquid flow. The dynamic behaviour of

this flow pattern cannot be captured with the tomographic technique used in this study. Nevertheless, it is obvious that liquid mixing is promoted at these locations.

2.3 Hydrodynamic analogy approach

A modelling approach based on hydrodynamic analogies between real and simplified flow conditions was developed by Shilkin and Kenig [11] for distillation columns filled with structured packing. The packing geometry was modelled as a bundle of inclined circular channels. The liquid was assumed to flow in form of laminar films over the inner surface of these channels, while the gas occupied the rest of the volume. Both phases were assumed as ideally mixed periodically, to take mixing induced by the packing geometry into account. The geometric simplification allowed a direct application of the partial differential equations governing momentum, heat and mass transport to describe the physical phenomena.

Based on the tomographic investigations of liquid flow morphology, the model of Shilkin and Kenig [11] is extended here for aqueous systems, by defining three different channel types. Beside the already existing type of irrigated channels in which mass transfer between gas and liquid phase occur, dry (one-phase gas-flow) and flooded (totally filled with liquid) channels are considered. Based on the insight that liquid mixing is promoted at the contact points of two adjacent packing sheets, these new liquid mixing points are included into the physical model presented in Figure 2.

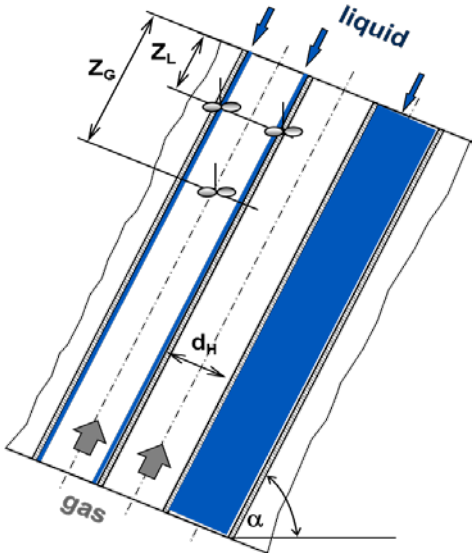

Figure 2: Physical model of the structured packing. d_H: hydraulic diameter of the channels. Z_L and Z_G: - distances between ideal mixing points of gas and liquid flow; α - inclination angle of packing.

The total number of all channels is defined by the packing geometry and specific surface area and is described in [11]. The channels comprise all wetted (gas/liquid), dry (gas) and flooded (liquid) channels:

$$NC_{tot} = NC_{G,L} + NC_G + NC_L \quad (1)$$

Liquid is distributed between the wetted and the flooded channels. The number of flooded channels can be calculated by using the hold-up ratio of flooded regions $h^r_{L,full}$ estimated by the image analysis method:

$$\frac{NC_L}{NC_{tot}} = \frac{V_{L,full}}{V_{Pac,tot}} = h_L \cdot h^r_{L,full} \quad (2)$$

The ratio wetted channels number/total channel number is equal to the fraction of the gas-liquid interfacial area related to the specific packing surface area:

$$\frac{NC_{G,L}}{NC_{tot}} = \frac{a_{eff}}{a_{pac}} \quad (3)$$

For the estimation of the distance Z_L between the ideal mixing points in the liquid phase, again, results of the image analysis are used. As pointed out before, mixing takes place at the contact points of two packing layers. The distance between the contact points is given by the geometry of the packing. Analysis of tomographic images shows that only a certain fraction of the liquid is located at the contact points. Thus, the distance between the points at which the entire liquid is mixed is increased:

$$Z_L = \frac{\text{distance between contact points}}{\text{hold-up fraction of C-P liquid}} \quad (4)$$

Momentum, heat and mass transfer equations are applied for the wetted channels and solved using the numerical solution method based on the so-called Tri-Diagonal Matrix Algorithm. The equations and the solution method are given in [11] in a detailed form. Radial and axial velocity, concentration and temperature profiles are the results of the numerical calculations.
Since no mass transfer in the dry and flooded channels occurs, the mean concentration in the liquid and gas phase is calculated as an average value of the calculated and initial concentrations weighted with the number of the according channel types.

3 Efficiency measurements

For the experimental investigation of the influence of liquid viscosity on mass transfer and for model validation, desorption of CO_2 from water and water/glycerin mixtures is chosen as a test system. The column set-up, the liquid system and the operating conditions are equivalent to the experimental set-up used during the tomographic investigations. The column with an inner diameter of 100mm is filled with three elements of MellapakPlus 752.Y structured packing.
The liquid is saturated with CO_2 in a mixing chamber under CO_2-atmosphere and afterwards distributed over the packing bed. The investigated range of liquid loads is between 5 and 25 $m^3/(m^2h)$ and the range of liquid viscosity is 1-20mPas. Air is used as a counter-current gas flow, with a gas capacity factor F of 0,64 $Pa^{0,5}$.
Liquid samples are taken above and directly below the packing bed. Thereby, the liquid is directly induced into a sodium hydroxide solution, so that the containing CO_2 is chemically bound. CO_2 concentration is determined indirectly, by titration of the sample with HCl.

4. Results and discussion

In order to verify the proposed modelling approach, CO_2-desorption process is simulated at operating conditions and inlet compositions of gas and liquid according to the experiments. The CO_2-desorption rate is chosen for the comparison of experimental and simulated values. It is determined as the ratio of the amount of CO_2 desorbed into the gas phase to the initial content.
Figure 3 shows the experimental and simulated CO_2-desorption rate for the investigated parameters. The latter shows a significant negative influence on the desorption rate. Rising liquid load also leads to decreasing separation efficiency.

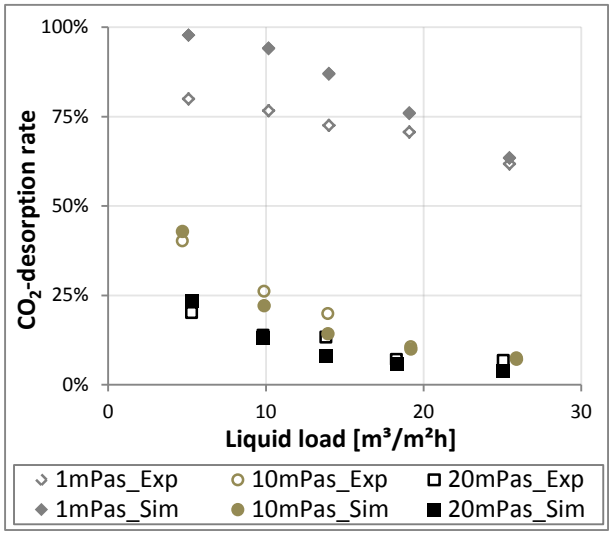

Figure 3: Comparison of experimental (Exp) and simulated (Sim) CO_2-desorption rates at different liquid loads and viscosities at a gas capacity F=0,64.

The comparison presented in Figure 3 shows very good agreement between the simulation results and experimental values. The model is capable of predicting the influence of liquid load and viscosity on mass transfer. A slight deviation between experiment and simulation is visible at low liquid loads and low viscosity (1mPas). At these conditions, the highest experimental uncertainty prevails regarding the tomographic and the separation efficiency measurements. For instance, due to very low liquid hold-up, the spatial resolution of the tomograph and the following image analysis may lead to an overestimation of the gas-liquid interfacial area. Nevertheless, the proposed modelling approach can be applied for the simulation of the separation efficiency of aqueous systems in a broad range of operating conditions and liquid viscosities.

5. Conclusions

In this work, the image analysis results of tomographic measurements of liquid distribution inside structured packing are used to develop hydrodynamic analogies between the real liquid flow and simplified flow patterns. The latter are implemented in a modelling approach for the calculation of the separation efficiency of structured packing.

Influence of liquid viscosity is studied experimentally and numerically, based on the desorption of CO_2 from saturated water and water/glycerine mixtures. Rising liquid viscosity leads to a significant decrease of separation efficiency. The experimental results are also used for the validation of the proposed modelling approach. Good agreement between experimental and simulated values for the CO_2-desorption rate is found.

Acknowledgements

The authors are grateful to the Deutsche Forschungsgemeinschaft (DFG) for financial support (research project KE 837/19-1) and to Sulzer Chemtech AG for providing the MellapakPlus 752.Y packing elements. Furthermore, the financial support of Max-Buchner-Forschungsstiftung (research project No. 2842) is greatly acknowledged.

Notation

NC_{tot} – total channel number [-]
$NC_{G,L}$ –number of wetted channels [-]
NC_G –number of dry channels [-]
NC_L –number of flooded channels [-]
$h^r_{L,full}$ – hold-up ratio of flooded regions [-]
h_L – liquid hold-up [-]
$V_{L,full}$ – Volume occupied by liquid [m³]
$V_{Pac,tot}$ – total packing volume [m³]
a_{eff} – specific gas-liquid interfacial area [m²/m³]
a_{pac} – specific packing surface area [m²/m³]

References

1. Suess, P., Spiegel, L., 1992. Hold-up of mellapak structured packings. Chemical Engineering and Processing 31, 119-124.
2. Böcker, S., Ronge, G., 2005. Distillation of viscous systems. Chemical Engineering & Technology 28, 25-28.
3. Aferka, S., Viva, A., Brunazzi, E., Marchot, P., Crine, M., Toye, D., 2011. Tomographic measurement of liquid hold up and effective interfacial area distributions in a column packed with high performance structured packings. Chemical Engineering Science 66, 3413-3422.
4. Green, C.W., Farone, J., Briley, J.K., Eldridge, R.B., Ketcham, R.A., Nightingale, B., 2007. Novel application of X-ray computed tomography: Determination of gas/liquid contact area and liquid holdup in structured packing. Industrial & Engineering Chemistry Research 46, 5734-5753.
5. Marchot, P., Toye, D., Pelsser, A.M., Crine, M., L'Homme, G., Olujic, Z., 2001. Liquid distribution images on structured packing by X-ray computed tomography. AIChE Journal 47, 1471-1476.
6. Schmit, C.E., Eldridge, R.B., 2004. Investigation of X-ray imaging of vapor-liquid contactors. I. Studies involving stationary objects and a simple flow system. Chemical Engineering Science 59, 1255-1266.
7. Viva, A., Aferka, S., Toye, D., Marchot, P., Crine, M., Brunazzi, E., 2011. Determination of liquid hold-up and flow distribution inside modular catalytic structured packings. Chemical Engineering Research & Design 89, 1414-1426.
8. Schmit, C.E., Cartmel, D.B., Eldridge, R.B., 2001. The experimental application of X-ray tomography to a vapor-liquid contactor. Chemical Engineering Science 56, 3431-3441.
9. Sidi-Boumedine, R., Raynal, L., 2005. Influence of the viscosity on the liquid hold-up in trickle-bed reactors with structured packings. Catalysis Today 105(3-4), 673-679.
10. Janzen, A., Steube, J., Aferka, S., Kenig, E.Y., Crine, M., Marchot, P., Toye, D., 2013. Investigation of liquid flow morphology inside a structured packing using X-ray tomography. Chemical Engineering Science 102, 451-460.
11. Shilkin, A., Kenig, E.Y., 2005. A new approach to fluid separation modelling in the columns equipped with structured packings. Chemical Engineering Journal 110, 87-100.

Columns Subject to Motion:

Maldistribution Sensitivity and Susceptibility

Markus Duss, Mario Roza

Sulzer Chemtech Ltd, Winterthur, Switzerland

Abstract

Separation columns built on non-stationary platforms or vessels (FPSO, FLNG) are subjected to motion. Motion results in offset of the column axis from the vertical and acceleration forces act on the system inducing maldistribution.

This paper introduces the concept of maldistribution susceptibility, which aims to quantify the maldistribution formation in packing and liquid distributor, and maldistribution sensitivity, which quantifies the impact on the separation.

The various mass transfer devices (trays, rings and structured packing) have different maldistribution susceptibilities under motion conditions. Whereas conventional downcomer trays are susceptible to form maldistribution, packing can mitigate the impact of motion better. Structured packing is favoured over random packing in most applications and has proven its expected performance in numerous applications.

The impact of initial maldistribution of the liquid distributor, horizontal accelerations inducing liquid maldistribution in the packing and vapour maldistribution due to uneven liquid flow must not be neglected when predicting the maldistribution parameter.

Keywords

Non-stationary platforms, FPSO, FLNG, column design, maldistribution sensitivity, maldistribution susceptibility

1. Introduction

Offshore produced oil and gas is processed more and more on platforms and Floating Production Systems (FPS) such as FPSO and FLNG[1]. Non-stationary platforms and FPS are subjected to motion and therefore all equipment needs to be designed accordingly. This paper addresses the design of separation columns operated under such conditions.

1.1 Offshore separation columns

Typical separation columns operated on platforms are glycol dehydration units to achieve the pipeline specification of the water dew point for natural gas and MEG recovery units used to inhibit hydrate formation. On FPSO units, crude stabilzers and or de-ethanizers, de-propanizer and de-butanizer columns are operated as well as VOC recovery columns on Shuttle Tankers. FLNG units in addition will require a de-methanizer (scrub or NGL extraction column) and a unit for gas sweetening.

1.2 Onshore design

The choice of mass transfer technology depends on the physical properties of the vapor and liquid phase and on the hydraulic loadings.

Applications involving low liquid loads are preferably designed using structured packing and thus glycol dehydration and MEG recovery units are commonly designed using structured packing made of metal sheets, such as Mellapak^{TM} or MellapakPlus^{TM}. More than 1'000 glycol units are successfully in operation.
For high pressure distillation systems, trays are in many cases the most economical solution and packing designs are often not competitive for onshore applications. The reason is that the physical properties tend to be critical: when distilling hydrocarbon systems, the liquid viscosity and surface tension become lower the higher the operating pressure is and the gas to liquid density ratio can be below 10. Such conditions restrict the optimal use of packing and the columns need to be operated at reduced capacity. Inherent small scale maldistribution inducing large scale maldistribution was considered to be the root cause for such behavior[2]. In columns with small diameters equipped with structured packing, such behavior was not found because large scale maldistribution cannot be induced.
Gas sweetening applications are often involving high liquid loadings, however because the physical properties are far from being critical, i.e. liquid density, viscosity and surface tension are typically high when using aqueous solutions of amines, random and structured packing are widely applied in such applications.
When these columns are operated under moving conditions, the optimal separation technology has to be adapted.

1.3 Design conditions
Offshore columns can be subjected to motions such as angular and translational motions. Figure 1 indicates the 6 different types of motion. Table 1 indicates typical motion conditions under which the column needs still to perform according to specification. However, the motion conditions depend on the platform type or vessel size and on the sea conditions at the production site. The position of the column on the deck is of importance since the resulting acceleration forces due to angular motion will depend on the distance from the center of rotation (figure 2).

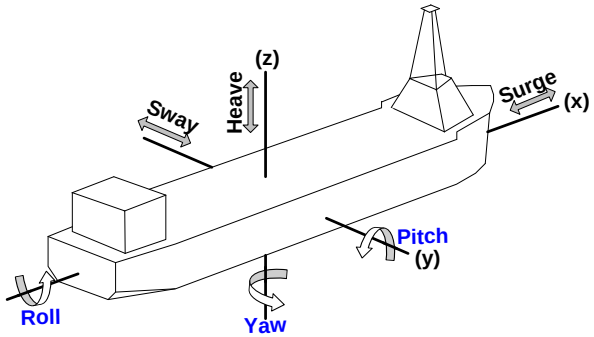

Figure 1: angular motion (roll, pitch, yaw) and linear motion (surge, sway, heave)

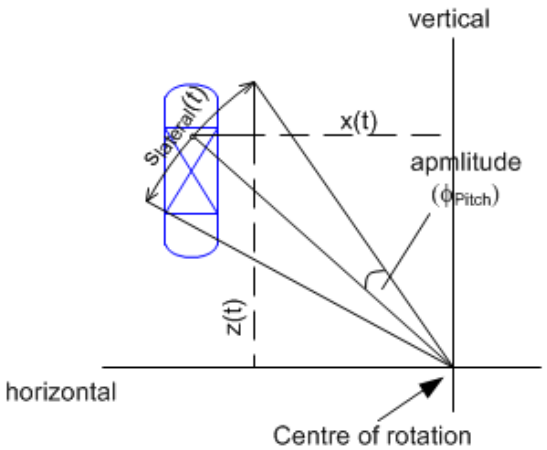

Figure 2: impact of the column position

Table 1: typical design values for columns subject to motion

Moving Conditions	Angular motion		Tilt
	Amplitude [°]	Period [s]	Angle [°]
Typical	3 to 5	14 to 16	0.5 to 1

Figure 2 indicates the lateral movement of single point of the column, $s_{lateral}$, due to a harmonic motion. Angular motions cause a deviation in horizontal direction x(t) or y(t) and in vertical direction z(t). Surge and sway result in a change in horizontal direction, and heave in vertical direction. The second derivative of these functions result in horizontal and vertical accelerations, $a_x(t)$, $a_y(t)$ and $a_z(t)$, respectively and corresponding vectors need to be summed up.

$$a_x(t) = \frac{d^2x(t)}{dt^2} \quad ; \quad a_y(t) = \frac{d^2y(t)}{dt^2} \quad ; \quad a_z(t) = \frac{d^2z(t)}{dt^2}$$

Horizontal accelerations will induce liquid maldistribution due to inertia, whereas vertical accelerations will predominantly impact the maximum capacity of the column.
Angular motions will additionally result in an offset of the column axis from the vertical, which is here referred to as dynamic tilt. Since the liquid is driven by gravity, dynamic tilt will cause liquid maldistribution close to the column wall.
For angular motion with periods longer than 12 seconds, dynamic tilt will have a dominant impact on liquid maldistribution in most cases[3], however, this analysis did not include linear motion. Generally, column designs need to include the impact of accelerations caused by linear and angular motion as well.
Permanent offset of the column axis from the vertical is referred to as static tilt, which can be caused by weather conditions or due to unbalanced product storage or offload conditions and will cause maldistribution similar as dynamic tilt.

2. Maldistribution sensitivity and susceptibility

2.1 Maldistribution sensitivity – Two column model

Maldistribution sensitivity attempts to quantify the impact of an uneven L/V-ratio in radial direction on the separation. Liquid and vapor maldistribution can originate from many different reasons and motion is only one of it. Since a rigorous approach to describe local maldistribution is still not possible, a simple method was proposed, which is called the two column model[4]. The method assumes that the column is split into two equal parts and the feed streams to the two columns are unevenly split. This will result in a deviation of the L/V-ratio and thus the product streams from the two columns are not the same. The sensitivity will depend on the stripping factor (ratio of slopes of equilibrium and operating line), the concentrations and the number of theoretical stages. After mixing the bottom or top product streams, respectively, a reduced performance is obtained compared to a simulation assuming a constant L/V-ratio (in radial direction), as assumed when simulating with a single column.
Equalizing the concentration difference in the assumed two column model can significantly reduce the impact of maldistribution on the separation. This can be physically achieved in packed columns by collecting, mixing and redistributing the liquid phase and can be simulated accordingly with the two column model. With a single pass down-comer tray it can be assumed that liquid is mixed inside each downcomer, i.e. after each stage and thus maldistribution would only weakly affect the separation. Such a tray would be expected to perform well, even when severe liquid maldistribution was assumed which this is not the case: due to the dynamic behavior of the liquid phase, downcomer trays cannot be represented correctly with this simplified approach, which assumes steady state. Using 2-pass downcomer trays amplifies the weakness of a tray design since even equalization of the liquid concentration is no longer assured.

2.2 Maldistribution susceptibility

2.2.1 Maldistribution susceptibility of packing – Dry area model

Static tilt results in deviation of the liquid flow path parallel to the column axis and therefore, liquid will flow along the wall on one side, whereas on the other side of the column a dry area will be formed[5]. The higher the packed bed and the smaller the column diameter, the higher the fractional dry area is. The fractional dry area is the dry packing area divided by the total area.

The impact of resulting acceleration forces on the formed maldistribution will depend on the physical properties, the hydraulic loads and the chosen column equipment. A given acceleration force will induce more liquid maldistribution when the friction factor of the liquid in contact with the packing surface is low. Accordingly it holds for dynamic tilt: liquid maldistribution formed during a period of the harmonic motion will depend on the effective liquid velocity in axial direction. To quantify maldistribution in terms of the formed fractional dry packing area, the model assumes that dry area is formed at the zone close to the wall and the liquid in bulk of the column, which is shifted only, will not cause maldistribution. From these assumptions it can be concluded that the larger the column diameter is, the less the formed fractional dry area is. The impact of motion might not depend on the height of a packed bed if the liquid residence time is longer than the period of the harmonic motion. However, the resulting fractional dry area due to motion in a packing section needs to be integrated over a time equal to the residence time of the liquid in the respective section, considering friction factors.

A shortfall of this model is that radial liquid spreading is not included and columns with small diameters will suffer from such simplifications. Tests have shown that the ability of radial liquid spreading is significantly better with structured packing than with rings[6]. In addition, structured packing is installed in elements (packing layers) and each vertical adjacent element is rotated by 90°. Therefore, only liquid in every second element is fully affected by motion or tilt in average for a corrugated sheet packing like Sulzer Mellapak. The reason is that a liquid film flowing down a vertical plane driven by gravity is weakly affected by a moderate horizontal motion perpendicular to the plane (see 3.1.2).

The liquid maldistribution parameter based on the fractional dry area cannot be retrieved straight forward, so it can be used to quantify the impact on the separation using the before described two column model. But the packing maldistribution parameter will be proportional to the fractional dry area and the constant of proportionality needs to be adjusted based on experimental data.

The vapor maldistribution parameter is recommended to be included and shall be determined, so the resulting pressure drops are the same in both of the assumed columns. Operation of the column at part loads (turn down) will result in a reduced maldistribution susceptibility for the packing.

2.2.2 Maldistribution susceptibility of liquid distributor

In order to reduce the relative differences in liquid head in radial direction for the liquid distributor, the liquid head needs to be increased. This is the reason why closed pipe distributors are predominantly applied. The required liquid head is either given by the liquid height, h or supplied by a pump. Figure 3 indicates a deviation in liquid head, dh due to tilt. Motion results most often in more severe deviations in liquid head than static tilt and will define the basis for the design. Contrary to the packing, the susceptibility of a liquid distributor increases with increasing column diameter and the design liquid head, h will depend on the column diameter. It shall

not be assumed that the initial liquid maldistribution is negligible compared to maldistribution formed in the packing section, since a design criteria for the liquid distributor is to achieve a certain percentage of the totally formed maldistribution (packing plus distributor). The maximum maldistribution parameter formed by the liquid distributor is calculated by dividing the cross sectional area into two equal areas so the dividing chord forms a horizontal line with the inclined plane. The liquid rate flowing from each side is then calculated by integration, considering the change in liquid head based on maximum tilt (static and dynamic) and accelerations along the length L. The maldistribution parameter is calculated by the difference of the flow rate from the two areas divided by the total flow rate.
Turn down will increase the initial maldistribution since the liquid level h will be reduced.

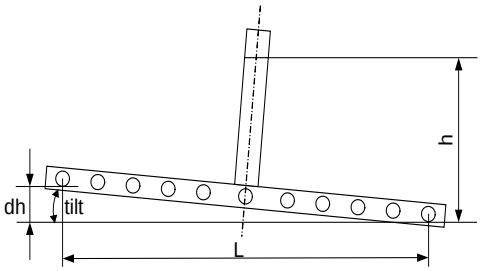

Figure 3: Impact of tilt on liquid head for a pipe type liquid distributor (VRG)

The total maldistribution parameter which shall be used for the sensitivity analysis as described in chapter 2.1 is the sum of the maldistribution parameters of the packing and the liquid distributor.
The quantification of the liquid maldistribution parameter of a system (susceptibility) must include the influence of column diameter, packing type, bed height, hydraulic loads, physical properties, liquid distributor design, motion conditions and the location of the column on the vessel. The vapor maldistribution parameter is then retrieved based on the liquid maldistribution parameter assuming that vapor will distribute to have no radial pressure gradient and requires a detailed hydraulic analysis.

3. Susceptibility of various mass transfer technologies

3.1 Packed columns

Structured packing has proven to operate satisfactory under moving conditions. Well designed packing and column internals allow minimizing risks of mal-performance.

3.1.1 Liquid distributors

In order to reduce initial maldistribution by the liquid distributor, pipe-types are best used (figure 4). Open troughs or channels adhere to splashing and sloshing and would have a high liquid inventory if designed for adequate liquid head.
Only in case the liquid feed is pumped, the required liquid head is supplied by the pump. In all other cases, the height of the liquid distributor has to be adjusted and will depend on the column diameter for otherwise equal conditions.

Figure 4: liquid distributor (VRG) on test rig prior to installation

3.1.2 Packing

For applications where structured packing is used onshore, the column will be most probably designed with the same packing type for motion conditions. This holds true for example for glycol contactors or MEG recovery units.

For applications where random packing is an option onshore, the use of structured packing is mostly preferred, too. Industrial examples are typically gas sweetening, sea water de-aeration or VOC recovery units. There are two main arguments for the use of structured packing:

- radial liquid and vapor spreading have proven to be better for corrugated sheet structured packing compared to random packing[6]
- with Mellapak, only every second packing element (layer) is fully affected to tilt and motion

The latter reason is often not recognized adequately: random packing shows a spherical shape and the fractional area perpendicular to the horizontal is small. Therefore, the liquid has the tendency to flow in vertical direction at any time, forming more dry area than with structured packing due to tilt (static and dynamic)[7]. The liquid flow path along an incline is not depending on the slope and for horizontal accelerations acting on the liquid it holds: forces acting perpendicular to the incline will not change the flow path. Though Mellapak does not consist of smooth planes (it has corrugated channels, holes and micro structures) the basic advantages can be best understood based on the liquid behavior on an inclined plate.

Onshore applications where the domain is with trays (high pressure hydrocarbon distillation) require special attention when designed with packing under moving conditions. Industrial experience showed that packed columns do not perform as good in large columns as in pilot columns with small diameter. Tests[8] with a reasonable large column of 1.22 m showed that the packing efficiency depends on the operating conditions (physical properties and hydraulic) and might show a hump in terms of HETP with changing throughput. Despite these draw-backs, hydrocarbon fractionation columns operated under elevated pressure and motion conditions are not designed with trays till now. By far the most of the built columns have been designed using structured packing[7]. However, a considerably larger column diameter and increase in column height will result as compared to onshore operated columns using trays.

3.2 Trays

Conventional downcomer trays are susceptible to form severe maldistribution due motion (sloshing) and tilt. Motion and tilt parallel to the down-comer orientation will affect tray performance differently than in perpendicular direction: downcomer flooding and vapor by-pass might both happen due to non-steady liquid hold-up.

Due to the high maldistribution susceptibility, conventional downcomer trays have not been considered for column designs subjected to motion till now. The attempt of using point efficiency trays (instead of cross flow) has been discussed due to a considerable potential to reduce foot print and height of the column but it has not yet been proven that a good and stable performance can be achieved under moving conditions with such devices.

4. Conclusion

It is proposed to distinguish between maldistribution sensitivity and susceptibility to avoid any confusion about the impact of the thermodynamic behavior (sensitivity) and the impact of the hardware (susceptibility). The assumed column configuration itself

will affect both, the sensitivity and susceptibility, depending on the number packing sections chosen.
Published literature assumes simplifications, such as neglecting initial maldistribution of the liquid distributor, not considering the impact of the column position on the vessel, or not considering liquid maldistribution due to horizontal accelerations and assuming an even gas flow in radial directions. Such simplifications can result in a relevant underestimation of the maldistribution susceptibility and thus the retrieved maldistribution parameter can be too optimistic in such cases.
Finally, vertical accelerations might not cause maldistribution but the capacity of the column can be affected in rare cases, when the column position is far from the center of rotation.

References

[1] Shimamura, Y., 2002. FPSO/FSO: State of the art, *J Mar Sci Technol* 7: 59-70
[2] Zuiderweg, F.J, Olujic, Z., Kunesh, J.G, 1997. Liquid backmixing, IChemE Symp. Ser. 142., 38: 512-518
[3] Plüss, R.C. and Bomio, P., 1987. Design aspects of packed columns subjected to wave induced motion, *I. Chem. Eng. Symp. Ser*. 104: 1-4
[4] Yuan, H.-C., Spiegel, L., 1982, Theoretical and Experimental Investigation of the Influence of Maldistribution on the Performance of Packed Columns, *Chem. Ing. Tech*., 54: 774–775
[5] Cullinae, J.T, Yeh, N., Grave, E., 2011. Effects of tower motion on packing efficiency, Brasil Offshore Conference
[6] Hoek, P.J, Wesselingh, J.A.., Zuiderweg, F.J., 1986. Small scale and large scale maldistribution in packed columns, *Chem. Eng. Res. Des.*, 64:431-449
[7] Roza, M. and Zuber, L., 2003. Most recent developments on design and operation of distillation and absorption columns under moving conditions, AIChE Spring meeting
[8] Fitz, C.W., Kunesh, J.G, Shariat, A., 1999. Performance of Structured Packing in a Commercial-Scale Column at Pressures of 0.02-27.6 bar, *Ind. Eng. Chem. Res*., 38: 512-518

CO_2 Capture from Coal Flue Gas: Measurement of Gas Stream Impurities and their Effect on Process Operation and Design

C.J. Satterley[1], B. Schallert[2], W. Albrecht[2], S. Neuhaus[2], H. Rode[2] & S. Reddy[3]
[1] E.ON New Build & Technology, Ratcliffe on Soar, UK
[2] E.ON New Build & Technology GmbH, Gelsenkirchen, Germany
[3] Fluor Corporation, 3 Polaris Way, CA 92698, USA

Abstract
Amine-based capture processes are currently considered as a leading technology for the capture of CO_2 from coal-fired power plant flue gas and is the process of choice for several large scale demonstration projects in Europe and North America.

One of the key challenges in application of this technology to coal-fired power plant is the presence of impurities in the flue gas, e.g. particulate/dust & SO_2. On a modern power plant with typical environmental controls, these impurities exist in the flue gas at the ppm level. This level is small enough to present a significant measurement challenge, but large enough to potentially impact on the operation of the CO_2 capture process through enhanced solvent degradation & emissions.

Since mid-2012, E.ON has successfully operated a 70 tonne CO_2 per day pilot plant facility at its Wilhelmshaven coal power plant in partnership with Fluor Corporation as part of its Technology & Innovation programme on CCS. Details of flue gas measurements undertaken directly upstream of the CO_2 absorber column are reported along with discussion of observed effectiveness of the installed flue gas pre-treatment and potential impacts on capture plant performance.

Keywords
Carbon Capture, Post-combustion, Amine, Flue Gas Impurities, Pilot Plant

1. Introduction

CO_2 capture from coal-derived flue gas can be achieved through a number of technologies including post-combustion capture. Capture from flue gas using amine-based solvents is widely considered to be the closest to market of the post-combustion technologies with numerous pilot facilities and large-scale demonstration projects in planning or operation around the world (e.g. Reddy et al. 2012, Anderson et al. 2012, Just 2013 and Gardiner et al. 2013).

Coal-derived flue gases contain a number of impurities such as SO_2, NO_x and fine particulate that have ability to affect the performance of the capture system and are not present in other flue gases where amine capture technologies are applied. Due to the environmental control technologies applied on a modern power plant and addition flue gas polishing in the capture plant these impurities are reduced to the ppm level. Over time, however, these low levels of flue gas impurities may still impact the recirculating solvent system due to gradual build-up of absorbed material or reaction products. Accurate measurement at these low levels is required to correctly quantify the input to the capture plant and track developments in solvent quality. However this can be challenging to achieve in the real power plant environment and new methods are sometimes required.

Since mid-2012, E.ON, as part of its Technology & Innovation Programme on CCS, has successfully operated a 70 tonne per day CO_2 capture pilot plant facility at its 800 MW Wilhelmshaven coal power plant in partnership with Fluor Corporation. This pilot plant treats approximately 16,000 m^3/h of flue gas with a design capture rate of 90% utilising Fluor's Econamine Plus^{SM} technology. A simplified schematic of the general capture process can be seen in Figure 1.

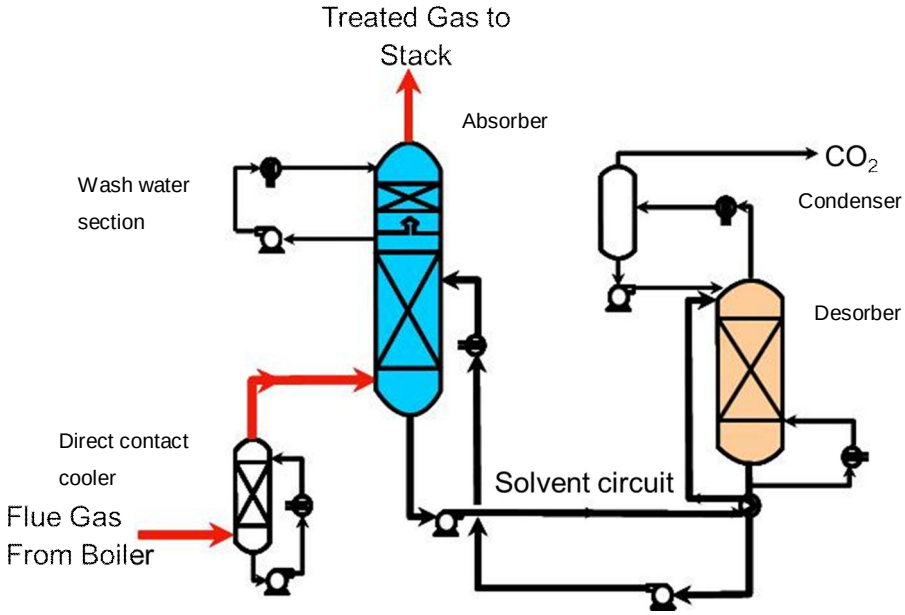

Figure 1: Simplified schematic of a general capture process including flue gas direct contact cooler, absorber and desorber columns, absorber water wash and desorber overhead accumulator.

2. Results and discussion

The results below will focus on measurements undertaken on the Wilhelmshaven flue gas upstream of the capture plant and after a direct contact cooler (DCC) (using NaOH as the desulphurisation reagent) supported by analytical data from solvent samples taken during plant operation. This study has focused on three impurities found within coal-derived flue gas; particulates, SO_2 and HCl. NO_x measurements are still ongoing and will be reported at a later date.

2.1 Particulate

Particulate matter is present in the flue gas at the inlet of the capture plant at Wilhelmshaven. A major component of this particulate will be fly ash from combustion. Table 1 shows a typical fly ash composition found in samples collected from the electrostatic precipitator hoppers at Wilhelmshaven. Fly ash is mainly an alumino-silicate base with significant amounts of iron, calcium, magnesium and potassium with other elements and trace elements (not shown).

Component	Concentration (wt %, C free)	Component	Concentration (wt %, C free)
SiO_2	59.2	MgO	1.7
Al_2O_3	23.7	Na_2O	0.7
TiO_2	1.1	K_2O	2.1
Fe_2O_3	6.8	SO_3	0.4
CaO	3.2	P_2O_5	0.7

Table 1: Typical fly ash composition of major components at Wilhelmshaven as sampled from the electrostatic precipitator ash hoppers.

The CO_2 plant at Wilhelmshaven is installed downstream of a wet limestone flue gas desulphurisation (FGD) system and so particulate entering the capture process is likely to contain carried-over solid material and some liquids from the FGD absorber (mainly calcium salts) in addition to the fly ash component. This may particularly increase the calcium and sulphate levels in the particulate entering the capture plant.

Manual gravimetric dust measurements were undertaken in late 2013 at the FGD outlet, inlet to the capture plant and after the DCC. These measurements were undertaken in compliance with the relevant German/European standard DIN EN 13284-1. Table 2 shows the results of these measurements. To ensure applicability beyond the Wilhelmshaven measurements were made at both the FGD outlet and DCC inlet to ensure that no significant changes in particulate concentrations exist due to the extended ductwork between the two parts of the plant (approx. 94 m). It can be seen from the measurement results that the DCC achieved an approx. 64% removal efficiency for particulate during the test period.

Measurement point	FGD outlet	DCC inlet	DCC outlet
Dust concentration (mg/Nm^3, dry, 6% O_2)	1.70	1.72	0.62

Table 2: Average dust concentrations observed during manual sampling at the FGD outlet, DCC inlet & DCC outlet at Wilhelmshaven over a period of 2 days in late 2013.

Filter samples taken during the testing were also analysed by inductively coupled plasma mass spectrometry for their elemental composition. Table 3 shows the average elemental composition of filter samples taken from the FGD outlet, before the DCC and at the DCC outlet (net values following subtraction of a blank filter

analysis). From these results it can be seen that, in general, the particulate capture directly upstream of the pilot plant have significantly increased levels of calcium sulphate (analysed as CaO & SO_3) indicating a significant contribution to the overall particulate load from carryover of FGD liquor. If it is assumed that silicate originates solely from fly ash then this contribution can be estimated to be in the region of 60 – 70% of the particulate load being carryover of FGD liquor based on these measurements. This indicates that this may also be a significant source of metals in the capture process.

	Concentration (wt %)		
Component	FGD outlet	DCC inlet	DCC outlet
SiO_2	23.2	17.5	20.3
Al_2O_3	9.3	7.0	8.3
TiO_2	7.2	8.3	5.9
Fe_2O_3	6.7	12.4	6.1
CaO	14.0	7.9	12.0
MgO	5.8	5.0	4.7
Na_2O	2.4	2.3	1.9
K_2O	0.6	0.5	0.5
SO_3	26.9	33.6	35.9
P_2O_5	2.2	1.3	2.1
Number of samples	1	2	4

Table 3: Average elemental composition of particulate filter samples at the FGD outlet, DCC inlet and DCC outlet.

Calcium-based reagents are not used anywhere in the capture process and therefore monitoring of calcium build up can be used to give an indication of particulate build up within the process. Figure 2 shows the trend in calcium levels in the solvent during the first approx. 1,500 hours of operation. Calcium levels are generally seen to rise, as expected, during the operational period. Observed reductions in concentration are due to the addition of make-up solvent and potential precipitation processes (Schallert et al. 2013). Metal ion levels in the solvent, such as Fe, may also have some input from particulate matter, however, corrosion of the fabric of the capture plant is also a potential source of such metals and therefore measurements would be highly plant specific. Further measurements are currently ongoing to assess the capture rate of particulate in the absorber and to assess if solvent Ca levels can be used as a reliable indicator of particulate absorption.

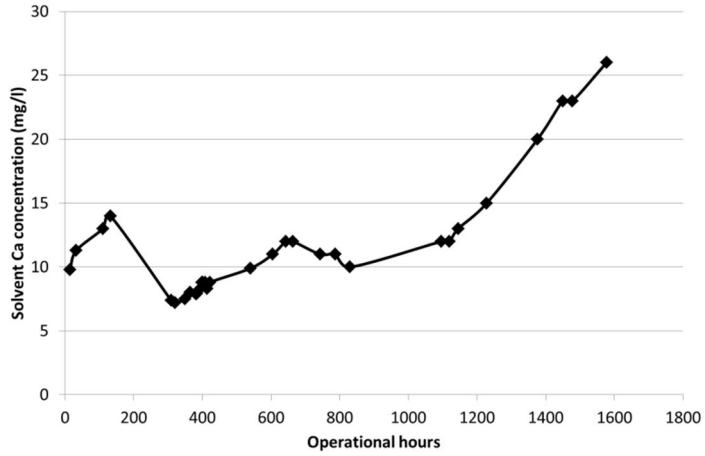

Figure 2: Solvent calcium concentration during the first approx. 1,500 hours of operation of the Wilhelmshaven pilot.

Particulate build up in the solvent is a potential issue for the operation of the CO_2 capture process. Previous work has shown that for a typical amine solvent (MEA) leaching of metals from particulate is enhanced compared to pure water alone (Schallert et al. 2013). Metals such as iron are known to catalyse oxidative degradation of amines (e.g. Sexton & Rochelle 2009) and it has been observed that the pH swing and presence of organic acid heat stable salts (HSS) in solvent can potentially results in the precipitation of calcium and transition metal salts (Schallert et al. 2013). Such precipitation may lead to fouling of plant components including heat transfer surfaces.

2.2 SO_2 & HCl

In order to obtain an assessment of the acid gas removal performance of the DCC an in-house wet chemistry method was used to measure the levels of SO_2 and HCl around the DCC. The method uses 3 temperature controlled gas washing bottles in series connected to a filtered pump and flow meter. Flue gas is sampled from the duct for a period of approx. 6 hours and drawn through the 3 washing bottles where acid gas components are captured. For these experiments the washing bottle specifications are shown in Table 4. This set-up was chosen as it has the potential to capture low levels of NO_2 and this application is currently under investigation.

Washing bottle	**1**	**2**	**3**
Volume (ml)	150	100	150
Composition	0.2 M $KHCO_3$	5 M Monoethanolamine	0.2 M $KHCO_3$

Table 4: Gas washing bottle specifications for SO_2 & HCl measurements at the Wilhelmshaven pilot.

Two measurements were undertaken in July 2013 and represent some of the variability expected in SO_2 concentration when treating flue gas from a commercially operated coal-fired power plant. Figure 3 shows the results of the measurements and indicate that the DCC is functioning effectively at reducing SO_2 to a low level but has little impact on the already low levels of HCl.

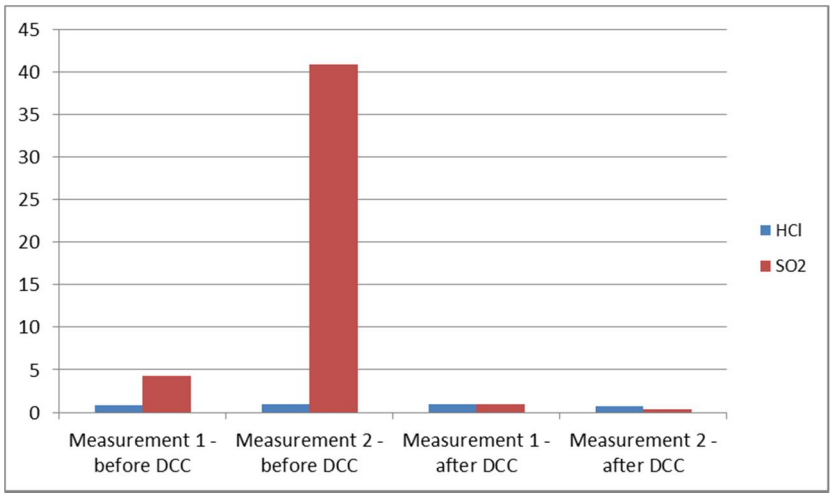

Figure 3: Gas wash bottle measurements of SO_2 & HCl around the DCC at Wilhelmshaven.

3. Conclusions

Results of the latest flue gas quality measurements upstream of a CO_2 capture plant have been presented. It can be seen from the above results that operation on coal-derived flue gas has specific challenges related to flue gas impurities, in particular particulate matter. Further research is required to understand the uptake of metals in the solvent and how this impacts and is impacted by degradation. Particulate entrainment has been observed to occur and may lead to long term issues with solvent degradation and fouling, this should be considered at the design stage for future plants.

Currently applied flue gas polishing technologies are effective at removing SO_2. However, there is a need to ensure that flue gas pre-treatment processes are optimized for all impurities to minimize the impact on the capture process.

References

- Anderson, V. Sanden, K., Wittmeyer, K. & Maree, Y. (2012). Operational experience and initial results from the first test period at the CO_2 Technology Centre Mongstad. Paper presented at the *International Conference on Greenhouse Gas Technologies (GHGT) 11*, Kyoto, 18 – 22 November.
- Gardiner, R. (2013). CCPILOT100+ Test Results and Operating Experience. Paper presented at the *International Energy Agency Greenhouse Gas R&D Programme Post-Combustion Capture Conference (PCCC) 2*, Bergen, 17 – 20 September
- Just, P. (2013). Shell Cansolv – Advancing CCS Deployment Worldwide. Paper presented at the *International Energy Agency Greenhouse Gas R&D Programme Post-Combustion Capture Conference (PCCC) 2*, Bergen, 17 – 20 September
- Reddy, S., Scherffius, J., Radgen, P. & Rode, H. (2012). Initial results from Fluor's CO_2 capture demonstration plant using Econamine FG plus Technology at E.ON Kraftwerke's Wilhelmshaven Power Plant. Paper presented at the *International Conference on Greenhouse Gas Technologies (GHGT) 11*, Kyoto, 18 – 22 November.
- Schallert, B., Neuhaus, S. & Satterley, C. (2013). Do we underestimate the impact of particles in coal-derived flue gas on amine-based CO_2 capture processes? *Energy Procedia*, **37**, pp. 817-825.
- Sexton, A., & Rochelle, G. (2009). Catalysts and inhibitors for oxidative degradation of monoethanolamine. *International Journal of Greenhouse Gas Control*, **3** (6), pp. 704 – 711.

Large diameter experimental evidence on liquid (mal)distribution properties of structured packings

Žarko Olujić, Helmut Jansen

Delft University of Technology, Delft, the Netherlands
Julius Montz GmbH, Hilden, Germany

Abstract
Comprehensive liquid distribution experiments were conducted with common size conventional and high capacity corrugated sheet structured packings in a 1.4 m internal diameter column hydraulics simulator using air/water test system at ambient conditions. The objective of the present study was to observe and quantify for various liquid loads and bed depths the relation between the quality of liquid distribution of a packed bed and uniformity and density of initial irrigation profiles, and, in particular, to demonstrate the effects of severe forms of initial liquid maldistribution.

Keywords
Distillation, Packed columns, Large diameter, Structured packings, Liquid maldistribution

1. Introduction

In answer to ever growing need for fuels and commodity chemicals as well as CO_2 capture installations the size of distillation, absorption and stripping columns tends to increase well beyond dimensions considered large in the recent past. Such a development confronts tray and packed column designers with challenges on both mechanical and process design side, and in the case of the latter the need for achieving a uniform liquid and vapour distribution and related uncertainties is a main concern.

The key to proper performance of large diameter packed columns containing structured packings is achieving and maintaining adequate quality of liquid distribution along a packed bed within the given range of operating conditions. Operating failures experienced in early years of application of large diameter packed columns, which can be attributed mainly to improper liquid distribution due to inadequate quality of liquid distributors at that time, have stimulated both academicians and practitioners to initiate and conduct experimental and theoretical studies on the quality of liquid distribution and its relation to mass transfer performance of a packed bed. Former have been usually conducted using air-water at ambient conditions as the test system, while the latter were total reflux distillation experiments carried out with some of established test mixtures [1,2,3].

Although air-water system has often been considered inadequate regarding pronounced differences in liquid spreading behaviour compared to organics [4], it was used widely, because of its practicality and affordable costs. Indeed, a relatively very high surface tension makes the water to be the worst case regarding the

spreading behaviour of liquids in packed beds. However, the fact that many distillations involve aqueous mixtures with considerable fraction of water (in alcohol distilling and many solvent regeneration applications water is often a high purity product), which is also a frequent case with solvents used in absorption and regenerated in stripping operations, indicates that the liquid distribution data obtained in air-water tests may be usable for practitioners.
Another issue in this respect is the scale of experimentation. Many efforts in this direction have been undertaken with test columns employing rather small diameters (< 0.5 m), including pronounced wall effects that make packed bed hydraulics to differ considerably from that exhibited in industrial scale columns [1,5]. Therefore industry was looking for experimentation at large enough scale, and the low and high pressure distillation columns with an internal diameter of 1.22 m available at FRI were considered sufficient in this respect. Indeed a number of devoted studies have been performed at FRI to define the relation between some imposed forms of severe initial liquid distributions and performance of a packed bed, showing that a structured packing may be more or less sensitive to certain type of initial maldsitribution than random packing, and that the structured packing can operate without significant loss of efficiency when the pour point density is reduced to one third of that considered normal in given case [3].
However the FRI tests have not provided direct insight into quality of liquid distribution of a packed bed and the depth of penetration of various forms of imposed initial maldistribution. To enable this, in mid-2000s, at the Delft University of Technology (TU Delft) a comprehensive research programme on similar scale has been arranged to study the liquid distribution behaviour of conventional and high capacity structured packings [2]. The experimental data presented here for the first time give an insight into the relation between the quality of initial liquid distribution and the hydraulic performance of a large diameter packed bed and provide a direct evidence on the depth of penetration of severe forms of large scale initial liquid maldistribution, similar to those employed in the FRI study [3].

2. Experimental set-up, procedure and data interpretation

A detailed description of the TU Delft column hydraulics' simulator containing a Perspex column with an internal diameter of 1.4 m, using air/water at ambient conditions as test system, can be found elsewhere [2,5]. Figure 1 shows an installed packed bed comprising five layers of Montz-Pak B1-250, with (above) a narrow trough distributor and (below) a liquid collecting section. The B1-250 is a conventional corrugated sheet structured packing with a corrugation inclination angle of 45^{o}, and a shallow embossed, imperforated surface. Each packing layer was assembled of three segments made to fit tightly into given space, and packed beds were arranged by stacking subsequent packing layers rotated by 90^{o} to each other. One meter of bed height contained five packing layers, and in present study the bed height was varied from 1 to 4 m.

Figure 1 Photograph of a short packed bed

Figure 2 shows layout of the narrow trough liquid distributor used in this study. It contains 152 drip tubes (99 pour or drip points per meter square cross sectional area). The picture on the right hand side shows the same distributor with the number of pour points halved by plugging the

outlet of every second drip tube. Figure 3 shows three severe forms of initial liquid maldistribution profile considered in this study, from left to right: one half of the distributor blanked (chordal blanking), periphery zone blanked (peripheral blanking) and the central zone of the distributor blanked (central blanking). In all cases approximately 50 % of the available pour points have been blanked.

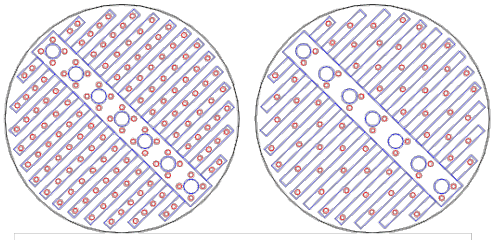

Figure 2 Layout of pour points: 100 vs. 50 pour points/m^2

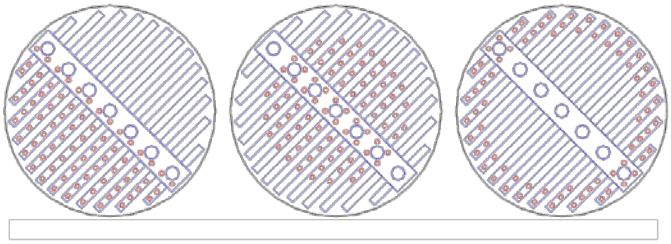

Figure 3 Three severe forms of initial liquid maldistribution considered in this study

Figure 4 shows the double wall liquid collection section, the liquid sampling directions and locations and a drawing with main dimensions of a funnel installed on the end of each of three moving rods. Each rod was moved gradually from one to the other side of the cross sectional area, which means 25 sampling points, leaving the ring close to the wall uncovered. The liquid leaving the packed bed via walls was collected in a 1 cm annulus occupying approximately 1.5 % of the cross sectional area. Funnels were equipped with electronic sensors indicating start and end levels, and the filling time was measured by stopwatch. Reproducibility of this simple but reliable time-volume technique proved to be high, except at vapour loads close to flooding point.

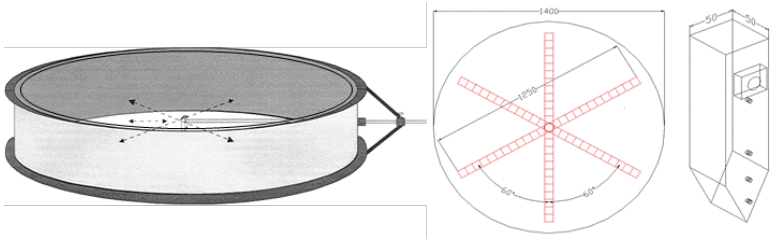

Figure 4 Double wall liquid collecting section, directions and locations of liquid sampling, and funnel dimensions

Since it appeared that the effect of gas load is not significant around loading point and within the preloading region [2], which is in accordance with observations made in earlier studies [7,8], and to avoid potential interference with ascending gas during liquid sampling, the data presented in this paper were obtained without presence of an ascending gas phase. All measurements reported here were conducted at a constant specific liquid load of 10 m^3/m^{2}h (m/h).

3. Results and discussion

Figure 5 shows a typical set of measured data for given situation, illustrating the effect of a strong reduction in the pour point density. The numbers shown on left hand side indicate the measured wall flow in m^3/m^{2}h (m/h), and are placed at the level corresponding with the values measured for the same conditions for three cross sectional liquid sampling directions. The fluctuating lines showing measured local velocities are accompanied by a horizontal line representing average value based on given constant specific liquid load (10 m/h in present case). Corresponding 2D liquid distribution profiles are shown on the right hand side, with, on top of it, a layout of the pour or drip points and the numbers 1 to 3 indicating the direction of liquid sampling. With a grid superimposed, with rectangular cells of the dimensions corresponding to that of the funnel, the empty cells were filled by numbers generated by linear

interpolation of measured values belonging to the same concentric circle. The vertical bar on the right hand side of Figure 5 indicates the corresponding liquid loads by a distinctive colour.

Such an approximation provided a basis for quantifying the magnitude of maldistribution using the characteristic values of the coefficient of (velocity) variation (C_v), which is per definition an overall mean velocity. The lower this value the lesser the deviation from uniform liquid distribution, i.e. plug flow.

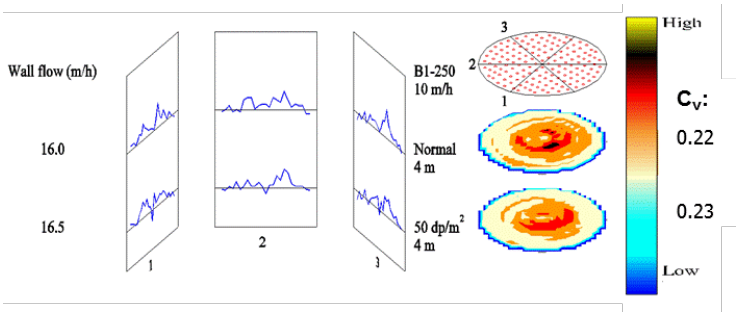

Figure 5 Effect of halving the number of drip points

More complex maldistribution indicators accounting for the extent of clustering in local velocities will be considered in forthcoming full (journal) version of this short paper.

Interesting to mention here is that the numbers shown represent in fact the inherent or “natural distribution” pattern of this packing, which corresponds with a mean deviation from ideal one of about 22 per cent. Owing to the fact that this packing performs well in distillation applications means that such a deviation from plug flow is not really harmful, but also that there is space for improvement. As shown elsewhere [2], under same conditions, the high capacity version of B1-250 packing (B1-250M) exhibited even a smoother performance (C_V values in the range: 0.12 to 0.2).

Figure 5 shows that for a 4 m packed bed halving the number of drip points from 100 d.p./m^2 to 50 d.p./m^2 does not influence distribution quality adversely. There are some differences in local distribution patterns but fluctuations in local velocity are nearly equal. This confirms previous experiences in this respect [3].

Figure 6 shows the effect of bed height on the liquid distribution quality of B1-250 packing, for a normal initial liquid distribution profile and three severe forms of large scale initial liquid maldistribution. As it can be seen from Figure 6, with a uniform initial distribution the quality of liquid distribution established after one meter is preserved until the bottom of a 4 m bed. Unchanging values of the coefficient of variation indicate that in this case there is no sign of any deterioration in the quality of liquid distribution. However a closer inspection of 2D profile at 4 m indicates a small cluster in the central zone with increased velocity, which suggests that at higher bed depths certain but not really harmful deterioration could be expected. One should note that this packing is often installed in practice with bed heights up to 8 m without affecting performance adversely. Interesting to mention here is that the characteristic

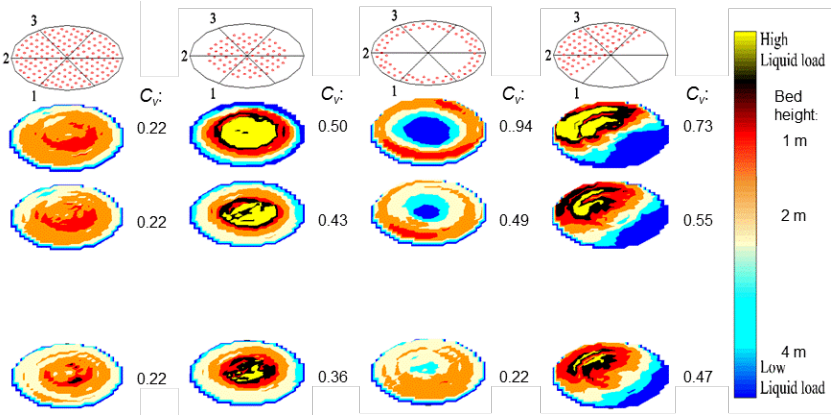

Figure 6 Effect of bed height on the liquid distribution quality for a uniform initial liquid distribution and three severe forms of large scale initial liquid maldistribution

value (C_v = 0.22) of the coefficient of variation indicates that the natural distribution of a well performing packing appears to be coarser than generally anticipated [6].
As expected, in case of initial maldistribution the quality of liquid distribution within the bed tends to improve gradually with the bed depth, to the extent depending on the form of initial profile. In case of blanking periphery zone, the profile after one meter exhibits much lower value than in other two cases, and improves gradually but at four meter it is still severely maldistributed. The initial smoothing effect is strong because the distance of the initial distribution perimeter and the column walls is rather short, and one or two layers are enough to get the liquid to column walls, but the rate of liquid transport towards walls appears to be low. In case of central blanking the distance to the column centre is larger and after 1 m the core of the packing is still dry (blue colour indicates zero velocity). With increasing bed depth the liquid flows from all sides towards the centrum at a relatively higher rate and after 4 m a nearly uniform distribution, equal in quality to that in normal situation is reached. This suggests that equalization progresses faster from the wall towards the centre than vice versa. As expected, the worst case in this respect is experienced with one half of the distributor blanked. With such an unsymmetrical initial profile, after 4 m there is still a significant fraction of the bed cross sectional area without liquid. Similar was observed during tests performed in early 1990s at DUT with a rectangular packed bed with approximately same cross sectional area [9].

Table 1 Wall flow (m/h) corresponding to the situation shown in Figure 7.

Bed height (m)	Normal	Peripheral blanking	Central blanking	Chordal blanking
1	9.2	2.2	18.2	8.2
2	12.5	5.1	21.5	12.1
4	16.0	9.2	19.6	14.2

Corresponding wall flows are shown in Table 1. With normal initial distribution the wall flow tends to increase and at 4 m it is well above the given specific liquid load. Interestingly, in case of chordal blanking the wall flow behaves similarly both in trend and absolute values. Also in case of peripheral blanking there is an increasing tendency from zero at the top to a value approaching at 4 m that of given specific liquid load. With overloaded wall zone, as experienced in case of central blanking, over the whole bed height the wall flow is nearly double of the given specific liquid load.
Figure 7 indicates a fairly good agreement between measured and predicted liquid distribution profiles for a 2 m bed. The model predictions were obtained using a simplified (interaction with column walls omitted) form of Stoter's "design model" [1,10] programmed in Excel, with cubic cell size of 7 cm (three per packing layer

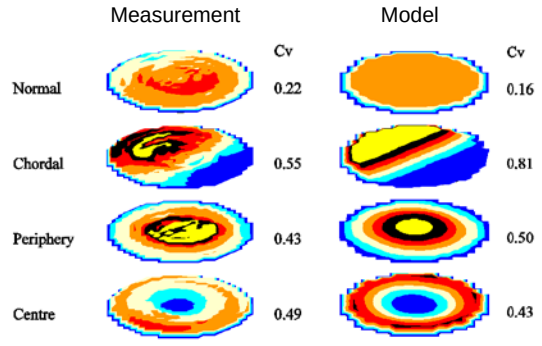

Figure 7 Comparison of measured and predicted quality of liquid distribution for a 2 m bed with different initial profiles

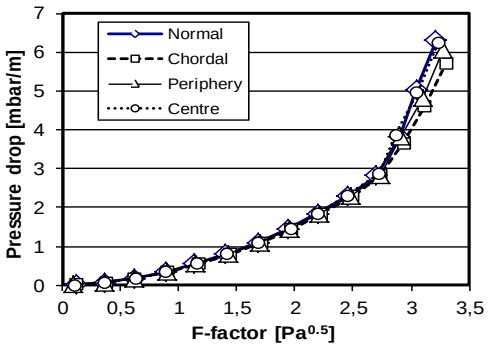

Figure 8 Pressure drop of an irrigated packed bed as a function of gas load for different forms of the initial liquid distribution profile

height), allowing for lateral transport of liquid in two directions and downwards in conjunction with characteristic values of corresponding spreading coefficients.
Figure 8 shows effect of initial distribution profile on pressure drop of a 4 m bed. In preloading region there is no visible effect, while in loading region the amount of pressure drop depends on the quality of liquid distribution. As expected, pressure drop decreases with increasing degree of liquid maldistribution [11] and the differences among different patterns tend to decrease with increasing bed depth.

4. Conclusions

With normal and symmetrically reduced pour point density there is no effect of bed depth. Regarding the observed value of the coefficient of variation it appears that the natural liquid distribution is coarser than generally anticipated. The wall flow tends to increase with increasing liquid load and bed depth.
A large diameter packed bed cannot restore to health from any severe form of initial maldistribution. It appears that the excessive liquid is transported faster from the periphery to the centre than in opposite direction. However, this is a slowly progressing process and for a large diameter bed it is an absolute necessity to have a uniform initial liquid distribution to perform accordingly.
Predictions of a simplified Stoter's large cell size model appeared to be in a fairly good agreement with experiments.
Pressure drop in the loading range is affected by the form of liquid maldistribution, and tends to increase with improving quality of the liquid distribution.

Acknowledgements

Roland van Baak and Johan Haaring, graduates of TU Delft, for carrying out a tedious and time consuming experimental work with utmost care and accuracy.

References

1. Stoter, F., Modelling of maldistribution in structured packings: from detail to column design, Thesis, Delft University of Technology, 1993, Delft, the Netherlands.
2. Olujić, Ž., Baak, R. van, Haaring, J., Kaibel, B., Jansen, H., Liquid distribution properties of conventional and high capacity structured packings, Chem. Eng. Res. Des. 84 (2006) 867-974.
3. Fitz, C.W., King, D.W., Kunesh, J.G., Controlled liquid maldistribution studies on structured packing, Chem. Eng. Res. Des. 77 (1999) 482-486.
4. Bennet, D.L., Ludwig, K.A., Understanding the limitations of air/water testing of distillation equipment, Chem. Eng. Prog. 90 (1994) 4, 72.
5. Olujić, Ž., Effect of column diameter on pressure drop of a corrugated sheet structured packings, Chem. Eng. Res. Des. 81 (2003) 108-115.
6. Edwards, D.P., Krishnamurthy, K.R., Potthoff, R.W., Development of an improved method to quantify maldistribution and its effect on structured packing column performance, Chem. Eng. Res. Des. 77 (1999) 656-662.
7. Stikkelman R.M., Gas and liquid maldistribution in packed columns, Thesis, Delft University of Technology, 1989, Delft, the Netherlands.
8. Kouri R.J., Sohlo J.J., Liquid and gas flow patterns in random and structured packings, I.Chem.E. Symposium Series No. 104 (1987) B193-B211.
9. Olujić, Ž., Stoter, F. de Graauw, J., Gas distribution in large-diameter packed columns, Gas Separation & Purifacation 5 (1991)59-66.
10. Olujić, Ž., Roelofse, A., Stoter, F., de Graauw, J., LDESP: A simulation and optimisation environment for structured packings, I.Chem.E. Symposium Series No. 142 (1997) 949-960.
11. Zuiderweg, F.J., Olujić, Ž., Kunesh, J.G., Liquid backmixing in structured packing in high pressure distillation, I.Chem.E. Symposium Series No. 142 (1997) 865-872.

MEGA Tower Design Considerations

Daniel R. Summers, Mark W. Pilling, Daryl C. Wiesman
Sulzer Chemtech USA, Inc., Tulsa, Oklahoma, USA

Abstract
Economic principles tell us that "Economies of Scale" drives us to larger and larger chemical plant sizes. Limits to plant sizes that were present decades ago have disappeared and the "norm" is now what we refer to as MEGA sized plants. With this in mind, distillation tower sizes are now being designed in excess of 14 meters in diameter and towers heights are in excess of 100 meters tall. In addition, very large rectangular towers are being employed in power plant flue gas streams to absorb carbon dioxide. This paper deals with design parameters that need to be considered when designing such MEGA towers. Parameters such as deflection, shop installation, support rings, bed depth and inter bed depth, beam count and sizes, vessel roundness and feed introduction will all be addressed in this paper.

Keywords: design, sizing, equipment, trays, packings, supports

1. Introduction

Sulzer Chemtech has been providing tower internals for over 60 years. During that time, tower diameters have increased significantly (more than threefold), see Figure 1, and tower elevations have exceeded 100 meters. Some factors that have assisted fabricators in attaining larger diameter towers over this time frame are: the development of high strength steels in the 1970's and 80's, the use of Finite Element Analysis (FEA), the employment of Computational Fluid Dynamics (CFD) and much improved understanding of liquid distribution.

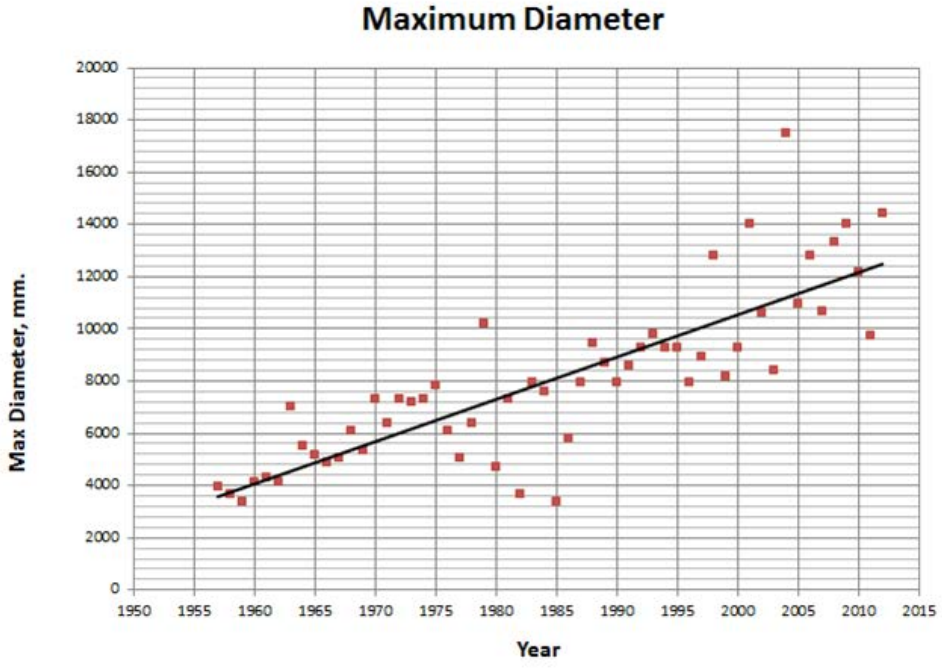

Figure 1 – Maximum Tower Diameter Designs

Tray and packing designs need to account for the obvious mechanical strength needed to support the lengths spanning larger and larger diameter towers. There are also functional (operational) issues that come into play with large diameter towers (e.g. mixing boxes for distributors and tray levelness). In addition, with the recent high interest in CO_2 capture from flue gas, there are also applications being examined using very large rectangular shaped vessels.

2. Discussion

Various Topics for design consideration for MEGA sized towers are itemized here

2.1 Support Ring Size

ASME code (Section VIII Division 1 UG-80) dictates that pressure vessels need to be round within +/- 1%. For large diameter towers, this means that support rings need to be wide enough to cover this tolerance range. Assuming that the outside diameter of a tray should extend halfway across a support ring and have a minimum of 13 mm (1/2") at the largest potential diameter to have a safe tray overlap for support, then the minimum support ring width needs to be:

$$\text{Ring Width}_{min} = 2\,(13 + \Delta) \qquad (1)$$

Where,

$$\Delta = 0.01\,(D / 2) \qquad (2)$$

D = Tower nominal diameter, mm

Ring Width_{min} = minimum ring width, mm

These equations form the curve shown in Figure 2. The curve is the minimum allowable support ring width for distillation trays and ring supported tower internals for continuous tray panels and beams. Typically Support Ring widths are rounded up to the nearest 10 mm (1/2"). Most people will use this curve as a basis for a "stair-step" support ring width table as a function of tower diameter.

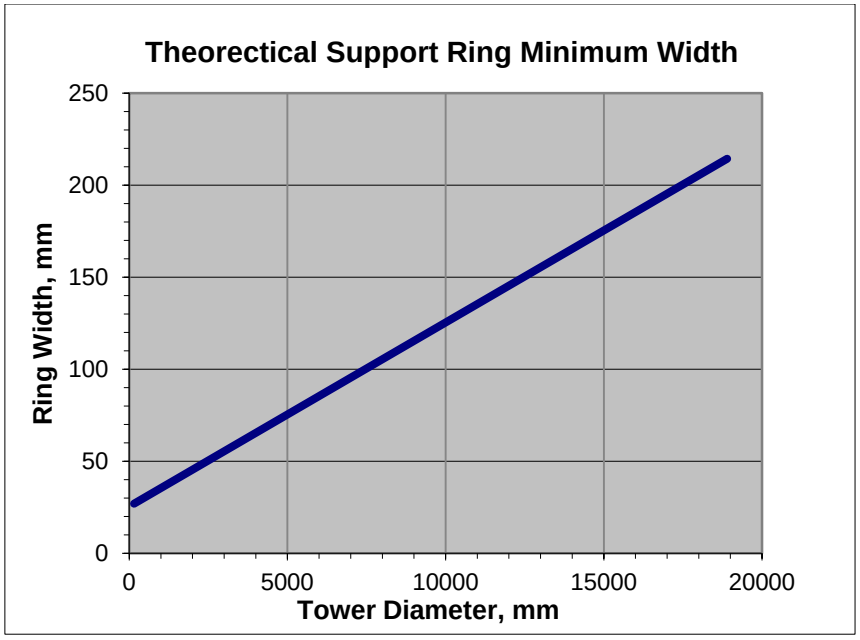

Figure 2 – Minimum Support Ring Widths

When dealing with MEGA towers, it is not mechanically possible that a tray deck panel would extend continuously across the entire diameter of the vessel. Most tray panels are limited to 3 meters in length due to handling issues. As such, with tray panel breaks and overlaps, it then becomes unnecessary to require that a 20 meter tower needs a support ring width of 225 mm as shown in Figure 2. The same applies to packed tower supports where they typically do not extend the entire diameter of the tower because there are support beams, as explained below. Therefore, support rings (whether they are horizontal or vertical) typically do not exceed 120 mm in width from the vessel wall.

2.2 Support Ring Levelness

Many tray suppliers in the past have indicated that tray support ring levelness should be +/- 3 mm. This is adequate for tower diameters up to 4 meters in diameter. Above 4 meter however, this levelness criterion becomes a burden for vessel fabricators and inspectors alike. A more reasonable levelness criterion is to impose a levelness tolerance based on maximum allowable degree of tilt. Sulzer Chemtech has adopted a "stair-step" levelness table(1). For MEGA sized towers in excess of this table, it would be advisable to maintain a levelness criterion based on a tilt angle of 0.10% of tower diameter. What this means is that for a 10 meter ID tower, the maximum allowable out of levelness for a tray would be 10 mm measured from high point to low point. Even if all the trays were tilted on the same side up to this allowable limit, the trays should still perform satisfactorily. This levelness criterion is shown in Figure 3. For distributors, the acceptable allowable limitation is the same but for parting boxes (pre distributors) we allow only 0.1 % out of levelness as a function of tower diameter.

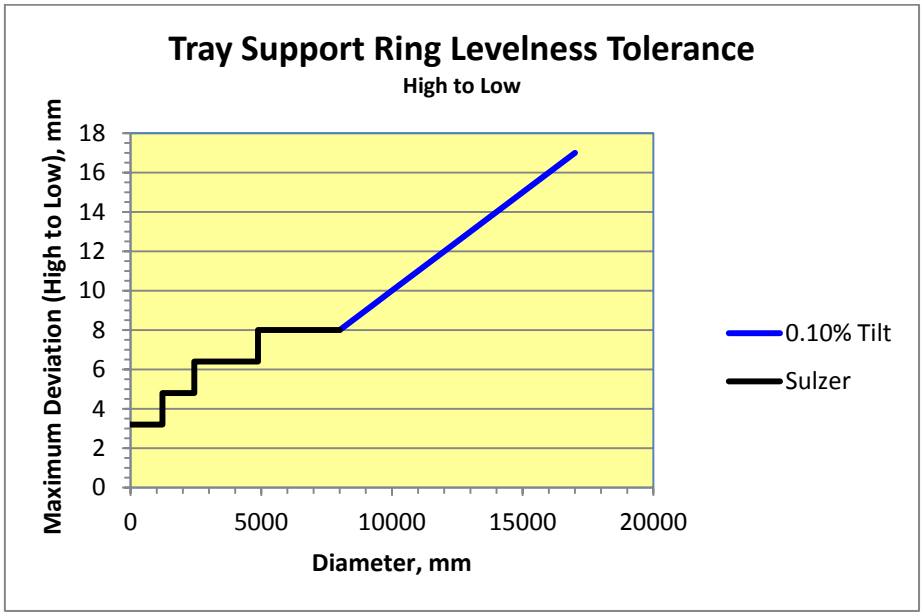

Figure 3 – Support Ring Levelness

2.3 Beam Requirements for Trays

As tower designs become larger in diameter, there comes a point at which the integral truss strength is insufficient to adequately support the tray decks. Sulzer Chemtech's standard, as well as the industry standard, is to design tray decks to

accommodate the operating loads without deflecting the tray decks more than 1/900 of the tower diameter[2]. This means that as tray panel lengths become longer with increasing tower diameter, the tray panels need to be strengthened either by being thicker, having deeper integral trusses or by being made shorter (with extra beams or downcomers). The economical tray design is one that minimizes the use of beams for tray support. Employing downcomers as support members is an effective means to minimize major supports beams on trays. However, adding downcomers to trays simply to add tray strength is not encouraged because the resulting shorter flow path length will have a significantly detrimental effect on tray efficiency. With the extensive use of push valves on today's tray designs, extra flow path length provides a significant improvement in tray efficiency even in excess of 100% tray efficiency[3].

When major support beams are employed, these sometimes can be so large as to block a significant portion of the up-flowing vapor. For example, a single 200 mm (8 inch) wide support beam in an 8 meter ID Tower will block 3.2% of the tower cross-sectional area. If lattice truss beams are employed, provisions should be made to allow liquid passage across the top of the structural member of the lower tray(s). Lattice Truss beams can be used to support two or more trays simultaneously.

Beam design, namely length, needs to take into account vessel out of roundness. As stated above for support ring widths, larger vessels will need longer beam seats and longer slots to account for the +/- 1% diameter out of roundness of pressure vessels.

2.4 Beam Requirements for Packing

Typically the support below a packed bed will need to be designed not only to hold the weight of the packing, but the expected liquid holdup, the hold-down grid, and the distributor on top of the bed. A "Rule of Thumb" for packed towers is that lengths of 3 meters can be spanned with structured packing support grids and with random packing Gas Injection Support (GIS) plates. Lengths greater than 4 meters will, most assuredly, need a major beam to help support these devices. For lengths between 3 and 4 meters, depending on the bed depth, holdup and the weight of other pieces of equipment (e.g. distributors, and hold down plates), a major beam may or may not be needed. This implies that that roughly for every 3 meter increment in tower diameter a major beam will be needed to support a packed bed. For a 12 meter diameter tower for example, 3 major beams will be needed to support each packed bed. Other factors will also determine the number of major beams needed for MEGA towers. These factors would include material length available to fabricate the support grid and the length and tonnage of the press break available to make the lengths needed. Designers also need to be aware of the pressure drop that results from having a significant amount of cross-sectional area blocked by the beams themselves.

Beam design, namely length, needs to take into account vessel out of roundness. As stated above for support ring widths, larger vessels will need longer beam seats and longer slots to account for the +/- 1% diameter out of roundness of pressure vessels.

2.5 Feed Introduction – Trayed Towers

Feed piping in large diameter towers is invariably different than in small diameter towers because inlet devices are <u>always</u> employed. It does not matter if the feed is

single or multiple phase, there needs to be internal piping because of the larger number of passes employed and the larger distances the feed must travel to get to the proper distribution points inside the vessel. For example, a simple liquid feed at the top of a tower from a single nozzle will have to be split to a 4-pass tray set at least once and possibly twice. In much smaller towers it is possible that a simple reflux stream could be introduced with no internal piping provided the feed is behind a false downcomer.
Intermediate feeds on multipass towers will need to be introduced at multiple locations for the same tray. This is because downcomers will prohibit internal piping to all compartments of a multipass tray. For a 4-pass tray, intermediate feed introduction should come from two nozzles located above a tray that has off-center downcomers. Here the liquid (or two phase mixture) can be introduced into two symmetrical compartments. For bottom feeds, such as reboiler returns, the bottom tray should be a tray that has side downcomers. Again, the reasoning is that the vapor (or two phase feed) can be introduced into two symmetrical compartments on either side of the center downcomer. With this in mind, the best tray count for a multipass tray set is to have an odd number of trays. This would enable the bottom tray to have side downcomers and the top tray to have side downcomers as well, thus minimizing the number of nozzles and maximizing symmetry in the tower.

In large diameter towers, the feed nozzles are also quite large. Therefore, the tray spacings at the feed points are much larger to accommodate the feed piping without interfering with the froth activity on the tray. As a result, tray spacings of 1000 mm or more will not be unusual in very large towers. The ability to place “oversize” vessel manholes is possible and may be cost effective especially to accommodate the larger feed piping and structural members.

2.6 Feed Introduction – Packed Towers

Probably one of the more challenging aspects of feed introduction in very large diameter towers is ensuring excellent liquid and vapor distribution to a packed bed. It is very important that the liquid distributors be level to within 0.1 % of tower diameter as explained above. Vapor feed distribution is one of the often overlooked problems encountered in the distillation industry. Packed towers have much lower pressure drop than towers with trays (approximately 10 times less than trays) and as such are much less forgiving when it comes to poor vapor introduction to a distillation tower. The pressure drop through a packed bed, especially at turndown, is simply not high enough to correct the flow of vapor and help spread it out over the full diameter of a large tower. Vapor inlet devices such as Vapor horns, Shell Schoepentoeters™ and Chimney trays are often needed to get vapor feeds to be distributed evenly below a packed bed regardless if it random packing or structured packing. Typically, for vapor flow, the best design tool is the use of CFD to represent the vapor entering the tower and to examine the various internals options to distribute the vapor in an optimal manner.

2.7 Flashing Feeds

These feeds pose an especially challenging design aspect, how to separate the liquid from the vapor while providing good distribution. The “safest” way to accommodate a flashing feed in a large diameter tower is to flash the feed above a chimney tray that

has sufficient residence time to allow the vapor to escape the liquid before the liquid passes to the packing or trays below. This will take a considerable amount of elevation to accommodate the flash, enable disengagement of liquid droplets from the flashing vapor and provide the "head" for liquid distribution. There are other devices that can be utilized depending upon the amount of flashing in the feed. If the flashing feed is 99% or more vapor by volume, then the flashing feed can be treated as a vapor feed. If the flashing feed is less than 3% by volume vapor, then the feed can be treated as if it were liquid. If the flashing feed is less than 50% by volume vapor then a flashing feed gallery or flashing feed boxes can be utilized directly above the packing distributor or tray inlet pan, see Figure 4.

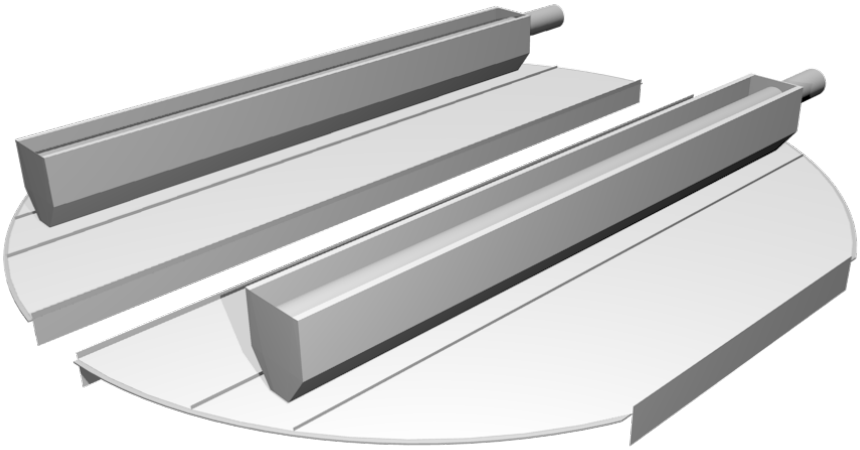

Figure 4 – Flashing Feed Boxes

3. Conclusion

MEGA sized towers are becoming more common place today. This paper provides insight into some of the parameters that need to be considered when designing today's MEGA sized equipment. We trust that we have addressed some of the important practical aspects of tower design as well as some of the mechanical issues that one will encounter in designing very large equipment. Our primary advice to the designer is that larger equipment design needs to account for the extra distances that liquids and vapors will travel to get to their ideal destinations.

Of course, MEGA is only relative to the time frame being discussed. 50 years from now, today's MEGA towers will probably be considered standard sized.

References

1.) Sulzer Standard Specification for Fractionation Trays, Rev 2.3 November 2013, Public Domain
2.) Fractionation Tray Design Handbook: Volume 5, Section 1.14.2, Pg. 2, Jan. 15, 1997, available to all FRI members
3.) Weiler, D.W. and Catani, S.J., "Performance of Linde Slotted Sieve Trays in the CCB Styrene Process", 74th AIChE National Meeting, Nov. 10, 1981

Dividing Wall Column for Industrial Multi-Purpose Use

Daniel Staak[1], Thomas Grützner[1], Brian Schwegler[2], Detlef Roederer[3]
[1]Center of Excellence Lonza Group, Visp, Switzerland
[2]MSAT Lonza Group, Visp, Switzerland
[3]Process Engineering, Visp, Switzerland

Abstract
Dividing wall columns (DWC) were first applied in commercial scale by BASF in the 80s. Since then a rapid development has taken place and the number of applications world-wide will reach a number over 200 in the coming years. Therefore a DWC will soon be a standard operation for the separation of a multicomponent mixture by distillation. However the open literature refers only to application in dedicated or mono plants for the separation of always the same mixture. For the distillation in Multipurpose Plants (MPP) DWCs where not applied. In MPP different products are produced campaign wise over the course of a year with different plant setups. The equipment in such MPPs, therefore, has to comprise a high level of flexibility. The distillation operations are normally carried out batchwise. The common opinion is that DWCs are not flexible enough for the operation in MPPs. However, Lonza set up a Multipurpose Dividing Wall Column (MDWC) in Visp, Switzerland in 2010. The experience shows that most of the hurdles regarding flexibility were easy to overcome. Since start-up all evaluated operations were successfully fit to the column and it did by far outperform the competing operations (e.g. batch distillation or side-draw distillation). This contribution reports on details of the technical solutions, operation experience and the workflow of fitting a process to a MDWC.

Keywords
Distillation, multipurpose plant, dividing wall column, operation, simulation

1. Introduction

Although distillation is a very old concept it still dominates the separation technology. Still today over 90% of the separation operations of multicomponent mixtures are carried out by distillation. Therefore, the energy consumption plays a major role in the operational costs of a process. Concepts to reduce this energy consumption are getting more and more important in times of rising energy- and raw material costs. The DWC is a concept that already leads to a CAPEX and OPEX reduction of approximately 30-40% [1]. The concept is very old and originates from the 30s [2]. However, it took until the mid 80s before the first industrial application was taken into operation [3]. With far more than 100 applications this technology can nowadays considered as mature. The basic concept is shown in Figure 1 (right bottom). A mixture consisting of three components A,B and C is fed to the column where A is the light-, B the medium- and C is the heavy boiling component. Conventionally two columns would be needed to separate this mixture (Figure 1, left bottom). Another alternative would be a side-draw column (Figure 1, right top). However the achievable purity of B in a DWC is higher and can be theoretically increased to

complete 100% and still having A and C in the desired purity. This is not possible with a side-draw-column.
Multipurpose production plants are used to produce different products in the same facility. The different products are produced campaign wise over the course of a year (typical 3-5 campaigns). In that case during the development phase the process is fitted to the plant, and not vice versa, how it is typically done in the design phase of non-existing equipment [4]. However the equipment used in these facilities has still to comprise a high degree of flexibility to allow a good plant fit. The distillation operations in these plants are very often carried out by batch distillation. Experience shows that for a majority of cases three fractions are distilled, whereas the intermediate fraction very often is the largest fraction and consist of the desired product whereas the bottom fraction consist of heavies formed during reaction or degradation and the overhead consists of undesired lights or solvent. These conditions are perfect for the application of a DWC. Besides the DWC has additional advantages compared to the competing distillation concepts (see also Figure 1). Compared to a standard batch distillation (equivalent size) the throughput and the degree of automation are higher. Like already mentioned the CAPEX and OPEX costs are lower compared to a two column sequence due to smaller unit footprint and reduced mixing effects. In comparison to a side draw column the DWC concept is superior and can achieve higher purities in all three components (considering comparable energy input and number of stages). The specific technical solutions to make it possible to operate a DWC in a Multipurpose Plant environment are described in detail below.

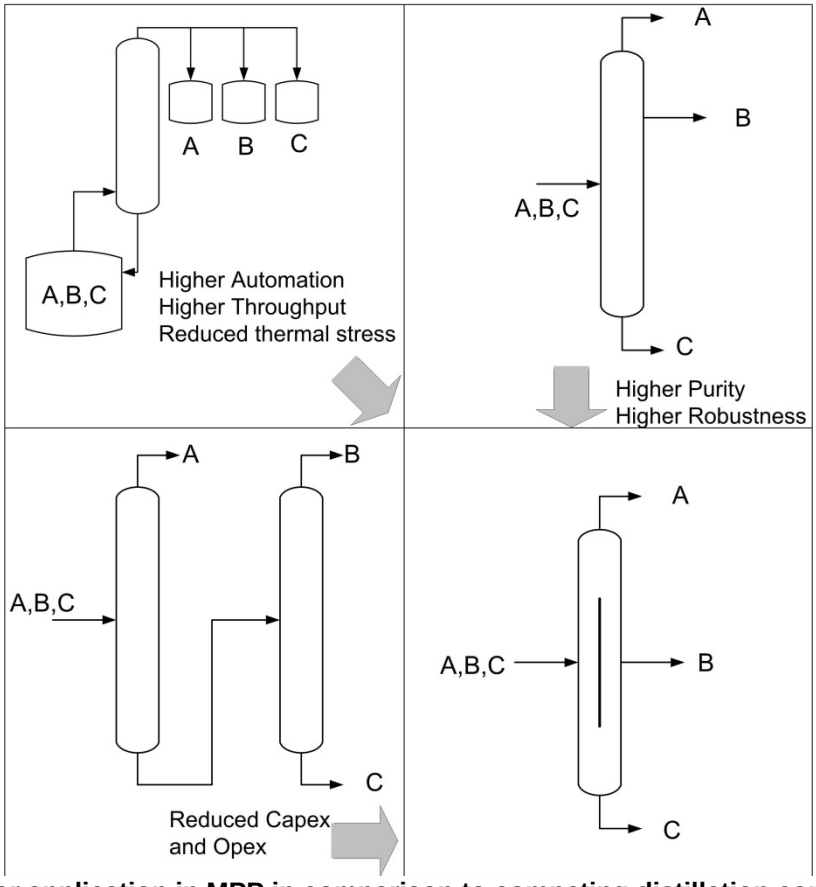

Figure 1 DWC for application in MPP in comparison to competing distillation concepts

2. Results and discussion

2.1 Design of a multipurpose dividing wall column

The column was constructed from Hastelloy C-22. This allows the distillation of even corrosive materials and is especially important since during the design phase possible future processes are not known. Using this material of construction opens the operating window and allows the handling of a large number of additional mixtures. Heating and cooling is possible between 160°C and 0°C (and even lower). To allow the condensing at such low temperatures two condensers are applied. The first in line is operated with normal cooling water and sufficient for most cases where no low temperatures are needed. The second one is operated with brine and only additionally applied if cooling at very low temperatures is needed. The operating pressure range is between 10 mbar and 2000 mbar (absolute). Other hardware design features are shown in Figure 2. The feed stream can be given on three different heights as well as the side draw. Also the feed stream can be split in two equal parts and applied to both sides of the dividing wall. This allows the operation as a normal column with the full capacity. The liquid split on both sides of the dividing wall can also be controlled and set to almost any desired ratio, even during operation. Experience shows that this has a large impact on the separation performance of the column.

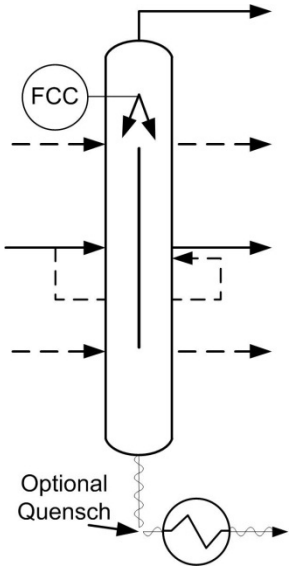

Figure 2 Design Features of MDWC

The column bottom, the pipes and the reboiler are especially designed to be able to handle sensitive materials and even solids. This is beneficial since the column is used to distill reaction mixtures which are very often not stable for a longer period of time. Therefore, the thermal stress should be as low as possible. Also solid formation and freezing is a possible issue. Hence, the bottom pipes are inclined, as short as possible, can be heated and cooled and also an immediate quench is possible.
The applied control scheme was designed to be as robust as possible. This is due to the fact, that the column operates a number of different processes over the course of a year. Stable operation and achieving always the desired product quality were therefore the main goals.

2.2 Modeling and Simulation

The time for a complete process development in multipurpose plants is much shorter in comparison to development timelines in dedicated plants which are designed from the scratch. A time frame of 3-9 month between first evaluation and plant start-up is usual. This also leads to special requirements regarding the distillation concept. Normally no time for piloting and even no time for measurement of vapor-liquid equilibriums are available.
Therefore the workflow for establishing the thermodynamic model comprises on a first level to gain all available data from literature and data bases such as the DDB (Dortmund Data Bank). But very often the needed data is not available. Therefore, on a second stage predictive methods like COSMO-RS or UNIFAC are applied. Lonza has established a technical guideline in which the accuracy of different predictive

methods for different classes of molecules is summarized. This gives the designing engineer a good guidance in regard to the reliability of the model and allows him to judge the accuracy of the results.

Model validation is carried out in the development phase by simple batch distillation lab trials using the real mixture. The model should be able to describe the course of temperature for the head and the bottom and the composition of each fraction. If this is not the case, the parameters of the thermodynamic model are optimized until the model is able to describe real behavior sufficiently. Also important criteria like solid formation or exothermic behavior are clarified at this stage.

Subsequent to the successful model validation, the fit of the separation task to the existing MDWC is carried out. This is done simply by simulation runs. The model is established in ChemCad™. To receive a quick and reliable convergence of the simulation model, a special modeling approach is used. The approach and the thermodynamic model is described in detail in [5]. The overall number of stages is set. Adjustable parameters like Reflux Ratio, Liquid Split, operating pressure etc. are optimized with the simulation model according to the desired constraints like composition of each outgoing flow, feed rate etc. The developed process is then transferred to the real production column without further piloting.

In Figure 3 a comparison between the simulation results and real plant data is shown. Whereas A* is a summary of all light boilers, B is the intermediate boiler (product) and C* is a summary of all heavy boilers. The thermodynamic data of the model were predictive.

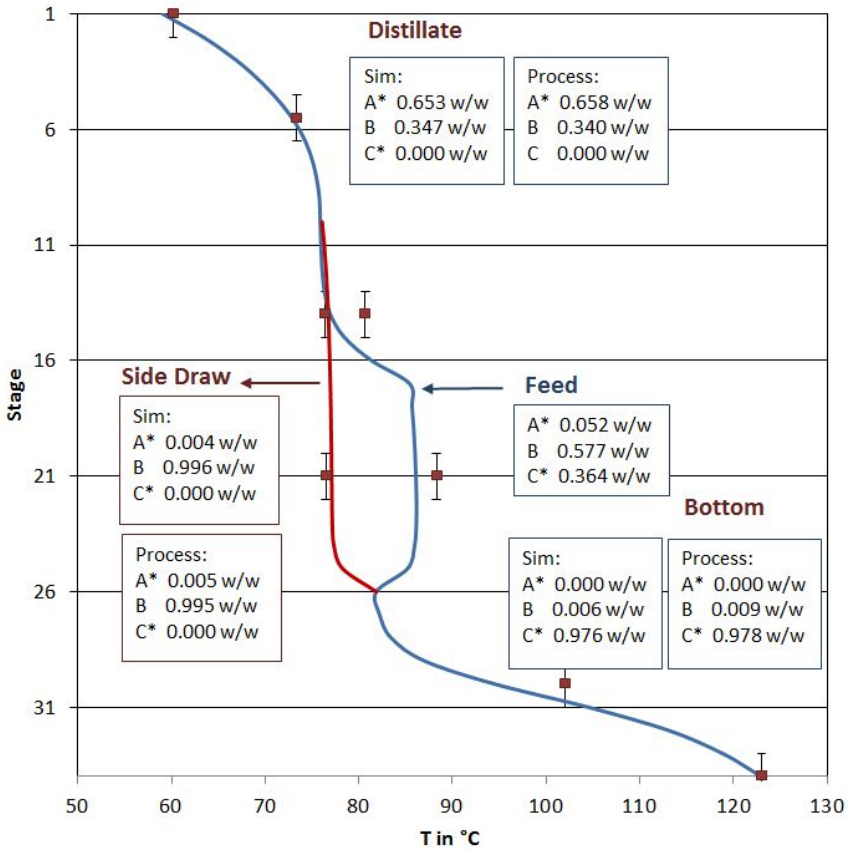

Figure 3 Comparison of Simulation results with real plant data

For the temperature profile can be seen that the simulation results reflect the real data very well, except for a region around the feed stage. This might be due to the applied enthalpy model, which was also predictive. Therefore, in a region where due to mixing lot evaporation and condensation occurs, the model might not be very precise. The compositions of the outgoing streams were in very good accordance with the simulation model.

2.3 Implemented production processes

The column is in operation since 2010 [5]. So far three different distillation tasks were evaluated and all three processes were afterwards operated in the MDWC. For each process a competing distillation concept has been substituted. Table 1 gives an overview. For each process the application of the MDWC was beneficial compared to the distillation alternative. For process 1 the MDWC achieved a strongly increased purity of the outgoing streams. The higher purity allowed the implementation of a recycling concept that led to a strong cost reduction. For process 2 a batch distillation was replaced. The MDWC was again able to achieve a higher purity. The received quality was already the premium quality. This quality, which was also requested by the market, was with the batch distillation only achieved if the already distilled product was distilled a second time. Additionally the distilled mixture was sensitive to thermal stress and was degrading at high temperatures. The strongly reduced residence time in the continuous operated MDWC in comparison to the batch distillation led to a yield increase of approx. 5%. The batch distillation was prior the bottleneck of the whole production process and therefore also the throughput could be increased (more than 50%) by applying the MDWC. The 3rd process replaced a thin film evaporator with an attached column. The major benefit for this process has been that the intermediate component is now received as a clear colorless liquid from the MDWC which was not the case in the original concept. This was due to the fact that this component has been the bottom product from the attached column.

Table 1

	Process 1	***Process 2***	***Process 3***
Replaces	*Column with side-draw*	*Batch distillation*	*Thin film evaporator with column*
Objective	*-Increase purity in side-draw and bottom stream*	*- Reduction of thermal load* *-Increase throughput*	*-colorless side draw*
Benefit	*Recycling of both streams became possible (cost reduction)*	*- 5% yield increase by reducing residence time under heat* *- Capacity increase of 50%*	*- Component was usable for application in another process*

3. Conclusions

Dividing wall columns did already prove their superiority in mono- or dedicated plants compared to standard distillation approaches for separation of ternary mixtures. However, the common opinion was that they are not flexible enough for the use in a multipurpose environment. Applying smart technical solutions added the desired flexibility. By that means the operation in a multipurpose plant became beneficial and the column showed its advantages in comparison to competing distillation concepts. Since the start-up in 2010 all evaluated processes were successfully implemented.
The fitting of a new process to the existing equipment is done merely based on simulation studies. Due to the lack of time no piloting is carried out typically. The thermodynamic model, underlying the simulation studies, is often based on predictive methods like COSMO-RS or UNIFAC. The reliability and the accuracy of the method for the given class of molecules can be assessed by an internal technical guideline. A model validation is carried out by lab batch distillation. This procedure accelerates the development speed and allows reducing the time between first evaluation and process start-up.

Due to the large commercial success the second multipurpose dividing wall column will start-up operation in 2014.

Acknowledgements

The authors are grateful for the contribution of Fabian Homberg (Technical University of Kaiserslautern) during his time at Lonza.
Parts of this conference contribution were previously published by the authors in Chemical Engineering and Processing.

References

[1] L. Humphrey, Separation processes: playing a critical role, *Chemical Engineering Progress* 91(10) (1995) 31–32.
[2] A.J. Brugma, Process and Device for Fractional Distillation of Liquid Mixtures,more Particularly Petroleum, US Patent 2.295.256, 1942 (filed 1936).
[3] N. Asprion, G. Kaibel: Dividing wall columns: Fundamentals and recent advances, *Chemical Engineering and Processing*, 49 (2010), 139-146
[4] G. Heckmann, F. Previdoli, T. Riedel, D. Ruppen, D. Veghini, U. Zacher, Processdevelopment and production concepts for the manufacturing of organic finechemicals at Lonza, *Chimia* 60 (9) (2006) 530–533.
[5] D.Staak, T.Grützner, B.Schwegler, D. Roederer: Dividing wall column for industrial multi purpose use, *Chemical Engineering and Processing,* 75 (2014) 48– 57

Process Intensification of the production process of biojet fuel

Claudia Gutiérrez-Antonio[1], Fernando I. Gómez-Castro[2], Juan G. Segovia-Hernández[2], Abel Briones Ramírez[3]
[1]Universidad Autónoma de Querétaro, Querétaro, México;
[2]Universidad de Guanajuato, Guanajuato, México;
[3]Exxerpro Solutions, Querétaro, México

Abstract
Aviation sector contributes with 2% of the total CO_2 emissions, and predictions estimate that air traffic will duplicate in the next 20 years, doubling fuel requirements and CO_2 emissions. International Air Transport Association has identified the development of aviation fuel from renewable feedstocks, known as biojet fuel, as the most promissory strategy to reduce CO_2 emissions. Recently, UOP Honeywell received a patent for its process to produce aviation fuel from renewable feedstock. The process considers the transformation of vegetable oil through hydrogenating, deoxygenating, isomerizing and selective hydrocracking to generate renewable fuels, which are purified later. Thereby, the process is integrated by two consecutive reactors and a conventional distillation sequence.

In this work, we propose the intensification of the production process of UOP Honeywell, through the use of thermally coupled distillation columns for the purification stage; moreover, we incorporate a turbine in order to generate electricity with the energy contained in the stream that leaves the reactor system. Then, we developed a model for the production of biojet fuel, obtaining an estimation of the conversion of the involved reactions. Also, the purification stage is optimized through a multiobjective genetic algorithm with constraints, which is coupled to a process simulator; so, we generate results considering the complete model of the process. Results show a high conversion of the vegetable oil (castor oil) to biofuels (biojet fuel and green diesel). The use of thermally coupled distillation columns allows getting a reduction in energy requirements in the separation stage. Also, energy can be generated in the process as result of the conditioning of the stream that is fed to the distillation train.

Keywords
Biojet fuel, process intensification, thermally coupled distillation sequences, multiobjective stochastic optimization

1. Introduction

In the transport sector, the aviation industry is responsible for 2% of total annual emissions of CO_2, about 623 million tons in 2009 [1]. The overall percentage is small; however, it is estimated that by 2020, global emissions of international aviation will be approximately 700% higher than in 2005, even if the engine efficiency will increase by 2% per year [2]. The International Civil Aviation Organization, ICAO, forecasts that air traffic will grow at a rate of 4.8% per year until 2036 [3], this finding is consistent with the reports of the International Air Transport Association, IATA, which estimates that air traffic will double by 2020, compared to 2005.

Therefore, both IATA as ICAO have established a four-pillar strategy to combat climate change problem [5]: 1) Technological improvements; 2) Operational improvements; 3) market-based measures; and 4) Alternative fuels. IATA estimates that this strategy will allow a 50% reduction in CO_2 emissions by 2050, relative to 2005 emissions levels, and neutral growth in CO_2 emissions from 2020 [1]. From the above alternatives, IATA identifies the development of biofuels as one of the most promising to reduce more significantly CO_2 emissions. The aviation fuel from renewable feedstocks, also known as biojet fuel, must be drop in, since changes in motor structures are not desirable; thereby, it has to present the same properties and chemical composition of the jet fuel [4]. Thereby, compounds known as synthetic paraffinic kerosene (SPK's) have been developed, and they are very similar to the jet fuel in energetic density and physical properties [6]. The SPK's contains small amounts of sulfur, generating less contaminant emissions in comparison with the conventional jet fuel. The only inconvenient of the SPK's is that they do not contain aromatics, so that they must be used in mixtures up to 50% of biojet fuel with the conventional jet fuel according to standard ASTM D7566. The SPK's can be produced from biomass in two ways [7]. The first one considers the gasification of the biomass, which is introduced to a Fischer-Tropsch process where the SPK's are generated. The second one considers the extraction of vegetable oils, which are chemically modified to produce the SPK's. In both cases, purification of the product stream is required to obtain the biojet fuel.

In 2009, UOP Honeywell received a patent for its process to produce aviation fuel from renewable feedstocks [8]. The process considers the transformation of vegetable oil to generate hydrocarbons fuels using two consecutive reactors and conventional distillation. In this work, we propose the intensification of the production process of biojet fuel through the use of thermally coupled distillation columns for the purification of the hydrocarbon stream; also, we incorporate a turbine in order to generate electricity with the energy contained in the stream that leaves the reactor system. Then, we developed a model for the production of biojet fuel, obtaining an estimation of the conversion of the involved reactions. Also, the purification stage is optimized through a multiobjective genetic algorithm with constraints, which is coupled to Aspen Plus process simulator; so, we generate results considering the complete model of the process. Results show a high conversion of the vegetable oil (castor oil) to biofuels (biojet fuel and green diesel). The use of thermally coupled distillation columns allows getting a reduction in energy requirements in the separation stage. Also, energy can be generated in the process as result of the conditioning of the stream that is fed to the distillation train.

2. Results and discussion

2.1 Biojet fuel production process

The process of UOP Honeywell considers the transformation of vegetable oil through hydrogenating, deoxygenating, isomerization and selective hydrocracking to generate hydrocarbons fuels [8], which later are separated to obtain biojet fuel.

An important aspect in the production of biojet fuel is eliminating the oxygen to ensure the thermal stability of the fuel; due to this the first reaction is the deoxygenation. From this reaction we obtain paraffins, but not in the range of the distillation curve of the biojet fuel. In a second step, reactions of catalytic cracking

and isomerizing occur to cut the hydrocarbons chain in the required range for the biojet fuel; also, the chain is branched to improve the freezing point of biojet fuel. The obtained product is a kerosene equivalent to jet fuel, but without aromatic compounds. The reaction system is a fixed bed reactor, and the reaction is exothermic. In general, the cracking conditions are lower than those for a traditional cracking process. The process uses a multifunctional catalyst to transform the vegetable oil into biofuels. It is important to mention that the quality of the SPK's is independent of the raw material employed, plant (jatropha, camelina, algae, and castor) or animal (tallow or fish oils) oils [8].

2.2 Modelling of biojet fuel production process

We consider as renewable feedstock castor oil with a flow stream of 100 kg/h, which composition was taken from Demirbas [10], and it is: palmitic acid (1.1 kg/h), estearic acid (3.1 kg/h), oleic acid (4.9 kg/h), linoleic acid (1.3 kg/h) and ricinoleic acid (89.6 kg/h). It is important to mention that there is no information available for the kinetic model or type of catalyst involved in the UOP Honeywell process due to confidential issues. Therefore, we estimate the hydrotreating reaction with the kinetic model develop by Sebos et al [11] for the hydrotreating of cottonseed oil:

$$(-r_{HDO}) = k_{HDO} \cdot C_{esto} \cdot (1 - x) \quad (1)$$

$$k_{HDO} = -\ln(1 - x) \cdot \dot{m}/m_{cat} \quad (2)$$

Where the subindex HDO implies hydro-deoxigenation, $\dot{m}$ is the feed stream flow and m_{cat} is the catalyst mass. Equation (2) is obtained for a feeding of 10% of cottonseed oil in fossil diesel, with temperatures between 305 and 345 °C, a pressure of 30 bar in a Cr/Al_2O_3 catalyst. Using the values reported by Sebos et al. [11] and eq. (2) we estimate the conversion of the castor oil in order to select the optimal catalyst mass; the result was 18 kg to get almost a total conversion (99.35%). According with Donis et al [12], when a triglyceride molecule is broken by a deoxygenation reaction the byproducts are water (6 mol by triglyceride mol) and one mol of propane. Also, it is possible that a decarboxilation reaction occurs, generating propane and carbon dioxide. We consider that both reactions occur: 50% of the triglycerides react by deoxygenation and 50% by decarboxilation. We assume that all fatty acids in castor oil are present as triglycerides.

For the reactions of isomerizing and cracking we take the results showed by Steijns et al [13] for the isomerization and hydrocracking simultaneous of n-dodecane. This implies that we are assuming that the n-alcanes from carbons 15 to 18 present a similar reactive behavior of the n-dodecane. According to Steijns [13], for pressures between 50-60 bar and temperatures of 240 °C the maximum conversion to isomers is around 32%, for a total conversion for n-dodecane of 50%. We take this conversion for estimation of the streams leaving the second reactor of the biojet fuel production process.

The generated hydrocarbon stream, at 240 °C and 60 bar, is conditioned at 19.7 psia and 27.22 °C in order to be fed to the distillation sequence, for the separation of the biojet fuel. We have design four schemes: direct and indirect both conventional and thermally coupled sequences. We consider recoveries of 99% in the key components to generate three products: light hydrocarbons (C3 to C7), biojet fuel (C8 to C16) and

green diesel (C17 and C18). The distillation sequences are optimized using a multiobjective genetic algorithm with constraints, coupled to Aspen Plus process simulator, and accelerated through neural networks, [14]. The algorithm generates a set of optimal designs that represent the best trade-off between the selected objectives; it manages several objectives simultaneously, manipulating integer and continue variables, and the link to Aspen Plus allows using the complete equilibrium model of the distillation columns (Radfrac module). The algorithm works as follows: the first generation is created from an initial design, and all individuals are sent to Aspen Plus to simulate them and get data about objectives and constraints; then, individuals are ranked in subpopulations, according with the number of satisfied constraints. The best individuals are selected to be the new parents of the second generation, and so on; the process ends when the maximum number of generations is reached. For the distillation sequences, the optimization problem is expressed as:

$$\begin{aligned} &\text{Min } (Q_i, N_i) \\ &\text{subject to} \\ &\mathbf{y}_m \geq \mathbf{x}_m \end{aligned} \qquad (1)$$

where Q_i and N_i are the heat duty and the number of stages of the column i, while $\mathbf{y}_m$ and $\mathbf{x}_m$ are vectors of obtained and required purities for the m components, respectively.

2.3 Analysis of results

With the proposed model, we simulate the biojet fuel production process taking as raw material castor oil (100 kg/h) For the hydrotreating reaction the operating conditions are 345 °C, 30 bar, 18 kg of Cr/Al_2O_3 catalyst, and the kinetic model described in eqs. (1) and (2), according with Sebos et al. [11]. In the hydrotreating reactor a high conversion, 99.36%, of the triglycerides to hydrocarbons plus water and carbon dioxide is obtained. Among the generated hydrocarbons, the major proportion corresponds to those in the range of a diesel (C17 and C18) instead of biojet fuel (C8 to C16). Therefore, the hydrocarbons must be separated from water and carbon dioxide, and fed to the second reactor where the isomerization and cracking are performed. For these reactions we consider that the operating conditions are 240 °C and 60 bar. In the isomerizing/cracking reactor an important modification of the hydrocarbons to generate biojet fuel occurred. There is a total conversion to hydrocarbons of 82%, while the conversion to biojet fuel is 22%, Table 1; conversion to biojet fuel is low, but consistent with the maximum conversion of 36% reported by UOP Honeywell [8].

In order to feed the hydrocarbon stream to the distillation sequence in adequate conditions, we propose a turbine to take advantage of the pressure on the stream. Simulations show that 74.5 Watts are generated during the process; which contribute to decrease the operating costs of the process.

The hydrocarbons stream is fed to a both conventional and thermally coupled distillation sequences. We consider two alternatives for each kind of scheme: direct and indirect; these sequences were optimized through a multiobjective genetic algorithm with constraints, accelerated with neural networks, coupled to Aspen Plus

process simulator [14]. As a result we obtained the Pareto front of both sequences, which includes a set of optimal designs that represent the best trade-offs between the objectives simultaneously optimized: number of stages and heat duty in each column of the sequence. This set of optimal designs include minimum heat duty, minimum number of stages and all designs that represent the best compromises between these extremes. Table 2 present the optimal designs, taken from the Pareto front, of both distillation sequences with minimum energy consumption.

Table 1. Composition of the output stream of the reaction stages

Component	nC3 to nC7	nC8 to nC14	nC15	nC16	nC17	nC18	iC15	iC16	iC17	iC18
Flow rate (kg/h)	10.12	21.60	0.215	0.229	19.07	20.19	0.069	0.073	6.10	6.46

Table 2. Optimal designs with minimum heat duty, both conventional and thermally coupled distillation sequences

Sequence	Conventional direct	Conventional indirect	Coupled direct	Coupled indirect
Total stages	129	238	125	127
Heat duty (Btu/h)	74, 598.79	79, 241.51	63, 610.73	75, 292.28

From Table 2, the minimum energy consumption is observed in the thermally coupled direct sequence, which is obtained even with the minimum number of stages. The thermally coupled direct distillation sequence requires 15% less energy than the conventional sequence with minimum heat duty. The reduction in energy requirements lead to a more sustainable process and minor production costs of biojet fuel. Thereby, the intensified process includes the reactive section, a turbine and a direct thermally coupled distillation sequence, Figure 1.

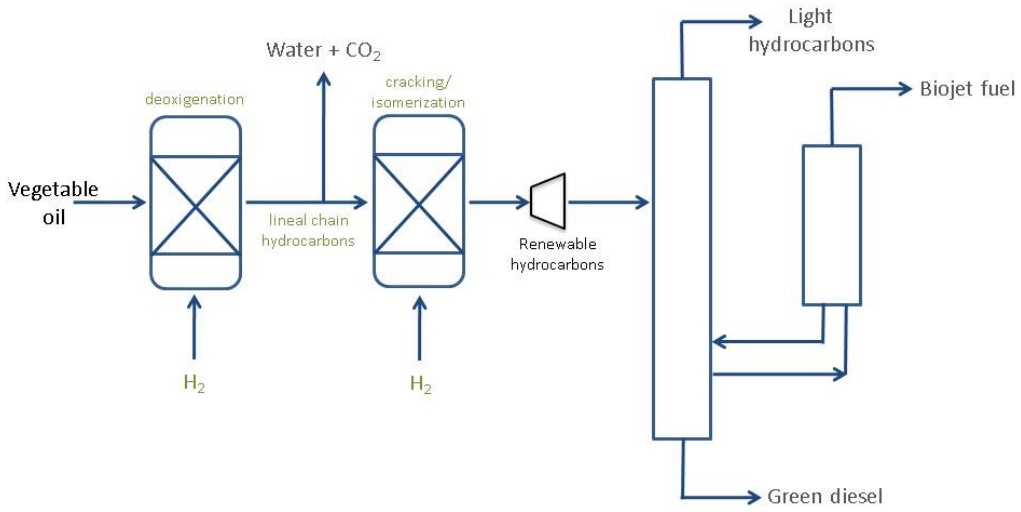

Figure 1. Intensified process to produce biojet fuel

3. Conclusions

We proposed the intensification of a production process of biojet fuel, through the use of thermally coupled distillation columns for the purification stage; also, we incorporated a turbine in order to generate electricity with the energy contained in the stream that leaves the reactor system. We estimated the conversion of reactions and amount of catalyst with base in other works previously reported. The results show that the proposed model gives good estimations of the conversion to hydrocarbons, 82%, and biojet fuel, 22%. Also, as a result of the modification of conditions of the stream of the reactor that will be feed to the distillation sequence around 75 Watts were generated in the process. The implementation of thermally coupled distillation sequences allows getting a reduction of 15% in the energy consumption of the separation stage, in comparison with the original process. The reduction in energy requirements lead to a more sustainable process and minor production costs of biojet fuel.

Acknowledgements

Financial support provided by Exxerpro Solutions and Universidad Autónoma de Querétaro for the development of this project is greatly appreciated.

References

[1] International Air Transport Association, 2009, A global approach to reducing aviation emissions – First stop: carbon neutral growth from 2020, 8 pp, www.iata.org, accesed on January 30th, 2014..
[2] European Commission, Reducing emissions from the aviation sector, Web page: http://ec.europa.eu accessed on January 30th, 2014.
[3] Chacin, E., 2010, La OACI y los combustibles alternativos sustentables de aviación, Taller de Financiamiento, Legislación, Logística y Distribución, Plan de Vuelo, 21 pp.
[4] Herrera-Vaillard, A. et a., 2010, Sustainable Aviation Fuel – Global Overviews, Reunión de arranque, Plan de Vuelo, 16 pp.
[5] Aeropuertos y Servicios Auxiliares, Estrategia de los cuatro pilares. Web page: http://biocombustibles.asa.gob.mx, accesed on January 30th, 2014.
[6] Bertelli, C., 2010, Bioturbosina, Taller de Refinación e Infraestructura, Plan de Vuelo, 16 pp.
[7] Jansen, J.P. et al., 2002, Large-scale production of biofuels through biomass (co-) gasification and Fisher-Tropsch synthesis, Report, TNO Environment, Energy and Process Innovation.
[8] McCall, M. J. et al., 2009, Production of aviation fuel from renewable feedstocks, Patent No. US 8,039,682 B2.
[9] Gutiérrez-Antonio, C.; Gómez-Castro, F. I., 2010, Estudio de benchmarking para las tecnologías de producción de bioturbosina, Internal technical report, CIATEQ, A.C.
[10] Demirbas, A., 2005, Biodiesel production from vegetable oils via catalytic and non-catalytic supercritical methanol transesterification methods, Prog. Energ. Combust., 31, 466-487.
[11] Sebos, I. et al., 2009, Catalytic hydroprocessing of cottonseed oil in petroleum diesel mixtures for production of renewable diesel, Fuel, 88, 145-149.
[12] Donnis, B. et al., 2009, Hydroprocessing of bio-oils and oxygenates to hydrocarbons. Understanding the reaction routes, Topics on Catalysts, 52, 229-240.
[13] Steijns, M. et al., 1981, Hydroisomerization and Hydrocracking. 2. Product distributions from n-decane to n-dodecane, Ind. Eng. Chem. Prod. Res. Rev., 20, 654-660.
[14] Gutiérrez-Antonio, C.; Briones-Ramírez, A., 2010, Speeding up a multiobjective genetic algorithm with constraints through artificial neuronal networks, Comp. Aided Chem. Eng., 28, 391-396.

Biocatalysts for enhanced CO_2 post-combustion capture efficiency in absorption columns

Anna-Katharina Kunze[1], Vera Penner[1], Maria T.Gundersen[2], John M. Woodley[2], Andrzej Górak[1,3], Philip Lutze[1]

[1]TU Dortmund University, Dortmund, Germany;

[2] Technical University of Denmark, Lyngby, Denmark

[3] Lodz University of Technology, Lodz, Poland

Abstract

The reduction of greenhouse gas emissions, especially CO_2, is an important topic with regard to its possible influence on the worldwide climate change. Reducing the CO_2 emissions by capturing the CO_2 is one possibility to reduce the emissions, but it is only promising if the energy for the capture process is reasonable towards the produced energy. Reactive absorption using amines as solvent systems prove its feasibility for CO_2 separation for decades, but it did not find wide spread large scale application, due to the high energy amount necessary for solvent regeneration as well as degradation of primary amine solvents, such as monoethanolamine. Therefore, process improvement by process intensification in the field of CO_2 separation is necessary to increase the efficiency of such processes.

This work investigates the feasibility of biocatalysts for technical scale application in packed bed absorption columns for post-combustion CO_2 capture. The enzyme called carbonic anhydrase is advantageous towards chemical catalyst, as it is not volatile, no toxic components are formed due to degradation and it is biodegradable. Therefore, a systematic screening on solvent systems for the application of carbonic anhydrase is carried out to prove the pH and temperature stability range of the enzyme. The best performance enzyme solvent systems are than applied in a miniplant scale absorption column to prove the technical feasibility.

Keywords

Reactive Absorption, carbonic anhydrase, enzyme, packed bed columns

1. Introduction

There is a need to reduce emissions of CO_2 as it is one of the most relevant greenhouse gases. Currently, state of the art for CO_2 separation is chemical absorption using aqueous amine solutions, such as e.g. monoethanolamine. Currently, the industrial application of CO_2 capture from power plant flue gas is restricted due to a significant reduction of the process efficiency caused by the high amount of energy necessary for the absorbent regeneration. In the past, it was reported, that 3.7 GJ/ ton CO_2 are necessary to achieve a 90 % removal for a absorption plant with a capacity of 5000 Nm³/h [1]. Furthermore, a loss of 1.4 kg

MEA per ton CO_2 was lost though oxidative degradation was observed [1]. Therefore, the use of 30 wt.-% MEA based reactive absorption is wide spread, large scale application in the future is restricted. But process intensification with a focus on new materials and new technologies for CO_2 separation could be beneficial and is there with the main focus of this work.
Process intensification of post combustion CO_2 capture could be realized by using solvents, which need less energy for regeneration. The trade-off between reduced energy for desorption and reduced absorption rate could be solved by applying catalysts for well-known reaction systems to enhance their reaction rate drastically.

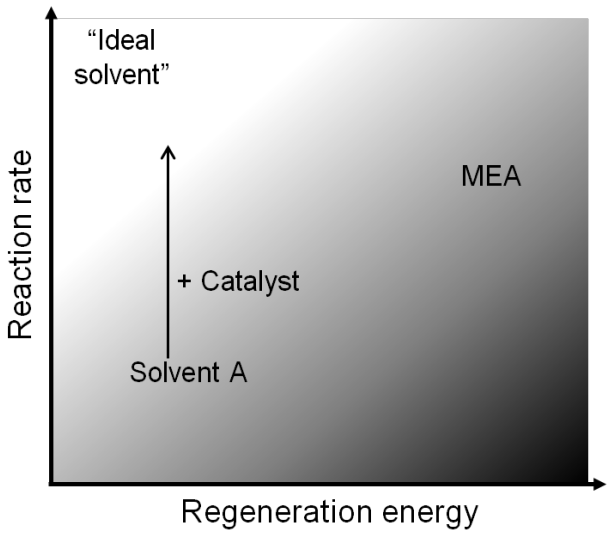

Figure 1: Qualitative trade-off between reaction rate and regeneration energy towards operational costs, represented by the grayscale

Catalysts here are chemical or biochemical species that enhance the reaction rate without an overall chemical transformation. Catalysis for reactive absorption is predominantly carried out with homogenous catalysts, which means the catalyst is soluble in the solvent. Another method that is applied especially in reactive distillation is heterogeneous catalysis, in which the catalyst is immobilized within the column or within the packing. This method is especially advantageous for thermally-sensitive catalysts that should not be in the solvent streams, which are sent to regeneration.
This work will show how enzymes could contribute as non-volatile, non-toxic and biodegradable biocatalysts to reactive absorption systems and therewith enhance the competitiveness of the solvent. The benefit of enzymes is that they are renewable raw materials in comparison to classical catalysts. The resulting higher process efficiencies would proof the potential for industrial application of CO_2 capture in the future.

2. Enzyme / solvent systems

The biocatalyst investigated in the present work is a carbonic anhydrase. Carbonic anhydrases are part of the enzyme class lyases and can be found in mammal, plant and bacteria cells [2]. Carbonic anhydrase catalyzes the hydration of CO_2 shown as the overall reaction:

$$CO_2 + H_2O \rightleftharpoons H_2CO_3 \quad (1)$$

Different aqueous solvents have been tested in literature and so far, one of the most promising is potassium carbonate K_2CO_3. Carbonic anhydrase could be integrated into the system to enhance the reaction rate up to a factor of 40 % for CO_2 absorption with K_2CO_3 [2].

The rate of the catalyzed reaction highly depends on the form of carbonic anhydrase and the operating conditions. Depending on the origin of the CA, also its stability due to denaturation is investigated. A decrease of enzyme stability results in a loss of activity due to unfolding of the protein chains. Critical factors for using the enzyme for industrial CO_2 separation are:

- pH: Carbonic anhydrase can be unstable at alkaline conditions [2]
- Temperature: Carbonic anhydrase can be unstable for temperatures higher than 50 °C [3]
- Impurities in the flue gas [3]

The use of aqueous potassium carbonate solution for CO_2 separation is known as the hot potash process, due to the temperature of the absorption solvent that enhances the reaction rate. Carbonic anhydrase could be able to fill the gap in absorption efficiency between the hot potash process and the absorption using potassium carbonate at lower temperatures of the overall process to save energy costs. Therefore, this work will present strategies how to apply carbonic anhydrase as a biocatalyst in reactive absorption processes and show how absorption efficiency is influenced by the enzyme. Additionally, a detailed modeling of carbonic anhydrase supported absorption processes in columns will be carried out to investigate the potential for process intensification due to the use of biocatalysts to enhance CO_2 post-combustion capture efficiency compared to a base-case process.
To evaluate the feasibility of enzymes to catalyze reactive absorption, first of all a systematic investigation of the enzyme stability needs to be carried out. The first step is to analyze the stability of the enzyme due to physical and chemical conditions, such as temperature and pH. The next step is the investigation of enzyme solvent systems. Therefore, a list of promising solvents that already prove their capability for reactive CO_2 absorption has been set up and Table 1 shows an extract of this list.

Table 1: Excerpt of the solvent list under investigation

Alkali carbonates	Amines
K_2CO_3	MEA
	MDEA
	DEEA

Before starting the absorption column experiments in miniplant scale a suitable solvent/enzyme system needs to be determined by a two-step investigation. First of all, the general stability towards temperature and pH was studied separately. Afterwards the stability of the enzyme in the solvents was tested by carrying out small scale experiments. Carbonic anhydrase stability in these systems has been

investigated and the most promising solvents have been chosen for experiments carried out in pilot scale absorption columns.
Major goal of this work is to show that reactive CO_2 absorption using biocatalysts has the ability to outperform conventional processes in special process configurations with regard to the necessary energy demand per separated ton CO_2. An experimental study on the performance of enzymes in packed columns is carried out and the results are modeled using a simulation platform by Aspen Tech®. Evaluation of an absorption process on a simulative basis is highly dependent on the model parameters introduced into the models.

3. Absorption in columns using enzyme catalyzed solvent systems

Mini plant scale absorption experiments are conducted to show the performance and the technical feasibility of the enzyme solvent system.
The experiments are carried out in an absorption column with an inner diameter of 56 mm and a packing height of 2.3 m. Figure 2 shows the flowsheet of the absorption mini plant. The mini plant consists of a packed bed absorption column that is run in counter current mode. It is connected in series with a humidifier column, in which the gas stream is saturated with water to prevent evaporation in the absorber column (not pictured in Figure 2). Pressurized air is mixed with 15 vol.-% CO_2 to simulate the conditions in a post combustion capture plant. The experiments in the absorption column are carried out in a temperature range between 30 –50 °C and at ambient pressure. Impurities, such as traces of SO_x and NO_x are neglected for the first investigations.

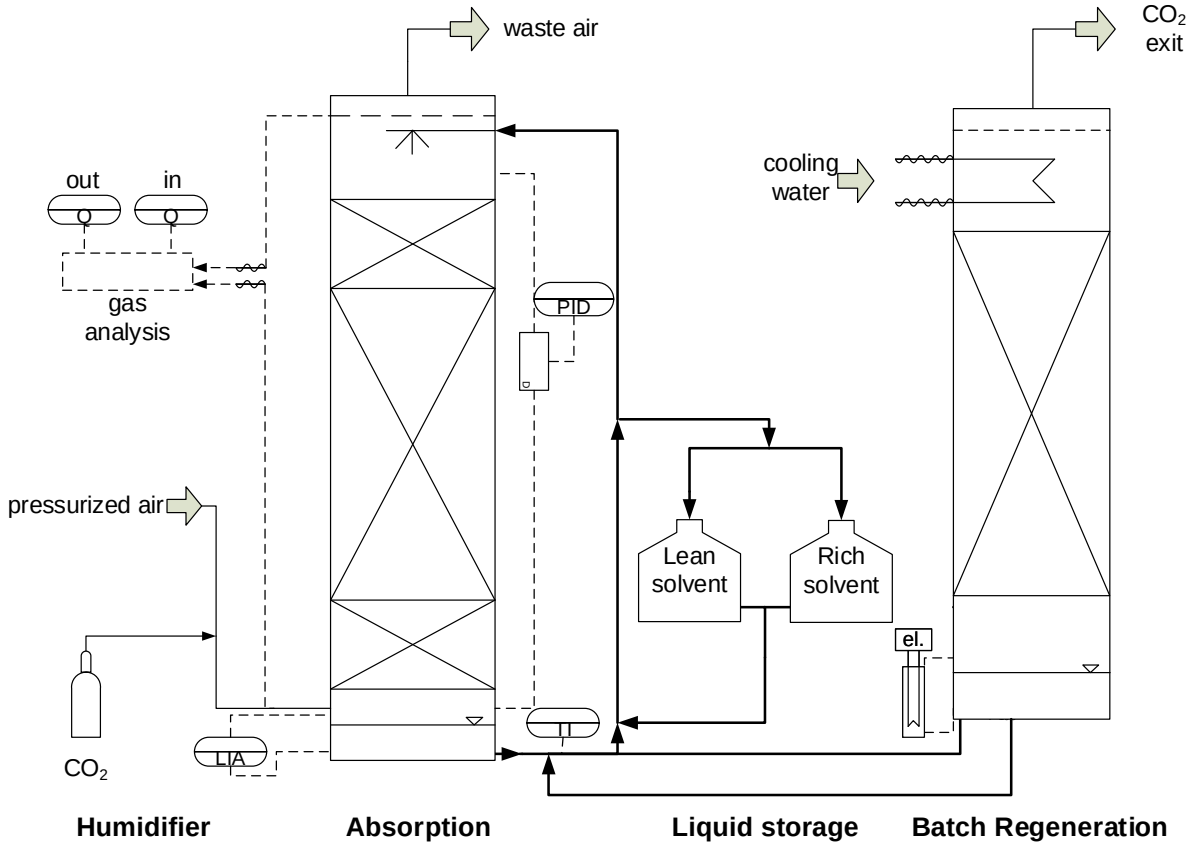

Figure 2: Experimental set-up

3.1 Benchmark miniplant experiments

Experiments investigating the solvent without the addition of the carbonic anhydrase have been carried out to see the influence of the enzyme. Therefore, experiments using a 3 mol.-% potassium carbonate solution have been carried out, as literature shows that this concentration is feasible for the addition of enzyme. The comparative studies at room temperature are shown in Figure 3.

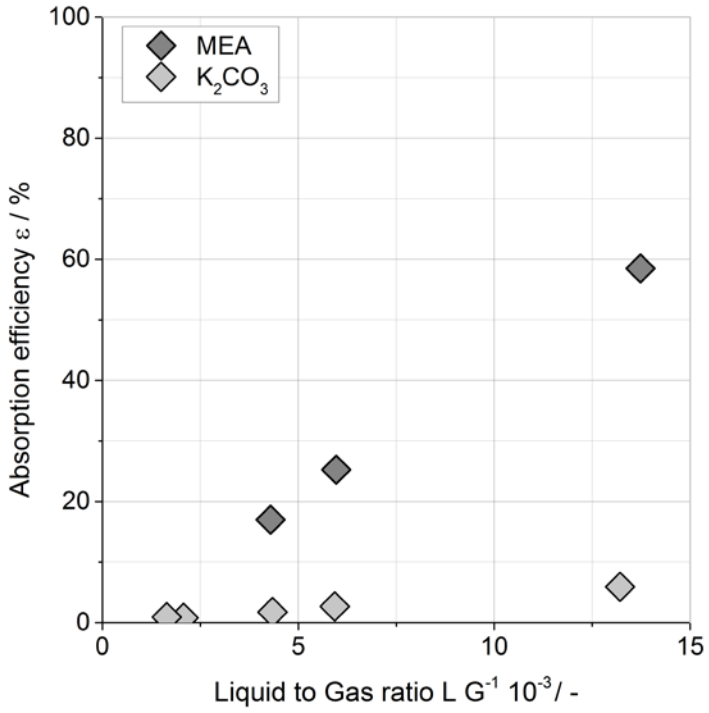

Figure 3: Comparative experiments of 3 mol.-% MEA and K_2CO_3 to show the potential of K_2CO_3 to be activated by carbonic anhydrase as a biocatalyst at 25 °C

For an absorption process at room temperature the enzyme would have to overcome a gap in absorption efficiency of a factor of 10 to achieve comparable absorption efficiencies as equivalent concentrated MEA as shown in Figure 3. On the other hand desorption enthalpy of the potassium carbonate is assumed to be 3 folds smaller than the one of MEA [4], which means that the liquid to gas ratio can be drastically increased.

4. Conclusions

The reduction of CO_2 emissions for fossil fuel based power plants gives a huge opportunity for process intensification. The application of new materials and new technologies could help to realize a more energy efficient separation and therewith a large scale application in the future.

This work investigated the application of a biocatalyst, the enzyme carbonic anhydrase to catalyze the reaction within a reactive absorption process. The reaction rate of solvent systems with a low reaction rate is enhanced but the beneficial low energy necessary for regeneration is used to save energy for the overall separation process.

Acknowledgements

The research leading to these results has received funding from the European Union Seventh Framework Programme FP7/2007-2013 under grant agreement n° 608535.

References

[1] **Knudsen, J.N., Jensen, J.N., Vilhelmsen, P.-J.**, et al., in *9th International Conference on Greenhouse Gas Control Technologies, GHGT-9*, Washington DC (**2009**).

[2] **Lindskog, S., Henderson, L.E., Kannan, K.K.**, et al., in *The Enzymes* (Ed: Paul D. Boyer), Academic Press (**1971**).

[3] **Russo, M.E., Olivieri, G., Marzocchella, A.**, et al., Post-combustion carbon capture mediated by carbonic anhydrase, *Separation and Purification Technology 107*, pp. 331–339 (**2013**).

[4] **Behr, P., Maun, A., Tunnat, A.**, et al., Optimization of CO2 Capture from Flue Gas with Promoted Potassium Carbonate Solutions, *GHGT-11 37*, pp. 1554–1565 (**2013**).

Biocatalytic reactive distillation: Fundamentals and experimental investigations

R. Heils[1], M. Wierschem[2], L. Hilterhaus[3], A. Liese[3], P. Lutze[2], I. Smirnova[1]
[1]Institute of Thermal Separation Processes and [2]Institute for Technical Biocatalysis, Hamburg University of Technology, Germany;
[3]Laboratory of Fluid Separations, TU Dortmund University, Germany

Abstract

In reactive distillation processes, the integration of reaction and separation in one unit operation reduces equipment and operational costs as well as increases conversion and selectivity. Therefore, an integrated setup of the reactive distillation can be advantageous for enzymatic reactions which often show low yields in a stirred tank reactor (STR) due to equilibrium limitation and/or product inhibition.
In this work, a silica-based coating was developed for commercial structured packings in order to immobilize lipase B from *Candida antarctica* (CALB) in reactive distillation columns. The biocatalytic coatings were successfully tested in a batch reactive distillation column for the transesterification reaction of ethyl butyrate with *n*-butanol. Under the given process conditions, the coatings showed sufficient stability and activity, even after repeated use.
The production of the biocatalytic coatings by means of a newly developed spray-coating setup is presented that resulted in an increased reproducibility of the coatings and reduction in precursor consumption. As an example for enantioselective enzymatic reactions, the kinetic resolution of racemic 2-pentanol was performed in a discontinuous reactive distillation setup in the presence of the biocatalytic coatings containing lipase CALB.
As future work, the obtained experimental data can be used for modeling and optimization of this process. Therefore, the kinetic of the transesterification reaction of ethyl butyrate with *n*-butanol is described by means of the Michaelis Menten double substrate model. The model parameters are presented in this work. In addition, the investigation of the hydrodynamic properties of the coated structured packings is also paramount.

Keywords
Reactive distillation, enzymes, biocatalytic coatings, kinetic resolution

1. Introduction

Reactive distillation is an integrated separation process that is well-established in industry for diverse etherification and esterification reactions (e.g. MTBE, TAME, methyl acetate) [Harmsen 2007]. By integrating the reaction and separation process into one operational unit, the equipment and operational costs can be reduced as well as the yield of equilibrium-limited reactions can be enhanced by removal of the product. Enzyme-catalyzed reactions often show a thermodynamic and/or kinetic limitation which can be overcome by this kind of integrated reaction/separation setups. In biocatalytic applications there are different examples of integrated processes, e.g. *in situ* adsorption, *in situ* extraction and reactive membrane processes [Bechtold et al., 2009]. Due to the thermal sensitivity of the enzymes, up to now the reactive distillation was not considered for enzymatic reactions, although improved immobilization methods and the discovery of more robust enzymes would in principle allow the application in reactive distillation processes.
The minimum requirement for the application of enzymes in distillation columns is that the enzymes are stabilized by means of immobilization on a solid carrier. The classical approach to introduce such a heterogeneous catalyst into distillation columns is by means of reactive packing structures like KATAPAK-SP. An alternative method is the coating of the column internals with a catalytically active coating, which is part of the presented work.

2. Results and discussion

2.1 Development of a biocatalytic coating for structured packings
Recently, a silica-based coating was developed for commercial structured packings in order to immobilize lipase CALB in reactive distillation columns [Smirnova et al. 2011] (Figure 1). The advantage of the coating procedure is that the increased surface area of the packing can be used both for a better vapor-liquid mass transfer and also as contact area for substrates and biocatalyst. The more uniform distribution of the catalyst over the complete packing segment promises an improved separation performance compared to catalyst pockets within catalytic structures like KATAPAK SP.

Figure 1 - Silica-based coating for immobilization of lipase CALB on structured packing (Montz A3-500 or Sulzer BX)

The silica-matrix of the coating is synthesized by the sol-gel reaction, which adds great flexibility to the immobilization method. By adjusting the sol-gel parameters the chemical and structural properties of the biocatalytic coating were adapted to the favored conditions of the enzyme. For the investigated transesterification reaction the immobilized lipase CALB showed an increased activity in hydrophobic coatings produced with alkyl-substituted silanes [Reetz et al. 1997; Heils 2012]. Furthermore, the composition of the sol-gel was adjusted so that it provides proper adhesion to the stainless steel surface of the structured packing. In addition, the coating has to be stable in organic solvents. For the preparation of the sol-gel, TMOS and MTMS were mixed with MeOH and stirred in an ice bath (solution A). In solution B, all water-soluble components were prepared, i.e., sodium fluoride (1 M) as catalyst, PEG, enzyme solution, and additional water. Solution B was then mixed with solution A, thus starting the polymerization reaction. The composition of the silica-gel used for the immobilization of lipase CALB onto the structured packings is summarized in Table 1.

Table 1 - Composition of silica-based coating for immobilization of lipase CALB on structured packings

	Component	Mass [g]
A	Methanol	12,88
	Methyltrimethoxysilane (MTMS)	10,90
	Tetramethyl orthosilicate(TMOS)	3,05
B	H_2O, dest.	4,78
	Enzyme CALB-L (Novozyme A/S)	4,00
	Sodium flouride, 1M	1,88
	Polyethylene glycol (PEG), MW 400	0,52
	∑	38,01

In our previous work, the production of the biocatalytic coatings by means of a simple dip-coating method is described [Heils 2013]. The main disadvantage of this method is the high waste stream of silica precursors of up to 97%. In a new coating procedure, a pressurized air driven spray pistol is used to apply the silica-gel onto the packing structure. The silica precursors and the catalyst for the polymerization reaction are combined only within the nozzle of the pistol so that waste streams are considerably reduced. The spray of the lipase CALB solution through the nozzle did not cause any additional deactivation of the enzyme compared to the dip-coating procedure.

2.2 Application of biocatalytic coatings in reactive distillation processes

Subsequently, the performance of the biocatalytic coating was investigated in a discontinuous reactive distillation setup for the transesterification reaction of ethyl butyrate with *n*-butanol. The glass column (d_i = 45 mm) was equipped with 960 mm of coated structured packings with no additional rectifying section. In order not to exceed a maximum temperature of 60 °C in the column, a vacuum of appr. 10 kPa was applied.

The stability of the biocatalytic coating was determined by monitoring the mass of the coating before each experiment in the reactive distillation (RD) column (Figure 2).

The major mass loss occurs after the first experiment with approximately 20 wt% coating (of the initial coating mass). Afterwards the loss of coating decreases to an average value of 2.2 %. The long-term stability was also tested in a stirred tank reactor (STR) containing an equimolar mixture of the substrates at 60 °C. Similar to the experiments in the RD column, the weight loss was highest after the first run (app. 19 %) and was rather stable for all further experiments with an average mass loss of 2.6 wt%. Due to the major weight loss after the first experiment, it is appropriate to wash the coatings in a short-chained alcohol/ester (< 5 C-atoms) before first use.

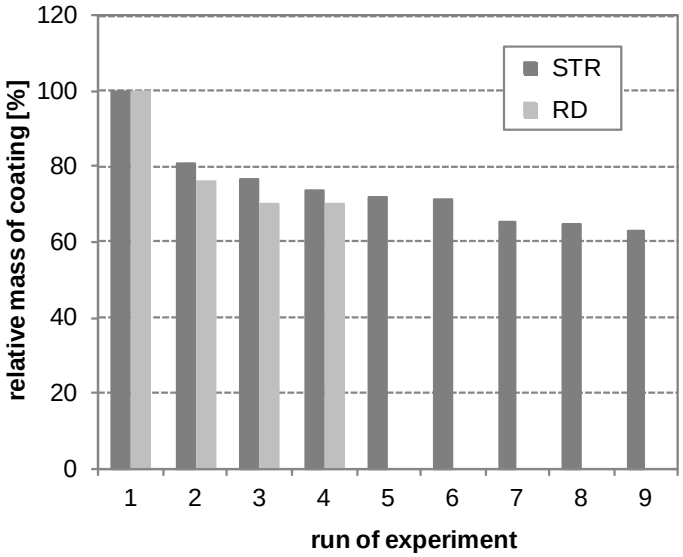

Figure 2 - Stability of the biocatalytic coatings in a mixture of ethyl butyrate and n-butanol. Conditions: Stirred tank reactor (STR), 60 °C, duration : 30 min; Reactive distillation (RD), 30 – 60 °C ($T_{distillate}$ – T_{bottom}), duration 6-9 h.

This successful introduction of enzymes in a reactive distillation column opened up a new application field for biocatalytic reactions. Literature research showed that for a maximum bottom temperature of 80 °C, 5 esterification and 108 transesterification reactions could be carried out in a reactive distillation setup. In addition, reactions with chiral molecules that cannot be realized with a chemical catalyst or only in several reaction steps were considered. Due to the increased selectivity of lipase CALB, the kinetic resolution of (R/S)-2-pentanol was chosen as an example for an enantioselective reaction in the reactive distillation setup (Figure 3: Kinetic resolution i.e., reactive separation of enantiomeric mixtures by selective catalysts).

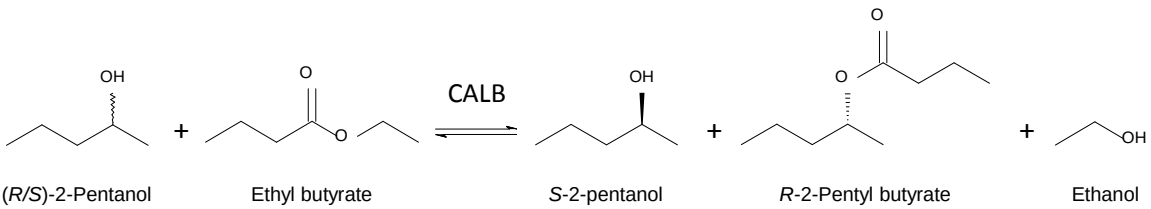

Figure 3 - Reaction equation for the kinetic resolution of racemic 2-pentanol with ethyl butyrate catalyzed by lipase CALB

The stability of the coating under process conditions was comparable to the previously considered system of ethyl butyrate/*n*-butanol. The product ethanol accumulates in the distillate of the column and is withdrawn to drive conversion. By means of a stepwise removal of distillate stream the reaction yield was raised to

86 % compared to app. 40 % yield at equilibrium concentration. The selectivity of the reaction in the reactive distillation column was still high, with $ee_{2\text{-}PeBu}$ values of 97 %.

$$\text{enantiomeric excess: ee\%} = \frac{\text{R-2-PeBu} - \text{S-2-PeBu}}{\text{R-2-PeBu} + \text{S-2-PeBu}} * 100\%$$

Furthermore, a feasibility study was carried out to demonstrate that enzymatic reactions are fast enough to be conducted in a continuous reactive distillation setup [Heils 2014]. The transesterification reaction of *n*-butanol with ethyl butyrate served as a model reaction. A Michaelis Menten double substrate model in combination with the Arrhenius model was used to describe the reaction kinetics for the concentration and temperature range expected within the distillation column. Initial rate measurements were carried out in a solvent system, to be able to vary the concentration of one of the substrates while the other is kept constant. The kinetic parameters were then fitted to the whole set of experimental data. The model was transferred to the solvent-free system with good agreement to the experimental value (Figure 4). Finally, process simulations were carried out with an Aspen Custom Modeler non-equilibrium stage model validated for a DN50 pilot-scale column. For an optimized setup and operating conditions, conversion rates of more than 90 % were achieved for *n*-butanol and 26 % for ethyl butyrate.

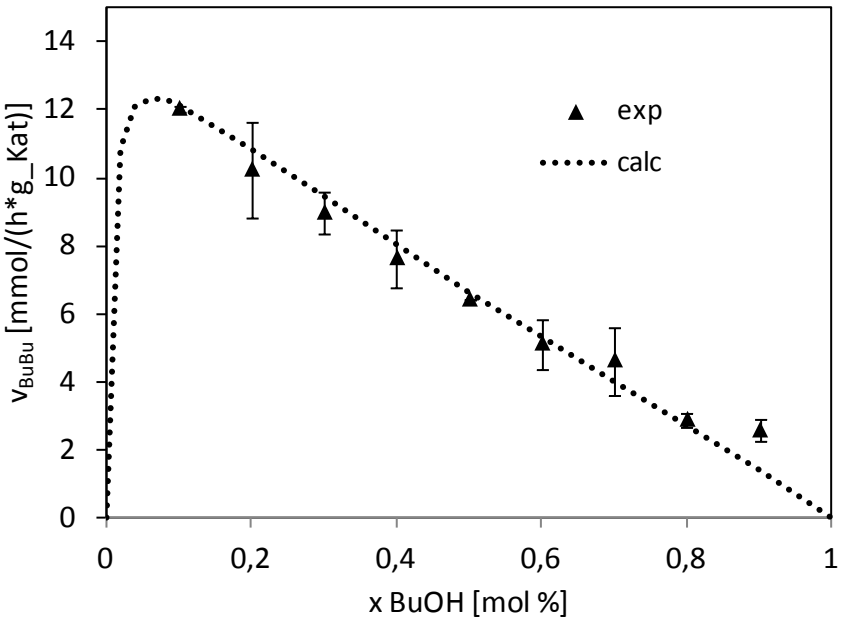

Figure 4 - Initial rate measurements for the transesterification reaction of ethyl butyrate with n-butanol in the presence of lipase CALB immobilized within the silica-based gel coating. The measurements were conducted at 60 °C in a solvent-free system.

3. Conclusions

A silica-based coating for structured packings has been developed in order to immobilize lipase CALB for application in reactive distillation processes. Hydrophobization of the gel matrix with alkoxysilanes improves the activity of the lipase for organic synthesis. The biocatalytic coating shows very good stability under the given process conditions, i.e. at temperatures up to 60 °C in organic solvents. For the production of the coatings, a new spray-coating setup is presented.

The proof-of-concept for the application of the biocatalytic coatings in the reactive distillation column has been demonstrated with a transesterification reaction of ethyl butyrate with *n*-butanol. As an example for enantioselective reactions, the kinetic resolution of racemic 2-pentanol has been carried out in the reactive distillation setup. By withdrawing the light-boiling product via the distillate stream, the reaction yield is increased clearly beyond the reaction equilibrium to a yield of 86 %.
For a simulation-based feasibility study of an enzymatic reaction in a continuous reactive distillation setup, the reaction kinetics of the transesterification reaction has been investigated and the model parameters are presented.
In summary, this work presents a new immobilization method for the introduction of enzymes in a reactive distillation column. In addition, the first realization of an enzyme-catalyzed kinetic resolution reaction in a reactive distillation column shows great potential for enantioselective synthesis.

Acknowledgements

The authors are grateful for the financial support of German Research Foundation (No. SM 82/9-1). We also thank Sulzer Chemtech Ltd. and Julius MONTZ GmbH for the provision of structured packings.

References

Bechtold, Matthias; Panke, Sven (2009): In situ product recovery integrated with biotransformations. In: *CHIMIA International Journal for Chemistry* 63 (6), S. 345–348.

Harmsen, G. Jan (2007): Reactive distillation: the front-runner of industrial process intensification: a full review of commercial applications, research, scale-up, design and operation. In: Chemical Engineering and Processing: Process Intensification 46 (9), S. 774–780.

Heils, Rene; Sont, Annika; Bubenheim, Paul; Liese, Andreas; Smirnova, Irina (2012): Integration of Enzymatic Catalysts in a Reactive Distillation Column with Structured Packings. In: *Industrial & Engineering Chemistry Research* 51 (35), S. 11482–11489.

Heils, Rene; Niesbach, Alexander; Wierschem, Matthias; Claus, Dierk; Soboll, Sebastian; Lutze, Philip; Smirnova, Irina (2014): Integration of enzymatic catalysts in a continuous reactive distillation column: reaction kinetics and process simulation. *submitted*

Reetz, Manfred T.; Zonta, Albin; Simpelkamp, Jörg (1996): Efficient immobilization of lipases by entrapment in hydrophobic sol-gel materials. In: *Biotechnology and Bioengineering* 49 (5), S. 527–534.

Smirnova, Irina; Liese, Andreas; Fieg, Georg; Hilterhaus, Lutz.; Bubenheim, Paul; Sont, Annika (2011): Ein in der Reaktivrektifikation einsetzbarer, einen Biokatalysator aufweisender Kolonneneinbau und dessen Verwendung in der Reaktivrektifikation, *Patent DE 102010 028788 A1*

Reactive Distillation, an Intensifying Tool in Biorefinery

D. Painer, S. Lux, M. Siebenhofer
Graz University of Technology/Institute of Chemical Engineering and Environmental Technology, NAWI Graz, Graz/Austria

Abstract
An alternative separation process for effluents from biorefinery, containing acetic acid, formic acid and water, is presented. This waste water treatment, for instance in the pulp and paper industry, was intensified by combination of chemical reaction with separation. The ternary system acetic acid/formic acid/water is an impressive example for non-separable mixtures from the distillation point of view. Facing both, a binary high boiling azeotrope and a ternary saddle point azeotrope, constituent isolation is impossible with simple distillation. Via reactive distillation the carboxylic acids are esterified with methanol and the low boiling esters can be separated easily in the distillate. Due to permanent removal of the reaction products methyl formate and methyl acetate, the reaction equilibrium is shifted to the product side. Formic acid esterification is faster than acetic acid esterification, explainable by the acid strength, therefore selective removal of formic acid is feasible. Validation was carried out in batch reactive distillation experiments, starting from all four distillation fields. With a molar ratio of methanol : formic acid = 2, complete elimination of formic acid from the ternary mixture was achieved.

Keywords
Reactive distillation, azeotropic mixtures, carboxylic acids

1. Introduction

Valuable by-products from biorefinery are hardly available in simple mixtures of appropriate composition. Dilute broths provide illustrative examples of multicomponent mixtures from the isolation point of view. Ternary mixtures of acetic acid, formic acid and water for instance, are representative by-product constituents of pulping processes. Facing both a binary high boiling azeotrope and a ternary saddle point azeotrope makes isolation of the pure acids challenging. The binary systems acetic acid/formic acid and acetic acid/water show low relative volatility. Complete separation of constituents by simple distillation is not possible due to the impressive vapor-liquid-equilibrium.
Reactive separations provide a flexible technological toolbox for such complex azeotropic mixtures. Chemical reactions change the substance properties whereby separation limits may be overcome. Through combination of equilibrium reactions with separation, the reaction products are isolated continuously and the equilibrium is shifted to the product side.

1.1 Vapor-liquid-equilibrium

The vapor-liquid-equilibrium is the basic need for any distillation process. According to the data in table 1 literature shows varying results for the ternary mixture acetic acid/formic acid/water.

	Boiling point °C	Acetic acid mol%	Formic acid mol%	Water mol%
Aristovich et al. 1960 [1]	107.1	15.4	49.1	35.5
Aristovich et al. 1962 [2]	107.1	12.5	48.2	39.3
Wisniak et al. 1977 [3]	107.0	16.8	46.9	36.3

Table 1: Literature data for the saddle point azeotrope of acetic acid/formic acid/water at 1.013 bar

Therefore the ternary vapor-liquid-equilibrium was reinvestigated at ambient pressure. The experiments were performed in a Fischer vapor-liquid-apparatus, type 0601. In Figure 1 the experimentally determined boiling point surface of the ternary system is presented.

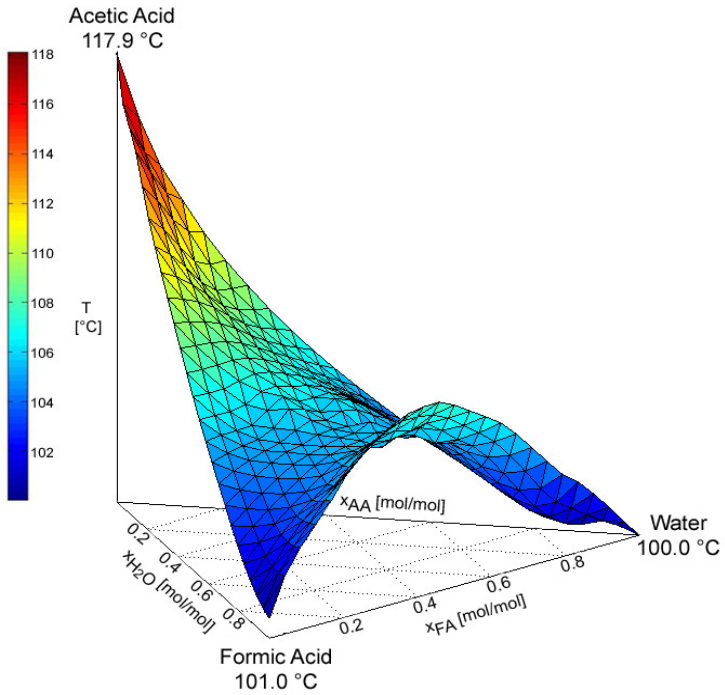

Figure 1: Boiling point surface of the ternary system acetic acid/formic acid/ water at ambient pressure, binary data from [4]

The composition of the saddle point azeotrope at ambient pressure was 14 mol% acetic acid, 49 mol% formic acid and 37 mol% water. The boiling point was detected at 105.6 °C.

1.2 Separation concepts

Reactive distillation via esterification of the acids with short-chain alcohols, namely methanol, allows for removal of the low boiling methyl esters in the distillate. Two concepts are conceivable. The difference in the acid strength of formic acid and acetic acid renders selective esterification of formic acid possible in a first step, preparing the major amount of aqueous acetic acid for further downstream processing.

Alternatively, both acids may be esterified in heterogeneous catalytic esterification with cation-exchange resins and excess methanol. The low boiling methyl esters are separated from the aqueous carrier by combination of simultaneous rectification and/or subsequent pervaporation.

1.2.1 Experimental setup

The batch reactive distillation experiments were carried out in a 30 cm vigreux column connected to a condenser and a reflux splitter. The reboiler was a 500 ml three-neck flask, equipped with a heating plate from Heidolph. The temperature was recorded in the reboiler, at the upper end of the vigreux column and below the condenser.

The continuous reactive distillation was investigated in a 2 m distillation column with 6 mm glass Raschig ring packings. The acid-water mixture and the methanol were directly fed to the reboiler, where the reaction was performed.

2. Results and discussion

Through combination of the process steps esterification, rectification and pervaporation, aqueous mixtures of acetic acid and formic acid can be completely separated.

Starting feed compositions were chosen in each distillation field for the reactive distillation experiments. The molar ratio of methanol : formic acid was varied between 1 and 2.4. For equal molar ratio of methanol and formic acid highly pure methyl formate was collected in the distillate. In the bottom product a significantly reduced amount of formic acid was determined.

With a molar ratio of methanol to formic acid of 2.4 complete elimination of formic acid was observed. The results are shown in figure 2.

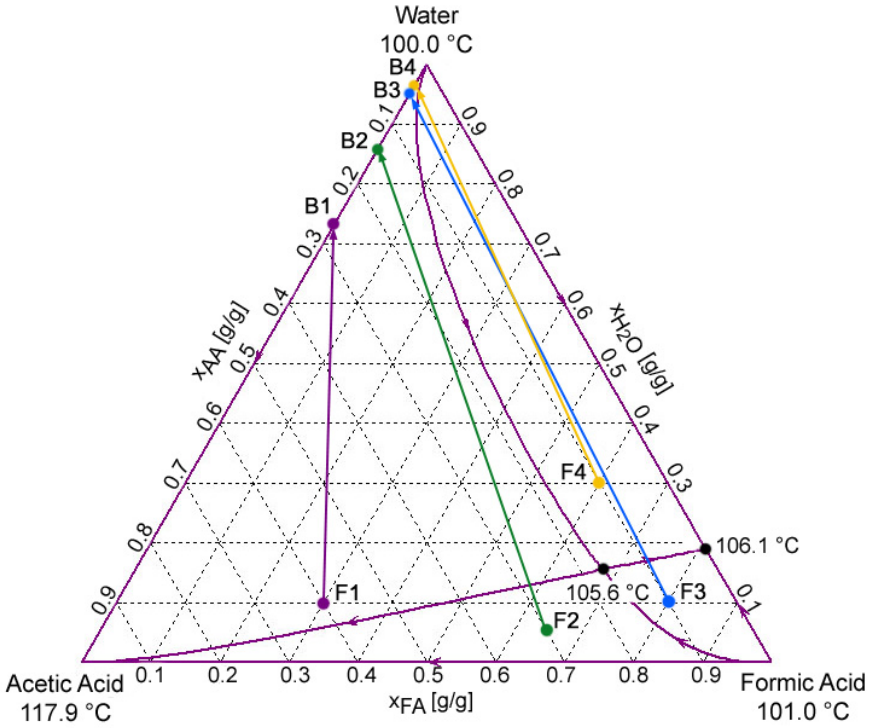

Figure 2: Batch reactive distillation results at ambient pressure; molar ratio of methanol : formic acid = 2.4; F…Feed, B…Bottom product

Starting from each distillation region the binary system acetic acid/water as bottom product was obtainable with a molar ratio of methanol to formic acid of 2.4. Formic acid reacts faster with methanol and it is removed completely from the feed mixture independent of the starting concentration.

Figure 3 shows the results from the continuous reactive distillation experiments with different molar ratios between methanol and the carboxylic acids.

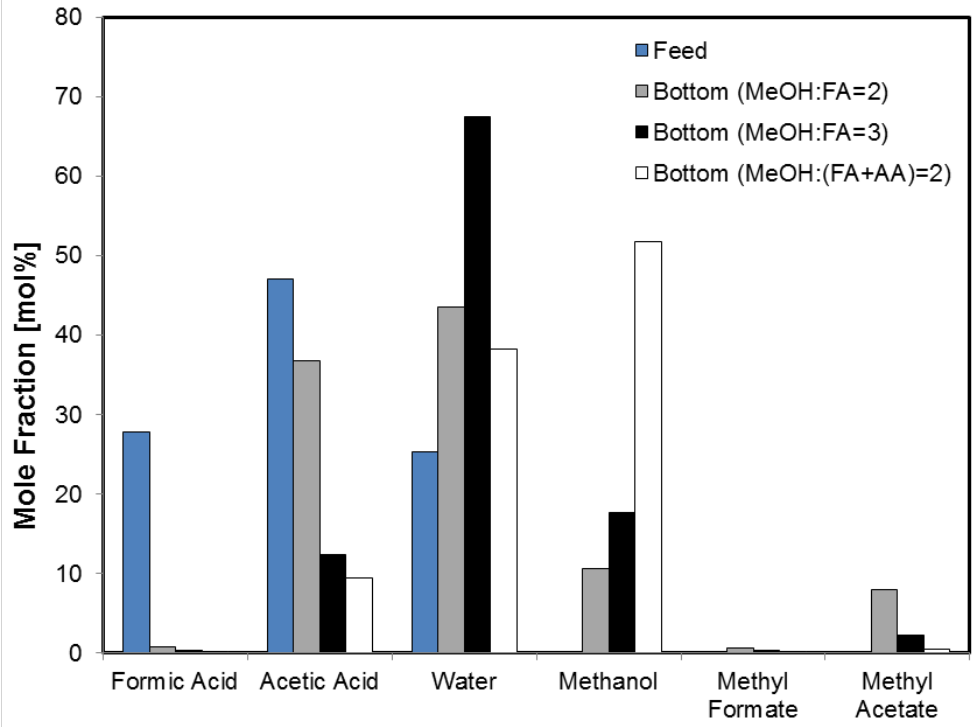

Figure 3: Composition of the bottom products of continuous reactive distillation with different molar ratio of methanol (MeOH) to formic acid (FA) and acetic acid (AA)

The results from continuous reactive distillation experiments validated the selective removal of formic acid from the ternary mixture. The molar ratio of methanol to formic acid of 2 already shows sufficient depletion of formic acid in the bottom product. Formic acid concentration decreases with increasing methanol in the feed.

3. Conclusions

The selective separation of formic acid from ternary mixtures of acetic acid/formic acid/water by reactive distillation was successfully demonstrated. In batch mode as well as continuous mode reactive distillation experiments complete separation of formic acid from acetic acid and water was demonstrated.

References

[1] Aristovich, V.Y., Lutugina, N. V., Malenko, Y.I., Morachevskii, A.G. 1960: Investigation of Liquid-Vapor Equilibria and Rectification Processes in the ternary system Water – Formic Acid – Acetic Acid. Zhurnal Prikladnoi Khimil 33, S. 2693-2698

[2] Aristovich, V.Y., Levin, A.I., Morachevskii, A.G. 1962: Vapor-liquid equilibriums in low-molecular-weight fatty acids-water systems. Tr. Vses. Nauchn.-Issled. Institute Neftekhim 5, S. 84-101

[3] Wisniak, J., Tamir, A. 1977: Vapor-Liquid Equilibria in the Ternary Systems Water-Formic Acid-Acetic Acid and Water-Acetic Acid-Propionic Acid. Journal of Chemical and Engineering Data 22, S. 253-260

[4] Gmehling, J.; Onken, U.; Arlt, W.; Grenzheuser, P.; Weidlich, U.; Kolbe, B.; Rarey, J.: Vapor-Liquid Equilibrium Data Collection. Dechema, 1991-2010

PROFLUX™ Severe Service Grid
Dealing with challenging applications

Izak Nieuwoudt[1], Patrick Quotson[2], Alessandro Ferrari[3]
[1]Koch-Glitsch, Wichita, Kansas, USA
[2]Koch-Glitsch, Wichita, Kansas, USA
[3]Koch-Glitsch, Bergamo, Italy

Abstract
Unit operations such as refinery vacuum towers, FCC main fractionators, coker fractionators, visbreaker fractionators and ethylene quench towers are plagued with fouling issues. Special tower internals are needed to extend run lengths in these fouling applications. A new product, called PROFLUX™ severe service grid, was developed with these applications in mind. PROFLUX severe service grid offers ease of installation, mechanical rigidity, acceptable separation efficiency, improved fouling resistance, high capacity, low pressure drop and good entrainment removal. This paper details performance data taken on this new product.

Keywords
Grid, Packing, Fouling, Vacuum, FCC, Ethylene, Refining

1. Introduction

Applications such as ethylene quench towers, refinery vacuum towers and FCC, coker and visbreaker fractionators pose significant challenges. These applications have zones that are considered as extremely fouling. To extend the run lengths of these units, special tower internals are used in the heavily fouling zones. In these applications some combination of the following performance indicators is desirable: mass and heat transfer efficiency; droplet de-entrainment; low pressure drop; fouling resistance; high capacity; mechanical resistance to process upsets; ease of installation; and ability to be cleaned. Conventional packings generally struggle with fouling and cleaning issues. Trays generally struggle to meet the fouling resistance and pressure drop requirements of these applications. Shed decks and baffle trays do offer better fouling resistance, but they do not offer much in terms of mass and heat transfer efficiency or droplet de-entrainment. Severe service grid products have been used in several of these applications, and have been combined with structured packing to increase the mass transfer efficiency and droplet de-entrainment. The challenge of improving equipment performance in these severe service applications is one of developing equipment that would simultaneously address issues around efficiency, capacity, pressure drop, de-entrainment, mechanical rigidity and fouling resistance. A novel product, called PROFLUX™ severe service grid, was developed to specifically address these issues. A photograph of PROFLUX severe service grid is shown in Figure 1. The key features of this product are[(1)]:

- The blades are shaped in a way that reduces the likelihood of fouling material adhering.
- The blades are spaced apart to remove contact points where stagnant liquid could coke or fouling material could be held up.
- A welded construction is used to obtain a high degree of rigidity.

PROFLUX severe service grid is currently available in two styles designated by the numbers 45 and 64. Style 45 has lower pressure drop, higher capacity and more fouling resistance than Style 64.

Figure 1: PROFLUX™ severe service grid

2. Results and discussion

2.1 Mechanical rigidity

In PROFLUX severe service grid mechanical rigidity is obtained by using an all-welded construction and by having the sheets with opposing crimp angles act as a type of lattice beam. Compression data in Figure 2 show that PROFLUX grid is significantly stronger than the conventional grid products that are being used in severe service applications – even with reduced material thickness. To achieve a 1 or 2 psi uplift resistance, through rods can be installed to enhance the mechanical integrity of the packing bed.

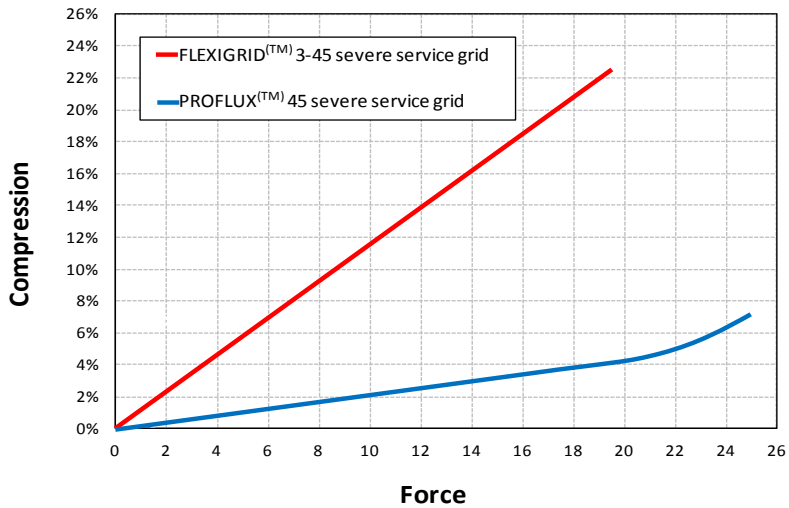

Figure 2: PROFLUX™ severe service grid compression strength

2.2 Fouling resistance

In PROFLUX severe service grid, fouling resistance is obtained by shaping the sheets in a way that reduces the settling of fouling material, as well as spacing the sheets apart to eliminate crevices where fouling material can be trapped and increase the residence time. PROFLUX severe service grid and a conventional grid product were subjected to identical conditions in an accelerated fouling test. From Figure 3 it is evident that the PROFLUX severe service grid showed less fouling than the conventional grid product. Due to its open structure and mechanical rigidity, PROFLUX grid can be cleaned, depending on the nature of the fouling.

Figure 3: Accelerated fouling tests on conventional grid packing (left) and PROFLUX™ severe service grid (right)

2.3 De-entrainment and hydraulic capacity

The maximum hydraulic capacity of low surface area packing cannot be defined without tying it to entrainment. At high vapor velocities, liquid can be sheared off surfaces and the resulting droplets would be blown out of the bed if the packing is incapable of capturing the droplets. The same is true for droplets that have been generated somewhere else and hit the bed from below. For low surface area packing products it is best to define the maximum useful hydraulic capacity as the C_s value at which a significant amount of entrainment is blown out of the bed. PROFLUX severe service grid and a conventional grid product were subjected to the following test: A 1.65 m deep bed was set up in a hydrocarbon distillation tower. A reflux rate of 2.4 $m^3/m^2/h$ was dialed in, and the tower was operated at 9 kPa Abs. Liquid laced with a tracer was sprayed below the packed bed with a nozzle operated at 5 bar dP. The vapor rate was increased by increasing the boil-up, and the amount of tracer above the bed was monitored. An increase in tracer levels above the bed is an indication that entrainment is breaking through the bed. The percentage of tracer breaking through the bed is plotted versus the vapor C_s value in Figure 4. It is evident that the PROFLUX severe service grid is more effective in removing entrainment and can be operated to significantly higher C_s values than the conventional grid product.

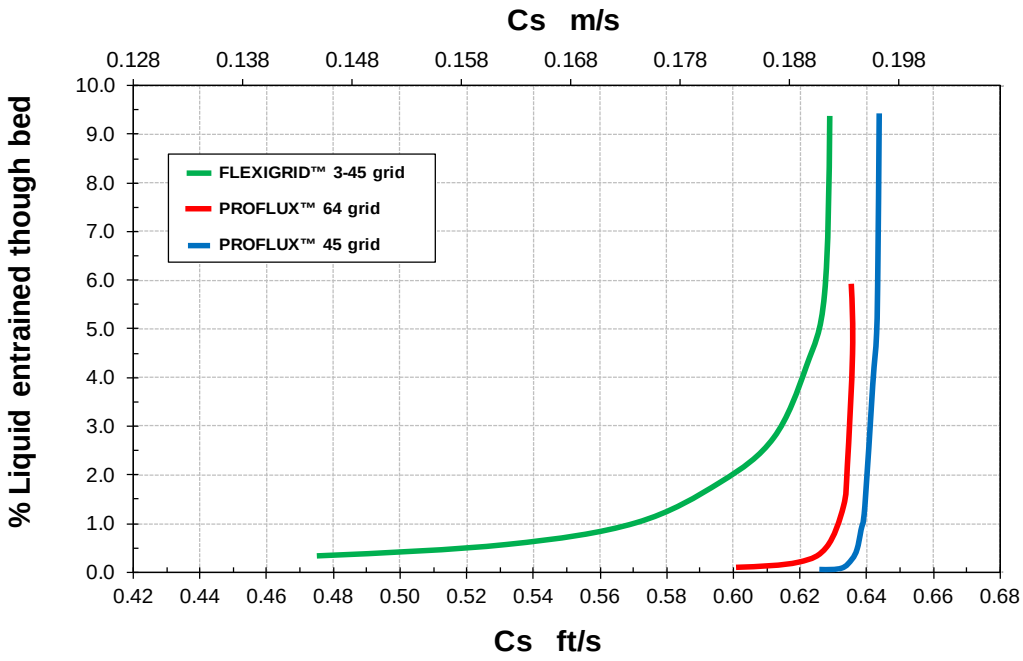

Figure 4: Entrainment removal efficiency of grid products. Tower operated with hydrocarbons at 9 kPa Abs and a constant liquid rate of 2.4 $m^3/m^2/h$.

2.4 Pressure drop

The aerodynamic shape of PROFLUX severe service grid sheets and the gaps between the sheets are used as means to reduce the pressure drop. As can be seen from Figure 5, the PROFLUX severe service grid has significantly lower pressure drop than the conventional grid product with same surface area. This difference is significant in the case of vacuum towers.

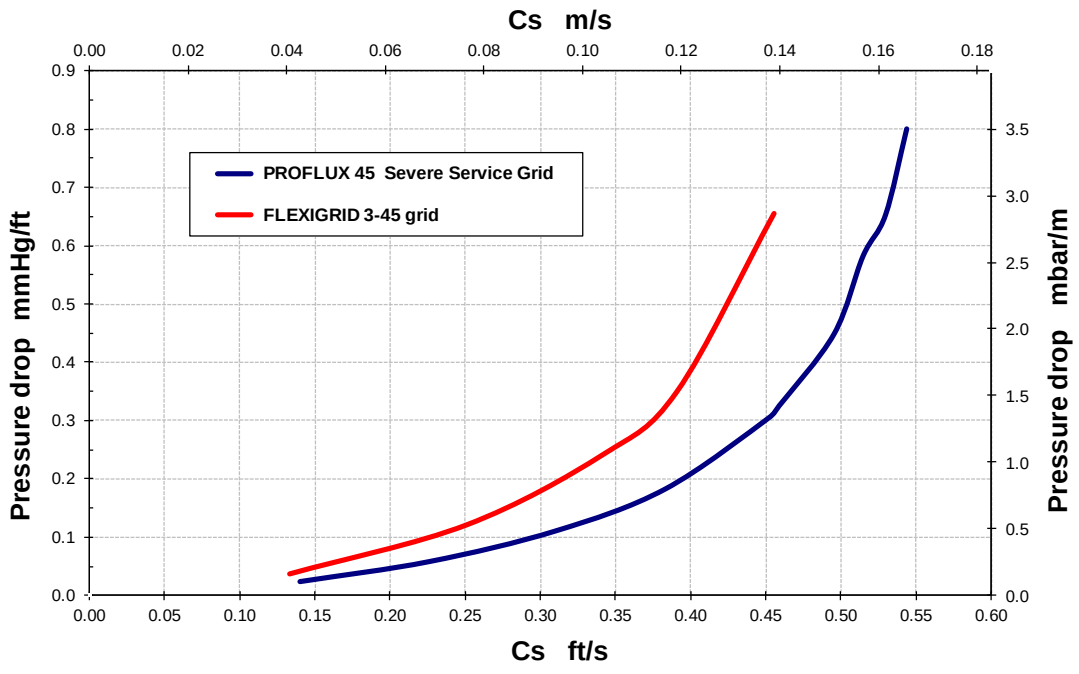

Figure 5: Pressure drop comparison. Total reflux distillation at 27 kPa Abs.

2.5 Mass transfer efficiency

PROFLUX severe service grid is typically used in applications where fouling resistance, high capacity, low pressure drop and good de-entrainment is of paramount importance. However, in these applications heat or mass transfer efficiency performance cannot be neglected. From Figure 6 it can be seen that that PROFLUX grid has mass transfer performance that is in line with what is required for the challenging services where it is being applied.

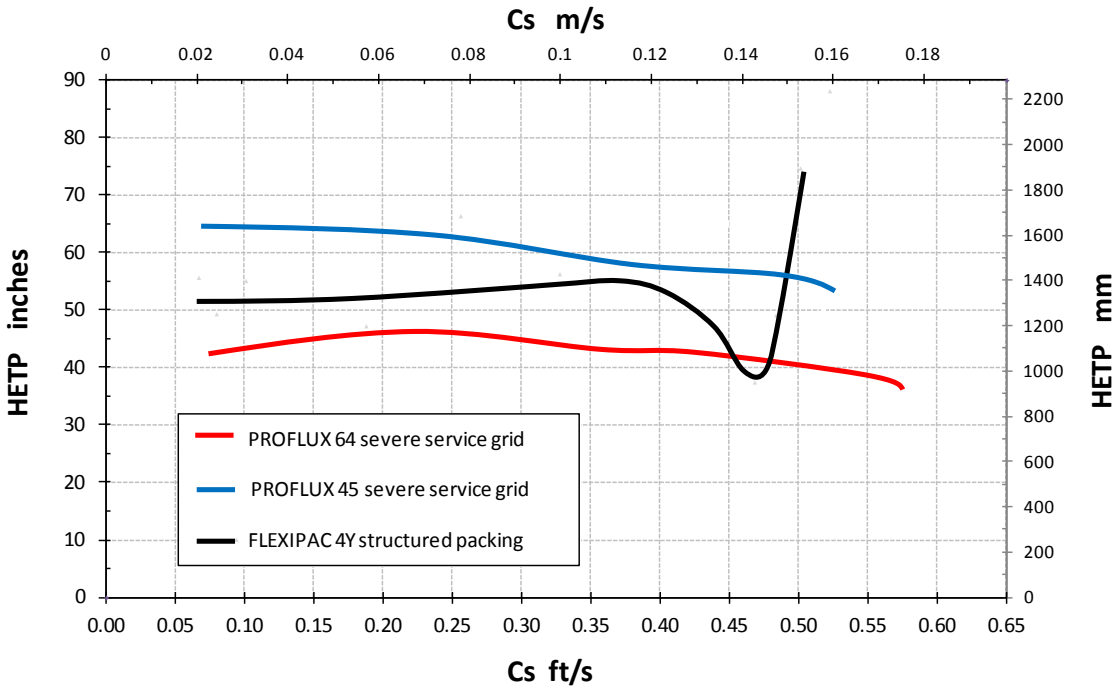

Figure 6: Efficiency comparison. Total reflux distillation at 10 kPa Abs.

2.6 Ease of installation

PROFLUX severe service grid has twice the layer height of conventional grid. Personnel protection restricts the maximum weight a person is allowed to lift. Since PROFLUX severe service grid is made from thinner material than conventional grid products, the increase in layer height does not cause a problem with lifting restrictions. This means that, for every element that is handled, a larger volume of the tower is filled compared to the conventional grid product. This reduction in installation time can shorten the duration of turnarounds. The welded bars on the PROFLUX severe service grid can be used as lifting points to facilitate easier handling of the elements. The open structure of the PROFLUX severe service grid also allows it to be cleaned in cases where the fouling is not too severe.

2.7 Industrial applications

Although a relatively new product, PROFLUX severe service grid has been installed in refinery vacuum towers, refinery atmospheric towers, FCC units, coker units, and a number of chemicals applications.

3. Conclusions

PROFLUX severe service grid provides the following benefits over conventional grid packing:

- Increased fouling resistance
- Reduced entrainment
- Increased hydraulic capacity
- Lower pressure drop
- Mechanical integrity

PROFLUX severe service grid lends itself to use in the following applications:

- Refinery atmospheric and vacuum towers
- FCC, Visbreaker and Coker towers
- Ethylene quench towers
- Towers with moderate separation requirements but high fouling tendency.

References

1. US Patent 8298412B

Effective mass transfer area of modular catalytic structured packings

Elisabetta Brunazzi
Department of Civil and Industrial Engineering, University of Pisa, Pisa, Italy

Abstract
This paper presents the results of a study carried out to examine the effective mass transfer area of the modular catalytic structured packing Katapak-SP. Information has been gathered by using the chemical absorption method and monitoring the composition profiles along the packed bed. Liquid load ranged between 5 and 27 $m^3/(m^2h)$. A procedure was developed taking into account the complex geometry of the packing. The use of both volumetric mass transfer coefficients correlations from the literature and data from own measurements, allowed chosing the proper operating conditions. A simple model to calculate the effective area is presented. The model is based on the packing geometry and the liquid flows distribution within the hybrid structure of the packing.

Keywords
Katapak-SP, Mellapak 752.Y, effective area, CO2 absorption

1. Introduction

Modular catalytic structured packings are used in an increasing number of industrial applications where reaction and separation (i.e. distillation, absorption, extraction…) can be efficiently integrated in single equipment. The commercially available Sulzer Katapak-SP packing, under study in this work, is characterized by a hybrid structure made of corrugated sheets of conventional distillation layers (separation elements) and catalytic baskets, i.e. wire gauze envelopes filled with catalyst particles, assembled in alternate sequence (reaction elements). The modular design allows varying the relative size of the separation and reaction zones by placing one or more corrugated sheets in between. This feature allows to arrange the packing to fit the requirements of each specific process, and makes Katapak-SP a highly competitive internal device for reactive separation columns. The ratio between catalytic baskets and corrugated sheets (tipically, 1:1, 1:2 or 1:3) identifies the packing configuration (Götze et al., 2001; Olujic and Behrens, 2006). Modelling attempts have pointed out that rate based models provide better results than stage models in describing reactive separation columns. Besides the kinetics parameters, of particular interest for the improvement of predictive models is the quantification of fluid dynamic related parameters, i.e. pressure drop, liquid hold-up, effective mass transfer area and coefficients (Viva and Brunazzi, 2009, Aferka et al. 2010).

In this study, we determined experimentally the effective mass transfer area of Katapak-SP packing. A chemical method (CO2 absorption from air into a caustic solution) was employed, for the first time, to study a packing with a complex geometrical structure like the Katapak-SP packing. Indeed, the hybrid structure determines the flows development inside the packed bed and consequently application of the method is not straightforward as it could appear at first glance. Volumetric mass transfer coefficients from the literature and some own measurements were used to enable a critical analysis of the measurement method and chose the proper operating conditions.

Then, a simple model based on flows distribution and packing geometry is presented to interpret the measured effective area.

2. Experimental method and setup

Chemical absorption rate data in the fast-reaction regime is frequently employed to determine effective gas-liquid interfacial area in packed columns (Danckwerts, 1970). Among the large variety of the two-fluid systems, the absorption of CO2 into NaOH solution is especially proper (Kolev et al. 2006, Rejl et al. 2009). CO2 reacts in the liquid phase with NaOH and forms bicarbonate and carbonate. The reaction is of second order and the formation of the bicarbonate ion is the limiting reaction. The value of its equilibrium constant at ambient temperature is large enough to allow considering the reaction as practically irreversible. The kinetics of the system has been extensively studied and characterised (Pohorecki and Moniuk, 1988, Kolev et al. 2006). Weimer and Schaber (1996) have investigated how the test conditions must be chosen, when studying conventional packings, in order to operate in the desired fast reaction of pseudo-first order condition. They found that using air (i.e. with only some 380 ppmv CO2), instead of a CO2 enriched gas stream, has no effect on the reaction regime, and that the method is preferable because this way, the use of chemicals is significantly reduced and more importantly caustic and carbonate concentrations change very slowly. The gas side resistance is limited by operating at high gas velocities (1-2 m/s). Effective gas-liquid interfacial area measurements using air and 0.1-1 molar NaOH solution have been recently reported by Tsai et al. (2011), Alix et al. (2011), Duss et al. (2010) to characterise structured packing. Aferka et al. (2011), used air and 0.3 molar NaOH solution to determine the effective interfacial area of MellapakPlus 752.Y, and the results were used to validate tomographic measurements.

In this paper the technique is applied, for the first time, to determine the effective interfacial area of catalytic structured packing. In particular, two modular configurations of Katapak-SP, i.e. 1:1 and 1:2, have been studied in the nominal size of 100 mm diameter and 200 mm height. They are made of stainless steel, glass particles of 1 mm diameter fill the catalytic baskets. Corrugated sheets are those encountered in MellapakPlus 752.Y. A comprehensive description of the packings geometry is provided in Viva et al. (2011).

The column has an internal diameter of 100 mm and is 2 m high. It is made of transparent plexiglass. Packed beds are constituted by nine Katapak-SP elements, rotated by 90° with respect to each other. The column was operated at atmospheric pressure and room temperature. Air is supplied by a compressor, pre-humidified and fed at the bottom of the column. A multiple point source distributor was used to feed the liquid at the top of the column. The column is attached to two 500 litre capacity storages, one for the fresh solution and one for the used solution, to ensure that the caustic solution concentration is constant during the tests. Nevertheless, liquid samples both at the inlet and the outlet of the packing were taken during the runs. The concentrations of hydroxides and carbonates in the liquid samples were determined by titration with HCl. Also temperature of gas and liquid were accurately measured during the runs. Ionic strength of the solution, hydroxides concentration and temperatures have a significant impact when evaluating the interfacial area (Duss at al., 2010) this is the reason why they need to be accurately measured and monitored.

Gas samples were withdrawn at different locations along the column. Besides monitoring inlet and outlet air streams, samplings were taken directly from the packed portion of the column to avoid end effects (Rejl et al. 2009) and monitor the gas composition profile along the packed bed. The CO2 concentration was measured by an infrared gas analyzer (Ecocontrol AD 30), calibrated with N2 for zero point and 590 ppm CO2/air span gas. The 4-20mA signal was recorded continuously on a data logger and stored on a PC. This feature allowed the CO2 concentration to be observed in real-time.

Use of the chemical method with a packing characterized by a hybrid structure like the Katapak-SP packing, requires, among others, the following aspects to be considered:

- Evaluation of the composition and ionic strength of the solution as it flows down the packed bed (model for the liquid flow)
- Large Hatta number throughout the packed bed (Ha >3)
- Limited gas side mass transfer resistance
- Significant variation in CO2 concentration in the gas phase to limit experimental errors

For the current study we found a satisfactory comprimise with the following operating conditions: gas F-factors were comprised between 0.8-1.5 $Pa^{0.5}$ (for each liquid load, the maximum F-factor was fixed by operating at pressure drop below 3-5 mbar/m, so as to work below the gas loading point; some runs were also conducted at higher gas rates, up to the flooding point, to determine the gas effect on the effective area); liquid loads ranged from 5 to 27 $m^3/(m^2\ h)$; the feed liquid was a 0.3 molar NaOH solution, some runs with 0.5 molar solution where also conducted as a check of the method.

To evaluate the effective interfacial area from the resulting experimental data we used the physico-chemical property values and reaction kinetic constants published by Pohorecki and Moniuk (1988).
One dimensional and stationary plug flows of gas and liquid were assumed within the packed bed as well as isobar and isotherm operating conditions. The material balance and rate equations on a differential section of the column were written in Matlab 7.0 and integrated over the packed bed to calculate the composition profiles along the column. The effective interfacial area was assumed to be constant. It is the only parameter to adjust in order to fit the measured CO2 profile and meet the NaOH concentration in the liquid bulk measured at the column inlet and outlet.
The hybrid structure of the packing determines the flows development inside the packed bed. Two zones can be distinguished within the packing, the open channels (OC), which correspond to the separation zone where the corrugated sheets are placed, and the catalytic baskets (CB). The mesh size of the wire gauze envelopes ensures easy access of liquid, prevents the particles cross-over and makes the baskets practically impermeable to the gas flow. Hence, it can be reasonable assumed that the gas flows entirely in the separation zone.
In previous studies on the same packings, Viva et al. (2011) deduced the distribution of liquid flowrate, between the reaction and the separation zones, from hold-up distribution measurements. The liquid specific load, *uL*, was written as the sum of two contributions:

$$uL = u_{OC} \cdot \Psi_{OC,S} + u_{CB} \cdot \Psi_{CB,S} \qquad (1)$$

where u_{OC} and u_{CB} stand for the liquid specific load outside and inside the catalytic baskets, respectively, and Ψ_{OC} and Ψ_{CB} are the superficial fractions on the column cross section occupied by the OC and CB zones. Liquid distribution changes with the liquid load and quantitative results are provided Viva et al. (2011).
In its way down the packed bed, the liquid solution flowing in the separation zone contacts the gas phase and absorbs CO2. As a consequence, its composition and ionic strength vary. To model the liquid behaviour, two extreme cases were considered: (a) the liquid is continuously and completely mixed in any packing cross section, (b) the liquid flowing in the separation zone never mixes within the packing with the liquid flowing in the reactive zone. The worse scenario occur at low liquid loads and with model (b). Both models were considered in the analysis of the experimental profile, and with the chosen conditions, we found that either models affect the calculated area by less than 2-3%.

In regard to the Hatta number criterion, estimates of the physical liquid side mass transfer coefficient (kl0) are needed. Correlations for kl0 from the literature (Rocha et al.1996, Behrens et al. 2006) were used to calculate Ha number and monitor the values along the packed bed for all the liquid loads. The used correlations predict values of kl0 of the order of 10^{-4} and 10^{-5} m/s. Own measurements not shown here for brevity, consisting of the desorption of CO2 from aqueous solutions into air, support these estimates. The worse conditions occur at the higher liquid loads. We found that the use of 0.3 molar NaOH solution allowed us satisfying the large Ha criterion. Additional runs were conducted with 0.5 M solution to check the results.

The gas side mass transfer resistance and its associated errors in the measured contact areas are minimised when dilute caustic solution and high gas velocities are used. For the present study (with the 0.3 molar solution) and with the chosen operating conditions, the gas side resistance affect the calculation of the effective area by less than 4-7%. The gas-side mass transfer coefficient was calculated from the correlation of Brunazzi et al. (1995) adapted to the Katapak-SP geometry. Furthermore, own measurements, not shown here for brevity, consisting of the absorption of SO2 into caustic solutions have supported this estimate.

3. Results and discussion

Figure 1 shows a sketch of the packed section of the column showing the location of the gas sampling stations (two for each level). CO2 concentration axial profiles for Katapak-SP 11 and Katapak-SP 12 are compared: measurements were conducted with the same liquid load (20 $m^3/h/m^2$) and gas F-factor (1 $Pa^{0.5}$). Points are the experimental values while the lines are the calculated profiles. The figure show that a higher CO2 mass transfer rate, and hence higher effective area, is obtained for Katapak-SP 12 compared with Katapak-SP 11. This can be explained with the higher specific geometric area of the packing, i.e. 282 and 210 m^2/m^3, respectively (Viva et al. 2011). No significant gas effects were observed for F-factors below the gas loading point. The influence of both the liquid load and packing type on the effective mass transfer area is illustrated in Figure 2, where data for MellapakPlus752.Y are also reported for comparison (Aferka et al., 2011). Every packing exhibited an increase in area with increasing liquid load. For MellapakPlus 752.Y packing this is naturally attributable to a greater portion of the packing being wetted and therefore available to participate in the mass transfer process. A correlation for the fractional

area of MellapakPlus packing as a function of liquid load can be easily obtained by interpolation of data shown Figure 2.

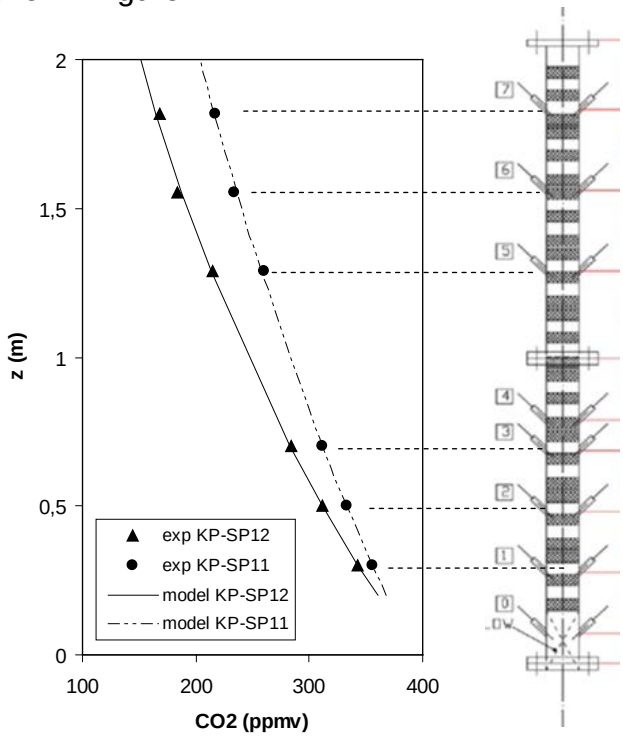

Figure 1: *Sketch of the packed section of the column (right) and CO2 concentration along the column axial coordinate (left). Liquid load = 20 $m^3/(m^2h)$, F-Factor = 1 $Pa^{0.5}$.*

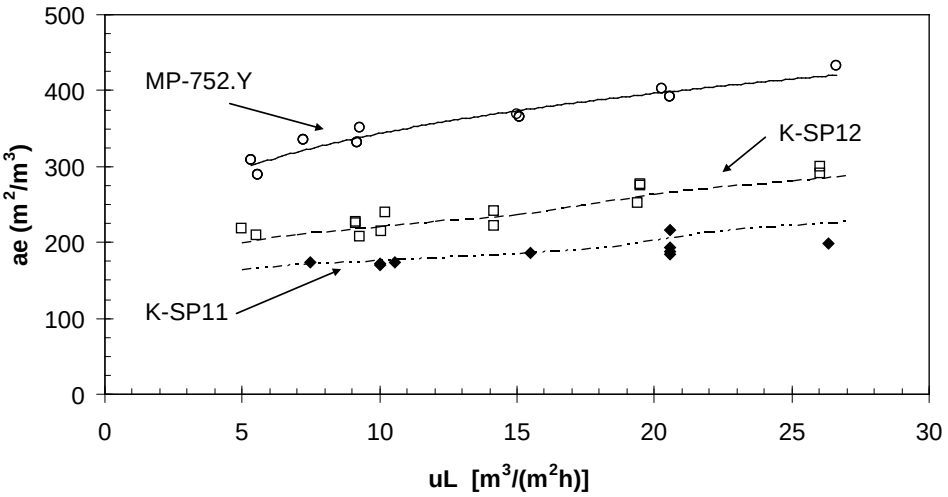

Figure 2: *Effective area as a function of liquid load. Comparison between calculated values (lines) and experimental data (points).*

For Katapak-SP the mass transfer process takes place in the separation zone. The effective area could be calculated as the sum of two contributions, i.e. the corrugated sheets and wire gauze of the catalytic baskets.

$$ae = (ae/ag)_{MP,u_{OC}} \cdot ag_{MP\_inK-SP} + ae_{WG} \qquad (2)$$

where *ae* is the Katapak-SP effective area for a liquid load of *uL*, $(ae/ag)_{MP,u_{OC}}$ is the fractional area of MellapakPlus packing for a specific load of u_{OC}, $ag_{MP\_inK\text{-}SP}$ is the

specific geometric area of the corrugated sheets in the Katapak-SP packing, ae_{wg} is the effective area of the wire gauze assumed completely wetted. A fairly good agreement is observed in Figure 2 with predictions of Equation (2).

4. Conclusions

A procedure based on chemical absorption was developed to calculate the effective area of Katapak-SP packing directly from experimental results. Effective area was measured for liquid load between 5 and 27 $m^3/(m^2\ h)$. A simple model based on flows distribution and packing geometry is presented which interpret fairly good the measured values.

Acknowledgements

The author is grateful to Sulzer Chemtech for supplying the packing materials and Dr. Markus Duss for useful suggestions. The contributions of Francesco Burattini, Francesca Maggesi and Aurora Viva to this work are gratefully acknowledged.

References

Aferka, S., Viva, A., Brunazzi, E., Marchot, P., Crine, M., Toye, D., 2010. Liquid load determination in a reactive distillation packing by X-ray tomography. Can. J. Chem. Eng. 88, 611-617.

Aferka, S., Viva, A., Brunazzi, E., Marchot, P., Crine, M., Toye, D., 2011. Tomographic measurement of liquid hold up and gas-liquid interfacial area distributions in a column packed with MellapakPlus 752.Y. Chem. Eng. Sci. 66, 3413-3422.

Alix, P., Raynal, L., Abbe, F., Meyer, M., Prevost, M., Rouzineau, D., 2011. Mass transfer and hydrodynamic characteristics of a new carbon packing: application to CO2 post-combustion capture. 2011. Chem. Eng. Res. Des. 89, 1658-1668.

Behrens, M., Olujić, Ž., Jansens, PJ., 2006. Combining reaction with distillation. Hydrodynamic and mass transfer performance of modular catalytic structured packings. Chem. Eng. Res. Des. 84, 381-389.

Brunazzi E., Nardini, G., Paglianti, A., Petarca, L., 1995. Interfacial area of mellapak packing: absorption of 1,1,1-trichloroethane by genosorb 300. Chem. Eng. Technol., 18, 248-255.

Danckwerts, P. Gas-liquid reactions. McGraw Hill, New York, 1970.

Duss, M., Menon, A., 2010. Optimized absorber design for post-combustion CCS. Proc. of the 9th D&A Conference, Eindhoven, The Netherlands, 12-15 September 2010, 109-114.

Götze, L., Bailer, O., Moritz, P., von Scala, C., 2001. Reactive distillation with Katapak. Cat. Today. 69, 201–208.

Kolev, N., Nakov, S., Ljutzkanov L., Kolev, D., 2006. Effective area of a highly efficient random packing. Chem. Eng. Proc. 45, 429-436.

Olujić, Ž., Behrens, M., 2006. Hold-up and pressure drop of packed beds containing a modular catalytic structured packing. Chem. Eng. Technol. 29, 979–985.

Pohorecki, R., Moniuk, W., 1988. Kinetics of reaction between carbon dioxide and hydroxyl ions in aqueous electrolyte solutions. Chem. Eng. Sci. 43, 1677-1684.

Rejl, J.F., Linek, V., Moucha, T., Valenz, L., 2009. Methods standardization in the measurement of mass-transfer characteristics in packed absorption columns. Chem. Eng. Res. Des. 87, 695-704.

Rocha, J.A., Bravo, J.L, Fair, J.R., 1996. Distillation columns containing structured packings: a comprehensive model for their perfomance. 2. Mass-trasnfer model. Ind. Eng. Chem. res. 35, 1660.

Tsai, R. E., Seibert, F., Eldridge, R. B., Rochelle, G.T., 2010. A dimensionless model for predicting the mass transfer area of structured packing. 2011, AIChE J, 57, 1173–1184.

Viva, A., Brunazzi, E., 2009. The influence of modular structure on the hydrodynamics of catalytic structured packings for reactive separation processes, Chem. Eng. Trans., 17, 1519-1524.

Viva, A., Aferka, S., Toye, D., Marchot, P., Crine, M., Brunazzi, E., 2011. Determination of liquid hold-up and flow distribution inside modular catalytic structured. Chem. Eng. Res. Des. 89, 1414-1426.

Weimer, T., Schaber, K., 1996. Ermittlung effektiver Phasengrenzflaechen durch Kohlendioxidiabsorption aus Luft. Chem, Technik 48, 237-288.

Influence of viscosity and packing geometry on distillation: Experiments and simulation

Christian Bradtmöller, Stephan Scholl
Institute for Chemical and Thermal Process Engineering, Technische Universität Braunschweig, D-38106 Braunschweig, Germany

Abstract
In a distillation process the physical properties of the mixture, operating conditions and the geometry of the packing determine fluid dynamics and mass transfer and thereby the performance of the column. Liquid viscosity has an impact on separation efficiency as well as on capacity. Therefore, in this study measurements were carried out with two test mixtures, one with elevated viscosity. Furthermore, the geometry was altered using two different structured packings. Based on experimental data, different predictive models are assessed with respect to their capability to describe the impact of viscosity on column efficiency.
Increase of viscosity by a factor up to 6 resulted in a decrease of separation efficiency by 50 %, higher pressure drop and lower capacity. Whilst separation efficiency at low viscosity was roughly met by the rate based models, the influence of increased viscosity could not be predicted correctly.
The results reveal that even at moderate viscosities column performance is affected significantly. Hence, if rate based models are applied to conditions deviating from those they were validated for, their accuracy has to be considered carefully.

Keywords
Distillation, viscosity, mass transfer efficiency, structured packings

1. Introduction

Structured packings are widely used in distillation and absorption processes, since they allow combining high capacity and good separation efficiency. These are determined by the geometry of the packing, operating conditions and the physical properties of the mixture. Significant effort has been made to find and improve predictive models for structured packings. Thereby the calculation of efficiency in dependence from geometry and physical properties is desired to avoid time consuming and expensive experiments. However, experiments are needed for model validation whenever major changes in physical properties or geometry are made. In this respect, liquid viscosity is especially important, since it has an impact on separation efficiency as well as on capacity, because it influences fluid dynamics and mass transfer in the liquid phase. Typically, efficiency tests are carried out using standard test mixtures, based on the comprehensive compilation of Onken and Arlt [1]. Most frequent systems are Chlorobenzene/Ethylbenzene (CB/EB) and Cyclohexane/n-heptane (C6/C7). Increased viscosities are represented by Trans-/ Cis-Decalin, however well below 1.5 mPa s. Hence, there is little or no data available in open literature concerning the influence of viscosity beyond this value. Böcker and Ronge [2] used polymers to increase viscosity and study its impact, but due to the

comparability of the measurements, most datasets used for the validation of existing rate based models are limited to the low viscous mixtures stated above.
The intention of this study is to systematically investigate the influence of viscosity and the ability of rate based models to predict the dependencies. Therefore, measurements with CB/EB as reference and a binary mixture of 2-Methyl-2-butanol and 2-Methyl-1-propanol (MB/MP) with increased viscosity were carried out. A system without polymers or any other non-volatile components was chosen in order to conduct experiments under total reflux, which is the standardized procedure for efficiency tests [3]. The utilized mixture allows an increase of viscosity by a factor of 6 in respect to CB/EB. Furthermore the effect of the corrugation angle was investigated by conducting experiments with Sulzer Mellapak 500.Y and 500.X, the latter having a higher inclination.
The influence of viscosity and geometry on separation efficiency depicted by the HETP value and on pressure drop is discussed. Furthermore, results are compared with two rate-based models. The Delft model [4,5] is applied since it contains no empirical parameters and can represent the geometrical conditions of the miniplant the experiments were conducted in. In addition, the widely used model by Rocha, Bravo, Fair [6] is applied.

2. Results and discussion

2.1 Experimental set up and data assessment

The experiments were conducted under total reflux in a miniplant column with an inner diameter of 50 mm. Heat losses were minimized by a vacuum jacket and electric trace heating. Hydraulic and mass transfer performance was measured for CB/EB and MB/MP under variation of the operating pressure. The reflux is preheated before being distributed. The column was equipped with four beds of structured packing. Representative samples were drawn from the reflux and below each bed. Two stainless steel structured packings differing in the inclination of corrugation were investigated. In case of Mellapak 500.Y (M500.Y) sheets are corrugated with an angle of 45° relative to the horizontal plane, for Mellapak 500.X (M500.X) the angle measures 60°. The beds have a height of 0.612 m each and are composed of six packing elements, rotated by 90°. Pressure was measured at the column head and below the first bed. Additionally pressure drop was measured for upper and lower halves of the column. Temperatures were determined within the beds and at the sampling points. For the cross sections where samples are drawn, volumetric flows and the separation factors are calculated. The geometric mean of the latter is used to determine separation efficiency, described by the HETP value. Presented gas loads are the arithmetic mean of the flows in these cross sections.

2.2 Influence of viscosity

The influence of viscosity was determined by applying the mixture CB/EB as reference and MB/MP as viscous mixture. Viscosity is furthermore varied by changing the operating pressure. Since liquid viscosity depends on the corresponding boiling temperature, its value can be adjusted by the applied pressure. The resulting dependence is shown in table 1.

Table 1: Viscosities of mixtures at boiling temperatures corresponding to given operating pressures

pressure [mbar]	Liquid viscosity [mPa s]	
	CB/EB	MB/MP
20	0.7	4.5
100	0.5	1.6
200	0.4	1.1
950	0.3	0.5

First measurements were carried out with CB/EB to establish a reference. This is necessary, since not only physical properties and the type of packing affect the separation efficiency, also the conditions resulting from miniplant scale influence packing performance. As depicted in figure 1 (A), separation efficiency measured for CB/EB is slightly higher compared to values measured in a column with a diameter of 1 m. Since the height of one packing element in this study was 102 mm instead of 150 to 200 mm in larger scale columns, liquid mixing at the intersection of packing elements and vapor distribution is promoted. Hence, mass transfer is increased and the measured pressure drop should be higher. Whilst the presented results support the first assumption, the latter is contradicted. This is assumed to be caused by the annular gap between packing and column wall, contributing a larger portion of the cross section in the miniplant scale. In this gap a certain amount of liquid and vapor can flow countercurrent with reduced friction. Thereby the flooding point is shifted to higher gas loads. Furthermore, the decrease of HETP for gas loads above the loading point, that contradicts the relation for the larger scale column, can be attributed to the geometry. Vapor coming into the gap from the triangular flow channels exerts a drag force on liquid covering the inner column wall. The liquid is retained enabling intensive mass transport. HETP drops significantly reaching the flooding point, since in this regime a bubble layer is formed in the gap around the uppermost bed, which still permits stable operation. Whilst HETP differs in this region depending from operating pressure, for lower gas loads a constant HETP of 0.22 m independent of pressure can be observed.

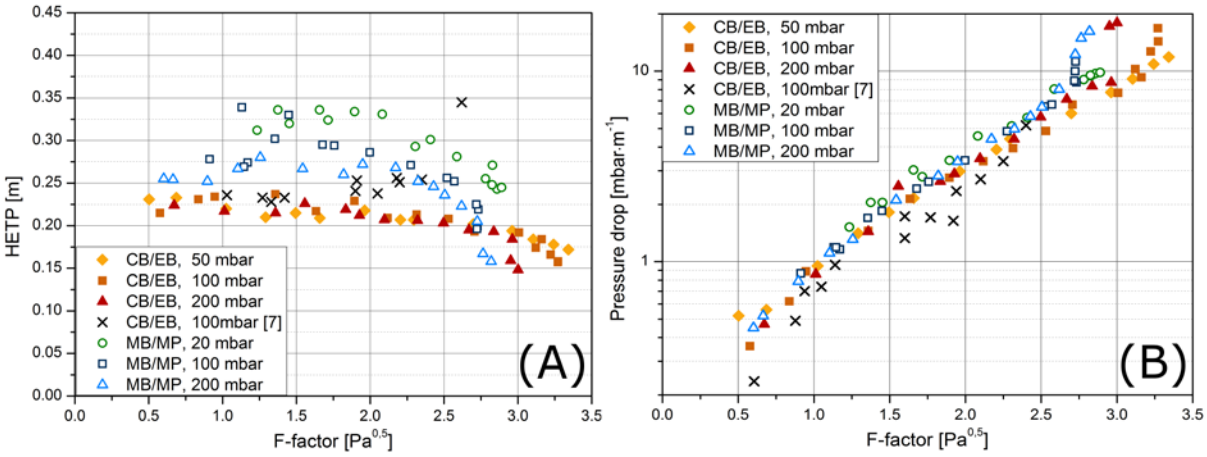

Figure 1: Packing efficiency (A) and pressure drop (B) as function of gas load (F-factor) at different operating pressures for chlorobenzene/ethylbenzene (CB/EB) and 2-Methyl-2-butanol/2-Methyl-1-propanol (MB/MP), values from [7] measured in column with 1 m diameter

If the results for CB/EB are compared to the separation efficiencies determined for the viscous mixture, a significant increase of the HETP is evident. At 200 mbar a value of 0.26 m was determined, with a pronounced decrease in the flooding region.

In comparison to CB/EB, flooding occurred at lower gas loads at all pressures and pressure drop were slightly higher. Furthermore it can be observed from figure 1 (B), that pressure drop for MB/MP at 20 mbar is higher compared to the other experiments with the viscous mixture. The effect is rather small, but if only the upper half of the column is considered, a distinct difference is obvious. As shown in table 1, the liquid viscosity of MB/MP significantly rises, with decreasing pressure, i.e. decreasing boiling temperature. Also the ratio of viscosities for MB/MP and CB/EB increases. Hence, for 100 mbar and 20 mbar further increased HETP values of 0.29 m and 0.33 m were determined. Since it was shown that the HETP is independent of pressure for CB/EB, the significant decrease of separation efficiency up to 50 % may be attributed to liquid viscosity.

2.3 Influence of geometry

Figure 2 (A) shows the influence of the corrugation angle of the packing. The separation efficiencies are considerably lower for M500.X. This effect is slightly higher at 20 mbar. Here the HETP exhibits with 0.4 m a value 19 % higher, whereas at 200 mbar an increase of 17 % occurs.

In general, two major effects have to be considered concerning the impact of inclination on separation efficiency. At otherwise constant conditions like hydraulic diameter of the flow channels, a larger flow angle causes thinner liquid films on the surface of the packing with a correspondingly higher liquid velocity. Furthermore, at constant superficial velocity of the vapor the effective velocity is reduced. This causes a less turbulent flow and thereby a lower mass transfer coefficient on the vapor side. Together with a reduced residence time of liquid, higher HETP values can be expected, which is supported by the experimental results.

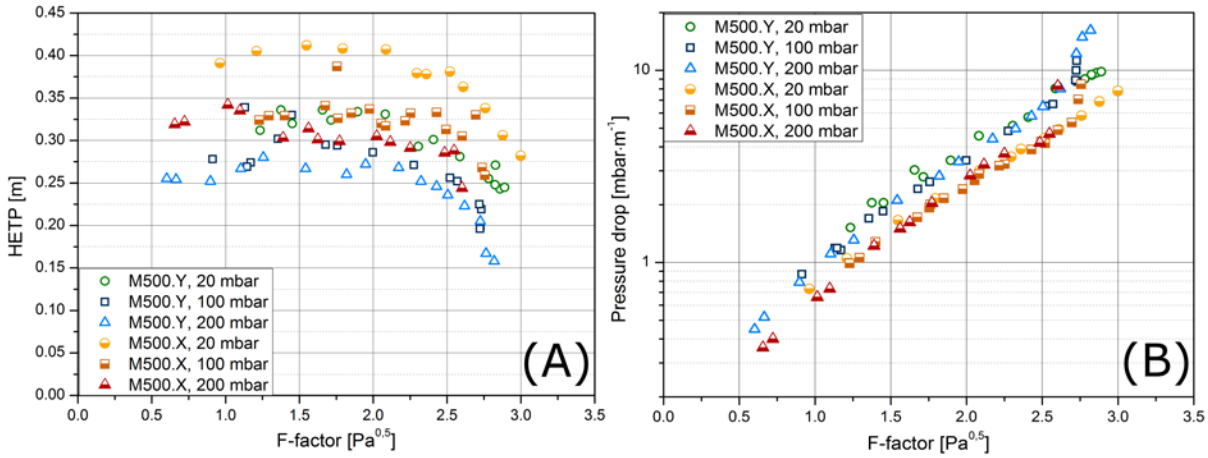

Figure 2: Packing efficiency (A) and pressure drop (B) as function of gas load (F-factor) at different operating pressures for Mellapak M500.Y and M500.X for 2-Methyl-2-butanol/2-Methyl-1-propanol (MB/MP)

Figure 2 (B) shows a significantly lower pressure drop for M500.X. The steeper angle of the corrugation reduces direction change losses at the transition of gas flow from one packing element to the next. Furthermore, losses at the column wall are decreased. Thereby pressure drop follows the same qualitative trend with operating pressure with slightly higher losses at 20 mbar for both packings. In contrast there is no consistent change of the maximum gas load. For 200 mbar flooding occurred at a lower gas load, whereas at 100 mbar and 20 mbar a marginal increase of the maximal gas loads was determined. Flooding is not shifted to higher loads

consistently, because the flooding mechanism changes. In the experiments carried out with M500.X the tendency of gas to flow into the annular gap was much lower. Thus, flooding is predominantly influenced by the packing´s geometry and the maximum gas load should better concur with results for large scale columns.

2.4 Modeling

After a significant increase of the HETP value for higher viscosities has been shown, the question arises if this dependency can be predicted by literature rate based models. Therefore the Delft model [4,5] is chosen since it contains no empirical constants, but parameters such as the height of a packing element and the length of flow channels which are directly obtained from the actual packing elements. Furthermore, the widely used model by Rocha, Bravo, Fair (RBF) [6] is applied to the test mixtures investigated before. Here the packing specific surface enhancement factor F_{SE} given for M500.Y in [6] is used for the calculation of wetted surface.

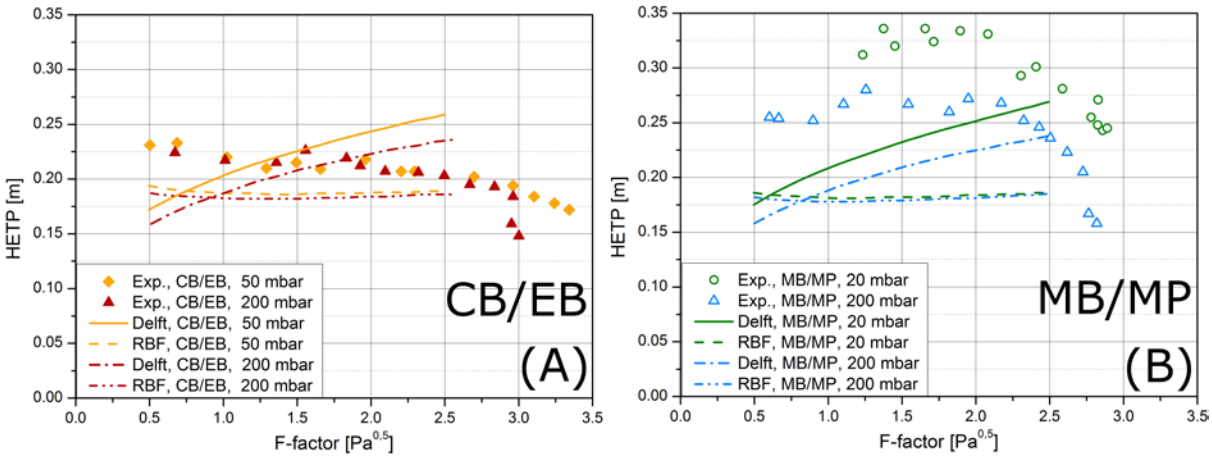

Figure 3: Comparison of measured HETP values for Mellapak 500.Y and predicted by (A) Delft model [4,5] and (B) Rocha, Bravo, Fair (RBF) [6]

For CB/EB the RBF model gives HETP values below the experimental results, but correctly describes the HETP to be comparatively independent of gas load, see figure 3 (A). Contrary the Delft model exhibits a strong dependency on gas load, yielding efficiencies better at low loads and beneath the experimental results for $F > 1.5$ $Pa^{0.5}$. Both models suppose the HETP to rise, if pressure is reduced. This tendency is more obvious for the Delft model. Thus, the models meet the range of the experimental results, but do not provide accurate values.

When changing to the viscous mixture MB/MP, both models significantly overestimate the separation efficiency, see figure 3 (B). Although HETP values by the Delft model are slightly higher compared to the results for CB/EB, the strong influence of physical properties is not assessed correctly. The RBF model even predicts a lower HETP. The marginally higher HETP values at 20 mbar in case of the Delft model are caused by the lower pressure and do not reflect the higher viscosity. Hence, it has to be concluded that the effect of increased viscosity with otherwise only moderately changing properties cannot be properly predicted with the applied models.

3. Conclusions

Separation efficiency tests were carried out in a miniplant column with CB/EB as reference and a mixture with increased viscosity to investigate the effect of viscosity on packing performance. A new test mixture, composed of 2-Methyl-2-butanol and 2-Methyl-1-propanol, was applied. This mixture offers viscosities by a factor up to 6 times higher compared to CB/EB and exhibits a pronounced increase of viscosity with decrease of operating pressure and the corresponding boiling temperature of the mixture. Structured packings with different inclination of the corrugated sheets were used to study the effect of geometry.

Measurements with Mellapak 500.Y revealed that the HETP values for the reference system fairly agree with experiments in larger scale columns for gas loads below the loading point. Above, separation efficiency increased due to the characteristics of the miniplant. The same effect was encountered for the viscous test system, but the HETP was determined to be significantly higher, rising with decreasing operating pressure. This effect can be assigned to be the impact of viscosity, since for CB/EB a HETP of 0.22 m independent of pressure was measured. At the lowest pressure under investigation the HETP increased by 50 % to 0.33 m for the viscous mixture. Experiments with Mellapak 500.X showed lower separation efficiencies and pressure drop as expected because of the higher inclination of the corrugation. Furthermore, the decrease of separation efficiency within the measurements with the viscous mixture was found to be even higher.

Rate based models were applied to both test systems and different operating pressures. While for CB/EB a performance within the experimentally measured range was determined, the models underestimated the influence of viscosity. Here an integral consideration of mass transfer and equations for wetted surface or a more elaborated modeling approach like hydrodynamic analogies [8] seems necessary.

However, the distinct decrease of separation efficiency, even observed for moderate viscosities, is a crucial insight with importance for column design.

Acknowledgements

This work was supported by Deutsche Forschungsgemeinschaft (DFG) under grant no. SCHO 842/12-1.

The authors wish to thank Sulzer Chemtech Ltd. for the provision of the packing material.

References

[1] U. Onken, and W. Arlt, Recommended test mixtures for distillation columns (second edition), The Institution of Chemical Engineers, 1990, Rugby, England

[2] S. Böcker, G. Ronge, Distillation of Viscous Systems, Chem. Eng. Technol., 2008, 28, 25-28

[3] Ž. Olujić, Standardization of Structured Packing Efficiency Measurements, 2008, http://www.tkk.fi/Units/ChemEng/efce/2008/presentations/Olujic-document.pdf

[4] Ž. Olujić, M. Behrens, L. Colli, A. Paglianti, Predicting the Efficiency of Corrugated Sheet Structured Packings with Large Specific Surface Area, Chem. Biochem. Eng., 2004, 18, 89-96

[5] Ž. Olujić, M. Behrens, Experimental Characterization and Modeling of the Performance of a Large-Specific-Area High-Capacity Structured Packing, Ind. Eng. Chem. Res., 2007, 46, 883-893

[6] J. A. Rocha, J. L. Bravo, J. R. Fair, Distillation Columns Containing Structured Packings: A Comprehensive Model for Their Performance. 2. Mass-Transfer Model, Ind. Eng. Chem. Res., 1996, 35, 1660-1667

[7] K. Bennett. M. Pilling, Efficiency Benefits of High Performance Structured Packings, presentation Sulzer Chemtech at Department of Energy Texas Technology Showcase, 2003, http://texasiof.ceer.utexas.edu/texasshowcase/pdfs/presentations/d2/mpilling.pdf

[8] T. Wolf, C. Bradtmöller, A. Janzen, S. Scholl, E. Y. Kenig, Chem. Ing. Tech., 2013, 85, 1404

Kettle Reboiler Hydraulic Studies

*Tony Cai**, Michael Resetarits, Simon Chambers*
Fractionation Research, Inc.,Stillwater, OK 74074, U.S.A

ABSTRACT

Kettle reboilers are widely employed in the chemical processing industry (CPI), and they are often considered to be troublesome. The problems are usually related to excessive pressure drops caused by liquid entrainment from the kettle reboilers. Information and data regarding kettle hydraulics and entrainment are generally lacking. One of the two industrial-size kettle reboilers at Fractionation Research, Inc's (FRI's) experimental distillation unit was equipped with four large observation windows that were strategically positioned for hydraulic studies. The reboiler is typically operated using different hydrocarbon systems and is run at column pressures ranged from 0.1 to 11.4 bara.

Extensive hydraulic studies on the kettle reboiler have been conducted by FRI. This paper presents a small portion of the results, including visual observations, pressure drops and entrainment data. Vaporization was found to be asymmetric. The depth of the boiling pool was found to be a weak function of the heat flux. At high horizontal vapor velocities, excessive liquid droplets (entrainment), were carried out of the reboiler and were observable via windows in the distillation column. The entrainment data were collected using gamma ray scanning of the kettle's vapor return line at various heat fluxes. At entrainment fraction above 10% (L/V mass basis), the kettle reboiler appeared to be flooded (as seen through the windows). Pressure drops across the vapor return piping between the column and the reboiler were measured. Liquid heads inside the kettle and column bottom sump were also measured. Pressure drop data were compared against entrainment measurements and visual observations. A good agreement was found between the measured data and the predicted values, until the onset of visible liquid entrainment from the kettle.

A literature correlation regarding kettle reboiler hydraulic capacity was applied to the FRI kettle reboiler. For all of the test systems, the literature correlation under-predicted the measured capacities very significantly.

Key Words: Distillation, kettle reboiler, pressure drop, entrainment, capacity

*Corresponding author. E-mail: cai@fri.org , Phone: 1-405-385-0354

Introduction

Kettle reboilers are widely used in the chemical processing industries (CPI). Many column failures have been caused by the problems associated with kettle reboiler circuits [1]. Researchers have conducted studies on the heat transfer and hydraulics of kettle reboilers [2,3,4,5]. An excessive pressure drop in a kettle reboiler circuit results in a high liquid level in the bottom of the associated column. If

the liquid level is close to or above the bottom of the reboiler vapor return nozzle, the column will be prematurely flooded; and it will lose capacity and separation efficiency. The excessive pressure drops are often related to the liquid droplet entrainment from the kettle reboiler.

Information and experimental data are insufficient regarding the hydraulics of and the entrainment of the kettle reboilers, especially industrial-size kettle reboilers. FRI has been conducting extensive hydraulic studies on one of its industrial-size kettle reboilers since 2011. This reboiler was equipped with four large viewing windows. Those windows were strategically positioned for the hydraulic studies. As far as the authors know, nobody has ever before put observation windows on an industrial-size kettle reboiler. Using these windows, FRI has collected very significant kettle reboiler data using different hydrocarbon systems operated at column pressures ranged from 0.1 to 11.4 bara with a maximum heat flux of 59 kW/m^2. These reboiler studies are considered by FRI's membership as a "Parallel Project" because these studies are not interfering with any FRI mass transfer programs.

Experimental setup

The FRI experimental unit consists of two commercial scale distillation columns and their support systems. For most of the current kettle reboiler studies, only the low pressure (LP) unit was employed. The low pressure unit is rated for operation from deep vacuum to 11.4 bara. Figure 1 is a sketch of the FRI LP kettle reboiler circuit, including some reboiler dimensions and the locations of the feed, bottom, steam inlet, condensate outlet, and vapor return nozzles. The left side of the figure is the column. Vapor enters into the column from the vapor return line of the kettle reboiler. Liquid from the bottom of the column and the feed flow are fed into the bottom of the reboiler.

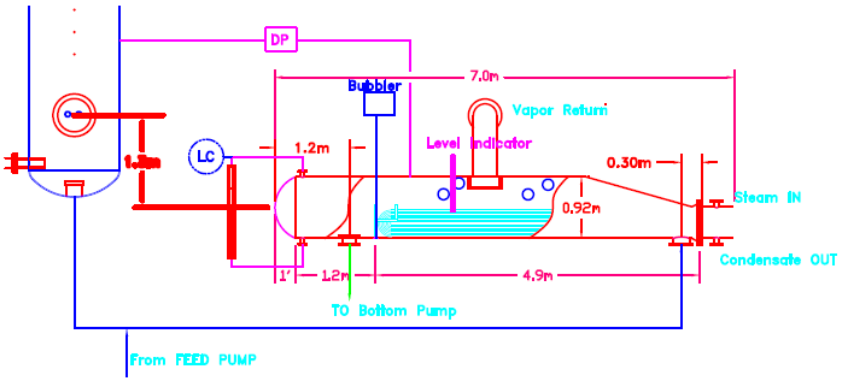

Figure 1. FRI LP Kettle Reboiler Circuit

Other parameters of the kettle reboiler are listed in Table 1 as follows:

Shell ID, mm	921
Height of Over-flow baffle/weir, mm	508
Diameter of Vapor nozzle, mm	457
U-tube bundle length, m	4.97
Tubes	183x15.9 mm OD
Total tube surface area, m^2	89

Table 1. Dimensions of FRI LP Kettle Reboiler

To better understand reboiler circuit hydraulics, pressure drops between the kettle reboiler and the column were measured. Figure 1 shows the locations of the differential pressure drop transmitter, and the bubbler that extends to the inside bottom of the kettle.

As shown in the Figure 1, four observation windows are strategically positioned in the kettle reboiler. Two of them are located between the overflow weir and the vapor return nozzle. The other two windows are located close to the steam inlet. Figure 2 shows the four windows. A metal metering stick (level indicator) was inserted into the top of the shell, directly above the U-tube bundle. This stick allows measuring of the boiling pool depths. There are two more windows on the distillation column bottom manway that are on the opposite side of the column vapor return nozzle. Those two windows allow observations of the vapor stream leaving the vapor return nozzle and entering the bottom of the column.

Figure 2. FRI Kettle Reboiler Observation Windows

Window observations

Some of previous kettle reboiler studies [5,6] used a slice of a heat exchanger that was electrically driven. The photographs and video footages from those studies showed that all of the tubes in the apparatus were boiling with equal vigor, and that the bubbling extended horizontally to the inside shell wall. Those studies suggested that the heavy bubbling inside the kettle make it impossible to see deep into any exchanger.

General

The FRI kettle reboiler was routinely run with the iso/n-butane, cyclohexane/n-heptane, and p/o-xylene systems. For all of the systems, even at the highest of heat fluxes, contrary to the previous studies by other researchers, the views of the functioning kettle reboiler through the windows were amazingly clear. It was usually possible to see individual tubes bubbling, and to see individual bubbles being created and then climbing within swarms to the boiling pool surface.

Nucleate boiling

In the early stage of this study, the investigators encountered a surprise. At very low flux rates, the tube surfaces were not the first places where bubbling occurred. Instead, the first surfaces to create bubbles were the rusted segmental support baffles and the rusted support rods. Figure 3 provides a photograph of this phenomenon. The rusted support hardware was at the same temperature as the

tubes, but, the rusted support hardware contained more, and more effective, nucleation sites. The rusted support hardware was, in fact, behaving like UOP High Flux tubing [6].

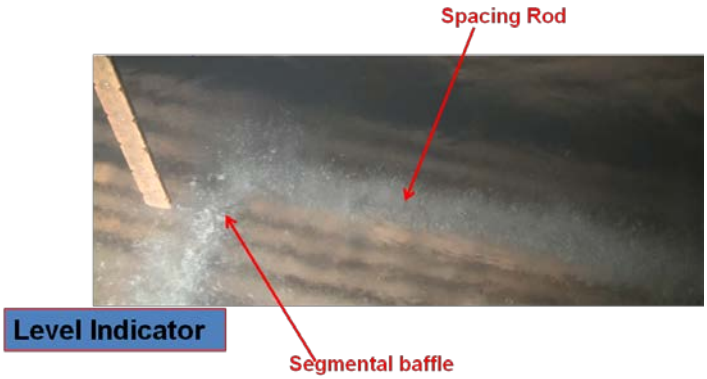

Figure 3. Nucleate Boiling on Baffle and Spacing Rod

Low and Medium Reboiler Heat Fluxes

At low and medium reboiler duties, the central and highest tubes boiled well before the lower/side tubes, the ones near the sides of the exchangers. There was usually clear liquid above these lower side tubes.

Different Test Systems

For all of the systems and pressures that were studied, the boiling pools above and around the reboiler tubes were usually calm. In fact, these pools appeared similar to the "bubble regime' on a distillation tray. Almost always, individual bubbles could be observed. There were no geysers, or washing machine type of actions, inside the kettle reboiler.

Figure 4 shows the view inside the kettle with the C4 system at 11.4 bara pressure at a heat flux of 59kW/m^2. This rate was about 115% of the kettle design rate. Even though a professional heat exchanger rating program predicted an extremely high entrainment rate at this condition [7], the liquid entrainment out the vapor product nozzle was nearly zero, as seen through the windows. The entrainment rates were significantly over-predicted by the professional model.

Figure 4. View inside Kettle with C4's system at 59 kW/m^2 Heat Flux

For the C6/C7 system at 1.62 bara pressure, when the kettle reboiler was operated at a heat flux of 38 kW/m^2, very significant liquid entrainment out the vapor product

nozzle was observed using the windows on the kettle and was confirmed using the column windows across the vapor return nozzle as shown in Figure 5**.**

Figure 5. View inside Kettle with C6/C7 system at 38 kW/m^2 Heat Flux

Gamma Scan Measurements

The vapor return line of the LP reboiler was gamma scanned by Tracerco at various heat fluxes for the C6/C7 system at 1.62 bara. Table 2 includes the measured entrainment fractions in the horizontal part of the vapor return line that was close to the column. It was demonstrated that Tracerco gamma scanning successfully quantified the liquid entrainment in the reboiler vapor return line. The entrainment measured by gamma scanning was consistent with visual observations from the windows on the kettle reboiler and from the windows opposite the vapor return nozzle.

Run No.	Heat Flux	Measured Process Density	Entrainment Fraction
	kW/m^2	kg/m^3	kg-liquid/kg-vapor
1	9.7	5.68	0.00
2	15.5	5.73	0.01
3	23.4	5.95	0.05
4	25.4	6.14	0.09

Table 2 Gamma Scan Results

Pool Depth Measurements

For all of the systems and pressures that were studied, the boiling pool depths were usually readable to ±10 mm. The flow of the boiling pool towards the overflow weir was usually weaker near the sides of the kettle. Appreciable data were collected regarding pool depths. Very surprisingly, pool depths were not significantly affected by reboiler heat fluxes, but were significantly affected by loadings over the tall weir.

Pressure Drop Results

Pressure drops between the top of the kettle and the bottom of the column were measured with various systems at different pressures. Figure 6 shows one of the resultant pressure drop graphs. The graph compares the measured and the predicted/calculated vapor phase pressure drops across the kettle vapor product piping. At high column capacity factors, Cs, the divergence of the curves is believed to be due to liquid entrainment in the vapor product piping**.**

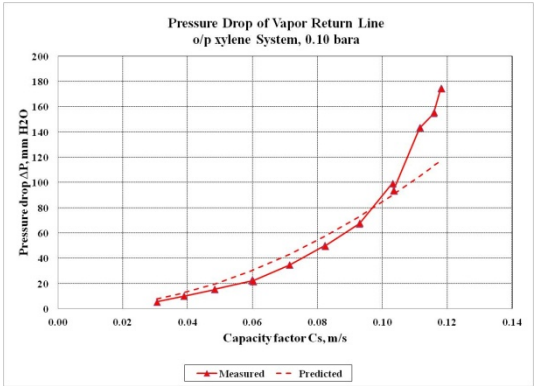

Figure 6**.** Pressure Drops across Vapor Return Line

Conclusions

Contrary to other studies published in the literature, the boiling/bubbling inside the kettle reboiler proved to be amazing clear and relatively calm. At low reboiler heat fluxes, bubbling begins on the heavily rusted segmental support baffles and support rods. The upper tubes create much more bubbling than the lower tubes. There is more vaporization in the steam end of the reboiler than the weir end. Liquid entrainment levels (in the vapor product line) as viewed from the distillation column windows are corroborated by the views from the kettle windows. Reboiler duty has an almost-negligible impact on boiling pool depth, but liquid weir loading has a significant impact on boiling pool depth. Literature correlations significantly over-predicted the entrainment rate, and under-predicted the kettle reboiler capacities.

Additional kettle reboiler studies are currently underway at FRI.

Acknowledgements

The authors gratefully acknowledge the support of the FRI membership for their continuous support to FRI research program. They are also grateful to Tracerco for gamma scanning the vapor return line. Professors Ken Bell and Rob Whiteley, both of Oklahoma State University, consulted regularly regarding these kettle reboiler studies.

References

1. H. Z. Kister (2003), Trans. IChemE, 81, A, 5-12
2. J. W. Palen and W. M. Small (1964), Hydrocarbon Processing, 43, 199-208
3. P. Milada et. al. (2006), International Journal of Heat and Mass Transfer, 49, 1214-1224
4. J. R. Fair and A. Klip (1983), CEP, March 1983, 86-95
5. B. M. Burnside et. al. (2005), International Journal of Heat and Mass Transfer, 48, 1000-1016
6. D. A. McNeil (2000), Applied Thermal Engineering, 22, 803-814
7. Fractionation Research, Inc.(2009), Internal Report

Maldistribution in Packed Columns – New Findings, Old Challenges

Dr. Tobias Keller[1], René Eiswirth[1], Dr. Alexey Shilkin[1], Dr. Carsten Knösche[1], Dr. Alexander Pavlenko[2], Dr. Nikolay Pecherkin[2], Dr. Vladimir Zhukov[2]
[1] BASF SE, Chemical and Process Engineering, Ludwigshafen, Germany;
[2] Kutateladze Institute of Thermophysics SB RAS, Novosibirsk, Russia

Abstract
To improve the reliable design and the economical efficiency of packed columns, a better understanding of the arising of liquid maldistribution is necessary. In the open literature, a cell model is commonly used to describe the liquid distribution behavior of structured packings. In this study, we performed point source experiments to study the spreading behavior of different types of structured packings and to develop a cell model based on the experimental results. To prove the capability of this cell model, maldistribution experiments were performed in an industrial-scale distillation column. The column had a diameter of 900 mm and was equipped with the structured packing Mellapak 350.Y, containing 19 layers with a total height of 4.016 m. The freon mixture consisting of R114 and R21 were used as a test system. The experimental data on the distribution of local liquid loads over the column cross section were compared with the predicted results using the cell model. It was shown that the cell model is not able to predict the experimental data. This demonstrates the need for more-detailed models that are able to predict not only the small-scale distribution behavior of structured packings but also large-scale distribution effects as well as the influence of the gas flow.

Keywords
Distillation, Liquid distribution, Cell model, Experimental validation

1. Introduction

The separation step of a chemical process is typically performed in distillation columns. If random or structured packings are used as column internals, a uniform distribution of the internal liquid flows over the cross-sectional area of the column is required for an adequate separation performance. On the other side, if liquid maldistribution does occur, the separation performance of the distillation column will be significantly reduced. To counteract this maldistribution, packed columns are equipped with liquid distributors. Usually, the design engineer applies an empirical rule of thumb including that the liquid should be collected and redistributed after a maximum bed height of 5 m or 10-15 theoretical stages [1]. In case of challenging separation tasks, the volumetric content of non-separating internals can thus be higher than 50% leading to significant investment costs.
To improve not only the reliable design of packed columns but also their economic efficiency, a better understanding of the arising of liquid maldistribution is necessary. The present work addresses this need through the experimental investigation and modelling of liquid maldistribution in a distillation column.

2. Results and discussion

To better understand the mechanism of maldistribution in distillation columns, which are equipped with structured packings, an experimental set-up was designed in this work to study the liquid distribution behavior of different structured packings in more detail. The experimental set-up will be introduced in Section 2.1. The experimental results that were obtained for different structured packings will be presented in Section 2.2. To predict the experimental data on liquid distribution, a cell model is introduced in Section 2.3. Results of maldistribution experiments performed in an industrial scale column will be shown in Section 2.4. The cell model will be used to predict the experimental data.

2.1 Experimental set-up and conditions

Because this work addresses the local liquid distribution behavior of structured packings, the experimental studies were not performed in a distillation column but in an experimental set-up that only requires two corrugated sheets of the relevant structured packing. The experimental set-up is shown in Figure 1.

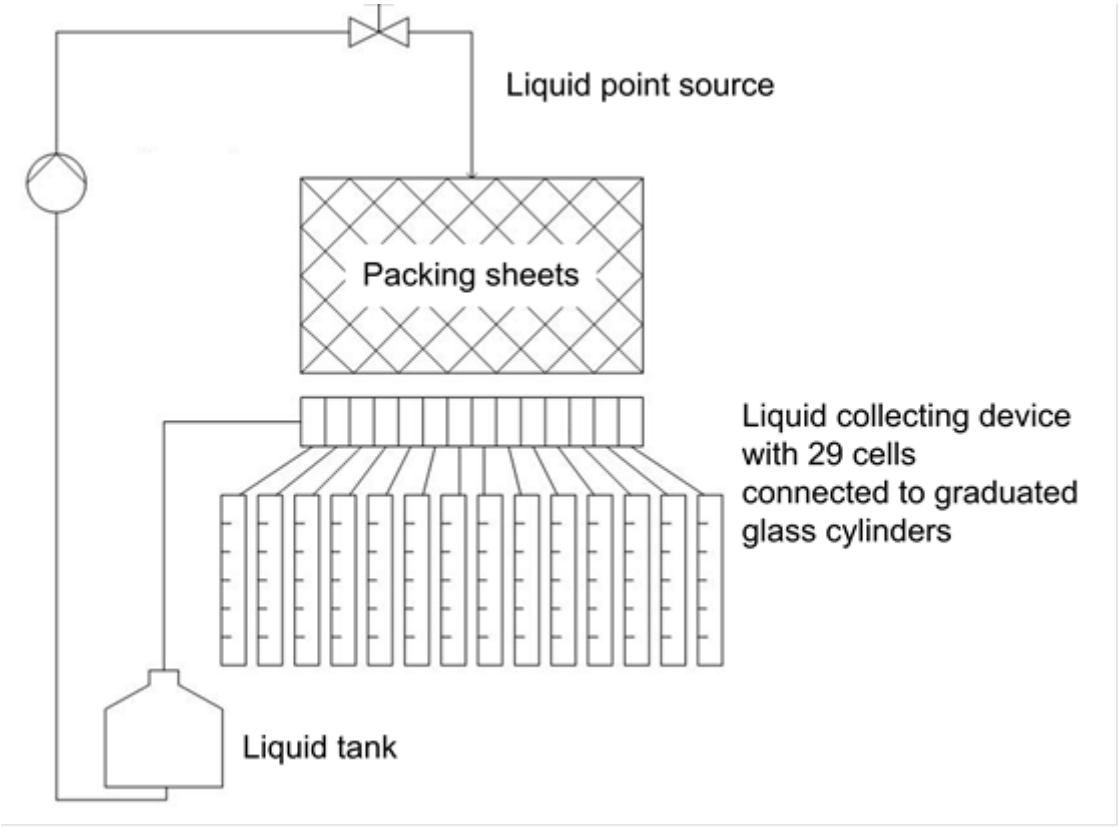

Figure 1: Experimental set-up for the determination of liquid distribution.

The essential part of the experimental set-up consists of two corrugated sheets of the corresponding packing to create the typical channel geometry of a structured packing. The liquid is introduced at the top of the packing sheets. A collector system for the liquid is installed below the packing sheets and consists of two different parts. The first part is used at the beginning of each experiment to ensure the pre-wetting of

the packing sheets. In this phase, the liquid is collected and recycled back to the feed tank. The second part of the collector system contains 29 separate cells and is used for the determination of the liquid distribution. Each cell is connected through a tube to a graduated glass cylinder to measure the local liquid load coming out of the packing. The collector system is manufactured in such a way that it is possible to switch between the two different parts.

Four different types of structured packings were studied: Montz B1-250, Montz B1-250M, Montz B1-350 and Montz B-350MN. Each packing sheet had a height of 200 mm and a width of 600 mm. The liquid distribution was studied at varying liquid loads within the range of wl = 1–10 m/h.

Previous experiments showed that the use of water leads to a low reproducibility of the experimental data because of the low wetting behavior of water. As a consequence, an aqueous surfactant solution with a surface tension of approx. 30 mN/m was used resulting in reliable experimental data.

To study the distribution mechanism of the liquid, especially with respect to lateral spreading effects, the liquid was centrally introduced with a point source at the top of the packing. For the placement of the point source, six different positions near to the center of the packing were chosen (see Figure 2). Because of the six different positions for the placement of the point source, six experimental runs were performed for each liquid load.

As already mentioned, two adjacent corrugated packing sheets were used for the experimental study. These two sheets are oriented at 180° to each other forming a series of inclined channels. Because it is difficult to find the exact center of the channel for the placement of the point source, the liquid was introduced on two different positions of the channel, namely on the front-side and on the back-side of the channel (see Figure 3).

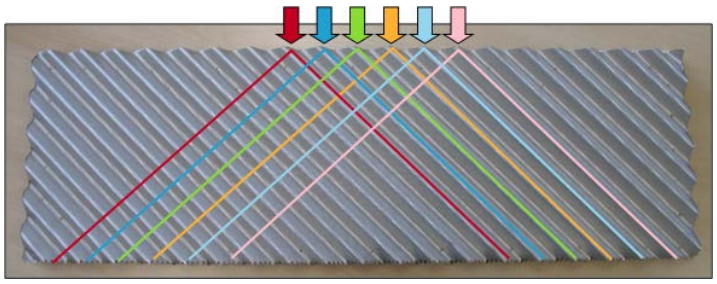

Figure 2: Overview of the six different positions that were chosen for the placement of the point source.

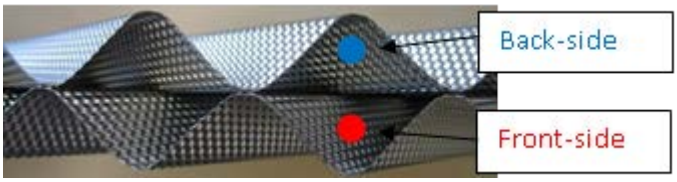

Figure 3: Front-side and back-side position for the placement of the point source.

2.2 Experimental results

In this work, four different types of structured packings – Montz B1-250, Montz B1-250M, Montz B1-350 and Montz B-350MN – were experimentally investigated at

different liquid loads (wl = 1–10 m/h) to get a detailed insight into the liquid distribution behavior. The following section will exemplarily present the results for the structured packings Montz B1-350 and B1-250M at a liquid load of wl = 1 m/h and wl = 10 m/h.

The experimentally determined liquid distributions of both packing types are given in Figure 4. These figures indicate the percentage of the total volume flow-rate that was collected in the individual cells of the collecting device below the packing sheets. The numbering of the cells is defined such that the cell, which is located directly below the introduction point of the liquid, has the number 0. Because of this normalization, it is possible to show the results of all six experiments with varying positions of the point source in a single diagram.

In case of the packing B1-350, the liquid distribution curve becomes higher and thinner with an increase of the liquid load. This peakedness observed at a high liquid load of wl = 10 m/h indicates an undesirable non-uniform liquid distribution behavior of the packing. Moreover, the results demonstrate that most part of the liquid does not follow the corrugations of the packing sheets but flows between the two sheets straight downwards. In contrast, the experimental results of the packing B1-250M show that no liquid leaves the packing sheets directly below the point source (cell number = 0). Most part of the liquid follows the corrugations of the packing sheets. The packing B1-250 was the only packing in our study, for which liquid was collected even in the cells -8 and +8 indicating that part of the liquid followed exactly the corrugation where the liquid was introduced.

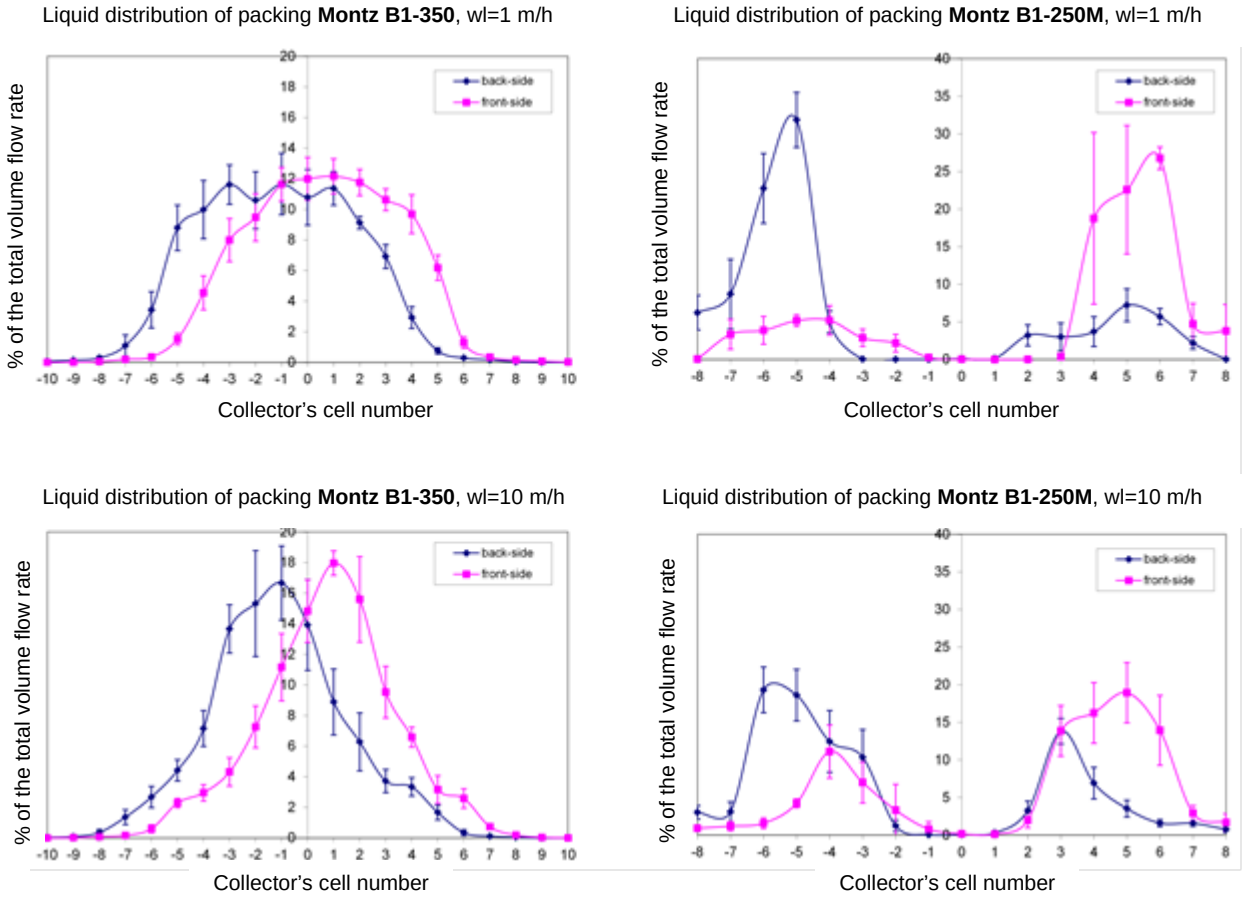

Figure 4: Experimentally determined liquid distribution curves at a liquid load of wl = 1 m/h and wl = 10 m/h for the structured packings Montz B1-350 and Montz B1-250M.

2.3 Cell model

The liquid distribution model used in this work is based on the cell model developed by Stoter [2]. This model is commonly used in the open literature and discretizes the structured packing into discrete cells which are interconnected to each other (see Figure 5). The dimensions of these cells and their communication with each other depend on the type, size and surface characteristics of the structured packing. The following flow paths are considered in the model: (1) flow in the channel direction, (2) flow over the crossings to the adjacent corrugation sheet and (3) flow over the channel ridge to the next channel. The model parameters a_1, a_2 and a_3 were determined by fitting the calculated results to the experimental data obtained for the different packing types.

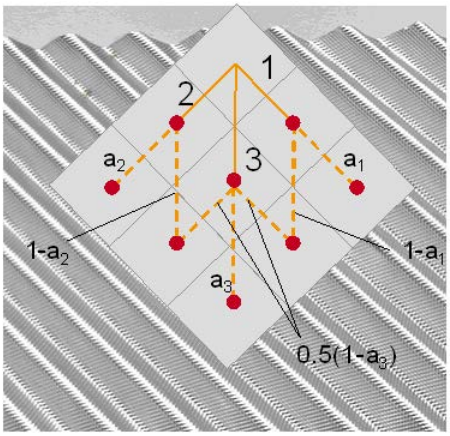

1) Flow in channel direction

2) Flow over the crossings

3) Flow over the channel ridge

Figure 5: Different flow paths that are considered in the cell model to describe the liquid distribution behavior of structured packings.

2.2 Maldistribution experiments in a distillation column

To validate the developed liquid distribution cell model, experimental studies were performed in a distillation column with a diameter of 900 mm using the R114 and R21 freon mixture [3]. The column was equipped with the structured packing Mellapak 350.Y, containing 19 layers with a total height of 4.016 m. To generate mal-distribution of the liquid flow over the cross-section of the packing, a complete row of holes in the bottom of the liquid distributor were deliberately blocked. The distribution of the local liquid flow rate was experimentally determined below the packing over the total cross section of the column. In total, 419 measuring points were installed, distributed uniformly over the column cross section. More detail about the experimental set-up and the experimental conditions that were studied can be found in the latest publication of Pavlenko et al. [3].

In the following, the results are exemplarily discussed for an experiment that was performed under total reflux conditions, at a liquid load of wl = 14 m/h and F-Factor of F = 1.27 $Pa^{1/2}$. The distribution topogram of the local liquid loads, which were measured below the packing section, is shown in Figure 6a. It can be seen that the distribution of local liquid loads is non-uniform.

The developed cell model was used to predict the liquid distribution. The simulated results are shown in Figure 6b. It can be seen that the cell model is not able to reproduce the liquid load distribution over the column cross section. Especially, the cell model was not able to predict the zones of lower liquid loads that were observed

near the wall on the right side. The comparison with the experimental data clearly demonstrates that a cell model, which is commonly used in the open literature, is not sufficient for a satisfying description of liquid distribution in an industrial-scale column. We think that large scale mixing effects need to be considered in a more detailed model. Large sale effects, which have not been considered yet, are caused by the small gaps between blocks of packings. Moreover, the effect of the vapor flow rate should be taken into account.

All of the other experimental data, which are not shown in this manuscript, clearly demonstrate that further experimental studies are still necessary to get a deeper understanding of the mechanism of liquid distribution, and the development of more detailed models is necessary for a reliable prediction of liquid distribution effects.

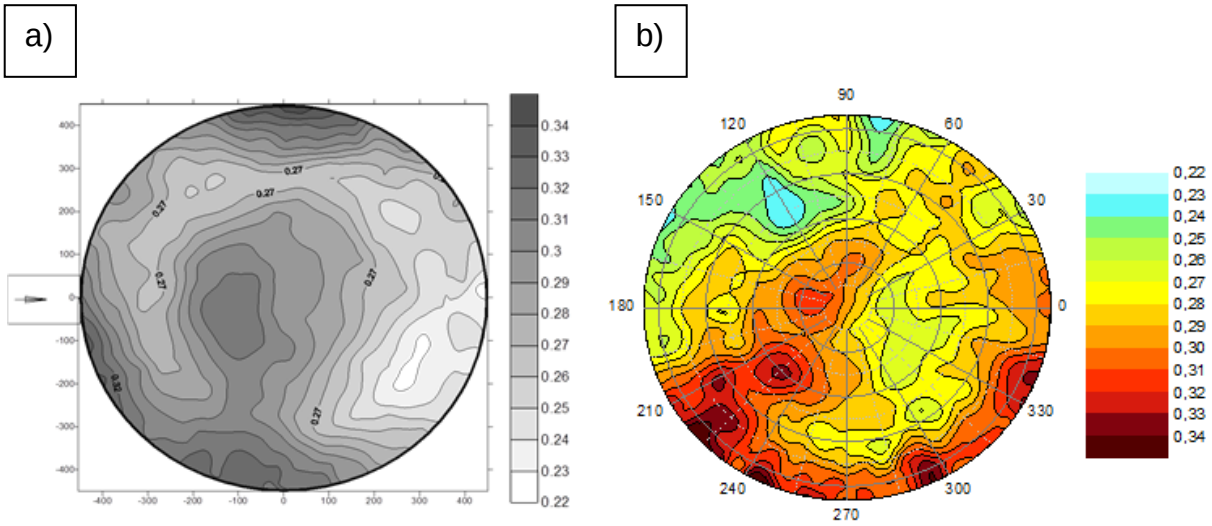

Figure 6: Distribution topograms of local liquid loads over the column cross section. The flow-rates are given in 10^{-2} m/s. (a) Experimental results and (b) predicted using the cell model.

3. Conclusions

The small-scale liquid distribution behavior of the following structured packings was experimentally studied: Montz B1-250, Montz B1-250M, Montz B1-350 and Montz B-350MN. The results showed that the structured packings have different liquid distribution behavior. The liquid load has a great influence on the liquid distribution. Based on the experimental data, a cell model, which is commonly used in the open literature, was developed. However, maldistribution experiments in an industrial column demonstrated that the cell model was not able to predict the experimentally determined liquid load distribution over the column cross section. Further experimental studies are needed to better understand the mechanism of liquid distribution. More detailed models must be developed to consider large scale mixing effects and the influence of the vapor flow rate.

References

[1] Z. Olujic et al., 2009,*Chem. Eng. Process.*, 48, 1089–1104.
[2] C. Stoter, 1993, *Modelling of Maldistribution in structured packings*, PhD thesis, TU Delft.
[3] A. Pavlenko et al., 2014, *AIChE J.*, 60, 690–705.

Investigation of Liquid distribution in Packed column with Cell model

Dipl. Ing. Miha Košir[1], *Guanghua Zheng*[1], *Marcus Grünewald*[1]

[1]*Ruhr-Universität Bochum, Laboratory of Fluid Separations, Bochum, Germany.*

Abstract

Gas-liquid counter-current packed columns are widely used as contacting devices in separation processes. They are mostly utilized for absorption, desorption and distillation columns. One significant parameter in packed columns is the homogeneity of distribution of gas- and liquid phase. The phase distribution influences parameters like pressure drop and residence time distribution but even more the mass transfer. In particular the effective area for mass transfer depends strongly on the quality of liquid and gas phase distribution.

Considering that fact that the insitu measurement of the interfacial area in packed columns is not possible, a new technique, the wire mesh sensor (WMS) has been established to characterize the homogeneity of flow in packed columns. The WMS is based on matrix-shaped adjustment of measuring elements and is characterized by a highly spatial and temporal resolution. Since both levels have different electrical permittivity values the distribution of gas and liquid phase can be identified.

The results of liquid phase distribution experiments have been evaluated with a cell model as described in literature. The targeted parameter, the splitting factor has been determined varying the operating parameters. Therefore, it is suggested to study the scale-up of liquid distribution by performing experiments in columns with different diameters. In addition an advanced cell model including equations which account the interaction of gas and liquid flow has been developed.

Keywords: Packed column, Phase distribution, Cell model

1. Introduction

In the process industry distillation and absorption columns are widely used as gas-liquid counter-current flow contactors for thermal separation processes.

In this contribution, the focus is laid on random packing which have been developed with variation in shapes, sizes and materials in the past years. In contrast to structured packings, random packings are less expensive. Therefore and due to higher loading capacities and lower specific pressure drop, mostly second generation random packings, like the Pall Ring are used in research. (Joham 2006,Potthoff 1992)

One of the significant parameter for investigation in packed columns is the homogeneity of distribution of gas- and liquid phase. The phase distribution influences parameters like pressure drop and residence time distribution but more than that the mass transfer phenomena. In particular the effective area for mass transfer depends strongly on the quality of liquid and gas phase distribution.

However, the phase distribution for both gas and liquid phase are strongly dependent on the geometry of random packing. Deviations from ideal phase distribution are described by maldistribution (Stoter, C.F. 1993). In this case, the liquid that streams down through the column assembles near the wall. The influence of maldistribution is bigger in columns with larger diameter, but in contrast, in this columns wall flow can be neglect (Stikelman 1989). Consequently, The redistributor or second distributor (liquid collector) is useful in order to maintain the desired flow patterns. This redistribution results in increasing costs for additional hardware within the column. Hence, It has to be investigated in which height a redistribution of liquid becomes necessary.

Therefore, the liquid phase distribution in columns with random packing is studied with the help of a of cell model. As described by (Stikkelman 1989, Olujic Ž.), cell models divide the overall columns in several cells, which are characterized individually with inlet and outlet streams of liquid phase. The stream direction as well the splitting factor, which describes the fraction of liquid flow in the under layer cell, are dependent on the position of the cell within the column. Liquid distribution is influenced by packing size, packing height, liquid holdup, contributor and liquid load rate, for example. Thus, a cell model helps to describe the liquid phase flow in packed column.

In the past, cell models were used to numerically study the liquid distribution in random packings by many researches. The first cell model was studied by Albright (1984), to investigate different types of liquid distributors. This model was set up with the assumption, that each random packing with a diameter of 25 mm concur to a single cell and that the liquid flows into a cell randomly and spreads without splitting in cells. In this model, the radial spreading of liquid is neglected. (Kammermaier 2008). Stikelman also investigated liquid and gas phase distributors in random and structured packings. In his work, he divided the column into orthogonal stacked layers and finally presented the random splitting mechanism.(Stikkelman 1989). Further investigations were done by Higler, who assumed that the liquid flow through the cell from the upper layer does not completely enter the underlying cells. The cell models of researches distinguish from one another by using different packings and different parameters (splitting factor, packing height, cell size, cell geometrie…) for cell model.

The aim of this contribution is the development and validation of a cell model for the study of liquid phase distribution. With regard to this newly developed cell model an easier scale up of packed column might be possible.

In addition to investigate the cell model experiments with the Wire-Mesh sensor (WMS) are performed. Within the last few years various measurement procedures were presented for structured and random packings to investigate details with the

multiphase flow. These were studied with x-Ray/Gamma ray tomography technique, which has spatial solution very high and temporal solution has low. This method is also expensive (Mahr 1975). Nevertheless, the WMS is applied for the study of phase distribution in multiphase flows. This system can also be used for hydrodynamic investigations in packed column. This measuring device can be described as invasive, but low-intrusive in comparison to other measuring technologies for phase distribution. The exerted Wire-Mesh sensor is multiphase reclaimer and enables the investigation of multiphase flows with high spatial and temporal resolution.

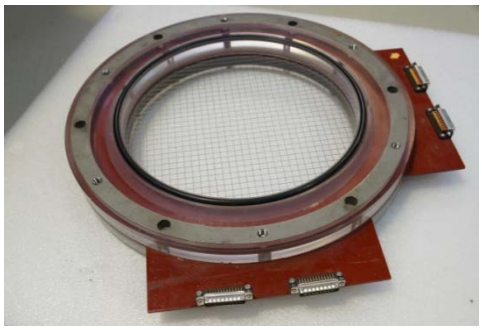

Figure 1: Wire Mesh sensor 32x32

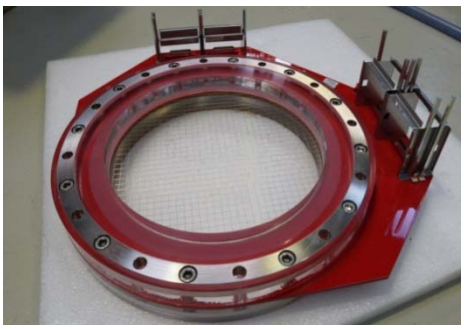

Figure 2: Wire Mesh sensor 64x64

The Wire-Mesh sensor used for our experiments (Figure 1) exists of 32x32 orthogonally arranged stainless steel wires, which are classified in two planes with a distance of 3 mm apart each other. The diameter of wires is 0,5 mm. The classification gives a total of 1024 sensing points thereof 840 are inside points. The circular cross-section of the packed column has a diameter of 288 mm. Measurements are performed with 400 Hz which is equivalent to 400 frames per second. The application of the wire-mesh sensor was successfully performed in packed column by Zheng (2011).

Figure 2 shows a WMS used for further measurements which exists of 64x64 orthogonally arranged wires from stainless steel. The wires are also classified in two planes with a horizontal distance of 0,9 mm. The diameter of the wire is 0,2-0,3mm. For this instrument the classification gives 4096 sensing points thereof 3174 inside points. The temporal resolution is 2000 Hz (frames per second), where as the cross section of the column does not change

The experiments were performed with deionized water and air. Water and air have different electrical permittivity values. Consequently, the capacitances, received in the sensing points of the WMS vary. By connecting the WMS to a computer, the measured data can be extracted and processed, resulting in images of phase distributions over time and diameter.

The experiments were performed in a packed column with adiameter of 288 mm as shown in Figure 4.

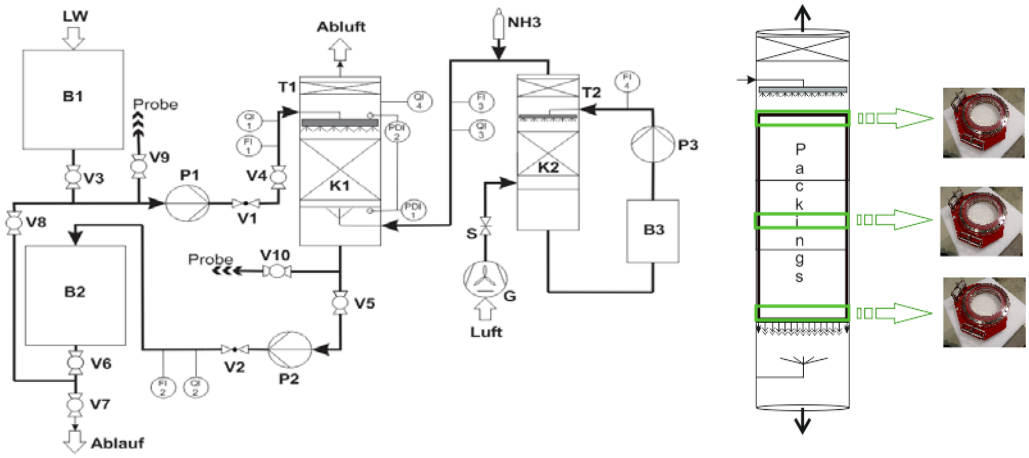

Figure 4: Process plant for measurements with Wire-Mesh sensor

2. Results and discussion

In the following section, the results of the application of a cell model coupled with results from measurements of the wire-mesh sensor are presented. To show the range of performance of the applied cell model, important parameters are varied. In further detail, variable liquid flow rates, random packing heights and flow patterns by different liquid inlet are investigated in the simulation.

The influence of liquid flow rate on phase distribution is shown in Figure 6, by the packing height of 0,3 m, column diameter 0,288 m and splitting factor 0,3.

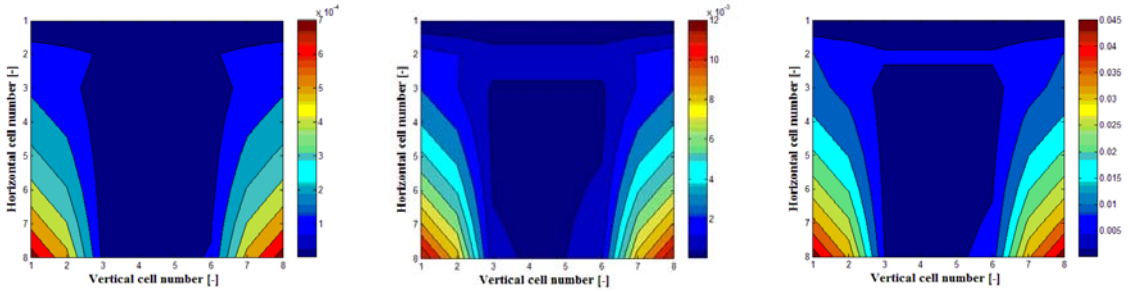

Figure 6: Simulation of variable liquid flow rates (1, 4 an 8 $m^3/m^2/h$)

The results show that the liquid flow rates are similar to liquid flow pattern and the increase of liquid flow rate does not influence the phase distribution. Splitting factor does not have an effect on the higher liquid flow rate of the phase distribution. There are differences on outlet (wall flow) of liquid flow rate, but similar distribution is in the core of cells.

For the research for gas-liquid distribution with Wire-Mesh sensor in packed column is used the random packing metal Pall Ring 25 (Figure 5).

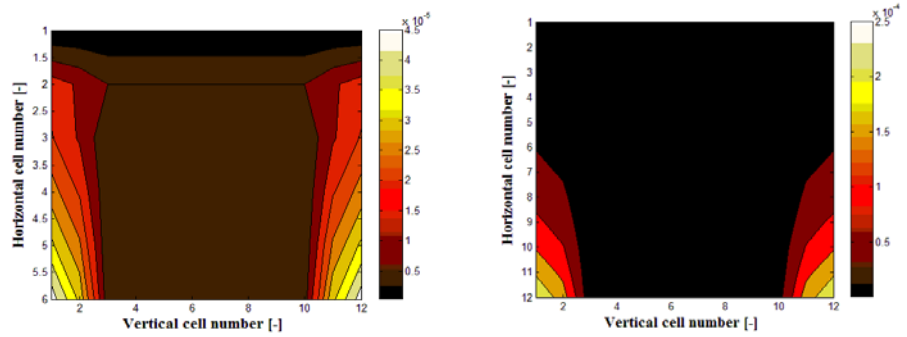

Figure 7: Simulation of random packing height (0,15 und 0,3 m)

Liquid distribution is investigated by 0,15 m and 0,3 m random packing heights (Figure 7).

It is shown that the packing height influences the phase distribution. However, the cell size and cell number are significant for the investigation of phase distribution. Maldistribution leads and starts earlier by the packing height of 0,15 m as by packing height of 0,3 m, but anyway maldistribution is noticed in both packing heights. The liquid flow is also stronger and accumulates on the wall in smaller height. Wall flow starts by the packing height of 0,3 m at the half of the packing height and the core area remains consistent. However, at the wall more liquid assembles as in packing height of 0,15 m. The higher is the packing height the later and the more liquid assembles on the wall. The packing height has strong impact on liquid distribution. Further studies should be done on the random packing height.

Flow patterns were investigated by different liquid inlet and are presented in Figure 8. The random packing is built on height 0,3 m, column radius is 0,144 m and the splitting factor with 0,3.

a) o o o o o 1 1 o o o o o b) o o o 1 1 1 1 1 1 o o o c) 1 1 1 1 1 1 1 1 1 1 1 1

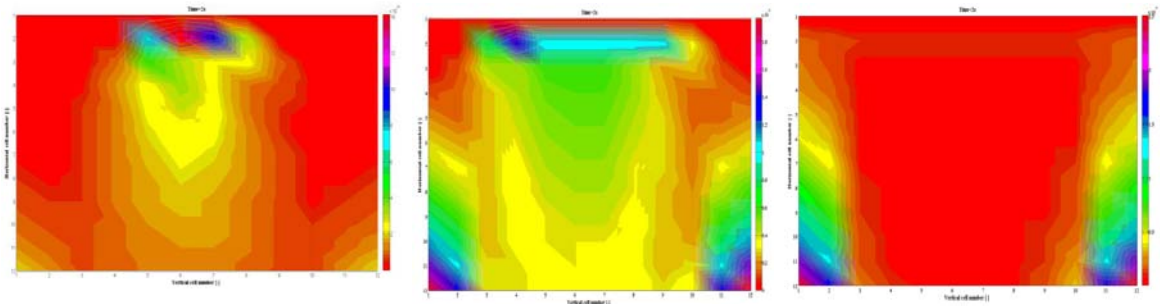

Figure 8: Simulation of flow patterns by different liquid inlet through a) two cells, b) six cells, c) twelve cells

At this investigation it is resulted the primary distribution of two cells at the middle of first row in core of column (a). The two cells are full irrigated and there is no liquid flow on the column wall. By observation of six irrigated cells increase the irrigation density and increase start of liquid assembling on the column wall. On the wall liquid flow assembles earlier by higher irrigation density than at lower irrigation density. It sees the full irrigated cells in the core and on the wall of column. The irrigated hole flow pattern by primary distribution (all twelve cells observed) is shown in c). In the

core of column the liquid flows congenial through the cells. The liquid assembles dramatically on wall of column. It can be still noticed the maldistribution.

However, it is shown that the flow pattern is not vertical equal. The reason can we find in the mechanism of stream classification. The cell study is done from left to right, from top to bottom. The cell classification is concerned that on the left side are two cells without liquid and one cell with liquid with liquid content. On the right side are two cells with liquid content and one cell without. It is resulted that we have in every cell maldistribution and unevenness.

3. Conclusion

For this research a cell model with equal sized cells was developed for the investigation of liquid distribution in packed column with random packing The measurements were performed with the help of a Wire-Mesh sensor. Various parameters which influence the liquid distribution such as liquid flow rate, packing height, liquid inlet for cell pattern in vertical and horizontal direction, were studied. Subsequently, with these results it is possible to draw conclusions regarding the hydrodynamics of the column.

However, it is found that packing height, splitting factor, liquid flow and liquid inlet flow as parameters of the cell effect the overall liquid distribution. As the results show, in almost every cell maldistribution of the liquid can be found. Therefore, more experimental work has to be done for different packings, different diameter of column and different destributors.

References:

Albright M.A.: Packed tower distributors tested, Hydrocarb. Proc. 63 9, 173-177, (1984)

Higler A., Krishna R., Taylor R.: Nonequilibrium Cell Model for Packed Distillation Columns-The Influence of Maldistribution, Ind. Eng. Chem. Res., 1999, 38, 3988-3999

Kammermaier, E.: Neuartige Einbauten zur Unterdrückung der Maldistribution in Packungskolonnen, Technische Universität München, Dissertation 2008

Joham, M.: Untersuchung des Stofftransportes in Füllkörperkolonnen unter Anwendung modern Programme, Ruhr Universität Bochum, Dissertation 2006

Olujic Ž., Development of Complete Simulation Model for Predicting the Hydraulic and Separation Performance of Distillation Columns Equipped with Structured Packings, Chem. Biochem. Eng. Q. 11 (1) 31-46 (1997)

Potthoff, R.: Maldistribution in Füllkörperkolonnen, Fortschritt-Berichte VDI, Reihe 3, Nr.294, VDI-Verlag, Düsseldorf, 1992

Stikelmann, R.M., de Graauw J., Olujic Ž, Teeuw H., Wesselingh H. : A Study of Gas and Liquid Distribution in Structured Packings, Chem. Eng. Technol. 12 (1989) 445-449

Stikkelman, R.M.: Gas and liquid maldistribution in packed columns, Delft University of Technology, dissertation, 1989

Stoter, C.F.: Modelling of maldistribution in structured packings: from detail to column design, Delft University of Technology, dissertation 1993

Caustic Wash Columns for Sour Gas Absorption

Hans-Jörg Zander
Linde AG, Engineering Division, Dr.-Carl-von-Linde-Straße 6-14, 82049 Pullach, Germany

Designing caustic towers for high caustic utilization helps to reduce operating costs such as caustic consumption, spent caustic flow to be treated, sulphuric acid needed for neutralization and salt freight to the sewer. If caustic utilization approaches and exceeds 100%, i.e. free NaOH is fully consumed and hydrogen sulfides and hydrogen carbonates are formed, the usual Hatta model describing mass transfer is no longer valid. Instead, a full discretization of the film considering all ionic species is inevitable. A model is presented to predict the column overall performance.

Keywords:
NaOH, caustic wash, sour gas removal, absorption, CO_2, H_2S

1. Introduction

Caustic wash columns are used for sour gas removal, especially CO_2 and H_2S, from gas streams. The gas phase and a NaOH solution is contacted in a trayed column, where the sour gases are absorbed and subsequently the reactions

$$\mathrm{CO_2 + 2\,NaOH \rightleftharpoons Na_2CO_3 + H_2O}$$
$$\mathrm{H_2S + 2\,NaOH \rightleftharpoons Na_2S + 2\,H_2O}$$

take place. As these reactions are widely irreversible, the column can be designed for very low lean gas concentrations down to ppm fractions. An absorption column setup including two caustic cycles is shown in figure 1. [3]

The spent caustic is non-regenerable and therefore withdrawn from the column to be oxidized. This converts the extremely toxic sulfide solution to sulfates, before neutralization with sulfuric acid degases CO_2 and forms sodium sulfate. In the end, the ions can be found in the spent water leading to a sewer salt freight. Due to these ion losses, caustic treatment is only suitable for the removal of traces.
A method reducing caustic consumption and spent caustic salt freight is proposed.

2. Caustic Absorption Principles

2.1 Basic Assumptions

One important variable describing the state of the liquid phase is the caustic alkalinity or strength before absorption

$$w_0 = \frac{m_{0,\mathrm{NaOH}}}{m_{0,\mathrm{NaOH}} + m_{0,\mathrm{H_2O}}}$$

The other variable is the caustic utilization

$$\eta = \frac{2 \cdot \mathrm{n_{CO_2}} + 2 \cdot \mathrm{n_{H_2S}}}{\mathrm{n_{NaOH}}}$$

which can be split specifically into CO_2 and H_2S utilization.

A utilization of 100% describes a state where caustic is quantitatively converted to Na_2CO_3 and Na_2S while no free caustic is available.

In contrast to this apparent species approach, it is well known that Na_2CO_3 and Na_2S solutions have an elevated pH. For example, a 5% Na_2CO_3 solution at 25°C has a pH of 11.6. This indicates that 100% caustic utilization can be exceeded through formation of dissolved $NaHCO_3$ and NaHS. This can be used to significantly reduce the caustic consumption and the sewer salt freight.

As the pH decreases when utilization exceeds 100%, the reverse reactions get significant in this region and a sour gas equilibrium back pressure becomes more and more important. Therefore, the maximum reachable caustic utilization depends on the available raw gas partial pressure. The absorption takes place in subsequent sections, at least a raw absorption section approaching equilibrium and a fine wash section operated at caustic excess.

2.2 Conventional Mass Transfer Modelling Approach

For caustic utilization below 100%, the reverse reaction is negligible and a NaOH excess is available, so CO_2 absorption is a pseudo-first order irreversible reaction:

$$r = k_{2^{\mathrm{nd}}\,\mathrm{order}} \cdot \left(c_{\mathrm{CO_2}} \cdot c_{\mathrm{OH^-}} - \frac{c_{\mathrm{CO_3^{2-}}}}{K} \right) \approx k \cdot c_{\mathrm{CO_2}}$$

Therefore, the liquid film theory can be applied to calculate mass transfer rates. Using the film thickness δ, the rate constant k, and the CO_2 diffusion coefficient D, the Hatta number is defined as

$$\mathrm{Ha} = \delta \cdot \sqrt{\frac{k}{D}}$$

A mass transfer enhancement factor is then given by

$$E = \frac{\mathrm{Ha}}{\tanh \mathrm{Ha}}$$

Therefore, as the CO_2 bulk concentration is zero, the mass transfer rate is

$$j_{\mathrm{CO_2}} = D \cdot \frac{c^*}{\delta} \cdot E$$

where c^* is the interfacial CO_2 concentration.

As the chemical reaction is fast enough for $\mathrm{Ha} \gg 3$ and therefore $\tanh \mathrm{Ha} = 1$, the film thickness cancels out, representing the fact that the CO_2 concentration goes to zero within the film. Therefore, CO_2 absorption can be used to measure effective interfacial areas. [1,2]

Using this mass transfer rate, the gas mole flow $\dot{n}_{\mathrm{vap}}$, the CO_2 outlet concentration of a tray with interfacial area A, Henry coeffient $H_{\mathrm{CO_2}}$ and mass transfer coefficients $k_l = D/\delta$ and k_g, the tray outlet concentration can be calculated according to

$$x_{\mathrm{CO_2}} = x_{0,\mathrm{CO_2}} \cdot \frac{1}{1 + \frac{A}{\dot{n}_{\mathrm{vap}}} \cdot \frac{p}{\frac{RT}{k_g} + \frac{H_{\mathrm{CO_2}}}{E \cdot k_l}}}$$

The reaction of H_2S with excess caustic is complete and very fast, therefore H_2S absorption is limited by the gas side mass transfer coefficient:

$$\mathrm{j_{H_2S}} = k_g \cdot \mathrm{c_{H_2S}}$$

This results in an H_2S outlet concentration of

$$x_{\mathrm{H_2S}} = x_{0,\mathrm{H_2S}} \cdot \frac{1}{1 + \frac{A}{\dot{n}_{\mathrm{vap}}} \cdot \frac{k_g \cdot p}{RT}}$$

The interfacial area A of the respective stage can be calculated using the common correlation equations for the selected tray type.

These equations describe the behaviour of one single tray. Several trays and liquid recycles are combined to a total column. The column profile predicts the purities that can be achieved with a given design.

2.3 Mass Transfer Modeling for High Caustic Utilization

In the more complex case of high caustic utilization above 100%, the valid range of this simple Hatta calculation is exceeded. To predict the column performance, a full film model discretizing the film volume was derived. This model contains the species H_2O, Na^+, OH^-, CO_2, HCO_3^-, CO_3^{2-}, H_2S, HS^- and S^{2-} and the liquid phase reactions

$$\begin{aligned}
\mathrm{CO_2 + OH^-} &\rightleftharpoons \mathrm{HCO_3^-} \\
\mathrm{HCO_3^- + OH^-} &\rightleftharpoons \mathrm{CO_3^{2-} + H_2O} \\
\mathrm{H_2S + OH^-} &\rightleftharpoons \mathrm{HS^- + H_2O} \\
\mathrm{HS^- + OH^-} &\rightleftharpoons \mathrm{S^{2-} + H_2O} \\
\mathrm{H_3O^+ + OH^-} &\rightleftharpoons \mathrm{2\,H_2O}
\end{aligned}$$

All of these reactions are limited by equilibrium. While the first reaction is kinetically controlled, all other reactions are instantaneous. The diffusion of the diluted dissolved gases CO_2 and H_2S in the liquid film volume can be described using Fick's law. Care has to be taken for diffusion of ions, as the motion of ionic species is coupled with electrostatics. The movement of one ion leads to an electrical field and this forces all other ions including itself. Ionic diffusion can be described on the basis of the Nernst-Planck equation [4]

$$j_i = D_i \cdot \nabla c_i + D_i \cdot c_i \cdot z_i^2 \cdot \frac{F}{RT} \cdot E$$

with the electrical field E, Faraday's constant F and the ionic charge z_i. Water is present in excess, its concentration can be calculated from the balance $\sum x_i = 1$.

The differential equation system describing the film is closed by a number of boundary conditions. The flow rates across the interfacial area are zero for all ionic species, while local equilibrium of CO_2, H_2S and H_2O is assumed. At the film layer boundary towards the liquid bulk phase, all concentrations are continuous.

A 1D finite-volume discretization of the mass balance equations across the liquid film results in algebraic equations. This discretization structurally represents the conservation characteristics of the balance equations. To reduce the number of variables to be solved for, a non-equidistant grid was used with an accumulation of grid points near the interface. The CO_2 hydrolysis reaction rate is described by a kinetic equation, while all other reaction rates are free variables as the reactions fully approach equilibrium. The equation system is closed using the respective equilibrium conditions.

As the kinetic equations cause the model equations to be strongly nonlinear, a Newton-based solver is used to converge the discretized equation system for each tray. The result is the concentration profiles and mass fluxes across the interfacial area of one single tray. Figure 2 shows an example of a concentration profile of the important species in the interface on a single tray.

The CO_2 concentration profile is bended as expected for reactive absorption. Therefore the mass transfer rate is enhanced compared to unreactive transfer, although the enhancement factor is smaller than in the low caustic utilization case. A OH^- profile influences all ionic equilibria causing profiles of the ionic concentrations. For caustic utilization below 100%, the profile is identical to the Hatta model prediction.

2.4 Overall Column Performance

As a caustic wash column absorbs sour gas on ppm levels, the gas throughput is orders of magnitude higher than the liquid consumption. Caustic is recycled within the column to increase the liquid load on the trays up to a reasonable hydraulic state.

The absorption equilibrium is strongly on the product side, therefore liquid recycling in any extent can be done without thermodynamic limitations. In a classical wash column, 2 or 3 caustic sections, each with one internal recycle, are used. In the raw wash section at the column bottom, the bulk amount of sour gas is removed, but the caustic is depleted, thus limiting the mass transfer rate. In the top wash section, caustic utilization is low and the free caustic concentration is therefore much higher. This strongly reduces the required number of trays compared to a column with only one section.

Three caustic cycles are required in the case of a caustic utilization above 100%. The lower cycle absorbs sour gas at its maximum partial pressure, which must be sufficiently high, as the absorption is limited by equilibrium and sour gas concentration can only decay to the equilibrium concentration. The middle section is a raw wash section, where caustic utilization is below 100% and no equilibrium limitation occurs. The upper section is the fine wash section in order to reach the specification absorbing with fresh caustic.

The column profiles can be calculated iteratively. First a sequential tray-by-tray calculation is done from bottom to top assuming constant liquid phase concentrations. Second a liquid phase correction step can be repeated until convergence is reached. Convergence of the column profile is attained after only a few calculation cycles, the calculation time is in the range of seconds. These calculations allow insight in the absorption process and a prediction of the overall column performance.

The model is validated by a comparison of the fully discretized model versus the Hatta model for the low caustic utilization case. Available data of laboratory and industrial plants have been used for a model validation. Measured data of an existing industrial column operated at high caustic utilization confirmed the design and the absorption model calculations.

3. Conclusion

The presented model is capable of describing the interfacial film and column profiles. The model prediction was validated using measured lab and industrial plant data. The maximum achievable caustic utilization is limited by equilibrium as well as kinetics. Higher partial pressures of CO_2 and particularly H_2S allow higher caustic utilization. High utilization requires increased effort to control the fresh caustic feed, as the safety distance to CO_2 break through is reduced. An additional third caustic cycle allows higher caustic utilization exceeding 100% based on carbonate and sulphide formation.

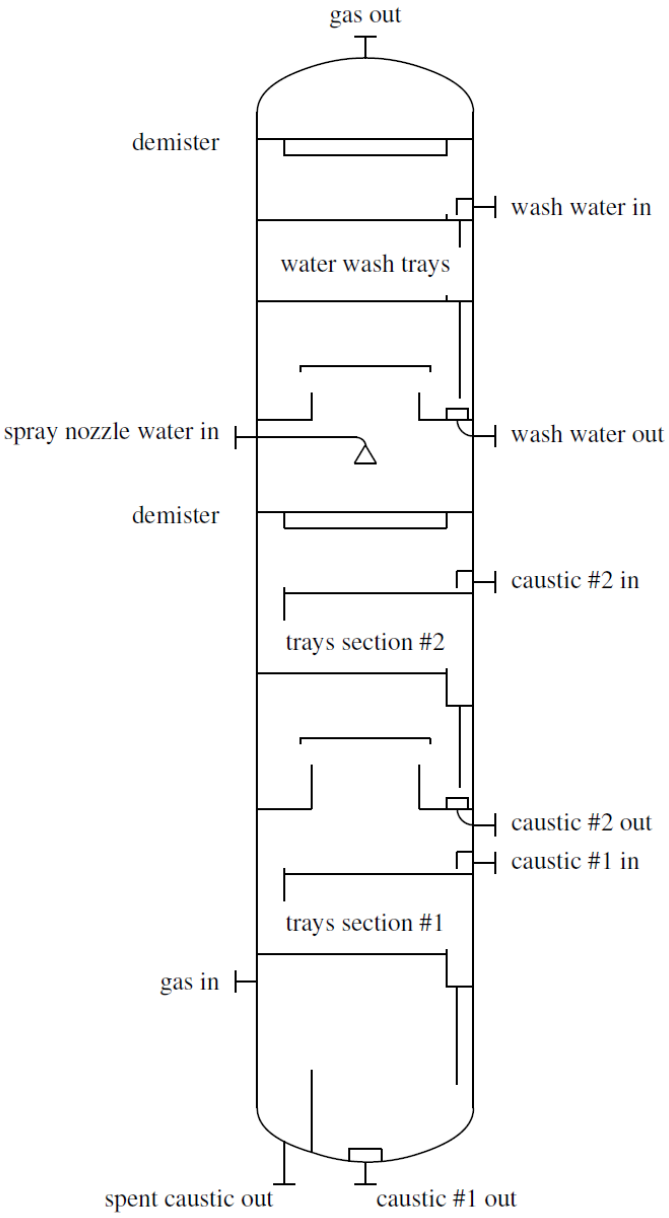

Figure 1: Caustic wash column setup with 2 caustic cycles and water wash section [3]

References:

[1] Baerns M., Hofmann H., Renken A.: Chemische Reaktionstechnik, 2. Aufl., Georg-Thieme-Verlag, Stuttgart, 1987.

[2] Fitzer E., Fritz W., Emig G.: Technische Chemie, 4. Aufl., Springer Verlag, Berlin 1995.

[3] Raab M.: NaOH-Wäschen in petrochemischen Anlagen aufgezeigt am Beispiel einer Äthylenanlage, Linde-Berichte aus Technik und Wissenschaft, 39/1976.

[4] Taylor R., Krishna R.: Multi-component Mass Transfer, Wiley, New York 1993.

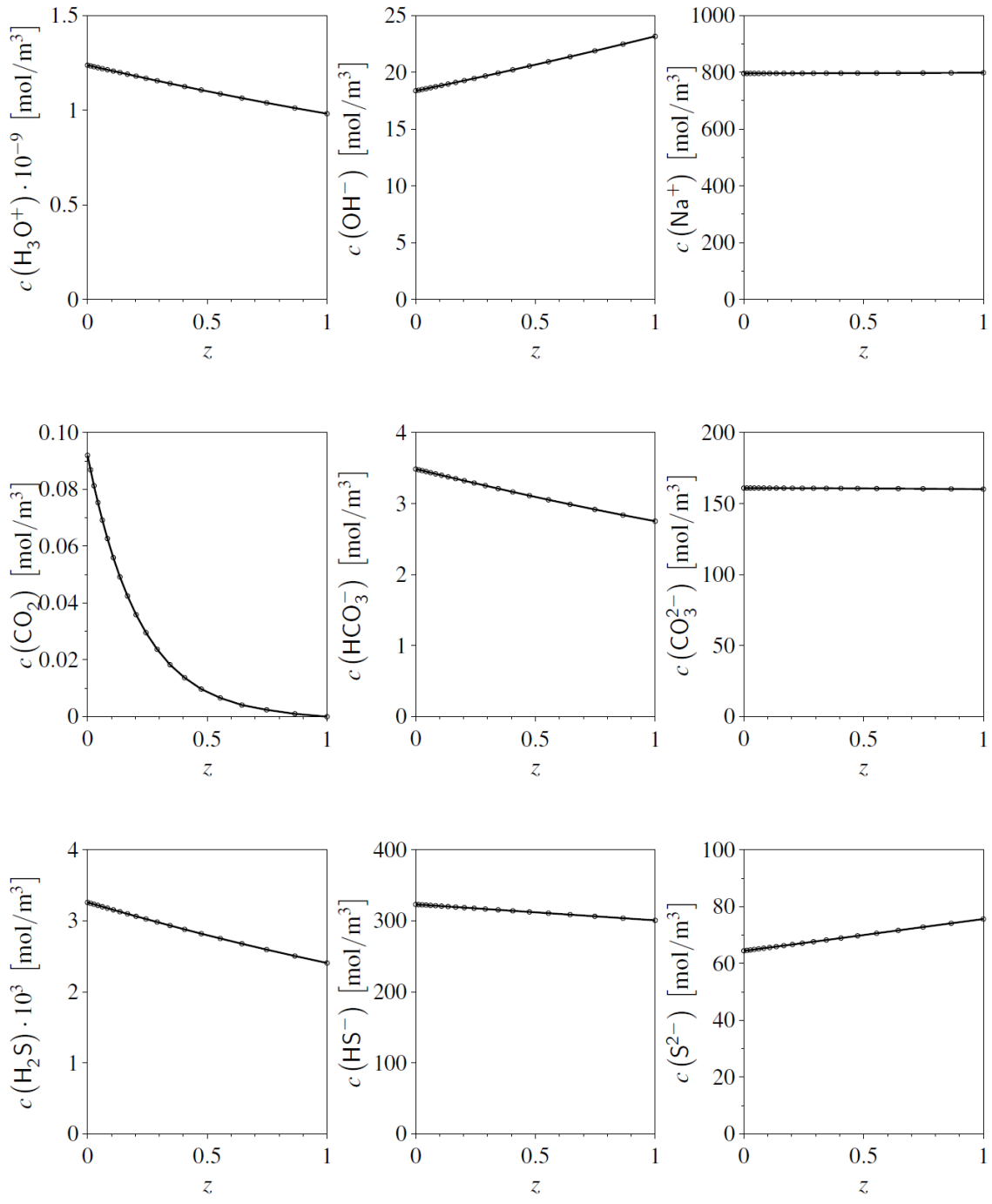

Figure 2: Film concentration profiles on a single tray as function of the normalized position.

Development and characterisation of a modular absorption column

S. Müller[1], S. Lier[1], M. Grünewald[1]
[1]Ruhr Universität Bochum, Bochum, Germany

Abstract

Increasing product differentiation and changing from commodities to specialized products are reasons for shortened product life circles in chemical engineering. Traditionally, large scale-plants possess inadequate flexibility in capacity and product portfolio based on their 'one purpose' development. Therefore apparatus with increased flexibility, like modular devices, becomes necessary to handle fluctuating customer demands. Due to modular assembly capacity can be increased either by equaling up modules from general structures or by numbering up equipment. Hence, a 'smart scale-up' of the complete modular apparatus becomes possible. In favor of smart scale-up only the operating parameters of the single module are necessary and thus reduced time-to-market periods for the products. In this contribution first experimental studies on a newly developed packed absorption module with rectangular cross section are compared with the operation behavior of a conventional packed column. In detail, this work presents results of measurements with Pall Ring 25M and Raschig™ Super-Pak 150 & 250. A comparison of experimental results between a packed absorption module and conventional packed columns shows the practicality of this new apparatus. With regard to identical packings, the module's results are comparable to conventional packed columns. Although the single module shows the expected losses in capacity for the gas and liquid load, it shows comparable results for the mass transfer efficiency in consideration of the reduced cross-section. In summary, the rectangular absorption column represents an interesting approach for the implementation of a modular multiphase unit.

Keywords: absorption, multi-phase, mass transfer, modular, scale up

1. Introduction and motivation

The chemical industry still focuses on economies of scale and therefore builds its plants as large and as optimized as possible (Riegel and Kent 2007, Behr et al. 2003, Ewers 2002). But this industry faces the difficulties of intensified global competition, shorter product life cycles, and volatile markets, which lead to insecure forecasts (Ewers 2002, Früh et al. 2008, Bott 2010, Drathen 2010). Industries, such as automotive or mechanical engineering, who have faced the same difficulties, have already implemented modular production concepts to increase flexibility (Ewers 2002, Skjott-Larsen and Schary 2007, Wiendahl 2009). Hence, factory modularization concepts can increase flexibility, in terms of capacity, assortment and location, and meet these challenges in the chemical industry, too. Applied to the chemical industry modules can be found in production plants, the production line, the unit operation, the apparatus or the single phenomenon respectively (Lier and Grünewald 2011).

Looking at the development of building the plant, there are two different scales within this hierarchy: A scale of equipment development, which ranges from the single

phenomenon to the unit operation and a scale of plant design, which ranges from the unit operation to the production plant. The main difference between these scales lies in the type of scale-up strategies. On the equipment scale, scale-up is reached by *equaling-up* the characteristic phenomena. In the end, the procedure of *numbering-up* results in a toolbox of equipment, each designed for the application in one-line production processes. Such equipment shows the same performance and behaves like the lab scale equipment, which is the starting point for process development. On the plant scale the desired throughput is provided simply by numbering-up one-line processes to a multi-line process (Lier and Grünewald 2011).

In this contribution the main focus lies on the scale of equipment. These include different units of the equipment toolbox. One separation unit for example can be implemented multiple times into the system. Furthermore it can meet the capacity needs for this process step because it can be multiplied several times within this step. Traditionally, large scale-plants possess low flexibility in capacity, product portfolio and location because of their development designed for one purpose. In order reach a maximum efficiency during operation they are designed to meet one point in capacity utilization most efficient. This development and design procedure takes a lot of time. Multiple steps in scale from laboratory, technical scale, pilot plant onto production plant are carried out. In each the phenomena and parameters are analyzed again (see figure 1). This takes a lot of effort and time. With the introduction of a transformable, modular approach a ‘smart scale-up’ becomes possible. Using this smart scale-up the operating parameters of only one single module in one scale have to be analyzed. Thus reduced time-to-market periods for the production of the products can be introduced. The challenge coming along with multiplying-up modular devices is an equal feed flow for every single module.

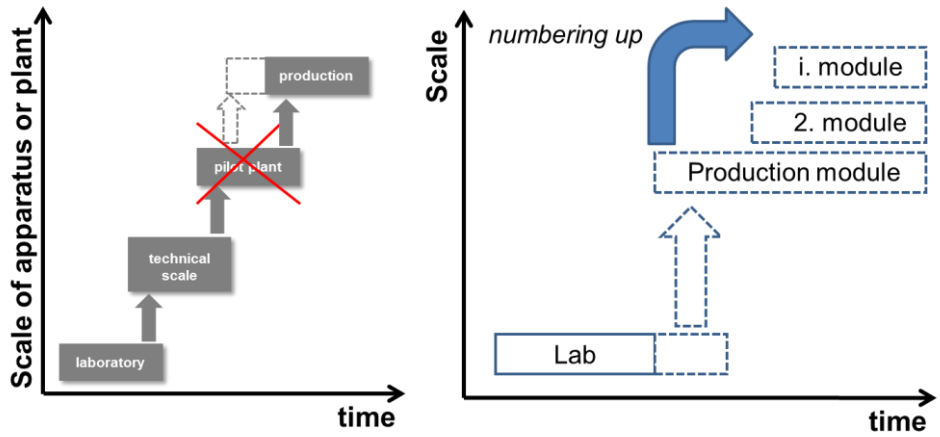

Figure 1: Smart Scale-up

Broken down to the scope of this article, separation steps and especially absorption, the problem of the conventional scale-up of these apparatuses is that the equipment often is unnecessarily oversized. Usually first mass transfer measurements in technical scale are carried out, the columns are designed and a high safety factor is applied (see figure 2). This column model based design is very cost intensive. On the one hand production scales cannot be tested before a hand and on the other hand

phenomena analyzed on lower scales cannot be transferred easily. With a transformable, modular approach as described above the single apparatus module can be observed and analyzed deeply in its scale and from there capacity can be increased by numbering-up these modules to the capacity goal. In this scale each module behaves as tested before and therefore ideally the whole process step behaves as forecasted. The challenge here lies in an equal feed flow for every single module.

Figure 2: Traditionally scale up

As mentioned before this contribution focuses on the development of modular multiphase units or, more precisely, of modular separation units. In some areas of chemical engineering modular devices are already state of the art, although they might not have been labeled “modular” so far. Apparatus types like plate heat exchangers or filter presses are established technologies with a long history of development (Hewitt 1981, Zimparov 2002, Price and Shaw 2001, Braun et al. 2000, Anlauf 2008). These modular devices are characterized by a simple rectangular geometry and standardized contact points of each single module. This simple geometry creates planar areas for the necessary contact points of each single module. With multiple connections of single modules the utilization of the modular device can be increased. In this way the aspect of scalability of transformable apparatuses is realized. But established modular devices show no implementation of separation technologies in modular apparatus concepts. Most of the existing modular apparatus concepts do not include unit operations for thermal separations, besides plate heat exchangers for evaporation or condensation tasks. The idea of developing a modular unit operation in technical scale is subject of our research group. They are dealing with the modularization of multiphase units like packed columns and bubble column reactors for example. For the design of these newly modular devices an adaption of existing modular apparatuses like plate heat exchangers or filter presses are used.

2. Results and discussion

The present article shows the first steps of development and characterization of a newly packed absorption column in technical scale. The concept of these apparatus implies a single module with rectangular cross section and planar outwalls (see Figure 3). The complete size of the single module is 2 m with a width of 0,5 m and a depth of 0,1 m. Due to the geometry and size of these technical apparatus, it is constructive possible to fit a single module into a rack of plate heat exchangers or even filter presses. According to the rectangular cross section a newly liquid pipe distributor has been developed. This experimental installation allows maximal liquid loads to 80 $m^3/(m^2*h)$ and gas loads to 5 $Pa^{0,5}$ for the single module. Firstly, experimental studies regarding hydrodynamics and mass transfer efficiency of the module have been performed to show the plausibility of this modular concept. Those

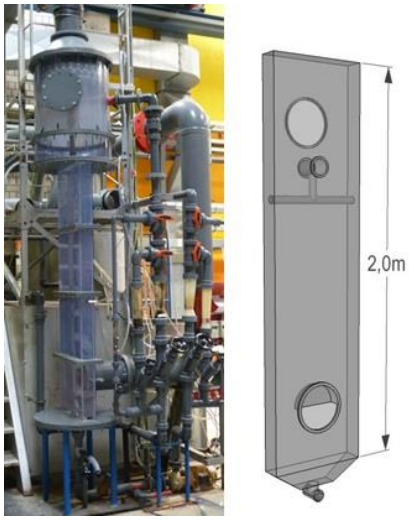

Figure 3: Realization in technical scale: rectangular absorption

studies have been performed with dumped and structured packings for liquid and gas loads up to the flooding point. In detail, this work presents results of measurements with Pall Ring 25M and Raschig™ Super-Pak 150 & 250. A comparison of experimental results between a packed absorption module and conventional packed columns shows the practicality of this new apparatus. The comparison includes an analysis of separating capacity by the HTU/NTU Model with the test system Ammonia-Air/Water. With regard to the rectangular cross section all experimental investigations have particular interest to the phase distribution in the module.

In figure 4 a comparison of the newly developed module and conventional round columns for the specific pressure drop with a liquid load of 40 m³/(m²*h) is shown. The hydrodynamic investigations implied packing heights from 0,7 to 1,0 m for the module, 1 m for a conventional packed column of our own research group with an inner diameter of 0,288 m and reference data of the packing producer (Chambers and Schultes 2007) for a packed column with a packing height of 3,05 m and an inner diameter of 0,43 m for the column. Due to identical packings, the module's results are comparable to conventional packed columns under the loading point. Particular the specific pressure drop of the RSP 250 in the module shows greater deviations over the loading point and expected losses in capacity compared with reference data. In opposite to these results the dumped packing of Pall Ring 25M in the module shows a loading and flooding point for higher gas loads than the conventional columns. With regard to the shortened distance for liquid and gas to the wall in the rectangular cross section, the pressure drop results can show deviant liquid phase distribution inside of the module. An optical analysis of the liquid distribution showed a high content of liquid on the larger inner walls of the module especially for the measurements with dumped packings.

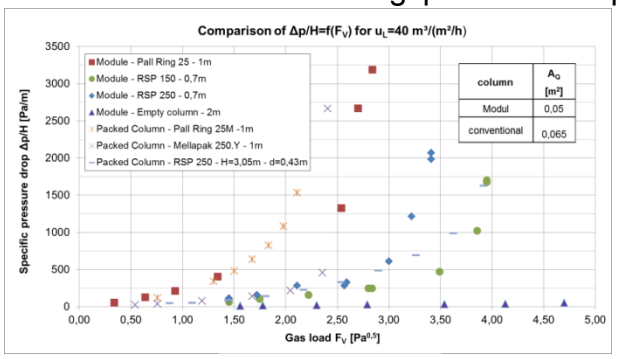

Figure 4: Comparison of specific pressure drop for packed columns and module

Another influencing factor for the shortened module packed bed is an inadequate gas distribution. With regard to the shortened distance between gas feed inlet and the bottom of the packing, gas maldistribution has a not negligible influence on hold up and so on pressure drop, especially for packing heights under 1 m. The influencing factor of gas distribution in this rectangular module is subject of several running projects at our research group. These studies imply CFD Simulations and experiments with fog for the visualization of the gas flow in the newly developed

module. Experimental and theoretical investigations are still in progress, but until now they show an extended distance for a fully developed gas flow profile is necessary, compared with conventional round columns. These studies exhibit already the need of a gas distributor for the newly module. The development of this gas distributor will be supported by additional CFD Simulations.

Due to these results, a detailed view on the results of the holdup measurements presents also a deviation between the module and the conventional packed column. Although the module demonstrates an earlier loading and flooding point at the comparison of pressure drop, the module shows higher capacity at the holdup (see figure 6). The results of the module with structured packings exhibit higher hold up values and a higher capacity compared with a packed column with related internals. Thereby the deviations of pressure drop for the module and the conventional columns are explainable for the structured packings. In addition, the comparison of the module and packed columns with dumped packings shows a different behavior as seen before. The holdup values of the module are up to 13 % smaller than the values of the conventional column with the identical column internals. These results were even for higher liquid loads seen and repeatable, but also explain the divergent results of the specific pressure drop measurements. Due to the divergent results of the dumped packings in the module a high influence of the gas and liquid flow profile gets obvious. Especially the hold up of the empty module exposes a characteristically course based on the shortened distance for the phases to the wall. With rising gas load the liquid phase gets pushed against the inner wall and thus the hold up decreases. Based on the higher void fraction of the dumped packing, the results mentioned before are explainable. A detailed examination of the wall effect inside the module is currently in progress.

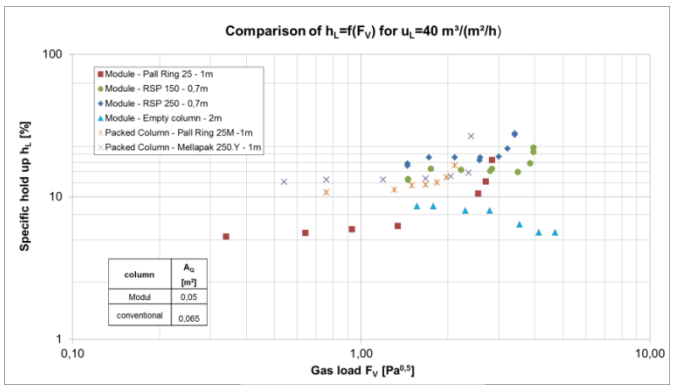

Figure 6: Comparison of specific hold up for packed columns and module

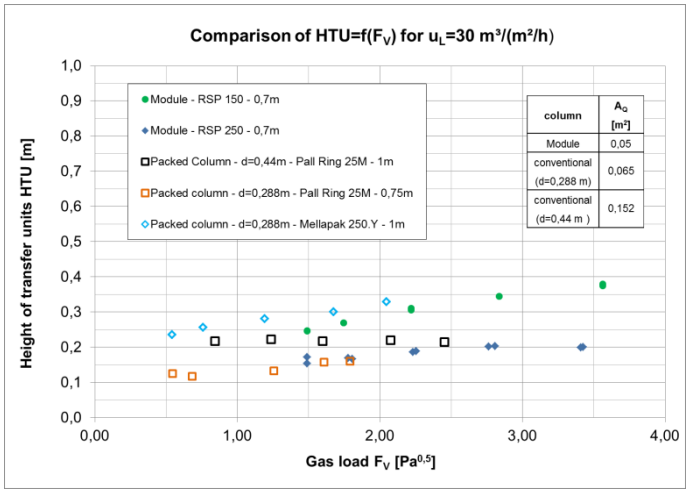

Figure 7: Comparison of HTU values for packed columns and module

Despite the influencing factors of phase distribution, the mass transfer performance of the module exhibits comparable results with conventional, round columns. In detail, figure 7 demonstrates a comparison of HTU values for the module and different round packed columns with a liquid load of 40 m³/(m²*h). With reference to the packing height, the module shows mass transfer performances of the

same value like packed columns with three times greater cross section area and column internals with comparable specific area. The variance in HTU values of the module with structured packings is small according to the influencing factors of phase distribution. Even conventional packed columns, with comparable packings in specific surface and higher packing height, exhibit a maximal deviance of 0,1 m. Additional tests of the mass transfer performance with identical column internals are currently in progress.

3. Conclusion and outlook

New challenges for chemical production concepts, like increasing product differentiation and changing from commodities to specialized products, cause in the need for new apparatus concepts. One idea of these new concepts is a transformable, modular approach of a multiphase separation unit. For the realization of a modular multiphase device a rectangular absorption module was developed and built in technical scale. First experimental studies of hydrodynamical and mass transfer measurements have been performed with different dumped and structured packings to show the plausibility of this modular concept. In summary, the module's results are comparable to conventional packed columns. Although the single module shows the expected losses in capacity for the gas and liquid load, it points out comparable results for the mass transfer efficiency in consideration of the reduced cross-section and enhanced wall effects of the liquid phase.

Particularly the results of the hydrodynamic investigations show greater deviations to the reference data. These results follow from different or even inadequate phase distribution due to the divergent cross section or shortened packing height. Continuative investigations of the liquid and gas phase distribution in the module are necessary for a full understanding of unit functionality. These studies are currently in progress and aim on one hand for an exact knowledge of phase behavior in the single module and on the other hand for distributing devices, like gas distributor, for an improvement of phase distribution. In summary, the rectangular absorption column represents an interesting approach for the implementation of a modular multiphase unit.

As aforementioned the utilization of the packed absorption module can be increased by a multiple connection of single modules, the so-called *equaling-up*. Purpose of this work is to demonstrate possible design studies to connect single modules in the future. These studies indicate the conduction of gas and liquid flows and possible integration of the modules into existing modular concepts like frames of plate heat exchangers.

References:

(Riegel and Kent 2007) E. R. Riegel, J. A. Kent, Kent and Riegel's handbook of industrial chemistry and biotechnology, Vol. 1; Springer, 2007

(Behr et al. 2003) A. Behr, V. A. Brehme, C. L. J. Ewers, H. Grön, T. Kimmel, S. Küppers, I. Symietz, Chem. Ing. Tech. 2003, 75 (4)

(Ewers 2002) C. L. J. Ewers, Pharma Supply Chain: Neue Wege zur effizienten Wertschöpfung, Der Pharmazeutische Betrieb, Vol. 47, ECV, 2002

(Früh 2008) K. F. Früh, U. Maier, D. Schaudel, Handbuch der Prozessautomatisierung: Prozessleittechnik für verfahrenstechnische Anlagen, Vol. 4; Oldenbourg Industrieverlag, 2008

(Bott 2010) T. Bott, Process 2010, 17 (6)

(Drathen 2010) H. Drathen, Process 2010, 17 (5)

(Skjott-Larsen and Schary 2007) T. Skjott-Larsen, P. B. Schary, Managing the global supply chain, Vol. 3, Copenhagen Business School Press DK, 2007

(Wiendahl 2009) H.-P. Wiendahl, Handbuch Fabrikplanung, Hanser Verlag, 2009

(Lier and Grünewald 2011) S. Lier, M. Grünewald, Chem. Eng. Tech., 34 (5), 2011

(Lier 2013) Lier, S., Entwicklung einer Bewertungsmethode für die Modularisierung von Produktionssystemen in der Chemieindustrie, Shaker Aachen, 2013

(Hewitt 1981) Hewitt, G. F., Heat Transfer Engineering, 3 (2), 1981

(Zimpranov 2002) Zimparov, V., Int. J. Energy Res., 26, 2001

(Price and Shaw 2001) Price, M., Shaw, D., Filtration & Separation, 38 (5), 2001

(Braun et al. 2000) Braun, A., Mrotzek, D., Ruhland, M., Chem. Ing. Tech., 72 (12), 2000

(Anlauf 2008) Anlauf, H., Chem. Ing. Tech., 80 (8), 2008

(Chambers and Schultes 2007) Chambers, S., Schultes, M., Reaching new performance levels with surface enhanced Raschig Super-Pak structured packings, Presentation AIChE Spring Meeting, 2007

Study of the effect of stripping components in absorption processes for CO_2-removal from power plant flue gases

Dipl.-Ing. Andreas Kossmann1, Dr. Peter Moser2, Prof. Dr.-Ing. Harald Klein1,
[1]Institute of Plant and Process Technology, Technische Universität München, Garching/Germany
[2]RWE Power Aktiengesellschaft, Essen

Abstract
In this work the influence of adding an organic component, immiscible with water, in the desorber of a Post-Combustion-Capture process is examined. Therefore, a model for a three-phase equilibrium was developed. Based on this model for phase equilibrium a multistage column model representing the desorber was set up. With this model and another model for the absorber, both implemented in MATLAB, the overall absorption process can be simulated. Moreover, a power plant model was set up in the commercially available process simulator UniSim Design.
The results show that depending on the choice of the organic component the boiling temperature of the reboiler can be significantly lowered. However, the overall penalty for power plant including CO_2 separation is in favor of the traditional two-phase regeneration. Next a sensitivity analysis will be made in order to check, whether there might be (fictitious) components with a lower overall penalty compared to the conventional regeneration.

Keywords
carbon capture, stripping components, modeling and simulation

1. Introduction

One possibility for removal of CO_2 in conventional coal-fired power plants is the so-called Post-Combustion-Capture process. In this process CO_2 is separated from the power plant flue gas by absorption. Amongst others aqueous amine solutions are considered as one possible solvent for absorption [1]. Advantageous of the Post-Combustion-Capture process is the fact that existing power plants could be retrofitted. A disadvantage, however, is the additional energy consumption occurring when regenerating the solvent in the desorber. For regeneration steam is taken from the turbines of the power plant. This reduces the overall efficiency of the power plant significantly [2].

In this work the influence of adding an organic component, which is almost immiscible with water, on the regeneration of the solvent and therefore, also on the overall efficiency of the power plant, is examined. This concept was originally proposed in [3] and is patented in [4]. By adding this organic component a miscibility gap is formed in the desorber and subsequently the boiling temperature decreases, an effect also known from steam distillation. As the temperature in the reboiler of the desorber is lower, the pressure and temperature of the required steam for heating the reboiler can also be lower. However, the amount of steam required for heating might be higher. This aspect shows potential for optimization and shall be investigated.

For calculation of the phase equilibrium a system of nonlinear equations has been set up in MATLAB. With some minor modifications this model for calculation of the phase equilibrium can be used for multistage columns. Thus both absorber and desorber can be modeled, in case of latter one for conventional two-phase and three-phase regeneration. The strong nonideal behavior of the liquid phase is modeled with the ElectrolyteNRTL activity coefficient property method [5].
For simulation of the combined power plant and CO_2 separation process a model for a power plant has been set up in the process simulator UniSim Design. A model for the reference power plant “North Rhine-Westphalia” shows satisfactory agreement with literature. The two models for CO_2 separation process and power plant are then combined by a graphical user interface in MATLAB.

2. Results and discussion

2.1 Three-phase regeneration with two different hydrocarbons in comparison with conventional regeneration

First simulations were made in order to compare the conventional two-phase regeneration with three-phase regeneration by adding organic stripping components. The results for the specific energy consumption for both the conventional two-phase regeneration as well as the three-phase regeneration, latter one with the two different hydrocarbons hexane and octane, can be seen in Figure 1. The specific energy consumption q is plotted against the ratio of solvent to flue gas mass flow rate L/G. It can be seen that the conventional two-phase regeneration, depicted in green, shows the lowest value of q = 3.55 MJ/kg CO_2 at the lowest ratio of L/G = 3.3. In case of three-phase regeneration by adding hexane q = 5.55 MJ/kg CO_2 at a ratio of L/G = 9.4. If adding octane instead of hexane q = 4.19 MJ/kg CO_2 at a ratio of L/G = 4.3. Looking at the reboiler temperatures, in case of the two-phase regeneration as expected the temperature is the highest with T_{Reboiler} = 124.2 °C. Adding hexane features the lowest reboiler temperature being T_{Reboiler} = 82.0 °C. In between is the value if octane is added as stripping component, in this case the reboiler temperature is T_{Reboiler} = 111.2 °C. It has to be noted that the desorber pressure was kept constant in all three cases at p = 2.1 bar.

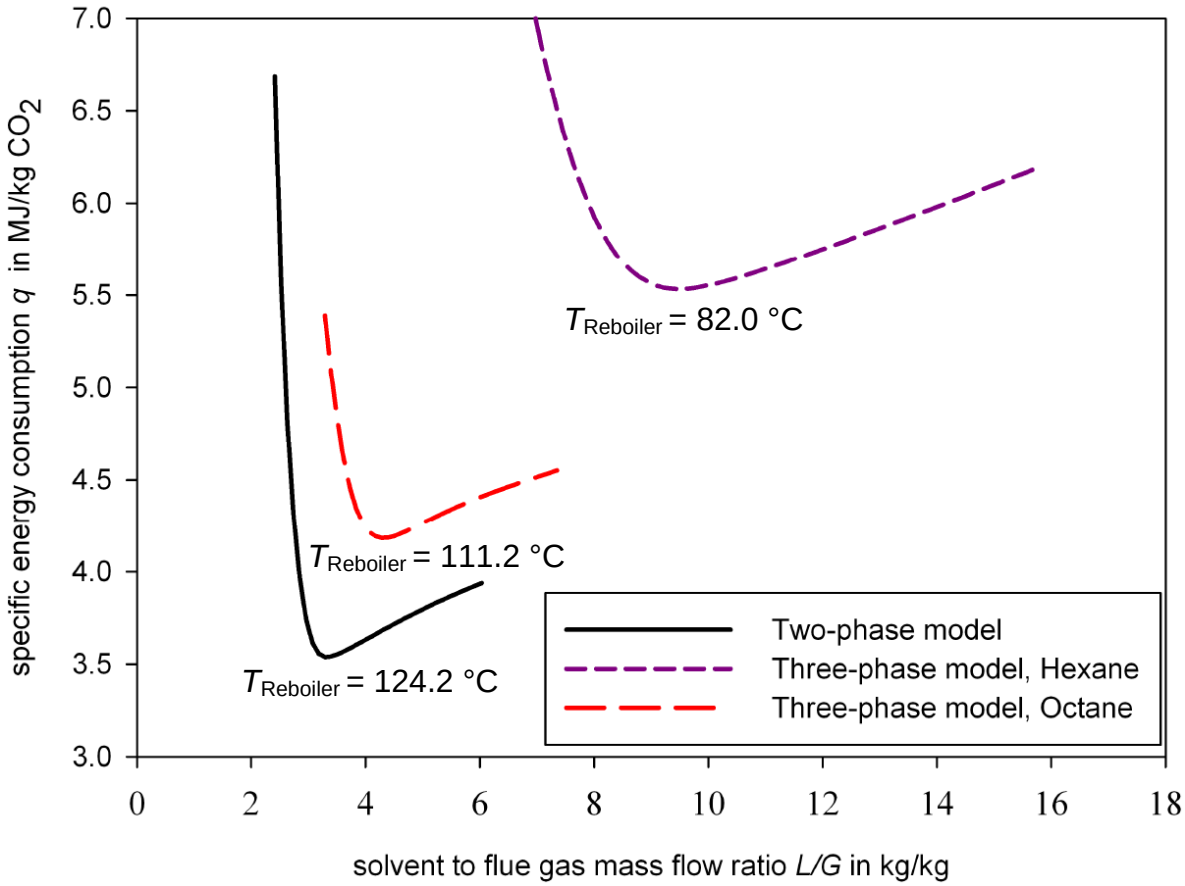

Figure 1: Specific energy consumption *q* for two-phase and three-phase regeneration dependent on the ratio of solvent to flue gas mass flow rate *L/G*

In order to find out which of the three above mentioned options features the lowest efficiency penalty for CO_2 separation in a power plant, simulations of a power plant including carbon capture were performed. The results of these simulations are summarized in Table 1.

	Two-Phase Regeneration	Three-Phase Regeneration Hexane	Three-Phase Regeneration Octane
Specific energy consumption *q* in MJ / kg CO_2	3.55	5.55	4.19
$T_{Reboiler}$ in °C	124.2	82.0	111.2
Steam extraction pressure from turbines in bar	3.34	2.06	2.28
Efficiency penalty			
by CO_2 separation	8.5%	11.7%	9.0%
by CO_2 compression	3.1%	3.1%	3.1%
Efficiency gain			
by heat integration	0.3%	0.0%	0.2%
Overall efficiency penalty	11.3%	14.8%	11.9%

Table 1: Results from power plant simulations including carbon capture for two-phase and three-phase regeneration

The results show that the efficiency penalty caused by CO_2 separation is the lowest for the conventional two-phase regeneration and is the highest in case of three-phase regeneration with hexane as stripping component. When looking at the steam extraction pressures from the turbines it is noticeable that for hexane steam at a comparable high pressure has to be used. Based on the reboiler temperature of 82.0 °C and a temperature difference of 10 °C between steam and solvent in the reboiler a steam pressure of 0.8 bar would be adequate. However, at that pressure the whole amount of steam available in the turbines is not sufficient for regeneration. For this reason steam at a higher pressure has to be used and this leads to such a high efficiency penalty when using hexane as stripping component. This result clarifies the importance of combining CO_2 separation process and power plant when evaluating the results. Looking at the results in Table 1 it can be seen that higher temperatures in the desorption column are moreover advantageous when it comes to integrating heat from the desorption column into the steam cycle.

In a next step the influence of the pressure in the desorber was examined for the case of adding hexane as stripping component. As mentioned in the previous paragraph the standard desorber pressure of 2.1 bar leads to problems because the energy provided on such a low temperature level is not sufficient for regeneration. Accordingly, on the pressure in the desorber was increased to 3.1 and 4.1 bar respectively. The results are summarized in Table 2.

	Three-Phase Regeneration Hexane as stripping component		
Pressure in bar	2.1	3.1	4.1
Specific energy consumption q in MJ / kg CO_2	5.55	5.20	4.98
$T_{Reboiler}$ in °C	82.0	94.0	103.2
Steam extraction pressure from turbines in bar	2.06	1.31	1.77
Efficiency penalty			
by CO_2 separation	11.7%	9.6%	10.0%
by CO_2 compression	3.1%	2.7%	2.5%
Efficiency gain			
by heat integration	0.0%	0.02%	0.04%
Overall efficiency penalty	14.8%	12.3%	12.5%

Table 2: Results from power plant simulations including carbon capture for three-phase regeneration with hexane as stripping components at different desorber pressures

From the results it can be seen that for the medium pressure of 3.1 bar the overall efficiency penalty is the lowest. In contrast to the lower desorber pressure of 2.1 bar the steam for heating can be extracted from the turbines at a significantly lower pressure and is nevertheless sufficient for regeneration. Moreover, the efficiency penalty caused by CO_2 compression is lower at 3.1 bar compared to 2.1 bar. However, at a higher pressure of 4.1 bar the overall efficiency penalty rises again. On

the one hand the efficiency penalty caused by CO_2 compression is lower compared to 3.1 bar as expected. On the other hand the negative effect of having to use more valuable steam at a higher pressure and temperature for heating caused by the higher boiling temperature in the reboiler predominates. Thus, the medium pressure of 3.1 bar features a minimum regarding the overall efficiency penalty but comparing it to the conventional two-phase regeneration or addition of octane it still performs worse.

2.2 Performance of (fictitious) components depending on component properties and rating regarding efficiency penalty

It is planned to check how (fictitious) components with certain properties will perform regarding the overall efficiency penalty for power plant including CO_2 separation. The physical properties which a stripping component would need, in order to perform better than the conventional regeneration, shall be investigated. A *q*-*T*-plot as shown in Figure 2 is drawn in order to illustrate the efficiency penalty depending on specific energy consumption *q* and reboiler temperature *T*.

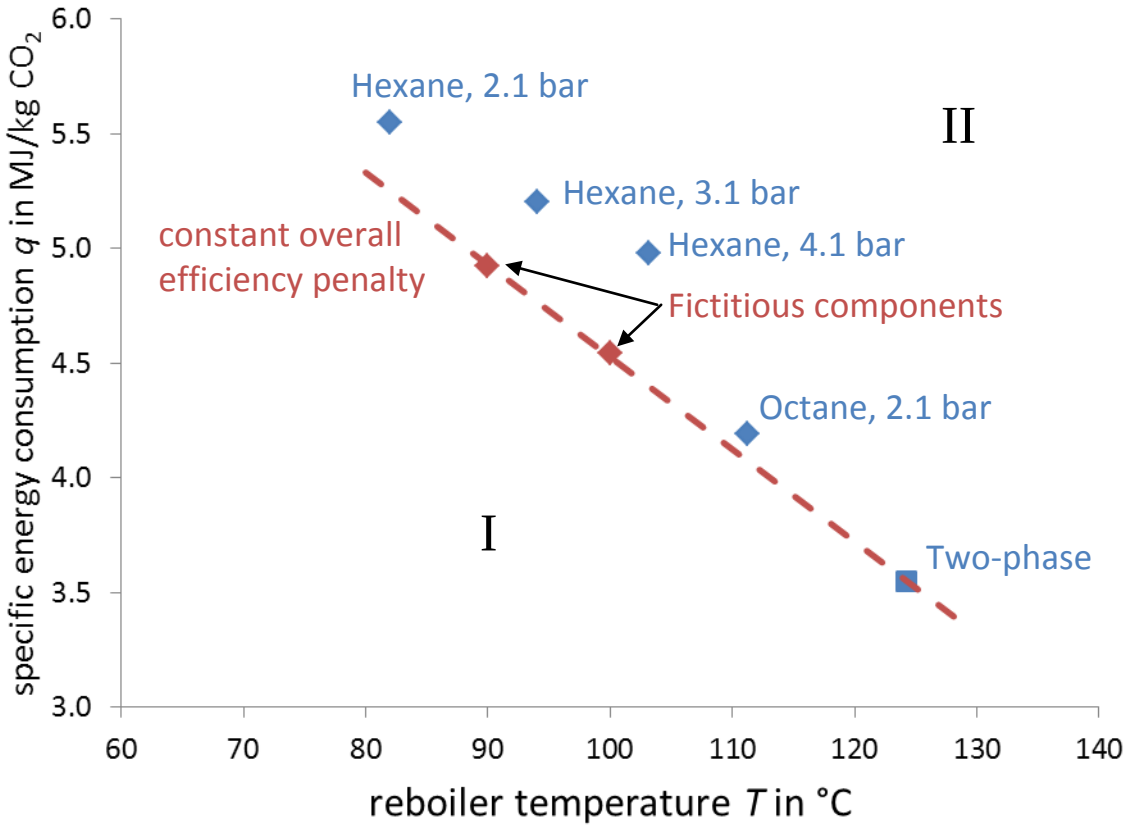

Figure 2: Overall efficiency penalty related to specific energy consumption *q* and reboiler temperature *T*; blue symbols: simulations of real components, red symbols: simulations of fictitious components, square: two-phase regeneration, diamonds: three-phase regeneration

The blue filled diamonds in Figure 2 represent the above described results for three-phase regeneration with octane and hexane as stripping components respectively, for latter one at the different desorber pressures. The blue filled square in Figure 2

represents the result for the two-phase regeneration. The red filled diamonds represent the results for three-phase regeneration with fictitious organic components added as stripping components. The specific energy consumption *q* and reboiler temperature *T* of these fictitious components are chosen in such a way that the overall efficiency penalty is in the range of the conventional two-phase regeneration. Accordingly, the dashed line represents points with a constant overall efficiency penalty for power plant including CO_2 separation. While points in the region above the dashed line, marked with II, perform worse compared to the conventional two-phase regeneration any points that would be in the region below the line, marked with I, would perform better.

3. Conclusions

The influence of adding an organic component, immiscible with water, in the desorber of a Post-Combustion-Capture process is investigated in this work. For this purpose a model for calculation of a three-phase equilibrium was developed. Furthermore, a multistage column model representing the desorber was set up based on the three-phase equilibrium calculation. With this desorber model and another model for the absorber, both implemented in MATLAB, the overall absorption process can be simulated. In order to combine the results from the CO_2 separation process with results from a power plant simulation, a model for latter one was set up in the commercial available process simulator UniSim Design.

The results show that for the two used hydrocarbons hexane and octane the boiling temperature of the reboiler can be significantly lowered. However, the overall penalty for power plant including CO_2 separation is in favor of the traditional two-phase regeneration. It has been shown that it can be decisive to judge the results from CO_2 separation not on its own but only in combination with results from the power plant simulation. Finally simulations have been made with the power plant model to determine which combinations of specific energy consumption and reboiler temperature feature the same overall efficiency penalty as the conventional two-phase regeneration. Based on this result it will be analyzed which properties a stripping component needs in order to perform better regarding overall efficiency penalty than the two-phase regeneration.

References

[1] Arthur Kohl and Richard Nielsen: Gas Purification. Gulf Publishing Company, 1997.

[2] John. Davison: Performance and costs of power plants with capture and storage of CO2. Energy (Oxford, U. K.), 32:1163–1176, 2007.

[3] Finn Andrew Tobiesen and Hallvard F. Svendsen: Study of a Modified Amine-Based Regeneration Unit. Ind. Eng. Chem. Res., 45:2489–2496, 2006.

[4] Matthias Krumbeck, Horst Mertikat and Peter Moser: Method based on two-phase distillation for utilization of low-temperature heat for regeneration of carbon dioxide-loaded solvents during carbon dioxide separation from waste gases by absorption. WO 2008107050 A1

[5] David M. Austgen, Gary T. Rochelle, Xiao Peng and Chau Chyun. Chen: Model of vapor-liquid equilibria for aqueous acid gas-alkanolamine systems using the electrolyte-NRTL equation. Ind. Eng. Chem. Res., 28:1060–73, 1989.

A new structured packing for reactive absorption

J. Roesler[1], L. Raynal[1], P. Alix[1], P. Broutin[1], J. Esquier[2], G. Perdu[2], L. Normand[2]
[1]IFP Energies nouvelles – Lyon, Solaize, France
[2] PROSERNAT, Paris La Défense, France

Abstract
Improving efficiency and flow capacity of structured packings can help reduce absorption column investment costs in acid gas treatment and CO_2 capture plants. IFPEN has recently patented a structured packing geometry with concepts that were applied to manufacture a number of packing elements with a geometric area of 200 m^2/m^3 named IFPACC 2X™. Hydrodynamic properties and effective area properties were evaluated in a 1 m diameter column. The performance results are compared to those of commercial packings. Relative to the Sulzer's Mellapak 250.X, for example, this new packing can offer a 10% higher flow capacity with the same effective area yet with less geometric area.

Keywords
Structured packing, gas sweetening, distillation, CO_2 capture, IFPACC

1. Introduction

One of the main investment costs in natural gas sweetening and CO_2 capture plants is associated with the absorption column[1]. This cost can be reduced with more efficient and more capacitive packings. To this avail, IFPEN has recently developed a new structured packing geometry[2] that provides high fractional areas (ratio of effective to geometric areas) while maintaining a high flow capacity. The base geometry is a classical assembly of wavy metal sheets as with many other commercial structured packings (Sulzer Mellapak, Koch-Glitsch Flexipac or equivalent...). The specific features that provide the improvements are the inclusion of indentations or "windows" in the packing that generate flow discontinuities. As a consequence, droplets will be generated that will enhance the effective surface area analogously to observations made on random packings[3]. Mixing within the liquid film will also be enhanced at the nodal points, or window edges, thus potentially increasing the liquid side mass transfer coefficient by reducing the contact time as used in the Higbie penetration theory. The concepts were applied to produce a number of packing elements named IFPACC 2X™. A picture of a sample packing bloc is shown in Figure 1. The geometric features of the packing are shown in Figure 2. The base structure has vertical corrugations angled at 30° that provide a geometric area of 200 m^2/m^3 from stainless steel sheets with surface embossing. A regular pattern of windows has been sheared through the sheets to achieve the improved performances. These openings do not add any surface area but generate flow discontinuity points. To date tests have been performed to determine pressure loss, flooding points and effective surface area.

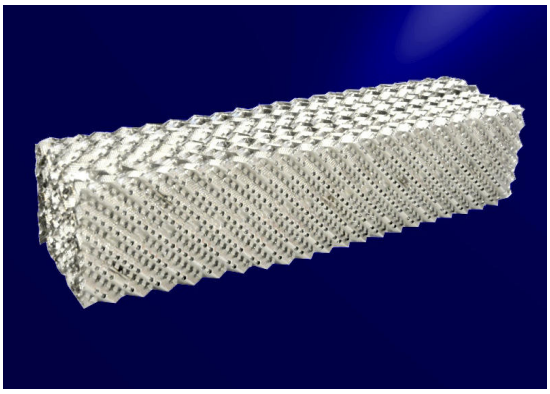

Figure 1 : Photography of an IFPACC 2X packing block.

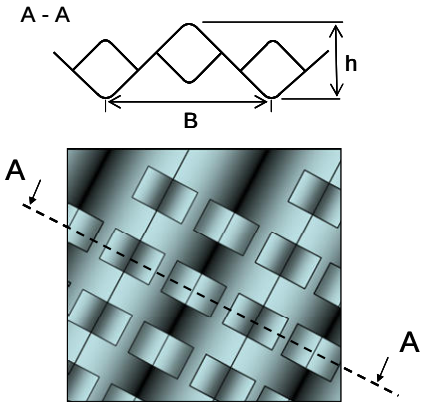

Figure 2: Geometric characteristics of the packing. Top view and profile along the A-A cut: h/B=0.46 .

2. Results and discussion

2.1 Materials and methods

The tests were performed in a 1 m diameter transparent column operating in a counter flow mode at near ambient pressures and temperatures. The bed consisted of 15 layers of IFPACC 2X packing blocks 210 mm high for a total height of 3.15 m. For comparison purposes, a 3 m bed of Mellapak 250.X (hereafter M250X) was also tested. The successive block layers were arranged at 90° angles. The liquid phase was recirculated with a maximum flowrate of 80 m^3/h and injected at the top through a commercial collector-distributor purchased from a packing supplier with 0.19 m ID liquid tubes and 81 injection points per square meter. The air was supplied by a series of compressors at a maximum flowrate of 9,000 Nm^3/h and rejected into the atmosphere after cyclonic separation of entrained liquid droplets. The gas was injected axially from the bottom through a 0.20 m diameter duct located 1.2 m bellow the packed bed.

The pressure drop measurements were performed using the air-water system. The effective area measurements were performed using the air/NaOH (0.1N) system [5, 6]. The inlet gas phase CO_2 concentration is thus near 400 ppmv and the liquid phase inlet NaOH concentration is close to 0.1 $mol.L^{-1}$. The chemistry for this system is well described by a pseudo-first order irreversible reaction in the fast reaction regime. In these structured packing systems the gas side resistance is negligible, therefore the local absorption flux is given by:

$$\phi_{CO_2} = \frac{\sqrt{D_{CO_2} \cdot k_2 \cdot C_{OH}^0}}{He} \cdot P_{CO_2} \cdot a_e \qquad (1)$$

The column absorption rate is calculated based on column inlet and outlet gas phase CO_2 concentrations that are measured using an on-line NDIR gas analyzer. The column inlet and outlet liquid solutions are also sampled and analyzed by HCl titration for every data point in order to determine the OH^- and CO_3^{2-} concentrations. This allows to check the mass balance between gas and liquid phases and to properly account for the loading effect on the kinetics. The experimentally measured

column absorption rates are compared to those from a one-dimensional column model that assumes isothermal, isobaric and stationary plug-flow conditions. The effective area is then determined by matching the calculated and measured global absorption fluxes.

The kinetic parameters for k_2 have been determined in the literature for virgin solutions of sodium hydroxide [7]. For our low concentration solutions there does not appear to be a well proven method of accounting for the effects of carbonation by CO_2 , whether on k_2, D_{CO2}, *He* or on the onset of reversible reactions. It is therefore important to operate only at low loadings in order to limit uncertainties on the determination of the effective area. The acceptable limit of carbonation in our laboratory has typically been 0.015 mol/L of CO_3^{2-} representing a 15% loading rate. However this limit represents an operational constraint and even at 15 % loading the measured effective areas are altered by several % as will be shown below.

In order to develop a correction for carbonation effects a test was performed at constant gas and liquid flow conditions to track the absorption flux evolution over an extended period of time. The results are shown in
Figure 3. The square symbols show the change in global absorption flux as a function of CO_3^{2-} relative to the first measurement made at a carbonation level of 0.01 mol/L of CO_3^{2-}. This value was selected as a reference for lack of data with a perfectly virgin solution and because the residual correction to zero carbonation, 1.5%, falls largely within the experimental uncertainties. As expected, calculated effective areas decrease with carbonation due to a reduced CO_2 absorption flux. No detailed analysis has been made to determine specific corrections to either k_2, D_{CO2}, *He* which operate as a whole in equation (1). A curve fit to these data simply serves as the basis for applying a global correction factor to back calculate the abortion flux at a reference carbonation load of 0.01 mol/L. The carbonation data extend to 0.04 mol/L, however, the carbonation limit for the tests was set to 0.025 mol/L.

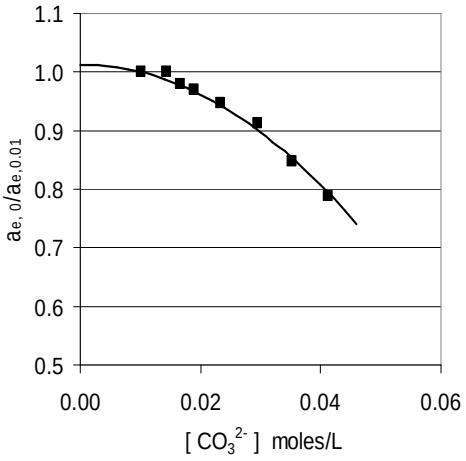

Figure 3: Calculated effective area variation as a function of liquid carbonation relative to a reference point defined as [CO_3^{2-}] = 0.01 moles/L for a 0,1N solution of NaOH.

2.1 Pressure drop and flood points

Pressure drop and flood points are compared to those of commercial packings Mellapak 2X (hereafter M2X), from the literature[10], and M250X, from this work, in Figure 4 (a) at a liquid load of about 60 $m^3/h/m^2$. The new packing shows initially the highest pressure drop, however, the flood point ends up between those of the other packings. The 10% higher gas flow capacity relative to the M250X is due to the lower geometric area. The lower capacity and increased pressure drop relative to the M2X, which has an equivalent geometric area, is due to the flow obstruction generated by the windows. At a higher liquid load of 90 $m^3/h/m^2$ the capacity gain relative to the M250X remains 10% and the pressure drop curves match up to the flood point as shown in Figure 4 (b).

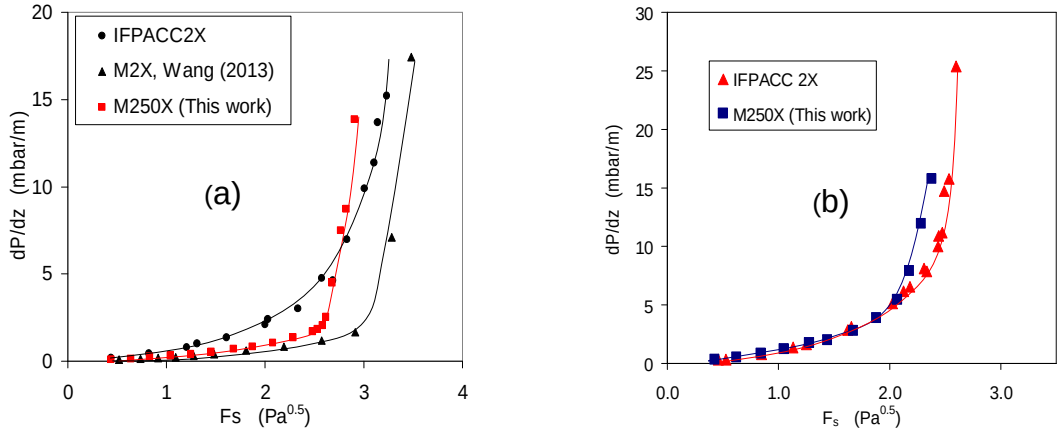

Figure 4: Comparison of IFPACC 2X™ pressure drop to measurements on commercial structured packings with geometric areas of a_g=200 and 250 m^2/m^3 at liquid loads of(a) 60 $m^3/m^2/h$ and (b) 90 $m^3/m^2/h$.

For practical design purposes the flood limit, $F_{s,f}$, can be be represented as a function of flow parameter, $FP = \dot{m}_L / \dot{m}_G \sqrt{\rho_G / \rho_L}$, the value of which is determined by the gas treatment plant processing requirements. Figure 5 shows the capacity gain of IFPACC 2X relative to M250X as a function of *FP*. The % gain in capacity is given by the dashed curve and is observed to be higher at lower FP values, i.e., for lower liquid to gas loading requirements.

2.2 Effective area

The measured effective areas are reported in terms of fractional areas (a_e/a_g) and compared to values of existing commercial packings in Figure 6. The IFPACC 2X packing is found to produce a 20 to 25% higher fractional area. Compared to the M2X (Figure 6a) which has the same geometric surface, this increase translates directly into a gain in effective area. Since the two packings also have the same basic corrugation geometry the area gain results most likely form the formation of liquid droplets at the" windows". In Figure 6b comparisons are made relative to M250X with both literature and in-house results. The latter are the most reliable for a quantitative comparison as they were obtained in the same facility and under the same conditions as for the IFPACC 2X. Relative to our measurements, the results of

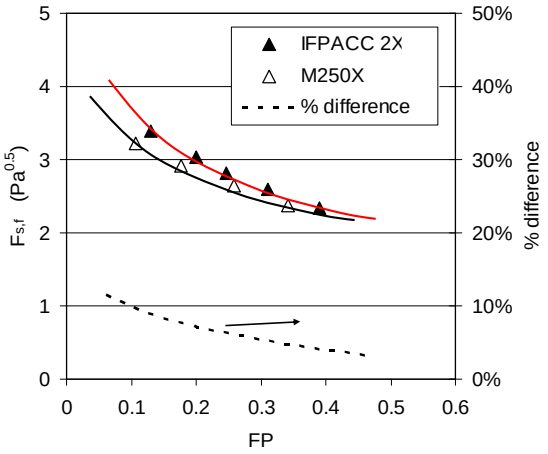

Figure 5: Comparison of flood limits as a function of FP for IFPACC 2X and M250X. Solid lines are curve fits to the data. The dashed line represents the % gain at a fixed *FP* value.

Tsai[8]. extend the data coverage to lower liquid loads but are 10% higher in the area of overlap. Based on the in-house results the IFPACC 2X has the same effective areas as the M250X as shown in Figure 7 where a power law fit through the data of either packing is observed to yield virtually the same curve. This is explained by the obviously higher fractional area than the M250X, that compensates for the lower geometric area. Note that in this figure the data of Tsai[8] have been reduced by 10% to match and provide continuity to the in-house data with M250X.

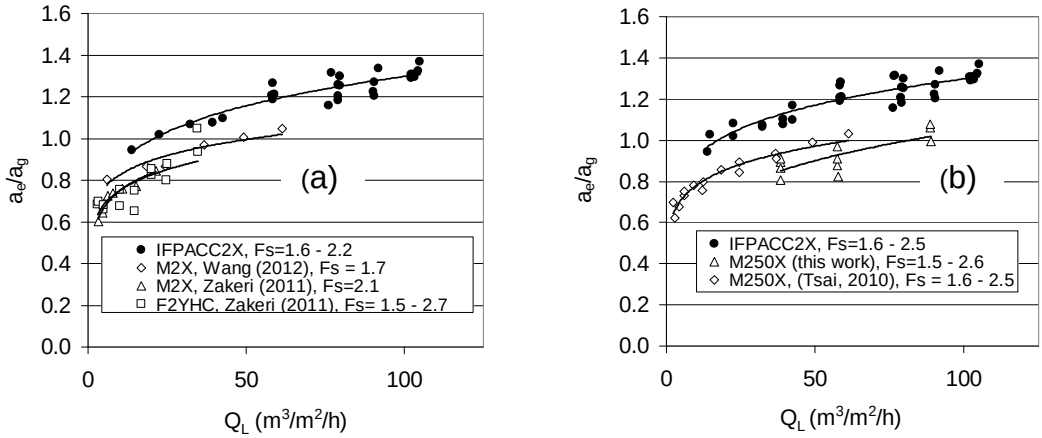

Figure 6: Fractional area comparisons of IFPACC 2X to other commercial packings with geometric areas (a) near 200 m^2/m^3 (M2X = Mellapak 2X, F2YHC = Flexipac 2Y HC) and (b) near 250 m^2/m^3 (M250X =Mellapak 250.X) for F_S from 1.5 to 2.6 $Pa^{0.5}$.

3. Conclusions

A new structured packing geometry concept has been developed targeting high capacities for gas sweetening and CO_2 capture applications. The performances of a first design, IFPACC 2X, are under assessment. The current results are very promising as flow capacities were found to exceed those of structured packings for similar applications while maintaining the effective area owing to the higher fractional

area. This last characteristic will allow future IFPACC generations to achieve yet better performances. Further testing is underway to determine liquid and gas side mass transfer coefficients. associated correlations will be implemented in rate-based simulation software for the design of gas sweetening units and CO_2 capture plants under the IFPEN technology brands, marketed by Prosernat.

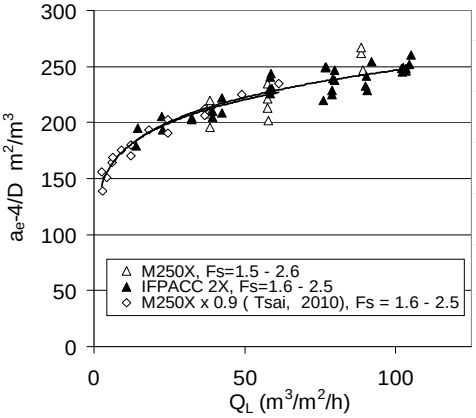

Figure 7: IFPACC 2X and Mellapak 250.X (M250X) intrinsic effective areas (the small geometric contribution of the column internal area, 4/D, has been subtracted out of the base measurement).

Nomenclature

References

1. Raynal, L., Bouillon P.A. , Gomez A. and Broutin P. , *Chem. Eng. J.* **2011**, 171, 742-752.
2. Raynal, L., Alix and P., French Patent FR 2.913.353, **2007**, US Patent 8,646,758, 2014.
3. Alix, P and Raynal L., *Energy Procedia* **2009**, 1, 845-852
4. Raynal L.,Gomez A., Caillat B. and Haroun Y., *Oil & Gas Science and Technology*, **2013**, 68, 6, 1093-1108.
5. Alix P., Raynal L., Abbe F., Meyer M., Prevost M. and Rouzineau D., *Chem. Eng. Res. Des.* 2011, 89, 1658-1668.
6. Tsai, R. E., Schultheiss, P., Kettner A., J. C. Lewis, Seibert F., Elridge R. B. and Rochelle G. T. , Ind. Eng. Chem. Res. 2008, 47, 1253-1260.
7 Pohorecki, R. and Moniuk W., Chem. Eng. Sci. **1988**, 43 (7), 1677-1684.
8. Tsai R. E., Mass Transfer Area of Structured Packing, University of Texas at Austin, Austin, TX, 2010. Ph.D dissertation.
9. Wang, C., Perry M., Rochelle, G.T. and Seibert, A.F.. , *Energy Procedia* **2012**, 23, 23 – 32
10. Wang C., Perry M., Seibert F and Rochelle G. T., AIChE Spring Meeting, San-Antonio, TX, April 28th – May 2nd **2013**, paper 85c.
11. Zakeri A., Einbu A., Wiig P. B., Øi E. L.,and Svendsen H. F., *Energy Procedia* **2011**, 4 , 606–613.
12. Zakeri A., Characterization of Packing Materials for CO_2 capture, Norwegian University of Science and Technology, Trondheim, Norway, **2011**, Ph.D dissertation.

Dynamic Models for Safety Shutdown of Distillation Columns

L. Bodizs, M. Hahn, A. Rix, J. Schallenberg. M. Vogt;
Evonik Industries AG, Marl, Germany

Abstract

To protect distillation columns from overpressure in emergency situations like loss of cooling, relief valves are commonly used. An alternative safeguarding method is safety shutdown of all energy inputs to the column. Especially in hazardous, corrosive or reacting systems, it is advantageous to keep the column holdup enclosed in the pressure system. Furthermore, the time required for start-up may be shorter if the holdup is not relieved to a flare. Shutting down the heat input to the column leads to a rapid collapse of the pressure profile and to fast draining of liquid from the internals. In the bottoms, the boiling temperature decreases with the amount of low boilers flowing back from the internals. During the dynamic draining process, the mixture's vapor pressure continuously changes and may increase considerably.

The maximum pressure rise from liquid mixing during the shutdown process must be considered in the mechanical design pressure of all connected equipment. Validated dynamic models are required to predict the pressure dynamics. During shutdown, the flow regime leaves the stable operating range and hydraulic models must be carefully selected. Experimental data from an industrial valve tray column is analyzed. A sieve tray weeping model is implemented in a dynamic model and fitted to experimental data. Simulation results show good agreement with experimental data.

Keywords

Distillation, safety shutdown, dynamic modeling, distillation hydraulics, liquid draining, weeping

1. Introduction

Loss of cooling causes a rapid increase of column pressure and is a standard scenario in HAZOP studies. To limit the maximum process pressure to a value below the vessel rating, safety relief valves are often used, wherever large flares exist anyway and temporary loss of holdup material is of little consequence. Calculation of relief loads by the unbalanced heat method [1] using steady-state simulation is straightforward and simple. As an initial guess, the relief rate may be estimated from the steady-state overhead vapor flowrate. If fully opened steam valves and clean heat exchanger surface are assumed, the calculated rate may be considerably higher. Whether credit for reboiler pinching may be assumed depends on the system under consideration [2]. Detailed simulations show, that complex dynamic transients are to be expected and that real relief rates may differ substantially from predictions of the unbalanced heat method [3]. Even large flare systems may reach their capacity after several plant revamps. Therefore, relief load mitigation studies have been published recently, showing, that relief loads can be greatly reduced or avoided altogether by shutdown of heat and gas flows to the column, see e. g. [4].

In specialty chemistry, however, relieving the columns' holdup to a flare during a column upset may be undesirable. Many components are highly reactive, corrosive or hazardous and are therefore best kept in the system designed for them. Furthermore, a distillation column is merely one unit in a multi-step production

process. In the relief case, the whole production chain needs to be stopped until the cause of the failure is corrected and restarting operations may become a rather time consuming procedure.
On the other hand, column shutdown using safety interlocks offers a chance to eliminate the need for relieving altogether, except for the fire case. Column high-high pressure is employed as a fast trigger to close valves in steam lines and possibly in feed and reflux lines using instrumentation of appropriate safety integrity level. Shutting down all heat inputs to the column causes a rapid collapse of the pressure profile and the trays cannot hold the liquid any longer. As the holdup drains, an increasing amount of low boilers is mixed with the relatively hot liquid in the bottoms. In a closed, adiabatic system, the resulting mixture vapor pressure may be higher than the trip pressure and even go through a maximum. This maximum pressure rise has to be considered in the design pressure of all equipment.
To compute the transient behavior of column pressure, validated dynamic models are essential. Little experimental information is available in literature, though. Can et al. [5] initiate a relief process by a step reduction of cooling water flow in a 100 mm diameter 22 tray bubble cap column in the methanol-water system. Before relief, top pressure and tray temperatures rise linearly. A dynamic model is implemented in SPEEDUP, but no hydraulic modeling details are provided. Staak et al. [6] report modeling and experimental work on the dynamics of column relief and shutdown. Their experiments in the methanol-water system show the importance of adequate hydraulic models and a simplified weeping model for sieve trays is presented. The model correctly predicts the dynamics of relief processes. Lifting forces acting on trays during relief are measured. After shutdown, a small pressure increase by post-evaporation is observed and correctly predicted by the dynamic model.
To date, no experimental data on safety shutdown of industrial size columns has been published. To provide lacking data, a plant test was performed in a tray column and simulated in ASPEN Dynamics. The most interesting experimental result is that liquid drains from the trays much faster than predicted by weeping models available in ASPEN Dynamics.

2. Results and discussion

2.1 Experimental data

An experiment was carried out in a production column separating a wide-boiling mixture, see **Figure 1**. The column has a diameter of 1176 mm and is equipped with 13 V1-moveable valve trays. The reboiler is heated with steam on tray temperature control; pressure is controlled by manipulating cooling water flow. During start-up, the column was run at a pressure of 4.5 bar in total reflux mode with feed, distillate and bottoms flow rates set to zero. The tray temperature controller was in manual mode, while reflux was on flow control. Temperature is measured at the top, on the pilot tray and in the bottom.
The operational diagram is shown in **Figure 2.** Flooding curves are calculated using the well-known Glitsch 13 equation [7]. Design loads (50, 100 and 120%) are given by open symbols for the top section and by filled symbols for the bottom section. Due to low liquid load during start-up, the experimental loads (diamonds) fall short of the design loads.
At t=1 min, the cooling water valve is closed. With a time delay of 40 s, the high pressure interlock is activated manually. All three control valves close within 16 s, see **Figure 3**. Except for heat loss to the environment, the column can now be considered as a closed system, as indicated by the dotted line in **Figure 1**.

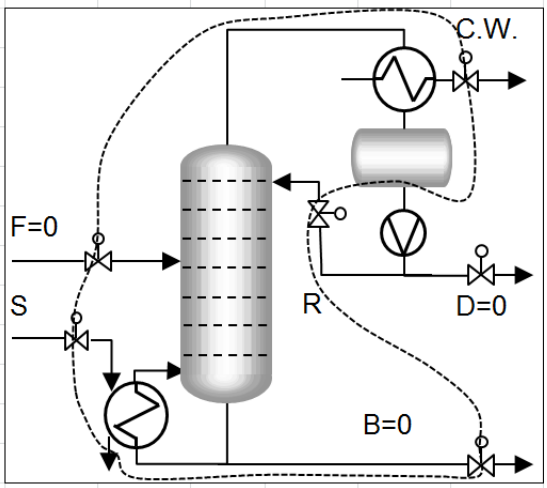

Figure 1: Column flowsheet.

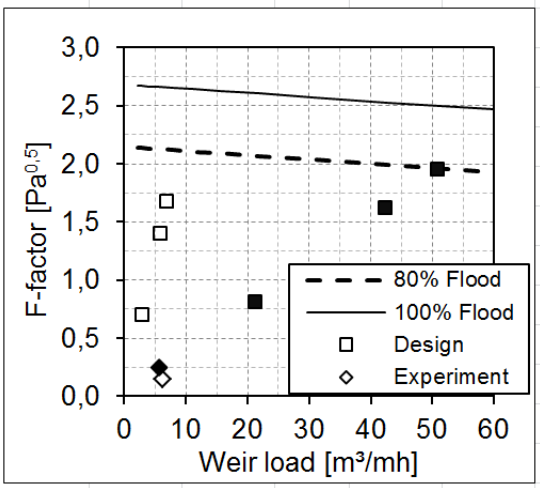

Figure 2: Load diagram.

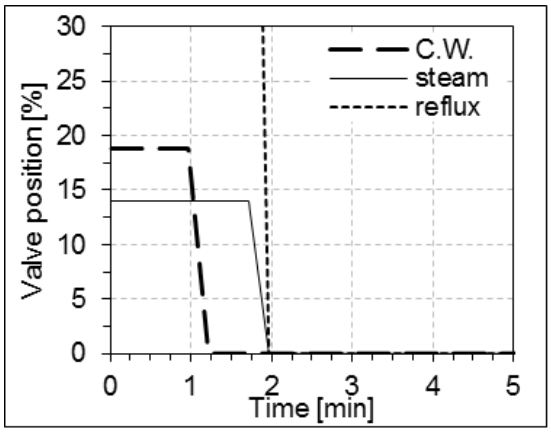

Figure 3: Closing of cooling water, steam and reflux valves.

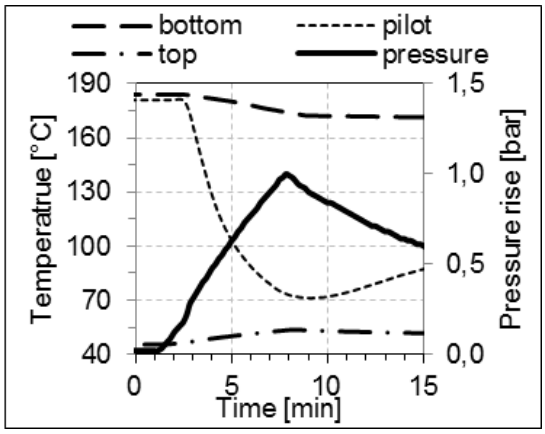

Figure 4: Response of tray temperatures and column pressure

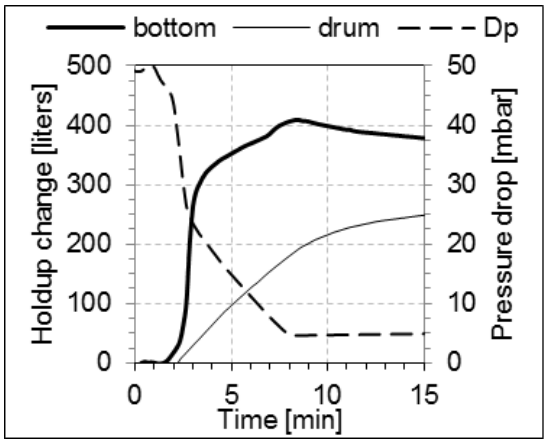

Figure 5: Levels of reflux drum, bottom and pressure drop.

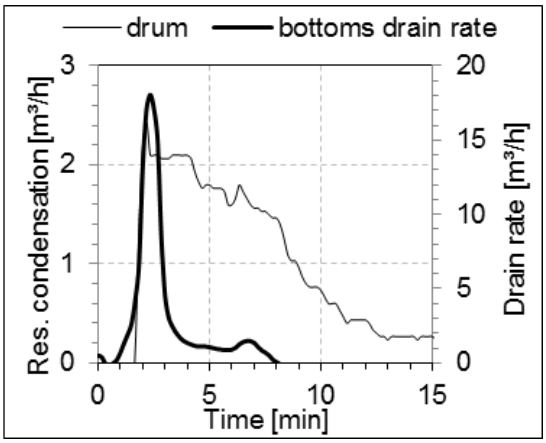

Figure 6: Calculated residual condensation in condenser and drain rate from the lowest tray

Immediately after closing the cooling water valve, column pressure starts to rise in a linear fashion. The maximum pressure increase of 1 bar is reached 410 s after closing cooling water flow. Afterwards, pressure starts to decline due to heat loss and residual cooling capacity of the condenser. The top temperature increases by more than 8 °C due to rising pressure and high boiler content, see **Figure 4**. Low boilers draining from the column cause a fast drop of temperatures on the pilot tray by

110 °C and by 11 °C in the bottoms. After about 15 min, the experiment was finished by re-opening the cooling water valve.
The hydraulic behavior during shutdown can be estimated from the pressure drop and level measurements given in **Figure 5**. Internal flow rates are estimated from the level data, see **Figure 6**. The steady-state pressure drop is ~ 4 mbar/tray indicating that the tower is in stable operating range. As soon as the steam valve is closed, the pressure profile collapses very fast. The liquid holdup quickly drains from the trays in about one minute, followed by a slower further build-up of liquid in the bottom. The rising holdup in the reflux drum clearly shows that the cooling water trapped in the condenser has considerable residual condensation capacity.
Figure 6 shows a maximum drain rate of more than 15 m³/h and that the residual condensation rate initially almost reaches the steady-state value. This residual condensation may play a decisive role in the columns dynamics.

2.2 Dynamic (hydraulic) modeling
During shutdown, the tray hydraulics move to zero flowrates, i.e. to the origin of the load diagram, see **Figure 2**. The hydraulic transients will mostly depend on tray parameters like initial holdup, dump point and drain rate.

2.2.1 Holdup models
Within ASPEN Dynamics, the Francis-weir equation is implemented, where clear liquid height is the sum of weir and overflow heights:

$$h_{Cl} = h_W + C_0 (V_L / L_W)^{2/3} \quad (1).$$

To model the true nature of the two-phase flow on sieve trays, Colwell [8] develops a holdup model considering the effect of gas load on froth height and density:

$$h_{Cl} = \alpha_L h_W + 7.3 (\alpha_L^{1/2} / C_D \cdot V_L / L_W)^{2/3} \quad (2).$$

The froth density α_L depends on a Froude number and its calculation requires iteration. In the model given by Bennett et al. [9], α_L only depends on gas load. A recent paper shows that the Colwell model is applicable to valve trays as well [10]. During shutdown, gas and liquid load quickly fall to zero, while the clear liquid height models mentioned above converge to the value of the weir height. However, recent experimental valve tray data [10] shows, that tray holdup quickly decreases below the dump point. Holdup models break down in the dumping region and need to be complemented by a weeping model.

2.2.3 Weeping models
On sieve trays, the weep fraction can be correlated using a Froude number and the transition from no weeping to dumping occurs in a small interval of gas load [11]. ASPEN Dynamics provides a weeping model, which needs to be tuned to describe a particular tray design:

$$F_{weep} = C_{DR} \rho_L h_{Cl} (1 - V / (V_0 C_{DP})) \quad (3).$$

The weep rate F_{Weep} must be adapted by fitting the constants C_{DP} for the onset and C_{DR} for the magnitude of weeping. V/V_0 is the ratio of actual to steady-state vapor flows at initialization, the ratio $V/(V_{0C}C_{DP})$ is clipped to values between 0 and 1.
Staak [6] simplifies the model derived by Wijn [12] by fitting to own sieve tray data:

$$L_{weep} = \Omega A_{hole} \rho_L \sqrt{2 g h_{cl}} \quad (4).$$

The weeping factor Ω is computed from:

$$\Omega = Min \left[1; k_3^{weep} \exp(-k_2^{weep} F_{hole} + k_1^{weep})\right] \quad (5).$$

The constants are given in [6]. On moveable valve trays, the valves will close during shutdown and the free area A_{hole} left for vapor flow will depend on the valve design.

2.3 Simulation results

Correct definition of tray type and geometry, as well as initial composition and holdup profiles in ASPEN Plus is essential to ensure good initialization of the ASPEN dynamics model. For all simulations, the Francis weir equation is used to model holdup. Within Aspen Dynamics, the weeping model must be fitted to the operating conditions on the tray. Because of the low gas load in the experiment, the value of the drain point constant C_{DP} was increased from the default value of 0.1 to 0.95. I.e. weeping sets in at a 5% reduction in gas load. Results are shown in **Figures 7** to **10**. In the ASPEN model with increased C_{DP} (dashed line), the dynamics of pressure change and temperatures are much too slow, because the predicted weeping rate is too small. An additional tenfold increase of the constant C_{DR} for the drain rate only leads to a slightly faster response (thin solid line). The ASPEN weeping model has a major disadvantage for shutdown simulation: Dumping (i.e. 100% weeping) only occurs, when vapor flow is zero.

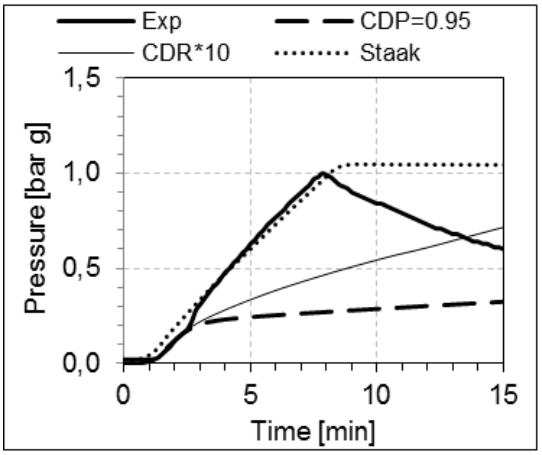

Figure 7: Pressure increase

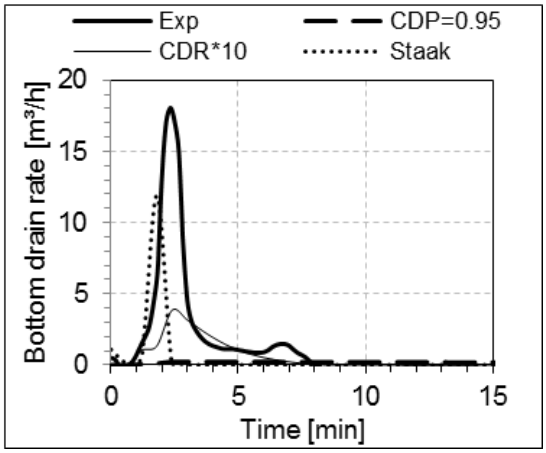

Figure 8: Drain rate from the lowest tray

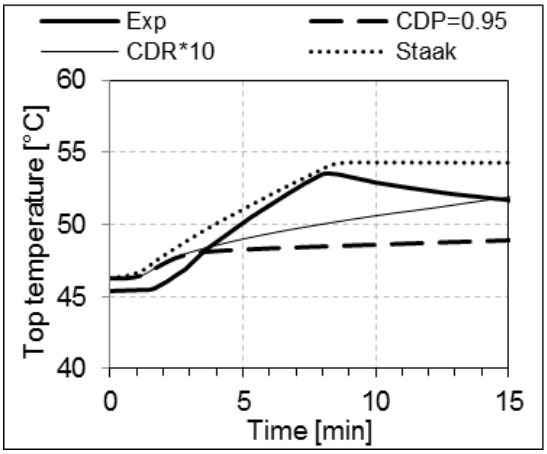

Figure 9: Top tray temperature

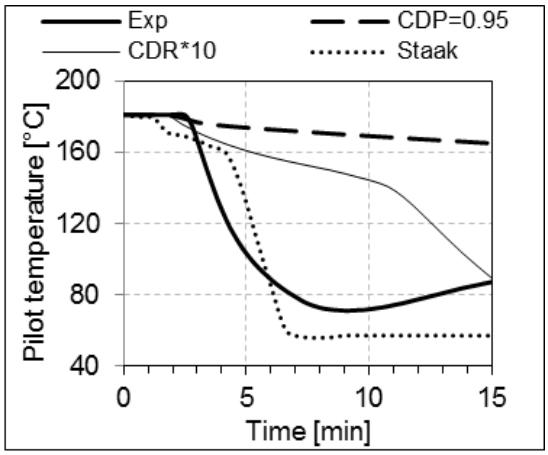

Figure 10: Pilot tray temperature

Adaption of the Staak weep model to valve trays is possible by considering the real valve type. Typically the open area left for draining in the closed position will range from less than 5 up to 20% of the value for open valves. Simulation results for 2% open area in closed valve position (dotted lines) show good agreement in pressure and temperature dynamics. Especially the top pressure and temperature transients are closely matched by the model up to the pressure peak. The decline in the real column pressure due to residual condensation and heat loss (non-insulated overhead pipe) is not predicted. The predicted drain rate from the lowest tray sets in very fast,

but does not quite reach the peak inferred from experimental bottom level data. The simulated pilot tray temperature is also very close to the experimental values. Note that the temperature measurement is located in the downcomer and the model assumption of perfect mixing on the tray no longer holds under shutdown conditions.

3. Conclusions

ASPEN dynamics is a useful tool to model shutdown. It allows easy access to property data used for design ensuring consistency for HAZOP discussions.

Experimental data on shutdown is provided from an industrial column. Due to the operational constraints of an industrial plant during start-up, the hydraulic load in the experiment was rather low, but well within the stable hydraulic operating region. Considering the hydraulic characteristics of valve trays, we expect very similar behavior at higher loads. Consistent with results from [6], the maximum pressure is reached within a few minutes. In the standard ASPEN model, however, the pressure peak is never fully reached, because the weeping model cannot be tuned to correctly predict the fast dumping of liquid from the trays. A literature sieve tray correlation is adapted to valve trays and is successfully employed to predict the process dynamics.

Column shutdown after loss of cooling causes a fast, but limited pressure increase, which needs to be considered in the mechanical design of all connected equipment. Experimental proof of a safeguarding method frequently used for distillation columns is provided. Properly designed, a closed system results in which relief is avoided completely, except for the fire case. At least, a considerable reduction of the relief rate is possible by shutting down energy inputs to the column. Definition of suitable weeping models capable of providing the high dumping rates observed is essential. The model developed captures the complex process dynamics. It can be used to design safety interlock systems and asses the dynamic performance in detail. Different structures of safety interlock systems, e. g. with or without shutdown of feed or reflux flows can be simulated.

References

[1] Sengupta, M. and Staats, F. Y.: A new approach to relief valve calculations. *Hydrocarbon Processing*, May 1978, 160-162

[2] Bradford, M. and D. G. Durrett: Avoiding common mistakes in distillation safety valves. Chemical Eng. July 8, 1984, 78-84

[3] Haribabu, C., Amudha, V., Khanna, V., and D. Bhattacharya: Calculating column relief loads, *PTQ Q2*, 2010, 55-65

[4] Abouelhassan, M.: Crude column relief mitigation, *PTQ Q4*, 2011, 133-137

[5] Can, Ü., Jimoh, M., Steinbach, J. and G. Wozny: Simulation and experimental analysis of operational failures in a distillation column. *Separation and purification technology* 29.2 (2002): 163-170.

[6] Staak, Daniel, et al. Safety assessment on distillation columns: From shortcut methods and heuristics to dynamic simulation. *AIChE Journal* 57.2 (2011): 458-472.

[7] Glitsch Inc.: Ballast tray design manual Bulletin No. 4900, 6th edition, Dallas, TX

[8] Colwell, C. J.: Clear liquid height and froth density on sieve trays. *Industrial & Engineering Chemistry Process Design and Development*, *20*(2) (1981), 298-307.

[9] Bennett, D. L., Agrawal, R. and P. J. Cook: New pressure drop correlation for sieve tray distillation columns. *AIChE Journal*, *29*(3), (1983) 434-442.

[10] Brahem, R., Royon-Lebeaud, A., Legendre, D., Moreaud, M. and L. Duval: Experimental hydrodynamic study of valve trays. *Chemical Engineering Science* 100 (2013), 23-32.

[11] Lockett, M. J. and S. Banik: Weeping from sieve trays. *Industrial & Engineering Chemistry Process Design and Development*, *25*(2), (1986), 561-569.

[12] Wijn, E. F. (1998). On the lower operating range of sieve and valve trays. *Chemical Engineering Journal*, *70*(2), 143-155.

Vapor/Liquid Parallel-Flow Channeling on Cascade Trays with Moving Valves

J. Bausa[1] *and B. Pennemann*[2]
[1]*Bayer Technology Services, Leverkusen, Germany;*
[2]*Bayer Material Science, Leverkusen, Germany*

Abstract
A hydraulic mechanism called 'vapor/liquid parallel-flow channeling' (VPC) is presented, which leads to tray efficiency loss due to disengagement of vapor and liquid flows. It occurs only on cascade trays. The occurrence of VPC is shown based on model calculations and experimental results from water/air tests.

Keywords
Distillation, valve tray column, liquid channeling, maldistribution, multiple steady states, vapor crossflow channeling

1. Introduction

Vapor crossflow channeling (VCC) is a known problem of trayed distillation columns with high liquid load and long flow path length. Here, the high liquid load generates a high hydraulic gradient on the tray, which in turn causes weeping/small gas loads at the inlet and high vapor load at the tray outlet. The weep as well as deficient vapor and liquid contact lower tray efficiency, and degrade column performance. One measure to alleviate vapor crossflow channeling is the use of cascade weirs which reduces the flow path length. However, the cascade can lead to another form of vapor-liquid maldistribution, we termed 'vapor/liquid parallel-flow channeling' (VPC). In contrast to VCC, it will occur even on trays with low liquid load.

2. Tray efficiency loss in a technical scale column

The work presented here is based on a real troubleshooting case of a plant distillation column just less than 3 m diameter equipped with cascade trays containing Varioflex moving valves type VV16-3L20.

While the product specifications were met in some cases, they were missed widely in others. Plant data revealed that for the same process operating conditions (feed/bottoms/distillate flow rate, pressure and reflux ratio) on-spec as well as off-spec cases were found. So, the column seemed to have two different steady states, which can run more or less stable under the same process conditions. These problems occurred particularly at small and medium loads, but not at high loads.

A column simulation showed that the number of trays installed is sufficient to achieve the desired separation. Even when decreasing the value for the expected tray efficiency considerably, product specifications could be met. It was concluded, that only an unrealistically low tray efficiency could explain the observed malfunction of the column.

Based on these findings a hydraulic phenomenon was suspected to cause the observed tray efficiency loss. But which kind of hydraulic malfunction could lead to the dramatic loss in tray efficiency? Based on literature, the first theory to be checked was 'vapor crossflow channeling' (VCC) (see Kister 1993, Kister 2006 and Resetarits and Pappademos 2001).

In case of VCC the hydraulic gradient on the tray results in a significant higher liquid level on the inlet side of the tray, as depicted in Figure 1. Due to the higher liquid level in the inlet area, hydrostatic pressure is also higher, which results in weeping. In addition, the higher hydrostatic pressure hinders vapor rising through this area. On the other hand, there is no weeping but increased vapor traffic on the outlet side of the tray, as liquid level is smaller. As part of the vapor flows countercurrent to the liquid, it even increases the gradient in liquid level.

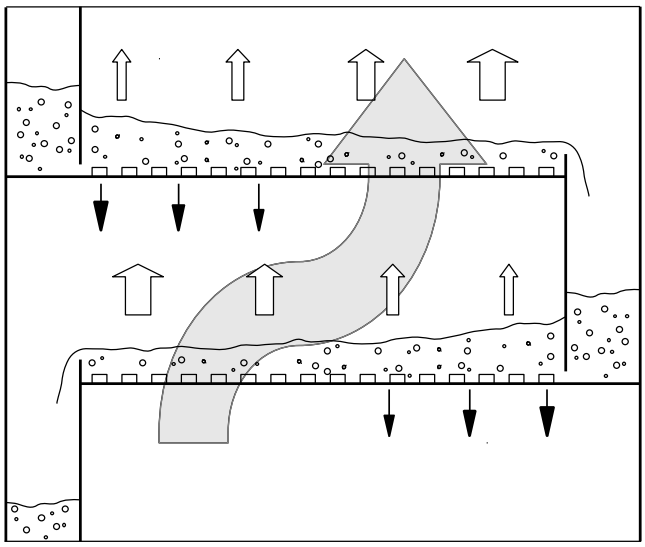

Figure 1: Vapor crossflow channeling.

As in the inlet area some of the liquid is weeping and vapor traffic is small, contact between liquid and vapor is worsened, resulting in poor tray efficiency. Similarly, this is what is observed in the above mentioned case as well.

According to Kister (2006), four criteria need to be fulfilled to allow for VCC:

- A large open area of more than 15 % or venturi valves.
- A high ratio (>2) of flow path length to tray spacing.
- A pressure of 4.8 bara (70 psia) or less.
- A high liquid flow rate (>45-54 $m^3/m/h$ (5-6 gpm/in.) of outlet weir).

In our case the fourth and most important one is not met by a large margin (liquid flowrate at outlet was about 4 $m^3/m/h$). But only when liquid flowrate on the tray is high enough, a strong gradient in liquid level may build up. Thus VCC is very unlikely in our case.

Based on VCC, a slightly different scenario was considered: What if all the liquid fed to the tray is weeping from the inlet half before the cascade weir (dumping)? If the liquid level on the inlet half is smaller than the weir height there will be no overflow over the cascade weir. Consequently the outlet half of the tray will run completely dry. However, the described state can only be stable, if pressure drop on both sides of the cascade is the same: the inlet side, which has some liquid level and only minimal vapor traffic, and the outlet side that has no liquid level but high vapor load.

The column is equipped with Varioflex valves of type VV16-3L20 which were developed by company Stahl in the 1970ies. As can be seen in Figure 2, at low vapor loads (closed position) only a 20 mm hole is provided for the vapor. However, at high

vapor loads, the caged disc is lifted and a much higher open area (5 x) is available. As a result, the Varioflex provides a very wide operating range with a turndown ratio of five.

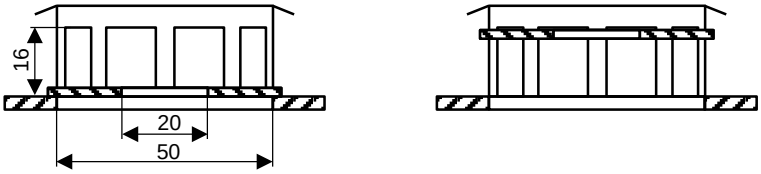

Figure 2: Varioflex valve type VV16-3L20 in closed (left) and open (right) position.

Varioflex valves have been tested extensively in the 1980ies by Bayer. Hence, proprietary data on pressure drop and weeping was available for this work. The pressure drop for different liquid levels and vapor loads is depicted in Figure 3. It shows the flat characteristic of the moving valve: While at low loads all valves are in their closed position and pressure drop increases with vapor load, at some load the valves start to open and pressure drop stays nearly constant. Only when all valves operate in their full open position, pressure drop again increases with vapor load.

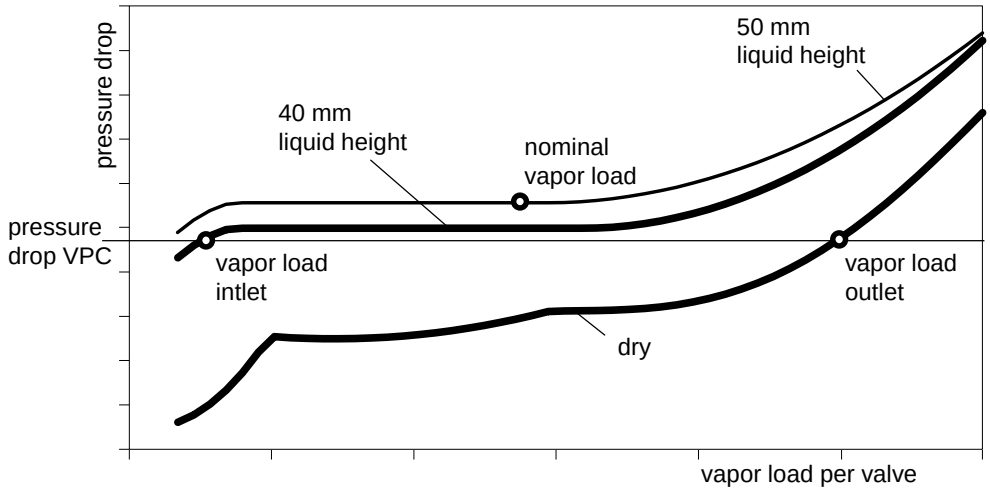

Figure 3: Pressure drop for Varioflex moving valve type VV16-3L20.

Figure 3 shows that the scenario stated above is possible for the VV16-3L20: The marked vapor load at the inlet with a liquid level of 40 mm (which is the cascade weir height, so barely no liquid will overflow) results in the same pressure drop as the vapor load at the outlet with no liquid level (dry). Obviously, the nominal vapor load is in the middle between both loads, as it is their mean value.

Thus, based on pressure drop considerations, the phenomenon called ‘vapor/liquid parallel-flow channeling’ (VPC) is at least possible. As depicted in Figure 4, the complete liquid entering the upper tray would be weeping through the valves on the inlet half, while only small amounts of gas pass them (about 20 % of nominal load, see Figure 3). As the liquid level on the inlet half does not reach the cascade weir height, there is no overflow and consequently no liquid feed to the outlet half of the tray. As the valves on the outlet half are running dry, they exhibit the same pressure drop, even at a much higher vapor load (about 180 % of nominal load).

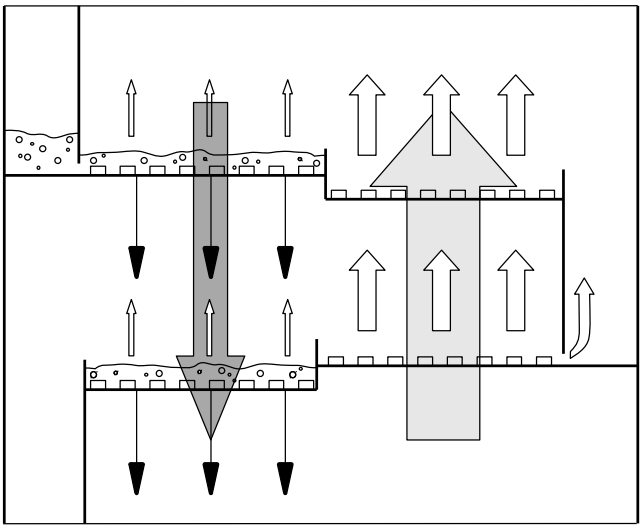

Figure 4: Scenario of ‘vapor/liquid parallel-flow channeling’ (VPC).

This scenario may even propagate downward through the column, as depicted in Figure 4: As only the left half of the lower tray gets liquid feed (weeping from the upper tray), this part may weep with low vapor load, while the other half runs dry with high vapor traffic. As the downcomer is empty, there is no sealing and vapor may even take this way. This way, vapor and liquid will find their way through the column in parallel and 90 % of the vapor will have no contact to the liquid. It is clear, that this will lead to very poor tray efficiency.

3. Modelling of hydraulics

To check conditions, under which VPC can occur, the following model equations were developed. Basis are empirical correlations for weeping per element w_{El} and pressure drop Δp as functions of vapor load per element V_{El} and clear liquid height h_L that were fitted to experimental data. It was assumed that VPC occurs, there is no overflow over the cascade weir and the liquid level on the outlet side is zero ($h_{L,out}$ = 0). Then the following set of equations can be derived from liquid balance, vapor balance and the condition of equal pressure drop on both sides.

$$L_t = \frac{N_{El}}{2} w_{El}\left(V_{El,in}, h_{L,in}\right)$$

$$V_t = \frac{N_{El}}{2} V_{El,in} + \frac{N_{El}}{2} V_{El,out}$$

$$0 = \Delta p\left(V_{El,in}, h_{L,in}\right) - \Delta p\left(V_{El,out}, h_{L,out} = 0\right)$$

Here, L_t denotes the total liquid load as volume flow rate, V_t the total vapor load as equivalent air flow and N_{El} the total number of valves on the tray. Based on this system of three equations, the three unknowns $h_{L,in}$, $V_{El,in}$, and $V_{El,out}$ can be calculated iteratively.

The model is based on the assumption that no overflow occurs at the cascade. If the calculated liquid height is higher than the cascade weir height this assumption is not met and VPC cannot occur. On the other hand, if the calculated level is less than the cascade weir height, VPC can occur.

However, normal column operation, where weir overflow occurs and both halves of the tray share the same liquid level and vapor load per valve, is always a solution to

the hydraulic conditions. This means, that in case of a calculated liquid level on the inlet half lower than the cascade weir height, two different possible hydraulic states exist for the tray. These two states for each tray are multiple steady states of the system.

Using the model equations, the liquid level on the inlet half of the tray in case of VPC was calculated for different vapor and liquid loads. As can be seen from Figure 5, vapor load has a high impact on the liquid level and is thus a good measure to avoid VPC. On the other hand the liquid flowrate has only minor impact in avoiding VPC. For the considered column VPC was shown to be possible below about 95 % of the nominal vapor load. At 100 % vapor load the liquid level is at 50 mm, which is already higher than the cascade weir and will lead to overflow.

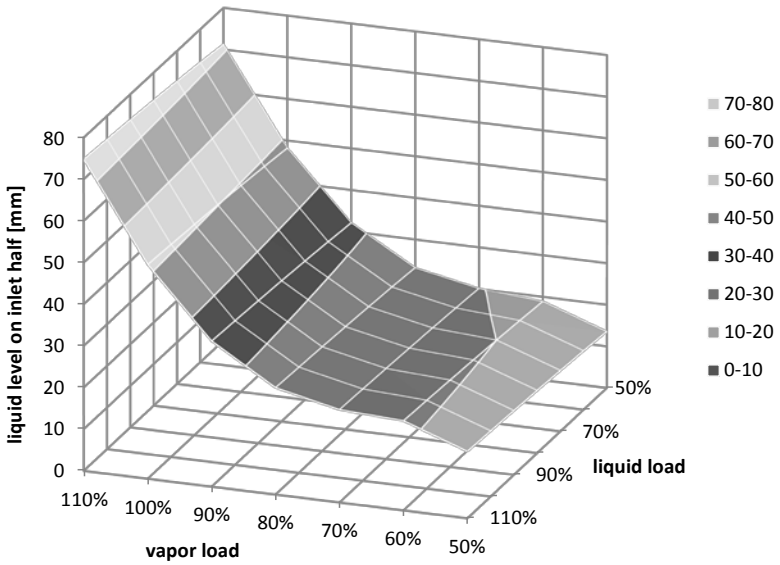

Figure 5: Calculated values of liquid level on inlet side in case of VPC for different vapor and liquid loads relative to the nominal load.

These findings were then tested in the problematic distillation column. It was found that indeed increasing liquid rate did not solve the problem, while increasing vapor load resulted in acceptable separation efficiency. However, while for the model equations a load of about 95 % of nominal load was sufficient to avoid VPC, in reality VPC maintained at 100 % load and was stopped at about 110 % load. The normal hydraulic operation state then stayed stable, even when decreasing vapor load to 100 %.

Interestingly the VPC-state always exhibits a lower pressure drop than the normal state: As can be seen in Figure 3, pressure drop at VPC is lower than at nominal vapor load and a liquid level of about 50 mm, which is required to overflow the 40 mm weirs. For nominal load a decrease of pressure drop due to VPC of 10 % was calculated. A lower pressure drop was also found for the plant column when running with bad efficiency. However, as it is unclear how many trays may suffer from VPC, the change in pressure drop could not be attributed to specific trays.

4. Experimental validation

To experimentally confirm the model predictions, water/air tests were carried out. As it was not possible to test a large tray with hundreds of valves, a small, rectangular

testing device with only 22 Varioflex VV16-3L20 valves was utilized, as depicted in Figure 6.

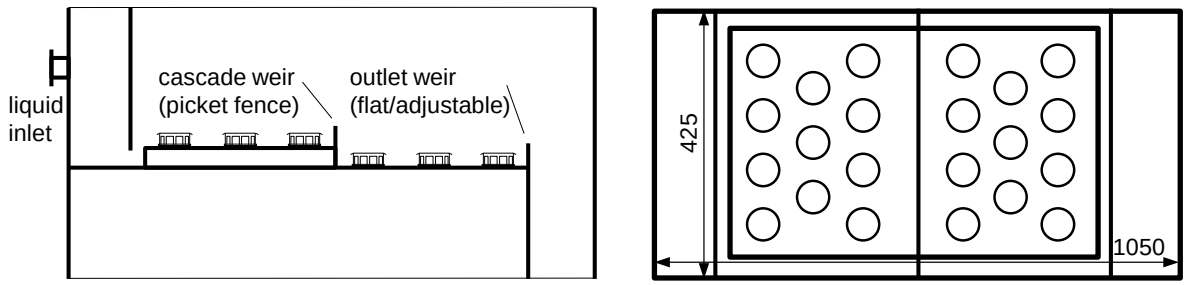

Figure 6: Experimental setup for water/air tests.

In order to run the tests under the same conditions as in the plant column, the following key parameters were kept the same: vapor load per valve (V_t/N_{El}), liquid load per valve (L_t/N_{El}), and cascade weir load ($L_t/L_{Cas.eff.}$). Here $L_{Cas.eff.}$ denotes the effective (*i.e.* not blocked) length of the picket fence cascade weir. Thus, overflow height and liquid level on the inlet side should be comparable to the technical column. The flat outlet weir was adjusted in a way that would lead to the same liquid height as in the plant column.

As can be seen in Figure 7, VPC was found to prevail on the tray at nominal load. Pressure drop was about 30 % less than calculated by the pressure drop calculations for uniform vapor distribution. Weeping rate was about 80 %, while no weeping at all would be expected for a uniform vapor distribution based on data from earlier tests. The tests also showed that changing the liquid rate between 50 and 150 % of nominal load had no remarkable influence on hydraulic state. Thus, the main predictions of the model could be proven by the tests.

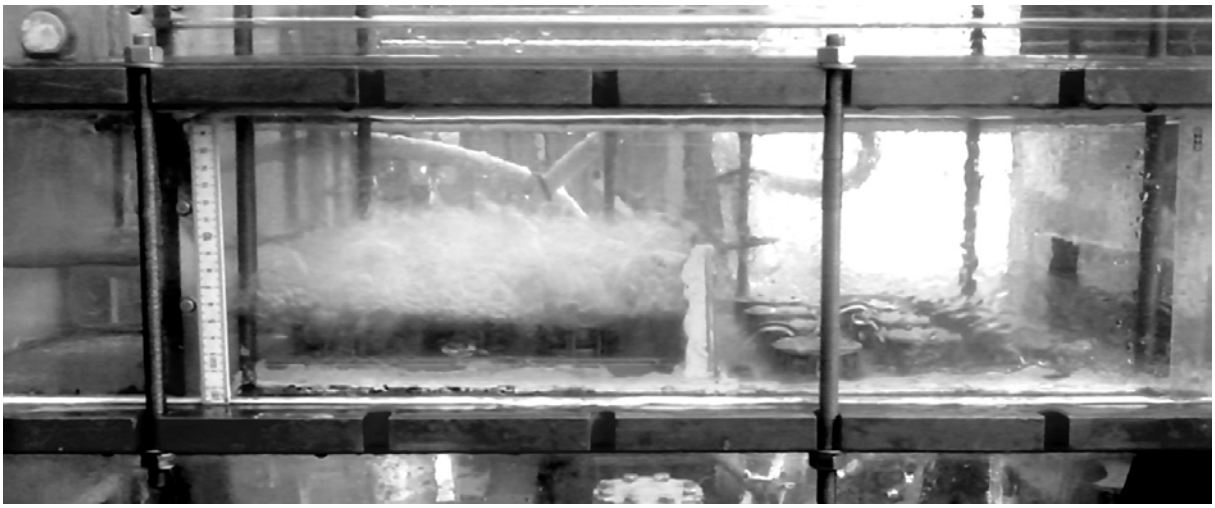

Figure 7: Water/air tests at nominal load exhibiting VPC.

However, there is one significant difference between the experimental setup and the plant tray: vapor leaving the valves typically entrains liquid droplets and throws them about 200-300 mm. As depicted in Figure 8, on a small tray, all valves are located near to a boundary and thus most of the liquid droplets entrained by vapor jets are leaving the segment. While on a larger tray, most of the valves have some distance to the boundary. Liquid entrained by vapor jets will most likely remain on the

segment. Thus, a small tray has a much higher tendency to run in the spray regime when losing liquid by spray and not by weir overflow.

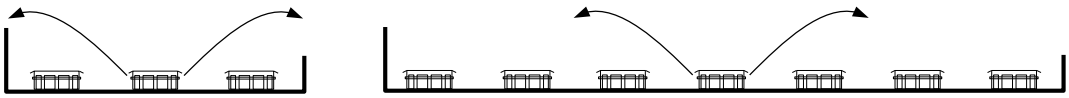

Figure 8: Effect of throw distance on small and large trays.

As a result of this effect, the outlet half ran in the spray regime with no liquid, even when the liquid level on the inlet side was high enough to overflow the cascade weir. In some cases under higher loads even the inlet side had no liquid level and ran in the spray regime, while the outlet side had a normal liquid level and was overflowing over the outlet weir. While in these cases vapor distribution was still non-uniform, no weeping occurred and the tray is expected to have acceptable separation efficiency. Only for special operation conditions and startup procedure it was possible to run the test tray with uniform vapor distribution and equal liquid levels on both sides.

5. Conclusions

In this contribution a maldistribution scenario for trayed columns termed ‘vapor/liquid parallel-flow channeling’ (VPC) is presented. For a column equipped with cascade trays and Varioflex VV16-3L20 valves the possibility of this phenomenon was demonstrated by model calculations and water/air tests. As VPC causes a dramatic loss in tray efficiency, it can be a severe problem for columns equipped with cascade trays.

It was also found, that cascade trays with valves have a high tendency to non-uniform vapor distribution, even when VPC does not occur. This can be caused by running only one of the halves of the tray in the spray regime. It is expected that non-uniform gas distribution caused by spray will be less pronounced on larger trays, as only a small portion of the spray will leave the segment and liquid can thus backup. However, it is recommended to use a cascade on valve trays only if there is real need to do so, as the cascade could introduce more problems than it solves.

All investigations were done for the Varioflex VV16-3L20. Since it has a large open area even if in closed position, it may be more prone to VPC compared with other valves. Thus, it seems necessary to check other valve types in the same way. This should then be extended to fixed valve and sieve trays. Although their pressure drop characteristic is not as flat as for valves, VPC is at least not impossible.

References

Kister, Henry (1993): Can valve trays experience vapour cross-flow channeling?, The Chemical Engineer, June 1993.

Kister, Henry (2006): Distillation troubleshooting, John Wiley & Sons Inc., Hoboken.

Resetarits, Michael R. and Pappademos, Nadia (2001): Factors influencing vapor crossflow channeling, AIChE Fall Annual Meeting, Reno, Nevada, November 2001.

Gamma Scan and Tomography Scan Data from a Distillation Column at Various Loadings

Lowell Pless[1], Ron Carlson[1] and Michael Schultes[2], and Simon Chambers[3],
[1] Tracerco, Pasadena, Texas, USA
[2] Raschig Ring Department, RASCHIG GMBH, Ludwigshafen, Germany
[3] Fractionation Research, Inc., Stillwater, Oklahoma, USA

Abstract

As first reported at a 2013 AIChE meeting, a unique combination of gamma scanning and FRI performance testing was executed on the FRI 1.22 m diameter High Pressure Test Column that contained a Raschig Super-Ring No. 2 high performance random packing and a trough type liquid distributor. The column was scanned several times from top to bottom during total reflux data collections with the cyclohexane/n-heptane system at 1.62 bara. The column was baseline scanned when dry and scanned at 45, 79, 100, and 102% of the packing Maximum Useful Capacity. Distributor liquid levels derived from the scan data compared extremely well against liquid level data from FRI bubblers. Tomography scans were performed at two different column elevations. At each elevation, 81 data points through the bed of packing were recorded: 9 scanning source positions with 9 different detector positions for each source position around the column circumference. Mathematical processing of the tomography scan data provided significant quantitative insights regarding liquid holdup and liquid flow patterns in random packed columns.

Keywords: Packing, gamma scan, maximum useful capacity, bubblers

Correspondence to author, e-mail: schambers@fri.org , Ph: 1-405-385-0354

1. Introduction

Fractionation Research Inc. (FRI) operates two industrial-size distillation test columns in Stillwater, Oklahoma. The Low Pressure (LP) column operates at pressures as low as 0.013 bara and as high as 11.4 bara. The High Pressure (HP) column can perform up to 34.5 bara. The HP column diameter is 1.22 meters. FRI has its own gamma scanning equipment which is employed in every test involving trays and packings. That equipment, however, is anchored in place on a single deck of the column, thus limiting the vertical scan range.

In June of 2012, FRI tested Raschig Super-Ring No. 2 [1,2] high performance random packing for the FRI membership. FRI received approval from Raschig to run concurrently special gamma scan tests[3]. Specifically, the random-packed column was scanned from top to bottom across a very wide range of internal flow rates. Dry scans were run with the test fluid hydrocarbon vapours present inside the column. Additionally, tomography scanning was performed at two elevations.

2. Results and discussion

2.1 Tower Set-Up and Operations

Figure 1 provides elevation drawings and photographs describing the FRI High Pressure Column as configured for the Raschig Super-Ring No.2 tests. The packed bed depth was 3.05 m. This packing had a void fraction of 0.98. A Raschig Type-D DT-S liquid distributor was employed above the packed bed.

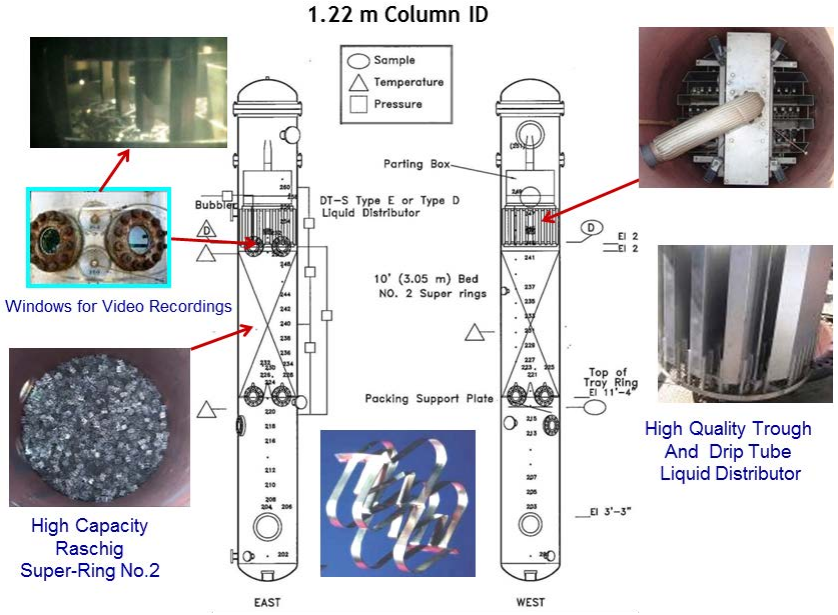

Figure 1. FRI HP Column Set-Up for Raschig Super-Ring Random Packing Test

For this special gamma scan work, the only system employed was the C_6/C_7 binary system at 1.62 bara. All of the wet runs were at total reflux (TR). Sample compositions were employed to calculate HETP's. The HETP's in **Figure 2** identified the percent Maximum Useful Capacity (MUC) of the random packing.

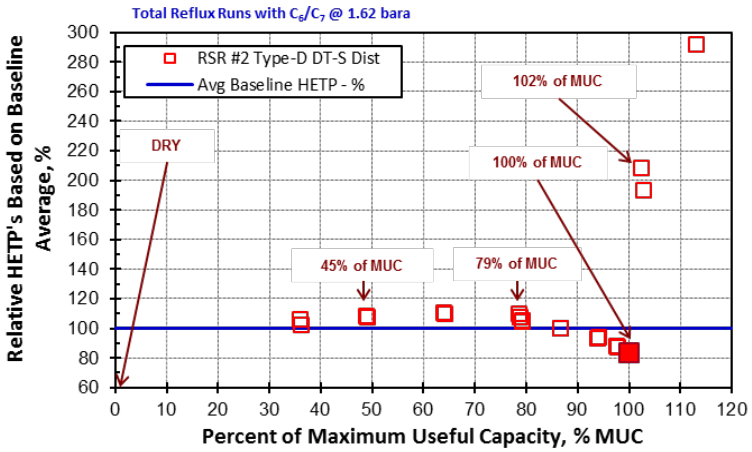

Figure 2. FRI HP Column Set-Up for Random Packing Test

2.2 TRU-SCAN® Method

The packed column was gamma scanned vertically from near the top of the installed liquid distributor down through the entire bed of packing. A gamma scan generates a density profile of the column, which can be used to identify the integrity of internals and to identify internal conditions. **Figure 3** is a representation of the scanline orientation used to obtain the TRU-SCAN® data.

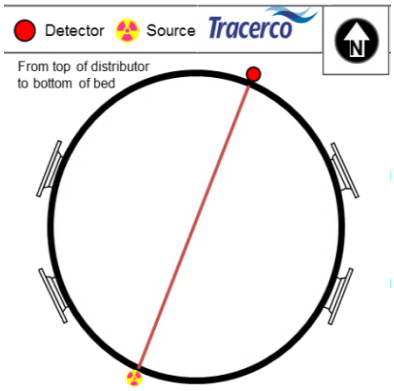

Figure 3. TRU-SCAN® Scanline Orientation in HP Column

2.3 Gamma Scan Results

Table 1 summarizes the operating conditions with process parameters that were calculated from the scan data.

Scan	% Maximum Useful Capacity	Data Curve	Average Bed Density, kg/m^3	Liquid Fraction @ Top of Bed	Liquid Fraction @ Mid-Bed	Liquid Fraction @ Bottom of Bed
1	Dry	Blue	155	0	0	0
2	45	Red	176	0.025	0.034	0.037
3	79	Black	185	0.046	0.048	0.049
4	100	Green	230	0.083	0.144	0.133
5	102	Orange	243	0.169	0.133	0.108

Table1: Summary of Liquid Fraction Data Collection

Figure 4 is a plot of the scan results. The vertical or Y-axis is tower elevation; the horizontal or X-axis is the density of the column fluids as calculated from the radiation counts. **Figure 4** includes a "clear vapor" reference line (vertical far right). The line is not based on a calculated number, but on the radiation intensity at which the lowest vapor density was observed. The "clear vapor" reference was presumed free of liquid and was used as the reference for calculating relative densities of the process fluids.

The gamma scan results revealed a disproportionate build-up of liquid within the packing at the middle (vertically) section of the bed. From **Figure 4** the maximum density observed on the green data curve is in the middle of the bed from 4.3 to 5.2 m, reference tower elevation. *As the HP Column approached flooding the area of liquid accumulation or excess liquid holdup shifted vertically*

from the middle of the bed to the top of the packed bed. **Figure 4** shows where the maximum density on the orange data curve is at the top of the bed.

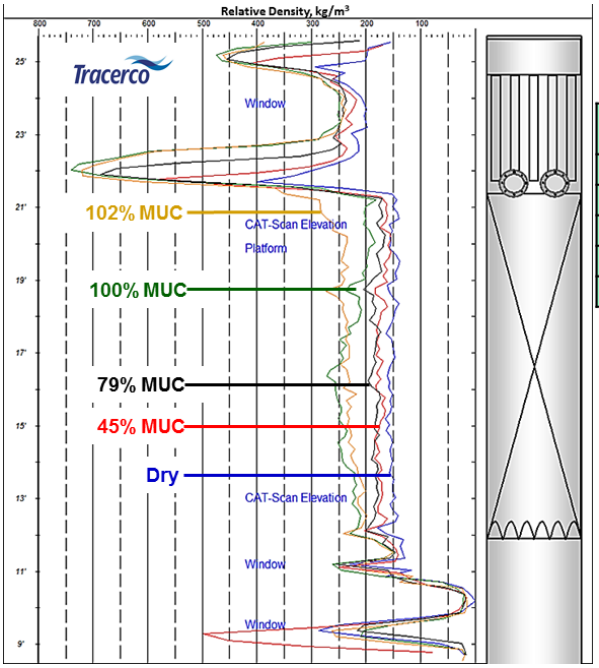

Figure 4. Complete Vertical Scans at One Dry and Four 'Wet' Rates.

Scan	% MUC	Data Curve
1	Dry	Blue
2	45%	Red
3	79%	Black
4	100%	Green
5	102%	Orange

View through Windows of Liquid Distribution Quality

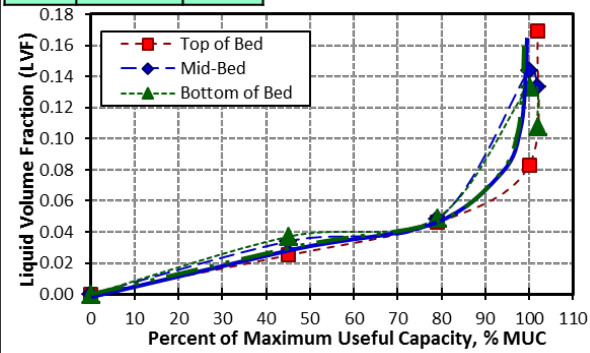

Figure 5. Liquid Volume Fractions as A Function of % MUC

Liquid volume fractions were determined using calculated relative process densities from the vertical scan data and from top, mid-bed and bottom liquid densities provided by FRI. **Figure 5** shows the liquid volume fraction trends versus the %MUC. The liquid retention trends in the bed corroborate the observations made with **Figure 4**. At 85-100 % of MUC the bottom and mid-bed liquid hold-ups were unexpectedly higher than the top of the bed, but more data points would be required in this operating region before reaching a general conclusion. The expected trends (dashed lines) in liquid volume fraction for the bottom and mid-bed were added on to **Figure 5**.

2.4 TRU-CAT™ Method

A TRU-CAT™ scan is a proprietary tomography scan method consisting of a series of gamma scans covering a full horizontal plane at a given column elevation. Each chord represents data points that collectively were regressed to provide a cross-sectional relative density profile of the HP Column.

The HP Column was scanned near the top of the bed of packing, approximately 230 mm into the bed, and near the bottom of the bed of packing, approximately 150 mm above the packing support. **Figure 6** is a representation of the tomography scan orientation used on the High Pressure Column.

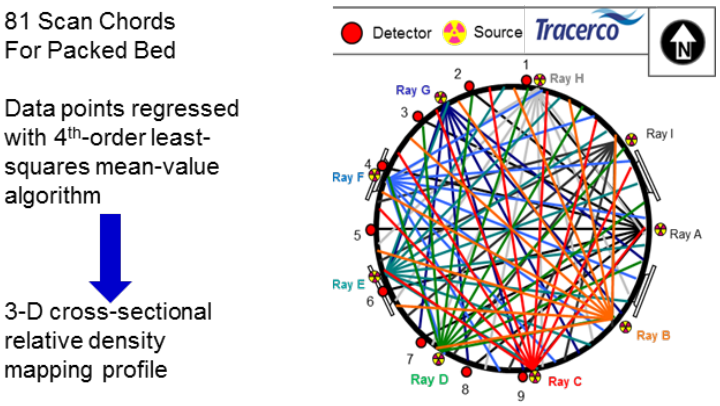

Figure 6. Tomography Scanline Orientation in HP Column

2.5 Tomography Scan Results

The results, in **Figures 7** and **8** are topographic images with contour. Colors indicating the relative densities were derived from a mathematical model fitted to the scan data taken and are not a plot of actual data.

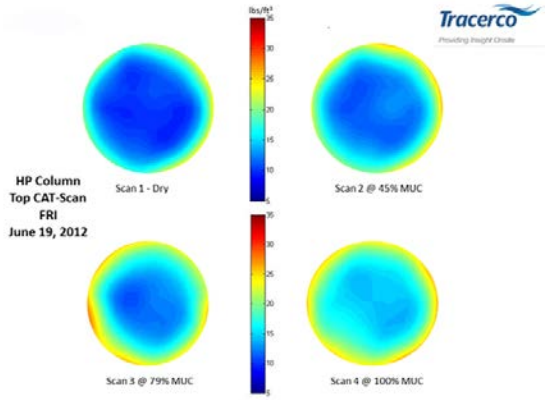

Figure 7. Top of Bed Tomography Scans

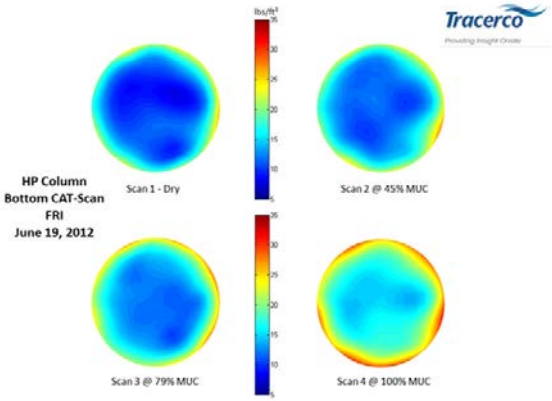

Figure 8. Bottom of Bed Tomography

A general tendency at rates approaching and surpassing 100% MUC was for the extra volume of liquid retention in the packing to accumulate against the walls.

2.6. Distributor Liquid Levels

The gamma scan distributor liquid levels shown in **Table 2** are each a composite level detected through all the distributor laterals that the scan radiation beam passed through. The measurement method follows:

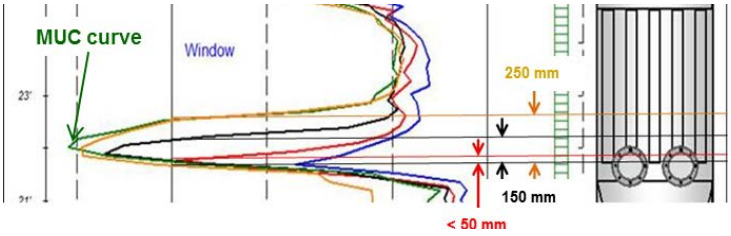

At all four wet operating conditions, the liquid depths in the distributor troughs measured from the gamma scans were compared to the liquid depths determined by FRI bubbler data. The table shows that agreement was excellent.

Percent of Maximum Useful Capacity	Data Curve	TRU-SCAN® Distributor Liquid Level, mm	FRI Bubbler Distributor Liquid Level, mm
Dry	Blue	Dry	Dry
45	Red	< 51	64
79	Black	152	165
100	Green	254	254
105	Orange	254	282

Table 2: DT-S Liquid Head Measurements TRU-SCAN® vs. Bubbler

3. Conclusions

Generally:

- CAT-scanning sometimes provides valuable information that is often unavailable from conventional scans
- Before column commissioning, dry gamma scans of the process fluid vapours can aid appreciably in the interpretations of wet scans for a column in operation.
- Total top-to-bottom scans facilitate troubleshooting efforts.

Regarding the scanning and cat scanning of the Raschig Super-Ring No.2 packing:

- Approaching the Maximum Useful Capacity (MUC), there was liquid build-up near the *middle* (vertically) of the packed bed compared to the top and bottom.
- At rates slightly higher than the MUC, there was a build-up of liquid near the *top* of the bed – as if the liquid was having a difficult time getting down the tower
- The gamma scan determined liquid heads in the distributor troughs agreed with the FRI bubbler (hydrostatic head) readings extremely well.

Abbreviations

HETP Height Equivalent to a Theoretical Plate
HP H Pressure
MUC Maximum Useful Capacity

Acknowledgements

Mr. Mike Resetarits contributed to the writing of this paper.

References

1. Schultes, M., 2001, "Raschig Super-Ring - A New Fourth Generation Random Packing", AICHE Meeting & Petrochemical, & Refining, Houston, Texas, 22–26 April.
2. Chambers, S., Pless, L., Carlson, R. and Schultes, M., “Gamma Scan and CAT-Scan Data From a Distillation Column at Various Loadings”, AIChE Spring Meeting, San Antonio, TX, April 28-May 2, 2013.
3. Pless, L., “Tower Scanning As a Quantitative Tool – Pack View™”, Topical 8, Distillation Topical Conference, AIChE Spring Meeting, San Antonio, TX, April 28-May 2, 2013.

Control of cyclic distillation systems

Costin Sorin Bildea,[1] Cătalin Pătruţ,[1] Anton A. Kiss[2]

[1]University Politehnica of Bucharest, Bucharest/Romania;

[2]AkzoNobel Research, Development & Innovation, Deventer/Netherlands;

Abstract

Cyclic distillation is an effective process intensification technique that allows key benefits such as: increased column throughput, lower energy requirements and higher separation performance. Despite these advantages, the application to industrial processes is limited, mainly due to serious controllability concerns. To address this challenge, this study is the first to prove that cyclic distillation is also well controllable, hence being able to provide in practice the expected key economic benefits.

In this work we developed a dynamic model which consists of two non-linear functions that map the initial conditions to the system state at the end of vapour and liquid periods, respectively, by solving the dynamic mass balance together with equilibrium relationships. A periodic state is reached when the initial condition is attained after successive application of the two maps. A discrete-time controller is used, with the temperatures in the lower and upper parts of the column as controlled variables and the vapour flow rate and the amount of liquid reflux as manipulated variable. A case study is presented, proving that the discrete PI algorithm in the velocity form gives excellent performance. Therefore, the system is able to cope with changes in the feed flow rate and composition.

Keywords

Cyclic distillation, dynamics, process modeling, process control

1. Introduction

Process intensification in distillation systems received much attention during the last decades, with the aim of increasing energy and separation efficiency. Various techniques, such as internal heat-integrated distillation, dividing-wall columns and reactive distillation were studied (Yildirim et al., 2011). Cyclic operation is considered as an innovative method for operating existing distillation columns (Flodman and Timm, 2012), leading to key benefits, such as: increased column throughput, lower energy requirements (Bausa and Tsatsaronis, 2001) and higher separation performance (Maleta et al., 2011). The cyclic operation is achieved in distillation by alternating two steps: a) Vapor period, when vapor flows upwards through the column and liquid is stationary; b) Liquid period, when vapor flow is stopped, reflux and liquid feed are supplied and the liquid holdup is dropped from each plate to the one below (Cannon, 1961, Gaska and Cannon, 1961). This mode of operation can be easily achieved by using perforated trays, without downcomers, combined with sluice chambers located under each tray (Maleta et al., 2011). If the vapor velocity exceeds the flooding limit, the liquid does not overflow from tray to tray during the vapor-flow period. When the vapor supply is interrupted, the liquid drops down by gravitation to the sluice chamber. When the vapor supply is started again, the sluice

chambers open and the liquid is transferred to the tray below. The principle of cyclic operation is schematically illustrated in Figure 1.

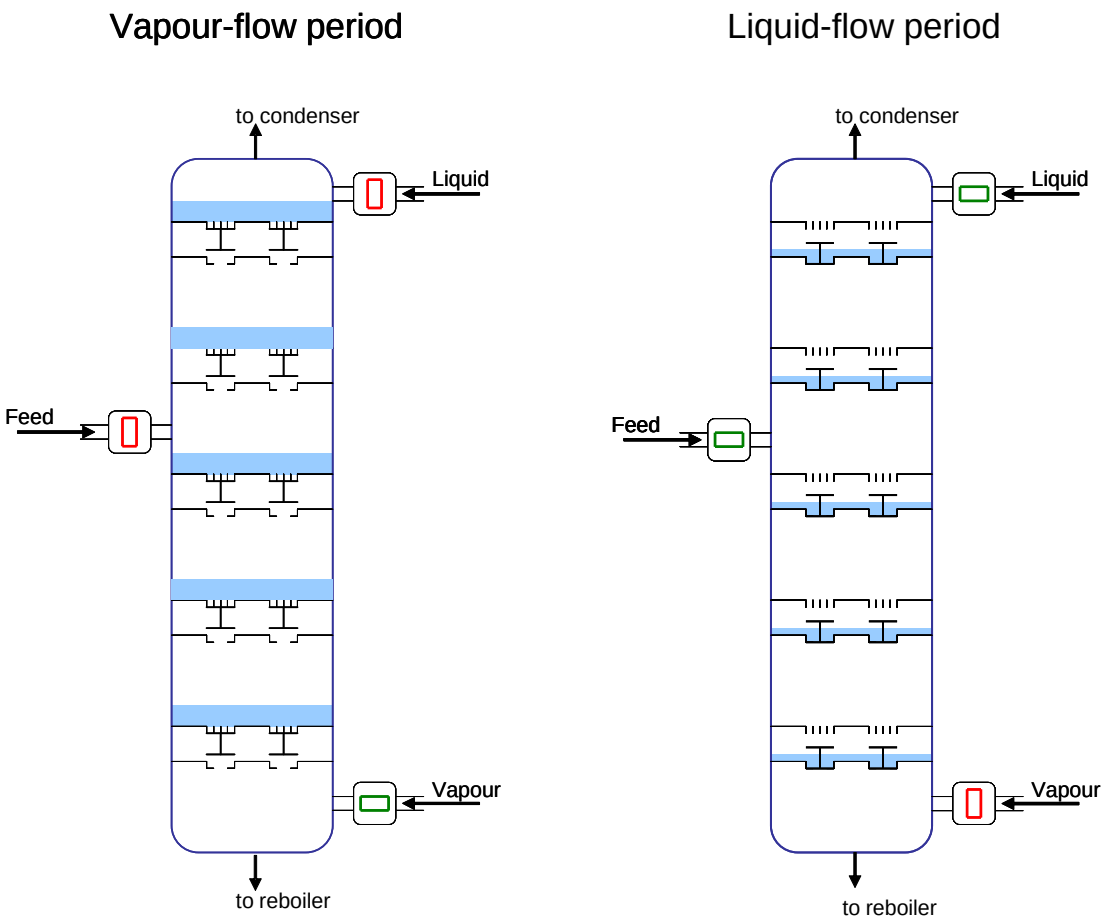

Figure 1. Schematics illustrating the working principle of cyclic distillation

Although the advantages of cyclic operation have been demonstrated experimentally, the information about control of cyclic distillation columns is rather limited. Matsubara et al., (1985) used both computer simulation and experiments to study the controllability of a cyclic distillation column stripping ammonia from an aqueous solution. For this particular system, the product composition was easy to be determined by conductivity measurements. However, for most practical systems, composition measurements are not available and inferential control is needed.

2. Problem statement

The literature review clearly proves the advantages of cyclic operation as compared to conventional, steady state operation of distillation. Several models are available to simulate the behavior of the cyclic distillation columns. When the assumption of linear equilibrium is employed, it is indeed possible to derive analytical solutions of the model equations. However, the accuracy of the results is limited. Moreover, these models are not applicable for control studies, as they do not take into account the nonlinearity of the system, the non-ideal vapor-liquid equilibrium, the dependence of the pressure versus the vapor and liquid flows and the dynamics of the temperature measurements. This paper fills this gap by presenting a rigorous model of cyclic distillation systems which is further used for a controllability study.

3. Mathematical model

The model of the cyclic distillation column has been derived under the following assumptions:

- Ideal stages (vapour-liquid equilibrium is reached)
- Equal heat of vaporization (this implies constant molar holdup and vapor flow rate)
- Perfect mixing on each stage
- Negligible vapour holdup
- Saturated liquid feed

Note that in contrast to the previously cited papers, no assumptions are made here with regard to the linearity of vapour-liquid equilibrium, negligible or constant pressure drop, infinite reboiler holdup or zero condenser holdup.

The vapour-flow period: For each component, j = 1, NC, the following equations describe the evolution of tray holdup:

Condenser: $$\frac{dM_{1,j}}{dt} = V \cdot y_{2,j} \quad (1)$$

Trays: $$\frac{dM_{k,j}}{dt} = V\left(y_{k+1,j} - y_{k,j}\right);\ k = 1, NT-1 \quad (2)$$

Reboiler: $$\frac{dM_{NT,j}}{dt} = -V \cdot y_{NT,j} \quad (3)$$

For each tray, *k* = 1,NT, the following relationships describe the liquid-vapor equilibrium:

$$P_k \cdot y_{k,j} - x_{k,j} \cdot \gamma_{k,j}\left(x_1, ...x_{NC}, T_k\right) \cdot P_j^{vap}\left(T_k\right) = 0 \quad (4)$$

$$x_{k,j} = \frac{M_{k,j}}{\sum_j M_{k,j}};\quad \sum_j y_{k,j} - 1 = 0 \quad (5)$$

For each tray, *k* = 3, NT, the pressure is calculated based on the vapor flow rate and the amount of liquid on the tray above:

$$P_2 = P_{cond} + \Delta P_{cond};\ P_k = P_{k-1} + \Delta P\left(M_{k-1}, V\right) \quad (6)$$

The state of the system at the beginning of the vapor-flow period is the same as the state at the end of the liquid-flow period:

$$\mathbf{M}\left(t=0\right) = \mathbf{M}^{(L)} \quad (7)$$

The state of the system at the end of the vapor flow period is found by integrating the equations (1)-(7)

$$\mathbf{M}^{(V)} = \mathbf{M}\left(t = t_{vap}\right) \quad (8)$$

The liquid-flow period: for each component, j = 1, NC, the following equations give the stage holdup at the end of the liquid-phase period:

Condenser: $$M_{1,j}^{(L)} = M_{1,j}^{(V)} - \left(D + L\right) \cdot x_{1,j}^{(V)} \quad (9)$$

Trays, rectifying section: $$M_{2,j}^{(L)} = L \cdot x_{1,j}^{(V)};\ M_{k,j}^{(L)} = M_{k-1,j}^{(V)},\ k = 2, NF \quad (10)$$

Feed tray: $$M_{NF+1,j}^{(L)} = M_{NF,j}^{(V)} + F \cdot x_{F,j} \quad (11)$$

Trays, stripping section: $$M_{k,j}^{(L)} = M_{k-1,j}^{(V)},\ k = NF+2, NT-1 \quad (12)$$

Reboiler: $$M_{NT,j}^{(L)} = M_{NT,j}^{(V)} - B \cdot x_{NT,j}^{(V)} + M_{NT-1,j}^{(V)} \quad (13)$$

Equations (1) - (6) and (9) - (13) can be written in the following condensed form, where $\Phi^{(V)}$ and $\Phi^{(L)}$ are mappings relating the state at the start and the end of the vapor- and liquid-flow periods, respectively.

$$\left(M^{(V)}, x^{(V)}\right) = \Phi^{(V)}\left(M, x\right) \quad (14)$$

$$\left(M^{(L)}, x^{(L)}\right) = \Phi^{(L)}\left(M, x\right) \tag{15}$$

Periodicity condition requires:

$$\left(M^{(L)}, x^{(L)}\right) = \Phi^{(L)} \circ \Phi^{(V)}\left(M^{(L)}, x^{(L)}\right) \tag{16}$$

A straightforward solution of equation (16) can be obtained by considering an initial state and applying relationships (14) and (15) until the difference between two iterations becomes small. However, the convergence can be accelerated (Toftegard and Jørgensen, 1989) by applying algebraic equations numerical methods (for example Newton).

4. Results and discussion

The design procedure described in our earlier work (Lita et al., 2012) was applied to the separation of an equimolar mixture of ethanol and propanol. The feed flow rate was set to 0.833 kmol/cycle, while the distillate and bottoms purities were set to 0.995. The cyclic distillation column has 21 stages of 1 m diameter, with the feed located on stage 11. The required vapour and liquid flows are V = 3.06 kmol/min and L = 0.417 kmol/cycle, respectively. The duration of vapour- and liquid-flow periods are 25 s and 5 s, respectively. The total pressure drop is 0.24 bar. Hydrodynamic calculations showed that, under these conditions, no weeping occurs.

Figure 2 presents results of dynamic simulation, as the composition of the top and bottom products at the end of the vapour-flow period. After 20 liquid-vapour cycles, the feed amount (left) and composition (right) are changed by 10% and 0.1, respectively. Large deviations of the product purities from the desired values can be observed, the need for control being obvious.

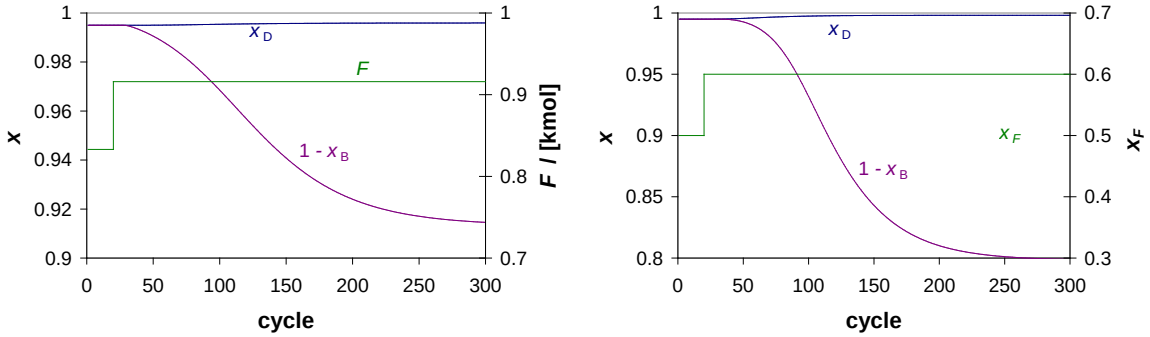

Figure 2. Distillate and bottoms purities for feed rate and composition disturbances

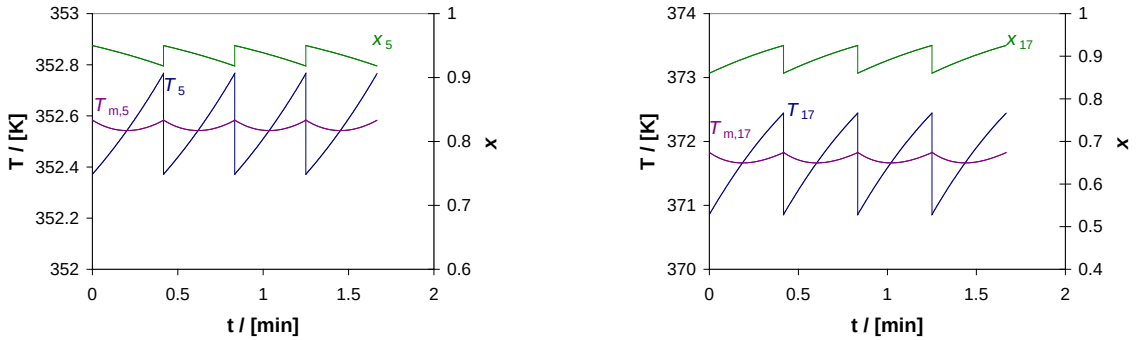

Figure 3. Dynamics of composition, temperature and temperature measurements during several vapor-liquid cycles

The control strategy measures two temperatures, at the top and bottom of the distillation column (stages 5 and 17), at the end of the vapor-flow period. The model was extended by including the dynamics of the temperature measurements as first-order elements with a time constant of 0.5 minutes. Figure 3 shows the dynamics of composition, temperature and temperature measurements during several vapor-liquid cycles, on the trays chosen for control. The lag of the temperature measurement is obvious.
Figure 4 shows the stationary temperature profiles which are established after a new stationary state is reached. The temperature profile is sensitive therefore it can be used for inferential control. Taking into account their sensitivities, temperatures on tray 5 and 17 are chosen for control purposes.

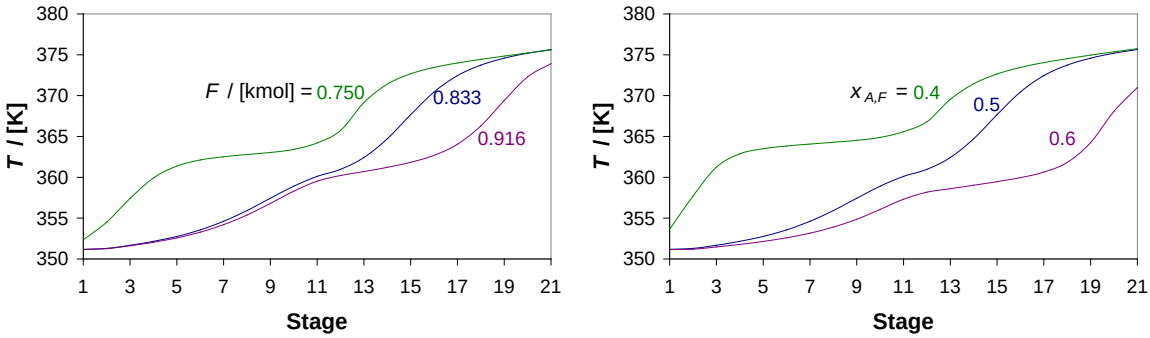

Figure 4. Stationary temperature profiles for different feed rate and composition

A discrete PI-algorithm adjusts the values of the vapor flow rate and reflux amount, for the next vapor-liquid cycle:

$$u_{k+1} = u_k + \alpha \cdot \varepsilon_{k+1} + \beta \cdot \varepsilon_k \qquad (17)$$

where u and are the manipulated and control errors, respectively, while α and β are the control tuning parameters.

The performance of the control system was tested for +/- 10% change of the feed flow rate, as well as for a change of the feed composition from x_F = 0.5 to 0.6 and 0.4. The results presented in Figure 5 and Figure 6 show that the product purities can be indeed kept to their set points. Remarkably, the disturbances in the feed flowrate and composition are rejected successfully with short settling times, low overshooting and small changes of the manipulated variables, therefore proving indeed the good controllability of cyclic distillation.

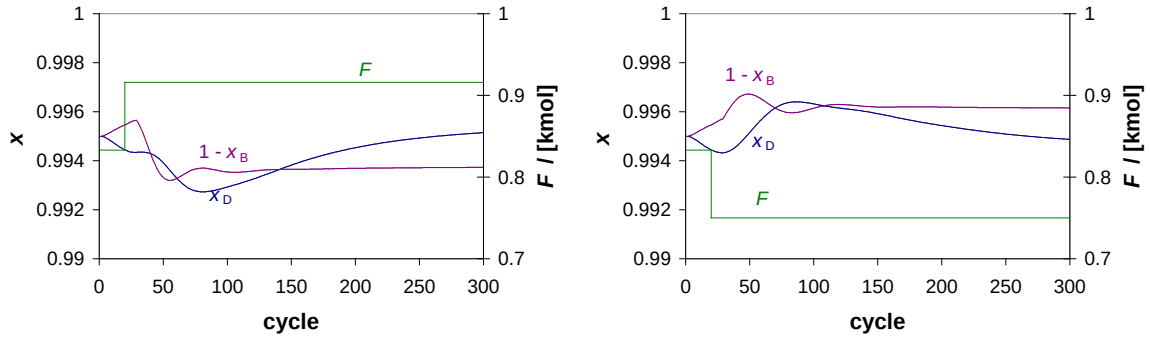

Figure 5. Performance of the control system for feed rate disturbances

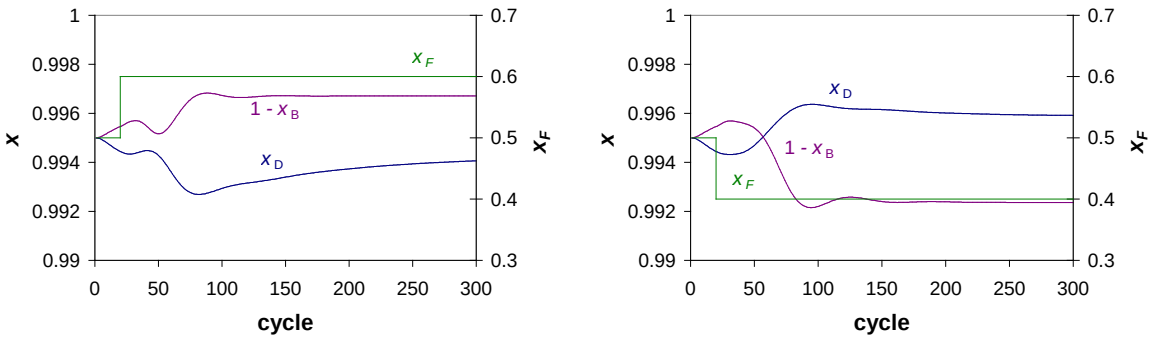

Figure 6. Performance of the control system for feed composition disturbances

4. Conclusions

Cyclic distillation can bring new life in old distillation columns, providing key benefits, such as: high column throughput, low energy requirements and high separation performance. This study presents a detailed model of cyclic distillation column, applicable to multi-component mixtures and including nonlinear vapor-liquid equilibrium, tray pressure drop relationships and temperature sensor dynamics. Dynamic simulation results prove that cyclic distillation columns can be easily controlled by adjusting the reflux and the vapor flow rate, in order to keep temperatures in the top and bottom sections close to their set points. Remarkably, disturbances in the feed flow rate and composition are successfully rejected with low settling times, low overshooting and small control action.

References

1. Bausa J., Tsatsaronis G., 2001, Reducing the energy demand of continuous distillation processes by optimal controlled forced periodic operation, Comp. & Chem. Eng., 25, 359-370.
2. Cannon M.R., 1961, Controlled cycling improves various processes, Ind. Eng. Chem., 53, 629-629.
3. Flodman H. R., Timm D.C., 2012, Batch distillation employing cyclic rectification and stripping operations. ISA Transactions, 51, 454-460.
4. Gaska R.A., Cannon M.R., 1961, Controlled cycling distillation in sieve and screen plate towers, Ind. Eng. Chem, 53, 630-631.
5. Kiss A. A., Bildea C. S., 2011, A control perspective on process intensification in dividing-wall columns, Chemical Engineering and Processing, 50, 3, 281-292.
6. Lita I., Bildea C.S., Kiss A.A., 2012, Modeling, design and control of cyclic distillation dystems, Procedia Engineering, 42, 1311 - 1322.
7. Maleta V.N., Kiss A.A., Taran V.M., Maleta B.V., 2011, Understanding process intensification in cyclic distillation systems, Chem. Eng. Process., 50, 655-664.
8. Matsubara M., Watanabe N., Kurimoto H., 1985, Binary periodic distillation scheme with enhanced energy conservation I - Principle and computer simulation, Chem. Eng. Sci., 40, 715-721.
9. Matsubara M., Watanabe N., Kurimoto H., Shimizu K., 1985, Binary periodic distillation scheme with enhanced energy conservation II - Experiment, Chem. Eng. Sci., 40, 755-758.
10. Toftegard B., Jørgensen S. B., 1989, An integration method for dynamic simulation of cycled processes, Comp. & Chem. Eng., 13, 927-930.
11. Yildirim O., Kiss A. A., Kenig E. Y., 2011, Dividing wall columns in chemical process industry: A review on current activities, Sep. Pur. Tech., 80, 403-417.

Troubleshooting a Hot Vapor Bypass Control Instability

Henry Z. Kister[1], Daryl W. Hanson[2]
[1]Fluor Corp., Aliso Viejo, CA [2] Valero Energy, San Antonio, TX

Abstract
Tower failure surveys[1,2] identified the hot vapor bypass as the most troublesome pressure and condenser control scheme in distillation. Most problems are due to poor configuration of hot vapor bypass piping[3-8]. When correctly configured, hot vapor bypasses are usually non-troublesome[6-8]. Recently, we encountered problems even though the hot vapor bypass piping was correctly configured. To investigate, we applied field testing and hydraulic analysis that identified a source of instability with hot vapor bypass schemes not previously reported. The problem identification led to successful solutions. This paper describes our experience, findings, and the lessons learnt for troubleshooting and design of hot vapor bypass schemes.

Keywords: Pressure control, Hot vapor bypass, Condenser control, Submerged condensers, Tower instability, Distillation troubleshooting

How Hot Vapor Bypass Controls Work

A hot vapor bypass is one of the flooded condenser pressure control schemes used for total condensers (no vapor product). In these schemes, the condenser area is partially flooded by condensate. The flooded tubes do not contact the vapor and perform little condensation. Raising condenser liquid level floods additional tubes, which lowers the condensation area, raising tower pressure. Conversely, reducing the liquid level in the condenser exposes more tubes, enhancing condensation, and lowering tower pressure. Although the flooded area performs little condensation, it serves the vital purpose of subcooling the condensate.

Fig.1 shows a correctly configured pressure control by hot vapor bypass. The condenser is at ground level. The drum is elevated, typically on the lowest platform, so the liquid level in the condenser is 3 to 6 m below that in the drum. The condensate is lifted to the drum by the vapor pressure difference between the condenser liquid surface, which is at the bubble point temperature, and the drum liquid surface, which is colder due to condensate subcooling.

Even a few degrees of subcooling can often raise the condensate 15 to 30 m, even more. To limit the lift to the desired height, hot tower overhead vapor is used to heat the drum liquid surface. The vapor pressure in the drum is set by the liquid surface temperature, not the subcooled temperature. Liquid is a good thermal insulator. The surface temperature is set by the heat balance between the hot vapor inflow and the heat outflow from the surface to the bulk liquid and from the vapor space to the atmosphere. Opening the bypass valve heats the liquid surface, thereby reducing the lift, while closing the valve allows the liquid surface to cool, thereby raising the lift.

The lift is manipulated to control the tower pressure. Opening the bypass heats the drum liquid surface, raising its vapor pressure, and therefore the drum pressure. This pushes drum liquid into the condenser, flooding more tubes, reducing condensation, and therefore raising the tower pressure. Conversely, closing the valve cools the drum liquid surface, reducing vapor pressure, and therefore the drum pressure, and sucking liquid from the condenser to the drum. This exposes additional condensing area and therefore lowers tower pressure.

The popularity of the hot vapor bypass scheme in large total condensers stems from its major capital savings. Locating large condensers at ground level eliminates the need for massive condenser support structures, piping cooling water to elevations, and provides easy access for maintenance, leading to handsome savings in steelwork, platforms, and maintenance. The subcooled liquid delivered to the reflux and product pumps minimizes

their NPSH and platform height requirements.

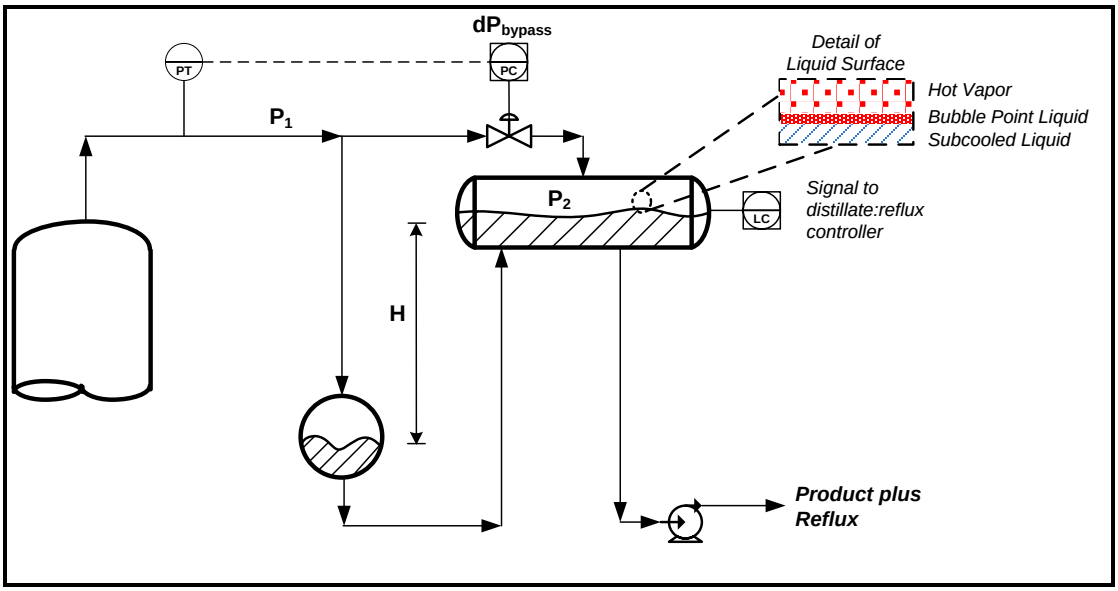

Figure 1: Typical Hot Vapor Bypass Controls

Depropanizer Hot Vapor Bypass Experience

Installation In this column, the hot vapor bypass was correctly configured (as in Fig. 1). The condenser liquid level was 3 - 4 m below that of the uninsulated drum. The control usually worked well when the (reflux plus product) flow rate was below 85 t/h. Beyond 85 t/h, the drum would often suddenly fill up. The drum level controller would increase reflux rate. The drum level would then dive, the reflux rate plummet, and the reflux pump cavitate. The only way to restore stability was to cut back reflux. The problem was more severe in summer. This restricted the column capacity.

A similar instability at times occurred at lower rates (Fig. 2). In Fig. 2 the reflux plus product rates were 60 t/h. At about 10:40 PM the hot vapor bypass differential pressure jumped from the normal 300 mbars to about 480 mbars in one minute, and to 830 mbars in five minutes. Over the same period the tower pressure declined only from 20 barg to 19.9 barg, opening the valve from 50% to 80%, while the drum liquid level jumped from 40% to 80%. Over the next 15 minutes, the pressure drop, valve opening and drum liquid level returned to their pre-event values, while the column pressure slightly rose to 20.1 barg. Throughout the event there was little change to the boilup, reflux and product flow rates and to the condenser outlet temperature.

Testing Pressure gauges were installed and measured dP across the condenser. Field measurements during an instability at high reflux and product rates showed that the condenser pressure drop rapidly fell (due to reduced head) and condensate temperature quickly rose as the liquid slugged from the condenser to the drum, suggesting that the condensate seal in the condenser could have been broken.

Hydraulic analysis We elected to perform our hydraulic analysis on the event in Fig. 2, in which the condensate seal was not broken, as evidenced from the condenser outlet temperature remaining unchanged. The pressure balance on the system gives

$$\Delta P_{\text{bypass valve}} + \Delta P_{\text{bypass line}} = \Delta P_{\text{cond}} + \Delta P_{\text{liq line}} + \Delta P_{\text{vap line}} + H \qquad (1)$$

ΔP is pressure drop, mbars. H is the head difference between the reflux drum and the condenser liquid levels, mbars. H is based on the difference between the liquid and vapor densities, due to the vapor static leg in the condenser inlet line.

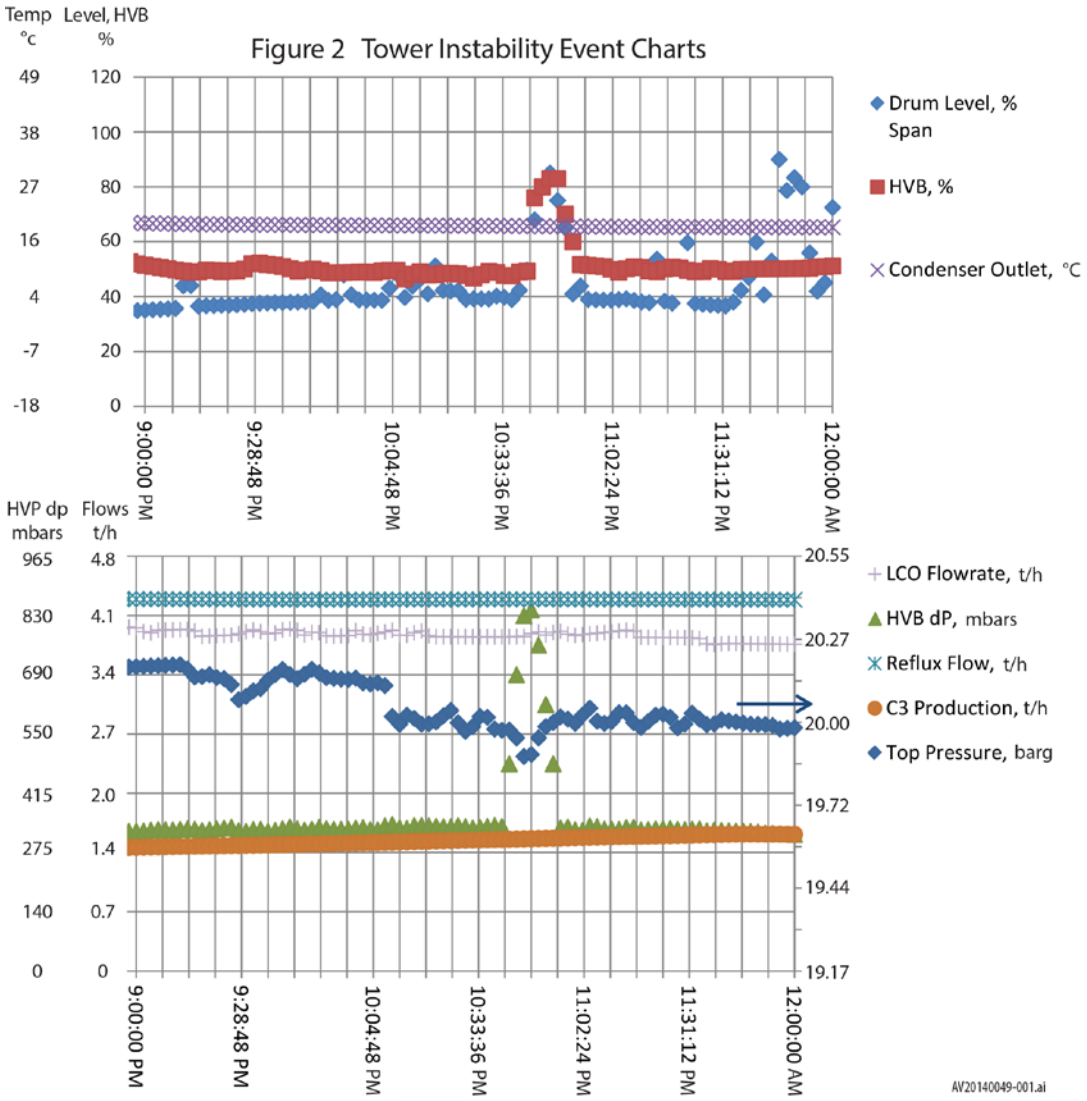

Table 1 shows the results of the pressure balance calculation at the beginning of the Fig. 2 event. There is a 76 mbars discrepancy, probably due to inaccuracy in the measurement of the pressure drop across the control valve or in the calculations.

Table 1. Depropanizer Hot Vapor Bypass Pressure Balance

Term	Left Hand Side of Eq. 1	Right Hand Side of Eq. 1
$\Delta P_{bypass\ valve}$ mbars	310	
$\Delta P_{bypass\ line}$ mbars	7	
ΔP_{cond} mbars		33
$\Delta P_{liq\ line}$ mbars		28
$\Delta P_{vap\ line}$ mbars		35
H, Liquid head, mbars		145
Total, mbars	317	241

Fig. 3 is a plot of flow vs. valve opening at various valve pressure drops based on the control valve characteristics. Fig. 3 shows that opening the valve from 50% at 310 mbars pressure drop to 80% at 830 mbars pressure drop increased the flow rate through the valve from 2,500 kg/h to 14,000 kg/h. Over the five minutes event, with approximately a linear increase in valve opening and pressure drop per Fig. 2, the additional vapor that entered the drum (above the normal rate) was about 500 kg.

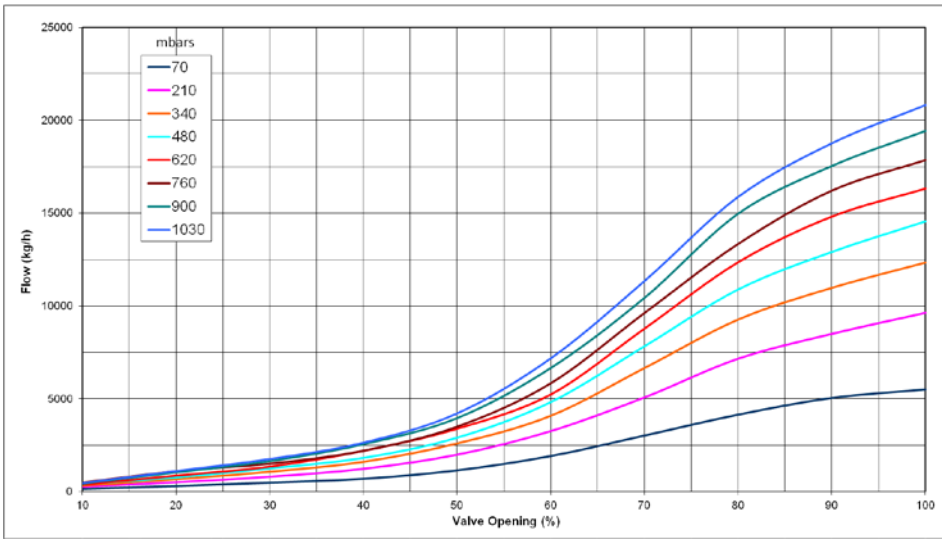

Figure 3. Valve Vapor Flow vs. Control Valve Opening

The drum is 2.75 m ID and 6.2 m long (tangent to tangent). To raise its liquid level from 40% to 80% on the level transmitter takes 9.5 tons. Adding this quantity of liquid to the drum over five minutes is a tremendous movement of liquid, tripling the quantity of liquid entering the drum from 60 t/h to 175 t/h. The key to understanding the mechanism is to determine where this huge amount of liquid can come from.

Mechanism From the control valve calculation above, the additional vapor entering the drum would be about 0.5 tons. This may be augmented by condensation of the vapor inventory in the drum, which was replaced by the liquid during the event, which would account for another 0.9 tons. Another explanation may be the onset of heavy rain. Heat transfer calculations described elsewhere[8] showed that this would account for additional liquid generation of 0.1 tons. This leaves 8 tons liquid to be explained.

One conceivable source remains: liquid from the condenser sucked into the drum. There are two condenser shells in parallel, each 1.2 m in diameter and 6.1 m long. Allowing for the tube volume, the condensers approximately hold 3.6 tons of liquid when full. We estimate that during the low rates of Fig. 2 (60 t/h reflux plus product), and at the cold ambient temperatures, only about 25% of the condenser heat transfer area performed condensation. So the condensers contained about 2.7 tons of liquid. By itself, this falls short of explaining the large liquid movement of 8 tons.

However, as liquid is sucked out of the condensers, additional tube area is exposed, increasing condensation. Emptying all the liquid from the condensers would quadruple the condensation area. The liquid generated by raising the condensation area from the 25% at the beginning of the event to 100% five minutes later is calculated at about 7.3 tons. This liquid together with the 2.7 tons drained from the condenser exceed the 8 tons increase in drum liquid. This means that some liquid remained in the condensers, retaining their liquid seal and the subcooled outlet temperature.

The intensified condensation dropped the tower pressure. The hot vapor bypass valve opened rapidly as the pressure fell. Eventually the hot vapor supply caught up with the disturbance. The drum liquid surface heated up, the drum vapor pressure rose, the differential pressure across the valve declined, the liquid returned to the condenser, column pressure went back up, and normal operation resumed.

In this event, the low rate operation and the low cooling water temperature led to a relatively large liquid inventory in the condensers and sufficient condensation capacity to cushion against totally emptying the condensers. At higher rates or warmer ambient temperatures, the liquid level in the condensers would have been lower, the flooded area smaller, and it

would have been much easier to lose the condensers liquid seals. This was the experience described earlier at high rates and especially during summer. Losing heat transfer upon loss of condensate seal is a common problem in condensing sides of reboilers[2,6].

Initiation Up to this point, we followed the movement of liquid produced by strong suction. However, we did not address the cause of this suction. To move 8 tons of liquid in 5 minutes takes a very strong suction force that needs to be identified.

Fig. 2 shows a fast rise in control valve differential pressure, i.e., of the difference between the tower and the drum pressures. Since the tower pressure changed only slightly (Fig. 2), the big change was in the drum pressure, 550 mbars over five minutes. The drum pressure is the vapor pressure of the liquid surface in the drum. A 550 mbar vapor pressure reduction corresponds to cooling of the liquid surface of the drum by only 1.4^{o}C. The problem now is to identify the source of a 1.4^{o}C cooling of the drum surface temperature.

One possibility is heavy rain. However, heavy rain would have increased the condensation rate only by 1,000 – 1,400 kg/h[8], easily offset by the additional 11,000 kg/h flow rise through the hot vapor bypass valve during the same period. Further, there were many other events (including the tests) that took place under dry ambient conditions. Another possibility is hot vapor impingement ruffling the liquid surface. However, at the beginning of the event the vapor velocity was about 2 m/s, giving a $\rho_v V^2$ of 150 kg/m s^2, too low to ruffle a liquid surface 1.5 meters below (ρ_v. is vapor density, kg/m^3, V is vapor velocity at the drum inlet nozzle, m/s). Also, this vapor flow rate was commonly used during normal operation.

At the first minute of the event, the valve pressure drop rose from 310 to 480 mbars, corresponding to a drop in drum liquid surface temperature of 0.5^{o}C. At 19.7 barg, the liquid surface was at 52^{o}C, while the bulk subcooled liquid in the drum was at 19^{o}C. As little as 1.5% of the subcooled liquid reaching the surface would explain a temperature fall of 0.5^{o}C.

The liquid enters via a 6” nozzle at the bottom of the drum, discharging upwards at 1.7 m/s at the beginning of the event, a velocity exceeding the good design practice of 1.2 m/s max. Normally, this would not have been an issue, but here, with the liquid level was only 1.1 m above, the initial momentum may have carried some of the subcooled liquid jet it to the surface, possibly piercing the hot liquid surface. Some of this may even occur during normal operation, with some surface cooling by the rising jet balanced by some of the hot vapor.

Instability may initiate upon step-up of the subcooled liquid reaching the surface. Fig. 2 shows that just prior to the pressure differential rise, the tower pressure fell by about 35 mbars and the drum level rose by about 2-3%. Both indicate a step-up in condensation rate, possibly initiating by heavy rain hitting the drum vapor space. The drum pressure fell, sucking liquid from the condenser. A level rise of 2% is equivalent to about 0.5 tons. Sucking 0.5 tons from the condensers would raise the exposed condensation area by around 50%, quickly reducing tower pressure. The bypass pressure drop remained constant at that time, meaning that both the drum and tower pressures fell by the same 35 mbars. The additional liquid flow, about 0.5 tons in two minutes, would increase the drum liquid inlet velocity from 1.7 m/s to 2.1 m/s. The intensified jet raised more subcooled liquid onto the liquid surface, generating a “fountain effect” that cooled the surface. The drum pressure fell, sucking more liquid from the condenser, the jet and the fountain intensified, the surface further cooled, more liquid was sucked from the condenser, and so on. This process is self accelerating. At the pressure differential peak, the liquid rate tripled, the liquid jet velocity exceeded 4.6 m/s, high enough for the jet to break right through the liquid surface, even at the higher level.

At the pressure differential peak, the hot vapor bypass flow reached 14,000 kg/h, the vapor inlet velocity 10 m/s, and the $\rho_v V^2$ 5,000 kg/m s^2, while the level rose (to 80%) to 0.64 m below the vapor inlet. Somewhere along the event, vapor impingement on the liquid surface would have begun raising more subcooled liquid to the surface, augmenting the instability.

Solution The low pressure drop in the system, a total of 100 mbars per Table 1, offered little hydraulic resistance to impede the self-accelerating fountain effect. Increasing the

pressure drop in the lines leaving the condenser can mitigate the self-accelerating process. As the condenser liquid is sucked into the drum, the additional friction pressure drop rapidly increases. The line pressure drop increases with the square of the flow, and severely retards the increase in liquid flow to the drum, giving the hot vapor a chance to catch up.

A manual throttling valve was installed in the line from the condenser to the drum (Fig. 4). The dP across the valve is maintained at 140 mbars. This completely eliminated the instability. The modified system can now operate stably with the reflux plus product up to even 140 t/h during both summer and winter.

Epilogue

Adding the throttling valve raised the hot vapor bypass pressure drop from about 100 mbars to 240 mbars. The throttling valve slows the rate of drainage from the condenser, making it more difficult to suck the condenser liquid into the drum.

This case brings to light an instability not previously reported in hot vapor bypass systems. The instability develops because different factors govern the valve pressure drop and the valve opening. The valve pressure drop is largely governed by the drum surface temperature. The valve opening is governed by the tower pressure controller. The two may vary independently and interact. Such interaction can be initiated by sudden cooling to the liquid surface in the drum. The vapor pressure at the drum liquid surface quickly drops, while the tower pressure, and therefore, the valve opening, remain temporarily constant. A good solution is to increase the pressure drop in the outlet of the condenser (Fig. 4). We have successfully eliminated instabilities in other similar systems using this throttling valve.

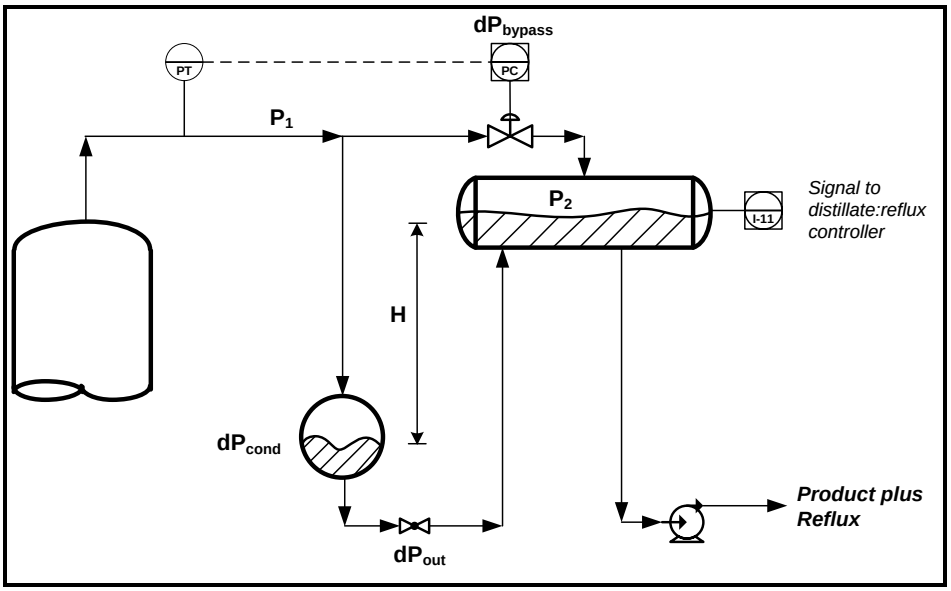

Figure 4: A Throttling Valve at the Condenser Outlet Eliminates Instability

References

1. Kister, H. Z., "What Caused Tower Malfunctions in the Last 50 Years?", Trans. IChemE, Vol 81, Part A, p. 5, January 2003.
2. Kister, H. Z. “Distillation Troubleshooting”, Wiley – Interscience, NJ, 2006.
3. Whistler, A. M., "Locate Condensers at Ground Level," Pet. Ref. 33(3), 1954, p. 173.
4. Hollander, L. "Pressure Control of Light-Ends Fractionators," ISA J. 4(5), 1957, p. 185.
5. Chin, T. G., "Guide to Distillation Pressure Control Methods," Hydroc.Proc. 58(10), 1979, p. 145.
6. Kister, H. Z., "Distillation Operation", McGraw-Hill, NY, 1990.
7. Smith, C. L., “Distillation Control – An Engineering Perspective”, Wiley, NJ, 2012.
8. Kister, H.Z., and D.W. Hanson, ”Can Well-Configured Hot Vapor Bypass Control Be Unstable?”, Distillation Topical Conference, AIChE Spring Meeting, New Orleans, March 30th – April 3rd, 2014.

Distillation Column Availability. The True Meaning of Capacity and how to Realize it

Jose L. Bravo, Chief Scientist Thermodynamics and Separations, Royal Dutch Shell

Abstract

The reliability/availability of distillation operations in Refineries and Chemical Plants is a very impactful parameter in the economics of such businesses. They also often also have HSSE and integrity implications. Availability can be viewed from the asset integrity and hardware point of view using statistical reliability models (mean time to failure) but a more proactive approach to monitoring can provide real time availability predictions. This proactive monitoring needs to be based on accurate models that convert process conditions to historical effects on the hardware. This paper will discuss a conceptual approach to monitor the health of a distillation system by tracking the process history and how it impacts the true capacity of a distillation system. Some examples will be used to illustrate the point

Keywords: Distillation, Column Availability, Flooding Predictor, Modeling

1.- The Issue

Chemical Engineers in general tend to be trained with a high performance bias. Meaning that ChEs learn how to design and operate equipment in process plants maximizing throughput, achieving strict specifications, and in the most energy-efficient way possible. When it comes to Distillation equipment the variables that ChEs normally concern themselves with are flowrates, purities, reflux rates, energy consumption, pressure drop, pressure, temperatures, approach to flood, etc.

This is congruent with the required performance of the equipment which is tasked to provide a production rate at a given specification. But, obviously, produced mass only comes out of distillation equipment when the distillation columns are running. If these are not available, production and economics suffer and it really doesn't matter how well designed, or efficient the columns are.

Engineers with ample plant experience learn to take distillation columns availability very seriously. In the case of refinery operations, the availability of the crude towers is clearly of supreme importance. Clearly, production engineers need to be aware of the potential and unanticipated failure of a column from three points of view

a. Safety and Integrity.- Unplanned failures of distillation equipment and peripherals can cause unsafe situations such as leaks, loss of containment, emergency releases, flaring, etc
b. Loss of planned production. - Losses in production can be much more painful in times of high margins for example. Also, re-processing of sticks is expensive
c. Effect on upstream and downstream equipment.- Particularly in complex and highly integrated process plants

A key concept here is the idea of “unanticipated failure” with possible consequences several orders of magnitude more severe. These losses of availability are mortal enemies of profitability and safety.

In a very general sense there are two kinds of unanticipated failures that cause a loss of availability

a. Mechanical or integrity failure
b. Process related failure

Clearly one can also imagine a mechanical failure that is caused by damaging process conditions outside the expected operating window of the equipment. Figure 1 below shows how dramatic the impact of process related losses of production are in the overall context of equipment reliability

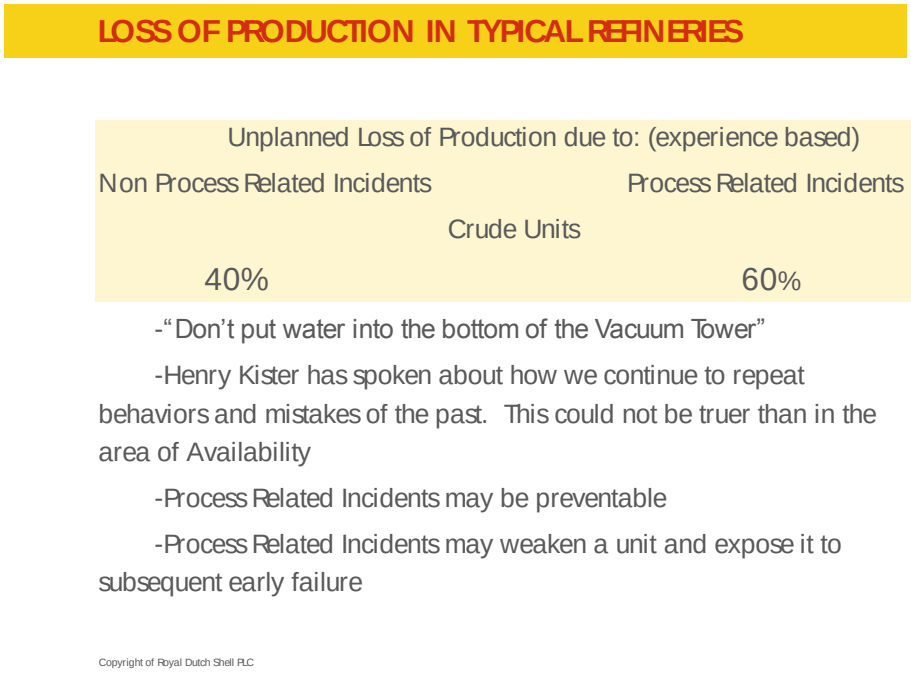

Figure 1. - Over an average year, up to 60 % of the production lost to unanticipated process upsets can be directly related to process incidents.

So, what good does it do us to strive for operation at say 95% of maximum hydraulic capacity when we lose 10% of our yearly production to unplanned process incidents? Reducing unplanned process incidents can have a more beneficial economic benefit that retrofitting columns with high capacity technology.

2.- The Data Matters

There is a very large amount of data available from process systems already that can be used to monitor, and maybe even prevent, unplanned outages in a proactive manner. The following quote captures this very eloquently;

"The aggressive adoption of wired and novel wireless technology to capture more measurements has significantly increased the volume of data available. This wealth of data puts us in an even better position to leverage predictive analytics technology. The technology …… makes use of a wealth of existing but unused data, representing a breakthrough in the area of equipment health."
Zaid Rawi, BP Machinery Predictive Analytics SPE Intelligent Energy Conference and Exhibition March 23-25, 2010, Utrecht, NL copyright 2010 Society of Petroleum Engine

Clearly, the effectiveness of proactive monitoring depends heavily on data. It also depends on reliable models and analytical tools.

3.- Some Examples

a. The case of the Incipient Flood.

The following is based on the use of the "Flooding Predictor" concepts as described by G. Dzyacky in US Patent: 5,784,536

In this story, a column that is expected to run at about 98% of hydraulic capacity experiences what appear to be random unexpected flooding episodes. Once the column floods, the control system backs the loads down in the column to return it to separation efficiency. This column production is reduced by the lowering of product flows and the necessary rework of off-spec material. The column normally had to be backed down to 50% of maximum hydraulic capacity to be able to re-establish operation within the next 4 hours.

These episodes of flooding happened in what appeared to be a random pattern and appeared to be related to changes in the feed composition. The column would flood even at constant feed, heat, and reflux rates.

In an average year this event would happen about once every month. This meant that in principle production losses were about 10 to 12 hours per incident or per month. The availability loss caused by these incidents alone was then in the order of 2% in any given year. Keep in mind that the column was asked to operate nominally at 98% of hydraulic capacity and the unplanned flooding episodes reduced it true production by an added 2%

Analysis of the situation taught us that the flooding at constant rates was caused when the change in composition caused the appearance of a second phase in the middle of the column. The reduction in boiling point that came with this combined with the heat available in the column and its inventory caused a surge in vapor flow that flooded the column. The composition change in the feed was a consequence of a deteriorating catalyst upstream.

Clearly, this had to be dealt with. Feed analysis and a feed-forward control system were deemed unusable because the time for analysis on-line was considered too long. But exhaustive data mining showed that several variables showed a pattern of behaviour simultaneously several minutes before the column flooded. These were

mainly oscillations in bottoms level and overhead flows. Also, the first order derivatives of the vapor flows and other variables with time showed simultaneous changes. These data were examined exhaustively and a correlation was noted. About 20 minutes before flooding, we could see the pattern already developing. If we backed off on feed and heat by 1% for 20 minutes and then ramp it up to spec, the flooding episode would be averted completely and the column could adapt.

The control system was then configured to detect this incipient flooding, correct, and then ramp up. As a consequence the column was able to operate for a full year without a single unplanned loss due to this issue.

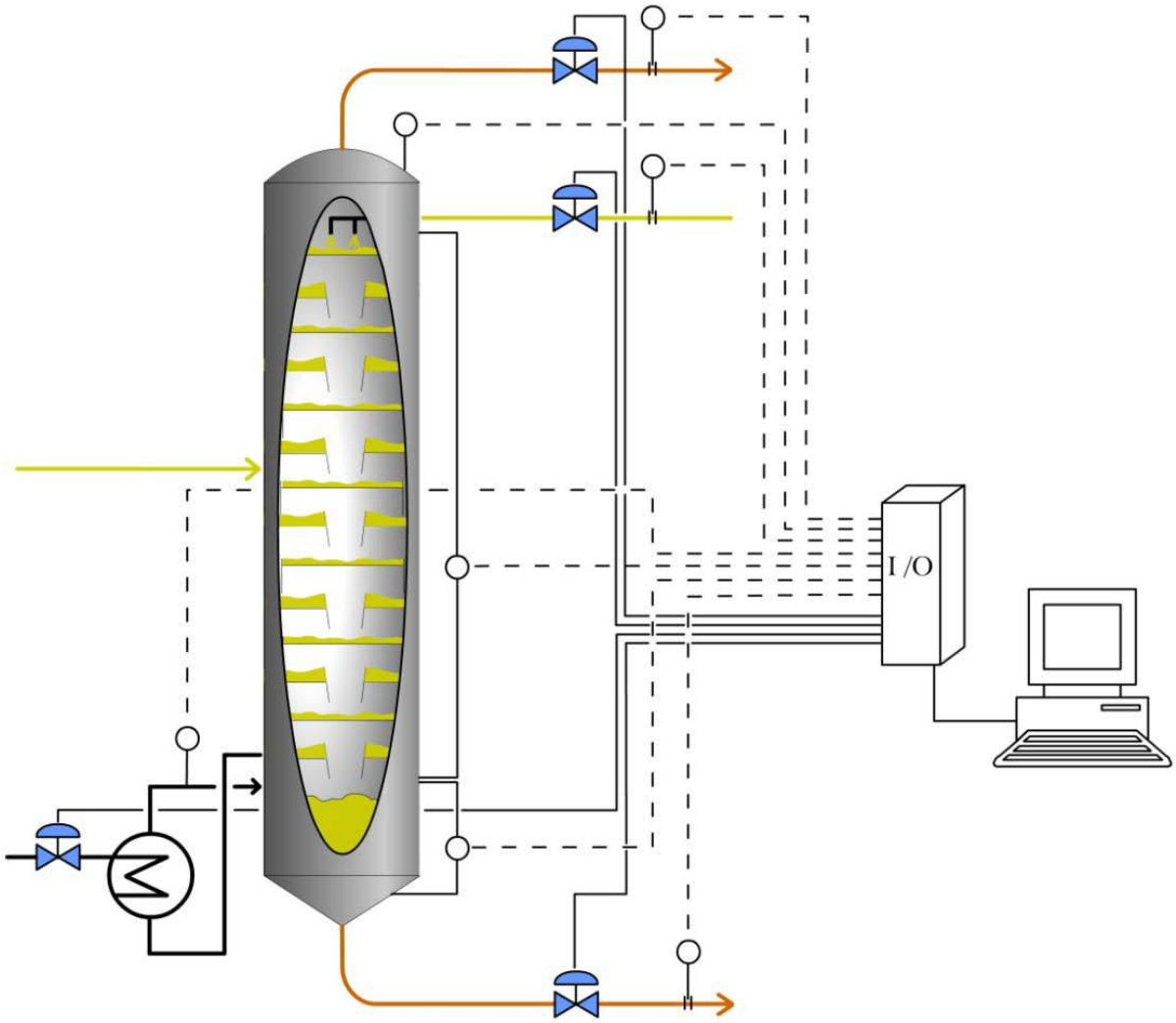

Figure 2. - A column instrumented to use a flooding predictor routine with feed, product, reflux, and heat rates, as well as pressure drops and levels as inputs

One item of note. This was a trayed column and we believe that the higher liquid holdup gave the time to do the adjustments to avoid flood. A packed tower, with is small liquid holdup, would respond much faster both to the stimulus and to the correction. The use of flooding predictors has to be calibrated to each specific column due to such uncertainties.

b. Dew Point Corrosion

One of the most feared phenomenons in the operation of Crude Distillation Systems is that of corrosion caused by condensed water with a very low pH that may appear in the cooler portions of the crude distiller or other main fractionation systems. Water vapor that condenses out of these mainly hydrocarbon vapor streams can be very corrosive since the first drops that occur at the dew point will be very highly concentrated in acids of sulphur and nitrogen. This condensation and corrosion is clearly undesirable since it reduces the life of connecting pipes, vessel heads, and heat exchangers. This is the type of unplanned process upset or change that reduces the long term availability of distillation equipment as well as puts integrity at risk

Very effective thermodynamic models (with electrolyte effects) are available in the market these days. The use of these models allows for accurate predictions of dew point and when combined with actual temperature measurements in strategic parts of the system, and reliable process simulations, they can be used to indicate the presence of unwanted condensation. The models can also assist in determining the Corrosivity of the water condensed.

When this is paired with a good corrosion and erosion model, the effects on the hardware can be quantified and combined with historical information to determine how close is a piece of metal ti its limit of thickness or brittleness.

So by the judicious use of process data, models, and thermodynamics, combined with history, one can always have an instant health report on the overhead system of a distillation column susceptible to dew point corrosion. This cumulative information can be used profitably to do several things like:

1. Determine if the hardware will last until planned turnaround
2. Decide if a more corrosive feedstock can be taken in at an advantaged price
3. Pre-order materials for a fast repair
4. Decide what the inspection protocol needs to be for the unit
5. Establish an effective protocol to maintain integrity

So the actual capacity of the system can be managed by its availability by reducing turnaround time, running advantaged feedstocks, preventing unwanted shutdowns for integrity issues that are caused by process conditions.

So once again, it is not about having the most efficient distillation technology; it is also about how to operate the system to its maximum without damaging it

4.- In Conclusion

The true capacity of a distillation system depends not only on its hydraulic and separation performance but also on how much of the time a distillation column is available for production. Unplanned shutdowns, slowdowns, and other disturbances end up reducing the total tonnage of material produced and in many cases contribute the lion’s share of lost production. Managing these events, preventing them, avoiding them, recovering from them, and quantifying their long term effects is with our reach with the current suite of Information Technology available to Refineries

and Chemical Plants. Better instruments, Better Data, Better Models, Better connectivity, Better intelligence, can for a low cost, increase availability (and thus ultimate capacity) of distillation systems.

Application of a control strategy with cooling distributed action in a distillation unit

Geysa N. Mello[1], Ricardo A. F. Machado[2], Cintia Marangoni[1]
[1]*University of Joinville Region, Masters in Process Engineering, Joinville/SC Brazil;*
[2]*Federal University of Santa Catarina, Chemical Engineering Department, Florianópolis/SC – Brazil*;

Abstract
Among other purposes, control systems are used to minimize periods of operation outside the desired condition that occur due to a disturbance in the process. In distillation units, this transition cannot be completely eliminated even with the implementation of well-adjusted advanced controllers because the operation in stages results in the propagation of the corrective action throughout the entire unit, increasing the global tower response. Based on this characteristic, a prior study evaluated a proposal for a control system with distributed heating action between the reboiler and one stage of the stripping section and these experimental results demonstrated reductions in the transition time using proportional-integral-derivative (PID) controllers when the control system used was composed of temperature loops for the reboiler, one stage of the stripping section and the top stage compared with the conventional dual control. Therefore, the objective of this work was to evaluate the proposed strategy considering the cooling distributed action between the condenser and one stage of the rectifying section. Tests were performed using the commercial simulator Aspen Hysys®, in dynamic mode, disturbing the feed temperature. The results demonstrated that the insertion of a rectifying stage temperature loop enables a reduction in transition time of 20% (6 min to 4.8 min) for the reboiler temperature loop and of 72.7% (26.4 min to 7.2 min) for the top temperature loop when compared with the conventional system. The internal profiles were evaluated, and the results revealed that similar final steady states were obtained when distributed and conventional systems were used, indicating that the proposal did not alter the process operation and contributes to minimizing transients with simple controllers such as PID.

Keywords
Distillation, internal heat sources, transition time, Hysys

1. Introduction

Systems that control variables in distillation columns are developed with varied objectives, including increasing production; minimizing operational transients, energy consumption and products out of specifications; and reducing process costs, eliminating risks inherent to the process and improving final product quality [1]. When the system is perturbed either by alterations in the operational points or by a desired change in conditions (set point alteration), that is, through external perturbations, the rapid achievement of steady state minimizes the time necessary to meet the desired product specifications. However, numerous difficulties in the control of these units are

responsible for the generation of long transients intrinsic to the process. Distillation columns have inherent process characteristics that represent a challenge for the reduction of transients and the application of control systems. Among these are non-linear behavior, which is associated with the coupling of variables; operational restrictions; elevated time constants; and a delay in the response [2]. This behavior results from the configuration of the column in stages, requiring successive heating and cooling actions for heat and mass transfer to occur in the stages; therefore, there is a propagation of a control action throughout the unit to establish the product quality standards. The result is a transient that is difficult to eliminate, even with well-adjusted control systems.

The most used system to reduce operation time away from the set point involves the implementation of control techniques, more specifically, advanced techniques that consider the unit dynamics in their structure. However, these systems tend to be difficult to implement, and simple industrial controllers, such as PID controllers (proportional-integral-derivative) are still widely used [3]. However, proposals for intensified units have been made with the aim of miniaturization and better energy use. Diabatic distillations are in this scope, where heat provided to the reboiler is distributed in the rectifying section stages and where the heat removed by the condensate is distributed between the trays in the rectifying section [4].

Connecting this concept of heat distribution in the trays of diabatic distillations with the objective of minimizing operational transients, a control scheme with distributed corrective action to minimize the effect of perturbations in temperature and feed composition was previously proposed and evaluated [5,6]. In this approach, the objective of controlling product quality in the streams at the base and top of the unit was performed by associating the conventional dual control with the temperature control of an internal stage of the unit. Studies that analyzed process dynamics when stages from the stripping section were used indicated that the approach was a valid option for reducing transients. However, in all of the tests performed, only heating points were considered. Due to the experimental nature of the constructed unit, the evaluation of heat removal making use of the trays in the unit could not be performed. Thus, the objective of this study is to evaluate the distributed corrective action proposal using cooling actions by applying PID type controllers to the reboiler temperature in the last tray and in one stage of the rectifying section to minimize perturbations in the feed temperature. It is important to emphasize that this study is focused on process dynamics and not on the design or tuning of the control system. The results presented in this work are only simulated once the experimental unit does not allow the evaluation of cooling actions using a tray in rectifying section as proposed. Thus, the simulations representing the unit dynamics were validated by reproducing the experimental results of previous studies [6], where the distributed action was evaluated using a tray in stripping section (heating action). From these simulation cases, the proposed work presented here was evaluated, considering only disturbances in feed temperature (and not feed flow or composition disturbances).

2. Methodology

This simulation study presented here was based on the continuous experimental unit used by the research group in previous studies [7] and; this unit contains 13 perforated trays, with the reboiler being stage zero and the accumulation tank being stage 14. The feed is added at tray 4. Simulations were performed using the Hysys® version 7.3 software from AspenTech, with the UNIQUAC thermodynamic package. The conditions used are listed in Table 1.

Two different control strategies were evaluated: a conventional strategy and a distributed strategy, in which PID type controllers were implemented in the following loops for the conventional system: (1) base temperature control, manipulating the thermal load provided to the reboiler, and (2) temperature control of the last stage, manipulated by the reflux flow rate. The distributed approach consisted of using these loops with the addition of another intermediate loop that was activated separately. Temperature control of tray 11 was manipulated by removing heat from this stage. The definition for the use of this stage was obtained from sensitivity analysis studies [8]. The parameters used for the controllers are listed in Table 2 and were determined from fine-tuning based on experimental values.

Table 1: Operational conditions and parameters of the distillation column.

Variable	Value
Feed temperature	Sub cooled (≈ 80°C)
Volumetric feed flow rate	300 L/h
Volumetric fraction of ethanol in the feed	0.2
Pressure at the top of the column	1.2 bar
Pressure drop along the column	0.15 bar
Reflux ratio	6

Table 2: Parameters used for the PID controllers.

Parameter	Reboiler	Tray 13	Tray 11
K_c	3.90*	0.70**	7.22*
τ_i (s)	7.45×10^{-2}	9.67×10^{-2}	2.57×10^{-2}
τ_d (s)	9.17×10^{-3}	1.00×10^{-2}	5.33×10^{-3}

* (°C/%heat transferred), ** (°C/%valve opening)

It is important to emphasize that from the experimental viewpoint, the addition and removal of heat must be promoted with the aid of devices coupled to the trays of the unit to permit this action. In the simulations, the software only permitted one simple energy current to be inserted into the stage and to be defined in terms of heat exchange. The range of 0 to 3.5 kW was defined (applied experimentally), where 100% corresponds to zero heat removal (minimum value) and 0% indicates that the total cooling value was applied (in this case, -3.5 kW).
The conventional strategy was validated based on the experimental results of the transition time when the unit was perturbed with a step of +14°C in the feed temperature. This same perturbation was applied in the experiments presented in this study.

3. Results and Discussion

Figure 1(A) presents the temperature profile of the reboiler for the first 0.2 h (12 minutes) following the feed temperature perturbation. An increase in the reboiler temperature occurs at the moment of the perturbation (according to the modification made); however, when the distributed strategy is applied, this oscillation is lower compared with the conventional strategy. A graphic depiction of the derivative of the reboiler temperature with respect to time is presented in Figure 1(B), where a reduction in the transition time is observed, demonstrating that the distributed strategy is more efficient compared with the conventional strategy. To minimize the

feed perturbation, 0.10 h (6 minutes) was needed for the conventional strategy, and 0.08 h (4.8 minutes) was needed for the distributed strategy, which is a 20% reduction.

The temperature profile in tray 13 is presented in Figure 2(A), where it is also verified for this variable that the distributed strategy achieves stability more rapidly than the conventional strategy. The derivative of the temperature of tray 13 with respect to time is presented in Figure 2(B). This graphic demonstrates that the efficiency of the distributed strategy can be reiterated because the transition time for the conventional strategy and distributed strategy was 0.44 h (26.4 minutes) and 0.12 h (7.2 minutes), respectively, resulting in a reduction of 72.72%.

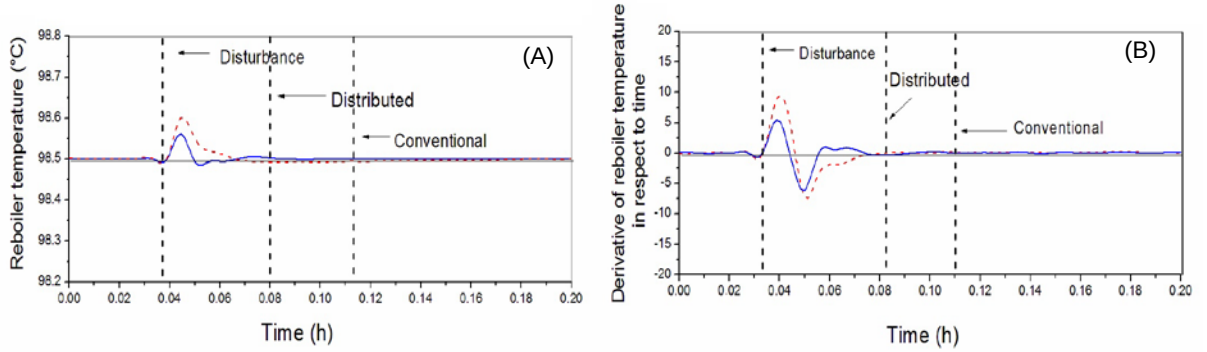

Figure 1: Reboiler temperature profile (A) and derivative of this variable with respect to time (B), comparing the conventional strategy (- - -) and the distributed strategy applied to tray 11 (—) relative to the set point value.

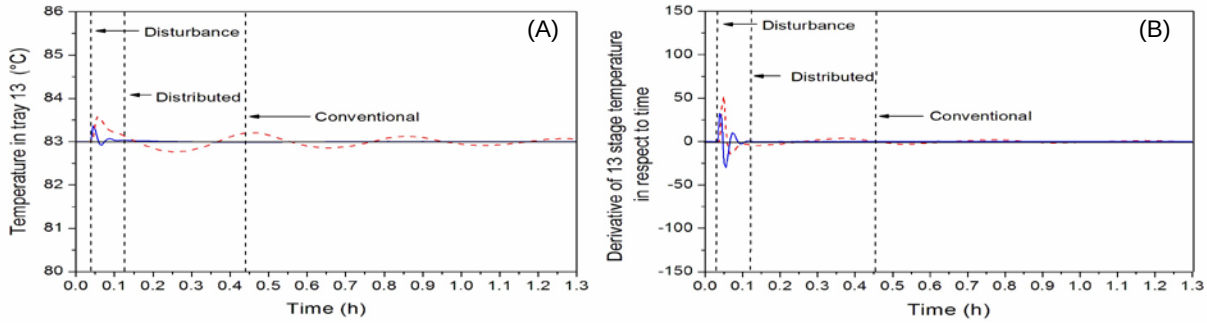

Figure 2: Temperature profile in tray 13 (A) and derivative of this variable with respect to time (B), comparing the conventional strategy (- - -) and the distributed strategy applied to tray 11 (—) in relation to the set point value (—).

These results can be corroborated through analysis of the control actions (manipulated variables), that is, through the profile of heat transfer to the reboiler and the reflux flow rate (Figure 3).

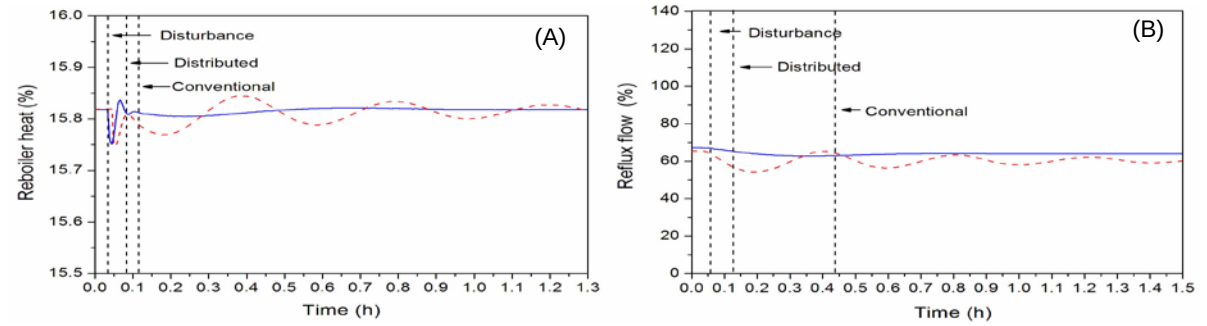

Figure 3: Heat profile of the reboiler (A) and reflux flow rate (B), comparing the conventional strategy (- - -) and distributed strategy applied to tray 11 (—)

The oscillations are observed to be reduced in the obtained profiles when the strategy implementing the distribution of heat exchange is applied. Because heat is being removed from the column at tray 11 in conjunction with the action performed in the reflux flow rate, more rapid temperature stabilization occurs during the stages. This behavior is more evident in the reflux flow rate profile, demonstrating that less is required from this variable when tray 11 is activated. For the heat transferred to the reboiler, the conventional approach is slower to initiate the correction process due to the need for propagation of the action from the reflux to the reboiler. This action is anticipated by the tray 11 controller, making the distributed control process faster.
The temperature of tray 11 was also analyzed, where local temperature control was applied. It is verified in Figure 4(A) that the conventional control strategy achieved the reference value even without the controller on this stage but with a constant oscillation around the set point. This behavior, as expected, is different when the distributed strategy is used, as the distributed strategy is more efficient compared with the conventional strategy, with a lower transition time. This result is demonstrated through the derivative of the temperature of tray 11 with respect to time (Figure 4B), where it is observed that the transition time for the conventional strategy and the distributed strategy is 0.47 h (28.2 minutes) and 0.14 h (8.4 minutes), respectively.

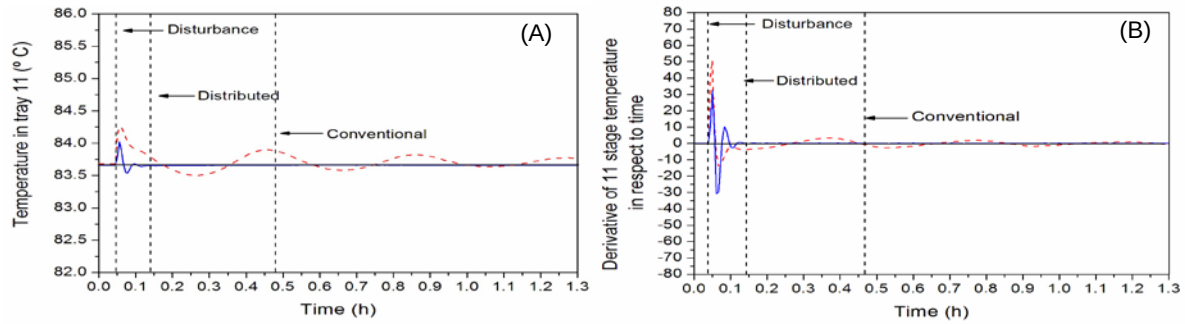

Figure 4: Temperature profile in tray 11 (A) and derivative of this variable with respect to time (B), comparing the conventional strategy (- - -) and distributed strategy applied to tray 11 (—) relative to the set point value (—).

Because the quantity of product produced out of specifications also depends on the time the process takes to return to the desired steady state after a perturbation occurs, an estimate of this quantity was obtained and is listed in Table 3.

Table 3: Quantity of product out of specifications (in volume) during the transition time for the conventional and distributed strategies using tray 11.

Flow rate(m^3/h)	Conventional Strategy	Distributed Strategy
Distillate	5.45×10^{-5}	1.95×10^{-6}

The data listed in Table 1 demonstrate that the volume of product out of specification in the distillate stream when the distributed control strategy is used corresponds to only 3.5% of the total volume produced using the conventional approach. That is, the reduction in the oscillations and transition time promoted by the proposed approach represent an elevated gain in product quality when considering the productive scenario.
Finally, the temperature, pressure and composition profiles in the stages along the unit (Figure 5) were evaluated, comparing their values before and after the perturbation with the application of the two evaluated strategies.

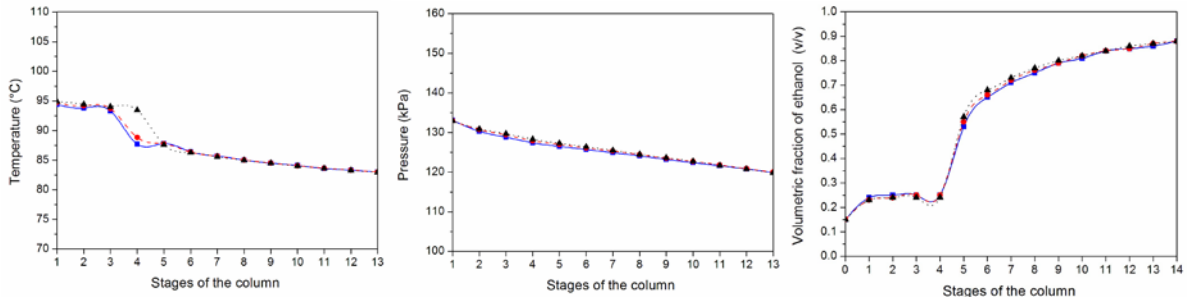

Figure 4: Profiles of temperature (A), pressure (B) and volumetric fraction of ethanol (C) during the stages of the column at steady state (-▲-) for the conventional strategy (-●-) and for the distributed strategy applied to tray 11 (-■-).

The insertion of an intermediate control loop, which composed the distributed strategy, did not affect the final steady state after the perturbation, demonstrating that this proposal did not alter the product quality, independent of the applied strategy. That is, the distributed action makes the control faster, without promoting alterations in the profiles of variables in the column stages.

3. Conclusions

In general, distributed control exhibited better performance compared with conventional control for the analysis of the distributed action in the rectifying section. The behavior of the variables became less oscillatory, and the controllers maintained the controlled variables closer to the desired values after the perturbation for all of the control loops that were affected by the perturbation.

The results presented consolidate the control approach with distributed action that has been proposed because the heating actions (proven experimentally by our group in previous studies) or cooling actions (evaluated in this study) can be used with classical, PID-type controllers to reduce the transient observed when a distillation unit is perturbed.

References

[1] Enagandula, S. and Riggs, J.B., 2006, Distillation control configuration selection based on product variability prediction, Control Eng Practice, 14: 743-755

[2] Skogestad, S., 2007, The dos and don'ts of distillation column control, Trans IChemE, Part A, Chem Eng Res Des, 85(A1): 13-23

[3] Astrom, K. J.; Hägglund, T. The future of PID control. Control Eng Practice, v. 9, p. 1163-1175, 2001

[4] Koeijer, G.; Røsjorde, A.; Kjelstrup, S. Distribution of heat exchange in optimum diabatic distillation columns. Energy. v. 29, p. 2425-2440, 2005

[5] Marangoni, C. and Machado, R. A. F. Distillation tower with distributed control strategy: Feed temperature loads. Chem. Eng. Technol, v. 30, p. 1292-1297, 2007

[6] Marangoni, C.; Machado, R. A. F.; Bolzan, A. Distributed Heat Supply for Distillation Control to Reduce Feed Composition Disturbance Effects. Chem. Eng. Technol., v. 36, p. 2071–2079, 2013

[7] Marangoni, C.; Pasetti, G.; Rico, J. E. N.; Machado, R. A. F.; Bolzan, A. Construção e Instrumentação com Tecnologia Fieldbus de uma Coluna Piloto de Destilação [Construction and Instrumentation with Fieldbus Technology of a Pilot Distillation Column]. Revista Petroquímica, v. XXVIII, n.267, p. 55-59, 2004

[8] Mello, G. N.; Machado, R. A. F.; Marangoni, C. Análise de Sensibilidade de uma Unidade de Destilação Fracionada para Implementação de Controle com Ação Distribuída [Sensitivity analysis of a Fractionated Distillation Unit for Implementation of Control with Distributed Action]. 11º Congreso Interamericano de Computacion Aplicada a la Industria de Proceso. Lima, Peru. 2013

Synthesis of a Membrane-Absorption-Hybrid System for the Removal of CO_2 from OCM Product Gas

Erik Esche[1], David Müller[1], Christian Bock[1], Günter Wozny[1]
[1]Technische Universität Berlin, FG Dynamik und Betrieb technischer Anlagen, Sekr. KWT-9, Straße des 17. Juni 135, D-10623 Berlin, Germany

Abstract
As part of the Cluster of Excellence "Unifying Concepts in Catalysis" a mini-plant for the Oxidative Coupling of Methane has been built at Technische Universität Berlin (TU Berlin). For the subsequent product gas separation an absorption desorption process and two gas separation membranes for the removal of carbon dioxide (CO_2) are installed. Initial optimization studies showed a decrease of the energy required per captured kilogram of CO_2 down to 2.64 MJ, while keeping the ethylene loss below 5%. In this contribution, the complexity of the membrane section is increased. By placing several membrane cascades in a row it is shown that the product loss of ethylene can be kept constant while the specific energy required for the removal of CO_2 is even further decreased.

Keywords
CO_2 Absorption, Gas Separation Membrane, MINLP, Optimization

1. Introduction and Motivation

Designing the carbon dioxide (CO_2) removal section of any chemical process is a challenging task. The standard process involving the Monoethanolamine (MEA) based absorption has been extensively modeled e.g. by Aboudheira et al. (2003). The main issue with most of the published models is their strong non-linearity which poses a problem when trying to perform preliminary optimization during the design stage. The design task is even further complicated in case hybrid structures are to be considered, which contain a number of different equipments for the same task.
In this contribution the energy efficient CO_2 removal from OCM (oxidative coupling of methane) product gas is discussed. OCM is an alternative process to directly convert bio or natural gas based methane into ethene. CO_2 is the main byproduct of the heterogeneous catalysis and an energy efficient design for its removal is essential to allow for the economic viability of the overall process concept.
Preliminary studies showed an energy demand for the CO_2 removal from the product gas of more than $5MJ/kg_{CO2}$ when using a standard absorption desorption process with 30wt% MEA solution at 32bar absorption pressure. However, at the same time considerable product loss of ethene (C_2H_4) of up to 10% was observed. To rectify this issue, polyimide (PI, Matrimid®) and polyethylene oxide (PEO) membranes were tested, which have a considerably lower energy demand but comparable selectivity issues. In Esche et al. (2013), a simple hybrid process consisting of a PI, a PEO membrane, and an absorption desorption process was investigated. The hybrid process concept is shown in Figure 1.

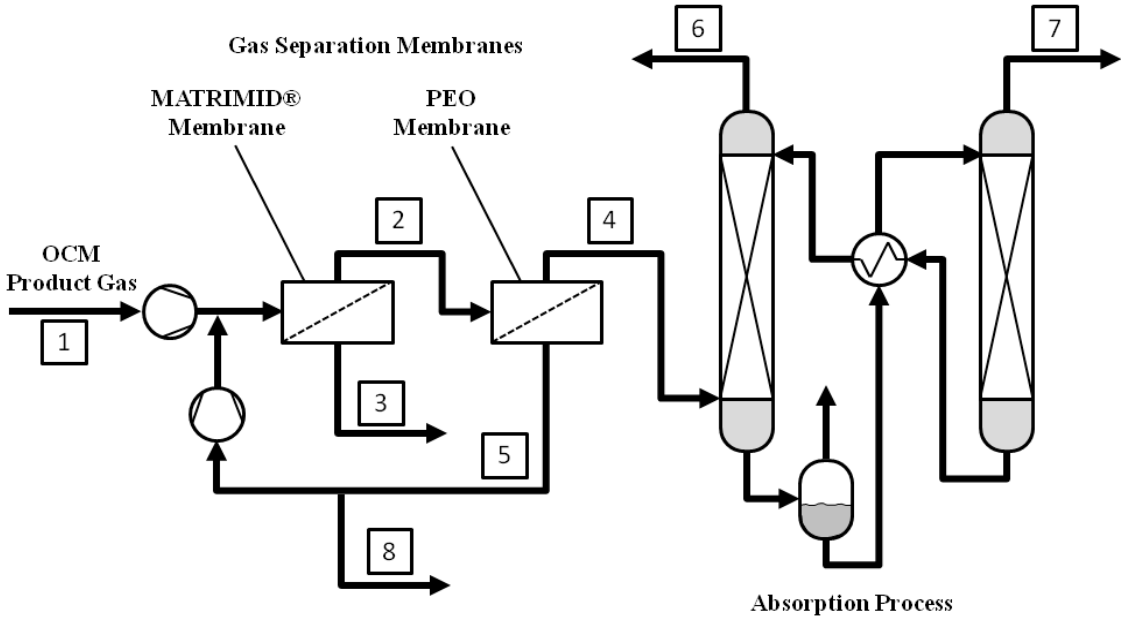

Figure 1: Flowsheet for the initial hybrid system for the removal of CO2 from OCM product gas (Esche et al., 2013).

The hybrid concept combines the advantage of the high CO_2 selectivity of the absorption at lower pressures (<15bar) with the advantageous energy demand of the less selective membranes. The hybrid system shows a total energy demand of 2.64MJ/kg_{CO2} with a C_2H_4 loss below 5%.

The following sections will, first of all, discuss the modeling and the assumptions made therein. Afterwards, the superstructure derivation and its stepwise optimization are described.

2. Modeling

Just as is the case with the initial hybrid system shown in Figure 1, the superstructures discussed herein consist of two fundamentally different equipments. Firstly, the membrane modules, independent of the actual membrane material, follow the diffusion solution model. Secondly, the amine-based, chemical absorption process is usually governed by chemical equilibria on each tray. Both models have already been published elsewhere (Esche et al., 2013 and 2014). Hence, only specifics regarding additional deliberations or extensions will be presented here. At TU Berlin a mini-plant exists, which contains both a full-scale absorption desorption section and PI and PEO membrane modules. Thus, the derived models are partially founded on or validated against experimental data.

2.1 The Membrane Model

The actual membrane modules at TU Berlin are of the envelope type. However, despite the complex flow profiles, previous studies (Song et al, 2013) showed that it is still viable to model the membrane modules one-dimensionally, i.e. concurrent flow between high and low pressure side is assumed, whilst the flow through the membrane is modeled based on the standard permeance equations published by Ohlrogge et al. (2005). The permeability data is provided by co-works at Helmholtz-Zentrum Geesthacht Centre for Materials and Coastal Research, Germany. The real gas behavior is included by calculating fugacity coefficients for the high pressure side

based on Peng-Robinson equation of state. In additional studies effects such as concentration polarization, pressure drop, and temperature effects were investigated.

2.1.1 Concentration Polarization

For a 0.5m² PI membrane the concentrations at the core of the high pressure flow and at the membrane itself were calculated according to standard film theory. Figure 2 shows the resulting molar fractions of CO_2 at the core of the flow and at the membrane surface. There is a maximum offset of 0.98% well reasoning the neglect of the flux profiles across the membranes.

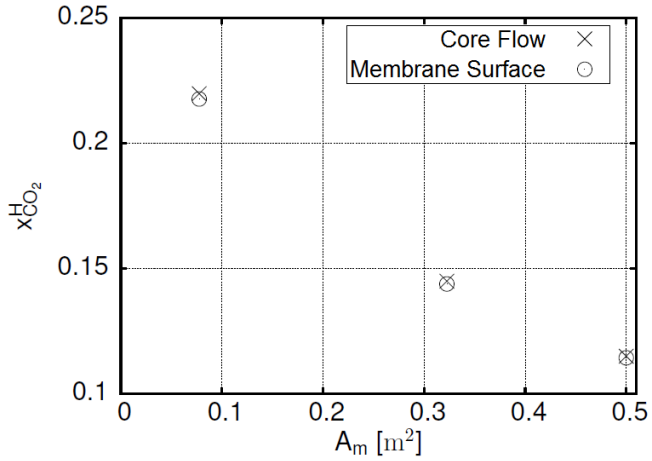

Figure 2: Investigation of the concentration polarization in a polyimide membrane, mole fraction of CO_2 at three different membrane positions.

2.1.2 Pressure Drop

As the pressure gradient is of course the driving force of the membrane process, the appearance of greater pressure drops on either high or low pressure side is of course detrimental and could cost additional compression duty. On the high pressure side the envelope membranes are held apart by lattice spacers. Da Costa et al. (1994) developed a method to model the pressure drop in spacer-filled channels. Their method is applied here, again for a membrane area of 0.5m² and a feed pressure of 7bar. The parameters to calculate the flow resistance were experimentally determined by T. Brinkmann and co-workers at Helmholtz-Zentrum Geesthacht. The pressure drop on the high pressure side is approximated at 51mbar. The same systematic cannot be applied for the permeate side. However, given the lower fluxes and lower pressures there, the permeate side pressure drop is assumed to be negligible. In total, a pressure drop of 51mbar would roughly amount to an additional compression duty of 4W, which should have no greater effect on the outcome of the optimization studies.

2.1.3 Temperature Effects

Among the gases present in the membrane feed, CO_2 has the largest permeability and at the same time also the largest Joule-Thomson effect. The expansion of carbon dioxide from 10 down to 1 bar causes a temperature drop from 298 down to 289K. Hence, there should be a noticeable cooling across the membrane. Of course, it is extremely difficult to pinpoint where exactly this cooling will appear. The gas permeances of both membrane types, considered herein, decrease considerably for a temperature reduction of 9K, while at the same time the selectivity of CO_2 with respect to C_2H_4 increases. As a compromise and given the higher volume flow on the feed side of each membrane, the cooling caused by the Joule-Thomson effect is

moved to the permeate side. An average temperature is assumed for the membrane and thus also for the calculation of the permeances.

2.2 The Absorption Desorption Model

The absorption desorption model used in this contribution does not follow the classical rigorous approach. Instead a short-cut model has been derived which handles CO_2 and MEA in the liquid phase as pseudo components using correlations for the CO_2 liquid load depending on pressure and temperature and the heat of absorption thereof. The entire model has been described extensively in Esche et al. (2014). The most important aspect is, that the short-cut model specially derived for optimization purposes shows both a very convenient computational behavior as well as being suitably accurate with respect to the actual existing mini-plant at TU Berlin. The mini-plant is configured for gas feeds of around 10Nm³/h, liquid recycle flows of up to 60kg/h, and an absorption pressure of up to 32bar. Details on the performance of the mini-plant using MEA solutions can be found in Stünkel et al. (2013).

3. Superstructure Optimization

The main structure of the hybrid system does not change with the addition of further membranes. The OCM product gas is first fed to the membrane network and the retentate outlet flow is then sent to the absorption unit. In the more complex superstructure a maximum of six membranes is considered. This is shown in Figure 3, in which the absorption section is omitted.

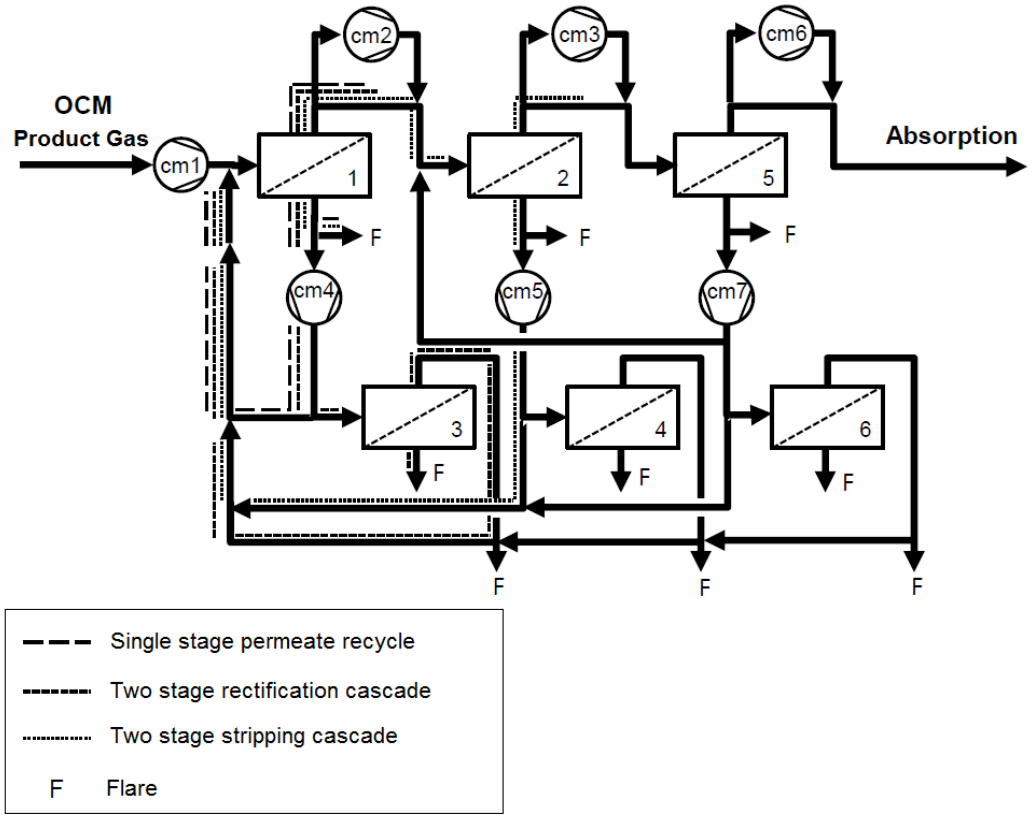

Figure 3: Setup of the membrane section in the membrane absorption network.

The generic superstructure offers several options of combining the different membranes. Both a single stage permeate recycle, a two stage rectification cascade, and a two-stage stripping cascade, in addition to more extensive combinations are

possible. In total, the superstructure offers 12 binary and 22 continuous decisions. Among these are the choice in the membrane material, recycle split factors, (re)compression pressure levels, membrane area, heating duty and scrubbing liquid flow in the absorption etc.

For the optimization studies the gas feed is fixed at 10Nm³/h with a feed composition of 26vol% CO_2, 40vol% CH_4, 10vol% C_2H_4, and 24vol% N_2. At least 90% of the whole amount of CO_2 needs to be separated from the feed gas stream, while an upper bound is enforced on the C_2H_4 loss, meaning the amount which is separated together with the CO_2. The objective function of the optimization problem is the specific energy required for removing the CO_2. The main contributors thereto are the desorption heating and the gas compressors.

The optimization problem was set up using the online modeling, simulation, and optimization environment MOSAIC developed at TU Berlin (Kuntsche et al., 2013). Therein the sets of equations were prepared and automatically exported to GAMS and AMPL. To solve the MINLP optimization problem local copies of Couenne, Bonmin, and IPOPT were employed. Additionally, all of the NEOS server's solvers were tested. Figure 4 shows the specific energy required for the removal as a function of the C_2H_4 loss.

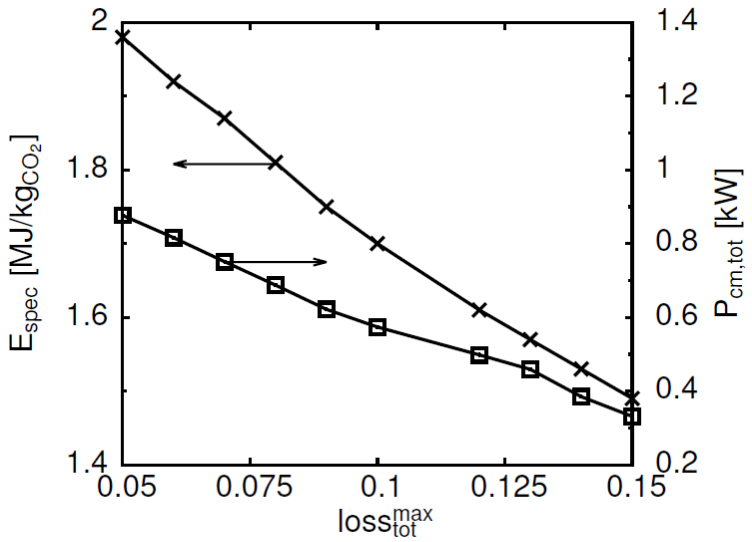

Figure 4: Changes in the optimal specific energy for the removal of CO_2 E_{spec} for changing bounds on the loss of C_2H_4 $loss_{tot}^{max}$.

Compared to the initial hybrid system sporting only a single PI, a PEO membrane, and the absorption desorption section, the final superstructure consists of six PI membranes. At a 5% C_2H_4 loss, roughly 2MJ/kg$_{CO2}$ were required for the separation. This is a further reduction from the initial hybrid by 24%. At this point, the absorption section is operated at a pressure of 5.4bar with a liquid recycle of 10kg/h and a desorption heating duty of 1.3kW. On the retentate side of the membrane network only the first recompression *cm2* is employed. The network can be understood as a series of three rectification cascades, the first and last of which operate at full recycle, whilst the second operates with a 13% purge at the permeate side of membrane 2. As is shown by Figure 4, accepting a greater ethen loss leads to a considerable reduction of the specific energy required for the CO_2 removal. The main reason is the decrease in the recycle flows of the membrane section which cause significantly lower recompression duties.

4. Experimental studies

Experimental studies have been carried out within the mini-plant at TU Berlin. Stünkel (2013) extensively investigated the stand-alone performance of the absorption desorption part using monoethanolamine (MEA) and methyldiethanolamine (MDEA) solutions at various operation conditions. In addition, they implemented a single membrane up front to the either MEA or MDEA filled absorption section. Song et al. (2013) extended the investigations to a basic PI and PEO cascade without recycle. Currently, work is under way to investigate the influence of the recycle in the membrane section. The more complex membrane networks are going to be implemented indirectly by synthesizing the outlets of the various network parts and feeding them to single membranes.

5. Discussion and Outlook

The combination of different types of equipment fulfilling the same or similar tasks within the same process is an interesting possibility to reduce the operation costs of various processes. The process discussed herein is a good example for how the challenge of combining high selectivity with energy efficiency.

The true challenge of course lies in the increase of the investment cost with each additional piece of equipment. The initial membrane system has already been proven to both have lower CAPEX and OPEX compared to the stand-alone absorption (Song et al., 2013). For the more complex structures, investigations are currently under way to properly estimate the investment costs and to incorporate them into the optimization problem seeing as the reduction in the equipment size for the absorption section cannot be neglected either.

Acknowledgements

The authors acknowledge the support from the Cluster of Excellence “Unifying Concepts in Catalysis” coordinated by the Technische Universität Berlin and funded by the German Research Foundation (Deutsche Forschungsgemeinschaft ``DFG''). Cooperation by the group of T. Brinkmann at Helmholtz-Zentrum Geesthacht Centre for Materials and Coastal Research is thanked for most sincerely.

References

Aboudheir, A., Tontiwachwuthikula, P., Chakmab, A., and Idema, R. (2003), Kinetics of the reactive absorption of carbon dioxide in high CO_2-loaded, concentrated aqueous monoethanolamine solutions. Chem. Eng. Sci., 58, 5195-5210.

Da Costa, A.R., Fane, A.G., Wiley, D.E. (1994) Spacer characterization and pressure drop modelling in spacer-filled channels for ultrafiltration, Journal of Membrane Science, 87, 79-98

Esche, E., Müller, D., Song, S., Wozny, G. (2013) Optimization of a Membrane-Absorption-Hybrid System for the Removal of CO2 from OCM Product Gas, 6th International Conference on Process Systems Engineering (PSE ASIA 2013), accepted for publication.

Esche, E., Müller, D., Kraus, R., Wozny, G. (2014) Systematic approaches for model derivation for optimization purposes, Chem. Eng. Sci., DOI: 10.1016/j.ces.2013.11.041i

Kuntsche, S., Barz, T., Kraus, R., Arellano-Garcia, H., Wozny, G. (2011) MOSAIC a web-based modeling environment for code generation, Comp. & Chem. Eng., 35, No. 11, 2257-2273

Ohlrogge, K. and Ebert, K. (2005), Membranen: Grundlagen, Verfahren und industrielle Anwendungen, Wiley-VCH, Weinheim, Germany

Song, S., Esche, E., Stünkel, S., Brinkmann, T., Wind, J., Shishatskiy, S., Wozny, G. (2013) Energy, Equipment, and Cost Savings by Using a Membrane Unit in an Amine-Based Absorption Process for CO_2 Removal, Chemie Ingenieur Technik, 85, No. 8, 1-8

Stünkel, S. (2013) Kohlendioxid-Abtrennung in der Gasaufbereitung des Prozesses der oxidativen Kupplung von Methan, Dissertation, Technische Universität Berlin, Germany

Performance of a novel modular concept for membrane distillation

A. Hagedorn[1], G. Fieg[1], D. Winter[2], D. Düver[2], J. Koschikowski[2], T. Mann[3]
[1]Institute of Process and Plant Engineering, Hamburg University of Technology (TUHH), Hamburg, Germany;
[2]Fraunhofer Institute for Solar Energy Systems (ISE), Freiburg, Germany;
[3]MAHLE Industrial Filtration GmbH, Hamburg, Germany;

Abstract

Membrane distillation is an innovative process combining known advantages of thermal processes for desalination with membrane technology resulting in an efficient hybrid process. The use of membrane distillation is not only limited to desalination and can be extended to a variety of other applications, e.g. food & beverage, pharmaceutical industry or petrochemistry. Especially where low-temperature waste heat is available membrane distillation is an energy efficient process for separating or enriching liquid components.

In the context of an industrial research-cooperation the application of membrane distillation in the field of seawater desalination is widely investigated. The performance of spiral wound membrane modules optimised with respect to heat recovery has already been studied in previous works of Fraunhofer Institute for Solar Energy Systems [1][2]. Regarding the planned field of application and based on these results a novel modular concept focussing on flux enhancement rather than on heat recovery has been developed. The performance of this novel modular concept was investigated in a pilot plant at TUHH and compared to results of the spiral wound module concept.

Furthermore, when dealing with seawater the occurrence of fouling and scaling has to be considered. The fouling and scaling behaviour was investigated with a flat sheet membrane test cell using synthetic seawater and indicator parameters. In addition, a plant concept was developed for pilot plant testing with seawater depicting real conditions and an integral seawater desalination process from seawater to drinking water.

In the presentation results of the experimental work are presented and a comparison to the known spiral wound concept will be performed. Additionally, first experimental results of the fouling and scaling behaviour are presented, discussed and analysed.

Keywords
Membrane distillation, Desalination, Energy efficiency, Fouling, Waste heat usage, Green technology

1. Introduction

Water can be considered as one of the most important resources on earth. Especially freshwater is needed for various reasons, e.g. as nutrient for humans and animals, in agriculture, for washing and cleaning, as heat exchanging medium in industry and as a resource for the production of various products.
Unfortunately, only a small amount of water on earth is freshwater and in addition easily accessible. Therefore, seawater is desalinated since many decades. Energy efficiency plays an important role for desalination technologies. One way to meet energy requirements is to improve existing technologies; another way is to work on new technologies. Membrane distillation is an innovative process combining known advantages of thermal processes for desalination with membrane technology resulting in an efficient hybrid process. The driving force of this process is a partial pressure difference over the membrane which is induced by a temperature gradient (Figure 1).

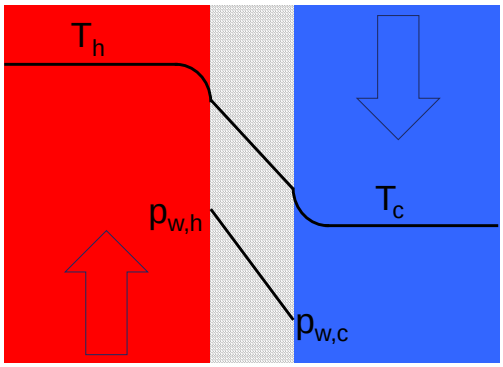

Figure 1: Principle of Direct Contact Membrane Distillation. Partial pressure difference of water over the hydrophobic porous membrane is established by a temperature gradient.

Waste heat with a temperature between 60 to 80 °C can be used to run the membrane distillation. No vacuum, and respectively no high pressure is needed like in other distillation or in other membrane processes. Since now this technology has not been applied to desalination processes in an industrial scale.
In the context of an industrial research-cooperation the application of membrane distillation in the field of seawater desalination is widely investigated. Regarding the planned field of application and based on these results a novel modular concept focussing on flux enhancement rather than on heat recovery has been developed. The performance of this novel modular concept was investigated in a pilot plant at Hamburg University of Technology (TUHH) and compared to results of the spiral wound module concept.

2. Results and discussion

Firstly, based on the knowledge of Fraunhofer ISE with spiral wound modules using Permeat Gap Membrane Distillation (PGMD) a novel concept was developed. The basis of this new concept is the Direct Contact Membrane Distillation (DCMD) process using a modified spiral wound membrane module. In Direct Contact Membrane Distillation one hot and one cold stream flow in counter-current mode only separated from each other through a thin membrane which establishes the phase boundaries of liquid-vapour and vapour-liquid phase. The vapour phase is restricted to the pores of the membrane.
The DCMD configuration was tested with a new module concept in a prototype scale with a pilot plant at TUHH. Additionally a simulation tool was used. What is new about the module concept is the module geometry and the flow configuration. A schematic diagram of the experimental set-up can be seen in Figure 2. The condenser circuit is depicted with a blue line, the evaporator (feed) circuit with an orange line. The module inlet temperature of the condenser and evaporator channel respectively is named T_{ci} and T_{ei} respectively. The module outlet temperatures are

named T_{co} and T_{eo} respectively. Specifications of the old and new module can be taken from Table 1.

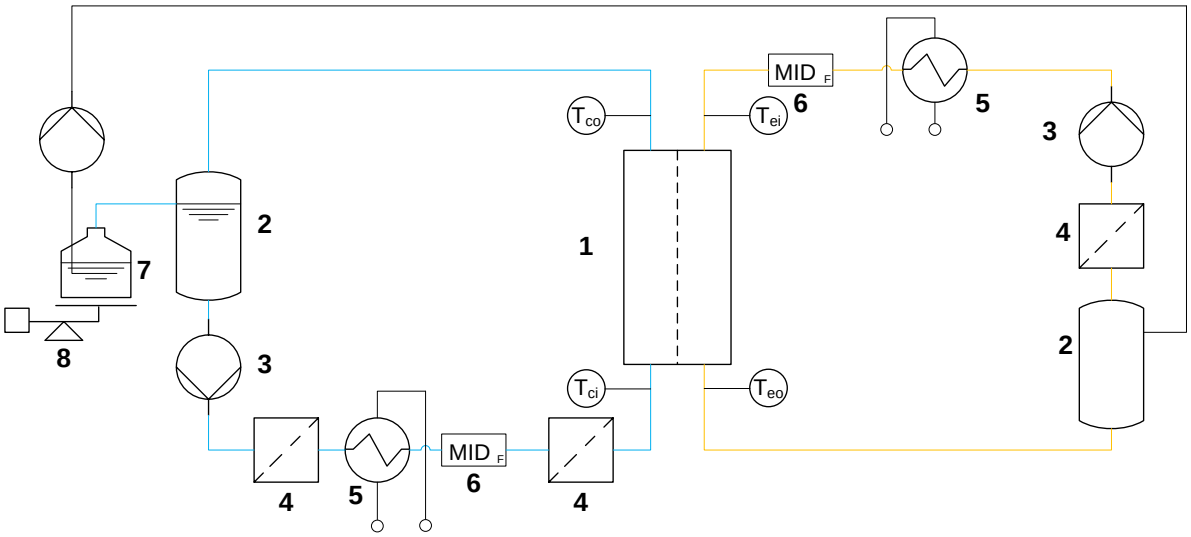

Figure 2: Schematic diagram of experimental set-up; 1 membrane distillation module, 2 feed water tank, 3 feed pump, 4 filter, 5 heat exchanger, 6 magnetic flow meter, 7 overflow tank, 8 electronic balance

Table 1: Specifications of investigated membrane distillation modules at pilot plant of TUHH.

Specifications	**#01**	**#02**
Process	PGMD	DCMD
Membrane	PTFE (dp = 0.2 µm; ε=80 %; δ = 70 µm)	PTFE (dp = 0.2 µm; ε=80 %; δ = 70 µm)
Membrane backing	PP	PP
Condenser foil	ETFE	-
Spacer	LDPE	LDPE
Shell	GFK	GFK
Face potting	Resin compound	Resin compound
Total membrane area	9.7 m²	0.64 m²

To characterize the performance of the modules flux and specific electrical / thermal energy demand the following definitions were considered. The flux is defined as the volume flow of product water related to the membrane area:

$$J = \frac{\dot{V}_D}{A_M}\left[\frac{L}{m^2 h}\right] \quad (1)$$

The consumed energy in terms of electrical and thermal energy is regarded separately from each other and related to the produced amount of water. Within this work only the specific thermal energy demand will be considered:

$$q_{spec,th} = \frac{\dot{Q}_{heat}}{\dot{V}_D}\left[\frac{kWh}{m^3 product}\right] \quad (2)$$

As described by many authors [1,2,4] the transmembrane flux can be enhanced by increasing the feed volume flow rate, the temperature difference across the membrane or the temperature level. Additionally, deaeration of the feed flow enhances the flux by reducing the transport resistance through the membrane pores but this also increases the technical complexity of the system significantly and impacts the investment costs of a plant. In industrial applications often strict boundary conditions are given for operation. So the operating conditions with the highest possible flux can rarely be chosen. As well not only the flux of a module (which is determining the plant volume) is crucial but also the consumed energy.

Therefore, the comparison of the two configurations is carried out considering these different aspects.

2.1 Comparison of concepts

To compare DCMD to PGMD set-up experimental evaluations have been conducted. Results of three different operating points are shown in Figure 3.

As can be seen the flux in DCMD configuration is exceptionally higher compared to PGMD. Accompanied with the DCMD set-up is a higher thermal energy demand as no heat is recovered in the module and therefore has to be recovered externally with higher energy losses. Concerning the specific electrical energy demand on the one hand in DCMD two fluid circuits have to be run with a pump each but on the other hand the pressure drop over the membrane module and the pumping power respectively is much lower. All in all a nearly identical specific electrical energy demand in DCMD and PGMD is achieved. The determined specific electrical energy demands are qualitative significant for this pilot plant and for comparison of concepts. When going into industrial applications pumps have higher efficiencies and therefore specific electrical energy demands will be lower. Advantageous of the DCMD set-up is the lower space needed for modules due to a significantly higher flux. To decrease energy demand in DCMD set-up a consideration of pumps and feed volume flow rates in industrial scale will be accomplished as well as an efficient modular combination of several modules to recover heat.

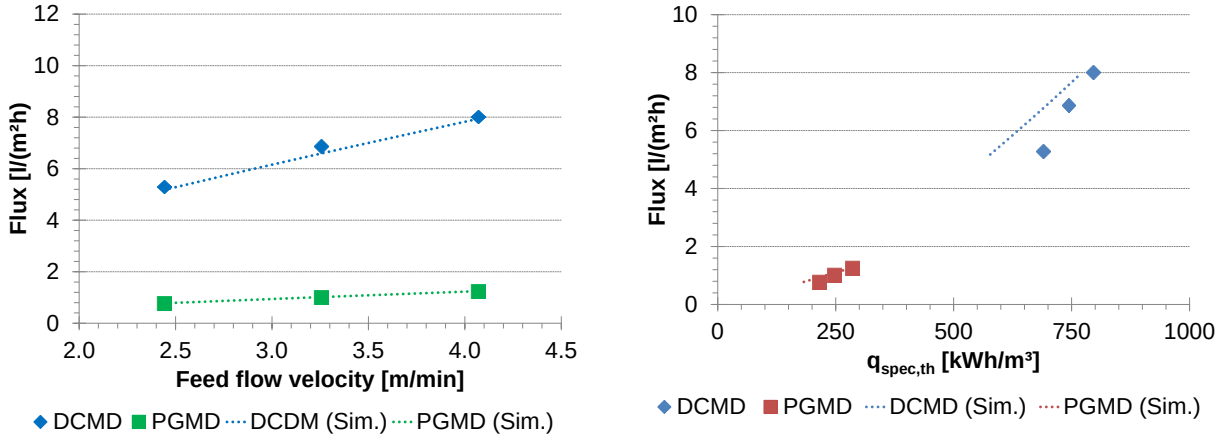

Figure 3: Experimental results of comparable operational parameters in PGMD and DCMD set-up. T_{ei} = 60 °C. Volume flow rate ratio in DCMD $\dot{V}_E/\dot{V}_C = 1$.

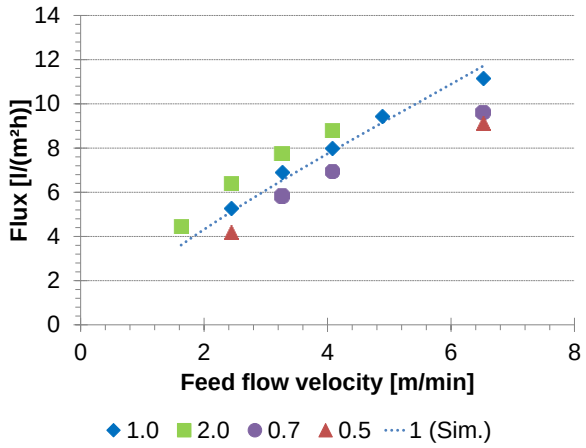

Figure 4: Experimental results of DCMD set-up. Variation of volume flow ratio ($\dot{V}_C/\dot{V}_E$).

Experiments with different volume flow ratios $\dot{V}_C/\dot{V}_E$ were performed. Figure 4 shows that a higher condenser channel volume flow compared to the evaporator channel flow (feed volume flow) leads to a higher flux. Unfortunately, energy demand is increasing as well with higher volume flow ratio. Further experiments will be performed to evaluate this observed trend.

2.2 Investigations on fouling & scaling behaviour

Like in reverse osmosis and evaporation processes one has to consider fouling and scaling effects. Although because of the hydrophobicity of the membrane it is assumed that these effects play a minor role compared to the previously mentioned desalination technologies, researchers already observed these effects in MD to a certain extend [5, 6].

First investigations focused on the effect of cleaning agents on the membrane. One acidic cleaning agent was investigated in a test unit [2] at Fraunhofer ISE. A mixture of natural sea salt with a conductivity of 50 mS/cm and 2% of the cleaning agent was recirculated in the test unit over 6 hours. No temperature gradient across the membrane was established. In Figure 5 the progress of the conductivity and the pH value related to each first value is presented.

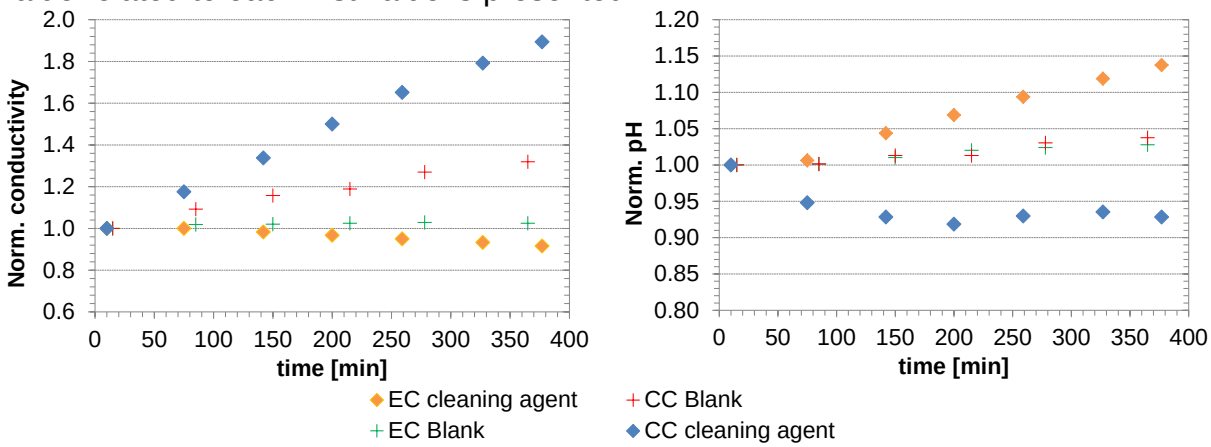

Figure 5: Influence of cleaning agent on conductivity and pH of evaporator (EC) and condenser channel (CC). Mixture of natural sea salt with a conductivity of 50 mS/cm and acidic cleaning agent, $T_{ei}=T_{ci}=30$ °C.

The conductivity of the condenser channel using the cleaning agent increases by 0.11 µS/(cm*min) while that of the blank only by 0.04 µS/(cm*min). In addition, the pH value decreases while those of the evaporator channel increases. The results indicate a component of the cleaning agent is evaporating through the membrane of which the pH value is sensitive to. Further investigations and comparison to other cleaning agents are in progress.

2.3 Concept for pilot plant

When dealing with seawater it is nearly impossible to determine the composition of it or to standardise it. In laboratory it is a challenge to depict natural seawater. The best way to proof a plant concept is to work under real conditions. Therefore, a plant concept for pilot plant was developed and will be tested in summer 2014. A flow diagram of the integral pilot plant concept is presented in Figure 6. The pilot plant consists of two different pre-treatment concepts. One is equipped with an automatic backwashing filter (50 µm (*MAHLE*)) and a cartridge filter (20 µm (*MAHLE*)); the other one consists of a gravel filter with 1-2 mm gravel (*MAHLE*) and as well a cartridge filter (20 µm (*MAHLE*)). These two options were chosen because they are comparatively inexpensive and use established components.

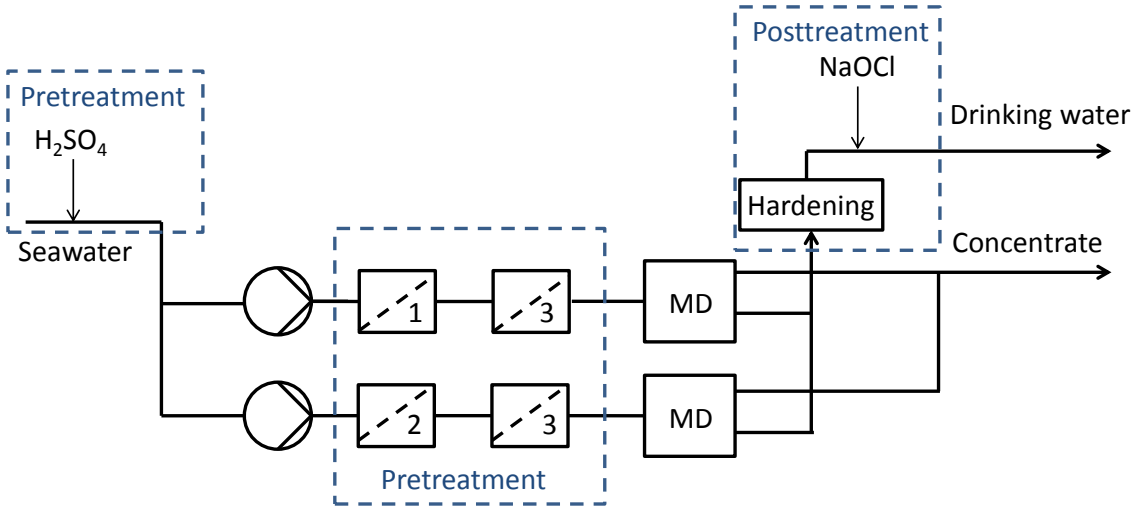

Figure 6: Flow diagram of the planned pilot plant; 1 gravel filter, 2 backwashing filter, 3 cartridge filter

3. Conclusions

A novel module concept for DCMD was developed and has been pre-tested. The performance was evaluated in the first experiments with a modified spiral wound membrane module. In on-going investigations, up-scaled modules are measured and investigations on a new pilot plant will be performed with natural seawater. Concerning a flux enhancement the Direct Contact Membrane Distillation is advantageous over the Permeat Gap Membrane Distillation. Especially when using modified channel geometry, flux can be improved due to the relatively high driving forces. By means of the internal heat recovery of the PGMD process the specific thermal energy demand of this process is lower compared to the DCMD process. To lower the specific energy demand in the case of this novel module a higher volume flow rate in the evaporator channel than in the condenser channel can be chosen. In addition, for industrial applications the interconnection of several modules to a network plays an important role to internally recover heat in the plant.

References

[1] WINTER, D.; KOSCHIKOWSKI, J.; WIEGHAUS M.: *Desalination using membrane distillation: Experimental studies on full scale spiral wound modules*. Journal of Membrane Science., 375, 104-112, 2011

[2] WINTER, D.; KOSCHIKOWSKI, J.; RIPPERGER, D.: *Desalination using membrane distillation: Flux enhancement by feed water deaeration on spiral-wound modules*. Journal of Membrane Science, 423-424, 215-224, 2012

[3] CATH, T.Y.; ADAMS, V.D.; CHILDRESS, A.E.: *Experimental study of desalination using direct contact membrane distillation: a new approach to flux enhancement*. Journal of Membrane Science, 228, 5-16, 2004

[4] KHAYET, S.; MATSUURA T.: *Membrane Distillation – Principles and Applications*. Amsterdam: Elsevier, 2011

[5] GRYTA, M.: *Fouling in direct contact membrane distillation process*. Journal of Membrane Science, 325, 383-394, 2008

[6] HE, F.; SIRKAR, K.K.; GILRON, J.: *Studies on scaling of membranes in desalination by direct contact membrane distillation: $CaCO_3$ and mixed $CaCO_3$/$CaSO_4$ systems*. Chemical Engineering Science, 64, 8, 1844-1859, 2009

Selectivity Engineering with Hybrid Reactive Distillation Column with Side Draw

Shabih Ul Hasan[+]*, Sanjay M Mahajani, Ranjan K Malik*
Department of Chemical Engineering
Indian Institute of Technology, Bombay-400076, India
[+]*Presently at Motilal Nehru National Institute of Technology, Allahabad-211004*

Abstract
The contribution deals with the development of design algorithm for hybrid Reactive Distillation (RD) column with side draw in order to get the desired selectivity in a multi-reaction system wherein, reactant is a saddle in the corresponding residue curve map. A model reaction scheme of van de Vusse type is studied as an illustrative example and a combined graphical-simulation algorithm is developed using the concepts of attainable region approach. The developed algorithm successfully finds at least one feasible design of hybrid RD column with side draw to give desired selectivity.This work is the continuation of our earlier work on selectivity engineering with hybrid RD columns (Amte et al. 2011; Amte et al. 2012; Hasan et al., 2013a,b).

Keywords
Design, Selectivity, Reactive distillation, Side draw, Surface of Reactive Stage Compositions.

1. Introduction

Reactive distillation (RD) can be advantageously used to improve the selectivity of the desired product in the multi-reaction system. Recently, Hasan et al. (2013a) have developed a conceptual design algorithm for single feed hybrid reactive distillation columns to achieve desired selectivities in case of single reactant multi-reaction schemes. It was also shown that hybrid RD columns are especially useful when the reactant is intermediate boiling or saddle in the residue curve map of the mixture (see section 8 (point 1) in Hasan et al., 2013a). This algorithm is restricted to pseudo ternary mixture and to the cases wherein, only one product undergoes further side reaction. In the present work we remove both the restrictions and found that when more than one product undergo further side reactions then hybrid RD columns with side draw are capable to give desired selectivities in case of single reactant multicomponent multi-reaction schemes. In this work, we developed a combined graphical-simulation algorithm by using the concepts of attainable region for the design of RD columns with side-draw in order to achieve desired selectivities in case of multicomponent multi-reaction schemes.

2. Design Methodology

The methodology starts with non-reactive distillation column (non-RD) and then introduces the reaction related attributes. For non-RD, we use the concept of visualization of the locus of feed stage compositions (LFSCs) in 3D composition space. For reaction related attributes we view the column as a reactor and relate it to the conventional reactors for which geometric interpretation is well studied through

the attainable region approach. Glasser et al. (1987) presented geometrical interpretation of CSTR in terms of process vectors *viz*. reaction and mixing. In order to know whether a point in the composition space is attainable or not, they derived a condition that the rate vector at that point is collinear with the mixing vector of feed and product stream. The component material balance of CSTR gives the required condition. It must be noted that the reaction takes place at the product composition in the case of CSTR. On the other hand, in an arbitrary reactor (R), if the composition at which reaction takes place is different than the product composition, then the collinearity condition is no longer valid. The composition at which reaction takes place is dependent on the type of reactor. One can control this composition by introducing separation attributes as is done the case of reactive distillation.

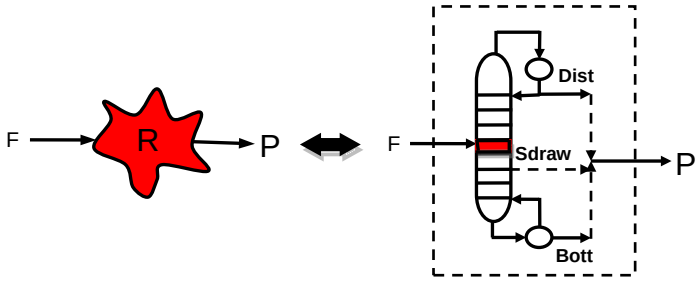

Figure 1. Analogy between Arbitrary reactor (R) and hybrid RD Column with side draw

Now, as shown in Figure1, let us consider a side draw column with single reactive stage. It may be noted that the reaction in the column does not take place at a composition corresponding to that of the product (P). The overall product composition is the one obtained by virtually mixing the overhead, side draw and bottom streams. The composition of the reactive stage depends on the distillation attributes such as reflux ratio, side draw to feed ratio, feed location, number of stages, etc. Therefore, the next exercise is to know –which are the points in the composition space that can be the potential reactive stage composition(s) giving the desired selectivity corresponding to the point of desired product composition. The following section determines the surface of such feasible reactive stage compositions.

2.1 Surface of Reactive Stage Compositions (SRSCs)

Consider an equi-molar van de Vusse type reaction scheme (Eq. 1) with only one reacting component A. All the reactions are irreversible except B to C with first, second and third reactions are of 1st order while the fourth reaction is of 2nd order. The feed is pure reactant A and the kinetic rate constants are given by [*k1 k2 k3 k4*]=[1 1 1 3].

$$\left.\begin{aligned} &A \xrightarrow{\text{desired } (k_1)} B \underset{\text{desired } (k_3)}{\overset{\text{undesired } (k_2)}{\rightleftarrows}} C \;\; and \;\; A \xrightarrow{\text{undesired } (k_4)} D, \\ &\left[r_A \; r_B \; r_C \; r_D\right] = \left[-k_1 x_A^* - k_4 x_A^{*2},\; k_1 x_A^* - k_2 x_B^* + k_3 x_C^*,\; k_2 x_B^* - k_3 x_C^*,\; k_4 x_A^{*2}\right] \end{aligned}\right\} \quad (1)$$

The material balances for components A and B on any arbitrary reactor, yield the following relation

$$\frac{x_{B,P} - x_{B,0}}{x_{A,P} - x_{A,0}} = \frac{r_B}{r_A} = \frac{k_1 x_A^* - k_2 x_B^* + k_3 x_C^*}{-k_1 x_A^* - k_4 x_A^{*2}} \quad (2)$$

where $x_{i,p}$ is the product composition of component *i*, $x_{i,0}$ is the inlet composition of component *i* and *x** denotes the compositions at which the reaction takes place in the reactor. The LHS of Eq. (2) is the slope of line joining points *A* (x_{A0}, x_{B0}) and *P* (x_{AP},

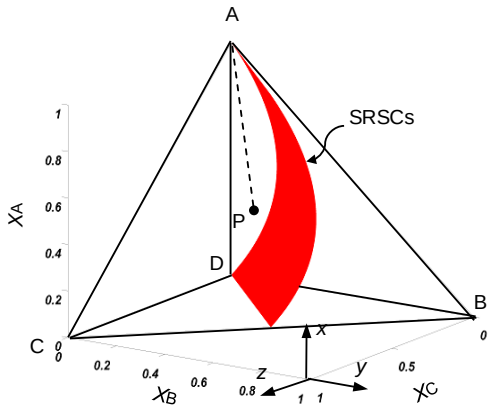

Figure 2. Surface of reactive stage compositions (SRSCs).

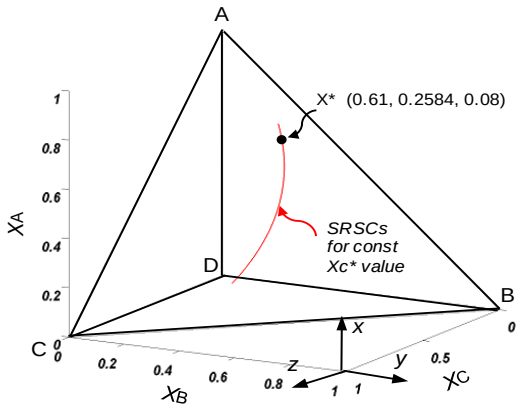

Figure 3. Selected reactive stage composition, X* on the curve of SRSCs.

x_{BP}) as shown in Figure 2. It should be noted that point P is on x-yplane and since Eq. (2) is independent of x_{CP},, its value is not required for plotting the SRSCs. Hence, for any desired point P in the composition space, Eq. (2) gives a relation between x_A*,x_B* and x_C*, which represents the SRSCs as shown in Figure 2. Moreover, it should be kept in mind that once we choose point *P* in the composition space it implies fixed selectivity, which we call as the desired selectivity and hence if the reaction occurs at any of the compositions on the SRSCs then the desired selectivity is ensured.

3. Design Procedure

Consider a reactor-separator system (Figure 4a) and a hybrid side draw RD column with one reactive stage (Figure 4b).

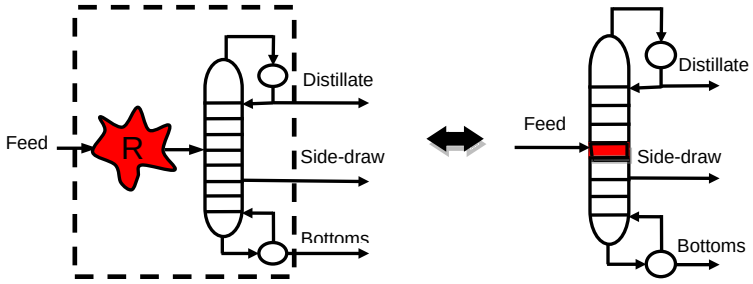

Figure 4. (a) Reactor separator system (Non-RD) and (b) hybrid (RD) column with side draw.

The approach presented in this work makes use of the fact that for a given conversion and under the assumption of *dominance of distillation over the reaction*, the column profiles of non-reactive side draw column (Non-RD; Figure 4a) and a side draw RD column (Figure 4b) are almost identical.To illustrate the design procedure we present an example a *van de Vusse* reaction as a model reaction scheme.

A simplified equimolar *van de Vusse* scheme (Eq. 1) with rate constants, [*k1 k2 k3 k4*] = [1 1 1 3] and volatilities as [α_A α_B α_C α_D]=[3 5 2 1], is chosen as an illustrative example.

Following are the proposed step-by-step design procedure:

Step-1: Select any point *P* (Figure 2) according to the desired selectivity of intermediate product, *B* in the composition space. This point represents the overall

output composition of side draw hybrid RD column (Figure 4b), obtained by virtually mixing distillate (*D*), Side draw (*SD*) and bottoms (*B*) streams. Hence, it can be considered as the feed to Non-RD column in Figure 4a.

Step-2: Join point *P* (0.3, 0.175) with *A* (1, 0) to calculate the slope of line *AP*, and hence obtain the surface of reactive stage compositions (SRSCs) using Eq. (2) as shown in Figure 2.

Step-3: Select any reactive stage composition, *X** on the SRSCs as shown in Figure 3. For the present example let $X^* = [X_A^* \; X_B^* \; X_C^*] = [0.61, 0.2584, 0.08]$. For clarity, instead of showing the entire surface, we draw a single curve of SRSCs for a constant value of X_C^*. Also only those compositions are plotted which lie within the 3D composition space as shown in Figure 3.

Step-4: Find the composition of all the components in the feed that is sent to the distillation column as we visualize RD as a combination of reactor followed by distillation column in series (Figure 4).We need to know the composition of all the components including *C* and *D* in the feed that is sent to the distillation column. The concentration of *C* is related to the extent to which individual reactions take place, which in turn depends on the Damkohler number (*Da*) number i.e. the ratio of characteristic liquid residence time to the characteristic reaction time (Eq. 3).

$$\mathrm{Da}=\left(\frac{\mathrm{W_{cat}}*\mathrm{k_{ref}}}{\mathrm{F}}\right) \tag{3}$$

We determine *Da* by applying material balance for either component *A* (Eq. 4) or component *B* (Eq. 5) for any arbitrary reactor in which reaction takes place at the selected composition , *X**. Further, by using material balance for component *C* (Eq. 6), one can find the composition of *C* in the feed to the distillation column.

$$x_{A,0} - x_{A,P} + Da\left(\frac{-k_1 x_A^* - k_4 (x_A^*)^2}{k_{ref}}\right) = 0 \tag{4}$$

$$x_{B,0} - x_{B,P} + Da\left(\frac{k_1 x_A^* - k_2 x_B^* + k_3 x_C^*}{k_{ref}}\right) = 0 \tag{5}$$

$$x_{C,0} - x_{C,P} + Da\left(\frac{k_2 x_B^* - k_3 x_C^*}{k_{ref}}\right) = 0 \tag{6}$$

Step-5: For the simulation of Non-RD column, along with the feed composition, we also have to specify the number of stages, feed location, side draw location and operating parameters. Number of stages can be chosen on the basis of cost considerations (e.g *N*=12, *reboiler* = 1st*stage*). Since the reactant *A* in our case is of intermediate volatility one can choose the feed location anywhere near the middle of the column (*Nfl* =7th stage). Side draw location depends on the volatility of that product whose composition is required to be adjusted through side draw to obtain the desired selectivity. In the present case it is component *C*. Hence, if the volatility of component *C* is less than the volatility of reactant *A* then the side draw location is below the feed location. (*Sdl*= 6th*stage*).

Step-6: Find the operating parameters such that the feed stage of Non-RD column coincides with the selected reactive stage composition, *X**. To obtain this intersection draw the family of curves representing LFSCs obtained for a range of reflux and reboil ratios by choosing initially some arbitrary value of *side draw to feed ratio* (say *SD*=0.2). Figure 5 shows three such families of curves for a range of reflux (5-to-

1000) and reboil ratios (5-to-500) at three different values of *SD*. Range of reflux ratio can be decided based on whether or not one of the LFSCs crosses the curve of SRSCs containing selected reactive stage composition, *X**, while the reboil ratio can start from any small value till the performance becomes insensitive at higher values of reboil ratios. It can be clearly seen in Figure 5 that the reactive composition, *X** of interest lies in the vicinity of curves obtained for *SD*=0.4.

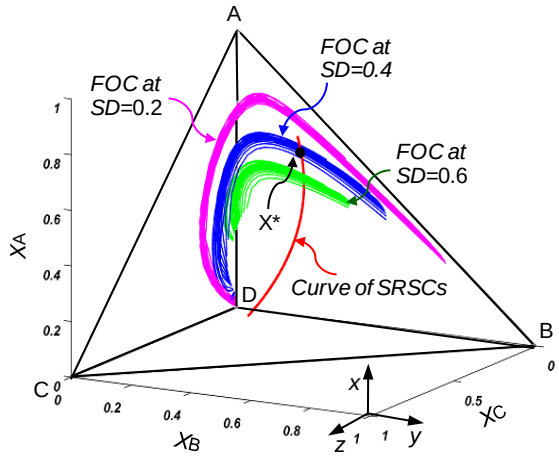

Figure 5. Family of curves (FOC) for a range of reflux and reboil ratios representing LFSCs.

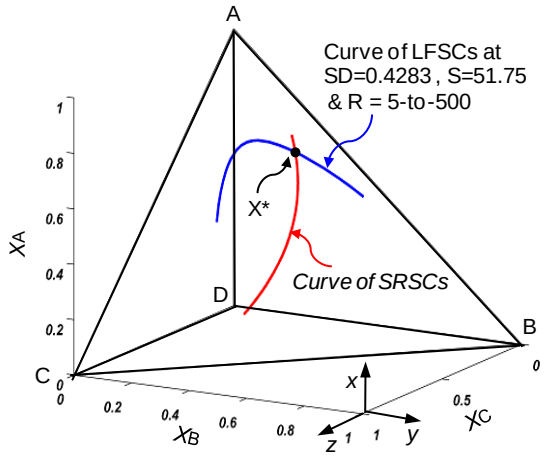

Figure 6. Feasible condition that satisfies our requirements.

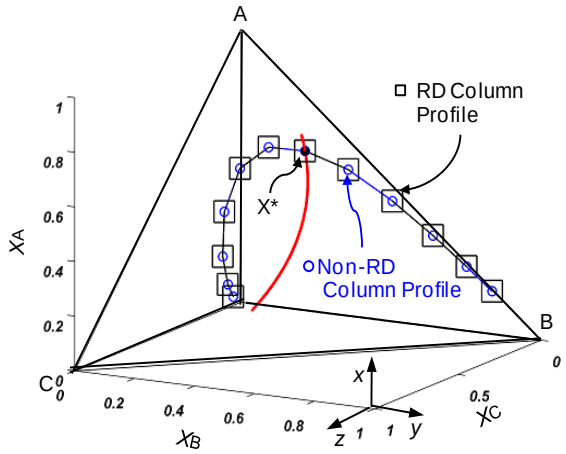

Figure 7. Identical composition profiles of Non-RD and RD side draw columns in 3D composition space.

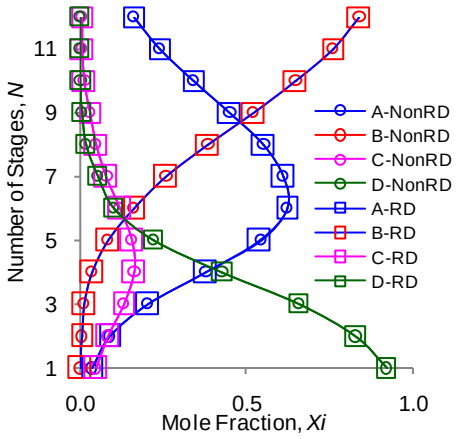

Figure 8. Column profiles along the length of column. The close overlap indicates that the design is feasible.

Step-7: Next step is to consider a range of *SD*, near the value 0.4 and narrow down the ranges of reflux and reboil ratios based on the results shown in Figure 5. The exact intersection of feed stage of Non-RD column with the selected reactive stage composition, *X** is shown in Figure 6. The values of three operating parameters *viz*. *SD*, *S*, and *R* at this intersection are found to be *0.4283*, *51.75* and *180*, respectively. The column profile for Non-RD side draw column in 3D composition space is then plotted as shown in Figure 7.

Step-8: Obtain the column profile for RD, with the feed as pure A and the feed stage as the reactive stage, using the same design and operating parameters as used for the Non-RD case. As discussed in our earlier work (Appendix A in Hasan et al., 2013a), it is necessary that the feed stage should be the reactive stage to avoid the *feed effect* on column profile. The profiles coincide (Figure 7 and Figure 8) to indicate that the design is feasible. Hence, the desired selectivity for the given complex

reaction scheme is attainable through hybrid RD column with side draw, the design specifications of which are given in Table 1.

Table 1. Design specifications for hybrid RD column with side draw

Column configuration	Non-RD Side draw column	RD Side draw column
Number of components, *NC*	4	4
Volatility [*A B C D*]	[3 5 2 1]	[3 5 2 1]
Number of stages, *N*	12	12
Feed location, *Nfl*	7^{th} Stage	7^{th} Stage
Feed flow rate, *F*	1	1
Feed composition, *Xf*	(0.3 0.175 0.0723)	(1, 0, 0)
Feed stage composition, *X**	(0.61, 0.2584, 0.08)	(0.61, 0.2584, 0.08)
Side draw location, *Sdl*	6^{th} Stage	6^{th} Stage
Number of reactive stages, *Nr*	-	1
Location of Reactive stage, *Nrl*	-	7^{th} Stage
Damkohler Number /Catalyst loading	-	0.4055
Reflux ratio, *R*	180	180
Reboil ratio,*S*	51.75	51.75
Side draw to feed ratio, *SD*	0.4283	0.4283
End Compositions after mixing the distillate, side draw and bottom streams	(0.3, 0.175, 0.0723)	(0.3, 0.175, 0.0723)

4. Conclusions

A combined graphical-simulation algorithm for the design of hybrid RD columns with side-draw, is developed using the concepts of attainable region. The design methodology utilizes the concept of visualization of the LFSCs of nonreactive distillation column and its intersection with that composition in space at which reaction takes place in RD column. The developed methodology successfully finds promising designs of hybrid RD column with side-draw, to give desired selectivity in case of multicomponent multi-reaction systems. Depending on the specification of number of stages, feed location and side draw location the developed algorithm generates multiple feasible designs which can be evaluated and compared in terms of capital cost, energy requirement and catalyst loading to determine a good/optimal design for the given set of design goals. The applicability of this approach, at present, is restricted to the systems with single reactant. However, the developed methodology holds a potential to be extended to the schemes with multiple reactants and is the next step of this work.

References

D. Glasser, D. Hildebrandt, C. Crowe, *Ind. Eng. Chem. Res.* 26 (1987) 1803-1810.

S.U. Hasan, R.K. Malik, S.M. Mahajani, *Chemical Engineering Science* 99 (2013a) 324–334.

S.U. Hasan, S.M. Mahajani, R.K. Malik, *Computer Aided Chemical Engineering* 32 (2013b) 313–318.

V. Amte, N. Sriharsha, R.K. Malik, S.M. Mahajani, *Chemical Engineering Science* 66 (2011), 2285–2297.

V. Amte, N. Sriharsha, R.K. Malik, S.M. Mahajani, *Chemical Engineering Science* 68 (2012) 166–183.

Conceptual design, simulation, and experiment for a reactive divided wall column

NGUYEN Trung Dung (1,2), David ROUZINEAU (1), Michel MEYER (1), and Xuan MEYER (1)

(1) Université Toulouse, ENSIACET - INPT, Laboratoire de Génie Chimique, UMR CNRS 5503

4 allée Emile Monso, BP 44362, 31432 TOULOUSE Cedex 4, France ;

(2) Hanoi University of Science and Technology, Hanoi, Vietnam

Abstract

The main objective of this paper is to present a design procedure for the R-DWC. In a first step, an original short cut method based on a hybrid method coupling a classical short cut adapted to a DWC by C. Triantafyllou and R. Smith (1992) and a predesign method developed in our lab by R. Thery et al. (2005). This method is able to rapidly determine a first approximation of structure parameters of R-DWC, in particular to determine two specific parameters (liquid and vapor splits) both technological and hydro-dynamical aspects will be considered. In a second step, a simulation tool (ProSim^{plus}) is used in order to validate and/or adjust the results of the previous step. In a third part, the description of a new pilot for the DWC system located in our lab is proposed. The main results provided by the pilot plant are given in order to validate the design procedure for non-reactive mixture. The result of this study indicates that the approach works well and provides both the basis for preliminary optimization and a good initialization for rigorous simulation. It is also a good proof that helps to increase the acceptance of R-DWC system in industrial processes.

Keywords: Design, Simulation, Pilot plant, Shortcut method, Reactive divided wall column, Divided wall column

1. Introduction

Reactive distillation (RD) and divided wall column (DWC) are concepts of process intensification. DWC is combination between separation and separation while RD column is combination between reaction and separation in one column. Both DWC and RD system can save both energy of use and capital cost. The integration of these two processes is R-DWC. Generally, reaction - separation occurs only in the prefractionator and separation process occurs in main column. Guido Daniel et al. (2006) presented a method in which R-DWC is decomposed into prefractionator and a thermally coupled main column. To design, a combination of the boundary value method for non-reactive zone in the main column and reactive zone in the prefractionator is applied. I.Mueller et al. (2007) decomposed step-by-step R-DWC into single non-reactive and reactive columns. For the non-reactive columns, the shortcut method suggested by Underwood, Fenske, and Gilliland is applied. For the reactive column, they applied the rate-based stage model in which bases on account of the actual mass and heat transfer rates and process hydrodynamics. Anton A. Kiss (2007, 2010, and 2012) proposed a method for design R-DWC. They used a sequence including a RD column and a conventional distillation column. And then, they considered the more integrated design that combines reaction and separation into one R-DWC. The key factor that allows such an integration of two columns into one unit is the similar pressure and temperature conditions. In this study, a proposed shortcut design method for the design of R-DWC is presented. It based on a hybrid

method coupling a classical shortcut adapted to a DWC system by C. Triantafyllou and R. Smith (1992) and a predesign method developed in our lab by R. Thery et al. (2005).

2. Design of reactive divided wall column

In this study, we only consider single-feed column with two restrictions that (i) reactive section limits only in the prefractionator and (ii) main column is only used to separate. To design the R-DWC, we propose a shortcut design method including two steps. Step 1: By using the predesign method of Thery et al (2005), the feed composition x^F is converted to the pseudo initial x^* by using a certain extent of reaction ξ. Step 2: The mixture is separated by non-reactive divided wall column and a classical shortcut adapted to a DWC system by C. Triantafyllou and R. Smith (1992) is applied.

2.1 Classification of feed composition region

Ivo Mueller et al. 2007 suggested that R-DWC is a highly integrated setup that can be used, if: (i) Reactive systems with more than two products which should be obtained as a pure fraction each; (ii) Reactive systems with inert component and with desired separation of both products and inert component. (iii) Reactive systems with an excess of a reagent, which should be separated purity before being recycled.

Depending on the feed composition and desired purities of products, we should decide using RD or R-DWC. The entire feed composition of reactive system can be classified into several sub-regions by the predesign method of R. Thery et al. (2005), in this part mainly relies on the work of S. Giessler et al. (1998). Then, each of the feed sub-regions has an arrangement to get desirable products (S. Giessler et al, 2001). This analysis also enables to get the maximum conversion yield, the distillate and bottom composition flowrates of the products for each studied feed composition.

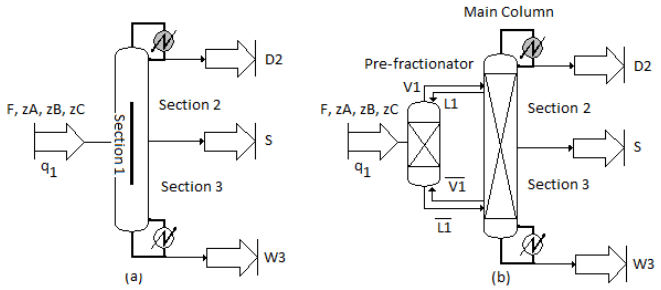

Figure 1: (a) Divided wall Column. (b) Thermally coupled distillation

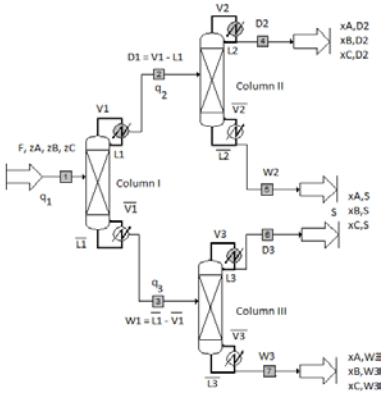

Figure 2: Simplified model design of divided wall column

2.2 Shortcut design method for Reactive divided wall column

C. Triantafyllou et al. (1992) presented a method to decompose DWC column into three traditional distillation columns as the Figure 1 and 2 in which the column I, II and III only take place separation process. The minimum vapor flowrate of the DWC system can be determined by the Underwood's equation. For R-DWC, I. Mueller et al. (2007) also applied the method to decompose into single reactive column (column I) and two non-reactive columns (column II and III). For reactive mixture, separation and reaction take place in the column I at the same time. Thus, to determine the minimum vapor flowrate for column I, both the minimum vapor flowrate for separated mixture and the minimum vapor flowrate for reactive mixture must be considered. For separated mixture, at the minimum reflux condition, the minimum vapor flowrate can be calculated by Underwood's equation:

$$V_{1,min}^{pure} = \sum_{i=A}^{C} \frac{\alpha_i . x_{i,D_1} . D_1}{\alpha_i - \theta}$$

For reactive mixtures, Domingos Barbosa and Michael F. Doherty (1987) presented an algorithm to find minimum reflux ratio r_{min}^{reac} for reactive mixtures. From that, we can calculate the minimum external reboil ratio s_{min}^{reac} and minimum vapor flowrate $V_{1,min}^{reac}$ for reactive mixtures:

$$V_{1,min}^{reac} = s_{min}^{reac} . W_1$$

The minimum vapor flowrate for the column I is chosen:

$$V_{1,min} = max\{V_{1,min}^{pure}(\theta);\ V_{1,min}^{reac}\}$$

Following the restrictions, the column II and III take place only separation. Thus, minimum vapor flowrate of the columns can determine the same as shortcut method of C. Triantafyllou et al. (1992).

Starting from this structure (Figure 2) an evaluation of NET for each section and reflux ratio for each column are computed based on a shortcut method of Fenske, Underwood and Gilliland and Kirkbride equations (Henry Z. Kister 1992).

3. Case study

The reaction of methyl acetate production is operated at standard pressure and temperature between 76 to 117°C. Making the purification of methyl acetate is very difficult because of azeotrope between methyl acetate and methanol (0.66/0.34). Thermodynamic data of this system is taken from Song et al. (1998). The azeotrope has the lowest boiling temperature. For the direct separation, it is as distillate product as Table 1. The reaction scheme is as follows:

Methanol (MeO) + Acetic acid (AcA) ↔ Methyl acetate (MeA) + Water (H2O)

Using predesign method of Thery et al. 2005, the entire feed composition of reactive system can be classified.

Table 1: Classification of feed composition in case of RD

Feed molar liquid composition		Distillate molar liquid composition				Bottom molar liquid composition				ξ	$K_D = \frac{D}{W}$
MeO	AcA	MeO	AcA	MeA	H2O	MeO	AcA	MeA	H2O		
0.1	0.9	0.34	0.00	0.66	0.00	0.00	0.93	0.00	0.07	0.066	0.11
0.2	0.8	0.34	0.00	0.66	0.00	0.00	0.83	0.00	0.17	0.132	0.25
0.3	0.7	0.34	0.00	0.66	0.00	0.00	0.72	0.00	0.28	0.198	0.43
0.4	0.6	0.34	0.00	0.66	0.00	0.00	0.56	0.00	0.44	0.264	0.66
0.5	0.5	0.34	0.00	0.66	0.00	0.00	0.34	0.00	0.66	0.330	1.00
0.6	0.4	0.34	0.00	0.66	0.00	0.00	0.01	0.00	0.99	0.396	1.50
0.7	0.3	0.34	0.00	0.66	0.00	0.45	0.00	0.00	0.55	0.3	0.83
0.8	**0.2**	**0.34**	**0.00**	**0.66**	**0.00**	**0.71**	**0.00**	**0.00**	**0.29**	**0.2**	**0.43**
0.9	0.1	0.34	0.00	0.66	0.00	0.88	0.00	0.00	0.12	0.1	0.19

In table 1, depending on the required purification of the products, if amount of MeOH in the feed composition is less than 10% or around 60%, we should use only RD because the purity of bottom products are high. For feed compositions containing MeOH < 60%, the bottom product is a mixture of H2O and AcAc. For feed compositions containing MeOH ≥ 70%, the bottom product is a mixture of MeOH and H2O. In those cases, we should use R-DWC to separate bottom product. In this paper, the feed composition x^F is chosen MeOH/AcAc = 0.8/0.2. The operation pressure is 1 atm, feed flowrate is 100 kmol/h and separation type is direct separation. The table 1 shows that the extent of reaction ξ = 0.2. The conversion of

AcAc is 100% and disappears in the separated mixture. In the table 2, the feed composition x^F is converted to pseudo-initial composition x^* and the specification of products for R-DWC is provided.

Table 2: Pseudo initial separation mixture and product specifications of the R-DWC

Component	Feed composition x^F	Pseudo initial mixture x^*	Distillate product	Side product	Bottom product
MeA	0.0	0.2	0.66	0.005	0.00
MeO	0.8	0.6	0.34	0.99	0.01
H2O	0.0	0.2	0.00	0.005	0.99
AcA	0.2	0.0	0.00	0.00	0.00

Table 3 shows the results obtained from the shortcut design method in which the detailed structure and operating variables of R-DWC system are listed.

Table 3: Structure results of the reactive divided wall column

Variables	
N_1	5
N_2	6
N_3	2
N_4	6
N_5	5
N_6	6
Reflux ratio R	7
Liquid split R_L	0.48
Vapor split R_V	0.57
Heat consumption Q_b (kW)	2.1

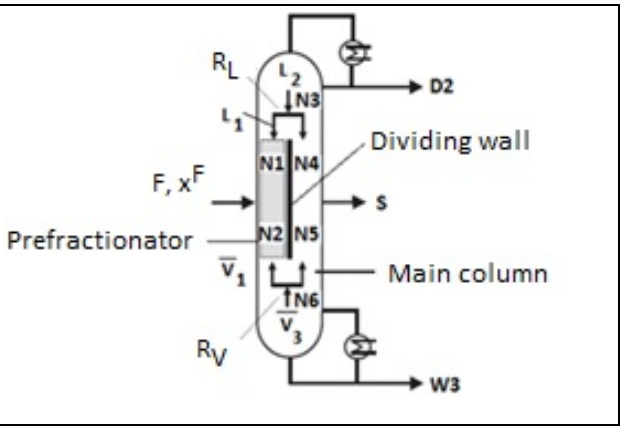

In this paper, we will use simulation tool to simulate the R-DWC system. The model for simulation is presented in the Figure 3. The first column is as the prefractionator where takes place reaction and the second column is as the main column where uses to separate products. The interconnecting streams 2, 3, 4, and 5 connected between two columns. The top, side and bottom product are the stream 6, 7, and 8, respectively. Feed flowrate is as the stream 1. Based on the information from shortcut design method, R-DWC will be simulated. The results show in the table 4.

Table 4: Simulation results of product compositions

Component	Distillate product	Side product	Bottom product
MeA	0.640	0.016	0.00
MeO	0.359	0.971	0.03
H2O	0.001	0.013	0.97
AcA	0.000	0.000	0.00

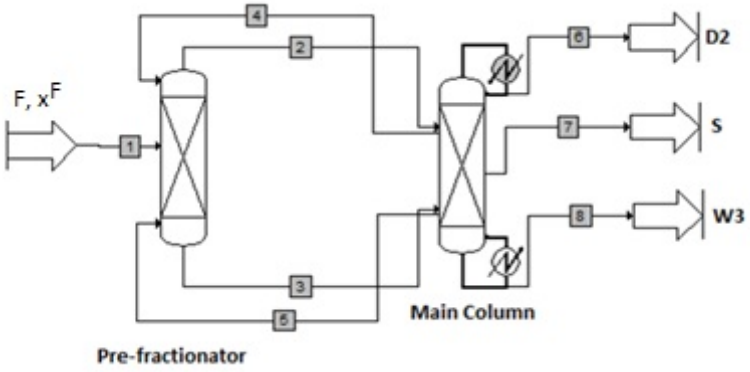

Figure 3: The model for simulation R-DWC system by ProSim[plus]

4. Validation for non-reactive divided wall column

A lack of knowledge for operation and control of divided wall column is significant reason to limit building the system in the industry. To bridge the gap, the pilot for divided wall column has already built by Gerit Niggemann and Georg Fieg (2011). The mixture consisting of n-hexanol, n-octanol, and n-decanol was studied with purities of key component around 99 wt %. In our laboratory, a pilot plant divided wall column was also set up (LGC, Toulouse, France, 2013).

Figure 4 shows the diagram of the pilot plant in our laboratory. The DWC column has a total height of 5.53 m and can be divided into 3 parts. For the top and bottom parts of the column, each part has 6 elements (height of element is 0.3 m and inner diameter is 80 mm). Middle part of the column divided into two sections (feed section and side section) has 4 elements (height of element is 0.2 m and inner diameter is 50 mm). The structured packing of use in the pilot is Sulzer DX for non-reactive mixture. The liquid split (R_L) and reflux ratio (R) will be controlled by timer. At the top column, the condenser is operated with cooling water. At the bottom column, the liquid in the reboiler is heated by vapor that operation pressure is 8 bar. Heat losses through the column will be reduced by jacket of the entire column. Temperature (T) of the along column will be determined by 14 temperature sensors as the Figure 6. Liquid samples (El) of the along column are taken from 11 points and are analyzed by using gas chromatography.

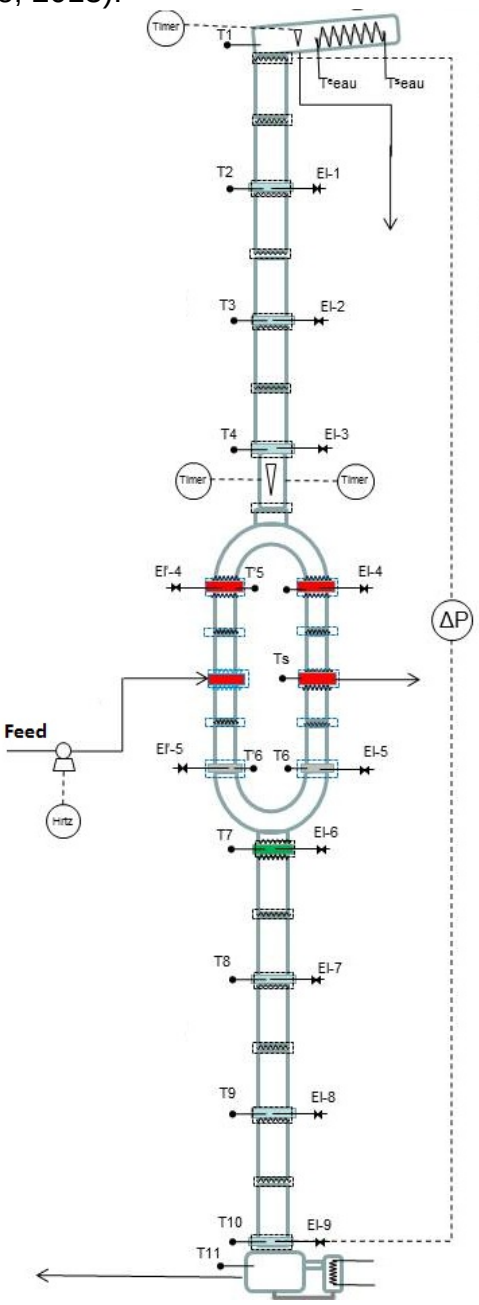

Figure 4: Flowsheet of the pilot plant

In this paper, firstly, the non-reactive mixture will be chosen to verify the procedure design DWC system. Secondly, in the future, the reactive mixture will be investigated with the Katapak packing in the reactive section. A ternary mixture of Methanol, 1-Propanol, and 1-Butanol is chosen for the experiment. The experiment data shows in the table 5.

The results of experiment will be obtained when the temperature points along the pilot remain constant. The model of simulation is as the Figure 5 in which prefractionator and main column take place only separation. Thermodynamic model is NRTL. The temperature and composition profile will be compare between experimental data and simulation as the Figure 5. The comparison shows that simulation results and experimental data are in good agreement with each another.

Table 5: Experiment data

Composition	Feed flowrate (kg/h)	Feed composition (mass fr.)	Liquid split (R_L)	Heat consumption (kW)	Reflux ratio
Methanol	5.14	0.4	0.5	5.17	3
1-Propanol		0.3			
1-Butanol		0.3			

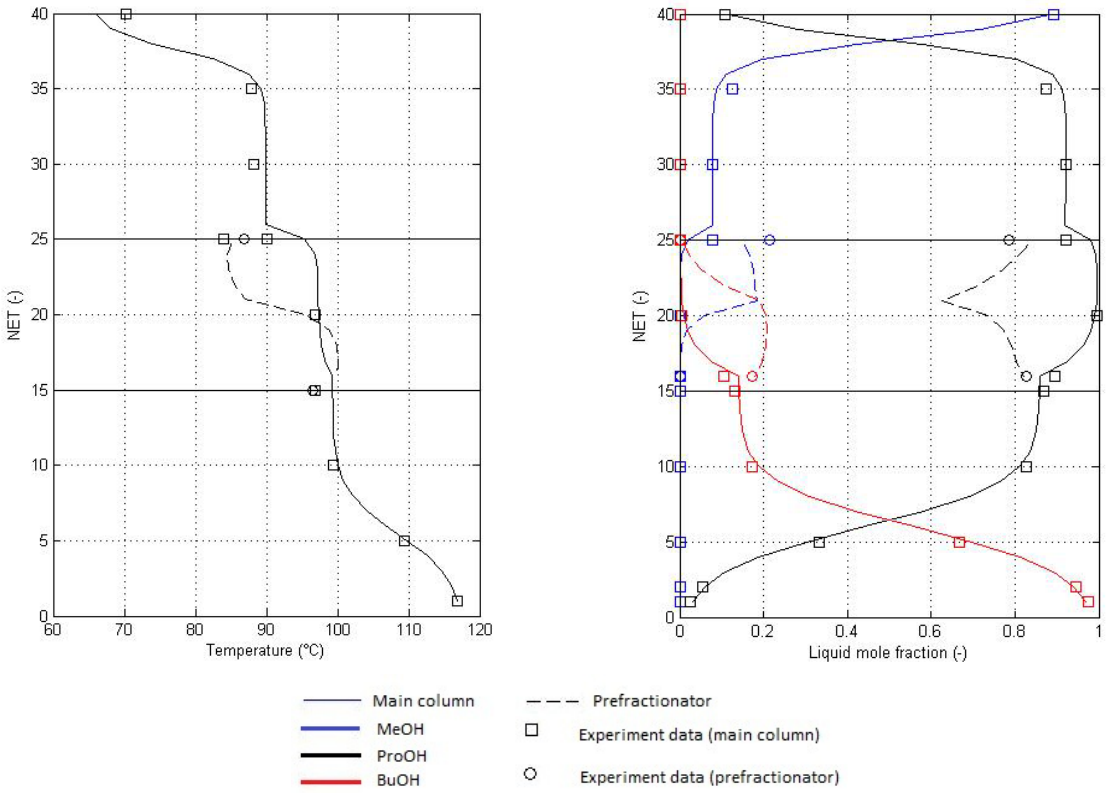

Figure 5: Temperature and composition liquid of simulation and experiment

5. Conclusions

The study presents a shortcut design method for the R-DWC. The result of this study indicates that the approach works well and provides both the basis for preliminary optimization and a good initialization for rigorous simulation. It is a good proof that helps to increase the acceptance of R-DWC system in industrial processes. The work also presents a pilot plant for DWC system and verifies the procedure design DWC system by a non-reactive mixture. In the future, a reactive mixture will be investigated.

References

1. C. Triantafyllou and R. Smith. (1992) 'The design and optimization of fully thermally coupled distillation columns', *Institution of chemical engineering*, vol. 70, no. A2, March, pp. 118 - 132.

2. Domingos Barbosa and Michael F. Doherty (1988), 'Design and minimum reflux calculation for single-feed multicomponent reactive distillation columns', *Chemical Engineering Science,* Vol. 43, No. 7, pp. 1523-1537

3. S. Giessler, et al. (2001), 'Systematic structure generation for reactive distillation processes', *Computer and Chemical Engineering,* 25, pp. 49 – 60.

4. R. Thery, X. M. Meyer, X. Joulia, and M. Meyer. (2005) 'Preliminary design of reactive distillation columns', *Chemical Engineering Research and Design,* vol. 83, Issue 4, pp. 379 – 400.

5. I. Mueller et al. (2007), 'Rate-based analysis of reactive distillation sequences with different degrees of integration', *Chemical Engineering Science,* 62, 7327 – 7335

6. Gerit Niggemann and Georg Fieg (2011), 'Validation of dividing wall column based on experimental data and dynamic simulations: Pilot plant and production scale column', *Industrial & Engineering Chemistry Research,* 51, 931-943.

A hybrid distillation – pervaporation system in a single unit for breaking distillation boundaries in multicomponent mixtures

Javier Fontalvo
Grupo de Investigación en Aplicación de Nuevas Tecnologías, Laboratorio de Intensificación de Procesos y Sistemas Híbridos,
Universidad Nacional de Colombia, Manizales / Colombia - jfontalvoa@unal.edu.co

Abstract
This work presents a theoretical investigation of an integrated pervaporation and distillation column. The pervaporation section consists of hollow fibres, with the separation layer on the outer diameter. Vapour and liquid flow facing the separation layer while the permeate stream is removed from the inside lumen. Several advantages have been identified from the process integration. There is no need for inter-stage heating since the latent heat required for pervaporation is supplied by condensation of the vapour in the pervaporation section. Additionally, vapour induces turbulence in the liquid phase enhancing the mass and heat transfer between the liquid and the membrane surface. In addition, the liquid phase within the column is close to saturated conditions, and thus its components are also close to their maximum driving force for pervaporation at the operation pressure. As a consequence, the membrane area is reduced compared to an Externally Connected Pervaporation-Distillation hybrid System (ECPDS). Due to a higher amount of liquid that is in contact with the membrane than in an ECPDS, the driving force of the transported component is improved, reducing the required membrane area. This investigation, it is shown that the hybrid column is able to overcome the distillation boundaries for multicomponent mixtures. Therefore, the hybrid column can perform separations that are not possible in a single distillation column.
Two case studies of ternary mixtures are analysed. The hybrid system behaviour is studied as function of the membrane area, position of the pervaporation section, membrane wetting, the component fluxes between the liquid and the vapour phases, component fluxes between the liquid and the membrane, and the temperature and concentration axial profiles.

Keywords
Distillation, pervaporation, process intensification, hybrid distillation and pervaporation systems.

1. Introduction

Hybrid processes combining distillation and pervaporation have gained considerable attention in the recent years[1–3]. Pervaporation is especially suitable for the separation of close boiling and azeotropic mixtures, where distillation is energy intensive or requires an auxiliary agent. However, the capital cost of pervaporation processes can be higher than distillation. Hybrid membrane-distillation processes can potentially exploit the advantages of distillation and pervaporation, while overcoming the disadvantages of both[4].

A conventional pervaporation-distillation hybrid system (ECPDS) consists of a distillation column and an externally connected pervaporation module[1,5]. A pervaporation unit consists of a series of pervaporation modules and inter-stage heat exchangers where the retentate flows between stages in liquid phase. Inter-stage heat exchangers are required because the retentate temperature drops due to the permeation and evaporation of the components through the membrane. In general, the pervaporation module can be used in a hybrid distillation system to remove a specific component from a side stream of the distillation column. Otherwise, it can be used as a final treatment stage. Applications for binary mixtures[4,6,7] and multicomponent mixtures[8,9] can be found in literature, where the effect of the membrane properties and operating variables on the hybrid process performance have been discussed.

It has been shown that a retentate stream composed of a mixture of liquid and vapour can reduce the membrane area requirements compared to conventional pervaporation units and membrane savings higher than 40 % can be achieved[10,11]. Also an important CAPEX reduction is expected since the inter-stage heat exchangers are not required. Vapour induces turbulence in the liquid phase within the module, increasing the mass and heat transfer between the liquid and the membrane surface. Simultaneously, the vapour supplies the energy required for the pervaporation process by condensation.

The novel concept is to integrate a pervaporation unit with a liquid-vapour feed and a single distillation column[12] (DPSU, Figure 1a). A pervaporation module with, for example, ceramic hollow fibre membranes, which are coated on the outside, replaces a section of packing or trays in a distillation column (Figure 1). The permeate stream is withdrawn from the inside lumen of the tubes through the column shell and condensed. In a DPSU, the reboiler supplies the required energy for the pervaporation process, while liquid and vapour flow in counter-current in the pervaporation section.

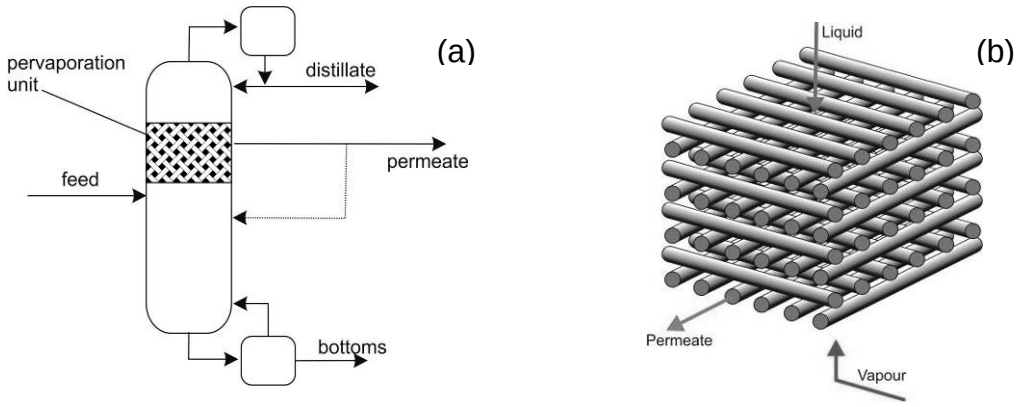

Figure 1. Hybrid distillation-pervaporation system in a single column (a) and membrane packed section in an integrated distillation pervaporation unit (b).

This work shows that in a single column the distillation boundaries can be overcome, making separation of more than two components technically feasible. Unlike ECPDS, a higher driving force is expected in a DPSU since the liquid along the pervaporation section is at or close to saturated conditions and the concentration of the removed component remains higher than in an ECPDS. Two case studies of ternary mixtures are investigated. The influence of different factors is studied such as: the membrane

area, position of the pervaporation section, membrane wetting, and temperature and concentration axial profiles.

2. Results and discussion

The DPSU consists of a pervaporation section and two zones of equilibrium distillation stages (Figure 2a). The equilibrium stage equations (MESH[13]) and the non-equilibrium equations for the pervaporation zone were solved simultaneously by implementing a Newton method[14] in Matlab®. The corresponding nonequilibrium equations are described in Appendix A. For the nonequilibrium zone, the following phenomena were considered: the mass and heat transfer between the vapour and the liquid, the vapour and the membrane, and the liquid and the membrane surface (Figure 2b). A wetting factor is used to take into account the fraction of liquid that is in contact with the membrane surface. Thus, pervaporation occurs on wet membrane surface areas while vapour permeation is carried out on dry areas. The pervaporation section modelled here consists of 3 mm external diameter tubes with the selective layer on the external face arranged with a cross in line configuration[11] with a packing density of 150 m^2/m^3. Permeance for each component in the mixture was considered constant and independent of temperature and concentration, see Table A1 (Appendix A). Previous simulations revealed that for binary mixtures an ECPDS is more convenient that a DPSU, so two cases for ternary mixtures are investigated in this work.

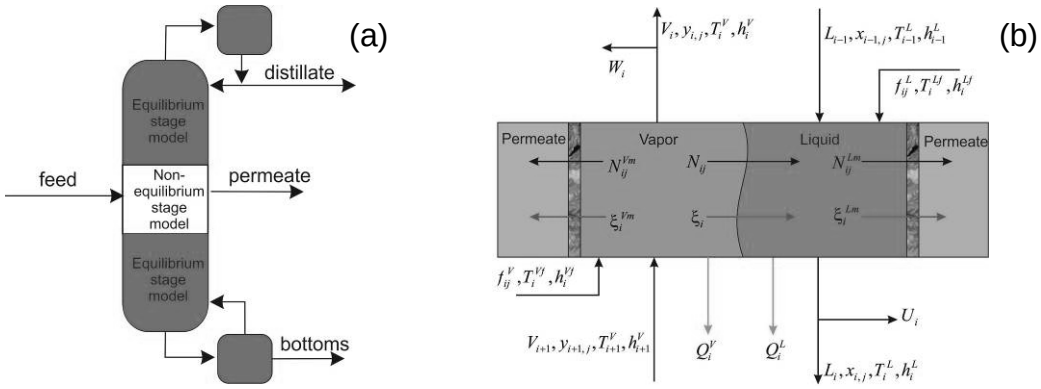

Figure 2. Simulation strategy for a DPSU. Zones were equilibrium and non-equilibrium stage equations were used (a) and sketch of a non-equilibrium pervaporation stage were flows, mass and energy fluxes are indicated (b).

2.1. Methyl Tertiary butyl ether (MTBE), 1-Butene, methanol mixture

MTBE is conventionally produced by the process licenced by Huels AG. Hömmerich and Rautenbach[8] showed that the process can be intensified by using distillation integrated to a methanol selective pervaporation membrane. A side stream is removed from the distillation column, fed to the pervaporation unit and the retentate is recycled to the distillation column.

The liquid molar fraction profile calculated inside the distillation column in the Huels process is shown in Figure 3 for a 23 stages column, feeding at stage 17. The methanol concentration in the MTBE product stream (bottom stream) is close to 7%. Methanol concentration in the bottom stream is strongly reduced by using the DPSU if the pervaporation section is placed at stage 20. The liquid concentration profile changes close to the distillation residue curves (not shown). However, in a DPSU the

concentration profile does not follow the same path because pervaporation is not limited by the liquid-vapour equilibrium.
In an ECPDS has been shown that increasing the side stream flow rate that is fed to the pervaporation unit, it is possible to reduce the methanol concentration in the product stream and the required membrane area[8]. Also, the liquid temperature in an externally connected pervaporation module drops along the membrane making necessary an inter-stage heating system. So, the required membrane area is higher than in a hypothetically isothermal pervaporation module.
In a DPSU the required membrane area is lower than in an ECPDS, mainly for two reasons:

- The whole liquid that flows through the DPSU column is fed to the pervaporation section, and thus the methanol concentration in the pervaporation module is higher than in an ECPDS. Higher methanol concentrations produces higher driving forces for methanol removal through the membrane and so, the required membrane area is lower than in an ECPDS.
- In the pervaporation section of a DPSU while methanol and other components are transported through the membrane, vapour is condensed which supplies mass and energy to the liquid and keeps the liquid temperature close to the bubble temperature. Therefore, the driving force for pervaporation is kept close to its maximum at a given pressure. It has been shown that this effect can reduce the required membrane area by 45%[11].

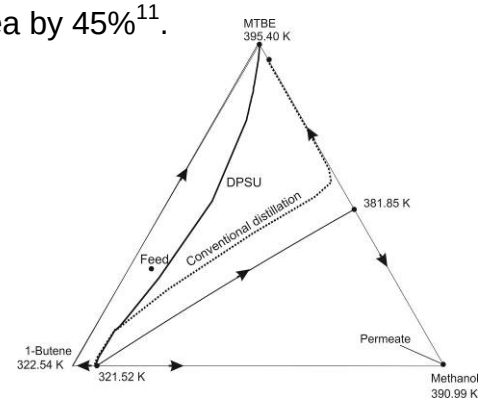

Figure 3. Liquid molar fraction profile calculated for a conventional distillation and a DPSU columns. Simulation conditions are shown in Table A1.

Figure 4 shows that the methanol concentration in the MTBE product stream is the lowest if the pervaporation membrane section is located at stage 20. At this stage, the methanol liquid activity is the highest (not shown) and so is its driving force for its removal by pervaporation. Thus, for the same membrane area a higher amount of methanol is removed. In fact, the qualitative shape of this curve is similar to the liquid methanol activity profile for the conventional distillation shown in Figure 3.

Also, it was found that the molar methanol concentration in the MTBE product is the lowest (0.0027) for a wetting factor of 1 and linearly increases to 0.0048 for a wetting factor of 0. Due to the mass and heat transfer resistance between the liquid and the vapour phase, the methanol activity in the liquid phase is slightly higher than in the vapour increasing the methanol removal by pervaporation than by vapour permeation (not shown).

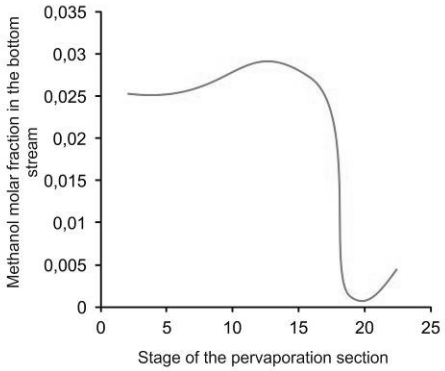

Figure 4. Effect of the pervaporation stage location on the methanol molar fraction in the MTBE product stream (bottom stream). Simulation conditions are shown in Table A1 but the location of the membrane section has been changed.

2.2. Ethanol, Ethyl Acetate, water mixture

The liquid vapour residue curve diagram for the ethanol-ethyl acetate-water mixture shows three distillation boundaries (Figure 5a). In a conventional distillation, the maximum molar ethanol concentration that can be achieved in the bottom stream is approx. 87% if the feed concentration is located in the right area of the composition diagram. If a water selective pervaporation membrane is placed inside the column, it is possible to increase the ethanol concentration in the product stream and also to overcome the distillation boundary depending on membrane area (Figure 5b).

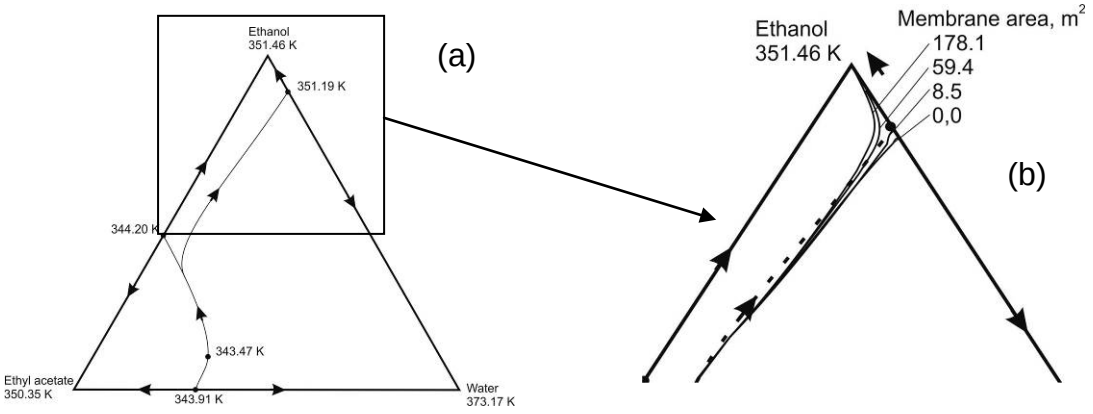

Figure 5. Distillation residue curve map for the ethanol-ethyl acetate-water system at 1 bar (a), liquid molar concentration for a DPSU using several membrane areas. Simulation conditions are shown in Table A1 but with several membrane areas (Table A2).

In general, composition trajectories in distillation do not cross distillation boundaries. Although, Baur *et al*.[15] have shown, by mass transfer considerations, that the composition trajectories in distillation might slightly cross the distillation pinch-point curves. In a DPSU the composition trajectory can completely overcome the distillation boundaries depending on membrane selectivity and area due to that the pervaporation process is independent on the liquid-vapour equilibria. Thus, a DPSU has the potential to obtain product streams with concentrations that in conventional distillation will be not possible.

Other simulations for a different mixture (acetone, methanol, isopropyl alcohol, water) with a DPSU have shown that in the pervaporation section of the column the temperature profile might slightly decrease from top to bottom. Due to the transport of

water through the membrane, the bubble point temperature of the mixture is changed which affects the temperature profile in the column.
The behaviour of DPSU columns requires more system insights and experimental data. The potential applications for mixtures and the possible implications for the separation of multicomponent mixtures are not well understood. This work is an initial approximation to understand the potential and particular behaviour of DPSU columns.

3. Conclusions

This work presents theoretical results of an integrated pervaporation and distillation system within a single column. Compared to conventional hybrid systems where the pervaporation unit is externally connected, several advantages are identified: (1) there is no need for inter-stage heating because the latent heat required for pervaporation is supplied with condensation of the vapour present in the distillation column, (2) vapour induces turbulence in the liquid phase increasing the mass and heat transfer between the liquid and the membrane surface, (3) since the liquid within the column is close to saturated conditions, their components are also close to its maximum driving force for pervaporation at a given pressure, (4) membrane area is reduced compared to an externally connected pervaporation unit (ECPU). (5) The hybrid column is able to overcome the distillation boundaries for multicomponent mixtures and (6) the hybrid column can performed separations that a single distillation column is not able to do.
Results for the Methyl Tertiary butyl ether (MTBE), 1-Butene, methanol mixture show that an optimal methanol separation is achieved if the pervaporation section is located where the methanol activity is at its maximum. Also, the membrane area slightly decreases as the membrane wetting increases. For the Ethanol, Ethyl Acetate, water mixture, it was found that the distillation boundaries can be overcome depending on the membrane area in the pervaporation section.
The DPSU column can perform separations that are not possible in conventional distillation. However, it requires more insight and experimental data to explore the potential applications, to obtain shortcut design methods and to find analysis tools.

Acknowledgements

This work was initially performed at the Eindhoven University of Technology (The Netherlands). I acknowledge prof. J.T.F. Keurentjes, M.A.G. Vorstman and J.G. Wijers for their contributions to this DPSU concept.

Appendix A. Nonequilibrium model for a DPSU and some specific simulation results

The DPSU consists of a pervaporation section and two zones of equilibrium distillation stages (Figure 2a). Liquid and vapour flows, compositions and temperatures as well as component flux through the liquid-vapour, liquid-membrane and vapour-membrane interfaces were calculated by using equilibrium stage equations (MESH[13]) for the zones with ideal stages and nonequilibrium equations for the membrane section of the column. Both, the MESH and the nonequilibrium equations were solved simultaneously by implementing a Newton method[14] in Matlab®. In this model, the input streams to the DPSU can be fed to the equilibrium stage zones or to the membrane section of the column. The equations used for the nonequilibrium zone were:

A1. Mass balance for stage i

$$M_{i,j}^{V} = v_{i,j}(1+r_i^{V}) + N_{i,j}^{Vm} a^{m}(1-\zeta) + N_{i,j} a - f_{i,j}^{V} - v_{i+1,j}$$

$$M_{i,j}^{L} = l_{i,j}(1+r_i^{L}) + N_{i,j}^{Lm} a^{m}\zeta - N_{i,j} a - f_{i,j}^{L} - l_{i-1,j}$$

A2. Mass transfer on the liquid-vapour interface

$$\left(R^{V}\right)_i = \left(N\right)_i - \left[k^{V}\right]_i \left(\frac{\left(v\right)_i}{\sum_{k=1}^{c} v_{i,k}} - \left(y^{I}\right)_i \right) - \sum_{k=1}^{C} N_{i,k} \left(\frac{\left(v\right)_i}{\sum_{k=1}^{c} v_{i,k}} \right)$$

$$\left(R^{L}\right)_i = \left(N\right)_i - \left[k^{L}\right]_i \left[\Gamma\right]_i \left(\left(x^{I}\right)_i - \frac{\left(l\right)_i}{\sum_{k=1}^{c} l_{i,k}} \right) - \sum_{k=1}^{C} N_{i,k} \left(\frac{\left(l\right)_i}{\sum_{k=1}^{c} l_{i,k}} \right)$$

A3. Mass transfer on the membrane surface

$$R_{i,j}^{Lm} = N_{i,j}^{Lm} - \tilde{P}_j \left(\frac{l_{i,j}\gamma_{i,j}P_j^{0}}{\sum_{k=1}^{c} l_{i,k}} - \frac{N_{i,j}^{m}P^{p}}{\sum_{k=1}^{c} N_{i,k}^{m}} \right)$$

$$R_{i,j}^{Vm} = N_{i,j}^{Vm} - \tilde{P}_j \left(\frac{v_{i,j}P^{R}}{\sum_{k=1}^{c} v_{i,k}} - \frac{N_{i,j}^{m}P^{p}}{\sum_{k=1}^{c} N_{i,k}^{m}} \right)$$

Where:

$$N_{i,j}^{m} = (1-\zeta)N_{i,j}^{Vm} + \zeta N_{i,j}^{Lm}$$

A4. Energy balances

$$H_i^{V} = h_i^{V}(1+r_i^{V})\sum_{j=1}^{c} v_{i,j} + \xi_i^{Vm} a^{m}(1-\zeta) + \xi_i^{V} a - h_i^{Vf}\sum_{j=1}^{c} f_{i,j}^{V} - h_{i+1}^{V}\sum_{j=1}^{c} v_{i+1,j} + Q_i^{V}$$

$$H_i^{L} = h_i^{L}(1+r_i^{L})\sum_{j=1}^{c} l_{i,j} + \xi_i^{Lm} a^{m}\zeta - \xi_i^{L} a - h_i^{Lf}\sum_{j=1}^{c} f_{i,j}^{L} - h_{i-1}^{L}\sum_{j=1}^{c} l_{i-1,j} + Q_i^{L}$$

$$H_i^{I} = \xi_i^{V} - \xi_i^{L}$$

$$\xi_i^{V} = h_i^{\bullet V}(T_i^{V} - T_i^{I}) + \sum_{j=1}^{c} N_{ij}\tilde{H}_{i,j}^{V}$$

$$\xi_i^{L} = h_i^{\bullet L}(T_i^{I} - T_i^{L}) + \sum_{j=1}^{c} N_{ij}\tilde{H}_{i,j}^{L}$$

$$\xi_i^{Vm} = \sum_{j=1}^{c} N_{i,j}^{Vm}\tilde{H}_{i,j}^{V}$$

$$\xi_i^{Lm} = \sum_{j=1}^{c} N_{i,j}^{Lm}\tilde{H}_{i,j}^{LV}$$

where $\tilde{H}_{i,j}^{LV}$ is the vapour phase molar enthalpy calculated at the liquid temperature.

A5. Equilibrium equations

$$Q_{i,j}^{I} = k_{i,j}^{I} x_{i,j}^{I} - y_{i,j}^{I}$$

$$S_{i,j}^{VI} = \sum_{j=1}^{c} y_{i,j}^{I} - 1$$

$$S_{i,j}^{LI} = \sum_{j=1}^{c} x_{i,j}^{I} - 1$$

Information used for simulations shown in this work is presented in Table A1. Although for Figure 5 several membrane areas were used the information in this table corresponds to a membrane area of 59.4 m2. Liquid and vapour flows above the membrane section, for separation of an Ethanol-Ethyl acetate-water mixture, are included in Table A2 and correspond to simulation results in Figure 5.

Mixture		MTBE-C4-MeOH	EtOH-EtAc-Water
Permeances (kmol /m^2 h bar)		MeOH: 0.0715	EtAc: 0.00005
		MTBE: 0.0005	EtOH: 0.0005
		C4: 0.00005	Water: 0.8
Type of selective layer membrane		Polymeric: methanol selective	Ceramic (Silica): Water selective
External molar reflux ratio		3.75	1.26
Type of condenser		Partial	Partial
Column pressure (bar)		6	1
Column diameter (m)		1.2	1.2
Number of equilibrium stages above (A) and below (B) the membrane section	A	20	12
	B	3	5
Membrane area (m^2)		17	59.4
Membrane packing density (m^2/m^3)		150	150
Feed Temperature (K)		334.3	344.0
Feed molar flow (kmol/h) Fed as a liquid		MeOH: 6.4	EtAc: 33
		MTBE: 30.1	EtOH: 58
		C4: 63.5	Water: 9
Liquid (L) and vapour (V) flows above the membrane section (kmol/h)	L	287.3	Liquid: 168.8
	V	243.2	Vapour:135.0

Table A1. Permeances, liquid and vapour flows and some specific information for simulations shown in this paper.

Membrane area (m^2)	Liquid (L) and vapour (V) flows above the membrane section (kmol/h)	
	L	V
8.5	168.6	134.9
59.4	168.8	135.0
178.1	169.0	135.1

Table A2. Liquid and vapour flows above the membrane section for simulations shown in Figure 5. Simulations conditions are those shown in Table A1.

Nomenclature

$v_{i,j}$ = Vapour flow from stage i of component j (kmol/h)

r_i = Dimensionless side stream at stage i.

$N_{i,j}$ = Flux through the liquid-vapour interface on stage i of component j (kmol/m^2 h)

$N_{i,j}^m$ = Flux through the membrane in contact with liquid (L) or vapour (V) for stage i of component j (kmol/m^2 h)

a^m = Membrane area (m^2)

a = Liquid-vapour interfacial area (m^2)

$f_{i,j}$ = Feed flow to stage i of component j (kmol/h)

$l_{i,j}$ = Liquid flow from stage i of component j (kmol/h)

ζ = Wetting factor. Fraction of membrane area in contact with liquid.

$(N)_i$ = Column vector of component fluxes for stage i. (kmol/m^2 h)

$[k]_i$ = Matrix of mass transfer coefficients for the liquid (*L*) or vapour (*V*) side for stage i. (kmol/m^2 h)

$\widetilde{P}_j$ = Permeance through the membrane of component j.

$\gamma_{i,j}$ = Activity coefficient of component j in stage i.

P_j^0 = Vapour pressure of component j at the stage temperature.

P^p = Permeate pressure.

P^R = Retentate pressure.

h_i = Entalphy of a liquid (*L*) or vapour (*V*) stream from stage i.

Q_i = Heat removed from a liquid (*L*) or vapour (*V*) phase in stage i.

$[\Gamma]_i$ = Matrix of thermodynamic factors.

$h_i^{\bullet}$ = Heat transfer coefficient in the liquid (*L*) or vapour (*V*) phase on the liquid-vapour interface.

T_i = Temperature of a liquid (*L*) or vapour (*V*) stream from stage i, or at the liquid-vapour interface (I).

$\widetilde{H}_{i,j}$ = Partial molar enthalpy of component j in the liquid (*L*) or vapour (*V*) stream from stage i.

$k_{i,j}^I$ = Distribution coefficient at the liquid-vapour interface.

References

(1) Kreis, P.; Gorak, A. Process Analysis of Hybrid Separation Processes Combination of Distillation and Pervaporation. *Chem. Eng. Res. Des.* **2006**, *84*, 595–600.

(2) Ahmad, S. A.; Lone, S. R. Hybrid Process (Pervaporation-Distillation): A Review. *Int. J. Sci. Eng. Res.* **2012**, *3*, 1–5.

(3) Drioli, E.; Stankiewicz, A. I.; Macedonio, F. Membrane engineering in process intensification—An overview. *J. Memb. Sci.* **2011**, *380*, 1–8.

(4) Fontalvo, J.; Cuellar, P.; Timmer, J. M. K.; Vorstman, M. a. G.; Wijers, J. G.; Keurentjes, J. T. F. Comparing pervaporation and vapor permeation hybrid distillation processes. *Ind. Eng. Chem. Res.* **2005**, *44*, 5259–5266.

(5) Kookos, I. K. Optimal design of membrane distillation column hybrid processes. *Ind. Eng. Chem. Res.* **2003**, *42*, 1731–1738.

(6) Sommer, S.; Melin, T. Design and optimization of hybrid separation processes for the dehydration of 2-propanol and other organics. *Ind. Eng. Chem. Res.* **2004**, *43*, 5248–5259.

(7) Pressly, T. G.; Ng, K. M. A break - Even analysis of distillation-membrane hybrids. *AIChE J.* **1998**, *44*, 93–105.
(8) Hommerich, U.; Rautenbach, R. Design and optimization of combined pervaporation / distillation processes for the production of MTBE. *J. Memb. Sci.* **1998**, *146*, 53–64.
(9) Lu, Y.; Zhang, L.; Chen, H. L.; Qian, Z. H.; Gao, C. J. Hybrid process of distillation side - connected with pervaporation for separation of methanol - MTBE - C4 mixture. *Desalination* **2002**, *149*, 81–87.
(10) Fontalvo, J.; Vorstman, M. a. G.; Wijers, J. G.; Keurentjes, J. T. F. Heat supply and reduction of polarization effects in pervaporation by two-phase feed. *J. Memb. Sci.* **2006**, *279*, 156–164.
(11) Fontalvo, J.; Vorstman, M. a. G.; Wijers, J. G.; Keurentjes, J. T. F. Separation of Organic−Water Mixtures by Co-current Vapor−Liquid Pervaporation with Transverse Hollow-Fiber Membranes. *Ind. Eng. Chem. Res.* **2006**, *45*, 2002–2007.
(12) Fontalvo, J.; Keurentjes, J. T. F.; Wijers, J. G.; Vorstman, M. A. G. Pervaporation process and apparatus for carrying out same **2007**, *WO/2007/03*, -.
(13) Seader, J. D.; Henley, E. J. Separation process principles. **2006**, *Second*, -.
(14) Powers, M. F.; Vickery, D. J.; Arehole, A.; Taylor, R. A nonequilibrium stage model of multicomponent separation processes-V. Computational methods for solving the model equations. *Comput. Chem. Eng.* **1988**, *12*, 1229–1241.
(15) Baur, R.; Krishna, R.; Taylor, R. Influence of mass transfer in distillation feasibility and design. *AIChE J.* **2005**, *51*, 854–866.

Experimental Investigation of the Synthesis of the Environmental Friendly Fuel Additive GTBE by Reactive Distillation

Hilke-Marie Lorenz, René Heiduschke, Patrick Schiffmann, Jens-Uwe Repke
TU Bergakademie Freiberg, Freiberg, Germany

Abstract

Reactive distillation (RD) is a hybrid process where reaction and distillation are combined in one column. Due to the limitation of the chemical equilibrium, both esterification and etherification reactions are typical reactions for RD processes. The tert-butyl ether of glycerol (GTBE) are promising fuel additives. The synthesis of GTBE can be realized in two different reaction pathways: The etherification of glycerol with isobutene or tert-butyl alcohol, respectively. The main disadvantage of the first way is the need of a high reaction pressure. In this work a feasibility study for the realization of a RD process for the GTBE synthesis at ambient pressure is conducted. Due to the poor data basis for this mixture (e.g. reaction kinetics, equilibrium data) several preliminary investigations were necessary. Based on these results a RD pilot plant was designed and built. Challenging tasks in the design were the gaseous unwanted by-product isobutene and the high boiling point of glycerol (290°C). The feasibility of the RD process has been shown in first experimental runs.

Keywords
Reactive distillation, tert-butyl ether of glycerol, biodiesel, process intensification, bio-based products, hybrid process

1. Introduction

Glycerol tert-butyl ether (GTBE) is considered to be an alternative for the ground water imperiling fuel additive ETBE/MTBE (octane booster) due to the advantageous environmentally friendly properties of GTBE. The used reactant glycerol is a by-product of the biodiesel production and its availability has increased strongly in the last years due to the rising production of biodiesel.

GTBE is a mixture of higher tert-butyl ethers (di- and triethers) of glycerol. The GTBE synthesis is currently in the focus of numerous research activities. The glycerol conversion is limited by the chemical equilibrium. There are two different reaction pathways described in literature: The etherification of glycerol (GLY) with isobutene (IB) or with tert-butyl alcohol (TBA). The etherification of glycerol to mono- (ME), di- (DE) and tri-tert-butyl ethers (TE) can be realized with isobutene (IB) under high pressure and under the presence of homogeneous or heterogeneous acid catalysts (Behr and Obendorf, 2002). An experimental study (Karinen and Krause, 2006) confirmed that two different isomers of ME and DE are primarily formed. A continuous process for the synthesis of GTBE using IB as reactant is described in (Behr and Kleyensteiber, 2013).
Klepáčová et al. (2005), however, describe the catalyzed etherification of glycerol and TBA using acid ion exchangers in an autoclave at low pressure. The multi-stage etherification reaction network of GTBE and TBA to primary (1), secondary (2) and

tertiary (3) ethers is shown in Figure 1. Beside the wanted etherification to these products, the dehydration of TBA to IB (4) takes place (Pico et al., 2012).

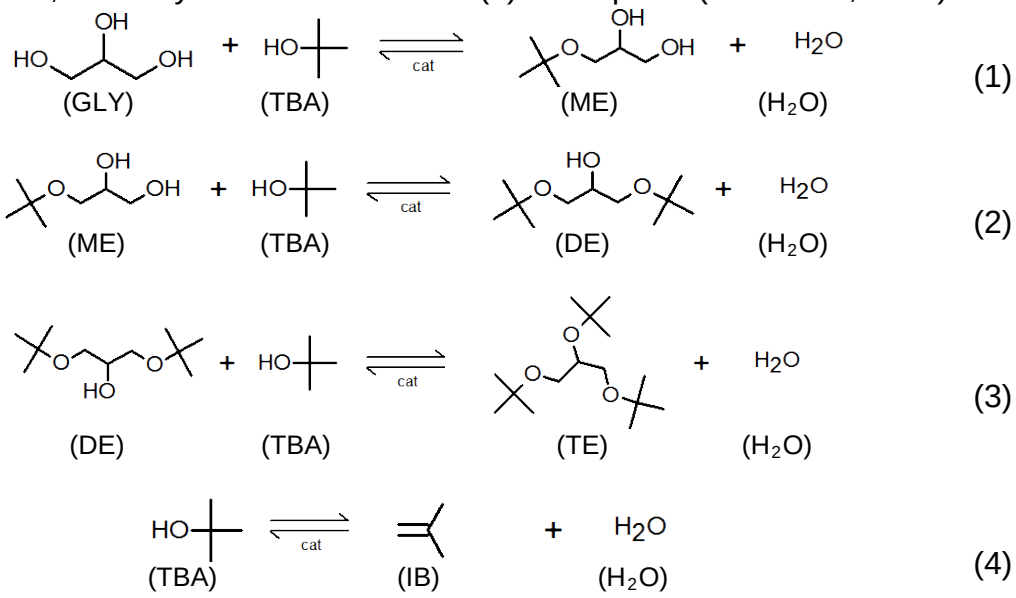

Figure 1. Reaction network for the etherification of glycerol and TBA (Pico et al., 2012).

The comparison of the two different reaction pathways (IB or TBA as reactant) shows a selectivity higher than 60% with IB, and less than 30% with TBA at autogenous pressure and temperatures of 60°C and 90°C, respectively (Klepáčová et al., 2005). In order to make the synthesis of GTBE economically attractive using TBA as reactant, reactive distillation (RD) can be used, which is a well known process alternative to overcome the limits of chemical equilibria, due to the continuous removal of the products. Thus, the reaction selectivity can be increased. Etherification reactions in RD processes are well established, as demonstrated by the synthesis of MTBE (Sundmacher et al., 1999). The experimental etherification of glycerol with TBA to GTBE in a reactive distillation column in lab scale is described in (Kiatkittipong et al., 2011), where conversions of glycerol of up to 80 % and selectivities between 40 and 60 % can be reached. Vlad and Bildea (2012) simulated a reactive distillation process for the GTBE synthesis in Aspen Plus™, where a total conversion of the reactants was reached.

In this work, an experimental investigation of the synthesis of GTBE in a reactive distillation process using glycerol and TBA as reactants in pilot-plant scale is presented. Physical properties such as boiling points and VLE are necessary to design the RD process and conduct the feasibility study (Shah et al., 2012). Neither the boiling points of DE and TE are known, nor are VLE data available. More than that, DE and TE are not yet commercially available. Nevertheless, the boiling point curve of the reaction mixture has been experimentally investigated. Based on these results the RD process has been designed in pilot-plant scale.

2. Preliminary investigation

As mentioned before, preliminary investigations in lab scale are necessary to design a RD column for the GTBE synthesis. Due to the experimental results of batch and semi batch experiments (2.1) the maximal assumed formation of the unwanted explosive IBU can be determined.

Due to unknown equilibrium behavior (VLE/LLE) of the mixture a batch distillation (2.2) is carried out to measure the boiling characteristics of the mixture.
TBA (Evonik industries) and bio based glycerol (Glacon Chemie GmbH) are used as chemicals with the catalyst Amberlyst^{TM} 36 (Dow Chemical*)*.

2.1 Reaction experiments

The batch reaction of glycerol and TBA (Figure 1) is performed in a 3 L lab-scale reactor (Figure 2a). The reactants as well as the heterogeneous catalyst are charged in the vessel. The batch reaction is performed at a temperature of 70 °C and ambient pressure. The molar ratio of TBA and glycerol is 2. (Schiffmann and Repke, 2013)

The dependency of the dehydration of TBA to IB (Figure 1) on the TBA concentration is investigated with a comparable semi batch reaction. Glycerol and the catalyst (Amberlyst^{TM} 36, 13,2 wt%) are charged in a 600 ml autoclave (Figure 2b) and TBA is fed to the mixture in 30 min steps. The overall molar ratio of TBA and glycerol is 3, which is higher than in the batch experiments.

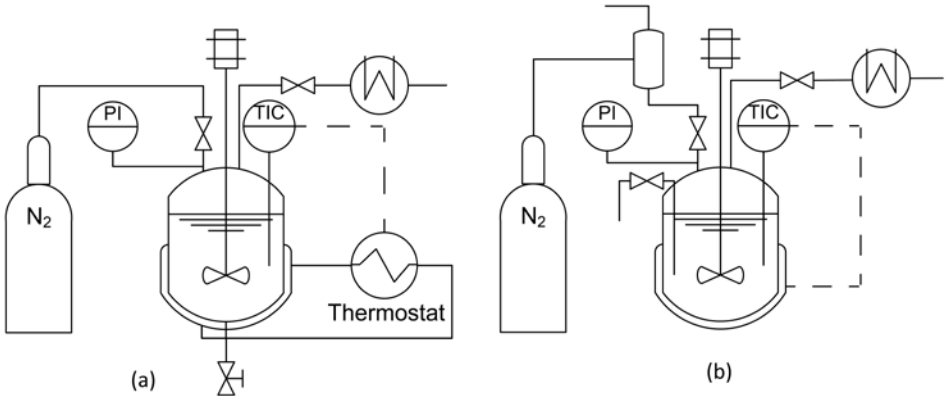

Figure 2. Experimental setup for the batch (a) and semi-batch (b) investigation.

2.2 Batch distillation experiments

In order to determine the boiling temperatures of a mixture of the reactants and the products a batch distillation is carried out. The existence of low boiling azeotropes can be determined, and further the boiling point of the glycerin-ether mixtures can be measured.

Behr and Obendorf (2002) mentioned a miscible gap between glycerol and DE and TE. For the mixture with TBA no LLE data for the quaternary LLE (Glycerol, TBA, DE, TE) were available. Water and TBA form two liquid phases with a critical upper solution temperature of 50°C. All samples are checked with regard to a phase separation.

2.3 Results and discussion

2.3.1 Reaction experiments

Figure 3 shows the selectivity of the desired products ME, DE and TE based on TBA over the reaction time for the batch reaction experiments. It can be seen that the formation of the mono ether is very fast compared to the reaction to the higher ethers. The selectivity of IBU at the end of the reaction is higher than 50%.

Only one sample after four hours (end of the reaction) is taken in the conducted semi batch experiment. A selectivity of IB of about 31,8% can be determined. Due to this decreasing selectivity of IB still a lower formation of IB in a RD process can be assumed.

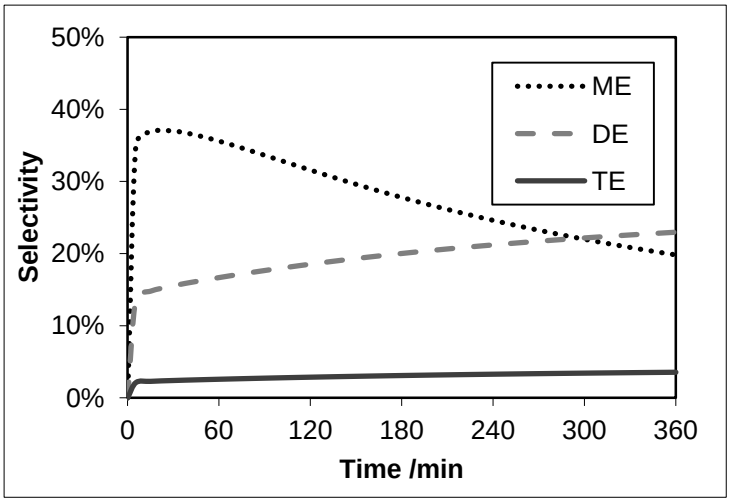

Figure 3. Selectivity of ME, DE and TE (based on TBA); fitted kinetic (Schiffmann and Repke, 2013); batch reaction experiments. Selectivity of IB represents the difference to 100 %.

2.3.2 Batch distillation experiments

For the batch distillation the reaction mixture of the investigated semi batch reaction experiments is used. Figure 4 shows the temperature curve of the distillate and the bottom over the distillation time. After the removal of the first fraction (IB) the binary TBA-Water azeotrope is distilled, small amounts of the diether are also found in the distillate. After four hours, measurable amounts of the triether can be found in the distillate (increasing distillate temperature). After the bottom temperature has reached 220°C the distillation has been stopped. All distillate fractions are homogenous, only the bottom product is forming two liquid phases at ambient temperature.

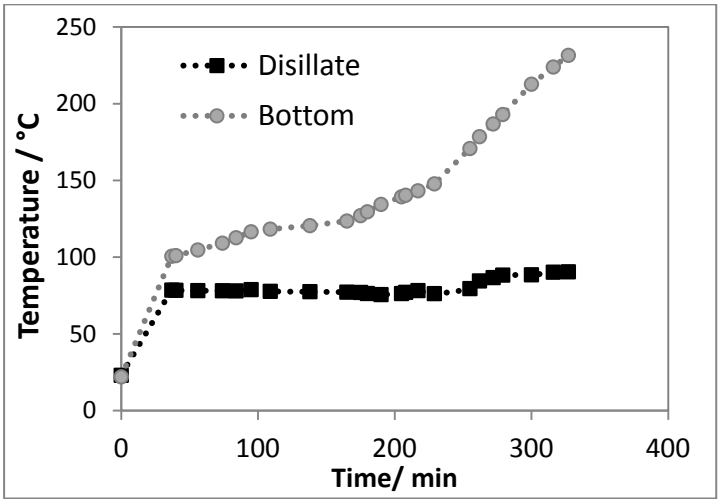

Figure 4. Temperature curve of distillate and bottom in the batch distillation of GTBE reaction mixture.

Based on these results a rough design of the configuration of the RD column can be assumed. The height of the column is limited by the building height. Due to the smaller amount of IBU formed in the semi batch, higher selectivity of GTBE in the RD is expected compared to the batch reaction. The formation of two liquid phases can be noticed only at low temperature. Due to the higher temperatures in the RD column, a homogenous liquid phase in the column is expected.

3. Design of the pilot plant reactive distillation column

Figure 5b shows the resulting column configuration of the pilot plant reactive distillation setup. Table 1 gives an overview over important column parameters. The column internals are made of hastelloy (Sulzer BX packings and Sulzer Katapack with Amberlyst^{TM} 36 as heterogeneous catalyst). The reaction part is situated in the stripping section; in the enriching section the separation stages are placed. The higher boiling reactant glycerol is fed above the reaction section, the lower boiling TBA is fed in the middle of the reaction section. The normal boiling point of glycerol is 290°C, which is higher than the maximal admissible temperature of the materials and the decomposition temperature of glycerol. Hence, no separation section is realized at the bottom of the column. The column features a partial condenser and a torch for the combustion of the non-condensed IB. First experimental runs demonstrate the feasibility of the process and will be shown in the presentation.

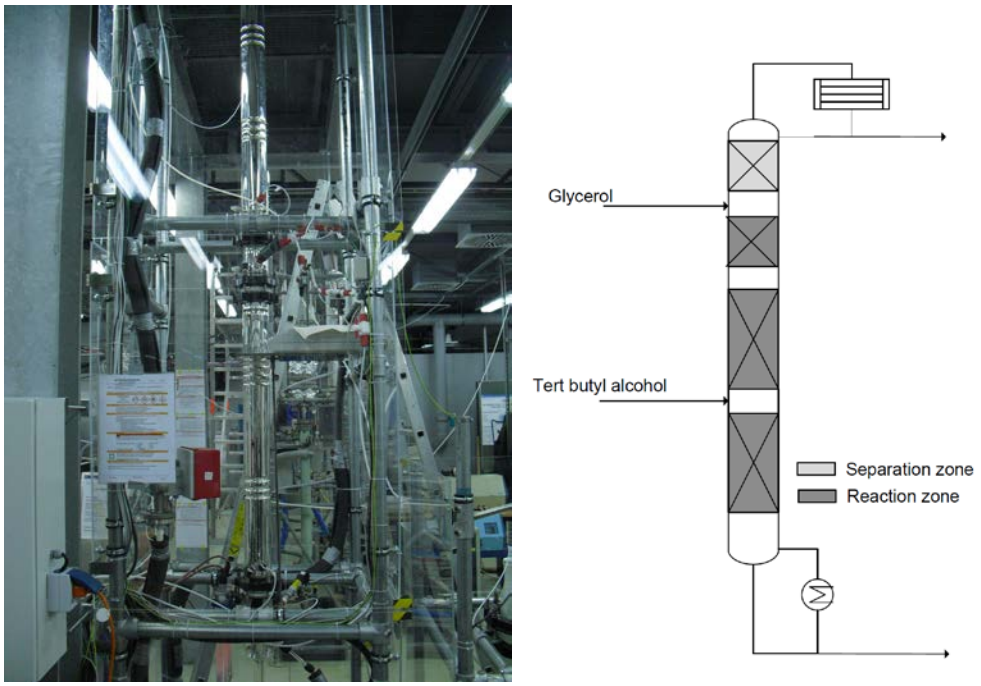

Figure 5: Experimental setup for the reactive distillation investigation (a), configuration of the RD column (b).

Table 1. Parameters of RD column

Total height	m	5.0
Packing height	m	2.4
Diameter	mm	50
Reboiler duty	kW	2.0
Separation zone	m	0.4
Reaction zone	m	2.0

4. Conclusions and outlook

The synthesis of GTBE from glycerol can be realized with IB or TBA. The lab-scale reaction of glycerol and TBA was performed at ambient pressure in batch and semi batch mode. Compared to the batch reaction a higher selectivity has been observed in the semi batch reaction. Due to the unknown LLE and VLE data of the reaction components, a batch distillation was performed. A clear separation between the

water/TBA azeotrope and the glycerin/ether fraction was demonstrated. Two liquid phases were only present at ambient temperature. Based on these results a RD column configuration was developed and a pilot-plant RD process was built.
The experimental results of the RD process will be discussed. The influence of process variables, such as the reactant ratio, reflux ratio and reboiler duty will be pointed out.
Based on the experimental results a simulation of a RD process for the GTBE synthesis in CHEMCAD^{TM} will be carried out.

Acknowledgements
We gratefully acknowledge Evonik Industries and Glaconchemie GmbH for the kind supply of the chemicals.

References

A. Behr, A. Kleyensteiber**,** 2013, Method for continuously producing tertiary butyl ethers of glycerol, U.S. Patent, US2013/0031829 A1, 7. Feb. 2013

A. Behr, L. Obendorf, 2002, Development of a process for the acid-catalyzed etherification of glycerine and isobutene forming glycerine tertiary butyl ethers, Engineering in Life Sciences, 2, 7, 185-189

R. L. Grob, E. F. Barry, Modern Practice of Gas Chromatography, John Wiley & Sons, Edition 4, 25. June 2004, Hoboxen (New Jersey), 978-0471229834,

F. W. Jones, 1998, Estimation of Flame-Ionization Detector Relative Response Factors for Oligomers of Alkyl and Aryl Ether Polyethoxylates using the Effective Carbon Number Concept, Journal of Chromatographic Science, 36, May, 223-226

R. S. Karinen, A. O. I. Krause, 2006, New biocomponents from glycerol, Applied Catalysis A: General, 306, 128-133

W. Kiatkittipong, P. Intaracharoen, N. Laosiripojana, C. Chaisuk, P. Praserthdam, S. Assabumrungrat, 2011, Glycerol ethers synthesis from glycerol etherification with tert-butyl alcohol in reactive distillation, Computers & Chemical Engineering, 35, 10, 2034-2043

K. Klepáčová, D. Mravec, M. Bajus, 2005, Tert-Butylation of glycerol catalysed by ion-exchange resins, Applied Catalysis A: General, 294, 141–147

M. P. Pico, A. Romero, S. Rodríguez, A. Santos, 2012, Etherification of Glycerol by tert-Butyl Alcohol Kinetic Model, Industrial & Engineering Chemistry Research. 51, 9500−9509

P. Schiffmann, J.-U. Repke, 2013, Production and Purification of Glycerol based Fuel Additives Combination of synthesis and pervaporation, Presented at 9th European Congress of Chemical Engineering together with 2nd European Congress of applied Biotechnology, The Hague, Netherlands, April 21-25, 2013

M. Shah, A. A. Kiss, E. Zondervan, A. B. de Haan, 2012, A systematic framework for the feasibility and technical evaluation of reactive distillation processes, Chemical Engineering and Processing: Process Intensification, 60, 55-64

K. Sundmacher, G. Uhde, U. Hoffmann, 1999, Multiple reactions in catalytic distillation processes for the production of the fuel oxygenates MTBE and TAME: analysis by rigorous model and experimental validation, Chemical Engineering Science, 54, 13-14, 2839-2847

R. Thery, X. M. Meyer, X. Joulia, M. Meyer, 2005, Preliminary Design of Reactive Distillation Columns, Chemical Engineering Research and Design, 83, 4, 379-400

E. Vlad, C. S. Bildea, 2012, Reactive distillation - a viable solution for etherification of glycerol with tert-butyl alcohol, Chemical Engineering Transactions, 29, 589-594

Temperature effect on the CO_2 absorption using ILs

Gomez-Coma, L; Garea, A; Irabien,
Chemical and Biomolecular Engineering. Universidad de Cantabria. Santander (Spain)

Abstract

Post-combustion process based on Ionic liquids (ILs) and a membrane contactor have emerged as new attractive alternative to traditionally systems because of their zero emission solvent features compared to amines and their controlled interfacial area and independent control of gas and liquid flow rates respectively [1-3].

The aim of the present work is to describe the temperature effect on efficient in hollow fibre membrane contactor using the ionic liquid 1-ethyl-3-methylimidazolium acetate, [emim][Ac].

The temperature ranges from 291 to 348K. A polysulfone hollow fibre membrane contactor was used where the IL flow through the shell side and the gas flows counter-currently on the inside of the hollow fibres. The gas stream has a typical composition of post-combustion processes including CO_2 (15%) and N_2.

The design of the CO_2 removal process by non-dispersive absorption using ionic liquids requires the study of the temperature influence in the efficiency improvement when the chemical reaction appears to be important.

Keywords
CO_2 capture; temperature; ionic liquid (IL), Polysulfone membrane contactor

1. Introduction

Research new strategies to mitigate the climate change is a major concern in recent years. The present work is focused on post-combustion capture. This process route is ideally suitable for conventional power stations and energy conversion systems. CO_2 at low partial pressure is separated from the gas stream after the fuel has been burned completely [4]. The flue gas from a typical post-combustion process is composed by 10-15% CO_2, 70-75% N_2 and lower concentrations of other components. The temperature reached in this type of system is between 313 to 348 K [5].

For this purpose, the hollow fibre membrane contactors have been proposed as a way to capture carbon dioxide and so reduce greenhouse gas impacts from fossil fuels in industrial processes. The main membrane contactors characteristics are a high surface area per unit volume, a controlled interfacial area and an independent control of gas and liquid flow rates respectively. As solvents, ionic liquids (ILs) have emerged as new attractive alternative solvents because of their zero emission features compared to amines [1-3].

The overall mass transfer behavior for gas absorption into different absorbents liquids appears to be important for the process design. Some studies are reported for different hollow fiber membrane contactor [1], but there is a lack of data for the temperature influence.

The study of the temperature effect in the non-dispersive absorption of CO_2 was carried out in a polysulfone hollow fiber membrane contactor using the ionic liquid [emim][Ac].

2. Results and discussion

2.1 Materials

A polysulfone hollow fiber membrane contactor in parallel configuration was supplied by VWR International Eurolab, S.L. (Spain). The main characteristics of this system are shown in Table 1. Carbon dioxide 99.7 ± 0.01 vol.% and pure nitrogen 99.999 ± 0.001 vol.% were purchased from Air Liquide (Spain). The ionic liquid was supplied by Sigma Aldrich. The 1-Ethyl-3-methylimidazolium acetate [emim][Ac] (≥90%) was chosen because of its high CO_2 solubility. To ensure that the ionic liquid is suitable for our process despite its relatively low purity, solubility rates were measured and, compared with literature data [6], similar values were obtained.

2.2 Experimental setup

The experimental setup is shown in figure 1. The feed gas mixture stream contains 15 vol.% CO_2 and N_2 (rest to balance) and it was adjusted by means of a mass flow controller (Brook instrument MFC 5850, Emerson Process Management Spain) that flows through the inside of the hollow fibers. The liquid absorbent flows counter-currently in a closed circuit through the shell side. The IL was pumped from the storage tank. Control and measurement in the liquid line (50 mL min^{-1}) was carried out

with a digital gear pump (Cole Parmer Instrument Company, Hucoa-Erloss S.A, Spain). Membrane contactor and IL were kept under isothermal conditions using an oven. Experiments were carried out from room temperature (291 K) to 348 K. Each experiment was replicated three times under the same operating conditions and the average value was calculated. The Gas flow rate was 70 mL min-1.

2.3 CO_2 Absorption

The CO_2 removal efficiency is defined as

$$Efficiency\ (\%) = \left(1 - \frac{C_{CO_2,out}}{C_{CO_2,in}}\right) \cdot 100 \tag{1}$$

Figure 2 shows the experiments at different temperatures with a gas flow rate of 70 mL min^{-1}, using the 1-Ethyl-3-methylimidazolium acetate [emim][Ac]. The outlet concentration dimensionless of carbon dioxide was calculated for each experiment at pseudo-steady-state, that ranged between 0.7-0.55.

The CO_2 removal efficiencies were calculated from inlet and outlet CO_2 concentrations for the absorption experiments (Table 2). From the obtained results a remark is pointed out, the temperature influence is significant because of the efficiency values from 291K to 348 K: 30 to 45%.

2.4 Overall mass transfer calculations

The mass transfer flux of carbon dioxide has been calculated according to the equation

$$\mathrm{N_{CO_2,g}} = \frac{\mathrm{Q_g}}{\mathrm{A}}\left(\mathrm{C_{CO_2,in}} - \mathrm{C_{CO_2,out}}\right) = \mathrm{K_{overall}}\,\frac{\Delta \mathrm{ylm}\ \mathrm{P_T}}{\mathrm{RT}} \tag{2}$$

In the steady state CO_2 fluxes are equal in the gas and liquid. The overall mass transfer $K_{overall}$ can be experimentally evaluated from the flux through the membrane and concentration gradient. Qg is the gas flow rate ($m^3\ s^{-1}$), A is the membrane area (m^2), PT is the total pressure in the gas phase and Δylm is the logarithmic mean of the driving force based on gas phase molar fractions. Taking into account the carbon dioxide concentration in the inlet ($y_{CO2,in}$) and the outlet ($y_{CO2,out}$) of the Ps membrane contactor, assuming that CO_2 concentration in the solvent is very far from the saturation in the experiments, Δylm can be calculated as:

$$\Delta ylm = \frac{(y_{CO_2,in}) - (y_{CO_2,out})}{ln((y_{CO_2,in})/(y_{CO_2,out}))} \tag{3}$$

Table 3 shows the overall mass transfer coefficients were obtained at different temperatures. The Koverall values increase significantly as the temperature rises: an increase of 60% in the temperature range 291-348 K

3. Conclusions

A polysulfone hollow fiber membrane contactor has been used to study the absorption of CO_2 in ionic liquid at different temperatures. The gas stream has a typical composition of post combustion processes including CO_2 (15%) and N_2. The ionic liquid 1-Ethyl-3-methylimidazolium acetate [emim][Ac] was used.

Higher values of CO_2 flux are achieved when the ionic liquid [emim][Ac] at higher temperature. An increase of 60%of the overall mass transfer coefficient is obtained when the temperature increases from 291 to 348 K.

The temperature effect is related to the chemical reaction. For this reason, a further work studying the enhancement factor, E_A, which determines the absorption rate of the reactant and quantifies how the mass transfer is enhanced by the presence of a chemical reaction, is necessary.

Acknowledgements
This research has been funded by the Spanish Ministry Economy and Competitiveness (Project ENE2010-14828).

Refereces

[1] J. Albo, P. Luis, A. Irabien. Desalin. Water Treat. 27, 54-59, (2011).
[2] J. Albo, P. Luis, A. Irabien. Ind. Eng. Chem. Res. 49, 11045-11051 (2010).
[3] P. Luis, T.V. Gerven, B.V. Bruggen. Prog. Energ. Combust. 38, 419-448 (2012).
[4] D.W. Bailey, P.H.M. Feron. Oil Gas Sci. Technol. 60, 461-474, (2005).
[5] M. Ramdin, T.W. De Loos, T.J.H. Vlugt. Ind. Eng. Chem. Res. 51, 8149-8177, (2012).
[6] M.B. Shiflett, A. Yokozeki. J. Chem. Eng. Data 54, 108-114, (2009).

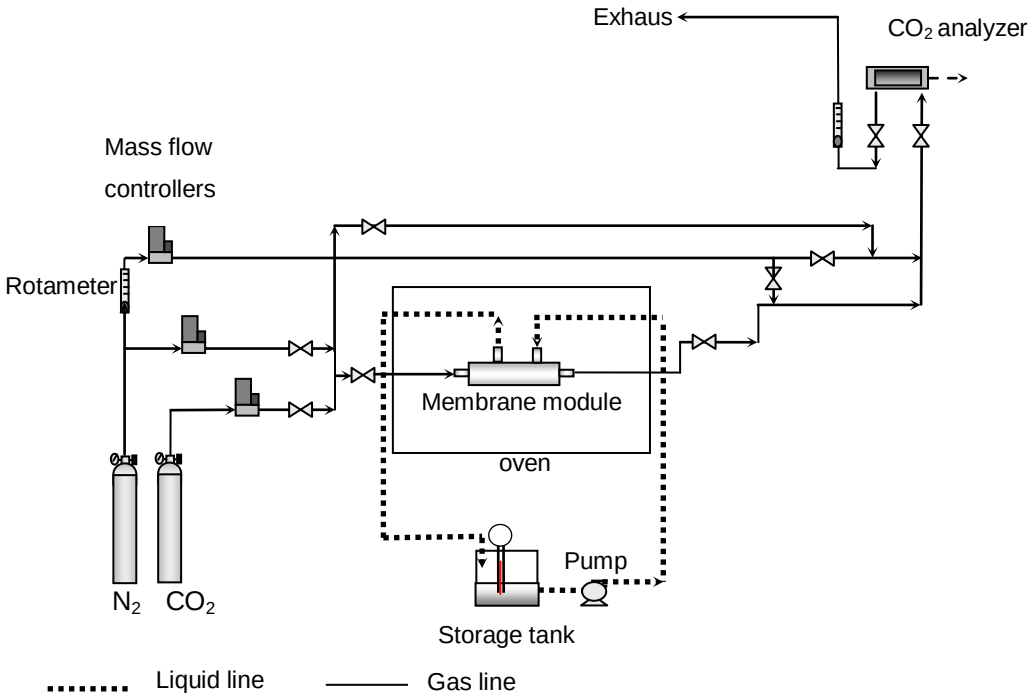

Figure 1

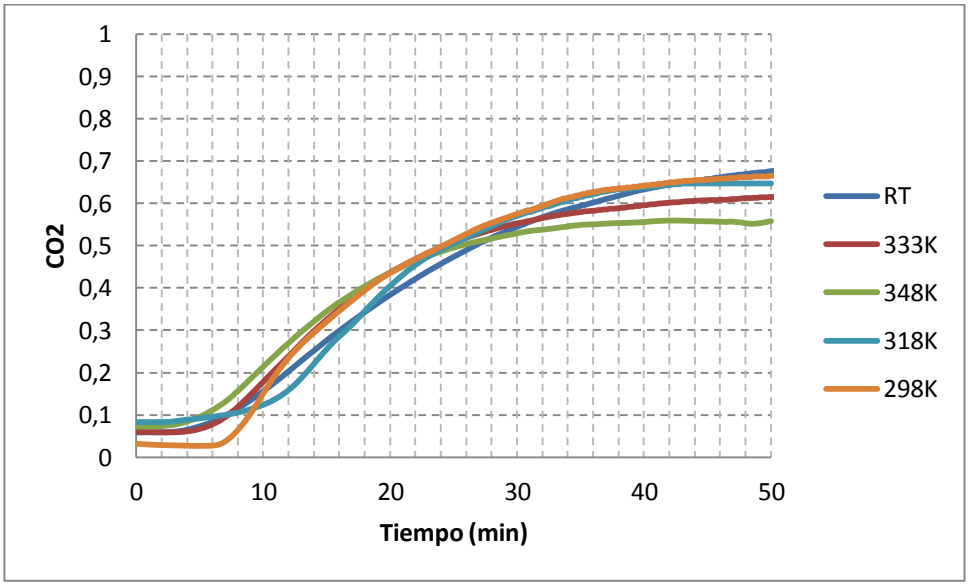

Figure 2

Table 1 Hollow fiber membrane contactor characteristics.

Membrane material	Polysulfone
Fiber o.d. d_0, (m)	1.3×10^{-3}
Fiber i.d. d_i, (m)	7×10^{-4}
Fiber length, L (m)	0.347
Number of fibers, n	400
Effective inner membrane area, A (m^2)	0.18
Membrane thickness, δ (m)	3×10^{-4}
Porosity (%)	43
Packing factor	0.43
Tortuosity[a]	2.33

aAsummed as 1/ε

Table 2 Experimental efficiency of [emim][Ac]

No.	T (K)	Efficiency (%)
1	291	30
2	298	33
3	318	37
4	333	40
5	348	45

Table 3 Experimental Koverall [emim][Ac].

No.	T (K)	$K_{overall}$ (10^6 m s^{-1})
1	291	2.2
2	298	2.6
3	318	3.2
4	333	3.4
5	348	3.5

Poster Programme

Complexities of the design of distillation based separation: extractive heterogeneous-azeotropic distillation

Andras Jozsef Toth[1], Agnes Szanyi[1], Peter Mizsey[1,2]*
[1] Budapest University of Technology and Economics, Department of Chemical and Environmental Process Engineering, P.O. Box 1521, H-1111, Budapest, Budafoki Street 8., Hungary;
[2]University of Pannonia, Research Institute of Chemical and Process Engineering, P. O. Box 125, H-8200, Veszprem, Egyetem Street 10., Hungary
**Corresponding author. E-mail address: andras86@kkft.bme.hu*

Abstract

The distillation based separation can be extremely complex if highly non-ideal mixtures are to be separated. In spite of different successfully applied unit operations there is still possibility to improve distillation technique and widen its toolbar. A new improvement in this area is the introduction of the extractive heterogeneous-azeotropic distillation. This unit operation includes the merits of the extractive and heterogeneous-azeotropic distillations in one unit without an extra material addition. In spite of the complexity of this unit operation it can be efficiently applied and complex separation technologies can be simplified with its application.

The separations of ternary and quaternary mixtures from the fine chemical industry show both in the modelled and the experimental results that the extractive heterogeneous-azeotropic distillation can be successfully applied.

The comparison of the modelled and experimental results in the case of concentrations close to high and/or zero purity concentrations shows differences between modelled and measured values. This highlights the paramount importance of the experiments if special extra fine chemicals with almost no impurities e.g. pharmacopoeial quality are to be produced by special distillation technique.

Keywords

complexities of design, non-ideal mixtures, extractive heterogeneous-azeotropic distillation

1. Introduction

Distillation is the most widespread separation process in the chemical industry. The components of a liquid mixture are separated on the basis of the difference in their volatilities. As the energy demand of the distillation is very high, the optimal design and operation of the process are important questions, both economically and environmentally [1].

If the separation of highly non-ideal mixtures should be made, that is quite often in fine chemical industries, where the separation of usually azeotropic mixtures and then fine chemical quality should be produced, it is extremely difficult to pay significant attention to the energetic and environmental issues. Such highly non-ideal mixtures usually contain different kinds of alcohols, esters, aldehydes, ethers and water. These compounds already predict that serious problems arise at their distillation based separation.

The separation of an ethanol, ethyl acetate, isopropyl acetate and water containing quaternary mixture from the fine chemical industry [2] called the attention of the necessity for the development of the distillation based separation that comprises the merits of different separation solutions.

A new hybrid separation alternative, the so called extractive heterogeneous-azeotropic distillation (EHAD) introduced by Szanyi et al. [3-5] and Szanyi [6] that combines the advantages of the extractive and the heterogeneous-azeotropic distillations (Figure 1). The heterogeneous-azeotropic option assumes that water is present in the mixture and limited immiscibility exists.

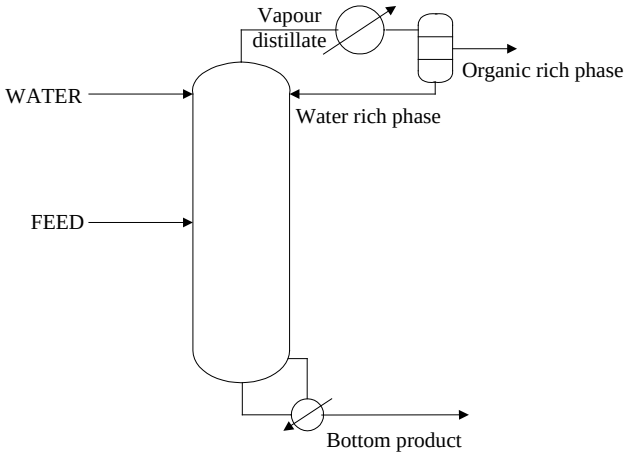

Figure 1 The extractive heterogeneous-azeotropic distillation

The EHAD differs from the heteroextractive distillation [7] since no new azeotrope is formed, namely the extractive agent/entrainer is water and this component is already present in the mixtures to be separated. Moreover, the extractive and relative volatility changing effect of the autoentrainer/extractive agent is fully utilized and there is no rectifying section in the column [6].

The efficiency of the EHAD can be represented with the motivating case study. This was first solved with a separation system of nine units, distillation columns and extractors [8]. With the application of the EHAD it could be simplified to four units (Figure 2) [2].

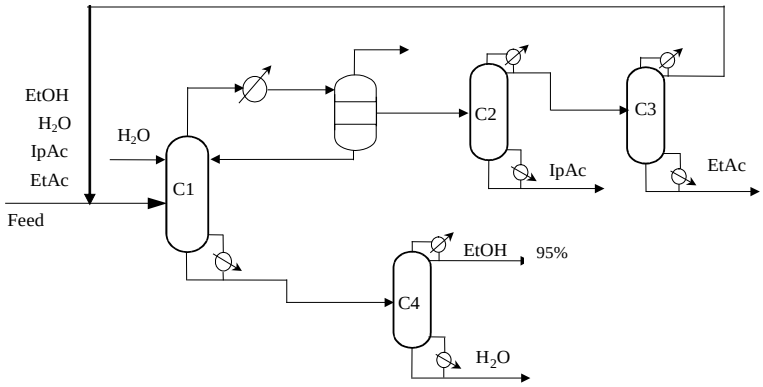

Figure 2 Solution of the motivating example with EHAD

Among the products there is the ethanol of 95 w/w% purity, so below the azeotropic point. In our investigation we considered the current industrial praxis where the dewatering of the ethanol can be completed with molecular sieve.
If fine purity is required e.g. biofuel or pharmacopoeial application further unit operations might be needed, e.g. rectification again.

2. Results and discussion

The applicability and effectiveness of extractive heterogeneous distillation is tested with computer simulations and experimentally. The test includes also the investigation of the accuracy of computer modelling.
First a terner mixture is selected: methanol (MEOH), ethyl-acetate (ETAC) and water. Before the experiments computer simulations are carried out with ChemCAD 6.4.2 [9] to reduce the required number of experiments and to find promising separation alternatives. Moreover, the optimal reflux ratio, the mass- and bottom flow rates, heating and cooling requirements can be also determined knowing the measured heat flow in the column. As an equilibrium model for the calculation of the highly non-ideal vapour-liquid equilibria the UNIQUAC method [10-13] is applied. If binary pairs are existing, where no UNIQUAC data are available, the UNIFAC method [14] is applied.
Since the EHAD works with limited immiscibility besides the vapour-liquid equilibria, liquid-liquid equilibria should be also calculated, that is, vapour-liquid-liquid (VLL) equilibria. The mentioned equilibrium models (UNIQUAC, UNIFAC) both have VLL equilibria option.

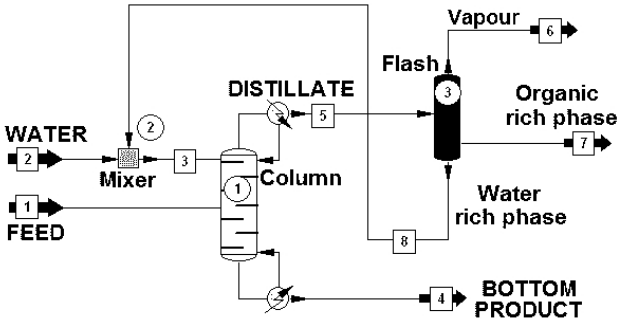

Figure 3 ChemCAD model for the separation of the ternary mixture

The operation of the EHAD and the complexities of the ternary mixture are shown in Figure 3 calculated with ChemCAD. There are two binary azeotropes, one

homogeneous and on heterogeneous. The operating lines show the operation of the EHAD. The entrainer, water, addition is also presented.
To save time and material first extensive simulation works should be completed. The simulation prepares and predicts the experiments. The experiments are completed on a laboratory apparatus shown in Figure 4.

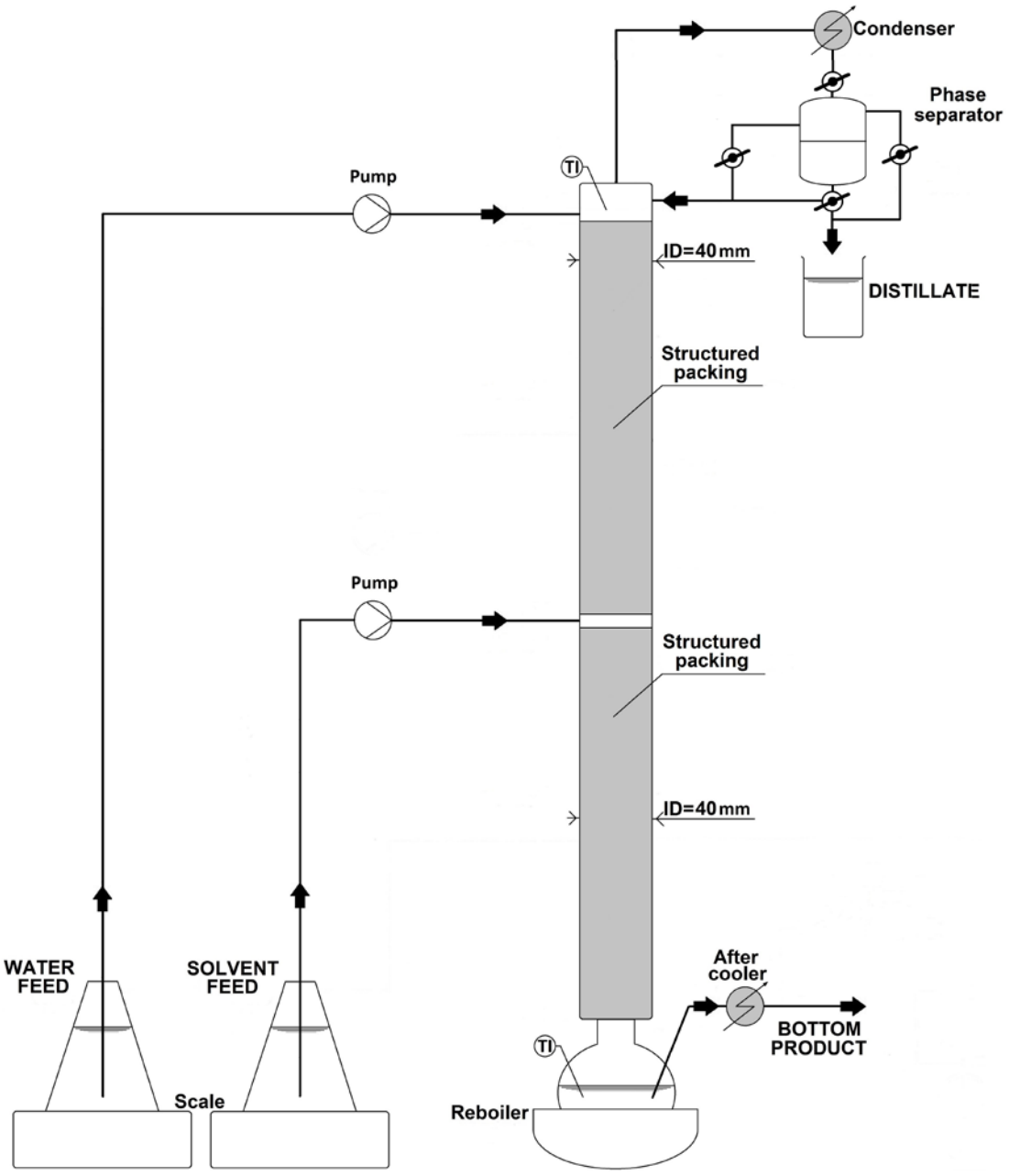

Figure 4 Extractive heterogeneous distillation column of laboratorial size

The modelling results are tested in laboratory experimental conditions. The main parameters of the experimental column are the following: structured packing, internal diameters of 40 mm. The column has 40 theoretical plates. (According to measurement carried out by methanol-water mixture.) The feed is not preheated and it is pumped in the middle of the column and the flow value is kept at 0.25 kg/h. The entrainer (water) is pumped in the top of the column and the flow value is kept at 1.23

kg/h. The column heating is controlled with a 300 W efficiency heating basket. The flow leaving the condenser goes to a phase split. The upper, organic reach phase is taken away. The lower, water rich phase goes back into the EHAD column as reflux. The content of the feed (F), distillate (D), bottom product (W) are measured with Shimadzu GC-14B gas chromatograph with a CP-SIL-5CB column connected to a flame ionization detector.

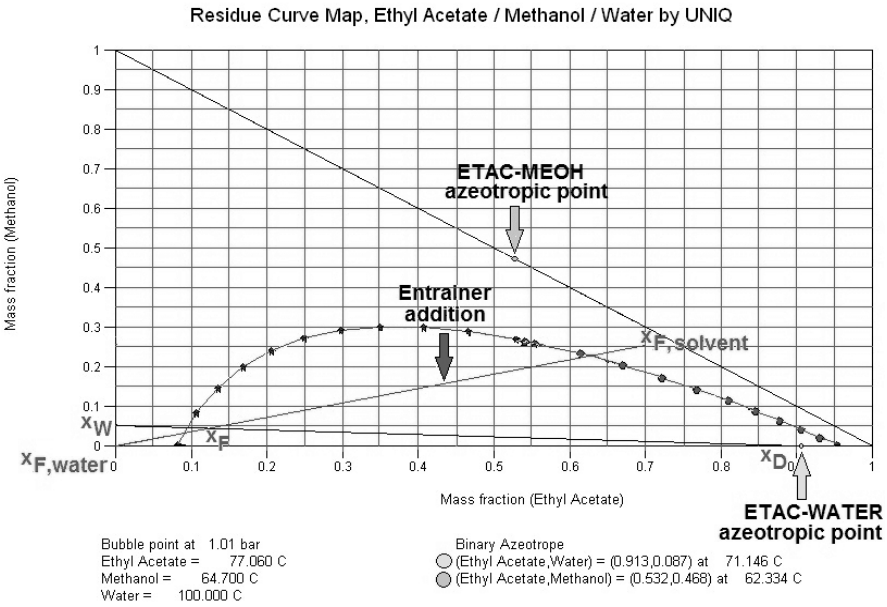

Figure 5 Calculated equilibria and operating lines of the EHAD

In Table 1 we can see the measured and calculated results. The comparison pays special attention to those regions where the measured and calculated concentrations are close to zero. This is usually a pretty uncertain region.

Table 1 Comparison of measured and simulated data for the ternary mixture

	Feed	Simulated data w %		Measured data w %	
	w %	D - top phase	W	D - top phase	W
Water	4	3.6	94.7	5.3	94.6
MEOH	26	0.102	5.2	0.227	5.4
ETAC	70	96.3	0.1	94.5	b.d.l.

b. d. l.: below detection limit

For instance at the production of extreme fine chemical, industrial examples show that this uncertainty can be even critical when only calculations are considered and this uncertainty underline the importance of the experiments.
The comparison of our previous modelling also strengthens this result [2]. These measurements and calculations were made for quaternary mixtures like in the case of the motivating example ethanol, ethyl acetate, isopropyl acetate and water and ethanol, ethyl acetate, methyl ethyl ketone and water.

3. Conclusions

The application of the extractive heterogeneous-azeotropic distillation improves significantly the possibilities for the separation of highly non-ideal mixtures. It opens

new areas for the design of distillation based systems. Difficult multicomponent separations can be easily and cost effective solved with the EHAD.
Modelling and experimental results show good agreement for the EHAD. Our results obtained on EHAD experiments and industrial distillation problems that close to zero concentrations e.g. pharmacopoeial purity the modelling cannot always deliver reliable results and the experiments and proper analytics have paramount importance.

Acknowledgements
The authors would like to acknowledge the financial help of TÁMOP-4.2.2.A-11/1/KONV-2012-0072 and KMR - 12-1-2012-0066.

References
[1] L. Hégely, Improvement of Batch Distillation Separation of Azeotropic Mixtures, PhD Thesis, Université de Toulouse, Toulouse, 2013.
[2] P. Mizsey, A. Szanyi, A. Raab, J. Manczinger, Z. Fonyo, Intensification of a solvent recovery technology through the use of hybrid equipment, in: G. Johan, S. Jan van (Eds.) Computer Aided Chemical Engineering, Elsevier, The Hague, The Netherlands 2002, pp. 121-126.
[3] A. Szanyi, P. Mizsey, Z. Fonyo, Novel hybrid separation processes for solvent recovery based on positioning the extractive heterogeneous-azeotropic distillation, Chemical Engineering and Processing: Process Intensification, 43 (2004) 327-338.
[4] A. Szanyi, P. Mizsey, Z. Fonyo, Optimization of nonideal separation structures based on extractive heterogeneous azeotropic distillation, Industrial and Engineering Chemistry Research, 43 (2004) 8269-8274.
[5] A. Szanyi, P. Mizsey, Z. Fonyó, Separation of highly non-Ideal quaternary mixtures with extractive heterogeneous-azeotropic distillation, Chemical and Biochemical Engineering Quarterly, 19 (2005) 111-121.
[6] A. Szanyi, Separation of non-ideal quaternary mixtures with novel hybrid processes based on extractive heterogenous-azeotropic distillation, PhD Thesis, Budapest University of Technology and Economics, Budapest, 2005.
[7] A.M.J.C. Wijesinghe, Development of Industrial Complexes of Special Rectification Techniques for Solvent Recovery, in, M.V. Lomonosov Institute of Fine Chemical Engineering, Moscow, USSR, 1985.
[8] A. Raab, Separation of highly nonideal mixture for solvent recovery, MSc Thesis, Budapest University of Technology and Economics, Budapest, 2001.
[9] CHEMCAD 6.4.2 5456, in, 2012.
[10] A. Klamt, G.J.P. Krooshof, R. Taylor, COSMOSPACE: Alternative to conventional activity-coefficient models, AIChE Journal, 48 (2002) 2332-2349.
[11] D.S. Abrams, J.M. Prausnitz, Statistical Thermodynamics of Liquid Mixtures: A New Expression for the Excess Gibbs Energy of Partly or Completely Miscible Systems, AIChE Journal, 21 (1975) 116-128.
[12] B. Wiśniewska-Goclowska, S.X.K. Malanowski, A new modification of the UNIQUAC equation including temperature dependent parameters, Fluid Phase Equilibria, 180 (2001) 103-113.
[13] K. Egner, J. Gaube, A. Pfennig, GEQUAC, an excess Gibbs energy model describing associating and nonassociating liquid mixtures by a new model concept for functional groups, Fluid Phase Equilibria, 158-160 (1999) 381-389.
[14] A. Fredenslund, R.L. Jones, J.M. Prausnitz, Group-contribution estimation of activity coefficients in nonideal liquid mixtures, AIChE Journal, 21 (1975) 1086-1099.

Solvent recovery from azeotropic mixtures by heteroazetropic and extractive batch distillation

Steven Vreysen[1], Tom Ooms[1], Guy Van Baelen[1], Vincent Gerbaud[2], Ivonne Rodriguez-Donis[3], Geert Vermeulen[4], Bart Van der Bruggen[5]
[1]Thomas More University College, Geel, Belgium;
[2]Université de Toulouse, CNRS, Laboratoire de Genie Chimique,Toulouse, France;
[3]Instituto Superior de Tecnologías y Ciencias Aplicadas (InSTEC). La Habana, Cuba;
[4]De Neef Chemical Processing, Heist-op-den-Berg, Belgium;
[5]KU Leuven, Leuven, Belgium

Abstract
Many fine chemicals and specialty chemicals are produced in batch processes, which generate solvent mixtures as 'waste'. Often these solvent mixtures form azeotropes, which cannot be separated with conventional distillation. This paper investigates the practical application of heteroazeotropic and extractive distillation for the recovery of solvents from 6 azeotropic solvent mixtures from industry. Heteroazeotropic distillation was possible if one of the two components was either very apolar or polar, because an entrainer with the opposite polarity could be selected. When both solvents have an intermediate polarity, extractive distillation was applied. Calculation of the OPEX and CAPEX of the separation of the toluene/ACN mixture by heteroazeotropic distillation using n-hexane as entrainer showed that the total separation cost is about half the cost of the new solvent. Moreover, LCA showed that the recovery of these valuable organic solvents from azeotropic mixtures has a lower environmental impact than the incineration of these mixtures and the production of new solvents.

Keywords
Solvent recovery; heteroazeotropic distillation; extractive distillation; entrainer selection; residue curve analysis; LCA

1. Introduction

Many fine chemicals and specialty chemicals are produced in batch processes, which generate solvent mixtures as 'waste'. Due to the interaction between these solvents often azeotropes occur. Therefore these solvents cannot be easily recovered by conventional distillation, and the solvent mixtures are mostly incinerated. However, the recovery of these solvents could be a direct cost saving for companies and a large benefit for the environment.

Azeotropic and extractive distillation techniques involving the addition of an entrainer are well established in the petrochemical industry to separate azeotropic mixtures. However, less is known about the potential applications of heteroazeotropic and extractive distillation in batch mode. This paper investigates the application of these techniques for the recovery of solvents from azeotropic solvent mixtures from industry. An experimental approach is preferred, rather than a modelling approach. Practical entrainer selection rules and processing guidelines are presented, based on real industrial practice.

2. Results and discussion

The separation of 6 real solvent mixtures from industry (see Tables 1 and 2) was studied by heteroazeotropic batch distillation or extractive distillation experimentally.

2.1 Entrainer selection

Rodriguez-Donis et al. (2001) were the first to provide exhaustive heterogeneous entrainer selection rules specific to batch columns. Skouras et al. (2005) simplified these rules to two principles: (1) The entrainer should form a heteroazeotrope with one of the original components and/or a ternary heteroazeotrope and (2) The vertex of the original component to be obtained in the still at steady-state should be connected with the steady-state reflux point of the entrainer-rich phase, with a distillation line in the direction of increasing temperature from the top of the column to the bottom. Skouras el al. (2005) formulated also two “screen out” guidelines for finding unfeasible entrainers: (1) The entrainer must not lead to the formation of maximum azeotropes with any of the original components and (2): The entrainer should preferably not lead to the formation of a ternary saddle homoazeotrope.

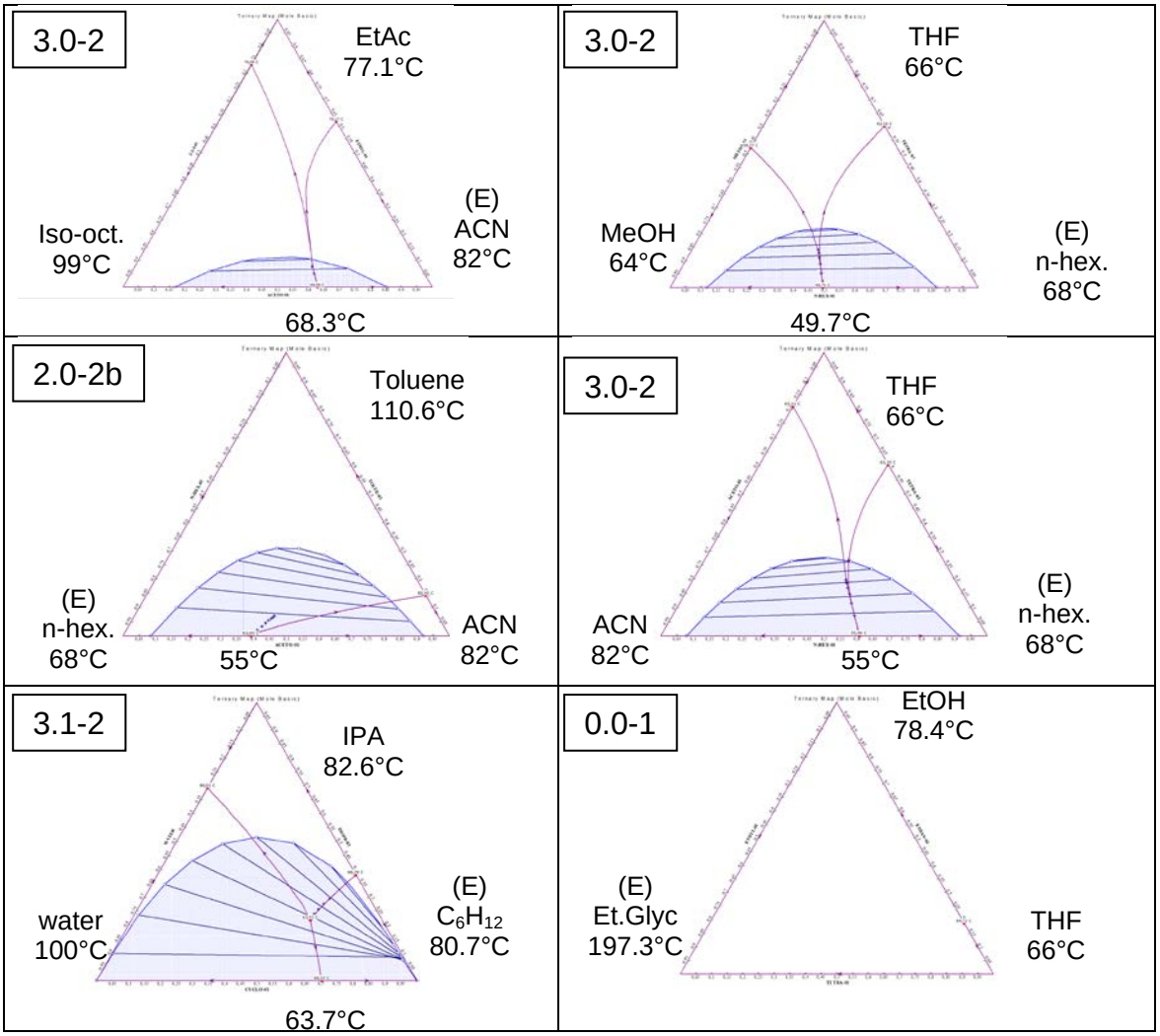

Table 1: Residue curve maps and Serafimov’s classification of the ternary systems. Obtained with Aspen software using the UNIFAC model. For iso-octane / ethyl acetate / acetonitrile the UNIFAC-DMD model was used, which corresponded better with the experimental results.

Ooms et al. (in press) stated also that the good performance of the heteroazeotropic batch distillation is not limited by the presence of extra homogeneous binary azeotropes. Hence, feasible ternary diagrams for minimum boiling azeotropes are the 2.0-2b, 2.0-2c and 3.0-2 class diagrams according to Serafimov's classification having a physical occurrence of 21.1%, 0.9% and 8.4%, respectively (Hilmen et al., 2002; Kiva et al., 2003). Table 1 shows also a case were a ternary heteroazeotrope was obtained. This ternary mixture belongs to the 3.1-2 Serafimov's classification, having a physical occurrence of 26% of ternary mixtures (Hilmen et al., 2002).

The entrainers used in the heteroazeotropic distillations were selected by the RegSolExpert® software (Gerbaud et al. 2006), except for the IPA-water and tetrahydrofuran-water system, where the entrainer selection was based on literature data (Luyben and Chien, 2010; Tang et al.,2013).

2.2 Experimental validation

Figure 1 shows the batch distillation column used for the experimental validation experiments. It has a length of 1.50 m and an inner diameter of 0.03 m. The column is filled with 3x3 mm raschig rings meaning about 44 theoretical plates. The boiler was heated with an electrical heating jacket. The liquid reflux was controlled through the open/close time of a solenoid valve. In all experiments total reflux was applied until the column reaches the steady state determined invariable temperature at the top of the column invariable temperature at the top of the column. Several fractions were collected according to the temperature variation at the top and further analyzed by gas chromatography GC-FID (model Chrompack CP9002).

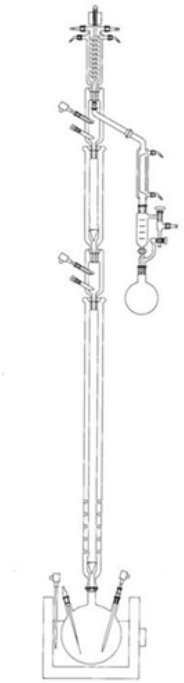

Figure 1: Sketch of the batch distillation column

Skouras et al. (2005) distinguished two operation modes of batch heteroazeotropic distillation which were reviewed recently by Hegely et al. (2013). In Mode I the composition of the reflux (and the distillate) equals that of the condensate, and the existence of two liquid phases is only exploited at subsequent separation of the distillate. In Mode II, distillation and phase separation occurs simultaneously and the reflux has different composition than that of the condensate. The entrainer-rich phase can be totally or only partially refluxed. Obviously more entrainer is needed in mode I or when the entrainer is only partially refluxed.

In the applied experimental approach always Mode I with a reflux ratio of 20/1 or 10/ was tested first. This test shows the feasibility of the proposed separation method. However, when the separation is done on an industrial scale the amount of entrainer

should be as low as possible and therefore Mode II should be applied, preferentially with total entrainer reflux. This was successfully tested for the toluene/ACN, THF/ACN, and IPA/Water mixtures.

However the for THF/ACN and IPA/Water a combination of Mode I and Mode II had to be applied for a higher reflux ration in order to obtain the desired purity. This combination corresponds with Mode II, strategy B, where the entrainer-lean phase is partially refluxed from Lang and Modla (2006).

Table 2 displays experimental figures for the distillation performed. The toluene/ACN and IPA/water mixtures were also separated on both pilot and industrial scale, with purities of the recovered solvents above 99 wt%. The tetrahydrofuran/ethanol mixture could be separated using an extractive distillation with a reflux ratio of 2 and an entrainer/vapor ratio of 0.5. The recovered ethanol and tetrahydrofuran both had a purity above 98 wt%.

Solvent mixture – entrainer (bp)	Heteroazeotrope (bp)	Reflux policy	Purity recovered solvents
Ethyl acetate (99°C) / Iso-octane (77.1°C) – Acetonitrile (ACN) (82°C)	Iso-octane / ACN (68.3°C)	Mode I reflux ratio 20/1	Ethyl acetate: 100 wt% Iso-octane: 100 wt% (after 2nd distillation)
THF (66°C)/ Methanol (64.7°C) – n-Hexane (68°C)	MeOH / n-Hexane (49.7°C)	Mode I Reflux ratio 10/1	THF: 99.5 wt%
Toluene (110.6°C) / ACN (82°C) – n-Hexane (68°C)	ACN / n-Hexane (55°C)	Mode II Total entrainer reflux	Toluene: 99.4 wt% ACN: 99.9 wt% (after 2nd distillation)
THF (66°C) / ACN (82°C) – n-Hexane (68°C)	ACN / n-hexane (55°C)	Model I & II Reflux ratio 10/1 + total entrainer reflux	THF: 99.8 wt% ACN: 99.9wt% (after 2nd distillation)
IPA (82.6C) / Water (100°C) – Cyclohexane (80.7°C)	IPA / Water / cyclohexane (63.7°C)	Mode I & II Reflux ratio 20/1 + total entrainer reflux	IPA: 99.9 wt%
THF (66°C) / Ethanol (76.4°C) – Ethylene glycol (197.3°C)	none	Extractive distillation E/V ratio 0.5	Ethanol: 98.1 wt% THF: 99.2 wt%

Table 2: Overview of experimental parameters and obtained purifty of the recovered solvents

2.3 Economical an ecological comparison with incineration

The separation of toluene and acetonitrile by a process which combines a heteroazeotropic distillation with hexane as entrainer and a conventional distillation for entrainer recovery was tested on industrial scale. Data from this test were used to calculate both CAPEX and OPEX of this process (Couper, 2003). These calculations show that the total separation cost (not including transport) is about 0.5 euro/kg recovered solvent. This is significantly less than the cost of new solvent (about 1 euro/kg for toluene and about 2 euro/kg for acetonitrile).

Also life cycle assessment (LCA) was performed for two alternatives, namely distillation and incineration with energy recovery. The system considered was the acetonitrile–toluene mixture with several compositions in order to determine the most appropriate technology depending on the characteristics of the mixture. The

Ecosolvent® v.1.0.1 software was used to perform the LCA, considering two scenarios and the following methods of impact assessment: Eco-indicator 99, cumulative energy demand, method of ecological scarcity (UBP'97), global warming potential and CO_2 balances.

Figure 2 (reproduced from Luis et al. 2013) shows that the recovery of ACN has a lower environmental impact than incineration, especially with a high ACN concentration in the solvent mixture. On the other hand focusing on toluene recovery gradually increases the environmental impact as the toluene content decreases. At 25 wt% of toluene, it may even get bigger than incineration. Comparison of batch vs continuous distillation shows no significant differences in terms of environmental impact.

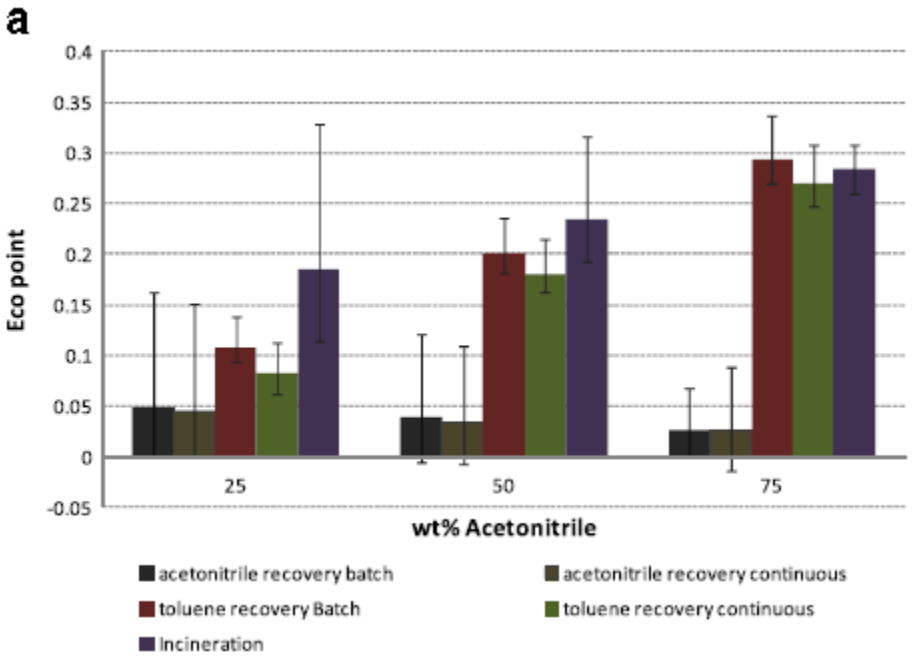

Figure 2: Comparison of Eco-indicator 99 of the mixure acetonitrile–toluene for incineration and batchand continuous distillation with acetonitrile or toluene as target compounds (Luis et al. 2013)

More results of this LCA study are presented in detail by Luis et al. (2013) and show that the solvents of which the production entails a large environmental burden should be recovered by means of distillation since the environmental credits obtained by the recovery are higher than those led by the energy production from incineration.

From these economic and LCA studies it can be concluded that rather expensive solvents (e.g., cost > 1 euro/kg), of which the production often entails a large environmental burden, should be recovered both from an economic and ecological point of view.

3. Conclusions

This paper shows that heteroazeotropic or extractive batch distillation is a technically feasible and a cost efficient technique to separate the studied azeotropic mixtures in a batch mode. Moreover LCA shows that the recovery of the valuable organic

solvents from azeotropic mixtures has a lower environmental impact than the incineration of these mixtures and the production of new solvents.

Acknowledgements
The authors also acknowledge financial support from The Environmental & Energy Technology Innovation Platform of Flanders (MIP).

References

Couper, JR. 2003. Procecc Engineering Economics. Marcel Dekker. New York, USA.
Gerbaud, V., Joulia, X., Rodriguez-Donis I., Baudouin, O., Rosemain, O., Vacher, A., Castelain, P. (2006). Practical residue curve map analysis applied to solvent recovery in non-ideal binary mixtures by batch distillation processes, Chem. Eng. Proc.: Proc. Intensification, 45 (8), 672-683.
Hegely L., Gerbaud V., Lang P. (2013). Generalised model for heteroazeotropic batch distillation with variable decanter hold-up. Sep. Purif. Tech., 115, 9-19.
Hilmen, E.K., Kiva, V.N., Skogestad, S. (2002). Topology of ternary VLE diagrams elementary cells. AIChE Journal, 48 (4), 752-759.
Kiva, V.N., Hilmen, E.K. , Skogestad, S. (2003). Azeotropic phase equilibrium diagrams: a survey. Chem. Eng. Sci., 58, 1903-1953.
Lang, P, Modla, G. (2006). Generalised method for the determination of heterogeneous batch distillation regions. Chem. Eng. Sci., 61 (13), 4262-4270
Luis P., Amelio A., Vreysen S., Calabro V., Van der Bruggen B. (2013). Life cycle assessment of alternatives for waste-solvent valorization: batch and continuous distillation vs incineration. Int. J. Life Cycle Assess, 18, 1048–1061.
Luyben W.L., Chien I.-L. (2010). Isopropanol–Water (Cyclohexane as the Entrainer), in Design and Control of Distillation Systems for Separating Azeotropes, Wiley & Sons, Inc., Hoboken, NJ, USA.
Ooms T., Vreysen S., Van Baelen G., Gerbaud V., Rodriguez-Donis I. (2013). Separation of ethyl acetate–isooctane mixture by heteroazeotropic batch distillation, Chem. Eng. Res. Des., Available online 19 October 2013.
Rodriguez-Donis I., Gerbaud V., Joulia X. (2001). Heterogeneous entrainer selection for the separation of azeotropic and close boiling temperature mixtures by heterogeneous batch distillation. Ind. Eng. Chem. Res., 40, 4935-4950.
Skouras S., Kiva V., Skogestad S. (2005). Feasible separations and entrainer selection rules for heteroazeotropic batch distillation. Chem. Eng. Sci., 60, 2895–2909.
Tang K., Bai P., Huang C., Liu W. (2013). Separation of Tetrahydrofuran-Ethanol Azeotropic Mixture by Extractive Distillation. Asian journal of chemistry, 2774-2778.

Rectification of lemongrass (*Cymbopogon citratus*) essential oil using centrifugal molecular distillation

Laura Plazas Tovar1, Glaucia Maria Ferreira Pinto2, Cesar Benedito Batistella1, Rubens Maciel Filho1, Maria Regina Wolf Maciel1
[1]University of Campinas-UNICAMP, Campinas, Brazil;
[2] Universidade Paulista-UNIP, Campinas, Brazil

Abstract
Essential oils are concentrated extracts from aromatic plants containing volatile organic compounds, with a predominance of one or two of them and responsible for organoleptic characteristics. *Cymbopogon Citratus*, scientific name of a plant also known worldwide as lemongrass, is one of the most important essential oils in commercial level, and it is characterized by high concentration of Citral. In this work, lemongrass (*Cymbopogon citratus*) essential oil was purified by re-distillation in high vacuum conditions (6.67 Pa), and this purification by re-distillation was referred to as rectification. Experiments were carried out using a centrifugal molecular distillation unit with an evaporation surface area of 0.0046 m^2. We studied three strategies of molecular distillation process (CMD), such as: (i) two rectification in four stages at constant evaporator temperature (60 °C and 80 °C) and (ii) a rectification in three stages at evaporator temperature range between 60 °C and 120 °C. Feed flow rate and condenser temperature were set as 1.5 mL min^{-1} and 10 °C, respectively.
Results showed that the rectification in three stages at different temperatures is more advantageous than the rectification in four stages at constant temperature. In reference to rectification in four stages at 60 °C, after two stages concentration of Citral reached 17.425 mg_{citral} mL^{-1} and at fourth stage, concentration of Citral aimed 22.152 mg_{citral} mL^{-1} in the distillate stream. On the other hand, rectification approach at different temperatures in each stage enabled to obtain 20.486 mg_{citral} mL^{-1} in the distillate stream using only three stages.
Analytical techniques and physicochemical characterizations by standard methods for oil and fat analyses were used to determine the density and free fatty acids. The rectification of the essential oil using CMD allowed to obtain and to purify the material preserving bioactive compounds as well as minimizing toxicity which ensure quality and safety in human consumption whether in food, cosmetic or medicinal fields, satisfying the oil quality criteria, since, the density and free fatty acids of essential oil obtained in the distillate stream ranged from 0.873 to 0.890 g mL^{-1} (at 27 °C) and from 1.19 to 2.06 wt % (oleic acid), respectively.

Keywords
Molecular Distillation, rectification, lemongrass essential oil, Citral concentration

1. Introduction

Lemongrass is a plant from the grass family and may have 1–2% of essential oil in a dry basis. The essential oil is characterized by a high content of Citral (a mixture of isomeric acyclic monoterpene aldehydes: neral (cis-Citral) and geranial (trans-Citral) [1], which is used as a raw material for the production of vitamin A and beta-carotene [2].

The potential of the centrifugal molecular distillation (CMD), is due to the fact that it is appropriate for the separation and purification of thermally unstable materials, without the hazard of thermal decomposition, as it is the case of many vitamins and essential oils, because the process works under high vacuum and relative lower temperatures [3,4]. In CMD process, it is necessary that: the vapor molecules generated find a free path between the evaporator and the condenser; the pressure be low and the condenser be separated from the evaporator by a smaller distance than the mean free path of the evaporating molecules. In these conditions, theoretically, the evaporation rate should only be governed by the rate of molecules that escape from the liquid surface and, therefore, phase equilibrium does not exist [5]. The CMD process has been widely applied for recovering carotenoids from palm oil [6], for octacosanol recovery from rice oil [7] and for purifying and deodorizing structured lipids [8-9].

The objective of this work is processing the lemongrass (*Cymbopogon citratus*) essential oil by re-distillation in high vacuum conditions (6.67 Pa) referred as rectification process. Two strategies under isothermal conditions and a strategy under non isothermal conditions were developed (Figure 1).

2. Experiments and methodology

2.1 Essential oil: Raw material

Essential oil of lemongrass was acquired from Ferquima Ltda. (São Paulo, Brazil). Samples were stored during, approximately, 03 months at -2 °C, up to the rectification by the CMD process.

2.2 Molecular distiller

The model used in this work was a centrifugal distiller system from Myers Vacuum Inc. (Kittanning, PA), with an evaporation surface area of 0.0046 m^2. The evaporator temperature (EVT) was controlled by an electrical heater system from 60 ^oC to 120 ^oC, while the condenser temperature was controlled by thermostatic baths at 10 ^oC. The typical pressure (P_s) of the system was 6.67 Pa, and the evaporator rotation velocity was 1350 rpm. Based on results reported in [10], the feed flow rate was keeping at 1.5 mL min^{-1}.

In the CMD process, two product streams are generated: distillate stream (rich in the volatile molecules that are condensed) and residue stream (rich in the heavier molecules).

In this work, different operating strategies were developed based on the fact that the residue stream obtained during the CMD is distilled again and a new distillate stream is obtained with an even higher concentration of volatile components (Figure 1). Moreover, the process of repeated distillation by CMD process was referred as rectification of lemongrass (*Cymbopogon citratus*) essential oil.

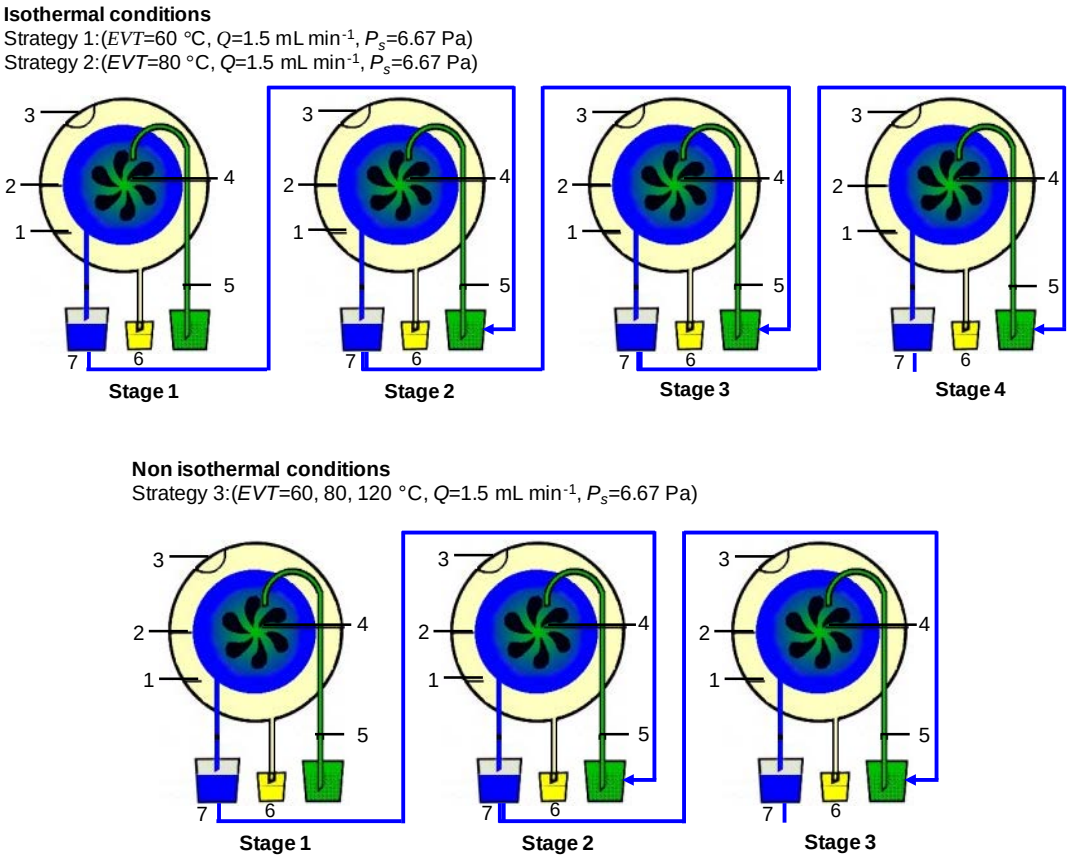

Figure 1: Simplified illustration of the rectification process of lemongrass (*Cymbopogon citratus*) essential oil by CMD process. 1. Condenser surface; 2. Centrifugal rotor; 3. Vacuum system; 4. Evaporator surface; 5. Feed stream; 6. Distillate stream and 7. Residue stream. Modified [11].

2.3 Analytical Characterization

Identification and quantification of the Citral in the process streams (distillate and residue) were carried out by Gas Chromatography coupled to Mass Spectrometry (CG-MS). Analyses were carried out in a Star 3600 CX gas chromatograph interfaced with a Varian Saturn 2000 mass spectrometer operated by WorkStation (6.6 version) software, using a Varian capillary column model 58/FFAP. The size of the column is: 50 m × 0.25 mm i.d., film thickness 0.2 µm. The oven temperature was programmed linearly from 50 to 200 °C at heating rates of 5 °C min^{-1}. Other operating conditions were: injector temperature, 250 °C; carrier gas: helium, adjusted to a volumetric column velocity of flow, 44 mL min^{-1} splitting ratio: 1:26. A volume of sample of 1 µL was injected in the equipment. Citral peak was identified by a comparison of its mass spectra when the pure spectrum of a component is obtained at certain operating condition. The quantification of Citral in the essential oil and in streams of CMD process was performed by external calibration curve constructed with standard stock solutions.

2.4 Physicochemical Characterizations

Free fatty acids (FFA): It was used the official method AOCS Ca 5a-40 [12].

Determination of density: It was used the ratio of mass to volume (1000 µL of sample).

Colorimetric measurements: The analyses were carried out in GBU-UV-VIS brand Cintra 10e Spectrophotometer, with the software Spectral 1.70, using CIE color space (L*, a*, b*) (CIELAB) [13], making a scanning in absorbance mode with wavelength from 380.0 nm to 780.0 nm, resolution of 1.5 nm, and interval data of 0.640 nm. The samples were analyzed without dilution.

3. Results and discussion

3.2 Distillates and residue streams analytical characterization

These evaluations show the importance of process, since it can obtain a larger amount of the distillate stream with quality parameters and without thermal degradation of the material during the process, since the temperatures used in the rectification process by CMD are softer due to high vacuum used. As the process is repeated in different stages, the concentration of volatile components in the distillate stream increases aiming 21.114 mg_{citral} mL^{-1} at third stage under isothermal strategy (60 °C) (see Table 1).

Table 1: Parameters to evaluate the rectification process of lemongrass (*Cymbopogon citratus*) essential oil by CMD process in terms of the mass fractions, concentration of Citral in the distillate and residue streams, free Fatty Acids (%FFA) and density

Strategy	Stage	EVT (°C)	Distillate streams				Residue streams				D/R
			CCD (mg_{citral} mL^{-1})	MF (%wt)	%FFA[a] (%wt)	Density[b] (g mL^{-1})	CCR (mg_{citral} mL^{-1})	MF (%wt)	%FFA[a] (%wt)	Density[b] (g mL^{-1})	
Raw material			19.816	-	2.13±0.03	0.899±0.001	19.816	-	2.13±0.03	0.899±0.001	
1	1	60	15.316	6.89	1.33±0.03	0.873±0.003	17.705	93.11	2.53±0.05	0.882±0.002	0.07
	2		17.425	24.51	1.42±0.00	0.886±0.003	17.684	75.49	3.09±0.02	0.883±0.002	0.32
	3		21.114	21.37	1.41±0.02	0.887±0.009	14.915	78.63	3.69±0.04	0.888±0.001	0.27
	4		22.152	21.68	1.44±0.01	0.886±0.002	14.712	78.32	4.13±0.06	0.888±0.004	0.28
2	1	80	13.403	18.83	1.28±0.04	0.878±0.002	15.476	81.17	2.51±0.01	0.891±0.010	0.23
	2		13.942	30.93	1.41±0.01	0.884±0.002	9.876	69.07	3.03±0.04	0.887±0.003	0.45
	3		17.738	33.32	1.55±0.02	0.886±0.002	9.749	66.68	3.79±0.03	0.892±0.002	0.50
	4		17.959	32.98	2.06±0.02	0.890±0.009	6.307	67.02	4.93±0.09	0.907±0.011	0.49
3	1	60	13.164	12.26	1.19±0.03	0.874±0.003	15.131	87.74	2.50±0.05	0.890±0.006	0.14
	2	80	17.911	33.44	1.25±0.01	0.886±0.001	14.240	66.56	3.04±0.03	0.887±0.001	0.50
	3	120	20.486	37.27	1.71±0.07	0.883±0.003	13.140	62.73	4.01±0.08	0.897±0.011	0.59

[a] It was calculated as the percentage of a specific FFA (% wt oleic acid)
[b] Density was determined, at atmospheric pressure and 27 °C
CCD: Concentration of Citral in the distillate stream; CCR: Concentration of Citral in the residue stream; D/R: Split ratio between mass of distillate stream and mass of residue stream; MF: Mass fraction
Data represent the means and standard deviations of experiments carried out in triplicate (value ± standard deviation)

Based on results provided for each strategy, it can establish the influence of the EVT and the number stages on the yield of the process expressed as mass fraction of distillate and residue streams. By analyzing the operational strategies at isothermal conditions (strategies 1 and 2), it is clear that significant variation in the efficiency of the process will continue until the third distillation stage. In stage 4, the change in yield are minimal (about 2%) when compared with the results reported in stage 3, so that three stages of re-distillation by CMD are sufficient to achieve significant changes in percentage values for the fraction of distillate and residue streams reporting a D/R values between 0.07 and 0.59 (Table 1).

3.3 Distillate and residue streams physicochemical characterizations

Considering the percentage of free fatty acids (%FFA), quantified in the distillate and residue streams obtained from the rectification process by CMD, as an indicator of quality for the oil, according to the quality parameters, the oils for human consumption must have a content lesser than 2.00 %wt [14]. The residue streams obtained under isothermal strategy (at EVT equal to 60 °C and 80 °C) and non isothermal strategy (at EVT from 60 °C to 120 °C) reported higher %FFA as the distillation stages rose (Table 1). However, considering both strategies, it can be observed that the %FFA values determined for the distillate streams is lower than the one determined for the initial sample of essential oil (2.13%) and according with quality parameter reported in [14].

On the other hand, in [15] density values for lemongrass essential oil destined for industrial applications (0.862 – 0.911 g mL^{-1}) are reported. Density values from 0.873 to 0.888 g mL^{-1} were reported for distillate streams from rectification process by CMD using the isothermal strategy at 60 °C. A similar range was determined for distillate streams obtained from rectification process by CMD using non isothermal strategy (0.874 to 0.883 g mL^{-1}). Thus, these streams are according with specification established for disposal of these materials at the industry level. Nevertheless, the residue streams showed higher densities than specifications as displayed in Table 1.
The quality of the products (distillate and residue streams) were also accompanied from the estimated coordinates and color properties according to the theory of CIELAB 1976 (L*, a*, b*, where L* refers to coordinate related to luminous intensity of a color, a* denotes the red/green value; and b* denotes the yellow/blue value, based on the CIE color space [13]). Table 2 presents the spot of chromatic coordinates (color space CIELAB), since each sample color occupies a unique location in the three-dimensional CIELAB color space.

Table 2: Characteristics of color (L*, a*, b*) of the essential oils obtained in the distillate and residue streams from rectification process by CMD

CMD streams	Strategy	EVT (°C)	Stage	L*	a*	b*
Raw material	-	-	-	101.006	-5.087	15.704
Distillate streams	1	60	1	98.831	-2.451	10.311
			4	99.600	-4.534	15.129
	2	80	1	102.098	-1.966	4.355
			4	100.270	-4.706	15.082
	3	120	1	101.626	-2.450	6.276
			3	101.540	0.355	11.290
Residue stream	1	60	1	99.049	5.061	41.839
			4	100.720	-6.913	20.294
	2	80	1	97.895	-8.434	34.332
			4	99.475	-6.488	22.537
	3	120	1	85.250	-7.422	43.785
			3	101.540	-2.819	7.042

The fractions are between the first and second quadrants (from CIELAB color space) with negative and positive values of a* and positive values of b*, or yellow color characterizing a mixture of, a pair of terpenoids with the molecular formula $C_{10}H_{16}O$ (the cis-isomer known as neral and the trans-isomer known as geranial).
In Table 2, the essential oils obtained in the distillate streams reported lower values along b* axis ($4.355 < b^* < 15.129$) and higher values along a* axis ($-4.706 < a^* < 0.355$) with higher values in the L* plane ($98.831 < L^* < 102.098$), when compared to the essential oils obtained in the residue streams. Therefore, a color measurement in

the +a direction depicts a shift toward red and along +b movement represents a shift toward yellow. On the L* plane, it was determined that distillate streams were lighter than residue streams. These results were not compared with published data due to the fact that the open literature does not report results related to them.

4. Conclusions

For effective concentration of Citral in the distillate streams using rectification process by CMD, special attention must be given to evaporator temperature (EVT) and number of stages (re-distillation by CMD) to achieve high mass fraction of distillate, high concentration of Citral in the distillate streams keeping requirements for commercial applications of essential oil. Furthermore, the rectification of lemongrass essential oil by CMD allowed higher concentration of Citral in the distillate stream using strategy 1 (isothermal conditions at 60 °C, Q=1.5 mL min^{-1} and P_s=6.67 Pa) and strategy 3 (non isothermal conditions 60 - 120 °C, Q =1.5 mL min^{-1} and P_s =6.67 Pa) as described in Table 1. Physicochemical evaluation indicated that the essential oil obtained in the distillate streams from rectification process by CMD provides good quality for commercial market through a clean technology, what is nowadays appellatives worldwide reducing the risk of degradation, reporting low %FFA (lower than 2.00 %wt oleic acid) and density range from 0.873 to 0.890 g mL^{-1}. Such color characteristics as a* and b* values were influenced by the type of streams (distillate and residue stream); the changes of these characteristics was evaporator temperature dependant.

Acknowledgements

This research was supported by the São Paulo Research Foundation (FAPESP) and the National Council for Scientific and Technological Development (CNPq).

References

[1] C.R. Rauber, S.S. Guterres, E.E.S. Schapoval, J. Pharm. Biomed. Anal. 37 (2005) 597–601.
[2] F.Q. Ferrua, M.O.M. Marques, M.A.M. Meirelles, Ciênc. Tecnol. Aliment. 14(Suppl.) (1994) 83.
[3] J. Cvengroš, J. Am. Oil Chem. Soc. 72(1995) 1193–1196.
[4] C.B. Batistella, E.B. Moraes, R. M. Filho, M.R.W Maciel, Appl. Biochem. Biotechnol. 98 (2002) 1187–1206.
[5] K.C.D. Hickman, Chemical Reviews, 34 (1943) 51–106.
[6] C.B. Batistella, E.B. Moraes, R. Maciel Filho, M.R. Wolf Maciel, Appl. Biochem. Biotechnol. 98 (2002) 1149–1159.
[7] F. Chen, T. Cai, G. Zhao, X. Liao, L. Guo, X. Hu, J. Food Eng. 70(1) (2005) 47–53.
[8] S.T. Jiang, P. Shao, L.J. Pan, Y.Y. Zhao, Biosyst. Eng. 93(4) (2006): 383–391.
[9] P.F. Martin, V.M. Ito, C.B. Batistella, M.R.W. Maciel, Separ. Purif. Tech. 48(1) (2006) 78–84.
[10] L.P. Tovar, G.M.F. Pinto, M.R.W. Maciel, C.B. Batistella, R.M. Filho, Ind. Eng. Chem. Res. 50(13) (2011) 8185–8194.
[11] Myers Vacuum Repair Services, Inc. Available via site. http://www.myers-vacuum.com/mv1.shtml Accessed 16 Jan 2014
[12] AOCS; Official methods and recommended practices of the American Oil Chemists' Society, AOCS: Champaign, 2004. AOCS; Official methods and recommended practices of the American Oil Chemists' Society, AOCS: Champaign, 2004.
[13] Commission Internationale de l'Eclairage (CIE). Recommendations on Uniform Color Spaces, Color-Difference Equations, Psychometric Color Terms; Suppl. No. 2 of Publ. CIE No. 15 (E–1.3.1); 1978
[14] BRAZILIAN RESOLUTION nº. 482, SEPTEMBER 23rd, 1999., v. 196, October 13. 1999. Section I, p. 82-87.
[15] L. Paviani, S.B.C. Pergher, C. Dariva, Braz. J. Chem. Eng. 23(2) (2006) 219–225.

Distillation based recovery of solvents used for tyre solubility

Edit Csefalvay[1], Nora Valentinyi[1], Andras Jozsef Toth[1], Jozsef Mark Tukacs[1,2], Ivan Gresits[1], Laszlo Racz[3], Szabolcs Solti[4], Peter Mizsey[1,5]

[1]Budapest University of Technology and Economics, Department of Chemical and Environmental Process Engineering, H-1111, Budafoki Street 8., Budapest, Hungary;

[2]Eotvos University, Institute of Chemistry, H-1117, Pázmány P.S.1/A, Budapest Hungary;

[3] Renergy Fund Kft. Újvilág S.15 Budapest Hungary

[4] Szelence Kamionmosó Kft. H-2600, Cserje S. 2/B. Vác, Hungary

[5] University of Pannonia, Research Institute of Chemical and Process Engineering, H-8200, Egyetem Street 10., Veszprem Hungary

Abstract

About 1.4 billion tyres for vehicles are manufactured annually all over the world. Every year an almost equal number of tyres are generated as waste. Knowing the composition of tyres, material recovery is a possible option for further utilization and can be realized with several techniques.

Beside the common constituents of tyres different solvents can be used for enhancing the rubber adhesivity and possible extracting of useful materials. In order to find the soluble components, solubility tests were carried out. Passenger car tyres were selected and eight different solvents. Shredded tyres with an average diameter of 0.2 mm were used in solubility tests in order to increase the mass transfer surface and decreasing the contact time. Temperature was varied from ambient to the value of boiling point of each solvent. Solvent was transported into the inner part of rubber by diffusion resulting in partial dissolution of the non-space polymer. The swelling of space polymer constituents could be observed at the same time. Swelling measured by mass by volumetric increase as well, and it was in correspondence with weight measurements and bulk densities. Extracts were analysed to define the dissolved components with X-ray fluorescence (XRF) spectrometer and GC-MS.

Solvents were recovered by common distillation. Volatile compounds extracted from the tyre were present in the distillate phase. GC-MS analysis proved the efficiency of the different solvents. 1,4-Benzenediamine, N-(1,3-dimethylbutyl)-N'-phenyl was determined in the distillates. The possible source of this amine was isocyanates as binding components of textiles to polymer. Another distillation step of the solvents proved that further purified solvents met the quality standards. Therefore it could be concluded that the proper recovery of the solvents needs the application of rectification so that, they could be reused again or for other industrial tasks.

Keywords

Shredded tyres, swelling, extraction, solvent recovery, distillation

1. Introduction

While refuel cars, sometimes petrol or any other organic solvents' droplets fall accidentally on the tyre from the charging pipe. At this point the question presents itself: does the petrol react with the tyre material? Can it damage the tyre, or just extract some of its components? Does this shorten the tyre's lifetime? To answer these questions several solvents were selected to our experiments. Examination extended to basic solvents which are main products of the chemical industry. Besides the everyday situation of petrol droplets, treatment of tyre material with solvents can contribute to enhanced separation of metal and rubber parts of tyre by swelling, which is a key factor in material recycling.

Swelling depends on the solvent itself and the rubber matrix and the network density. Denser the network less the swelling factor [1,2]. Besides swelling, extraction and chemical reaction can take place, as well, but the dominant phenomenon is swelling that can be measured either by mass or volume [3].

Based on these considerations different solvents can be used for enhancing the rubber adhesivity and possible extracting of useful materials. In order to find the soluble components, solubility tests were carried out. Passenger car tyres were selected and eight different solvent such as cyclohexane, dichloro-methane, acetone, normal-hexane, normal-heptane, gasoline, ethyl-acetate, and gamma-valerolactone were applied. Solvent selection was based on relevant literatures [4-9] and environmental concerns were taken into account.

Shredded tyres with an average diameter of 0.2 mm were used in solubility tests in order to increase the mass transfer surface and therefore decrease the contact time. Temperature was varied from ambient to the value of boiling point of each solvent. Solvent was transported into the inner part of rubber by diffusion resulting in partial dissolution of the non-space polymer. The swelling of space polymer constituents could be observed at the same time. Swelling, extraction and the opportunity of chemical reactions were tested. Experiments were scheduled as follows:

- preparation of shredded tyres by washing with distilled water,
- vacuum drying of shredded tyres,
- weight of shredded tyres,
- dipping of samples into solvent, saturation with solvents,
- measure of mass and bulk volume of shredded tyres after 1 h, 2 h, 4h, 24h, 48h.

After the experiments, the recycling of solvents with distillation was carried out aiming for a complete recycling. By fractionate distillation each 10 ml of distillate was analyzed by GC-MS to make sure of the distillate is pure solvent and determine the rate of recycling. In order to determine the extracted components of shredded tires the bottom product was analyzed by X-ray fluorescence (XRF) emission technique.

2. Results and discussion

Table 1 summarizes the results of swelling tests including increase in mass and volume at different temperatures for each selected solvents.

Table 1 summary of increase in mass and volume relating to the selected solvents at different temperatures

solvent	Boiling point of solvent [°C]	Density of solvent [g/cm^3]	Increase in mass %			Increase in volume %			Extrac-tion
			20°C	30°C	50°C	20°C	30°C	50°C	
dichloro-methane	40	1.325	181.08	181.95	-	105.53	103.75	-	yes
cyclohexane	81	0.779	121.13	126.90	121.86	139.17	133.33	134.43	yes
n-hexane	69	0.659	44.46	52.11	48.80	52.78	66.53	65.69	yes
acetone	56	0.791	5.32	5.17	-	11.25	11.69	-	yes
ethyl-acetate	77	0.901	27.93	21.79	30.62	23.80	15.13	18.33	yes
n-heptane	98.4	0.684	-	61.16	-	-	82.33	-	yes
gamma-valerolactone	208	1.050	-	17.35	-	-	37.78	-	no
Petrol (95)	54-186	0.72-0.77	112.62	110.69	108.63	130.74	125.63	126.05	yes

Swelling was spectacular in the case of dichloro-methane: the transparent solvent turned to black and enormous increase was measured in mass: the final mass was 2.8-times the initial, i.e. about 180% increase could be reached. Due to relatively high density of dichloro-methane the increase in mass was higher than that of in volume. Dividing the final mass measure after 48 h of dipping by final volume of samples it equals to the solvent density (281.08/205.53=1.3). Regarding the effect of temperature no significant effect on increase in mass or volume could be detected, opposite to our expectations. Molecular diffusion can be enhanced with increasing temperature, but the back diffusion from solid to liquid phase is enhanced, too resulting in an occasional deviation between the measured values.

Acetone caused insignificant change in the samples in mass (5%) but noticeable in volume (11%). The degree of solvents' effect on mass from smallest to the greatest is as follows: acetone, gamma-valerolactone, ethyl-acetate, n-hexane, n-heptane, petrol, cyclohexane and dichloro-methane. Due to the different relative densities, ranking of effects on volume differs: most significant volumetric change could be achieved when dipping the tyre samples into cyclohexane or petrol. Considering petrol's effect it can be stated that with increasing contact time the swelling is more intensive, but the significant increase takes place in the first 15 minutes. Noteworthy to emphasize that in our experiments shredded tyre samples were dipped into the solvent, and the effect of contact surface was out of scope of our study. When one parks a car in a bog pool of petrol or a sump, the deformation of tyres should be taken into account.

GC-MS analysis of solvents proved that not only swelling but extraction and reaction took place inside the rubber matrix. 1,4-Benzenediamine, N-(1,3-dimethylbutyl)-N'-phenyl was detected in samples of all tested solvents except gamma-valerolactone. Amine compounds are usually used in a form of isocyanates as binding components between textile and rubber in tyres.

After the distillation of used solvents, the remaining black gel-like bottom products were analysed by XRF. Elemental composition of bottom product verified that chemical reaction took place between the solvents and the rubber matrix. The bottom products contained 3.42-7.12 wt% (related to the total mass of bottom product) of sulfur. The detection of sulfur clearly indicates the breaking up of sulfur-hydrogen and disulfide bonds i.e. the cross bindings of rubber polymers. Considering the effect of temperature on sulfur extraction, a reversed ranking could be observed which was inconsistent to our expectations. Diffusion was enhanced by temperature, however extracted sulfur content decreased, consequently we assume that the solvent reacted with the polymer chains while breaking up the cross bindings at lower temperatures. Among other traces of elements zinc was in remarkable amount (5.4 wt%) in the bottom product of experiments with cyclohexane at 50°C.

Recycling of solvents

Taking into account the small quantity of solvent recycling experiments were carried out in batch mode. Due to the low boiling points of solvents (except gamma-valerolactone) atmospheric distillation was carried out. Distillates were collected in 10 ml fractions, and each fraction was analysed. When extraction occurred during the dipping and volatile compounds were extracted, they could be detected in the distillate phase. In the cases of n-hexane, cyclohexane and ethyl-acetate a distillate/feed ratio of 0.66 could be reached. Until this point he temperature was constant i.e. the boiling point of the solvent. After the recovery of 66.7% of solvents as distillate the temperature increased which points to the fact that the rest of feed contained solvent modified state and the extracted compounds. In all cases the 1,4-Benzenediamine, N-(1,3-dimethylbutyl)-N'-phenyl amine component was detected in the 7^{th} fraction but it was in traces. The low concentration of amine in the solvent is in ppm range. When these solvents would be recycled to the process for the same aim, the ppm concentration of amine is allowable and an increased recycling rate of 77.8% could be reached.

3. Conclusions

1. As a conclusion it can be stated that out of the eight tested solvents seven do have effect on shredded tyres. Greatest swelling by volume was reached by using cyclohexane, but deviation between the different temperatures was 5% and could be neglected.
2. Similar swelling could be reached in the case of dichloromethane, but the increase in mass was more significant than that of in volume due to the relatively high density of the solvent.
3. Considering the extracted inorganic compounds, sulfur showed a remarkable part, and highest quantity was 7.90wt% of bottom product. (Dipping in ethyl-acetate at 30°C).
4. GC-MS analysis verified the reaction of solvents with rubber matrix. 1,4-Benzenediamine, N-(1,3-dimethylbutyl)-N'-phenyl was detected in samples of all tested solvents except gamma-valerolactone. This amine could be formed from isocyanates (used as binding components between textile and rubber in tyres).

5. A distillate/feed ratio of 0.66, i.e. recovery of 66.7% of solvents could be achieved by atmospheric distillation.

Acknowledgements

This work was supported by project KMR_12-1-2012-0066 entitled “Selective and complete reutilization of the compounds of waste tires” (in the consortium of the Szelence Ltd. and the Budapest University of Technology and Economics).

References

[1] Czvikovszky Tibor, Nagy Péter, Gaál János A polimertechnika alapjai, Kempelen Farkas Hallgatói Információs Központ, 2007 (in Hungarian)
[2] J. S. Dick, Rubber Technology, Compounding and Testing for Performance, Carl Hanser Verlag, 2001
[3] J.M.G. Cowie, Polymers: chemistry and physics of modern materials (Inter. Textbook Co. Ltd, 1973) p 258.
[4] D.M. Money, G. Harrison, Liquefaction of scrap automobile tyres in different solvents and solvent mixes, Fuel 78 (1999) 1729–1736
[5] John R. Kershaw, Supercritical fluid extraction of scrap tyres, Short Communication , Fuel Vol. 77, No. 9/10,(1998) pp. 1113-l 1151
[6] K.A. Dubkov, S.V. Semikolenov, D.P. Ivanov, D.E. Babushkin, G.I. Panov, V.N. Parmon, Reclamation of waste tyre rubber with nitrous oxide, Polymer Degradation and Stability, Volume 97, Issue 7, July 2012, Pages 1123–1130
[7] Faten Sadaka, Irène Campistron, Albert Laguerre, Jean-François Pilard, Controlled chemical degradation of natural rubber using periodic acid: Application for recycling waste tyre rubber, Polymer Degradation and Stability 97 (2012) 816e828
[8] Debapriya De, Amit Das, Debasish De, Brojendranath Dey, Subhas Chandra Debnath, Bidhan Chandra Roy, Reclaiming of ground rubber tire (GRT) by a novel reclaiming agent, European Polymer Journal 42 (2006) 917–927
[9] B Adhikari, , D De, S Maiti, Reclamation and recycling of waste rubber, Progress in Polymer Science. 25 (2000) 909–948

Surface area and interfacial area measurements for spray absorption

Yash Tamhankar[1], Brett King[1], Rob Whiteley[1], Tony Cai[2], and Clint Aichele[1]
[1]School of Chemical Engineering, Oklahoma State University, Stillwater, USA
[2]Fractionation Research Incorporated, Stillwater, USA

Abstract
Spray absorption efficiency is strongly influenced by the surface area of drops. The measurement of dropsize distributions is critical in estimating the cumulative drop surface area. However, not all of the surface area offered by drops is available for absorption. Reaction and then saturation of solvent mass contained inside the drops result in unavailable surface area. Further, size of drops, drop-drop interactions, and wall impact can significantly alter the available surface area. Hence, it is essential to ascertain the interfacial area available for mass transfer. This paper presents surface area quantification based on drop size distribution measurements made with a Phase Doppler Interferometer (PDI), inside a 0.2032 m glass column with counter-current gas flow. The interfacial area measurements are made using CO_2 - 0.1 N NaOH system. A full cone, low pressure drop nozzle is tested in this work. The effect of gas rate and liquid rate on the surface area is elucidated, and the measured interfacial area is compared to a previously developed correlation. Data from these experiments will provide insight into drop surface area generation and absorption in spray towers.

Keywords
spray, absorption, surface area, interfacial area, dropsize distributions, phase doppler interferometer (PDI)

1. Introduction

Gas absorption into a swarm of liquid drops (sprays) is widely used in the chemical industry. The rate of mass transfer into liquid drops is proportional to the surface area offered by the drops. Knowledge of surface area is critical in estimating the efficiency of sprays. Drop size distributions from liquid sprays can be conveniently measured using a Phase Doppler Interferometer (PDI) which facilitates the calculation of surface areas. However, not all of the surface area is available for mass transfer. Drop size, extent of saturation, coalescence, and wall impact can significantly affect the available surface area.

In packed columns, the specific surface area (a_p) is the measure of the surface area offered by the solid packing material per unit volume of the column. The specific surface area remains constant throughout the packed bed height. However, in a spray column, all of the surface area for gas-liquid contacting is offered by the liquid or solvent itself, either in the form of drops or inner wall flow. Drop-drop interactions, drop break up, and wall impact can change the available specific surface area across the height of the column. Hence, there is a need to calculate the specific surface area of a spray rigorously. Spray specific surface area (a_s) can be conveniently expressed in terms of the surface area of all drops per unit volume of liquid sprayed [1]. The volume of liquid sprayed does not change across the height of the spray column, and

hence provides a better basis for calculating the surface area. In this work, the specific surface area of sprays is reported in terms of the cumulative surface area of all drops normalized by the cumulative volume of all drops, across a horizontal plane.

2. Background

Absorption of CO_2 in NaOH has been studied extensively by multiple researchers with the objective of measuring chemical absorption rates and for quantifying the effective surface area or the interfacial area (a_e). Mehta and Sharma [2] tested multiple nozzles in two spray columns and found that the amount of gas absorbed to be a function of the surface area of the drops, relative velocity of drops, and the residence time of drops inside the column. Taniguchi [3] measured absorption rates over a wide range of liquid and gas rates and found them to be well predicted by the solid sphere model. Dimiccoli [4] found the mass transfer flux occurring at the inner wall to be insignificant compared to the flux during drop flight. Turpin *et al* [5] developed an interfacial area correlation to calculate the interfacial area as a function of the gas and liquid velocities. Bandyopadhyay and Biswas [6] investigated CO_2 capture using a two-phase critical flow atomizer. Size distributions were measured using a Phase Doppler Particle Analyzer (PDPA). In spite of the large volume of work on absorption and interfacial area measurements with CO_2-NaOH system, surface area quantification inside the spray plume based on radial and axial measurements of droplet distributions is absent. Apart from one study [6], no effort in quantifying surface areas inside the spray plume with a point technique such as PDI/PDPA has been attempted. In addition, there is a paucity of data regarding interfacial area measurements at high liquid and gas velocities.

3. Experimental Section

3.1. Experimental Set Up

3.1.1. Column

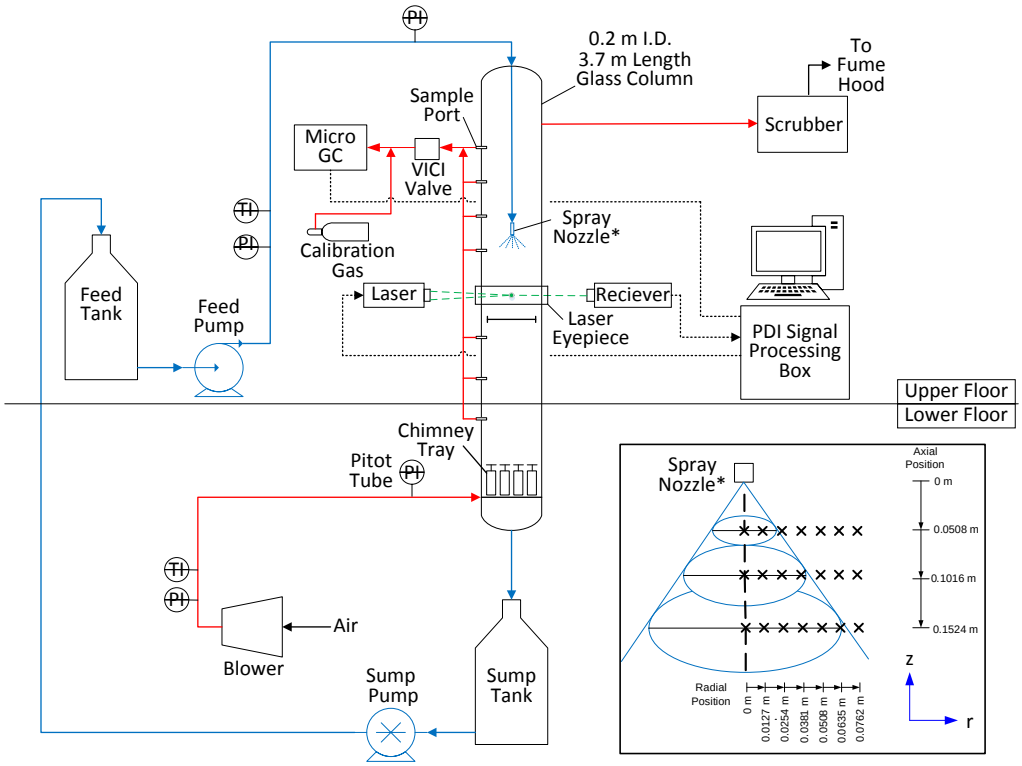

Figure 1. Schematic of experimental set-up (not drawn to scale).

The experimental set up shown in Figure 1 consists of a borosilicate glass column, made of nine sections (QVF) and a cylindrical column head and a cylindrical bottom, 0.06 m^3 feed and sump tanks, feed pump, spray nozzle, air blower, and a gas chromatograph for gas composition measurements. The drop size and velocity measurements are made using a 1-dimensional Phase Doppler Interferometer (PDI) system (100 MD, Artium Technologies, USA) mounted on a rail system. Counter-current gas is injected into the bottom of the column through a glass tee by means of a centrifugal blower. Gas samples are drawn from a custom insert plate at the top of the column. The solvent is pumped from the feed tank using a centrifugal pump, through a rotameter, to the nozzle. The liquid pressure is measured directly before the nozzle. The gas flow rate delivered to the spray column was measured using a pitot tube-differential pressure gauge assembly.

3.1.2. PDI System

The PDI system measures droplet velocity in the spray axial (vertical) direction (downward velocities: +ve; upward velocities: -ve). The PDI technique measures droplet diameter and velocity based on the phase shift and frequency shift of refracted signals from drops [7]. To permit PDI measurements through wall flow on inner walls of the glass column, a customized eye-piece was developed [8].

3.1.3. Chemicals

0.0568 m^3 of 0.1 N NaOH solution was prepared and charged to the feed tank by mixing 234 g of NaOH flakes (98 wt%, Alfa-Aesar) in de-ionized water. Counter-current (indoor) air was used as feed gas for all the experimental runs.

3.2. Experimental Conditions

Table 1 – Experimental Conditions

Temperature (ºC)	30
Liquid rate. 10^5 (m^3/s)	7.6, 12
Gas velocity (m/s)	0, 1.42
Nozzle	Lechler 1/2" 460.803
Nozzle type	Full cone
Spray angle	60º
PDI axial measurements .10^3 (m)	0.0508, 0.1016, 0.1524
PDI radial measurements .10^3 (m)	0, 12.7, 25.4, 38.1, 50.8, 63.5, 76.2

3.3. Calculation

3.3.1. Surface Area

Surface area calculations are based on the measured drop size data reported by the PDI. The method involves curve (polynomial) fitting the radial variation of both the total surface (T_S) and total volume (T_V) recorded by the PDI, and the subsequent integration across a horizontal plane of the spray plume. T_S and T_V, as defined by Equation 1 and Equation 2, represent the surface area and volume of all drops passing through the measurement point for a set acquisition period, respectively.

$T_S = \pi \sum_i n_i {d_i}^2$ (Equation 1)

$T_V = \frac{\pi}{6} \sum_i n_i {d_i}^3$ (Equation 2)

The specific surface area of the spray (a_s) in this case would be the ratio of the integral of the total surface to the total volume in one horizontal plane, as shown in Equation 3.

$$a_s = \frac{2\pi \int_{r=0}^{r=r'} T_S(r)dr}{2\pi \int_{r=0}^{r=r'} T_V(r)dr} \quad \text{(Equation 3)}$$

3.3.2. Interfacial Area

Under the assumption of pseudo first order reaction, the interfacial area can be calculated using the following equation. The pseudo first order assumption is valid in this case due to the speed of the reaction between CO_2 and NaOH. The physio-chemical constants in Equation 4 are evaluated and checked against the work of previous investigators [9, 10].

$$a_e = \frac{N_{CO2}}{V\,\Delta C_{CO2}{}^{*}\,\sqrt{D_{CO2}\,k_2\,C_{NaOH}}} \quad \text{(Equation 4)}$$

4. Results and Discussion

4.1. Surface Area

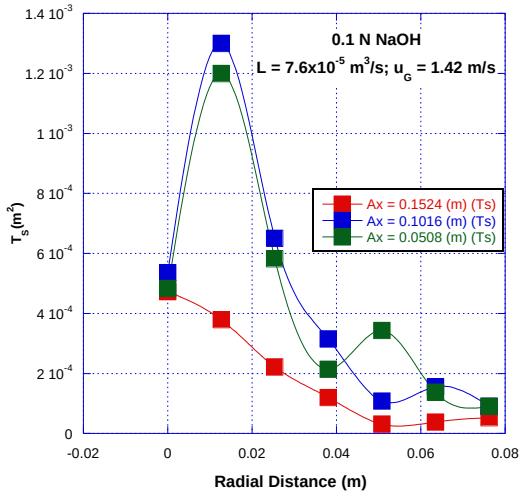

Figure 2 –Total surface variation

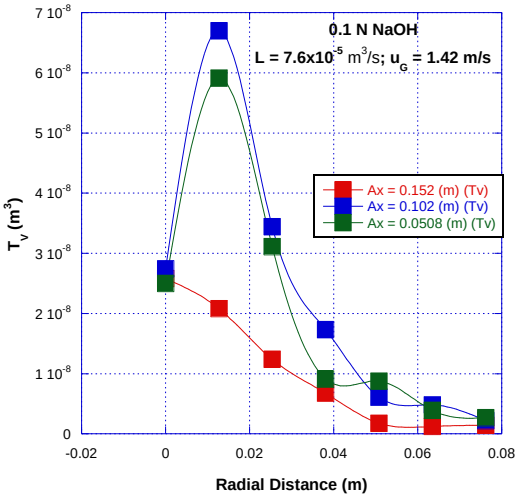

Figure 3 –Total volume variation

The radial variation of total surface (T_S) and total volume (T_V) at all the three axial locations is shown in Figures 2 and 3, respectively. Both T_V and T_S increase away from the geometric center of the column and then decrease. Large drops get ejected away from the spray center, resulting in higher values of T_V and T_S. The dropping off of the curve coincides with the movement of the measurement point outside of the spray plume.

The effect of gas rate and liquid rate on the calculated spray surface areas are shown in Figures 4 and 5, respectively. The spray surface area is found to be greater without countercurrent gas flow than with gas flow, for all the axial locations. With gas flow, a large number of drops are entrained in the up-flowing gas. These upward moving drops travel outside of the spray plume, and are not captured by the PDI and spray surface area calculation procedure because the upper limit of the integral for both the total surface and total volume is limited to the boundary of the spray plume at that particular axial location.

The spray surface area is found to increase with axial location and then decrease, as shown in Figure 5. The increase in spray surface area can be attributed to drop break up and drop-drop interactions. Liquid drops emerge from the spray nozzle at ballistic

velocities. These drops start interacting with the ambient gas and attain the ambient velocity at a certain axial distance downstream of the nozzle tip. At higher discharge velocities, greater axial distance is traversed by the drops before attaining the ambient velocity. Drops which have slowed down get entrained outside of the spray plume. With the lower liquid rate, drops tend to reach the ambient velocity 0.1016 m downstream of the nozzle. Beyond this axial distance, drops start getting entrained and hence the spray surface area is seen to decrease. This trend is not seen with the higher liquid rate because the drops slow down beyond the axial measurements used in this study.

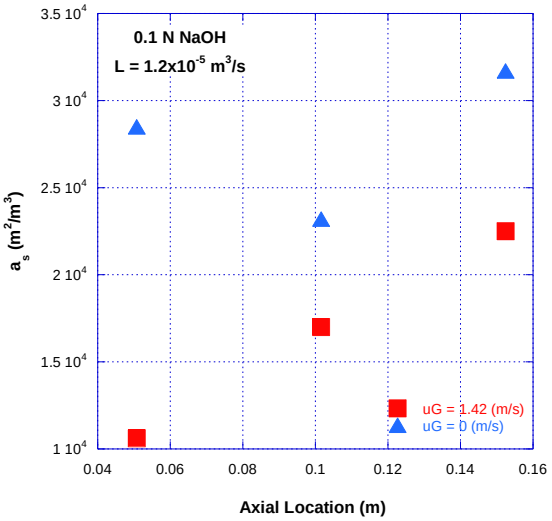

Figure 4 – Effect of gas rate on a_s

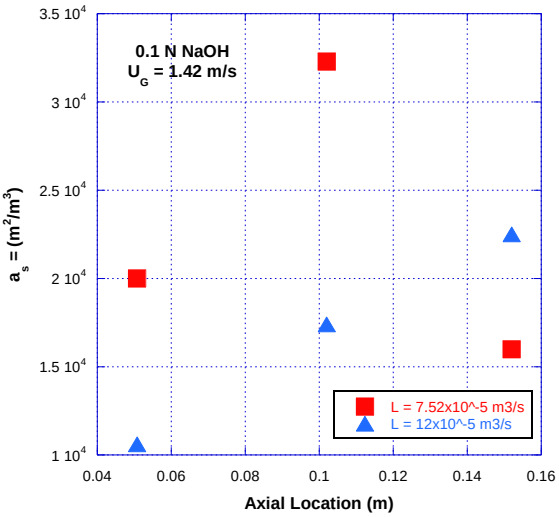

Figure 5 – Effect of liquid rate on a_s

4.2. Interfacial Area

Table 2 below summarizes the interfacial area measurement results.

Table 2 – Interfacial area results.

Present Work	Run # 1	Run # 2	Mehta & Sharma [2]
$CO_{2,in}$ (ppm)	768	830	-
$CO_{2,out}$ (ppm)	755	812	-
G . 10^3 (m^3/s)	47.2	47.2	8.3 – 16.8
L . 10^3 (m^3/s)	0.076	0.076	0.083 – 0.21
Measured a_e (m^2/m^3)	332	475	30 - 50
Calculated a_e (m^2/m^3)	294	294	82.9 – 155.6

The interfacial area was found to vary from 332 – 475 m^2/m^3 based on the measured differences in the CO_2 composition. Comparison of the measured interfacial area with published results of Mehta and Sharma [2] show an order of magnitude difference. This deviation is a result of the larger gas rates employed in this work. Previous investigators [5, 6] have shown the interfacial area to vary with gas rate to the power of 0.74 – 0.87. The measured interfacial area matches the prediction (calculated a_e) from Turpin [5] correlation to within 12 - 38%.

5. Conclusions

A new methodology has been developed to quantify surface areas inside spray columns from droplet size distributions measured by a PDI. The spray surface area is found to change across the axial height of the column, and with both the liquid and

gas rate. As expected, the interfacial area measured inside the column using CO_2 - 0.1N NaOH at high gas velocity was an order of magnitude greater than that seen in a comparable column. This work provides critical insight into spray behavior for absorption applications.

Nomenclature

a_e	interfacial area, m^2/m^3	L	liquid rate, m^3/s
a_p	packing specific area, m^2/m^3	n	count of drops
a_s	spray surface area, m^2/m^3	N_{CO2}	CO_2 flux, kmol/s
C_{CO2}	CO_2 concentration, $kmol/m^3$	r	radius or radial distance, m
C_{NaOH}	NaOH concentration, $kmol/m^3$	r'	spray plume radius, m
d	droplet diameter, m or μm	T_S	total surface, m^2
D_{CO2}	diffusivity of CO_2, m^2/s	T_V	total volume, m^3
G	gas rate, m^3/s	u_G	gas velocity, m/s
k_2	second order rate constant, $m^3/kmol.s$	V	volume of contactor, m^3

References

1. Nukiyama, S. and Y. Tanasawa, *Experiments on the Atomization of Liquids in an Air Stream: Reports 1 to 6*. 1950: Defence Research Board, Department of National Defence.
2. Mehta, K. and M. Sharma, *Mass transfer in spray columns.* British Chemical Engineering, 1970. **15**(11): p. 1440-1558.
3. Taniguchi, I., Y. Takamura, and K. Asano, *Experimental study of gas absorption with a spray column.* Journal of chemical engineering of Japan, 1997. **30**(3): p. 427-433.
4. Dimiccoli, A., M. Di Serio, and E. Santacesaria, *Mass Transfer and Kinetics in Spray-Tower-Loop Absorbers and Reactors.* Industrial & Engineering Chemistry Research, 2000. **39**(11): p. 4082-4093.
5. Turpin, A., A. Couvert, A. Laplanche, and A. Paillier, *Experimental study of mass transfer and H_2S removal efficiency in a spray tower.* Chemical Engineering and Processing: Process Intensification, 2008. **47**(5): p. 886-892.
6. Bandyopadhyay, A. and M.N. Biswas, *CO2 capture in a spray column using a critical flow atomizer.* Separation and Purification Technology, 2012. **94**(0): p. 104-114.
7. Bachalo, W.D. and M.J. Houser, *Phase/Doppler Spray Analyzer For Simultaneous Measurements Of Drop Size And Velocity Distributions.* Optical Engineering, 1984. **23**(5): p. 235583-235583.
8. Tamhankar, Y.S., J.R. Whiteley, M.R. Resetarits, and C.P. Aichele, *Spray Droplet Characterization Inside a Glass Column through Dense Wall Flow.* Atomization and Sprays, 2014. **24**(2): p. 115-128.
9. Pohorecki, R. and W.d.w. Moniuk, *Kinetics of reaction between carbon dioxide and hydroxyl ions in aqueous electrolyte solutions.* Chemical Engineering Science, 1988. **43**(7): p. 1677-1684.
10. Tsai, R.E., *Mass transfer area of structured packing*. 2010, PhD Dissertation, University of Texas at Austin.

Proposal for a new test mixture with elevated viscosity at distillation conditions

Christian Bradtmöller[1], *Stephan Scholl*[1]

[1] *Institute for Chemical and Thermal Process Engineering, Technische Universität Braunschweig, D-38106 Braunschweig, Germany*

Abstract

Standardized test mixtures are needed to determine the efficiency of distillation columns and their internals. Despite the wide range of different test mixtures and the variations in their physical properties, no standard test mixture is available that contributes viscosities above 1.5 mPa s at typical distillation conditions. To investigate the impact of viscosity on separation efficiency and validate models for higher viscosities, a new test mixture is proposed. A screening was carried out to identify components that satisfy the requirements for separation efficiency tests. Based on this, the binary mixture 2-Methyl-2-butanol/2-Methyl-1-propanol was chosen, showing liquid phase viscosities up to 5 mPa s. For this mixture vapor-liquid-equilibria were measured. A slight negative deviation from ideal behavior is accounted for using the NRTL model. Furthermore, liquid density and viscosity were determined for both pure substances as well as their mixtures. Non-idealities are modeled with a Redlich-Kister approach. Thus, vital information for the assessment of separation efficiency with a new test mixture is given and subsequent studies on the influence of viscosity on fluid dynamics and separation efficiency in distillation columns are enabled.

Keywords

Test mixture, viscosity, rectification, vapor-liquid-equilibrium

1. Introduction

The separation efficiency of column internals is an important factor in column design and operation. The efficiency is determined by the internals´ geometry, operational conditions and mixture properties. The influence of the latter has to be known for an optimal design in respect to energy consumption and capacity. In this context liquid viscosity is especially important, since it affects the fluid dynamics and thereby separation efficiency as well as capacity.

Although great effort has been made concerning the development of predictive models, still experiments have to be conducted to obtain accurate data for column performance [1]. These experiments are carried out with standardized test mixtures. Onken and Arlt [2] compiled the properties of recommended systems, with chloro-benzene/ethylbenzene (CB/EB) and cyclohexane/n-heptane (C6/C7) being most widely used. However, there is no test mixture that contributes viscosities above 1.5 mPa s at typical distillation conditions. Predictive models are correspondingly based on low viscosities. Hence, there is demand for a mixture with higher viscosity to enable studies on the effect of increased viscosity as well as the validation of models. A data-bank-based screening was conducted and possible mixtures were identified with their separation factor and viscosity as most important criteria. The exact values of these properties along with liquid density have to be calculated for

the analysis of experimental data and predictive models. This relates to the temperature dependent properties of the pure substances as well as the respective concentration dependence in mixtures.
Hence, vapor-liquid-equilibria (VLE) were determined at different pressures. These were complemented with measurements of liquid density and viscosity in the corresponding range of boiling temperatures. The NRTL model is used to describe the VLE data and a modified Redlich-Kister approach for liquid density and viscosity.

2. Results and discussion

2.1 Screening for a viscous test mixture

Experiments for the assessment of the separation effectiveness of different column internals are typically conducted for a binary system with the column operated under total reflux conditions [3]. The number of effective separation stages is extracted following the approach of Fenske-Underwood. To satisfy the underlying assumptions of this approach the component system has to meet a comprehensive set of criteria:

- both constituents should be well-defined pure components available at high purity to eliminate trace effects of high or non-boiling impurities,
- specifically racemic systems should be avoided,
- relative volatility should be in the range of $1.3 \leq \alpha = (y/x)_1/(y/x)_2 \leq 2.0$, to allow for a reasonable separation with 15 to 20 theoretical stages [1],
- complete miscibility should be given over the full concentration and temperature range,
- boiling temperatures at $p \geq 20$ mbar should be in the range of 50 °C to 150 °C,
- VLE should be close to ideal, i.e. α being almost constant over the column height,
- liquid phase viscosity at separation conditions should be around 0.5 mPa s to 10 mPa s with a small concentration but pronounced temperature dependency,
- no viscosity increasing non-boiling components should be added to avoid concentration of the non-boiling component near the vapor liquid interface. Otherwise the local viscosity instead of the bulk viscosity had to be considered [4],
- the liquid phase should show Newtonian flow behavior,
- components should have a low hazard potential with respect to EHS issues,
- to ease experimental procedures the melting point should be below 40 °C and
- price and availability of the candidates should be acceptable.

On this basis a mixture of two primary alcohols, 2-Methyl-2-butanol/2-Methyl-1-propanol (MB/MP) was chosen.

2.2 Measurement and modeling of vapor-liquid-equilibrium

VLE were determined in a range from 20 mbar to 950 mbar and the vapor pressures were measured in the resulting range of boiling temperatures. First the experimental set-up and the used equations are introduced. Results are presented including a set of NRTL parameters. This allows the calculation of separation factors for any concentration in the investigated pressure range.

2.2.1 Experimental

The chemicals, (MB, purity 99+%, extra pure) and (MP, purity 99%, ReagentPlus), were purchased from Acros Organics, and used without further purification. Experiments were carried out isobarically in a dynamic still, VLE 100, Pilodist GmbH, Meckenheim, Germany. Temperature was measured with a calibrated four wire Pt-100, with an estimated accuracy of ±0.02 K. The accuracy of the pressure is estimated to be 0.1 kPa. Samples of 0.1 mL were drawn with syringes for all

pressures except for 20 mbar. Here volumes of 0.8 mL were received in sample tubes. Composition analysis was carried out with a Shimadzu GC 2010 gas chromatograph. Presented results are the mean of two injections, providing an uncertainty of ±0.002 mol_{MB}/mol_{total}.

2.2.2 Modeling of vapor pressure and VLE

Model parameters were obtained by minimizing the squared ratio of differences between measured and calculated variables divided by the measured value. NRTL parameters were obtained by minimizing the differences of separation factors. Thereby the datasets were normalized with the number of experiments for one pressure.

Vapor pressures were measured in the dynamic still and are calculated according equation 1.

$$\ln\left(p_{s,i}\right) = a_i + \frac{b_i}{T_s} + c_i \cdot \ln\left(T_s\right) + d_i \cdot T_s^{e_i} \tag{1}$$

Activity coefficients were calculated according to the NRTL model as follows:

$$\ln\left(\gamma_1\right) = x_2^2 \cdot \left[\tau_{21}\left(\frac{G_{21}}{x_1 + x_2 G_{21}}\right)^2 + \frac{\tau_{12} G_{12}}{\left(x_2 + x_1 G_{12}\right)^2}\right] \tag{2}$$

$$\ln\left(\gamma_2\right) = x_1^2 \cdot \left[\tau_{12}\left(\frac{G_{12}}{x_1 + x_1 \cdot G_{12}}\right)^2 + \frac{\tau_{21} \cdot G_{21}}{\left(x_1 + x_2 \cdot G_{21}\right)^2}\right] \tag{3}$$

where the parameters τ_{ij} and G_{ij} are given by

$$\tau_{ij} = \frac{\Delta g_{ij}}{R \cdot T}, \qquad G_{ij} = \exp\left(-\alpha_{ij} \cdot \tau_{ij}\right), \qquad i,j = 1,2, \quad i \neq j$$

2.2.3 Results

Figures 1 and 2 present the VLE for the binary system at different pressures.

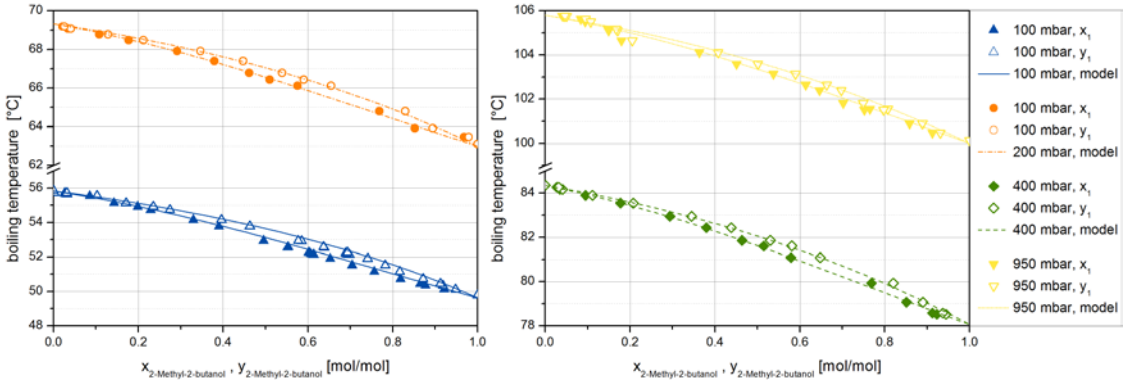

Figure 1: T-x/y-diagram of 2-Methyl-2-butanol / 2-Methyl-1-propanol at different pressures

The vapor-liquid equilibrium shows a slight negative deviation from ideal behavior. At infinity dilution values of γ_1 = 0.83 … 0.92 and γ_2 = 0.84 … 0.95 were measured, the first value corresponding to a pressure of 20 mbar and the latter to a pressure of 950 mbar. Thus, higher pressures cause smaller deviations from ideal behavior. Boiling temperatures reach a maximum of about 0.5 K above the values expected for ideal behavior. Resulting from the increasing non-idealities as well as the ratio of

vapor pressures the separation factor rises with decreasing pressure. Furthermore, a dependency of the concentration can be observed. This dependence on concentration is more pronounced at lower pressures. The NRTL model is able to describe the whole dataset reasonably well. The interaction energy parameters Δg_{ij} could be used without implementing a temperature dependency, although boiling temperatures range from 23 °C at 20 mbar to 105 °C at an operating pressure of 950 mbar.

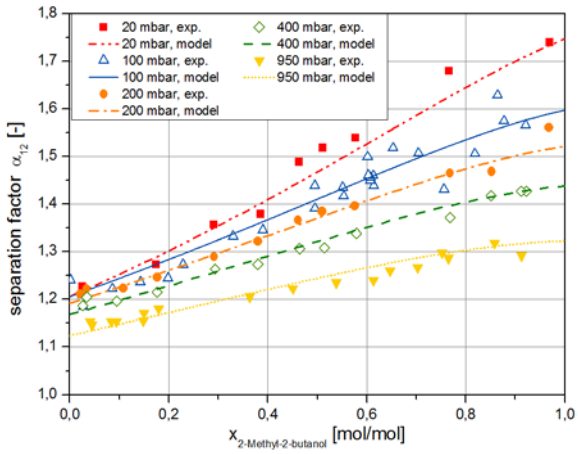

Figure 2: Separation factors of 2-Methyl-2-butanol / 2-Methyl-1-propanol at different pressures

Especially for distillation experiments at low pressures, the change in composition from head to bottom of a column accompanied by the increase in pressure has to be considered. In this case the calculation of separation efficiency should be carried out with the geometric mean of the separation factors along column height. These can be determined with the parameters stated below.

Table 1: Parameters for vapor pressure curves and NRTL model

	vapor pressure		NRTL
2-Methyl-2-butanol	a= $1.2211 \cdot 10^{2}$ b= $-1.0254 \cdot 10^{4}$ c= $-1.4044 \cdot 10^{1}$	d= 0 e= 0	Δg_{12} = 3990.3 Δg_{12} = -3328.3 α_{12}= 0.211
2-Methyl-1-propanol	a= $9.6329 \cdot 10^{1}$ b= $-9.1854 \cdot 10^{3}$ c= $-1.0222 \cdot 10^{1}$	d= $4.4954 \cdot 10^{-7}$ e= 2	

2.3 Measurement and modeling of density and viscosity

For the assessment of experiments, the dependency of density on temperature and composition has to be known to accurately calculate volumetric flows in different cross sections within the column. In this study density was measured from 20 °C to 70 °C. Additionally, the viscosity has to be known. Both properties were measured for the pure substances as well as mixtures at different temperatures. The Redlich-Kister [5] approach was used to deduce suitable correlations.

2.3.1 Experimental

Density was measured with a Mettler Toledo DE51, Mettler, Gießen, Germany, with a resolution of 0.01 kg/m³, temperature was set with an accuracy of ± 0.05 K. Viscosity was determined with a cone and plate system with a Physica MCR 101, Anton Paar, Graz, Austria, equipped with a temperature chamber, minimizing deviations in temperature. Temperature was measured with an accuracy of ± 0.03 K.

2.3.2 Equations for density and viscosity

To model the temperature dependence of the pure components, the following equations were used. Liquid density was modeled with equation 4, adapted from the Racket equation [6], liquid density is computed using equation 5. These equations were chosen, since they are used in the DIPPR® database (equations 105 and 101) and are commonly applied in commercial flowsheet simulation software.

$$\frac{\rho_i}{kg/m^3} = \frac{a_i}{b_i^{\left(1+\left(1-\frac{T/K}{T_c/K}\right)\right)^{d_i}}} \cdot \frac{M_i}{kg/kmol} \tag{4}$$

$$\ln\left(\frac{\eta_i}{Pa \cdot s}\right) = a_i + \frac{b_i}{T} + c_i \ln(T) + d_i \cdot T^{e_i} \tag{5}$$

Instead of excess functions, the mixture densities are presented, since these are needed to determine mass balances for different cross sections of a distillation column. Therefore, the excess molar volume V^E is calculated using a Redlich-Kister [5] approach.

$$\rho_m = \frac{x_1 \cdot M_1 + x_2 \cdot M_2}{\frac{x_1 \cdot M_1}{\rho_1} + \frac{x_2 \cdot M_2}{\rho_2} + V^E} \tag{6}$$

with $V^E = x_1 \cdot x_2 \cdot \sum_{k=0}^{2} A_k \cdot (x_1 - x_2)^k$ and: $A_k = a_k + b_k \cdot T + c_k \cdot T^2$

To determine the viscosity of the mixture, a strong temperature dependency of the non-idealities has to be accounted for. Hence, the Redlich-Kister approach is adapted, using the additional factor f_1 to calculate the deviations.

$$\eta_m = x_1 \cdot \eta_1 + x_2 \cdot \eta_2 + x_1 \cdot x_2 \cdot f_1 \cdot \sum_{k=0}^{1} A_k \cdot (x_1 - x_2)^k \tag{7}$$

with: $f_1 = \frac{\eta_1 + \eta_2}{2}$ and $A_k = e^{a_k + \frac{b_k}{T} + c_k \cdot \ln(T)}$

2.3.3 Results

For both properties non-idealities were seen, which are a function of temperature. Especially at low temperatures, the viscosity of the mixtures shows much higher values than calculated by a mixing rule and the contributions of the pure components. The distribution of these deviations is not symmetrical. Therefore, the Redlich-Kister approach was used to model mixture properties, as for k ≥ 1 in equations 6 and 7, non-symmetric distributions can be handled very well.

In case of the density, at 20 °C the maximum of the deviation is measured at a concentration of x_{MB} = 0.7 mol_{MB}/mol_{total}. At lower temperatures the maximum is shifted to lower concentrations, reaching a value of x_{MB}=0.4 mol_{MB}/mol_{total} at 70 °C. This shift goes along with a decrease of the maximum deviation with rising temperature. A value of k = 2 in equation 6 and a second degree polynomial were able to reproduce these temperature dependencies.

The deviation of the viscosity is rather symmetric, but temperature has a strong impact on the absolute values. At 20 °C a viscosity 1.4 mPa·s above the ideal value is measured. With increasing temperature, the deviation declines to 0.1 mPa·s at

60 °C. Since mixture properties are not available at higher temperatures and a negative deviation cannot be presumed, the deviation is assumed to level for higher temperatures. This dependence could be modeled by applying an exponential approach for A_k and by normalizing deviations with the viscosity of the pure components by implementing the factor f_1. Thereby it is possible to describe the viscosity properly over the whole range of concentration and temperatures.

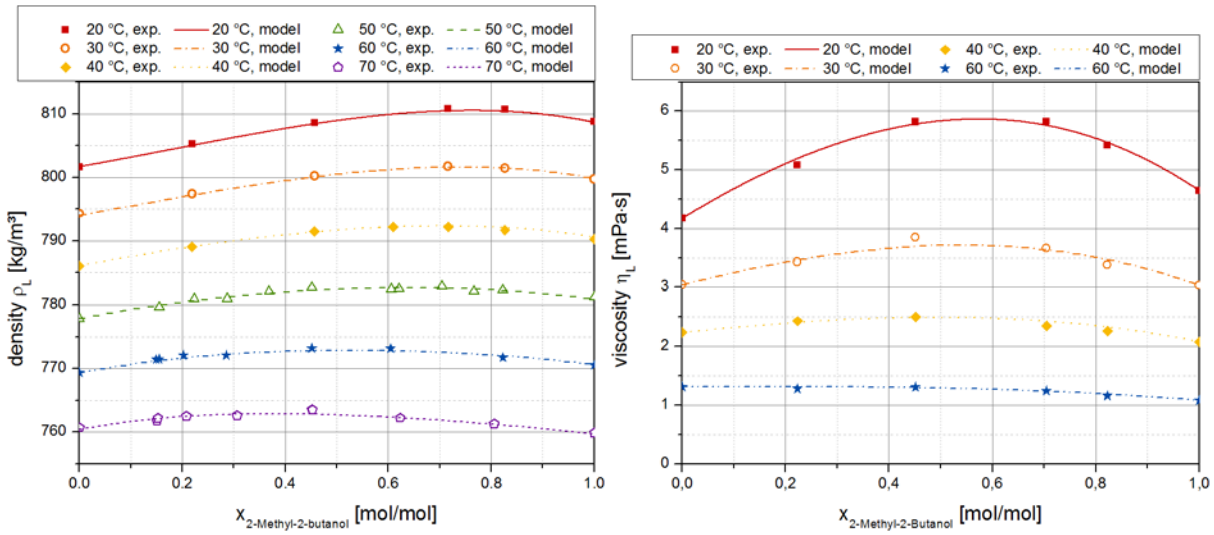

Figure 2: Experimental and modeled values of density and viscosity at different temperatures as function of composition

Table 2: Parameters for the modeling of density and viscosity of pure components and mixtures

	Parameters for density		Parameters for viscosity	
	Pure	**Mixture**	**Pure**	**Mixture**
2-Methyl-2-butanol	a = 0.1223 b = 0.1029 T_c = 545.2000 d = 0.1379 M_i = 88.1500	$a_0 = -7.4310 \cdot 10^{-4}$ $a_1 = -5.1130 \cdot 10^{-3}$ $a_2 = -1.0978 \cdot 10^{-4}$ $b_0 = -1.0382 \cdot 10^{-5}$ $b_1 = -1.1741 \cdot 10^{-6}$ $b_2 = 2.5204 \cdot 10^{-6}$ $c_0 = 2.3316 \cdot 10^{-8}$ $c_1 = 5.0099 \cdot 10^{-8}$ $c_2 = -6.2798 \cdot 10^{-9}$	a = -191.6332 b = 11581.8476 c = 25.7814 d = 0.1358 e = 0.1405	a_0 = 63.1017 a_1 = 19.1467 b_0 = 1.6095 b_1 = 40.6774 c_0 = -11.0640 c_1 = -3.7039
2-Methyl-1-propanol	a = 0.4756 b = 0.1897 T_c = 547.7300 d = 0.1683 M_i = 74.1230		a = -46.8575 b = 4337.6539 c = 4.6803 d = 0 e = 0.7398	

3. Conclusions

A screening for substances with elevated viscosity under distillation conditions was carried out. The mixture of 2-Methyl-2-butanol/2-Methyl-1-propanol was identified as a potential test mixture. The measurement of the vapor-liquid-equilibrium at different pressures revealed non-idealities relevant for separation efficiency tests. Therefore, the NRTL model was applied and separation factors were successfully calculated. Furthermore, liquid density and viscosity were measured and parameters were derived to model the properties of the mixture.

Since no polymer is used to enhance viscosity, packing efficiency can be determined according to standardized procedures under total reflux. Compared to CB/EB the proposed binary mixture exhibits five times higher viscosities. These strongly increase if operating pressure is lowered. Hence, the mixture offers an excellent possibility to investigate the influence of viscosity on separation efficiency.

Acknowledgements

This work was supported by Deutsche Forschungsgemeinschaft under Grant no. SCHO 842/12-1.

References

[1] M. Ottenbacher, Ž . Olujić, T. Adrian, M. Jödecke, C. Großmann, Structured packing efficiency-Vital information for the chemical industry, Chem. Eng. Res. Des., 89, 2011, p 1427-1433
[2] U. Onken, and W. Arlt, Recommended test mixtures for distillation columns (second edition), The Institution of Chemical Engineers, 1990, Rugby, England
[3] Ž. Olujić, Standardization of Structured Packing Efficiency Measurements, 2008, http://www.tkk.fi/Units/ChemEng/efce/2008/presentations/Olujic-document.pdf
[4] R.E. Tsai et al., Influence of viscosity and surface tension on the effective mass transfer area of structured packing, Energy Procidia, 1, 2009, p 1197-1204
[5] O. Redlich, A.T. Kister, Ind. Eng. Chem., 40, 1948, p 345-348
[6] B. E. Poling, G.H. Thomson, D. G. Friend, R. L. Rowley, W. V. Wilding, Perry´s chemical engineers´ handbook, Editor D. W. Green, R. H. Perry, 8th edition, Mc-Graw-Hill, New York, 2008, p 2-503 et seq.

Desorption Kinetics of CO_2 from aqueous Amine-Carbonate-Blends

Alexander Tunnat[1], *Peter Behr*[1], *Klaus Görner*[1]
[1]*Affiliation: Chair of Environmental Process Engineering and Plant Design*
Universität Duisburg-Essen, Leimkugelstraße 10, 45141 Essen

Abstract
Within this work a well known and critically validated experimental setup is used in order to gather kinetic and thermodynamic data for the absorption and desorption of CO_2 from different aqueous amine solutions and amine-carbonate blends. A wetted wall reactor is used to directly measure the absorption and desorption fluxes of CO_2 at ambient pressure up to 353 K. A quasi adiabatic reaction calorimeter is employed to measure the heat capacities and absorption enthalpies of the different solvents. All measurements are in a fairly good agreement with available literature data.
Accounting these data a simplified kinetic model was developed and modified in order to evaluate the performance of novel solvents in larger scale processes based on a reliably measurable lab data.
Performed calculations indicate that energy demands and required amine concentrations can significantly cut down by using amine-carbonate blended solutions instead of pure amine solutions (i.e. 30 wt.-% Monoethanolamine, MEA).

Keywords
Absorption kinetics, desorption kinetics, process modeling, basic data, CO_2, CCS

1. Introduction

For process optimizations including solvent systems a very detailed understanding of the process itself and the employed solvents is essential. In order to perform a reliable process simulation one has to be certain about the employed models and the physical and chemical data these models are based on. Pure and blended aqueous amine solvents have become the reference regarding large scale post combustion carbon capture processes.
So far a lot of attention has been paid to the absorption process of CO_2 into different reactive solutions. In order to measure these kinetics a wide range of different setups [1, 2] and mathematical models [2, 3] is known. Some enclosing reviews [4, 5] indicate a thorough understanding of these processes. At the same time, only limited data are provided concerning the desorption kinetics of CO_2 from different reactive solvents [6-9].
For our measurements a wetted wall reactor is used in order to measure the absorption and desorption kinetics of CO_2. A critical validation of our experimental setup, method of measurement and data analysis as well as comparisons to available desorption kinetics data are given in [10, 11].
Furthermore a simple kinetic model is used to calculate detailed absorption column profiles and evaluate the effective kinetics a long the height of packing in the column. This model is based on discretising the entire absorption column and calculating mass and heat transfer for every element of column height and volume. Measured

kinetic and thermodynamic lab data can directly be implemented in this model. Some of these data from a previous model are already published [12].

2. Results and discussion

2.1 Desorption Data

Apart from previously presented measurements of pure amine solutions [10,11] we are currently focusing on carbonate-amine blends.

Prior to performing the desorption experiment each solvent was exposed to a CO_2 atmosphere (1 atm, 14 vol.-% CO_2, comparable to coal fired power plant flue gases) until the equilibrium loading was reached.

Figure 1 shows the measured desorption fluxes j [mol m^2 s^{-1}] versus the CO_2 loading of the solution [mol CO_2/mol solvent]. Hence the red dots represent a pure MEA solution. Here it can be seen that the equilibrium loading decreases with an increasing carbonate fraction of the solution. Furthermore desorption fluxes decrease with an increasing carbonate fraction, respectively shift to slightly lower loadings.

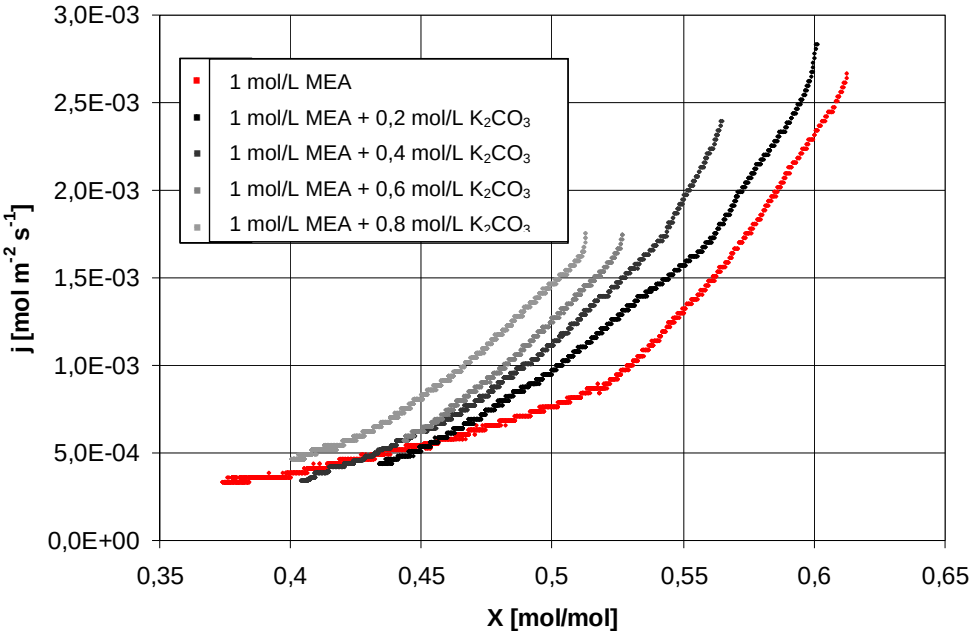

Figure 1: Measured desorption fluxes from pure and blended MEA solutions at 333 K

This decrease of the desorption rate can mainly be contributed to the comparably high stability of the MEA-carbamate. Therefore the increase of basicity by adding carbonate to the solution does not lead to a significantly increasing carbamate hydrolysis. The rather stable OH^--CO_2-bond formed by the direct reaction of CO_2 with OH^--ions in the solution even leads to a decrease of the measured desorption fluxes.

The following Figure 2 shows a similar plot for pure and blended Piperazine solutions. Here comparable trends can be found for the correlation of total solvent concentration and equilibrium CO_2 loading. Here, in contrast to the blended MEA solutions, an increase in desorption fluxes can be found with an increasing carbonate fraction. By employing a solution of 1 mol/L Pz and 0,6 mol/L potassium carbonate a significant increase of measured desorption fluxes compared to the pure amine solution can be found.

Reference desorption measurements of pure, even highly concentrated carbonate solutions did not show desorption kinetics that allowed to contribute the increase of desorption fluxes to the simple addition of reactants in the solution. Here it is a matter of carbamate stability and hydrolysis [13, 14], whereas the low carbamate stability of Pz leads to a high rate of carbamate hydrolysis and therefore also to a higher rate of CO_2 desorption.

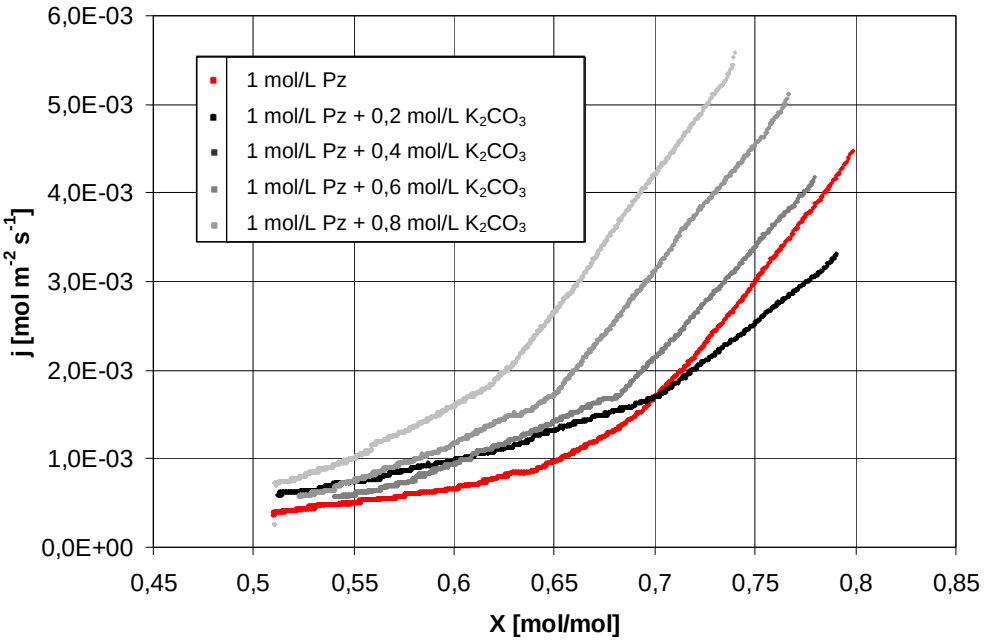

Figure 2: Measured desorption fluxes from pure and blended Piperazine (Pz) solutions at 333 K

2.2 Process Modeling

Figure 3 shows an generic heat and loading diagram for the absorption column of an existing plant (3 m height of packing, 20 m³/h gas stream, 0,1 m³/h solvent stream).

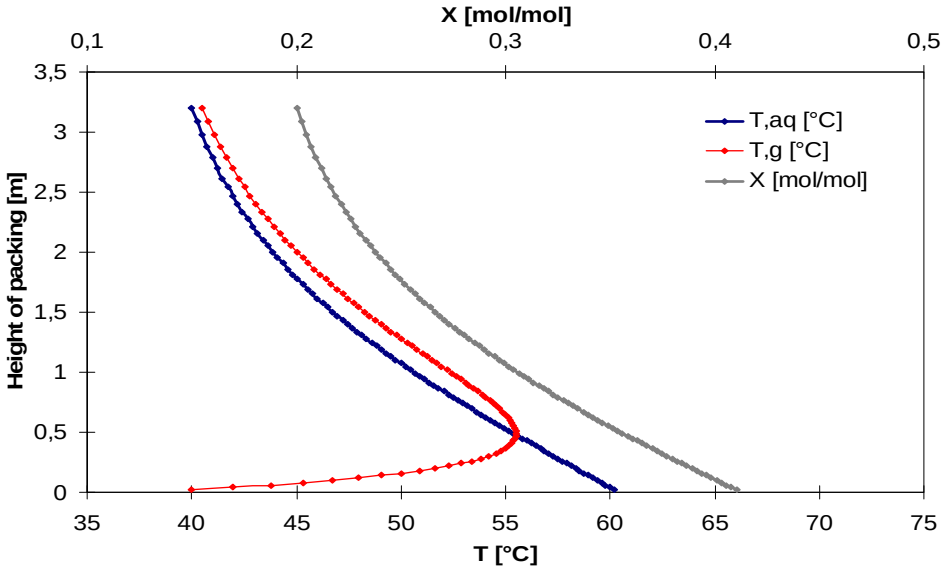

Figure 3: Generic absorption profile for 30 wt.-% MEA, loading and temperature

Here one can see, that most of the heat of absorption is released in the lower half of the column. This has mainly to be contributed to the higher CO_2 vapor pressure at the bottom of the column.
This also results in the highest effective mass transfer at the bottom of the column, as shown in Figure 4. This has to be contributed to the higher CO_2 vapor pressure here, which even compensates the decrease of absorption kinetics due to the increasing liquid loading from the top to the bottom of the column.

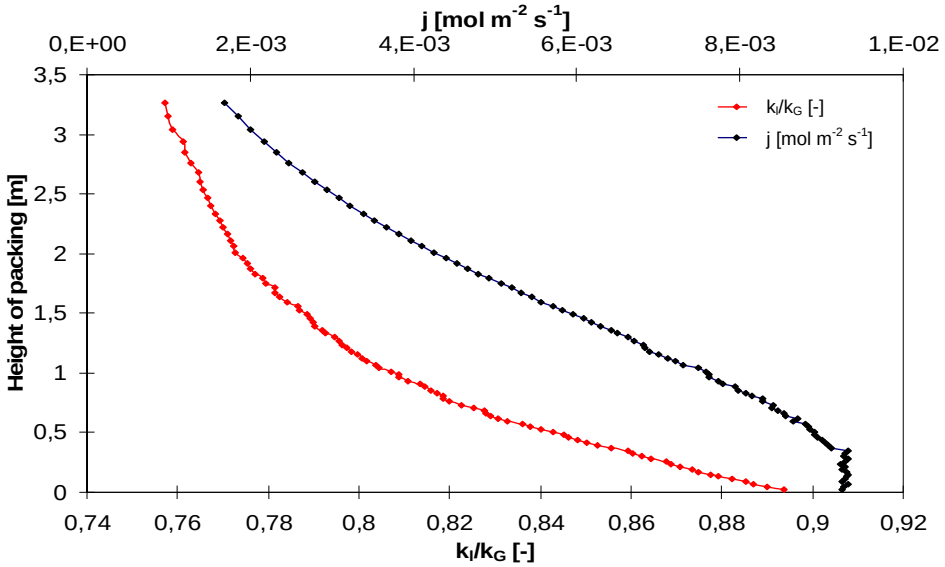

Figure 4: Generic absorption profile for 30 wt.-% MEA, effective mass transfer

Furthermore it is shown, that the liquid side mass transfer resistance (k_l) accounts to up to 90 % of the overall mass transfer (k_G) resistance in the column. Mass transfer overall is strongly controlled by the liquid side, although its influence decreases from the bottom to the top of the column due to a decreasing liquid loading and decreasing CO_2 vapor pressure in the gas phase.
Figure 5 shows a parity plot of measured and calculated overall CO_2 absorption efficiencies ($y=1-c(CO_{2,lean})/c(CO_{2,rich})$).

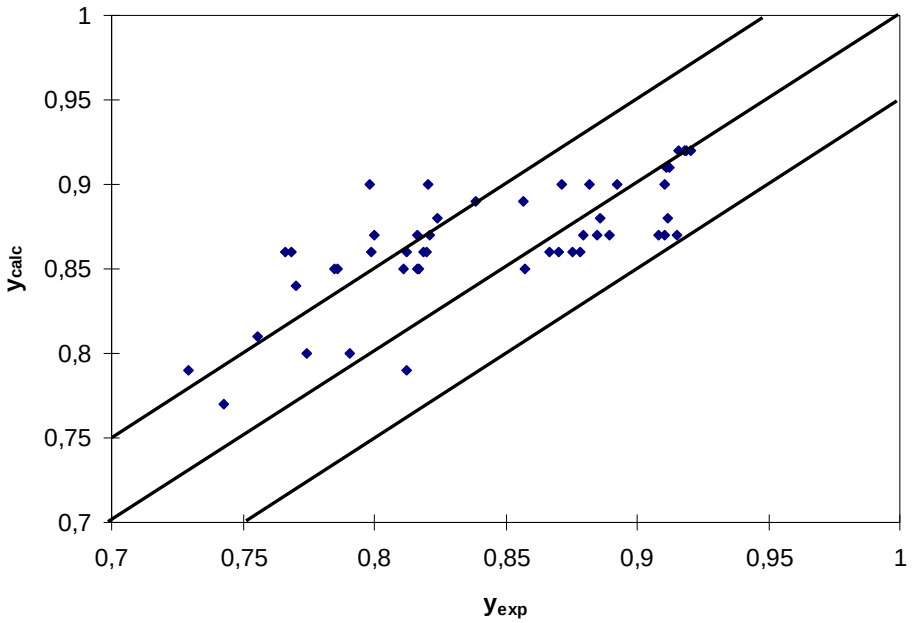

Figure 5: Parity plot of measured and calculated overall absorption efficiencies (y)

In Figure 5 a parity plot of measured and calculated overall absorption efficiencies is shown. This validation of our previously described model was based on about 100 experimental data points. Overall our model predicts the experimental values within 10 % deviation. Some experimental values are over-predicted by our model by more than that due to process instabilities during the measurement. Overall it has to be noted, that our model rather tends to overpredict the measured values. This can also be attributed to the model employed for calculating the hydraulic area within the column especially for low L/G ratios. This extend of overprediction can also be found for other simplified models [15].

3. Conclusions

Within this work some kinetic desorption experiments were performed. Apart from pure amine solutions also blended amine potassium carbonate solutions were examined. A direct comparison between blenden MEA and Pz solutions shows, that the blended Pz solutions desorb CO_2 at significantly higher rates than the blended MEA solutions. Furthermore it is indicated, that the carbamate stability has a significant influence on the effective desorption kinetics. Hence the less stable Pz carbamate leads to a significant increase in desorption rate when combined with an additional base such as potassium carbonate. Further experiments will focus on slightly higher concentrated blends in order to optimize desorption kinetics for technical application. It has already been shown that the use of such amine carbonate blends offers the possibility to reduce the energy demands for solvent regeneration due to lower heats of absorption [12].

Furthermore we developed a kinetic model to describe mass transfer in a packed column. Based on a few easily measurable lab data it is possible to evaluate the performance of a certain solvent for technical application. A critical model validation based on about 100 experimental data points from a rather small post combustion capture plant was performed. This validation shows a good agreement with experimental results within an acceptable uncertainty.

Current efforts focus on the completion of comparable experiments with a larger pilot plant (2x6 m height of packing, 1200 m³/h gas stream, 10 m³/h solvent stream) in order to validate our model on a larger scale as well.

Acknowledgements

Financial support for this work provided by the Federal Ministry of Education and Research through project 01RC1003C and project 0327786A is greatly appreciated.

References

[1] P.V. Danckwerts, Gas Liquid Reactions, McGraw-Hill, 1970.

[2] A. Jamal, A. Meisen, C. Jim Lim, Kinetics of carbon dioxide absorption and desorption in alkanolamine solutions using a novel hemispherical contactor-I. Experimental apparatus and mathemathical modelling, Chem. Eng. Sci. 61, pp. 6571-6589, 2006.

[3] J. Landau, , Desorption with a chemical reaction, Chem. Eng. Sci. 47, pp. 1601-1606, 1991.

[4] A. Aboudheir, P. Tontiwachwuthikul, A. Chakma, R. Idem, Kinetics of the reactive absorption of carbon dioxide in high CO_2-loaded, concentrated aqueous monoethanolamine solutions, Chem. Eng. Sci., 58, pp. 5195-5210, 2003.

[5] P.M.M. Blauwhoff, G.F. Versteeg, W.P.M. van Swaaji, A study on the reaction between CO_2 and alkanolamines in aqueous solutions, Chem. Eng. Sci. 38, pp.1411-1429, 1983.

[6] H. Kierzkowska-Pawlak, H., Chacuk, A., Kinetics of CO_2 desorption from aqueous N-methyldiethanolamine solutions, Chem. Eng. J., 168, pp. 367–375, 2011.

[7] A. Jamal, A. Meisen, C. Jim Lim, Kinetics of carbon dioxide absorption and desorption in aqueous alkanolamine solutions using a novel hemispherical contactor—II:Experimental results and parameter estimation, Chem. Eng. Sci., 61, pp. 6590-6603, 2006.
[8] E.S. Hamborg, G.F. Versteeg, Absorption and desorption mass transfer rates in chemically enhanced reactive systems. Part II: Reverse kinetic rate parameters, Chem. Eng. J. 198-199, pp. 561-570, 2012.
[9] H. Kierzkowska-Pawlak, A. Chacuk, Carbon Dioxide Removal from Flue Gases by Absorption/Desorption in Aqueous Diethanolamine Solutions, Air&Waste Manage. Assoc. 60, pp. 925-931, 2010.
[10] A. Tunnat, P. Behr, K. Görner, Untersuchungen der Desorptionskinetik von CO_2 aus wässrigen Amin- und Carbonatlösungen zur Optimierung von CO_2-Abscheideprzesse, 45. Kraftwerkstechnisches Kolloquium, Dresden, Konferenzband, 2013.
[11] A. Tunnat, P. Behr, K. Görner, Desorption Kinetics of CO_2 from water and aqueous Amine Solutions, TCCS-7 Conference, Trondheim, 2013, to be published, Energy Procedia.
[12] P. Behr, A. Maun, A. Tunnat, K. Görner, Optimization of CO_2 capture from flue gas with promoted potassium carbonate solutions, Energy Procedia, 37, pp. 1554-1565, 2013.
[13] V. V. Mahajani, P. V. Danckwerts, Carbamate-Bicarbonate Equilibrium for Several amines at 100 °C in 30 % Potash, Chem. Eng. Sci. 37, pp. 943-944, 1982.
[14] S. S. Laddha, P. V. Danckwerts, The Absorption of Carbon Dioxide by Amine-Potash Solutions, Chem. Eng. Sci. 37, 665-667, 1982.
[15] F. A. Tobiesen, H. F. Svendsen, Experimental Validation of a Rigorous Absorber Model for CO_2 Postcombustion Capture, AIChE Journal, 53, Pages 846-865, 2007.

Continuous Gas Dehydration with Ionic Liquids as an Absorbent

Florian Heym, Michel Krannich, Wolfgang Korth, Andreas Jess
Chair of Chemical Engineering, Bayreuth, Germany

Abstract

In the gas processing industry, the dehydration of natural gas plays a decisive role. It is necessary to remove the water vapour present in the wet gas stream. The most effective practice to remove water from natural gas is to use triethylene glycol (TEG) in the gas dehydration process. Although this physical absorption is an industrially mature process, glycols run off due to evaporation losses and oxidative decomposition. Thus, making ILs promising alternatives to glycols because they possess low vapour pressure, high stability against oxygen decomposition and high affinity to water. In a continuously operating absorption and desorption column, long-term experiments for gas dehydration and the subsequent regeneration of the ionic liquid (IL) 1-ethyl-3-methylimidazolium methanesulfonate [EMIM][$MeSO_3$] were conducted. The experimental data point out quite satisfactory results with regard to the efficiency of gas drying with [EMIM][$MeSO_3$]. In addition, a comparison of the column height between TEG and the ionic liquid [EMIM][$MeSO_3$] for a predefined drying task shows that the IL takes up to four times lower column height than the TEG as absorbent. Furthermore, a regeneration of the ionic liquid with air at moderate temperatures (T = 90 °C) is possible, which is impossible for the oxygen sensitive glycols.

Keywords

absorption, continuous gas drying unit, HTU/NTU-model, gas dehydration process, ionic liquid

1. Introduction

Raw natural gas coming out of a gas well usually contains significant amounts of water vapour and various other impurities. Since corrosion and hydrate formation in pipelines is associated with water, the gas industry desires a dew point of about -5 °C representing 4000 ppm in the gas phase [1]. Hence, the dehydration of natural gas is the first and most important step during the natural gas processing. In industry, water is removed in absorption units containing glycols like triethylene glycol (TEG) as absorbent. Typically, industrial glycol dehydration units consist of an absorber, flash tank, heat exchangers and a regenerator. Here, the natural gas stream containing water is conducted in counter flow to TEG. The water loaded TEG stream is regenerated in a desorption unit and the lean TEG liquid is returned to the absorber [2-4]. Although TEG has a high boiling point of 287 °C losses by evaporation during absorption and mainly during regeneration at elevated temperatures cannot be avoided. According to literature [1] the loss at normal operating conditions is around 10 litres of glycol per million standard m^3. Thus, for a typical throughput of up to 10 million m^3 per day of natural gas, the loss amounts to around 100 litres per day. This is not much, but more than nothing. Furthermore, TEG decomposes in presence of oxygen and forms organic acids which lead to corrosion. Therefore, the dehydration

of air as well as the regeneration of TEG by stripping with air is impossible [5-7]. An ideal solvent for dehydration of a gas by absorption (scrubbing) of water vapour should have a low vapour pressure and a high affinity to water. In addition, it should be stable during thermal stress and chemically stable against oxygen. It should have a low viscosity and low toxicity.
Hygroscopic ionic liquids (ILs) like 1-ethyl-3-methylimidazolium methanesulfonate [EMIM][$MeSO_3$] seem to be promising alternatives to the industrially used glycols. Their very low vapour pressure (several decades lower than TEG) minimizes the losses of the absorbent due to evaporation of several decades. Furthermore, the regeneration of the water loaded IL is possible either by distillation or stripping at moderate temperatures of 90 °C with air [8, 9].
However, apart from choosing the suitable ionic liquid, the design of a continuous gas drying process (absorption and desorption column) with the hygroscopic ionic liquids as new absorbents requires the knowledge of crucial parameters. These parameters are the activity coefficient γ_{H_2O}, which might be temperature-dependent, the loading/flooding point of columns and mass transfer coefficient k_G of water in the ionic liquid [10-12]. For the presented system H_2O-[EMIM][$MeSO_3$], these parameters were determined in a continuous absorption unit. Based on these data, a continuous absorption/desorption plant was designed using the HTU/NTU-model (HTU = Height of one transfer unit, NTU = Number of transfer units) [13].

2. Results and Discussion

2.1 Experimental Methods

For the continuous gas drying experiments with subsequent regeneration of the ionic liquid [EMIM][$MeSO_3$], a continuous adsorption/desorption plant (Figure 1) was used.

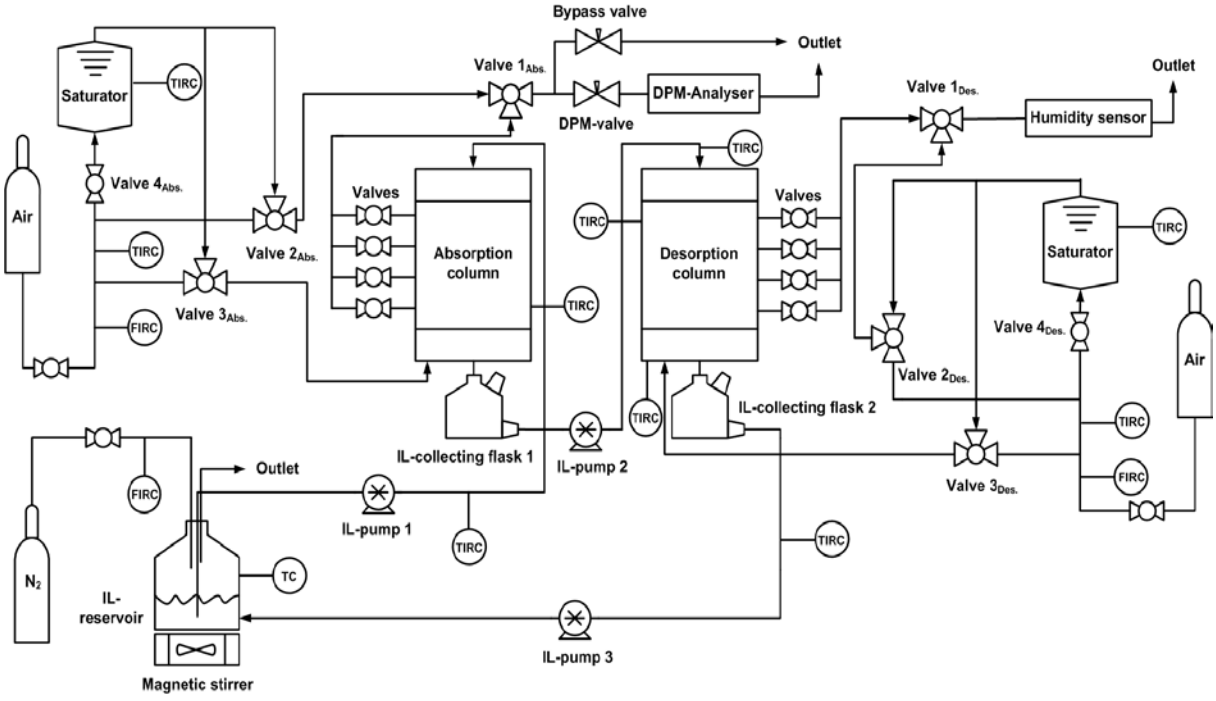

Figure 1: Experimental setup of the continuous absorption/desorption plant

The setup consists of two gas supply units for air, two temperature-controlled water saturators, two temperature-controlled absorption/ desorption columns (cylindrical

and double-walled glass column with 4 valves, fill height: 66 cm, diameter: 3.54 cm) two peristaltic pumps (Heidolph, Pumpdrive 5201), one membrane dosing pump (Hanna Instruments, BL5), one humidity sensor (Hygrosens, HYT-221) and a dew point meter (Michell Instruments, S4000 Remote Klimatik). This setup enables long-term absorption/desorption experiments. The column temperature of the absorption was varied between 30-50 °C while the regeneration was operated at 90 °C. Each experiment (absorption/desorption) is divided in three main parts (see Figure 2). First the degree of saturation of the corresponding feed gas of the absorption/desorption unit is measured. During the second step the feed gas is passed through the column in counter flow to the loaded or regenerated ionic liquid respectively. In the last step the degree of saturation of the corresponding feed gas was measured again in order to check if the degree of saturation has changed during the measurement. The experimental results were subsequently compared with theoretically predicted values.

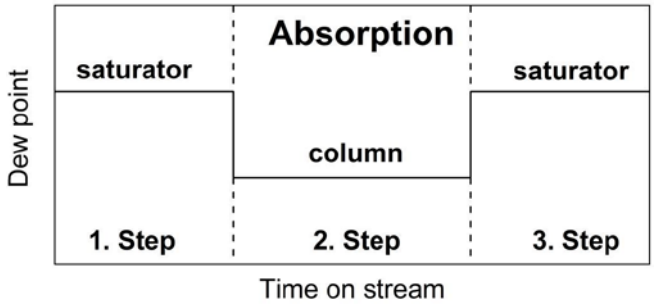

Figure 2: Schematic profile of the three main parts of a gas drying with the ionic liquid [EMIM][$MeSO_3$]. In this case exemplary for the absorption

The design of a continuous absorption/desorption plant with the HTU/NTU-model requires the important parameters like the temperature-dependent activity coefficient γ_{H_2O}, loading/flooding point and the mass transfer coefficient k_G. By using the correlation of Mersmann et al., the loading/flooding point was validated [10]. The activity coefficient was determined with a continuous absorption unit. Measurements for the mass transfer coefficient were conducted and compared with Onda's correlations [11].

2.2 Activity Coefficient of Water in Water/IL mixture

The temperature-dependent activity coefficient γ_{H_2O} in ILs was measured in a continuous absorption unit. In these measurements, the water content of the ionic liquid [EMIM][$MeSO_3$] (0-5 wt%) and the temperature (30-90 °C) were varied. For a temperature range of 30-50 °C (absorption) and a temperature of 90 °C (desorption), the activity coefficient can be approximated by equation (1) and (2).

$$\gamma_{H_2O}(T = 30 - 50\,°C) = 0.075 + 0.925 \cdot x_{H_2O}^{2.7} \quad (1)$$

$$\gamma_{H_2O}(T = 90\,°C) = 0.105 + 0.895 \cdot x_{H_2O}^{2.3} \quad (2)$$

The temperature-dependent activity coefficient is needed for the column design with the HTU/NTU-model [13, 14].

2.3 Mass transfer coefficient k_G

Another important parameter for the column design is the mass transfer coefficient k_G which describes the mass transfer between gas and liquid phase. The k_G-value has to be determined for both the absorption and the desorption. Figure 3 represents the results for the measured mass transfer coefficients at a temperature of 30-50 °C (absorption) and 90 °C (desorption) which are compared with the theoretically calculated k_G-values [11].

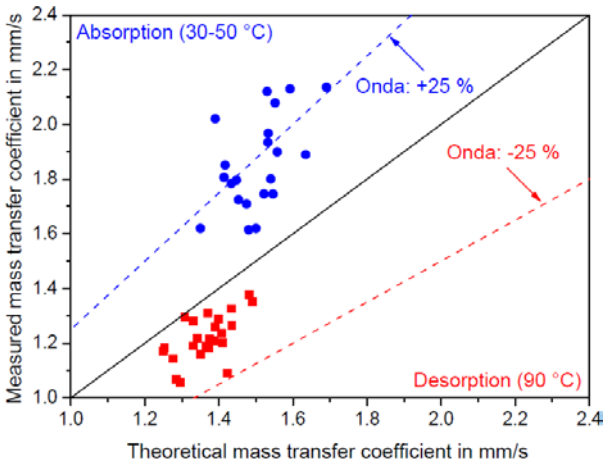

Figure 3: Comparison of the measured mass transfer coefficient k_G with the theoretical mass transfer coefficient k_G for the system H_2O-[EMIM][$MeSO_3$]

The measured mass transfer coefficients for the absorption and desorption are within the error range of ±25 % according to Onda. In summary, it can be noted that a column design based on the calculated mass transfer coefficients according to Onda [11] is definitely possible.

2.4 Continuous gas drying experiments

In the absorption/desorption plant (see Figure 1), long-term experiments for gas drying and regeneration of the ionic liquid [EMIM][$MeSO_3$] were conducted. During these experiments the absorption and desorption temperature, water vapour content, the fluid and gas load factor as well as the size and kind of packing (Raschig rings, sphericals) were varied. At the beginning of each gas dehydration measurement, a theoretical drying task with the HTU/NTU-model was predicted. Table 1 exemplifies the theoretical operating conditions for the continuous gas drying process with 6 mm Raschig rings. It is important to mention that the dew point of the moist gas stream (absorption, starting point) corresponds approximately to the ambient temperature (atmospheric humidity of 100 %) of the natural gas production plant.
In this measurement, the column temperature of the absorption was 30 °C while the regeneration was operated at 90 °C. Figure 4 shows the results for the gas drying experiment. In this case, the measured dew point for the absorption and desorption is plotted over the time.

Operating Condition	
IL stream in l/h	1.7
Gas stream at loading point (abs. /des.)	950/1030
Water content of IL in wt%	4.0
Dew point (abs., start) in °C	9.0
Dew point (abs., end) in °C	-12.9
Dew point (des., start) in °C	24.5
Dew point (des., end) in °C	29.4

Table 1: Theoretical operating conditions for a gas drying task with the ionic liquid [EMIM][$MeSO_3$] (abs. = absorption; des. = desorption)

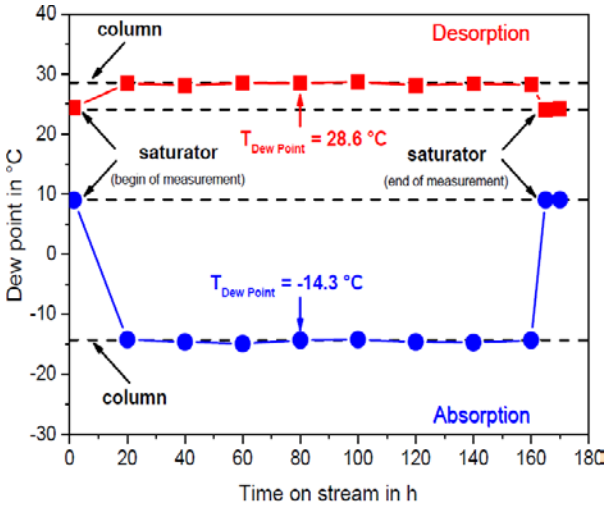

Figure 4: Measured dew point of the dry gas at the outlet of the absorption unit (T = 30 °C) and the measured dew point of the loaded air at the outlet of the desorption unit (T = 90 °C) against the duration time (one week)

The lower line (blue curve) represents the course of the measured dew point for the absorption and the dew point of desorption is shown by the upper line (red curve). At the beginning of the measurement (1. Step, see Figure 2), the desired dew points from Table 1 are adjusted with the absorption and desorption saturator. After the constant setting of the both saturator temperatures, the saturated gas streams are switched to the absorption and desorption column. In this case, a drop (absorption) or an increase (desorption) of the dew points is determined (2. Step). The water loaded gas stream is dried in counter flow to the ionic liquid in the absorption column. For the absorption, this results in a decrease of the dew point. In the desorption column, the water loaded IL is regenerated by the second air gas stream. Here, the air stream deprives the IL the water which was absorbed during the absorption and the measured dew points increase. At the end of the experiment, the air gas streams of the absorption and desorption is switched back again from both columns to the respective saturators (3. Step). Thereby, the starting dew points of the saturators should be reviewed if the saturation degree has changed. The comparison between the measured and the calculated dew points as well as the water content in the IL-reservoir and after the absorption column are presented in Table 2.

Table 2: Comparison between theory and experiment for the gas drying task (abs. = absorption; des. = desorption)

Operating condition	Theory	Experiment
Dew point (abs., Start) in °C	9.0	9.1
Dew point (abs., End) in °C	-12.9	-14.3
Dew point (des., Start) in °C	24.5	24.1
Dew point (des., end) in °C	29.4	28.6
Water content of IL (reservoir) in wt%	4.0	4.3
Water content of IL (after absorption) in wt%	4.3	4.6

The dew points at the entry of the absorption and desorption exhibit only a minimal changing during the measurement. Overall, the ionic liquid dries the water loaded gas stream in the absorption column to a dew point of around -14 °C. Generally, the measured values for the absorption and desorption temperature as well as the water content of the IL [EMIM][$MeSO_3$] show only a minimal deviation from the theory. Deviations can be attributed to the mass transfer coefficient according to Onda.
In summary, it can be seen that the theoretical column design with the HTU/NTU-model is in principle possible. Deviations from this can be explained by variations of the process parameters (no constant temperature in absorption/desorption column, fluctuating dew points in saturator columns) during the measurement. In addition, the measured mass transfer coefficients for the absorption and desorption are within the error range of ±25 % according to Onda. Overall, this experiment shows very satisfactory results especially with respect to the length of the experiment from one week.

2.5 Comparison between ionic liquid [EMIM][$MeSO_3$] and TEG

In order to assess the suitability of the ionic liquid as a drying agent in the gas processing, the common absorbent triethylene glycol is used as a reference substance. Therefore, a theoretical column design with the HTU/NTU-model for a predetermined drying task is carried out for both adsorbents. The separation task exists that the dew point of the moist gas stream is dried in a packed absorption column (variation of packing materials: 5 or 6 mm Raschig rings, 6 mm spherical; column diameter: 1 m) from 15 °C to -10 °C. The dew point of -10 °C is a characteristic value for the drying degree of the gas [1]. In the gas dehydration process, the absorption temperature is 30 °C. It should be noted that this drying task is performed with different gas flow rates. In addition, the loading point is always assumed for the gas volume flow. Furthermore, the column diameter of 1 m is a typical value for a glycol dehydration absorber [1]. Final-ly, the respective drying height for the different packing materials is calculated in a volume flow range between 200-1000 m^3/h.

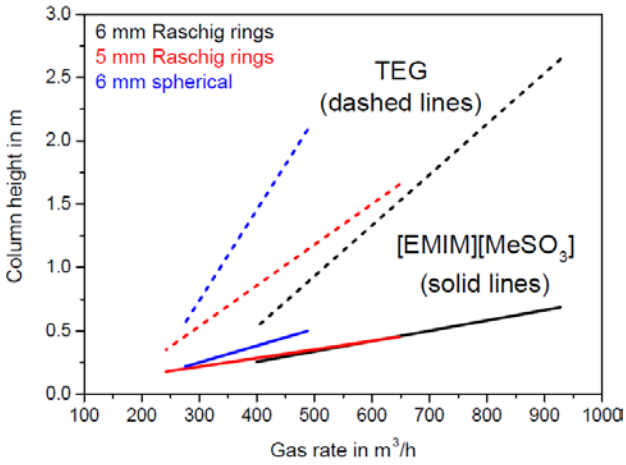

Figure 5: Comparison of the column height between the washing fluids TEG and [EMIM][$MeSO_3$] for different packing materials (column diameter = 1 m)

Figure 5 shows a comparison of the column height between TEG and the ionic liquid [EMIM][$MeSO_3$] for various packing materials at different gas flow rates. The main point of the diagram is that the ionic liquid needs for all three packing materials lower column heights than for triethylene glycol. For 6 mm Raschig rings, the ionic liquid (height = 0.7 m) requires for the same drying task a four times lower height than is needed by TEG (height = 2.7 m). In glycol dehydration plants, a typical column height of an absorber is about 3.6 m [1] so that the theoretically calculated value for TEG with the HTU/NTU-model is comparable. The advantage of this lower column height for all three packing materials is that the ionic liquid can dry more of the moist gas stream than TEG.

3. Conclusions

In a continuously operating absorption and desorption unit, long-term experiments for gas drying and regeneration of the ionic liquid were conducted. Here, the absorption and desorption temperature, water vapour content, flow rate of the IL and gas as well as the size and kind of packing (Raschig rings, sphericals) were varied. Ionic liquids are proposed as gas dehydration agents, due to their pronounced hygroscopicity. The experiments seem to be carried out carefully and the chosen ionic liquid showed satisfactory water absorption capacity. Thus, a column design with the HTU/NTU-model can be realized for the ionic liquid. Compared to the industrially used washing fluids such as triethylene glycol, the ionic liquid requires for the same drying task (6 mm Raschig rings, gas rate = 900 m^3/h) a four times lower column height. In conclusion, the ionic liquid can dry more of the moist gas stream than TEG in the same column height. Furthermore, the regeneration of the ionic liquid (T = 90 °C) is possible by stripping with air which is not possible for the oxygen sensitive glycols. At high gas flow rates up to 15 % less ionic liquid is required as in the case of TEG. Therefore, the ionic liquid [EMIM][$MeSO_3$] represents a promising alternative to the conventional industrially used washing fluids.

References

[1] A. Kohl, R. Nielsen, Gas Purification, Gulf Professional Publishing, Houston, 5th Edition, 1997
[2] T. Sun, A. S. Teja, J. Chem. Eng. Data, 2003, 48, 198-202

[3] B. Bestani, K.S. Shing, Fluid Phase Equilibria, 1989, 50, 209-221
[4] C. H. Twu, V. Tassone, W. D. Sim, S. Watanasiri, Fluid Phase Equilibria, 2005, 228-229, 213-221
[5] L.C. Polderman, Oil Gas J., 1957, 55, 107-112
[6] W.G. Lloyd, J. Chem. Eng. Data, 1961, 6, 541-547
[7] P.W. Brown, W.J. Jr. Rossiter, K.G. Galuk, Solar Energy Materials, 1961, 6, 541-547
[8] F. Heym, J. Haber, W. Korth, B.J. Etzold, A. Jess, Chem. Eng. Technol., 2010, 33 (10), 1625-1634
[9] F. Heym, B.J.M. Etzold, C. Kern, A. Jess, Green Chem., 2011, 13, 1453-1466
[10] A. Mersmann, M. Kind, J. Stichlmaier, Thermal separation technology, Springer Verlag, Berlin Heidelberg, 1st Edition, 2011
[11] K. Onda, H. Takeuchi, Y. Okumoto, J. of Chem. Eng. of Japan, 1968, 2 (2), 56-62
[12] U. Domanska, M. Krolikowski, J. Chem. Thermodynamics, 2012, 54, 20-27
[13] B. Lohrengel, Einführung in die thermischen Trennverfahren, Oldenburg Wissenschaftsverlag GmbH, 2007
[14] K. Sattler, Thermal Separation Processes: Principle and Design, Weinheim Wiley-VCH Verlagsgesellschaft, 1st Edition, 1997

Gas-Phase Mass-Transfer Characteristics of Mellapak 250Y Structured Packing under Distillation Conditions

František Rejl, Lukáš Valenz, Jan Haidl
Institute of Chemical Technology, Prague
Technická 5, 166 28 Prague 6, Czech Republic
frantisek.rejl@vscht.cz

Abstract
The packing efficiency is usually presented in the form of the dependence of *HETP* on the load. As an integral quantity, *HETP* cannot be recalculated to another conditions, namely to other systems. This disadvantage is overcome when rate-based approach is applied instead, but the knowledge of the mass-transfer coefficients is inevitable.
This contribution summarizes results of the measurement of the gas phase volumetric mass-transfer coefficient (k_Ga) for Mellapak 250Y structured packing under distillation conditions. The k_Ga has been determined using novel "profile method" out of the molar fraction profiles along the column packing under the total reflux and atmospheric pressure for several alcohol systems and cyclohexane-heptane standard test system.
The results demonstrate the agreement of k_Ga prediction of several dedicated mass-transfer models (Billet-Schultes, Rocha-Bravo-Fair, Delft model) with the experimental data. Revealed k_Ga dependence on the gas flow is also discussed. The different distribution of the mass-transfer resistance between the phases for alcohol and organic systems is demonstrated.
Combination of the results with the extrapolation of the absorption derived Sh_G correlation enabled estimation of the distillation effective interfacial area, perhaps the most obscured mass-transfer parameter and in the same time a key for the evaluation of the mass-transfer coefficients.

Keywords
mass-transfer, structured packing, interfacial area, distillation, absorption

1. Introduction

Characterization of the packing efficiency as well as the column design using HETP value is a proven method, which, however, brings several known problems based on the weak relation between real physical phenomena in the column and their description by stage-wise concept. This is overcome by rate-based approach, for which, the parameters (volumetric mass-transfer coefficients k_La, k_Ga) must be known.
Measurement of the volumetric mass-transfer coefficients under absorption conditions is generally possible as there exist systems with the mass-transfer resistance limited to the single phase as well as the systems in which the mass-transfer rate is controlled by the interfacial area. For the distillation the situation is far more complicated, as the mass-transfer resistance is usually distributed between the

both phases and separation is not straightforward. Currently there are only limited attempts to determine effective interfacial area during distillation process.

Table 1:					
M250Y		C_6/C_7		M/E	
u_G [m/s]		0.75	1.18	0.86	1.79
B [m/h]		12.8	20	5.66	11.8
k_La [s^{-1}]	EXP	0.032	0.04	0.012	0.021
	RBF	0.031	0.04	0.02	0.03
	BS	0.025	0.034	0.016	0.027
	DELFT	0.079	0.094	0.055	0.075
k_Ga [s^{-1}]	EXP	2.9	5.07	4.07	9.3
	RBF	2.78	4.80	2.84	7.05
	BS	2.94	5.65	3.61	7.26
	DELFT	1.82	2.77	2.28	4.29
a [m^{-1}]	RBF	181	217	135	180
	BS	83	112	68	92
	DELFT	240	245	215	231

This situation is reflected by the insecurity of the predictions of the mass-transfer coefficients and active interfacial area values provided by three respected models (RBF [1], BS [2], DELFT [3]). While predictions of the volumetric mass-transfer coefficients for C_6/C_7 and for the methanol/ethanol system are similar for RBF and BS models, the DELFT model predicts much larger mass-transfer resistance for the gas phase (see Table 1). Which of these predictions is closer to the truth can't be easily told, as the *HETP* values calculated on the basis of these data don't differ much and roughly correspond with the experimental ones. The predictions of the fundamental mass-transfer parameters (k_L, k_G, a) by individual models differ in multiples. This is a direct consequence of no reliable method for the effective area determination under distillation conditions. While this outcome could be (hardly) satisfactory for the column designers, the unclear fundamental of the distillation process on the packing is rather alarming.

The distribution of the mass-transfer resistance between the phases considerably affects the shape of the binary concentration profiles along the column packing (see Figure 1) and this fact enables evaluation of the k_La, k_Ga as optimized parameters of the distillation rate-based model, which produces concentration profiles matching the experimental ones.

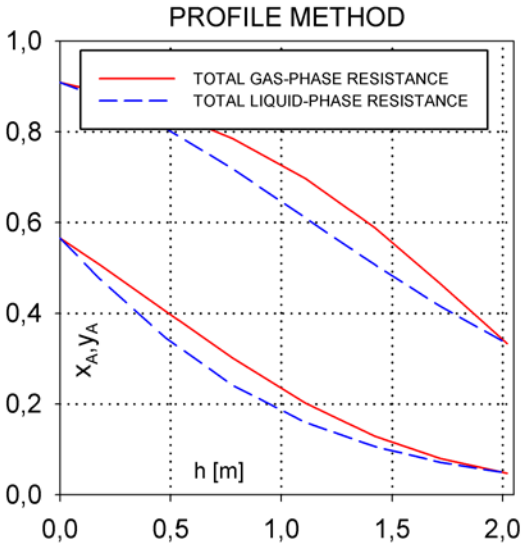

Figure 1: molar fraction profiles in the column under total reflux

This so called "profile method" was used to analyze distillation data measured on several distillation systems (methanol/ethanol, ethanol/propanol, methanol/propanol, cyclohexane/n-heptane) and two types of the metal structured packing (Sulzer Mellapak 250Y and Mellapak 452Y).This contribution presents volumetric mass-transfer coefficients in the gas phase, k_Va, measured under distillation conditions and attempts to correlate them in the dimensionless form on the basis of the variation of the following parameters a) physical properties of the system through involvement of several types of the system b)

flow of the phases through change of the reboiler power, c) characteristic dimension through change of the packing.
Speaking in advance, it seems that the values of $k_L a$ and $k_G a$ under distillation conditions are rather well predicted by the RBF and BS models. Under just slight simplifications with minor impact on the results the key equations of these models describing the gas-phase mass-transfer are

$$Sh_G = C_{BS}(packing) \cdot Re_G^{3/4} \cdot Sc_G^{1/3} \quad \text{BS} \quad (1)$$

$$Sh_G = C_{RBF}(packing) \cdot Re_G^{0.8} \cdot Sc_G^{1/3} \quad \text{RBF} \quad (2)$$

These equations differ in the values of the multiplication constant and also in the value of the Reynolds criteria power, but consistently predict form of the system-related term as "$Sc_G^{1/3}$".
In contrast to the distillation the values of the mass-transfer coefficients k_G can be deduced under the absorption conditions. For several Mellapack packings [4] the $k_G a$ data have been measured using the air/SO_2/lye and interfacial area, a, using the air/CO_2/lye system and the resulting k_G data have been correlated in the form

$$Sh_G = 0.409 \cdot Re_G^{0.622} \cdot Re_L^{0.0592} \quad (3)$$

Now let us simply assume that the system-related term "$Sc_G^{1/3}$" works well and enables transfer of the gas-phase mass-transfer data between absorption and distillation. Under this assumption the absorption derived correlation (3) can be generalized into the form

$$Sh_G = 0.439 \cdot Re_G^{0.622} \cdot Re_L^{0.0592} \cdot Sc_G^{1/3} \quad (4)$$

Effective mass-transfer area under the distillation conditions can be subsequently estimated from the values of the $k_G a$ determined using "profile method" and k_G values computed on the basis of the correlation (4).

$$a = \frac{k_G a}{k_G} \quad (5)$$

2. Results and discussion

For alcohol systems the mass-transfer resistance is distributed between both phases while for the cyclohexane/n-heptane the gas phase mass-transfer resistance is clearly dominant. For larger loads the liquid-phase resistance in the C_6/C_7 system vanishes (see Figure 2).

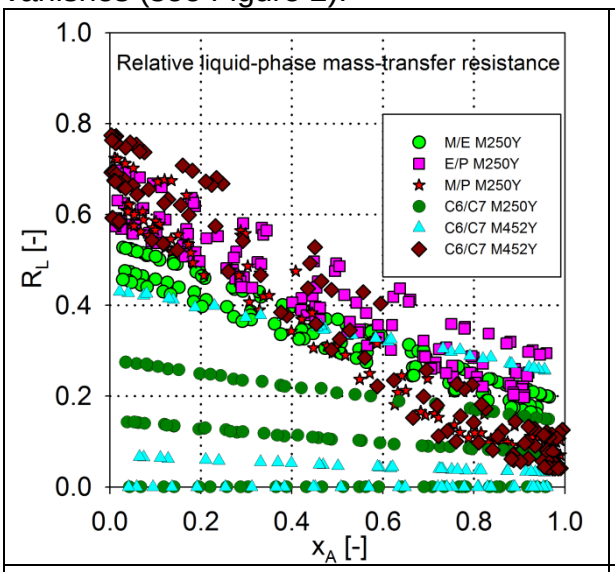

Figure 2: DISTILLATION relative mass-

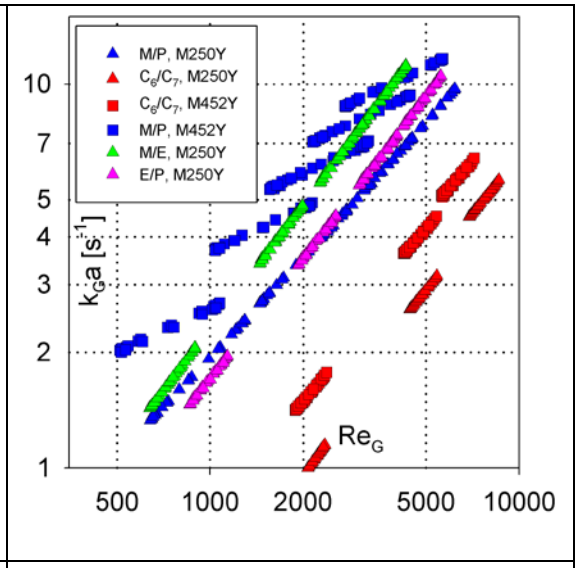

Figure 3: DISTILLATION $k_G a$ by the

transfer resistance of the liquid phase	“profile method”

Evaluation of the volumetric mass-transfer coefficients is more secure and more precise for the phase with larger mass-transfer resistance, which is the gas-phase. These data ($k_G a$) are therefore chosen for this presentation and together are presented in the Figure 3. As can be anticipated (and as is also predicted by the models) $k_G a$ values are higher for M452Y packing and for the alcohol systems. The data for individual packings and systems vary greatly and attempt to reduce them has been performed.
Dependence of the mass transfer coefficient k_G on the flows and physical properties of the system is assumed in the dimensionless form

$$Sh_G = C_1 \cdot Re^{\alpha} \cdot Sc^{1/3} \quad (6)$$

while the effective interfacial area is in the first approximation assumed to follow simple relationship

$$\frac{a}{a_G} = C_2 \cdot Re^{\beta} \quad (7)$$

Under such assumptions the $k_G a$ data obtained for various systems and packing dimensions can be expressed in the form

$$k_G a = Sh_G \cdot \frac{D_G}{d_{eq}} \cdot \frac{a}{a_G} \cdot a_G = C_3 \cdot Sc^{1/3} \cdot \frac{D_G}{d_{eq}} \cdot a_G \cdot Re^{\gamma} \quad (8)$$

which is rearranged into

$$\frac{k_G a}{Sc^{1/3} \frac{D_G}{d_{eq}} a_G} = C_3 \cdot Re^{\gamma} \quad (9)$$

The term in the denominator serves for recalculation of the $k_G a$ data from one system and packing size to another one, and the left hand side of the equation should be sole function of the Reynolds criteria – hydrodynamic function presented at the right-hand side of the equation.
The reduced data presented in the Figure 4 have been evaluated with the assumption of the plug flow in both phases. The data are clearly distributed into the three groups - those measured on the a) methanol/ethanol and ethanol/propanol system on the M250Y packing; b) methanol/propanol and C_6/C_7 system on the M250Y packing c) methanol/propanol and C_6/C_7 system on the M452Y packing. All the data measured on the methanol/ethanol, ethanol/propanol and C_6/C_7 system exhibit similar Reynolds criteria power γ (relationship 9) in the range 1.07-1.23, while the data measured on the methanol/propanol system exhibit significantly lower power (γ=0.93 for M250Y and γ=0.76 for M452Y). Perhaps this behavior is related to the high relative volatility of the methanol/propanol system and corresponding sharp separation, which makes the evaluation of the data more difficult.
When methanol/propanol data are not considered, such behavior suggests that powers α and β could be constants and their sum equals to ~1.15. Due to the distribution of the data into groups according to the systems and packings the form of the recalculation factor

$$Sc^{1/3} \cdot \frac{D_G}{d_{eq}} \cdot a_G \quad (10)$$

doesn’t seem to work well in this case, although the constant power γ of the hydrodynamic function at least suggests that the hydrodynamic of the phases under various conditions is analogical.

An attempt to remedy the situation has been performed through evaluation of the $k_G a$ data with the more realistic assumption of the plug flow with axial dispersion in the liquid phase. The fit of the experimental data is in average 42% better than in the case of the plug flow. Once again the reduced data doesn't form single function of the Reynolds criteria, but are dispersed in the broad (+/- 30%) region with methanol/ethanol data being high extreme and C_6/C_7 data the low one. With exception of the methanol/propanol data measured on the M452Y packing the data provide Reynolds criteria power γ (9) in the range 0.72-0.88, which is significantly lower than in the case of the plug flow. The absolute values of the (9) left-hand side remain almost the same, however. Important change in the behavior consists in the vanishing of the dependence on the packing type.

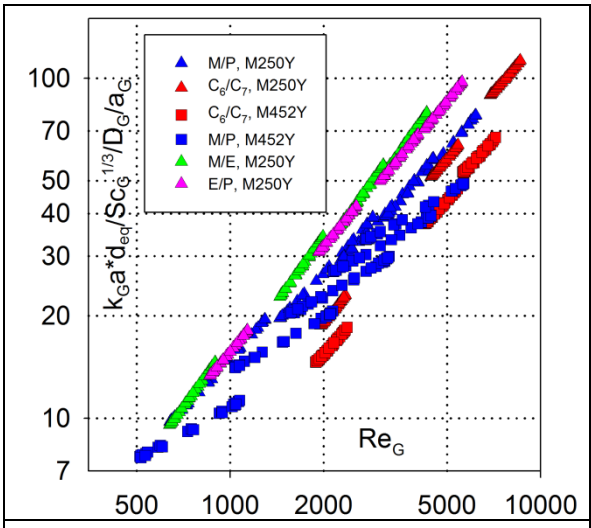

Figure 4: values of the recalculated $k_G a$ (9) evaluated under the PLUG FLOW assumption

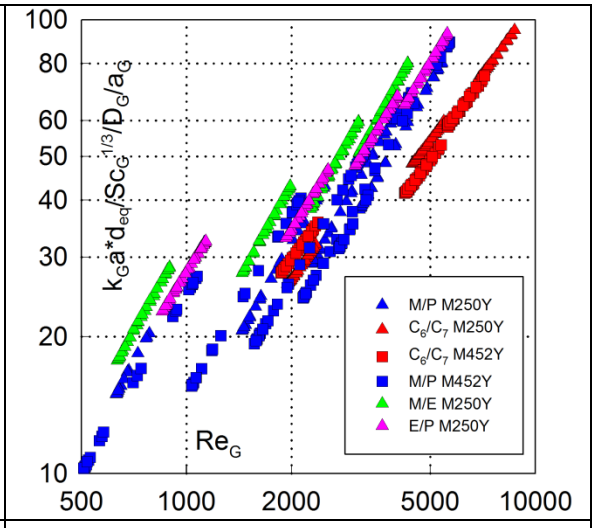

Figure 5: values of the recalculated $k_G a$ (9) evaluated under the PLUG FLOW +AXIAL DISPERSION assumption

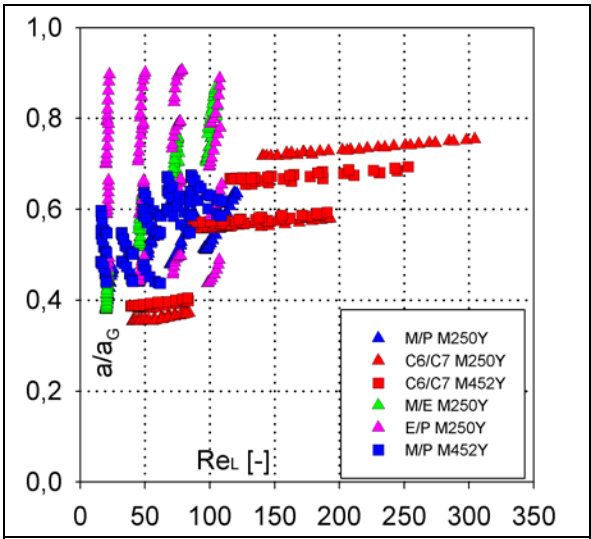

Figure 6: DISTILLATION interfacial area under the PLUG FLOW assumption

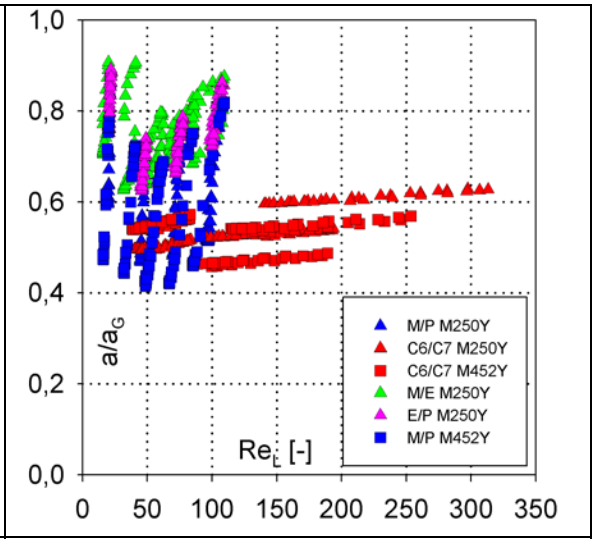

Figure 7: DISTILLATION interfacial area under the PLUG FLOW +AXIAL DISPERSION assumption

The effective distillation interfacial area evaluated using absorption data recalculated to the distillation conditions according to the relations (4,5) are present in the Figures (6,7). In both cases the resulting effective area forms ~ 50-90% fraction of the geometrical area of the particular packing. Effective area evaluated for C_6/C_7 system is nearly independent of the mixture composition while that for M/E and E/P system changes dramatically. Dependence on the liquid load seems to be low when the plug flow with axial dispersion model is chosen for k_Ga evaluation. Surprisingly the results suggest that the effective interfacial of the C_6/C_7 system is lower than that of the alcohol systems.

3. Conclusions

The distillation is usually treated as a process with the dominant mass-transfer in the gas-phase. The data indicates that this is correct for the C_6/C_7 system, especially for larger loads, while for systems consisting of alcohols the mass-transfer resistance is distributed between the both phases.

The distillation k_Ga data are well described by the RBF and BS model for the C_6/C_7 system. For the methanol/ethanol system the k_Ga values are about 25% underestimated by these models. Common correlation of the distillation k_Ga data was not successful. While the hydrodynamics of the phases seems to be analogical, the recalculation of the data between the systems brings problems even when more sophisticated model for the liquid phase hydrodynamics is introduced for k_Ga evaluation.

The estimates of the effective interfacial area can't be conclusive due to weakly proven and actually rather challenged recalculation procedure from one system to another. As is, they support the idea of the effective interfacial area forming just about 50%-90% of the geometrical area of the packing although the packing is completely wet for all the conditions, as visually confirmed.

The system transfer procedure is only planned to be verified more thoroughly. Therefore the conclusions with respect to the distillation effective interfacial area should be viewed only as an attempt to shed some light on this perhaps most obscured mass-transfer parameter until reasonable direct measurement method is developed.

Does anybody have any idea?

Acknowledgements

Support of Grant Agency of the Czech Republic through the project No. 13-01251S is gratefully acknowledged.

References

[1] Rocha, J.A., Bravo, J.L., Fair, J.R., 1996. Distillation columns containing structured packings: A comprehensive model for their performance. 2. Mass transfer model. Ind. Eng. Chem. Res. 35, 1660–1667.

[2] Billet, R., Schultes, M., 1999. Prediction of mass transfer columns with dumped and arranged packings. Updates summary of the calculation method of Billet and Schultes. Trans IChemE 77 (Part A), 498–504.

[3] Olujic', Ž., Behrens, M., Colli, L., Paglianti, A., 2004. Predicting the efficiency of corrugated sheet structured packings with large specific surface area. Chem. Biochem. Eng. Q. 18 (2), 89–96.

[4] Rejl, F.J., Valenz, L., Haidl, J., Kordač, M., Moucha, T. On the modeling of gas-phase mass-transfer in metal sheet structured packings. To be published in the Chemical Engineering Research and Design.

Hydrodynamic Behaviour of Packed Columns Operated under Supercritical Conditions

*H.H. Franken, J.H. Knoetze and C.E. Schwarz**
Department of Process Engineering, Stellenbosch University
Private Bag X1, Matieland, 7602, South Africa
** Tel: +27 21 808 4487 Fax: +27 21 808 2059, E-mail: cschwarz@sun.ac.za*

Abstract

The purpose of this paper is to describe a pilot plant that was designed and constructed for the measurement of the hydrodynamic behaviour of a packed column operating with a supercritical fluid vapour phase. A lack of hydrodynamic data for supercritical packed countercurrent extraction/fractionation columns was identified, especially in columns with random packing. The pilot plant consists of two columns of 17 mm and 38 mm diameter and 3.5 m and 1.5 m packed height, respectively, and is able to operate up to 300 bar and 473 K. For initial testing the system CO_2/Polyethylene glycol 400 (PEG 400) was used. The pressure drop, liquid hold-up, column overheads and bottoms were measured at 313.15 K and 120 bar for several fluid flow rates. Hydrodynamic data was successfully measured and interpreted. It is found that the overhead liquid mass fraction correlates well to literature data.

Keywords
Hydrodynamics, Liquid hold-up, Pilot Plant, Pressure drop, Random Packing, Supercritical.

1. Introduction

Supercritical fluids (SFs) present an attractive alternative to traditional solvents, being able to distinguish between components with regard to their functional group, while using less intrinsically harmful compounds [1, 2]. Supercritical fluid extraction (SFE), in turn, has advantages over classical extraction with rapid mass transfer, sharp, highly efficient separations and easy recovery of solutes possible [3]. SFE can achieve high degrees of efficiency and compares well to classical extraction methods in energy requirement, facility scaling and operating costs [4, 5, 6].

Although the potential of SFs as solvents have been known for more than a century, very little experimental work has been done on the hydrodynamic behaviour of packed columns under supercritical conditions. This can be attributed to the relative success in the use of atmospheric hydrodynamic models to approximate SF column design and a predominant culture of overdesign in process engineering. Even though subcritical hydrodynamic models may provide a good approximation, they do not successfully predict the effect of the significantly higher density and viscosity, and lower surface tension of a SF, which leads to costly inaccuracies in column design.

Rathkamp et al. [7], researched the efficiency and energy requirements of columns operating with supercritical CO_2 using a water/ethanol system in a 25.4 mm column

packed with 6.4mm metal raschig rings. Seibert and Moosberg [8], also using a water/ethanol system, measured efficiency and liquid hold-up using a 98.8 mm column with sieve trays, 12.7 mm ceramic raschig rings and #15 IMTP. Sievers [9] and Woerlee [10] were among the first to measure flooding under supercritical conditions, using water and hexadecane, respectively. They both used the same 36 mm column packed with a gauze type packing (Montz-pak type A3) and were the first to clearly state that hydrodynamic data measured at supercritical conditions are not consistent with well-known generalized pressure drop correlations of the time [11, 12]. Lim et al. [13] investigated liquid hold-up in a 31.8 mm column with a knit mesh packing, and observed a positive correlation between a rise in system pressure and a rise in liquid hold-up. Machado [14], using palm oil distillate in a 25 mm column, packed with Sulzer EX, measured flooding points consistent with the work of Woerlee [10]. Using the same experimental setup, Buddich [15, 16] investigated orange peel oil/CO_2 and water/ethanol/CO_2 systems. Meyer [17], again using the same experimental setup, measured not only flooding, but also the pressure drop and physical properties of soybean oil/CO_2 and fish oil/CO_2 systems. Meyer [17] compared his results with well-known flood point correlations [18, 19, 20], and concluded that models applicable at vacuum and normal pressures do not readily predict high pressure systems (P > 70 bar). Stockfleth and Brunner [21, 22] performed a full hydrodynamic study, investigating liquid hold-up, flooding, pressure drop and foaming for water/CO_2, olive oil distillate/CO_2 and tocopherol/CO_2 systems. Using the semi-empirical models proposed by Stichlmair et al. [23], modified for the density of the supercritical phase, they achieved relative success in predicting hydrodynamics, except for the flooding point.

2. Motivation and Aims

A few shortcomings may be identified from literature. Firstly, most of the significant research that has been performed is on structured packing, causing a severe lack of data on random packing. Secondly, most of the research neglects to investigate the mutual solubility of both phases. Thirdly, no investigation with regard to column diameter has been made at supercritical conditions, as at the small diameters used in supercritical columns, wall effects could become significant. Fourthly, no work has been done on SFs other than CO_2. Finally, no hydrodynamic correlations have been tailored specifically to SF conditions and no fundamentally based correlation exists that can predict flooding in SFE columns. Simply put, these shortcomings force industry to perform expensive and lengthy pilot plant studies in order to obtain a reliable design. In order to overcome these shortcomings a number of comprehensive studies are required. There thus exists a need for a set-up able to measure hydrodynamic data applicable to SFE processes systematically. The aim of this paper is to (1) describe a pilot plant that is able to investigate hydrodynamics at supercritical conditions for a wide range of systems and (2) to present preliminary results gathered.

3. Materials and Methods

3.1 Pilot Plant Setup

A basic process flow diagram of the designed and constructed pilot plant can be seen in Figure 1 and specifications for the pilot plant are provided in Table 1. The

pilot plant consists of two columns and can measure the liquid hold-up, pressure drop, flooding and entrainment over a wide range of liquid and solvent flow rates. Pressure drop is measured using an Endress+Hauser Deltabar S PMD75 with an accuracy of 0.075 % of its range of 50 kPa. Temperature is measured by multiple J type thermocouples, accuracy ±1.5 K. Solvent mass flow is measured using a Micro Motion D12 flow sensor and RFT 9729 remote flow transmitter combo. All electronic data is logged using a custom PLC setup. Liquid mass flow rate is determined from prior calibration of the pumps and confirmed by doing a liquid mass balance over the column.

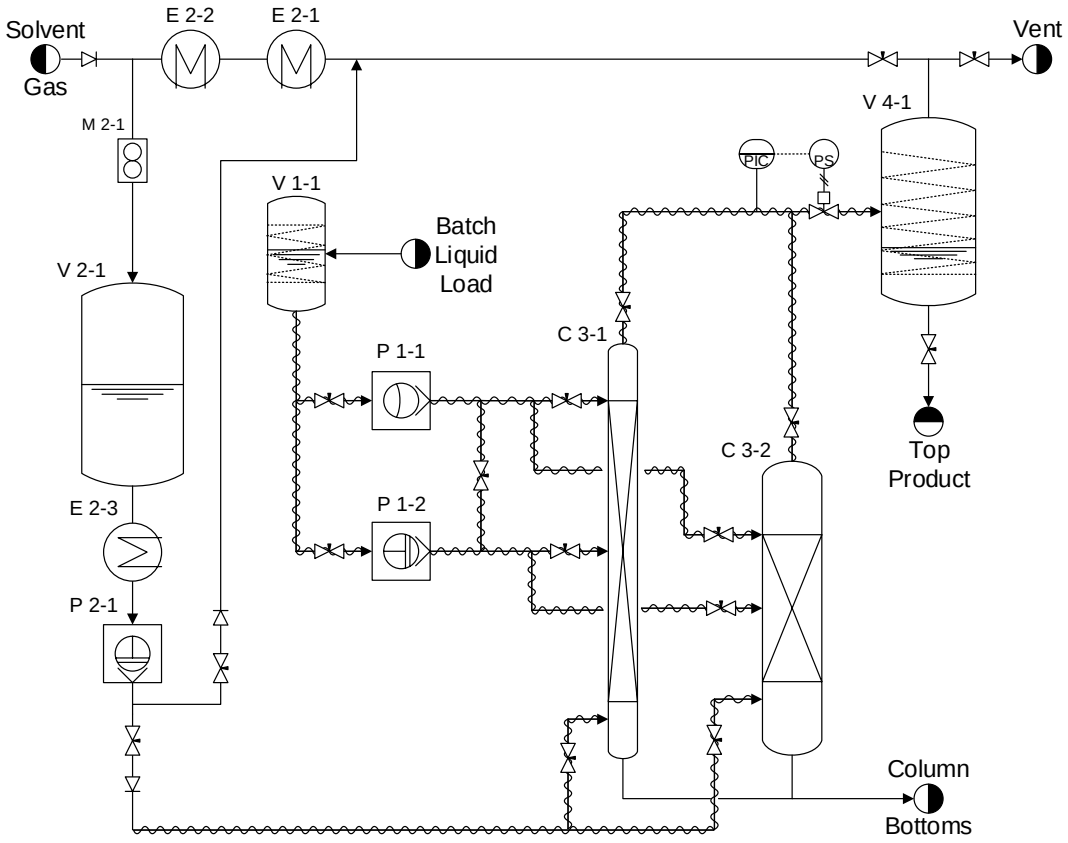

Figure 1: Schematic representation of the pilot plant set-up

Table 1: Legend for Figure 1 and pilot plant specifications

Figure 1 Legend		Plant Specifications	
V 1-1	Liquid Feed Tank	Maximum system pressure	300 bar
P 1-1	Small Capacity Diaphragm Pump	Maximum system temperature	473 K
P 1-2	Large Capacity Piston Pump	Separator pressure	~ 50 bar
E 2-1	Water Pre-cooler	Liquid flow rate range	0 - 8 ℓ/h
E 2-2	Chilled Condenser	Solvent flow rate range	0 - 55 ℓ/h
M 2-1	Mass Flow Meter	Column C 3-1 Diameter	17 mm
V 2-1	Solvent Buffer Tank	Column C 3-1 Packed Height	3.5 m
E 2-3	Pump Feed Chilled Pre-cooler	Column C 3-2 Diameter	38 mm
P 2-1	Solvent Diaphragm Pump	Column C 3-2 Packed Height	1.5 m
C 3-1	Small Diameter Column	Column Packing	1/4" Dixon Rings
C 3-2	Large Diameter Column	Packing void fraction	91 %
V 4-1	Overhead Product Separator Vessel	Packing surface area	900 m^2/m^3

3.2 Liquid-Solvent Systems

To investigate the fundamental hydrodynamic behaviour, it is vital to use systems that limit mass transfer. Mass transfer directly affects flow rates and fluid properties, complicating the interpretation of results. As a virtually endless number of possible combinations can be formulated, the scope is initially limited to using CO_2 as the supercritical phase of choice. CO_2 is inexpensive, safe, and environmentally friendly and does not react with process components. Indeed, CO_2 is the most popular SF [3], with wide use in industry.

Liquids used in previous hydrodynamic studies at supercritical conditions were typically aqueous mixtures, which exhibit high solubility, or organic oils, which still have a significant solubility in CO_2, and neither are thus ideal liquids. Consulting literature, it was found that polyethylene glycol (PEG) is a good candidate for hydrodynamic studies. PEG is available in a wide range of molecular weights, safe, inexpensive and exhibits a low solubility in supercritical CO_2 (as low as 0.7 wt% at 120 bar and 313.15 K [24, 25]).

4. Results and Discussion

Initial experiments were performed using the 38mm diameter column, packed with ¼" Dixon dings, with a CO_2/PEG 400 system at 120 bar and 313.15 K. Due to the operating nature of the pilot plant, it was decided to keep the solvent feed rate constant and vary the liquid feed rate.

Typical results for measured liquid hold-up and pressure drop are shown Figure 2. Figure 2A shows a gradual increase of the hold-up, followed by a sharp rise and a subsequent plateau being reached. In Figure 2B similar behaviour is seen in the pressure drop over the column with a sharp increase noted consistent with the increase in liquid hold-up.

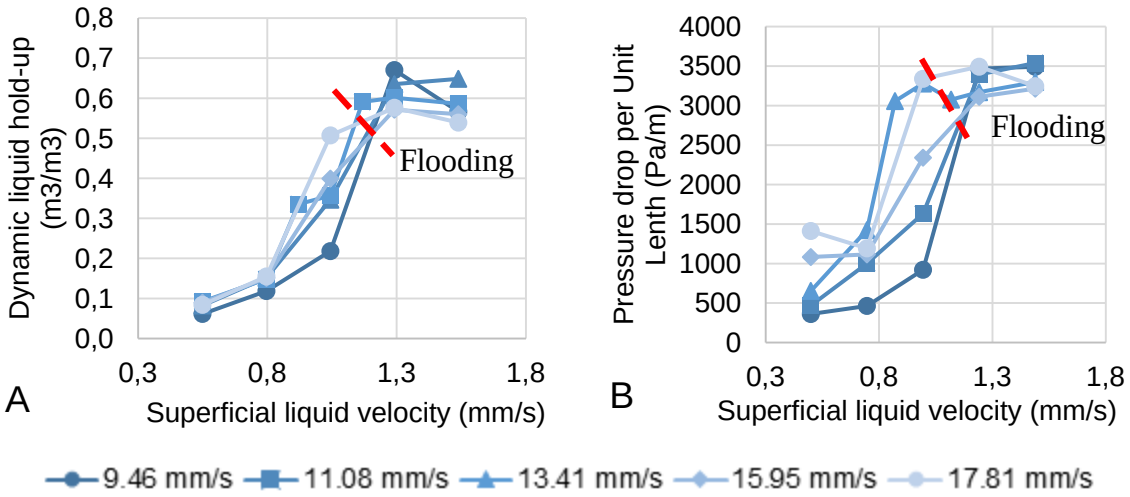

Figure 2: (A) Dynamic hold-up, (B) Pressure drop per unit length at 313.15 K and 120 bar at various solvent flow rates as a function of SF velocity.

The plateau corresponds with an increase in the column overheads and a decrease in the bottoms leading to the column being hydrodynamically inoperable, as can be seen in Figure 3, correlating to an operational flooding point in this state.

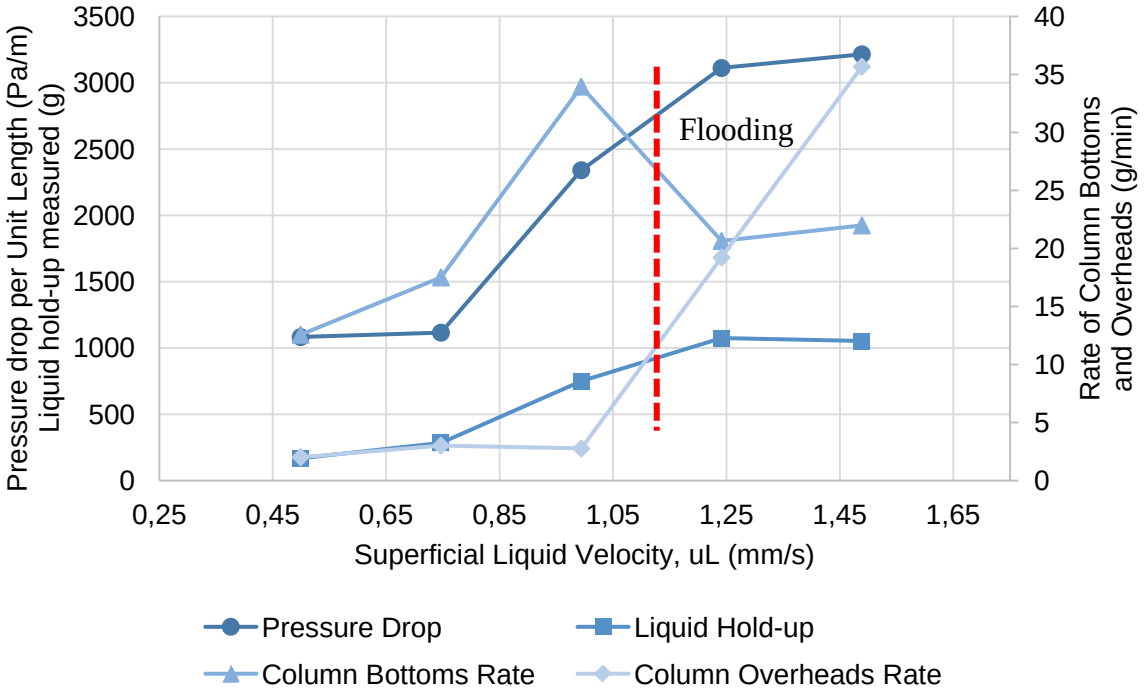

Figure 3: Pressure drop, dynamic liquid hold-up and average column bottoms and overheads rate vs. superficial liquid velocity for a superficial gas velocity of 11.08 mm/s.

Figure 4 compares the PEG solubility achieved in the pilot plant to literature data and shows that the solubility values obtained from pilot plant data compares well to available literature data, confirming this aspect of the pilot plant accuracy.

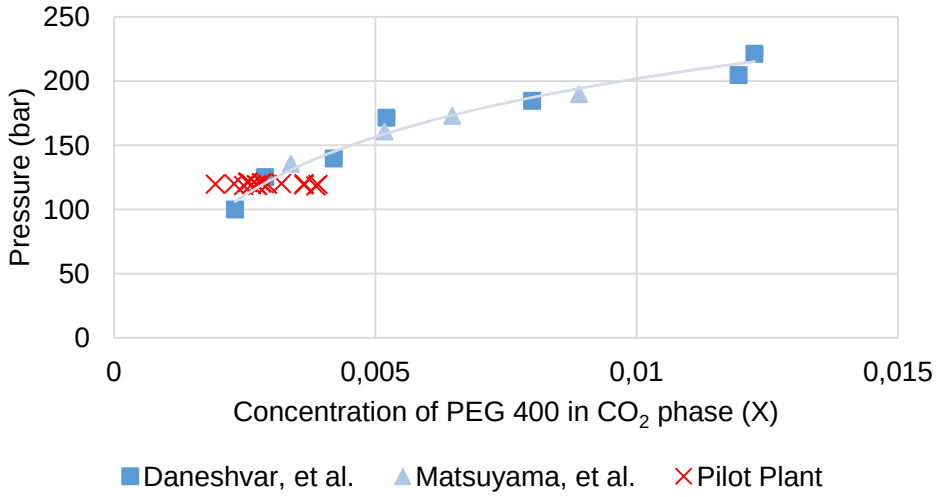

Figure 4: Comparison of pilot plant extracted fraction to literature data at 313.15 K.

5. Conclusions

This paper presents an experimental set-up and initial results of a study measuring supercritical hydrodynamics. In order to conduct the investigation, a pilot plant was designed and constructed. Initial testing was performed with a CO_2/PEG 400 system at 120 bar and 313.15 K, with the measurement of liquid hold-up, pressure drop, column bottoms and overheads at various fluid flow rates. The measured hydrodynamics indicate a possible region of interest where the pressure drop and liquid holdup rapidly increases, but the column overheads and bottoms seems to stay within operability limits, only increasing at a higher liquid flow rate. Finally the extracted fraction of PEG 400 is compared with literature data and found to correlate very well. Based on these results it can be concluded that this set-up produces reliable data.

References

[1] C. Schwarz and I. Nieuwoudt, J. Supercrit. Fluids, Vol. 27, p 133-144, 2003.

[2] C. Schwarz, F. Fourie and J. Knoetze, J. Supercrit. Fluids, Vol. 51, Issue 2, p. 128-135, 2009.

[3] C. Schwarz and J. Knoetze, [As published in 'Supercritical Fluids' by M. Belinsky. Nova Science Publishers], 2010.

[4] J. Crause and I. Nieuwoudt, J. Supercrit. Fluids, Vol. 27, p. 39-54, 2003.

[5] G. Hytoft, R. Gani and A. Fredenslund, Houten, The Netherlands: Springer Netherlands, 1993.

[6] M. Perrut, Ind. Eng. Chem. Res., Vol. 39, p. 4531-4535, 2000.

[7] P. Rathkamp, J. Bravo and J. Fair, Solvent Extr. Ion Exch., Vol. 3, p. 367, 1987.

[8] A. Seibert and D. Moosberg, Sep.Sci. Tech., Vol. 23, p. 2049, 1988.

[9] E. Sievers, Delft, The Netherlands: Ph.D. Dissertation, Technische Universität Delft [As referenced by : Stockfleth, R., Ph.D. Dissertation, Technischen Universität Hamburg, Hamburg, Germany, 2001], 1994.

[10] G. Woerlee, Delft, The Netherlands: Ph.D. Dissertation, Technische Universität Delft. [As referenced by : Stockfleth, R. and Brunner, G., Ind. Eng. Chem. Res., Vol. 40], 1997.

[11] T. Sherwood, G. Shipley and F. Holloway, Ind. Eng. Chem., Vol. 30, p. 765-769, 1938.

[12] M. Souders and G. Brown, Ind. Eng. Chem., Vol. 38, p. 98-103, 1934.

[13] J.S. Lim, Y. Lee, J. Kim, Y.Y. Lee and H. Chun, J. Supercrit. Fluids, Vol. 8, p. 127, 1995.

[14] N. Machado, Hamburg, Germany: Ph.D. Dissertation, Technische Universität Hamburg. [As referenced by : Stockfleth, R. and Brunner, G., Ind. Eng. Chem. Res., Vol. 40], 1998.

[15] M. Budich, Düsseldorf, Germany: VDI-Verlag, 1999.

[16] M. Budich and G. Brunner, Fluid Phase Equilib., Vol. 158, p. 759, 1999.

[17] J.-T. Meyer, Hamburg, Germany: Ph.D. Dissertation, Technische Universität Hamburg. [As referenced by : Stockfleth, R. and Brunner, G., Ind. Eng. Chem. Res., Vol. 40], 1998.

[18] A. Mersmann, Chem. Eng. Tech., Vol. 37, p. 218, 1965.

[19] J. Eckert, Chem. Eng. Prog., Vol. 66, Issue 3, p. 39, 1970.

[20] J. Maćkowiak, Frankfurt: Salle & Sauerland, 1991.

[21] R. Stockfleth and G. Brunner, Ind. Eng. Chem. Res., Vol. 38, p. 4000-4006, 1999.

[22] R. Stockfleth and G. Brunner, Ind. Eng. Chem. Res., Vol. 40, p. 347-356, 2001.

[23] J. Stichlmair, J. Bravo and J. Fair, Gas Sep. Purif., Vol. 3, p 19-28, 1989.

[24] M. Daneshvar, S. Kim and E. Gulari, J. Phys. Chem., Vol. 94, p. 2124-2128, 1990.

[25] K. Matsuyama and K. Mishima, Fluid Phase Equilib., Vol. 249, p 173-178, 2006.

Absorption Hydraulic and Mass-Transfer Characteristics of Raschig Super-Pak 250

L. Valenz, F.J.Rejl, J. Haidl

Institute of Chemical Technology, Prague, Czech Republic

Abstract

This paper refers on the hydraulic and mass-transfer characteristics of metal sheet Raschig Super-Pak 250 structured packing under absorption conditions. The pressure drop measurements were performed with air – water system. The mass-transfer characteristics were measured using standard absorption systems of oxygen desorption from water (k_La measurement), SO_2 chemisorption into the NaOH aqueous solution (k_Ga measurement) and CO_2 chemisorption into the NaOH aqueous solution (effective area, a, measurement). Measurements were performed with four elements of the packing with diameter of 0.29 m and total height of 0.93 m. The evaluated values of mass-transfer characteristics are compared with the ones obtained for Mellapak 250Y structured packing on the same experimental device and the ones recently published in Wang, C., Perry, M., Rochelle, G., T., Seibert, A., F., Energy Procedia, 2012, 23, 23. The hydraulic (C_S, C_{Fl} and $C_{P,0}$) and mass-transfer (C_L and C_V) parameters of the Billet-Schultes model (Billet, R., Schultes, M., Chem. Eng. Res. Des., 1999, 77, 498) obtained using the experimental data are presented.

Keywords

hydraulic and mass-transfer characteristics, structured packing

1. Experimental part

Mass-transfer coefficients in the liquid and in the gas phase, k_L, k_G, and effective interfacial area, a, are the basic rate-based mass-transfer characteristics of the packings. They are used together with their hydraulic properties for the design of the absorptions columns and strippers as well as for comparison of the packings. As the models predicting mass-transfer and hydraulic properties of the packings are still not sufficiently evolved with respect to the prediction of the exact packing shape influence on these properties, they have to be measured for each new packing.

In this contribution above mentioned data have been measured for Raschig Super-Pak 250, RSP 250, belonging to the class of the high capacity packing which provide significantly larger capacity without sacrificing of the mass-transfer properties. The packing differs substantially from the classical corrugated sheet packings as it forms sinusoidal, 50% open channels from the single metal sheet.

Absorption mass-transport properties in terms of the mass-transfer coefficients and effective interfacial area of the RSP 250 packing has been measured by Wang et al. [4] at SRP using column of 0.42m i.d. Hydraulics as well as *HETP* of the RSP 250 measured on 0.42m i.d. SRP column has been published by Chambers and Schultes [5].

This contribution presents hydraulic and mass-transfer data measured on the 0.29m i.d. column measured using proven standard systems [1] and has been correlated using

Billet-Schultes model [2], thus providing set of the constants for this packing, which has not been published yet.

The experiments have been carried out in the column with a 0.29 m inner diameter. The packed bed consisted of four elements of the packing rotated mutually by 90° with a total bed height of 0.93 m. Liquid distribution over the cross-section of the column was carried out by the pipe type distributor with drip-point density of 630 dp/m^2. Gas entered the column through a large drum where the flow was calmed and preceded into the column through the grid which secured its uniform distribution.

Volumetric mass-transfer coefficient in the liquid phase, k_La, has been measured by oxygen striping from the water to the stream of the nitrogen. The system exhibits mass-transfer resistance solely in the liquid phase. k_La has been evaluated from the oxygen concentrations in the liquid phase under the assumption of the plug flow of the liquid phase out of the relation (1). The oxygen concentration has been measured by optical oxygen probes.

$$k_L a = \frac{u_L}{H} \ln \frac{c_{O_2,L}^{in}}{c_{O_2,L}^{out}} \tag{1}$$

Volumetric mass-transfer coefficient in the gas phase, k_Ga, has been measured by sulfur dioxide absorption from the air into the aqueous solution of the sodium hydroxide. Due to the instantaneous reaction at the interface the system exhibits mass-transfer resistance solely in the gas phase. k_Ga has been evaluated from the sulfur dioxide concentrations in the gas phase under the assumption of the plug flow of the gas out of the relation (2). The sulfur dioxide concentration has been measured by infrared analyzer.

$$k_G a = \frac{u_G}{H} \ln \frac{c_{SO_2,G}^{in}}{c_{SO_2,G}^{out}} \tag{2}$$

Effective interfacial area has been measured by absorption of the diluted CO_2 from the air into the aqueous sodium hydroxide solution, which is the system, where the gas-phase relative mass-transfer resistance is low and the rapid reaction of CO_2 with OH^- consumes quantitatively CO_2 within the liquid film. In such case, the mass-transfer rate is determined by the reaction-transport phenomena in the liquid film and is determined solely by the physical quantities of the system. Effective interfacial area can be calculated by combination of the relation for the CO_2 local mass-transfer rate and its balance along the height of the packing

$$a_{R_G=0} = \frac{\left(K_{OG}a\right)_{CO_2}}{He\sqrt{D_{L,CO_2} k_{OH} c_{OH,ave}}} = \frac{1}{He\sqrt{D_{L,CO_2} k_{OH} c_{OH,ave}}} \cdot \frac{u_G}{H} \cdot \ln \frac{c_{CO_2,G}^{in}}{c_{CO_2,G}^{out}} \tag{3}$$

Value of the reaction term $He\sqrt{D_{L,CO_2} k_{OH} c_{OH,ave}} = 2.24 \cdot 10^{-3}$ m/s (20 °C and 1 M NaOH solution) was determined by still level experiments (Linek et al. [6]) as this procedure circumvents the errors induced by application of different physical data of solubility and diffusivity by the authors.

Pressure drop of the packing has been measured with the air-water system. The pressure drop related to 1 m of the packing has been evaluated out of the relation (4).

$$\frac{dp}{dH} = \frac{p^{in} - p^{out}}{H} \tag{4}$$

2. Results and discussion

The liquid phase volumetric mass-transfer coefficient of the RSP 250 packing follows approximately power law relation to the liquid phase velocity with power of 0.67. In this respect the behavior is very similar to that of the Mellapak 250Y, M250Y. The absolute k_La values of the packings are quite similar up to the B~40m/h, at higher liquid loads the RSP 250 k_La are 10-15% larger (see Figure 1). In comparison with the data provided by Wang [4] we have found them to be ~40% higher. This comparison involves recalculation of the k_L data between air/toluene/water and nitrogen/oxygen/water system and is therefore indirect.

The data has been correlated using Billet-Schultes correlation [2] with the relative mean deviation of 16% and resulting C_L value is 1.446 (see Table 1).

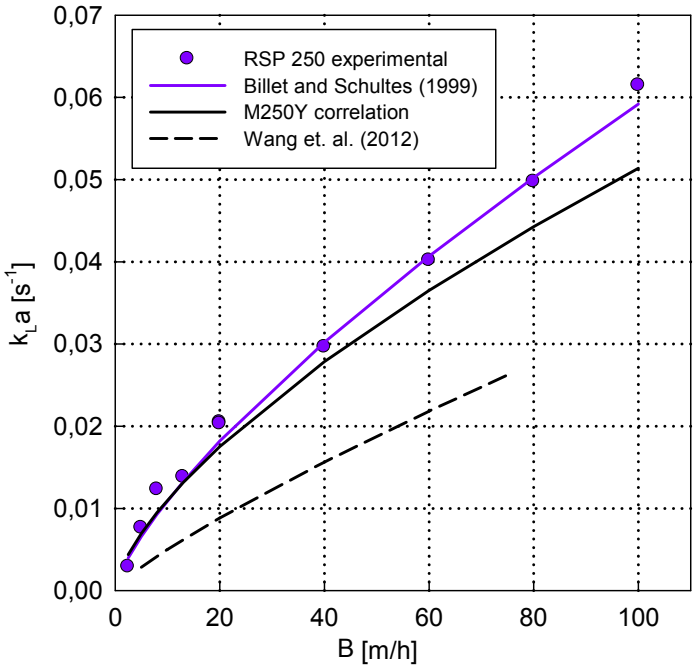

Figure 1: k_La of the RSP 250 measured with the nitrogen/oxygen/water system

The volumetric mass-transfer coefficient in the gas phase, k_Ga, of the RSP 250 has been measured under various gas and liquid loads (see Figure 2). Resulting k_Ga are 39-81% higher than that of the M250Y (see Figure 3) which is caused by both, higher effective interfacial area as well as higher mass-transfer coefficient k_G under similar phase flows. The obtained data are ~80% higher than those obtained by Wang [4], possibly as a result of different experimental arrangement differing significantly in the packed bed height and corresponding SO_2 concentration range.

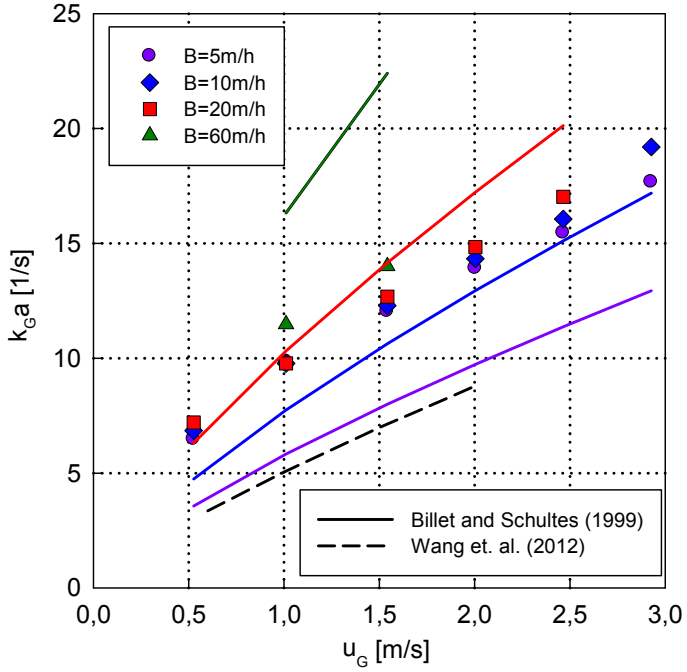

Figure 2: $k_G a$ of the RSP 250 measured with the air/sulfur dioxide/sodium hydroxide aq. sol.

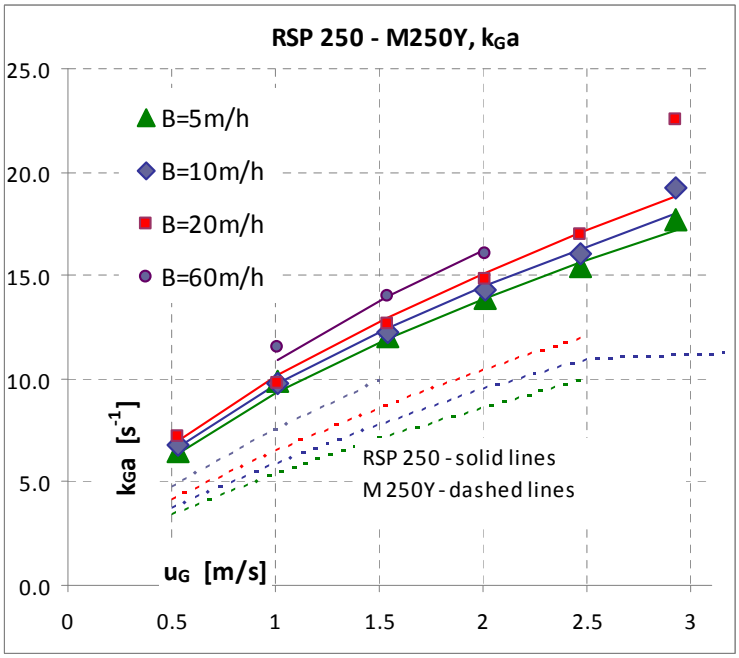

Figure 3: comparison of the $k_G a$ values for RSP 250 and Mellapk 250Y

The data has been correlated using Billet-Schultes correlation [2] with relative mean deviation of 26% and resulting C_V value is 1.023 (see Table 1). The correlation predicts more significant effect of the liquid flow on the $k_G a$ values than was found experimentally.

The effective interfacial area of the RSP 250 packing evaluated from our data is in close agreement with that found by Wang [4], deviation doesn't exceed 10% (see Figure 4). The effective interfacial area is larger than RSP 250 geometrical area for the liquid loads above B~10m/h which is in the agreement with the findings of Wang [4] and of the packing

vendor. This is in contrast with what was found for M250Y. The effective interfacial area of the RSP 250 is 20-50% higher than that of M250Y.

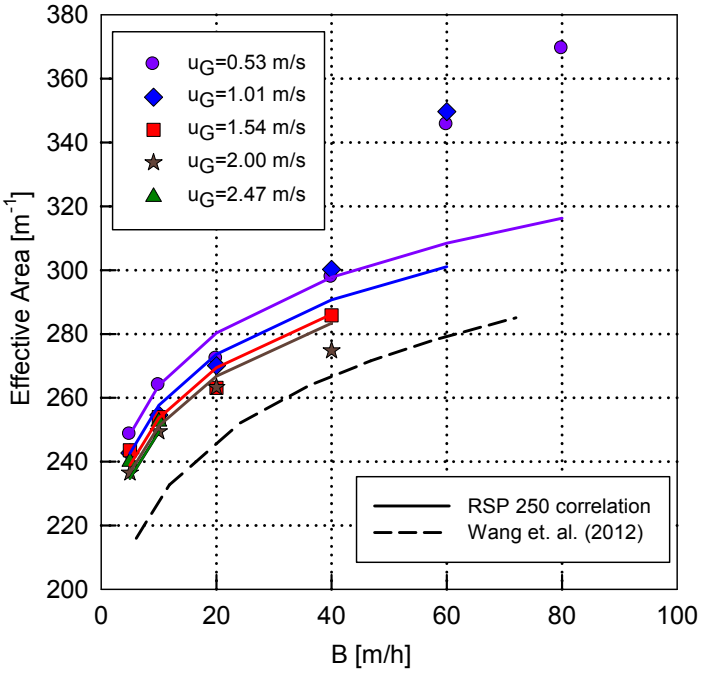

Figure 4: effective interfacial area, *a*, of the RSP 250 measured with the air/CO_2/sodium hydroxide aq. sol.

The pressure drop of the RSP 250 has been measured under various gas and liquid loads (see Figure 5). The obtained data correspond well with the ones published by Chambers and Schultes [5] up to the loading point achieved at our column. The capacity is about 20% lower in comparison with data from Chambers and Schultes [5] possibly as a result of different experimental arrangement differing in the column inner diameter and packed bed height. The capacity of the packing is comparatively high in comparison with M250Y packing measured in the same column.

The pressure drop values has been correlated using Billet-Schultes correlation [2] with relative mean deviation of 16% and resulting hydraulic parameters, C_S, C_{Fl}, $C_{P,0}$, are summarized in Table 1.

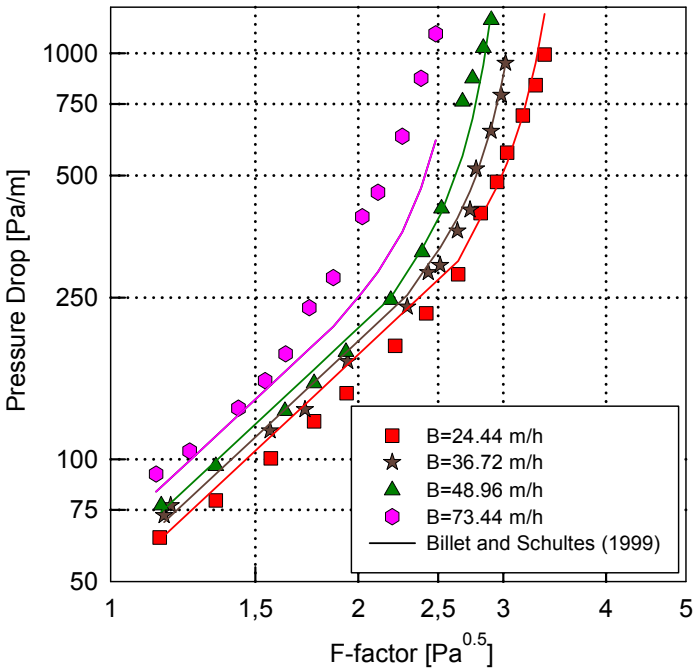

Figure 5: pressure drop of the RSP 250 measured with the air/water system

Table 1: Hydraulic and mass transfer parameters of Billet-Schultes model [2]

parameter	C_S	C_{FI}	$C_{P,0}$	C_L	C_V
value	3.89	2.67	0.260	1.446	1.023
mean relative deviation	16.4 %			15.8 %	25.7 %

3. Conclusions

Basic mass-transfer characteristics k_La, k_Ga, a and pressure drop of the metal sheet Raschig SuperPak 250 has been measured under absorption conditions in the i.d. 0.295m column using standard systems.

There was found, that the liquid phase volumetric mass-transfer coefficient, k_La, of the RSP 250 is very close to that of Mellapak 250Y up to the B~40m/h, at higher liquid loads it is 10-15% larger.

The interfacial area of the packing is found to be larger than its geometrical area for the liquid loads above B~10m/h which is in contrast with what was found for M250Y. This behavior suggests that there exists some phenomenon forming additional mass-transfer area, possibly generation of the droplets. The effective interfacial area of the RSP 250 is 20-50% higher than that of M250Y.

The volumetric mass-transfer coefficient in the gas phase, k_Ga, of the RSP 250 is 39-81% higher than that of the M250Y which is caused by both, higher effective interfacial area as well as higher mass-transfer coefficient k_G.

The capacity of the packing is comparatively high in comparison with M250Y packing. The hydraulic and mass transfer parameters of the Billet-Schultes model [2] for the metal RSP 250 structured packing have been evaluated on the basis of the obtained absorption data.

Acknowledgements

Support of Grant Agency of the Czech Republic through the project No. 13-01251S is gratefully acknowledged.

References

[1] Rejl, F.J., Linek, V., Moucha, T., Valenz, L., 2009. Methods standardization in the measurement of mass-transfer characteristics in packed absorption columns. Chemical Engineering Research and Design 87, 695-704.

[2] Billet, R., Schultes, M., 1999. Prediction of mass transfer columns with dumped and arranged packings. Updates summary of the calculation method of Billet and Schultes. Trans IChemE 77 (Part A), 498–504.

[3] Rejl, F.J., Valenz, L., Haidl, J., Kordač, M., Moucha, T. On the modeling of gas-phase mass-transfer in metal sheet structured packings. To be published in the Chemical Engineering Research and Design.

[4] Wang, C., Perry, M., Rochelle, G., T., Seibert, A., F., 2012. Packing characterization: Mass transfer properties. Energy Procedia 23, 23-32.

[5] Chambers, C., Schultes, M. 2007. Reaching new performance levels with surface enhanced Raschig Super-Pak structured packings. AIChE Spring meeting, April 22-26 2007, Houston.

[6] Linek, V., Sinkule, J., Brekke, K., 1995. A critical evaluation of the use of absorption mass transfer data for the design of packed distillation columns, Chem. Eng. Res. Des. 73 (Part A), 398–405.

Reactive Absorption Rates of CO_2 into Solutions of MEA/n-Propanol on a Wetted Wall Column

L.J. du Preez, L.H. Callanan, C.E. Schwarz, J.H. Knoetze[1]

[1]*Department of Process Engineering, Stellenbosch University*

Private Bag X1, Matieland, 7602, South Africa

Abstract

Effective interfacial mass transfer area is a vital efficiency parameter of separation column internals. Under the fast reaction regime, the absorption rate of CO_2 into solutions of MEA/n-Propanol is controlled by the reaction in the liquid film and is predominantly dependent upon the available effective area provided by the presence of MEA at the interface. This reactive absorption system was investigated using a cylindrical wetted wall experimental set-up. Absorption rates were measured in the fast reaction regime under conditions where the MEA at the liquid surface undergoes appreciable interfacial depletion. The liquid flow rates were varied to study the effect of liquid turbulence on the absorption rate and the surface renewal rate of MEA. The predominant resistance to mass transfer was in the liquid phase. The specific absorption rate was found to be a function of temperature, CO_2 partial pressure, degree of surface depletion and the degree of liquid turbulence. Image analysis of the gas-liquid interface revealed the wave motion noticed on the falling liquid film surface. The images used in the analysis were collected from high definition video footage of the gas liquid interface using an endoscopic camera. All three types of waves (capillary, composite and roll waves) commonly occurring on falling liquid films were identified. The increase in liquid phase turbulence with an increase in liquid flow rate and flow path length was noticed from the wave motion on the liquid surface changing from capillary waves (lower turbulence) to composite and roll waves (higher turbulence).

Keywords

Wetted Wall, Specific Absorption Rate, Carbon Dioxide, Mono-ethanolamine, Image Analysis

1. Introduction

Under certain conditions, the reactive absorption of CO_2 into alcoholic solutions of MEA falls in the fast reaction regime [1], which makes it a suitable system for calculating the effective interfacial mass transfer area of separation column internals from absorption rate data [1,2]. Under the fast reaction regime, the absorption rate is controlled by the reaction and is predominantly influenced by the available effective interfacial area provided by the presence of MEA at the interface. Absorption rates measured on a device with an assumed known interfacial area therefore provides insight to the effective area available for mass transfer [1].

A smooth wetted wall experimental set-up was constructed and used to study the absorption rate of carbon dioxide (CO_2) into an assumed known area of solutions of

mono-ethanolamine (MEA) dissolved in n-propanol. The experimental aims of this study were:

- Measuring the specific absorption rate (absorption rate per interfacial area) of CO_2 into solutions of MEA/n-Propanol at two MEA concentrations (0.08 M and 0.2 M), two temperatures (25°C and 30°C) two column heights (60 and 90 mm), three different liquid flow rates (0.874, 1.016 and 1.345 mL/s) and a gas flow rate of 78 mL/s.
- Measuring the specific and total absorption rates under fast liquid phase reaction conditions where appreciable interfacial depletion of MEA occurs. This meant measuring specific absorption rates at various CO_2 partial pressures (partial pressure range of 2.15 – 19 kPa)
- Collecting high definition video footage of the falling film gas-liquid interface and analysing the footage to reveal the wave motion on the gas-liquid interface.

The experimental data allowed the evaluation of the effect of temperature, interfacial area, degree of interfacial depletion and liquid turbulence on the total and specific absorption rates of CO_2 into solutions of MEA/n-Propanol. Image analysis of the falling liquid film was required to evaluate the nature of the surface ripples (waves) on the liquid film and how these waves are influenced by liquid phase turbulence. New insight into how all of the above mentioned effects influence the available effective interfacial mass transfer area may be obtained from the evaluation of the data.

2. Materials and Method

The wetted wall column used in this study is illustrated in Figure 1. The wetted wall column had a diameter of 26.4 mm and the height of the column was adjustable to achieve a range of gas-liquid interfacial areas. The liquid phase was distributed evenly on the outer surface of the wetted wall by over-flowing through 24 evenly spaced 1 mm holes in the column. The gas phase (CO_2/N_2) was distributed evenly around the base of the wetted wall column with the use of a donut shaped distributor. A boundary layer analysis of the gas phase revealed that a laminar gas phase was encountered at the gas-liquid interface, with insignificant resistance to mass transfer in the gas-phase. For effective area measurements, it is crucial that gas- phase resistance to mass transfer is kept to a minimum [2].

Temperature control of the absorption conditions were obtained by submerging the wetted wall column in a water bath. The gas and liquid lines were circulated through a pre-heater and insulated with heat tracing to ensure a uniform temperature for the entire experimental set-up. The inlet and outlet temperature of both the gas and liquid lines were measured along with the temperature inside the PVC dome. The temperature readings were within the accuracy of the PT-100 temperature probes (±0.5°C).

The gas phase was saturated with n-propanol before entering the dome, to prevent solvent evaporation from the falling film. Both the gas and liquid flow rates were measured and regulated with rotameters. The liquid rotameter was calibrated with a measuring cylinder and a stop watch and the gas rotameters with a soap bubble flow meter. The absorption rate of CO_2 was calculated from the difference between the CO_2 vol% readings before and after absorption and by assuming ideal gas behaviour:

$$\dot{n}_{CO_2} = \frac{P_{\text{dome}}\dot{V}_G}{RT} \cdot \left(\text{vol\% CO}_2\right) \qquad \textbf{1}$$

The vol% CO_2 data were measured by a Dräger® PIR 7200 CO_2 analyser (accuracy 0.01 vol%). The experimental set-up was validated by performing experimental runs similar to those of a previous study on the same absorption system [3].

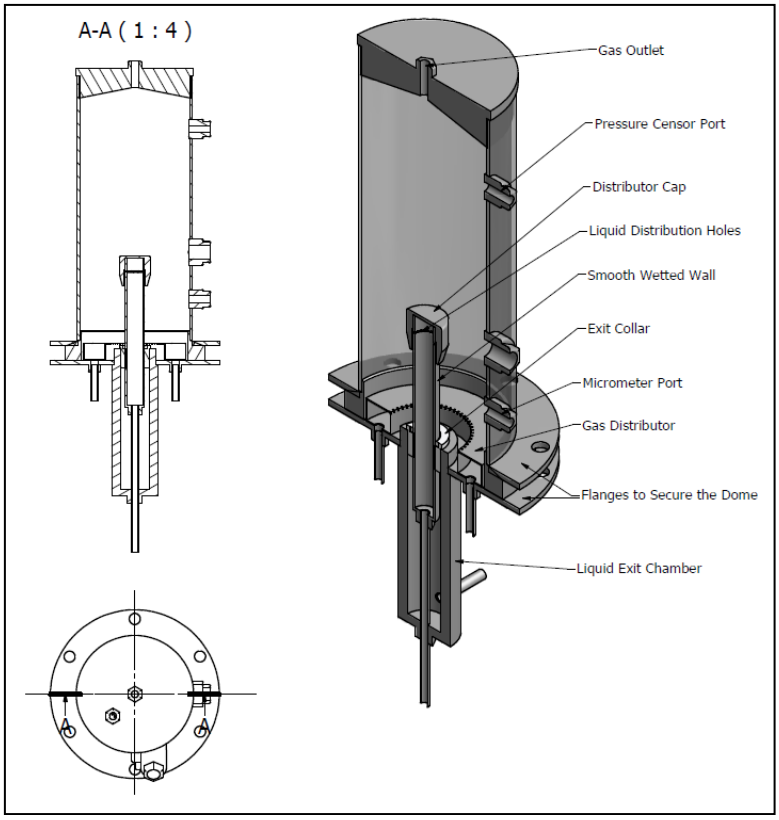

Figure 1: Wetted wall column and PVC dome experimental set-up

The PVC dome of the wetted wall experimental set-up was fitted with specially manufactured fittings to accommodate glass tubes with optic windows enclosing one end of the tube. These glass tubes served as the view ports for the Stryker® 1188 HD endoscopic camera used for collecting the 720p video footage of the gas-liquid interface. The dome was further fitted with a port to accommodate a Mitutoyo® series 128 depth micrometer (±0.01 mm accuracy) for measuring the thickness of the falling liquid film.

2. Results and discussion

An analysis of the specific absorption rate provides insight into the effective interfacial area available for mass transfer. The specific absorption rate was calculated by dividing the total absorption rate by the estimated gas-liquid interfacial area. The estimated interfacial area was calculated by taking the measured film thickness into account and assuming the liquid interface to be smooth for the purpose of the calculation. The specific absorption rates of CO_2 into a 0.2 M MEA/n-propanol solution at 25°C, 30°C, column heights of 60 mm and 90 mm and a range of CO_2 partial pressures are illustrated in Figure 2. A decrease in absorption rate was noticed for an increase in temperature. This was in agreement with previous research [2,3,4].

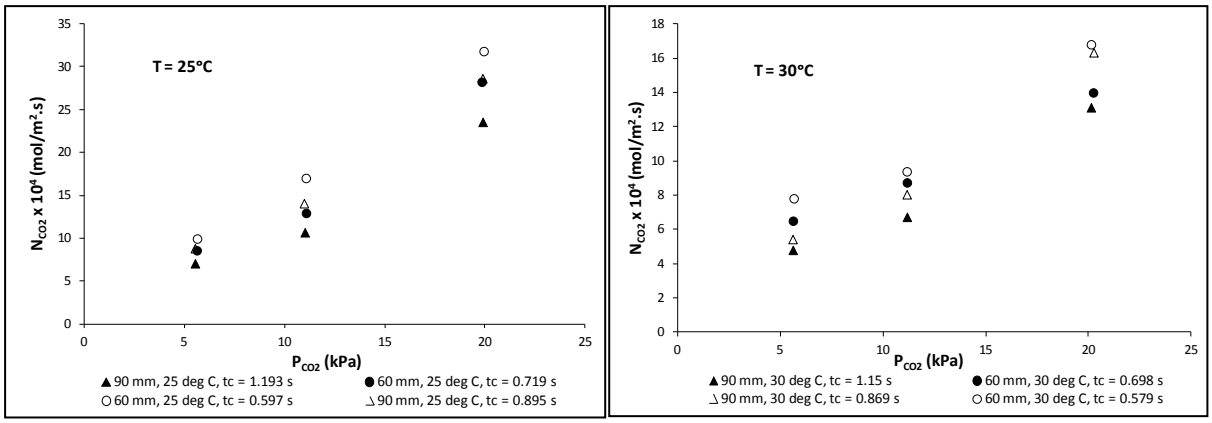

Figure 2: Specific Reactive Absorption Rates into 0.2 M MEA in n-Propanol as a Function of CO_2 partial pressure

The effect of temperature on the reactive absorption rate involves the consideration of both CO_2 solubility and the equilibrium of the liquid phase reaction. The liquid phase reaction is reported as equation 2 [3,6]:

$$1)\ CO_2 + RNH_2 \underset{k_2}{\overset{k_1}{\rightleftharpoons}} RNH_2^+COO^-$$

$$2)\ RNH_2^+COO^- + RNH_2 \underset{k_4}{\overset{k_3}{\rightleftharpoons}} RNHCOO^- + RNH_3^+ \qquad \textbf{2}$$

The solubility of CO_2 in n-Propanol, decreases with an increase in temperature [5]. When considering the solubility of CO_2 in pure n-Propanol, its molar solubility decreases by 4.73% with an increase in temperature from 25°C to 30°C [5]. This does not account for the average of 38.4% decrease in total absorption rate for the 0.2 M MEA solutions or 32.6% decrease for the 0.08 M MEA solutions. A possible explanation for this difference may be found when considering the exothermic nature of the reaction and the effect of temperature on the equilibrium of the reaction. The exothermic reaction of CO_2 with MEA obeys reversible reaction kinetics [6]. According to Le Chatelier's principle, an increase in temperature will cause a shift in the reaction equilibrium towards the reactants for an exothermic reaction. This shift causes a decrease in the concentration difference of CO_2 between the gas and liquid phases, which decreases the driving force for absorption.

The data points in Figure 2 represent absorption rates at different contact times with a predominantly higher specific absorption rate noticed at shorter contact times. This indicates that there is a degree of depletion of MEA in the liquid film at the interface and that the degree of depletion increases with an increase in contact time. From the measured specific absorption rate it is possible to discuss the results from both an interfacial depletion and interfacial renewal rate perspective. Interfacial renewal can only happen if there is interfacial depletion and so these effects are always linked.

At higher CO_2 partial pressures there will be a higher surface depletion rate due to the higher driving force for absorption and the faster reaction kinetics in the liquid film at the higher reagent concentrations. This may explain why the specific absorption rate at shorter column heights is higher than that for longer column heights. The higher degree of surface depletion for longer column heights decreases the effective area available for absorption. The number of moles of MEA available for reaction in the liquid film was calculated from the MEA concentration and the volume of liquid in

the film. From the molar amount of CO_2 absorbed into the liquid film at steady state and the reaction stoichiometry, the number of moles of MEA that could possibly react, was calculated. The calculation showed that the range of percentage of MEA that could possibly react for all experimental runs performed was 0.43% - 4.36% of the MEA available in the film. This indicates that whilst appreciable interfacial depletion does occur, there is sufficient MEA left in the bulk liquid for surface renewal to easily and continuously take place

From the mole balance calculation it was found that at higher liquid flow rates there is a higher percentage of MEA that reacts per second due to a higher liquid turbulence increasing the surface renewal rate and contributing to the higher driving force for CO_2 absorption. This could be an explanation for the higher CO_2 absorption rate noticed at shorter contact times. For the same CO_2 partial pressure, column height and liquid flow rate, there was a larger percentage MEA that reacted per second for the 0.08 M MEA solution, than the 0.2 M solution. Under these conditions, equal surface renewal rates on a basis of the volumetric rate of liquid carried to the surface due to turbulence may be assumed. There will thus be a lower molar amount of MEA reaching the interface per second for the 0.08 M solution. A similar partial pressure driving force for CO_2 will thus cause a greater percentage of MEA molecules to react per second, leading to a higher surface depletion of MEA for the 0.08 M solution compared with the 0.2 M solution. Both interfacial depletion and interfacial renewal may thus be assumed to occur.

The video footage of the gas-liquid interface, collected with the endoscopic camera was analysed for wave motion using an in-house developed Matlab® image analysis algorithm. The gas-liquid boundary is defined by a threshold of greyscale intensity (0 (white) to 256 (black) for negative resolution images). The threshold value is selected manually based on visual observation of the wave motion on the liquid surface. The threshold value in each frame is then plotted and filtered using a moving average with a 15 frame window. Each filtered threshold value is thus the average of the preceding 15 frame's threshold values. The filtered frames are then re-recoded at a desired frame rate to produce a video that shows the wave motion of the threshold line, indicating the wave motion of the gas-liquid interface.

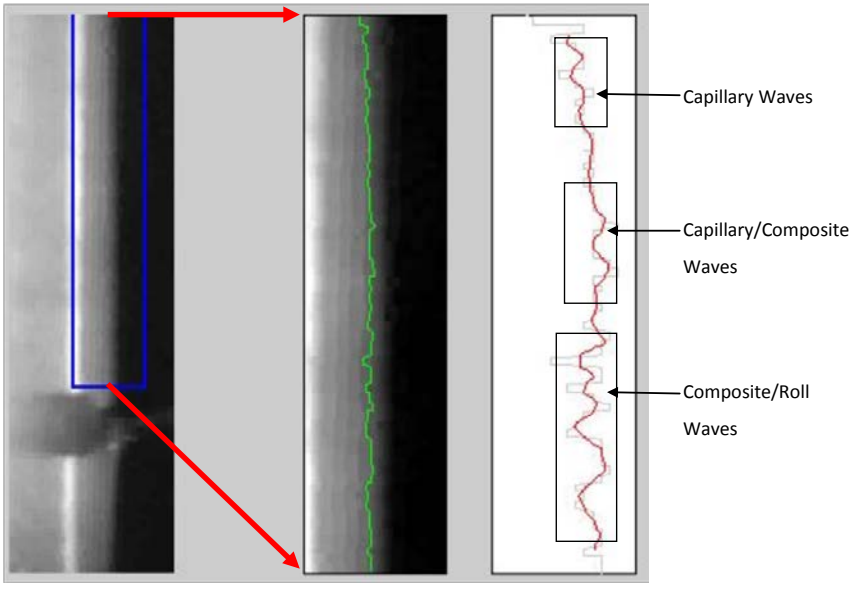

Figure 3: Image analysis result for a liquid flow rate of 1.345 cm^3/s indicating the three types of waves found in falling liquid films

A screen shot of a typical re-recoding of an image analysis result for a liquid flow rate of 1.345 cm^3/s is illustrated in Figure 3. All three types of waves described in literature [7] (capillary, composite and roll waves) may be identified. In the entrance region of the liquid film, capillary waves are most common and as the flow length increases, composite and roll waves start to appear. From the image analysis results it may be concluded that the assumption of a smooth gas-liquid interface for the liquid flow rates used in this and previous studies [2,3,4] is an over-simplification. The true interfacial area may more accurately be determined with wave functions fitted to the image analysis data.

3. Conclusions

The absorption rate data showed that the specific absorption rate of CO_2 into MEA/n-propanol is a function of temperature, CO_2 partial pressure, degree of surface depletion and the degree of liquid turbulence. Specific absorption rate decreases for an increase in temperature. This is partly due to the decrease in solubility of CO_2 with an increase in temperature. At longer column heights, the specific absorption rate of CO_2 decreases. This may be attributed to a degree of depletion of MEA in the liquid film for the longer liquid flow path, causing a decrease in the available effective area for absorption. At higher liquid flow rates, the increased turbulence causes an increase in the surface renewal rate, which increases the effective area available for absorption. Image analysis of the gas-liquid interface revealed the wave motion noticed on the falling liquid film surface. The increase in liquid phase turbulence with an increase in liquid flow rate and flow path length was noticed from the wave motion on the liquid surface changing from capillary waves (lower turbulence) to composite and roll waves (higher turbulence).

Acknowledgements

This work is based on the research supported in part by the National Research Foundation of South Africa (Grant specific unique reference number UID 83966), Stellenbosch University's OSP project on Energy and the Environment, and Sasol Technology (Pty) Ltd. The authors acknowledge that opinions, findings and conclusions or recommendations expressed in any publication generated by the supported research are that of the authors, and that the sponsors accept no liability whatsoever in this regard. Opinions expressed and conclusions arrived at are those of the authors and are not necessarily to be attributed to the sponsors.

References

[1] Charpentier, J. C., 1981. Mass Transfer Rates in Gas-Liquid Absorbers. In: T. B. Drew, ed. *Advances in Chemical Engineering.* New York: Elsevier, pp. 2-133

[2] Tsai, R. et al., 2008. Influence of Surface Tension on Effective Packing Area. *Industrial Engineering Chemistry Research,* Volume 47, pp. 1253-1260.

[3] Erasmus, A., 2004. *Mass Transfer in Structured Packing,* Stellenbosch: PhD Dissertation: University Stellenbosch.

[4] Luo, X., Hartono, A. & Svendsen, H., 2012. Comparative Kinetics of Carbon Dioxide Absorption in Unloaded Aqueous Monoethanolamine Solutions Using Wetted Wall and String of Discs Columns. *Chem. Eng. Sci,* Volume 82, pp. 31 - 43.

[5] Tokunaga, J., 1975. Solubilities of Oxygen, Nitrogen and Carbon Dioxide in Aqueous Alcohol Solutions. *Jour. Chem. Eng. Data,* Volume 20, pp. 41 - 46.

[6] Du Preez, L.J., 2014. *Reactive Absorption Kinetics of CO_2 in Alcoholic Solutions of MEA: Fundamental Knowledge for Determining Effective Interfacial Mass Transfer,* Stellenbosch: PhD Dissertation: University Stellenbosch.

[7] Yu, L.-M., Zeng, A.-W. & Yu, K., 2006. Effect of Interfacial Velocity Fluctuations on the Enhancement of the Mass-Transfer Process in Falling-Film Flow. *Ind. Eng. Chem. Res.,* Volume 45, pp. 1201 - 1210.

Experimental investigation of the three dimensional velocity field of falling liquid film flow on an inclined surface and micro structures

A. Marek, J.-U. Repke
Institut für Thermische Verfahrenstechnik, Umwelt- und Naturstoffverfahrenstechnik, Technische Universität Bergakademie Freiberg, Leipziger Str. 28, Freiberg, Deutschland; Tel. +49 (0)3731 39 2801, Fax. +49 (0)3731 / 39 3652, E-Mail: andre.marek@tun.tu-freiberg.de

Abstract
For the analysis of gravity driven liquid film flow on an inclined surface of structured packing material a novel non-intrusive measurement system is applied to measure the three dimensional velocity field. Therefore a measurement cell is built up, which enables the detailed flow analysis. To avoid optical distortions at the gas / liquid interface through the appearance of waves the whole measurement cell is made of transparent PDMS and the measurement orientation is from the back of the cell. A refractive index matching is done to avoid optical distortion at the complex solid/liquid interface.
The new measurement system is validated on a smooth inclined surface and it can be shown that it is suitable to measure the three dimensional velocity field and the film thickness of the liquid film. With the validated measurement system, a series of experimental investigation are carried out on surfaces with different micro structures. For a bidirectional micro structure the velocity field show that the velocity component transversal to the main component is induced.

Keywords:
Film flow, Stereo PIV, PDMS, refractive index matching

1 Introduction

In the field of downstream processes like distillation or absorption, structured packings have been established for several decades. The efficiency of packed columns depends on the flow behavior of the liquid phase inside the packing segments where the gas and liquid phase brought in contact for heat and mass transfer. Packing segments usually consist of macro structures in the range of one centimeter that promotes the gas-liquid interaction with a low overall pressure drop. Micro structures, usually in the range of less than one millimeter, increase the stability and the spreading of the liquid film on the packing surface. Several authors investigated the effect of macro structures on mass transfer [1, 2]. However, the influence of the micro structures has been considered less. Compared with the smooth surface without micro structures, (Schultes [3]) found mass transfer intensification and assumed a more turbulent flow regime in distillation runs. A detailed experimental analysis done by (Kohrt et al. [4]) showed a mass transfer intensification of up to 80% on different micro structured surfaces. The influence of surface wetting area and the gas side mass transfer resistance were precisely controlled and can be excluded by those studies.
The fluid dynamics of film flow on micro structured surfaces has been investigated theoretically ([5, 6, 7, 8]) and experimentally ([9, 10, 11, 12, 13, 14]) with intrusive

and non-intrusive measurement systems in a two dimensional space. To elucidate the mass transfer intensification the three dimensional fluid dynamic behavior of the complex gravitational driven liquid film has to be investigated.
In this work, the three dimensional velocity field of falling liquid film flow on smooth and micro structured surfaces is investigated. Therefore a novel measurement system is applied. A transparent measurement cell is designed to measure the liquid film flow from the back of the measurement cell to avoid disturbance at the gas/liquid interface. To avoid disturbance at the solid/liquid interface a refractive index matching is done between the measurement cell and the used liquid. Here, systematic fluid dynamic analysis is carried out to identify the impact of micro structured surface on the fluid dynamic as a base for a better understanding of the mass transfer intensification reported by Kohrt [4].

1.1 Experimental setup

To analyze the fluid dynamics a transparent measurement cell is built up as shown in figure 1. It is a mould of transparent Polydimethylsiloxane (PDMS) and enables to create different micro structured surfaces. To avoid optical distortion at the wavy gas/liquid interface the measurement orientation is from the back of the measurement cell. To avoid optical distortion at the complex micro structured solid / liquid interface a refractive index matching is done between the PDMS and the liquid water/glycerol. The properties of the liquid are:

- Water / glycerol (weight %: 46 / 54)
- viscosity: 9,6 mPas
- refractive index: 1.41.

The liquid is pumped from a tank to the measurement cell behind the surface and is fed with an overflow weir on top of the surface without any distortion. The inclination angle is 60 degree, which resembles industrial packing elements.

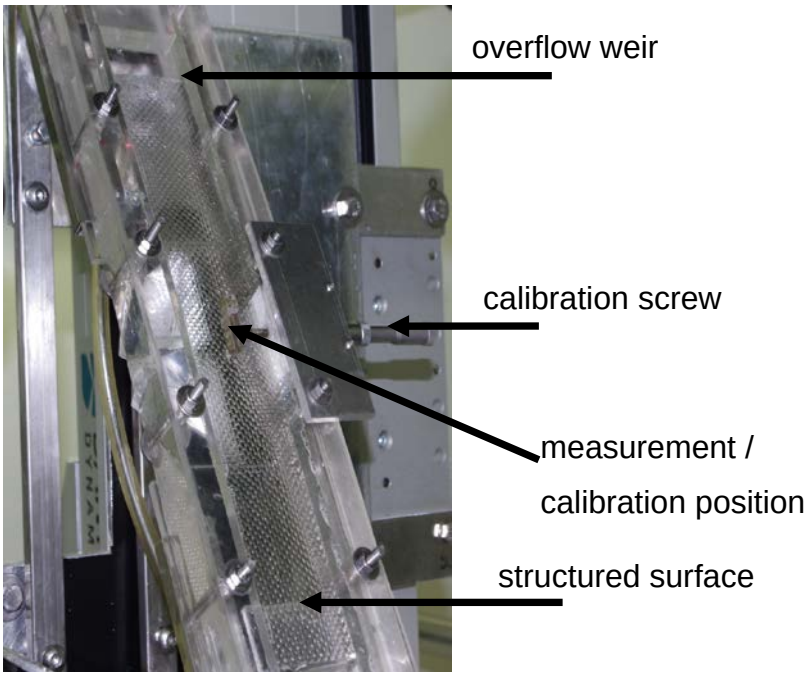

Figure 1: film flow measurement cell

1.2 Measurement setup

To measure the three dimensional velocity field, a new micro Stereo Particle Image Velocimetry (µSPIV) method is used [15, 16]. Two locally displaced cameras, by 45° to the center giving the lowest reconstruction error [17], record the two dimensional velocity field. The three dimensional (two component - 3D2C) velocity field is reconstructed from these recordings. The cameras used are two HiSense Neo (5MP, 16bit) cameras from Dantec Dynamics with 12x optical micro lens in front (Navitar). To ensure an orthogonal camera orientation to the measurement cell, prisms are used as shown in figure 2 (left). The limitation of the chosen micro lens is the small depth of field. In standard SPIV applications it is common to evade this restriction by a lens translation method or an angular lens displacement. Both methods are not working in this case since the image to lens plane distance is larger than the object to lens plane distance. To overcome this limitation a three millimeter aperture is used to extend the depth of field of the micro lens to approximately 6 millimeter.

For the calibration of the object plane a micro target (DDO Coating) is used with the dimension of 2x5 millimeter. The two dimensional target has to be moved at the measurement position to get a three dimensional calibration to evaluate the camera recordings. For this purpose the calibration target is moved with a calibration screw (as shown in figure 1) several times in the light sheet of the laser. The used laser is a standard Nd:YAG laser with a wavelength of 532nm and a repetition rate of 15Hz. To measure the fluid dynamics in the experiment 10µm hollow glass spheres are used which match the density of the working fluid closely. The time between to µSPIV recordings is adapted in the way that the mean particle displacement is close to 8 pixel [17].

The complete measurement setup is shown in figure 2 (right). The measurement cell is positioned on a 3D traversing system in the middle. The cameras are behind the measurement cell and also inclined and disposed by 45° to the centerline. The laser is located above the measurement cell.

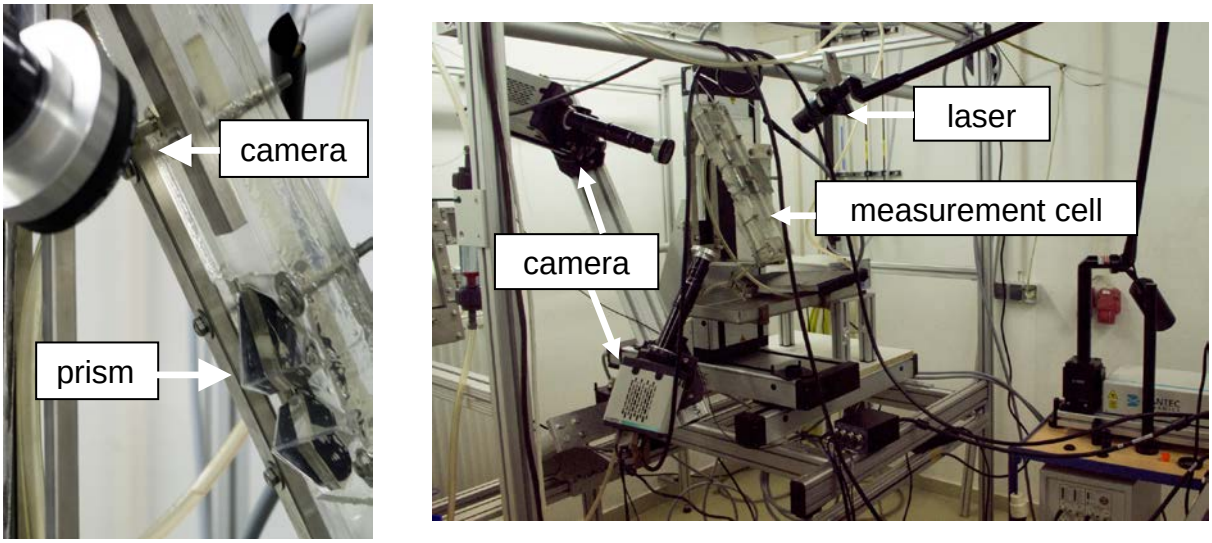

Figure 2: (left) camera orientation behind measurement cell and prism for orthogonal camera orientation to measurement cell, (right) complete measurement setup in the lap

1.3 Analysis of µSPIV recordings

For the analysis of the µSPIV recordings DynamicStudio v.3.41 software from Dantec Dynamics is used. For the time averaged velocity field a total of 500 µSPIV

recordings are utilized. In a first step the background noise is removed from the recordings by subtracting the mean image of all recorded pictures. In the next step an adaptive cross correlation with flexible interrogation areas, which is needed due to the high velocity gradients in the flow, ascertains the velocity vectors. Additionally a peak validation of the cross correlation map removes spurious vectors. In the last step the average of all 500 vector fields for each camera is calculated and reconstruction of the three dimensional velocity field is performed. The three velocity components can be calculated with:

$$U = \frac{U_1 \cdot \tan\alpha_2 + U_2 \cdot \tan\alpha_1}{\tan\alpha_2 + \tan\alpha_1} \tag{1}$$

$$V = \frac{V_1 \cdot \tan\beta_2 + V_2 \cdot \tan\beta_1}{\tan\beta_2 + \tan\beta_1} \tag{2}$$

$$W = \frac{U_1 - U_2}{\tan\alpha_2 + \tan\alpha_1} = \frac{V_1 - V_2}{\tan\beta_2 + \tan\beta_1} \tag{3}$$

Subscript 1 addresses for camera one and 2 for camera 2. The *U* velocity component is in mean flow direction, *V* perpendicular to *U*, and *W* transversal to *U*. More information on SPIV reconstruction can be found elsewere [18].

2 Results and discussion

2.1 Validation of the measurement system

The validation of the measurement system is done by comparing the results of the velocity profile on a smooth surface without micro structures with the theoretical Nusselt solution [19] for velocity profile and film thickness.

$$u(y) = \frac{g \cdot \sin\alpha \cdot \delta^2}{\nu}\left(\frac{y}{\delta} - \frac{1}{2}\left(\frac{y}{\delta}\right)^2\right) \tag{3}$$

$$\delta_N = \sqrt[3]{\frac{3 \cdot \dot{V} \cdot \nu}{B \cdot g \cdot \sin\alpha}} \tag{4}$$

There g is the gravity acceleration, α the inclination angle, δ the film thickness, δ_N the theoretical film thickness, y the coordinate orthogonal to the surface $\dot{V}$ the flow rate, ν the viscosity and B the wetted width of the surface. In figure 3 the measured velocity profile, calculated from all velocity component, is compared with equation 3 for Re=35, with the width of the

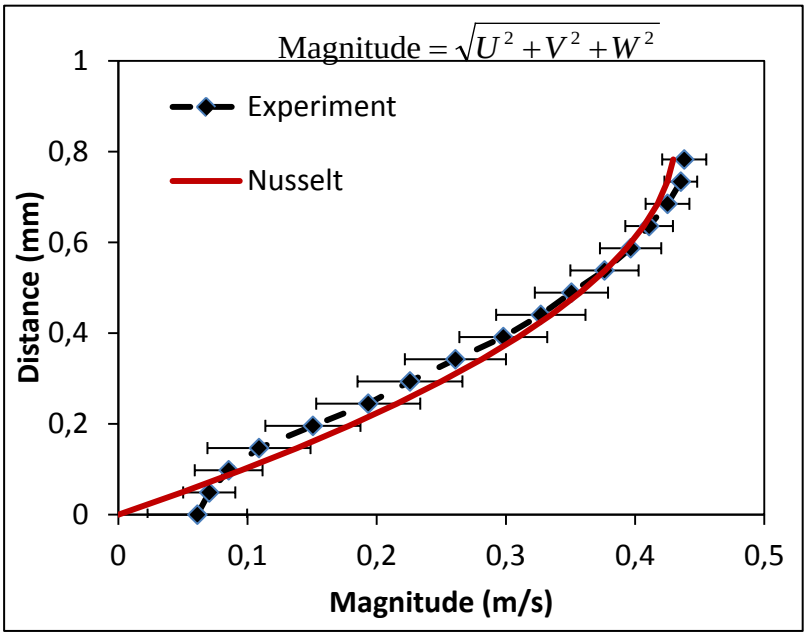

Figure 3: comparison of measured velocity profile and theory

surface as characteristic length. As can be seen, the measured profile shows good agreement to the theoretical solution. The highest deviation appears near the solid / liquid interface. The reason is the very small particle displacement due to the small velocity in this area.

2.2 Fluid dynamics on micro structured surfaces

The fluid dynamics of a micro structured surface are analyzed. In general these micro structures have a tetrahedral shape with a height of 0.55mm and a length of 1.85mm. The velocity field for Re=25 is shown in figure 4. To visualize the influence of the micro structures the vectors are not scaled depending on their magnitude. It can be seen that the highest velocities appear at the gas/liquid interface and close before and above the structures. In the bulk flow region the mean velocity is dominant. Between and before the micro structures a deflection of the liquid can be seen. It can be stated that through the micro structured surface the velocity field in the liquid film is clearly influenced and an induction of transversal and perpendicular velocity components takes place. Due to the higher mixing efficiency compared with a smooth surface the conclusion can be drawn that a higher mass transfer on the micro structured surface can be expected. This is the first approach to clarify the mass transfer intensifation found by Kohrt [4].

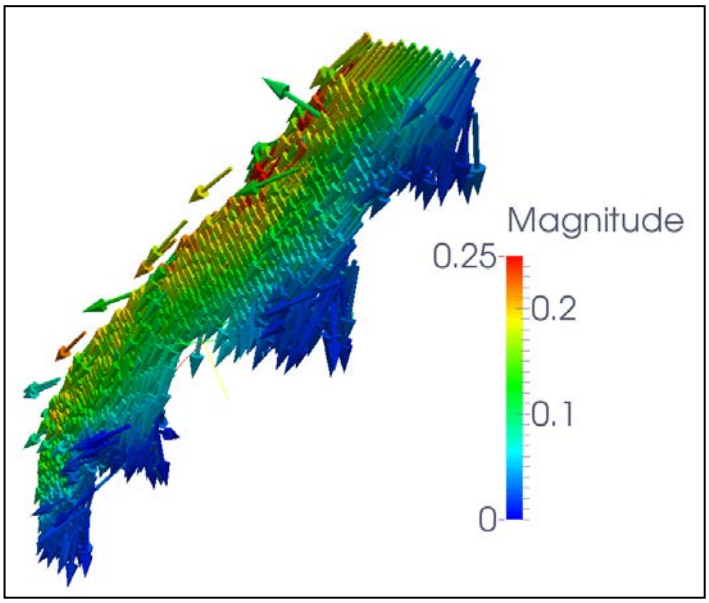

Figure4: velocity field of liquid film flow on micro structured surface

3 Conclusion

For the analysis of the velocity field of falling liquid film flow on micro structured surfaces a measurement cell is built up and a novel µSPIV method is used to determine the three dimensional velocity field. The measurement orientation is from the back of the measurement cell to get rid of optical distortions at the wavy gas/liquid interface. With a refractive index matching optical distortions at the complex solid/liquid interface are suppressed. The validation of the measurement system showed good agreement with literature. For the velocity field on the micro structured surface it was shown that there is a clear influence on the velocity field, by induction of additional velocity components, which is caused by the micro structures and it can be deduced that also the mass transfer is influenced by this. In the next step the influence of a countercurrent gas stream will be analyzed.

Acknowledgments

The authors would like to thank the Deutsche Forschungsgemeinschaft (DFG) RE 1705/8-1 for the financial support.

References

[1] Olujic, Z., Joedecke, M., Shilkin, A., Schuch, G., Kaibel, B., 2009. Equipment Improvement trends in distillation. Chem. Eng. Process. 48, 1089–1104.
[2] Fischer, L., Buehlmann, U., Melcher, R., 2003. Characterization of high-performance structured packing. Trans. IChemE A 81, 79–84.
[3] Schultes, M., 2008. Raschig Super-Pak – Eine neue Packungsstruktur mit innovativen Vorteilen im Vergleich. Chemie Ingenieur Technik 80 (7), 927–933.
[4] Kohrt M., Ausner I., Wozny G., Repke J.-U. 2011. Texture influence on liquid-side mass transfer. Chemical Engineering Research and Design 89(8), 1405-1413
[5] Trifonov, Y.Y., 2004. Viscous film flow down corrugated surfaces. J. Appl. Mech. Tech. Phys. 45 (3), 389–400.
[6] Valluri, P., Matar, O.K., Hewitt, G.F., Mendes, M.A., 2005. Thin film flow over structured packings at moderate Reynolds numbers. Chem. Eng. Sci. 60, 1965–1975.
[7] Luo, H., Pozrikidis, C., 2007. Gravity-driven film flow down an inclined wall with three-dimensional corrugations. Acta Mechanica 188, 209–225.
[8] Baxter, S.J., Power, H., Cliffe, K.A., Hibberd, S., 2009. Free surface Stokes flows obstructed by multiple obstacles. Int. J. Numer. Methods Fluids,
[9] Zhao, L., Cerro, R.L., 1992. Experimental characterization of viscous film flow over complex surfaces. Int. J. Multiphase Flow 18, 495–516.
[10] Negny, S., Meyer, M., Prevost, M., 2001. Study of a laminar falling film flow over a wavy wall column. Part II: Experimental validation of hydrodynamic model. Int. J. Heat Mass Transfer 44, 2147–2154.
[11] Wierschem, A., Scholle, M., Aksel, N., 2003. Vortices in film flow over strongly undulated bottom profiles at low Reynolds numbers. Phys. Fluids 15 (2), 426–435.
[12] Ataki, A., Kolb, P., Buehlmann, U., Bart, H.-J., 2006. Wetting performance and pressure drop of structured packings: CFD and experiments. Proc. Distillation Absorption , 534–543.
[13] Argyriadi, K., Vlachogiannis, M., Bontozoglou, V., 2006. Experimental study of inclined film flow along periodic corrugations: the effect of wall steepness. Phys. Fluids 18, 012102.
[14] Helbig, K., Nasarek, R., Gambaryan-Roisman, T., Stephan, P., 2009. Effect of longitudinal minigrooves on flow stability and wave characteristics of falling liquid films. J. Heat Transfer 131, 011601.
[15] Marek A., Repke J.-U. 2013. Investigation of the three dimensional velocity field of falling liquid film flow on micro-structured packing surfaces, 2013, 9th World Congress of Chemical Engineering, Seoul, Korea
[16] Marek A., Repke J.-U. 2013. Three dimensional hydrodynamics of liquid falling film, 2013, AIChE Annual Meeting, San Francisco, USA
San Francisco, USA
[17] Bohl D. G., Koochesfahani M. M., Olson B. J., 2001. Development of stereoscopic molecular tagging velocimetry. Exp. in Fluids 20, 2001
[18] . Raffel, M., Willert, C.E., Wereley, S.T., Kompenhans, J., 2007. Particle Image Velocimetry, A Practical Guide.
[19] Nusselt, W.: Die Oberflächenkondensation des Wasserdampfes. 1916. VDI-Zs, 60 (27), 541-546

The experimental data on the phase transitions in the system with ethyl acetate synthesis reaction

Artemiy Samarov, Alexander Toikka, Maria Toikka, Maya Trofimova, Alexandra Golikova and Nikita Tsvetov
Saint Petersburg State University, Department of Chemical Thermodynamics and Kinetics, Saint-Petersburg, Russia

Abstract
This paper present some results of new complex experimental study of solubility and liquid-liquid equilibrium for the quaternary system acetic acid – ethanol – ethyl acetate – water and for the ternary sub-systems acetic acid – ethyl acetate – water and ethanol – ethyl acetate – water with liquid phase splitting at 303.15 K and 313.15 K. Binodal surfaces, binodal curves, tie-lines and compositions of critical states of liquid-liquid equilibrium were determined. LLE data were correlated by UNIFAC and NRTL models.

Keywords
Liquid-liquid equilibria, ethyl acetate, esterification, quaternary reacting systems.

1. Introduction

The ethyl acetate synthesis is one of important processes of chemical engineering. The design of this process had been developed in many aspects, including the run of reaction and phase transitions in reaction media. The essential for this task belongs to thermodynamic studies of solubility, liquid-liquid equilibrium (LLE), vapor-liquid equilibrium (VLE) and chemical equilibrium (CE). The design of ethyl acetate synthesis may combine mass transfer and chemical processes, in other words it could be organized as a coupled process. Such coupled processes are of well-known significance for the development of resource- and energy-saving green technologies. In spite of the fact that there are a numerous data sets (LLE, CE and VLE) on acetic acid – ethanol – ethyl acetate – water system some of these need corrections. Our analysis of experimental data led to conclusion that additional experiments are necessary for overall thermodynamic analysis. The critical analysis of existing literature data on the system with ethyl acetate synthesis reaction would be also presented in the lecture. First of all the lack of experimental information concerns the data on phase splitting and the peculiarities of liquid-liquid envelope at polythermal conditions which may be significant for process design. Accordingly the aim of presented work was to carry out the complex and detailed study of solubility and LLE: these data are more limited in comparison with VLE. We also obtained a new experimental data on CE on ester synthesis (and hydrolysis) reaction at few temperatures.

2. Results and discussion

The experimental study of solubility, LLE and CE was carried out at 303.15 – 313.15 K. We also used the data (293.15 K) that had been obtained in our recent works[1, 2]. Determination of disposition of the binodal surface was performed by cloud-point techniques method. The initial homogeneous binary mixtures ethanol – ethyl acetate and acetic acid – ethyl acetate and ternary sub-system acetic acid – ethanol – ethyl

acetate were titrated with bidistilled water. The estimated accuracy of an experimental data was ± 0.002 mole fraction.

The compositions of coexistent phases were determined by gas chromatographic (GC) analysis (Cristal 5000, Chromatec, Russia). The study of CE was carried out also with the use of GC (for equilibrium composition determination). Firstly, binary, ternary and quaternary mixtures of known overall composition within the heterogeneous region were prepared in glass vessels (5 ml) by gravimetric method. After reaching phase equilibrium, samples were taken from both phases with 1µl chromatographic syringe (“Hamilton”, USA) and analyzed by GC. We used a gas chromatograph “Chromatec Crystal 5000.2” (Russia) with thermal conductivity detector (TCD) and packed column Porapak R (1m long and 0.003m i.d.). Helium with a flow rate of 60 ml/min was used as a carrier gas. The operating temperature of a column was 468 K, vaporizing injector was maintained at 503 K, and TCD temperature was 513 K. Method of internal standard and relative calibration were used to calculate compositions of equilibrium liquid phases. Ethanol was used as an internal standard and accepted as a linking component. New experimental data on the coexisting organic and aqueous phases were obtained for quaternary system and two ternary subsystems with limited miscibility (acetic acid – ethyl acetate – water and ethanol – ethyl acetate – water). In order to construct the binodal surface in the composition tetrahedron the solubility for quaternary system acetic acid – ethanol – ethyl acetate – water was studied for the initial solutions of constant ratios of concentrations of acetic acid and ethanol (3:1, 5:3, 1:1, 3:5 and 1:3) (Figure 1). Such choice of sections gave the opportunity to present the binodal surface in clear and convenient form.

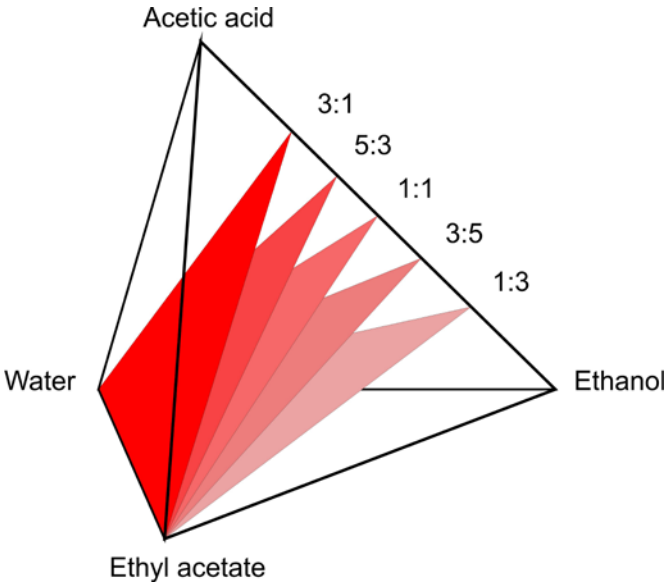

Figure 1. Planes of composition tetrahedron for the study of solubility and LLE.

The study of solubility was also carried out for compositions belonging to the chosen ratios, i. e. sections of composition tetrahedron. Projection of solubility curve for various ratios concentrations of acetic acid and ethanol (Figure 1) in composition

triangles are presented in Figure 2. Such view of located solubility curve provides guidance on quality obtained experimental data.

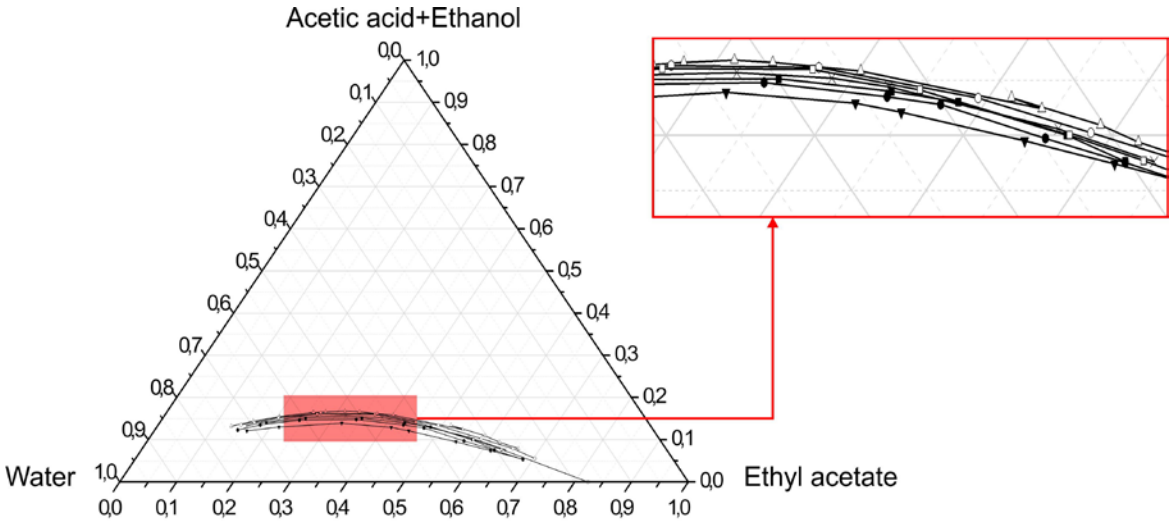

Figure 2. Projection of solubility curve in ternary systems: acetic acid – ethyl acetate – water (▼–▼) and ethanol – ethyl acetate – water (Δ–Δ); quaternary systems 1:3 (○–○); 3:5 (□–□); 1:1 (x–x); 5:3 (■–■); 3:1(●–●)

On the base of experimental data the surfaces of phase and chemical equilibrium at 303.15 K and 313.15 K were constructed in the composition tetrahedron. The diagrams of solubility in acetic acid – ethanol – ethyl acetate – water system at 313.15 K are presented in Figure 3 (the view for several sections of composition tetrahedron).

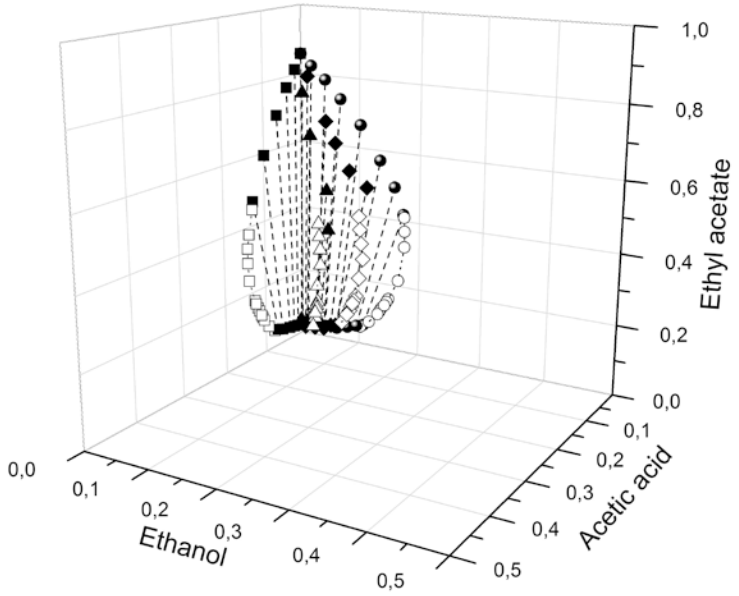

Figure 3. The view of binodal surface of acetic acid – ethanol – ethyl acetate – water system at 303.15 K. Tie-lines in ternary systems: acetic acid – ethyl acetate – water (■–■) and ethanol – ethyl acetate – water (●–●); ▲–▲ and ♦–♦ – selected tie-lines in quaternary system. Solubility curves in ternary systems: acetic acid – ethyl acetate – water (□) and ethanol – ethyl acetate – water (○). Points ◊ and Δ – selected solubility

data for quaternary solutions with constant ratios of concentrations of acetic acid and ethanol: 1:3 (◊) and 1:1 (Δ).

This view of solubility curves and experimental tie-lines qualitatively presents the disposition of binodal surface. Region of liquid-liquid envelope occupies a small area of composition tetrahedron: maximum overall concentration of acetic acid and ethanol on the binodal surface is ~ 0,2 mole fraction.

The run of critical curves of LLE was determined on the base of LLE data. The compositions of critical states were additionally confirmed by visual control during the studies of solubility by cloud-point technique: in the vicinities of critical points the critical opalescence was fixed. The set of critical points forms a critical curve in composition tetrahedron of quaternary system. The run of critical curves is presented in Figure 4 for 303.15 K and 313.15 K with our recent data at 293.15 K[2].

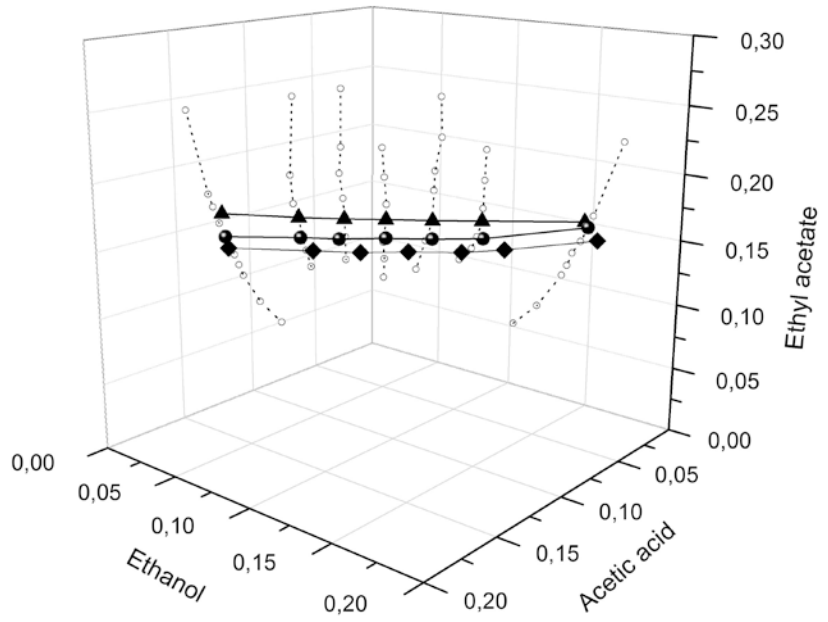

Figure 4. The critical curves of acetic acid – ethanol – ethyl acetate – water system at polythermal conditions: ♦ – 293.15 K[2], ● – 303.15 K, ▲ – 313.15 K.

The polythermal data sets gave also the opportunity to determine the disposition of the critical surface in composition space. The possibility of crossing CE and LLE surfaces (i.e. the establishing heterogeneous CE) is considered. The run of stoichiometric lines in composition tetrahedron relatively liquid-liquid envelope is considered.

The UNIFAC and NRTL models were used to calculate VLE and to correlate the experimental data for the quaternary system. The calculated values were compared with experimental data. Both models show a low deviation that indicates the possibility of simulation of LLE in acetic acid – ethanol – ethyl acetate – water system on this base.

In spite obtained data sets do not include conditions close to boiling temperatures at atmospheric pressure (that is important for ordinary distillation) there is the opportunity to calculate the phase properties for more higher temperatures. On the

other hand the data for temperature considered is more suitable for the design of extractive or reactive extraction processes.

3. Conclusions

The new detailed experimental data on solubility and LLE for quaternary system acetic acid – ethanol – ethyl acetate – water and two ternary systems ethanol – ethyl acetate – water and acetic acid – ethyl acetate – water at 303.15 and 313.15 K was obtained. The run of critical curves in composition tetrahedron was determined. The comparison of LLE data with the values calculated by UNIFAC and NRTL models indicates that experimental and calculated data are in sufficient agreement. The new data may be useful in the design of technological processes associated with reactive extraction and reactive distillation.

Acknowledgements

Authors are grateful to Russian Foundation for Basic Research (project 13-03-00985a) for the support of this study.

References

1. A.M. Toikka, M.A. Toikka, M.A. Trofimova, *Russ. Chem. Bull.* 61 (2012) 662-664.
2. M.A. Trofimova, A.M. Toikka, M.A. Toikka, *Fluid Phase Equilib.* 313 (2012) 46-51.

Hydrodynamics and mass transfer in viscous absorption media

Felix Ortloff[1], *Frank Graf*[1], *Thomas Kolb*[1]

[1]*DVGW Research Center, Engler-Bunte-Institute at KIT, Karlsruhe, Germany*

Abstract

Ionic liquids (IL) are proposed as absorption media for the upgrading of biogas, as they feature some advantages over common solvents. While conventional solvents are usually applied as aqueous mixtures, pure IL exhibit an increased viscosity in consequence of the strong ionic interactions peculiar for this class of substances. Hence, the material properties of ionic liquids typically range outside of the validity limits of common correlations for the prediction of mass transfer of gases in packed bed absorption columns, e. g. Billet & Schultes[1] or Mackowiak[2] etc.

Therefore, in a first step, pressure drop, liquid hold-up and mass transfer of CO_2 have been measured in a lab scale packed bed column of 0.1 m in diameter using classic Raschig-Rings as packing material. Furthermore, the results of the ongoing examinations with a larger diameter column (d = 0.25 m) and advanced packing material, e. g. Raschig-Super-Rings will be presented in comparison to the aforementioned small scale setup. On the basis of these results, it will be discussed, if and how common correlations for the prediction of mass transfer can be adapted for viscous absorption media.

Keywords

Hydrodynamics, mass transfer, packed bed, viscous absorption media, ionic liquids

1. Introduction

Ionic liquids can be used as physical sorbents, chemical sorbents (e. g. by amine-functionalization) or as mixtures of both. In any case, they feature a negligible vapor pressure and a hygroscopic character. When using certain ionic liquids as physical solvents, a high and selective solubility for carbon dioxide (CO_2) can be achieved.

Functionalized ionic liquids for chemisorption of CO_2 feature competitive absorption kinetics and gas loading, but an explicit reduction in heat of absorption and heat capacity in comparison to conventional solvents (e. g. MEA, DEA).

These properties can lead to energetic savings and process integration in comparison with state-of-the-art technologies in cases where CO_2 has to be removed from fuel gas streams, such as biogas upgrading, IGCC-CCS or from flue gas streams, in case of e. g. post combustion CCS.

For such kind of mass transfer tasks, structured and randomly packed columns are the most frequently used gas-liquid (G/L) contactors. Within this type of apparatuses, the liquid usually flows gravitationally from the top to the bottom of the column. In absorption processes, the gas phase commonly passes the liquid phase in a counter-current mode.

In order to improve mass transfer, the specific effective surface area a_e and Reynolds number (Re) for both, gas and liquid phase have to be maximized. On the other hand, pressure drop should be minimized in order to keep operational costs low.

For the dimensioning of gas-liquid contactors, numerous empirical or partly analytical design correlations for hydrodynamics (dry and wetted pressure drop, static and dynamic liquid hold-up and load ranges of gas and liquid phase) as well as for mass transfer (volumetric mass transfer coefficient $k_L \cdot a$) are available[3].

While some correlations for hydrodynamics have been checked with viscous media (η_L < 100 mPa·s), most of the design correlations for mass transfer are not applicable without further verification as viscosity of ionic liquids (η > 30 mPa·s) does not match the validity ranges.

Thus, a series of experiments has been performed, beginning with hydrodynamics (basically for validation of the experimental setup), then advancing to mass transfer measurements, to obtain information on the applicability of common design correlations.

2. Results and discussion

The experimental results (presented in this abstract) have been generated in a lab scale column of 0.1 m in diameter, filled with Raschig-Rings (metal, Ø: 6, 8 and 10 mm, resulting in specific surface areas of 900, 630 and 500 m^{-1}). The H/d-ratio of the packed bed was kept constant (≈ 5). For liquid distribution a perforated plate was used, the gas was premixed and added to the column via a pipe elbow (directed towards the bottom of the column). As absorption media, water (η=0.001 Pa·s, ρ=1000 kg/m³, σ=0.072 N/m), Gensorb® 1753 (η=0.0075 Pa·s, ρ=1030 kg/m³, σ=0.033 N/m) and the ionic liquid [EMIM][Tf], 1-ethyl-3-methylimidazolium triflate (η=0.05 Pa·s, ρ=1380 kg/m³, σ=0.042 N/m) were used (u_L < 40 m³/m²·h) at T = 293 K. The liquid hold-up h_L in the column was measured online via gravimetric sensors. During mass transfer measurements, CO_2 was absorbed from an oil-free compressed air carrier gas stream. The residual CO_2 content at the outlet of the column was determined with a NDIR photometer (Uras26 by ABB Ltd.).

2.1 Liquid hold-up $h_{L,dyn,0}$

The total liquid hold-up (V_L/V_P) of the column consists of a static part $h_{L,static}$ (wetted packing, but no actual liquid or gaseous feed), which usually is neglected in view of the dynamic part $h_{L,dynamic}$. The dynamic hold-up can be further subdivided into a part below the loading line of the column, where the counter-current gas velocity shows no effect on the liquid hold-up $h_{L,dyn,0} \neq f(u_G)$ and into a part above the loading line, where the liquid hold-up ($h_{L,dyn}$) and the pressure drop feature a strong growth with increase of gas velocity, until flooding of the column occurs.

In the small scale setup, as used in the first part of this work, steady operation above the loading line is critical, probably due to wall effects. The liquid hold-up h_L was experimentally determined up to the flooding point, but reproducibility was not satisfying. Hence, only liquid hold-up $h_{L,dyn,0}$ below the loading line is compared with the results of four widely used correlations, namely Mersmann & Bornhütter[4], Mackowiak[2,5], Billet & Schultes[1] and Engel[6], see Figure 1.

Obviously, liquid hold-up $h_{L,dyn,0}$ is slightly underestimated by three of the four examined correlations (a, b and c). It seems that only Engel (d) is able to give an adequate prediction for the liquid hold-up $h_{L,dyn,0}$ for the three examined material

systems. A general refusal of applicability for Mersmann & Bornhütter, Mackowiak and Billet & Schultes should not be derived from these experimental results, because in cases (a, b and c), the geometric surface area, at least for Raschig-Rings with a diameter of 6 and 8 mm is outside of the authors´ specific validity limits (see Table 1).

Indeed, weighting of viscosity´s influence on liquid hold-up does not differ heavily in the four compared cases (0.19 to 0.33), but rather it seems, that the deviations are a result of the underestimation of geometric surface area´s influence, which is assumed to be highest (0.91) in Engel´s case (for comparison see Table 1).

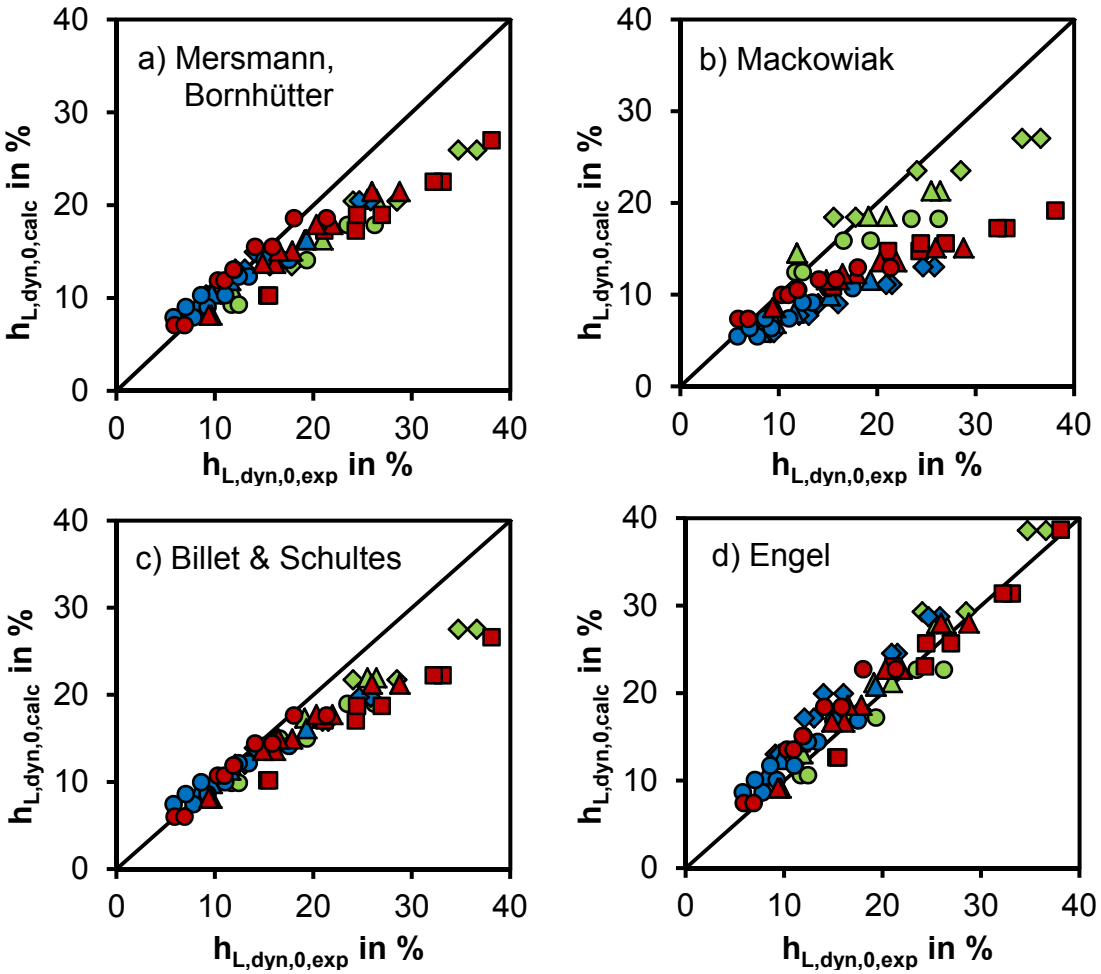

Figure 1: Parity plots for experimental and calculated values of $h_{L,dvn,0}$ for water (●), Genosorb® 1753 (●) and ionic liquid (●). Packing: Raschig-rings, d = 6 (■), 8 (▲) and 10 (●) mm

Nevertheless, Engel´s correlation gives a good prediction for the small scale setup and Engel is the only author accounting for the surface tension´s influence on hold-up. Therefore, Engel´s correlation was selected for further evaluation of pressure drop and mass transfer measurements in the present study.

Further on, the results for the liquid hold-up of the small scale setup will be compared with the experiments in the larger column (d = 0.25 m) in order to determine, whether the other authors´ correlations can deal with viscous absorption media when validity limits are obeyed.

Table 1: Overview over four widely used correlations for the prediction of liquid hold-up below the loading line: $h_{L,dyn,0}$, with weighting of material and operational parameters

Author and correlation for liquid hold-up $h_{L,dyn,0}$	u_L	σ_L	η_L	ρ_L	a	ε	C_1
a) Mersmann, Bornhütter[4] (1993), valid for a: < 250 m^{-1}							
$h_{L,dyn,0} = C_1 \cdot \left[\left(\frac{\upsilon_L}{g^2}\right)^{\frac{1}{3}} \cdot \frac{u_L \cdot a}{6 \cdot \varepsilon^2}\right]^{0.57}$	0.57	-	0.19	-0.19	0.57	-1.14	4.34
b) Mackowiak[2,5] (2011), Re_L < 2 (for IL), valid for η_L < 92 mPa·s, a < 215 m^{-1}							
$h_{L,dyn,0} = C_1 \cdot \left(\frac{3}{g}\right)^{\frac{1}{3}} \cdot a^{2/3} \cdot (u_L \cdot \upsilon_L)^{1/3}$	0.33	-	0.33	-0.33	0.66	-	0.75
c) Billet & Schultes[1] (1999), Re_L < 5 (for IL), valid for ν_L < 142 $mm^2 \cdot s^{-1}$, a < 545 m^{-1}							
$h_{L,dyn,0} = \left(C_1 \frac{1}{g}\frac{\eta_L}{\rho_L} u_L a^2\right)^{\frac{1}{3}} \cdot \left(C_h \left(\frac{u_L \rho_L}{a \eta_L}\right)^{0.15} \left(\frac{u_L^2 a}{g}\right)^{0,1}\right)^{\frac{2}{3}}$	0.56	-	0.23	-0.23	0.63	-	12
d) Engel[6] (1999), valid for η_L < 230 mPa·s, a < 1330 m^{-1}							
$h_{L,dyn,0} = C_1 \cdot \left(\frac{u_L \cdot a^{0.5}}{g^{\frac{1}{2}}}\right)^{0.66} \cdot \left(\frac{\eta_L \cdot a^{2/3}}{\rho_L \cdot g^{\frac{1}{2}}}\right)^{0.25} \cdot \left(\frac{\sigma_L \cdot a^2}{\rho_L \cdot g}\right)^{0.1}$	0.66	0.1	0.25	-0.35	0.91	-	3.6

2.2 Pressure drop Δp

Pressure drop calculations (in this case: Engel´s correlation[6] was used) for dry packed bed columns and turbulent gas flow are usually performed with correlations based on modifications of Ergun-equation, taking a packing specific drag coefficient ζ into account and modelling the actual packing as an aggregation of particles, tubes or rods with equivalent porosity ε and interfacial area a. For pressure drop calculations of a loaded packing, it is usually assumed that the porosity of the dry bed is reduced by the liquid hold-up ($\varepsilon_L = \varepsilon - h_L$), resulting in an increase of gas velocity, friction between the gas and liquid phase and thus also in pressure drop.

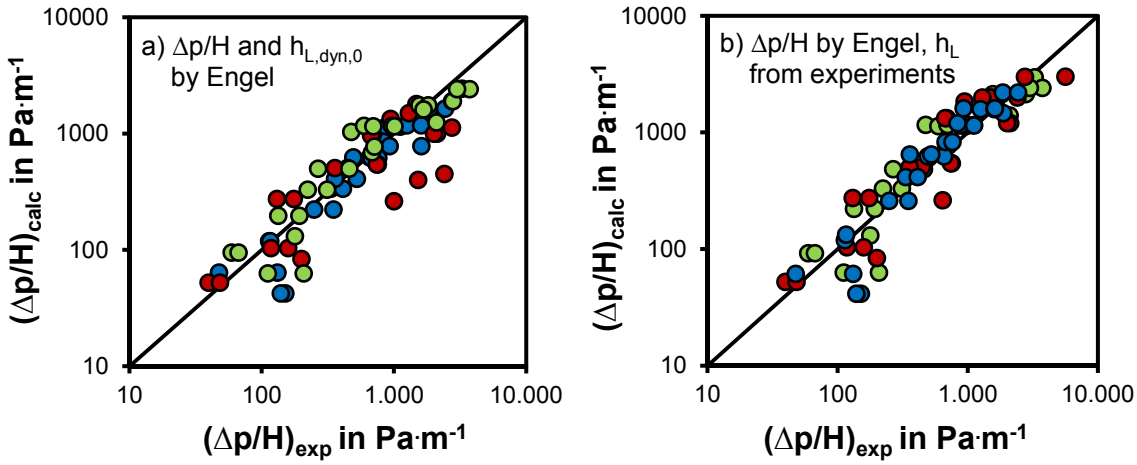

Figure 2: Parity plots for a) Δp/H with $h_{L,dyn,0}$ calculated with Engel´s correlation and b) Δp/H with experimental values for h_L for water (●), Genosorb® 1753 (●) and ionic liquid (●). Packing: Raschig-Rings, d = 10 mm

On the basis of an appropriate relation between Reynolds number (Re) and the packing specific drag coefficient ζ, the pressure drop of a dry packing can be described reliably. Besides, the liquid hold-up h_L turns out to have major influence on the pressure drop of a loaded packing. Figure 2 shows the specific pressure drop for calculated (with Engel´s correlation) and experimental values of $h_{L,dyn,0}$. Obviously, a suitable relation between material properties, operational parameters and the liquid hold-up $h_{L,dyn,0}$ (e. g. Engel) results in adequate values for Δp/H.

2.3 Volumetric liquid side mass transfer coefficient $k_L{\cdot}a_e$

Models for the prediction of volumetric mass transfer coefficient $k_L{\cdot}a_e$ are based on empirical or semi-empirical approaches. Usually one of the two fundamental theories on mass transfer is incorporated - Lewis & Whitman´s film model, resulting in a linear correlation between k_L and diffusion coefficient $D_{i,L}$ or (in recent models) Higbie´s more often applied non-steady penetration theory (see equation 1), giving k_L a dependency upon diffusion coefficient with a power of 0.5.

$$k_L \sim \sqrt{\frac{D_{i,L}}{\tau}} = \bar{u}_L \cdot \sqrt{\frac{D_{i,L}}{l_c}} \qquad (1)$$

The dimensionless contact time τ originally (in sense of Higbie´s model) accounts for the time in which a fluid element arises from the bulk liquid phase and enters a direct exchange with the gas phase. This time period can be correlated with a characteristic contact length l_c, for which (on an empirical basis) some characteristic diameter of the packing element is applied. Within equation (1), the effective liquid velocity $\bar{u}_L$ is calculated from the superficial liquid velocity u_L divided by the liquid hold-up h_L of the column. Hence, the liquid hold-up also has an impact on mass transfer prediction.

$$\bar{u}_L = \frac{u_L}{h_L} \qquad (2)$$

Besides the liquid side mass transfer coefficient, the effective interfacial area a_e is often correlated, incorporating at least one of Reynolds Weber or Froude number in an author specific empirical weight.

In order to determine whether one of the aforementioned authors´ liquid side volumetric mass transfer correlations is able to predict mass transfer of CO_2 in viscous absorption media in the present experimental setup, the experimental results of this work and literature data are compared with the appropriate calculated values of Mackowiak´s and Billet and Schulte´s correlation (see Figure 3).

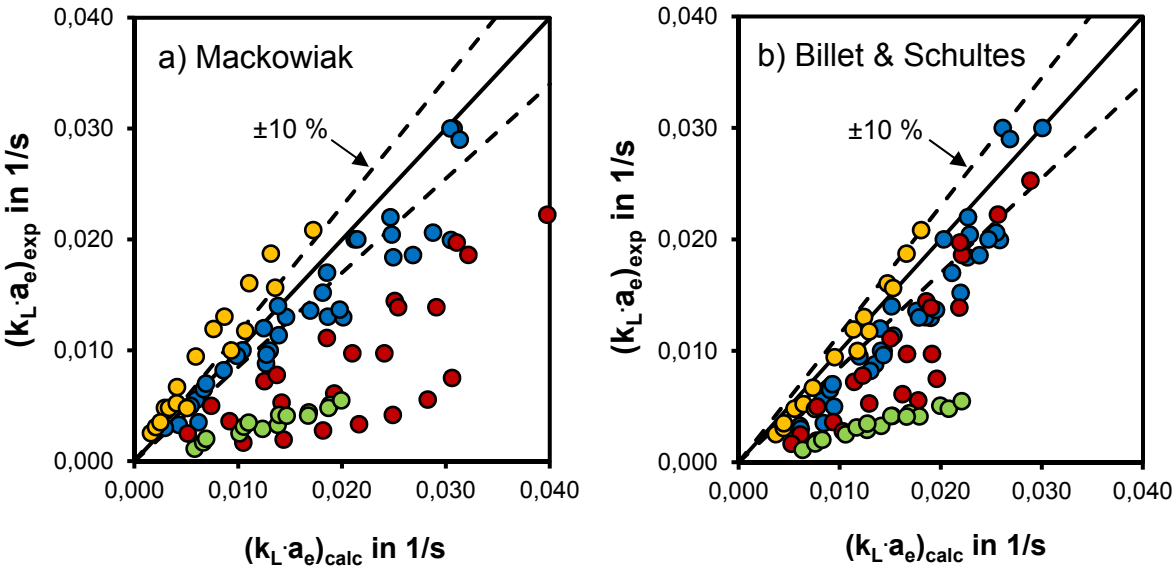

Figure 3: Parity plots for ($k_L{\cdot}a_e$) for correlations of a) Mackowiak[2,5] and b) Billet and Schultes[1] for liquid phase: methanol[7] (●), water[2,8] (●), water+glycerin[9] (●) and [EMIM][Tf] (●); Packing material: Raschig-Rings, d = 10-50 mm; Pall-Rings, d = 25 mm; HiFlow-Rings, d = 20 mm

As shown in Figure 3, the experimental data for low viscous absorption media, such as methanol (data from: Yoshida et al.[7]) with Raschig-Rings, d = 15 (m = metal), 25 mm (m) and water (this work and Onda[8] et al.) with Raschig-Rings, d = 10 (m), 15

(c = ceramic), 50 mm (c), Pall-Rings, d = 25 mm (m) and HiFlow-Rings, d = 20 mm (c) can be predicted with an acceptable level of accuracy by Mackowiak´s and Billet & Schulte´s correlations. Onda´s data for water is reproduced fairly well with the present experimental setup. Additionally, data from Mangers[9] with a water+glycerin-system (Raschig-Rings (glas), d = 10 mm) was added. Already with Mangers data, a clear trend towards overestimation of mass transfer in viscous absorption media becomes visible, which is confirmed by this work´s data on mass transfer of CO_2 with the ionic liquid [EMIM][Tf] using Raschig-Rings (m), d = 10 mm. Table 2 shows the weighting of the incorporated material properties for the two aforementioned design correlations. Both predict a positive influence of liquid viscosity on mass transfer (Mackowiak (Re < 2): $k_L a_e \sim \eta_L^{0.17}$, Billet & Schultes (Re < 5): $k_L a_e \sim \eta_L^{0.09}$). However, measurements show a reduction of $k_L a_e$ with an increase of η_L. This shows that additional efforts need to be undertaken to clarify the influence of liquid viscosity η_L on mass transfer in packed bed absorption columns.

Table 2: Two widely used correlations for the prediction of liquid side mass transfer $k_L a_e$ and weighting of material and operational parameters

Author and Korrelation for $k_L \cdot a$	**u_L**	**D_L**	**η_L**	**ρ_L**	**σ_L**	a	**ε**
a) Mackowiak[2,5] (2011), Re_L < 2 (validity limits Re < 2: n. a.; Re > 2: Sc_L = 5.100 – 10.000)							
$k_L \cdot a_e = \frac{3.842 \cdot D_L^{0.5}}{(1-\varphi_P)^{\frac{1}{3}} d_h^{\frac{1}{2}} \left(\frac{3}{g}\right)^{\frac{1}{6}} a^{\frac{1}{3}} \nu^{\frac{1}{6}}} u_L^{\frac{1}{3}} \cdot 6.49\, a^{\frac{2}{3}} \frac{\Delta\rho^{0.5} g^{1/6} \nu^{\frac{1}{3}}}{\sigma_L^{0.5}} u_L^{\frac{1}{3}}$	0.67	0.5	0.17	0.67	-0.5	0.58	-0.25
b) Billet & Schultes[1] (1999), Re_L < 5 (for IL) (valid for ν < 1.66 $mm^2 \cdot s^{-1}$)							
$k_L \cdot a_e = C_L 12^{\frac{1}{6}} \bar{u}_L^{0.5} \left(\frac{D_L}{d_h}\right)^{0.5} \cdot 1.5(a d_h)^{-0.5} \left(\frac{u_L d_h}{\nu_L}\right)^{-0.2} \left(\frac{u_L^2 \rho_L d_h}{\sigma_L}\right)^{0.75} \left(\frac{u_L^2}{g d_h}\right)^{-0.45}$	0.62	0.5	0.09	0.67	-0.75	0.18	0

3. Conclusions and outlook

The validity ranges of the examined correlations allow the prediction of liquid hold-up $h_{L,dyn,0}$ for viscous absorption media. Engel´s correlation is even able to predict the liquid hold-up $h_{L,dyn,0}$ of all three examined material systems in the present small scale experimental setup (for a > 500 m^{-1}). Pressure drop is also predictable when liquid hold-up $h_{L,dyn,0}$ is described correctly. On the basis of the results on hydrodynamics, this work´s experimental setup has been validated successfully.

In contrast to hydrodynamics, correlations for volumetric mass transfer coefficient $k_L \cdot a_e$ do not produce reliable results, as mass transfer is systematically overestimated for viscous absorption media. To provide a more substantial experimental database, mass transfer measurements in viscous absorption media are currently performed in a larger scale column (d = 0.25 m). On basis of both, the small and large scale experiments, existing design correlations are to be adapted for the prediction of mass transfer of CO_2 in viscous absorption media with η_L > 30 mPa·s.

References

[1] Billet, R.; Schultes, M.: Trans IChemE 77 (1999), 498-504
[2] Mackowiak, J.: Chem. Eng. Research and Design 89 (2011), 1308-1320
[3] Wang, G. Q. et al.: Ind. Eng. Chem. Res. 44 (2005), 8715-8729
[4] Bornhütter, K.; Mersmann, A.: Chem. Eng. Technol. 16 (1993), 46-57
[5] Mackowiak, J.: ISBN: 3-540-00493-9, Springer, Berlin, 2003.
[6] Engel, V. et al.: Chem. Eng. Technol. 24 (2001) 5, 459-462
[7] Yoshida, F.; Koyanagi, T.: Ind. and Eng. Chem. 50 (1958), 365-374
[8] Onda, K. et al.: J. Chem. Eng. 1 (1968), 56-62
[9] Mangers, R.J.; Ponter, A.B.:Ind. Eng. Chem. Proc. Des. 19 (1980), 530-537

Control Benchmark for Solvent Recovery by Distillation

Peter Lützen[1], Miguel Mauricio-Iglesias[1], Jakob Kjøbsted Huusom[1], Jens Abildskov[1]
[1]Dept. of Chemical and Biochemical Engineering, Technical University of Denmark, Kgs. Lyngby, Denmark

Abstract
Over the years many different strategies for controlling distillation columns have been developed, but only few comparisons between the strategies have been made and described in the literature. The goal of this paper is to compare three different control strategies, on a system consisting of a single heat integrated distillation column. The three methods investigated are: decentralized PID, self-optimizing control and MPC. The strategies are compared using the integral of absolute error, total variation, integral of profit and difficulty of implementation. The control strategies are evaluated by introducing a series of large disturbances on the feed: temperature, concentration of key component and total flow. We find that self-optimizing control gives a suitable control, and easy implementation, compared to the more advanced model predictive control.

Keywords
Distillation control, Model predictive control, MPC, Self-optimizing control, Null-space method, PI-control, Benchmark

1. Introduction

The need for tight control of a process has always been of great importance, especially within the field of distillation control, where great savings in energy and operational cost often can be obtained by using a suitable control strategy. However the transfer of research results in control design to the process industry is sometimes hindered by the complexity of the new developments. The purpose of this contribution is to compare the practical consequences of three different control strategies on a real case-study, considering the ability of the resulting controllers to achieve the operational goals, as well as the complexity associated with this implementation. The investigated strategies have been chosen to cover a broad range of control strategies and levels in the control hierarchy. The chosen controllers are:

- A classical decentralised two-input, two-output (TITO) PI control, aimed at the regulation of the system
- A TITO self-optimising control [1] with regulatory and economic evaluation
- Offset free model predictive allowing centralized regulation of the process [2]

2. Description of the process and methods

The pairing of the controller in the PID strategy is performed by using the Relative Gain Array (RGA) method [3]. The tuning of the PID strategy is obtained using the Internal Model Control (IMC) method by Garcia et al. [4] and Rivera et al. [5]. The self-optimizing controller (SOC) is designed following the null space [6]. For tuning and implementing the SOC strategy the same IMC method is used as with the PID control strategy. The implementation of the MPC is based on an algorithm given by

Huusom et al. [7], and the offset free MPC equations used are given by Rawlings and Mayne [2]. The tuning is done by trial and error since no tuning scheme seems to have been established to implement the offset free MPC method used [8].

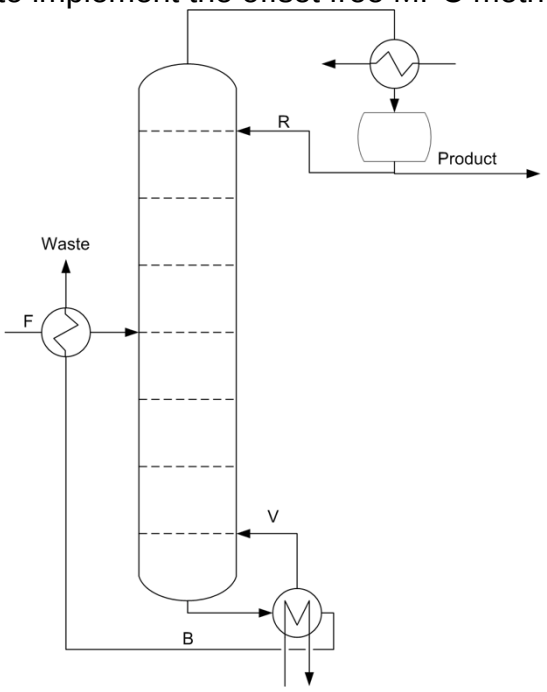

Figure 1: Process unit recovering ethanol from a process waste stream consisting of ethanol, water and acetaldehyde.

These three control strategies are tested on a distillation model of an actual industrial process unit consisting of a distillation column, recovering solvent grade ethanol from an industrial waste stream containing water, ethanol (EtOH) and trace amounts of acetaldehyde (AA). The product from the investigated column is then passed on to a second column where the acetaldehyde is removed. The column is in operation continuously but the feed undergoes large step changes since the production upstream is batch based. The model is developed in MATLAB and a graphical description of the system is shown in Figure 1. The mathematical model used for simulating the column is a modified version of the column A of Skogestad [9], where several assumptions are made in order to decrease computation time, while retaining sufficiently accurate simulation results. Among the assumptions are:

- Energy balance, calculating the energy needed to heat and evaporate the vapour throughout the column
- The VLE is characterised by the modified Raoult's equation using UNIFAC to determine the activity coefficients
- Linear hydrodynamics [9]
- A constant vapour flow in the rectifying and stripping section of the column
- Liquid level in the reboiler and condenser is perfect level controlled
- Each stage is at bubble point throughout the column

The parameters used in the simulation of the column are displayed in Table 1, together with the target concentration of the product stream. The column has two measured variables: the concentration in the top, calculated via density measurement, and the temperature at the bottom. When the self-optimizing control strategy is implemented it is assumed that a temperature at any stage could be

measured. The manipulated variables are the energy to the reboiler and the reflux flow.

Feed stage	Stages	Feed temp.	Feed concentration	Target product concentration
12	23	28°C	AA: 0.5 mol% EtOH: 14 mol% Water: 85.5 mol%	AA: 2 mol% EtOH: 68 mol% Water: 30 mol%

Table 1: Parameters and set points used in the simulation of the system

The three different control strategies are compared, and evaluated by imposing a series of disturbances on the system. These disturbances are given in Table 2. Common to all disturbances is the large magnitude, which is imposed in order to test limits of the control strategies at extreme conditions, but also simulate the upstream batch production.

Disturbance stream	Magnitude	Type	Scenario
Concentration of key component in feed (z_F)	±15%	Step	Disturbance in the feed composition of the key component, because of instability upstream
Temperature of feed (T_c)	±7°C	Step	Disturbance in the feed temperature, because of different batch temperatures or instabilities from unit operations upstream
Total flow of feed (F)	±20% over 400 min.	Ramp	Disturbance in the feed stream, because of drifting in upstream equipment

Table 1: List of disturbances introduced to the system

The evaluation is made at 2 levels; the local level which is evaluated by means of the integral of absolute error (IAE) and total variation from set-point (TV) and at the global level, where the integral of the profit function over the evaluated period is utilized. The equations used for IAE, TV and the profit function are given below:

$$IAE = \int_0^T |e|\,dt \approx \sum_n^\infty (|e(t)| \cdot \Delta t) \qquad TV = \sum_n^\infty |u_{n+1} - u_n|$$

$$Cost = \int_0^T |p(t)|\,dt \approx \sum_n^\infty (|p(t)| \cdot \Delta t) \quad p(t) = p_D D(t) + p_B B(t) - p_F F(t) - p_V V(t)$$

The final comparison between the three strategies is performed by comparing the empirical result obtained by the equation above, with an assessment of the complexity and difficulties in implementing the different strategies.

3. Results and discussion

With the model implemented and tested the tuning and evaluation of the 3 methods is conducted.

3.1 Response to disturbances

The disturbances conducted on the system are given in Table 2, and three graphical examples for the control systems behavior on a disturbance are shown in Figure 2-4. The result of the 3 evaluation methods applied on the different disturbances is given in Table 3-4.

As seen in Figure 2-4, all control strategies are able to stabilise the system, and bring the measured variables back or close to the desired set point, but the SOC need more aggressive use of the manipulated variables, compared to the other strategies. This may be an indication of a too aggressive controller but both the PID and SOC

has been tuned to the same time delay/close loop time constant, in order to make a fair comparison.

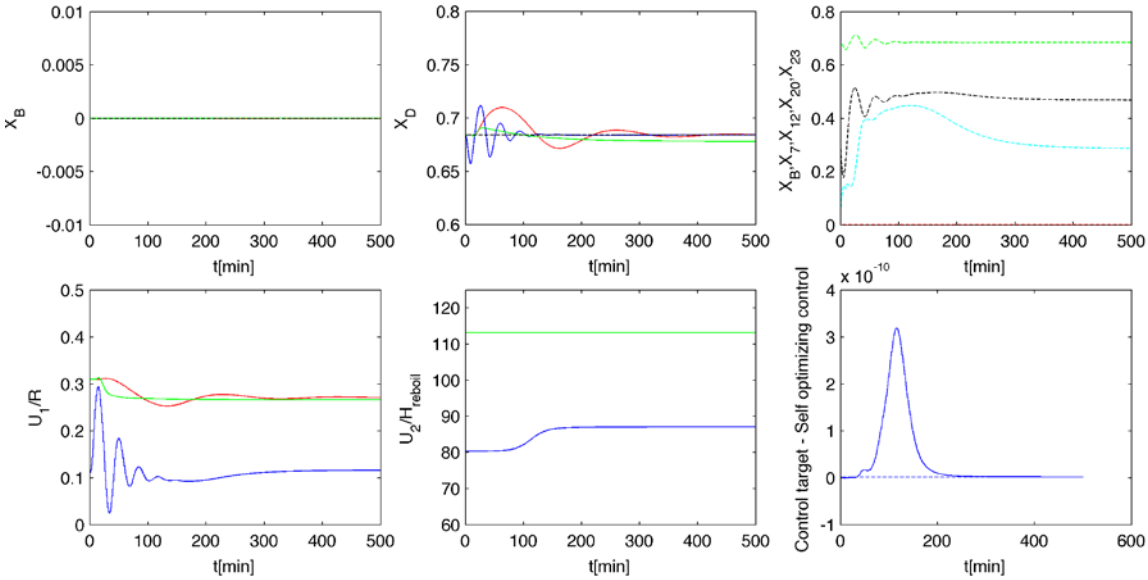

Figure 2: Disturbance of +15% in the amount of ethanol in the feed, (•), PID controller, (•) Self-optimized control, (•) Model Predictive Control, (−−) X_B, (−−) X_7, (−−) X_{12}, (−−) X_{20}, (−−) X_{23}

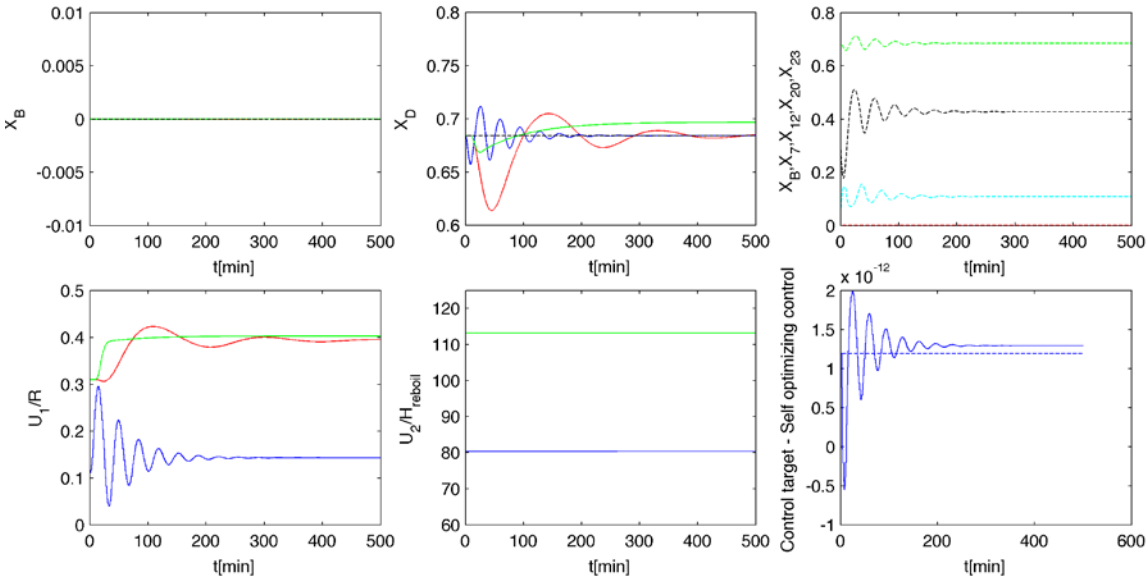

Figure 3: Disturbance of +7°C in the temperature feed, (•), PID controller, (•) Self-optimized control, (•) Model Predictive Control, (−−) X_B, (−−) X_7, (−−) X_{12}, (−−) X_{20}, (−−) X_{23}

3.2 Evaluations of the disturbances

The evaluation is performed at two levels: First the single controller is evaluated and later the entire system. Comparing the result of the IAE given in Table 3 for the two measured points it is clear that all the controllers are able to keep the concentration at the bottom of the column constant. However, from comparing the IAEs at the top it is clear that the self-optimizing controller shows the largest IAE. However, this is to be expected since the controller finds the optimal set point based on a profit function, calculating the maximum profit, rather than a minimization function, where the offset from the set-point is minimized.

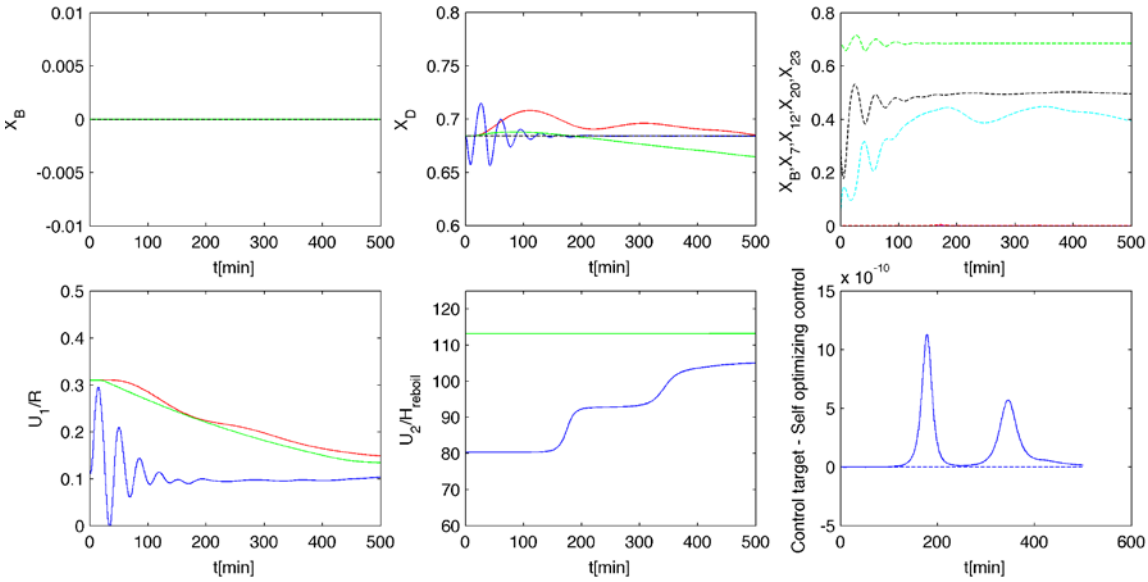

Figure 4: Disturbance of +20% ramp over 400 min in the magnitude of the feed, (•), PID controller, (•) Self-optimized control, (•) Model Predictive Control, (−−) X_B, (−−) X_7, (−−) X_{12}, (−−) X_{20}, (−−) X_{23}

The second parameter on which the strategies are compared is the total variation of the manipulated variables. All three control strategies have a very low TV when manipulating the reflux of the column. Looking at the TV of the energy given to the reboiler the self-optimizing control obtains much higher values, showing that this strategy has a large need to change the energy in order to obtain a stable and optimal control.

	X_B - Integral of Absolute Error [mole frac.]			**X_D - Integral of Absolute Error [mole frac.]**		
	PI	**SOC**	**MPC**	**PI**	**SOC**	**MPC**
z_F +15%	9.52×10^{-11}	4.22×10^{-8}	9.57×10^{-11}	2.91	1.07	2.19
z_F -15%	5.84×10^{-11}	7.90×10^{-10}	5.82×10^{-11}	4.35	3.01	2.25
t_F +7°C	5.59×10^{-11}	6.72×10^{-10}	5.57×10^{-11}	5.83	1.40	4.75
t_F -7°C	1.02×10^{-10}	6.04×10^{-8}	1.03×10^{-10}	6.66	1.81	3.89
F +20%	2.81×10^{-10}	2.24×10^{-7}	2.89×10^{-10}	4.97	1.38	3.56
F -20%	3.34×10^{-11}	4.38×10^{-10}	3.30×10^{-11}	11.92	1.53	5.45

	U_1/Reflux – Total Variation [kmol]			**U_2/Reboiler – Total Variation [kmol]**		
	PI	**SOC**	**MPC**	**PI**	**SOC**	**MPC**
z_F +15%	0.10	0.83	0.05	3.68×10^{-6}	6,69	0.01
z_F -15%	0.15	2.34	0.05	2.26×10^{-6}	0,05	0.01
t_F +7C	0.20	1.09	0.09	2.16×10^{-6}	0,03	0.03
t_F -7C	0.23	1.42	0.08	3.94×10^{-6}	7,86	0.02
F +20%	0.16	1.07	0.18	1.09×10^{-5}	24,79	0.02
F -20%	0.39	1.18	0.41	1.29×10^{-6}	0,05	0.04

Table 3: Integral of absolute error and total variation over 400 minutes

	PI [currency]	SOC [currency]	MPC [currency]
z_F +15%	4406.9	5636.16	4510.5
z_F -15%	1912.9	3403.22	1830.1
t_F +7°C	3268.5	4715.37	3061.9
t_F -7°C	3087.3	4290.49	3246.4
F +20%	3905.7	4974.00	4199.8
F -20%	2484.3	3769.09	2022.9

Table 4: Integral of profit function over 400 minutes

The last level is the overall comparison, where the integral of the profit is compared. As shown in Table 4 the self-optimizing controller is the control strategy that obtains the largest profit when a disturbance is imposed on the system. This is mainly due to the fact that the profit function is used when calculating the optimal set-point and measurement combination, and the control is able to operate at much lower boilup that the other control strategies. When comparing the implementation of the three control strategies, the PI strategy is by far the easiest to implement, and it would be possible to implement and tune it with very limited knowledge of the system. The self-optimizing control strategy is also quite easy to use, especially when it is possible to obtain a linearized model of the system, but the null space method used, also makes it possible to find the optimal gain matrix, by introducing a series of disturbances to the system [6]. The MPC implementation used here requires a known linear model of the system and together with the usage of online optimization. This makes it by far the most advanced and implementation heavy control strategy to implement. In addition the lack of tuning methods for the offset MPC [8] makes the implementation even more laborious and increases the uncertainties of correct tuning.

4. Conclusions

From the data presented it is clear that the PID is the easiest to implement, but not the most accurate controller, neither in offset nor cost. The SOC is the best controller for minimizing the cost of a disturbance, but also the most aggressive controller. The MPC shows really good and accurate control, but is very heavy to implement and requires online optimization. The simplicity of implementing the self-optimizing control theory, the lack of online calculations, and the usage of a profit function make this the best-suited control strategy for the distillation column investigated.

References

[1] S. Skogestad, “Plantwide control: the search for the self-optimizing control structure,” Journal of Process Control, vol. 10, pp. 487–507, 2000.

[2] J. B. Rawlings and D. Q. Mayne, Model Predictive Control: Theory and Design. Nob Hill Pub, 2009.

[3] E. H. Bristol, “On a new measure of interaction for multivariable process control,” IEEE Transactions on Automatic Control, vol. 11, pp. 133–134, 1965.

[4] C. E. Garcia and M. Morari, “Internal model control. 1. a unifying review and some new results,” Ind. Eng. Chem. Process Des. Dev., vol. 21, pp. 308–323, 1982.

[5] D. E. Rivera, M. Morari, and S. Skogestad, “Internal model control. 4. pid controller design,” Ind. Eng. Chem. Process Des., vol. 25, p. 252-265, 1986.

[6] V. Alstand and S. Skogestad, “Null space method for selecting optimal measurement combinations as control variables,” Ind. Eng. Chem. Res., vol. 46, pp. 846–853, 2007.

[8] J. K. Huusom, N. K. Poulsen, S. B. Joergensen, and J. B. Joergensen, “Tuning of methods for offset free mpc based on arx model representations,” in American Control Conference, 2010.

[8] J. K. Huusom, N. K. Poulsen, S. B. Joergensen, and J. B. Joergensen, “Tuning siso offset-free model predictive control based on arx models,” J. Process Contr., vol. 22, pp. 1997–2007, 2012.

[9] S. Skogestad, “Dynamics and control of distillation columns: A tutorial introduction,” Trans IChemE, vol. 75, pp. 539–562, 1997.

Operating lines of cyclic distillation

Volodymyr Maleta[1], Oleksandr Shevchenko[2], Olesja Bedruk[3]
[1]Volodymyr Maleta, Tallinn, Estonia;e-mail:info@maletacd.com
[2]Oleksandr Shevchenko, Kiev, Ukraine;
[3]Olesja Bedruk, Kiev, Ukraine.

Abstract
The most effective separation in distillation columns takes place in the hydrodynamic regime where is perfect displacement of the liquid and vapor streams. It can be reached when the distillation column is operated in cyclic mode: lack of outflow of liquids to the trays vapor admission; lack of mixing of liquids in adjacent trays upon outflow of liquid. Industrial implementation of the cyclic mode was made possible by the development of special mass transfer contact devices (US 8,158,073 B2 and 8,333,940 B2), which actually provide optimal process conditions. Today, cyclic distillation columns are implemented in stripping column, rectification column and DWC-column with diameter from 400 to 1700 mm. The first column already worked for 7 years and fully confirmed the benefits of cyclic mode based on a (theoretical stage model with perfect displacement and operation line. This article is devoted to this model and to the theory of the process operation lines in cyclic distillation. Created mathematical model of the cyclic distillation was confirmed by industrial operation. Using the operation lines for describing the cyclic distillation enables us to determine the potential and perform column design operated in a cyclic mode.

Keywords
Cyclic distillation,operating lines,theoretical stage model with perfect displacement, trays efficiency, process intensification

1. Introduction

Improving efficiency of the process of mass transfer in distillation columns got much attention during the last decades, with the aim of lower capital expenditure, reduced energy requirements and significant savings of operating costs. One of these methods of mass transfer process intensification is cyclic distillation [1,2,3,5]. The required process conditions to achieve this are as follows: lack of outflow of liquids to the trays vapor admission; lack of mixing of liquids in adjacent trays upon outflow of liquid [6,7]. Pursuant to Lewis' work [8], the greatest effect is achieved upon perfect displacement by liquid and vapor and sing-direction movement of liquid on adjacent contact degrees. In such conditions the efficiency of Murphy's tray may significantly exceed the local efficiency.

The theoretical results about a high efficiency of the cyclic mode have been confirmed under conditions of industry implementation hydro-selection column with diameter 400 mm in production ethanol food grade [2].To determine theoretical limits and prospects of using cyclic distillation technology as process of intensification solution for distillation, reactive distillation, stripping and absorption we propose

usageof theoretical stage model with perfect displacement (cyclic theoretical stages). In this article, we demonstrate the method of construction operation line of cyclic distillation according theoretical stage model with perfect displacement.

2. Results and discussion

Upon description of distribution the concentration of volatile component (VC) on the contact stage operating in the mode of cyclic distillation, there is used an equalizing of material balance in differential mode (Figure 1b). The change of VC amount in Hdx_n liquid is equal to change of VC amount in $Gd\tau\ (y_n - y_{n-1})$ vapor, or

$$\frac{dx_n}{d\tau} = -\frac{G}{H}(y_n - y_{n-1}) \qquad (1)$$

where H- is the amount of liquid on the tray, mol; G – is vapor consumption, mol/s; y_n – VC concentration in vapor at the output from tray, %;y_{n-1}– is VC concentration in vapor at input to the tray, %;x_n– is VC concentration in liquid on the tray, %; τ – is the vapor supply time, s; and n – is the tray number.

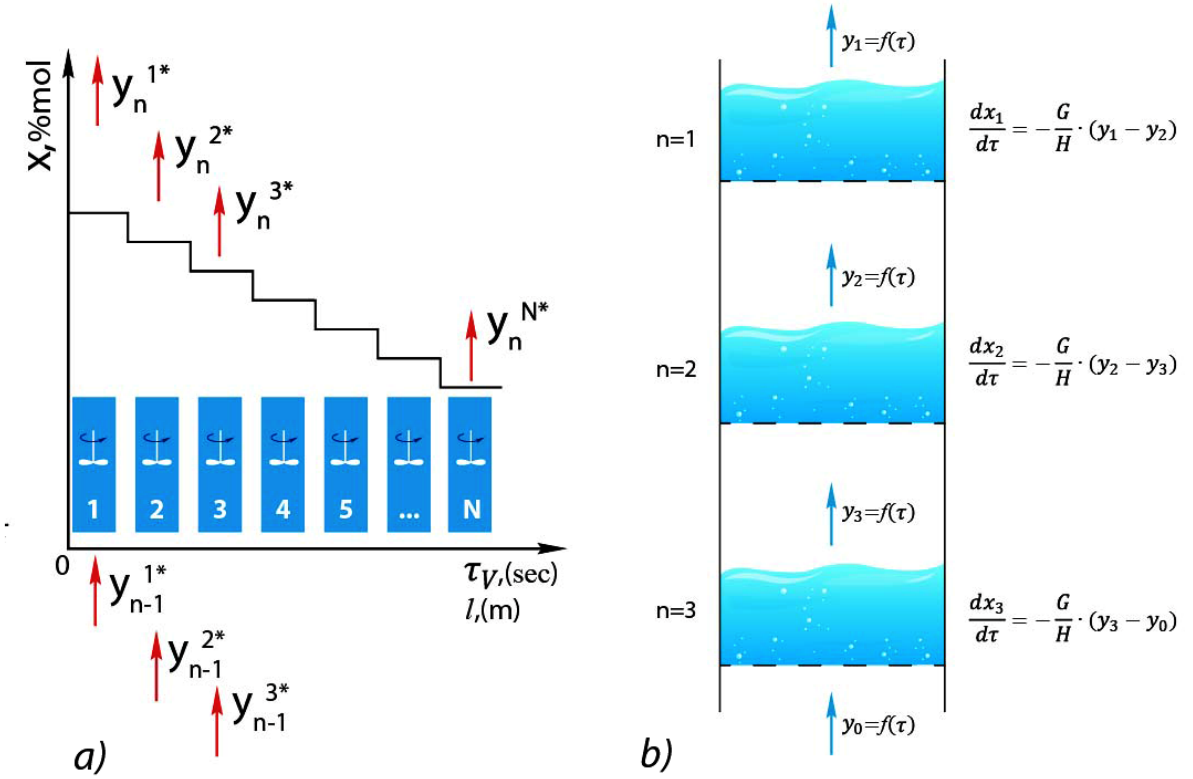

Figure 1: Overview of cyclic distillation processes. a) hydrodynamic model ofperfect displacement in liquid and vapor; b) operation model of cyclic distillation.

The perfect hydrodynamic mode of liquid overflow from one tray to another is described with the following balance$x_n(0) = x_{n+1}(\tau_v)$,where τ_v– is the vapor supply time, s.Let's consider the cyclic distillation from the single point of view, namely the time of mass transfer on the tray. The mass transfer time coincides with vapor supply time τ_v (Figure 1a,b).

$$\frac{Dx_n}{D\tau} = -\frac{G}{L\bar{\tau}}(y_n - y_{n-1}), \qquad (2)$$

where $\bar{\tau} = \frac{l_T}{v_l}$ - is the time of stay of the liquid on the tray, s.

Therefore, the cyclic and stationary processes are described with similar material balance equations (1) and (2), according to the nature of vapor and liquid interaction $y_n(x_n) \rightarrow x_{n+1}$ we determine that the cyclic process is similar to the stationary one upon single-direction movement of liquid on adjacent contact phases and perfect displacement by liquid and vapor [4].

2.1. The method of construction operating lines of cyclic distillation

The suggested system of equations is solved analytically. Generally, the concentration profiles on each stage are recorded as follows:

$$x_n(\tau) = e^{-\frac{Gm}{H}\tau} \sum_{i=1}^{n} C_i \frac{(\frac{Gm}{H}\tau)^{n-1}}{(n-i)!}, \qquad i = \overline{1,n} \qquad (3)$$

Meanwhile the source conditions are as follows:

$$x_i(0) = C_i$$

We use this technique for obtaining of the cyclic process operating line [2]. Upon known interim concentration profiles in liquid and vapor for a random point of time $\tau_i \in [0, \tau_v]$. By changing the time points $\tau_i \in [0, \tau_v]$, we graphically find any number of points referred to the operating line (Figure. 2).

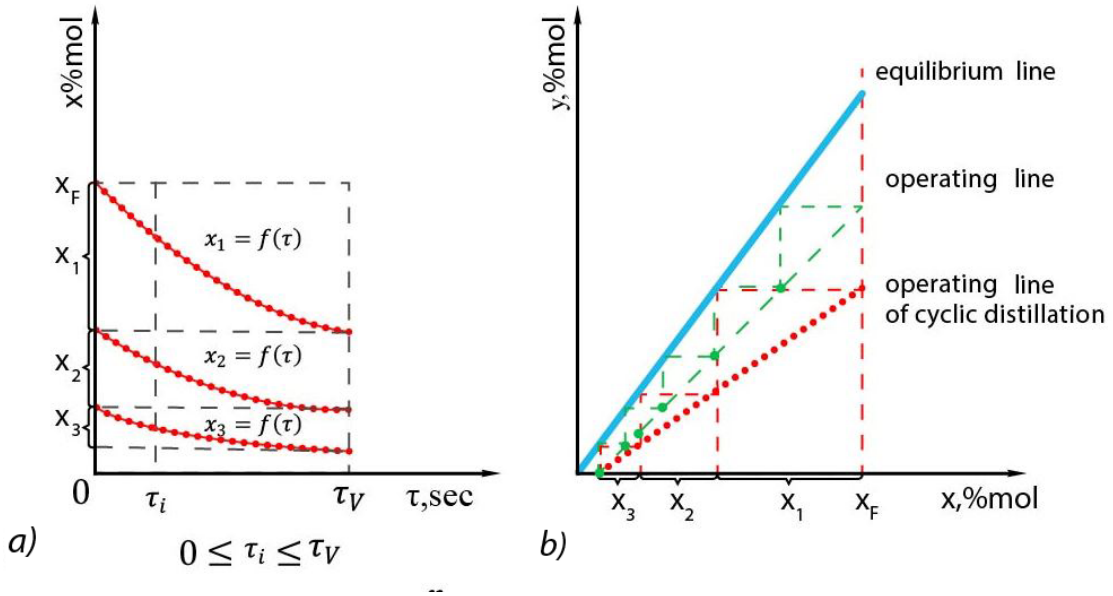

Figure 2: The methodology of construction of the perfect displacement mode operating line is as follows: a) Temporary concentration profiles in liquid; b) depicting of the perfect displacement operating line in У – Х coordinates;1 – equilibrium line; 2 – perfect mixing operating line; 3 – perfect displacement operating line.

2.2. Influence of model parameters on mass transfer efficiency

The modeling results are presented on Figure 3. As can be seen on the picture, the perfect displacement operating line (line 5, $\mathrm{F}=1,\mathrm{E}_0=1$) is not straight but concave which is a mirror reflection of the equilibrium line concave. The line is continuous. The liquid flow dynamics, expressed through the value of the multiplication factor of liquid delay transfer F influences on the mass transfer process as follows. At$\mathrm{F}<1$ (line 6, Figure 3).When $\mathrm{F}\to 0$, the average time of liquid stay on the tray$\bar{\tau}\to\infty$, the mixture separation efficiency reduces and operating parts are converged into a point. In this case the process operating line coincides with operating line of perfect mixing with inclination tangent L/G(line 3, Figure 3). For linear equilibrium dependency$y^*=\mathrm{mx}$ and, for example, four trays, the above position is proven analytically if the VC concentration on the tray is not changed. According to the suggested calculation technique, this condition is met when the amount of liquid on the contact stage$\mathrm{H}\to\infty$, $\mathrm{F}\to 0$, and $\bar{\tau}\to\infty$. By means of serial transformations it is clear that when $\mathrm{F}\to 0$, this line inclination tangent is equal to L/G, at any values of τ_i, in the distance of $\tau_i\in[0,\tau_v]$, i.e.

$$\lim_{\mathrm{F}\to 0}\mathrm{A}=\lim_{\mathrm{F}\to 0}\frac{\mathrm{mF}}{\mathrm{a}\tau_v}=\frac{\mathrm{mFL}}{\mathrm{mGF}}=\frac{\mathrm{L}}{\mathrm{G}},\tau_i\in[0,\tau_v] \qquad (4)$$

where A – slope angle $(\tan\alpha)$ofcyclic distillation operation line.

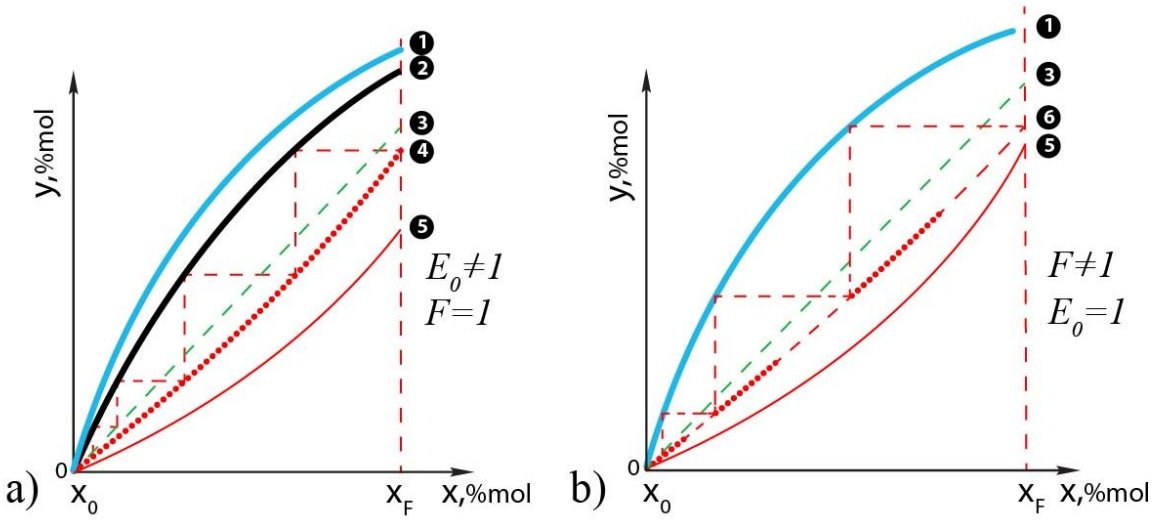

Figure 3: Influence of model parameters on the position and shape of operating line of cyclic distillation: a)1-equilibrium line; 2- kinetic line; 3 – operating line (L/G); 4 - operating line of cyclic distillation $(\mathrm{F}=1;\mathrm{E}_0\neq 1)$; 5 -operating line operating line of cyclic distillation $(\mathrm{F}=1;\mathrm{E}_0=1)$; 6 -operating line operating line of cyclic distillation $(\mathrm{F}\neq 1;\mathrm{E}_0=1)$.

The leading role in the separation process is played by point efficiency valueE_0. InFigure 4 it is clear that E_0 influences not only on equilibrium achievement degree (this known fact is used upon calculation of stationary process columns), but also on the operating line position. In view of E_0 reduction the 4 - kinetic line and 5 - operating line cyclic distillation get approximate to each other therefore reducing the separation efficiency. The ultimate position of both lines at $\mathrm{E}_0\to 0$ will be the operating line L/G.

2.3. Operation line of cyclic distillation for full distillation column

Using mathematical model constructed operation line of cyclic distillation for full distillation column Figure 4.The method of construction is similar to the method described for Figure 4. The Figure 4a shows that in case with minimum of the reflux number of cyclic distillation, the operating line passes below the diagonal. This fact confirms high efficiency of mass transfer in a cyclic mode. The Figure 4b shows that threshold the efficiency of the distillation column in cyclic mode which has been operating at infinite reflux – is operational line of cyclic distillation like a mirror image with respect to the diagonal line of equilibrium.

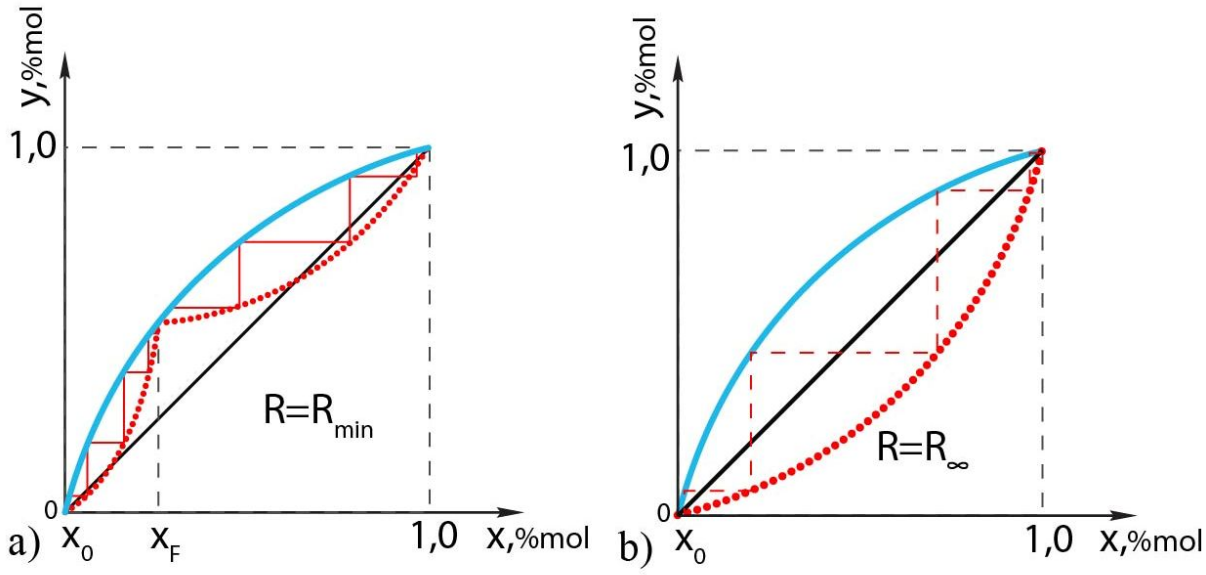

Figure 4: Operation line of cyclic distillation for full column a) $\mathrm{R} = \mathrm{R}_{\min}$; b) $\mathrm{R} = \mathrm{R}_{\infty}$

3. Conclusions

Cyclic distillation open new possibilities for process intensification of mass transfer as results, we got reducing of energy, capital costs significantly and increased quality of the products. In additional benefits, cyclic distillation can be effectively used for advanced techniques such as DWC-column, reactive distillation and membrane technology.

Defining limits and prospects of cyclic distillation application in chemical, petrochemical, oil refining and other industries requires establishing of reliable process model. Solution of this equation system is an explicit function of the concentration profiles of light component in the liquid and vapor on each stage, which can be called as cyclic theoretical stages of distillation. This function depends on the steam supply time and can be represented graphically similar to a classical method of theoretical stage. The only difference between the operating lines of the cyclic and conventional process is that the points of concentration in the vapor and liquid come up to all current value time interval of steam supply. Thus, the theoretical stage is a single point on the operating line, which is a straight line, and the theoretical stage of cyclic distillation is a continuous portion of the operating line having the curvature. The most important difference between the two operating lines is visible in a graphical interpretation of the X - Y coordinates with an infinite number of reflux $R = \infty$. For a theoretical stage operating line is the diagonal $(\mathrm{L}/\mathrm{G} = 1)$ and for the

cyclic distillation operating line is a mirror reflection of the equilibrium line in reference to diagonal line. Using the operation lines to describe the cyclic distillation enables us to determine the potential and perform complete calculation of column mass-transfer apparatus operating in a cyclic mode.

All advantages of cyclic distillation are confirmed in industrial operation data columns in the ethanol and petrochemical areas.

Acknowledgements
We thank Prof. Vitaliy Taran (National University of Food Technologies, Ukraine) for open prospects of the cyclic distillation and developed this area to the industrial implementation together with us.

References

1. Maleta V.,LawrenceP.,Uncovering significant energy efficiencies with cyclic distillation through process intensification: Exploiting latest advances in modeling technology.ACHEMA 2012.
2. Maleta, V.N., Kiss, A.A., Taran, V.M., Maleta, B.V., Understanding process intensification in cyclic distillation systems, Chem. Eng. Proc. 50, 655–664 (2011).
3. Maleta V.N., Journal of Chemistry and Chemical Engineering (USA).Hydrodynamics of Liquid Flow in the Model of Theoretical Stage with Perfect Displacement, Volume 5, Number 1, January 2011, Pages 25-29.
4.Малета В.Н., Таран В.М., Дубовик В.А. Сопоставление циклического и стационарного процесса ректификации // Известия вузов СССР. Пищеваятехнология (1986) №6 с.52-55.
5.Sommerfeld T.; Verle N. Schrodt ; Paul E. Parisot; Henry H. Chien, Studies of Controlled Cyclic Distillation: I. Computer Simulations and the Analogy with Conventional Operation Jude //Separation Science and Technology, 1520-5754, Volume 1, Issue 2, (1966). 245 – 279.
6. Cannon MR, Controlled cycling improves various processes. Ind. Eng. Chem. 1961; 53:629-629.
7. MC. Whirter I.R. and Canon M.R. Controlled cycling distillation // Ind. Eng. Chem. (1961). V.53.No.8 632-634.
8. Lewis W.K. Rectification of binary mixtures // Ind. Eng. Chem. (1936) V.38 No.4 399-403.

Criterion of energy effectiveness of extractive distillation in the partially thermally coupled columns

Andrey Timoshenko, Elena Anokhina

Lomonosov Moscow University of Fine Chemical Technology, Moscow, Russia

Abstract

The aim of this work is the development of the reasons of different energy effectiveness of extractive distillation systems with the partially coupled heat and material flows (PCEDS) for various mixtures and entrainers. The estimation of effectiveness was carried out of PCEDS application for separation of seven binary mixtures with different initial composition and various entrainers. The criterion of summary power consumption in the boilers of the columns under the optimum operating parameters was used. It was concluded on the base of the obtained results that PCEDS effectiveness depends on the value of reflux ratio in entrainer recovery column (RRC) of conventional extracted distillation flowsheet. If reflux ratio in that apparatus will have small value, then energy consumption decreasing through the use PCEDS will be insignificant. Thus the criterion for evaluation of PCEDS energy efficiency for binary mixtures separation can be formulated as follows: PCEDS is useful if the reflux ratio at the entrainer recovery column has value equal to or greater than 1.

Keywords

Extractive distillation, complex column, energy saving

Introduction

Extractive distillation (ED) is used in the industry for the separation of mixtures with close relative volatilities and azeotropes. The classical ED (CED) flowsheet for the separation of binary mixture (Figure 1a) includes extractive column (EC) and entrainer recovery column (RC). Power consumption reduction of ED is the urgent task of the chemical technology.

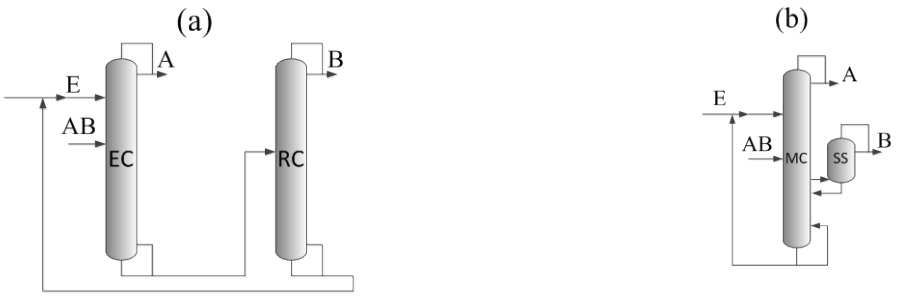

Figure 1. Classical ED flowsheet (a) and ED systems with the partially coupled heat and material flows (b), A,B – components of initial feed, MC – main column, SS – side section, EC – extractive distillation column, RC – entrainer recovery column

Recently ED systems with the partially coupled heat and material flows (PCEDS) are applied for saving energy. PCEDS is single complex column which consist of the main column (MC) and the refining side section (SS) for the cases of binary mixtures separation by ED with heavy boiling entrainer (Figure 1b). In these Figure heat exchangers, such as condensers, boilers, refrigerators for entrainer are not shown. Power consumption reduction by PCEDS differs considerably for the various mixtures up to ~30% [1], and only by ~ 4.7% [2]. Until now it was unclear why some cases the application PCEDS significantly reduced power consumption and the other practically gave no effect. Therefore, we carried out a systematic study to investigate energy consumption reduction dependence by PCEDS on various factors of the process.

Results and discussion

Thus the aim of this work is the development of the reasons of different energy effectiveness of PCEDS for various mixtures separation with different entrainers. As the energy efficiency criterion ($\mathrm{D}Q$) was used relative reduction of energy consumption in the boiler of PCEDS (Q_{reb}^{PCEDS}) in comparison with the CED boilers total energy consumption (Q_{reb}^{CED}): $\mathrm{D}Q = \frac{Q_{reb}^{CED} - Q_{reb}^{PCEDS}}{Q_{reb}^{CED}} \cdot 100\%$.

We carried out the estimation of DQ of PCEDS application for separation of seven binary mixtures with various entrainers (E). As objects of study were selected extractive distillation of different azeotropic mixtures with various entrainers: dymethyl formamide (DMFA), water, ethylene glycol (EG), butyl propionate (BP), dimethyl sulfoxide (DMSO), propylene glycol (PG) (Table 1).

Table 1. Some characteristics of the separated azeotropic mixtures at 101.3 kPa pressure.

No mix-ture	Binary mixtures	t_{AZ}, °C; min/max boiling point az.	x_1^{AZ}, mass %	Entrai-ner	Distillate of EC or MC	Distillate of RC or SS
I	Acetone (1) – Chloroform (2)	64.5 max	22.0	DMFA	Acetone	Chloroform
II	Acetone (1) – methanol (2)	55.6 min	86.3	DMFA, water	Acetone	Methanol
III	Allyl alcohol (1) – allyl acetate (2)	95.1 min	62.9	EG	Allyl acetate	Allyl alcohol
IV	Isobutyl alcohol (1) – isobutyl acetate (2)	107.4 min	78.3	BP	Isobutyl alcohol	Isobutyl acetate
				DMFA	Isobutyl acetate	Isobutyl alcohol
V	methyl acetate (1) – methanol (2)	54.0 min	81.3	EG	Methyl acetate	Methanol
VI	ethyl acetate (1) – ethanol (2)	71.8 min	69.0	DMSO PG	Ethyl acetate	Ethanol
VII	methyl acetate (1) – chloroform (2)	67.7 max	25.58	DMFA, EG, DMSO	Methyl acetate	Chloroform

For mixture IV, V, VI quantity and composition of feed, as well as product quality were set according to data [3], [4], [2] respectively. In all cases the initial feed has a boiling point temperature. Vapor-liquid equilibrium equations, characteristics of initial feed and product flows compositions are fixed by calculations are presented in Table 2. ASPEN + have used to simulate the ED.

Table 2. Concentrations of initial feed and products flows and VLE models

Mixture	Feed, kg/h	x_1^F, mass %	Pressure, kPa	Entrainer feed, X_E mass %	Distillate of EC or MC, mass %	Distillate of RC or SS, mass %	Bottom product of RC or MC, X_E mass %	Type of VLE model, parameters references
I with DMFA	100	22.0	101.3	99.90	99.50	99.90	99.90	NRTL,[5]
II with DMFA	100	86.3	101.3	99.90	99.50	99.50	99.90	NRTL,[6]
II with water Case 1 Case 2	100	 86.3 20.0	101.3	99.90	99.50	99.50	99.90	 NRTL,[8] NRTL,[8]
III with EG	100	20.0	101.3	99.90	99.50	99.50	99.90	NRTL,[9]
IV with BP	1500	41.0	101.3	99.60	97.60	99.60	99.60	UNIQUAC, [3]
IV with DMFA	1500	41.0	20	99.60	99.60	97.60	99.60	UNIQUAC, [3]
V with EG	12200	77.9	101.3	99.90	99.50	99.99	99.90	NRTL,[7]
VI with DMSO	11279	77.8	30	99.90	99.50	99.99	99.90	NRTL,[7]
VI with PG	11279	77.8	101.3	99.90	99.50	99.99	99.90	NRTL,[7]
VII with DMFA	1000	25.58	101.3	99.90	99.50	99.90	99.90	NRTL,[10]
VII with EG	1000	25.58	101.3	99.90	99.50	99.90	99.90	NRTL,[10]
VII with DMSO	1000	25.58	25	99.90	99.50	99.90	99.90	NRTL,[10]

We use the criterion of summary power consumption in the boilers of the columns (Q_Σ) and the optimization method of scanning of the factor space to identify the optimal operating parameters. Optimization variables include for classical ED flowsheets the total number of theoretical trays (N_{total}) (except ED of mixture IV with BP), entrainer-to-feed ratio (E:F), the entrainer temperature (t_E), the entrainer and the feed trays locations (N_E and N_F). The number of theoretical plates for ED of mixture IV with BP was set in accordance with the data [3]. Results are presented in Table 3. For the PCEDS the optimization variables include the entrainer temperature (t_E), the entrainer-to-feed ratio (E:F), the entrainer, the feed and the side section outlet trays locations (N_E, N_F, N_S), the value of flow rate directed to side section (FS). The total number of theoretical plates for PSEDS set the same as for traditional ED flowsheets. Results are presented in Table 4.
We carried out a comparison of the total energy consumption at boilers of the traditional two-column ED flowsheets and PCEDS flowsheets for separation of these mixtures. Table 5 and Figure 2 show the data of the value of energy consumption reducing by applying PCEDS systems compared to classical ED flowsheets.

Table 3. Energy consumption of classical ED flowsheets for different mixtures separation under optimal parameters

Mixture and entrainer	Extractive (EC) or recovery (RC) column	Total number of trays, N_{total}	Entrainer / feed trays location, N_E/N_F	Entrainer temperature, t_E, °C	Entrainer-to-feed ratio, (E:F)	Reflux ratio, (R)	Q_{reb}, kW	Q_{reb}^{CED}, kW
I with DMFA	EC	22	4 /10	60	3.50:1	2.20	28.10	55.20
	RC	22	–/6	–	–	3.60	27.10	
II with DMFA	EC	35	4/18	70	4.90:1	3.00	66.10	85.80
	RC	10	–/5	–	–	2.80	19.70	
II with water Case 1	EC	35	17/27	70	1.20:1	3.30	56.00	86.60
	RC	14	–/9	–	–	6.10	30.70	
II with water Case 2	EC	35	12/23	70	1:1	11.2	36.06	113.1
	RC	14	–/9	–	–	2.00	76.50	
III with EG	EC	24	5/15	100	3.60:1	1.40	38.20	54.6
	RC	9	–/5	–	–	1.10	16.40	
IV with BP	EC	50	10/35	120	1.87:1	5.09	651.4	1050
	RC	30	–/15	–	–	4.07	399.3	
IV with DMFA	EC	60	14/46	101.06	1.76:1	6.50	639.6	1226
	RC	20	–/7	–	–	4.40	586.6	
V with EG	EC	50	3/33	40	2.87:1	1.04	4763	7513
	RC	10	–/6	–	–	0.18	2751	
VI with DMSO	EC	30	4/17	40	0.78:1	0.66	1925	2882
	RC	10	–/6	–	–	0.19	957.6	
VI with PG	EC	50	4/33	40	2.97:1	0.95	4487	6719
	RC	10	–/6	–	–	0.40	2233	
VII with DMFA	EC	30	4/12	80	3.45:1	2.60	246.8	573.9
	RC	15	–/5	–	–	5.00	327.1	
VII with EG	EC	35	3/14	90	4.50:1	2.00	330.0	568.6
	RC	12	–/5	–	–	0.80	238.6	
VII with DMSO	EC	22	3/11	30	0.9:1	1.04	89.80	182.5
	RC	9	–/4	–	–	0.12	92.70	

The difference in the energy effectiveness can be deal with: the different types of azeotropes, different entrainers, different processes at the PCEDS and CED extractive section and above it and some effects at another four sections of flowsheets. Mixtures I and VII have a one type of azeotropes with high boiling point and the others have azeotropes with minimum boiling point. The explicit dependence on the type of the azeotrope is not observed. There is some dependence on the type of entrainer e.g. PCEDSs with DMF at all the cases have relatively high efficiency. But the relationship is not precise. Efficiency criterion DQ values are different for cases with DMF nearly twice (16.0-32.1%), for cases with EG more than 8 times (1.4-11.7%) (Table 5). We have analyzed the profiles of temperature and component concentrations in the extractive sections and above them and found no difference for the PCEDS and CED. Thus reduction of energy consumption is associated with the processes occurring in the flowsheets sections located below the feed plate. Process

of hard boiling component and entrainer separation mainly exists in this part of the scheme.

Table 4. Energy consumption of PCEDSs under optimal parameters

Mixture	Main col. number of trays N^{MC}	Side col. number of trays N^{SS}	Entrainer/ feed /side section outlet trays location $N_E/N_F/N_S$	Entrainer temperature, t_E, °C	Entrainer-to-feed ratio (E:F)	Flow to side section, FS, kg/h	Reflux ratio main col. R^{MC}	Reflux ratio side col. R^{SS}	Q_{reb}^{PCEDS}, kW
I with DMFA	34	10	4 /11/24	60	3.50:1	120	1.90	1.20	40.90
II with DMFA	40	5	4/18/36	70	4.80:1	19	3.00	0.30	72.60
II with water Case 1	40	9	18/26/35	70	1.50:1	33	3.10	2.40	69.60
II with water Case 2	40	9	12/22/34	70	1.20:1	175	10.6	1.60	100.4
III with EG	28	5	5/15/25	100	3.50:1	23	1.40	0.30	50.80
IV with BP	65	15	10/35/52	120	1.90:1	2500	4.68	1.86	839.4
IV with DMFA	73	7	15/43/58	101.06	1.97:1	1400	6.50	1.00	860.5
V with EG	54	6	3/33/51	40	2.91:1	2700	0.95	0.04	7407.3
VI with DMSO	34	6	4/16/30	40	0.82:1	2530	0.64	0.05	2812
VI with PG	54	6	4/33/51	40	2.93:1	2640	0.96	0.11	6541
VII with DMFA	40	5	4/11/29	80	3.67:1	1150	2.67	1.18	389.6
VII with EG	42	5	3/15/38	90	4.18:1	770	1.62	0.22	501.9
VII with DMSO	27	4	3/11/23	30	0.80:1	750	1.30	0.06	180.7

Table 5. Reduction of energy consumption by using PCEDSs

Mixture	Recovery column reflux ratio, RRC	DQ, %
I with DMFA	3,60	25,9
II with DMFA	2,80	16,0
II with water, Case 1	6,10	19,6
II with water, Case 2	2,00	11,2
III with EG	1,10	7,10
IV with BP	4,07	20,1
IV with DMFA	4,40	29,8
V with EG	0,18	1,40
VI with DMSO	0,19	2,40
VI with PG	0,40	2,70
VII with DMFA	5,00	32,1
VII with EG	0,80	11,7
VII with DMSO	0,12	1,00

It is characterized by the reflux ratio in the entrainer recovery column. Criterion DQ value does not exceed 3% for values of reflux ratio less than one in the entrainer recovery column (Table 5, Figure 2).

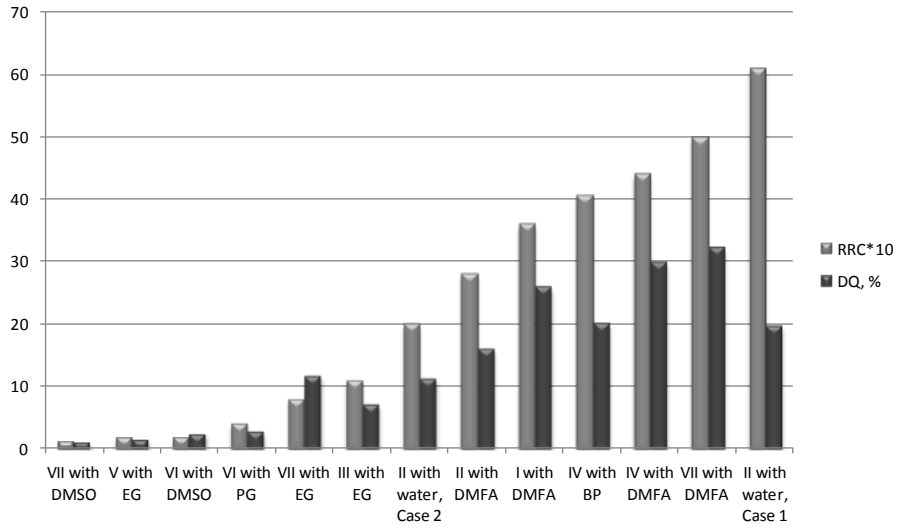

Figure 2. Reflux ratio in entrainer recovery columns (RRC) and reduction of energy consumption by using PCEDS for different mixtures separation

Conclusions

Thus we made the conclusion that PCEDS effectiveness depends on the value of reflux ratio in entrainer recovery column (RRC) of conventional ED flowsheet. If reflux ratio in that apparatus will have small value, then energy consumption decreasing due to using PCEDS will be insignificant. It is evident that reduction of energy consumption is not directly proportional reducing RRC. However, if to estimate as a significant reduction in energy consumption at a level equal to or greater than 10%, it can be stated that it is observed at RRC value close or equal to 1. Thus the criterion for evaluation of PCEDS energy efficiency (DQ>10%) for binary mixtures separation can be formulated as follows: PCEDS is useful if the reflux ratio at the entrainer recovery column has value equal to or greater than 1.

Work was carried out according to the state task of the Russian Ministry of Education and Science # 10.99.2014/K.

References

1. Timoshenko A., Anokhina E., Timofeev V. Russia Patent 2207896, 2003.
2. San-Jang Wang, Hsiao-Ping Huang and Cheng-Ching Yu. // Ind. Eng. Chem. Res. 2010. V.49. №2. P. 750–760.
3. Muñoz R., Montón J.B., Burguet M.C. // Separation and Purification Technology. 2006. V. 50. P. 175–183
4. Heinz Erpenbach, Klaus Günther, Georg Kohl Patent USA 5296630, 1994.
5. Anokhina E.A., Dolmatov B.B., Timoshenko A.V. // Khimicheskaya tehnologiya. 2008. V.9. N8. P. 402–407.
6. Anokhina E.A., Pankova I.A., Timoshenko A.V. // Khimicheskaya promyshlennost segodnya. 2009. N3. P. 44–49.
7. Rudakov D.G., Anokhina E.A., Timoshenko A.V. // Khimicheskaya tehnologiya. 2013. V. 14. N 3. P. 163–171.
8. Anokhina E.A., Sidorova Ju.I., Timoshenko A.V. // Vestnik MITHT. 2011. V. 6. N 5. P. 118–124.
9. Anokhina E.A., Timoshenko A.V., Novikova E.N. / Book of Abstracts «Resurso i energosberegajushie tehnologii v khimicheskoy i neftekhimicheskoy promyshlennosti». Moskva, RHTU, 2006. P. 41–42.
10. Anokhina E.A., Shlejnikova E.L., Timoshenko A.V. // Vestnik MITHT. 2013. V. 8. N2. P. 18–25.

Application systems with thermally coupled flows in extractive distillation of benzene-cyclohexane-toluene mixture with N-methylpyrrolidone

E. Anokhina, A. Timoshenko, A. Rebrovskaya, A. Fedyushina,

Lomonosov Moscow University of Fine Chemical Technology, Moscow, Russia

Abstract

In this paper evaluation of extractive distillation energy efficiency of schemes with partially coupled thermally and material flows for benzene-cyclohexane-toluene mixture with N-methylpyrrolidone as entrainer is considered. There are three different conventional schemes of this mixture separation by extractive distillation. Seven new extractive distillation schemes with partially coupled thermally and material flows were constructed on the base of three initial traditional extractive distillation schemes. We compared all 10 schemes by the total energy consumption of the boilers. We have determined that the lowest energy consumption (7256.2 kW) among the three conventional schemes has the scheme where extractive distillation is used at the first column and cyclohexane is recovered as a distillate. Benzene and toluene are distillates of the second and the third columns. The better schemes with partially coupled thermally and material flows are those that consist of a single complex column with two side sections. Their power consumptions decrease by 18-28% in comparison with conventional extractive distillation schemes with two outlets columns.

Keywords

Extractive distillation, thermally coupled distillation systems

Introduction

Extractive distillation (ED) is a method of separation of azeotropic mixtures and mixtures of components with low relative volatility. One way to reduce ED energy consumption is to use distillation systems with partially coupled thermally and material flows (PCDS). There is only one version of such a system for binary mixtures ED with heavy boiling entrainer (E) which is a single complex column with the refining side section. That system decreases the ED of acetone-chloroform mixture energy consumption up to 30% [1]. There are several schemes with PCDS for ternary mixtures ED. Algorithm for the synthesis of such schemes were presented in [2, 3].

In this paper evaluation of ED energy efficiency of schemes with PCDS for benzene (B) - cyclohexane (CH) - toluene (T) mixture with N-methylpyrrolidone (NMP) as entrainer is considered.

Results and discussion

The B-CH-T mixture contains a B-CH binary azeotrope with a minimum boiling point. There are three different conventional schemes of this mixture separation by ED (Figure 1). Each of them consists of three columns with two outlets. At the first

column of the schema I (Figure 1a) toluene as bottom product and azeotropic benzene-cyclohexane mixture as distillate are obtained. This mixture is separated by ED with NMP as entrainer in the second column. CH is the distillate of ED column and B is the distillate of entrainer recovery column. At the schema II (Figure 1b) NMP is used as entrainer in the first column, distillate is CH. B and T are distillates of the second and entrainer recovery columns respectively. NMP also applies as entrainer at the first column of the schema III (Figure 1c). CH is separated as distillate of the first column, B-T mixture as distillate and entrainer as the bottom product of the second column are obtained. B-T mixture is separated at the third column.

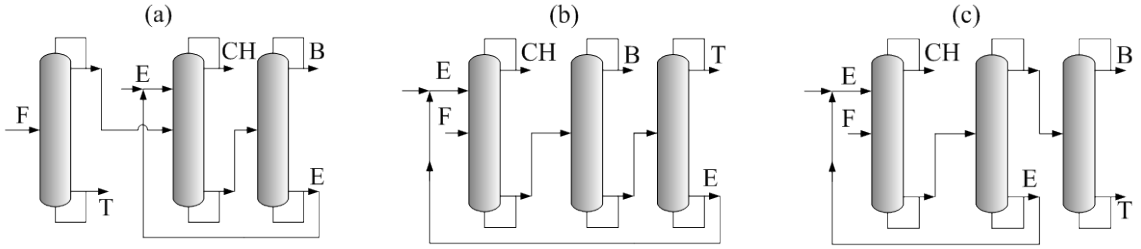

Figure 1. Conventional ED schemes for benzene-cyclohexane-toluene mixture separation with NMP: a) schema I, b) schema II, c) schema III, F – B-CH-T initial mixture, E - entrainer

The process of synthesis of schemes with PCDS was based on the algorithm proposed by authors [2, 3]. This approach is based on displaying schemes in the form of graphs. Vertices of the graph represent the intersections dividing or limiting column's sections. Undirected edges explicate of vapor and liquid flows inside the column and directed edges represent streams between the columns. The scheme which is base for synthesize of new technological solutions is preimage, and the resulting one - image. Vertices connected by oriented edges are merged during the transformation from preimage to the image. As preimages for the extractive distillation PCDS synthesis were used conventional ED schemes.

The schema I transformation produces the single schema I.1 ED with PCDS (Figure 2a). The schema II transformation gives three ED schemes with PCDS: schema II.1 (Figure 2b), schema II.2 (Figure 2c) and schema II.3 (Figure 2d). Schema III produces also three ED schemes with PCDS: schema III.1 (Figure 2e), schema III.2 (Figure 2f) and schema III.3 (Figure 2g). Thus seven new schemes involving PCDS were constructed on the base of three initial conventional ED schemes. Five of them consist of one simple distillation column and one complex column with one side section (Figure 2a–c, e, f). Each of the other two is a single complex column with two side sections (Figure 2d, 2g).

We compared all 10 schemes by the total energy consumption of the boilers $Q_\Sigma = \sum_{i=1}^{n} Q_i^{reb}$ (i – number of boilers in the schema). Q_Σ value was determined for each scheme under optimal values of operating parameters. The initial mixture flow rate was 15000 kg/h with a composition of B, CH, T - 78, 12, 10 mass % respectively. The purities of products were assigned for B and CH as 99.9 mass %, for T as 99.75 mass %. The entrainer flow rate contains 99.99 mass % NMP. The entrainer temperature is fixed and equal to 70 °C. Aspen$^+$ is used for distillation simulation and NRTL model is used to predict the activity coefficients. Optimization was carried out by scanning of factor space.

Optimization variables include for schemes I-III the total number of trays (N_{total}), entrainer flow rate (E), the entrainer and the feed trays locations (N_E and N_F).

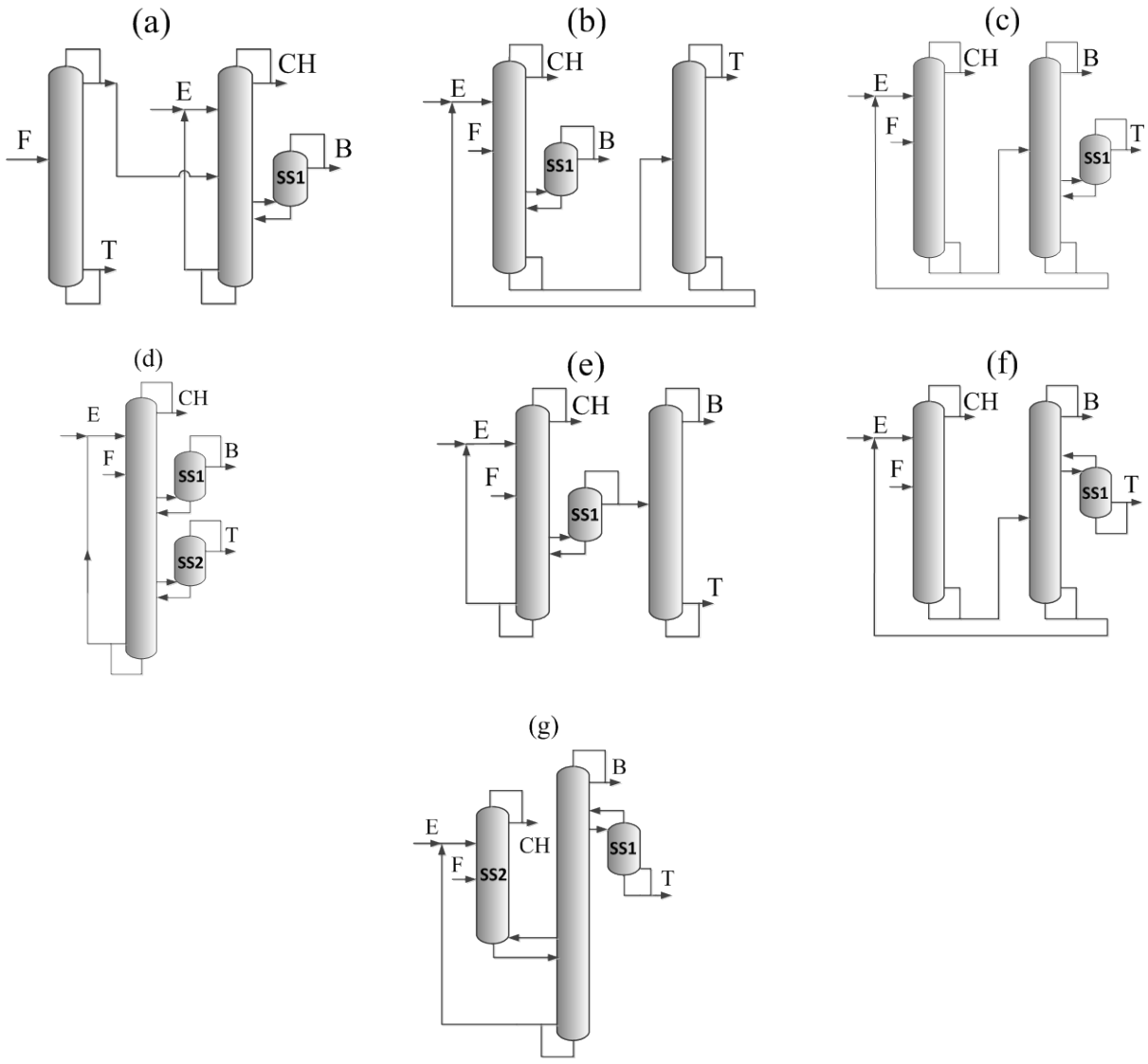

Figure 2. PCDS ED schemes for benzene-cyclohexane-toluene mixture separation with NMP: schema I.1 - (a), schema II.1 - (b), schema II.2 - (c), schema II.3 - (d), schema III.1 - (e), schema III.2 - (f), schema III.3 - (g). SS – side section

At the first stage we determined the optimal value of total number of theoretical plates (N_{total}) for the each column of schemes I-III at a fixed entrainer flow rate E= 25000 kg/h. The selection criterion was energy consumption in the columns boilers (Q^{reb}.). Optimal initial feed plates were found for each column with determined N_{total} . For extractive distillation columns the optimal entrainer feed plates were also determined. Figure 3 shows the dependence of the energy consumption at boiler of ED column of scheme I on the number of theoretical plates.
It can be seen that the energy consumption in the boiler of ED column of scheme I increased slightly (~ 5.3%) with a decreasing the number of plates from 50 to 38. With total number of the column trays decreasing of every two plates increase energy not more than 1.5%. With a further reduction of the number of plates increase Q^{reb} becomes more visible. Reducing the number of plates from 38 to 36 it is 2.2%, from 36 to 34 - 3.5%, from 34 to 32 - 3.9%. Therefore, during all further calculations we assigned the number of theoretical plates in the ED column of scheme I equal to 38 ones.

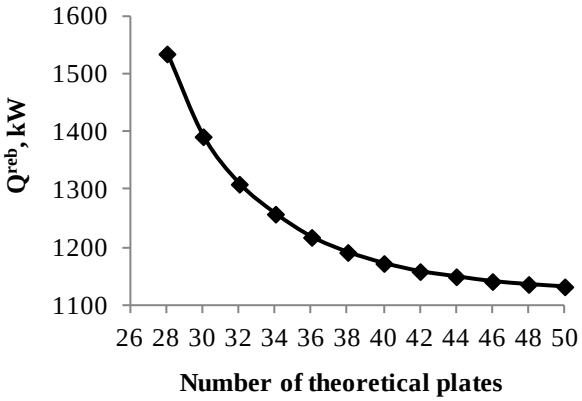

Figure 3. Dependence of the energy consumption at boiler of ED column of scheme I on the number of plates

We have carried out a similar analysis for all columns of the schemes I-III.
The number of plates in the columns is shown in Table 1. The number of ED column theoretical plates for the three schemes was the same. Of course, these values can be considered as optimal only in a certain extent since they are found at fixed temperature and entrainer flow rate, excluding the use of the cooling water, without heat recovery of entrainer flow rate, etc.

Later we have determined entrainer flow rate, entrainer and feed plates in the columns which provide minimum Q_{Σ} for the schemes I-III. Results are presented in Table 1.

Table 1. Optimal operating parameters and energy consumption of conventional ED schemes

Schema	Column	N_{total}	N_E/N_F	R*	E, kg/h	Q^{reb}, kW	Q_{Σ}, kW
Schema I	Column 1	22	– /12	1.62	–	3836.1	7675.3
	Column 2	38	4/17	3.69	18000	1366.8	
	Column 3	10	5	0.21	–	2472.4	
Schema II	Column 1	38	4/18	5.31	17000	1625.8	*7256.2*
	Column 2	22	–/11	2.32	–	4890.0	
	Column 3	14	–/9	2.25	–	740.4	
Schema III	Column 1	38	4/17	4.06	19000	1482.1	7556.0
	Column 2	14	–/9	0.33	–	2887.9	
	Column 3	22	– /12	1.48	–	3186.0	

*R – reflux ratio

According to our calculations, the greatest influence on the value of the optimization criterion provides entrainer flow rate. It should be noted that the optimal flow rate of NMP for the full schema is substantially lower than this value found for the individual ED column. For example, in schemes II and III, the minimum energy consumption at the boiler of the ED column is achieved with NMP flow rate equal 29000 kg/hr and the minimum total energy consumption of scheme II and scheme III are reached by NMP flow rates 17000 kg/h and 19000 kg/h respectively. The optimum flow rate of NMP at ED column of scheme I (27000 kg/h) is somewhat lower than in schemes II and III. Entrainer optimal flow rate for the scheme I is 18000 kg / h. Thus the presence of toluene in ED column of schemes II and III complicates separation of an azeotropic mixture of benzene and cyclohexane, as noted by the authors [4]. Optimal NMP flow rate has the smallest value in scheme II. The reason is that in scheme II the increasing of ED column boiler energy consumption (NMP flow rate is

below the optimum value for individual ED column) is compensated by energy consumption decreasing at the boilers of another two columns instead of only one, as in the schemes I and III. The optimum locations of the initial and NMP feeds plates of ED columns for all three schemes are practically equal. Thus, the numbers of theoretical plates of extractive sections for all schemes are almost the same and equal 13-14 (Table 1). One can see that scheme II has the minimum value of energy consumption (7256.2 kW) among the three conventional schemes. In scheme II ED is used at the first column and CH is recovered as a distillate (Figure 1b). However, it should be noted that the difference between the energy consumption of schemes I-III is small, the excess in comparison with the optimum one are 5.8 and 4.1% for schemes I and III, respectively.

For the schemes with PCDS the optimization variables include the entrainer flow rate (E), the entrainer, the feed and the side outlet trays locations (N_E, N_F, N_{S1} for all schemes and N_{S2} additionally for schemes II.3 and III.3), the flow rate directed to side section (FS). The total number of theoretical plates in the columns of each of the schemes-images was equal to the total number of plates in the columns corresponding to schemes-preimages. Results of optimization are presented in Table 2.

Table 2. Optimal operating parameters and energy consumption of PCDS ED schemes

Schema	Column		N_{total}	$N_E/N_F/N_{S1}/N_{S2}$	R	E, kg/h	FS, kg/h	Q^{reb}, kW	Q_Σ, kW
Schema I.1	Column 1		22	– /12/–/–	1.62	–	–	3836.1	7550.1
	Column 2	MC*	43	4/17/38/–	3.67	18000	–	3714.0	
		SS1	5	–	0.11	–	12300	–	
Schema II.1	Column 1	MC	49	4/18/36/–	6.63	17000		5588.7	6329.4
		SS1	11	–	1.42	–	27500	–	
	Column 2		14	–/9/–/–	2.25	–	–	740.7	
Schema II.2	Column 1		38	4/18/–/–	5.31	17000	–	1625.8	6618.1
	Column 2	MC	27	– /11/23/–	2.05	–	–	4992.3	
		SS1	9	–	0.33	–	1800	–	
Schema II.3	Column 1	MC	54	4/18/37/51	6.3	17000	–	5901.5	5901.5
		SS1	11	–	1.3	–	26000	–	
		SS2	9	–	0.86	–	2250	–	
Schema III.1	Column 1	MC	43	4/17/38/–	4.30	19000	–	4102.3	7289.3
		SS1	9	–	0.12	–	14000	–	
	Column 2		22	– /12/–/–	1.48	–	–	3187.0	
Schema III.2	Column 1		38	4/17/–/–	4.06	19000	–	1482.1	5440.7
	Column 2	MC	25	–/20/16/–	1.33	–	–	2910.6	
		SS1	11	–	–	–	11000	1048.0	
Schema III.3	Column 1	MC	25	–/–/16/20	1.3	–	–	4233.6	*5390.1*
		SS1	11	–	–	–	12000	1156.5	
		SS2	38	4/17/–/–	4.1	19000	12200	–	

* MC – main column, SS – side section

Table 2 shows that the lowest total energy boilers consumption (5390.1 kW) is observed for schema III.3 (Figure 2g). Its power consumption is lower by 28.7% than the schema-preimage III (Figure 1c). The next is schema III.2 (Figure 2f). Its power consumption is 5440.7 kW and it is lower 28.0% than the schema-preimage III. The third is schema II.3 (Figure 2d) with the power consumption 5901.5 kW. It is on the 18.7% lower compared to the total energy consumption for schema-preimage II (Figure 1b).

Previously, on the basis of the results obtained for binary mixtures ED, we concluded that the efficiency of schemes with partially coupled thermally and material flows depends on the reflux ratio in the entrainer recovery column in scheme-preimage. When R values in this column significantly smaller than 1, energy saving by the use of PCDS ED schemes is relatively small (less than 10%) [5]. It is confirmed by the results obtained by us in this work.

Let us consider heat integration of columns 2 and 3 in scheme-preimage I (Figure 1a). It leads to the complex column with side refinery section in the scheme-image I.1 (Figure 2a). R in the entrainer recovery column of scheme I has a small value (0.21). Energy consumption in the boiler of complex column is only by 3.3% less than the total energy consumption in the boilers of columns 2 and 3 of Scheme I.

Let us consider heat integration of columns 2 and 3 in scheme-preimage II (Figure 1b). It leads to the complex column with side refinery section in the scheme-image II.2 (Figure 2c). R in the entrainer recovery column of scheme II has a value substantially higher than in the previous example (2.25). Energy consumption in the boiler of complex column is by 11.3% less than the total energy consumption in the boilers of columns 2 and 3 of Scheme II. Thus the result for case 2 is much better than for the case 1.

Conclusions

Thus maximum energy efficiency is achieved for ternary mixture separation at the maximum thermally coupled systems which consist of only one complex column with two side sections. Their power consumptions decrease by 18-28% in comparison with conventional ED schemes with two outlets columns.

Work was carried out according to the state task of the Russian Ministry of Education and Science # 10.99.2014/K.

References

1. Timoshenko A., Anokhina E., Timofeev V. Russia Patent 2207896, 2003.
2. Timoshenko A.V., Anokhina E.A., Ivanova L.V. Theoretical foundations of chemical engineering. 2005. V.39. No 5. P. 463-470.
3. Timoshenko A.V., Anokhina E.A., Ivanova L.V. Europeen congress of Chemical Engineering. 2007. Book of Abstracts. V.2. P.551-552.
4. Gayle A.A., Zalischevskiy G.D. N-metilpirrolidon. Poluchenie, svoystva i primenenie v kachestve selektivnogo rastvoritelya. // SPb.: Himizdat, 2005.
5. Rudakov D.G., Anokhina E.A., Timoshenko A.V. // Khimicheskaya tehnologiya. 2013. V. 14. N 3. P. 163–171

Extractive distillation with the mixture of ionic liquid and organic solvent as entrainers

Zhigang Lei, *Xiaomin Xi, Chengna Dai, Biaohua Chen*

State Key Laboratory of Chemical Resource Engineering, Beijing University of Chemical Technology, Box 266, Beijing, 100029, China
Email: leizhg@mail.buct.edu.cn

Abstract

Extractive distillation with ionic liquids (ILs) can be used for the separation of azeotropic or close-boiling mixtures. However, by far, all studies have been limited to the use of single ILs as entrainers, and the use of single ILs may change the whole flowsheet of current extractive distillation process using traditional organic solvents because the ILs must be recovered in a flash drum operating at a very high vacuum.

In this work, the separation of ethanol/water was selected as a model system, and the mixture of ethylene glycol (EG) and $[EMIM]^+[Ac]^-$ were suggested as entrainers, which utilize the salting effect of IL. The vapor-liquid equilibrium (VLE) data were measured for the ternary system of ethanol (1) + water (2) + EG (3), as well as the quaternary system of ethanol (1) + water (2) + EG (3) + $[EMIM]^+[Ac]^-$ (4) at atmospheric pressure (101.3 kPa). It was found that the relative volatility of ethanol (1) to water (2) is enhanced upon the addition of the IL into the traditional solvent EG. The measured ternary and quaternary data were correlated using the NRTL equation. On this basis, process simulation was done, in which the model parameters of NRTL equation was input into the equilibrium stage (EQ) mathematical model. It was found that for the separation of ethanol and water azeotropic mixture, the overall heat duties on reboilers without and with heat integration (HI) using the new entrainers decrease 15.02% and 16.51%, respectively, when compared to the benchmark solvent EG.

Keywords: ionic liquids (ILs), extractive distillation, VLE (vapor-liquid equilibria), process simulation, energy saving

1. Introduction

Nowadays, ionic liquids (ILs) have become efficient entrainers in extractive distillation because of their unique advantages such as nonvolatility, salt effect, high separation ability, regeneration, liquid state around room temperature, and thermal and chemical stabilities. Extractive distillation with ILs can be used for the separation of azeotropic or close-boiling mixtures. However, by far, all studies have been limited to the use of single ILs as entrainers, and the use of single ILs may change the whole flowsheet of current extractive distillation process using traditional organic solvents because the ILs must be recovered in a flash drum operating at a very high vacuum [1, 2].

In this work, the separation of ethanol and water has been chosen as a model system for azeotropic mixtures, because ethanol is a green alternative energy source.

The present ethanol dehydration process with extractive distillation is energy-intense, with ethylene glycol (EG) as entrainer [3]. As we know, selection of a suitable entrainer is the key technology of extractive distillation [4]. Meanwhile, in the family of ILs, $[EMIM]^+[Ac]^-$ (breaking the ethanol and water azeotrope at x_{IL} = 0.013) has a significant effect on increasing the relative volatility of ethanol to water [5]. Thus, a new kind of physically mixed entrainers with the combination of ethylene glycol and IL was proposed in this work aiming to obtain higher relative volatility (or selectivity) of ethanol to water. And the mixture of EG and $[EMIM]^+[Ac]^-$ as entrainers have the unique advantage that there is no additional streams and equipment required based on the state of the art of extractive distillation processes with EG as entrainer. It should be mentioned that the new entrainers proposed in this work can also be applied to the separation of other aqueous solutions due to their similar separation mechanism.

The present paper will be organized as the following steps: i) measuring the isobaric vapor-liquid equilibrium data for the ternary system of ethanol (1) + water (2) + EG (3) and the quaternary system of ethanol (1) + water (2) + EG (3) + $[EMIM]^+[Ac]^-$ (4) at 101.3 kPa; ii) determining how much heat duty could be saved in the extractive distillation process using the new entrainers in comparison with the benchmark entrainer EG. For this purpose, the mathematical model for extractive distillation process was established, into which the phase equilibrium model (i.e. the NRTL model) obtained in this work was incorporated.

2. Results and discussion

2.1 VLE experiments

A circulation vapor–liquid equilibrium still (a modified Othmer still) was used for the VLE data determination. The details about this apparatus were described in our previous publications. The VLE data for ternary system of ethanol (1) + water (2) + EG (3) at 101.3 kPa were measured, and the EG concentrations in liquid phase were about 0.05, 0.10, and 0.15 in mole fractions, respectively. Meanwhile, the quaternary system of ethanol (1) + water (2) + EG (3) + $[EMIM]^+[Ac]^-$ (4) at 101.3 kPa were also measured. The mixed entrainers added into the system were about 0.05, 0.10, and 0.15 in mole fractions, respectively, while the IL concentrations in the mixed entrainers were about 0.2 and 0.4 in mass fractions, respectively.

As shown in Figure 1, when the total concentration of mixed entrainers remains constant (0.05 in mole fraction), the addition of $[EMIM]^+[Ac]^-$ into EG leads to a high ethanol content in the vapor phase, and, therefore, a large relative volatility of ethanol to water. The greater IL concentration, the higher relative volatility of ethanol to water. This conclusion also holds for other concentrations of mixed entrainers (i.e., 0.10 and 0.15 in mole fractions), which are not shown herein, due to the limitation of maximum 6 pages required. We relate this phenomenon with a strong salting-out effect brought by IL. The salting-out effect follows the order: $w4 = 0.4 > w4 = 0.2 > w4 = 0$. Therefore, the VLE experiments indicates that the IL $[EMIM]^+[Ac]^-$ is a promising additive for intensifying the conventional entrainer EG.

2.2 Data regression

The NRTL model was used for correlating the VLE data of the systems containing ILs. The following minimized objective function (OF) was used to correlate the binary interaction parameters (Δg_{ij} and Δg_{ji}):

$$\mathrm{OF}\,(\%) = \frac{1}{N}\sum_{i=1}^{N}\left|\frac{\gamma_i^{\exp} - \gamma_i^{\mathrm{cal}}}{\gamma_i^{\exp}}\right| \times 100 \qquad (1)$$

where N is the number of data points, and γ_i^{exp} and γ_i^{cal} are the experimental and calculated activity coefficients of component i, respectively. The Marquardt method was used to fit the model parameters as given in Table 1, where the binary interaction parameters Δg_{12} and Δg_{21} come from the literature [6]. In all cases, the maximum average relative deviation (ARD) is 7.23%.

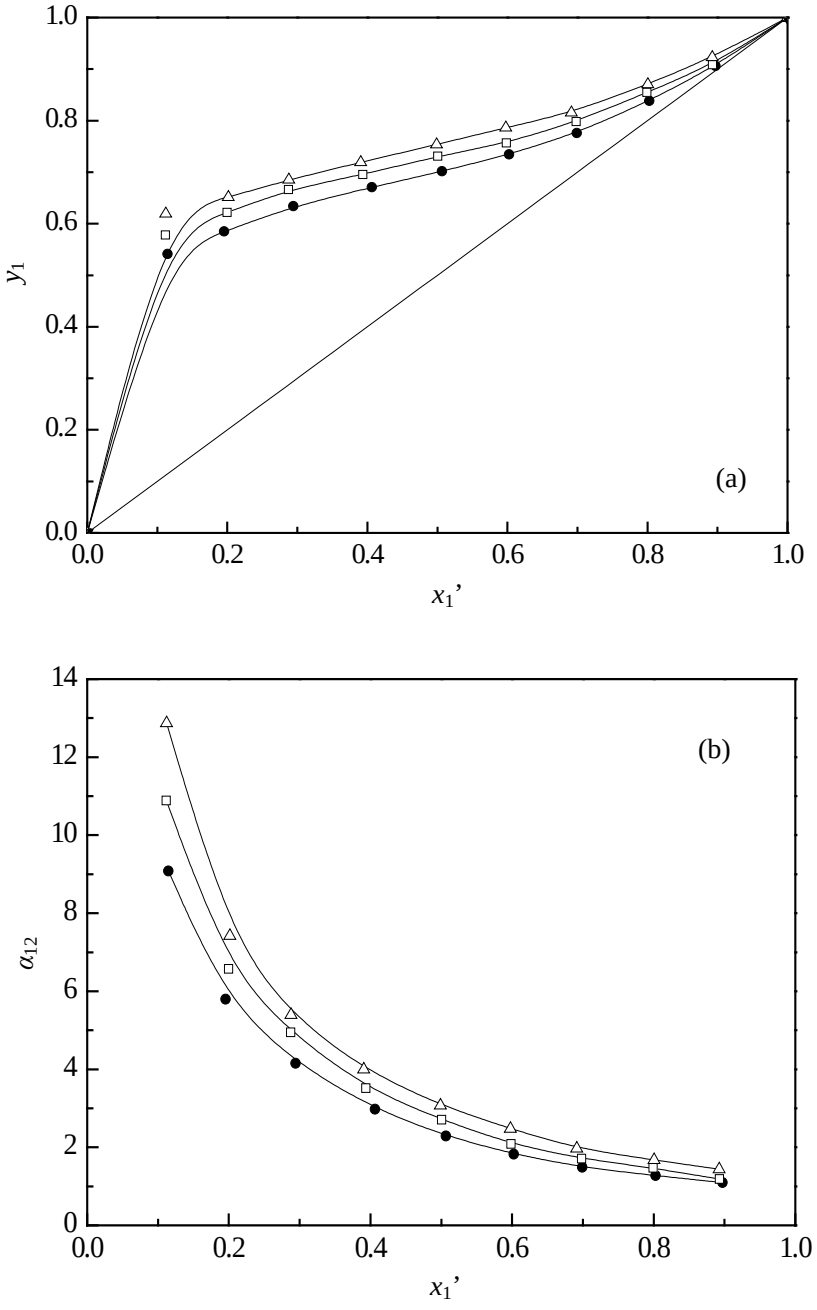

Figure 1. Isobaric VLE data (a) and relative volatility (b) for the ethanol (1) + water (2) + mixed entrainers (5% in mole fraction) system at 101.3 kPa.
Scattered points, experimental data; solid lines, correlated results using the NRTL model. ●, $w4 = 0$; □, $w4 = 0.2$; △, $w4 = 0.4$. The symbols x_1', y_1 and α_{12} represent mole fraction of ethanol in the liquid phase on an IL-free basis, equilibrium mole fraction of ethanol in the vapor phase, and relative volatility of ethanol (1) to water (2), respectively.

Table 1. Estimated values of binary parameters in the NRTL model

Component *i*	Component *j*	α_{ij}	Δg_{ij} / J·mol^{-1}	Δg_{ji} / J·mol^{-1}
ethanol (1)	water (2)	0.40	-2216.0 + 6.7055 *T*	3698.8 + 4.2758 *T*
ethanol (1)	EG (3)	0.30	1530.82	-743.87
Water (2)	EG (3)	0.30	-2549.37	-3924.44
ethanol (1)	[EMIM]$^+$[Ac]$^-$ (4)	0.30	-4282.64	-2775.43
water (2)	[EMIM]$^+$[Ac]$^-$ (4)	0.30	-3449.16	-7003.56
EG (3)	[EMIM]$^+$[Ac]$^-$ (4)	0.47	-682.73	-5101.27

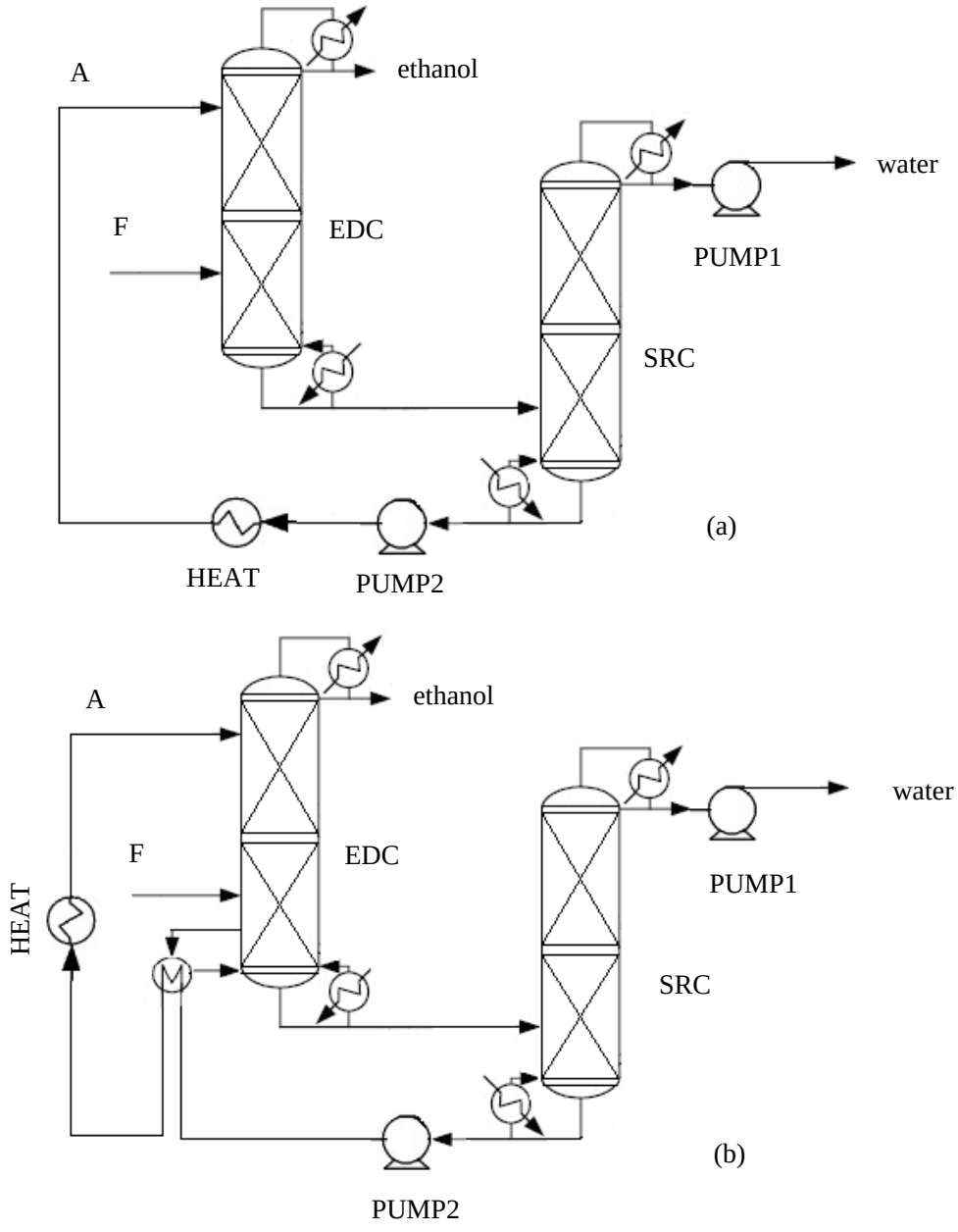

Figure 2. Flowsheets for extractive distillation process without (a) and with (b) heat integration (HI). F and A represent the feed stream and entrainer stream, respectively.

2.3 Process simulation

In principle, the flowsheet of extractive distillation processes with the single EG as entrainer is the same as with the mixture of EG and $[EMIM]^+[Ac]^-$ as entrainers, consisting of an extractive distillation column (EDC) and a solvent recovery column (SRC), as shown in Figure 2.

The process simulation was carried out in Aspen Plus software (version 7.1), in which the rigorous equilibrium (EQ) stage model RadFrac was established. The equations that model EQ stage are known as MESH equations, the M equations represent the mass balance, E the phase equilibrium relation, S the summation equations, and H the enthalpy balance. Herein the NRTL model parameters obtained from the section of phase equilibrium model for the VLE data were incorporated into the MESH equations. However, we are indeed aware that heat integration (HI) is necessary for an economic and feasible extractive distillation process. The entrainer from the bottom of the SRC contains a large amount of heat, which can be used to heat the stream near the bottom of EDC in order to reduce the energy cost of the reboiler. Thus, process A (without HI) and process B (with HI) were established.

The optimized specifications were determined using Design Specs module and sensitive analysis in Aspen Plus with the following constraints: i) mole purity > 99.0% for ethanol at the top of EDC; ii) mole purity > 99.3% for water at the top of flash drum; and iii) the mole fraction of water in entrainer at the bottom of SRC less than 0.2%, which allows for ensuring a high purity of ethanol product obtained at the top of EDC. The comparison of the operating performance between Process A and Process B was made. It was found that the overall heat duties on reboilers in the processes using the new entrainers without and with heat integration decrease 15.02% and 16.51%. That is to say, whether HI strategy is considered or not, the new mixed entrainers seem to be more promising in saving energy.

3. Conclusions

This work focuses on intensifying the extractive distillation process with the new mixed entrainers of EG and $[EMIM]^+[Ac]^-$ as an alternative of the single EG for the separation of ethanol and water, and the following conclusions can be obtained:

(i). The VLE experiments showed that it is an effective way to increase the relative volatility of ethanol to water by adding some $[EMIM]^+[Ac]^-$ into the benchmark solvent EG;

(ii). The NRTL model is capable for describing the experimental VLE data for the ternary system of ethanol (1) + water (2) + EG (3), as well as the quaternary system of ethanol (1) + water (2) + EG (3) + $[EMIM]^+[Ac]^-$ (4);

(iii). Based on the experimentally measured VLE data, the rigorous equilibrium (EQ) stage model RadFrac was used to simulate the extractive distillation process. It was found that the new entrainer is indeed more promising in saving energy.

It should be mentioned that the strategy of IL intensification presented in this work is easy to be implemented in practice by general chemical engineers, without changing the whole flowsheet but only by replacing the traditional solvent with the new entrainers as proposed in this work.

Acknowledgements

This work was financially supported by the National Nature Science Foundation of China under Grants (Nos. 21121064 and 21076008), and the Research Fund for the Doctoral Program of Higher Education of China (No. 20120010110002).

References

1. Meindersma, G.W., Quijada-Maldonado, E., Aelmans, T.A.M., Hernandez, J.P.G., de Haan, A.B. Ionic liquid in extractive disillation of ethanol/water: from laboratory to pilot plant. In: Visser AE, Bridges NJ, Rogers RD. Ionic liquids: Science and applications. Washington DC: American Chemical Society, ACS Symposium Series, 2012:239-257.
2. Jork, C., Kristen, C., Pieraccini, D., Stark, A., Chiappe, C., Beste, Y.A., Arlt, W. *J. Chem. Thermodyn.* 2005, 37, 537-558.
3. Kamihama, C., Matsuda, M., Kurihara, K., Tochigi, K., Oba, S. *J. Chem. Eng. Data* 2012, 57, 339-344.
4. Li, Q.S., Zhang, J., Lei, Z.G., Zhu, J.Q., Zhu, J.J., Huang, X.. *Ind. Eng. Chem. Res.* 2009, 48, 9006-9012.
5. Pereiro, A.B., Araújo, J.M.M., Esperança, J.M.S.S., Marrucho, I.M., Rebelo, L.P.N. *J. Chem. Thermodyn*. 2012, 46, 2-28.
6. Tang, Y., Huang, H., Chien, I. *J. Chem. Eng. Jpn*. 2003, 36, 1352−1363.

Solvent-screening and characterization for reactive gas scrubbing

A. Radnjanski[1],*J.Pfaff*[1], *G. Ewert*[1], *M. Grünewald*[1]
[1]*Ruhr University Bochum, Bochum, Germany;*

Abstract

One of the challenges of solvent screening for CO_2 capture is to select a solvent that has low regeneration energy demand, fast absorption rate and high solvent stability. The aim of this work is to investigate novel amine blends and to demonstrate their impacts on the process performance. Furthermore, the goal is to understand the influence of each amine on the process performance in the blend and to show if individual amine properties can be combined. This is demonstrated with an example of an EDA (ethylenediamine)/ AMP (2 amino-2 methyl 1-etnaonol) blends. For that purpose, screening experiments were carried out involving measurement of the cycle capacity and degradation rate. Results show, that the combination of an amine with a high regeneration efficiency and stability, such as AMP with an amine that has fast reaction kinetics and high CO_2 affinity, such as EDA may well affect the overall absorption desorption process. Based on the experimental results the amine make-up due to the solvent degradation, required solvent circulation rate, as well as the required heat duty were predicted on an example of a 1000MW coal-fired power plant and a comparison between the individual amines and their blends was made

Keywords
CO_2 capture; Absorbent; Amine blends; Degradation;

1. Introduction

Among the CO_2 capture technologies, the reactive absorption with chemical solvents is considered to be a promising process for CO_2 capture from industrial flue gases. The amine-based solutions, used as solvents, have excellent effectiveness and efficiency to absorb CO_2 even from gases with low CO_2 concentration, but the main drawback of the aqueous amine solutions is their high regeneration energy demand and low solvent stability. Generally, the used solvents have to offer fast absorption kinetic, low regeneration demand, high absorption capacity and long term stability. Remarkably, no single solvent combining all these characteristics has been discovered yet. For that reason, the application of mixed amine solvents in CO_2 capture has recently gained interest.[1-3] In order to achieve a blend with a good performance, the influence of individual amines has to be taken into account.

The focus of this study is primary amines and their blends. EDA is a primary amine with two functional amino groups (NH_2), which makes this amine very reactive and thus able to effect high volume acid gas removal at a fast rate. Primary, sterically amine such as AMP has slower absorption rate, but its less reactive performance is characterized by lower stripping energy requirements compared to EDA and its degradation occurs at very low rates. Therefore, screening experiments involving measurement of the cycle capacity and degradation rate were carried out. For the estimation of the cyclic capacity, equilibrium loadings at different CO_2 partial pressures were measured. The cyclic capacity is important not only for a better

separation performance but also for the required solvent circulation rate. It also has an impact on the energy demand in the desorption column [4]. The degradation rate was determined with batch experiments as a function of Amine concentration, temperature and CO_2-loadings. Two kinds of degradation were investigated. The oxidative degradation, initiated by the presence of O_2 in flue gas and the thermal decomposition of the amines, caused by supplying heat in the regeneration step. The prediction and the control of the amine degradation is of large importance, because it results in an extensive amine loss, corrosion of the plant, increased operation problems, such as foaming and fouling and thus leading to significantly higher maintenance costs.

2. Results and discussion

2.1 Equilibrium CO_2-loadings

The equilibrium loadings at different CO_2 partial pressures were measured at temperatures of 40 and 120 °C, which represent absorption and desorption conditions, respectively. Equilibrium isotherms for pure 30 wt.% EDA und AMP solutions as well as two blends with concentration of 5,5 wt.%EDA-24,5 wt.%AMP and 15 wt.%EDA-15 wt.%AMP were measured. The obtained results are illustrated in figure 1. It can be seen that the achieved loading strongly depends on the CO_2 partial pressure. With increasing partial pressure of CO_2, the loading in the liquid phase also increases. Due to the two amino groups, EDA can reach a higher level of CO_2 loadings at 40°C, compared to AMP. Under desorption condition, a better regeneration efficiency of AMP can be observed. When sterically hindered amine (AMP) reacts with CO_2 forms an unstable carbamate, which is readily hydrolyzed, leading mainly to formation of bicarbonate ion, which can be easily regenerated. On the other site EDA builds stabile carbamate and for their regeneration more energy is required. Furthermore, the figure compares the equilibrium isotherms of the individual amines with their blends. It can be noticed that the blend with higher concentration of AMP has a poorer absorption performance and better regeneration efficiency, compared to the blend with the less AMP concentration, showing the bigger influence of AMP due to its higher concentration. It is obvious that the equilibrium isotherms of 15%EDA-15%AMP blend lie approximately in the middle between the isotherms of the pure amine solutions, illustrating the equal influence of each amine component of the blend.

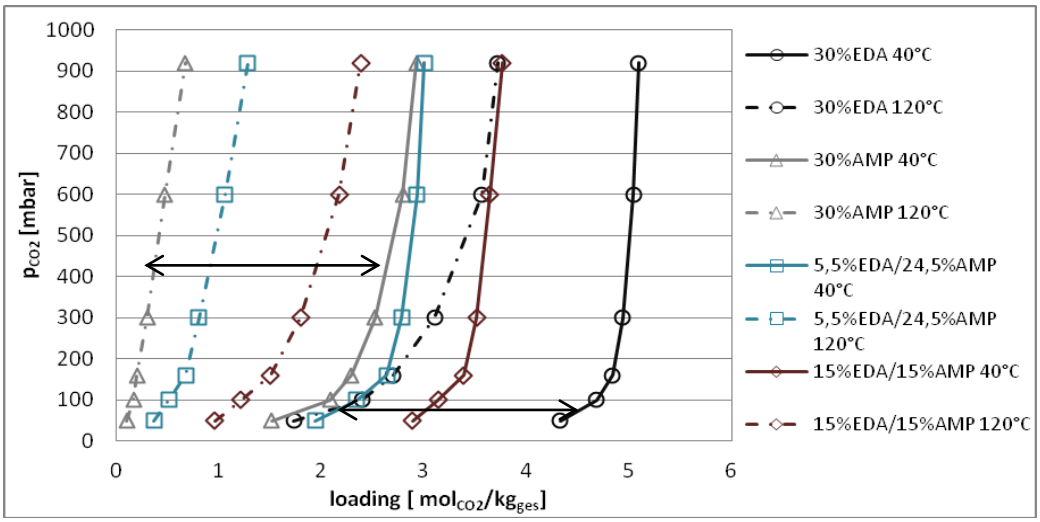

Figure 1: Equilibrium isotherms of pure and blended amine at 40 (solid lines) and 120°C (dashed lines)

The theoretical cycle capacity defined as the difference between the loadings at 40 and 120°C is an important parameter, as it determines the solvent flow rate. With increasing cycle capacity, the solvent flow rate decreases, leading to smaller process equipment. As can be seen in the figure 1, EDA has higher cyclic capacity than AMP, only at very low CO_2 partial pressures up to 180 mbar. At higher partial pressures, AMP shows better cyclic performance. The proper choice of the solvent strongly depends on the CO_2 partial pressure in gas feeds.
For the selection of a suitable solvent, not only the reached loadings, but also the time to achieve them is an important factor. The more time for the chemical reaction is needed, the higher the column has to be built, leading to higher investment costs. [4] In the absorber, the solvent does not reach the equilibrium loading because of the kinetic limitation of the process and thus cannot utilize the high cyclic capacity. Therefore, the reaction rate has to be considered. From the initial slope of the loading curves over the time, qualitative absorption rate can be obtained (figure 2). By comparing the slope of the curves the following order can be derived: 30 %EDA (100%) > 15%AMP/15%EDA (87%) > 5,5%EDA/24,5%AMP (71%) > 30%AMP (41%). It is obviously, that AMP reacts relatively slowly with CO_2 compared with EDA due to their different reaction mechanism, as it was already mentioned. For that reason the adding of EDA to an aqueous AMP solution enhances the reaction rate with CO_2.

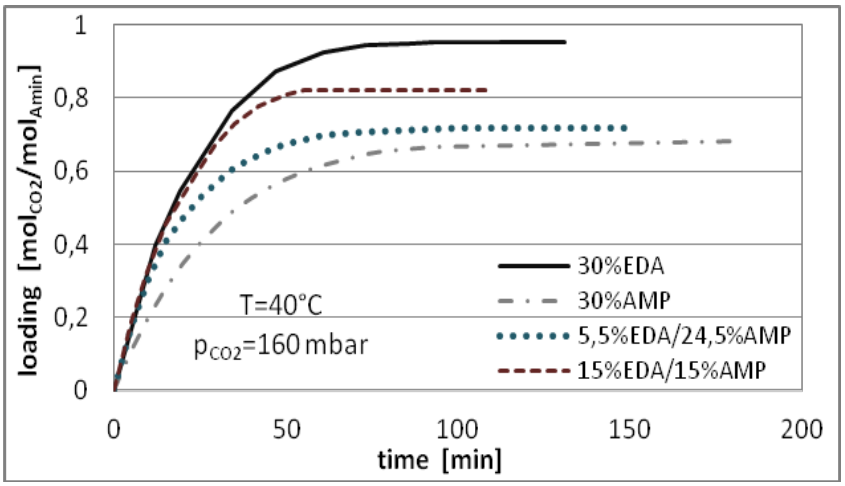

Figure 2: Equilibrium time-loadings curves

The results confirmed the conclusion of many research works, that the combination of an amine with a high regeneration efficiency, such as AMP, with an amine that has fast reaction kinetics and high CO_2 affinity, such as EDA, may well affect the overall absorption desorption process.

2.2 Degradation

Another important point, by selecting of an appropriate solvent, is the stability behavior of the amine solution. Therefore, the oxidative and thermal degradation rates were studied with batch experiments over the range of conditions. The extent of the degradation was calculated as percentage of compound loss τ. The degradation compounds are quantified by gas chromatography mass spectrometry (GC-MS) and the remaining amine concentration were analyzed using a high performance liquid chromatography (HPLC). Several previous studies have indicated that in the presence of O_2 and corrosion inhibitors, amine solvents can undergo oxidative

degradation at absorption conditions [5-8]. The focus of the oxidative degradation experiments was to investigate the behavior of the homogenous and blend amine systems under the influence of those parameters. Figure 3 illustrate the concentration-time curves of loaded with 0,5 mol_{CO2}/mol_{amin} amine solvents under the influence of O_2 and the catalytic effect of dissolved metallic Ions (Fe and Cu) at 55 °C. The results show that homogeneous amines, as well as, blended solvent are both resistant to oxidative degradation. This is confirmed through the constant concentration-time curves, figure 3.

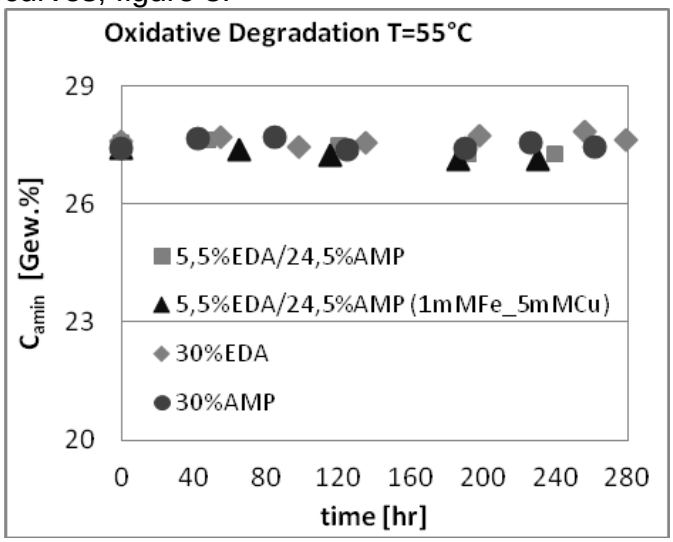

Figure 3: Oxidative degradation of homogeneous and blended amine solvent at 55°C

Under desorption condition the influence of the temperature and the CO_2-loading on the degradation rate was investigated. All analyzed amine systems at desorption conditions degrade in the presence of CO_2. The temperature has the largest effect on the degradation rate. An increase in 15 °C duplicates the loss of the bland over the course of the experiment, figure 4a, while increasing the CO_2 loading leads to increasing the degradation rate of approximately 4%, figure 4b.

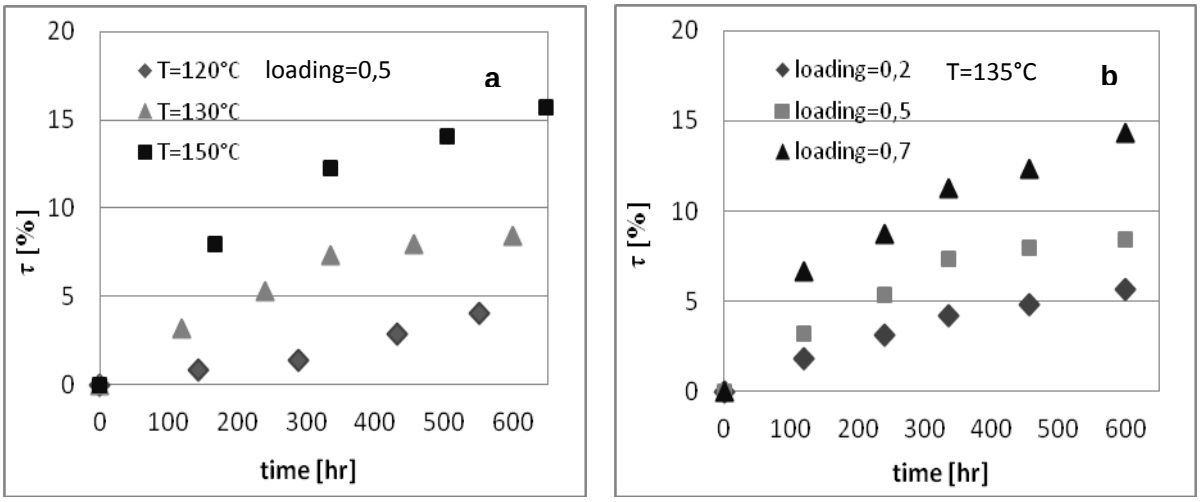

Figure 4: Degradation rates of 5,5%EDA/24,5%AMP with temperature (a) and loading (b)

The concept of using mixed amines is based on utilizing the advantages of each amine. The degradation behavior of amine blends compared, to the individuals amines is plotted in fig. 5.

Based on the figure we can observe that all aqueous amine solutions do degrade under desorption conditions. In terms of degradation potential, starting with the most degraded are: 30% EDA < 15%EDA/15%AMP < 5,5%EDA/24,5%AMP < 30%AMP. The results also demonstrate the same tendency of influence of the individual amine in the blends, as indicated in the experiments carried out for the equilibrium loading. This shows that by using mixed amines as solvent, the content of the single amine is one of the most important factors for utilization of the amine properties.

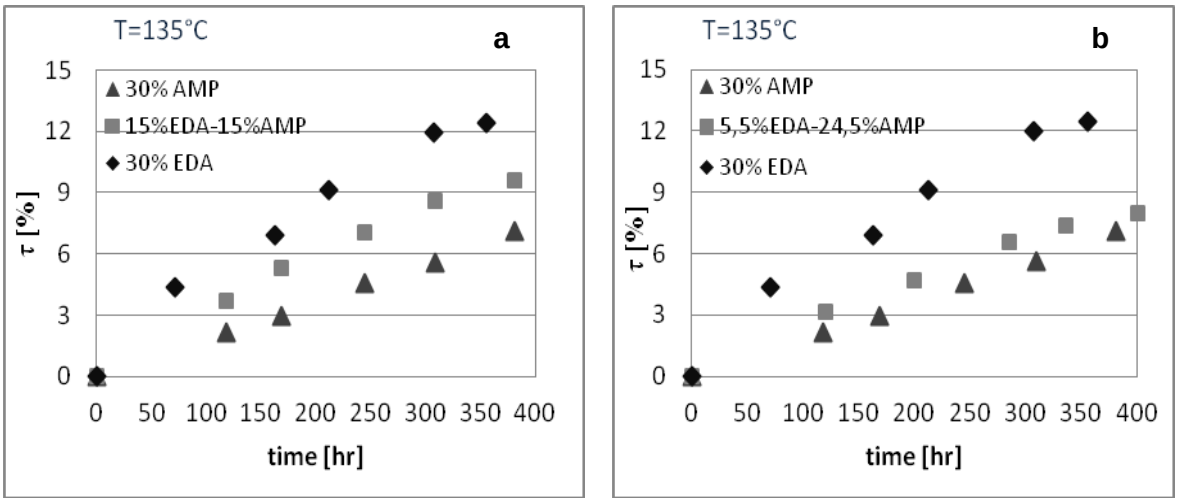

Figure 5: Comparison of degradation rates of homogeneous and blended amine at 135°C

Impact on process design

In order to show how the investigated amines affect the absorption desorption process, a comparison of the amine make-up due to solvent degradation, required solvent flow rate, as well as, the required heat duty are illustrated in figure 6. The experimental obtained degradation rates were used to predict the amine make-up caused by the solvents loss. Based on the measured equilibrium isotherms, two important process parameters can be calculated: solvent circulation rate and specific reboiler heat duty, using the modified Kremser model [9]. These calculations were derived from example of a 1000 MW coal-fired power plant with 16 vol.% CO_2 and 90% CO_2 separation.

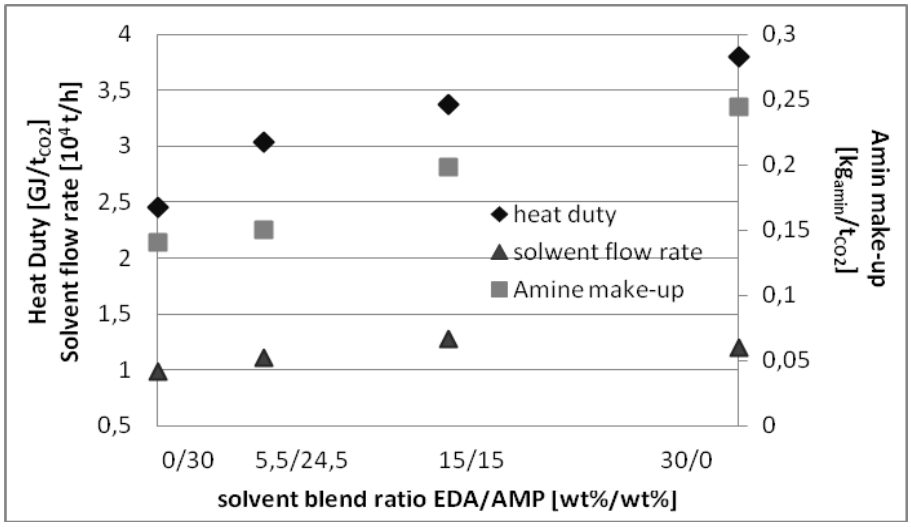

Figure 6: Comparison of heat duty, solvent demand and amine make-up

Based on the results in figure 2 and figure 6 can be seen, that the main disadvantage of AMP is its slow reaction kinetic. Aqueous EDA solution has high absorption kinetic but the effectively performance with regard to the other important parameter is not sufficient. Therefore, the solvent performance of EDA/AMP blends decreases with increasing EDA concentration in the blend. Considering the results, 5,5%EDA/24,5%AMP blend can be seen as a promising solvent for CO_2 capture achieving moderate absorption rate combined with low circulation and degradation rate, as well as, low heat duty demand. In comparison with the most used and investigated CO_2-Absorbent monoethanolamine (MEA), the amine blend of 5,5%EDA/24,5%AMP has to up 30% less energy duty and 43% less solvent flow rate than 30%MEA. In addition to that, the amine make-up demand of the blend is up to 116% less then MEA. Regarding the absorption kinetic, the blend has approximately 28% slower reaction kinetic compared to MEA.

3. Conclusions

This work shows that with mixing of different amine structures, it is possible to emphasize the positive characteristics of the individual amines and to suppress their disadvantages. In the search of a blended amine solvent for CO_2 capture, the type of the individual amines and the composition of the blend have to be considered. The optimum blending ration of EDA and AMP considering the important process parameters was evaluated and showed that the proper choice and composition of the blended amine structures can be a powerful tool for the process optimization.

References

[1] Aroonwilas A, Veawab A. Characterization and comparison of the CO_2 absorption performance into single and blended alkanolamines in a packed column. Industrial & Engineering Chemistry Research 2004; 43: 2228–2237.

[2] Zhu D, Fang M, Lv Z, Wang Z, Lou Z. Selection of blended solvents for CO_2 Absoprtion from coal-fired flue gas. Part1: Monoethanolamine (MEA)-based solvents. Energy & fuels 2012; 26: 147-153.

[3] Adeosun A., El Hadri H, Goetheer E, Abu-Zahra M R M. Absorption of CO_2 by Amine Blends Solution: An Experimental Evaluation. International Journal of Engineering And Science 2013; 3: Issue 9: 12-23.

[4] Schäffer A, Brechtel K, Scheffknecht G. Comparative study on differently concentrated aqueous solutions of MEA and TETA for CO2 capture from flue gases, Fuel 2012; 101: 148-153.

[5]Gouedard C, Picq D, Launay F, Carette P-L. Amin degradation in CO_2 capture. I. A review. International Journal of Greenhouse Gas Control 2012; 10: 244-270.

[6] Lepaumier H, Picq D, Carrette P L. Degradation Study of new solvents for CO_2 capture in post-combustion, Energy Procedia 2009; 1: 893–900.

[7] Bedell S A. Oxidative degradation mechanisms for amines in flue gas capture. Energy Procedia 2009; 1: 771-778.

[8] Sexton A J,Rochelle G T. Catalysts and Inhibitors for MEA Oxidation. Energy Proced 2009; 1: 1179-1185.

[9] Notz R J. CO_2-Abtrennung aus Kraftwerksabgasen mittels Reaktivabsorption. Stuttgart, Univ. Diss. 2009.

Study of the potential of new hybrid solvents for the post-combustion CO_2 capture process

*Julien Gervasi, Lionel Dubois and Diane Thomas**

Chemical Engineering Department, Faculty of Engineering, University of Mons,

*Rue de l'Epargne, 56, 7000 Mons, Belgium, *Diane.Thomas@umons.ac.be*

Abstract

In the context of reducing industrial CO_2 emissions by the post-combustion CO_2 capture process applying chemical absorption, many studies aim at finding new solvents that can replace the conventional ones, such as aqueous solutions of monoethanolamine (MEA), especially to reduce the operating costs and the global energy requirement of the process. In this paper, we focused on the hybrid solvents. These ones result from the mixing between a chemical (usually an amine) and a physical (ether, alcohol, etc.) solvent. Compared to other studies, our approach was based on the use of acetals as physical solvents.

Globally, this work confirms that these new hybrid solvents, composed of amine and acetal, seem to be a very promising alternative to classical solvents but such systems still need more investigations in order to optimize the solvent composition and to better understand the demixing phenomenon observed. After the selection of the most promising hybrid solvents, absorption-regeneration tests will be performed with a micro-pilot unit.

Keywords

CO_2 capture, post-combustion, hybrid solvents

1. Introduction

Today, we are facing the climate imbalance due to greenhouse gases emissions, like CO_2, most emitted gas by the transport and the industries (cement plant, power plant, etc.). In order to reduce CO_2 emissions, there are solutions like the CO_2 capture and its use or conversion in a chemical process, or its geological storage.

Nevertheless, these points need a quite pure CO_2 flow that can be obtained with different process. In the "Carbon Capture and Storage (CCS)" concept, we focused on the post-combustion capture process, an "end of pipe" technology which does not need any modification of the industrial process itself. The overall capture unit is made up of two columns. The first one, namely the "absorption column", is used to absorb the CO_2 into a solvent like the benchmark MEA (monoethanolmine) 30% wt. After this first step, the loaded solvent is regenerated in a "stripper" by heating it (in a reboiler) to its boiling point to produce a quite pure CO_2 gas flow and a lean solvent which is reused in the absorption column. This CO_2 capture process shows high operating costs, especially regarding the heating energy needed for the solvent regeneration at the stripper (around 3.5 GJ/tCO_2 [1-3] for the benchmark MEA 30%). To reduce this energy consumption, many studies try to find a new solvent that can solve this issue. In this purpose, among the different solvents possibilities, our work focuses on the hybrid solvents. These result of the mixing between a chemical solvent (classically an amine) and a physical solvent (ethers, alcohols, etc.). Such solvents bring the advantages of each component: the low regeneration energy of the physical solvent, the high absorption capacity of the physical solvent at moderate CO_2 partial pressures, the

better absorption performances of the chemical solvents at low CO_2 partial pressures and the high absorption kinetics due to the chemical reaction with CO_2.The innovative aspect of our work is the use of acetals as physical part of the hybrid solvent. Such compounds, which can be described as two ether groups attached to the same carbon, are already used in various applications (painting, pharmaceutical chemistry, cosmetics, etc.) that makes them quite cheap. Among the acetals available, first screening tests reveal that the focus should be put on the 2,5,7,10 -Tetraoxaundecane (TOU) as physical compound of the hybrid solvent. Regarding the chemical part of the solvent, different amine based compounds were considered, namely the monoethanolamine (MEA), the diethanolamine (DEA), the methyldiethanolamine (MDEA), the 2-amino-2-methyl-1-propanol (AMP) and also the piperazine (PZ) as absorption activator. In order to characterize and compare new hybrid solvents in terms of absorption and regeneration performances, two types of experiments were performed in our study.

2. Experimental devices and procedures

2.1 Absorption experiments

The apparatus used for the comparison of the absorption performances measured with different hybrid solvents includes a gas-liquid contactor, a gas supply, and a gas sampling part, illustrated on Figure 1. The gas-liquid contactor, namely a glass double-stirred cell reactor (0.15 m in diameter and 0.245 m in tank height) has a constant gas-liquid interfacial area. It has six lid holes: two for the gas inlet and outlet, two for the liquid temperature probe (type Pt100) and for the electronic pressure probe for the gas phase, and the two last for the gas stirring bar (helical shape of 5 cm, located in the upper part of the reactor) and for the liquid stirring bar (PTFE anchor with a wingspan of 8 cm, located in the lower part) agitated separately by two stirring motors. The reactor is pre-filled with 1 10^{-3} m^3 of the solution to be tested. The jacket of the cell is flowed by water coming from an external thermostating system whose heating power is automatically controlled providing the desired solution temperature within the cell. The absorption solution is stirred to ensure proper mixing of the liquid phase but also to maintain a perfectly flat gas-liquid interface (without wrinkles). The gas phase, previously humidified in a gas bubbler, is composed of N_2 and CO_2 at the desired concentration ($y_{CO2,in}$ = 10 vol. %) and is continuously fed into the reactor.

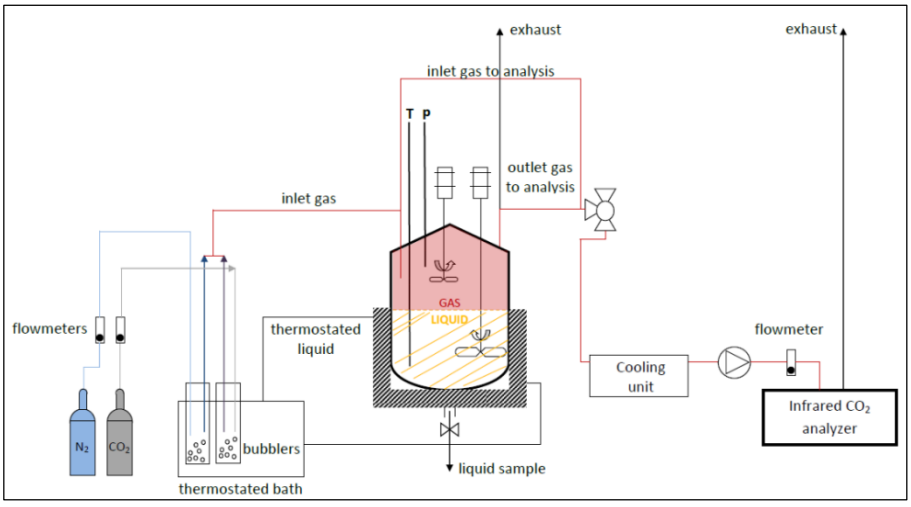

Figure 1: Double-stirred cell reactor used for the absorption tests

The total inlet gas flow rate is metered by a rotameter. Sampling of gas at the input and the output of the contactor is performed continuously through a cooling unit followed by an IR analyzer (Fuji Electric, model: ZRJ-3) giving respectively the temporal evolution of $y_{CO2,in}$ and $y_{CO2,out}$ and allowing to calculate the temporal evolution of the CO_2 absorption ratio (A) for different scrubbing solutions:

$$A(t) = (G_{CO2,in} - G_{CO2,out}(t)) / G_{CO2,in} = (y_{CO2,in} - y_{CO2,out}(t)) / (y_{CO2,in}(1-y_{CO2,out}(t))) \quad (1)$$

where $G_{CO2,in}$ and $y_{CO2,in}$ are respectively the CO_2 flow rate and volume fraction in the gas phase at the inlet of the contactor, $G_{CO2,out}$ and $y_{CO2,out}$ being the CO_2 flow rate and volume fraction in the gas phase at the outlet of the contactor. All semi-continuous tests reported here were carried out at atmospheric pressure and at a temperature equal to 298 K. Hydrodynamic conditions, namely gas flow rate (8.33 10^{-5} m³/s) and stirring speeds (35 rpm for the liquid phase and 500 rpm for the gas phase), were kept constant in all the experiments, comparing only the use of different chemical and hybrid solvents. For the liquid phase, samples of the solvent were analysed in terms of pH (pH meter Mettler Toledo, electrode LE438 in polypropylene) and by a Total Organic Carbon analyser (Shimadzu, TOC-VCSH, NDIR detector) which gives informations about the concentration of inorganic compounds, leading to the quantity of CO_2 absorbed per volume unit of solvent.

2.2 Regeneration experiments

The regeneration tests were performed in the device presented on Figure 2. It is composed of a three-necked flask of 0.25 10^{-3} m³, a thermo-regulated heating system (Ika, RCT Basic, maximum heating power of 600 W) with a Pt100 temperature sensor immersed in the solution and a magnetic stirring system (operating stirring speed of 500 rpm) to ensure the homogeneity of the liquid phase. A condenser (length of 0.35 m) installed at the top of the flask and flowed by cooling water (278 K) provided by an external cooling system aims at condensing the vapor products issued from the evaporation of the aqueous CO_2-solvent solution. In a first step, the hybrid solvent is gradually loaded with CO_2 up to its saturation thanks to a gas bubbler flowed by a pure CO_2 flow rate. At the end of the saturation step, the pH of the loaded solvent is measured and its CO_2 concentration (in terms of inorganic carbon concentration, IC (0) [mg C/m³]) is determined with theTOC analyser. The solution (volume of 0.25 10^{-3} m³) is then transferred in the regeneration cell in which it is stirred (stirring speed of 500 rpm) and heated (constant heating power of 600 W) up to its boiling point. The duration of the test was fixed at 120 min. During the test, samples of the solution are regularly withdrawn and analyzed to determine their pH and their CO_2 concentration (C_{CO2} [mol/m³]) deduced from the inorganic carbon content, IC (t) [mg C/m³]) allowing

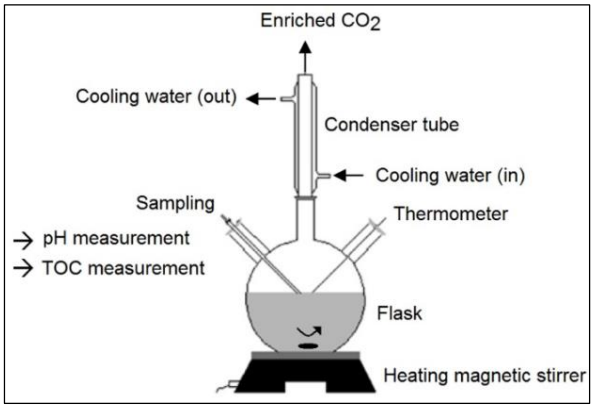

Figure 2: Regeneration apparatus

to deduce the regeneration efficiency ($\eta_{regen}(t)$) (t)) of the solution, conventionally defined as:

$$\eta_{regen}(t) = (IC\ (t) - IC\ (0)) / IC\ (0) \quad (2)$$

Although such tests do not give direct access to the regeneration energy of the hybrid solvents, the comparison of the temporal evolution of the regeneration efficiency at identical operating conditions can advantageously allow evaluating the regeneration potential of such solvents.

3. Results and discussion

The absorption and regeneration results obtained with various hybrid solvents are compared to the MEA 30 wt.% ones (reference solvent). The proportion of 2,5,7,10 - Tetraoxaundecane - TOU (physical part of the solvent) and the amine (chemical part of the solvent) were chosen taking another existing hybrid process as reference, namely the Sulfinol [4] one. The tested systems were generally made of 30 wt.% of amine, 35 wt.% of TOU and 35 wt.% of water.

3.1 Absorption results

The first absorption tests were performed with the reference solvent (MEA 30%) and the temporal evolution of the absorption performances is compared to the hybrid solvent one (composed of MEA 30% and TOU 35%) on Figure 3 (a). The initial absorption performances of the hybrid solvent are clearly better than the MEA 30% ones (53% against 31%). Unfortunately, the absorption performances decrease dramatically during the absorption test. This phenomenon can be linked to the progressive apparition of a layer in the solvent at the gas-liquid interface. As illustrated on Figure 3 (b), this layer is becoming bigger while the CO_2 is absorbed by the solvent but this demixing phenomenon prevents the CO_2 to be directly absorbed into the solvent which leads to the decrease of the absorption performances. This is linked to the particular hydrodynamics of our contactor.

Additional tests like TOC/IC/pH measurements and FTIR (Fourier Transform Infrared Red spectroscopy) analyses, show that the light phase was poor in CO_2 and mainly composed of TOU, and that the heavy phase was rich in CO_2 and mainly composed of MEA. In an industrial process, it is possible to take advantage of the demixing phenomenon, as for example in the DMX^{TM} process [5-6]. Figure 3 (a) also illustrates that the C_{CO2} (in the heavy phase) is logically increasing more quickly for the hybrid

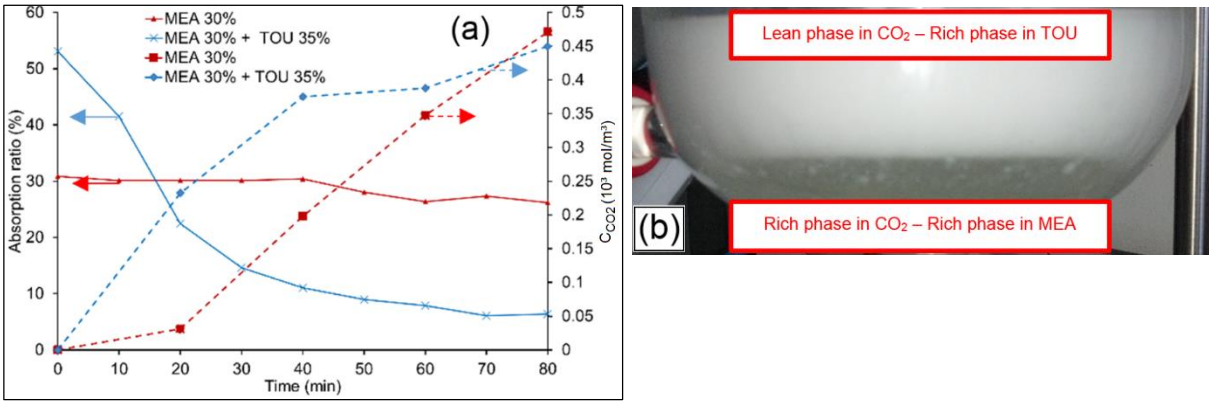

Figure 3: (a) Temporal evolution of the absorption ratio and of the CO_2 concentration measured with MEA 30% and MEA 30% + TOU 35% solvents (b) Demixing phenomenon illustrated with pure CO_2 bubbling

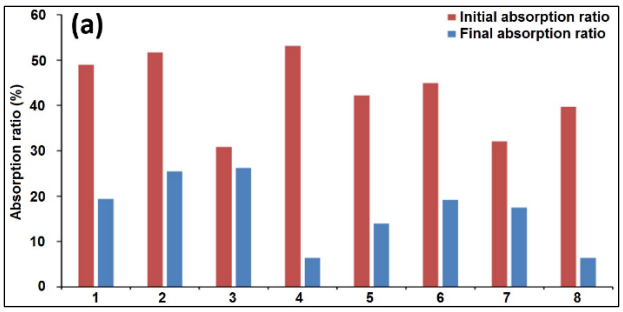

(b)	N°	Solvent (aqueous solution)	Final C_{CO2} (10^3 mol/m³)
	1	AMP 20% + PZ 10%	0.63
	2	AMP 20% + PZ 10% + TOU 35%	0.92
	3	MEA 30%	0.47
	4	MEA 30% + TOU 35%	0.45
	5	MDEA 20% + PZ 10%	0.41
	6	MDEA 20% + PZ 10% + TOU 35%	0.43
	7	DEA 20% + PZ 10%	0.37
	8	DEA 20% + PZ 10% + TOU 35%	0.40

Figure 4: (a) Initial and final absorption ratio of different amine(s) based and hybrid solvents (b) Final CO_2 concentration of the different solvents tested

solvent than for MEA 30%, the final CO_2 concentrations being almost identical (around 0.45 10^3 mol CO_2/m^3).The absorption performances of different hybrid solvents are compared in terms of initial (unloaded solution) and final (loaded solution) absorption ratios, and in terms of final CO_2 concentration on Figure 4 (a) and (b) respectively. For all the systems where a similar demixing phenomenon was observed, the initial absorption performances of the hybrid solvents (with TOU 35%) are better than the amine(s) based solvents ones, especially for MEA 30% and DEA 20% + PZ 10%. The decrease of the absorption ratio due to the CO_2 loading of the solution is also clearly illustrated, especially in the presence of TOU. The best final absorption performances of hybrid solvents were measured with the blend composed of AMP 20% + PZ 10% + TOU 35%, this solution leading to the highest final CO_2 concentration (namely 0.63 and 0.92 10^3 mol CO_2/m^3 for the solvent without and with TOU, see Figure 4 (b)), all the other C_{CO2} being in the range 0.37 to 0.47 10^3 mol CO_2/m^3.

3.2 Regeneration results

The regeneration performances of different solvents are compared in terms of temporal evolution of the CO_2 concentration (C_{CO2}) and of the regeneration efficiency (η_{regen}) on Figure 5 (a) and (b) respectively.

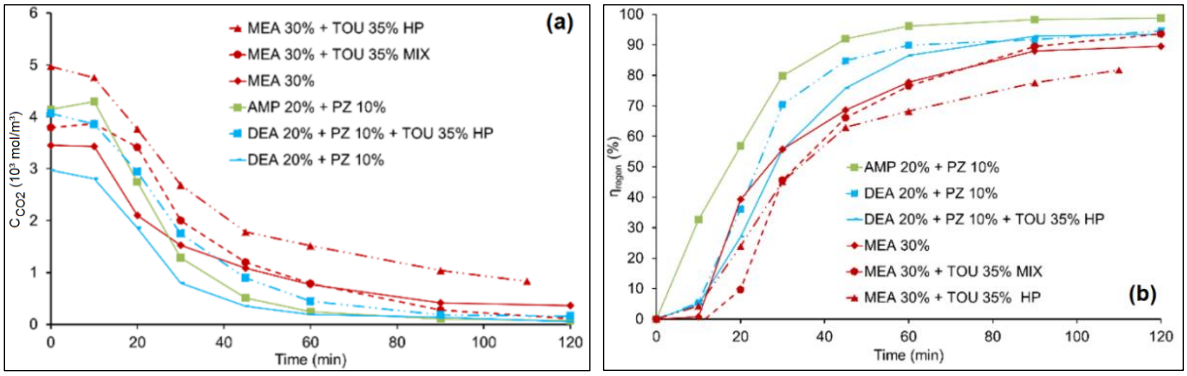

Figure 5: Temporal evolution of C_{CO2} (a) and of η_{regen} (b) of the solvents

Note that the regeneration of the AMP 20% + PZ 10% + TOU 35% solution was not possible due to crystallization problems during the saturation step before the regeneration test. Moreover, two types of regeneration tests were performed with MEA 30% + TOU 35%: with the mix of the two phases (noted “MIX” in the graph legend) and by regenerating the heavy phase only (noted “HP” in the graph), namely the CO_2 rich phase. Regarding the blend composed of DEA 20% + PZ 10% + TOU 35%, only the heavy phase was regenerated. It can be observed on Figure 5 (a) and (b) that logically, C_{CO2} is decreasing during the regeneration test which lead to an increase of the regeneration efficiency. The highest initial CO_2 concentration was measured with the MEA 30% + TOU 35% HP solution (namely 4.97 10^3 mol CO_2/m^3) and the lowest with

the DEA 20% + PZ 10% solution (2.97 10^3 mol CO_2/m^3). This parameter gives an idea of the absorption capacity of the solution.
Regarding more specifically the final regeneration efficiency, the best performances were measured with the AMP 20% + PZ 10% solution (η_{regen} around 99%). Concerning the hybrid solvents, η_{regen} (around 95%) for DEA 20% + PZ 10% + TOU 35% HP and for MEA 30% + TOU 35% MIX are higher than for MEA 30% (around 90%). Note that even if η_{regen} for MEA 30% + TOU 35% HP (82%) is lower than the one of the mixed phase solution, the interest of regenerating only the rich phase is already confirmed in other studies [5-6] in terms of lower energy consumption linked to a lower liquid flow rate fed into the regeneration column.

4. Conclusions

This work was carried out with the purpose of highlighting new solvents than can replace the conventional ones, such as MEA, for the post-combustion CO_2 capture process by chemical absorption. The innovative aspect of this study was the use of acetal, and especially the TOU, as physical part of new hybrid solvents composed of amine(s) based compound(s). In order to compare the absorption and regeneration performances of the solvents two types of experiments were performed. Firstly, a double stirred cell reactor was used to compare the absorption efficiencies of the solvents with fixed operating conditions at 298 K. From all the screening tests performed with different blended solutions (composed of a conventional amine such as MEA, DEA, MDEA, AMP, PZ and TOU), it was highlighted that the addition of the acetal compound improves significantly the absorption efficiencies, especially at the beginning of the test (at low CO_2 loadings of the solution). Indeed, the results showed a decrease of the performances with an increase of the CO_2 loading of the solution which is partially linked to a demixing phenomenon and which is still under investigations.
Secondly, regeneration tests of some chemical and hybrid solvents were performed with the use of a regeneration cell allowing to compare regeneration efficiencies of the solvents at a fixed heating power. The promoter effects of the acetals were also highlighted in terms of higher cyclic capacities and better regeneration efficiencies in comparison with MEA 30% ones.
Globally, even if such hybrid solvents still need more investigations, this work confirms that the new hybrid solvents, composed of amine and acetal, seems to be a very promising alternative to classical solvents. As perspectives of this work, after the selection of the most promising hybrid solvents, absorption-regeneration tests will be performed with a micro-pilot unit and the solvents will be analyzed in the light of other characteristics which are important regarding the industrial application (such as the corrosivity or the volatility).

Acknowledgements

J. Gervasi is grateful to the Chemical Engineering Department of the University of Mons, for this research achieved during his master's thesis and research fellowship.

References

[1] M. Karimi et al., *Chem. Eng. Res. Des.*, 2011, 89 (8), 1229.
[2] J.N. Knudsen et al., *Energy Procedia*, 2009, 1, 783.
[3] P. Moser et al., *Energy Procedia*, 2011, 4, 1310.
[4] M. T. Angaji et al., *J. Nat. G. Sci. Eng.*, 2013, 15, 22.
[5] L. Raynal et al., *Energy Procedia*, 2011, 4, 779.
[6] L. Raynal et al., *Chem. Eng. J.*, 2011, 171 (3), 742.

A pilot plant study investigating the effect of process parameters on CO_2 capture with MEA solutions

C.E. Schwarz, J.J. Miskin, L.R. Kritzinger, L.H. Callanan, J.H. Knoetze*
Department of Process Engineering, Stellenbosch University
Private Bag X1, Matieland, 7602, South Africa
** Tel: +27 21 808 4487 Fax: +27 21 808 2059, E-mail: cschwarz@sun.ac.za*

Abstract

The purpose of this paper is to describe a pilot plant for CO_2 capture studies and to investigate the effect of process parameters on the CO_2 capture feasibility using a 30 weight % MEA solution. A pilot plant set-up for CO_2 capture studies has been designed, constructed and verified. The set-up consists of two 200 mm diameter interlinked columns (absorber and stripper) with a heat exchanger for energy integration and a CO_2 gas recycle loop. The set-up has been designed for use with various solvents and a range of CO_2 feed gas compositions and L/G ratios. Experiments conducted at similar operational conditions as in the literature gave similar results thus proving reliable data can be generated on the pilot plant. The regeneration energy requirements for the CO_2 removal was investigated at a range of CO_2 feed gas compositions and a range of L/G ratios, all at a 90 % CO_2 removal efficiency and values varied between 4 and 15 MJ/kgCO_2 removed. The results showed that less regeneration energy is required per unit CO_2 removed for higher CO_2 compositions in the feed as well as at high L/G ratio. Additionally, by lowering the capture efficiency less regeneration energy is required.

Keywords

CO_2 capture, experimental, pilot plant, monoethanol amine (MEA)

1. Introduction

An exponential increase in anthropogenic CO_2 emissions in the last 150 years, together with a reduction in natural carbon sinks such as forests, have disrupted the carbon cycle and resulted in an increase in the CO_2 concentration in the atmosphere. A significant amount of these CO_2 emissions result from the combustion of fossil fuels, mainly for energy and transportation purposes. While alternative energy sources are becoming increasingly popular and implementation more widespread, the world will still be dependent on the combustion of fossil fuels throughout at least the 21st century. In particular, power generation is still heavily dependent on coal-fired plants. In 2008, 41 % of global electricity was generated via coal combustion [1]. While it is expected that this figure will drop in the future, predictions are that by 2035 approximately 32 % of global electricity will still be generated by coal fired power plants [1]. Typically flue gas emissions from natural gas and coal fired power stations range between 3 and 12 v/v % of CO_2. Considering the amount of CO_2 produced,

even partial capture of this CO_2 would significantly reduce the amount of CO_2 released to the atmosphere.

Reactive absorption of the CO_2 is currently being considered as a possible method to reduce the CO_2 emissions. Even though it may not be the optimum solvent, the majority of studies have been conducted using an aqueous mono-ethanol amine (MEA) solution, usually a 30 weight % solution. While a significant amount of work has been conducted on the underlying chemistry of the reactive absorption process, only a limited number of studies considering the effect of the process parameters and set-up have to date been considered. As the feasibility of a post-combustion CO_2 capture process is dependent on the process parameters and set-up, it is vital to understand the influence of the process parameters. Studies can be conducted on process simulators, yet real hydrodynamic and mass transfer efficiencies as well as equipment needs to be investigated. In particular, pilot and demonstration plant scale studies are vital in understanding the underlying interactions and behaviour of the CO_2 capture systems.

The aim of this paper is to, firstly, present a pilot plant that is able to investigate the process parameters and set-up of a post-combustion CO_2 capture process and, secondly, to determine the regeneration energy required for the capture of CO_2 using a 30 weight % MEA solution as a function of the feed CO_2 content, the liquid to gas (L/G) ratio and the CO_2 removal efficiency.

2. Experimental set-up

2.1 Requirements for set-up

The overarching aim of the pilot plant set-up is to conduct CO_2 capture studies for a range of solvents and feed gas compositions using a range of column internals and hydrodynamic conditions (L/G ratios and column loadings). As such a counter-current absorption column interlinked with a regeneration stripping column equipped with a reboiler is required. A heat exchanger between the two columns is also necessary to incorporate heat integration. While initially designed and commissioned using an aqueous MEA solution, the column should be able to operate with a range of reactive solvents provided regeneration can occur at temperatures below 150 ^{o}C.

The column diameter should be a balance between a larger diameter that is more representative of industrial applications and a smaller diameter where experiments are not as costly to run. The packed height of the absorption column should be sufficient for 95 % CO_2 removal with a feed gas containing 15 % CO_2, but removal should not exceed 99 %. Liquid and gas sample points are required at a number of locations with the possibility of online CO_2 and O_2 gas sampling. The column should be able to operate at L/G ratios of 0.5 to 3 (mass basis) and a lean solvent loading of up to 0.25 (mole basis). The CO_2 removed from the absorbent in the stripper column needs to be recycled to reduce operating costs and a surge tank is required to dampen gas fluctuations and improve control of the gas recycle loop. A wash-water section at the top of the absorption column is required to remove any entrained MEA before the cleaned gas is vented to the atmosphere.

2.2 Pilot plant set-up

Within the requirements outlined above, a pilot plant set-up was designed and constructed. A schematic representation of the pilot plant is given in Figure 1 and the column specifications are summarized in Table 1. The pilot plant consists of two columns (absorber column (E203), the stripper column (E105)), each with a diameter of 200 mm and a packed height of 3.68 m and 4.16 m, respectively. Auxiliary equipment includes the intergrated heat exchanger (E208), the surge tank (E205) and the gas blowers (E201A and E201B) as well as a range of pumps, valves and other equipment. The present study was done with Flexipak 250 Y.

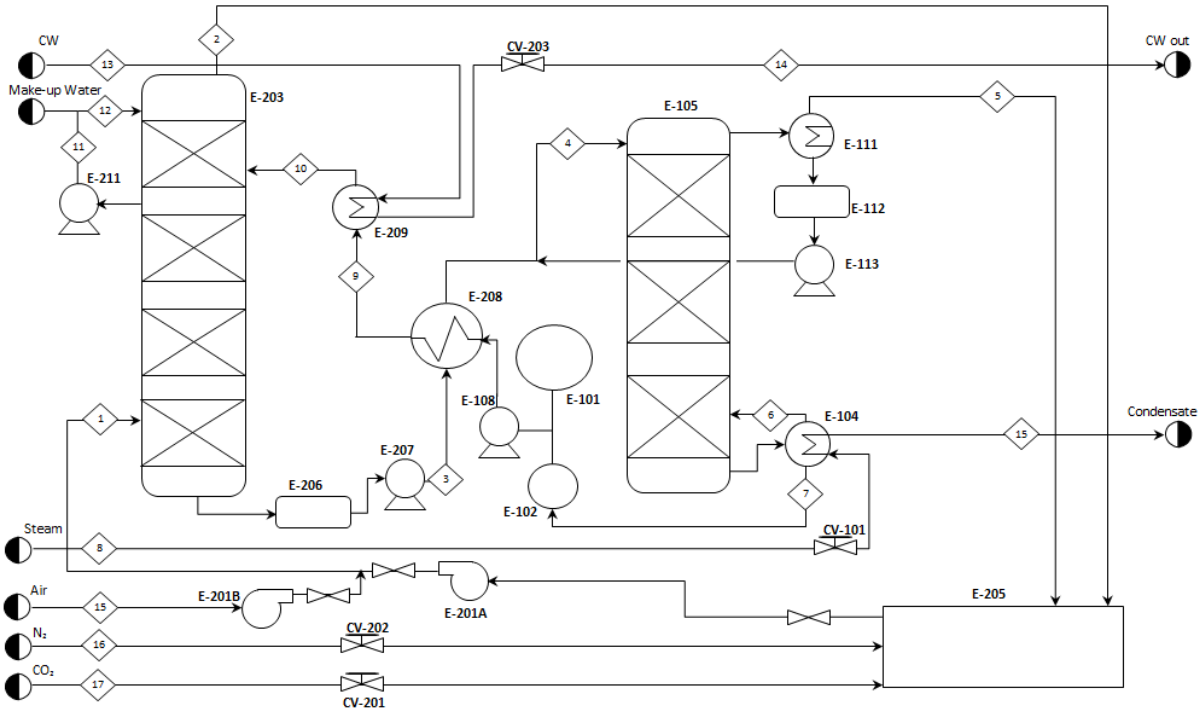

Figure 1: Schematic representation of pilot plant set-up

Table 1: Pilot plant specifications

Absorber column diameter	200 mm
Absorber column packed height	3.68 m
Absorber column packing	Flexipak 250 Y
Stripper column diameter	200 mm
Stripper column packed height	3.68 m
Stripper column packing	Flexipak 250 Y
Liquid flow rate range	150 to 650 kg/h
Gas flow rate range	100 to 700 kg/h

2.3 Verification of set-up

The system was verified by comparing the CO_2 concentrations and temperature profiles obtained in the absorber with similar studies reported in the literature. As the different studies used different set-ups, the influence of the set-up and variations in results thereof were accounted for through Aspen Plus ® simulations. At high capture efficiencies (92 % experimental, 90 % literature), similar concentration profiles to those of Mangalapally and Hasse [2] were obtained. Additionally, at low capture efficiencies (55 % experimental, 50 % literature) similar concentration profiles to those of Notz et al. [3] were obtained. Also, for similar operating conditions, albeit using different column internals, similar regeneration energy profiles to that of Notz et al. [3] were obtained. However, in all cases slightly different set-ups using different packing materials were used. To account for the variations in the set-up an Aspen Plus ® model was built and the model successfully predicted the behaviour of the various set-ups and accounted for the behavioural differences between the studies. Further details regarding the verification of the set-up can be found in Kritzinger [4].

3. Results and discussion

The purpose of a CO_2 capture plant is to remove CO_2 from, amongst others, flue gas from coal fired power stations before it is released to the atmosphere. The CO_2 removal process is energy intensive and thus one needs to minimize the amount of energy required to regenerate the solvent. Experiments were conducted at 90 % CO_2 removal for a range of liquid and gas flow rates and for a range of CO_2 feed compositions. The regeneration energy requirements for these conditions are shown in Figure 2. Trends from Figure 2 indicate that an increase in L/G ratio as well as a higher CO_2 concentration in the feed results in less regeneration energy required per kg CO_2.

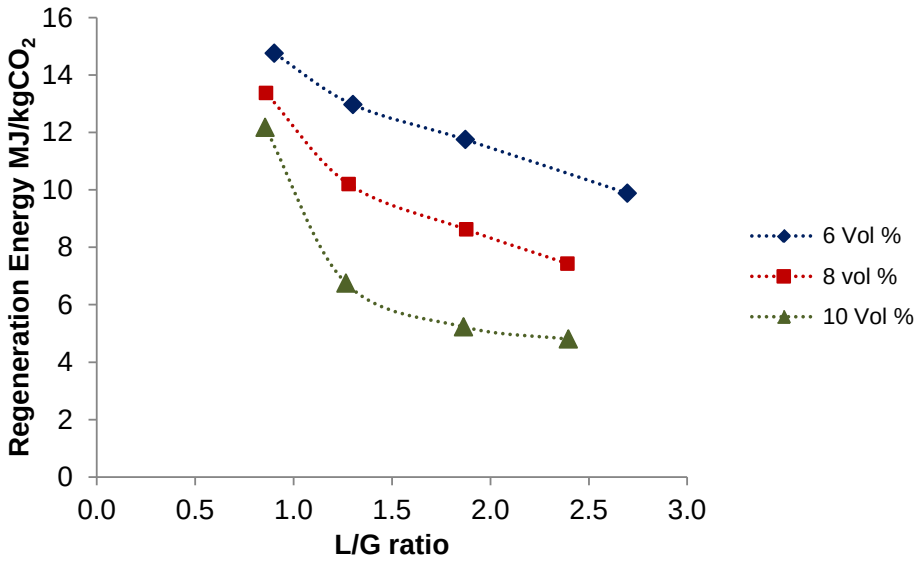

Figure 2: Regeneration energy as a function of L/G for three CO_2 inlet concentations at 90 % CO_2 removal efficiency

Figure 3 shows the effect of the CO_2 removal efficiency on the regeneration energy requirements at a L/G ratio of 2 and a CO_2 inlet concentration of 9 vol %. It is clear that at lower CO_2 removal efficiencies less energy is required per unit CO_2 removed.

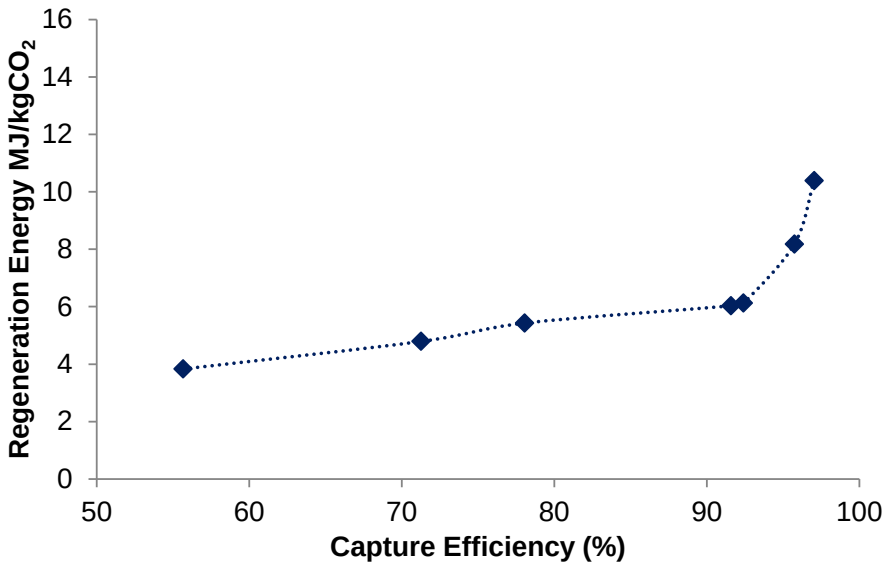

Figure 3: Regeneration energy as a function of CO_2 removal efficiency at L/G = 2 and and a CO_2 inlet concentation of 9 vol %

From the trends observed in Figure 2 and Figure 3 it is clear that at certain operating conditions less energy is required per unit CO_2 removed. Typically, at a specific CO_2 inlet concentration, the process requires less energy at higher L/G ratios and lower capture efficiencies. However, from a hydrodynamic point of view, the L/G ratio will effect the optimum column diameter. Selection of the L/G ratio would therefore be an optimization problem based on a balance low capital costs and low energy requirements. The results also clearly show that up to approximately 90 % CO_2 removal, the regeneration energy requirements per unit CO_2 removed does not significantly change with capture efficiency. However, as with many separation processes removal of the last amounts of CO_2 requires large energy inputs.

4. Conclusions

A versatile CO_2 capture pilot plant set-up was designed, constructed and, using literature information in conjunction with an Aspen Plus ® model verified. The effect of the L/G ratio on the energy required for the solvent regeneration was investigated and it was found that at 90 % CO_2 capture efficiencies for feed gas compositions between 6 and 10 v/v% CO_2 and at L/G ratios between 0.9 and 2.4 regeneration energies between 4 and 15 MJ/kg were required with lower regeneration energies at higher L/G ratios and for higher CO_2 feed compositions. Additionally, the lower the capture efficiency, the lower the regeneration energy per unit CO_2 removed. Future studies will investigate the interaction of the parameters and consider other MEA concentrations and other absorbents, all in an attempt to reduce solvent regeneration energy.

Acknowledgements

This work is based on the research supported in part by the National Research Foundation of South Africa (Grant specific unique reference number UID 83966) and Sasol Technology (Pty) Ltd. The authors acknowledge that opinions, findings and conclusions or recommendations expressed in any publication generated by the supported research are that of the authors, and that the sponsors accept no liability whatsoever in this regard. Aspen Plus ® is a registered trademark of Aspen Technology Inc.

References

[1] M.E. Boot-Handford, J.C. Abanades, E.J. Anthony, M.J. Blunt, S. Brandani, N. Mac Dowell, et al., Carbon capture and storage update, Energy Environ. Sci. 7 (2014) 130–189.

[2] H.P. Mangalapally, H. Hasse, Pilot plant study of post-combustion carbon dioxide capture by reactive absorption: Methodology, comparison of different structured packings, and comprehensive results for monoethanolamine, Chemical Engineering Research and Design. 89 (2011) 1216–1228.

[3] R. Notz, H.P. Mangalapally, H. Hasse, Post combustion CO_2 capture by reactive absorption: Pilot plant description and results of systematic studies with MEA, International Journal of Greenhouse Gas Control. 6 (2012) 84–112.

[4] L.R. Kritzinger, Establishing a Pilot Plant Facility for Post Combustion Carbon Dioxide Capture Studies, Masters Thesis in Chemical Engineering, Stellenbosch University, 2013.

Time and cost efficient scale-up for reactive gas-scrubbing with the mini-plant technology

J. Pfaff[1], A. Radnjanski[1], G. Ewert[1], M. Grünewald[1]
[1]Ruhr Universität Bochum, Bochum, Germany

Abstract
The reactive CO_2-absorption of flue gases from power plants has an enormous targeted plant size, leading to cost and time intensive scale-up procedure. The aim of this work is to demonstrate the potential and limitations of mini-plant-technology in the scale-up process development for reactive absorption and thermal regeneration. Therefore, a mini plant was built and tested with the standard amine Monoethanolamine. Two sets of experiments with variation of CO_2 removal rate, as well as, variation of L/G-ratio, were carried out and the obtained results are presented and discussed. Furthermore, a process simulation of the reactive absorption and thermal regeneration was developed in Aspen Plus ®. The process model was validated with literature results from a lab scaled pilot plant [1]. Both sets of experiments were simulated with input data from the literature. The results have shown that the process behavior can be represented with the simulation. From the mini-plant experiments it can be seen that the obtained results show the same qualitative behavior of the process like the lab scaled pilot plant measurements but with several quantitative differences. The results reveal that all relevant process parameters of the absorption/desorption process could be qualitatively analyzed using a methodology composed of mini-plant technology and accompanied simulation studies.

Keywords
Reactive CO_2-absorption, mini-plant, scale-up, simulation

1. Introduction

The design of new processes, as well as, the modification of established ones is based on validation of theoretical process analysis through experimental investigations. The effort of the process development, and therefore the time consumption and the scale-up costs, mainly depend on the targeted plant size. A current issue with large scale columns is the frequently discussed reactive CO_2-absorption with amine-based solvents in the context of post combustion capture (PCC). For a 400 MWel power plant with only one absorption column, a column diameter of 16 m is required [2].
A typical PCC process consists of two main parts: an absorber and a stripper. In the absorption, CO_2 solves in the solvent and afterwards reacts exothermically with the amine. In the desorption column the CO_2-loaded solvent (rich) is regenerated by supplying heat. The necessary driving force for regeneration is provided at higher temperatures and the amine-acid gas reaction can be reversed. The lean solvent is returned back to the absorber for cyclic use.
All different aspects of the scale-up procedure make the post- combustion capture process very extensive. The typical procedure of the process development can be classified in four steps: a laboratory phase, a laboratory scale pilot plant (LSPP) phase, a pilot plant (PP) phase and a demonstration plant (DP) phase [3]. The

purpose of the laboratory phase is to screen and characterize appropriate solvent candidates. The main parameters that have to be considered are solubility of CO_2 under absorber and desorber conditions, as well as solvent properties such as volatility and degradation rates (oxidative and thermal). Based on the results from the lab phase some potential solvent candidates for the LSPP-phase can be selected. In the LSPP-phase the most promising solvents can be tested for the first time in a continuous cyclic operation. The obtained results give basic information about the process and its operability. A qualitative comparison of important process parameters such as CO_2 removal rate, energy demand and mass transfer kinetic is the main criteria in this phase. In the PP-step the process is operated under real conditions, usually with a bypass of the flue gases from a power plant. Absolute information about the operability, stability and emissions can be obtained at this stage. DP-phase of the PCC process test includes also the storage of CO_2. The aim of this phase is to develop as much as possible a detailed plan for a commercial PCC-plant and to reduce the technical and financial risks of the scale-up for commercial operation [3].

The description of the different development phases makes it clear that the scale-up of the PCC-process is really costly and time consuming. For this purpose the present work reports about an alternative scale-up procedure, which is time and cost efficient compared to the typical. As already described above, the first step for an efficient scale-up is a qualitative comparison between the selected solvents from the laboratory-phase. Instead of measuring those in a LSPP, a qualitative comparison could be done on mini-plant scale. The mini-plant technology is widely accepted as an alternative for the characterization of process and solvent performance due to cost and time efficiency. However, until now mini-plants have been rarely ([9],[10]) applied for the design of reactive gas scrubbing processes in project planning. The mini-plant reflects all typical process performances and all relevant process parameters could be depicted. This allows for a cost and time efficient solvent selection.

With a selected solvent and the kinetic parameters, a simulation which builds the PCC process can be developed. With the rate based simulation, all relevant process parameters, like optimal column internals, minimal energy requirement or process modifications, such as intercooling, can be analyzed, which otherwise would be measured in the PP-phase. The main drawback of the scale-up procedure is the disability to describe the fluid dynamic behavior in the large column. For a more detailed process planning and for reducing the risk of the stakeholders, the problems with the mega equipment have to be solved. However, this falls outside the scope of this paper.

The aim of this work is to understand the potentials and limitations of the mini-plant-technology in combination with process simulation in the scale-up process for reactive absorption with thermal regeneration. For this purpose, a mini-plant, consisting of an absorption and desorption column was built and a rate based simulation was developed. Using the example of the standard amine Monoethanolamine (MEA) the possibilities and limitations of the scale-up procedure were tested.

2. Results and discussion

2.1 Qualitative solvent screening with mini-plant experiments

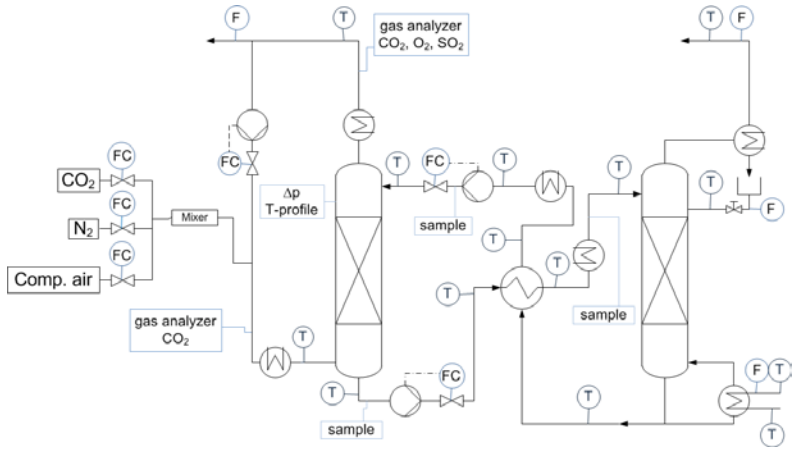

Figure 1: Flow scheme of the mini-plant

Figure 1 shows the flow sheet of the continuous mini-plant. A mixture of N_2, O_2 and CO_2 were used to simulate the flue gas. The absorber with a diameter of 26 mm and a packed height of 2,35 m, is filled with structured packing. The desorber has a diameter of 34 mm and a packing height of 0,6 m and is filled with random packing. With an IR gas-analyzer the CO_2 concentration in the inlet and outlet of the absorption column, as well as the O_2 and SO_2 in the outlet can be measured. The CO_2-concentration in the liquid phase is qualified by FTIR and the amine concentration is analyzed using a HPLC.
The main parameter, the CO_2 removal rate [separated CO_2 flow/CO_2 flow in the flue gas], can be calculated in three different ways. The CO_2-balances are in a good agreement for all of the data measured on the MEA-series, with an average derivation between gas- and liquid of 3,83%.

Variation of the CO_2 removal rate

As already described, the main parameters for an economical PCC process are the CO_2 removal rate and the reboiler duty in the desorption column. For a better understanding of the interaction between these parameters, in the first set of experiments the reboiler duty is varied, while all other parameters are kept constant.

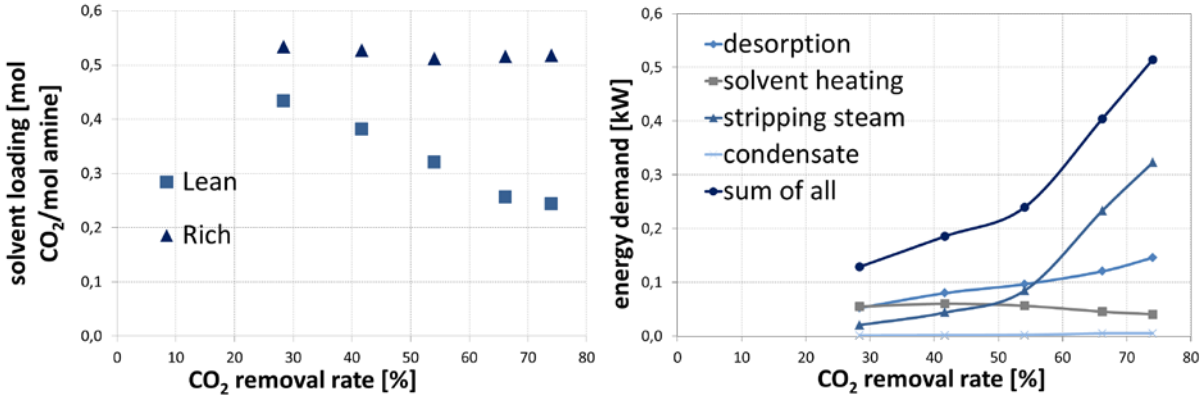

Figure 2: (a) Liquid loading and (b) regeneration energy demand versus the CO_2 removal rate

Figure 2 (a) shows the comparison of CO_2 rich and lean loadings as a function of the CO_2 removal rate. When reboiler duty is increased the leanloading decreases because of the higher regeneration supply. Due to the higher driving force in the absorption, the CO_2 removal rate increases simultaneously. It is obvious in Figure 2 (a), that the rich loading in all experimental sets is constant. By comparing them with

the operation line, it can be concluded that the equlibrium loading has been reached in all experiments.
Figure 2 (b) shows the energy demand, or the four contributions in which the regeneration energy requirement can be devided [1] as a function of the CO_2 removal rate. The regenetation of CO_2 consists of the energy demand necesarry to reverse the chemical reaction between the solvent and the CO_2. Furtheremore, the rich solvent pumped into the desorption column has to be heated to the sump temperature. At high desorber temperatures the water evaporates. One part of the reboiler duty is needed for the evaporation and another part is needed for heating the condensed water at the top of the column up to sump temperature. The function called “sum of all” is the reboiler duty minus the heat losses. Each of those energy contributions could be meassured with the mini plant equipment.
The energy contribution for the regeneration part increases with the removal rate because it is a linear function of the absorbed CO_2. For a constant liquid stream the energy demand for heating the solvent has to be constant during the experimental set. The small slight of the curve could be explainend with the increased sump temperature caused by the higher boiling temperature by lean loadings. The strongest influencing parameter on the CO_2 removal rate is the evaporated water steam. When increasing the steam amount, the water concentration in the gasphase increases resulting in a smaller CO_2 partial pressure. By lowering the CO_2 partial pressures, the equilibrium CO_2-loading in the liquid phase decreases and therefor the loading of the lean solvent decreases too. As shown, this leads to a higher CO_2 removal rate.

Variation of the L/G-ratio

Another parameter that influences the requiered energy demand is the circulated solvent flow or the liquid to gas ratio (L/G [kg/kg]). With a higher L/G ratio, more liquid has to be pumped and heated. Otherwise, with a lower L/G ratio, the required lean loading has to be lower for the same CO_2 removal rate, leading to the higher regeneration demand. Several studies arguing that the function of the energy demand versus the L/G-ratio has a minimum under LSPP or PP conditions have been puplished (e.g.[1], [4],[5],[9],[10]).
In the second experimental sensitivity study, the solvent flow rate was varied at a constant gas flow. The other parameters, mainly the removal rate are specified. Therefore, the reboiler duty in every experimet has to be adjusted.

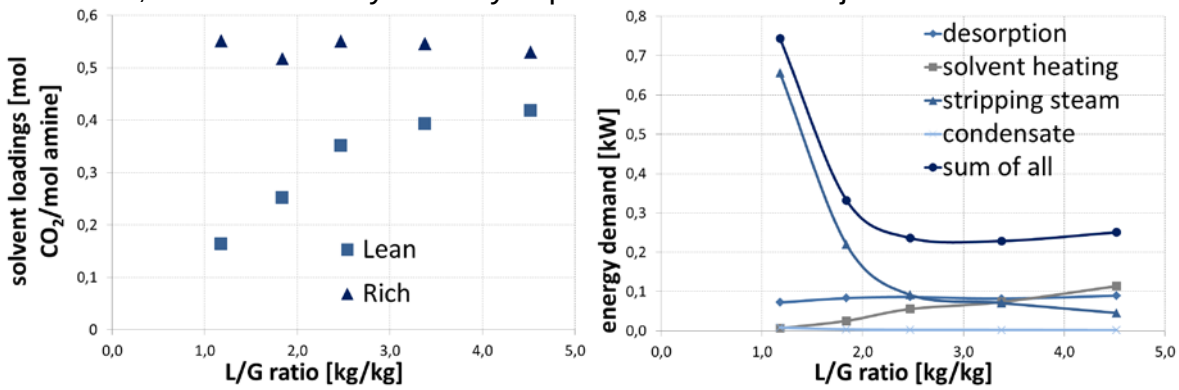

Figure 3: (a) Liquid loading and (b) regeneration energy demand versus L/G-ratio

Figure 3 (a) shows the obtained lean and rich loadings by variedted L/G-ratios. With increasing L/G-ratios, the driving force in the absorption decline and the lean loading increases. Figure 3 (b) shows the impact of the L/G-ratio on the four energy contributions, as well as the overall regeneration energy demand. The part corresponding to the heat of the desorption is nearly constant because of the

specified removal rate. With higher L/G-ratios, the solvent flow rate increases and therefore the energy contribution for heating the solvent increases too. The effect of the L/G-ratio on the required stripping steam is the most noticeable feature. With decreasing L/G-ratios, the lean loading also decreases, but the temperature in the desorber sump remains nearly constant. At this temerature, the equilibrium line is fixed and the only variable parameter for reaching lower lean loading is the CO_2 partial pressure. This leads to higer amounts of stripping steam at a lower L/G ratio. The opposite effects of the required stripping steam at low L/G-ratios and for heating the solvent at high L/G-ratios, lead to a minimum in the reboiler duty. This set of experiments illustrates that the relation between energy demand and L/G-ratio can be reproduced by the mini-plant experiments.
Summarizing the results of both sets of experiments reveal that the mini-plant apparature is suitable for a time and cost efficient qualitative solvent screening. For better understanding of the process as well as for testing the process modifications a process model has to be performed.

2.1 Process simulation with Aspen Plus®

A simulation is carried out with a rate based model that reproduced the PCC process. The non-ideal behavior of the liquid phase is described by the Electrolyte-NRTL method. The descriptions of the chemical reactions in the absorber are made with kinetic reactions and due to the high temperatures in desorber with equilibrium constants. All constants are taken from the data in the literature [6], [7], [8]. To determine the VLE condition, the values of the Henry coefficients ($H_{H2O-CO2}$, $H_{MEA-CO2}$) are implemented in the model. The binary mass transfer coefficients and the interfacial area are calculated with correlations of Billet and Schultes. The hold-up is calculated with a correlation of Bravo et al.
The validation of the process simulation can be performed with experimental results. The results from the mini-plant experiments are not appropriate for validation of the process simulation, due to the wall effects and high heat losses. Notz [1] has published a very detailed description of many experimental sets from a LSPP at the University of Kaiserslautern, which were used in this work for verification of the simulation model. Input data for the simulation are: pressures and temperatures of all streams, the mass flows and compositions of inlet gas and liquid stream in the absorption and the total reboiler duty.
To examine the validity of the simulation model a comparison was made between lean and rich stream obtained experimentally and predicted with the simulation. The average deviation between simulation and LSPP results is 4,27%, showing a good agreement.

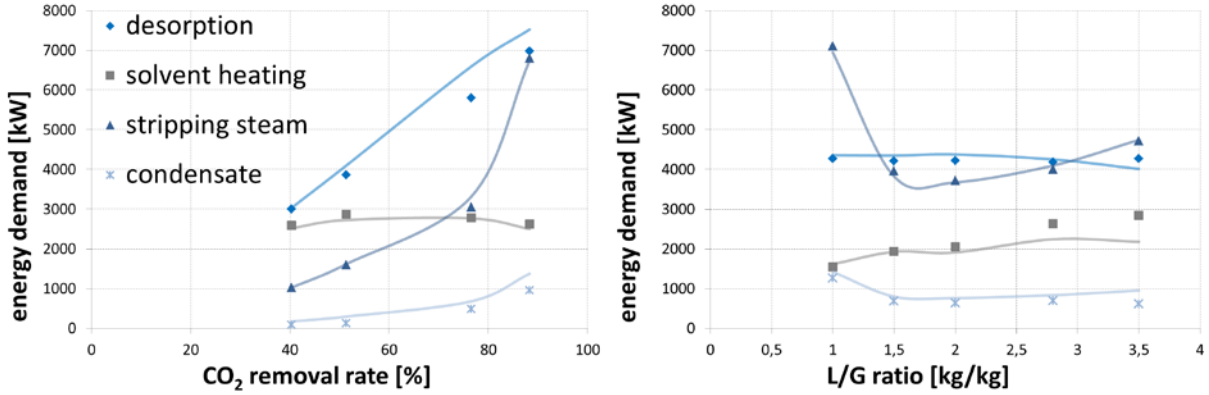

Figure 4: Comparison between the simulated (solid lines) and measured [1] (filled symbols) regeneration energy demand versus (a) the CO_2 removal rate and (b) the L/G-ratio

The four energy contributions versus the CO_2 removal rate and the L/G-ratio are mapped in Figure 4. The simulation results show a good agreement with the experimental values. Only the energy contribution for heating the solvent in Figure 4 (b) shows a slight deviation. This could be explained with a difference in the temperature between simulation and experiment of 2 K. All other temperature and concentration profiles in both columns are in good agreement with the experiments.
By comparing the LSPP results with the mini-plant results it can be concluded that both show qualitatively the same operation behavior. The quantitative differences between the LSPP and the mini-plant results can be explained on the basis of the process equipment. Important parameters in this context are the duty of the rich/lean heat exchanger and the low effective interfacial area in the mini-plant desorption column. However, for a qualitative solvent screening they display the same dependence on several process variations and both can be used.

3. Conclusions

The present contribution demonstrates that the mini-plant is able to represent the qualitative process behavior. Based on the behavior of the liquid loadings and the four energy contributions, the main process parameter can be clearly demonstrated. It can be concluded that the mini-plant equipment is a suitable tool for qualitative solvent screening. In addition, a rate-based simulation which builds up the PCC-process was also presented. The simulation was validated with literature data from a lab scaled pilot plant [1]. The results show a good agreement between experimental and simulated data, i.e. by the liquid loading of 4,27%. The same can be demonstrated with the four energy contributions, as well as with the temperature and concentration profiles along the columns.
By comparing the different plants it can be seen that both show the same tendencies. Only the ratio between the energy contributions is different and this can be explained with the differences in the plant equipment. The mini-plant can produce good qualitative results and can also be used as lab scaled pilot plant for solvent pre-screening. To summarize, it can be said that the combination of time-efficient experiments with the process simulation may contribute to reduce the scale-up procedure for reactive absorption plants such as the PCC process.

References

[1] Notz, R. (2009): CO_2-Abtrennung aus Kraftwerksabgasen mittels Reaktivabsorption. Berlin: Logos, PhD thesis, University Stuttgart

[2] Duss, M., Menon A., (2010): Optimized absorber design for post-combustion CCS. In: Conference Distillation and Absorption 2010, Eindhoven Netherlands

[3] Tönnies I., et al. (2011): CO_2-Abtrennung aus Kraftwerksabgasen auf dem Weg von der Forschung und Entwicklung zur industriellen Anwendung. CIT 83 (7), 1005-1015

[4] Moser P., et al. (2011): The post-combustion capture pilot plant Niederaussem – Results of the first half of the testing programme. Energy Procedia 4, 1310–1316

[5] Knudsen J., et al. (2009): Experience with CO_2 capture from coal flue gas in pilot-scale: Testing of different amine solvents. Energy Procedia 1, 783–790

[6] Pinsent B., et al. (1956): The kinetics of combination of carbon dioxide with hydroxideions. Trans. Faraday Soc. 52, 1512-20

[7] Hikita H., et al. (1977): The kinetics of reactions of carbon dioxide with monoethanolamine, diethanolamine and triethanolamine by a rapid mixing method. Chem. Eng. Journal. 13, 7-12

[8] Freguia S. (2002): Modeling of CO_2 Removal from Flue Gases with Monoethanola-mine. Master thesis, The University of Texas at Austin

[9] Stünkel S., et al. (2011): Carbon dioxide capture for the oxidative coupling of methane process – A case study in mini-plant scale. Chem. Eng. Res. Des 89, 1261-1270

[10] Zhang R., et al. (2011): RSAT™ process development for post-combustion CO2 capture:

Scale-up from laboratory and pilot test data to commercial process design. Energy Procedia 4, 1660-1667

A Systematic Approach to Design an Energy Efficient Distillation Column using a Process Simulator

Arnab Dutta, Ranjan K. Malik

Department of Chemical Engineering, Indian Institute of Technology - Bombay
Powai, Mumbai 400 076, India

Abstract

In this work, we target to present a systematic methodology for generating an energy efficient design of a distillation column. Combining the concepts of Column Grand Composite Curve (CGCC), Invariant Rectifying Stripping Curves (IRSC), and Exergy Loss profile analysis, we come up with a hybrid methodology which leads to an energy efficient design starting from scratch. Overall exergy loss analysis is integrated with the shortcut design procedure, and this leads to feed conditioning ahead of rigorous simulations. Column is then subjected to rigorous simulations using Aspen Plus and is analysed using IRSC technique for proper feed location. Finally, using the thermal targeting tools of Aspen Plus (Exergy Loss profile and the CGCC), decision is made to introduce side-exchangers. The column so obtained has a uniform exergy loss profile compared to the base case which results in a significant reduction in overall exergy loss, thus increasing the thermodynamic efficiency of the process. The proposed methodology has worked well on multicomponent hydrocarbon systems. The results show that the task of implementing various modifications like change in reflux ratio, fixing proper feed location, feed conditioning, and using side-exchangers becomes more systematic and yields an energy efficient design. The methodology is illustrated through case studies.

Keywords

Distillation, thermodynamic efficiency, CGCC, exergy loss, IRScurves

1. Introduction

The distillation process, though very energy intensive, is not energy efficient. Therefore, it is necessary to identify various energy saving opportunities through a detailed thermodynamic analysis. Improving energy efficiency of a distillation column deals with introducing various column modifications that reduce irreversibility associated with the column, thus minimizing the lost work (exergy loss) which in turn increases the thermodynamic efficiency of the column under study. The design of a multicomponent distillation column is normally carried out by starting from a shortcut method, - using reflux ratio (or number of stages) as per heuristics documented in literature. The configured column is then subjected to rigorous simulations using a process simulator to arrive at a better design; the resulting design is further modified to improve its thermodynamic efficiency using the available energy targeting tools. This approach of designing a distillation column (referred to as “Conventional Method” in this paper) is quite tedious and evolutionary in nature.

2. A Brief Literature Review

Dhole and Linnhoff (1993) introduced the concept of Column Grand Composite Curve (CGCC) to identify appropriate column design modifications. Using the results of an already converged simulation, the enthalpy deficit at each stage is obtained and

is plotted corresponding to the stage temperature in a Temperature vs Enthalpy diagram. It is called the CGCC. It is based on the concept of light and heavy key model. However, this approximation of pseudo-binary concept may not hold rigorously for non-ideal systems. The methodology based on CGCC does not give a systematic procedure for a grass root design of an energy efficient distillation column. Zemp *et al.* (1997) used an alternative approach based on the second law of thermodynamics and proposed that the thermodynamic optimization of a distillation column should go in the direction of producing a more uniform exergy loss distribution. At each stage, availability balance is carried out which results in exergy loss at each stage (Pinto *et al.*, 2011; Seader and Henley, 2006), thus an exergy loss profile is obtained from the converged column simulation and the section with largest exergy loss is identified. Based on the shape of the exergy loss profile, column modifications are proposed that reduce exergy losses in sections with large driving forces and increase loss in section with small driving forces, thus leading to a more uniform distribution of exergy loss. Though this concept identifies process sections that are thermodynamically inefficient, it does not provide any quantitative information regarding column modifications. Bandyopadhyay *et al.* (1999) introduced a novel pair of temperature-enthalpy curves known as the Invariant Rectifying-Stripping Curves (IRSC) for distillation columns. IRS Curves are invariant to the column configuration (feed location and number of stages) and depend only on sharpness of separation as well as operating pressure of the column. Using results of an already converged column simulation and the pseudo-binary concept of a light and heavy key, IRS Curves can be generated for multicomponent systems. However, unlike binary systems, the invariant nature of IRS Curves does not hold rigorously for multicomponent systems (Bandyopadhyay *et al.*, 1999) and hence its applicability is limited in case of multicomponent systems. Recently, many studies (for example, Salehi *et al.*, 2012; Pinto *et al.*, 2011) have appeared in literature with the motive to increase the thermodynamic efficiency of the distillation process by minimizing exergy loss. Though a variety of energy targeting tools are now available, there is still no systematic approach to design an energy efficient distillation column starting from scratch. The objective of this paper is to come up with a systematic methodology for design of an energy efficient distillation column by combining the concepts of CGCC, IRS Curves and Exergy Loss profile analysis. In this work, CGCC and column Exergy Loss profile are generated using the Aspen Plus simulator and IRS Curves are generated using results of a converged Aspen Plus simulation through an Excel spreadsheet. The developed methodology is demonstrated by two case studies of designing multicomponent distillation columns.

3. Methodology

The DSTWU and the RADFRAC modules of Aspen Plus were used for the shortcut design and rigorous simulations of the distillation column, respectively. The CGCC and the column Exergy Loss profiles were generated using the thermal analysis tools of RADFRAC module. The overall exergy loss, based on utility conditions and the thermodynamic efficiency were calculated as follows (Seader and Henley, 2006):

Entropy Balance: $\sum_{out\ of\ system}(nS + \frac{Q_{out}}{T_{source}}) - \sum_{into\ system}\left(nS + \frac{Q_{in}}{T_{sink}}\right) = \Delta S_{irr}$ (1)

Lost Work (LW) = $T_0 * \Delta S_{irr}$ (2)

Minimum work of separation: $W_{min} = \sum_{out\ of\ system} nb - \sum_{into\ system} nb$ (3)

Availability Function: $b = H - T_0 * S$ (4)

Thermodynamic Efficiency: $\eta = \frac{W_{min}}{W_{min} + LW}$ (5)

STEP-1: For the given system the initial thermal condition of the feed (vapor fraction, vf = vf_0) was evaluated via flash calculation in Aspen Plus. The condenser pressure is set based on the methodology illustrated by Seader and Henley (2006) for the given cooling utility and distillate composition. A condenser pressure drop of 7kPa and a pressure drop of 0.7kPa per stage was incorporated. Let R = 1.3* R_min.

STEP-2: For given specfications, run DSTWU at vf = vf_0 to obtain minimum reflux ratio (R_min), and with reflux ratio (R) = 1.3* R_min, get the number of stages N.

STEP-3: A subcooled or a superheated feed cannot be fed reversibly into the column (Bandyopadhyay, 2002), the vapor fraction is varied within the range [0,1]. For each vf, operate DSTWU at a reflux ratio 1.3 times the corresponding minimum reflux ratio. Evaluate corresponding overall exergy loss using Eq. 2. An optimal thermal condition (vf*) corresponds to that value of vf for which the overall exergy loss is minimum. The shortcut procedure being an approximate method, vapor fraction of feed so obtained is approximately close to the actual value and may require further investigation.

STEP-4: Run RADFRAC for vf_0. This simulation corresponds to base case design.

STEP-5: For vf*, the number of stages (N) and the feed stage location (F) reported by DSTWU are used to run RADFRAC and generate Exergy Loss profile and CGCC.

STEP-6: If there is flatness observed near the pinch point in CGCC, or a high exergy loss is visible at the feed stage, check for proper location of feed in the column using the feed stage location methodology based on IRS Curves (Bandyopadhyay *et al.*, 1999) and move the feed to the appropriate location in the column. If flatness still prevails above the CGCC pinch then there is further scope for feed pre-heating, whereas if the flatness appears below the pinch then there is scope for feed cooling.

STEP-7: Consider the distance between the CGCC pinch and the vertical (Temperature) axis for reflux ratio modification. Let this distance be = $HPinch$

$H'Pinch = 0.75 * HPinch$ (To avoid pinched design) (6)

Modified condenser duty: $Qc\_new = Qc\_old - H'Pinch$ (7)

$Qc\ approximately\ proportional\ to\ R$ => $Qc\_old/Qc\_new = R\_old/R\_new$ (8)

$R\_new = R\_old * Qc\_new/Qc\_old$ [More true for vapor phase distillates] (9)

- If $R\_new \approx R\_min$

  Stop the iteration as very large number of stages will be required

- Else

  Run DSTWU with $\boldsymbol{R\_new}$ to get modified F and N and continue STEP-7.

STEP-8: Generate column exergy loss profile for the last design obtained and calculate the total exergy loss in each section.

Exergy loss in rectifying section: $\boldsymbol{Ex\_r}$ = Sum of exergy loss of all stages in [2, F-1]

Exergy loss in stripping section: $\boldsymbol{Ex\_s}$ = Sum of exergy loss of all stages in [F+1, N-1]

$$\boldsymbol{Ex\_d\_old = Ex\_r - Ex\_s} \quad (10)$$

Load for side-exchanger is varied up to 75% (to avoid pinched design) of the heat duty obtained from the Stage-H plot (CGCC), corresponding to the stage where the side-exchanger is implemented so as to minimize the column exergy loss.

- If $\boldsymbol{Ex\_r} > Ex\_s$ then there is a scope for side-condenser

  To determine the location, two different stages are considered

  Location 1: Stage = F-1, i.e., farthest from the main condenser

  Location 2: Find the stage Nr in the rectifying section where exergy loss is maximum. The side-condenser is implemented at stage = Nr+1; thus reducing exergy loss in the section between stage 1 and Nr+1.

  The location corresponding to minimum column exergy loss is chosen.

- If $\boldsymbol{Ex\_r} < Ex\_s$ then there is a scope for side-reboiler

  To determine the location, two different stages are considered

  Location 1: Stage = F+1, i.e., farthest from the main reboiler

  Location 2: Find the stage Ns in the stripping section where exergy loss is maximum. The side-reboiler is implemented at stage = Ns-1; thus reducing exergy loss in the section between stage N and Ns-1.

  The location corresponding to minimum column exergy loss is chosen.

STEP-9: Evaluate $\boldsymbol{Ex\_d\_new} = \boldsymbol{Ex\_r} - \boldsymbol{Ex\_s}$ corresponding to last run from Step-8.

- If $\boldsymbol{Ex\_d\_old} * \boldsymbol{Ex\_d\_new} < 0$

  there is further scope for implementing side-exchanger

  Go to STEP-8.

- Else

  No scope for side-exchanger. Final design is obtained.

4. Results and Discussion

The proposed methodology was applied to evolve the designs of distillation columns for the following two multicomponent hydrocarbon systems (Table-1). The desired specifications were met by varying distillate rate and reflux ratio in each case. The designs so obtained are compared with the designs generated by the "Conventional Method" in terms of overall thermodynamic efficiency, i.e., for the entire process.

Table 1: Systems for case studies

System	Case-1: Heptane-Octane-Nonane-Decane-C15	Case-2: Methane-Ethane-Propane-N-butane-N-pentane
Source	Dhole and Linnhoff (1993)	Seader and Henley (2006)
Property Method	Peng-Robinson	Peng-Robinson
Feed Data		
Flow Rate (kmol h^{-1})	1000	360
Compositions (mole fr.)	0.2 each	0.2; 0.4625; 0.3; 0.03; 0.006
Temperature (K)	373.15	313.7
Pressure (atm)	2	27.2
Specifications (mole)	0.9% Nonane in distillate 0.9% Octane in bottoms	98% recovery of Ethane & 2% recovery of Propane in distillate

4.1 Case Study 1

This case study is taken from Dhole and Linnhoff (1993). The final design obtained in this work was compared with the final design of Dhole and Linnhoff.

Table 2: Results for Case Study 1

Column Design Details	Base Case	Dhole and Linnhoff, (1993)		Proposed Method
		As in Paper	As simulated	
Number of theoretical stages	24	30	30	28
Feed stage location	12	---	15	13
Reflux ratio	1.66	---	1.38	1.99
Distillate rate (kmol h^{-1})	398	398	398	398
Bottoms rate (kmol h^{-1})	602	602	602	602
Column pressure (atm)	1.97	1.97	1.97	1.97
Distillate temperature (K)	413.6	413.4	413.6	413.6
Bottoms temperature (K)	480.3	476.9	480.3	480.3
Final feed temperature (K)	373.1	441	440.9	439.4
Feed preheater duty (kW)	----	7320.3	7320.3	6763.9
Condenser duty (kW)	-6178.3	-5739.1	-5094.9	-7378.8
Side-condenser: Location (Stage/Temperature(K)) Duty (kW)	----	 5/420.2 -2928.1	 5/419.7 -2928.1	No Side condenser
Reboiler duty (kW)	18710.6	9721.3	8842.9	5182.7
Side-reboiler: Location (Stage/Temperature(K)) Duty (kW)	-----	 20/453.1 4392.2	 20/458.5 4392.2	 26/464.9 7993.7
Column exergy loss (kW)	1341.1	----	568.1	579.8
Exergy loss in rectification/stripping section (kW)	82/ 509.5	----	108.3/ 263.5	131.8/254. 7
Exergy loss at feed stage (kW)	497.8	----	149.3	137.6
*Overall Exergy Loss (kW)	2210.7	----	1868.1	1674.9
Overall Thermodynamic Efficiency (%)	62.3	----	66.2	68.6

*Overall exergy loss is calculated based on the utility conditions.

The final design so obtained using the proposed methodology shows an increase in overall thermodynamic efficiency of the process from 62.3% for the base case design to 68.6%, which is also higher than that obtained from Dhole and Linnhoff (1993).

4.2 Case Study 2

The second system, with specifications, as described in Table-1 was first used to arrive at a design using the “Conventional Method” using Aspen Plus. The final design, thus obtained, was compared with the ultimate design achieved using the proposed methodology as described in Section-3. This system was particularly chosen so as to highlight how side-condensers can be beneficial when refrigerant is used as a coolant in the main condenser. This case study showcases the applicability of the proposed methodology at sub-ambient conditions.

Table 3: Results for Case Study 2

Column Design Details	Base Case	Conventional Method	Proposed Method
Number of theoretical stages	19	26	28
Feed stage location	8	10	12
Reflux ratio	2.14	1.19	0.96
Distillate rate (kmol h^{-1})	240.2	240.2	240.2
Bottoms rate (kmol h^{-1})	119.8	119.8	119.8
Condenser pressure (atm)	27.22	27.22	27.22
Stage 2 pressure (atm)	27.29	27.29	27.29
Reboiler pressure (atm)	27.41	27.45	27.47
Distillate temperature (K)	262.87	262.87	262.87
Bottoms temperature (K)	350.31	350.4	350.43
Final feed temperature (K)	313.7	307.15	305.88
Feed preheater duty (kW)	----	-131.8	-169.8
Condenser duty (kW)	-1390.8	-773	-623.7
Side-condenser: Location (Stage/Temperature(K)) Duty (kW)	 ----	 6/286.65 -366	 5/287.22 -439.2
Reboiler duty (kW)	960.4	843.3	805.2
Column exergy loss (kW)	227.5	136.2	123.8
Exergy loss in rectification/stripping section (kW)	134.7/45.1	73.2/35.7	69.1/31.6
Exergy loss at feed stage (kW)	8.8	8.5	8.5
*Overall Exergy Loss (kW)	360.2	250.6	221.1
Overall Thermodynamic Efficiency (%)	21.4	28.2	30.8

*Overall exergy loss is calculated based on the utility conditions.

It can be seen that the overall thermodynamic efficiency of the improved design has increased by 44% as compared to the base case, and a 9% increase compared to the design obtained using the “Conventional Method”.

5. Conclusions

The proposed methodology, as presented in Section-3, has resulted in improved designs for both the case studies. From results of Case Study 2, it is quite evident that the proposed methodology works well in sub-ambient conditions. Locations of side-exchangers are chosen in such a way that it not only reduces the column exergy loss but also utilizes a better utility in side-condensers or side-reboilers compared to the utility used in the main condensers or reboilers. Final designs so obtained using the proposed methodology have higher thermodynamic efficiency compared to the designs done by the “Conventional Method”. Thus, the proposed methodology gives a much needed systematic approach to design an energy efficient distillation column.

References

1. G.R.Salehi, A.Salehi, and F. Kimiaghalam, *Energy Science &Technology*, 3(2): 2012 (63-73).
2. F.S.Pinto, R.Zemp, M.Jobson, and R.Smith, *Chemical Engineering Science*, 66: 2011 (2920-2934).
3. J.D.Seader and E.J.Henley, *Separation Process Principles*, John Wiley & Sons, New York, 2006.
4. S. Bandyopadhyay, *Chemical Engineering Journal*, 88(1-3): 2002 (175-186).
5. S. Bandyopadhyay, R.K.Malik, and U.V.Shenoy, *Computers & Chemical Eng.*, 23:1999(1109-1124).
6. R.J.Zemp, S.H.B.Faria, and M.L.O.Maia, *Computers & Chemical Eng.*, 21S: 1997 (S523-S528).
7. V.R.Dhole and B.Linnhoff, *Computers & Chemical Eng.*, 17(5-6): 1993 (549-560).

Energy efficient separation alternatives for the production of ethanol from lignocellulosic biomass

Cristian F. Triana[1], Eric S. Fraga[1], Philip Lutze[2] and Eva Sorensen[1]
[1]University College London, Department of Chemical Engineering, London, UK;
[2]TU Dortmund, Laboratory of Fluid Separations, Dortmund, Germany;

Abstract

Bioethanol production from lignocellulosic biomass is a promising alternative for energy generation from renewable sources; however, its implementation in industry presents challenges because of the high levels of energy consumed in the separation stages. This work focuses on the evaluation of different configurations of separation units including single distillation, double-effect distillation, and double-effect distillation combined with pervaporation and vapour permeation. The double-effect distillation system is found to have a significantly lower energy consumption that a single column unit. The double-effect distillation unit can be combined with pervaporation and vapour permeation system in order to dehydrate the ethanol solution (>99 mole %). The combination with vapour permeation showed better results than with pervaporation in terms of purity and energy consumption during the process, showing that double-effect distillations coupled with vapour permeation represent an efficient alternative to reduce the energy consumption in the ethanol production process from biomass.

Keywords

Ethanol, Distillation, Double-Effect, Pervaporation, Vapour Permeation, Membranes

1. Introduction

Ethanol production process from lignocellulosic biomass represents an alternative to the use of fossil fuels, whose prices keep increasing and that have negative effects on the environment through global warming. Although the production of bioethanol from lignocellulosic biomass presents many benefits, the energy demand of this process is high, currently making it non-competitive with traditional sources of energy such as oil and coal. The most energy-consuming part of the process is the separation stage which usually consists of several distillation columns for the collection of ethanol from the fermenting broth and for dehydration of the product to biofuel standard concentrations (e.g. using membranes, adsorption, etc.). This work focuses on the evaluation of different separation alternatives for the ethanol process which may reduce the overall energy consumption, including different arrangements of distillation columns and the integration of distillation columns with membrane operations into hybrid separations. In the following, double-effect distillation, and double-effect distillation combined with pervaporation and vapour permeation into a hybrid separation system, will be considered.

1.1. Double-effect distillation

Double-effect distillation systems, where the overhead vapour from one column is used to supply heat to the reboiler of another column operating at a lower pressure, have the potential to greatly reduce utility costs. The utilization of the heat released by the condenser of the high-pressure column into the reboiler of the low-pressure column represents an increase in the efficiency of the process and the energy integration thereof, [1,2]. An example of this configuration is shown in Figure 1.

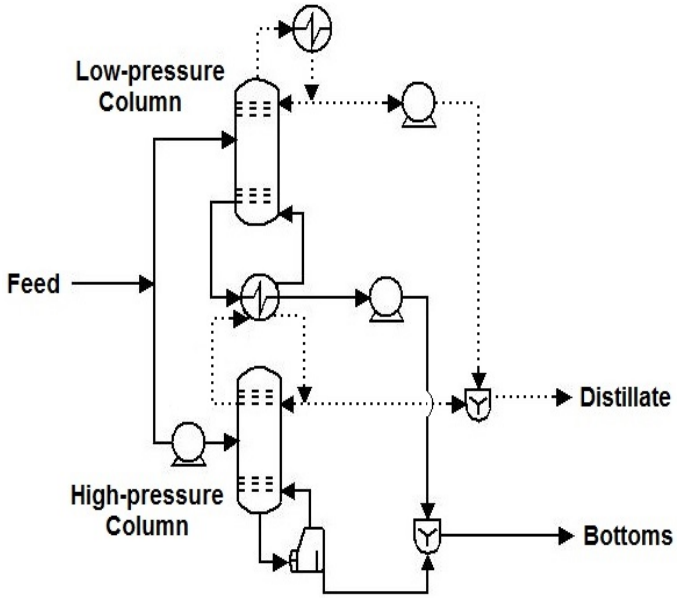

Figure 1: Scheme for the configuration of the double-effect distillation system, [1,2].

1.2. Vapour permeation

Vapour permeation is a process where vapour is fed into the system and the permeable component is transferred through the membrane allowing a separation between the components. In the case of the ethanol production process, vapour permeation is gaining more attention in industry since its implementation is believed to reduce the overall energy consumption in the process with high product purity [3,4,5].

1.3. Pervaporation

Pervaporation is another membrane-based operation in which, unlike vapour permeation, a liquid solution is fed into the membrane module and because of the pressure difference some of the liquid evaporates and permeates through the membrane. The evaporation of the solution makes the temperature of the system drop and additional external heating is required in order to guarantee the operating conditions inside the membrane module, [6,7].

2. Results and discussion

This work presents alternative configurations for the separation stages of the ethanol production process which aims to reduce the associated energy consumption. A combination of conventional distillation, double-effect distillation and membrane separation is presented. Initially, a shortcut model developed in ChemCAD which is

based on the FUG method was used to determine the minimum number of stages, the minimum reflux and the heat input for the reboiler. The results of this method were used in a distillation column and a double-effect distillation system developed in gPROMS to evaluate the reflux ratio that presents the minimum energy consumption. The specifications for the shortcut model are the following:

- The feed consists of 50 mole/sec at saturated-liquid conditions with a concentration of 5 mole % of ethanol at 101.3 kPa.
- The percentage of ethanol recovered at the top of the distillation column is 99%.
- The operating pressure for the high-pressure column in the double-effect distillation is 303.9 kPa in order to provide sufficient heat to the reboiler of the low-pressure distillation.

The column design obtained with ChemCAD is implemented into a dynamic model of a single distillation column and a double-effect distillation system using gPROMS. Using the optimisation tool of gPROMS (gOPT with an NLP approach), the optimal reflux ratio which minimises the heat input in the reboiler is determined for both configurations taking into account the following constraints:

- $X_{D-Ethanol} \geq 0.82$
- $Ethanol\ recovery \geq 0.99$

The results of the simulation of the Shortcut model using ChemCAD and the result of the simulation and minimisation of the dynamic models developed in gPROMS are presented in Table 1.

Table 1: Results of the simulation and optimisation of the distillation systems.

Parameter	Shortcut Model ChemCAD	Single distillation column gPROMS		Double-effect system gPROMS	
		Before optimisation	After optimisation	Before optimisation	After optimisation
Number of stages	20	20	20	20*/20**	20*/20**
Pressure (kPa)	101.3	101.3	101.3	303.9	303.9
Heat duty reboiler (kW)	838	838	459.7	838**	344.2**
Condenser heat released (kW)	808	797	438.5	812.2*	304.2*
Reflux Ratio	6	6	2.74	6* / 6**	4.3* / 4.7**
Ethanol mole fraction distillate	0.84	0.82	0.83	0.83	0.83
Ethanol mole fraction bottoms	0	0	0	0	0
Temperature top of column (K)	351.4	351.2	351.2	351.2*	351.2*
Temperature Bottom of the column (K)	373	372.9	373.0	406.8**	406.8**
Total work by pumps (kW)	N/A	N/A	N/A	0.283	0.283

* Low-pressure distillation column
** High-pressure distillation

Table 1 presents the results of the optimisation of the reflux ratio and the minimum heat input in the reboiler for the single distillation column and the double-effect distillation system. The double-effect configuration presented a significant reduction in the heat input of 59 % (compared to the non-optimised model) in comparison with the single distillation column which presented a reduction of 45%. These results show that double-effect distillation, given the operating conditions previously introduced, can be an efficient alternative for the separation of ethanol from the fermentation broth and will be considered for the application of the membrane technology as follows. The following step is the implementation of membrane-based systems to increase the purity of ethanol beyond the azeotrope (>99 mole %). The membranes considered in this work for vapour permeation and pervaporation were Poly vinyl alcohol and Polyacrylonitrile ultrafiltration PAN-B5, respectively, [5,6]. The operating conditions of these membrane systems are shown in Table 2.

The arrangement proposed in this work for the ethanol dehydration consists of two in-series membrane modules followed by two in-parallel membrane modules. Note that, a further analysis (not included in this work) of the membrane configuration and the optimal number of distillation trays is required in order to implement a more rigorous methodology that leads to an optimal design of the separation units and to an optimal process integration. Figures 3 and 4 show the arrangements of the double-effect distillation system coupled with vapour permeation and pervaporation considered in this work, respectively. For the pervaporation system, additional heat exchangers are required at the exit of modules 1 and 2 (See Figure 4) in order to increase the temperature of the outlet stream of those modules to the required temperature conditions of the modules (See Table 2 for operating conditions of the membrane modules), [6].

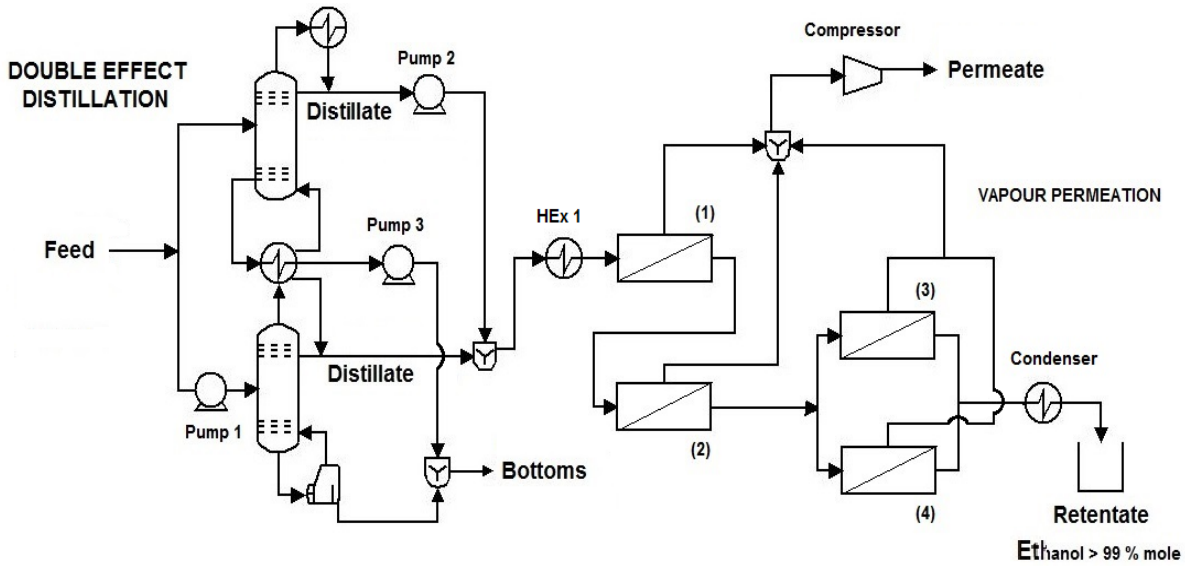

Figure 3: Scheme for a double-effect distillation system with vapour permeation (DEVP)

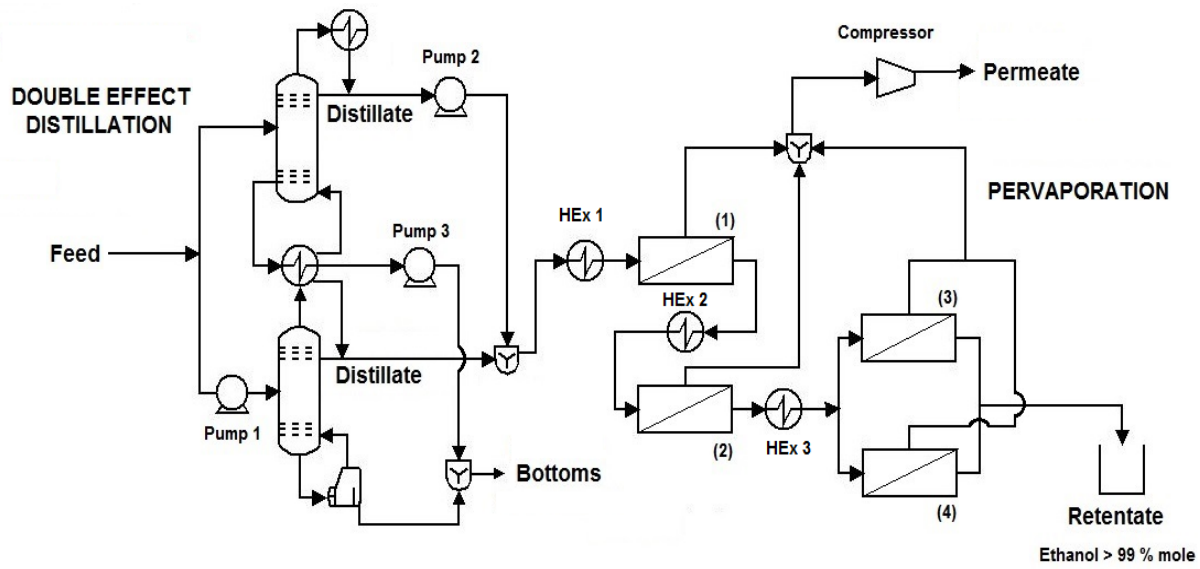

Figure 4: Scheme for a double-effect distillation system with pervaporation (DEP)

The results of the simulation of the combination of the vapour permeation and pervaporation modules with the double-effect distillation system previously introduced are shown in Table 2.

Table 2: Results of the simulation of a double-effect distillation system coupled with membrane-based separation units

Parameter	Vapour Permeation	Pervaporation
Ethanol concentration (% mole)	0.993	0.990
Feed pressure (kPa)	303.9	303.9
Permeate pressure (kPa)	0.1	0.4
Feed temperature (K)	382*	343.15**
Area membrane modules (m^2)	20	6
Energy heat exchanger 1 (kW)	7.172	-10.53
Energy heat exchanger 2 (kW)	N/A	13.57
Energy heat exchanger 3 (kW)	N/A	5.69
Energy condenser VP (kW)	43.51	N/A
Work by adiabatic compressor (kW)	15.04	15.12
Total work by pumps (kW)	0.283	0.283

* Inlet temperature of the feed in a Poly vinyl alcohol membrane for vapour permeation, [5].
** Inlet temperature of the feed in a PAN-B5 membrane for pervaporation, [6,7].

Table 2 shows that the DEVP configuration presents a slightly better separation than the DEP system (99.3 mole %). The kinetic models used in this work for the evaluation of the molar flux through the membranes are very dependent of the operating conditions used in the experiment, the selectivity and the effective membrane area and therefore there is a difference in the concentration of ethanol. Moreover, in terms of energy consumption, the DEVP configuration requires less energy than DEP since no heat exchangers are required to increase the temperature after each module. The DEVP system, although it requires a larger membrane area than the DEP and more trays for the distillation columns, represents an efficient alternative in the reduction of energy consumption. The DEP system also shows good results but additional membrane modules are likely to be required to increase the purity of ethanol.

3. Conclusions

This work considered the energy consumption in the separation stage of the production of ethanol from lignocellulosic biomass. The use of a double-effect distillation system was considered and compared to the use of a single column in terms of minimum energy consumption. The results of the optimisation showed that the double-effect system presented the lowest heat duty. The double-effect distillation system was then coupled to vapour permeation and pervaporation systems in order to dehydrate ethanol. A concentration of 99.3 mole % of ethanol was obtained with a double-effect distillation system combined with vapour permeation showing that this is an attractive method to reduce the overall energy consumption in the ethanol production process from lignocellulosic biomass.

Acknowledgements

Special thanks to the Colombian Institute of Science and Technology (COLCIENCIAS) for their financial support.

References

[1]. J. Pohlmeier, A. Rix, 1996. Interactive plant and control design of a double-effect distillation column. Computers & Chemical Engineering. 20, 395-400.
[2]. V. Bansal, R. Ross, J.D. Perkins, E.N, Pistikopoulos, 2000. The interactions of design and control: double-effect distillation. Journal of Process Control. 10, 219–227.
[3]. T. Pettersen, K.M Lien, 1995. Design of hybrid distillation and vapor permeation processes. Journal of Membrane Science. 99, 21-30.
[4]. T. Roth, P. Kreis, 2009. Rate based modelling and simulation studies of hybrid processes consisting of distillation, vapour permeation and adsorption for the dehydration of ethanol. 19th European Symposium on Computer Aided Process Engineering – ESCAPE 19, 815-819
[5]. T. Roth, P. Kreis, A. Górak, 2013. Process analysis and optimization of hybrid process for the dehydration of ethanol. Chemical Engineering Research and Design. 91, 1171-1185.
[6]. M. Tsuyumoto, A. Teramoto, P. Meares, 1997. Dehydration of ethanol on a pilot-plant scale, using a new type of hollow-fiber membrane. Journal of Membrane Science. 133, 83-94.
[7]. J. Marriott, E. Sorensen, 2003. The optimal design of membrane systems. Chemical Engineering Science.58, 4991–5004.

Dividing wall columns for heterogeneous azeotropic distillation

Quang-Khoa Le[1], Ivar J. Halvorsen[2], Oleg Pajalic[3], Sigurd Skogestad[1]*
[1]Norwegian University of Science and Technology (NTNU), Trondheim, Norway;
*[2]SINTEF, Trondheim, Norway; [3]Perstorp AB, Perstorp, Sweden. *skoge@ntnu.no*

Abstract
The aim of this work is to implement heterogeneous azeotropic distillation schemes in a dividing wall column (DWC) for a feed mixture of water (W), acetic acid (HAC) and an organic component (X). The original design makes use of X to act as an entrainer to facilitate the separation of water and HAC, and we also propose a DWC design based on this idea. This DWC design reduces the capital cost, but the energy usage is almost unchanged. To achieve energy savings and further reductions in capital costs, we need to use a Petlyuk DWC. We introduce isobutyl acetate (IBA) as an additional entrainer for the Petlyuk DWC, and achieve energy savings of about 20%.

Keywords

Dividing Wall Column (DWC), heterogenous azeotropic distillation, Petlyuk arrangement, energy saving.

1. Introduction

Distillation is one of the most energy-consuming processes in the chemical industry. Thus, reducing its energy requirement, which also leads to lower operating costs, is a priority target of chemical manufacturers all over the world. One of the most promising technologies is a Petlyuk distillation arrangement implemented in a Dividing Wall Column (DWC), see Figure 1(a). Indeed, for a three-component separation, this arrangement provides a potential energy saving of up to 30% compared to a conventional two-column sequence. The Petlyuk-DWC is also more compact, with only one column shell, one reboiler and one condenser, which typically reduces the capital cost by 30% [3]. The main disadvantages with the DWC arrangements are that they are less flexible and that the operation and control is more difficult. The Petlyuk-DWC was first patended by Wright in 1949 [5], but it was only taken into industrial use in 1985 by the German company BASF [3]. Since then there have been many installations, with more than 100 industrial applications reported in 2006 [3].

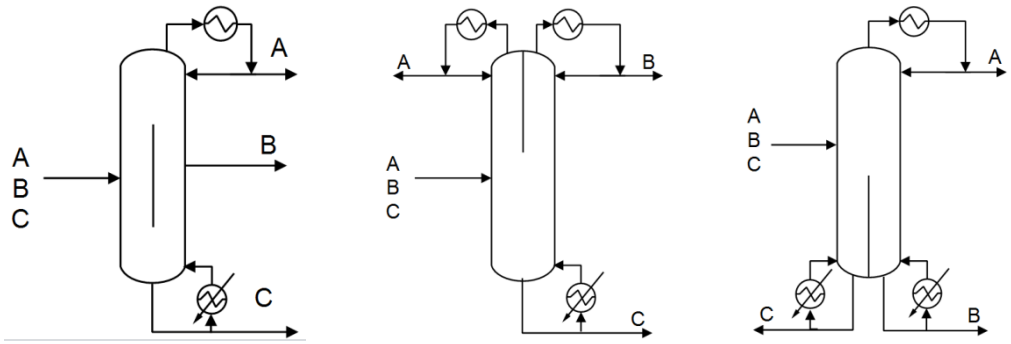

(a) *Petlyuk-DWC* (b) (c)

Figure 1: Dividing Wall Column (DWC) configurations for separating three components (A,B,C)

There are also other dividing-wall arrangements for a three-component separation, in which the partition wall is located either at the upper or at the lower part of the column shell, see Figures 1(b) and 1(c), but these require an additional condenser or reboiler. These are equivalent to a side-rectifier and a side-stripper configuration, respectively.

Another approach to make distillation more efficient and compact is to make use of liquid-liquid separation (decanting), whenever applicable. Indeed, *heterogeneous azeotropic distillation* is widely used in the chemical industry to separate azeotropes and close-boiling binary mixtures [1, 4]. The main idea is to “break” the binary azeotrope (A,B) by adding a third component (C), known as the entrainer [4] or solvent [1]. The entrainer (C) is generally a component that does not mix well with at least one of the components (A) in the original binary mixture, thus causing the two components (A,C) to evaporate more easily and to stay in the top part of the column, where they form an azeotrope. When condensed, the overhead vapor (close to azeotrope) forms two liquid phases which are separated in a decanter. All of the entrainer phase (C) is recycled to the column, while part of the other phase (A) is recycled (refluxed) and the remaining is taken as overhead (distillate) product. The resulting overall separation can be counterintuitive, for example, with the lightest of the original binary components ending up as the bottom product. The earliest example of heterogeneous azeotropic distillation is the breaking of the water-ethanol azeotrope using benzene as the entrainer [4]. However, azeotropic distillation arrangements are generally difficult to design and operate, because of distillation boundaries, complex thermodynamics with liquid-liquid phase split, non-linear dynamics, and the existence of multiple steady state solutions [2].

The objective of this paper is to consider heterogenous azeotropic DWC distillation applied to the separation of water (A=W) and acetic acid (B=HAC). This mixture forms a tangent pinch (“almost azetrope”) at the pure water end, where the liquid and vapor compositions are similar, making separation by conventional distillation difficult. A common industrial way of separating this mixture is to use an entrainer, for example, isobutyl acetate (C=IBA) [7].

However, in our case the original mixture actually contains a third component which can act as an entrainer (C=X). Component X is an organic component with a boiling point around 150C and with water it form a heterogeneous azeotrope with a boiling point around 98C. In addition, the feed contains small amounts of heavy organic components. In summary, we want to separate 100 kg/h of the following four-component feed mixture into pure components:

A = Water (W)	Bp=100C	8.87 wt%
B = acetic acid (HAC)	Bp=118C	54.55 wt%
C = organic (X)	Bp=150C	35.9 wt%
D = Heavy organics (HO)	Bp~200C	0.68 wt%

The heavy organics (D=HO) have almost no effect on the results in this paper. The paper is organized as follows: In Section 2 we give simulation results for the conventional configurations which is presently used in Perstorp (Figure 2). Aspen is used to simulate and optimize the process based on the data given by Perstorp. We then consider two different DWC arrangements for integrating the two distillation columns (C14 and C108 in Figure 2). First, we consider the arrangement in Figure 1b, which is quite straightforward to design and simulate (section 3).

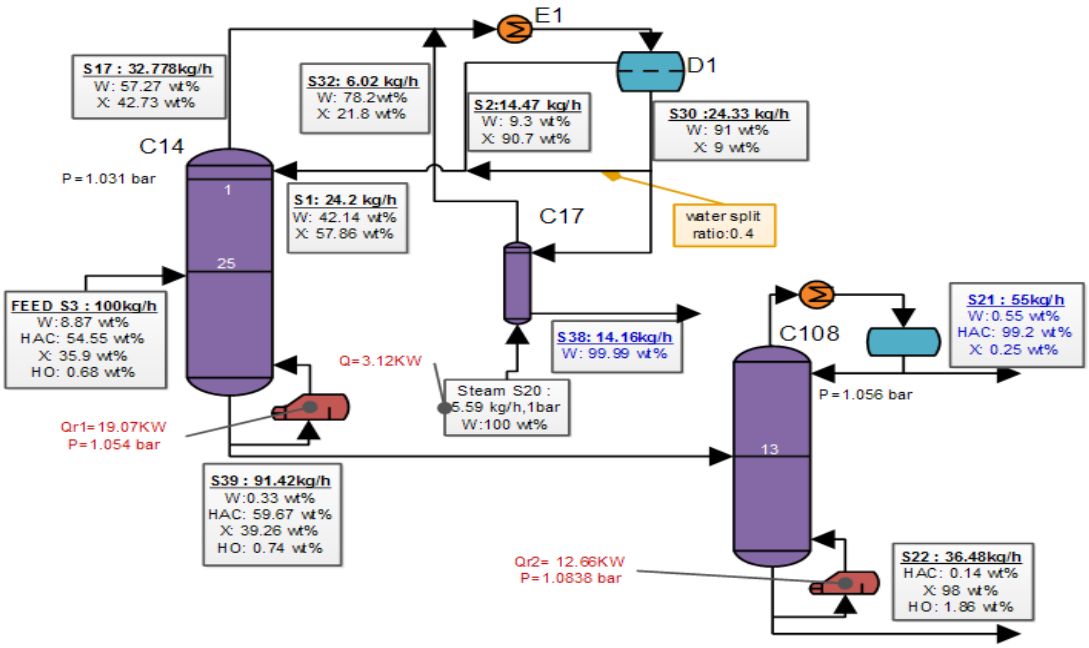

Figure 2: Original design with two distillation columns (C14, C108), decanter (D1) and stripper (C17). Overall Q=34.85 kW

Next, we consider the Petlyuk arrangement in Figure 1a, which is much more difficult to simulate (section 4.1), and which actually cannot be applied directly to this feed mixture (section 4.2). To make it work, we need to add a new entrainer (section 4.3), and we choose to use isobutyl acetate (IBA).

2. Conventional configuration

Figure 2 shows the flowsheet for the original conventional direct-sequence employed to separate the feed. The stream flows and the reboiler heat duties are also shown. The feed is introduced to the first column, C14. The overhead vapor of C14 (point S17 in Figure 3), which is close to the azeotrope of water and component X, is condensed and separated into two liquid phases in the decanter (D1). The organic phase, rich in X, is totally refluxed back to the top of column C14. The aqueous phase, containing mostly water, is partially refluxed, while the rest is send to the stripper column (C17) where steam (pure water) is used to strip off the remaining X which is recycled to the condenser. Almost pure water product is withdrawn at the bottom of the stripper. The bottom product of C14 goes tothe second column C108. The top product of this column is the HAC-rich product, while the bottom stream is rich in X and HO. The total energy required is 34.85KW.

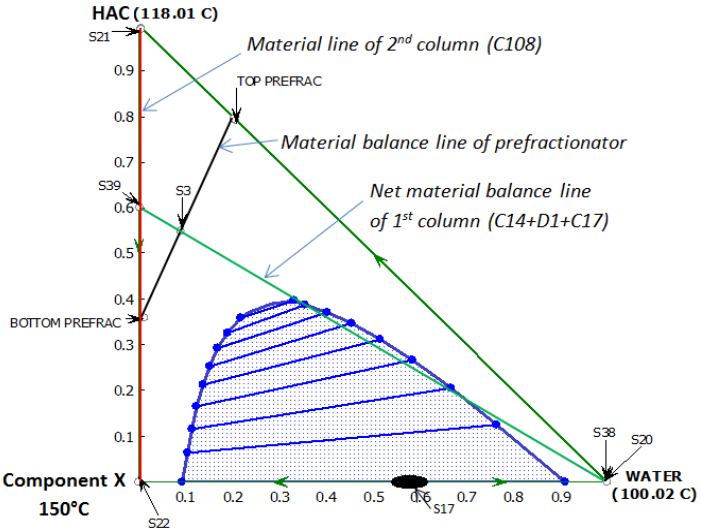

Figure 3: Phase diagram for Water-HAC-X

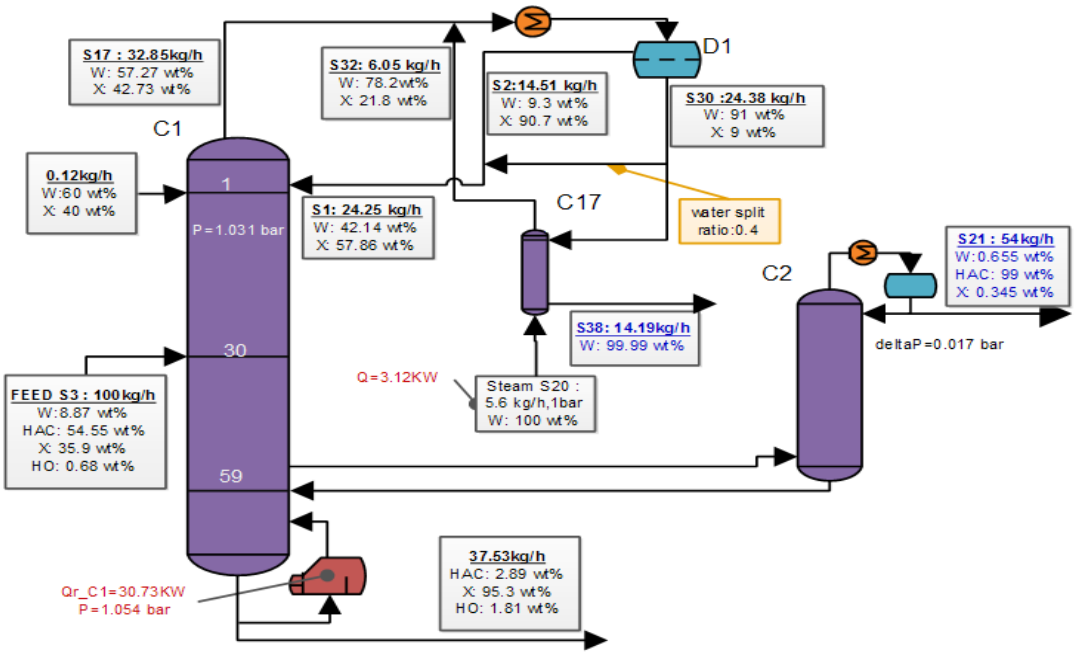

Figure 4: Side rectifier configuration (equivalent to DWC configuration in Fig. 1b with wall in upper part of column). Overall Q=33.85 kW

3. DWC with the wall placed at the upper part of the column

We consider the simple DWC solution in Figure 1b with the partition wall placed at the upper part of the column. This arrangement eliminates one reboiler, but still needs two condensers. Assuming negligible heat transfer across the wall, this configuration is equivalent to the simulated flowsheet in Figure 4.

Some observations can be made from the simulation results. First, we cannot avoid a slippage of HAC into the bottom stream of C1 (2.89 wt% versus 0.14% in the original design). Second, this configuration consumes 33.85KW which is only slightly lower than the energy required for the conventional design. Hence, energy savings are not achieved, but the capital costs are expected to be lower.

4.DWC Petlyuk arrangement

4.1 Simulation

Next, consider the three column section arrangement in Figure 5a which is thermodynamically equivalent to the Petlyuk DWC in Figure 1a. However, the arrangement in Figure 5a has many recycles between the column sections and it is difficult to get numerical convergence when using commercial simulators (e.g. Aspen, Hysys, Unisim). Thus, for simulations we used the three-column arrangement in Figure 5b with no recycles between the columns. The heat duty removed from the condenser in C1 in Figure 5b is used to virtually superheat the top product of C1 (or equivalently, used in a side heater in C21) and the reboiler duty required in C1 is supplied from virtually subcool the bottom product of C1 (or equivalently, used in a side cooler in C22). The boilup rate in C22 is adjusted until the heat duties in the reboiler of C21 and in the condenser of C22 become equal. More details about this

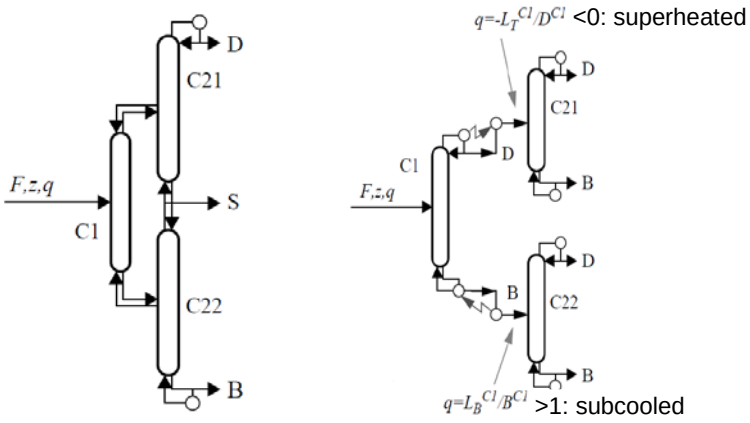

(a) *(b)*

Figure 5: Petlyuk arrangement (a) and simulation representation (b)

approach are found in Appendix D in [6]. The configuration in Figure5(b) is equivalent to that in Figure 5(a) for optimal operation with an infinite number of stages [6], but it has been found to give almost identical results also with a finite number of stages [6].

4.2 DWC Petlyuk with original feed mixture

A direct application of the Petlyuk idea to integrate the two original columns (C14 and C108 in Figure 2) does not work. The reason is that the nonideal thermodynamics make the heavist component (X), which eventually must end up in the *bottom* product in C108, appear as an azeotrope with water (W) at the *top part* of column C14. Because of this it is not possible to get an HAC-sidestream in the Petlyuk column with no X.

4.3 DWC Petlyuk with IBA added as entrainer.

However, it is possible to operate the column system such that X does not go to the top, for example, by reducing the amount of water reflux, as we found out when simulating the original design in Figure 2. Instead, HAC g0oes to the top and since the resulting water-HAC mixture is difficult to separate, we need to add an entrainer in the top. Our first approach was to use X as the entrainer because this avoids adding a new component. We found it to be workable, but X is not an ideal entrainer because the water phase contains about 10 mol% of X (Figure 3) and simulations showed that we need quite a lot of energy to strip off X. There are many better entrainers such as isobutyl acetate (IBA), n-butyl acetate and ethyl acetate [7]. We chose IBA (Bp. 116C) which is almost immiscible with water and forms a low-boiling azeotrope at 88C (so IBA and water don't like each oher) and forms a high-boiling azeotrope with HAC at 123C (so IBA and HAC like each other). The IBA remains in the top in a closed cycle, and only little IBA makeup is needed [7].

The simulation results are shown in Figure 6. Note that the number of trays in MAINCOL in Figure 6 is equal to the sum of stages in C21 and C22 in Figure 5b. The amount of IBA needed in the simulations was surprisingly small (only about 3 wt% IBA in the overhead vapor which is far from the azeotrope at 78 wt%). The reason is probably that only a small amount of IBA is needed to „bind" HAC and make it less volatile. To minimize the need for IBA makeup further and make the water product purity comparable with the original design, we added a stripper (C4), similar to that in the original design, but the required amount of steam is quite small and only

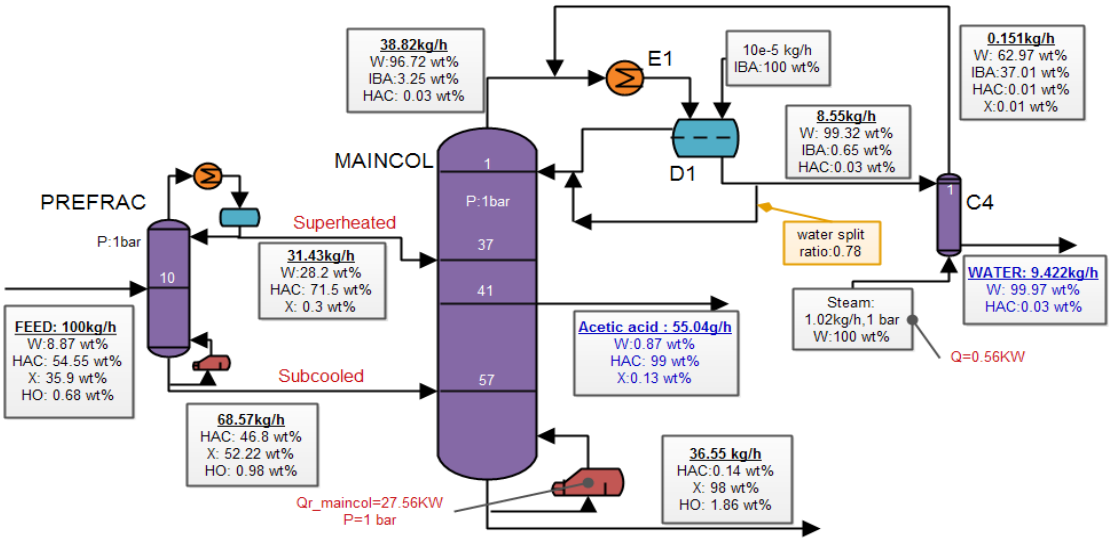

Figure 6: Simulation of Petlyuk-DWC with IBA as entrainer. Overall Q=28.12 kW

contributes 0.56 kW.The total heat input for this Petlyuk arrangement is 28.12 kW, which corresponds to *an energy saving of 19%*, compared to the conventional design. In addition, there will be savings in the capital costs, which are probably more important. The reason for the somewhat low energy savings of 19% is partially because this is a quite easy split (with relative volatilities for W-HAC-X equal to 7.8: 2.8:1 at the feed tray of prefractionator).

5. Conclusions

This work shows applies dividing wall columns (DWC) to ternary heterogeneous azeotropic distillation. For the feed mixture of water (W), acetic acid (HAC) and an organic component (X), the original design makes use of X to act as an entrainer to facilitate the separation of water and HAC (Figure 2). We propose a DWC design based on this idea (Figure 4). This DWC design reduces the capital cost, but the energy usage is almost unchanged. To achieve energy savings and further reductions in capital costs, we need to use a Petlyuk DWC (Figures 5a and 6). However, because component X is heavier than W and HAC, X cannot be used as the entrainer for this design. Thus, we introduce isobutyl acetate (IBA) as an additional entrainer and achieve energy savings of about 20%. A challenge for discovering and designing new integrated schemes is to develop systematic methods to supplement the present *ad-hoc* engineering approach.

References

[1] M. Benedict and D.R. Rubin, Extractive and Azeotropic Distillation. I. Theoretical Aspects, Trans. Am. Inst. Chem. Eng., 41 (1945), 353-370
[2] S. Widagdo and W.D. Seider, Azeotropic distillation, AICE J., 42 (1996), 96-130.
[3] G.Parkinson, Dividing-wall columns find greater appeal, Chem. Eng. Prog., 103, 5 (May 2007), 8-11
[4] H.H. Pham and M.F. Doherty, Design and synthesis of heterogonous azeotropic distillations - III. Column sequences, Chem. Eng. Science, 45 (1990), 1845-1854
[5] R.O.Wright, Fractionation apparatus, US Patent No. 2471134 (1949)
[6] I.J. Halvorsen, "Minimum Energy requirements in complex distillation arrangements", PhD thesis, Dept. of Chemical Engineering, NTNU 2001:43 (available from the home page of S. Skogestad).
[7] W.L. Luyben and I-L. Chien, "Design and Control of Distillation Systems for Separating Azeotropes ", John Willey & Sons Inc, 2010.

Hydrodynamics and Fouling in Polymeric Falling Film Evaporators for Multi-Effect-Distillation

C. Dreiser, H.-J. Bart
Chair of Separation Science and Technology, University of Kaiserslautern, Kaiserslautern, Germany

Abstract
To gain the knowledge of surface specific relations regarding wettability and scaling affinity for novel materials in apparatus design falling film and crystallization fouling studies are presented for various polymeric surfaces and a benchmark stainless steel. For the model salt solutions of calcium sulfate and calcium carbonate the interfacial energy difference between deposit and heat transfer surface is isolated as essential factor affecting scaling. This relation can be used for further optimization of the already scaling resistant polymeric surfaces. The falling film wettability is correlated for a plane surface as well as for the polymer film heat exchanger (PFHX) specific polymer-spacer geometry. The significant high thermal performance as well as the low scaling affinity and the cleaning in place strategy of the PFHX are beneficial for industrial applications in corrosive environment.

Keywords
Wetting, falling film, polymer heat exchanger, surface properties, fouling.

1. Introduction

Heat and mass transfer processes in falling film flow regimes take place in many thermal unit operations (absorption, distillation, falling film heat exchangers). Several experimental and theoretical investigations have been carried out to describe the wettability and falling film break-up in such processes [1-3]. The wetting performance as well as the fouling or scaling propensity is very sensitive to surface properties (roughness and topology, surface free energy and polarity) [4,5]. Especially fouling causes tremendous costs and high energy demand due to operational problems with heat exchangers [6] or columns [7]. Therefore, correlations for the prediction of surface wettability of flat surfaces should be discussed as well as general relations of crystallization fouling propensity on various surfaces.

Polymeric heat exchangers and column internals have been developed as cost-efficient alternatives in handling of corrosive media [7-9]. Christmann et al. [10] introduced a concept of a thin polymer film heat exchanger applicable e.g. for thermal desalination process conditions. High overall heat transfer coefficients and a sufficient mechanical stability are achieved by applying a wall thickness of 25 µm in combination with a supporting spacer grid [11]. However, in the following the design criteria of such novel heat exchangers in respect to the specific hydrodynamic and thermal situation will be discussed. As to this the paper presents surface related results of falling film wettability and crystallization fouling propensity of calcium sulfate ($CaSO_4$) and calcium carbonate ($CaCO_3$) solutions as major occurring industrial scaling species. Exemplarily results are given for a stainless steel surface (1.4571 or

316Ti) as benchmark and the polymer surfaces polypropylene (PP), polysulfone (PSU) and polyether ether ketone (PEEK) in different modifications (Aptiv® series).

2. Results and discussion

2.1 Wetting on polymeric heat transfer surfaces

Falling film break-up should be avoided in heat exchanger operation due to heat transfer performance and scaling propensity [12]. To predict the critical liquid load Γ^+ or Re^+ for the falling film on a vertical plane surface correlations of the following equation exist [13,14]:

$$Re^+ = \frac{\Gamma^+}{\eta_L} = a \cdot \left(Ka \cdot \left(1 - cos\theta\right)^3 \right)^b \tag{1}$$

where η_L is the dynamic viscosity of the liquid, θ the contact angle and Ka the Kapitza number:

$$Ka = \frac{\sigma_L^3 \cdot \rho_L}{\eta_L^4 \cdot g} \tag{2}$$

in which ρ_L is the density and σ_L the surface tension of the liquid and g the gravitational acceleration. Figure 1 presents the application of the correlation on a PEEK surface with a = 1.69 and b = 0.2, also found by Hartley and Murgatroyd [13].

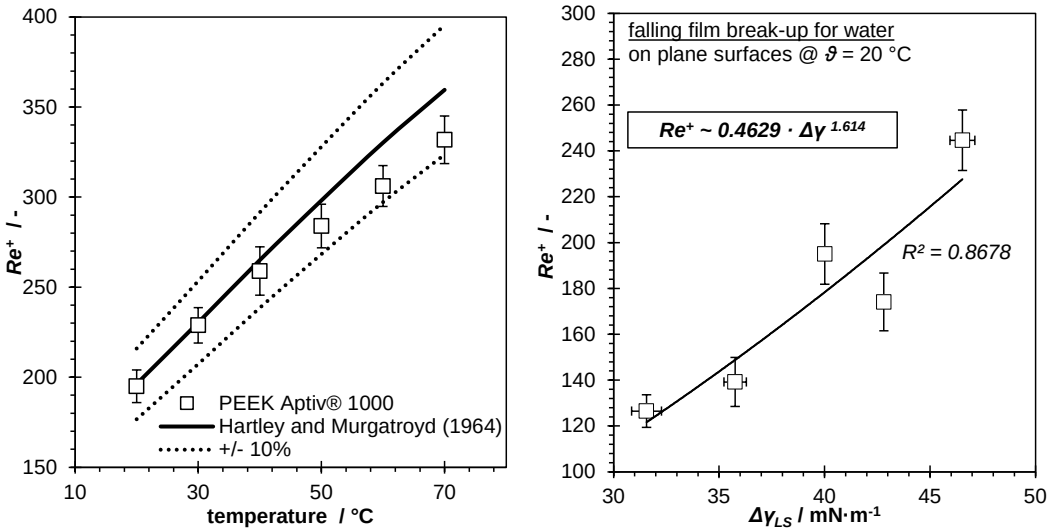

Figure 1: Experimental and correlated falling film critical Reynolds numbers Re^+ for water on a polymer surface (left) and relation between surface free energy difference between liquid and solid $\Delta\gamma_{LS}$ and the critical Reynolds number for various surfaces (right).

The critical falling film Reynolds number can be predicted within an adequate accuracy for polymer surfaces under knowledge of temperature dependent physical properties of the liquid and wetting characteristics of the surface (contact angle). These wetting characteristics depend on the surface free energy of a solid and the difference to the surface energy of the wetting liquid. Smaller interfacial energy differences increase the falling film wettability for the same liquid (Figure 1) and should be the aim of surface finishing technologies. Plasma treatment techniques e.g. showed a wetting enhancement of almost 30 % observed in contact angle measurements [4]. The observed reduction in corresponding experimental Re^+-values is incentive for a stable heat transfer operation at low film thicknesses.

2.2 Fouling on polymeric heat transfer surfaces

The additional thermal resistance of a fouling layer R_f reduces the actual overall heat transfer coefficient U_f compared to the state of the clean surface U_c. Fouling itself, however, is strongly affected by present process conditions like initial foulant concentration c_0, bulk temperature ϑ_b and initial wall temperature $\vartheta_{w,t=0}$. At studied process conditions of thermal desalination plants the scaling propensity of calcium sulfate and calcium carbonate solutions was found to be significantly lower on polymer surfaces compared to stainless steel (Figure 2 left) [5,12]. Besides a lower mean arithmetic roughness the surface free energy impacts the kinetics of crystallization fouling. Figure 2 (right) represents the deviation between the measured adhesive strength of gypsum on various polymeric surfaces and the stainless steel surface. The 10 to 20 times lower adhesion of the deposit on the polymers contributes to the cleanability compared to stainless steel.

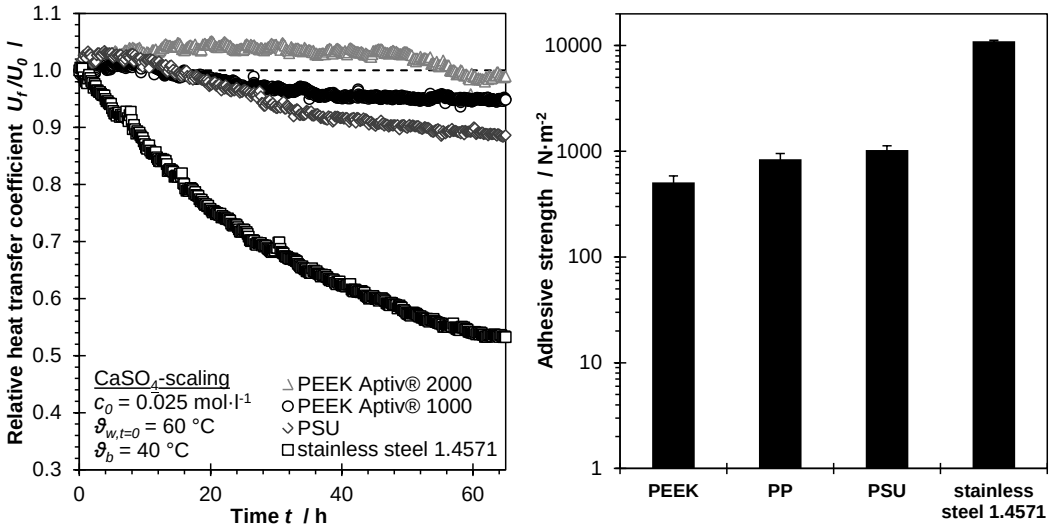

Figure 2: Heat transfer loss due to crystallization fouling [12] (left) and adhesive strength of gypsum on various surfaces (right).

A general characterization of scaling affinity can be performed by calculating the interfacial energy difference between surface and deposit. In analogy to wetting performance (see above) a smaller value results in larger adhesion ergo increase in scaling amount (Figure 3 left).

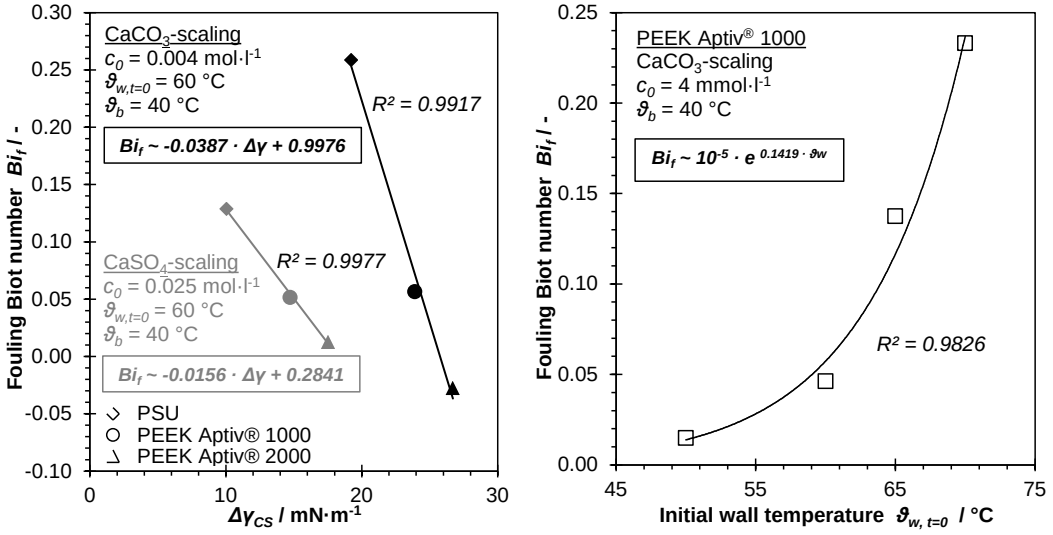

Figure 3: Scaling quantity of calcium sulfate and calcium carbonate solution as function of the interfacial energy difference between deposit and heat transfer surface $\Delta\gamma_{CS}$ for various materials [12] (left) and impact of initial wall temperature on calcium carbonate scaling [15] (right).

For an global interpretation and comparison to other heat transfer equipment the non-dimensional fouling Biot number is introduced as the overall heat transfer coefficient of the clean surface and the product of the thermal fouling resistance as $Bi_f = U_c \cdot R_f$ [16]. A large fouling Biot number indicates a domination of the overall thermal resistance by fouling. These results are relevant for custom-designed surface finishing technologies. A larger value of interfacial energy difference increases the activation energy of crystallization fouling kinetics and should be achieved in surface design. The impact of initial wall temperature is of exponential behavior for calcium carbonate scaling (Figure 3 right). As described by Dreiser and Bart [12] the calcium carbonate scaling kinetics can be derived from experiments under variation of wall temperature and lead to an activation energy of 71.6 kJ·mol^{-1} for the PEEK (Aptiv® 1000) surface, which is about 40 % higher compared to the stainless steel surface, contributing to the significantly lower scaling affinity of the polymeric surfaces.

2.3 Polymer film heat exchanger (PFHX) performance

When applying thin polymer films (25 µm) with a supporting spacer grid as heat transfer surface the hydrodynamics differ from the flat vertical plane without any support. Eq. 1 was adapted for critical Reynolds number measurements of water and the film-spacer combination by adjusting *a* to 1.65. The results are shown in Figure 4 (left). This adapted correlation was also found to be applicable on an extended range of Reynolds numbers by performing experiments with a glycerin/water-mixture. The polymer/spacer combination acts as turbulator, which enhances the heat transfer significantly. Figure 4 (right) compares the overall heat transfer coefficients for falling film heating under variation of falling film Reynolds number Re_{ff} at fixed heating side flow rate $\dot{m}_c$, falling film inlet temperature $\vartheta_{ff,in}$ and temperature difference $\Delta\vartheta$. Under consideration of wall thicknesses and thermal conductivity of the heat transfer surfaces the overall heat transfer coefficients of the 2 mm steel surface should be in the range of a 25 µm PEEK surface (with regard to Nusselt-correlations). It should be noted that the plane geometry can be modeled in good accordance with existing Nusselt-correlations (dashed line). However, the PEEK-spacer combination yields a considerably higher thermal performance as expected.

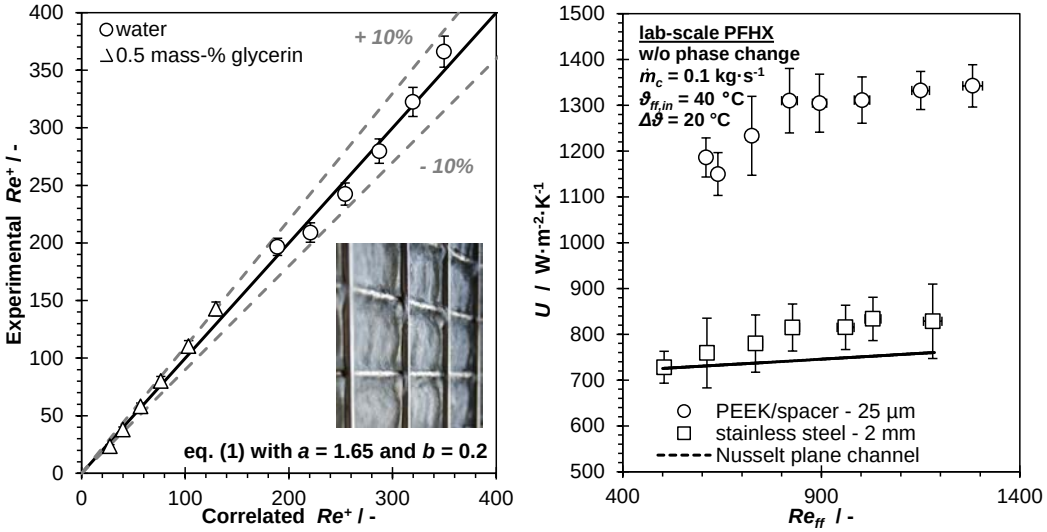

Figure 4: Experimental and correlated falling film critical Reynolds numbers for PEEK/spacer combination (left) and thermal performance for falling film heating compared to a stainless steel plate (right).

The good thermal performance of the PFHX gives space for potential safety factors in wall thickness. Compared to other polymer-based heat exchangers no additional heat

transfer area is required to compete with metallic plate heat exchangers. A further benefit is given by the low scaling affinity of the polymers. Besides the facts discussed above the spacer-induced turbulence also decreases scale deposition. In contrast to a strongly fouled stainless steel surface the PEEK/spacer-combination showed no measurable heat transfer drop due to deposition over one week of operation with calcium sulfate solution. Therefore, the heat exchanger has been operated at low Reynolds numbers (rivulet flow conditions) to force scaling due to high local supersaturation (Figure 5).

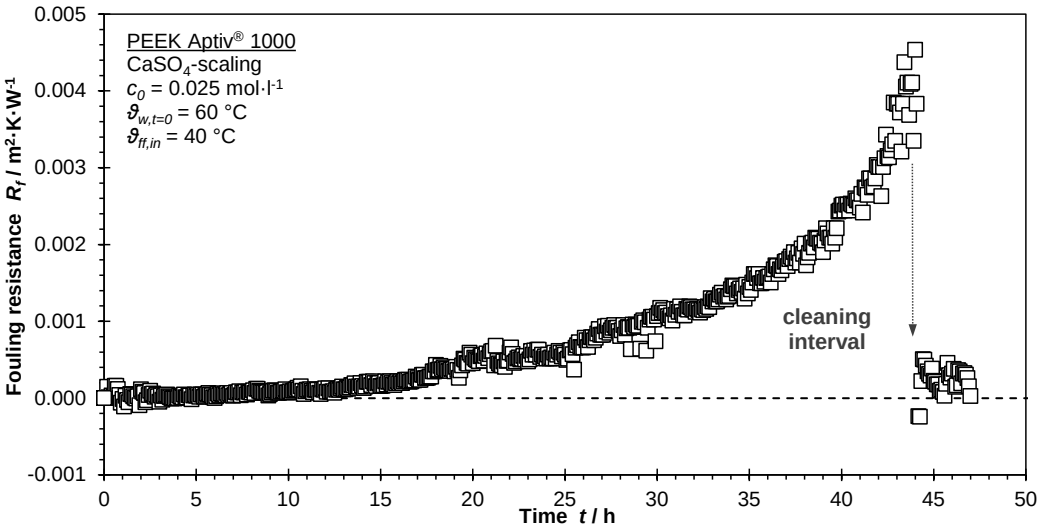

Figure 5: Calcium sulfate scaling and cleaning in a falling film heat exchanger with PEEK/spacer combination operated at rivulet flow regime ($Re < Re^{+}$) [15].

Although crystallization fouling did occur, after the cleaning in place process of only a few minutes overall heat transfer coefficients, which are almost as high as for the clean surface, could be reproduced. The basis of the cleaning procedure is a pressure pulse at the flexible thin polymeric heat transfer surface to dump off the stiff deposit layer. Details of the cleaning procedure are given by Dreiser et al. [15]. A frequently applied cleaning procedure is very promising for PFHX long term operation without significant heat transfer drop or maintenance downtimes, which is a common industrial problem. The general result is a highly efficient operation as well as small necessity to overdesign of the heat transfer area to compensate scaling with this apparatus concept.

3. Conclusions

General observations on flat surfaces contribute to the impact of interfacial effects of various surfaces on wettability as well as scaling propensity of the two model salt solutions of calcium sulfate and calcium carbonate. The observed differences in interfacial energy allow an early conceptual stage material selection (including surface finishing technologies like plasma treatment) for applications with corrosive media (heat exchangers, column internals, crystallizers etc.). The low scaling propensity on polymeric surfaces can be explained by a larger interfacial energy difference, smaller specific adhesion of deposit and larger activation energy of the process of scaling compared to a stainless steel surface. With the knowledge of physical properties and small scale wetting characteristics (contact angle) the falling film wettability (critical Reynolds number) can be correlated for flat polymer surfaces as well as for the apparatus specific geometry. This polymer/spacer geometry acts as film promoter which results in higher heat transfer coefficients and reduced scaling

propensity due to increased turbulence. The thermal performance, low scaling tendency and fast cleaning in place strategy is an incentive for industrial application of the PFHX in corrosive environment.

Acknowledgements
The authors would like to thank the Deutsche Forschungsgemeinschaft (DFG) for the financial support.

References

[1] B. Szulczewska, I. Zbicinski, and A. Górak, *Chem. Eng. Technol.* 26 (2003) 5, 580-584.
[2] A. Hoffmann, I. Ausner, J.-U. Repke, and G. Wozny, Trans IChemE, Part A, *Chem. Eng. Res. Des.* 84(A2) (2006), 147-154.
[3] M. S. El-Genk, and H. H. Saber, *Int. J. Heat Mass Tran.* 44 (2001), 2809-2825.
[4] C. Dreiser, and H.-J. Bart, *J. Mater. Sci. Eng. A* 3 (2013) 9, 591-600..
[5] C. Dreiser, L. J. Krätz, and H.-J. Bart, in *Proc. of the Int. Conf. on Heat Exchanger Fouling and Cleaning X* (2013), Eds.: Müller-Steinhagen, H., Malayeri, M.R., and Watkinson, A.P., Budapest, Hungary, 291-295.
[6] R. Steinhagen, H. Müller-Steinhagen, and K. Maani, *Heat Transfer Eng.* 14 (1993) 1, 19-30.
[7] D. Großerichter, and J. Stichlmair, Trans IChemE, Part A, 81 (2003), 68-73.
[8] D. M. Bigg, G. H. Stickford, and S. G. Talbert, *Polym. Eng. Sci.* 20 (1989) 16, 1111-1116.
[9] D. A. Reay, *Heat Recov. Syst. CHP* 9 (1989) 3, 209-216.
[10] J. B. P Christmann, L. J. Krätz, and H.-J. Bart, *Desalination* 308 (2013), 56-62.
[11] J. B. P Christmann, L. J. Krätz, and H.-J. Bart, *Appl. Therm. Eng.* 38 (2012), 175-181.
[12] C. Dreiser, and H.-J. Bart, *Appl. Therm. Eng.* 65 (2014), 524-529.
[13] D. E. Hartley, and W. Murgatroyd, *Int. J. Heat Mass Transfer* 7 (1964), 1003-1015.
[14] H. Coulon, *Chem.-Ing.-Techn.* 45 (1973) 6, 362-368.
[15] C. Dreiser, L. J. Krätz, and H.-J. Bart, in *Proc. of the Int. Conf. on Heat Exchanger Fouling and Cleaning X* (2013), Eds.: Müller-Steinhagen, H., Malayeri, M.R., and Watkinson, A.P., Budapest, Hungary, 296-301.
[16] P. J. Fryer, *J. Soc. Dairy Technol.* 42 (1989) 1, 23-29.

The destructive vibration of column trays

W. Zhang, P.H. Taylor and R.C. Darton,
Department of Engineering Science, University of Oxford, Oxford, UK

Abstract
The occasional structural failure of both sieve and valve trays operating at low vapour rates has been attributed in the literature to fatigue of tray parts caused by flow-induced vibration. We suggest that synchronous oscillation of flow at the tray perforations can occur when they are evenly spaced, and present a correlation for the oscillation frequency based on the data of Priestman *et al.* (1979). We show how effective elastic constants can be calculated for perforated tray panels, and draw attention to the stress concentration around holes near the tray edge that exposes trays to fatigue cracking during vibration. Vibration analysis of an idealized tray structure identified the first 30 modes with resonant frequencies between 25 and 70Hz, the range where excitation by flow-induced pressure pulsations is possible.

Keywords
Tray damage, vibration, resonance, modal analysis, pulsation

1. Introduction

At the 3rd International Symposium on Distillation, Brierley reported incidents at ICI in which trays were damaged by flow-induced vibration, in severe cases leading to collapse of tray sections and even a cracked column shell (Brierley *et al.*, 1979). Cracking of beams and tray panels has been reported, the parts commonly showing evidence of fatigue failure; workers reported that such a column “sounded like a bee-hive” due to parts chattering (Winter, 1993). Vibration damage mostly occurred at low vapour flow rates, and was experienced with both sieve and valve trays, sometimes after only a few hours of operation. It seems that such vibration only occurs at specific conditions: Brierley commented that “the source of vibration has been observed to move up or down a column with changing heat input to the reboiler.”

Brown (1958) had reported pressure fluctuations in the range 3.3 to 32Hz in the chamber below a perforated plate (see Chan and Prince (1966) who produced further data and a theory). Kupferberg and Jameson (1970) found that in a plate with multiple holes, as opposed to a single orifice, the frequency of pressure fluctuations did not equal the bubble formation frequency, so that theory for single bubble formation could not be applied. Regimes of jetting and bubbling at a single orifice were investigated by Muller and Prince (1972). They identified two regimes, likely to occur in commercial trays, in which regular pressure fluctuation in the chamber below the orifice was induced by gas-liquid interaction on the plate. These were the ‘imperfect bubble’ regime (where bubbles break through the surface before they are fully formed) and ‘pulsating jet’ at higher gas velocities; both required relatively shallow pools of liquid, not more than 30-40 mm in depth.

In research supported by ICI, Priestman *et al.* (1979) found pressure fluctuations in the range 12-40Hz in an air-water simulator fitted with sieve trays. They concluded that regular pressure pulsations could be induced by synchronous bubbling or jetting behaviour (oscillations) at the tray holes, and that the effect of pulsations, perhaps magnified by resonance, could be the cause of tray damage.

We have investigated this problem using a combination of insights and data from literature studies of oscillating flow at tray perforations with structural analysis of perforated plates and vibration mode analysis of tray structures.

2. Results and discussion

2.1 Oscillating liquid and pressure pulsations: frequency

Both Muller and Prince (1972) and Priestman and Brown (1988) observed liquid oscillation at the tray hole. Liquid moves away from the hole, then falls back towards, and to some extent into it; as the next cycle starts, liquid is blown out of the hole, and away again. During these movements, the gas velocity rises and falls, and pressure in the inter-tray space varies as well. Working with sieve trays 406 mm square, Priestman *et al.* (1979) found the frequency of pressure pulsations to increase linearly with the hole velocity but to vary little with hole diameter (d). Increasing the liquid head on a tray also increased the frequency in most cases. Photography revealed a circular spread of liquid from the hole at each cycle, with a diameter similar to the hole pitch. The pulsation frequency decreased as pitch (s) increased, and they concluded that the hole edge to hole edge distance $(s-d)$ was a crucial factor. This key observation helps us to understand the mechanism by which oscillations are synchronized. It implies that adjacent holes interact on a time scale comparable with that of the oscillations (25-80ms), which is similar to the time scale on which a variation in liquid head would be communicated between adjacent holes $(\sim (s-d)/\sqrt{(gH_L)})$ where H_L is the liquid height on the tray. This is much longer than the time for a pressure disturbance to travel the same distance in the vapour phase (<0.1ms). Local variations in pressure in the inter-tray space are evened out rapidly. Thus we would not expect the volume of the inter-tray space to affect the pulsation frequency, and this was confirmed by these experiments: a fivefold variation in the inter-tray volume had little effect on the frequency observed.

For a tray with regular perforation spacing (square or equilateral triangle pattern), the time for communication between adjacent holes will be the same all over the tray. This will promote the synchronous variation of vapour/liquid interactions at all holes. The exception will be for those holes at panel edges where the adjacent holes may, for construction reasons, not be placed at the usual regular distance. Also, for holes near the wall, weir or inlet downcomer, adjacent holes will be absent on one side. In three of the trays (C, D, E) the number of holes was reduced (403, 256, 108) whilst keeping the pitch (equilateral triangle pattern) and hole diameter the same. As a result these trays show the effect of leaving an area unperforated: reducing the perforated fraction from 84% to 24% reduced the oscillation frequency by ~10%. Figure 1 shows the frequency for

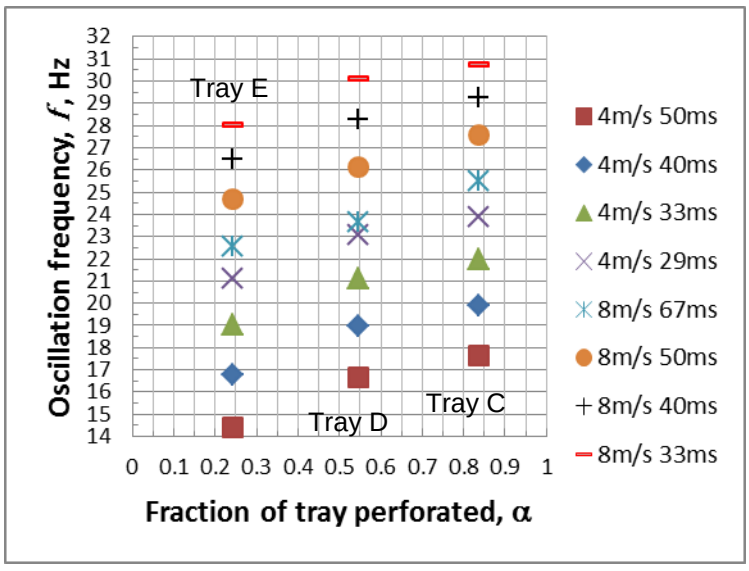

Figure 1: Data for trays C, D, E. Priestman *et al.* (1979)

values of the parameter $(s-d)/\sqrt{(gH_L)}$, interpolating from measurements at 4m/s and 8m/s hole velocity. Denoting $f(\alpha)$ as the oscillation frequency for a fractional perforation α, the data were fitted by $f(\alpha) = f(1)(1+0.2\alpha)/1.2$. The trays used in developing our correlation for oscillation frequency are listed in Table 1. If these trays behave similarly to the series C, D, E, we might expect the frequency measured for trays A, B, and C to be some 2-3% lower than if the whole tray area had been perforated. For trays N and O, which have a perforated fraction greater than 1.0, some holes on the edge of the perforated area are closer to the walls than the hole pitch.

Tray	A	B	C	H	I	L	N	O
Number of holes	403	391	403	108	104	108	38	38
Hole diameter, pitch, mm	4.76, 19.05	6.35, 19.05	9.53, 19.05	9.53, 38.1	12.3, 38.1	15.87, 38.1	12.3, 66.0	15.87, 66.0
Fraction of tray perforated*	0.839	0.814	0.839	0.969	0.939	0.969	1.136	1.136

Table 1: Trays used in correlating frequency data, Priestman *et al*. (1979)
* Fraction of tray with normal perforation pattern; rest is bare metal.

The pulsation frequency data for the 8 trays of table 1 are correlated in Figure 2. Measurements were made either at constant hole velocity, or constant liquid height, as indicated in the legend to Figure 2. The correlation ($r^2 = 0.974$) is

$$\frac{fd}{U} = 0.005\left(1+\sqrt{\frac{\rho_L g d^2}{\gamma}}\right) + 0.46\left(\frac{d}{s-d}\right)\sqrt{\frac{gH_L}{U^2}} \qquad (1)$$

where f is the frequency and U is the mean gas velocity through the holes.

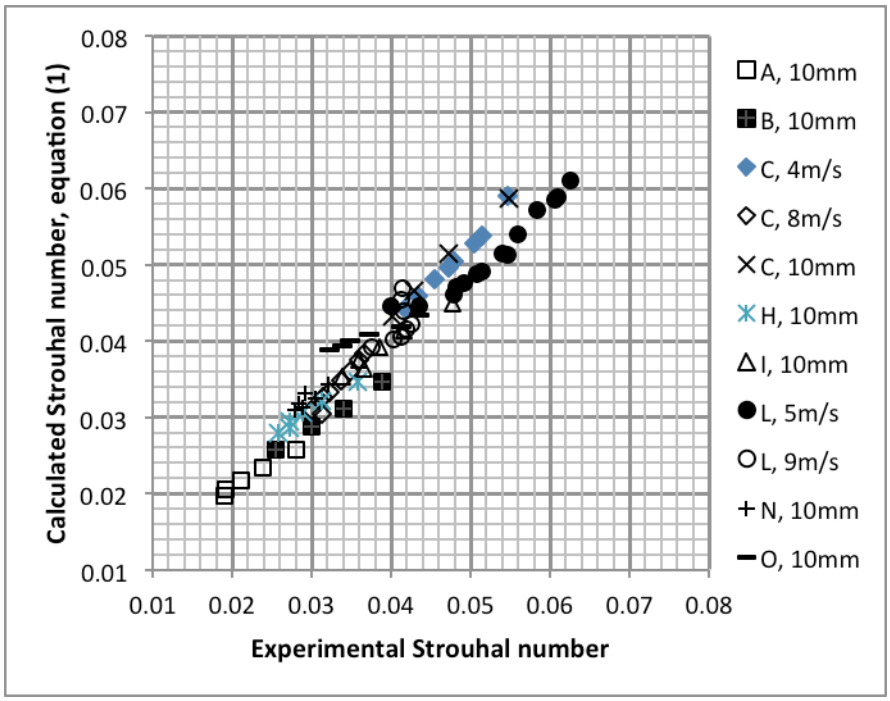

Figure 2: Correlation of pulsation frequency. Data of Priestman *et al.* (1979)

Although neither was varied in the experiments with air and water, both the liquid density ρ_L and the surface tension γ are included to ensure dimensional consistency. The correlation shows that the Strouhal number fd/U, is a function of the Bond number $\rho_L g d^2/\gamma$, the geometric ratio $d/(s-d)$ and the the Froude number $U/\sqrt{(gH_L)}$.

2.2 Pressure pulsations: amplitude

Pressure pulsations on adjacent trays cannot be in-phase because the pressure drop must fluctuate to be consistent with gas flow through the perforations. The pressure in the inter-tray space can be calculated from the unsteady state continuity equation, and this suggests that the RMS pressure fluctuation $\boldsymbol{p}$ will vary as $\boldsymbol{P\kappa A_h u/Vf}$. $\boldsymbol{P}$ is the mean pressure, κ the isentropic expansion factor of the gas, $\boldsymbol{A_h}$ the total hole area on the tray, $\boldsymbol{V}$ the volume of the inter-tray space and $\boldsymbol{f}$ the frequency. $\boldsymbol{u}$ is a measure of the variation in hole velocity, and is a fraction of its mean value $\boldsymbol{U}$. At high values of $\boldsymbol{U/\sqrt{(gH_L)}}$ we expect that $\boldsymbol{u/U \rightarrow 0}$ as a steady jet forms which entrains droplets rather than causing bulk liquid oscillation at the hole, and at low values of $\boldsymbol{U/\sqrt{(gH_L)}}$ oscillations will be suppressed by heavy weeping.

2.3 Holes in a plate – effective material properties and stress concentration

Perforated plates will be more flexible than solid plates of the same material, thus at long bending scales compared to the hole spacing the resonant frequencies will be lower. Locally to each hole there will also be a stress concentration effect.

Initially we consider a perforated sheet supporting an externally imposed stress in one direction (Figure 3a). The pattern of the holes is taken as square but the method is applicable to any regular pattern. We start with the known stress distribution for a single circular hole in an infinite plate (Timoshenko and Goodier, p90). We then sum the effects of many such stress distributions each centred on a hole away from the centre of the plate, neglecting any cross-hole interactions. This provides an estimate of the effect of the surrounding holes on the origin O in Figure 3a. The stresses here are modified from the undisturbed values σ_0 in the vertical direction and zero horizontally. We now insert the actual hole at the origin and make an estimate of the actual local stresses accounting approximately for the influence of the other holes. Given this value we now repeat the procedure but using the first approximation for the local stress field for all the other holes and calculate a second approximation at the central hole. This procedure could be repeated but it is not necessary as the stresses already obtained are accurate enough. We then calculate the vertical extension and horizontal contraction of the plate over a unit cell around a single hole to provide estimates for both the effective Young's modulus (E^*) and Poisson's ratio (ν^*) for the perforated plate, assuming (E, ν) in the bulk material. Figure 3b shows the analytical approximations based on the superposition of holes and data fits by O'Donnell (1962) based on his experiments with perforated plates. Even a small hole area ratio (free area) leads to significant reduction in the effective Young's modulus, but the change in the effective Poisson's ratio is much smaller.

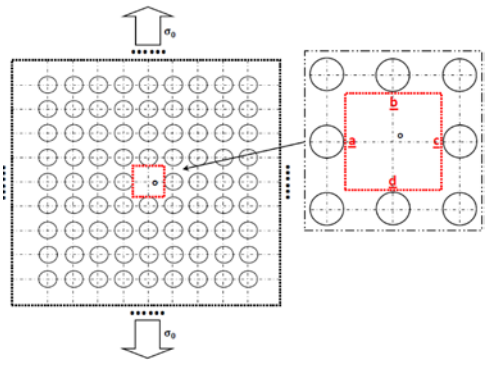

Figure 3a: Perforation pattern and stress calculation unit cell

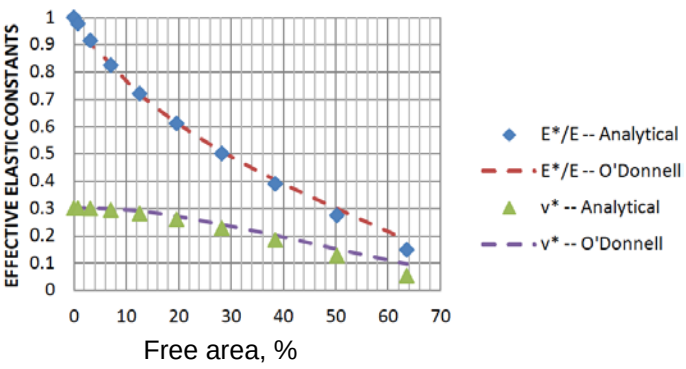

Figure 3b: Effective elastic constants, from analytic approximation and experiments

Given the effective material properties it is straightforward to estimate the overall bending stiffness (per unit length) of the plate as $D^* = E^* t^3/12(1-\nu^{*2})$, with t the plate thickness (Timoshenko and Woinowsky-Krieger, p5). The reduction in the effective Young's modulus is significant, but the role of the effective Poisson's ratio is small. Figure 4a shows a comparison of the analytic approximation based on the effective elastic moduli, a finite element analysis of a unit cell in a perforated plate performed using SolidWorks (both as symbols), and two curve fits (from O'Donnell (1962) and CODAP(1985)). Although the results are presented for plates with square perforation patterns, other patterns give very similar results as shown by O'Donnell.

At a scale local to an individual hole there is amplification of the stress field compared to the unit cell area-averaged value, as shown in Figure 4b for global load in one direction. The stress amplification for small free area is 3x (Timoshenko and Goodier, p90) but this grows significantly as the free area increases. Thus, fatigue cracking, running from the boundary supports towards the closest hole and from hole to hole, is a serious risk when perforated plates vibrate.

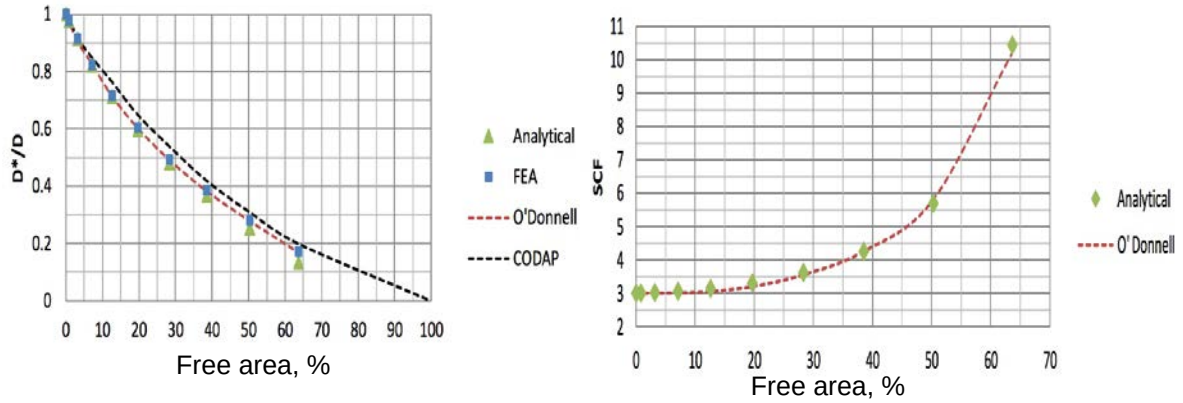

Figure 4a: Reduced effective bending stiffness

Figure 4b: Local stress concentration factor for uni-directional loading

2.4 Vibration analysis

We can use the effective elastic moduli (E^*, ν^*) when performing vibration analysis to estimate the resonant frequencies and mode shapes which might be excited, if these modes are long compared to the hole pitch. As an example we consider an idealised tray structure approximately 2m x 2m, with panels of width 406mm set side by side, joined and supported by small U-angle sections. All the dimensions are chosen to be representative of what would be found in a typical distillation column. The panels are stainless steel, 2mm thick with 15% free area. A vibration analysis of this geometry was conducted with the finite element package SolidWorks, allowing for the

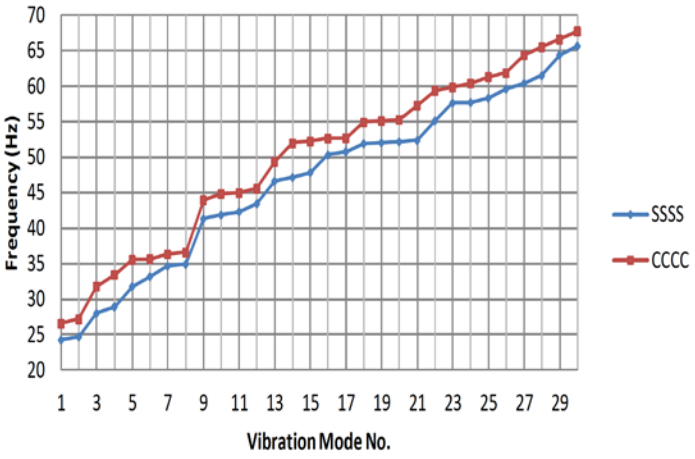

Figure 5. Structural vibration resonance frequencies of idealized tray structure

presence of the fluid layer on the tray. The frequencies and associated mode shapes of the first 30 modes were identified, as shown in Figure 5. The first 30 structural modes occur in the range 20-70Hz associated with tray vibration. Results for two cases are shown, the lower when the tray perimeter is simply supported (SSSS - restrained against motion out of plane but no rotational restraint on each edge, acting as a frictionless hinge) and the higher where both translation and rotation at the edge is suppressed (CCCC – all boundaries rigidly clamped).

These calculations illustrate that the edge conditions play a relatively minor role – a convenient finding, as in practice the edge conditions are likely to be intermediate between simply supported and rigid clamping. The results show that there are plenty of vibration modes in the range of observed tray pressure pulsation frequencies. Thus, during operation at conditions which enable coupling between flow-induced pulsations and the structure, and with relatively low structural damping, it would not be surprising if damaging levels of vibration were to occur.

4. Conclusions

Fatigue cracking and failure of column trays can happen when they vibrate in resonance with pressure pulsations in the inter-tray space. These pressure pulsations occur over a certain range of operating conditions and result from synchronous oscillation of bulk liquid at the tray perforations. The oscillation frequency increases as hole velocity increases, as hole spacing decreases and at greater liquid heights on the tray. The bending stiffness of trays decreases as the free area increases, reducing the resonant frequency. We can use effective elastic constants calculated for a perforated plate to identify the vibration frequencies of tray designs which include supports and beams. A typical tray for a column of diameter several metres shows many resonant frequencies in the range (25-70Hz) where pressure pulsations might be expected. Stress is amplified close to tray perforations, and fatigue cracks running from tray supports to the nearest hole and from hole to hole are a serious risk during vibration.

References

Brierley, R.J.P., Whyman, P.J.M. and Erskine, J.B. (1979) “Flow induced vibration of distillation and absorption column trays” in Distillation 1979, IChemE Symp. Ser No 56, 2.4/45

Brown, R.S. (1958) “Bubbling from perforated plates” PhD thesis University of California, Berkeley

Chan, B.K.C. and Prince, R.G.H. (1966) “Dynamic characteristics of perforated distillation plates operating at low loads” AIChE Journal 12, 232-237

CODAP (1985) Code Francais de Construction des Appareils a Pressions (French Code for Construction of Unfired Pressure Vessel)

Kupferberg, A. and Jameson, G.J. (1970) “Pressure fluctuations in a bubbling system with special reference to sieve plates” Trans IChemE 48, T140-T150

Muller, R.L. and Prince, R.G.H. (1972) “Regimes of bubbling and jetting from submerged orifices” Chem. Eng. Sci. 27, 1583-1592

O’Donnell W.J. and Langer B.F., (1962) “Design of Perforated Plates”, Journal of Engineering for Industry, Trans. ASME, 84, Paper No. 61—WA-115

O’Donnell W.J., (1967) “A Study of Perforated Plates with Square Penetration Patterns”, Pressure Vessels and Piping: Design and Analysis, vol. 2, pp.1089-1097

Priestman, G.H. and Brown, D.J. (1988) “Flow-induced vibration and damage in sieve tray columns” Chem. Eng. Commun. 63, 181-192

Priestman, G.H., Brown, D.J. and Kohler, H.K. (1979) “Pressure pulsations in sieve-tray columns” in Distillation 1979, IChemE Symp. Ser No 56, 2.4/45

Timoshenko S.P. and Goodier J.N. (1970) Theory of Elasticity (3rd edition), McGraw-Hill

Timoshenko S.P and Woinowsky-Krieger S. (1959) Theory of plates and shells (Second Edition), McGraw-Hill

Winter, J.R. (1993) “Avoid vibration damage to distillation trays” Chem. Eng. Progress 89(5), 42-47

How Packing Performance in Gas Treating Is Affected by Tower Geometry

Nathan A. Hatcher[1], Clayton E. Jones[1], Ralph H. Weiland[2]
[1] Optimized Gas Treating, Inc., Buda, TX, USA
[2] Optimized Gas Treating Inc., Coalgate, OK, USA

Abstract

Estimating the transfer unit height (HTU) or the height equivalent of a theoretical plate (HETP) can be exceedingly difficult in many applications, but none is more difficult than in gas treating with amines. Values for HTUs and HETPs in gas treating have complex dependency not just on hydraulic conditions and the specifics of the packing itself, but also on local temperatures and compositions which vary quite widely within the packed bed. If an ideal stage model in any form is used, the difficulties of HTUs and HETPs cannot be avoided because they are the only connection between ideal stages and reality.

By abandoning the ideal stage concept altogether, a mass transfer rate model of the separation completely avoids the problem. In addition, it can reveal some critically important design information, as demonstrated by the case study included in this paper.

When a tower has a mid-column feed or draw, it is sometimes economically attractive to swage the tower diameter around the mid-tower feed point. Technically, this change in column diameter is suggested entirely by hydraulic considerations, and economically by the lowered cost of a high pressure tower shell and the reduced volume of packing required. However, such a swage of diameter can result in radically different mass transfer behaviour on opposite sides of the swage. This paper uses mass transfer rate-based simulation to reveal the potential performance failure of a high-pressure packed absorber for CO_2 removal in an LNG production application that may result from ignorance of this previously unrecognised fact.

Keywords

Tower swage, rate model, LNG, split flow, amine, gas treating

Introduction

To prepare gas for liquefaction, its CO_2 content typically is reduced to 50 ppmv or below by absorption into an amine treating solvent. Most solvents are based on *N*-methyldiethanolamine (MDEA) promoted with lesser amounts of piperazine, although 2-(2-aminoethoxy)ethanol, known commercially as DIGLYCOLAMINE® agent (DGA®) and ADG has found use in this application. Frequently, absorbers are operated at high pressure.

There are several pitfalls to avoid in designing the CO_2 removal system:

- Absorbers that use fast reacting solvents such as piperazine-promoted MDEA may be subject to instabilities should operating conditions deviate significantly from process licensor recommendations.
- Energy consumption sometimes can be greatly reduced and solvent circulation lowered if the absorber is operated with a small, fully lean solvent feed to the column top, and a larger semi-lean solvent flow to a location part way down the tower. This is the absorber side of a split flow processing scheme. The bulk of the CO_2 is removed by the large solvent flow that needs to be only partially stripped, while final cleanup (polishing) is done in the top of the absorber using a relatively small flow of well-stripped solvent. Using a partially stripped solvent saves reboiler energy. In addition, the difference in liquid flow rates is itself large, suggesting a potential savings in absorber shell costs by using a reduced shell diameter in the top part of the high-pressure absorber and a concomitant savings in total packing volume. Absorbers are primarily mass transfer devices and, as such, there is a possible effect on mass transfer performance of reducing the tower diameter, especially if the tower is packed.
- So-called split-flow plants can be especially sensitive to departures from normal operating conditions, to the extent that even a slight change in a crucial process parameter can lead to failure-to-treat by a very wide margin. In these cases, small changes do *not* necessarily lead to the expectedly small responses in performance.

These pitfalls are by no means unique to treating gas in LNG production. For example, ammonia production where CO_2 is removed to a few hundreds of ppm is subject to the same concerns. Hydrogen production and the manufacture of various synthesis gases are other examples. The commonality, however, is the removal of CO_2 to concentrations measured in tens and hundreds of ppm using solvents having fast reaction kinetics with carbon dioxide.

The first and last items have been addressed for both absorbers and regenerators in other articles[1, 2]. The focus of the present paper is to identify a potential design pitfall involving split-flow absorbers in deep CO_2 removal applications, particularly in LNG units in which the upper packed bed is contained in a smaller diameter shell than the lower bed, i.e., absorbers with a so-called mid-tower diameter swage. Mass transfer rate-based simulation is used to analyse a specific example. Our approach is first to explain some of the basic principles on which mass transfer rate-based simulation relies, then use a detailed case study to expose a design issue that can cause an otherwise excellent design to fail.

Mass Transfer Rate-based Simulation

There are two fundamentally different methodologies for simulating any column used to separate mixtures of chemical species into pure components: ideal-stage and mass transfer rate-based. Calculations employing ideal stages have been used for about 80 years. However, the method suffers from a serious drawback—to connect ideal stages to real trays and tower packing, numerical values for tray efficiency and height equivalent to a theoretical plate (HETP) are needed. An unfortunate fact is that, especially in amine treating, there is no reliable way to determine the right values, other than using good quality data from an already operating plant. The approach can be used to fit the ideal-stage model to data, but it

must be honestly viewed strictly as a regression or fitting model, one that completely lacks predictive power.

One of the easiest ways to understand the principles of mass transfer rate-based simulation is by analogy with heat transfer. Heat exchangers have been designed this way for so long that after a first course in heat transfer we really don't give much thought to the fact that the methodology's basis is a heat transfer rate model. The simplest case is a shell and tube exchanger heating water with condensing steam on the shell side. The shell-side temperature is constant at the saturation temperature of the steam but on the tube side (for simplicity, one-pass) the water temperature gradually rises along the length of the tubes. If this heat exchanger were modeled as a single ideal stage, the outlet water temperature would be in equilibrium with the steam and it would be at the steam temperature regardless of the physical size of the exchanger itself. The efficiency in this model would be the value needed to achieve a match with the real measured outlet temperature, determined empirically *after the fact*. This certainly cannot be called predictive—it's just a fit to measured data. Admittedly this illustration is somewhat extreme because it is patently not the way we design heat exchangers. However, it is still the most commonly used method for designing much more expensive and complex mass transfer equipment such as distillation and absorption columns. The penalty for over-simplification is overdesign to compensate for the inherent uncertainty.

At its core, a mass transfer rate model focuses on the *rate* of exchange of chemical components between two phases as driven by the extent to which temperatures and species concentrations between phases are *not* at equilibrium. This is the very antithesis of the ideal-stage model with its assumption of perfect equilibrium, not disequilibrium. Figure 1 shows schematically two phases being contacted in some portion of the biphase on a tray or in a segment of packing within a column. At the heart of any true mass transfer rate model is the premise that the mass transfer process is characterised by mass transfer coefficients in the vapor and liquid phases. In no sense are these adjustable parameters any more than are film coefficients for heat transfer. The flow of high and low viscosity fluids across trays and over packing agitates the fluid and results in unique values for mass transfer coefficients. Engineers are not free to pick and choose coefficient values to obtain the preferred result or some preconceived notion of what the separation should be. On the contrary, values of the coefficients are a function of fluid flows, fluid properties, and the mechanical design of the specific tower internals as expressed in *well-established correlations*. The parallel with heat transfer is extremely close. Tower performance is predetermined and predictable in exactly the same way and to exactly the same extent as heat exchanger performance. This is the basis for the ProTreat® simulator, the original mass transfer rate-based tool used today for the simulation of a wide variety of gas treating processes.

Every tray is a real tray, and a column contains a certain number of real trays. Each is modeled as a real tray, not just to get the flooding hydraulics and pressure drop right, but to determine the *actual* chemical separation each tray achieves. Each tray has its own unique and very well-established mass transfer characteristics that depend on the temperature, pressure, flows, and compositions on the tray and on its mechanical design. If one is dealing with packing, the continuous nature of contact in a packed column is handled by dividing the height into a large number of short segments and numerically integrating across the column. Each short segment has

its own unique characteristic mass transfer coefficients and interfacial areas that depend on the particular packing (vendor, brand, material, size) in each segment.

It should be expected that the separation a given column is *predicted* to achieve depends very much on exactly what specific internals are in the column. This is completely in line with the reality of processing using actual real equipment, and it is precisely what ProTreat simulation predicts. This has the authenticity that simply cannot be achieved with theoretical stages regardless of embellishments.

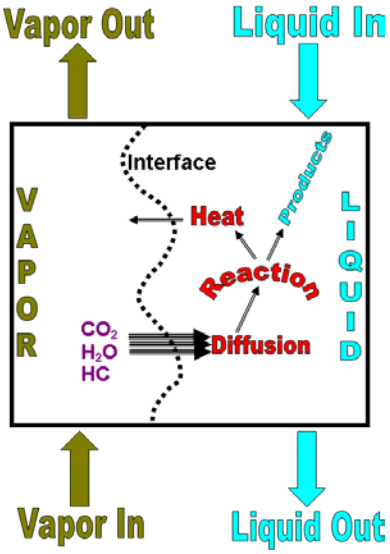

Figure 1 Schematic of Mass Transfer Between Vapor and Liquid Being Contacted Within the Biphase of an Absorber

Case Study: Split Flow Plant with Swaged Column Diameter

Case studies are one of the most effective ways to uncover design pitfalls. This case arose out of a design study for a new LNG plant by a major engineering firm and process licensor. The gas was 17.5% CO_2, 80% methane, and 2.5% ethane flowing at about 28000 Nm^3/h. The gas temperature and pressure were 70°C and 31 barg, respectively. The solvent contained 45 wt% of an MDEA-based specialty amine specifically formulated for deep CO_2 removal in LNG applications. The absorber itself was comprised of two 9.1-m deep beds of No. 2 Raschig Super-Rings with solvent feed nozzles positioned at the top of the upper and lower beds. Fully lean solvent with a CO_2 loading of 0.005 mol/mol entered at the top of the upper bed at a flow rate of 450 m^3/h. The semi-lean solvent with a CO_2 loading of 0.38 mol/mol entered via the lower nozzle at the much higher flow rate of 2725 m^3/h.

Simulations were done using the ProTreat® simulator, and the first case was with the absorber of a uniform diameter calculated to achieve 80% of flood at the most flood-prone point in the tower. The simulator predicted that 26 ppmv CO_2 would be achieved in the treated gas and that the upper half of the column would be nearly lean-end pinched. In other words, the treating level would closely correlate with the loading in the fully-lean solvent. The tower diameter was calculated to be slightly less than 4.5 m; this diameter was set by the much larger total solvent flow through the lower packed bed (3175 m^3/h vs. 450 m^3/h). At 4.5-m diameter, the

upper half of the tower was obviously going to be grossly oversized for the 450 m^3/h solvent flow through the upper bed. This was an opportunity to save possibly considerably on shell cost and total required packing volume by swaging down the column diameter between the two packed beds. The absorber was re-simulated, this time for 80% flood in *each* of the two beds with a diameter change between them. The tower diameter needed for the upper one-half of the column was reduced to only 2.6 metres, and it translated into a potential savings in packing volume from 145 m^3 to only 48 m^3 (67%) for the upper bed (the lower bed remains unchanged). However, simulation of the swaged absorber also saw the predicted treating level go from 26 to nearly 200 ppmv CO_2, not even close to specification!

The blue and red curves in Figure 2 show the carbon dioxide profiles in the two 9.1-m deep beds of the absorber for the cases of uniform and swaged diameter, respectively. Apparently a deeper packed bed will be needed in the upper section for the swaged tower to reach the same 26 ppmv CO_2 level achieved by the uniformly-sized column; however, the reason for the perhaps surprising disparity remains to be explained. In terms of ideal stages, the HETP or HTU in the upper bed has nearly doubled despite the better coverage of packing with liquid at the higher liquid loading. Practitioners accustomed to dealing with ideal stages and HETPs or HTUs may well be astounded that such a simple reduction in column diameter could require a much deeper bed of packing. The reason for the disparity lies in the dry packing surface area in the swaged down upper bed. It has only 1/3rd of the area as the large-diameter bed. Table 1 shows the packing wetted area per unit volume of packing and the liquid-side mass transfer coefficient for the uniform diameter and swaged diameter cases.

Table 1 Interfacial Areas and Liquid Film Coefficients for Mass Transfer

	Single Diameter	Swaged Diameters
Specific Wetted Area, a (m^2/m^3)	83	92
Total Area, A, in Entire Section (m^2)	12000	4400
Liquid Film Coefficient, k_L (m/s)	0.001	0.002
$k_L A$ (m^3/s), refers to Entire Tower Section	12.0	8.8

Carbon dioxide absorption rates in fast reacting systems are controlled by mass transfer resistance in the liquid phase; indeed, absorption rates are directly proportional to the total wetted area of the packing. Although the wetted area *per unit of packed volume* is lower in the large diameter upper bed (implying the absorption rate should be lower and treating worse) there is also three times the packed volume there; hence, the total wetted area is about 12000 m^2 in the large diameter section vs. only 4400 m^2 in the swaged down section. The liquid-film coefficient also plays a role which makes the proportionality anything but direct and prevents wetted area from being used as a simple scaling factor. Suffice it to say that it is highly unlikely a design based on an ideal stage simulation and estimated HETP values would have succeeded at all had the upper packed bed been in a swaged down shell. Of course, one would inevitably apply safety factors but the question remains as to whether the safety factors would be generous enough to salvage the design. In any event, the purpose of the case study was to point out just how far off the mark conventional wisdom can lead.

The savings in packing volume and the cost of the tower shell have come with a price of their own. Further simulation showed that to reach the same 26 ppmv CO_2

as achieved without swaging, an additional 6.1 metres of packing would be required in the same 2.6-m diameter shell. The required packing volume needed to achieve the same treating as the uniformly sized shell is about 80 m^3—still less than in the original uniformly sized shell, but not as great a savings as originally thought. The dashed line in Figure 2 shows that the corresponding composition profile for the now 15.2-m deep upper bed also tapers off to a value of about 25 ppmv, determined primarily by solvent lean loading. In operation, the 15.2-m deep upper bed would be lean end pinched.

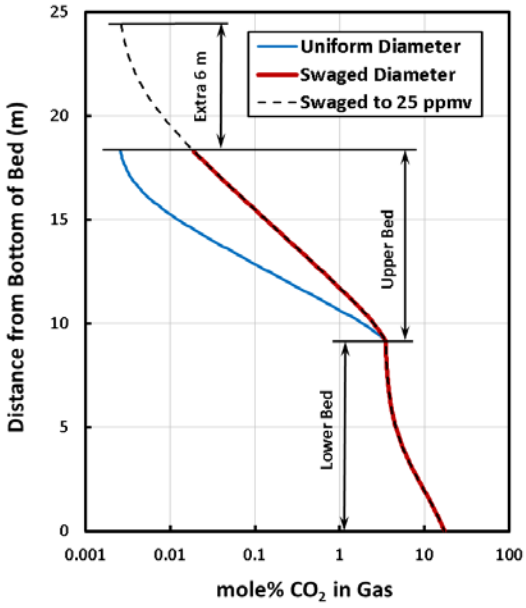

Figure 2 Profiles of CO_2 Concentration when LNG Tower is (1) of Uniform Diameter (Blue), (2) Swaged Diameter with 9.1-m Upper Bed (Red), and (3) Swaged Diameter with 15.2-m Upper Bed (--- Black)

The first lesson worth remembering is that regardless of the potential capital cost savings that might result from swaging tower diameters, there may be a column height penalty that, if not recognised, could result in a completely failed design. In fact, swaging the tower shell can spell disaster if one is unaware (as most are) of the effect on mass transfer performance that results. Another is the great difficulty in avoiding this situation when using ideal stages and HETPs—there are simply not enough data, and the little existing data lack sensitivity to operating parameters in amine systems where chemical reactions play such an important role. In these kinds of situations (and probably in all situations involving packing in amine treating) the only rational, safe, and reliable way forward is simulation that makes exclusive use of a true mass transfer rate-based approach. Anything less introduces needless uncertainty and results in expensive overdesign.

References

1. Hatcher, N. A. and Weiland, R. H., “Amine Regenerator Instabilities”, *Hydrocarbon Engineering*, October, 2012.
2. Weiland, R. H., and Hatcher, N. A., “Foundations of Failure”, *Hydrocarbon Engineering*, December, 2011.
3. Kern, Donald Q., *Process Heat Transfer*, McGraw-Hill Book Co., New York, 1950.

Hydraulics and mass transfer characteristics of fluidized packed beds for gas-liquid systems

Prof. Dr.-Ing. J. Maćkowiak[1], Dr.-Ing. J. F. Maćkowiak[1], Dr.-Ing. J. Szust[1]

[1]ENVIMAC Engineering GmbH, 46149 Oberhausen, Germany

Abstract

In this work, the results of extensive experimental investigation of fluidized beds are presented. Hydraulic behavior and mass transfer of a fluidized bed have been investigated in a two-tray test column with a diameter of d_C = 0.6 m. The hydraulics of fluidized beds with special packing made of polypropylene have been investigated using the air/water system under ambient conditions in the gas load range up to the flooding point and at specific liquid loads between 0 and 80 $m^3m^{-2}h^{-1}$. Based on the Suspended Bed of Droplets (SBD) model [1], a model equation has been developed on the basis of the experiments, allowing, for the first time, a prediction of the fluidization point and the pressure drop in the entire operating range of the fluidized packed bed. Separation efficiency and effective mass transfer area have been determined using the standard absorption test system CO_2/air-1n NaOH, the results have been compared with those of random 50 mm Pall rings (PP). The design data developed in this work has successfully been used for the design of an industrial plant.

Keywords: Fluidized bed, absorption, fluid dynamics, separation efficiency, column design

1. Introduction

Packed columns are widely used in gas cleaning processes, such as absorption and desorption processes, also called (wet) scrubbing and stripping. Columns filled with random packings cover a large part of such applications in industrial practice, especially when liquid side mass transfer resistance is dominating and when solid impurities are present in the liquid or in the gas phase. In these cases random packings have advantages compared to structured packings. Special random packings with large open area, so called lattice type packings, have been developed for gas-liquid applications with solid impurities [1].

However, there are industrial applications where fouling and clogging cannot be avoided by using even lattice type random packings. In such cases the immobilized packings fail or cause serious operational problems due to their susceptibility to clogging during the treatment of solid loaded media. Gas-liquid systems which cause severe problems in these columns are characterized either by a very high solid load or the liquid side is close to its solubility limit and small differences in operating conditions or dead zones inside the column lead to solid formation and incrustations which quickly block the column.

In contrast to columns with random packings, fluidized packed beds might be used in gas-liquid operations like scrubbing and stripping in systems with a high solid content. Continuous movement of the packings allows self-cleaning of the packing and

thus promises stable operation even in systems with very high solid content. Unless the advantage in “dirty” systems, fluidized packed beds are far less common compared to fixed packed beds, this is partly due to the lack of reliable design data for this type of apparatus. Experimental data of hydraulics and mass transfer characteristics fluidized beds is scarce in literature and limited to specific packing types and a narrow operating range [2]. In order to provide reliable data for design tasks, the results of an extensive experimental investigation of hydraulics and mass transfer on fluidized beds in a technical scale test plant is presented.

2. Experimental set-up

The experimental investigation of the hydraulics and mass transfer characteristics of a fluidized bed have been performed on a test column with a column diameter d_C = 600 mm. Two trays have been installed inside the column with a single static packing height of H_{stat} = 0,45 m, thus a total static height of 0,9 m was achieved. Above the static packing 0,55 m room for expansion was left, leading to a total height of H_{tot} = 2 m, see Figure 1.

As a fluidized bed packing (FBP), ellipsoid packings made from polypropylene have been used, the characteristic size of one packing is d_P = 35 mm (FBP 35). The fluidized bed packings have a closed surface and are hollow from the inside. In the test column, liquid is fed on top via different distribution devices such as spray nozzles and pipe distributor whereas gas is flowing from the bottom of the column upwards through the packed bed. After exceeding a specific gas load, the packed bed is lifted up by the gas phase leading to a highly mixed three phase fluidized zone.

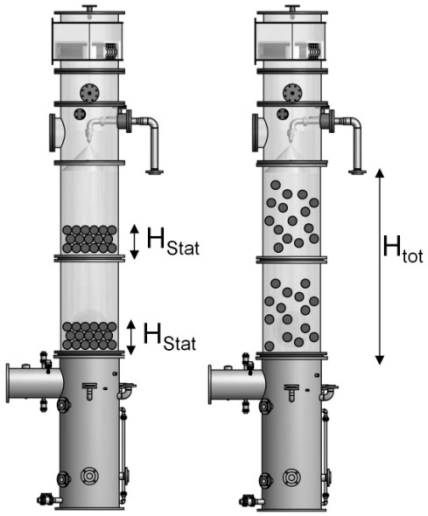

Figure 1: Layout of the test plant with static bed (left side) and fluidized bed (right side).

The column walls of the test plant are made of transparent PVC, allowing the determination of the expanded bed height and the observation of the bed movement during operation. The test column is equipped with state-of the art measurement devices and control technology, minimizing measurement errors and allowing electronic data storage and evaluation.

The characteristic parameters of the studied fluidized bed packing have been summarized in Table 1. The fluidized bed packing (FBP) has an experimentally determined surface area of the static bed of a_{stat} = 111 m^2m^{-3} which is comparable to the widely known 50 mm Pall ring. In order to allow a better comparison of the achieved

results, the characteristic data of a 50 mm Pall ring made of polypropylene studied in the same test column have been added to Table 1.

Table 1: Parameters of the investigated ellipsoid fluidized bed packing (FBP 35) referred to static bed in comparison to a 50 mm Pall ring made of polypropylene (PP).

Parameter	Symbol	Unit	FBP 35	Pallring 50mm PP
Packing size	d_P	[mm]		50
Void fraction	ε_{stat}	[m^3 m^{-3}]	0,44	0,92
Packing density	G_{stat}	[kg m^{-3}]	185	72
Spec. area (stat.)	a_{stat}	[m^2 m^{-3}]	111	110
Packing density	N_{stat}	[m^{-3}]	30.484	6.700

The hydraulics of fluidized beds have been investigated using the air/water system under ambient conditions in the gas load range up to the flooding point and at specific liquid loads between 0 and 80 $m^3m^{-2}h^{-1}$. The separation efficiency of the fluidized bed packing has been studied in the same test plant using the standard test system CO_2/air-1n NaOH under atmospheric conditions.

3. Hydraulics of fluidized beds

3.1. Results of experimental investigation

Beside the pressure drop characteristics, particular attention was paid to the determination of the fluidization point. This point characterizes the lower limit of the operating range of the fluidized bed and thus is crucial to characterize the operating range of the fluidized bed.

Figure 2 shows the results of the hydraulics investigation of the fluidized packing in the studied range. As can be seen in Figure 2, the pressure drop rises quickly with increasing gas load factor F_V until the fluidization begins.

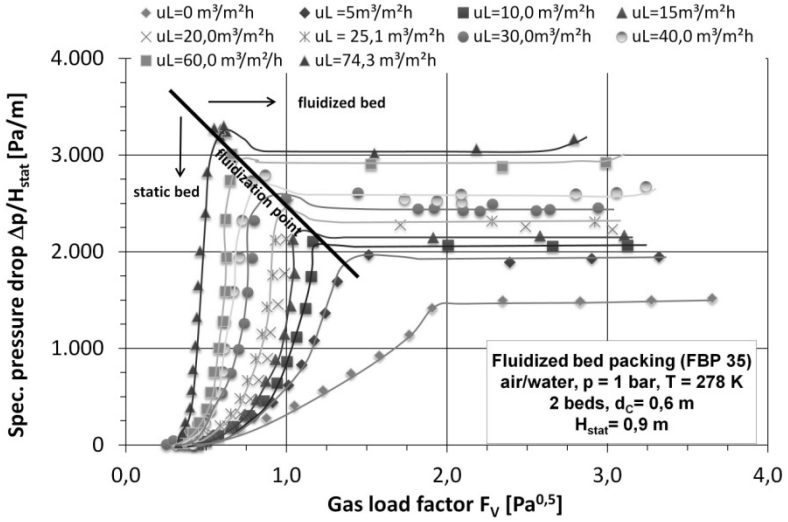

Figure 2: Pressure drop characteristics of the studied fluidized bed packing in dependency of the gas load factor F_V for various liquid loads for 0 to 80 $m^3m^{-2}h^{-1}$.

Once the fluidization has started and the packing starts to move inside the bed finally reaching its expanded bed height H_{exp}, the pressure drop remains almost constant throughout even when gas load is further increased. The pressure drop increases again, when the flooding point is reached. The flooding point of the fluidized bed is defined as the upper operation limit for the static packed bed, in this case the fluidized bed packing expands toward the support grid of the bed above.

According to Figure 2, the pressure drop increases for higher liquid loads because liquid hold-up h_L rises, leaving less free volume for the gas to pass upwards. In comparison to immobilized packings, the pressure drop of a fluidized bed is almost constant for a given liquid load throughout the entire operation range.

The fluidization point of the fluidized packed bed depends on the liquid load, see Figure 2. The higher the liquid load is, the lower the gas load has to be to start fluidization. This is due to buoyancy, leading to a higher lifting force at higher liquid hold-ups.

3.2. Modeling of the hydraulics of fluidized beds

For design purposes, a prediction of the fluidization begin and the pressure drop at that point are crucial, as these two parameters determine the most important points of the operation range of a fluidized bed packing. So far, no correlation to determine the fluidization point based on a physical model is known. In this work, based on the SBD model [1], a model equation has been derived for the first time, allowing a prediction of the fluidization point based on the assumption, that the fluidization point of the fluidized bed is equal to the flooding point of the static bed. The model equation previously developed for droplet flow in packed columns [1] has been adopted and adjusted to the fluidized bed characteristic data, see eq. (1), the packing specific resistance coefficient ψ_{Fl} has been determined based on the experiments in Figure 2.

The presented equation allows a prediction of the gas velocity at the fluidization point $u_{V,Fl}$ with an average deviation of 5,9%, see Figure 3a.

$$u_{V,Fl} = 0,693 \cdot \psi_{Fl}^{-1/6} \cdot \varepsilon^{6/5} \cdot \left[\frac{d_h}{d_T}\right]^{1/4} \cdot \left[\frac{d_T \cdot \Delta\rho \cdot g}{\rho_V}\right]^{1/2} \cdot \left(1 - h_{L,Fl}^0\right)^{7/2} \cdot K_{\rho_V} \quad \left[ms^{-1}\right] \tag{1}$$

With liquid hold-up at the flooding point $h_{L,Fl}^0$ acc. to eq. (2) for different phase flow ratios λ_0 [1], d_h representing the hydraulic diameter of the packed bed, d_T the droplet diameter acc. to Sauter and $K_{\rho v}$ being a correction factor for gas density [1].

$$h_{L,Fl}^0 = \frac{\sqrt{\lambda_0^{\,2} \cdot (m+2)^2 + 4 \cdot \lambda_0 \cdot (m+1) \cdot (1-\lambda_0)} - (m+2) \cdot \lambda_0}{2 \cdot (m+1) \cdot (1-\lambda_0)} \quad \left[m^3 m^{-3}\right]$$

$$m \text{ acc. to } [1],\ \lambda_0 = \left(u_L / u_{V,Fl}\right) \tag{2}$$

$$\psi_{Fl_m} \cong 1,66 \text{ (from experiments)}$$

Following the SBD-model, the specific pressure drop can be calculated based on the modeling concept developed for packed columns [1], eq. (3) shows the adjusted relation for the studied fluidized bed packings:

$$\frac{\Delta p}{H_{stat}} = 3,8 \cdot \mu \cdot \frac{1-\varepsilon}{\varepsilon^3} \cdot \frac{F_V^2}{d_P \cdot K} \cdot \left(1 + \frac{h_{L,Fl}}{1-\varepsilon}\right) \cdot \left(1 - \frac{h_{L,Fl}}{\varepsilon}\right)^{-3} \quad \left[Pa\, m^{-1}\right] \tag{3}$$

With K being the wall factor correction and d_P the particle diameter [1].

Eq. (3) for the determination of the specific pressure drop related to the static packing height allows the prediction of the pressure drop at the flooding point of the static bed and thus in the operating range of the fluidized bed up to ca. 85% of the flooding point with an average accuracy of 2,6%, see Figure 3b.

Compared to standard random packings, like the 50 mm Pall ring (PP), the specific pressure drop of the fluidized bed packing is approx. 10-20 times higher under the same operating conditions.

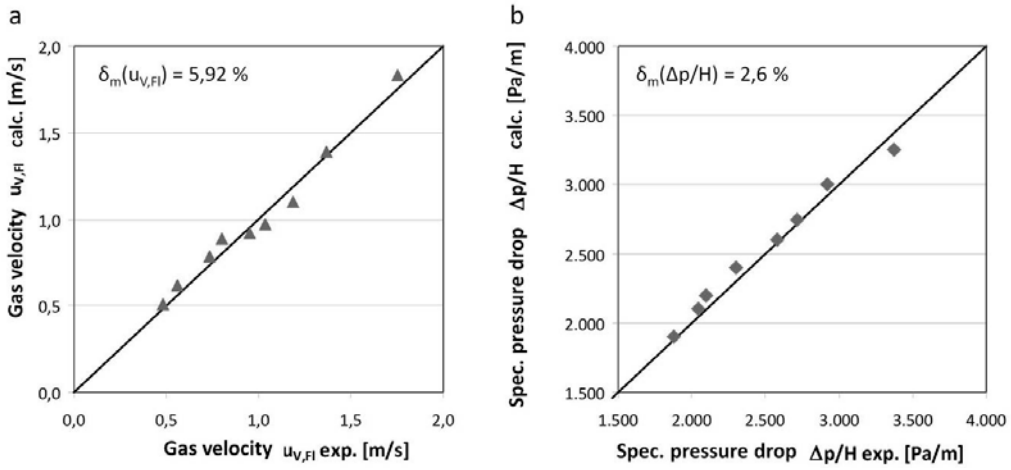

Figure 3: Parity plot of calculated and experimental a) gas velocities at the flooding point $u_{V,FL}$ of the static bed which equals the fluidization begin (left) and b) pressure drop in the operating range of the fluidized bed acc. to SBD-model [1].

4. Mass transfer of fluidized beds

As many of the mass transfer applications in gas cleaning technology are limited by the liquid side, the absorption of carbon dioxide (CO_2) in caustic soda under ambient conditions has been studied, allowing the determination of the effective separation area acc. to the procedure presented in [3].

Figure 4 shows the dependency of the volumetric mass transfer coefficient *($k_{OV}a_e$)* of the fluidized packing determined from the experiments with the standard test system CO_2/air-1n NaOH evaluated based on the HTU-NTU-model as a function of the specific liquid load u_L, see eq. (4).

$$H = HTU_{OV} \cdot NTU_{OV} = \frac{u_V}{k_{OV} \cdot a_e} \cdot NTU_{OV} \quad [m] \tag{4}$$

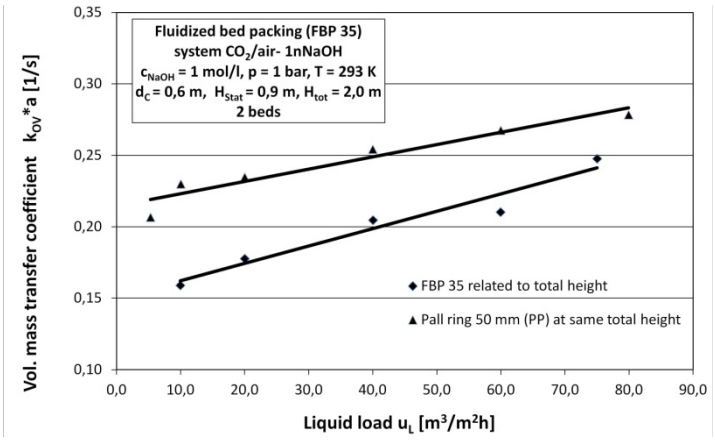

Figure 4: Separation efficiency of the fluidized bed packing referred total height, compared to values for a 50 mm Pall ring (PP) determined with the standard test system CO_2/air-1n NaOH under ambient conditions.

In dependency which height H is used in eq. (4), namely the static or the total height, the separation efficiency of fluidized beds might be interpreted in completely different ways, especially when compared to random packings. Thus, or a correct comparison with random packed columns, the total height H_{tot} should be used in eq. (4), because this height is relevant e.g. in revamp projects. Using the total height in the evaluation, the "correct" separation efficiency of the studied fluidized bed packings is approx. 20% lower compared to the standard 50 mm Pall ring (PP), see Figure 4.

5. Conclusions

5.1 In this work, hydraulics and mass transfer of a fluidized packed bed (FPB) have been investigated in a technical scale test column (d_C = 0,6 m). Based on the experiments, new model for fluidized packed beds describing the fluidization point and the pressure drop has been presented. Compared to 50 mm Pallrings (PP), the pressure drop is approx. 10-20 times larger, although it remains constant in the fluidized operating range. Separation efficiency and effective mass transfer area of the FPB have been determined and compared with 50 mm Pall ring made of the same material (PP). The separation efficiency and the effective mass transfer area of the FPB 35 are ca. 20 % lower than those of the 50 mm Pall rings.

5.2 The design rules developed in this work have been used to design an industrial scale column for a high pressure gas cleaning application with a diameter of d_C = 1,4 m. The plant is in continuous operation for 2 years now, all design parameters have been met, see exemplarily Figure 5.

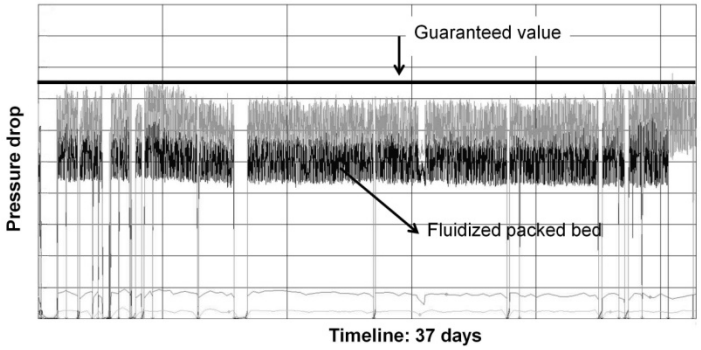

Figure 5: Pressure drop curve for over one month of industrial operation always showing values lower than guaranteed values.

5.3 Fluidized beds thus can be recommended as a solution for gas-liquid applications with a very high solid load. Compared to random packings, a significantly higher pressure drop is the "price" for the trouble-free handling of such systems.

6. Literature

[1] MAĆKOWIAK, J., Fluid Dynamics of Packed Columns. Springer, Berlin, 2010.
[2] BILLET, R., Packed Towers. VCH, Weinheim, 1995.

[3] DUSS, M., MAIERHOFER, H., NUTTER, D.E., Effective interfacial area and liquid holdup of Nutter rings at high liquid loads. Chem. Eng. Technol. 24 (2001), p. 716-724.

Investigation of pillow-plate condensers for the application in distillation columns

J.M. Tran[1], S. Sommerfeld[2], M. Piper[1], E.Y. Kenig[1]
[1]Chair of Fluid Process Engineering, University of Paderborn, Germany;
[2]Bayer Technology Services GmbH, Distillation & Phase Separation, Leverkusen, Germany

Abstract
Pillow-plate heat exchangers (PPHE) represent a new and promising concept which can be, among others, used in distillation as integrated top-condensers. Today, its application in process industries is growing. However, up to now, no reliable design methods for PPHE are available in the open literature, and this hinders further expansion. To overcome this limitation, we carried out a comprehensive experimental study on condensation, with the aim to develop PPHE design methods. This helps to facilitate the estimation of the application potential of new condensers in comparison with commonly used heat exchangers.
Two different lab-scale experimental setups at the University of Paderborn were used complementarily for the investigation of heat transfer during condensation in PPHE. In addition to the lab-scale experiments, pilot-plant measurements were carried out at Bayer Technology Services GmbH. This allows both an analysis of PPHE in different scales and a comparison of the obtained results with conventional geometries.

Keywords
distillation, pillow-plates, condensation, heat exchanger, energy efficiency

1. Introduction

Design of new processes and retrofit of existing technologies require a proper choice of the specific heat transfer equipment perfectly fitting to the technological targets. Because of the large diversity of available devices, this is not easy. On the one hand, conventional heat exchangers, e.g. plain shell-and-tube or plate heat exchangers, which have been extensively studied in the past, can be used. On the other hand, there exist innovative and promising heat exchanger types, for which only few basic data are available. Pillow-plate (PP) condensers represent the latter type. They offer several potential advantages over conventional heat exchangers, for instance, intensified heat transfer, compact, light and pressure-resistant construction, low pressure drop on the side of the product media, as well as low capital and operating costs. An important reason for limited implementation of PP condensers in process industries is the lack of proven design methods in the open literature. Only basic studies by Mitrovic et al. [1,2] are available, and the existing data on PP geometries, media and operating conditions are limited. The data transferability between different PP is also uncertain. This does not allow any reliable design and performance prediction for the PPHE operators. In our group, extensive experimental and numerical studies have been carried out, aiming at overcoming this limitation [3-6].

Two experimental setups were used complementarily for the determination of pressure drop and overall heat transfer coefficients, comprising cooling medium and condensation side. Additional pilot-plant measurements were carried out at Bayer Technology Services GmbH.

The manufacturing of PP consists of the following steps. First, two sheets – usually made of stainless steel – are placed one on another. Next, the plate is welded according to a specified welding spot grid, and it is then reshaped by using hydroforming. To be used in condensers, several PP are arranged vertically and parallel to each other as a stack, with alternating cooling and condensation channels. Figure 1 shows a sketch of a single PP with the geometric parameters used at the University of Paderborn (UPB). The geometric variability of this heat exchanger type is very high.

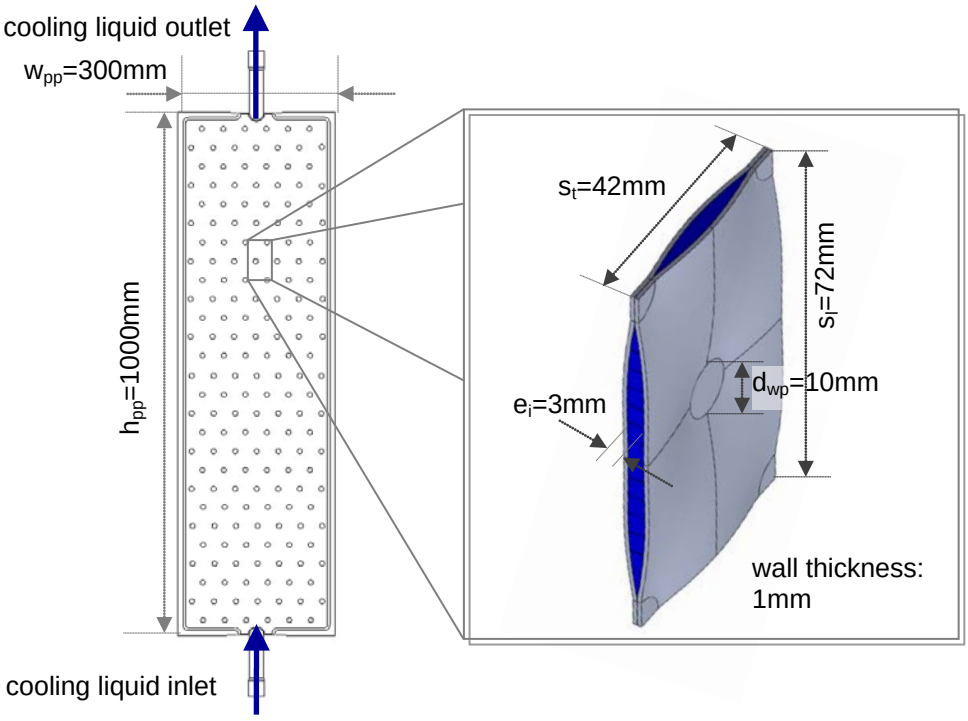

Figure 1: PP geometry used for the experimental investigations at UPB.

2. Experimental Setups

2.1 Lab-scale plant for pillow-plate condensation experiments at UPB

A lab-scale condensation plant at UPB is used to determine the overall film condensation heat transfer coefficients and pressure drop. The condensing medium is steam in presence of nitrogen as a non-condensable component (usually 0.01 to 3 vol. percent). The plant is operated at low pressures (100 to 800 mbar abs) with a resulting condensation temperature in the range of 46 to 94°C. This plant contains two separate PP condensers, both consisting of three PP, 300 mm wide and 1000 mm long each. The vapor enters each condenser from above, with a mean velocity of 5 to 25 meters per second in the upper condenser, and flows downwards together with the condensate film. The cooling liquid is water, flowing in counter-current to the vapor and condensate with mean velocities of 0.3 to 1.4 meters per second. In case of total condensation, only the first of the two PP condensers is used; in case of partial condensation, both condensers are used. Typical heat flow rates are in the

range of up to 90 kW. This plant is used for a comparison to the results gained from the PP condensation pilot plant at Bayer Technology Services.

2.2 Lab-scale plant for the determination of cooling-side (internal) heat transfer and pressure drop

In addition, heat transfer coefficients of the condenser cooling channel were estimated in a second lab-scale plant. Together with the measured overall heat transfer coefficients, these data permit the heat transfer coefficients in the condensation channels to be determined, too. A scheme of this setup is shown in Figure 2. In this setup, a PP is being heated by dissipating electrical energy supplied by a rectifier. The heat is absorbed by the cooling medium flowing through the PP, from the bottom to the top. Using seven temperature measuring points along the wall of the PP and two measuring points in the fluid, mean heat transfer coefficients on the cooling-side can be calculated. Pressure drop is measured along the PP using different pressure measuring points. In this way, both the specific pressure drop of the fully developed fluid flow inside the PP and additional pressure drop caused by the inlet and outlet arrangements can be determined.

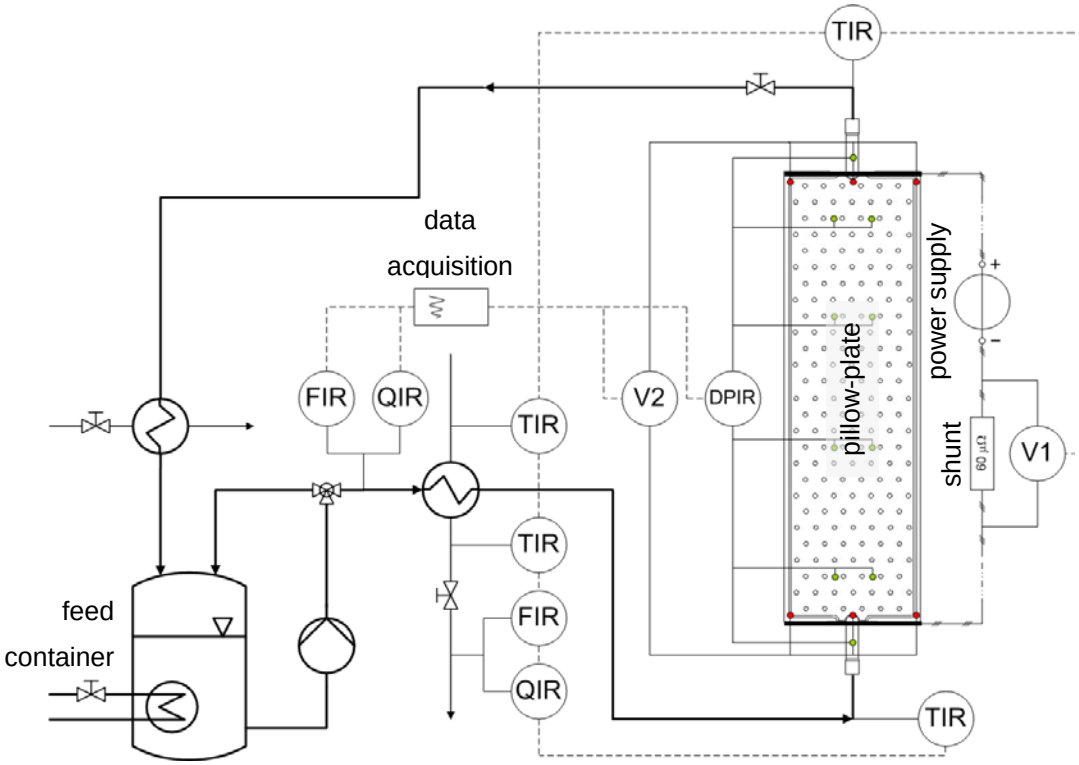

Figure 2: Scheme of the experimental lab-scale plant used for the determination of cooling-side heat transfer coefficients and pressure drop in PP.

2.3 Pilot plant at Bayer Technology Services GmbH

A PP condensation pilot plant was built at Bayer Technology Services GmbH (BTS) (see Figure 3). In contrast to the lab-scale condensation plant at UPB, the plant at BTS is capable of handling a bigger condenser and higher heat fluxes (i.e. higher resulting condensate Reynolds numbers). In combination with the condensation plant at UPB, this allows investigations on different scales. In the measurements at BTS, an integrated PP top-condenser (six PP, dimensions 500x1800 mm each) was used in a DN600 column with chloro-benzene (CB) in presence of non-condens-ables. A fiber optic temperature measurement technique was used in one of the condensation channels for the determination of the axial temperature profile.

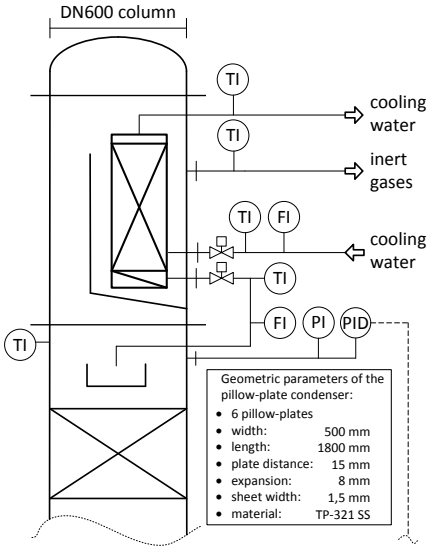

Figure 3: Scheme of the experimental pilot plant at BTS used for the determination of overall heat transfer coefficients.

3. Results and discussion

Figure 4 gives the data for a sample axial CB temperature profile measured in the pilot-plant PP condenser at BTS. In this sample measurement, the low volume fraction of non-condensables at the inlet (0.02 vol. percent) has no significant influence on the condensation curve leading to a flat axial CB temperature profile in the entrance region of the heat exchanger. This allows an estimation of the heat transfer area at which the condensation mostly takes place. In this case, this is the first quarter of the condenser (this corresponds to 166 kW), while in the other three quarters, residual condensation, bulk gas cooling and condensate subcooling with a total heat transfer rate of 75 kW occur.

In this case, the overall heat transfer coefficient for the first quarter of the apparatus is 691 W/m^{2}K and the log mean temperature difference is 88 K. The cooling-side heat transfer coefficient $h_{m,CM}$ is extracted from CFD simulations and experiments at UPB, with a PP similar to the BTS-PP. The resulting $h_{m,cond,exp}$, which is derived from the values mentioned above, is 1.0 kW/m^{2}K. For a first comparison with published correlations for film condensation on flat vertical surfaces, a mean value for $h_{m,cond,calc}$ can be estimated to be 0.7 kW/m^{2}K, by taking into account a superposition of the laminar and turbulent film condensation [7,8], the waviness of the film [9] and temperature-dependent film properties.

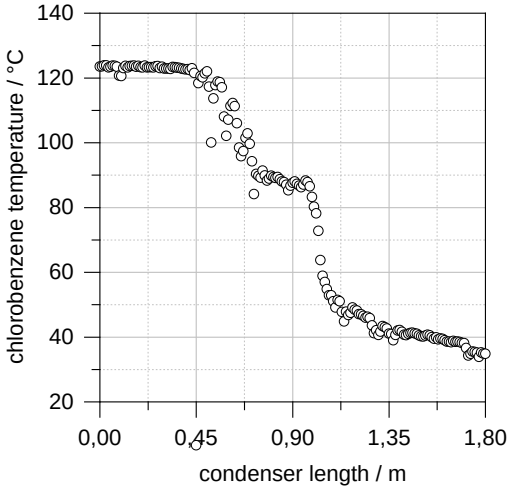

Figure 4: Sample axial CB temperature profile measured in the pilot-plant PP condenser at BTS using a fiber optic measurement technique.

Certainly, a more sophisticated analysis is necessary, which would take the opposed influences of the shear forces according to [10] and the mass transfer resistance

caused by the non-condensable component diffusion layer into account. A condensation model, which is currently being developed and implemented in a Visual Basic programming environment at UPB, can be applied for this purpose in the future.

Further important aspects are the heat transfer and pressure drop characteristics on the cooling-side, which are apparently influenced by the characteristic welding spots. Figure 5 shows the heat transfer coefficients and specific pressure drop on the cooling-side for a PP investigated at UPB. These results were obtained using the setup shown in Figure 2. The corresponding geometrical parameters of the PP can be seen in Figure 1. For an evaluation based on Reynolds and Nusselt numbers, relevant geometric parameters have to be known. These include hydraulic diameters, cross-sectional areas and heat transfer areas – each for both the inner cooling and outer condensation channels. In [1,2], the hydraulic diameters and cross-sectional areas were determined by simplifying the complex geometry to a gap between plane vertical plates. This simplification results in reduced accuracy and predictivity, because the measured liquid hold-up in the PP is used as an input for this calculation. In our new approach, the complex geometrical structure of the PP was reproduced by means of deformation simulations, and the resulting exact hydraulic diameters and cross-sectional areas were subsequently evaluated. On this basis, an easier applicable calculation method was derived, yielding values with minor deviations from the exact values. The inner and the outer heat transfer areas are other important parameters, which were assumed to be the outer projection surface.

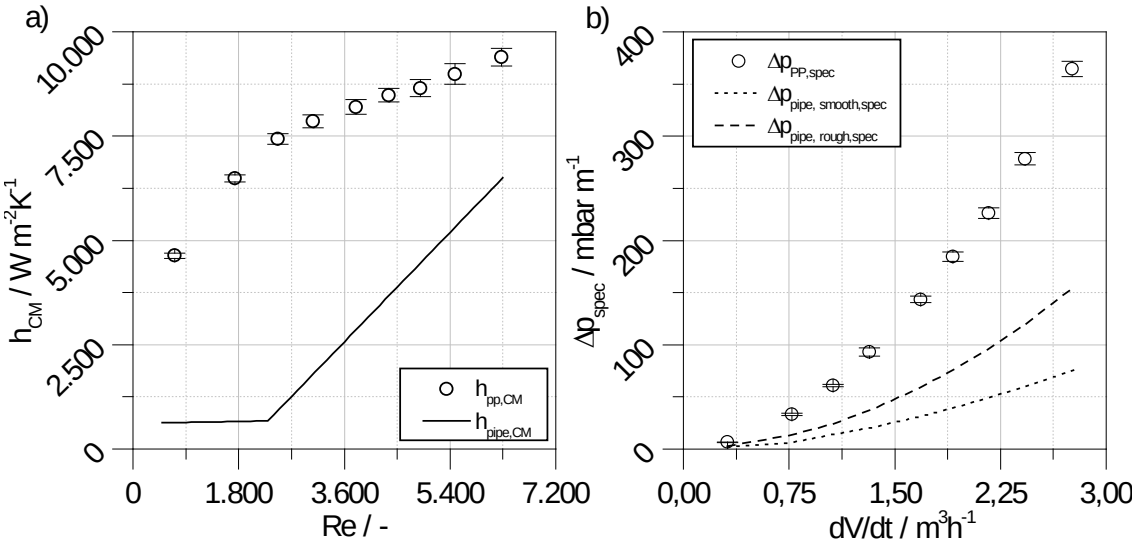

Figure 5: Measured h_{cm} in comparison to a pipe with the same d_h as the PP (a): the curve does not intersect the origin of coordinates, because constant heat flux density is specified; measured $\Delta p_{,spec}$ on the cooling medium side in comparison to a smooth/rough pipe (b): roughness parameter K = 0.2 mm [11] with the same d_h as the PP.

As can be seen in Figure 5, the heat transfer coefficients on the cooling medium side in the PP are significantly higher compared to a pipe with the same hydraulic diameter – already at low Reynolds numbers. The cooling liquid flows inside the PP and is being continuously redirected by the welding spot grid. This leads to thin boundary layers and a good heat transfer performance. However, interior pressure drop is also increased, so that an optimum has to be found.

4. Conclusions

PPHE represent a promising alternative to conventional heat exchanger types. With the three different-type and different-scale experimental plants, data for total condensation of steam and chlorobenzene (CB), with and without influence of non-condensables, were obtained. These data include both overall and condensation-side heat transfer coefficients. Moreover, cooling-side heat transfer coefficients in the PP geometries used at UPB were measured. First results for heat transfer, both on condensation side and on cooling medium side, were given. Due to their characteristic three-dimensional structure, PPHE show high heat transfer coefficients on both sides, and this results in lower required heat transfer area and higher potential for heat integration, e.g. in distillation processes. The results obtained at UPB and BTS target on performing a preliminary analysis of PP condensers for a given application. By overcoming implementation limitations and by identifying further relevant application areas of PPHE, substantial energy savings can be achieved.

Notation

d_h	hydraulic diameter, mm
d_{wp}	diameter of the welding spots, mm
e_i	inner expansion of the pillow-plate, mm
h	heat transfer coefficient, W $m^{-2}K^{-1}$
h_{PP}	height of the pillow-plate, mm
K	roughness parameter according to [11], mm
Δp_{spec}	specific pressure drop, mbar m^{-1}
Q	heat, W
q	heat flux, W m^{-2}
Re	Reynolds number, $ud_h\nu^{-1}$
s_l	longitudinal distance of the welding spots, mm
s_t	transversal distance of the welding spots, mm
w_{PP}	width of the pillow-plate, mm

Subscripts

calc	calculated
CB	chlorobenzene
CM	cooling medium
cond	condensation
exp	experimental
m	mean
PP	pillow-plate

Acknowledgements

The financial support of the German Federal Ministry of Education and Research (grant number 033RC1013E) is greatly acknowledged.

References

[1] J. Mitrovic and B. Maletic. *Chem. Eng. Technol.*, 34: 1439–1448, **2011**.
[2] J. Mitrovic and R. Peterson. *Chem. Eng. Technol.*, 13: 907 – 920, **2007**.
[3] M. Piper, A. Olenberg, J.M. Tran, and E.Y. Kenig. *Proceedings of the 9th World Congress of Chemical Engineering*, 672, **2013**.
[4] M. Piper, J.M. Tran, and E.Y. Kenig. *Chem. Ing. Tech.*, 85: 1455–1456, **2013**.
[5] J.M. Tran, M. Piper, and E.Y. Kenig. *Proceedings of the 9th World Congress of Chemical Engineering*, 314, **2013**.
[6] J.M. Tran, M. Piper, and E.Y. Kenig. *Chem. Ing. Tech.*, 85: 1456, **2013**.
[7] W. Nußelt. *Z. VDI*, 60: 541–546, 569–575, **1916**.
[8] J. Müller. *Fortschr. Ber. VDI*, 3 (270): 1, 1992.
[9] S.S. Kutateladze and I.I. Gogonin. *Int. J. Heat. Mass Transfer*, 22: 1593–1599, **1979**.
[10] R. Numrich, R. Claus, and M. Hadley. *Eurotherm Seminar, Paris*, **1995**.
[11] L.F. Moody. *Transactions of the ASME*, 66 (8): 671–684, **1944**.

Debottlenecking the Retrofitted Thermally Coupled Side-Rectifier in Naphtha Splitter Process

*Le Quang Minh, Le Cao Nhien, Feng Wei, Choi Bonggu, Lee Moonyong**

Schoof of Chemical Engineering and Technology, Yeungnam University

Gyeongsan 712-749, Rep. of Korea

**Email address (Corresponding author): mynlee@yu.ac.kr*

Abstract

Improving the separation of heavy naphtha from hydro-treating process, naphtha feed stock is separated into light naphtha, heavy naphtha and light kerosene in sequence. In this work, systems and methods of naphtha feed stock are destined both for a conventional distillation sequence and enhanced configuration with less energy consumption than conventionally possible, while producing less greenhouse gas emissions. The feasibility in retrofitting of two existing columns to thermally coupled distillation sequence (TCDS) has been demonstrated by several authors and in our previous result. Using the proposed approach, this work focused on the design options that remove the bottleneck phenomenon with which the integration of the existing shells. The pseudo-components for defining a liquid fraction have been described through using a commercial process simulator. The results showed that the operating cost could be reduced dramatically through novel combinations, such as TCDS with a side reboiler. Reducing CO_2 footprint is another benefit which can be derived from the proposed sequence.

Keywords: debottlenecking, naphtha splitter, thermally coupled distillation sequence, CO_2 footprint reduction, pseudo-component, process integration

Introduction

In the refinery and petrochemical industry, distillation units consume a large amount of energy requirement. To improve the fractionation of naphtha boiling range, naphtha feed stock is separated sequentially into light naphtha, heavy naphtha and light kerosene. In this study, it was identified the bottleneck of the main column in naphtha splitting process when being retrofitted to TCDS. A systematic approach using the response surface methodology was used for the design and optimization of the retrofitted TCDS. To remove the entrainment flooding in the retrofitted TCDS, it was considered the equipment and process modifications utilizing the existing reboiler as a side reboiler with particular emphasis on the use of existing hardware.

1. Conventional naphtha splitter process

Figure 1 presents a schematic diagram of the conventional naphtha splitter process. The existing column configuration uses two splitter columns: the naphtha splitter unit (NSU) and paraffinic fractionation unit (PFU). Typical product streams are light naphtha (Lt. Naphtha), heavy naphtha (Hv. Naph) and light kerosene (Lt. Kerosene) product, respectively. The detailed process is described as follows:

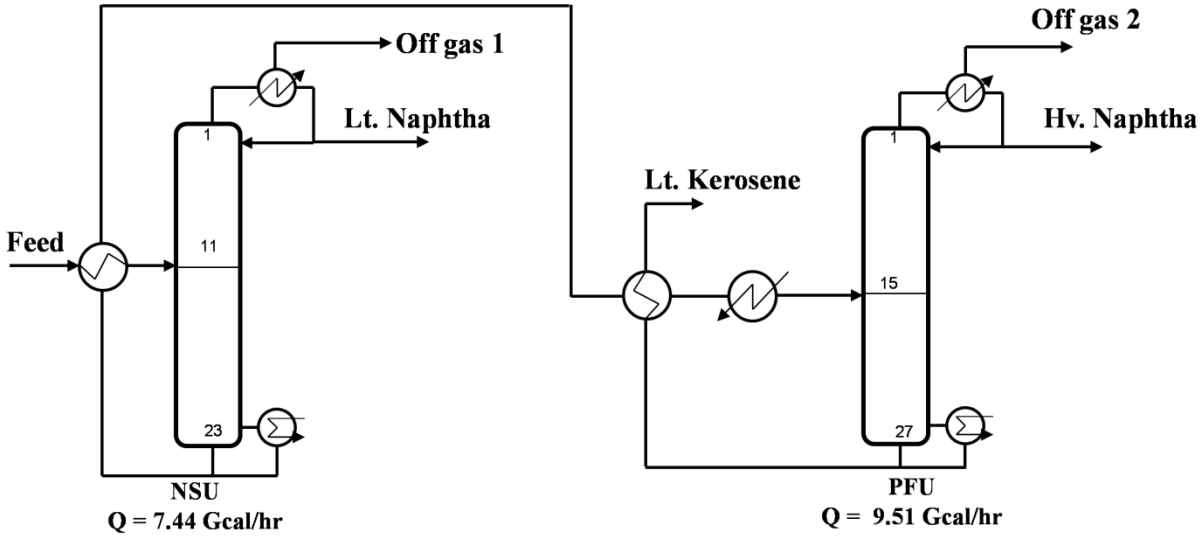

Figure 1. Schematic diagram of the naphtha splitter process

In this study, rigorous simulation was performed using the commercial software - Aspen HYSYS 8.0. The Peng-Robinson equation of state was selected to predict the vapor-liquid equilibrium of the mixture. **Table 1** lists the hydraulics and energy performances of the existing columns. The base case simulation model revealed the energy consumption of the NSU and PFU to be 7.44 and 9.51 Gcal/hr, respectively.

Table 1. Column hydraulics, and energy performance of the existing columns sequence

	NSU	**PFU**
Number of trays	23	27
Tray type	Valve	Valve
Column diameter (m)	2.8	3.1
Number of flow paths	1	1
Tray spacing (mm)	609.6	609.6
Max flooding (%)	81.77	82.13
Condenser duty (Gcal/hr)	3.27	8.09
Reboiler duty (Gcal/hr)	7.44	9.51

In this study, the main design parameters of the existing columns were evaluated for retrofitting to TCDS. The existing capacity of reboilers and condensers should also be checked for the reusability with the minimal modifications. To determine the maximum flooding of a particular column, the rating mode was simulated using the

internal specifications. All columns were designed with a maximum of 85% of the flooding point load to prevent flooding in the column.[1, 2]

2. Design and optimization of TCDS

Retrofitting the existing distillation sequence begins with the development of preliminary designs for complex systems, and minimizes the heat duty supplied to the reboilers through the optimization procedures. In this study, the response surface methodology (RSM) based optimization approach was used to examine the effects on the reboiler[3]. **Table 2** lists the factors and levels used in this case study. Thirteen simulations were run to optimize 2 parameters of the TCDS structure: the feed (N1) and vapor (N2) stream location. For each run, vapor flow to the side rectifier was varied to minimize the reboiler duty while achieving the required product purity. MINITAB software was used for both response surface fitting and to optimize the reboiler duty. The generalized second-order polynomial model was obtained as:

$$Y = 14.3662 - 0.1683X_1 + 0.0367X_2 + 0.1633X_1^2 + 0.0383X_2^2 + 0.0025X_1X_2 \quad (1)$$

where Y is the predicted response (reboiler duty), and X_1 and X_2 are the coded values of the vapor and feed stream locations, respectively.

Table 2. Coded levels of the factors

Factor	Levels		
	-1	0	1
Feed stream location in the side rectifier (N1)	3	6	9
Vapor stream location in the main column (N2)	16	18	20

The smallest reboiler duty was observed at the coded levels of the number of trays for the vapor stream location, and the feed rectifying section of 0.5151, and -0.4949, respectively (**Figure 2**). Under these conditions, the minimum reboiler duty using the retrofitted TCDS was predicted to be 14.3134 Gcal/hr (equivalent to 17.3% energy saving).

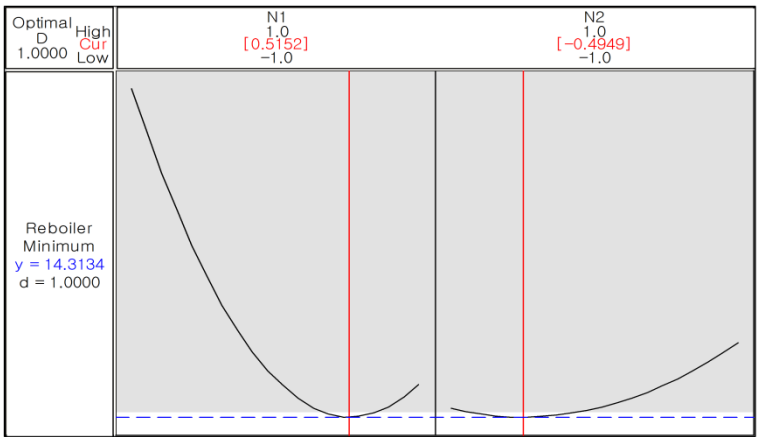

Figure 2. Optimization plot by the RSM

3. Debottlenecking retrofitted TCDS with a side reboiler

Knowing to what extent the area available for vapor flow on each stage is used when a column is operating at its maximum throughput is essential for determining at which stages, the vapor and liquid traffic should be reduced, and which stages can accommodate the increased flow. The following indicator of the hydraulic performance of an existing distillation column, the fractional utilization of area (FUA), was used as proposed by Liu and Jobson[4]:

$$\mathrm{FUA} = \frac{\text{Area required on stage i for vapor flow}}{\text{Area available on stage i for vapor flow}} \tag{2}$$

where the area required for vapor flow is calculated for a given approach to the flooding conditions (e.g. when the vapor velocity is 85% of the flooding velocity).

As seen from **Figure 3**, the FUA of the existing PFU varies from stage to stage: it began to increase from the feed stage, with some stages requiring all the available area (i.e., FUA = 1), whereas those in the rectifying section could accommodate significantly higher flows. When the existing PFU column is retrofitted to the main column of the TCDS, the bottom section of the PFU is likely to be bottlenecked because it needs to cover all the vapor flows that are shared by the main column and side rectifier. **Figure 3** shows that the FUA in the main column of the TCDS (i.e., the retrofitted PFU) increases dramatically from the vapor stream location (17th stage) and create a bottleneck in the stripping section. As shown in **Figure 3**, the FUA value is larger than 1 in the stripping section of the main column in the retrofitted TCDS.

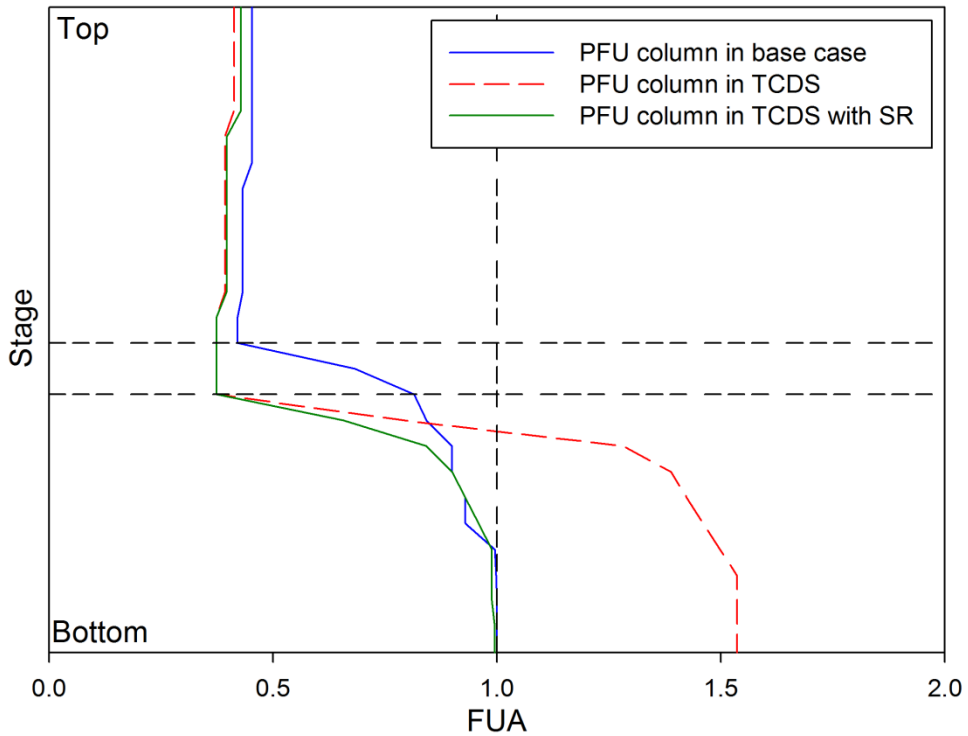

Figure 3. FUA profiles of existing PFU and main column in TCDS

Figure 4 shows the simplified flow sheet outlining the retrofitted TCDS with a side reboiler. Note that the retrofitted TCDS allows preheating the feed with the product streams only, which also provide a decrease in reboiler duty, while the existing conventional sequence requires external heat to preheat the feed. The natural values of the variables can be derived from the coded levels to carry out the rigorous

simulation. The maximum area utilization (in the stripping section) decreases to 1 by adopting the side reboiler, as can be seen the FUA plot in **Figure 3**, and can be even smaller. When the maximum area utilization is less than 1, the feed flow to the column can be increased until the maximum area utilization in the stripping section becomes 1, which corresponds to an increase in throughput. The heat duty in the reboiler decreased with increasing heat duty in the side reboiler. Note that in this retrofit case the reboiler of the existing NSU can be utilized as the side reboiler of the retrofitted TCD, as shown in **Figure 4**. In this study, the aim was to reduce the energy requirements. Therefore, the chosen side reboiler duty was 4.35 Gcal/h, which provides 17.1% savings in terms of the reboiler duty (equivalently to 16.8% in term of operating cost). In addition, the use of TCDS showed that the CO_2 footprint can be reduced up to 15.6% significantly[5].

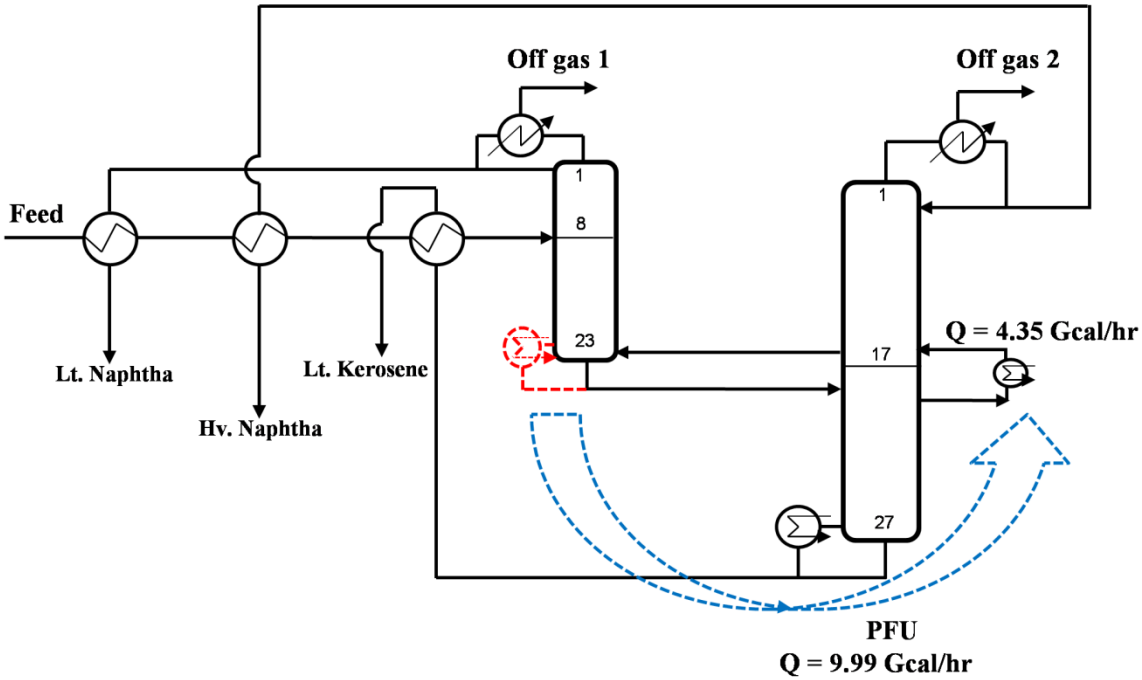

Figure 4. Simplified flow sheet illustrating the TCDS with a side reboiler

4. Conclusions

This study reported the benefits of retrofitting the conventional process to the TCDS sequence, particularly in the oil refining industry. The proposed method combining the RSM and FUA was applied to the retrofit of the conventional naphtha splitter process. Furthermore, retrofitting of a TCDS with a side reboiler could not only utilize the existing columns, but also increase the process capacity. The proposed retrofitted naphtha splitter process provided significant savings (16.8%) in operating cost with a minimal modification. Consequently, the proposed TCDS with the systematic retrofit design approach can be a promising option to increase both the separation efficiency and capacity, and thus to mitigate the CO_2 emissions (15.6% reduction) in the existing conventional naphtha splitter process.

Acknowledgement

This research was supported by Basic Science Research Program through the National Research Foundation of Korea (NRF) funded by the Ministry of Education,

Science and Technology (2012012532).

References

1. R. Premkumar, and G. P. Rangaiah, *Chem. Eng. Res. Des.*, **87**, 47-60 (2009)
2. N. V. D. Long, and M. Y. Lee, *Com. Chem. Eng.*, **37**, 119-124 (2012)
3. N. V. D. Long, and M. Y. Lee, *Ind. Eng. Chem. Res.*, **52**, 12635-12645 (2013)
4. Z. Y. Liu, and M. Jobson, *Trans. IChemE.*, **82**, 3-9 (2004)
5. M. A. Gadalla, et al., *Environ. Sci. Technol.*, **39**, 6860-6870 (2005)

Experimental study of vapor absorption by lithium bromide solution in tube and mesh alternating structure

Wu Jiafeng, Chen Yaping, Yi Zheyu, Cao Ruibing
School of Energy and Environment, Southeast University, Nanjing, P. R. China

Abstract

To further enhance the absorption of the LiBr solution systems, a new absorption structure is well designed and characterized in this paper. Stainless steel mesh is folded in zigzag as the packing and inserted to the gaps of the horizontal tubes. Thus, the simultaneous heat and mass transfer absorption on the conventional tube bundle surface is replaced by an alternating process. The absorbent flows through the tube outsides and packing regimes successively. In tube regimes, the inside cooling water removes the heat accompanied with the mass transfer, while in mesh regimes the adiabatic mass transfer is the main process. Experimental investigation is conducted to characterize the absorption heat and mass transfer performance of the absorption body with this alternative structure and compare with the conventional horizontal serpentine coil absorption bodies. The results confirm the feasibility to promote the absorption by using the mesh packing into the LiBr solution absorbers. The mesh packing provides the expanded absorption area in the absorption body, and simultaneously slows down the flow and well mingles the solution, which are beneficial for the mass transfer of the absorption. Furthermore, the adiabatic absorption process in the mesh packing leads to the increase of solution temperature at the inlet of next tube column, which can increase the total absorber cooling load but little effects on the absorption heat transfer coefficient.

Keywords

Absorption enhancement, LiBr solution systems, Heat and mass transfer, Stainless steel mesh packing

1. Introduction

The absorption of gases by solutions is a process controlled by heat and mass transfer, which is employed in many industries. Due to the low heat and mass transfer coefficient, most of the absorption bodies can accumulate huge volumes and thus necessitate lots of metal material, which becomes a major effect to restrict deteriorate the system performance [1]. Thus it has been of great importance to improve the performance of these absorbers.

Several methods have been proposed to enhance the absorption heat and mass transfer. Among them, the methods of absorber structure transformations attracted the most attentions. For example, the absorption properties could be significantly increased by using the complex heat and mass transfer structure surfaces [2-5]. The film-inverting [6-8] is another absorption enhancement program by increasing the concentration gradient at the gas-liquid surface by using the film guide configurations. Packing absorber is widely utilized because its special advantage in compensating the lack of mass transfer area in the ammonia absorption systems [9, 10], while it is rarely mentioned for the LiBr solution absorption systems [11].

However, the lack of mass transfer surface is a primary problem for absorbers. In order to further enhance the absorption in the LiBr solution systems, the utilization of packing is essential. For this reason, a new absorption structure is designed at the base of traditional horizontal serpentine coil LiBr solution absorbers. Stainless steel mesh is folded in zigzag and integrated to the gaps of the horizontal tubes as the packing, thus, a tube and mesh alternating structure is constructed.

In this alternating structure, the mass transfer area is expanded by the mesh layer, while the alternating structure limits the substantial temperature fluctuation. Therefore, both the crystallization and the decline of absorption driving force are avoided, which is superior to the packing absorbers with separating heat and mass transfer process. In addition, the mesh layer is also a complex structure surfaces and a good mixer of the solution, which is beneficial for the absorption heat and mass transfer.

The heat and mass transfer performance is tested on the absorption body with this alternative structure (or the design absorption body) in this paper, and the absorption data are compared to the horizontal serpentine coil absorber without the packing (or the control absorption body) under the same experimental conditions. The simulation results of the horizontal serpentine coil absorber (the control absorption body) are also presented in the paper for verifying the reliability of the experiment.

2. Experimental Setup and Data Reduction

2.1 The structure of the tube and packing alternating structure absorption body

Figure 1 is the schematic of the design absorption body in the experiment. Stainless steel mesh is folded as zigzag and integrated to the conventional horizontal serpentine coil as the packing. Four interlocked serpentine coils constitute the horizontal tube bundle. Each serpentine coil has 8 horizontal tube sections, with the horizontal length of 480 mm and tube pitch of 50 mm. The mesh packing is replaceable, while in this experiment, 40 grid stainless steel mesh is adopted and the packing structure is shown in Figure 2. The bottom polyline of the packing is parallel with the horizontal tubes and is aligned to the top of the cooling water tube, and then the solution could be gathered and flow to the next tube. The end faces of the packing are blocked by the mesh to prevent the leakage of the solution.

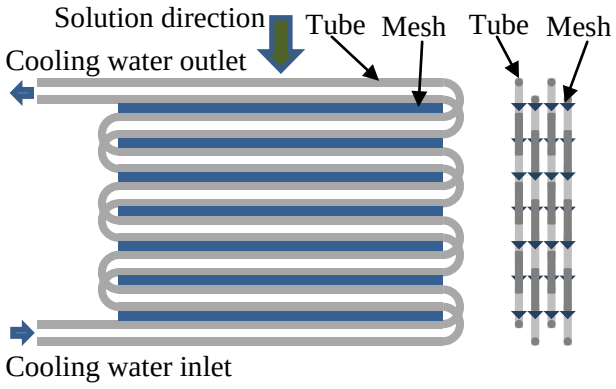

Figure 1: Absorption body schematic diagram

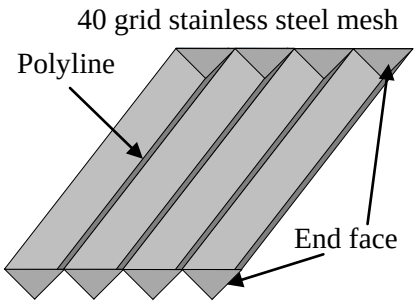

Figure 2: Packing schematic diagram

With the addition of the mesh packing layer, the simultaneous heat and mass transfer absorption on the tube bundle surface is replaced by an alternating process. The absorbent flows through the tube and packing regimes in turn. In tube regimes,

the cooling water removes the heat accompanied with the mass transfer, while the adiabatic mass transfer is the main process in mesh regimes.

2.2 Experimental setup

Figure 3 is the schematic diagram and photo of the experimental setup, which is a continuous-mode single-pressure stainless steel apparatus. The upper part of the system is the absorber while the desorber is located at the bottom part. In the experiment, the LiBr dilute solution in the desorber is heated by the adjustable heaters, and the steam is then separated from the solution. The steam goes through the mesh filter and enters the upper portion of the absorber. The concentrated solution gathered at the bottom of desorber is transported by the concentrated solution pump to the top of the absorber and sprayed to the test section. A pre-cooler is set between the desorber and solution pump to adjust the concentrated solution temperature at the inlet of absorber, and the solution pump can control the mass flow rate of concentrated solution.

The LiBr concentrated solution at the top of absorption body is sprayed by a distributer. When the solution passes through the absorption body, the absorption occurs and the cooling water takes away the heat released during the absorption. The cooling water and the solution form the counter flow in the test section. With the drive of a dilute solution pump, the dilute solution at the outlet of the absorption body can flow back to the desorber.

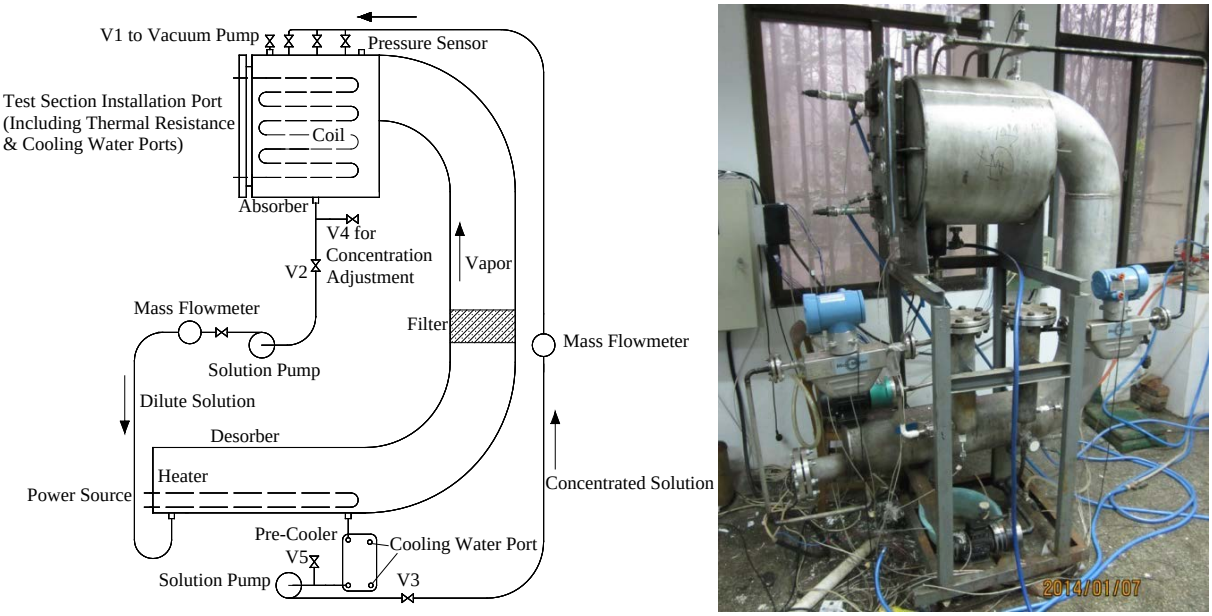

Figure 3: Experimental system schematic diagram and photo

2.3 Data measurement and reduction

Vacuum and sealing conditions are extremely important for the absorption process. Here, two pressure transducers are employed on the experimental system. One is used for testing the sealing before experiment. The experiment must be conducted only when the system in dry condition is vacuumed to lower than 10 Pa using a vacuum pump and the absolute pressure is kept to less than 100 Pa for 24 hours. The other pressure transducer is used for recording the pressure condition of the absorber (p) during experiment.

The state parameters of the concentrated and dilute solutions are measured by the mass flowmeters. By collecting the digital signals of the mass flowmeters, the

concentrated and dilute solutions' mass flow (G_c and G_d), density (ρ_c and ρ_d) and temperature (T_c and T_d) can be acquired simultaneously. Then, the concentrated and dilute solutions' concentration (X_c and X_d) and saturation temperature (T_{cs} and T_{ds}) can be calculated [12].

The cooling water temperature (T_i and T_o for inlet and outlet temperature, respectively) and volume flow (V_w) are measured by the thermal resistances and volume flowmeter, respectively. The concentrated solution temperature at the outlet of the desorber is also monitored in the experiment for the safety of the system, and the temperature measuring points are located inside the absorption body and absorber chamber for reference.

In the experiment, the solution inlet mass flow rate (Γ), absorber cooling load (Q) and the total mass absorption rate (G) are

$$\Gamma = \frac{G_c}{2nl} \quad (1)$$

$$Q = c_w \rho_w V_w (T_o - T_i) \quad (2)$$

$$G = G_d - G_c \quad (3)$$

where, n and l are the column number and length of the horizontal tube, which are 4 and 0.48 m, respectively. c_w and ρ_w are the cooling water specific heat and density, respectively.

The log mean temperature difference of the absorber (ΔT) and the absorption heat transfer coefficient (h_s) are calculated as [13]

$$\Delta T = \frac{(T_{cs} - T_o) - (T_{ds} - T_i)}{\ln[(T_{cs} - T_o)/(T_{ds} - T_i)]} \quad (4)$$

$$\frac{1}{h_s A_o} = \frac{4\Delta T}{Q} - \frac{1}{h_w A_i} - \frac{\ln(r_o / r_i)}{2\pi\lambda(8l)} \quad (5)$$

where, A_o is the surface area of a serpentine coil, and the second and the third term in Eq.(5) are the thermal resistance of the cooling water side and the tube, respectively.

In order to confirm the reliability of the experiment, a simulation is conducted on the control absorption body for comparison. The three regime absorption models [13, 14] i.e. falling film, droplet formation and droplet fall regimes are applied in the simulation.

3. Results and discussion

In order to compare the heat and mass transfer data of the design and control absorption bodies, experiment conditions are steadily controlled to keep the same absorber pressure at 2.5±0.02 kPa, and the same LiBr concentrated solution spray temperature and concentration at 40±0.2 ℃ and 55.75±0.15%, respectively. In addition, the cooling water inlet temperature is controlled at 10.5±0.3℃, while the volume flow rates are 6.5±0.15 l/min and 4.0±0.1 l/min for the design and control absorption body, respectively.

Figure 4 and 5 show the heat transfer results of the experiment. The maximum deviation of the simulation and experimental results of the control absorption body is 8.37%, which verify the accuracy of the heat transfer measurement in Figure 4. Most of the data show the absorber cooling load in design absorption body is larger than that in the control absorption body. While in Figure 5, the absorption heat transfer coefficient in design absorption body is larger than that in the control absorption body only at large mass flow rate.

Figure 6 and 7 are the mass transfer results of the experiment. The maximum deviation of the simulation and experimental results of the control absorption body is 15.4% in Figure 6. The design absorption body owns a higher mass absorption rate and a lower outlet solution concentration for most of the experimental cases, thus, both Figure 6 and 7 indicate the mass transfer enhancement of the design absorption body compared to the control absorption body.

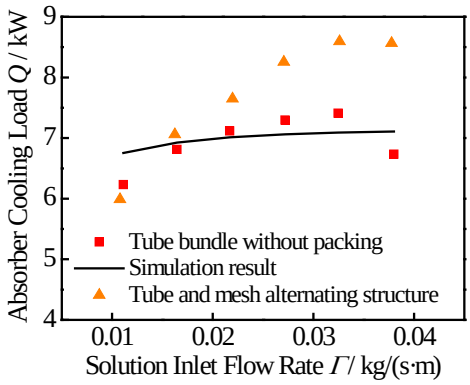

Figure 4: Absorber cooling load versus solution inlet mass flow rate

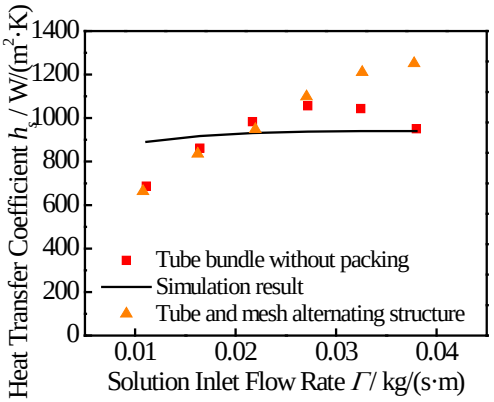

Figure 5: Absorption heat transfer coefficient versus solution inlet mass flow rate

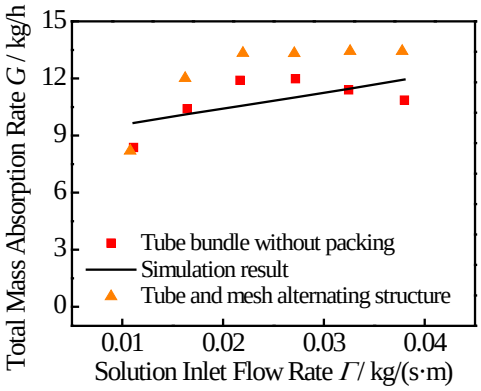

Figure 6: Total Mass absorption rate versus solution inlet mass flow rate

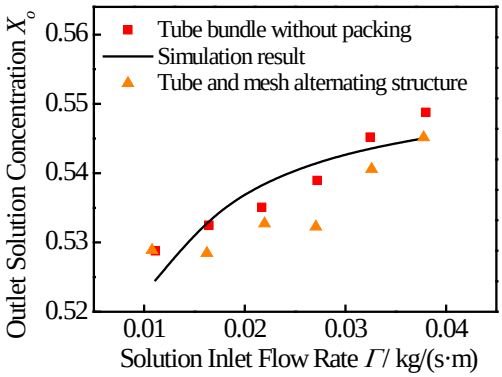

Figure 7: Outlet solution concentration versus solution inlet mass flow rate

The experimental results show an absorption heat and mass transfer enhancement of the design absorption body except the absorption heat transfer coefficient data. Therefore, it is a feasible method to promote the absorption by using the mash packing into the LiBr solution absorbers. On one hand, the mesh packing offers the expanded absorption area in the absorption body, and can slow down the flow and well mix the solution. As the experimental data shown in Figure 6 and 7, all these factors are beneficial for the mass transfer of the absorption. On the other hand, the adiabatic absorption process in the mesh packing leads to the solution temperature increase at the inlet of next tube column, which can increase the total absorber cooling load (see Figure 4), but there is no enhancement on the absorption heat transfer coefficient (see Figure 5). In addition, because of the slower solution velocity leading by the mesh packing, the splash of droplet is reduced when the absorbent hit the tubes, which is another positive factor for the absorption brought by the mash packing.

4. Conclusions

A new horizontal tube and mesh packing alternative structure absorption body is designed in this paper. Stainless steel mesh is folded as zigzag and integrated to the gaps of the horizontal tubes as the packing. Comparative experiment is conducted between the design and control absorption bodies. The experimental result shows an absorption heat and mass transfer enhancement gain, which confirm the feasibility to promote the absorption by using the mesh packing into the LiBr solution absorbers. The heat and mass transfer enhancement of the design absorption body could be concluded to three reasons: 1) the mesh packing offsets the lack of tube bundle absorption area and the absorbent is well mixed in the packing regime; 2) the mesh packing leads to the decrease of the solution velocity between the horizontal tubes, thus, the retention time of the solution in the absorption zone is extended and the droplet splash is reduced when the solution meets the tubes; 3) the adiabatic absorption process in the mesh packing leads to the increase of the solution temperature at the inlet of next tube column, which augments the heat transfer rate from the absorbent to the cooling water.

Acknowledgements

The authors gratefully acknowledge support from the National Natural Science Foundation of China (No. 51206022) for this research.

References

[1] J D Killion, S Garimella, A review of experimental investigation of absorption of water vapor in liquid films falling over horizontal tubes, HVAC&R Research, 9: 111-136, 2003.
[2] N Isshiki, K Ogawa, Enhancement of heat and mass transfer by CCS tubes, Ab-Sorption 96, International Ab-Sorption Heat Pump Conference, Montreal, Quebec, Canada, 1996, pp. 335-341.
[3] W A Miller, The synergism between heat and mass transfer additive and advanced surface in aqueous LiBr horizontal tube absorbers, International Sorption Heat Pump Conference, Munich, Germany, 1999, pp. 307-321.
[4] Y P Chen, Y B Li, M H Shi, Numerical simulation of characteristics of falling film absorption on vertical corrugation plates for aqueous Li-Br solution, Proceedings of the 6th International Symposium on Heat Transfer, Beijing, China, 2004, pp: 630-634.
[5] Y P Chen, Y B Li, M H Shi, Experimental study on falling film absorption with aqueous Li-Br solution on two-scale corrugation plate surfaces, Proceedings of 3rd ISHTEEC, 2004, pp: 335-339.
[6] M R Islam, N Wijeysundera, J C Ho, Performance study of falling-film absorber with film- inverting configuration, International Journal of Refrigeration, 2003, 26: 909-917.
[7] X Y Cui, J Z Shi, C Tan, Z P Xu, Investigation of plate falling film absorber with film-inverting configuration, Journal of Heat Transfer-Transactions of the ASME, 131: 072001, 2009.
[8] Y P Chen, C J Shi, M H Shi, Heat and mass transfer enhancement during absorption process with double-side film-inverting configuration, Journal of Chemical Industry and Engineering (China), 59: 19-24, 2008.
[9] J Sieres, J Fernández-Seara, F J Uhía, Experimental characterization of the rectification process in ammonia-water absorption systems with a large-specific-area corrugated sheet structured packing, International Journal of Refrigeration, 32: 1230-1240, 2009.
[10] A M Selim, M M Elsayed, Performance of a packed bed absorber for aqua ammonia absorption refrigeration system, International Journal of Refrigeration, 22: 283-292, 1999.
[11] N Goel, D Y Goswami, Experimental verification of a new heat and mass transfer enhancement concept in a microchannel falling film absorber, Journal of Heat Transfer- Transactions of the ASME, 129: 154-161, 2007.
[12] ASHRAE Handbook, Fundamentals: American Society of Heating, Refrigerating and Air-Conditioning Engineers, Inc., 2009.
[13] I Kyung, K E Herold, Y T Kang, Experimental verification of H2O/LiBr absorber bundle performance with smooth horizontal tubes, International Journal of Refrigeration, 30: 582-590, 2007.
[14] V D Papaefthimiou, I P Koronaki, D C Karampinos, E D Rogdakis, A novel approach for modeling LiBr-H2O falling film absorption on cooled horizontal bundle of tubes, International Journal of Refrigeration, 35: 1115-1122, 2012.

Dividing Wall Column as Energy Saving Retrofit Technology

Igor Dejanović[1], *Helmut Jansen*[2], *Žarko Olujić*[3]

[1]*The University of Zagreb, Zagreb, Croatia*
[2]*Julius MONTZ GmbH, Hilden, Germany*
[3]*Delft University of Technology, Delft, the Netherlands*

Abstract

Dividing Wall Column (DWC) is a fully heat coupled single shell column that replaces two columns connected in series to obtain three products at required purity. As proven in many industrial applications a three product DWC enables on average 30 % saving in energy and an equivalent saving in capital, accompanied by nearly halving the required plot area compared to conventional two or three column sequences. This however is related to new designs, and only few applications have been reported where an existing column has been revamped. These, however, have been originally single columns with a side product, which, by the virtue of the nature of a DWC, are obvious candidates for a revamp. Present paper uses an aromatics plant base case to show that existing two or three column sequences can be transformed in a cost-effective way into DWCs to allow energy saving equivalent to that achievable in new designs. This makes DWC to an interesting retrofit option for process industries willing to achieve significant energy savings in existing plants.

Keywords

Distillation, Dividing wall column, Column revamp, Energy saving

1. Introduction

With an ever growing demand for high quality commodity chemicals at lowest possible cost, distillation, which is both energy and capital intensive, is expected to remain the dominant separation technology in the foreseeable future. In order to comply with globally proclaimed requirement for increasing sustainability of new designs, the economic incentives are so strong that inherently conservative process industries are interested in industrial development and implementation of energy saving distillation technologies.

An encouraging technological breakthrough in this respect occurred in the mid-1980s, by introduction of the first Dividing Wall Column (DWC), i.e. a single shell, fully thermally coupled distillation column for obtaining three high purity products [1,2]. Such a column as proven in many industrial applications in the meantime enables on average 30 % saving in energy and an equivalent saving in capital, accompanied by nearly halving the required plot area compared to conventional two or three column sequences. Recent review papers give an overview on the state-of-the art of DWC technology [2,3,4]. Present academic effort is oriented towards moving user companies in refining, gas processing, petrochemical and chemicals manufacturing industries to consider and implement more complex configurations for

obtaining four or even more pure products, which allow a substantial increase in energy and capital saving gains compared to well established conventional, three-product DWC technology [5,6,7]. However, process industries seem to be reluctant to make a decisive step in that direction. The reason for this may be a lack of established design procedures and fear of unstable operation.

However, the associated risk could be lessened if novel configurations would first be tested in revamps of existing column sequences, where heat coupling could bring desired energy saving result. Usually column revamps are undertaken to enable an increase in production capacity. However, as mentioned above, legislation imposed push to reduce CO_2 emissions to a significantly lower level than allowed in the past will inevitably lead to an increase in the number of revamps of distillation sequences with energy savings as primary goal.

There are a number of tray columns in some refineries that have been revamped into a DWC. However, typical side product columns are a natural candidate for a revamp, and, as reported elsewhere [8,9] these efforts turned to be a full success, leading even to a significant capacity increase, which motivated the user companies involved to look enthusiastically for other similar opportunities in their plants. Similar outcome has been reported for an aqueous system with acetic as side product in a most recent publication by Long and Lee [10].

In the literature there are only few papers addressing explicitly application of DWC in retrofits, i.e. transformation of existing two-column sequences into DWCs. The pioneer in this respect is a paper by Amminudin and Smith [11], addressing among other aspects also practical issues related to such an application. The base case in this study was an existing NGL separation train including three columns connected in series. It appeared that installation of a partition wall into one of existing columns to transform it into a DWC would be too complicated and time consuming, so preference was given to an external, heat coupled prefractionator (Petlyuk) arrangement. A recent, frequently cited paper by Premkumar and Rangaiah [12] approached this subject in a typically academic way, using overall design and cost estimation methods available in open literature to allow a comparison of potential alternatives on basis of their cost-effectiveness. Despite related insufficiencies, this approach provided a good indication of potential gains by turning two column sequences into DWCs. In five of six cases studied a DWC as a retrofit option delivered same energy savings as new designs, when compared to conventional arrangements.

However, in case of a DWC a more detailed technical analysis is required to see whether a revamp is a good option. Most important, achievable energy saving need to be so high that corresponding vapour throughput will fit at critical place into shell diameter of existing conventional columns. This is a main concern, while two shells connected in series will provide more than sufficient height to accommodate increased stage requirement. If a four-product case is considered then existing three shells are available and need to be arranged accordingly. However, this may turn to be difficult or even impossible, depending on the extent of spread in operating pressures of individual columns. The methods developed to allow conceptual design and detailed enough dimensioning of packed three- and four-product DWCs can be used for this purpose [6,13].

This paper explores the potential for implementation of a DWC as an energy saving retrofit option. Using an industrially relevant, aromatics plant base case, it shows that existing two or three column sequences can be converted in a cost-effective way into DWCs to allow energy saving equivalent to that achievable in new designs.

2. Base cases

Figure 1 shows a conventional three-column sequence for separation of a multicomponent aromatics feed into four fractions with given specifications. It is based on an actual plant which was originally designed and operated as an indirect sequence, i.e. with columns C1 and C2 connected in series. In two-column sequence the toluene was lightest component of the heavies. To allow separation of chemical grade toluene another column (C3) was designed and added to the flowsheet.

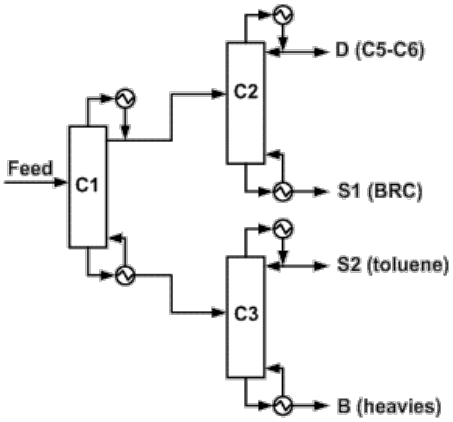

Figure 1 A three-column sequence for separation of a multicomponent aromatics feed into four fractions

Table 1 shows feed rates and compositions of the feed and products according to specifications for separation into four fractions. These data served as basis for design and assessment of a three-product DWC and various alternatives of a four-product which could be constructed as packed column using available know how [5,6,13].

Present paper aims on opposite, i.e. uses existing knowledge and means to convert conventional tray columns into a packed DWC.

Table 2 shows operating pressures, stage and reboiler duty requirements and dimensions of the conventional columns contained in the sequence shown in Figure 1. All columns contain conventional single path sieve trays, with a tray spacing of 0.6 m. Given tangent to tangent heights include active height occupied by trays and vapour-liquid disengagement spaces above the top tray and below the bottom tray, respectively. Revamp in present case means removal of the trays and tray support rings, arranging the required internal configuration, distributing partitioned sections and belonging stages over one or two shells, using the same high performance packing (Montz-pak B1-350MN), which was used for design of a new DWC for the same purpose [6].

3. Results and discussion

3.1 Three-product DWC case

Results of the detailed design of a new DWC as a replacement of the three-product sequence containing columns C1 and C2 from Figure 1, published in [5], suggest that column C2 will suffice, leaving column C1 available for some other purpose. Namely, a packed DWC for the same purpose operating at a top pressure of 2.7 bar would require a shell diameter of 1.7 m and total height of 37.3 m. Difference in required and available diameter suggests that significant capacity increase could be expected in addition to a 49% reduction in energy requirement compared to conventional sequence.

Detailed simulation of this case has indicated that the throughput of the revamped column could be factor 1.57 larger than the original one. Increasing production capacity implies corresponding increase in reboiler and condenser duties, by 56 % and 55 %, respectively. Interesting to observe here is that energy required to operate a DWC with 57 % larger capacity would be still below that required in case of original sequence. Certainly, existing reboiler and condenser will be insufficient, but to provide additional heat supply demand the reboiler and condenser of column C1 could be used, by connecting them in parallel with existing ones. This will avoid

additional investment, and the costs to implement required modifications of piping are a minor part of total costs associated with such a revamp job. Total installed costs associated with this case would be in the range of 713,500 US $, which is 48 % of the capital costs required in case of a new design. Indeed, such a revamp would be a highly profitable action.

Table 1 Base case feed and product rates and compositions

	Feed	C4-C6	BRC	Toluene	Heavies
Flow rate (t/h)	31.7	7.44	3.87	8.0	12.41
Mass fraction					
N-Hexane & lighter	0.2517	0.9869	0.1642	-	-
Benzene	0.0855	0.0131	0.6750	-	-
3-Methylhexane	0.0204	-	0.1608	0.0026	-
Toluene	0.2474	-	-	0.9718	0.0061
Ethilbenzene & heavier	0.3950	-	-	0.0256	0.9939

Table 2 Base case columns data

	C1	C2	C3
Top pressure (bar)	1.7	2.7	1.013
Shell diameter (m)	2	2	1.8
Shell height (m)	40.5	39.5	39.5
Stage requirement (-)	40	38	38
Sieve trays (#)	61	59	59
Reboiler duty (MW)	3.81	4.15	3.15

Alternative option, better suited if an increase in capacity is a secondary goal, would be to consider taking 1.7 bar column as the candidate for retrofit. At this pressure bottoms temperature would be significantly lower, which would further increase energy savings through increased relative volatility and reduced reboiler duty.

3.2 Four-product DWC case

According to the results of detailed design of various configurations of a fully thermally coupled four-product DWC [5-7], the number of stages determining the shell height is 130. This requires more shell height than available in any of the three columns from the flowsheet shown in Figure 1. However, this is not a problem because two existing shells connected in series provide enough height to accommodate required number of stages.

So two existing columns connected in series are first option for transformation of conventional three-column sequence into a four-product DWC. However this is not as straightforward as it appears. Namely, only one (C2) of the existing columns can operate at the pressure of 2.5 bar at the top, corresponding to that of new DWC design. As shown elsewhere [6], in such a case the vapour throughput is reduced to a volumetric flow rate that fits well into column C2. The column C1 has the same internal diameter (2 m); however it cannot be operated at a pressure exceeding its design pressure (1.7 bar at the top). Therefore, this column will need to handle a much larger vapour volume, which may lead to vapour velocities exceeding flooding limit of the chosen packing (B1-350MN). A remedy could be using a coarser, less efficient packing in 1.7 bar column (i.e. B1-250 or B1-250MN), provided enough height will be available for installation. If this proves insufficient, connecting two lower pressure columns (C1 and C3) in parallel could work in this respect. These options are considered and the most suitable elaborated in what follows by implementing the internal configuration of the simplest (so called “2-2-4” configuration) among four-product DWC alternatives [6]. Namely, this DWC requires only a relatively short segment of the column arranged with two partition walls in parallel.

Owing to the fact that the maximum vapour and liquid loads in new DWC design are at the bottom of the column, the lower half of the DWC will be accommodated in column C2, operated at a top pressure of 2.5 bar. This implies that this column will

contain, from bottom to the top, two beds in conventional part of the column and as much as reasonable of the stages on the prefractionator and the main column side. The available height (39.5 m) of 2.5 bar column (C2) dictates placing the bed above the side product draw-off into the bottom part of the 1.7 bar column (C1). Since two beds belonging to rectification and stripping sections of the prefractionator are much shorter, on this side of the partition wall there is a lot of empty space available in vertical direction. This allows moving downwards the rectification section bed which is in new design on the level of the middle and main column sections, i.e. installing it in high pressure column. This, in turn, allows enlarging the cross sectional area of middle and main column sections, needed to compensate for increase in vapour volume due to operation at lower pressure (1.7 bar). Interesting to mention here is that in this way it is avoided to have three packed sections in parallel, as employed in new DWC design [6].

Figure 2 shows schematically the result, i.e. the lay-out and internal configuration of the four-product DWC arranged using two available columns connected in series, each containing only one partition wall, with condenser pressure set at 1.7 bar.

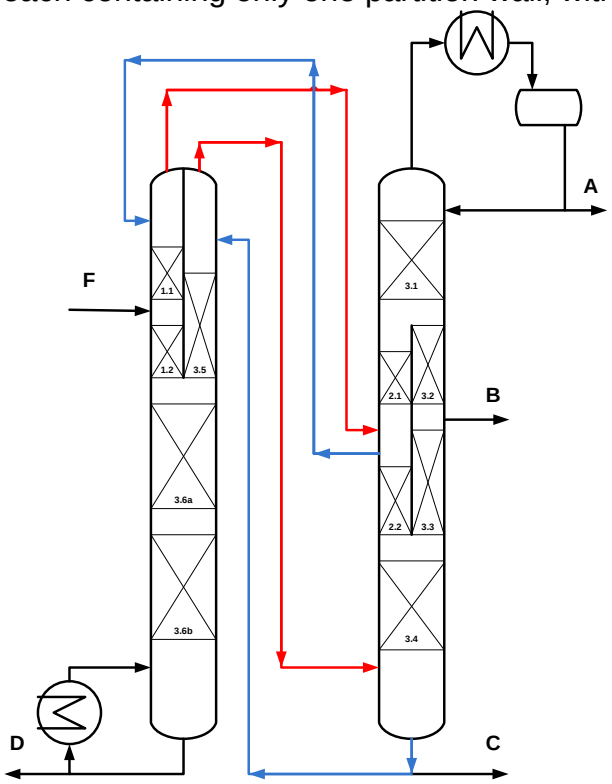

Figure 2 Schematic representation of a four-product DWC arranged as two column shells (C2 and C1) connected in series

The estimated installed costs for this revamp are approximately 1,249,000 US $, while energy saving on yearly basis is about 1,160,000 US$, indicating an attractive payback time (around one year). In other words, compared to conventional sequence, future earnings could be increased yearly by this amount, which could contribute to a significant increase in profitability of such an aromatics processing plant. No doubts, similar benefits could be expected in other applications.

Nevertheless, there are additional complexities and constraints associated with such a revamp, which could emerge as a reason to avoid it. First of all, the time available for revamp, which may turn to be insufficient to arrange modifications of two existing tray columns required to accommodate a packed DWC. Trays and tray support rings need to be removed, which is a routine activity inside the shell. However, to accommodate such a complex configuration with packings and auxiliary equipment a lot of local welding inside the shell will be needed to provide required structural strength and support for numerous packed beds, liquid collectors and distributors. It is anticipated that for this application non-welded partition wall will suffice, which is important because it minimizes effort and time needed to install partition walls and packed beds in a quite confined space. Also it is certain that a number of additional manholes will be required to allow installation and access to redistribution sections for future inspection and maintenance as well as nozzles for feed, side draw-off, instrumentation, and for liquid and vapour traffic between two columns. Also, the pressure drop associated with

transport of vapour from first into second column has not been accounted for as a part of pressure drop balance determining the vapour split in first column. This and other potential uncertainties need to be evaluated properly and accounted for during detailed process and mechanical design phase.

4. Conclusions

Conceptual process design considerations and aspects related to conversion of a conventional two columns sequence into a three-product DWC and a three column sequence into a four-product DWC have been addressed and discussed, indicating that both options could be highly beneficial, leading to high returns and consequently to a significant increase in profitability of aromatics processing plants.

In three-product case, one of existing columns could accommodate the DWC. In this case the energy saving translates into such a reduction of vapour load with respect to that of the conventional sequence that the production capacity could be increased by 57 %, creating a double win situation.

In four-product case, two existing columns connected in series could accommodate chosen DWC configuration. Most distinguishing advantage of this revamp lies in the fact that a complex configuration is reduced to two single partition wall columns, which suggests that there should not be additional complexities and concerns related to operability.

DWC technology should definitely be considered as a retrofit option, and could significantly contribute to energy saving efforts in process industries.

References

1. Kaibel, G., Distillation columns with vertical partitions, Chem. Eng. Technol. 10 (1987) 92-98.
2. Dejanović, I., Matijašević, Lj., Olujić, Ž., Dividing wall column–a breakthrough towards sustainable distilling, Chem. Eng. Proces. 49 (2010) 559-580.
3. Asprion, N., Kaibel, G., Dividing wall columns: fundamentals and recent advances, Chem. Eng. Proces. 49 (2010) 139-146.
4. Yildrim, Ö., Kiss, A.A., Kenig, E.Y., Dividing wall columns in process industry: A review of current activities, Sep. Pur. Technol. 80 (2011) 403-417.
5. Dejanović, I., Matijašević, Lj., Halvorsen, I.J., Skogestad, S., Jansen, H., Kaibel, B., Olujić, Ž., Designing four-product dividing wall columns for separation of a multicomponent aromatics mixture. Chem. Eng. Res. Des. 89 (2011) 1155-1167.
6. Olujić, Ž., Dejanović I., Kaibel, B., Jansen, H., Dimensioning multi-partition dividing wall columns, Chem. Eng. Technol. 35 (2012) 1392-1404.
7. Halvorsen, I.J., Dejanović, I., Skogestad, S., Olujić, Ž., Internal configurations for a multi-product dividing wall column, Chem. Eng. Res. Des. 91 (2013) 1954-1965.
8. Slade, B., Stober, B., Simpson, D., Dividing wall column revamp optimises mixed xylenes production, IChemE Symposium Series No. 132 (2006) amendment 1-10.H.
9. Spencer, G., Plana Ruiz, F.J., Consider dividing wall distillation to separate solvents, Hydrocarbon Processing 84 (2005) 7, 50B-50D.
10. Long, N.V.D., Lee, M.Y., Optimal retrofit of a side stream column to a dividing wall column for energy efficiency maximization, Chem.l Eng. Res. Des. 91 (2013) 2291-2298.
11. Amminudin, K.A., Smith, R., Design and optimization of fully thermally coupled distillation columns – 2: Application of dividing wall columns in retrofit, Chem. Eng. Res. Des. 79 (2001) 716-724.
12. Premkumar, R., Rangaiah, G.P., Retroffiting conventional column systems to dividing-wall columns, Chem. Eng. Res. Des. 87 (2009) 47-60.
13. Dejanović, I., Matijašević, Lj., Jansen, H., Olujić, Ž., Designing a packed dividing wall column for an aromatics processing plant, Ind. Eng. Chem. Res. 50 (2011) 5680-5692.

Effect of Liquid Spreading on Distillation Performance of Structured Packing

Marc Wehrli, Florian Kehrer, Ansor Gäbler
Sulzer Chemtech Ltd, Winterthur, Switzerland

Abstract
It is known that maldistribution can significantly impair distillation efficiency of packed beds. Known cross-channel type packings can cope with such non-ideal conditions to some extent, but there are limitations, especially with increasing column diameter and bed height. The effect of lateral liquid spreading is studied by means of a standard packing M1 and a special variant M2 with reduced spreading angle. According to theory maldistribution has no effect on efficiency in a sufficiently small column. This is confirmed by experiment: both variants show the same efficiency in a small column, but M2 has a much lower performance in a large column with a diameter of 1m. A special distillation test in a small column is proposed that is suitable to identify in an economical way potential maldistribution issues of a structured packing.

Keywords
Distillation, maldistribution, mass transfer efficiency, structured packing

1. Introduction

For assessing distillation efficiency of structured packing total reflux tests with standard binary systems[1] have become state of the art. It is understood that such tests are carried out under optimal conditions, including uniform vapor and liquid distribution. – Reality in productive, possibly large scale distillation plants is different, and *maldistribution* (deviation from plug flow) cannot be avoided. As a consequence, maximum distillation efficiency cannot be achieved any more. Very practical needs have triggered numerous research projects and publications dealing with the phenomenon of maldistribution, e.g. Huber and Hiltbrunner[2], Yuan and Spiegel[3], Stichlmair and Fair[4], Cai et al.[5], Schneider[6], Duss[7].

It has been known that the sensitivity to maldistribution greatly depends on the packing's capability to laterally spread or mix the phases. A packing with good liquid spreading mixes liquid better and thus will provide better performance despite imperfect irrigation. This effect is only visible in sufficiently large columns. According to Huber et al.[2] the ratio of column diameter D to characteristic length d of the packing (e.g. the hydraulic diameter) plays a major role. At D/d=20 or smaller, the packing efficiency will neither be affected by maldistribution nor will any improvement due to better liquid spreading be visible.

Most structured packing types are built according to the cross-channel principle. Each element consists of corrugated vertically extending material sheets, which are placed next to each other. The corrugation of adjacent sheets forms channels that are inclined in opposite direction with the angle φ as measured from the vertical axis. Vapor mainly follows these channels. Hence, good lateral distribution parallel to the sheets is achieved. For further improvement of mixing, elements are stacked upon each other with a rotation of about 90° around the axis. Liquid spreading is less directly influenced by the corrugation. Non-uniform distribution of vertical liquid flux L

and incomplete wetting both affect mass transfer negatively, which results in a bad distillation efficiency.
Among others the Sulzer structured packing Mellapak^{TM} and MellapakPlus^{TM} are built according to the cross-channel principle. All of them provide already a very good lateral liquid spreading. On the quest for even further improvement a major difficulty is related to the fact that maldistribution effects cannot easily be assessed in small columns. In the present paper it shall be shown, how lateral mixing affects distillation efficiency in two columns of different diameter, and how the effect of lateral mixing can be quantified experimentally in a column of small diameter despite the known limitations.

2. Results and discussion

2.1 Packing characteristics

Mellapak 250.Y has a specific surface area of 250m^2/m^3. Surface texturing, perforation, liquid/solid contact angle, φ=45° inclination of corrugation and the pattern of contact points between adjacent packing sheets determine the liquid film flow and the spreading of the liquid. Liquid flow can be observed experimentally on a vertically installed corrugated sheet by feeding a certain amount of water or alcohol at a distinguished point close to the top edge of the sheet. However, this approach does not provide significant enough information to identify minor changes, which may already impact the distillation efficiency. A better, although quite crude looking approach leads to more significant observations: Two packing elements of sufficient diameter are stacked on top of each other and put on a frame one meter above the ground. Water is fed centrally on the upper packing by means of a hose, and the pattern of the liquid leaving the lower packing element is observed. The area on the ground covered by the liquid trickling down can be measured. The installation and the observed collecting area for Mellapak 250.Y (M1) and a different packing (M2) are shown in Figure 1.

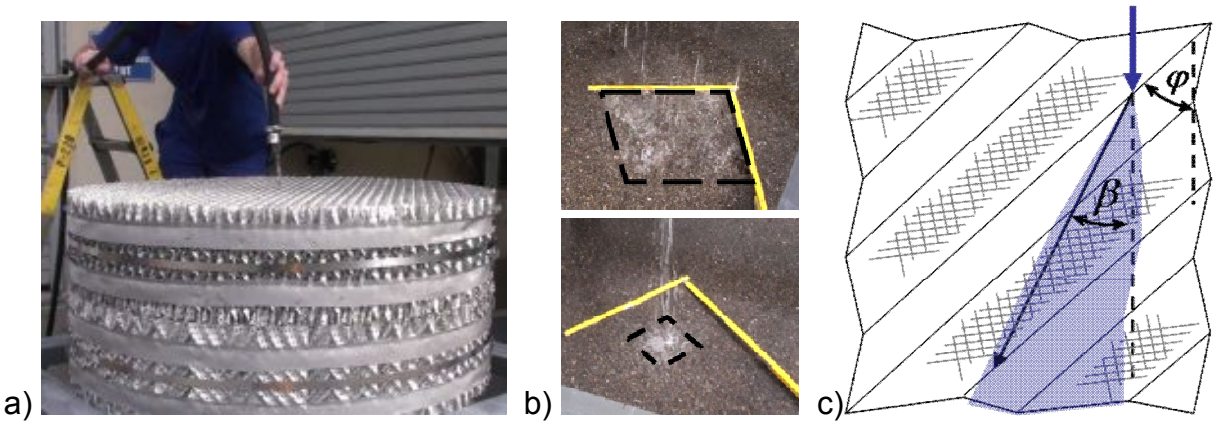

Figure 1: a) Set-up for water distribution test. Water is fed centrally at the top, the collecting area of the water trickling down on the ground is observed. b) Collecting areas for packing M1 (top) and modified packing M2. c) Definition of maximum angle of liquid spreading β.

A modified version M2 of the packing has been built that shares most details with the standard packing M1, however, the direction of liquid flow is different. To distinguish the two packing variants we use the maximum angle of liquid spreading β as observed indirectly via the experiment of Figure 1. Some details of M1 and M2 are

given in Table 1. Both packing variants are expected to realize the same number of theoretical stages $n_{expected}$=2.8m^{-1} under very ideal plug flow conditions with complete wetting, which can be realized with M1 at 100% capacity in a column of D=1m inner diameter (NTSM=Number of Theoretical Stages per Meter).

Table 1: Characteristics of the experimental packing variants M1 and M2

	Spec. surface area / m^2/m^3	Hydr. diameter d / m	Inclination angle φ of corrugation / °	Max. angle β of liquid spreading / °	$n_{expected}$ in NTSM / m^{-1}
M1	250	0.016	45	32	2.8
M2	250	0.016	45	10	2.8

2.2 Standard distillation tests

For the distillation test at total reflux using the standard binary mixture Ethylbenzene with 20% Monochlorobenzene first a column of an inner diameter of D=250mm is chosen. At a ratio D/d=15.6 the result should be insensitive to maldistribution. Both packing variants indeed provide very similar efficiency results as shown in Figure 2. The efficiency is scaled with the expected value $n_{expected}$, and the F-factor is arbitrarily normalized with the capacity that can be achieved with M1 in a column of D=1m at a head pressure of 960mbar, i.e. $F_{normal}=F/F_{100\%,960mbar}$. The typical decline of theoretical stages at capacity limit or flooding cannot be observed in this diagram. Instead, efficiency tends to increase due to stabilization of froth, which is typical for flooding in small columns. In the more relevant range below F_{normal}<1 and 1.3, for 960 and 100mbar respectively, both versions M1 and M2 have identical efficiency although slightly below the expected value $n_{expected}$.

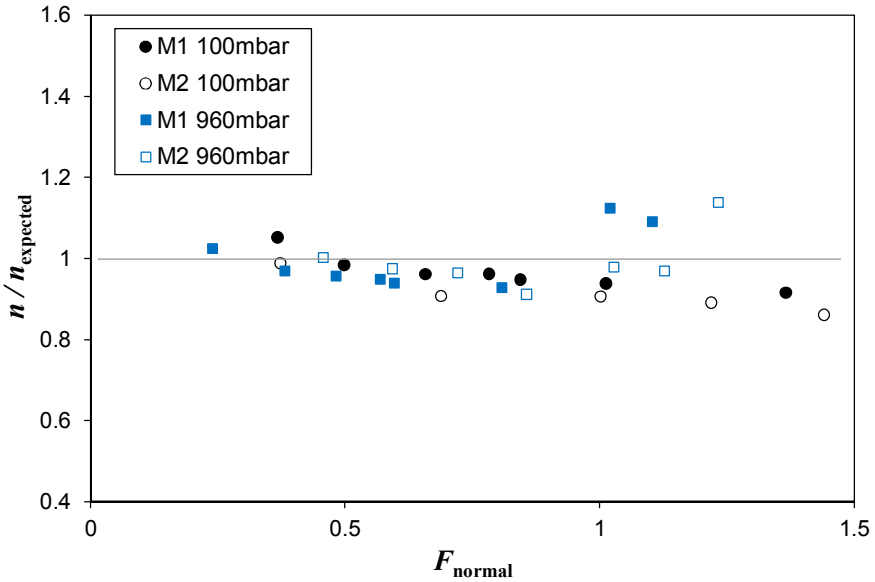

Figure 2: Total reflux efficiency data obtained in a column with inner diameter D=250mm. Head pressure 100mbar and 960mbar. Results for Packing variants M1 (standard) and M2 with bed height 3.5m and 2m.

If the two packing variants are tested in a large column of inner diameter D=1m, the results look very different. The efficiency of M1 meets the expected performance, whereas M2 reaches only $n/n_{expected}$ below 0.6 as can be seen in Figure 3.

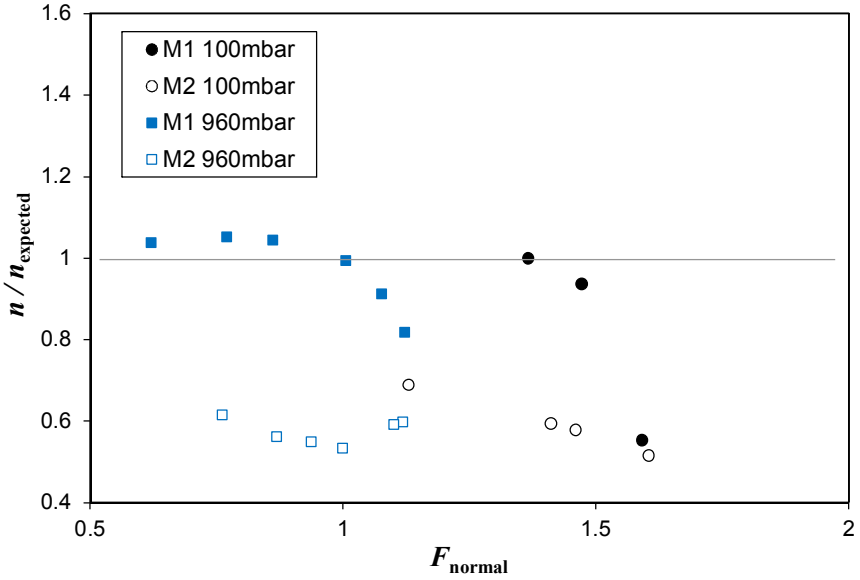

Figure 3: Total reflux efficiency data obtained in a large column with inner diameter D=1000mm for packing variants M1 and M2. Head pressure 100mbar, 960mbar. The packing beds were 4.8m high.

Although the tests have been carried out with the same uniform liquid distribution and a vapor return nozzle according to standards, a certain formation of maldistribution cannot be avoided. The capability of a distillation unit to cope with an imposed maldistribution or to avoid formation of maldistribution depends on specific geometrical features of the structured packing, which promote mixing and dispersion or lateral spreading of the phases.

It appears reasonable to assume that large scale maldistribution can always develop inside the packing bed. Its scale is characterized by the diameter D of the column. To evaluate the effect of maldistribution on efficiency we use the approach presented in Huber et al.[2] which provides analytical solutions for certain liquid flow distributions, which are constant along the bed. The equations can also be used for numerical integration in the case of an arbitrary smooth liquid flow distribution. For our purpose Huber's equation 7' shall be rephrased as follows:

$$C = \frac{1}{18\bar{L}} \int_0^R \left(\int_0^r \frac{\partial L}{\partial r} r \, dr \right)^2 \frac{dr}{r}$$

Whereas the partial differential $\partial L / \partial r$ describes local radial variation of the vertical liquid mass flux L due to maldistribution. Its average value is denoted by $\bar{L}$. The value C is used to determine the distillation efficiency of the packing bed in terms of measured approximate average Numbers of Theoretical Stages per Meter (NTSM) compared to expected NTSM:

$$\frac{n}{n_{\text{expected}}} = \frac{1}{1 + n_{\text{expected}} \dfrac{C}{\text{D'}}}$$

The dispersion factor D´ accounts for radial mixing of components within the packing and includes the effect of lateral spreading of liquid. Huber assumes proportionality between the dispersion factor, the gas flow rate and a characteristic length d of the packing. Experiments of Dzhonova et al.[9] show that proportionality with d is only maintained if d is sufficiently small. In this context it seems reasonable to correlate the coefficient with the spreading of liquid. For M1 a value of D´ is chosen that

delivers appropriate efficiencies. For M2 the value is set in proportion according to $D' \sim (\tan \beta)^2$. A linear maldistribution is assumed varying along the radius as $L = \overline{L} + \overline{L}\ell(3r/D - 1)$, where the factor $\ell = 0.2$ determines the deviation from uniformity such that 10% more liquid is flowing close to the column wall. The resulting values for n/n_{expected} are provided in Table 2 under "Prediction". Measured average ratios (from the diagrams in Figures 2, 3 and 4) are also provided. The agreement for the standard tests with column diameters D=250mm and D=1000mm is acceptable.

Table 2: Maldistribution effect for packing variants M1 and M2, expressed in ratio n/n_{expected} between approximate average measured NTSM value below flooding and expected NTSM as measured under ideal conditions. Prediction shows results according to Huber's model.

	Standard D=250mm		**Standard D=1000mm**		**Sensitivity test 250mm**	
	Measured	Prediction	Measured	Prediction	Measured	Estimation
M1	0.95	0.99	1.02	0.96	0.80	0.84
M2	0.95	0.97	0.58	0.67	0.30	0.16

2.3 Sensitivity test for liquid spreading

In the process of optimizing a structured packing, the impact of geometrical modifications on its efficiency is of interest. Total reflux distillation in a small diameter column is suitable to assess efficiency under ideal conditions. But we have seen that such a test is insensitive to maldistribution if D/d is too small. To predict the performance of a packing under conditions that favor maldistribution, a test with a larger column is required. Alternatively, a new test is suggested with the following modified geometrical conditions:

- Test in small diameter column, e.g. D=250mm
- *Single point* liquid feed at the top of the bed
- *Short packing* bed, e.g. 4D or 1m

This experiment measures the efficiency of a short packed bed with a single point liquid distribution and the effect of liquid spreading. A packing with improved liquid spreading will deliver better efficiency than a packing with bad spreading. The resulting ratio n/n_{expected} will in most cases be below unity. Results of such tests with M1 and M2 are given in Figure 4. They confirm that the bad liquid spreading of M2 translates directly into a poor efficiency. Even M1 achieves not more than a ratio of 0.80 at lower F-factor, but it is significantly better than M2. This shows that the proposed test provides results that are sensitive to liquid spreading. The achieved efficiency of M1 agrees approximately with single point irrigation results obtained by Olujic et al[9] with a similar packing of the same specific surface area.

In the set-up of the sensitivity test, maldistribution is very high at the top of the bed and decreases with the spreading of the liquid. Huber's model is only designed to predict the change in efficiency in a fully irrigated bed with a constant maldistribution not varying along the height. – Although not all conditions are satisfied, we try to employ the model just for the sake of a qualitative check. The packing bed is split along its height into five layers. For each layer the function L is described by means of a Gaussian distribution, such that 95% of its area covers the cross section of the bed according to the irrigation achieved with the spreading angle β. For M1 the liquid reaches the column wall already in the 2nd layer, for M2 only at the bottom of the 4th layer. The efficiency is evaluated for each layer using its own constant liquid maldistribution, and finally averaged to provide the performance of the bed.

Accordingly obtained $n/n_{expected}$ are listed in Table 2 under “Sensitivity test”. They confirm the results qualitatively, but the efficiency of M2 is underestimated.

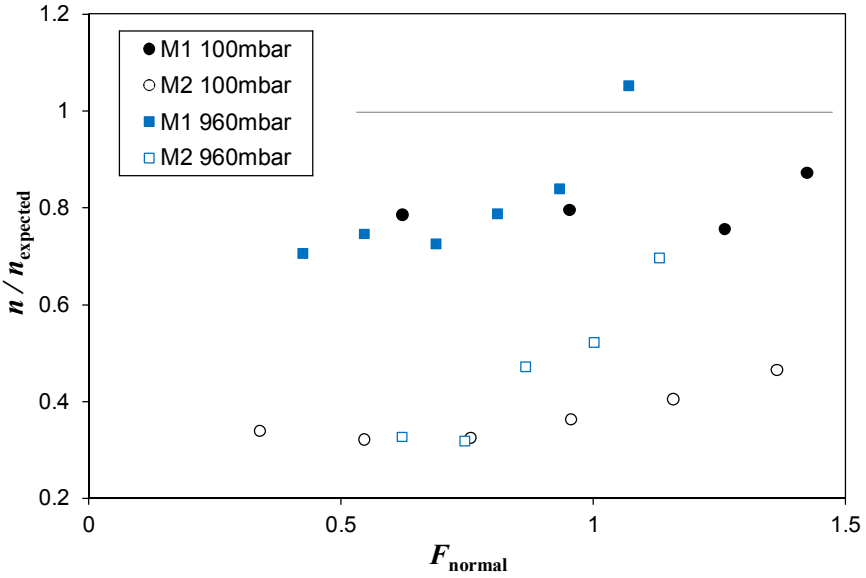

Figure 4: Sensitivity test in small column with inner diameter D=250mm. Total reflux efficiency data obtained with packing variants M1 and M2, head pressures 100mbar, 960mbar. Bed height: 1m.

3. Conclusions

Total reflux distillation tests with a modified structured packing of reduced liquid spreading capability confirm that small column tests are insensitive to maldistribution. However, potential maldistribution issues can be detected using a short bed test with a central liquid feed. Resulting efficiency is sensitive to liquid spreading and can therefore be used to identify even minor improvements achievable by geometrical modifications of a structured packing. The proposed method is inexpensive and suitable to assess the liquid spreading capability of a packing and its effect on efficiency. The model calculations according to Huber et al.[2] support the experimental findings.

References

1. U. Onken, W. Arlt, Recommended test mixtures for distillation columns (2nd edition), The Institution of Chemical Engieneers, 1990, Rugby, England.
2. M. Huber, R. Hiltbrunner, Füllkörperrektifizierkolonnen mit Maldistribution, Chem. Eng. Sci., 1966, 21, 819-832
3. H.C. Yuan, L. Spiegel, Theoretical and experimental investigation of the influence of maldistribution on the performance of packed columns at partial relfux, Chem. Ing. Tech., 1982, 54(8)
4. J. Stichlmair, J.R. Fair, Distillation: principles and practice, Wiley-VCH, New York 1998
5. T.J. Cai, B.X. Chen, C.W. Fitz, J.G. Kunesh, Effect of bed length and vapor maldistribution on structured packing performance, Chem. Eng. Res. Des., 2003, 81, 85-93
6. O. Schneider, Maldistribution in Packungskolonnen, Ausmass, Auswirkungen und Gegenmassnahmen, Fortschr.-Ber. VDI Reihe 3 Nr. 823, Düsseldorf 2004.
7. M. Duss, A new method to predict the susceptibility to form maldistribution in packed columns based on pressure drop correlations, IChemE Symposium series no. 152, 2006, 418-430
8. D. Dzonova-Atanasova, N. Kolev, S. Nkaov, Determination of liquid radial spreading coefficients of some highly effective packings, Chem. Eng. Technol., 2007, 30 (2), 202-207
9. Z. Olujic, A. Roelofse, F. Stoter, J. de Graauw, LDESP: A simulation and optimisation environment for structured packings, IChemE Symposium series no. 142, 1997, 949-960

Development and Testing of Trays with Downward Flowing Valves

Giuseppe Mosca[1], Ang Chew Peng[2], Mark Pilling[3]
[1]Sulzer Chemtech AG, Winterthur, Switzerland;
[2]Sulzer Chemtech Pte Ltd; Singapore;
[3]Sulzer Chemtech USA, Inc., Tulsa, Oklahoma

Abstract
Distillation column tray technology is considered by many to be quite mature. This is even more so when considering tray deck orifices. This paper will briefly discuss the operating characteristics of valve trays and finally demonstrate performance improvements for a new type of valve, the Sulzer Umbrella Valve (UFM™ valve), that generates a downward vapor flow component onto the tray deck.

Although a myriad of valve sizes, shapes and configurations have been tested over the past decades, it appears that there is still some room for improvement. By properly controlling the vapor flow leaving the valve, the generation of interfacial area can be improved and a more uniform overall vapor velocity can be obtained. This leads to better efficiency and higher vapor side capacity for the tray. Overall, the net result is an improvement of approximately 10% over existing high performance devices.

CFD results will be shown to outline the development process. Distillation results from both the Chlorobenzene/EthylBenzene and Cyclohexane/Normal Heptane test systems, showing efficiency and capacity gains for Umbrella Valves, will be discussed. The data are from Sulzer in-house laboratory distillation testing as well as from an independent test facility with commercial scale columns.

Keywords (Subheading – Arial 12 pt. bold, left-aligned)
Umbrella, UFM, Trays, Valves, High Performance

1. Introduction

Distillation is a rather mature technology. Over the past two centuries, a wide variety of different deck types have been produced and tested. Bubble cap trays were first commercially used more than 200 years ago for beer distillation. Sieve trays were developed in the mid 1800's with valve trays following much later. From this experience, we can observe certain clear trends. First, bubble cap trays, with their unique vapor flow characteristics, used for many years as the mainstay of tray designers, are used today generally only in niche applications where turndown is critical. This is due mainly to the higher cost of these trays in conjunction with their performance capabilities.[1] Also, over time, we have seen that deck orifice size and valves sizes have decreased. We find that smaller orifices generate less pressure drop and tend to have better de-entrainment capabilities. This is especially true for trays operating in the spray regime.[2,3]

Since the advent of “mini” valves in the latter part of the 1990’s, there have been few confirmed results seen in the area of tray deck improvements.[4] But with the huge magnitude of the global Chemical Processing Industry, there are always significant driving forces to improve distillation technology. As is well documented, distillation is an energy intensive process.[5] Any improvements in tray or packing efficiency will directly lower column energy requirements. Finally, capacity improvements are always desirable and tangible for project justifications. So, in the end, tray designers are always looking for improved technology.

2. Results and discussion

2.1 Sulzer Chemtech Investigations into Improved Tray Deck Performance

Sulzer Chemtech started this internal research and development effort with the proposal that there could be a valve design that would more effectively mix the vapor and the liquid streams flowing through and across the tray deck. However, to be commercially viable, this had to be done without creating excessive pressure drop, limiting capacity, or being too mechanically complex or expensive.

The first stage in this process involved taking a closer look at the vapor flows through conventional valves. At first glance, one would assume that the vapor leaves a conventional valve (with a vertically oriented orifice) in a near horizontal flow direction. However, when observing trays in an air/water simulator at relatively high vapor to liquid ratios, it could be seen that the liquid at the deck level was clearly being carried upward at an angle that was significantly steeper than horizontal. Of course vapor must ascend through the tray deck and flow upward to the tray above, but the surprising thing was that the vapor flowed upward so quickly after leaving the valve orifice. From this it was rather evident that any liquid near the tray deck was being left un-contacted by the bulk of the vapor. This phenomenon, known as “jetting”, results in tray efficiency losses.[6] The flow patterns through these trays were subsequently modeled using computational fluid dynamics (CFD) and the results confirmed the previous in-house visual observations. What was also seen was a distinct confluence of the vapor leaving adjacent valve to form larger, high velocity streams between the valves. This is shown in Figure 1.

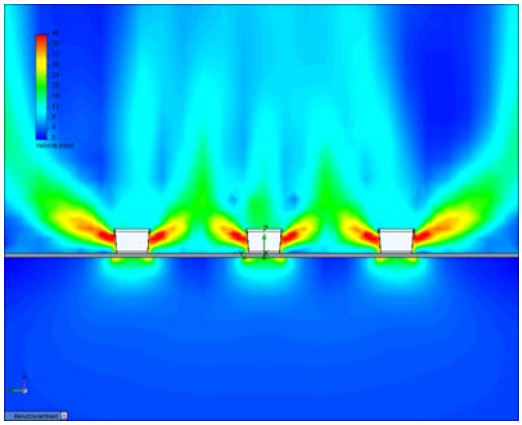

Figure 1: CFD Results with Conventional Valves

From this, we see that vapor emitting from valves with a generally horizontal top surface (such as fixed valves and conventional round or rectangular valves), will be projected upwards at some angle with respect to the horizontal, resulting in limited contact time between vapor and liquid on the tray deck. It was then proposed that by altering the vapor streams to flow in a downward direction on the tray decks that this would likely enhance mixing at the deck level and improve tray efficiency. A second perceived benefit was that the downward flowing vapor could be more evenly dispersed, creating the lowest possible vapor velocities to decrease entrainment and therefore improve deck capacity.

Initially, a few different designs were proposed. The most promising design was a modified concave "umbrella" shape, hence the name Umbrella Valve. One variant of this valve, the Umbrella Floating Mini or UFM^{TM} valve is the topic of this paper and is shown in Figure 2 in a commercial configuration.

Figure 2: UFM^{TM} Valve Trays

2.2 CFD Results from the Umbrella Valve

The new valve design features downward turned edges (as shown in Figure 3) to redirect the vapor leaving the valves. CFD studies were then conducted on the Umbrella Valves under similar conditions. The results show high vapor velocity zones close to the tray decks. Conversely, the regions above the valves have approximately 40% lower velocity than that of conventional valves that release vapor laterally.

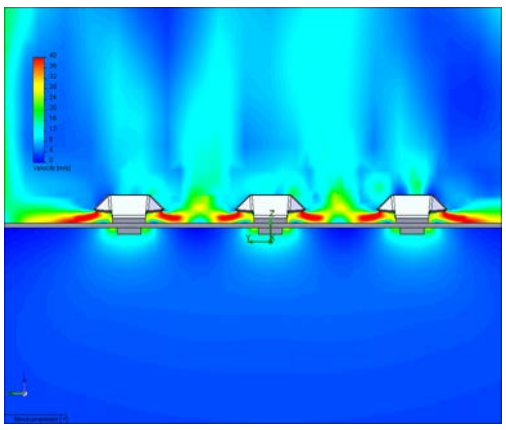

Figure 3: CFD Study of Vapor Flow from Umbrella Valves

To further study the vapor flows through these valves, an additional series of CFD runs was performed using a matrix of eight Umbrella Valves in the horizontal plane. Figures 4-6 show the CFD plane view at increasing elevations from the tray decks. This evaluation helps to focus on the vapor interaction between the valves.

Figure 4 is an overhead view of the UFM valve matrix showing the vapor velocities at 1 mm above the tray deck. The black oval shows the most representative region on the tray deck between 4 active valves. In this region, there are distinct zones of high vapor velocity indicated in red. These zones represent the vapor leaving the valves laterally at the top surface of the tray deck (where the liquid should be). These high energy zones provide good mixing to maximize vapor/liquid interfacial area.

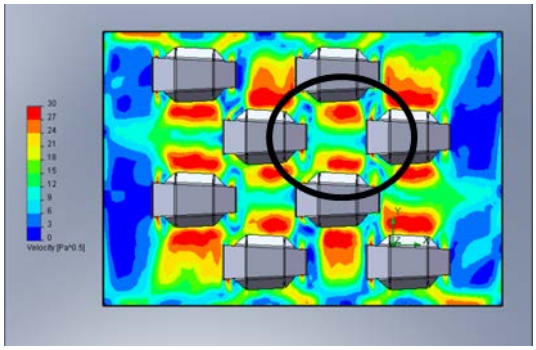

Figure 4: Top View of Tray Deck with Umbrella Valves. (Elevation 1 mm)

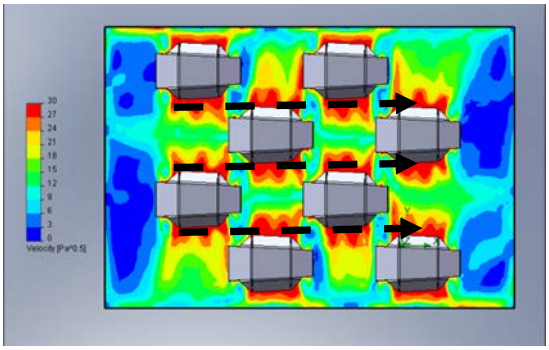

Figure 5: Top View of Tray Deck with Umbrella Valves. (Elevation 3 mm)

Figure 5 shows an overhead view of the valves at elevation of 3 mm above tray deck. There are regions of high vapor velocity indicated by red zones. The cross-current liquid flow, represented by black arrows, coincides with the regions of high vapor velocity. This should lead to higher vapor/liquid mixing in these areas just above the deck level.

Figure 6 shows an overhead view of the valves at an elevation of 10 mm above tray deck. At this elevation, the vapor velocities have dissipated noticeably, leaving a calmer and much more uniform upward vapor flow pattern arising from the tray decks. The lower velocities should reduce the liquid entrainment levels from the tray deck and improve capacity.

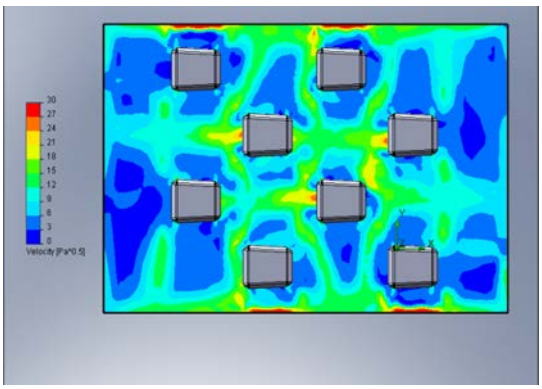

Figure 6: Top View of Tray Deck with Umbrella Valves. (Elevation 10 mm)

These CFD studies support the hypothesis that valves which direct vapor downwards to the tray deck could very likely provide enhanced tray performance. As designed, the downward vapor flow provides strong vapor/liquid mixing near the tray deck to enhance efficiency but also provides a more uniform, slower vapor velocity above the tray decks for reduced entrainment and improved capacity. Obviously, these results are mathematical simulations. The next meaningful step was then to test prototypes in an actual distillation column.

2.3 Sulzer Chemtech Test Results

The UFM trays were first tested in Sulzer Chemtech's Winterthur test facility using the 1 m diameter test column with a chlorobenzene/ethylbenzene test system operating at atmospheric pressure at total reflux conditions. The results (shown in Figure 7) show the UFM valve tray compared Sulzer's high capacity MVG™ fixed valve trays. Both trays sets had identical designs (i.e., all tray and downcomer design parameters were constant except for the valve type). As can be seen, the UFM valve trays maintained a higher separation efficiency over a wider operating range as compared to MVG valve trays. When evaluated at an 80% separation efficiency, the UFM valve trays provide 10% higher capacity than MVG valve trays, making UFM the highest capacity valve in the broad Sulzer Chemtech portfolio.

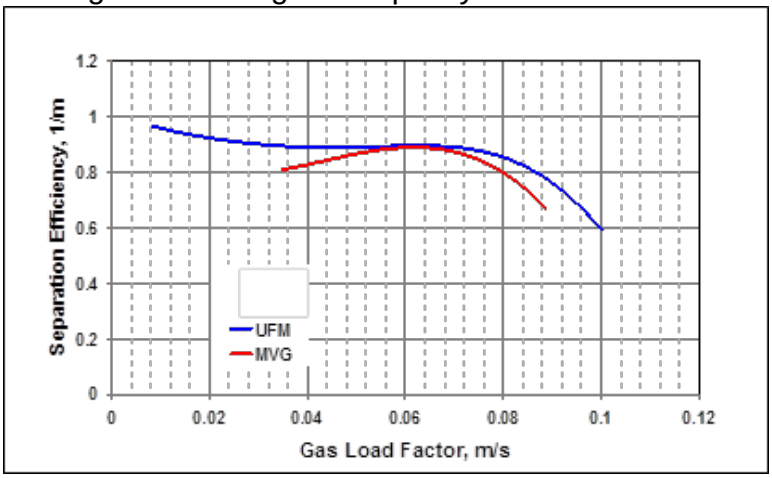

Figure 7: Efficiency curves of MVG™ fixed valve Tray and UFM™ Valve Tray

2.4 Independent Test Results

The UFM valve trays were next tested at a leading independent industrial test facility using its 1.2 m diameter column in a cyclohexane/n-heptane test system at 160 kPa (1.6 bar), under total reflux conditions. Results are compared against Nutter B valve trays tested at Fractionation Research, Inc. in the same, identical test system. Figure 8 shows that the UFM valve trays provide an increase of over 30% in useful capacity over the conventional Nutter tray. Also interesting is the fact that the UFM valve trays show a near constant efficiency level of 100% over nearly the entire operating range. This supports the theory of continually good mixing on the tray deck and minimal entrainment up until the hydraulic flood point.

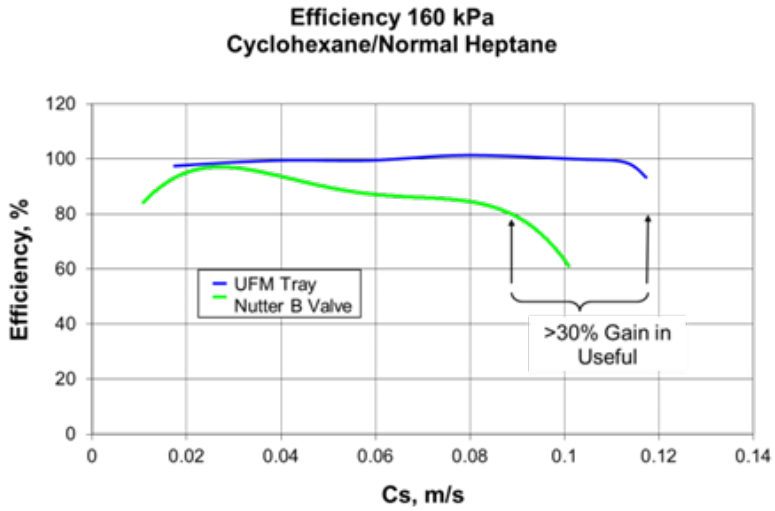

Figure 8: Efficiency curves of UFM™ Valve Tray and Nutter B Type Valve Tray

3. Conclusions

A new valve has been developed with a distinctive concave shape to route vapor downward and uniformly to the tray deck to improve vapor/liquid contact and capacity. Testing in two separate commercial scale facilities show that the Sulzer UFM Valve trays provide a clear advantage in both efficiency and capacity versus conventional and high performance valve trays. These trays have been installed in over 40 columns world-wide in applications ranging from high pressure services like amine contactors and deethanisers to refinery crude columns. To date, all columns are performing as expected. This proven commercial performance as well as the preceding research shown in this paper, support the theory that control of vapor flow direction with valve designs, can substantially improve tray performance.

References

1. Kister, H.Z., Distillation Design, McGraw-Hill, 1992, p. 260
2. Kister, H. Z. and J.R. Haas, Entrainment from Sieve Trays in the Froth Regime, Presented at AIChE Spring National Meeting, March 1988
3. Nutter, D.E. and D. Perry, Sieve Upgrade 2.0 – The MVG™ Tray, Presented at the AIChE Spring National Meeting, March 1995
4. Nutter, D.E., High Capacity Tray for Gas-Liquid Contact Apparatus, US Patent 5,360,583, November 1994
5. Shah, V.H. & Agrawal, R., A Matrix Method for Multicomponent Distillation Sequences, AIChE Journal, 56: 1759-1775 (2010)
6. Vennavelli, A.N., J.R. Whitely, and M.R. Resetarits, New Fraction Jetting Model for Distillation Sieve Tray Efficiency Prediction, Ind. Eng. Chem Res. 2012, 51 (35), pp 11458-11462

Influences of the experimental setup configuration on mass transfer measurements in absorption systems

Verena Wolf[1], Markus Lehner[1], Karin Hoffmann[2]
[1]Montanuniversitaet Leoben, Leoben, Austria;
[2]RVT Process Equipment GmbH, Steinwiesen, Germany

Abstract
The standardization of mass transfer measurements for absorption systems is a key factor for the deduction of accurate mass transfer models for random and structured packings. Several papers (Hoffmann et al., Rejl et al., Kunze et al.) already deal with this problem and recommendations are given for appropriate test systems, the execution of the experiments and particularly also for the experimental setup to be used. However, systematic investigations of the influences of the experimental setup configuration on the results of mass transfer measurements in absorption systems are published rarely.
Mass transfer measurements with the system ammonia – air / water have been performed at a pilot plant consisting of a DN 600 saturation column and a DN 450 measuring column, both made from polypropylene, and equipped with different random and structured packing. Although the used experimental setup of the pilot plant follows strictly the recommendations published in Hoffmann et al., experimental results may differ significantly depending on, for example, the locations of the gas and liquid sampling in the column, the raw gas concentrations of ammonia or the pre-treatment of packing.
The paper presents the results of the test series considering different effects on the derived mass transfer performance of the packing and addresses also problems as well as solutions concerning the sampling in a two-phase regime. The aim is to provide a valuable contribution to the efforts for the standardization of mass transfer measurements in absorption systems.

Keywords
Absorption, mass transfer measurement, standardization, packing, experimental setup

1. Introduction

A lot of influences exist on mass transfer measurements which need to be considered. Where about, many of them are already mentioned in Hoffman et al.. In this paper the effects of the chosen raw gas concentration, sampling position and the pre-treatment of plastic packing are reflected.

2. Results and discussion

2.1 Experimental setup

The experimental plant at the Montanuniversitaet Leoben consists of a DN 600 saturation column and a DN 450 measurement column made of polypropylene. The

air is sucked from the environment and flows through the saturation column where it is saturated with water. After passing a tube type gas distributor, the gas streams through the measurement column. Afterwards, it enters a radial blower (frequency converted gear, max. 5000 m^3/h, max. 5000 Pa pressure increase) and is then finally released to the environment. The gas flow is measured by a flow grid (airflow) downstream of the blower. Furthermore, the temperature of the gas is measured at every in- and outlet of both columns (Endress & Hauser, PT 100 type Omnigrad M TR 13; WIKA, type 55) which have their own liquid circulation. The packing is irrigated by a trough type liquid distributor (128 dripping points per m^2, free cross sectional area of 41%, operating range 5-30 $m^3/(m^2h)$). Where about the saturation column possesses a closed liquid circulation, in the measurement column the liquid is used in single passage. It is collected below the gas entrance of the column in a pan type collector and conducted to a bin outside of the column. The used radial pumps are able to handle a volume flow of 50 m^3/h. The liquid flow is measured by a magnetic inductive flow meter (Krohne, type optiflux 4000) and the temperature of the inlet stream at the measurement column is gauged by a resistance thermometer (Voltcraft, type K).

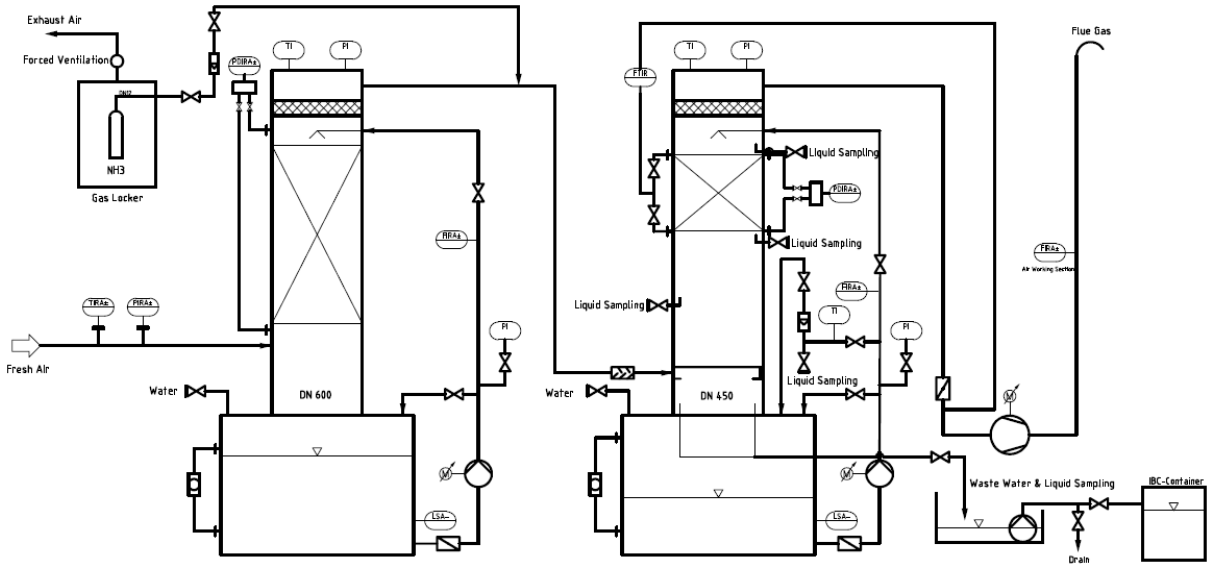

Figure 1: P&I diagram of the experimental plant „packing column“ Montanuniversitaet Leoben

The mass transfer characteristic has been determined by using the absorption model system ammonia (NH_3) – air / water. The mass transfer resistance for this system is located in both phases although it is predominant in the gas phase (Hoffmann et al.). The gaseous ammonia is injected in the gas duct between the saturation and the measuring column and has to pass a static mixer to ensure an optimal mixing. Stationary conditions are reached after 1 to 2 minutes by achieving a constant NH_3 concentration in the gas outlet stream. The concentrations of the ammonia in front of and behind the packing are measured for each operating point (constant F-factor and liquid load) by an FTIR spectrometer (Gasmet Technologies Oy, DX4000) in real time at a frequency of 1 Hz. The concentration of ammonia in the liquid phase is analysed by photometric determination after it was preserved by the use of hydrochloric acid as receiver (Gucher). The mass transfer measurements are operated at the same liquid loads as the gauging of the fluid dynamic.

2.1.1 Sampling

Concerning the sampling of the liquid and the gas phase, following has to be considered: the sample should be representative, which means that there should not be any disturbing components present and the sample volume should be high enough. On the other side, it is very important to avoid a significant disturbance of the gas and the liquid phase and thus maintaining the fluid dynamic conditions unchanged. Furthermore, the sampling positions should be located in such a way that only the mass transfer capacity of the packing itself is measured, which means the sampling should take place straight above and below the packing. Therefore, various sampling devices have been developed which are described below.

Gas sampling

For the analysis of the gas phase an amount of 1.4 l/min is sucked from the column (optional from above or below the packing) through a heated pipe (180°C) to the pre-heated FTIR spectrometer, where the concentrations of water, ammonia and carbon dioxide are analysed. Based on the fact that ammonia is readily soluble in water and as there is interference between water and ammonia concerning their infrared spectra, it is essential that only gas is sucked in and no water droplets. As the sampling position is located straight above and below the packing, in particular in the two-phase regime, a special sampling device is necessary, which was developed especially for this purpose at the Chair of Process Engineering. The measurement pipe which leads directly to the FTIR spectrometer is situated in a double-tube, where a small, but long (over the whole cross section of the column) slot is milled in both pipes, the inner one at the top and the outer one at the bottom side as shown in Figure 2.

Liquid sampling

The liquid should also be taken straight above and below the packing. For this purpose a sampling device has been developed which is illustrated in Figure 3. It is designed in such a way that the liquid is collected in the bulk phase of the column. It avoids the sampling of liquid next to the column walls which interaction with the gas is limited and which is therefore not representative (Grünewald et al.).

During sampling the total volume of the liquid sample collector is emptied three times before the sample is taken to ensure a fresh and representative sample. Furthermore, the horizontal position of the three possible liquid collectors is chosen in a way that they do not interact with each other. In particular they are situated in such a way that every one of them collects the liquid at the same diameter inside the column but they are shifted by angles of 45 and 90 degrees.

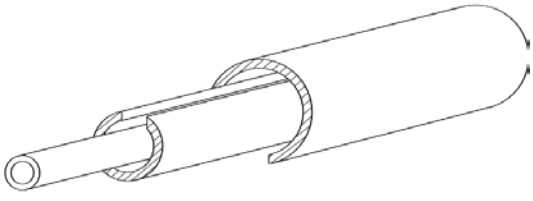

Figure 2: Schematic view of the gas measuring probe

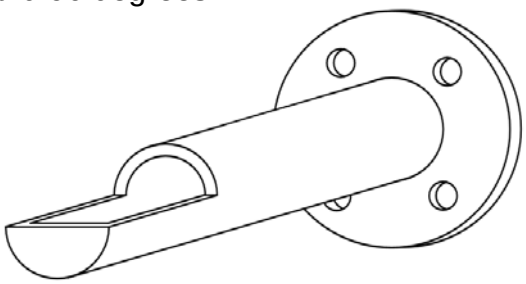

Figure 3: Schematic view of the liquid sampling device

2.2 Results

Although the used experimental setup of the pilot plant follows strictly the recommendations published by Hoffmann et al., further influences on the experimental results have been observed, which are described below. All

experiments were done with random plastic packing with a nominal size of 50 mm, a void fraction of 94 % and a specific surface area of 90 m^2/m^3. The uncertainty analysis has been performed based on the propagation of uncertainty of Gauß (DIN 1319), where about the F-factor was considered as a function of gas volume flow, diameter of the column, gas temperature and ambient pressure. The uncertainty of the F-factor concerning all measurements in this paper is ± 0.004. The HTU values are calculated from the measured concentrations as described in Lehner et al. and the calculated uncertainty of all HTU values in this work is ± 0.025.

2.2.1 Location of sampling

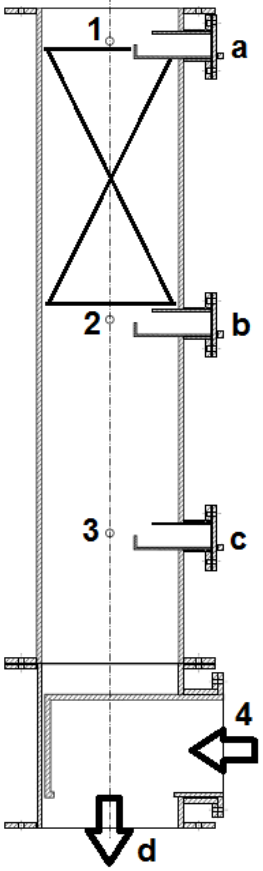

Figure 4: Positions of sampling

Hoffmann et al. recommend that the sampling position for the gas and the liquid phase should be situated directly below the packing to eliminate the mass transfer which takes place below the packing but they also suggest locating the sampling in the inlet and outlet tubes to get a representative sample. Therefore, the influence of the sampling location has been examined. All examined sampling positions are marked with numbers (gas sampling) or letters (liquid sampling) in Figure 4. In fact only the sampling positions below the packing were varied. Therefore, the liquid inlet (a) and the gas outlet concentration (1) were measured straight above the packing. The gas inlet concentration was measured straight below the packing (2) and alternatively in the inlet tube (4). The liquid outlet concentration was measured directly below (b) as well as 60 cm below (c) the packing and in the outlet tube (d). The results of these measurements are depicted in Figure 5 together with the mass balance calculations, where the HTU values are plotted against the F-factor. The mass balance is calculated by comparing the total NH_3 amount of the inlet gas and liquid stream with the one of the outgoing streams and the determination of the deviation of thus received values. Comparing the measurements [g:1-2, l:a-b] and [g:1-2, l: a-c] it can be recognized that the HTU values differ only by 2% but the mass balance has an deviation of about 60%. Further it can be seen that the HTU values of the measurements [g:1-2, l:a-b] and [g:1-2, l:a-d] show a deviation of 10% and the mass balance already of about 150-300%.

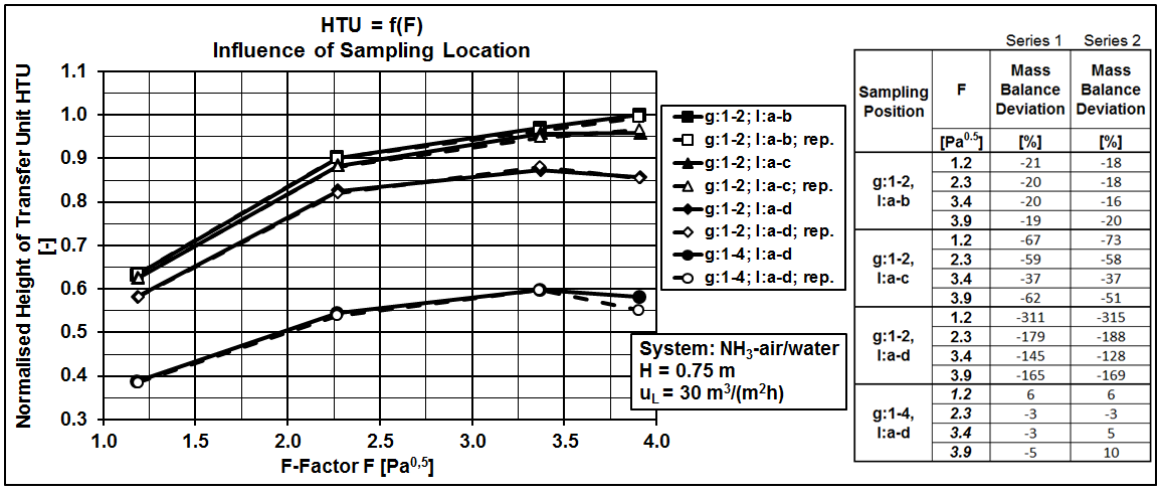

Sampling Position	F	Series 1 Mass Balance Deviation	Series 2 Mass Balance Deviation
	[Pa$^{0.5}$]	[%]	[%]
g:1-2, l:a-b	1.2	-21	-18
	2.3	-20	-18
	3.4	-20	-16
	3.9	-19	-20
g:1-2, l:a-c	1.2	-67	-73
	2.3	-59	-58
	3.4	-37	-37
	3.9	-62	-51
g:1-2, l:a-d	1.2	-311	-315
	2.3	-179	-188
	3.4	-145	-128
	3.9	-165	-169
g:1-4, l:a-d	1.2	6	6
	2.3	-3	-3
	3.4	-3	5
	3.9	-5	10

Figure 5: Influence of sampling location and mass balance therefore

Of course the huge difference concerning the mass balance can be explained due to the not closed mass balance area. Therefore, the measurement [g:1-4, l:a-d] took this into consideration which is also visible in the best matching mass balance in Figure 5. However, these sampling positions lead to 65% lower HTU values than [g:1-2, l:a-b] due to the interaction of gas and the liquid droplets in the column section below the packing. Therefore, it is obvious, that the sampling position has a huge influence on the determined HTU values, whereas the liquid concentrations do not have such a deciding effect on the HTU values. A closed mass balance is not an indicator for the right sampling positions.

2.2.2 Raw gas concentration

The amount of ammonia dispensed into the air should be high enough to limit any measurement mistakes on the one hand but on the other hand ammonia gas should also not be wasted. Therefore, it was investigated if the chosen raw gas concentration has an influence on the measured mass transfer performance. As demonstrated in Figure 6 an almost doubled raw gas concentration leads to 10% lower HTU values. This indicates that the influence of the chosen gas concentration cannot be neglected. Furthermore, additional examinations would be necessary to give an indication which gas concentration should be used, in order to achieve comparable measurements.

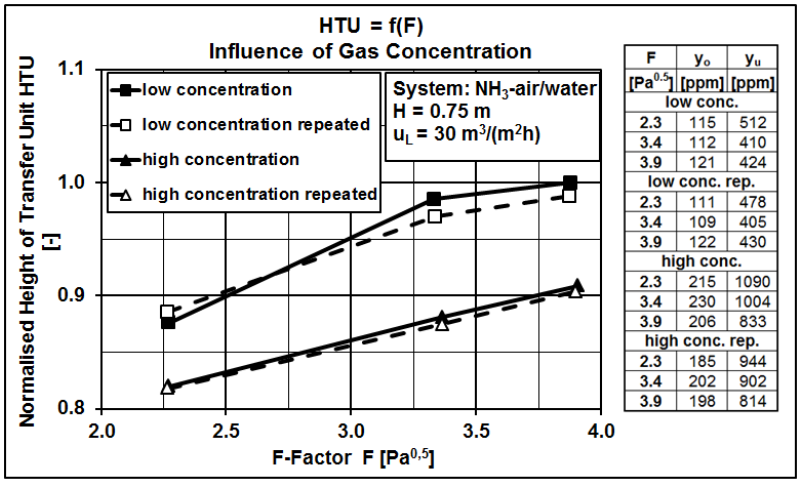

F [Pa$^{0.5}$]	y_o [ppm]	y_u [ppm]
low conc.		
2.3	115	512
3.4	112	410
3.9	121	424
low conc. rep.		
2.3	111	478
3.4	109	405
3.9	122	430
high conc.		
2.3	215	1090
3.4	230	1004
3.9	206	833
high conc. rep.		
2.3	185	944
3.4	202	902
3.9	198	814

Figure 6: Influence of gas concentration

2.2.3 Pre-treatment of plastic packing

In general, it is known that plastic packing improve their mass transfer performance during operation compared to their virgin state at the start-up. However, there are no publications about how long or in which way plastic packing should be pre-treated before they are examined in mass transfer measurements. Results concerning the fluid dynamic behaviour of this issue are published by Wolf and Lehner. Woicke et al. have already reported the occurring effect concerning the mass transfer performance. Nevertheless, the results in Figure 7 should point out how long it takes to establish stationary conditions. The HTU values at the 4th and 5th irrigation are about 40% lower at an F-factor of 1.2 Pa$^{0.5}$, 20% at F-factors 2.3 Pa$^{0.5}$ and 3.2 Pa$^{0.5}$ and 11% lower at an F-factor of 3.9 Pa$^{0.5}$ than the ones found at the 1st irrigation. The therefore deduced recommendation is to perform first mass transfer measurements under the same conditions with a brand-new plastic packing as long as it takes to achieve stationary conditions. Only then valid measurements are obtained.

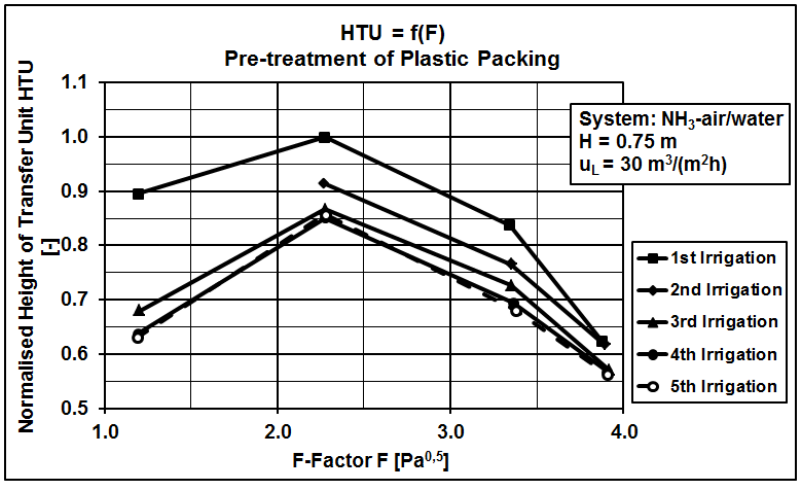

Figure 7: Influence of the pre-treatment of plastic packing

3. Conclusion

It has been shown that the influences of the chosen raw gas concentration, the sampling location as well as the pre-treatment of plastic packing have a significant influence on mass transfer measurements and should therefore not be neglected.

Symbols

DN	Diameter Nominal
F	F-factor [$Pa^{0.5}$]
FTIR	Fourier transformed infrared
G	Gas phase
H	Height of packed bed [m]
HTU	Height of an overall gas-side transfer unit [m]
l	Liquid phase
NTU	Number of the overall gas-side transfer units [-]
p	Pressure [Pa]
u_L	Liquid load [$m^3/(m^2h)$]

References

DIN 1319, Grundlagen der Messtechnik, Beuth, Berlin 1983.

Grünewald, M. et al. (2011): Auslegung von Absorptionskolonnen – Neue Problemstellungen für eine altbekannte Aufgabe. Chemie Ingenieur Technik, Vol. 83 (7), p. 1026–1035.

Gucher, A. (2013): Entwicklung eines Verfahrens zur quantitativen Bestimmung von Ammoniak in der Flüssigphase einer Absorptionskolonne. Masterarbeit. Montanuniversität Leoben, Lehrstuhl für Verfahrenstechnik des industriellen Umweltschutzes, Leoben.

Hoffmann A. et al. (2007): Standardization of Mass Transfer Measurements – A Basis for the Description of Absorption Processes. Trans IChemE, Part A, Vol. 85 (A1), p. 40-49.

Kunze A.K. et al. (2012): Die Notwendigkeit einer Standardisierung von Stofftransportmessungen in der Ab- und Desorption. Chemie Ingenieur Technik, Vol. 84, p. 1931-1938.

Lehner, M. et al. (2011): Hydrodynamic and Mass Transfer Characteristic of a Novel Grid Structured Plastic Packing. Heat and Mass Transfer Vol. 47 (8), p. 1035-1041.

Rejl J.F. et al. (2009): Methods standardization in the measurement of mass-transfer characteristics in packed absorption columns. Chemical Engineering Research and Design, Vol. 87, p. 695-704.

Woicke, N. et al. (2012): Größere Stoffaustauschleistung – Verbesserung der Benetzbarkeit von Kunststoffpackungen. CIT plus, Vol. 15 (11-12), p. 56–58.

Wolf, V., Lehner, M. (2013): Einflüsse bei der experimentellen Bestimmung der hydraulischen Parameter von Füllkörpern und Packungen. 9. Minisymposium der Verfahrenstechnik, Book of Abstracts. p. 73-77.

Shortcut Method for the Design of Non Ideal Mixtures Separation Using Extractive Distillation Dividing Wall Columns

Khadidja Benyahia [1], Hassiba Benyounes [1], Vincent Gerbaud [2, 3]
[1]U.S.T. Oran, Laboratoire de chimie physique des matériaux, catalyse et environnement, Oran, Algérie;
[2]Université de Toulouse, INP, UPS, LGC (Laboratoire de Génie Chimique), 4 allée Emile Monso, France;
[3]CNRS, LGC (Laboratoire de Génie Chimique), F-31432 Toulouse, France.

Abstract
To improve the energy efficiency of process, a thermally coupled distillation columns configuration, dividing wall extractive columns (DWC) has been proposed for separation of non ideal mixture. The process is made of an extractive distillation column and a post-fractionator column used for the solvent regeneration.
This work describes a shortcut method based on equations of Fenske - Underwood - Gilliland and Kirbrige equation, which can be used to determine the values of design parameters required for rigorous simulation and process optimization, including reflux ratio, the number of stages in all sections of the DWC column and the split of the internal liquid and vapor. The effectiveness of the design method is demonstrated by applying to non-ideal zeotropic systems, heptane - toluene – aniline, and azeotropic systems, acetone - methanol – water, respectively. The results are validated by rigorous simulations and show that the proposed method provided proper feasible parameters for the separation.

Keywords
Extractive distillation, shortcut method, reflux ratio, split ratio, energy efficiency, azeotropic mixture.

1. Introduction

Distillation is the most common used separation technique in the chemical and petrochemical process industries, but is also the most energy intensive operation unit. To overcome this problem several heat integrated and fully thermally coupled distillation systems were studied[1-2], and it was proved that thermally coupled configurations, such as the dividing distillation columns (DWC), are promising energy alternative solutions[3-5]. This key advantage is also applicable for a DWC, which has the minimum vapor flow rate for the particular separation compared to the conventional system.
Reduction in vapor flow contributes to lower duties of reboiler and condenser, and consequently capital and operating costs. Furthermore, DWC uses only one reboiler and one condenser when compared to two reboilers and two condensers for a conventional two columns system. This would add to the savings in capital as well as operating cost.
Design of DWCs has been studied in the open literature using basic equations[6] and using commercial simulators[7]. Fenske–Underwood–Gilliland (FUG) equations were used as part of shortcut method for initialization followed by rigorous simulation with simulators such as Aspen Hysys.

Usually, extractive distillation is performed in a sequence of two columns, first of them separating azeotropic mixture while the other one recovering the solvent that is recycled back. The DWC technology is not limited to ternary separations alone, but it can be used also in azeotropic separations and extractive distillation[8-12].
In this study the shortcut method and rigorous simulation were used to define the best operating parameters for separation of azeotropic mixture acetone – methanol using water as entrainer in extractive dividing wall column (E-DWC) which is thermodynamically equivalent to thermally coupled distillation column. The rigorous simulation is carried out to optimize the obtained parameters from shortcut method.

2. Methodology

In this work, we consider the separation of non ideal azeotropic mixture containing A and B with the heavy entrainer F_E. Where A is light component recovered in distillate product, B is the middle boiling component recovered in the side stream product, and the entrainer F_E is the heavy component recovered in the bottom product. The main feed and entrainer specifications are shown in table 1.
The process flowsheet of extractive DWC distillation column (E-DWC) is presented in the figure 1. We propose column configuration of extractive DWC with four sections (figure 1.c): section 1 corresponds to the rectifying section, section 2 is the extractive section, section 3 is the stripping section and section 4 corresponds to the post-fractionator.

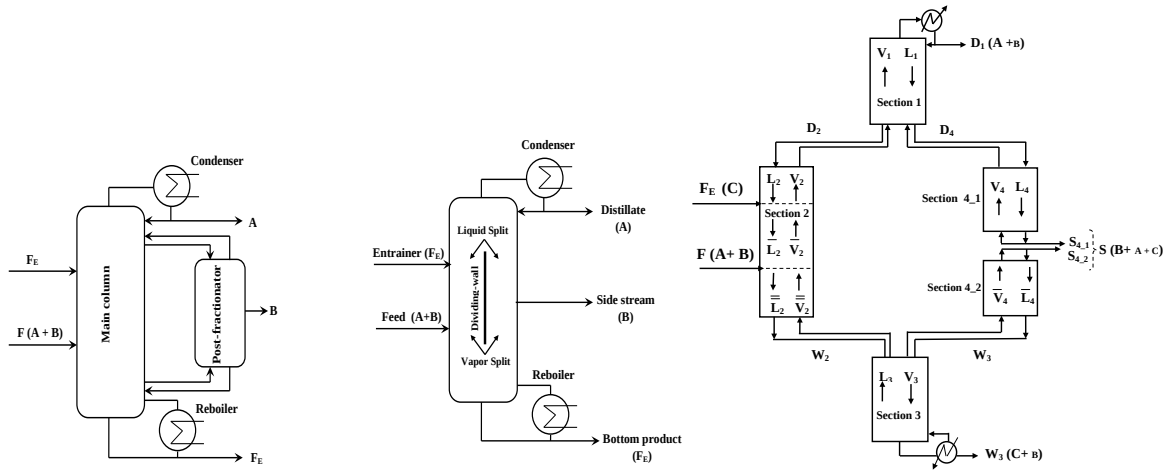

(a) (b) (c)

Figure 1: (a) Fully thermally coupled extractive distillation column; (b) Extractive dividing wall column; (c) Used model for extractive dividing wall column.

Table 1: The main feed and entrainer feed specifications of the case study

Specifications		Molar flow, kmole/h	Mole fraction (z_i)	Relative volatility (α_{ij})	Boiling temperature, °C
Feed	Acetone (A)	1	0.5	8.326	56,1
	Methanol (B)		0.5	3.537	61
Entrainer	Water (F_E)	0.55	1	1.000	100

This work is developed using shortcut method based on Fenske, Underwood, Gilliland and Kirbride equations[13-15].
The minimum vapor flow is calculated on the basis of the given roots limited by the values of the relative volatilities α_A, α_B and α_C (2), the maximum one is chosen. The liquid $L_{min,k}$ and vapor $V_{min,k}$ flows are combined to form distillate flow D_k (3). The shortcut design procedure for DWC column of non ideal mixture is described on figure 2.

$$1 - q = \sum \frac{\alpha_i . z_i}{\alpha_i - \theta} \quad i = \{A, B, C\} \qquad (1)$$

Where $\alpha_A > \theta_1 > \alpha_B > \theta_2 > \alpha_C$, θ_1 and θ_2 are the roots of Underwood equation

$$V_{min,k} = \sum \frac{\alpha_i . x_{iD\,k}}{\alpha_i - \theta} \quad k = 1,2,3,4 \text{ (section number)} \qquad (2)$$

$$L_{min,k} = V_{min,k} - D_k \qquad (3)$$

$$N_{min,2} = \frac{\ln (Z_i/Z_i)_{D2} (Z_j/Z_i)_{W2}}{\ln \alpha_{ij}} \quad i, j = \{A, B, C\} \qquad (4)$$

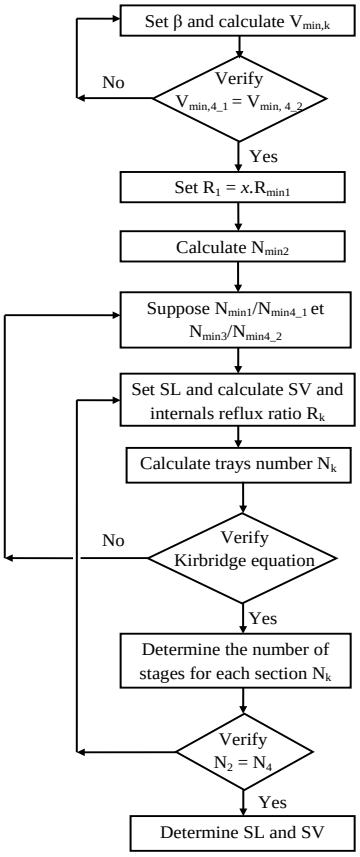

Figure 2: Shortcut design procedure for non ideal mixture extractive dividing wall column.

We note that β, $N_{min,1}/N_{min,4\_1}$, $N_{min,3}/N_{min,4\_2}$, S_L and S_V are the degrees of freedom of the shortcut design procedure for DWC column. At first, the minimum reflux ratios and reflux ratios are defined; then the number of stages is calculated for each section using Gilliland correlation (5). The two degrees of freedom $N_{min,1}/N_{min,4\_1}$ and $N_{min,3}/N_{min,4\_2}$ are defined when the Kirbride equations (6) and (7) are satisfied.
The calculation based on shortcut method needs to set the specifications of feed and products of extractive DWC column for investigated azeotropic system acetone –

methanol in the presence of water as solvent for breaking the azeotope. The binary mixture acetone – methanol mixture is taken at its boiling liquid thermal feed state (q = 0).

$$\frac{N-N_{min}}{N+1} = 0.75\left[1-\left(\frac{R-R_{min}}{R+1}\right)^{0,5688}\right] \quad (5)$$

$$\frac{N_1}{N_{4\_1}} = \left[\frac{D_1}{S_{4\_1}} \times \frac{x_{AD\,1} D_1}{x_{BS\,4\_1} S_{4\_1}}\right]^{0,206} \quad (6)$$

$$\frac{N_{4\_2}}{N_3} = \left[\frac{S_{4\_2}}{W_3} \times \frac{x_{BS\,4\_2} S_{4\_2}}{x_{CW\,3} W_3}\right]^{0,206} \quad (7)$$

3. Results and discussion

The design parameters obtained using shortcut method of Fenske – Underwood – Gilland are given in table 3. The obtained parameters by shortcut method are validated by rigorous simulation based on equilibrium model and the results are also shown in table 3.The values of S_L and S_V are chosen so that there are the same number of trays in section 2 and section 4 (figure 3).

Table 3: Operating parameters of E-DWC column obtained by shortcut method and rigorous simulation for system acetone – methanol with water as entrainer

Parameters	Shortcut methode	Rigorous simulation
Vapor split ratio (S_L)	0.463	0.663
Liquid split ratio (S_V)	0.697	0.633
Reflux ratio R	3.16	4.48
Reboiler ratio φ	3.781	3.8
Total number of stages	27	27
N_{rectif} (S_1)	8	8
N_{strip} (S_3)	8	8
Number of stages post-fractionator side	11	11
Side stream withdrawal stage	14	14
Feed stage of extractive entrainer	10	10
Feed stage of binary mixture acetone-methanol	16	16
Operating pressure, bar	1	1
Acetone recovery, %	98	97
Methanol recovery, %	98	95
Water recovery, %	98	97
Acetone purity, % mol	98	95
Methanol purity, % mol	96	94
Water purity, % mol	98	96

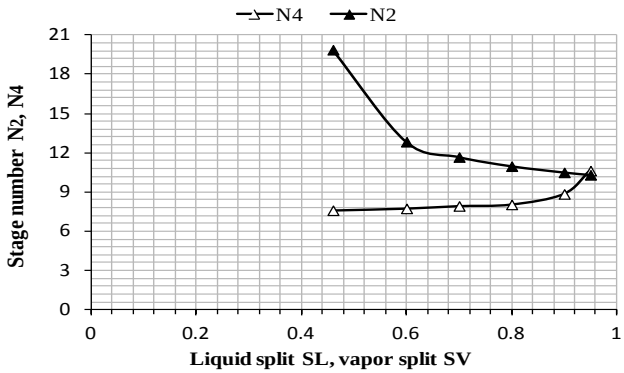

Figure 3: Schematic diagram of stage number in section 2 and section 4 versus liquid split S_L and vapor split S_V for acetone – methanol – water.

The residue curve map (RCM) and the ternary diagram showing the composition profile along the E-DWC column are illustrated in figure 4.

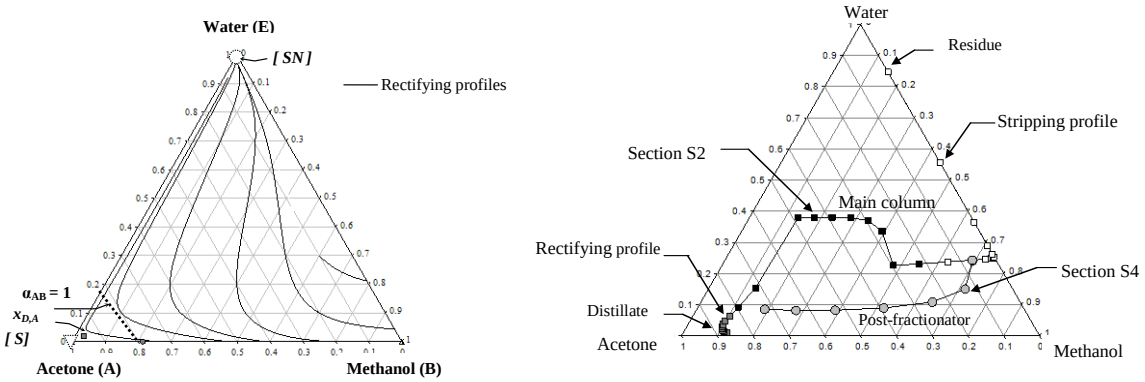

a **b**

Figure 4: Residue curve map of ternary mixture acetone –methanol-water (a) and composition profile inside the extractive dividing-wall column, as ternary diagram (b).

The table 4 represents the comparison of reboiler and condenser duties for conventional to-columns sequence versus the proposed E-DWC column. We note that energy saving around 28.43% is possible in E-DWC column configuration.

Table 4: Comparison of reboiler and condenser duties for E-DWC column

	Direct sequence Extractive distillation			Extractive E-DWC		
	DC1	DC2	Total	Main column	Post-fractionator	Total
Reboiler duty kJ/h	58340	53360	111700	79940	0	79940
Condenser duty kJ/h	55550	52790	108340	77080	0	77080

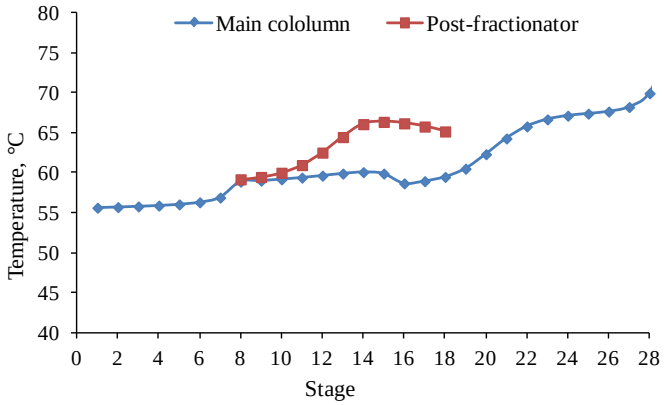

Figure 5: Temperature profile in E-DWC column for system acetone – methanol in the presence of water as entrainer

3. Conclusions

In this study we propose a shortcut method for design of extractive distillation column with internal dividing wall (DWC). The case of non-ideal azeotropic system was considered to validate this method. It is noted that according to the results that liquid and vapor splits ratio are the key parameters in the design of the DWC column. The method provided feasible design parameters of the extractive column with internal separating wall, which can be used for initialization of rigorous simulation of the process.

The novel DWC configurations for extractive distillation are not only technically feasible but also very attractive economically, leading to reduced significant overall energy savings of 28 %.

References

1. F. Petyluk, V. Platonov and D. Slavinski, Int Chem Eng. 5(3) (1965) 555–561.
2. K. Amminudin,R. Smith, D. Thong, G. Towler, Chem. Eng. Res. Des. 79 (2001) 701.
3. Radu Ignat, Alexandru Woinaroschy, Chem. Eng. Trans. 25 (2011) 647 – 652.
4. R. Premkumar, G.P. Rangaiah, Chem. Eng. Res. and Des. 87 (2009) 47 – 60.
5. Z. Fidkowski, and L. Krolikowski, AIChE J. 33 ( ) 643–653.
6. C. Triantafyllou, and R. Smith, Chem. Eng. and Processing 43 (2004) 339-346.
7. M. Emtir, E., Re´v and Z. Fonyo´. Z, Applied Thermal EnG. 21 (2001) 1299-1317.
8. A. Kiss, J. D. Suszwalak, R.M. Ignat, Chem. Eng. Trans. 35 (2013) 1279 – 1284.
9. R. M. Ignat, A. Kiss, Chem. Eng. Trans. 29 (2012) 619 – 624.
10. A. Kiss, R.M. Ignat, Sep. pur. technol. 98 (2012) 290 – 297.
11. A. Kiss, R.M. Ignat, Energy techology 1 (2013) 166 – 170.
12. C. Bravo-Bravo, J.C. Segovia-Hernandez, C. Gutierrez-Antonio, A.L. Duran, A. Bonilla-Petriciolet, A. Briones-Ramirez, Ind. Eng. Chem. Res. 49 (2010) 3672 – 3688.
13. Underwood, A. J. V. Chem. Eng. Prog. 44 (1948) 60.
14. Gilliland, E. R.. Ind. Eng. Chem. 32 (1940) 1220.
15. Kirkbride, C. G. rs. Pet. Ref. 23 (1944) 321.

Design and Optimization of HIDiC Distillation Columns Using a Boltzmann-Based Estimation of Distribution Algorithm: Influence of Volatility

Roberto Gutiérrez-Guerra[a], Rodolfo Murrieta-Dueñas[a], Jazmin Cortez-González[a], Juan Gabriel Segovia-Hernández[a], Salvador Hernández[a], Arturo Hernández-Aguirre[b].
[a]Universidad de Guanajuato, Campus Guanajuato, Departamento de Ingeniería Química, Noria Alta s/n, 36050, Guanajuato, Gto., Mexico.
[b]Centro de Investigación en Matemáticas, A.C., Departamento de Computación, A.P. 402, Guanajuato, Gto., CP 3600, México.

Abstract

The heat-integrated distillation columns (HIDiC) are configurations proposed to enhance the energetic efficiency and the total annual cost (TAC) of the current distillation sequences. At the same time, these distillation configurations are characterized for involve multiple freedom degrees and several constraints to be accomplished. In this study, the optimization of the HIDiC sequences using a Boltzmann-Based Estimation of Distribution Algorithm is performed. The goal is the minimization of the total annual cost. The results showed that the highest benefits of the HIDiC configurations are obtained when they are used to separate low relative volatility mixtures (from 1.12 to 1.5). Under this condition, important energy saving (from 50% and 87%) is obtained. In addition, considerable reductions of the TAC (16%) compared with the corresponding conventional sequences were determined.

Keywords

HIDiC sequence, optimization, BUMDA.

1. Introduction

The HIDiC columns have shown large energy savings and feasible costs in the separation of close boiling mixtures (Jana et al., 2010; Suphanit et al., 2010; Nakaiwa et al., 2000, 2003). Furthermore, the multiple freedom degrees (continuous and discrete variables) that model the HIDiC sequences disclose the possibility to expand such ones benefits through the optimization of these configurations. Thus, the application of optimization algorithms is an opportunity area to minimize the energy consumption and reducing the total annual costs, in relation with the conventional columns.

The HIDiC sequence is generated by separating the rectifying section (SR) and the stripping section (SS) of the conventional column. Then, both sections are connected by the compressor and the throttling valve. So, SR operates at higher pressure and temperature than SS. This operation makes possible the integration of internal energy (Qint.) between SR and SS. Hence, the reboiler duty and the condenser duty are reduced.

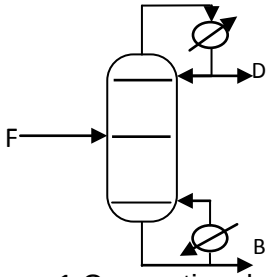

Figure.1 Conventional column.

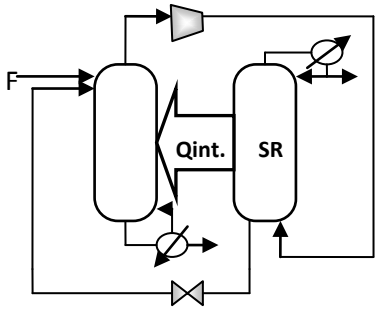

Figure 2. HIDiC sequence.

The constrained BUMDA algorithm (Valdez et al., 2013) has been implemented to treat continuous and discrete variables. In addition, a reset mechanism able to intensify the exploration was attached to it. The key elements that conforms the BUMDA algorithm are: the Bolztmann distribution and a truncation method (cut of the population on the best individuals). By one side, the Boltzmann distribution continuously approximates to the fitness function, g(x), through the model, P(x), presented in Equation 1. In this case, β involves the selection pressure and the variance. Besides, the normalization parameter Z is evaluated by the summation of the exponential function of the numerator, on the whole search domain, as it is indicated in Equation 2. On the other side, the truncation method promotes the convergence toward the optimum value. Observe that

the Boltzman distribution was approximated by a normal distribution, $Q_i(x)$, Equation 3. It was done with the aim to use a finite population. Notice that the subscript "i" represents each individual evaluated.

$$P(x) = \frac{e^{\beta\ g(x)}}{z} \quad (1) \Longrightarrow \quad (2) \qquad Q_i(x) = Q_i(\mu_i, v_i) = \frac{e^{\left[-\frac{(x_i-\mu_i)^2}{2v_i}\right]}}{(2\pi v_i)^{1/2}} \quad (3)$$

Notice that after the first evaluation, (Po), every new generation (Pt) is produced using the half of the population of the before generation (best individuals), based on the mean (μ) and variance (v) of the population. In addition, the function evaluations number (NumEvalMax) is considered as stop criteria of the optimization process. In this work, 3000 function evaluations were used for each case study. The cycle "if" proposed controls the optimization process with the function evaluations number. This means that if NumEval<3000, more individuals will be evaluated. Otherwise, the optimization process is finalized. The design-optimization strategy is performed via the interface Matlab-Excel-Aspen Plus. The rigorous simulations are made employing the RadFrac model in Aspen Plus.

The simulations were made with a PC with an i5 processor core, clock frequency at 2.8 GHz, and 16 GB of RAM. On average, for each case study, 145s were used for evaluation of the function.

2. Results and discussion

2.1 Cases study

In this work, seven binary hydrocarbon mixtures were analyzed, considering a range of relative volatility from 1.12 to 2.40, such as it is shown in Table 1. The thermodynamic model used to simulate all cases study was Chao-Seader, except for the cases M6 and M7, which were evaluated by the UNIQUAQ model. Besides, the composition of the feed was established as 50% mol. In addition, a feed rate of 100 kmol/h as a saturated liquid was used. The thermodynamic models used in this work were selected after revising the literature about the separation of these kinds of mixtures. The Chao-Seader model is recommended to represent the vapor and liquid phases in the separation of the hydrocarbon mixtures, Seader-Henley, 2006. On the other side, even when the other

mixtures are made of hydrocarbon, a more elaborated thermodynamic model (UNIQUAQ) was selected to model these mixtures, which represent binary isomers. The election of UNIQUAQ was derived of the results shown at the work developed by Rodrigues et al., 2005. The results of such one study showed the feasibility of the UNIQUAQ model to represent these systems in the separation.

2.2 Optimization strategy

The fitness function of the problem is presented in Equation 4, which is a function of two continuous variables, compression ratio (CR) and the reflux ratio (RR), and one discrete variable, the total number of stages (NT). The constraints of the problem are the recovery ($x_{recovery}$) and the purity (x_{purity}) of the components, which were defined as 0.995 (mol fraction). Also, it was established 3 °F as the minimum temperature driving force between the stages of SR and SS ($\Delta T_{SR\text{-}SS}$) for the energy integration (Qint.), and 0.3 kPa as pressure drop by stage.

$$Min(TAC) = f\left(CR, RR, NT\right) \tag{4}$$

Subject to

$$X_{purity} = X_{recovery} = 0.995 \pm \delta\,;\quad \delta = 0.0003\,;\quad \Delta T_{SR-SS} \geq 3°F$$

Where δ represents the tolerance allowed around the purity and recovery targets.

The TAC was evaluated using the Guthrie's method (Guthrie, 1974), considering 8000 operation hours per year. The operation cost includes the heating steam (0.016 USD/kg), cooling water (0.0148 USD/m^3), Turton et al., 2004, and electricity (0.1 USD/kWh), Nakaiwa et al., 2000. The capital costs involve the column shells, the reboiler, the condenser, the compressor and the heat transfer areas. Moreover, the total heat duty of the HIDiC (Qcons-HIDiC) is given by the reboiler duty plus the compressor duty. As it can be seen in Figure 3, all mixtures separated in the HIDiC column present large energy savings in relation with the conventional systems. The minimum energy saving achieved was of 50% and the maximum was of 87%. In addition, the TAC varies between 16% and HIDiC designs with a cost 37% higher compared with the conventional sequences. On the other side, it is possible to denote that as the relative volatility becomes smaller than 2.4, the energy required by the HIDiC sequence tends to be reduced, reaching a minimum in the relative volatility of 1.7 (energy saving of 55%). Nonetheless, as the relative volatility changes from 1.7 to 1.38, the energy saving tends

to decrease (50% of energy saving). After this value, the tendency shows that a reduction in the relative volatility leads to increase the energy savings, obtaining an energy saving of 87% in the system with relative volatility of 1.12. Comparatively (in the same Figure 3), the TAC is continually reduced from the relative volatility of 2.4 to the relative volatility of 1.248, where a minimum value is reached in the curve, which represents a TAC with 16% of saving. However, if the relative volatility is diminished even more, the TAC raises its value and the HIDiC sequence becomes economically equal (relative volatility equal to 1.23) or even more expensive (relative volatility of 1.12) in relation with the conventional column.

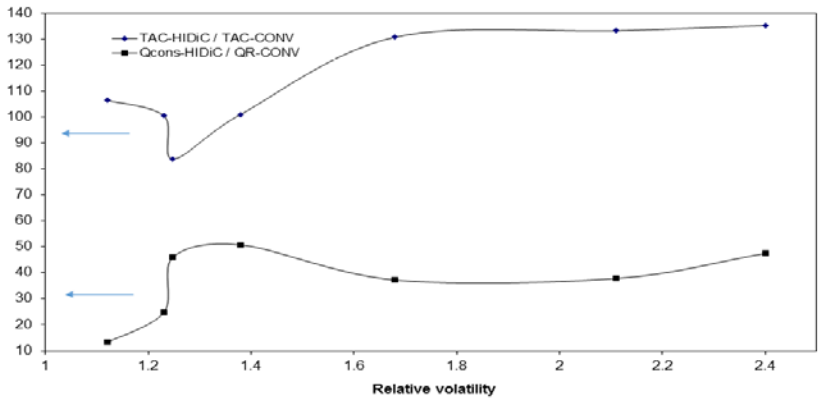

Figure 3. Tendency of the energy savings and the TAC of the HIDiC sequences, best designs.

Table 1. Optimization variables of the best HIDiC designs.

Case study	Optimization variables			Constraints	
	NT	CR	RR	Recovery	Purity
M1	28	2.15/1	0.22	0.9949	0.9949
M2	28	1.99/1	0.27	0.9949	0.9950
M3	56	1.86/1	0.38	0.9949	0.9949
M4	72	1.29/1	4.18	0.9950	0.9950
M5	74	1.34/1	9.63	0.9951	0.9952
M6	78	1.46/1	2.55	0.9947	0.9953
M7	138	1.56/1	4.25	0.9953	0.9953

Additionally, the optimization variables of the best HIDiC designs obtained for each case study are shown in Table 1. The results indicate that these configurations operate with low values of compression ratio and relatively small reflux ratios in most of the cases. Besides, it is clear that the optimization strategy applied was able to keep the constraints into values established, which reflects its robust performance.

4. Conclusions

The minimization of the total annual of the HIDiC sequences using the BUMDA algorithm, considering the effect of the relative volatility of the mixtures, was developed. The optimization problem of the HIDiC configuration was successfully performed by the BUMDA algorithm. The optimizer was able to achieve an intensified search, constantly focused on the best solutions. Thus, it was established that the most important benefits of the HIDiC configurations were determined in HIDiC sequences employed to separate low volatility mixtures, from 1.12 to 1.5. In this range, the HIDiC technology led to important energy savings (50%-87%) and the TAC might vary from 84% to 106% compared with the corresponding conventional sequences.

Acknowledgement

Financial support from CONACYT (México) and Universidad de Guanajuato is gratefully acknowledged.

References

1. Guthrie, K. M., Process Estimating Evaluation and Control; Craftsman Book Co.: Solana Beach,1974.

2. Jana, A.K., Mali, S.V., 2010, Analysis and control of a partially heat integrated refinery debutanizer, Comp. Chem. Eng., 34, 1296–1305.

3. Nakaiwa, M., Huang, K., Endo, A., Ohmori, T., Akiya, T., Takamatsu, T., 2003, Internally heat-integrated distillation columns: a review. Trans IChemE, 81,162–177.

4. Nakaiwa, M., Huang, K. Naito, K. Endo, A., Owa M., Akiya, T. Nakane, T. and Takamatsu T., A new configuration of ideal heat integrated distillation columns (HIDiC). Comp. Chem. Eng. 2000, 24: 239–245.

5. Rodrigues, W.L., Mattedi, S., Abreu, J. C. N., 2005, Experimental vapor-liquid equilibria data for binary mixtures of xylene isomers, Brazilian Journal of Chemical Engineering, 22, 03, 453 – 462.

6. Seader, J.D. and Henley, E., Separation Process Principles. (John Wiley and Sons, USA), 1998.

7. Suphanit, B., 2010, Design of internally heat-integrated distillation column (HIDiC): Uniform heat transfer area versus uniform heat distribution. Energy, 35, 1505–1514.

8. Turton, R.; Bailie, C. R.; Whiting, B.W.; Shaewitz, A. J. Analysis, Synthesis, and Design of Chemical Processes. Prentice Hall, Apendix A, 2004.

9. Valdez, S. I.; Hernandez, A., Botello, S. A Boltzmann based estimation of distribution algorithm, Information Sciences, 2013, 236:126–137.

Corona induced absorption of noxious constituents

P. Letonja, T. Friedrich, M. Siebenhofer
University of Technology Graz, Institute of Chemical Engineering and Environmental Technology, Inffeldgasse 25 CII, 8010 Graz, Austria

Abstract
DC-Corona discharge has been an established technology in off-gas dedusting. Recent research activities target the effect of brush geometry on the discharge characteristics and on applications in off-gas as well as wastewater treatment.
This contribution presents the results of degradation of hazardous pollutants from off-gas with DC-Corona discharge. A corona discharge reactor equipped with brush type discharge electrode was investigated.
In wastewater treatment applications degradation of selected constituents like acetone, EDTA, phenol etc. was recorded for specific corona current. Complete elimination of acetone and partial degradation of EDTA and phenol was recorded at a corona current of 0.3-0.45mA. In off-gas treatment applications oxidation of sulfur dioxide and nitrogen oxide was investigated.

Keywords
Electrostatic precipitators, Wet Collectors, Ozone, NO-absorption, SO_2-absorption

1. Introduction

Recent research activities in corona induced reactions target the effect of brush geometry on the discharge characteristics and on applications in off-gas as well as wastewater treatment.
A tube type corona discharge reactor equipped with brush discharge electrodes was investigated. The current/voltage data was modeled to develop an adapted correlation for brush discharge. The effect of brush discharge corona current on formation of oxidizing constituents was investigated.
DC-corona discharge with brush type discharge electrodes generates UV-radiation as well as ozone.
In off-gas treatment applications oxidation of nitrogen oxide and sulfur dioxide and absorption in water was investigated.

2. Apparatus set up and basics

The set up consists of a continuously rinsed tube-type electrostatic precipitator made of glass. The tube of 1 m net length and 76 mm inner diameter is equipped with brush electrodes of different brush diameter and wire diameter. During operation the water film acts as earthed counter electrode. The rinsing water is collected in a circulation tank from where it is pumped to the top of the precipitator and redistributed on the collector electrode. The gas phase enters the precipitator at the bottom.

Corona discharge of an electrostatic field is initiated by exceeding the critical corona field intensity E_0. For given radius r of the discharge electrode and the relative density δ of the gas the corona starting field intensity E_0 can be estimated[1], shown by equation 1.

$$E_0 = 3000 \cdot \delta + 90 \cdot \sqrt{\frac{\delta}{r}} [KV/m] \qquad \textbf{(1)}$$

with the relative gas density δ

$$\delta = \frac{T_o \cdot P}{T \cdot P_o}$$

at T_0 = 293 [K] and P_0 = 1013 hPa and the radius r of the discharge electrode.

After having determined the corona starting field intensity E_0 the corona onset voltage U_0 can be calculated with equation 2[2]. Calculation has to consider the type of electrostatic precipitator. For tube type electrostatic precipitators equation 2 is applied.

$$U_0 = E_0 \cdot r \cdot \ln\left(\frac{R}{r}\right)\left[\frac{\sqrt{Kg \cdot m}}{s^{-1}}\right] \qquad \textbf{(2)}$$

with the tube radius R [m] and the radius of the discharge electrode r [m]. For convenience the algorithm is rather applied in electrostatic SI units according to the conversion factors for voltage U [kV]

$$1KV = 1 \cdot 05 \cdot 10^{-2}\left[\frac{\sqrt{kg \cdot m}}{s}\right]$$

and current I [A]

$$1A = 9 \cdot 49 \cdot 10^{4}\left[\frac{kg^{0.5} \cdot m^{1.5}}{s^2}\right]$$

For wire type discharge electrodes and low current density the specific corona current i [mA/m] is evaluated with equation 3a[3].

$$i = \frac{U * 2 * K * \left[\frac{U - U_0}{R^2}\right]}{\ln\left(\frac{R}{r}\right)} \left[kg^{0.5} m^{0.5} S^{-2}\right] \qquad \textbf{(3a)}$$

with the ion mobility K = 17 bis 21 $[m^{1.5}\ kg^{-0.5}]$ for negative discharge voltage.

For brush type discharge electrodes modeling of the specific corona current i needs some adjustment since wire radius r_w as well as brush radius r_b may be varied. Equation 3b shows the algorithm for modeling the specific corona current i for brush type discharge electrodes.

$$i = \frac{U^2 * \sqrt{3} * K * \left[\frac{U - U_0}{U_0}\right]^3}{(R - r_b)^2 \ln\left(\frac{R - r_b}{r_b}\right)} \left[kg^{0.5} m^{0.5} S^{-2}\right] \quad \textbf{(3b)}$$

Finally the grade precipitation efficiency T(x) is derived from the Deutsch equation[4], represented by equation 4 for tube type precipitators,

$$T(x) = 1 - e^{-\frac{2*w(x)*L}{R*v}} \quad \textbf{(4)}$$

with the grade precipitation efficiency T(x), the particle rate of migration w(x), the length of the tube L and the gas velocity v.

The particle rate of migration w(x) is calculated with equation 5.

$$w(x) = \frac{E_a * E_P * x}{4 * \pi * \eta} \left[\frac{m}{s}\right] \quad \textbf{(5)}$$

With the discharge field intensity E_a [$kg^{0.5}$ $m^{-0.5}$ s^{-1}], the precipitation field intensity E_p [$kg^{0.5}$ $m^{-0.5}$ s^{-1}], the particle diameter x [m] and the dynamic viscosity of the gas η [Pas]. The discharge field intensity is deduced from the corona starting field intensity E_0[5]. The precipitation field intensity E_p is derived from equation 6[6].

$$E_p = \sqrt{\frac{2 * i}{K}} \quad \textbf{(6)}$$

3. Results and discussion

3.1 Current/voltage characteristic

Investigations were conducted with wire type and brush type discharge electrodes to determine the different shape of current/voltage characteristics for same operation voltage. The specific corona current i of brush type discharge electrodes is much higher than of wire type discharge electrodes. Figure 1 shows the comparison of current/voltage characteristics of brush type and wire type discharge electrodes. This data confirm the effect of geometry of discharge electrodes on current/voltage characteristics.

Experimentally recorded current/voltage data with wire type discharge electrodes are in accordance with equation 3a while current voltage data of brush type discharge electrodes are best modeled with equation 3b.

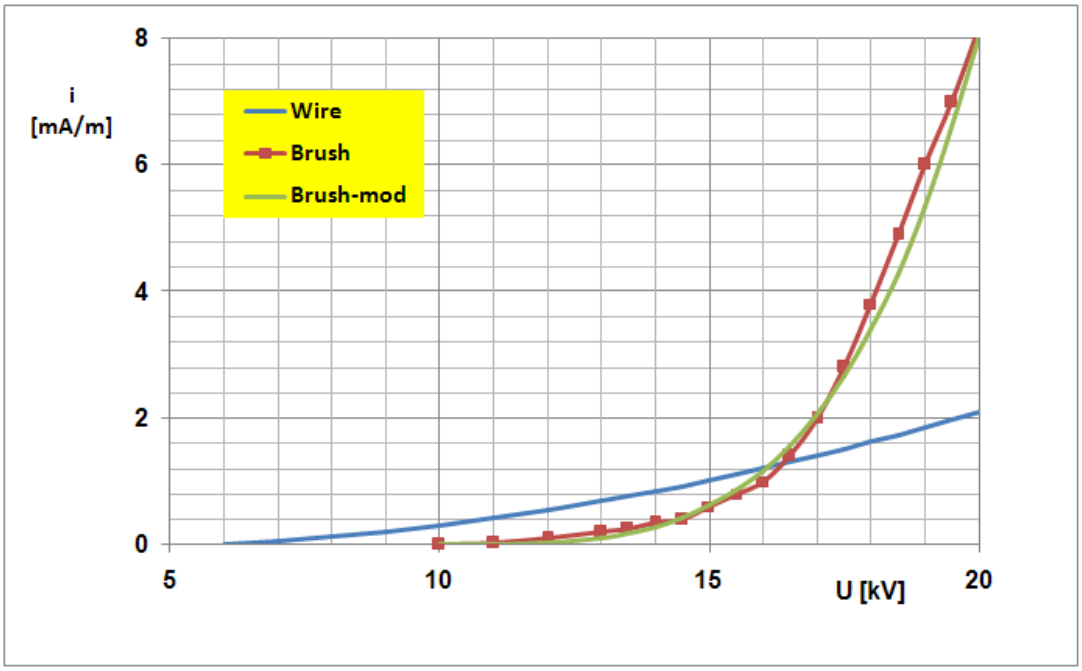

Figure 1: Comparison of current/voltage characteristics of wire type and brush type discharge electrodes. Operation data: Temperature and pressure: ambient, tube diameter: 32 mm, brush radius r_b: 4 mm, wire radius r_W: 0.075 mm

3.2 Ozon formation, UV-radiation and applications

Any electrical discharge in air does form ozone. While off-gas dedusting by electrostatic precipitation with wire type and barbed wire type discharge electrodes may suffer from ozone emission, wastewater treatment and off-gas treatment may make use of ozone formation through corona discharge with brush type electrodes[7]. Figure 2 shows the effect of corona current on ozone formation in a tube type wet electrostatic precipitator, equipped with brush discharge electrodes with different electrode radius but constant wire radius.
Figure 2 indicates linear correlation of ozone formation and the specific corona current with a distinct change in ozone formation close to the breakthrough voltage[8].

Correlation of corona current and UV-C radiation intensity was confirmed with a Rahn actinometer. From actinometric investigations the radiation intensity of λ = 254 nm radiation at U = 20 kV and I = 1 mA was determined to be I_{254}= 2 W, which is equivalent an amount of 10 % of the power input.

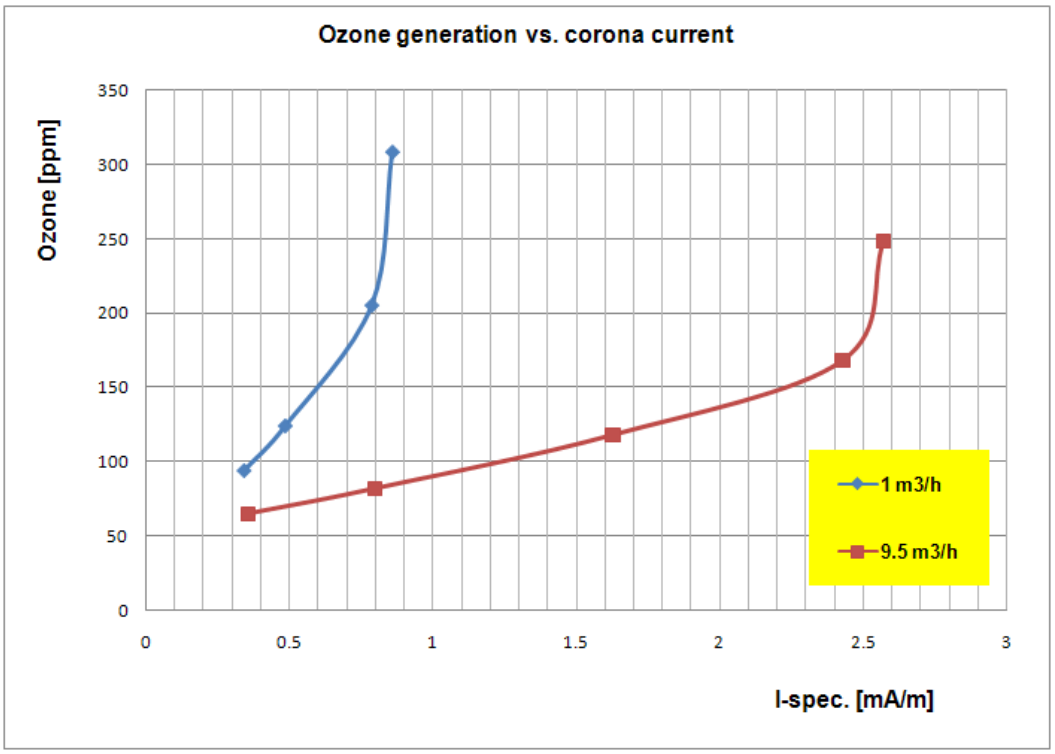

Figure 2: Effect of operation current and brush diameter on ozone formation during corona discharge in a tube type wet electrostatic precipitator at ambient temperature and pressure, tube diameter: 32 mm.

Figure 4 shows the effect of corona discharge on ambient air spiked with NO.

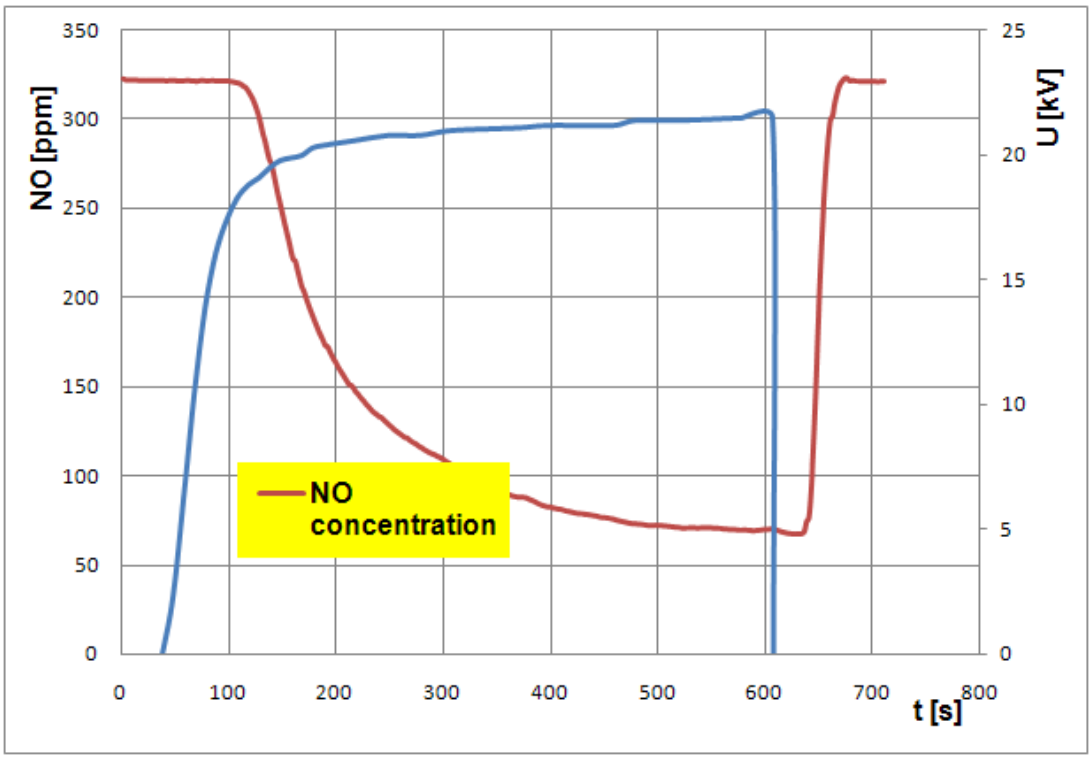

Figure 4: Effect of UV-irradiation on oxidation of humidified NO in ambient air

4. Summary

Wet electrostatic precipitation has still a domain in off-gas purification, demonstrated with NO and SO_2 oxidation. Design and construction have both proven predictible and liable. Subject of this project was the investigation of technological aspects of brush type discharge electrodes in wet electrostatic precipitation. Since brush type discharge electrodes produce a significant amount of ozone as well as UV-C radiation, extended applicability in wastewater treatment as well as off-gas treatment is expected.

Symbols and Abbreviations

δ	Relative gas density
η	dynamic viscosity of the gas [Pas]
E_o	Corona starting field intensity [kV/m]
E_p	Precipitation field intensity [kV/m]
E_a	Discharge field intensity [kV/m]
I	Radiation intensity
I	Current [A]
i	Specific corona current [A/m]
K	Particle mobility [Vs/m^2]
L	Length of the reactor [m]
P	Pressure [hPa]
R	Radius (distance between discharge electrode and collector) [m]
r	Radius of the discharge electrode [m]
T	Temperature [K]
T(x)	Grad precipitation efficiency [-]
U	Operation voltage [kV]
U_o	Corona onset voltage [kV]
v	Gas velocity [m/s]
w	Particle rate of migration [m/s]
x	Particle diameter [m]

References

[1] Peek F. W., Dielectric Phenomena in High Voltage Engineering, McGraw Hill Publ., New York, 1929.

[2] White H. J., Ind. Electrostat. Prec., Addison-Wesley Publ. Co, 1963.

[3] Cooperman P., Trans. Am. Inst. Electr. Eng. 79 (1960), p 47

[4] Deutsch W., Ann. Physik 68 (1922), p 335 - 344

[5] Siebenhofer M., Chem.-Ing.-Tech 63 (1991) 9, p 904-910

[6] Kalaschnikow S., Zeitschrift für Technische Physik 14 (1933), p 267

[7] Tahir M. S., Application of Corona Discharge in Off-gas and Wastewater Treatment, PhD Thesis, University of Technology Graz, 2011

[8] Friedrich T., Einfluss der Strom/Spannungs-Charakteristik eines Rohrnass-elektrofilters auf die absorptive Abscheidung von SO_x und NO_x, TU Graz, 2012

Selective hydrogenation and separation of C3 stream by thermally coupled reactive distillation

Xing Qian, He Tian, Yiqing Luo, Xigang Yuan[*]*, Kuo-Tsong Yu*
School of Chemical Engineering and Technology, State Key Laboratory of Chemical Engineering, Tianjin University, Tianjin, China

Abstract
In this paper, a novel process for C3 stream selective hydrogenation in ethylene plant is proposed. The proposed process combines the propylene catalytic reactive distillation for the hydrogenation with the column of depropanization to achieve a thermally coupled distillation column configuration. In the proposed process, the reactive distillation improves the selectivity of the hydrogenation reaction with a lower investment cost for the equipment and the thermal coupling of the distillation columns, which leads to a dividing wall column (DWC), increases energy efficiency of the system. The feasibility of the proposed process is tested by rigorous simulation employing AspenPlus^{TM} software. Optimization on decision variables in the process is also performed based on the process simulation. The results show that, on the premise of the product yield and purity (propylene mole fraction: 99.60%), the reactive distillation process can save 11.3% utility cost comparing to the conventional reaction-and-distillation process, and the thermally coupled reactive distillation can save 17.4% annual utility cost than the traditional reaction-and-distillation process.

Keywords
reactive distillation; C3 stream selective hydrogenation; thermally coupled distillation

1. Introduction

Propylene is a fundamental raw material in chemical industry. The conventional way in ethylene plant to separate cracking feedstock for obtaining propylene is either the sequential separation process, or front-end deethanization process, or front-end depropanization process. In all the process, distillation is used for the separation. The final step to produce propylene is the processing of the C3 stream, which is mainly composed of propylene and propane. The largest consumption of propylene is by the production of polypropylene, which requires high purity of propylene (mole fraction: 99.60%). However there exist impurities in C3 stream: methyl acetylene and propadiene (MAPD) that come from the cracking. MAPD must be removed from the C3 stream so that the obtained propylene meets the specifications for the subsequent process for polymerization. The concentration of MAPD in the C3 stream is so low (around 4% mass fraction) that a distillation column is not economical for the removal [1]. Instead, a selective hydrogenation reactor is usually introduced into the C3 stream processing and used to convert MAPD into C3 alkene component. In this way, propylene is purified and its yield is increased as well.

[*] To whom correspondence should be addressed. Email: yuanxg@tju.edu.cn

Distillation is a capital- and energy-intensive operation. Recent research demonstrated that a portion of energy can be saved by process integration or coupling between reaction and distillation and/or among columns of distillation [2]. This paper proposes an integrated, hybrid and novel process which combines the selective hydrogenation reaction with the propylene distillation column, and integrates two distillation columns into one thermally coupled reactive distillation column.

2. Thermally Coupled Reactive Distillation Process and Simulation

The proposed process is based on the traditional front-end deethanization process, which is shown in figure 1. In such a process, the deethanizer's bottom stream, of which the major composition is simplified as three main components (A: C_3H_6, B: C_3H_8, MAPD and C: C_4-C_7) as given in table 1, is fed into the depropanizer. The top distillate stream of the depropanizer goes into a selective hydrogenation reactor, and the outflow of the reactor feeds into the propylene distillation column to get a propylene product of 99.60% in mole fraction.

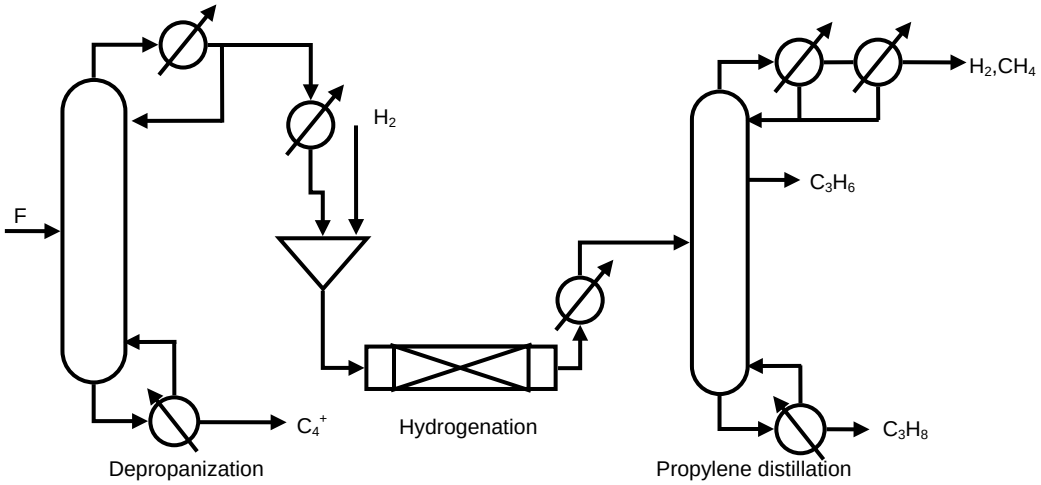

Figure 1 The conventional reaction-and-distillation process

Table 1 Feed data

Variable names	Variable values
mole flux (kmol/hr)	2219.174
component mole fraction (A B C)	z_i=[0.557,0.051,0.392]
temperature (K)	277.15
pressure (atm)	17.383

The proposed thermally coupled reactive distillation (TCRD) process is shown in figure 2a and it is thermodynamically equivalent to reactive dividing wall column (RDWC) as shown in figure 2b. Obviously, comparing to the conventional reaction-and-distillation process as shown in figure 1, the reactor is moved into the distillation column and the condenser of the depropanizer is eliminated in the TCRD process. In the RDWC configuration, the number of distillation column is decreased to one by introducing a vertical partition (wall), and such an arrangement can increase energy efficiency significantly [3]. Reactive distillation can simplify the process. An important advantage of the reactive distillation for such a system is that the reaction temperature can be stabilized by eliminating hot spot on the catalysis and, at the same time decrease the chance of deep hydrogenation, which may lead to the increase of by-product (propane) formation [4, 5]. All these, reactive distillation and

thermally coupling, lead to a lower investment and operating costs, which will be discussed in section 3.

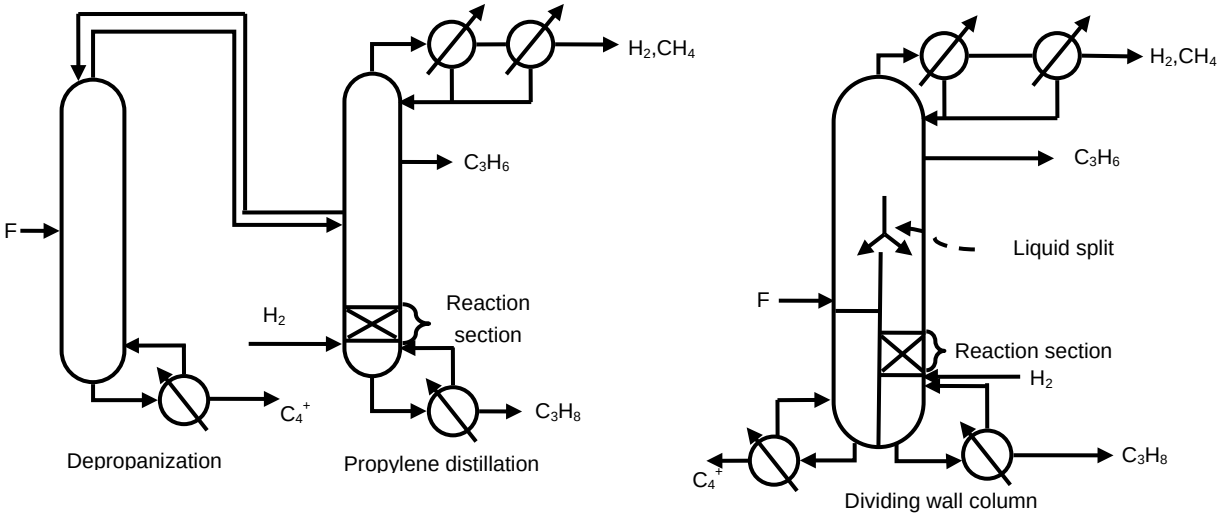

(a) thermally coupled configuration (b) DWC configuration

Figure 2 The thermally coupled reactive distillation column

Before the simulation of the processes, short-cut method based on the Winn-Underwood-Gilliland approach is used to provide initial designs for the distillation columns. Then, with the initial values given by the short-cut method, the traditional reaction-and-distillation process as shown in figure 1 is simulated rigorously employing AspenPlus^{TM} software (property method: RK-Soave). The kinetics comes from the work done by Yu [6].

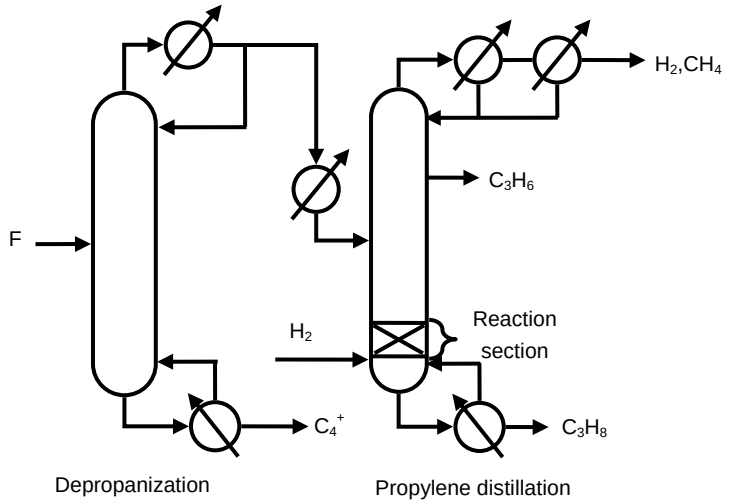

Figure 3 The reactive distillation process

Note that the short-cut model DSTWU in AspenPlus^{TM} cannot be used to calculate columns with a side product stream. The main function of the propylene distillation column is to separate propylene and propane; the goal of the short-cut calculation is getting the stage number and reflux ratio of the propylene distillation column for the separation between propylene and propane. So in the short-cut method the selective

hydrogenation reaction is not taken into consideration. The results of the short-cut method are shown in table 2, which are used as initial values of rigorous simulation.

In order to make comparisons, reactive distillation process without thermal coupling as shown in figure 3 is also simulated.

3. Results and discussion

3.1 The traditional reaction-and-distillation process

The results of rigorous simulation of the traditional reaction-and-distillation process, as depicted in figure 1, are shown in table 3. The stage numbers of the two distillation columns calculated in the short-cut method are used in the rigorous simulation. However, as there are hydrogen and methane in rigorous simulation introduced by selective hydrogenation, ten stages are employed to separate the hydrogen and methane from propylene. Also, the top distillate stream of the propylene distillation column is hydrogen and methane in rigorous simulation and the side withdraw stream is propylene. As a result, the reflux ratio with respect to the top product of hydrogen and methane is much higher than that in short-cut calculation. Another difference is the feed stage number of the propylene distillation column. As there is a reaction section in the propylene distillation column, the compositions in the column are different from those in a simple two-product distillation column as calculated in the short-cut method.

Table 2 Initial values for the rigorous simulation

Variable names	Variable values
Minimum reflux ratio	R_{min1},R_{min2}=[0.88, 13.01]
Minimum stage number	N_{min1},N_{min2}=[20, 96]
Reflux ratio	R_1,R_2=[1.06, 15.62]
Stage number	N_1,N_2=[43,175]
Feed stage number	N_{F1},N_{F2}=[25,54]

Table 3 Results of the rigorous simulation

Variable names	Variable values
Reflux ratio	R_1,R_2=[1.3, 73.75]
Stage number	N_1,N_2=[43,185]
Feed stage number	N_{F1},N_{F2}=[20,109]

3.2 The reactive distillation process

As the hydrogenation reaction is exothermic, the heat of the reaction can be used to provide the heat of vaporization and consequently decrease the reboiler duty of the propylene distillation column [5]. The one of the tasks of simulation of reactive distillation process as shown in figure 3 is determination of reaction section in propylene distillation column.

Figure 4 shows the mole fraction of MAPD in the propylene distillation column without a reaction section. As the concentration of MAPD increases along the stage number of the propylene distillation column, the maximum concentration of MAPD is near the bottom. So the reaction section of the reactive distillation column is arranged at the lower part of the column. The mole fraction of MAPD within the reactive distillation column is shown in figure 4. To achieve the same yield of propylene as the traditional reaction-and-distillation column, the reaction section within the reactive distillation

column contains at least 13 stages (the 171st to 184th stage). In this simulation of reactive distillation, the feed of H_2 is introduced at the 184th stage.

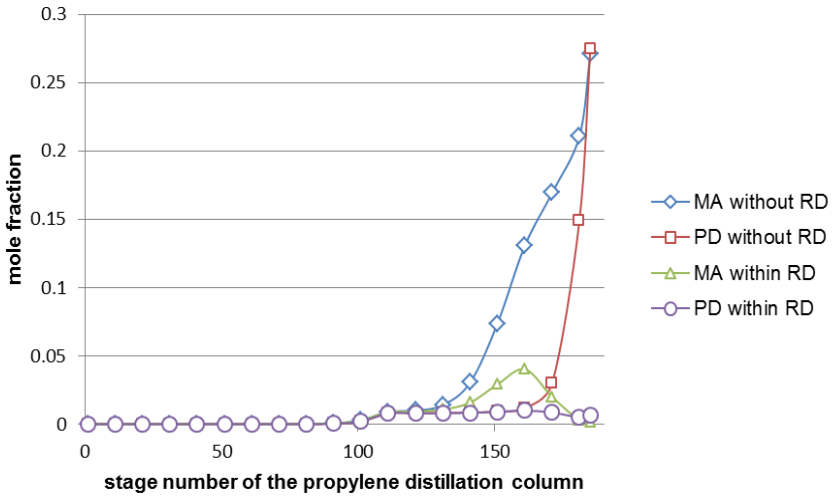

Figure 4 Mole fraction of MAPD along the stage number without or within reactive distillation

3.3 The thermally coupled reactive distillation process

In order to achieve the minimum annual cost of cold and hot utilities in the process as shown in figure 2, optimization on decision variables in the process is performed by simulation. The hot utility is the low pressure steam (5bar, 160℃) represented as U1. And the cold utility consists of two degrees: one is the cold water (15℃ to 25℃) represented as U2 and the other is the refrigeration propylene (-5℃) represented as U3. By optimization of the stage numbers of the various column sections, the vapor feed stream of the propylene distillation column from the top of the depropanizer is fed to the 109th stage, while the liquid withdraw stream is from the 108th stage of the propylene distillation column.

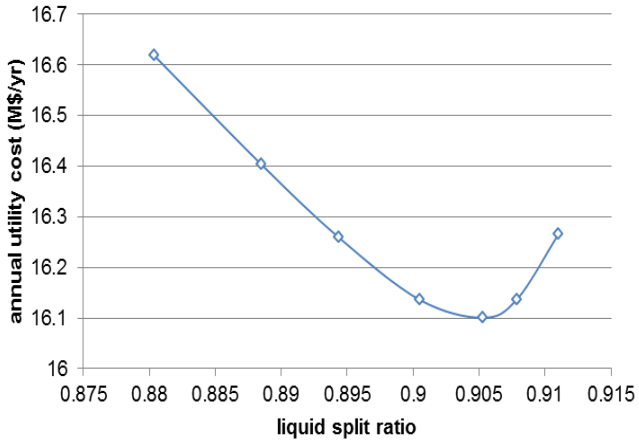

Figure 5 Annual costs for utilities with varying liquid split ratio

The most dominant variable in the optimization is the liquid split ratio, which is defined as the ratio of liquid that goes to the propylene distillation column (reactive distillation column), as shown in figure 2b. Through simulations, the relationship

between liquid split ratio and the annual utility cost is shown in figure 5. And the optimal liquid split ratio, as shown in figure 5, is 0.905, which is used in the thermally coupled reactive distillation in this paper.

The results in the Table 4 show that, the reactive distillation process can save 11.3% utility cost comparing to the conventional reaction-and-distillation process, and the thermally coupled reactive distillation (TCRD) process can save 17.4% annual utility cost than the traditional reaction-and-distillation process.

Table 4 Comparison of energy consumption in different simulations

Annual energy cost (M$/yr)	The conventional process	The reactive process	The thermally coupled process
Cost for U1	7.1	7.1	6.9
Cost for U2	12.2	10.0	9.0
Cost for U3	0.2	0.2	0.2
Total Cost	19.5	17.3	16.1
SAVING(%)	-	11.3	17.4

4. Conclusions

This paper proposes a reactive dividing wall column (RDWC) or the thermally coupled reactive distillation (TCRD) process, which combines the selective hydrogenation reaction with the propylene distillation column, and integrates two distillation columns into one thermally coupled reactive distillation configuration.

The results of our simulation show that the proposed process is economically attractive and can save annual utility cost up to 17.4% with comparison to the traditional reaction-and-distillation process. Comparing to the conventional reaction-and-distillation process as shown in figure 1, the reactor is moved into the propylene distillation column and the number of the heat exchangers is decreased in RDWC as shown in figure 2. On such a basis, the RDWC option may increase further the economic efficiency by lowering down the investment cost.

Acknowledgements

The authors acknowledge the National Basic Research Program of China (973 Program: 2012CB720500) for supporting this research.

References

1 Olujić, Ž., Jödecke, M., Shilkin, A., Schuch, G. and Kaibel, B., "Equipment improvement trends in distillation", *Chem. Eng. Pro.* **48**, 1089-1104 (2009).
2 Dejanović, I., Matijašević, L. and Olujić, Ž., "Dividing wall column—a breakthrough towards sustainable distilling", *Chem. Eng. Pro.* **49**, 559-580 (2010).
3 Yildirim, Ö., Kiss, A. A. and Kenig, E. Y., "Dividing wall columns in chemical process industry: A review on current activities", *Sep. Purif. Technol.* **80**, 403-417 (2011).
4 Yu, Z. Q., Gao, B. L. and Zhang, J. Y., "Selective hydrogenation of C3 fraction in a catalytic distillation column", *Modern Chemical Industry (China)* **21**, 23-26 (2001).
5 Taylor, R. and Krishna, R., "Modelling reactive distillation", *Chem. Eng. Sci.* **55**, 5183-5229 (2000).
6 Yu, Z. Q., Gao, B. L., Xu, J. M., Liu, K. Y. and Zhang, J. Y., "Kinetic study of C3 cut liquid-phase selective hydrogenation over supported metal catalyst", *Industrial Catalysis (China)* **10**, 11-16 (2002).

Petlyuk column and the alternatives for multicomponent distillation- A perspective from systematic process synthesis

Ben-Guang Rong

Department of Chemical Engineering, Biotechnology and Environmental Technology, University of Southern Denmark, Niels Bohrs Alle 1, Odense, Denmark

Abstract

The Petlyuk configuration has the minimum energy requirement for a multicomponent distillation. However, the equipment implementation of Petlyuk configuration is complex and difficulty in terms of both design and control, especially when a mixture involving four or more components. For example, although the dividing-wall column (DWC) for ternary Petlyuk configuration has received wide applications in industries, the dividing-wall column for quaternary Petlyuk configuration has not been the same applications. In this work, the synthesis on the alternative intensified distillation systems for Petlyuk configuration was investigated. For four or more components Petlyuk configuration, we present two types of intensified alternatives: the intensified systems with dividing-wall and the intensified systems without dividing-wall. First, the mechanism for generation of the original Petlyuk configuration was examined. Second, in order to generate all possible intensified alternatives, the simple column configuration for the separation sequence of Petlyuk configuration is found to be the necessary starting point. Third, five strategies are introduced to change the structure of the simple column configuration in terms of both condensers/reboilers and column sections. These strategies can be used to systematically synthesize the alternative intensified configurations for the Petlyuk configuration. The objective of this work is to present the synthesis method and to systematically generate the two types of intensified alternatives for Petlyuk configuration. The alternative intensified systems are amenable to be easier in both design and control due to the simplicity in the structures. The numerical design and optimization, as well as dynamics and control of these new alternative configurations are underway.

Keywords:

Petlyuk column, new alternative, process synthesis, intensified system, dividing wall column, nonsharp split

1. Introduction

Distillation is the widely used separation technology not only for fossil-based, but also for renewable-based products manufacturing. Synthesis of new intensified distillation systems with significant reductions on energy and capital costs is ever being an active research topic for both academics and industries. Among the feasible configurations for multicomponent distillation, the Petlyuk configuration has been proved to have the minimum energy requirement than other possible configurations. This is due to that the Petlyuk configuration has the lowest thermodynamic irreversibility with the nonsharp splits and thermal couplings. For an N-component

mixture, the Petlyuk configuration needs N-1 columns with one condenser and one reboiler in the product column. The implementation of Petlyuk configuration for ternary distillations has achieved remarkable success in the form of dividing-wall column (DWC). A single shell column with one dividing wall (DWC) can perform a ternary separation with three pure products. Such DWC columns have been successfully used in many industrial separations with substantial savings on both energy and capital costs.

Motivated by the ternary Petlyuk column, the Petlyuk configuration has ever been the preferred configuration for four or more component mixtures (Olujic et al., 2012). However, examining the separation sequence of Petlyuk column for four or more component mixtures, it is known that it has the maximum number of individual splits due to the nonsharp splits. Even though the final configuration has only N-1 columns with only one condenser and one reboiler, the maximum number of thermal couplings makes the system much more complex for both design and control. When coming to the dividing-wall column for Petlyuk configuration for four or more component mixtures, it is even more difficult to design and control a single shell equipment to implement the multiple dividing walls. Therefore, the original Petlyuk configuration so far is not well implemented in industries for four or more component distillations compared to ternary mixtures.

In this work, the synthesis of the alternative intensified distillation systems than Petlyuk configuration for four-component distillation was investigated. First, the mechanism for generation of the original Petlyuk configuration is examined. Then, new mechanisms for synthesis of alternative intensified configurations are presented. These mechanisms are then used in a systematic manner to synthesize the possible new intensified alternatives. Two types of alternative intensified systems are obtained each with only two columns. The alternative intensified systems are amenable to be easier in both design and control due to the simplicity in the structures.

2. Petlyuk configuration for quaternary distillation and its original DWC

Petlyuk et al. (1965) summarized four features for the fully thermally coupled configuration for an N-component distillation. 1) the total number of sections required for separating an N-component mixture is equal to N(N-1), instead of 2(N-1) in the conventional scheme; 2) it is sufficient to have only one condenser and one reboiler independent of the number of components to be separated; 3) the key components in each column are the two components with the extreme volatilities; 4) N products of a given purity are obtained in the product column.

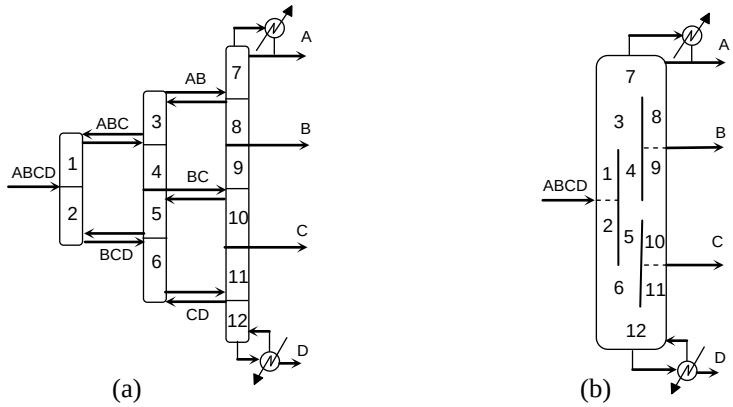

Figure 1. (a) Quaternary Petlyuk configuration; (b) Dividing-wall-column of quaternary Petlyuk configuration

In an earlier work to synthesize the heat-integrated configurations for Petlyuk arrangements, we illustrated that the Petlyuk configuration was generated from the unique nonsharp separation sequence in which all of the mixtures with three or more components are separated by the symmetric sloppy splits (Rong et al., 2006). Such unique separation sequence was called fully sloppy separation sequence. For quaternary mixtures, the fully sloppy sequence is: A<u>BC</u>D →A<u>B</u>C →B<u>C</u>D →A/B → B/C→C/D. The quaternary Petlyuk configuration is presented in Figure 1(a).

For an N-component mixture, the total number of thermal couplings in the Petlyuk arrangement is (N-2)(N+1)/2. There are N-2 thermal couplings associated with the submixtures involving the most volatile component, which are located at the top ends of the columns. Similarly, there are N-2 thermal couplings associated with the submixtures involving the least volatile component, which are located at the bottom ends of the columns. There are (N-2)(N-3)/2 thermal couplings associated with the submixtures composed of only the middle components, which are located at the intermediate locations in the columns. The two ends of the product column are connected with the only condenser and the only reboiler. The commonly studied single shell dividing-wall-column for quaternary Petlyuk configuration is presented in Figure 1(b) (Christiansen et al., 1997).

The Petlyuk configuration in Figure 1a with three columns has five thermal couplings which is complex for both design and control. The single shell DWC column in Figure 1b has three dividing walls which is too difficult for both equipment implementation and its design and control. In the following, we will derive new configurations with two columns which are amenable to both design and control.

3. The systematic method for synthesis of intensified alternatives for Petlyuk configuration

Starting from the fully sloppy separation sequence with the intended individual splits, it is clear that we need different strategies to deal with the condensers and reboilers, as well as the individual simple columns to achieve a distillation configuration with less number of columns and heat exchangers. For example, Figures 2a and 2b present two configurations with three columns (N-1 columns). However, to fully explore the possibility to generate the new configurations, we have found that the

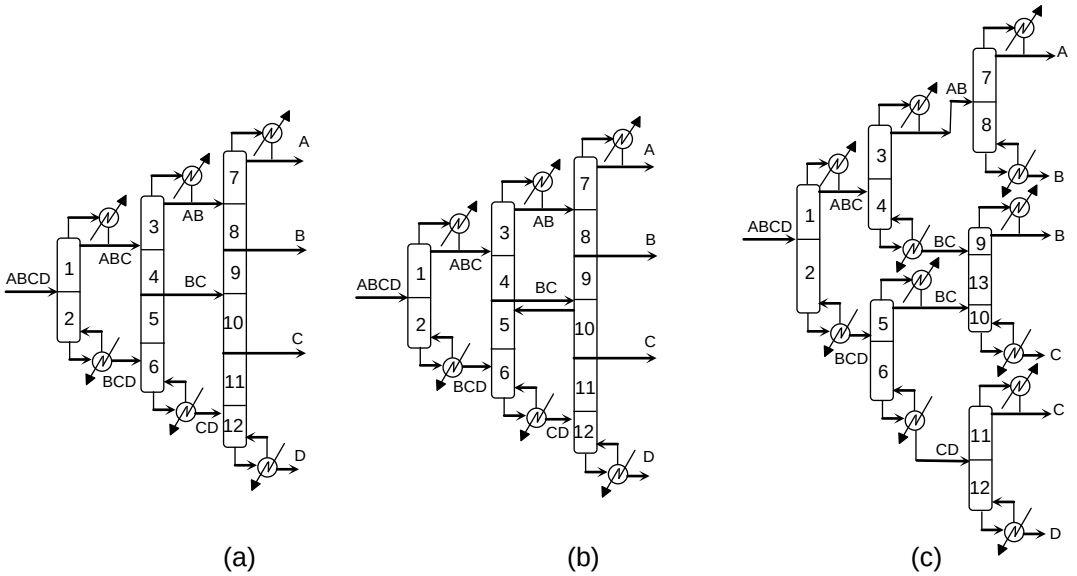

Figure 2. The configurations for the fully sloppy separation sequence of a quaternary mixture

simple column configuration (SCC) of the sloppy separation sequence is the necessary representation, which is shown in Figure 2c. This is because that the SCC configuration keeps all the structural flexibility, from which different mechanisms can be explored to change its structure, and from which all possible intensified distillation systems can be generated.

To synthesize the new intensified distillation systems with fewer columns and heat exchangers, we have introduced five strategies which are aiming at changing the structure of the SCC configuration, at the same time, also aiming at reducing the number of columns and heat exchangers.

Strategy 1*:* Heat-Integration strategy to combine the individual columns. This strategy is used to combine two columns by heat integration between a condenser and a reboiler involving only intermediate components. This will reduce the number of columns and heat exchangers than the SCC configuration.

Strategy 2*:* Thermal coupling strategy to eliminate a condenser or a reboiler. This strategy is used to eliminate a condenser or a reboiler which is associated with a mixture of binary or more components. This will reduce the number of heat exchangers than the SCC configuration.

Strategy 3: Rearrangement of column sections strategy to generate the thermodynamically equivalent structures. This will generate the thermodynamically equivalent thermally coupled structures which have different columns than the original thermally coupled configuration.

Strategy 4: Elimination of the single-section-side columns strategy to produce the intensified distillation systems. This strategy is used to eliminate the single-section-side columns which will generate the intensified distillation systems with fewer columns.

Strategy 5: Incorporation of the prefractionation or the single-section-side columns strategy to produce the dividing wall columns. This will reduce the number of columns than the SCC configuration.

In the following, as an example for the simple column configuration shown in Figure 2c, we will illustrate the synthesis of the two types of the intensified alternatives by systematically applying the above strategies.

4. The intensified alternatives with dividing wall

The single shell DWC column in Figure 1b has three dividing walls. The three walls divide the column shell into three layers for vapor and liquid distributions, which is

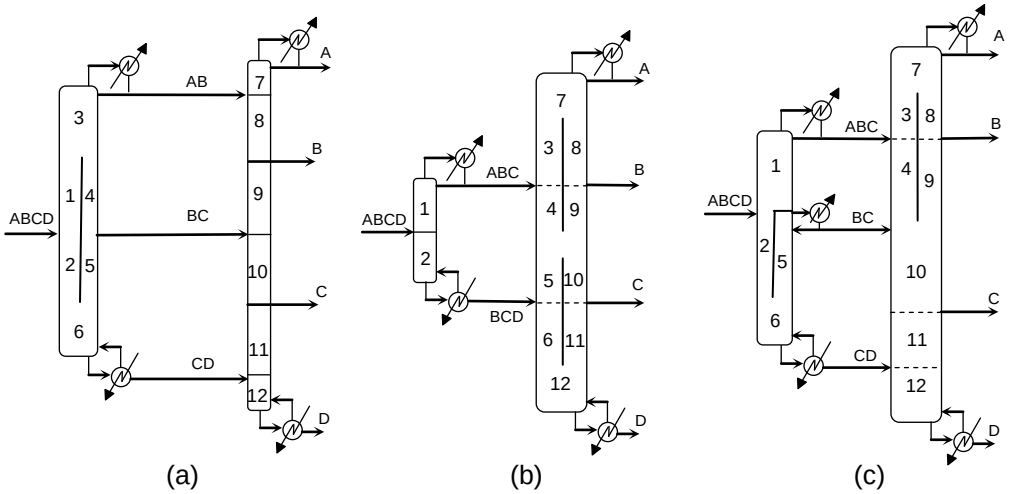

(a) (b) (c)

Figure 3. The intensified alternative DWC columns for quaternary distillation

difficult for both equipment implementation and its design and control. Here, we present the synthesis of DWC columns in which each column is only allowed to be divided into two layers. The key is to rearrange the columns so that the prefractionation or the single-section-side columns can be incorporated into another column through dividing walls. Figure 3 presents three such DWC columns, each of them has only two columns.

Example 1: generation of alternative Figure 3(a): Starting from the SCC in Figure 2c, we can use four steps to generate the Figure 3(a). Step 1: combining the columns co-producing the middle products B and C through strategy 1. Step 2: combining the columns co-producing the intermediate mixture BC through strategy 1. Step 3: eliminating condenser ABC and reboiler BCD through strategy 2. Step 4: Incorporating the feed prefractionation column into the subsequent column with a dividing wall through strategy 5, this will generate the alternative Figure 3(a).

Example 2: generation of alternative Figure 3(b): Starting from the SCC in Figure 2c, we can use three steps to generate the Figure 3(b). Step 1: combining the columns co-producing the middle products B and C through strategy 1. Step 2: eliminating condenser AB, reboiler BC, condenser BC and reboiler CD through strategy 2. Step 3: incorporating the prefractionation columns for ABC and BCD with dividing walls through strategy 5, this will generate the alternative Figure 3(b).

In similar manner, all the other possible DWC columns can be generated by systematically applying the above strategies.

5. The intensified alternatives without dividing wall

The original quaternary Petlyuk configuration shown in Figure 1a has three columns, in which five two-way thermal couplings communicate between the columns. It is difficult for practical implementation due to the complexity in design, control and operation. Here, we present the synthesis of new intensified distillation systems which have fewer columns than that of Petlyuk configuration. The synthesis procedure is still starting from the SCC shown in Figure 2c, then systematically applying the above strategies to reduce the number of columns and the number of heat exchangers. The key is to generate the thermodynamically equivalent structures in which there are single-section-side columns. A single-section-side column is either serving as transporting an intermediate mixture or as purifying a final product. In certain cases, they can be eliminated to obtain the intensified distillation systems with fewer columns. Figure 4 presents three such new alternative intensified systems, each of them has only two columns.

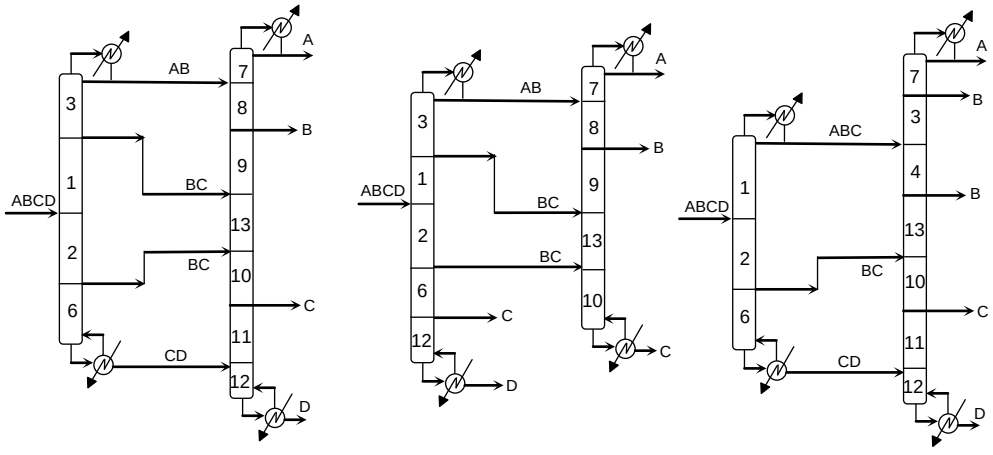

(a) (b) (c)

Figure 4. The intensified alternative inter-transporting systems for quaternary distillation

Example 3: generation of alternative Figure 4(a): Starting from the SCC in Figure 2c, we can use four steps to generate the Figure 4(a). Step 1: combining the columns co-producing the middle products B and C through strategy 1. Step 2: eliminating condenser ABC and reboiler BCD through strategy 2. Step 3: removing the movable sections 3 and 6 to rearrange the column sections through strategy 3. Step 4: eliminating the single-section-side columns 4 and 5 through strategy 4, this will generate the alternative Figure 4(a).
Example 4: generation of alternative Figure 4(b): Starting from the SCC in Figure 2c, we can use four steps to generate the Figure 4(b). Step 1: combining the two columns co-producing the middle product B through strategy 1. Step 2: eliminating condenser ABC, reboiler BCD and reboiler CD through strategy 2. Step 3: removing the movable sections 3, 6 and 12 to rearrange the column sections through strategy 3. Step 4: eliminating the single-section-side columns 4, 5 and 11 through strategy 4, this will generate the alternative Figure 4(b).

Similarly, all the other possible alternatives with fewer columns than Petlyuk configuration can be generated by applying the above strategies in a systematic manner. Furthermore, the number of heat exchangers of the intensified systems shown as in Figures 3 and 4 can be further reduced by replacing the condensers and reboilers associated with mixtures with thermal couplings.

6. Conclusions

The Petlyuk configuration is proved to have the minimum energy requirement than other possible configurations for a multicomponent distillation. However, the Petlyuk configuration with the theoretical minimum energy consumption for four or more component mixture is very difficult for practical application due to its complexity. The reason is that the fully thermally coupled Petlyuk configuration has too many thermal couplings between columns, which are difficult for control and operation. On the other hand, its single shell dividing-wall-column needs to implement multiple dividing walls in one column which is even more difficult for equipment design, control and operation.

In this paper, two types of intensified alternative distillation systems for quaternary Petlyuk configuration are presented: the intensified alternative systems with dividing wall, and the intensified alternative systems without dividing wall. All the intensified distillation systems use fewer columns than the Petlyuk configuration. The distinct features of the intensified distillation systems make them attractive in terms of economics, simultaneously, they are also amenable to systems' design, control and operation.

The method presented in this work is applicable to generate both types of the intensified distillation systems for Petlyuk configuration with a feed mixture of any number of components.

References

A.C. Christiansen, S. Skogestad, K. Lien, 1997, Complex distillation arrangements: Extending the Petlyuk ideas, Comput. Chem. Eng., 21, S237-S242.
Z. Olujic, I. Dejanovic, B. Kaibel, H. Jansen, 2012, Dimensioning multipartition dividing wall columns, Chem. Eng. Technol., 35, 1392-1404.
F.B. Petlyuk, V.M. Platonov, V.M. Slavinskii, 1965, Thermodynamically optimal method for separating multicomponent mixture, Inter. Chem. Eng., 5(3), 555-561.
B.-G. Rong, I. Turunen, 2006, New heat-integrated distillation configurations for Petlyuk arrangements, Chem. Eng. Res. Des., 84(12), 1117-1133.

The Extractive Dividing Wall Column in real production process– groundbreaking process intensification in the industrial practice

Daniel Staak, Thomas Grützner
Center of Excellence Lonza Group, Visp, Switzerland

Abstract

The extractive distillation for the separation of azeotropic or narrow boiling mixtures is known for a long time and well established within the chemical industry. For the separation of zeotropic ternary mixtures more and more dividing wall columns are applied since two decades. Both processes pose already a high degree of intensification yielding in a high potential to reduce both, CAPEX and OPEX. The streamlining of processes by intensification is crucial for chemical companies, especially in the western world, to compensate high energy prices and competition from low cost countries.

The combination of extractive distillation and dividing wall column allows the separation of two narrow boiling or azeotropic components using a suitable third component in only one column shell instead of two columns.

The dividing wall column for this extractive application was developed by Lonza and has a dividing wall that extends to the upper end of the column. Therefore this column comprises two vapor pipes and two condensers. This is the main feature of the discussed column as well as the main difference to conventional dividing wall columns. Within this configuration it is possible to carry out the entrainer distillation as well the regeneration of the entrainer within only one single column. The process itself is already known from literature but the realized column is the first publication of a device in industrial operation.

Keywords
Extractive distillation, extractive dividing wall column, operation, simulation

1. Introduction

Distillation plays an outstanding role among other thermal separation processes within the chemical industry. 90% of all separation units and 5% of the global energy demand account to distillation [1]. Steadily rising energy and raw material costs in the past as well as increasing market competition have been the major drivers to steadily search for potential energy savings, even for a mature operation like distillation. This pressure yielded in energy improved and intensified distillation processes, e.g. the heat integrated distillation column (HIDiC) and the dividing wall column. Contrary to the HIDiC which is still to a great extend an academic field of investigation the DWC is already widely applied in the chemical industry. It took decades after the idea of DWC has been established until the first commercial unit has been set-up by BASF in Ludwigshafen (Germany) in 1985 [2]. Since then > 160 units are operated world-wide, mainly at BASF-sites but also in other companies. Lonza operates 4 columns in

Visp (Switzerland). The main advantages of DWC are the considerable savings in energy consumption and investment costs, which are typically in the range of 30%-40% [3]. In order to separate narrow-boiling or azeotropic mixtures (A,B) an additional substance (entrainer) can be added to the system that selectively interacts with one of the components and influences the relative volatility. For instants in Figure 1 the volatility of component B decreases. As a result the light boiler (A) can be withdrawn as a pure substance overhead whereas the heavy boiler (B) and the entrainer (Ent.) are discharged in the bottom of the column and separated in a subsequent column. The recovered entrainer is then recycled to the first column (Figure 1, left). C is in this example an additional component with a lower volatility than A and B and is not difficult to separate.
Both concepts, the DWC (Figure 1, right) and the extractive distillation setup Figure 1, left) can very beneficially be combined in one single column shell [4]. The resulting column poses again a dividing wall (Figure 1, middle). The main difference to the standard concept of a dividing-wall column is that the partitioning wall extends to the upper end of the column. Two vapor streams results from this setup and, therefore, to vapor lines and two condensers are necessary.

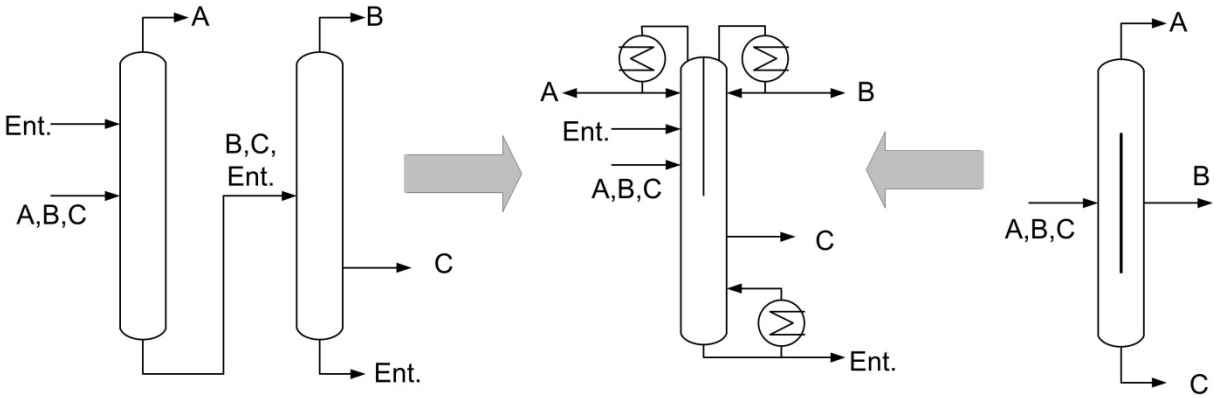

Figure 1 Standard Extractive Setup (left), Extractive DWC(middle) and Standard DWC (right)

As already mentioned, the extractive dividing wall column (EDWC) allows the separation of the whole system in one single column. The entrainer is typically fed to the left side of the dividing wall above the feed and hinders the component B to reach the top of the column. The pure light boiling component A is in this case withdrawn overhead in the left column section. The entrainer together with B is send to the section below the dividing wall and separated there. Pure entrainer is withdrawn from the bottom of the column and recycled directly. Pure B is withdrawn from the column head on the right side of the dividing wall.
Different construction principals are possible and were published by different authors [5, 6, 7].

2. Results and discussion

2.1 Separation Task

Due to very similar boiling points, A and B form an extremely narrow boiling system and, therefore, simple distillation cannot be applied. The relevant components occurring in the system are summarized in Table 1. A comprehensive solvent screening based on literature search and predictive methods indicated that Ethylenglycol is promising candidate. Ethylenglycol interacts stronger with component B (hydrogen bond of the hydroxyl-group) compared to component A

(more steric hindrance) and reduces the relative volatility of B. Additionally component C should be separated from the Product B. But the boiling difference between B and C is sufficient to draw C as a side product.

Table 1 Main components occurring in the system

Component	Boiling point at 0.1 bar°C	Mass fraction in feed %
A	76	3
B (Product)	76	86
C	85.5	5
Ethyleneglycol (Entrainer)	140	-

2.2 Designing process of the Extractive dividing wall column

2.2.1 Development of the thermodynamic model

Once the entrainer is defined subsequently the accuracy is proofed of the thermodynamic system by measurements of certain most relevant equilibria. If the measurements proof the results from predictive modeling the whole data is transformed to NRTL sets and used for the following flowsheet modeling.
Besides the components mentioned in Table 1, a number of other components are present in the system and taken into account in the thermodynamic model. However, these components play only a minor role and are not discussed in detail. The fact that measurements and binary interaction parameters were not available from literature or data bases for these binary systems, made it necessary to use predictive thermodynamic models to describe the behavior. Especially for the entrainer screening this approach is very beneficial since it is much faster and less expensive than carrying out own experiments in order to receive the desired data. Typically UNIFAC and COSMO-RS are used for predictive modeling. Experience shows that the accuracy of these approaches is absolutely adequate for the overwhelming number of systems and applications.

2.2.2 Model validation

Due to financial and timing reasons no piloting of the process was carried out. Instead the necessary validation of the thermodynamic model was carried with a single lab-batch-distillation. In the lab experiment the different characteristic sections of the column (marked in different grey), were imitated in the batch distillation over the course of time by altering the batch operation conditions. The experimental approach is visualized in Figure 3.

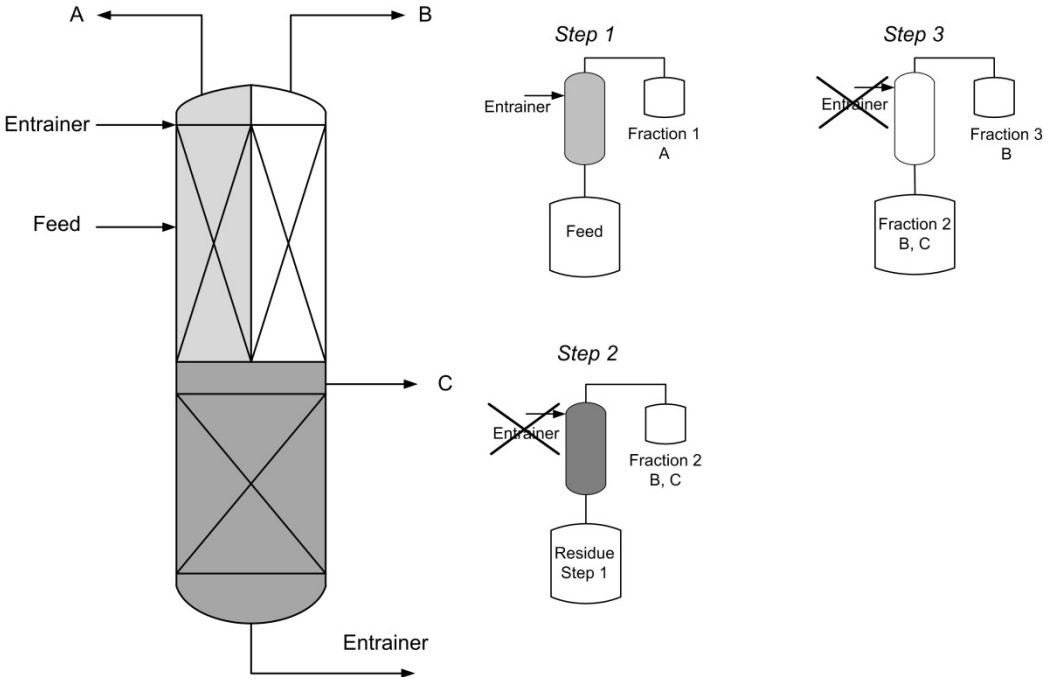

Figure 2 Approach used for experimental validation of the EDWC

The left side of the dividing wall (separate A from the entrainer and B) was approximated in the batch column by charging the feed to the bottom vessel and feeding the entrainer constantly to the top of the column (step 1). The distillate flow showed high purities of component A and, thus, the principle separation was proofed. The bottom section of the EDWC should separate pure entrainer in the bottom of the section and a mixture of B and C overhead. This was approximated in step 2 by simply using the residue of step 1(B,C, Entrainer, no A). The right section of the column should separate component B from C (step 3). Therefore the distillate of step 2 was used (only B and C) and distilled. Overhead pure B was received. So the batch distillation did proof the principle of the extractive distillation. Also the previous developed thermodynamic model was applied to describe the three steps of this batch distillation. All trends and compositions were in very good accordance with the experimental results. Therefore the model was successfully validated and further piloting was disclaimed. The design of the production scale column (diameter, number of stages, heat duty etc.) was based only on simulation studies with the validated model.

2.2.3 Unit operation modeling

In the commercially available flowsheeting tools (e.g. ChemCad or Aspen Plus) are no unit operation models for DWC or EDWC available. So the user has to build its model. The applied approach is shown in Figure 3. As the real column the model possess two condensers and one reboiler. The left and the right part of the dividing wall is represented by a column (with a condenser and no reboiler each). The lower column represents the part below the dividing wall and is equipped with a reboiler and no condenser. Via an additional sidedraw in the lower column component C is discharged. The final column design (e.g. number of stages in each section, feed locations) was carried out by using the simulation model shown in Figure 3 and carry out optimization runs and sensitivity analysis using the ChemCad inherent tools.

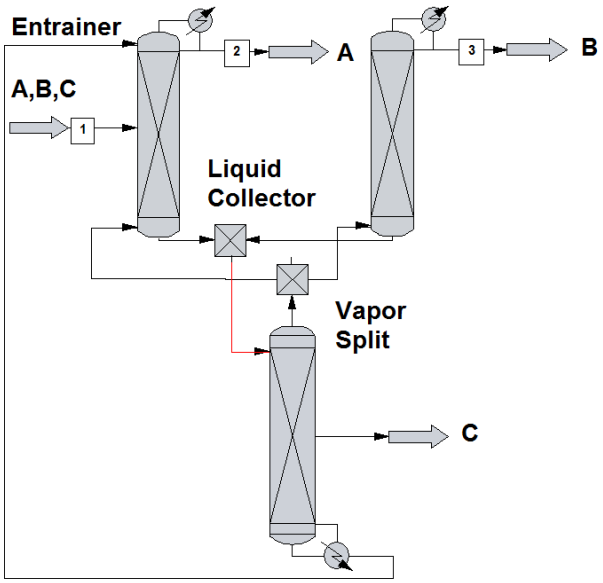

Figure 3 Extractive Dividing Wall simulation model

2.2.4 Production plant

The control loop uses only PI controllers and is straight-forward and shown in Figure 4. The feed is maintained at a fixed setpoint. The bottom level is maintained by level control acting on the bottom stream. The differential pressure, and, hence, the hydrodynamic regime over the column, is kept constant by manipulating the reboiler duty. This approach is frequently used at Lonza's dividing wall distillation columns and allows a stable operation of the column ensuring that the column is constantly operated in a desired window of the gas and the liquid load.

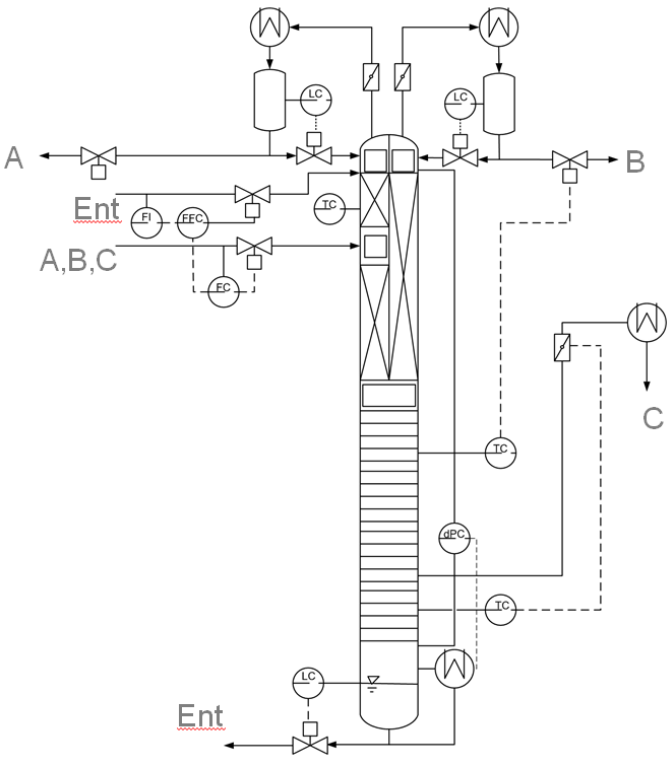

Figure 4 Applied control scheme for the commercial size Extractive Dividing wall column

Controlling the distillate stream and the side draw by maintaining sensitive temperatures along the column keeps the temperature profile stable. The entrainer flow is set on a specific ratio of the feed stream and controlled by mass flow meters. The component C (vapor draw off) is regulated by a control valve in the vapor line and this controls the temperature below the side draw. Regarding the control loops on the right hand side: By this configuration C is separated from B by the temperature control loop above the side draw and C is separated from the entrainer by the temperature control loop below the side draw. The instrumentation and control loops discussed here showed very good performance and allow a stable operation of the column.

3. Conclusions

The combination of the concept of extractive distillation with the concept of dividing wall column creating an Extractive Dividing Wall Column proved to be very beneficial. The CAPEX was reduced about 40%. The thermodynamic model used for the simulation comprised partly predictive methods and partly phase equilibrium measurements. A model validation was carried out by special designed lab-batch-distillation. The design and layout of the column was carried out based only on simulation studies. No piloting was carried out. The operational-expirience of the commercial size column proved the rightness of this approach. The controllabiltiy of the column is very good. The column is in operation since 2012. The predicted and desired puritys and yields were always achieved.

Acknowledgements

The authors would like to thank the BASF colleagues for the scientific exchange and for generously granting a license agreement.
We are gratefoul for the contribution of Jan-Oliver Drunsel (Technical University of Kaiserslautern) in regard to entrainer selection and measurement of phase equilibria.

References

[1] L. Humphrey, Separation processes: playing a critical role, *Chemical Engineering Progress*, 91(10) (1995), 31–32.
[2] N. Asprion, G. Kaibel: Dividing wall columns: Fundamentals and recent advances, *Chemical Engineering and Processing*, 49 (2010), 139-146
[3] Y. C. Ho, J. D. Ward, C. C. Yu: Quantifying potential energy savings of divided wall columns based on degree of remixing, *Industrial & Engineering Chemistry Research,* 50 (2011), 1473–1487.
[4] O. Yildrim, A. A. Kiss, E. Y. Kenig: Dividing wall columns in chemical process industry: A review on current activities, *Separation and Purification Technology*, 80 (2011), 403-417.
[5] B. Kolbe, S. Wenzel: Novel distillation concepts using one-shell columns, *Chemical Engineering and Processing: Process Intensification*, 43 (2004). 339-346
[6] C. Bravo-Bravo, J.G. Segovia-Hernandez, C. Gutierrez-Antonio, A. L. Duran, A. Bonilla-Petriciolet, A. Briones-Ramirez: *Extractive Dividing Wall Column: Design and Optimization,* Ind. Eng. Chem. Res. (49), 2010, 3672-3688
[7] B. Heida: *Method for extractive distillation*, EU Patent EP 1 596 954 B1 **2010** (filed 2003)

Pilot plant mass transfer efficiency evaluation for toluene + methylcyclohexane separation by extractive distillation with [HMIM][TCB]

Esteban Quijada-Maldonado[1]; G. Wytze Meindersma[2], André B. de Haan[3]
[1]University of Santiago, Santiago, Chile
[2]Eindhoven University of Technology, Eindhoven, The Netherlands
[3]Delft University of Technology, Delft, The Netherlands.

Abstract
Separation of the close-boiling mixture: toluene – methylcyclohexane (MCH) has been carried out by extractive distillation (ED) using the ionic liquid [HMIM][TCB]. High solvent-to-feed ratios are needed to maintain one liquid phase and increased liquid phase viscosities are expected compared to the reference solvent NMP. Experiments in an extractive distillation pilot plant were carried out at a solvent-to-feed mass ratio of 5 to evaluate the effect of solvent selectivity and viscosity on the separation performance and mass transfer efficiency. The results confirm that at the used operating conditions one liquid phase was maintained and that with [HMIM][TCB] a MCH purity >99.7% could be achieved. The liquid phase viscosities in the ED column when using [HMIM][TCB] appeared four times higher than with NMP. As a result the mass transfer efficiency decreased, which was reflected in a doubling of the HETP (height equivalent to a theoretical plate) compared to NMP.

Keywords
Ionic Liquid, Extractive Distillation, Mass Transfer, Pilot Plant

1. Introduction

Ionic liquids (ILs) are potential candidates to replace conventional solvents in separation processes, such as extractive distillation (ED), as a result of their ability to enhance the separation of azeotropic/close boiling mixtures [1,2]. Due to the close boiling points and the presence of azeotropes the separation of aromatics from non-aromatics at medium aromatic content (65 - 90%) is preferably carried out through ED. Currently polar solvents such as N-methyl-2-pyrrolidone (NMP) are widely used for this separation. Recently we have shown that the IL 1-hexyl-3-methylimidazolium tetracyanoborate, [HMIM][TCB], is a promising alternative solvent given its higher selectivity and non-volatility compared to NMP [3,4]. The present work evaluates the performance of [HMIM][TCB] in an ED process for the separation of toluene (T_b=111 °C) and methylcyclohexane (MCH, T_b=101 °C) in comparison with NMP, the most commonly used solvent for this separation [1].

2. Experimental

2.1 Pilot plant

Figure 1 provides a schematic of the extractive distillation pilot column. This column is equipped with Mellapak® 750Y structured packing provided by Sulzer® and

designed to operate in continuous mode. To prevent maldistribution, the column contains three liquid distributors. An electrical thermosyphon reboiler provides energy for boiling up. During the experiments, the liquid level of this reboiler was controlled visually. At the top of the column, a vertical condenser with an internal funnel provides reflux, which is controlled by adjusting the distillate rate. Cooling water was used to condense the vapor. Heat losses are prevented to the maximum extent possible by a double layer of Armaflex HT® insulating material and an electrical tracing system. Four coriolis-type flow-meters are installed to ensure accurate flow measurements at the feed, solvent, bottoms and distillate streams. Six liquid circular collector basins are installed inside the packing segments to collect liquid samples that were analysed by GC (accuracy 2%). Along with this, the liquid temperature of the collected liquid is also measured at these points (±0.1 K). Liquid samples can also be withdrawn from the distillate stream and at the reboiler. A summary of the column dimensions is given in Table 1.

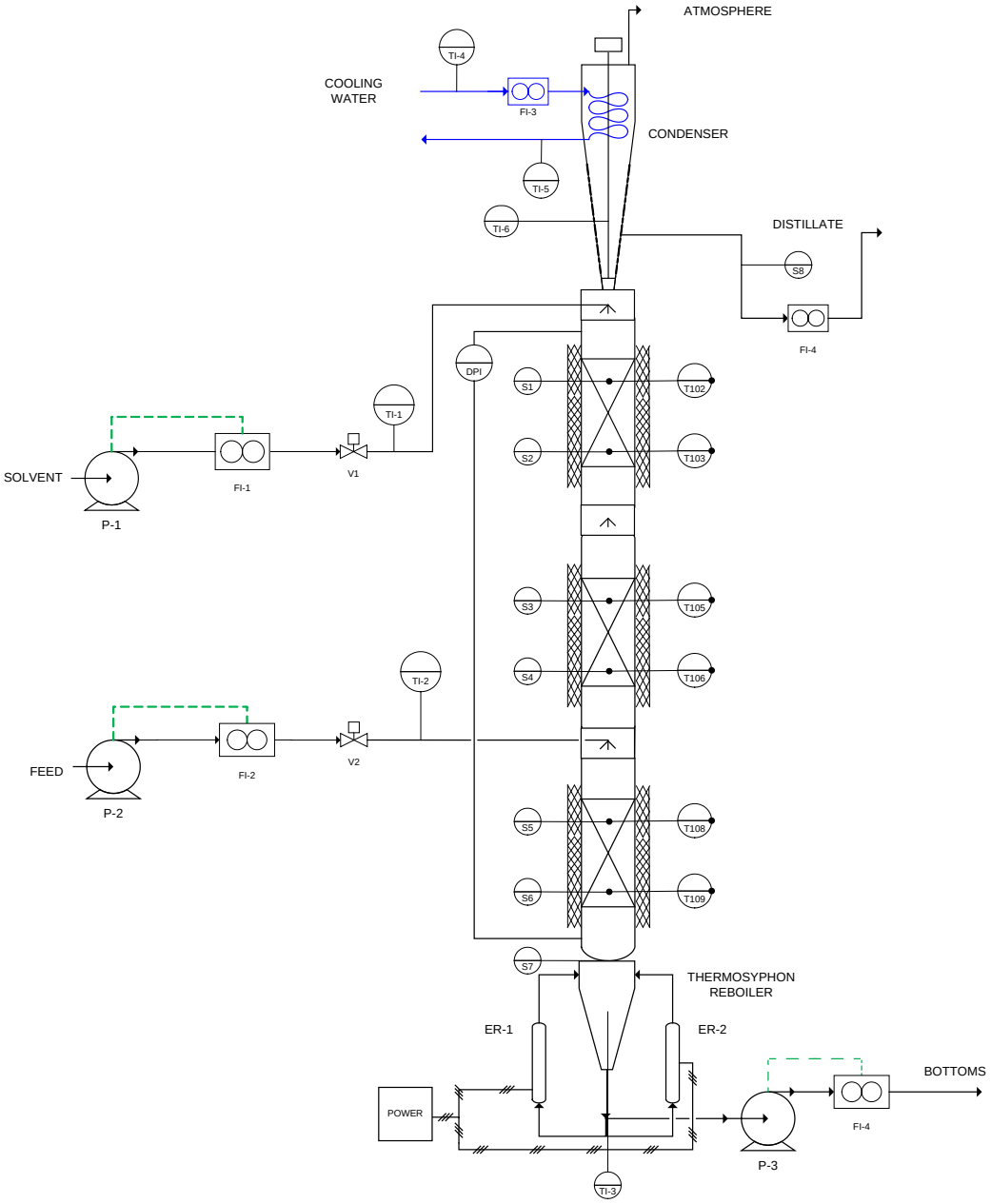

Figure 1. Simplified P&ID of the extractive distillation pilot column

Table 1. Column dimensions

Feature	Value
Packing type	Sulzer Mellapak® 750Y
Packing height	3.120 [m]
Packing material	Stainless steel 316L
Column diameter	0.049 [m]

2.2 Experimental conditions

The conditions (concentration and temperature) of the feed and solvent streams were kept constant during all experiments. The feed flow remained constant at 2 kg/h throughout the experiment and the solvent-to-feed ratio was 5 for all experiments. The feed composition was 30% MCH and 70% toluene and the feed temperature was 90 °C. There were four runs carried out, one with NMP as the reference solvent and three with the IL [HMIM][TCB] as the solvent. The operational conditions of all experiments are given in Table 2.

3. Results and discussion

3.1 Top product purity

A S/F ratio of 5 was used to avoid the formation of two-liquid phases. The temperature in the column was around 100 °C near the condenser in all runs. Table 2 summarizes the results of the analyses of the top product of all runs.

Table 2. **Product purity, reboiler duty and distillate rate of all experiments.**

Solvent		Reboiler duty (kW)	Distillate rate (kg/h)	Concentration of MCH (wt%)	Concentration of toluene (wt%)	Concentration of solvent (wt%)
1a	NMP	1.02	0.3	96.5	0	3.5
1b	IL	0.61	0.3	100	0	0
2	IL	1.02	0.3	99.82	0.08	0
3	IL	1.02	0.6	99.67	0.03	0

The lowest MCH purity was obtained with NMP as solvent and the highest MCH purity with the IL as solvent. This results clearly demonstrates the advantage of the non-volatility of the IL compared to NMP, which is present in a considerable amount in the distillate. For the IL a lower reboiler duty is apparently better for the separation. The product purity is 100% with 0.61 kW and 99.82% with 1.02 kW with the same distillate rate of 0.3 kg/h. As expected a higher distillate rate results in lower product purity. The conclusion is that the pilot plant performs well and that a high purity of the product (MCH) can be achieved with [HMIM][TCB] as solvent.

3.2 Viscosity and height of transfer unit profiles

Figure 2 shows the viscosity profiles and the liquid phase height of transfer unit profiles as calculated respectively for all the experimental cases (I.a, I.b, II and III). The liquid phase viscosities were obtained experimentally using an Ubbelohde viscometer and subsequently correlated using the Eyring-Patel-Teja model [5].

Finally, the correlation has been used to calculate viscosities from the experimental composition profiles in the pilot column.

In this work, the components of the ternary mixture have relatively low surface tensions enhancing the degree of wetting of the packing surface approaching to the complete wetting. Additionally, highly viscous forces increase the degree of wetting of the packing surface. For these reasons it is considered a valid approach to estimate the liquid k_L and vapor k_V mass transfer coefficients by the Bravo et al. [6] mass transfer correlation to calculate the height of transfer units assuming full wetting of the specific packing surface a:

$$H_L = \frac{u_L}{k_L a} \qquad \text{and} \qquad H_V = \frac{u_V}{k_V a} \tag{1}$$

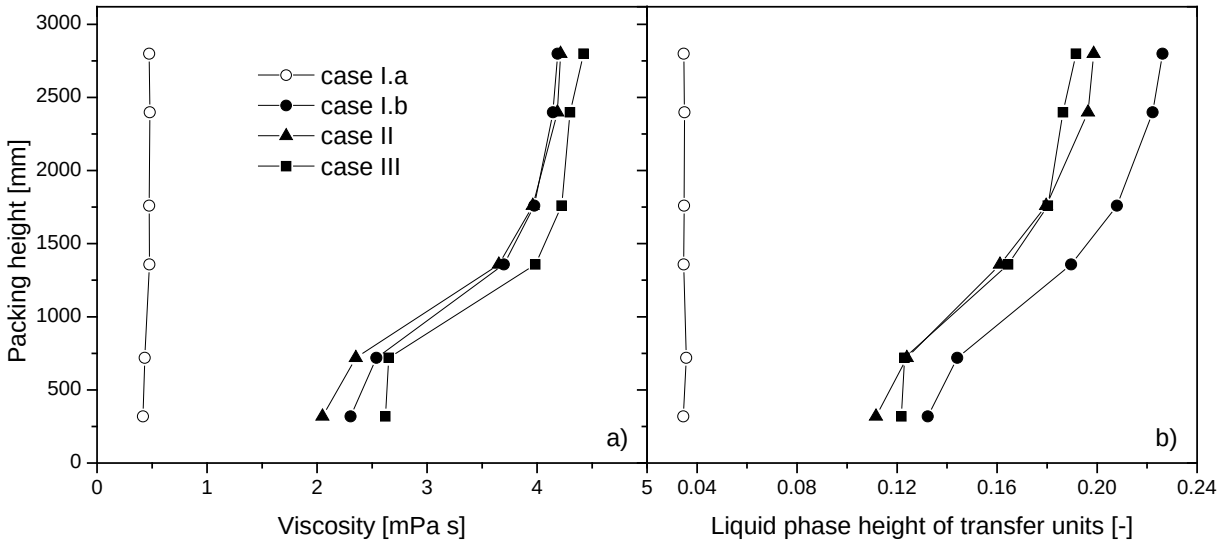

Figure 2. Calculated liquid phase viscosity (left) and liquid phase height of transfer unit (right) profiles for the ED of toluene – MCH.

In Figure 2 the influence of [HMIM][TCB] on the liquid viscosity can be clearly observed. While the separation of the toluene – methylcyclohexane mixture with NMP (Case 1.a) shows low viscosities, [HMIM][TCB] exhibits high values reaching 4 [mPa s] in the rectifying section. This behavior is observed for all three cases where the IL is involved with only small differences between them. Next, the liquid phase height of transfer unit profiles for all the cases are presented. The effect of viscosity on these profiles is clearly noticed since they follow the same trend. Case I.b shows the highest liquid phase transfer unit height values because of the lowest vapor to liquid ratio. In distillation processes it is well recognized that the main resistance to mass transfer is in the vapor phase. The large differences between NMP and the IL in figure 2 illustrate that the liquid phase may indeed provide a larger contribution to the overall mass transfer resistance when using a more viscous IL.

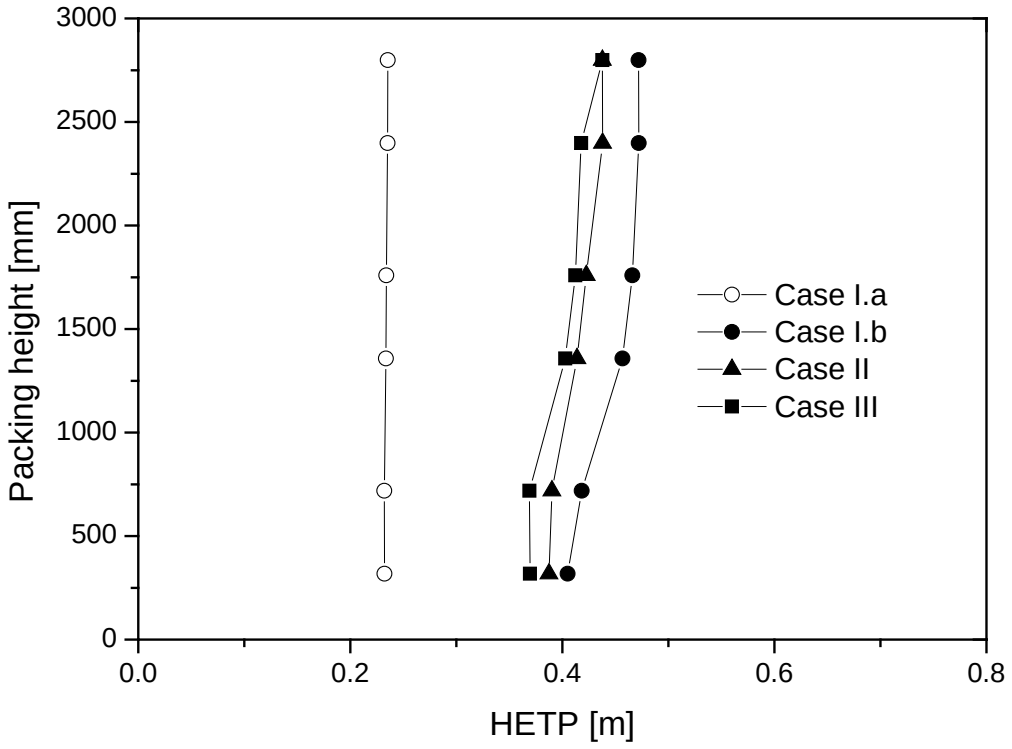

Figure 3. Calculated HETP profiles for the ED of toluene – methylcyclohexane for all studied cases.

3.3 Comparison of HETP

The mass transfer efficiency in the packed column is expressed by the height equivalent to a theoretical plate:

$$HETP = H_{OV}\,\frac{\ln(L)}{L-1} \qquad (2)$$

in which the overall height of transfer units is calculated as:

$$H_{OV} = H_V + L H_L \qquad (3)$$

which is composed of the height of a transfer unit in the vapor phase, H_V and the height of transfer unit in the vapor phase times the stripping factor, $L H_L$. The HETP has been calculated from the experimental results using the following approach (for details see [6]). The stripping factor L is obtained from the experimental liquid phase compositions from the pilot plant and using the UNIQUAC model parameters [7]. By doing this, it is assumed that the compositions in the liquid phase are in equilibrium with the calculated compositions in the vapor phase. Hereafter, the obtained vapor compositions are used to calculate the mass transfer coefficients in the vapor phase. Next, the liquid and vapor molar flow rates are calculated using ASPEN® Plus in equilibrium mode and taking into account the operating conditions from every

experiment. Finally, the superficial velocities in the vapor and liquid phases are calculated based on the molar vapor and liquid flow rates respectively.

Figure 3 shows the calculated HETP profiles over the ED pilot plant for all the cases. It can be observed that the impact of the liquid phase resistance on the mass transfer efficiency is significant. As previously noticed, the high viscosities produced inside the pilot plant by the high *S/F* ratios when using [HMIM][TCB], resulted in a decrease of mass transfer efficiency with regard to the reference solvent NMP even though the use of the IL solvent produces much higher relative volatilities, 9.4 instead of 2.8 for NMP. As a result the HETP when using [HMIM][TCB] is about twice as high as the HETP when using NMP. This also illustrates that the higher relative volatility in case of the IL partly compensates the much stronger effect of the IL on liquid viscosity and liquid phase transfer unit, as shown in figure 2.

4. Conclusions

The operation and the mass transfer efficiency for the separation of toluene – methylcyclohexane mixtures using the ionic liquid 1-hexyl-3-methylimidazolium tetracyanoborate and the reference solvent *N*-methyl-2-pyrrolidone were compared in an extractive distillation pilot plant equipped with Mellapak® 750Y structured packing.

With the IL a more pure distillate was obtained, mainly due to its non-volatility. Compared to NMP high viscosities were observed as a consequence of the high solvent-to-feed ratios needed to avoid the formation of two phases and the relatively high viscosity of the ionic liquid. As a result the use of the IL as solvent exhibited lower mass transfer efficiencies for all the studied cases. The HETPs when using [HMIM][TCB] were almost as twice as high as obtained with NMP.

Acknowledgements

This research was carried out with financial support of the Ministry of Economic Affairs, Agriculture and Innovation, EOS Long Term program, project number EOSLT06016, supervised by AgentschapNL.

References

1. J.C. Gentry, S. Kumar, R.Wright-Wytcherley, *Hydrocarbon Process.* 93(2004) 62-66
2. Z.Lei, C. Li and B.Chen, *Sep.Purif.Rev.,* 32(2003) 121-213
3. J.P. Gutierrez, G.W. Meindersma, A.B. de Haan, *Ind. Eng. Chem. Res.* 51(2012) 11518-11529
4. J.P. Gutierrez, *PhD Thesis Eindhoven University of Technology* (2013)
5. E. Quijada Maldonado, *PhD Thesis Eindhoven University of Technology* (2013)
6. J.L.Bravo, J.A.Rocha, and J.R.Fair, *Hydrocarbon Process*., 64(1985) 91-95
7. J.P.Gutierrez, W.Meindersma, and A.B.de Haan, *J.Chem.Thermodyn.* 43(2011) 1672-1677

Process analysis of microwave assisted reactive distillation

Kathrin Werth[1], Anton A. Kiss[2], Giorgos Stefanidis[3], Philip Lutze[1]

[1]Laboratory of Fluid Separations, TU Dortmund University, Dortmund, Germany;
[2]AkzoNobel Research, Development & Innovation, Deventer, Netherlands;
[3]Laboratory of Intensified Reaction & Separation Systems, Delft University of Technology, Delft, Netherlands

Abstract

A promising approach to intensify reactive distillation processes is the application of microwave fields. Recent research results indicate that microwave radiation might affect the thermal separation of molecules and accelerate chemical reactions. To determine the potential of microwave assisted reactive distillation in a first instance the separation of binary mixtures with microwave and conventional heating is investigated experimentally. The binary mixtures consist of ethanol which is a good microwave absorber, and a carbonate which is relatively transparent to microwaves – thus aiming at the preferred evaporation of ethanol. The experimental results indicate that there is no evidence for the influence of the applied microwave field on the thermal separation of these binary mixtures. The composition of distillate and bottom does not differ for conventional and microwave heating at macroscopic scale. Thus no enhancement of separation efficiency in distillation could be observed comparing the conventional and microwave distillation experiments. The potential impact of microwave radiation on the reaction is studied theoretically considering selective superheating of the catalyst by microwaves. The simulation results of the reactive distillation process indicate that no significant enhancement of conversion is possible. Consequently the performance of the reactive distillation process could not be improved by microwaves, neither on separation nor reaction level.

Keywords

Distillation, microwave assisted processes, reactive distillation

1. Introduction

Reactive distillation (RD) integrates reaction and separation into one apparatus this leading to increased conversion and selectivity by overcoming equilibrium limitations. However, its application is restricted by a common operating window between reaction and separation, while the achieved purities may still be limited by the occurrence of azeotropes. In chemical synthesis it is known that microwaves (MW) have the potential to enhance reaction rates [1]. Furthermore, recent research results indicate that MW radiation may affect the thermal separation of mixtures by e.g. increasing the concentration of the low boiling components in vapor [2], and may even influence the position of an azeotrope in terms of temperature and composition [3]. Therefore, a promising approach to intensify RD and widen its application window is the integration of MW fields into RD columns.

To prove the feasibility and the potential of the concept of MW assisted RD a systematic investigation of the impact of MW radiation on the thermal separation of

mixtures, and on the reaction is necessary. For that reason the transesterification of dimethyl carbonate with ethanol to produce diethyl carbonate is chosen as case-study. This reaction has been successfully realised in a RD column already [4]. Since the effects and mechanisms of MW heating are still not understood in the first step both separation and reaction are analysed separately. In the following an experimental investigation of the influence of MW radiation on the VLE and distillation of binary mixtures is presented. Subsequently a theoretical study of the MW assisted RD process based on current experimental data is described briefly.

2. Materials and methods

It is shown in literature that the boiling behavior of pure components can be affected in an electromagnetic field due to a number of reasons, e.g. superheating [5] or surface hydrodynamic instabilities [6]. The change in boiling behavior under MW radiation might also influence the evaporation of mixtures. Therefore, we wanted to study whether the thermal separation of binary mixtures can be favorably disturbed (i.e. enhancement of separation efficiency) in the presence of a MW field.
In literature it is claimed that one possible reason for the effect of MWs on the thermal separation of mixtures might be selective heating of components in MW fields caused by their different dielectric properties. Components which are capable to convert electromagnetic energy into heat very easily (e.g. polar components with a high dielectric loss) might be evaporated preferentially [3]. However, components which are not affected strongly by the MW field - such as nonpolar components with low dielectric loss - may remain mainly in the liquid phase. The dielectric loss describes the amount of input MW energy which is lost to the sample by heat dissipation [7]. To identify the effect of MW radiation on the evaporation behavior two different binary mixtures were chosen, each consisting of one component which is strongly affected by MWs (alcohol) and a second component which is relatively transparent to MWs (carbonate). Because of its high ability to store and convert electromagnetic energy into thermal energy ethanol (EtOH) was selected as the component which is affected by MWs very well. Dimethyl carbonate (DMC) and diethyl carbonate (DEC) represent components which would not be affected that much because a low dielectric loss of the components can be assumed. All of these components are present in the transesterification reaction of dimethyl carbonate with ethanol which is a reaction conducted in RD columns [4]. The system of DEC and ethanol shows ideal thermodynamic phase behavior with ethanol as low boiling component. In the DMC/ethanol systems a minimum azeotrope is present.

The experiments were performed in a small lab scale distillation setups. To evaluate the results experiments were conducted with both MW heating and conventional heating. The distillation setup (Figure 1) consists of a glass flask which was placed in the reboiler and was connected via glass tube to a distillation head with total condenser. In the MW experiments a Discover CEM single-mode microwave cavity was used as reboiler while the conventional heating experiments were performed with a heating mantle. The temperature is measured near the vapor liquid interface with fiber optic sensors which are appropriate for applications in MW fields.
Binary mixtures of different compositions were filled into the glass flask and the liquid was stirred continuously to guaranty a good temperature distribution. All experiments were run under total reflux conditions at atmospheric pressure. For the MW heating experiments a constant MW power was applied. MW power between 50 and 100W were chosen depending on the composition of the feed mixture to control the

evaporation rate and minimize the superheating of the liquid. When steady state was reached samples of distillate and bottom were taken. The distillate sample is taken at the top of the column from the condensed vapor and the bottom sample is taken directly from the reboiler. The composition of both samples was determined via gas chromatography.

Figure 1: Lab scale distillation setup for microwave experiments, flowing conditions indicated.

3. Experimental results

Following the results of the conventional and microwave assisted distillation experiments for the binary systems (DMC/ethanol and DEC/ethanol) are presented. Figure 2 shows the results for the distillation of DMC and ethanol for some selected experiments. The composition of distillate and bottom is displayed as molar fraction of ethanol at the top of the column or respectively in the reboiler similar to a common concentration profile in distillation columns.

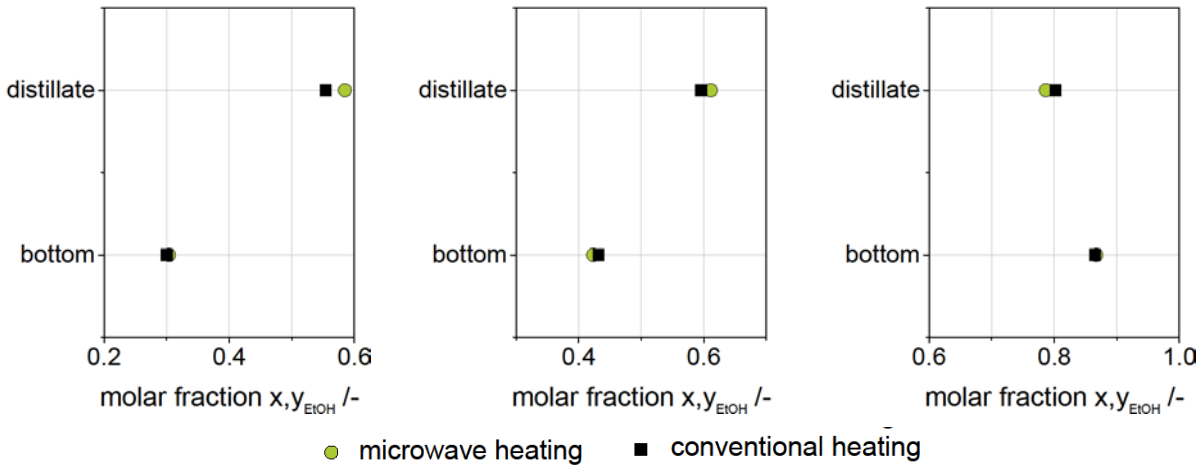

Figure 2: Molar fraction of ethanol in distillate and bottom for different feed composition of ethanol and DMC, each for conventional and MW assisted distillation experiment.

For a given bottom composition the molar fraction of ethanol in distillate is similar for conventional and MW assisted distillation experiments. Considering the uncertainties of measurements the slight difference in compositions cannot be regarded as a MW effect. One key issue is the temperature measurement because the measured values strongly depend on the position of the fiber optic sensor in the liquid. Thus no similar temperature in the reboiler can be ensured in the conventional and MW experiments (deviation around 1-2°C). It should be noted that in the setup also the temperature profile in the column cannot be measured. Furthermore, the analysis error of the gas chromatography (GC) should be taken into account (1-2.2%). There are also some unknown parameters which should be considered here. Since the absorbed MW power cannot be measured in the CEM microwave cavity the energy input and thus the reboiler heat duty is unknown. In addition, no information is available about the MW field – such as uniformity, stationarity or geometry.

An overview of all experimental results comparing the distillation under conventional and MW heating is provided in Figure 3. The molar fraction of ethanol in the distillate at the top of the column is plotted versus the corresponding molar fraction of ethanol in the bottom. One should keep in mind that in this set of experiments no vapor liquid equilibrium (VLE) was measured but a multistage distillation was considered.
The molar fraction of ethanol in distillate and bottom are in good agreement for conventional and MW assisted distillation. The separation behavior of both investigated binary mixtures in the distillation column setup does not change significantly for conventional and MW heating. If MW radiation has a strong influence on the evaporation in the bottom a change of vapour composition at the top of the column would be expected.

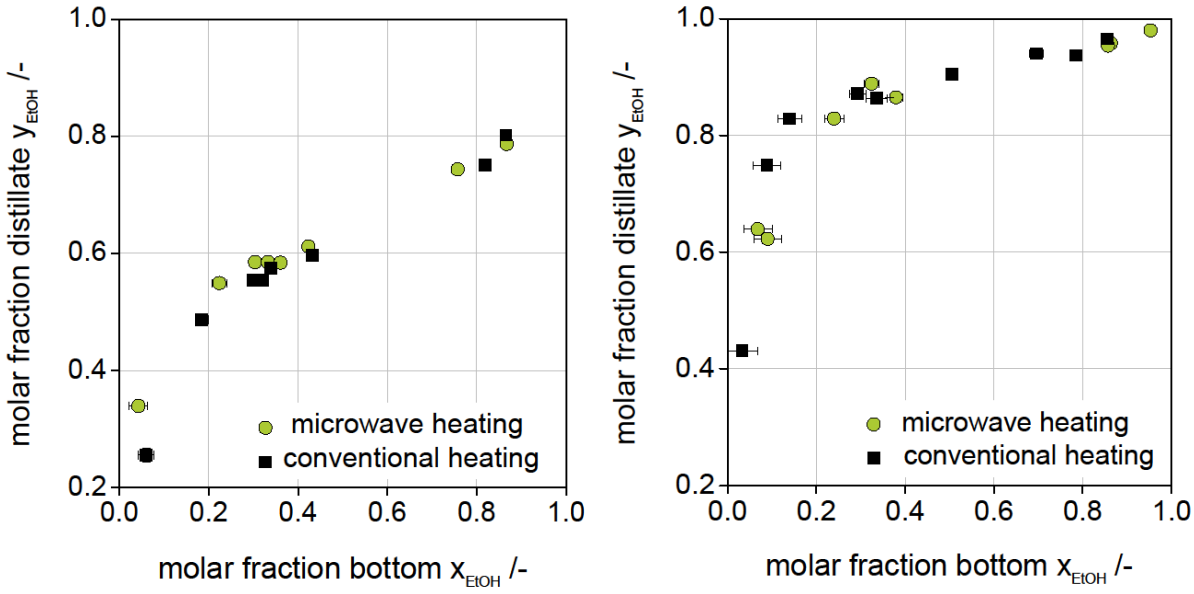

Figure 3: Molar fraction of ethanol in distillate and bottom for conventional and MW assisted distillation experiments for the binary system DMC/ethanol (left) and DEC/ethanol (right).

4. Discussion

MW assisted RD aims at a more efficient separation and accelerated chemical reaction leading to an improved process performance. Following the influence of MWs on the separation and reaction is discussed.

4.1 Influence of microwaves on the separation

In the conducted experiments the targeted impact that MWs enhance the separation efficiency in thermal separation is not observed on the macroscopic distillation scale. Also if there might be a small effect on the equilibrium composition at the vapor liquid interface when a MW field is applied the effect is dominated by the mass transfer in the still and in the column. However, it cannot be excluded that MW radiation has an effect on the separation when using MWs at micro scale, directly at vapor liquid interface.

Furthermore, the hypothesis that MWs might shift the azeotrope as proposed in literature [3] was investigated for the non-ideal system of DMC and ethanol. The results indicate that an influence of MW radiation on the VLE cannot be verified experimentally because otherwise the azeotrope would have been shifted, which is not the case here. However, no influence on the position of the azeotrope in terms of temperature and composition could be observed. In none of the distillation experiments an enrichment of distillate above the azeotropic composition was possible. But it should be noted that the dielectric properties which are changing with composition and temperature are unknown for the DMC/ethanol system. It might be possible that there are more appropriate systems for which the effect of selective heating (strongly depending on the dielectric properties of the mixture) may be more pronounced. The measurement of the dielectric properties would be necessary in order to get further insight.

4.2 Influence of microwaves on the reactive distillation process

Although no effect of an applied MW field in the separation was found, MWs may still have an impact on RD processes. Appling a MW field in the reactive section of the RD column could lead to local heating (e.g. hot spots on the solid catalyst) and thus enhanced reaction rates and higher conversion. To determine the potential of MW assisted RD processes an adapted model was developed based on a detailed model of conventional RD [8]. The adapted reaction model integrates a selective superheating of the catalyst into the Arrhenius approach.

Conventionally the transesterification of DMC with ethanol is catalyzed homogeneously by sodium ethoxide because the reaction rates of common heterogeneous catalysts are too low [9]. In homogeneously catalyzed RD no selective heating of catalyst would be possible due to good heat transfer in liquid phase. Therefore, reaction temperature and thus reaction rate is limited by the boiling temperature of the system. Even though MW heating might lead to elevated boiling temperatures, for this system around 10K higher [5], this is not enough to remarkably improve column performance since the reaction rate is already fast under conventional conditions.

But the local heating of solid catalysts might be an option to enable a heterogeneously catalyzed reaction which would allow a simplified catalyst recycling. In the simulation studies a MW field was integrated in the reactive section of the RD column to generate an additional power input and simulate a local heating of the catalyst. The results showed that very high superheating ($\Delta T>20K$) would be necessary to enhance reaction rates significantly. However, conversion is still very low. Furthermore, the realization of such high superheating in the column would not

be possible so heterogeneous catalysts would not be appropriate for this MW assisted RD process.

5. Conclusions

In this study the feasibility of MW assisted RD was evaluated. First the influence of MW radiation on the separation of binary mixtures was investigated experimentally, by comparing distillation using conventional and MW heating. Then the influence of MWs on the chemical reaction was determined theoretically.

The distillation with conventional and MW heating showed comparable results for the compositions of distillate and bottom for a given feed mixture. In general an influence on the evaporation behavior by applying a MW field could not be observed. Taking the uncertainties of measurement and the unknown parameter into account the deviation in distillate and bottom composition for the conventional and MW experiment is negligible and no microwave effect could be assumed. In the theoretical study of the MW assisted RD it was investigated if enhanced reaction rates and thus higher conversion could be reached by applying a MW field in the reactive section of the column. But no remarkable effect of MWs on the performance of the RD process could be found.

Hence, the current results indicate that for the investigated chemical system the integration of a MW field into the RD column will neither enhance the separation efficiency at macroscopic scale as present in a RD column nor enhance the reaction rate significantly.

Acknowledgements

The research leading to these results has received funding from the European Community‘s Seventh Framework Programme under grant agreement no. FP7-NMP-2012-309874.

References

[1] P. Lidström et al., *Microwave assisted organic synthesis – a review*, Tetrahedron 57 (2001) 9225-9283.

[2] E. Altman et al., *Process Intensification of Reactive Distillation for the Synthesis of n-Propyl Propionate: The Effects of Microwave Radiation on Molecular Separation and Esterification Reaction,* Ind. Eng. Chem. Res. 49 (2010) 10287-10296.

[3] X. Gao et al., *Influence of a microwave irradiation field on vapor–liquid equilibrium*, Chem. Eng. Sci. 90 (2013) 213-220.

[4] T. Keller et al., *Transesterification of dimethyl carbonate with ethanol in a pilot-scale reactive distillation column,* Chem. Eng. J. 180 (2012) 309-322.

[5] F. Chemat et al., *Microwave super-heated boiling of organic liquids: Origin, effect and application*, Chem. Eng. Technol. 24 (2001) 735-744.

[6] D. Stuerga et al., *Microwave heating as a tool for coupling Marangoni and Hickman instabilities*, Springer, 1996.

[7] C.O. Kappe et al., *Practical Microwave Synthesis for Organic Chemists*, Wiley-VCH, 2009.

[8] T. Keller and A. Górak, *Modelling of homogeneously catalysed reactive distillation processes in packed columns: Experimental model validation,* Comput. Chem. Eng. 48 (2013) 74-88.

[9] T. Keller et al., *Transesterification of Dimethyl Carbonate with Ethanol To Form Ethyl Methyl Carbonate and Diethyl Carbonate: A Comprehensive Study on Chemical Equilibrium and Reaction Kinetics,* Ind. Eng. Chem. Res. 50 (2011) 11073-11086.

Recovery of PVA Byproduct Methyl Acetate via Reactive and Extractive Distillation

*Lida Xie, Liying Cai, Huidong Zheng, Suying Zhao**
[1]Lida Xie, Fuzhou University, Fuzhou,China;
[2]Liying Cai, Fuzhou University, Fuzhou,China;
[3]Huidong Zheng, Fuzhou University, Fuzhou,China;
[4]Suying Zhao, Fuzhou University, Fuzhou,China;*

Abstract

A packed-bed reactive and extractive distillation (RED) column is developed to recovery PVA by-product MA. The azeotrope of MA and MeOH which is provided by a PVA plant is used as experimental materials. MeOH is transformed to MA in the RED column which is catalyzed by ion-exchange catalyst. The effect of four operation parameters, *R* the reflux ratio, *S/F* the volume ratio of the extractive solvent to the feed mixture, the composition of the extraction agent, S_V the initial space velocity on the performance of the RED column are investigated. According to the experimental results, a set of operational parameters is recommended. Under the conditions of *R* 2.5, *S/F* 2, w_{AA} 3.5~5%, S_V 0.16 ~0.33 h^{-1}, the conversion of MeOH is about 96%, the purity of top product MA is higher than 99.5%. Compared to the traditional MA recovery process in the production of PVA, this reactive and extractive distillation process is energy-saving and environment protection for the simplification of recovery process.

Keywords

Methyl acetate; Reactive and extractive distillation； Polyvinyl alcohol

1. Introduction

Methyl acetate (MA) is one of bulk commodity chemicals and is employed as the solvent in the production of glues, nail polish removers, perfumery and dyes etc, or as the reactant or the extracting agent. The joint production of MA in the manufacturing of PVA is huge, and approximate 1.68 ton of MA is generated per ton PVA.[1] But this byproduct MA could hardly be used directly in industry for its a mixture, which is typically co-mingled in a stream containing MA, methanol (MeOH), light organic impurities, and potentially polymer solids and water. At present, the hydrolysis is applied to deal with this MA byproduct industrially, and MA is hydrolyzed into acetic acid (HAc) and MeOH, then both of them are recovered subsequently.[2] Because the MA hydrolysis reaction is reversible and the reaction equilibrium constant is relatively small[3], reactive distillation is a favorable alternative for the advantages compared to the conventional fixed-bed process: (a) lower capital investment, (b) lower energy consumption, and (c) higher product yields.[4] However, for the strong restrictions on HAc concentration in the hydrolysate, the industrial MA hydrolysis conversion is around 70% even with reactive distillation. Multiple distillation/separation steps are required to recover MeOH and HAc from MA-MeOH-HAc-water quaternary system for the existence of two azeotropes of MA-water and MA-MeOH. Recovering high purity MA with the esterification reaction of methanol and acetate acid in a RED column will overcome the separation problem of azeotropes. It is an attractive process comparing to the conventional MA hydrolysis process.

In this article, the performance of a packed-bed RED column for the recovery of MA from MeOH-MA azeotrope using an ion-exchange catalyst is investigated. The performance of RED column is evaluated based on the MA concentration in the top product and the conversion of MeOH. The influence of several variables for the performance of RED column is analyzed.

2. Results and discussion

The sketch of an experimental setup for the reactive and extractive distillation was shown in Figure 1, the column consisted of glass columns (28 mm inner diameter) with four major sections: the solvent recovery section (height of 400mm), the extractive distillation section (height of 160 mm), the reactor section (height of 1240 mm), and the bottom stripping section (height of 690 mm). All trials were performed at the normal temperature and pressure. The effects of operation parameters, including the reflux ratio (*R*), the volume ratio of solvent to feed (*S* / *F*), the composition of the extraction agent and the space velocity (S_V) on the purity of MA in the distillate and the conversion of MeOH were investigated.

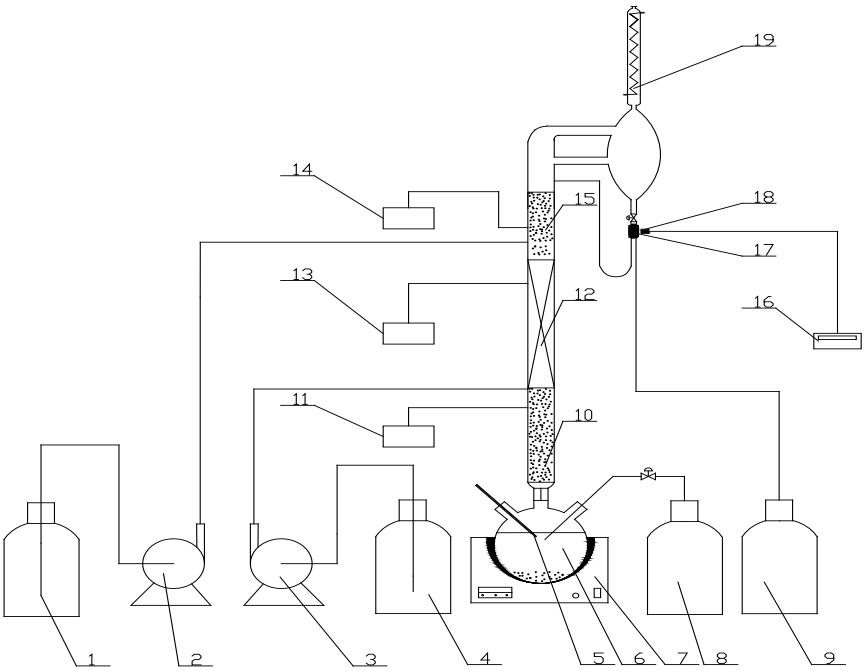

Figure 1.Sketch of reactive and extractive distillation process

(1)(4) feed tank, (2) (3) feed pump, (5) thermometer, (6) reboiler, (7) thermostatic bath, (8) bottom production tank, (9) production tank, (10) stripping section, (11),(13),(14) temperature controller, (12) reactor section, (15) extractive distillation section (16) reflux ratio controller, (17) splitter, (18) magnetic valve, (19) condenser.

2.1 Effect of the R

To investigate the effect of the *R*, operations are carried out at the *R* of 1, 2, 2.5, 3 and 4 under three *S/F* values**,** respectively.

As shown in Figure 2, the mass fraction of MA in the top product ($x_{D,MA}$) is decreased with the increase of *R* when *S/F*=1， especially when *R* is more than 2.5. The profiles of $x_{D,MA}$ are almost the same when the *S/F* is 2 and 3. The value of *R* for the maximum $x_{D,MA}$ is very close when *S/F* is 2 and 3, which means that *R*=2.5 is the optimum value when the *S/F* is range from 2 to 3. It must be noticed that if the concentration of MA in the top has to satisfy the product standard, which means that $x_{D,MA}$ is more than 99.5%, it provides a limitation for the operating conditions. Additionally, Figure 3 shows that the concentration profile is also an indicator of the MeOH conversion (X_{MeOH}), which means that high conversion always suggests a greater concentration gradient and vice versa. In fact, the relationship between the X_{MeOH} and *R* is similar to that of $x_{D,MA}$ and *R*.

The results indicate that there exists a maximum concentration of the MA in the distillate with the increasing of *R* under different *S/F*, respectively, which agrees with the conclusion that too low or high reflux ratio is not good for the separation and reaction.[4]

2.2 Effect of the S/F

As shown in Figure 3, the slope of the initial section of each curve is relatively steep which means that the improvement of conversion of MeOH is obvious by

increasing the *S/F*. However, a flat section can be seen under high *S/F* in each curve which means that little improvement of X_{MeOH} can be made when the RED column is operated in this range of *S/F*. The profiles of these curves in Figure 3 suggest that increasing the *S/F* is more efficient in increasing the X_{MeOH} under small *S/F* than under large *S/F*. The reason can be explained by two aspects. On the one hand, when *S/F* is small, increasing the *S/F* will improve the separation performance remarkably, which means that the esterification products, MA, can be removed from the reaction zone more completely; on the other hand, increasing the *S/F* will introduce additional MeOH into the reaction zone. The concentration of MeOH will be increased and the concentration of esterification products will be diluted in the reaction zone with the introduction of solvent. Both effects will promote the X_{MeOH}. However, when the *S/F* has reached a relatively large value, further increase of *S/F* has little effect on both separation and reaction. Therefore, the gradient becomes small for each line under high *S/F*.

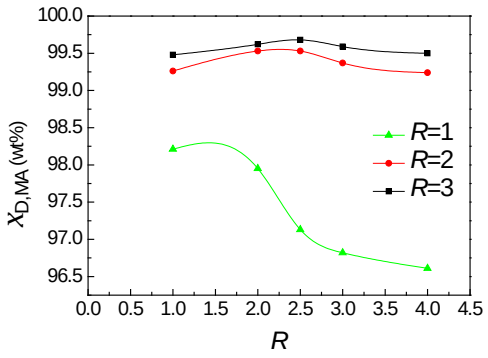

Figure 2. The influence of *R* on $x_{D,MA}$ under different *S/F*

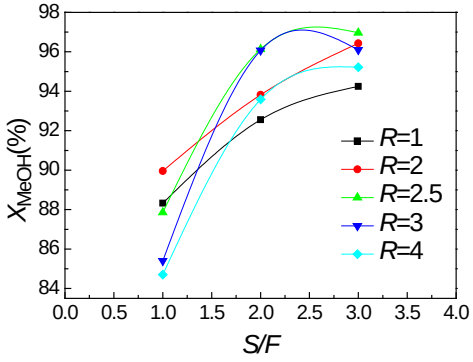

Figure 3. The influence of *S/F* on X_{MeOH} under different *R*

2.3 Effect of the composition of the extraction agent

A few acetic anhydride were added into the solvent as an adjuvant and an extraction agent, in order to improve the purity of MA. The experiments were performed at the *R* of 2.5, *S/F* of 1, 2, 3 and the mass fraction of acetic anhydride in entrainer solvent w_{AA} of 3.5wt%, 5wt%.

The experimental data are tabulated in table 1. As shown from table 1, when *S/F* is 1 and 2, the concentration of MeOH is prominently decreased, while little change can be obtained, when *S/F* =3. The concentration of water is almost keep constant except *S/F* =1. Experiments also find that the conversion of MeOH is almost the same under the same operation parameters of *R*, *S/F* and w_{AA}=0, especially when *S/F* is 2 and 3. The result shows that, the introduction of acetic anhydride in the esterification of HAc with MeOH is favorable for the acceleration of the forward reaction by Le Chatelier's principle, when the conversion of MeOH is relatively lower, the effect can be observed more significantly and vice versa, and it hardly to decrease the concentration of MeOH and water through increase w_{AA} when w_{AA} is as high as 5wt%

and *S/F* is higher than 2.

Table 1. The composition of distillate (wt%) under different w_{AA} and *S/F*

S/F	w_{AA}	$x_{D,MA}$	$x_{D,MeOH}$	$x_{D,water}$
1	3.5	97.13	1.70	1.15
	5	98.10	1.31	0.58
2	3.5	99.51	0.18	0.28
	5	99.67	0.089	0.23
3	3.5	99.68	0.076	0.23
	5	99.70	0.082	0.21

2.4 Effect of the S_V

The influence of the S_V on the composition of $x_{D,MA}$ is shown in Figure 4. The initial space velocity was varied between 0.16 and 0.34 h^{-1} at the *R* of 2.5, *S/F* of 2 and w_{AA} of 3.5wt%. Figure 4 shows that with the increasing of S_V, the concentration of MA in the top rises slowly and the rest composition in the distillate decrease slightly. A higher $x_{D,MA}$ can be expected under even large S_V value, but the experiments of more higher S_V value are restricted by liquid flooding. So higher S_V is favorable, which within the liquid flooding velocity value. In the present work, a S_V value ranging from 0.16 to 0.33 h^{-1} is recommended according to different *R* and *S/F*.

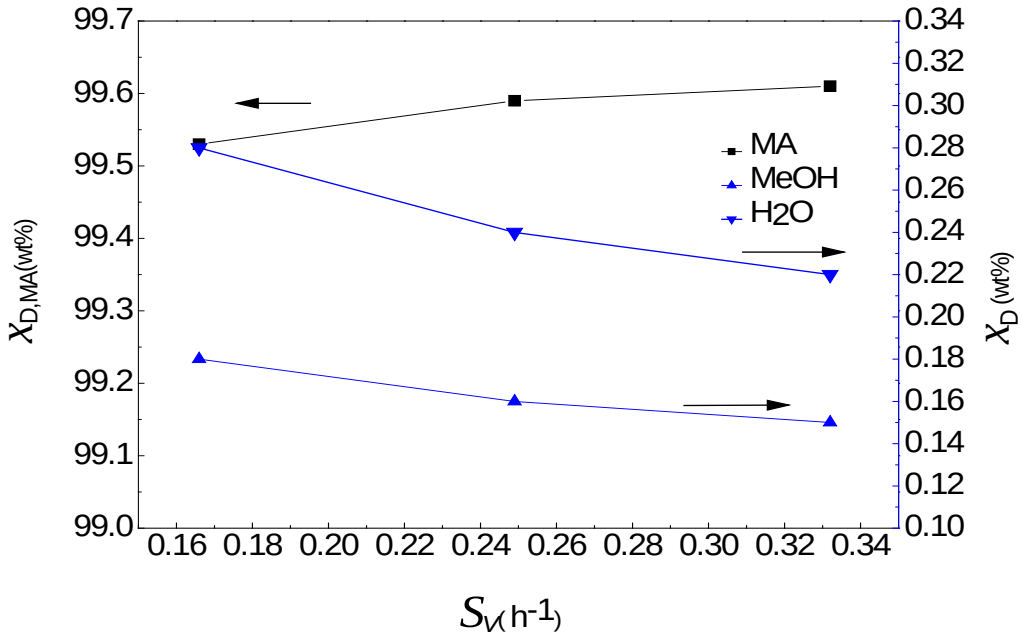

Figure 4. The influence of S_V on x_D

3. CONCLUSION

The PVA by-product MA which is co-mingled with MeOH as an azeotrope can be transformed into high-purity MA in a packed RED column. The conventional complex MA hydrolysis process, which at least including a MA-MeOH azeotrope distillation column, a MA hydrolysis RD column, a hydrolysate distillation column, an extractive column and a MeOH distillation column can be greatly simplified by a RED column. Suitable operation parameters are also recommended in this paper. The purity of MA is higher than 99.5%, the conversion of MeOH is about 96% under the recommend operational conditions.

Acknowledgement

The authors would like to thank the National Natural Science Foundation of China (Grant No. 21376053).

References

(1) Xu B, Zhang W, Zhang X, et al. Kinetic study of transesterification of methyl acetate with n -butanol catalyzed by NKC -9 [J]. International Journal of Chemical Kinetics, 2009, 41(2): 101-106.

(2) Xiao J, Liu J, Li J, et al. Increase MeOAc conversion in PVA production by replacing the fixed bed reactor with a catalytic distillation column [J]. Chemical engineering science, 2001, 56(23): 6553-6562.

(3) Du Y, Wang L. Kinetic Study on the Hydrolysis of Methyl Acetate [J]. Journal of Fuzhou University (Natural Science), 1999, 27(4): 98-102.

(4) Bessling B, Löning J M, Ohligschläger A, et al. Investigations on the synthesis of methyl acetate in a heterogeneous reactive distillation process [J]. Chemical engineering & technology, 1998, 21(5): 393-400.

Investigation on hygroscopic electrolyte solutions for capturing air humidity as an alternative drinking water resource

S. Biehler[1], M.Blicker[2], T. Hirth[1,2]
[1]Institute for Interfacial Process Engineering and Plasma Technology IGVP, University of Stuttgart, 70569 Stuttgart, Germany;
[2]Fraunhofer Institute for Interfacial Engineering and Biotechnology IGB, 70569 Stuttgart, Germany

Abstract
Scarcity of drinking water is an existent and intensifying challenge mankind is faced with. New technologies for water treatment and alternative fresh water resources are mandatory to relieve this distress. Harvesting the humidity of air using highly hygroscopic electrolyte solutions in an absorption-desorption process offers in principle an unlimited resource of drinking water, especially for areas with no access to sustainably utilisable surface or ground water sources.
In this study, different preselected electrolyte solutions were tested and compared in a flatbed reactor to evaluate their qualification as highly hygroscopic desiccants for the application of producing water from air humidity. Besides lithium chloride (LiCl) and calcium chloride ($CaCl_2$), well-known from air conditioning technology, two other salts, namely potassium formate (KCOOH) and potassium acetate (CH_3COOK), could be identified.
As a second step, the ability of a multistage vacuum membrane distillation unit was examined for desorption purpose of diluted LiCl and CH_3COOK solutions. The specific energy demand in kWh per gained kg of distillate was determined depending on the maximum heating temperature, the inlet brine concentration and the inlet brine flow rate. The results show a good performance of the system and a potentially low specific energy demand.

Keywords
water scarcity, liquid desiccant, electrolyte, membrane distillation

1. Introduction

Preliminary studies for air-conditioning purposes using aqueous solutions of electrolytes as liquid desiccants were carried out amongst others by Al-Farayedhi et al. (1), Fumo et al. (2) and Xiu-Wei et al. (3) (4). Studies regarding resourcing of drinking water were performed by Kabeel (5) as well as Audah et al. (6), all of them using LiCl and/or $CaCl_2$. Despite the main drawback of high corrosivity, LiCl exhibits very high performance in contrast to that of $CaCl_2$. Research for alternative electrolytes avoiding these drawbacks is thus mandatory.

1.1 Absorption performance in a flatbed reactor

In order to reveal an alternative electrolyte to lithium chloride (LiCl) and calcium chloride ($CaCl_2$), six other preselected aqueous solutions of electrolytes and two ionic liquids are tested in a flatbed reactor regarding their absorption performance of water vapor from a conditioned airstream. The absorption performance is determined by the decrease of absolute humidity through the reactor at different inlet air humidity aH_{in} and overall system temperature T according to Equation (1). Low values of

humidity and temperature are chosen to compare the absorption performance under relatively tough conditions and avoiding condensation throughout the entire experiment.

$$\Delta aH = aH_{out} - aH_{in} \quad (1)$$

The absolute humidity aH in g/m³ is given by Equation (2):

$$aH = \frac{p}{R_D \cdot T} = \frac{1}{R_D \cdot T} \cdot rH \cdot 611.2 \cdot e^{\frac{22.46 \cdot (T-273.15)}{243.12+(T-273.15)}} \quad (2)$$

where p is the partial pressure in Pa, R_D = 461.51 J/(kg K) is the gas constant for water vapor, T is the temperature in K and rH is the relative humidity in %. The mechanism behind the mass transfer of water from the gaseous phase to the liquid solution is based on diffusivity according to Fick's first law and may be written as Equation (3):

$$\dot{n} = k \cdot A \cdot (p - p_{sol}) \quad (3)$$

where $\dot{n}$ is the molar flux in mol/(m² s), k is the mass transfer coefficient in mol/(m² s mbar), A is the interface in m² and p and p_{sol} are the water vapor pressures in the air and over the solution respectively in mbar. The latter is dependent on the electrolyte and its concentration in the solution.

The chosen test values for the inlet air humidity are 5.00, 6.25 and 7.50 g/m³ and for the temperature 10.0, 15.0 and 20.0 °C, in total nine different combinations. The used solvent concentration is 95% of the saturation concentration depending on the temperature and the electrolyte as shown in Table 1. For electrolytes with only one value, no further tests are done. The ionic liquids are used in a pure state, as they are liquid by nature. The gas volume flow rate is kept constant at 3.73 l/min.

Besides LiCl and $CaCl_2$, six other electrolytes are tested, namely potassium formate (KCOOH), potassium acetate (CH_3COOK), lithium acetate (CH_3COOLi), magnesium bromide hexahydrate ($MgBr_2*6H_2O$), magnesium chloride ($MgCl_2$) and potassium phosphate (K_3PO_4), plus the two ionic liquids 1-ethyl-3-methylimidazolium thiocyanate and the corresponding triflate.

Electrolyte	**x1 [mass-%] 10°C**	**x2 [mass-%] 15°C**	**x3 [mass-%] 20°C**
LiCl	41.8	43.5	44.5
KCOOH	72.4	72.9	73.5
CH_3COOK	66.5	67.3	68.3
$CaCl_2$	37.8	39.0	40.5
CH_3COOLi	-	-	27.6
$MgBr_2 * 6 H_2O$	-	-	47.9
$MgCl_2$	-	-	33.4
K_3PO_4	-	-	31.5
EMIM-thiocyanate	-	-	100.0
EMIM-triflate	-	-	100.0

Table 1: Used concentrations of the investigated electrolytes at different temperatures

1.2 Desorption performance using a multistage-vacuum membrane distillation
To regenerate diluted electrolyte solutions in order to regain their physical potential and to yield the captured water, a thermally driven multi-stage vacuum membrane distillation unit from the company *memsys clearwater Pte. Ltd.* is investigated. In the unit, water vapor is produced in stage one by heating up the diluted solution. The latter flows afterwards to stage two. The produced vapor condenses at a thin plastic foil, transferring heat to stage two, causing further water evaporation due to lower system pressure. Initially introduced heat is thus be reused several times and the solution gets more and more concentrated. The condensate is collected in every stage and drained to a distillate tank. The solution exits the last stage as concentrated brine. In this investigation, a three-stage unit is used.
The two main objectives of this study are the validation of the functional capability of the unit working with high concentrated electrolyte solutions and the resulting specific energy demand q in kWh_{th}/kg. It is defined as Equation (4):

$$\boldsymbol{q = \frac{P_{heat}}{\dot{m}_{dist}}} \quad (4)$$

where P_{heat} is the heating power in kW_{th} and $\dot{m}_{dist}$ is the distillate flux in kg/h. The testing parameters are the maximum heating temperature T_{max} of 70.0, 75.0 and 80.0 °C, the feed inlet flow rate $\dot{V}$ of 1.2, 1.6 and 2.0 l/min and the feed inlet concentration x_{in} in mass-%. Aqueous solutions of LiCl and CH_3COOK are applied with varied concentrations x_{in} shown in Table 3.

2. Results and discussion

2.1 Flatbed reactor
Besides LiCl and $CaCl_2$, only CH_3COOK and KCOOH yield significant absorption performance under the testing conditions. Figure 1 displays the decrease of humidity through the reactor at different temperatures and inlet air humidities according to Equation (1).

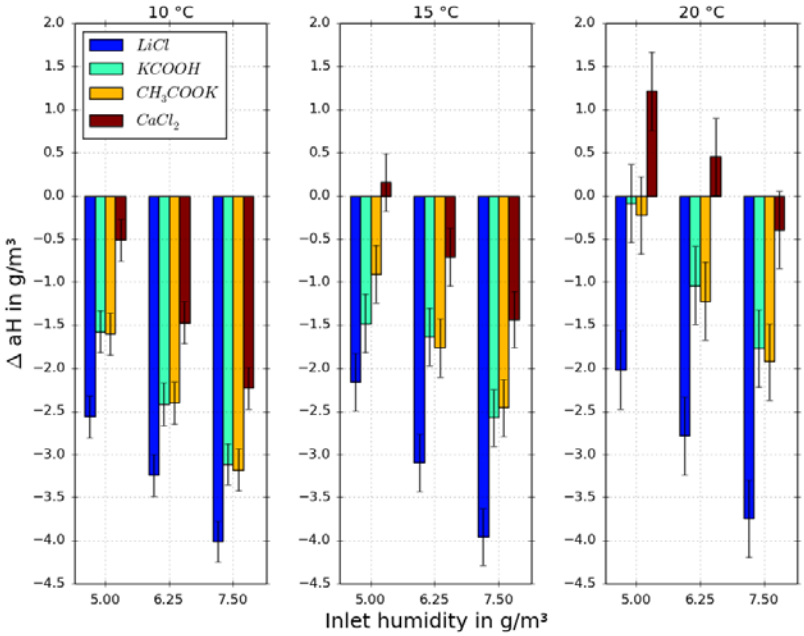

Figure 1: Decline of the absolute humidity through the reactor for four different electrolyte solutions at temperatures ranging from 10 to 20°C and air humidity ranging from 5.0 to 7.5 g/m³

Thus, negative values represent an absorption process.
LiCl shows the best overall performance followed by the two potassium electrolytes that show only a slight difference between each other. However, the concentration of KCOOH is higher. Solutions of $CaCl_2$ only absorb at temperatures of 10 and 15°C. At 20°C, all tests run with $CaCl_2$ caused an increase in humidity, hence a desorption process. The remaining electrolytes and ionic liquids exhibit very low absorption performance, or even cause desorption. At 20°C and 7.5 g/m³ inlet air humidity, the humidity changes are -0.5 g/m³ ($MgCl_2$), +6.6 g/m³ (CH_3COOLi), +3.8 g/m³ (MgBr2), +4.6 g/m³ (K_3PO_4), -1.9 g/m³ (EMIM-thiocyanate) and -1.1 g/m³ (EMIM-triflate). Therefore, these electrolytes are discarded and will not be tested under further conditions.
The relative deviations of the absorption performance of CH_3COOK, KCOOH and $CaCl_2$ compared to LiCl in % are displayed in Table 2.

T [°C]	**10**			**15**			**20**		
aF_{in} [g/m³]	**5.00**	**6.25**	**7.50**	**5.00**	**6.25**	**7.50**	**5.00**	**6.25**	**7.50**
CH_3COOK	-37.7	-25.8	-20.8	-57.8	-43.0	-37.9	-89.0	-56.1	-48.7
KCOOH	-38.6	-25.4	-22.4	-31.6	-47.1	-34.9	-95.6	-62.6	-52.7
$CaCl_2$	-80.0	-54.6	-44.4	-107.2	-77.0	-63.8	-160.1	-116.2	-89.4

Table 2: Relative deviations of the decrease of humidity in % of aqueous solutions of CH_3COOK, KCOOH and $CaCl_2$ compared to LiCl

The influence of the inlet air humidity aH_{in} on the humidity drop is dominant compared to the influence of the overall system temperature T. The inlet air humidity is directly proportional to the molar flux, in reference to Equations (2) and (3). Thus, an increase in humidity results in a higher vapor pressure, which is equal to a higher driving pressure gradient. The influence of the temperature is weak. Although, with increasing temperature, the solution concentration is higher, the negative effect of the higher temperature cannot be compensated as the value of ΔaH decreases. The solvent concentration is considered as constant during each single run.

2.2 Membrane distillation

Since a steady state distillate flux was observed throughout all experiments, the three-stage membrane unit was deemed suitable for separating water from highly concentrated electrolyte solutions.
The evaluation of the specific energy demand *q*, according to Equation (4), shows that it is minimized by lower feed inlet concentrations, lower feed flow rates and higher temperatures, independent of the electrolyte used. The results are displayed in Figure 2 and Figure 3 for CH_3COOK and LiCl, respectively. Missing values for LiCl are caused by a limited availability of the membrane system for testing. For LiCl, the range of *q* varies from 0.70 to 6.5 kWh/kg, while for CH_3COOK, values range from 0.94 to 4.8 kWh/kg. Throughout all tests, no external heat recovery of the outgoing mass flows was applied to preheat the feed.

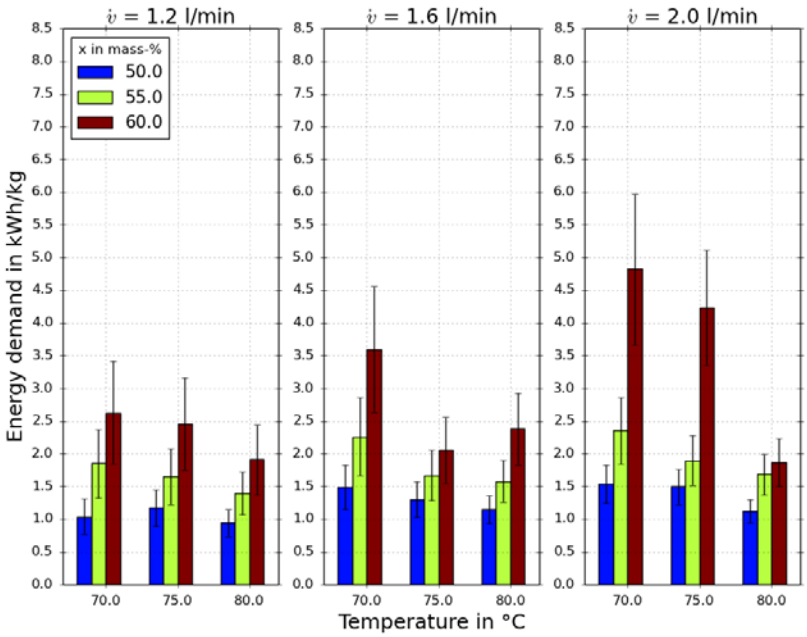

Figure 2: Specific energy demand in kWh/kg distillate for CH_3COOK at different feed flow rates, temperatures and feed concentrations

The feed inlet concentration has the highest impact on the specific energy demand, followed by the maximum system temperature and the feed flow rate. The water vapor pressure of the solutions is strongly dependent on the concentration and less dependent on the temperature, as shown in Table 3. Higher vapor pressure in stage one of the membrane unit is equivalent to a higher internal latent heat transfer and a higher distillate production. In contrast, less water vapor is separated from solutions of higher concentration, thus more sensible heat remains in the outgoing brine. Higher feed flow rate positively affects the vapor mass and heat transfer through the membrane and along with it, the distillate flow rate. But due to lower retention time more latent heat remains in the brine thus compensating this positive effect.

T [°C]		**70.0**			**80.0**		
LiCl	x [mass-%]	22.0	26.0	30.0	22.0	26.0	30.0
	p [mbar]	206.8	177.3	145.3	316.4	272.9	225.4
CH_3COOK	x [mass-%]	50.0	55.0	60.0	50.0	55.0	60.0
	p [mbar]	194.9	175.0	153.3	295.7	265.9	233.3

Table 3: Water vapor pressures in mbar over aqueous solutions of LiCl and CH_3COOK depending on applied temperature and concentration

3. Conclusions

3.1 Flatbed reactor

Two electrolytes besides LiCl and $CaCl_2$ for water vapor absorption purposes could be validated and described, namely CH_3COOK and KCOOH. Their absorption performances are very similar and range between those of LiCl and $CaCl_2$. The influence of the absolute air humidity is dominant compared to the overall system temperature. As the corrosivity of the potassium electrolytes is low compared to that of LiCl, they represent promising alternatives for air drying purposes.

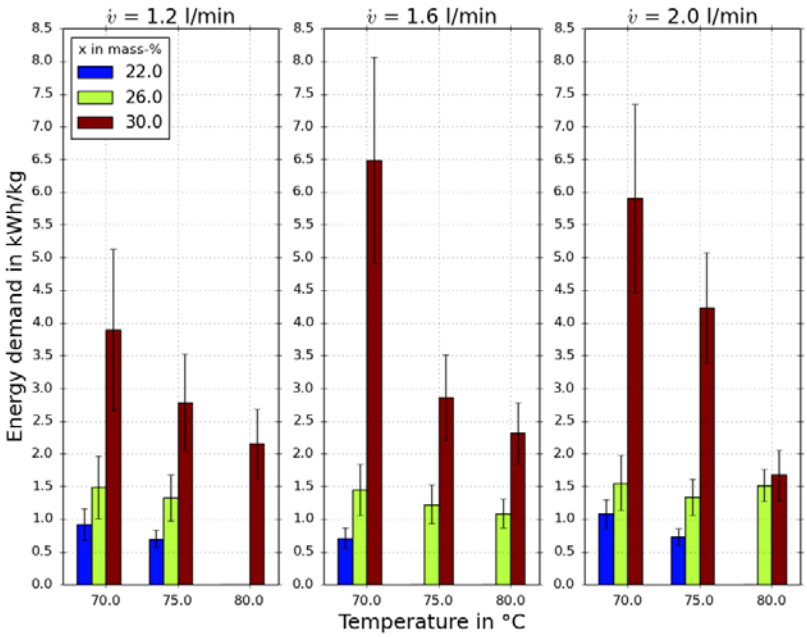

Figure 3: Specific energy demand in kWh/kg distillate for LiCl at different feed flow rates, temperatures and feed concentrations

3.2 Membrane distillation

The membrane unit was successfully tested up to 80°C using solutions of LiCl and CH_3COOK. The influence of the feed concentration, the maximum heating temperature and the feed flow rate are displayed. For the separation of water, a lower margin of the specific energy demand is attested using CH_3COOK. This will be further lowered using higher heating temperatures.

References

1. **Al-Farayedhi, A A and Gandhidasan, P and Antar, M A and Abdul Gaffar, M S.** Experimental study of an aqueous desiccant mixture system: Air dehumidification and desiccant regeneration. *Proceedings of the Institution of Mechanical Engineers, Part A: Journal of Power and Energy.* 2005, S. 669-680.

2. **Fumo, Nelson and Goswami, D. Y.** Study of an aqueous lithium chloride desiccant system: air dehumidification and desiccant regeneration. *Solar Energy.* 2002, Bd. 72, S. 351-361.

3. **Xiu-Wei, Li and Xiao-Song, Zhang and Geng, Wang and Rong-Quan, Cao.** Research on ratio selection of a mixed liquid desiccant: Mixed LiCl - CaCl2 solution. *Solar Energy.* 2008, Bd. 82, S. 1161-1171.

4. **Xiu-Wei, Li and Xiao-Song,Zhang and Shuo,Quan.** Single-stage and double-stage photovoltaic driven regeneration for liquid desiccant cooling system. *Applied Energy.* 2011, Bd. 88, S. 4908-4917.

5. **Kabeel, A.E.** Water production from air using multi-shelves solar glass pyramid system. *Renewable Energy.* 2007, Bd. 32, S. 157-172.

6. **Audah, N. and Ghaddar, N. and Ghali, K.** Optimized solar-powered liquid desiccant system to supply building fresh water and cooling needs. *Applied Energy.* 2011, Bd. 88, S. 3726-3736.

Design of Energy Efficient Distillation Process for Azeotropic Waste Photoresist Thinner Recovery

*Yus Donald Chaniago[1], Gyeong Min Kim[1], Bong Gu Choi[1], Riezqa Andika[1], Kee-kahb Koo[2] and Moonyong Lee[1]**
[1]Yeungnam University, Gyeongsan, Republic of Korea
[2]Sogang University, Seoul, Republic of Korea

**Email: (mynlee@yu.ac.kr)*

Abstract

In TFT-LCD and IC manufacturing processes, photoresistor thinner generates waste thinner when the unreacted photoresistor is removed from the product. Target constituents of photoresistor thinner (Propylene Glycol Monomethyl Ether and Propylene Glycol Monomethyl Ether Acetate, referred to as PGME and PGMEA) have been retrieved by applying distillation. In this work, a systematic design is applied to recover PGME and PGMEA by avoiding the azeotropic barrier, which occurs in the mixture of waste thinner in the atmospheric pressure, as well as to recover high purity of main product. Furthermore, an advanced distillation configuration is used to improve the energy efficiency of conventional distillation based recovery process. The results of this study contributes to the waste photo thinner recycling industry for how to design conventional distillation columns and to improve energy efficiency of waste thinner distillation process by using advanced distillation.

Keywords
Waste photoresist thinner, azeotropic, distillation, heat-integrated distillation

1. Introduction

Thinners are basic materials for removing photoresists on the substrate edges or dispensing nozzles during semiconductor and display production. In semiconductors industry, thinners are used for wafer, reducing photoresist usage, and cleaning equipments. For TFT-LCD displays thinners are used to clean photoresist dispensing nozzles and coating cups[1]. Huge amount of thinner are used in semiconductor Industry and some technologies were established in Korea to develop thinner recycling technology. The mixture of propyleneglycol monomethyl ether (PGME) and propyleneglycol monomethyl ether acetate (PGMEA) are waste thinner (WT) that is generated from TFT-LCD and IC manufacturing processes when unreacted photoresistor is removed from the products using photoresistor thinner (PT). PGME and PGMEA have been also used as alternatives for chlorofluorocarbons (CFCs) which had been extensively utilized for cleaning electronic components.
The waste thinner has been retrieved by several methods, and distillation can be one of them. However, to recover the target constituents of PTs (PGME and PGMEA), the co-existing compounds in the WT may hinder the distillation and reduced the

recovery of the target compounds of PT. The azeotropic phenomenon is supposed to be the hindering mechanism of the distillation[2].
The objective study of this work is to develop PGME-PGMEA recovery column without using entrainer to resolve azeotropic barrier at atmospheric pressure of the conventional distillation column and some modification of operation condition for advance column. High purity PGME and PGMEA is priority target of waste photoresist thinner recovery in this study. The results of this study may contribute to the waste recycling industry for how to improve distillation process further to raise the recovery efficiency.

2. Feasibility Study

Aspen Plus as one of powerful simulation tools for chemical processes was used to predict separation feasibility of mixture. The NRTL fluid package was chosen as a thermodynamic method of simulation. The UNIFAC method was applied to estimate the missing binary-interaction parameters of NTRL system. Residue curve map (RCM) was also established. The RCM is a powerful tool for better understanding of the design and operation of distillation columns, especially when the separation involves azeotropic mixtures. The RCM can be used to check separation feasibility of homogeneous and heterogeneous. In heterogeneous system, the RCM can be made to exploit liquid-liquid phase behavior to design desired separation[3].
Waste thinner mixture is from one industry in Korea. PGME, PGMEA and water are waste photoresist components as distillation feed. Three azeotropes include one homogenenous and two heterogeneous azeotropes. Data of singular point was generated by Aspen Plus.

Table 1. Singular points of mixture (%mole)

Temp (C)	Classification	Type	No. Comp.	PGMEA	PGME	WATER
146.02	Stable node	Homogeneous	1	1	0	0
120.09	Saddle	Homogeneous	1	0	1	0
100.02	Stable node	Homogeneous	1	0	0	1
98.86	Saddle	Homogeneous	2	0	7.07	92.9
97.4	Unstable node	Heterogeneous	3	9.8	0.54	89.7
97.41	Saddle	Heterogeneous	2	10.1	0	89.9

Three azeotope points are low boliling point azetrope and heterogeneous azeotropes of ternary mixture. Target constituents (PGME and PGMEA) have higher boiling points than water. Water is supposed to be dominant component on the top product. Three components are low boiling point azeotrope at 97.4 C and maximum composition of water is 89.7 %mole. No azeotrope forms between PGME and PGMEA. In this mixture, water are azeotrope to PGME and PGMEA. It is obvious from feasibilty data, water should be removed first to reduce azeotrope component in the mixture. Water can be evaporized until it reaches maximum composition on the top product. Because water is the lightest component, a direct sequence distillation configuration can be applied to remove water. PGME in the feed occupies 11 %mole,

PGMEA 15 %mole, and water 74 %mole. Total flowrate is 23.24 Kmol/hr. **Figure 1** shows the feasible separation.

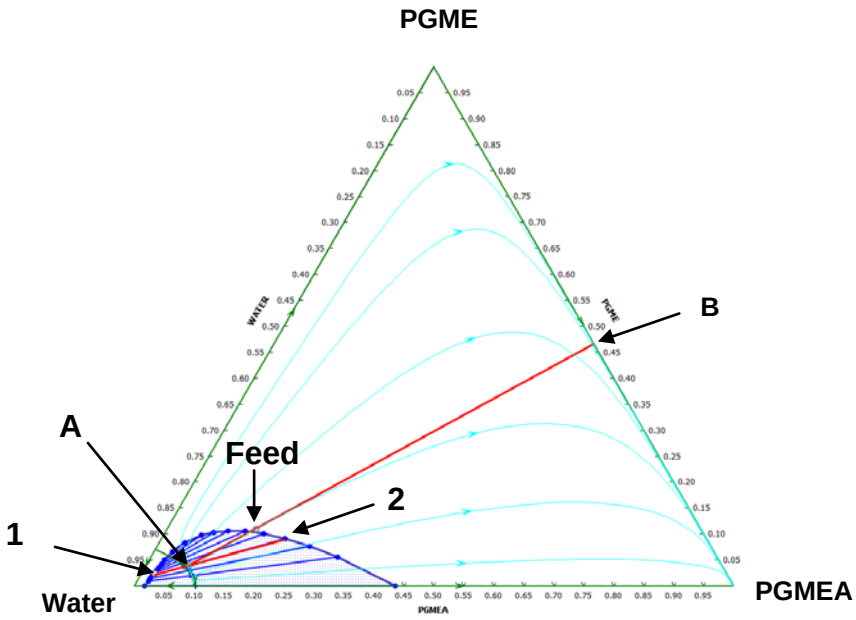

Figure 1. Feasible separation of waste photoresist thinner components

To obtain maximum composition of water in the top stream, a straight line through feed point (F) from an initial unstable point can be drawn until it reaches point B. Point A indicates maximum feasible water composition on the top product. Distillation barrier is reached at point A and on this point, feasible distillate composition cannot be changed anymore. Point A is in the liquid-liquid region. It can be seperated by a liquid-liquid separator. In the first column, main target is to reduce water as much as possible on the bottom. This is for eliminating the azeotrope component in the bottom product of first column. Water can be stripped to the top and the top vapor product toward to condenser. Liquid product of condenser is seperated in the decanter to be organic rich and water rich. Point 1 is water rich while point 2 is organic rich. Because almost all water is stripped on the top, the bottom product is rich of thinner components, but because there is azeotrope barrier for this ternary components, some PGME and PGMEA is stripped on the top product. Point 2 is organic rich and still contains some PGME and PGMEA. In order to increase recovery of PGME and PGMEA, organic phase is recycled to the column.

Table 2. Feasible composition of first column

	Composition %Mole				
	Feed	A	B	1	2
H2O	74	88.7	0.1	95.5	25.4
PGME	11	4	53.9	2.3	16.5
PGMEA	15	7.3	46	2.2	58.1

A = Top product ; B = Bottom product ; 1 = Water rich ; 2 = Organic rich

3. Process development

Aspen Hysys was used to simulate distillation process using the RCM result. Grassroot conventional columns are designed at non-optimal condition. The objective was to seperate PGME and PGMEA at the last column. First column (C-1) is a concentrator of PGME and PGMEA. As mentioned at section 2, this column aimes to strip water as much as possible. Some amount of PGME and PGMEA is still stripped on the top stream and seperated by decanter. Organic phase is then returned to the column to increase PGME and PGMEA recovery. **Figure 2.a** shows a conventional direct sequence distillation using a decanter at the first column, namely design 1. Another design, namely design 2 (**Figure 2.b**)uses one extra column after a concentrator. Extra column (C-2) has lower energy consumption compared to the concentrator (C-1).Top product from C-1 is water rich and organic phase in the decanter (D-1) is toward to the extra column instead of returning to C-1 as reflux. Water rich stream from D-1 is proceed also to D-2. Organic liquid of D-2 is recycled to C-2 as reflux, this is for enriching organic composition in the bottom of C-2. Water product is drained from D-2 containing 95.8 %mole of water. Organic rich streams from the bottom of C-1 and C-2 go to the main column (C-3). Total reboiler duty of design 2 is slightly lower than design 1 but the recovery of PGME and PGMEA of design 1 is apparantly higher than design 2. Table 3 compares performance of the two configurations.

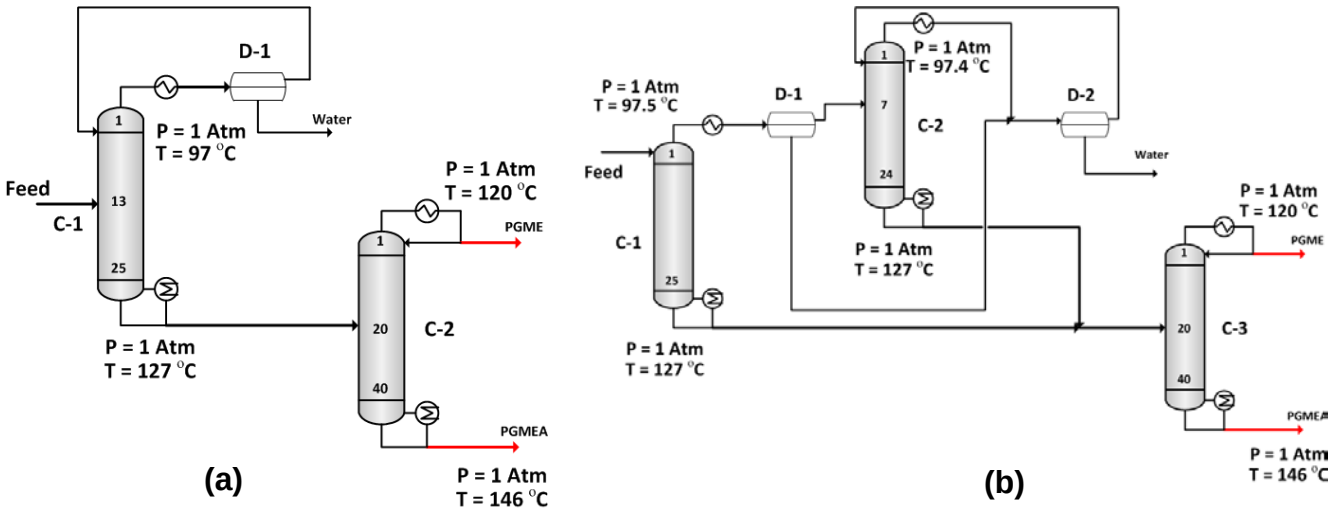

Figure 2. Conventional process of waste thinner recovery column, (a) Design 1, (b) Design 2

4. Advanced Column

Design 1 was chosen to be an enhanced column because the recovery of PGME and PGMEA is higher than that of design 2 and it requires only two columns. Energy efficiency can be improved by utilizing a thermally coupled configuration. **Figure 3** shows a thermally coupled distillation column associated with the direct sequence.

Table 3. Comparison of two configurations for PGME-PGMEA separation

	Distillate (%Mole)		Bottom (%Mole)		Recovery		Total Reboiler Duty	
	Design 1	Design 2	Design 1	Design 2	Design 1	Design 2	Design 1	Design 2
H2O	0.34	0.5	0	0				
PGME	99.37	99.22	0.03	0.4	89.57	85.22		
PGMEA	0.28	0.28	99.97	99.6	89.61	88.63		
MegaWatt (MW)							0.6053	0.6023

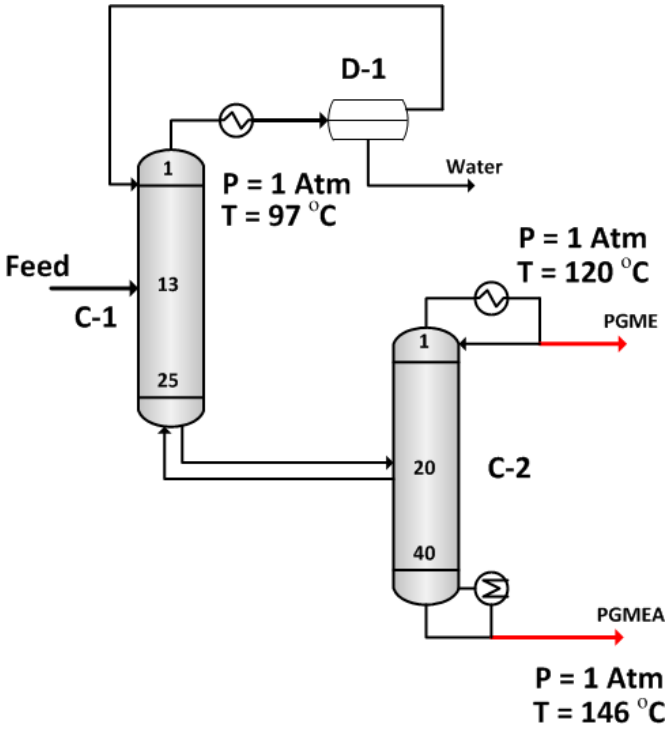

Figure 3. Thermally coupled distillation column of waste thinner recovery column

Total reboiler duty of thermally coupled distillation column was 0.58 MW with similar product specification, the improvement looks marginal. Further energy saving can be achieved through the heat-integration between the two columns in the direct sequence, called a multi-effect configuration where one column is operated at higher pressure than the other column, and condenser duty of higher pressure column can provide required reboiler duty in the lower pressure column[3]. Another study was done for multi-effect distillation of light hydrocarbon separation that was more beneficial for energy efficiency[4].

Figure 4 describes a heat integrated distillation column between C-1 and C-2. In this case, C-2 pressure was increased to 1.7 atm on the bottom and 1.65 atm on the top. This pressure was adjusted only to increase temperature top stream of C-2 and this stream could be used as a heat source of C-1 bottom. Pressure of C-2 was also

adjusted to keep the minimum temperature approach of HE-1 about 10 °C. Total reboiler duty of advanced case is 0.3514 MW, which is about 42% energy saving in the reboiler compared to design 1 case.

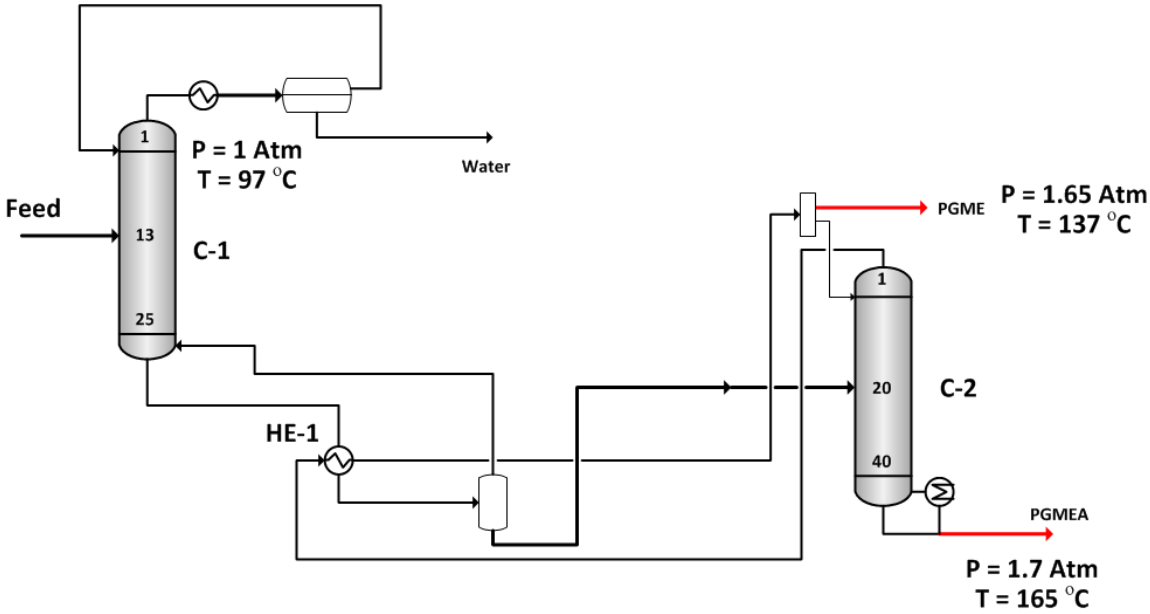

Figure 4. Heat integrated column of waste thinner recovery column

5. Conclusions

This study reports a new design of waste thinner recovery column and also the benefit of heat-integration to improve energy efficiency of waste thinner recovery column. Reboiler energy saving could be achieved about 42%. However, the conventional case is non-optimal design and there are some room for optimization and further enhanced energy efficiency, especially for C-2.

Acknowledgement

This study was supported by the R&D Center for Valuable Recycling(Global-Top Environmental Technology Development Program) funded by the Ministry of Environment.(Project No.:11-A13-OD). This study was also supported by Basic Science Research Program through the National Research Foundation of Korea funded by the Ministry of Education, Science and Technology (2012012532).

References

1. ENF Technology, *www.enftech.com*
2. J.F. Chang, *NCUIR, Taiwan* (2011)
3. W.D. Seider, J.D.Seader and D.R.Lewin, *John Wiley and Sons, Inc. 2nd Ed.*
4. H. Engelie, S.Skogestad, *Chemical Engineering and Processing*, **44**, 819-826 (2005)
5. S.H. Ahn et.al, *USPTO*, US 7387988 B2 (2008)

Thermal separation of ionic liquid recycling in biomass fractioning

Jakobsson Kaj; Abdulawahab Moshood; Alopaeus Ville
Aalto University, Espoo/Finland;

Abstract
Thermal separation processes for ionic liquid (IL) recycling was modeled in biomass fractionation processes using ionic liquids as fractionating agents. Three promising ILs were chosen having water as the antisolvent 1) 1-ethyl-3-methylimidazolium acetate ([emim][OAc]) 2) A distillable ionic liquid formed from 1,1,3,3-tetramethylguanidine and propanoic acid. 3) A switchable ionic liquid formed from 1,8-Diazabicyclo[5.4.0]undec-7-ene and butanol. The modelling of the chemical systems relied on various estimation methods for modelling of physical property, VLE and energy variables. The simulated pressure levels and the presence of reactions in the chemical systems are pointing towards short path distillation as the technical implementation of such processes.

Ionic liquid, biomass fractionation, modelling, simulation

1. Introduction

Lignocellulose materials have been identified as a CO_2-neutral, renewable and sustainable source of bioenergy and biochemicals. Because of these attractive qualities of lignocellulose materials attention has been focused on fractionating its components —cellulose, hemicelluloses and lignin.

Biomass fractionation can be accomplished with various techniques like steam explosion; hot water extraction and kraft pulping which employ harsh conditions, toxic chemicals and even incur some biomass component loss, mainly hemicellulose (Tan and Lee, 2012). In the search for more sustainable technology the ionic liquids (ILs) seem to be promising fractionating agents (Anugwom et al., 2012; Hyvarinen et al., 2011; Kilpeläinen et al., 2007; King et al., 2011; Mäki-Arvela et al., 2010).

Following the biomass fractionation with an IL, the resulting extract is a multicomponent liquid mixture in which the components are dissolved biomass components cellulose, hemicellulose, lignin, the employed IL and probably some degraded biopolymers and other impurities. From this solution the dissolved component(s) are recovered by precipitating the dissolved components with an antisolvent such as water and/or methanol (ethanol in some cases). The precipitation is performed in turns and in different conditions for different components. (Mäki-Arvela et al., 2010; Tan and Lee, 2012; Wei et al., 2012)

The last step of the fractionating process is to recover the used ILs from the dissolved components (the remaining antisolvent and water) for recycling. This type of process has been suggested based on laboratory experience and theoretical opinion (King et al., 2011; Mäki-Arvela et al., 2010; Ober and Gupta, 2012). From the industrial point of view, the recyclability is a vital process step for making potential ILs applications economical. In the following we discuss modelling of thermally-driven separation and the recycling of ILs for some interesting chemical systems. See Figure 1 for a schematic representation of such a process.

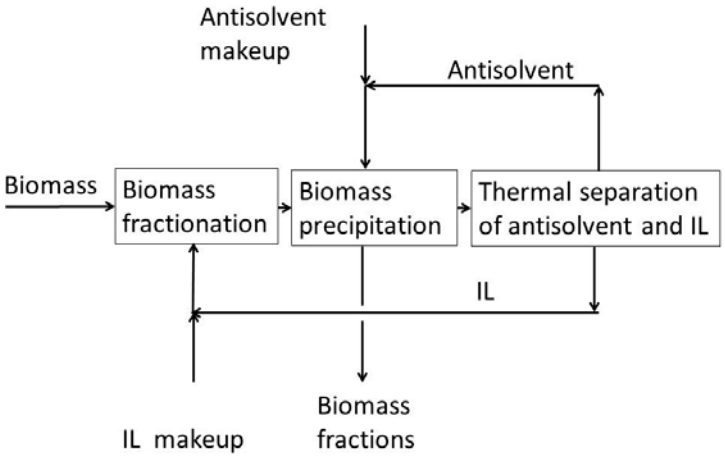

Figure 1. A Schematic block diagram of biomass fractionation with ionic liquid

2. Results and discussion

2.1 The Chemical Systems

Three promising ILs were chosen for the modelling of biomass fractionation and recycle process having water as the antisolvent (Anugwom et al., 2012; King et al., 2011). 1) *1-ethyl-3-methylimidazolium acetate ([emim][OAc])* is able to dissolve biomass at a relatively mild condition, tolerance to about 10 wt% of antisolvent (water in particular) without significant effect on its dissolution ability and the nontoxic nature due to its organic anion. (Mäki-Arvela et al., 2010). 2) *A distillable ionic liquid (DIL)*. DIL is formed from organic base and acid. Here we used 1,1,3,3-tetramethylguanidine (TMG) and propanoic acid.

$$TMG + C_2H_5COOH \leftrightarrow [TMGH][\ C_2H_5CO_2]$$

3) A switchable ionic liquid (SIL). SILs are synthesized by reacting mixture of organic base and alcohol in the presence of a sour gas—either carbon dioxide or sulphur IV oxide. In this case, 1,8-Diazabicyclo[5.4.0]undec-7-ene (DBU) is the base used for SIL synthesis and butanol the alcohol.

$$DBU + C_4H_9OH + CO_2 \leftrightarrow [DBUH][\ C_4H_9CO_3]$$

2.2 VLE, CPE and physical property modelling

Modelling thermally-driven separation requires a thorough thermodynamics study in vapour-liquid equilibrium (VLE) or chemical and phase equilibrium (CPE) and the other physical properties. In earlier works varying assumptions about the potential solvent's chemistry have been made: 1. normal molecular liquids; 2. completely dissociated in liquid phase; 3. partly dissociated. The first assumption dominates in the literature with acceptable VLE data prediction. Such models commonly utilize different equation of state (EOS) models for the vapour phase and activity coefficient for liquid phase. Peng-Robinson is by far the most used EOS while NRTL and UNIQUAC are the popular options in the liquid phase. (Alvarez and Saldaña, 2012; Anderko et al., 2002; Kato et al., 2004; Maia et al., 2012; Wang and Anderko, 2011). Other VLE studies for ILs can be found for example (Bedia et al., 2013; Döker and Gmehling, 2005; Ferro et al., 2012; Hector et al., 2013; Römich et al., 2012). The solution and vapour chemistry of ILs is still debatable (Wang and Anderko 2011).

In this work the physical properties are either calculated with the group contribution methods or by indirect optimization of model parameters.

2.2.1 VLE model of [emim][OAc] - Water

For the VLE modelling of [emim][OAc] the gamma-phi model is utilized while IL is treated as molecular specie. An ideal vapour is assumed throughout this modelling This approach have yielded acceptable results in earlier works (Döker and Gmehling, 2005; Kato et al., 2004; Revelli et al., 2010).

The saturated vapour pressure and the liquid activity coefficient parameters are needed. Due to nonavailability of measurement data, negligible values or even naught are commonly assumed for ILs vapour pressure for the purpose of VLE modelling (Döker and Gmehling, 2005; Revelli et al., 2010). In this work, values similar to ILs vapour pressure data found in the literature were employed to fit the vapour pressure in the simulation.

Römich et al. 2012 reported 85 xpT data points and the interaction parameters for [emim][OAc]-H_2O between a temperature range of 293.15 K to 353.15 K. Using the reported interaction parameters, the temperature-dependent NRTL parameters were optimized using the reported interaction energies.

2.3 Modeling of chemical and phase equilibrium of SIL and DIL -water

In the modelling chemical and phase equilibrium (CPE) of the SIL and DIL the vapour and liquid are assumed to be ideal in both cases. The vapour pressure of the SIL, DIL and DBU was estimated with the Riedel correlation in our in-house code.

The reaction equilibrium can be modelled approximately with indirect data found in the literature (Heldebrant et al., 2008; King et al., 2011).

For the SIL ([DBUH][$C_4H_9CO_3$]) the standard state enthalpy and Gibbs free energy of formation and the heat capacity are available in common physical properties databases for carbon dioxide and butanol but not for DBU and the SIL. Three different group contribution methods were used to estimate the standard state enthalpy and Gibbs free energy of DBU as ideal gas; the Joback method and two other methods developed for biological systems by Mavrovouniotis (1991) and Jankowski et al. (2008); (Poling et al., 2001). The other two methods asides Joback were employed because the nitrogen ring group (—N<) is absent in the Joback group table, hence, the aliphatic equivalent was employed for the estimation.

The heat capacity as ideal gas was estimated with the Harris and Seaton's property estimation method. Heldebrant et al. 2008 reported enthalpy, entropy and Gibbs free energy data for eighteen different CO_2 capturing reactions forming different SILs at 1 atm and 25 degree Celsius. These data include that of the SIL considered, thus, the standard state thermodynamics properties of the SIL in liquid state was back-calculated. In this calculation, the ideal gas standard state properties for DBU were converted to liquid state using the enthalpy of vaporization, also estimated with our in-house code. The liquid state properties of butanol were found at the DIPPR 801.

The equilibrium constant is estimated with the reported Gibbs energy of reaction and then extended with the van't Hoff equation. With the extended value of equilibrium constant, the heat capacity of the SIL was optimized using standard thermodynamical relationships. The liquid state heat capacity of DBU was calculated by backward difference method using the liquid state enthalpies calculated from the previously estimated ideal gas heat capacity and the Watson's extension of the enthalpy of vaporization.

The calculated coefficients were validated by calculating the heat capacity at 300K; the determined value—1.73 J/(g-K)—at least passed the test of 1.2 to 2 J/(g-K) range predicted by Heldebrant et al. 2008.

In the case of the DIL ([TMGH][$C_2H_5CO_2$]), the thermogravimetric analysis graph that is reported in King et al. 2011 was traced for the dissociation profile of the DIL with

respect to temperature. Using these data and the known stoichiometric reaction of the dissociation the corresponding amounts of propionic acid and TMG were calculated. Consequently, the reaction equilibrium constant was estimated for the temperature range. The activity coefficients were assumed to be unity throughout this calculation. It is possible to use UNIFAC method for the TMG-propionic acid interaction parameters but this method is not matured enough for the IL interaction computation.
Just like in the case of the SIL, the liquid state thermodynamics data for propionic acid were collected from the DIPPR 801 while that of TMG was calculated from the ideal gas estimation using Aspen property estimation. Our in-house code was also used for TMG property estimations for validation purpose, both software programs; however, yield similar values. Similarly, standard thermodynamical relationships were used to fit the DIL heat capacity and to optimize the DIL standard state enthalpy and Gibbs free energy.

2.1.3 Other estimated physical properties

The normal boiling point, density and critical properties of the ILs were estimated based on the method by Valderrama and Rojas (2009).
Römich et al. (2012) reported some specific heat capacity data for [emim][OAc]-water mixture for a temperature range of 293.15K to 363.15K. These data were extrapolated to calculate the specific heat capacities of pure [emim][OAc] at reported temperatures. The extrapolated values were compared with specific heat capacities calculated from an additive method reported in Soriano et al. (2010) and both estimates show considerable agreement. Enthalpy of vaporization for the ILs at 298K was estimated from a predictive rule given in Verevkin et al. (2008) and extended with Watson correlation for other temperatures.
The Joback method is used to estimate all physical properties needed for DBU except the ideal gas heat capacity that was calculated with Harris and Seaton's property estimation method. Using the optimized values for the ILs standard state enthalpy of formation, Gibbs free energy and heat capacity as liquid described in the standard state equivalents as ideal gas were back-calculated by setting the reference temperature at 298.15 K. All the estimated values were fed into Aspen Plus for the flowsheet simulation.

2.3 Processes and simulations

The model for separation of ILs consisted of a simplified fractionation section and rigorous thermal separation section based on 20 kg/s cellulose feed. The biomass dissolution, precipitation and filtration were mimicked with in Aspen Plus with two splitters and a mixer unit. The feed into the process was 80 kg/s feed of ILs and 50% cellulose dissolution, 100 kg/s feed of antisolvent (water).
In all cases the thermal separation was arranged with three flashes. The process arrangement resembles to a three stage multiple-effect evaporator. Thus the only energy input goes to the first flash tank. The antisolvent was evaporated and both the antisolvent and IL was recycled into the process. The process was optimized for energy consumption. In *[emim][OAc]-water* a temperature maximum of 400 K was used to avoid [emim][OAc] to decompose and the temperature differences were restricted to ensure usability of the condensed vapours. The pressure window in the first and second flash tanks was chosen to ensure operation of the tanks around atmospheric condition. 99.2 weight percent of [emim][OAc] was realized in the recycle stream. In *SIL and DIL cases* the temperature limits were lower due to the estimated equilibrium constants of the chemical system in order to avoid the

switching into the molecular form of the ILs. IL mass fraction in recycle streams were all set to about 95% for comparation purpose. The main results of the simulations are presented in Table 1.

		emimOAc			SIL			DIL		
Unit		flash 1	flash 2	flash 3	flash 1	flash 2	flash 3	flash 1	flash 2	flash 3
Temperature	K	386	370	345	300	290	290	280	330	330
Pressure	kPa	199	109	1.5	3.3	1.7	0.3	24	14	3
SEPARATION	Weight Frac IL in Vapour	97 ppm			109 ppb			0.005		
	Weight Frac IL in Liquid	0.95			0.96			0.95		
ENERGY	Qflash MW	108			69			79		
	MJ/kg IL	1.42			1.05			1.0		

Table 1. Simulation results of the thermal separation section of the three fractionating processes of biomass.

It can be seen from the results that the energy consumption of *[emim][OAc]-water* case is slightly higher than that of the other cases. On the other hand the used pressure levels are closer to normal pressure. The obtained pressures and the presence of reaction indicate techniques such as short path distillation to be used as the implementation of these separations.
It is a common opinion that in the processes there will be forming high boiling degraded biopolymers that will eventually contaminate the used ILs and there will be probably some decomposition of the ILs as well. Thus a regeneration section of the ILs must be included in the process. In the DIL and SIL process it is tempting to switch the ILs into their molecular form and distillate the ILs. However, it is noteworthy to consider that both SIL and DIL are formed from molecular components that form an azeotropic mixture with water.

3. Conclusions

In this work a preliminary analysis for ionic liquid recycle schemes was done. The obtained results give ideas towards the type of processes we are aiming for in biomass fractionation. The pressure levels and the presence of reactions are pointing towards short path distillation as the technical implementation. The presented results are based on many estimated physical property, VLE and energy parameters. Thus the modeling cannot be used for too detailed design and analysis of these processes. On the other hand this work also shows the short comings of our estimation methods and data at hand and invites the attention of experimentalist to these kinds of chemical systems and processes.

Acknowledgements

Financial support from FIBIC Ltd. (Fubio Joint Research 2 Research programme) and the National Technology Agency of Finland (TEKES).

References

Alvarez, V. H.; Saldaña, M. D. A. Thermodynamic prediction of vapor–liquid equilibrium of supercritical CO_2 or CHF_3 + ionic liquids. The Journal of Supercritical Fluids 2012, 66, 29-35.

Anderko, A.; Wang, P.; Rafal, M. Electrolyte solutions: from thermodynamic and transport property models to the simulation of industrial processes. Fluid Phase Equilib. 2002, 194–197, 123-142.
Anugwom, I.; Mäki-Arvela, P.; Virtanen, P.; Willför, S.; Sjöholm, R.; Mikkola, J. -. Selective extraction of hemicelluloses from spruce using switchable ionic liquids. Carbohydr. Polym. 2012, 87, 2005-2011.
Bedia, J.; Ruiz, E.; de Riva, J.; Ferro, V. R.; Palomar, J.; Rodriguez, J. J. Optimized ionic liquids for toluene absorption. AIChE J. 2013, 59, 1648-1656.
Döker, M.; Gmehling, J. Measurement and prediction of vapor-liquid equilibria of ternary systems containing ionic liquids. Fluid Phase Equilib. 2005, 227, 255-266.
Ferro, V. R.; Ruiz, E.; de Riva, J.; Palomar, J. Introducing process simulation in ionic liquids design/selection for separation processes based on operational and economic criteria through the example of their regeneration. Separation and Purification Technology 2012, 97, 195-204.
Hector, T.; Uhlig, L.; Gmehling, J. Prediction of different thermodynamic properties for systems of alcohols and sulfate-based anion Ionic Liquids using modified UNIFAC. Fluid Phase Equilib. 2013, 338, 135-140.
Heldebrant, D. J.; Yonker, C. R.; Jessop, P. G.; Phan, L. Organic liquid CO2 capture agents with high gravimetric CO 2 capacity. Energy and Environmental Science 2008, 1, 487-493.
Hyvarinen, S.; Damlin, P.; Grasvik, J.; Murzin, D. Y.; Mikkola, J. Ionic liquid fractionation of woody biomass for fermentable monosaccharides. Cellul. Chem. Technol. 2011, 45, 483-486.
Jankowski, M. D.; Henry, C. S.; Broadbelt, L. J.; Hatzimanikatis, V. Group contribution method for thermodynamic analysis of complex metabolic networks. Biophys. J. 2008, 95, 1487-1499.
Kato, R.; Krummen, M.; Gmehling, J. Measurement and correlation of vapor–liquid equilibria and excess enthalpies of binary systems containing ionic liquids and hydrocarbons. Fluid Phase Equilib. 2004, 224, 47-54.
Kilpeläinen, I.; Xie, H.; King, A.; Granstrom, M.; Heikkinen, S.; Argyropoulos, D. S. Dissolution of wood in ionic liquids. J. Agric. Food Chem. 2007, 55, 9142-9148.
King, A. W. T.; Asikkala, J.; Mutikainen, I.; Järvi, P.; Kilpeläinen, I. Distillable acid-base conjugate ionic liquids for cellulose dissolution and processing. Angewandte Chemie - International Edition 2011, 50, 6301-6305.
Maia, F. M.; Tsivintzelis, I.; Rodriguez, O.; Macedo, E. A.; Kontogeorgis, G. M. Equation of state modelling of systems with ionic liquids: Literature review and application with the Cubic Plus Association (CPA) model. Fluid Phase Equilib. 2012, 332, 128-143.
Mavrovouniotis, M. L. Group contributions for estimating standard Gibbs energies of formation of biochemical compounds in aqueous solution. Biotechnol. Bioeng. 1990, 36, 1070-1082.
Mäki-Arvela, P.; Anugwom, I.; Virtanen, P.; Sjöholm, R.; Mikkola, J. P. Dissolution of lignocellulosic materials and its constituents using ionic liquids—A review. Industrial Crops and Products 2010, 32, 175-201.
Ober, C. A.; Gupta, R. B. pH Control of Ionic Liquids with Carbon Dioxide and Water: 1-Ethyl-3-methylimidazolium Acetate. Ind Eng Chem Res 2012, 51, 2524-2530.
Revelli, A.; Mutelet, F.; Jaubert, J. (Vapor + liquid) equilibria of binary mixtures containing light alcohols and ionic liquids. The Journal of Chemical Thermodynamics 2010, 42, 177-181.
Römich, C.; Merkel, N. C.; Valbonesi, A.; Schaber, K.; Sauer, S.; Schubert, T. J. S. Thermodynamic properties of binary mixtures of water and room-temperature ionic liquids: Vapor pressures, heat capacities, densities, and viscosities of water + 1-ethyl-3-methylimidazolium acetate and water + diethylmethylammonium methane sulfonate. J. Chem. Eng. Data 2012, 57, 2258-2264.
Palatino Linotype
Soriano, A. N.; Agapito, A. M.; Lagumbay, L. J. L. I.; Caparanga, A. R.; Li, M. A simple approach to predict molar heat capacity of ionic liquids using group-additivity method. Journal of the Taiwan Institute of Chemical Engineers 2010, 41, 307-314.
Tan, H. T.; Lee, K. T. Understanding the impact of ionic liquid pretreatment on biomass and enzymatic hydrolysis. Chem. Eng. J. 2012, 183, 448-458.
Valderrama, J. O.; Rojas, R. E. Critical properties of ionic liquids. Revisited. Industrial and Engineering Chemistry Research 2009, 48, 6890-6900.
Verevkin, S. P. Predicting enthalpy of vaporization of ionic liquids: A simple rule for a complex property. Angewandte Chemie - International Edition 2008, 47, 5071-5074.
Wang, P.; Anderko, A. Modeling chemical equilibria, phase behavior, and transport properties in ionic liquid systems. Fluid Phase Equilib. 2011, 302, 74-82.
Wei, L.; Li, K.; Ma, Y.; Hou, X. Dissolving lignocellulosic biomass in a 1-butyl-3-methylimidazolium chloride–water mixture. Industrial Crops and Products 2012, 37, 227-234.

Distillation columns integrated with organic Rankine cycle

Dmitriy Sladkovskiy[1], *Nickolay Lisitsyn*[2]

[1]*St.Petersburg State Institute of Technology (technical university), Saint-Petersburg, Russia;, St.Petersburg State Institute of Technology (technical university), Saint-Petersburg, Russia*

[2]*St.Petersburg State Institute of Technology (technical university), Saint-Petersburg, Russia;, St.Petersburg State Institute of Technology (technical university), Saint-Petersburg, Russia*

Abstract (Subheading – Arial 12 pt. bold, left-aligned)

This paper presents theoretically very efficient method to generate electrical power for industrial facility utilizing a distillation. The main idea is to integrate distillation column and Organic Rankine cycle (ORC). It is allows to increase the efficiency of the power generation cycle over than 90% however operating power range is limited up to 1-2 MW.

The purpose of the research is to analyze the efficiency of integration the ORC and distillation column. The analysis is realized by means of Aspen HYSYS. Paper consist detailed description of the model.

This abstract shows 3 potential distillation columns for integration with ORC: i-butane/n-butane separation, deisopentanizer and naphtha splitter. Net power output and exergy efficiency is used as key performance indicators. Results of the analysis show that the performance strongly depends on the particular separation process.

Keywords (Subheading – Arial 12 pt. bold, left-aligned)

Distillation, Organic Rankine Cycle (ORC), simulation, power generation

1. Introduction (Subheading – Arial 12 pt. bold, left-aligned)

Fractional distillation is the most common form of separation technology used in petroleum and chemical process industries. It consumes greater than 40% of the energy used by the refining or chemical plants due to low energy efficiency of a distillation column.

It is well-known that significant energy savings can be achieved if complex column configurations and heat integration are used, although it withdraw the attractive advantages of conventional distillation column such as flexibility, low capital investment and low operational risk.

A wide range of distillation columns can be integrated with organic Rankine cycle to reach as high as 95% efficiency of electricity generation. The Organic Rankine Cycle (ORC) is a proven method of converting low temperature heat to electrical energy. The ORC process works like a Clausius–Rankine steam power plant but uses an organic working fluid instead of water. The disadvantage of such cycle is that the efficiency does not exceed 24%.

The integration of distillation column and ORC allows to increase the efficiency of the power generation cycle and to reduce it’s capital cost by combining heat exchanger equipment.

This idea was patented in 1984 (Don Carson, UOP)[1] but so far we have not found any publication concerning practical implementation or performance analysis.

The purpose of this paper was to analyze the efficiency of integration the ORC and various distillation columns using simulation on Aspen HySys.

2. Combined cycle principle

Figure 1 shows the basic principle of distillation column integrated with ORC. The liquid stream from the column's bottom is pressurized by a pump. The high pressure liquid is heated and vaporized in the reboiler (vaporizer). The resultant high pressure vapor stream drives the expander (expansion turbine), which is coupled to the electricity generator or another rotating equipment. Vapor stream expands to the operation pressure of the column. The expander exhaust vapour enters the column bottom to supply heat for separation process. Inside the column, the downflowing reflux liquid provides cooling and condensation of upflowing vapors. Both the working fluid condensation and mixture separation processes take place in distillation column. Required cooling for the vapor condensation is supplied by the overhead condensing system of the column.

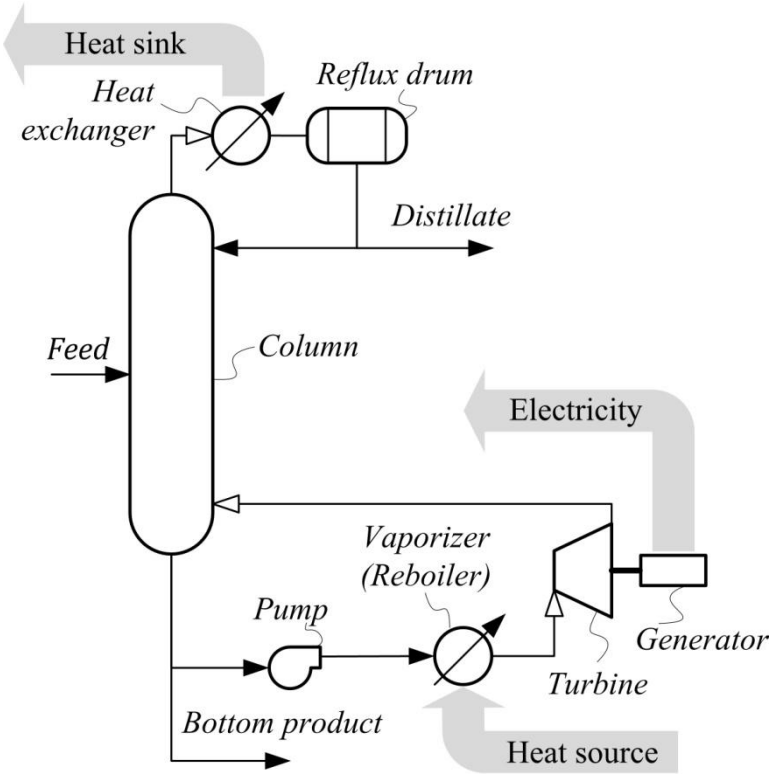

Figure 1. Distillation column integrated with ORC

When distillation column integrated with ORC is considered, the reboiler heat load is used not only for power generation. Most of heat is used for separation. The heat required for the distillation remains the same as in conventional column. If turboexpander effectively utilizes the energy of adiabatic expansion without heat loss, the power generation thermal efficiency of distillation column integrated with ORC is closer to 100%. According to the first law of thermodynamics this efficiency value is almost independent from turboexpander adiabatic efficiency because the flow energy of pressurized vapor, not converted to mechanical work, will be transformed to internal energy which is used to produce vapor for separation. In practice, the efficiency can decrease due to mechanical and generator losses.

It should be noted that the vapour from the expander can be superheated. Therefore the flow rate through the vaporizer is slightly reduced.

The modeling of the distillation column integrated with ORC is presented in the following section.

3. Modeling

Aspen HYSYS is used as simulation environment. Model consists of basic column with two pump-around and the ORC unit operations (pump, vaporizer, expander). Figure 2 shows the model process flow sheet with represented sub-flowsheet of the column. The pump-arounds are used as vaporizers. The vapour fraction of return streams is specified to 1. The “Desuperheater @SF” is intended to take into account the desuperheating duty of vapour from the expander. The liquid flowrate through the vaporizer is calculated using “Vaporizer @SF”.

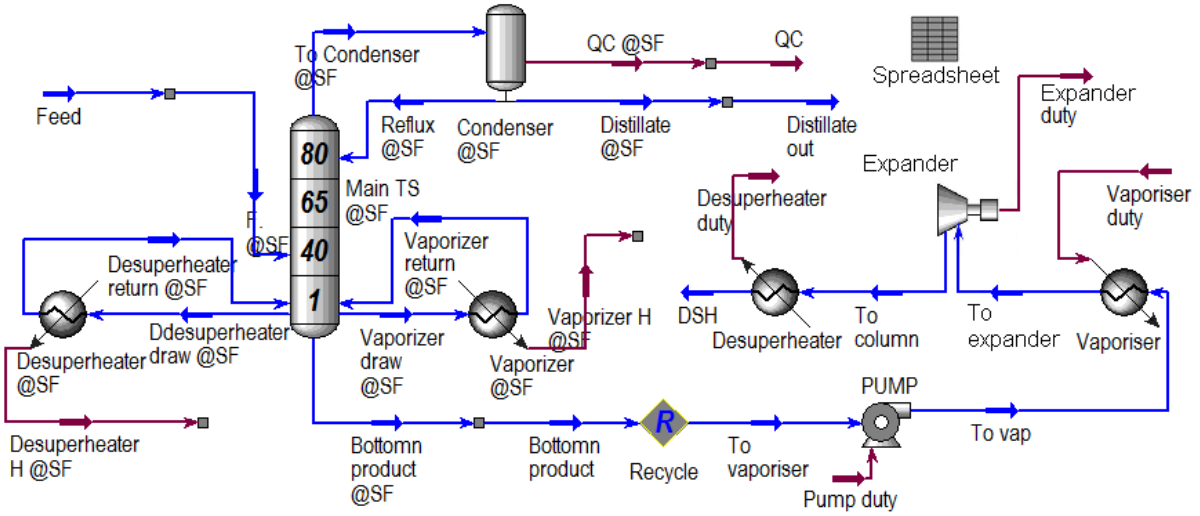

Figure 2. Model process flow diagram

The recycle transmits from stream “Bottom product” to stream “To vaporizer” only temperature, pressure and composition. Flow rate of the stream “To vaporizer” is equal to stream “Vaporizer draw@SF”. It is specified by integrated spreadsheet. Duty of “Desuperheater” is specified manually by iterative method.

To calculate the entire model the following simulation procedure is used:

1. Column and power cycle specification (desired draw rate and quality of products, turbine inlet pressure)
2. Distillation column calculation (Evaluation of bottom temperature, bottom product composition and flowrate through the reboiler)
3. Organic Rankine cycle calculation (Evaluation of pump duty, turbine output power and vapor desuperheating duty)
4. Specifying vapor desuperheating duty to the column’s “Desuperheater @SF” pump-around
5. Steps 2-5 are repeated until heat and mass balance between column and ORC are convergenced

Assumptions. The pump is assumed to have an isentropic efficiency of 75%. and the expander isentropic efficiency is 84%. Also the mechanical efficiency of expander gear (99%) and electricity generator efficiency (96%) are taken into account. These generic values are within the range of typical efficiencies for machines of this type.

Performance indicators. Considered scheme allows to produce electricity. Therefore net output power is one of the key parameters. It is determined from:

$$W_{net} = W_{exp} \cdot \eta_{mg} \cdot \eta_{me} - W_{pump} \cdot \eta_{mp}$$

where, W_{pump} − pump duty of distillation column integrated with ORC, MW; W_{exp} – turboexpander output power, MW; η_{mg} – mechanical efficiency of turboexpander gear; η_{me}– electricity generator efficiency; η_{mp} – mechanical efficiency of pump.

Values W_{pump} and W_{exp} are calculated using HYSYS according to specified adiabatic efficiencies. HYSYS calculates the expansion process rigorously by following the isentropic line from the inlet to the exit pressure [2].

For measuring the thermodynamic perfection of a process the perfection degree (exergy efficiency) is used. It is defined as the ratio of the useful exergy effect to the consumption of the driving exergy [3]. The perfection degree of conventional column is determined from

$$\eta_{cc} = (B_D + B_B) / (B_F + Q_R \cdot (1 - T_0/T_R))$$

where, B_D − exergy of distillate stream, MW; B_B− exergy of bottom product stream, MW; B_F− exergy of feed stream, MW; T_0 − environmental ambient temperature, ºC; T_R − temperature in conventional column reboiler, ºC; Q_R − reboiler duty of conventional distillation column, MW.

The perfection degree of distillation column integrated with ORC includes works of pump and expander:

$$\eta_{cc} = (B_D + B_B + W_{exp} \cdot \eta_{mg} \cdot \eta_{me}) / (B_F + Q_{ORC} \cdot (1 - T_0/T_{ORC}) + W_{pump} \cdot \eta_{mp})$$

where, T_{ORC}− temperature of DCORC vaporizer, ºC; Q_{ORC} − vaporizer duty of integrated scheme, MW.

Considering pressure equal to 101 kPa and temperature equal to 15 ºC as the specified dead reference state the exergy of the material process streams is determined from:

$$B = m \cdot (h_i - h_0) - T_0 \cdot (s_i - s_0) \cdot 10^{-3}$$

where, h_i, h_0− stream mass enthalpy at process and reference states, kJ/kg; s_i, s_0− stream mass entropy at process and reference states, kJ/kg ºK; m − stream mass flow rate, kg/s;

Simulation results using this model for several case studies is described in the following section

4. Case studies

This abstract shows 3 potential distillation columns for integration with ORC: i-butane/n-butane separation (gas fractionation unit), deisopentanizer (isomerization unit) and naphtha splitter (crude distillation unit).

Each case determines composition and outlet turbine pressure of power generation cycle. Table 1 describes the performance analysis which was carry out in terms of simulation procedure defined above.

As for basic ORC expander inlet pressure and temperature affect on net power generation, expander inlet and outlet temperature. For distillation column integrated with ORC the working fluid has the same composition as bottom product. The outlet pressure of the expander is equal to column bottom pressure. Bottom pressure depends on condensing temperature of distillate, which in turn, depends on the cooling utility temperature.

Increasing of expander inlet pressure leads to rise of difference between expander outlet temperature and bottom product boiling temperature [4]. That is, also, leads to working fluid flow rate decreasing.

Table 1. Simulation results summary

	C4 distillation		DIP		Naphtha splitter	
	CC	DC with ORC	CC	DC with ORC	CC	DC with ORC
Feed	$i\text{-}C_4$ $n\text{-}C_4$		$C_5\text{-}C_6$		NBP 62-180	
Bottom product	$n\text{-}C_4$		C_6		NBP 105-180	
Feed flow rate, t/h	25		40		120	
Distillate flow rate, t/h	12.5		6		53.8	
Number of theoretical trays	80		60		50	
Reflux ratio	7.9		15.7		0.9	
Column bottom pressure (expander inlet pressure), bar	8.5	8.5(30)	2.6	2.6(12)	2.3	2.3(10)
Vaporizer outlet temperature, ºC	72	137	84	153	162	239
Vaporizer flow rate, t/h	106	98	116	96	50	37
Vaporizer duty, MW	9.1	10.0	10.8	12.0	4.4	4.8
Net power out, kW	-	868	-	1126	-	361
Perfection degree, %	15.7	35	6.6	32	31.4	34

3. Conclusions

Integration of distillation column with ORC increases overall heat load of the column by 5-10% but almost whole of extra heat transforms to electricity power. The heat required for the distillation remains the same as in conventional column. The theoretical DC with ORC electricity generation efficiency is more than 90% if conventional column vaporizer duty is taken into account. The exergy efficiency of integrated scheme is higher than of conventional column and its determined by the properties of working fluid (bottom product).

Only thermodynamic properties and thermal stability of column's bottom product impacts on DC with ORC feasibility, but not the temperature difference between top and bottom of the column. This is an advantage of suggested technology to compare with heat integrated column with heat pumps where temperature difference is quite important.

For studied cases output electricity power is 0.3-1.1 MW. It's strongly depends on heat source and column feed flow rate.

According to the simulation results and the fact that such chemical components and their mixtures as propane, i-butane, n-butane, i-pentane et al. are utilized or considered as ORC working fluids, the distillation column integrated with ORC is seem to be practically feasible.

References

1. D. Carson. Electrical power generation by fractionation column reboiler. Patent. US4428202. 1984.

2. Aspen HYSYS operations guide. Version 3.2", Cambridge, USA. pp. 398-400.

3. J. Szargut. Exergy Method: Technical and Ecological Applications, WIT pres 2005. ISSN 1369-7331. pp. 4-7

4. D. Sladkovskiy. Improvement of Distillation Column Efficiency By Integration With Organic Rankine Power Generation Cycle. Proceedings of the AIChE annual meeting. 2013, november 3-8. San Francisco, USA

HIDiC – Design, Sensitivity and Graphical Representation

Meyer K.[1], Ianniciello L.[2], Nielsen J.E.[3], Bisgaard T.[1], Huusom J.K.[1], Abildskov J.[1]
[1]CAPEC-PROCESS, Dept. Chem. Biochem. Eng., DTU, Kgs. Lyngby, Denmark
[2]Université de Toulouse, INP-T, ENSIACET, Toulouse, France
[3]Harper-Vedel, Søborg, Denmark

Abstract
We have explored the applicability of recent design methods based on H-xy diagrams for the HIDiC [i,ii] also for non-ideal and azeotropic systems. When applied together with sensitivity analysis and verification through rigorous simulations based on a newly developed and detailed HIDiC model [iii], these concepts widen the scope of HIDiC design of a larger range of industrially relevant separations.

Keywords
Modeling and simulation, design, distillation columns, uncertainty, sensitivity analysis

1. Introduction

Distillation is the most used unit operation for separation of fluid mixtures in the process industry as it can continuously process large quantities and the technology is very well established. Interest in optimizing energy costs have led to alternative and intensified configurations such as MVR columns, dividing wall columns and internally heat integrated distillation columns (HIDiC) with or without external reflux/boil-up. The best known efforts made to develop heat-integrated distillation have been made in the Netherlands [iv] and in Japan [v]. HIDiC [iv] are mainly suited for symmetric columns with nearly similar numbers of stages in each section. Key challenges are: Devicing control structures, designing equipment allowing sufficient heat transfer area and lack of methods for process design. The design of a heat-integrated distillation process capable of accomplishing a given separation is clearly more complicated than designing a conventional distillation column accomplishing the same separation. Classical short-cut methods such as that of McCabe-Thiele do not provide the necessary information for a conceptual design of a HIDiC. Previous efforts towards methods for design of HIDiC comprise the works from Nakanishi [vi] for packed columns using a simulation model based on constant relative volatility. Later efforts comprise the works of Sun [vii]. This method was based on a constant heat duty per stage. The heat transfer area required for some stages are then very large compared to others (e.g. in the bottom part of the stripping section with lower temperature difference a relatively large heat transfer area is required), revealing the impracticality of the constant heat duty design scenario. The method of Sun et al. was later coupled with pinch analysis and composite curves in temperature-enthalpy representation. Later the method of Sun was followed up by the method of Gadalla [viii], who introduced an approach to conceptual design of heat integrated distillation columns based on constant available heat transfer areas as opposed to Sun (2003). A modification [ix] resolves design procedure for i-HIDiCs into two hierarchical phases: Thermodynamic and hydraulic analysis. In the thermodynamic design, the temperature profiles for both column sections are used as a design tool to generate design alternatives. In addition the model is proposed based on hydraulic calculations and tray geometry analysis, to quantify the column capacity for heat transfer. That design procedure starts by simulating a conventional column for the

given design problem. First, a HIDiC is simulated without any heat transfer between the two columns (basic design). Then, a complete HIDiC with full heat integration is simulated by increasing the level of heat transfer between the individual columns step by step until the condenser duty is reduced to zero (ideal i-HIDiC).

A path which we will explore here is that of Ho et al. [i, ii] based on Ponchon/Savarit diagram analysis, since energy/enthalpy is explicit in this representation. This design method has been labeled the Extended Ponchon-Savarit method. One key feature making Ponchon/Savarit diagram based methods particularly attractive is the graphical character of the technique. This method is currently only, known to us, reported for design of nearly-ideal zeotropic binary separations. However, the graphical character of the Ponchon/Savarit technique will only be preserved for HiDICs if one specifies the heat duty per stage. Then the heat transfer area required for each stage will be determined by a relation among the stagewise temperature profile and the heat duty exchanged. As mentioned, this seems impractical. It is more practical to design heat exchange areas. Also, since modular mass production will be necessary to keep CAPEX low, it seems advantageous to use similar areas per stage. Here we will explore a method that based on specification of feed flow and composition (F, z_F) and product streams (D, x_D) plus (B, x_B) incorporates steps from different sources among those mentioned above:

i. For a conventional column accomplishing the separation: Determine the number of ideal stages, R_{min}, N_{min}
ii. Set $R = 1.5\ R_{min}$
iii. Couple stages pairwise and set heat exchange areas to zero
iv. Increase ratio of rectifier pressure to stripper pressure and adjust reflux ratio/boil-up to satisfy performance criteria ($x_D = x_{D,spec}$ and $x_B = x_{B,spec}$)
v. Check if minimum temperature difference for heat integrated stages $\min[\Delta T] > \Delta T_{target}$? If not go to iv, if yes go to vi.
vi. Save result, increase heat exchange area and go to vii.
vii. Uncertainty analysis of performance measures to design variables

Steps iii-v requires rigorous simulations of MESH equations.

2. Results and discussion

For illustrating the steps concepts of design of heat-integrated distillation column, the procedure is applied to a separation task of industrial relevance. The task is to separate the non-ideal, azeotropic mixture, isopropanol and water, which is of interest in connection with regeneration of solvent after pectin precipitation steps.

2.1 Procedure

In the following mole fractions are for isopropanol. The feed is saturated liquid. The required specifications are listed in Table 1.

Table 1. Separation Specification.

Quantity	z_F	q	x_D	x_B	*P (column)*	ΔT_{target}
Specification	0.17	1	0.57	0.001	1 atm	5 K

2.1.1 Design Conventional Separation and Couple Stages Pairwise

According to step i, a conventional column satisfying the specified separation is designed using conventional methods. A minimum reflux ratio of 0.2 is obtained, giving a reflux ratio of 0.30 and thus 8 equilibrium stages including a re-boiler, with a feed location at the 5th equilibrium stage. The Wilson activity coefficient model has

been employed for calculating the activity coefficients. Ideal vapor phases are assumed. The final configuration is illustrated in Figure 1. Rigorous simulations suggests that the 8th stage should not be integrated since the temperature is significantly higher than the remaining stages in the stripping section which results in large required pressure ratio.

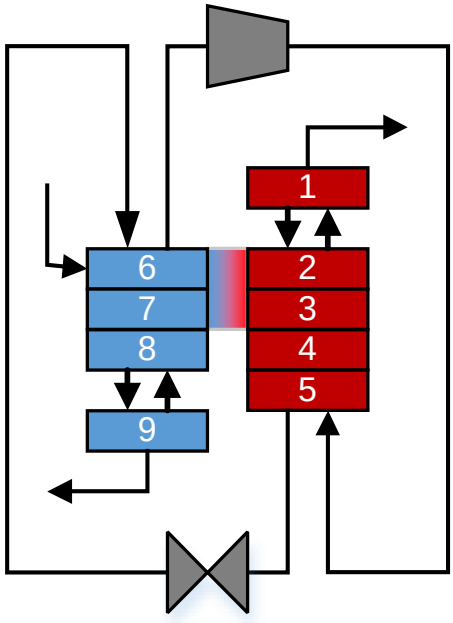

Figure 1. Configuration of heat-integrated distillation column for separation of isopropanol-water.

2.1.2 MESH simulations

Based on our previous steady-state model [iii], which includes a model for the HIDiC consisting of mass and energy (MESH) balances, rigorous simulations have been made using the algorithm in Section 1. The results are reported in Table 2. A linear relation is observed between the required pressure ratio, and duties when increasing the amount of internal heat transfer (increasing *A*) area. Obtaining a HIDiC results in a 24% energy reduction for both condenser and re-boiler. In steam 1.07 kW was saved by adding 0.148 kW electricity. Graphical representations of the HIDiC are shown in Figure 3. Based on active tray area estimation of conventional columns with a flooding factor of 80%, the obtained ideal HIDiC has a tray area of 0.0016 m^2 which is 1/133 the size of the required heat transfer area. Providing such an area is of course a challenge to equipment designers. Graphical representations of the ideal HIDiC are shown in Figure 3.

2.1.3 Candidate Evaluation

The choice of the most appropriate thermodynamic and thermo-physical models and physical parameters is critical to obtain a feasible and operable process design. But even if appropriate models have been chosen, these models impose uncertainties which may propagate through the calculation steps to such an extent that the final design might not be feasible or lead to poor performance.

For example, once designs have been obtained, one knows the number of stages, the flows, work of compression, heat duties, areas required for heat exchange. All of this is based on the assumption that the area available is used in a uniform fashion.

That is, that all area is covered by fluid (on each side) such that the underlying U = 500 kW / m^2 K is realized. It is also required that the underlying thermodynamic property estimates (presumably relative volatilities, vapor pressures and latent heats are the more important) are accurate. Likewise the pressure ratio can be a variable to which sensitivity is presumably great.

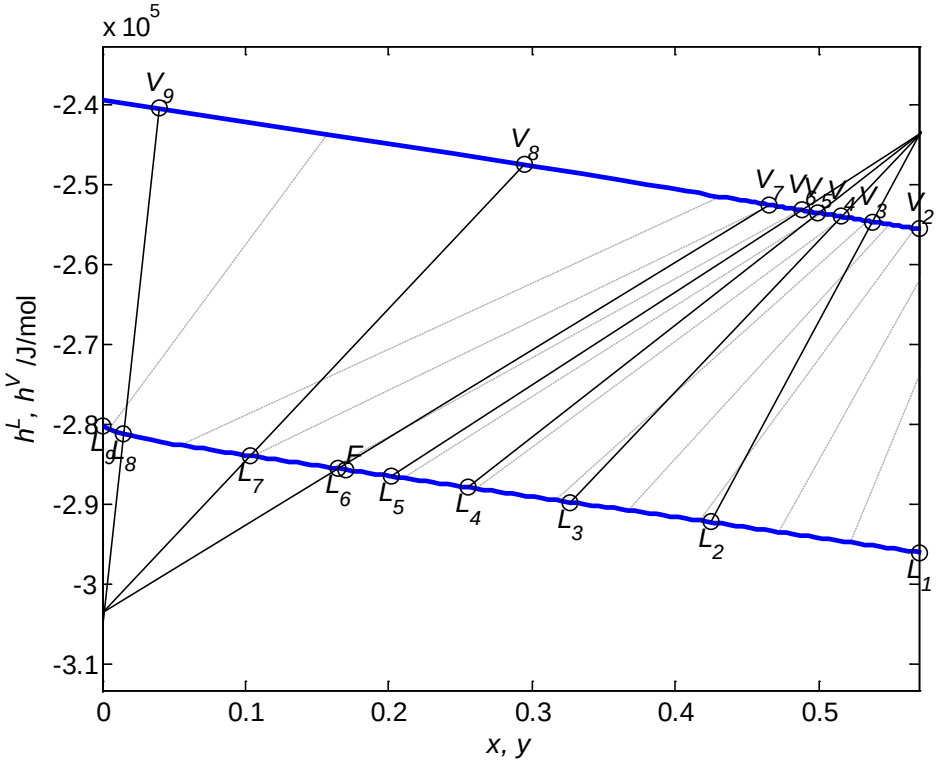

Figure 2. Hxy-representation of CDiC design.

Therefore it is advantageous to evaluate the sensitivity of process design to the uncertainties in design variables and property estimates obtained from thermo-physical property models.

Table 2. Rigorous HIDiC Simulations.

A/m^2	P_{rec}/P_{str}	min$[\Delta T]$ /K	Q_C/kW	Q_R/kW	W_S/kW
0	1	-4.32	-4.32	4.53	0
0	1.31	5.00	-4.36	4.53	0.132
0.0500	1.31	4.85	-4.13	4.29	0.132
0.050	1.32	5.00	-4.12	4.29	0.135
0.100	1.32	4.84	-3.89	4.06	0.136
0.100	1.33	5.00	-3.88	4.04	0.139
0.150	1.33	4.84	-3.65	3.82	0.139
0.150	1.33	5.00	-3.63	3.79	0.143
0.200	1.33	4.82	-3.41	3.57	0.143
0.200	1.34	5.00	-3.38	3.54	0.147
0.215	1.34	4.95	-3.31	3.47	0.147
0.215	1.35	5.00	-3.30	3.46	0.148

U = 500 kW/m^{2}K

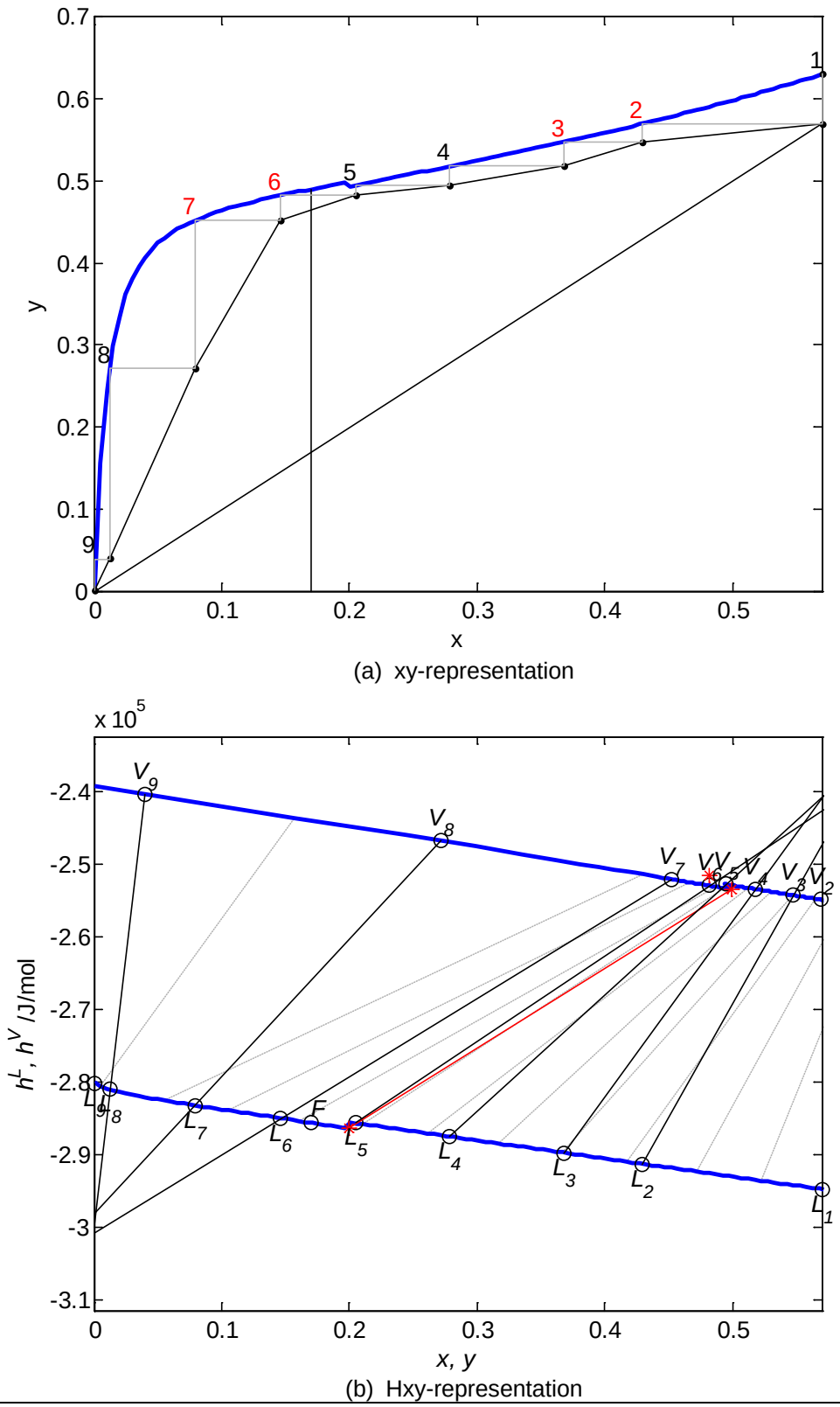

Figure 3. HIDiC Design, xy- (a) and Hxy- (b) representations. A = 0.0215 m^2; P_{rec}/P_{str} = 1.35. In (a), heat-integrated stages are labeled with red. In (b), the red dot above V_6 denotes the supersaturated vapor leaving the compressor. The red dots connected with a line represent the resulting liquid and vapor of an isenthalpic flash of the throttled liquid leaving the rectifying section.

Uncertainty and sensitivity analysis can be combined to determine which properties are of critical importance from a process design point of view and to establish an acceptable level of accuracy for different thermo-physical property methods employed. The results can then provide valuable identifications of the most sensitive parameters. For example, whether the sensitivity of a given design is most sensitive with respect to U, A, UA, P_r / P_s, relative volatility, and in which of these cases special precautions are required to ensure performance according to design.

3. Conclusions

We have described initial steps to formulating a procedure for designing HIDiCs. While the cases shown are limited, we believe this method has the advantage of combining existing computational schemes with uncertainty analysis in order to address the weakest spots of process designs. This helps the user to determine if additional property measurements and which experiments are most urgently required or to find more accurate values in the literature. A tailor-made and more efficient experimentation schedule is the result. In general, systematic sensitivity analysis should be part of process design efforts and is expected to contribute to better-informed and reliable design solutions in chemical industries. Further, the computational algorithm behind the Extended Ponchon-Savarit method, and its representation can also be applied to multi-component mixtures [x] in an H-xy diagram, although the full utility of this feature is not fully known yet. Substantial heat transfer areas seem to be required to realize the full potential of HIDIC technology.

References

[i] Ho T.J., Huang C.T., Lee L.S., Chen C.T., 2010. “Extended Ponchon-Savarit Method for Graphically Analyzing and Designing Internally Heat-Integrated Distillation Columns”, Ind. Eng. Chem. Res., 49: 350–358.

[ii] Wakabayashi T., Hasebe S., 2013. “Design of heat integrated distillation column by using H-xy and T-xy diagrams”, Comp. Chem. Eng., 56: 174-183.

[iii] Bisgaard T., Huusom J.K., Abildskov J., 2013. "A Modeling Framework for Conventional and Heat Integrated Distillation Columns", 10th IFAC International Symposium on Dynamics and Control of Process Systems. International Federation of Automatic Control. December 18-20, Mumbai, India.

[iv] Bruinsmaa O.S.L., Krikken T., Cot J., Saric M., Tromp S.A., Olujic Z., Stankiewicz A.I., 2012. "The structured heat integrated distillation column", Chem. Eng. Res. Design, 90: 458–470.

[v] a) Nakaiwa M., 2003. “Internally Heat-Integrated Distillation Columns: A Review”, IChemE Vol 81,Part A, Jan 2003, p 162-177; b) M. Nakaiwa et al., 2009. “Innovation in distillation processes”, Translation from Synthesiology, Vol 2, No 1, p 51-59, 2009.

[vi] T. Nakanishi, T. Takamatsu, M. Nakaiwa, K. Aso, H. Noda, N. Kuratani, 1999. "A case study of HIDiC design and energy saving", Computers and Chemical Eng. Suppl.: S855-S858.

[vii] a) Sun, L., Z. Olujic, A. de Rijke and P.J. Jansens, 2003, Industrially viable configurations for a heat integrated distillation column, Better processes for bigger profits, Proceedings of the 5th International Conference on Process Intensification for Chemical Industry, Maastricht, The Netherlands, 13-15 October, BHR Group ,151; b) M. Gadalla, Z. Olujic, L. Sun, A. De Rijke and P. J. Jansens, 2005. "Pinch Analysis-Based Approach To Conceptual Design Of Internally Heat-Integrated Distillation Columns", Chemical Engineering Research And Design, 83(A8): 987–993.

[viii] M. Gadalla, Z. Olujic , A. de Rijke and P. J. Jansens, 2005. "A new approach to the design of internally heat-integrated tray distillation columns". ESCAPE 15: 805. L. Puigjaner and A. Espuña (Editors).

[ix] Mamdouh Gadalla, Zarko Olujic, Laureano Jiménez Esteller, Gonzalo Guillén-Gosálbez, 2007. "A design method for internal heat integrated distillation columns (iHIDiCs)", ESCAPE 17: 1041. V. Plesu and P.S. Agachi (Editors).

[x] J.A. Reyes, A. Gómez, A. Marcilla, 2000. „Graphical Concepts To Orient the Minimum Reflux Ratio Calculation on Ternary Mixtures Distillation“, Ind. Eng. Chem. Res., 39: 3912-3919.

Biocatalytic Reactive Distillation

M. Wierschem[1], A. Niesbach[1], S. Soboll[1], R. Heils[2], L. Hilterhaus[3], A. Liese[3], I. Smirnova[2], P. Lutze[1]

[1]Laboratory of Fluid Separations, TU Dortmund University, Germany;

[2]Institute of Thermal Separation Processes, Hamburg University of Technology, Germany;

[3]Institute of Technical Biocatalysis, Hamburg University of Technology, Germany;

Abstract

Several crucial global challenges such as shortage of material resources in general, energy and water specifically, increasing food demand, environmental pollution and ageing societies as well as the development of new products are drivers for the increasing interest in biocatalytic reactions. Enzymes are enantio- and regioselective and are capable of using a wide array of substrate molecules and are still able to produce the desired product at high selectivity. Reactive distillation integrates reaction and separation in one unit operation which allows overcoming an equilibrium-limited conversion. Therefore, the combination of reactive distillation and enzymatic reactions creates synergies enabling efficient production of totally new products or existing products using other pathways.

As a case study, the lipase catalyzed transesterification of ethyl-butyrate with *n*-butanol is highlighted which is an equilibrium limited reaction. To provide the catalyst into the reactive zone, firstly a surface coating and secondly, catalytic packings filled with enzyme granulate can be used. The hydrodynamics of both reactive packings are investigated experimentally to develop suitable correlations for both packings. Then a detailed rate-based model of a continuous reactive distillation is developed in Aspen Custom Modeler ®. Subsequently, the detailed model is validated against experimental data of a pilot-scale reactive distillation column to check the agreement between experiments and modeling. This model enables the optimization of a biocatalytic reactive distillation system using both kind of packings and including all surrounded pumps and recycles for a production at industrial scale.

Keywords

Reactive Distillation, Biocatalysis, Hydrodynamics, Reactive packing, Modeling,

1. Introduction

In general, process intensification is a desired attempt to sustainable processes. Reactive distillation is one option to improve resource and energy management and can be used to enhance existing processes or synthesize new products. Specifically, the demand for optically active substances increases through their growing use for pharmaceutical and agricultural purposes [1]. The production of chiral compounds still lacks in the efficient usage of energy and raw material. Those processes show tedious separation tasks, due to the similarity of the chiral compounds chemical and physical properties. Since often only one enantiomer of the chiral compound is

applicable, a separation of both is necessary. Crystallization or extraction are widely applied for this separation. However, those desire a number of additional unit operations, for example to recycle solvents, which leads to a large energy consumption as well as high operating and investment costs. To reduce the amount of required steps, a reactive distillation column for the production of chiral compounds is a promising concept. Reactive distillation integrates reaction and separation in one unit operation and gaining synergy effects. The *in-situ* product removal (ISPR) positively affects the chemical equilibrium of a chemical reaction with a shift to its product site.

Enzymes are highly selective catalysts regarding their ability to selectively distinguish between stereo- and regioisomers. Since they are acquired from renewable resources, they are green catalysts and their catalytic properties can be formulated with protein or genetic engineering. To use enzymes, mild process conditions, as temperature and pH, are required, but are also advantageous.

Chemo-enzymatic reactive distillation integrates chemical and enzymatic reaction with separation in one unit operation. This combines the high (regio- and stereo-) selective ability of the enzyme and the high productivity of the chemical reaction (Figure 1). Several effects occur resulting from the integration. The chemical reaction products are converted by the enzymatic reaction and are separated thermally from each other, as well as the reaction products of the enzymatic step.

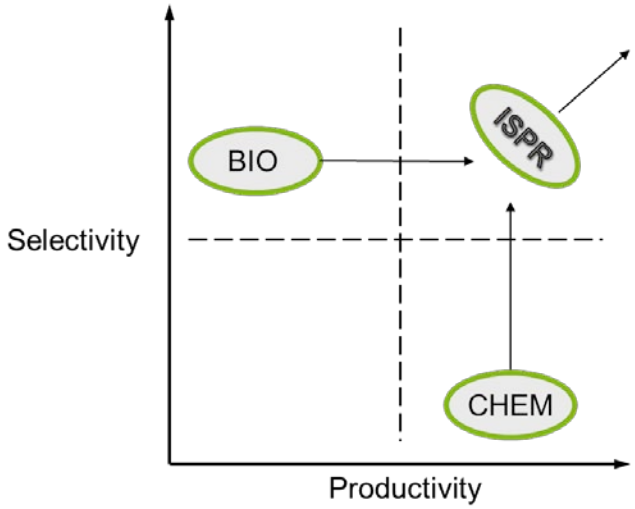

Figure 1: Effect of combining chemical reaction and biocatalysis with *in-situ* product removal (ISPR) in a reactive distillation.

In this study, to firstly proof the concept of an enzymatic reaction in a reactive distillation column it is necessary to answer the question how enzymes may be used inside distillation columns and if the provided activity is enough to run the distillation column. Different versions of enzyme provision have been developed [2]. This makes the description of the packings hydrodynamic necessary in order to model the reactive distillation process. To obtain hydrodynamic data, pressure drop and hold-up will be measured with a varied gas and liquid load [3]. The obtained data together with data of kinetics and physical properties of the substances form the basis for the developed model in Aspen Custom Modeler ® (ACM). The data will be transferred to ACM, where a rate-based model already is implemented. The model has been used

to design the experiments and to show the potential of this concept. Afterwards, the fully detailed model will be validated comparing simulated and experimental results from the biocatalytic reactive distillation.

2. Materials and Methods

In this section the methods and materials for measuring hydrodynamics and the setup of the reactive distillation column are presented (Figure 2).

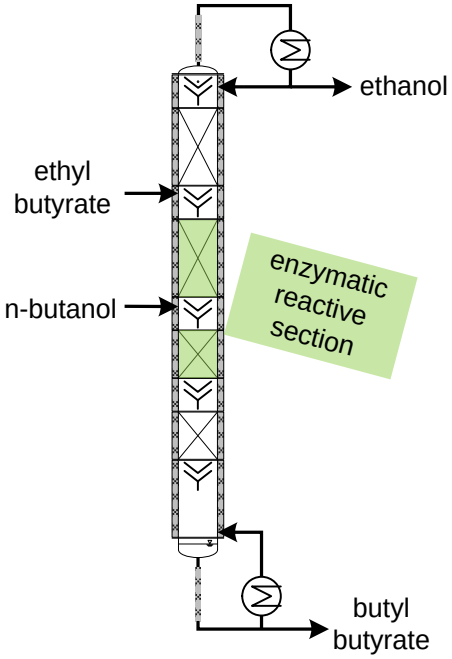

Figure 2: Scheme of the pilot-plant reactive distillation column equipped with reactive packing applied with enzyme

2.1 Hydrodynamics

To evaluate the pressure drop and liquid hold-up of the packings a column setup is prepared. For this purpose column sections of a diameter of 50 mm (DN50) are equipped with the packing. The packing is rotated 90 degrees to the other one to provide the mixing of the phases [4]. At the top of the column the liquid is fed to a liquid distributor which guarantees a defined liquid flow. At the bottom there is a connection for the gaseous feed, so that countercurrent flow is ensured. Feed pipes are equipped with mass and volume flow meter. The pressure drop can directly be measured with a u-tube manometer connected to the top and bottom liquid distributor. The liquid hold-up is calculated by a mass balance. The materials for this evaluation are water and nitrogen as the liquid and gas. Different liquid and gas loads are applied to the column and pressure drop and liquid hold-up are detected.

2.2 Reactive distillation set-up

The reactive distillation is investigated in a pilot-plant distillation column of a diameter of 50 mm of around 5.3 m packing height, of which two of six sections are equipped with (enzymatic) reactive packing. The two sections above the reactive section and the two sections below are equipped with uncoated Sulzer BX^{TM} packing. The

sections are connected by liquid distributors. To these distributors sample withdrawing points and PT100-thermocouples for vapor temperature measurement are attached. The column is controlled by Siemens Simatic^{TM} PCS7. An adiabatic operation mode is guaranteed by use of an outer mineral wool layer connected to a heating wire. The flow rates of feed, bottom and distillate streams are calculated with a balance and the mass increase/decrease over time. Samples are withdrawn from the different liquid distributors and analyzed by gas chromatography.

3. Results and discussion

In this contribution, the lipase-catalyzed biocatalytic reactive distillation of the transesterification of ethyl butyrate and *n*-butanol is investigated (Figure 3).

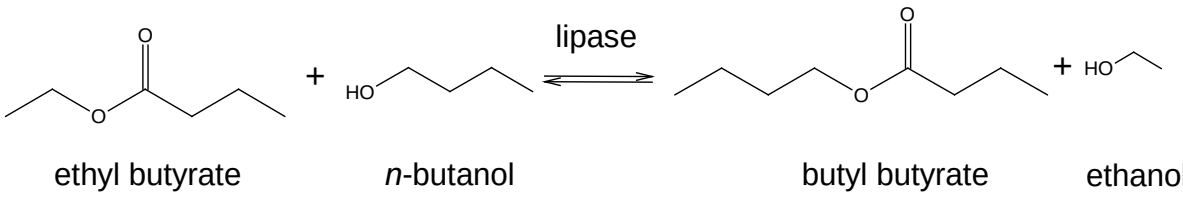

Figure 3: Reaction scheme of the transesterification of ethyl butyrate with *n*-butanol

3.1 Selection and development of packing

A homogeneous addition of the enzymes is not feasible since they will pass the reboiler and will denature at high temperatures. For the immobilization of enzymes within the column, different concepts will be presented. One method is the coating of wire gauze packing with a sol-gel, that contains entrapped enzymes. Another method is the immobilization by covalent bonding on small beads which are then integrated in catalytic packing. The sol-gel coating in the one case covers the gaps between the wires of the gauze packing (Figure 4).

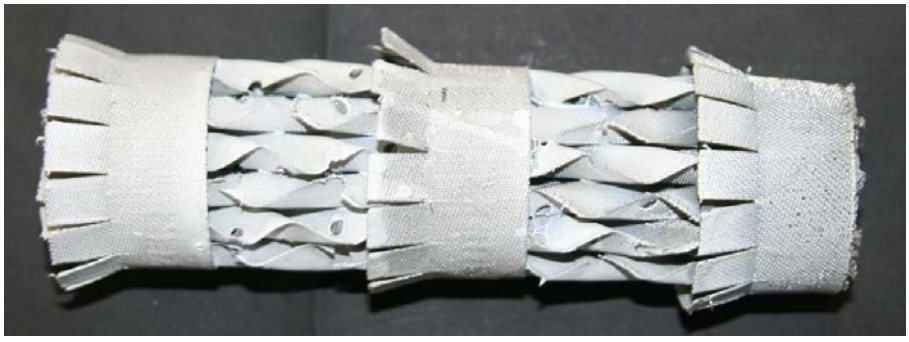

Figure 4:Sol-gel coated wire gauze packing Sulzer BX

3.2 Modeling and model validation

The modeling of the biocatalytic reactive distillation is accomplished in ACM. A non-equilibrium stage model using effective diffusion coefficients and used for the simulations is developed by Klöker *et al.* [5] and extended in this work. The model is adapted to the presented substance system and utilizes heat and mass transfer calculations. Missing parameters such as activity coefficients are calculated by UNIQUAC method as well as physical and thermodynamic data. Implementing coated packing to the model means to correlate the liquid hold-up h_L. The

determined empirical correlation for the hold-up including liquid load U_L and the f-factor F_F

$$h_L = 32.5\, {U_L}^{0.2591} + (367\, U_L + 0.1044) F_F$$

is derived from experimental data shown below (Figure 5). The experimental data shows that the pressure drop is similar for coated and uncoated packing.

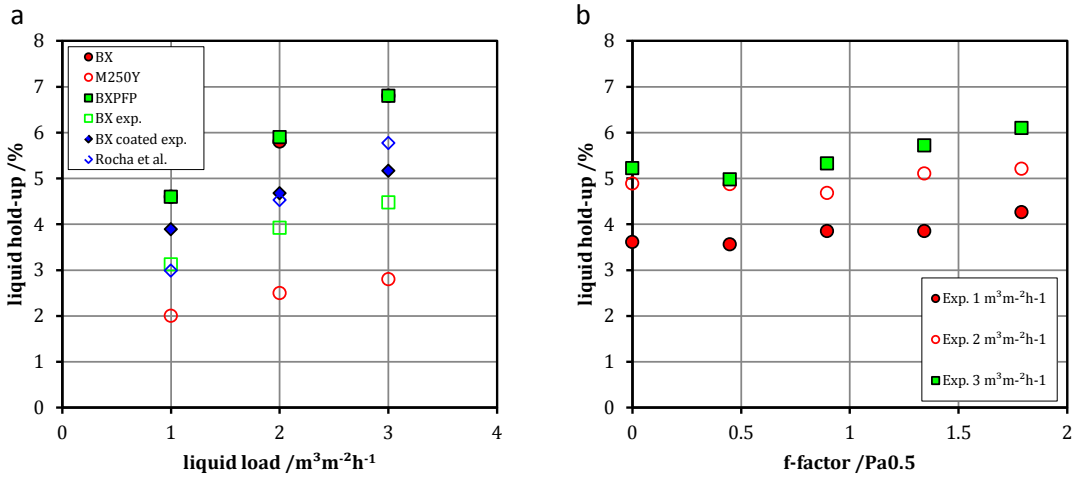

Figure 5: Liquid hold-up related to a) liquid load and b) f-factor. In a) hold-ups for different packing types (BX, Mellapak 250Y, and plastic BX (BXPFP)), experimental data of coated and uncoated BX-packing as well as correlations from Rocha et al. [6]. In b) experimental hold-ups for different liquid loads (1, 2 and 3 $m^3m^{-2}h^{-1}$) are shown.

The good accordance of the correlation and the experiments is shown in a parity plot as well as the simulation data for the set-up with enzyme-coated Sulzer BX packing (Figure 6).

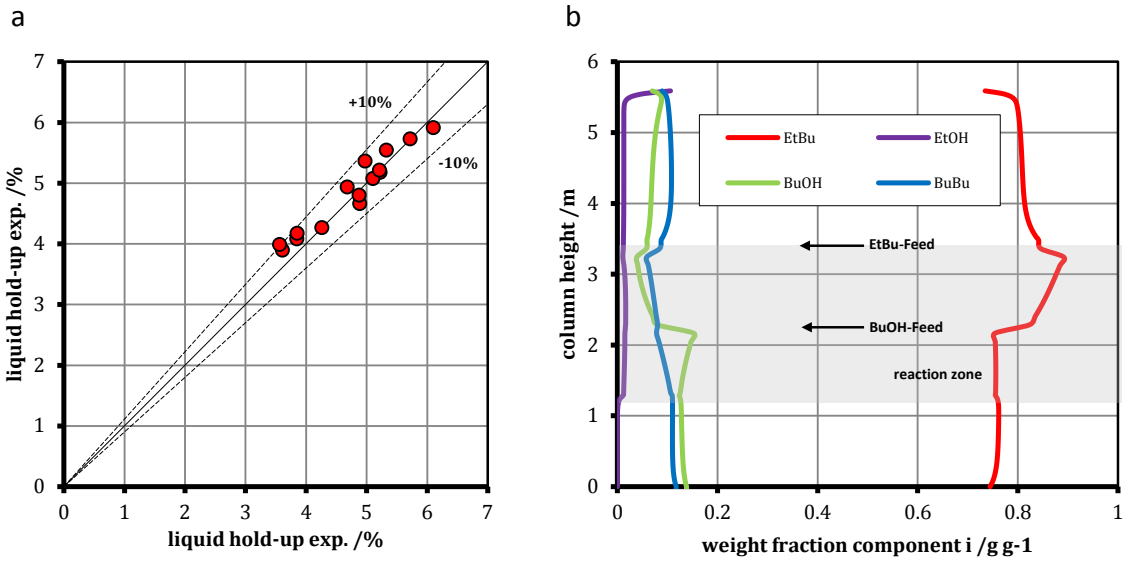

Figure 6: a) Parity plot for the simulated and experimental liquid hold-ups. b) Concentration profile of the liquid phase of the column. Feed positions and the reaction zone as a gray layer are shown.

3.3 Process Simulations and optimization

Simulated concentration profiles of the biocatalytic reactive distillation experiments are shown and will be compared to experimental data. The model is validated if a high accuracy between experiment and simulation is obtained. The outcome of the process simulations for coated packing is shown in Figure 6 b. There the weight fraction of the components is shown over the column height. It is obvious that there is a high concentration of the substrate ethyl butyrate in the liquid phase to shift the equilibrium to the product side (molar feed ratio of ethyl butyrate:*n*-butanol 2:1). The substrate *n*-butanol gained a conversion higher than 60%. With this set-up a bottom concentration of nearly 0.12 g/g butyl butyrate is achieved, whereas ethanol completely is withdrawn at the column head. The configuration of the feed positions has been selected due to higher conversions compared to other configurations. These process configurations and operating parameters experiments are conducted and are then compared to the process simulation results. Based on these, to find the optimal process variables an optimization problem will be solved with an evolutionary algorithm. The algorithm is looking for the global optimum by altering the process variables.

4. Conclusions and outlook

In this study, the concept for the realization of the chemo-enzymatic reactive distillation is shown and necessary pre-experiments were conducted. The hydrodynamics of two concepts of catalytic packing have been studied in order to attain correlations to model a biocatalytic reactive distillation column. If the temperature limits for the enzymes are not exceeded in the column this model has been (i) used to verify the operating window and (ii) to identify the potential of the application in a reactive distillation. Currently, the simulated process is compared to the experimental results of a pilot-scale biocatalytic reactive distillation. The validated model is then used to find the optimal process variables. For further studies, regarding the concept of the chemo-enzymatic reactive distillation, a combination of a chemical and an enzymatic reaction in one distillation column will be investigated.

Acknowledgements

The author thanks Sulzer Chemtech Ltd for the support and provision of Sulzer BX wire gauze packing. The author has received funding from the Ministry of Innovation, Science and Research of North Rhine-Westphalia in the framework of CLIB-Graduate Cluster Industrial Biotechnology, contract no: 314 - 108 001 08

References

[1] Breuer, M. *et al.: Industrial Methods for the Production of Optically Active Intermediates.* Angew. Chem. Int. Ed. 43, p. 788–824 (2004)

[2] Heils, R. *et al*.: Integration of Enzymatic Catalysts in a Reactive Distillation Column with Structured Packing. Ind. Eng. Chem. Res. 51, p. 11482−11489 (2012)

[3] Hoffmann, A.: *Scale-up von Reaktivrektifikationskolonnen mit katalytischen Packungen*. Shaker, Aachen (2005)

[4] Olujic, Z.: *Standardization of structured packing efficiency measurements* (2007)

[5] Klöker, M. *et al*.: *Rate-based modelling and simulation of reactive separations in gas/vapour–liquid systems*, Chem.Eng. Process. 44, p. 617–629 (2005)

[6] Rocha, J. A. et al.: *Distillation Columns Containing Structured Packings: A Comprehensive Model for Their Performance. 1. Hydraulic Models*, Ind. Eng. Chem. Res. 32, p. 641-651 (1993)

Methyl Acetate Synthesis, Novel Process Concepts

Susanne Lux, Thomas Winkler, Matthäus Siebenhofer
Graz University of Technology, Institute of Chemical Engineering and Environmental Technology, Graz, Austria

Background
Application of reactive distillation in methyl acetate synthesis is one of the most striking examples of process intensification. Although dating back to the eighties this process is still a benchmark which is worth matching with. Synthesis and isolation of methyl acetate serves as a welcome basic project in this research. Synthesis of methyl acetate is limited by the chemical equilibrium. In the absence of catalysts it suffers from low reaction rates. Azeotropic product mixtures as well as low relative volatility of binary systems hinder product isolation.

Goal
Aim of this project was to design an alternative process for methyl acetate synthesis based on heterogeneous catalytic esterification, pervaporation and distillation. Product isolation through pervaporation is not limited by the vapour-liquid equilibrium. Application of membranes featuring hydrophilic surface properties allows for permeating methanol and water whereas methyl acetate is enriched in the retentate phase.

Project
A process for membrane supported methyl acetate synthesis was developed. The reaction was conducted under acetic acid limiting conditions. Pervaporation modules were arranged in series to increase the methyl acetate content in the retentate ensuring a product quality of $w > 0.995$. Separation of the ternary permeate mixture of methyl acetate, methanol and water was carried out in a tray distillation column. The top product methyl acetate/methanol was recycled and the reaction product water left the system at the bottom of the column.

Keywords
Methyl acetate, azeotrope, pervaporation, hydrophilic membrane

1. Introduction

The production of high pure methyl acetate (MeOAc) via liquid-phase esterification of acetic acid (HOAc) and methanol (MeOH) is challenging due to its reaction kinetics, low reaction rate in the absence of a catalyst, and difficulties in product isolation. This synthesis is a typical example of an equilibrium-limited reaction in which the conversion is low due to the limits imposed by the thermodynamic equilibrium. Methyl acetate isolation is hindered by thermodynamic implications through azeotrope formation. Methyl acetate forms low boiling azeotropes with both the reactant MeOH and the by-product water (H_2O).
The state of the art process for methyl acetate synthesis is a reactive distillation process, well known as the Eastman-Kodak process[1].

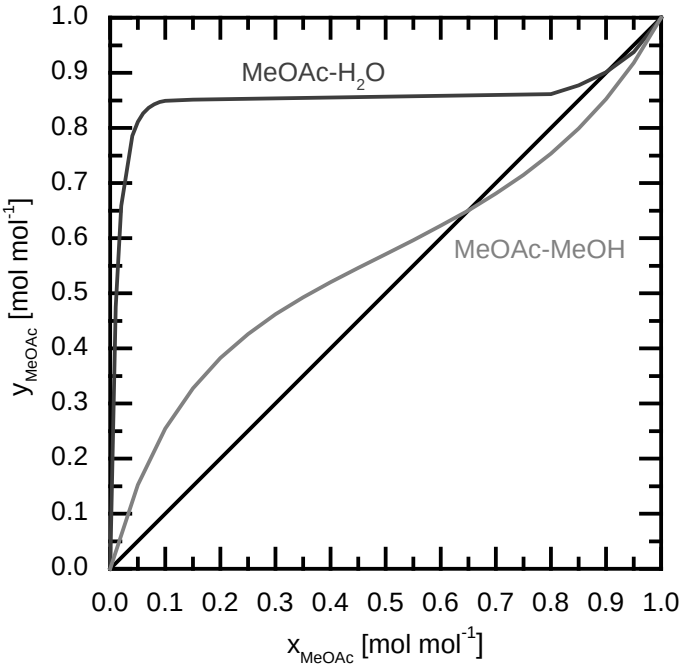

Figure 1. Vapour-liquid equilibria of the binary systems MeOAc–MeOH und MeOAc–H_2O at p = 1 atm (NRTL)[2,3]

In the course of this project an alternative membrane-supported process route for methyl acetate synthesis was designed. It is characterized by the combination of chemical reaction and pervaporation. Pervaporation processes are applied when conventional unit operations are cost intense and uneconomic due to limitations in thermodynamics (equilibrium, azeotropes). In recent years there has been a significant rise in the number of pervaporation processes for industrial applications, due to the progress in the field of membrane technology.

Pervaporation in combination with conventional unit operations offers a promising alternative which features several advantages. As separation through pervaporation is governed by the solution-diffusion behaviour of the components in the membrane, thermodynamic limitations caused by the vapour-liquid-equilibrium can easily be overcome. Due to reduced process temperatures in pervaporation, side reactions such as the dehydration of methanol to dimethyl ether and water are suppressed. Additionally, reaction with pervaporation can handle (stand) higher water contents of reactants than reactive distillation technology. This opens up a new perspective in methyl acetate synthesis.

Studies on pervaporation-assisted methyl acetate synthesis are scarce. Assabumrungrat et al.[4] conducted a theoretical study on the synthesis of methyl acetate in pervaporation membrane reactors and highlighted the high potential thereof. However, appropriate membranes are essential for successful application. Depending on the degree of crosslinking of the membranes and the composition of the feed, composite membranes generally show specific swelling behaviour. This affects their selectivity and the permeate fluxes during pervaporation. Therefore successful membrane selection still needs experimental support and modelling of the permeate flux has to account for composition dependent swelling.

In order to successfully design a pervaporation-assisted process for methyl acetate synthesis the esterification reaction and the pervaporation step were investigated individually and carried out in series in semi-batch mode. Based on the outcome of investigations the overall process was designed.

2. Results and discussion

2.1 Heterogeneous catalytic esterification of acetic acid and methanol

The esterification reaction itself was catalysed by commercial cation exchange resins, e.g. Amberlyst® 15. The operation temperature was kept well below boiling point. The reaction kinetics was modelled with an adsorption based approach based on the Langmuir-Hinshelwood mechanism accounting for the fact that the reactants show different adsorption behaviour on the resin due to their different polarity. The determination of the adsorption coefficients was established by conducting isolated experiments with non-reactive binary mixtures of the reaction solution. The temperature dependencies of the adsorption coefficients were determined by measuring the adsorption enthalpies. The reaction rate coefficients were determined by investigating the influence of the reaction temperature, the initial ratio of the reactants, the size of the catalyst and the amount of catalyst. The reaction was performed under acetic acid limiting conditions and excess methanol and water were then separated from methyl acetate by pervaporation.

2.2 Pervaporation

In pervaporation the liquid feed stream is split into a retentate and a permeate phase via selective dense membranes. The permeate side is evacuated to create differences in the chemical potential as driving force. When using membranes with hydrophilic surface properties the polar components methanol and water can permeate the membrane to be removed as a vapour. Due to its lower polarity methyl acetate is enriched in the retentate phase. In contrast, methyl acetate can permeate the membrane when membranes with organophilic surface properties are used.

In methyl acetate production the binary mixture methyl acetate/methanol is the technological bottleneck of the isolation process. Therefore the membrane screening was based on the separation of the binary methyl acetate/methanol mixture.

A membrane screening for hydrophilic membranes was conducted using commercially available polymer membranes (PERVAP™2255-30, PERVAP™2255-70, PERVAP™2255-80). The active layer of the membrane consists of crosslinked PVA. The membranes differ in their degree of crosslinking. Selectivity and permeate fluxes for the three membranes were compared. An increase in the degree of crosslinking of the membrane leads to a significant improvement in selectivity. The maximum permeate flux of the investigated PVA-membranes ranges from 0.9 to 9.4 $kg \cdot m^{-2} \cdot h^{-1}$. An adapted solution-diffusion-model was developed to describe the membrane behaviour. It accounts for the influence of swelling phenomena in the active layer of the membrane.

2.3 Pervaporation-assisted methyl acetate synthesis

A reaction scheme for the membrane-supported methyl acetate synthesis was developed. The reaction was conducted under acetic acid limiting conditions. Pervaporation modules (membranes PERVAP™2255-70 and PERVAP™2255-80) were arranged in series to increase the methyl acetate content in the retentate ensuring a product quality of $w_{MeOH} > 0.995$ kg kg^{-1}.

The separation of the ternary permeate mixture containing methyl acetate, methanol, and water was realised in a tray distillation column. The top product was recycled and the reaction by-product water was drawn out of the system at the bottom of the column.

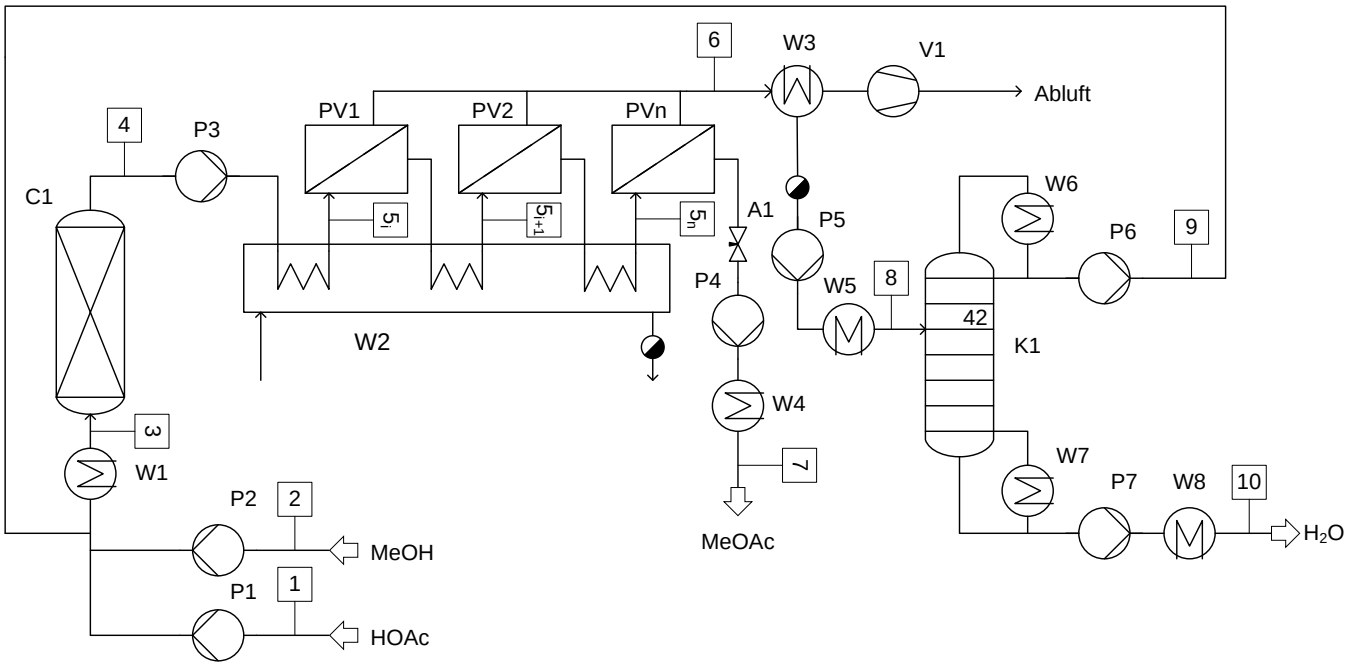

Figure 2: Pervaporation-assisted process for methyl acetate synthesis

3. Conclusions

Based on the outcome of experimental investigations pervaporation-assisted isolation of methyl acetate is presented as an alternative route to the state of the art process.

Acknowledgements

The authors acknowledge Sulzer Chemtech AG for kindly providing membrane samples.

References

1. V. H. Agreda und L. R. Partin. Reactive distillation process for the production of methyl acetate. Patent 4,435,595 (US), March 6, 1984.
2 J. Gmehling, U. Onken, and W. Arlt. Aqueous-organic Systems: Supplement 1. Chemistry data series: Vapor-liquid equilibrium data collection. DECHEMA, 1998.
3 J. Gmehling, W. Arlt, and U. Onken. Vapor-liquid Equilibrium Data Collection. Chemistry Data Series. Dechema, 1982.
4. S. Assabumrungrat, J. Phongpatthanapanich, P. Praserthdam, T. Tagawa and S. Goto, Chemical Engineering Journal, 2003, 95, 57–65.

Process Intensification for the Absorptive Upgrading of Biogas

Joachim Kerber[1], *Jens-Uwe Repke*[1]
[1]*TU Bergakademie Freiberg, Institute of Thermal, Environmental and Natural Products Process Engineering, Germany*

Abstract
Membrane gas-solvent contactors incorporate the advantages of absorption and membrane gas separation process in one unit-operation. In the presented work, such a membrane contactor is used for upgrading biogas to bio natural gas. Therefore, carbon dioxide (CO_2) has to be separated from methane (CH_4).
A lab-scale membrane contactor with a dense, polymeric gas separation membrane has been designed and first experiments have been carried out. Water and a 0.1 M K_2CO_3 solution were used as solvents.
First permeation results with CO_2 using a dense polymer membrane are presented. It can be seen that the use of a K_2CO_3 solution increases the membrane flux. The influence of the solvent velocity, the solvent pressure and the transmembrane pressure in particular on the mass transfer is demonstrated. It is shown that the transmembrane pressure has the largest impact on the transmembrane flux.
A mass transfer model incorporating the mass transfer through the dense selective membrane and the reaction kinetics on the permeate side is used to quantify the influence of the chemical absorption and the membrane on the total mass transfer resistance.

Keywords
Biogas Upgrading, Membrane Contactor, Potassium Carbonate, Gas Permeation, Hybrid Process

1. Introduction

Upgrading biogas to bio natural gas (BNG) is a promising approach to substitute regenerative biogas for finite fossil gas. Moreover, the upgraded gas can be fed in the existing natural gas grid and thus be used more efficiently than CO_2-rich biogas. For producing bio natural gas, the main part of the carbon dioxide needs to be removed from the biogas, which is crucial for the economic feasibility of the upgrading process. There are different commercially used processes for the upgrading step, e.g. amine scrubbing, pressure swing adsorption, pressurized water scrubbing and, recently increasing, gas permeation membrane processes.
The conventional separation processes are technically mature but do not make use of synergies between the respective processes which could offer additional benefits. Gas permeation membrane processes in contrast have a high potential to lower the separation costs due to their simple operation but lack high separation efficiencies within the demanded limits.
Hence, for process intensification, an integration of dense gas separation membranes with other unit operations is advantageous. The integration of a membrane in an absorption process combines the advantages of the respective unit operations i.e. a very high and defined specific mass transfer area and a high selectivity for CO_2. In such membrane contactors, the membrane acts as a barrier between the gaseous and the liquid phase (cf. *Figure 1*). Unlike conventional

absorber columns, membrane contactors exhibit neither entrainment nor flooding [Reed et al.,1995].

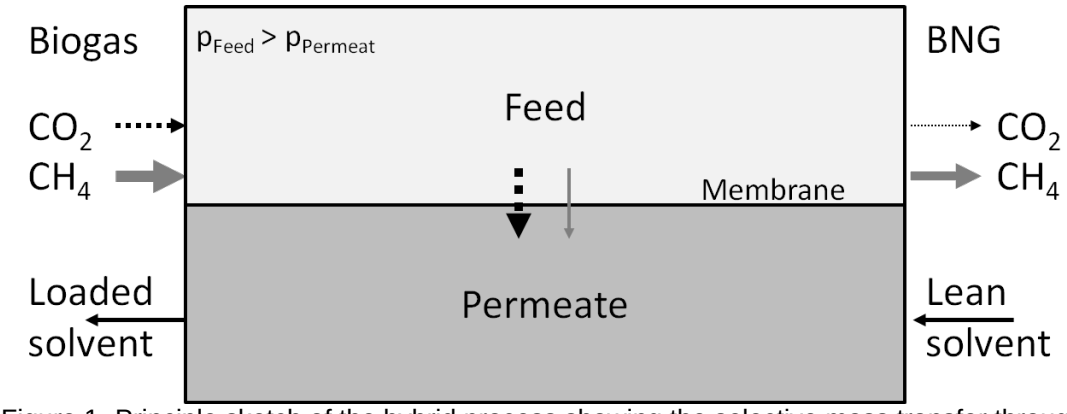

Figure 1. Principle sketch of the hybrid process showing the selective mass transfer through a dense membrane

Since the membrane in the contactor represents an additional resistance $1/k_m$ to the overall mass transfer K compared to a conventional absorption process,

$$\frac{1}{K} = \frac{1}{k_g} + \frac{1}{k_m} + \frac{H}{E \cdot k_l} \qquad (1)$$

its influence on the total mass transfer has to be overcompensated by the plus of mass transfer area A_M according to equation 2.

$$\dot{N}_i = K \cdot A_M \cdot \Delta f_i \qquad (2)$$

Compared to conventional absorption columns with average specific mass transfer areas of around 100-250 m²/m³, industry-scale membrane contactors typically have a much higher mass transfer area per unit volume of more than 500 m²/m³ [Reed et al., 1995]. The test cell used in these experiments exhibits a specific area of 1000 m²/m³.

Different membrane types are suggested to be used in membrane contactors, mainly porous membranes (cf. [Luis 2012]), but also porous membranes coated with an absorbent-impermeable but unselective layer to improve the operability [Nguyen et al., 2011]. More than that, using dense CO_2-selective absorbent-impermeable gas permeation membranes in membrane contactors to further increase the selectivity of the process represents a novel approach for further process intensification and will be presented here. In such a dense membrane contactor, a pressure difference across the membrane can be realized which is an additional optimization parameter for the process.

In this work, a membrane contactor with such a dense, selective membrane is investigated using different chemical and physical solvents in order to determine the influence of the membrane on the overall mass transfer and the selectivity of the process depending on the fluid characteristics incorporation the pressure difference across the membrane.

2. Theoretical framework

In order to determine the influence of the membrane on the total mass transfer resistance in the contactor, a rigorous mass transfer model incorporating the membrane resistance and the chemical absorption on the retentate side was developed. With this model, it is possible to quantify the mass transfer resistance caused by the membrane and the permeate solvent, respectively. The model can be

used to find an optimal operation point by minimizing the mass transfer resistance in the contactor.

2.1 Mathematical description of membrane flux in a membrane contactor

The mass transfer in a dense membrane can be described using Fick's law

$$J_i = D_i \cdot \frac{c_i^G - c_i^L}{\delta}. \quad (3)$$

Assuming a membrane-gas phase equilibrium on the membrane-feed surface and a membrane-liquid phase equilibrium on the membrane-solvent surface [Wijmans and Baker, 2006], the membrane flux J_i can be written as

$$J_i = \frac{P_i}{e} \cdot \Delta f_i = k_m \cdot \left(f_i^G - f_i^L\right) \quad (4)$$

where the permeability P_i is defined as

$$P_i = K_i \cdot D_i. \quad (5)$$

K_i being the sorption coefficient and D_i the diffusion coefficient, this model is called solution-diffusion model.
The fugacities can be described using Henry's law on the permeate side (cf. Table 1) and an φ-approach on the gas side:

$$f_i^L = \gamma_i^{L^*} \cdot x_i^L \cdot H^L \quad (6)$$

$$f_i^G = \varphi_i \cdot y_i \cdot p \quad (7)$$

2.2 Mass transfer resistance on the liquid permeate side

The resistance on the liquid side of the membrane can be quantified by the mass transfer coefficient k_L. It can be calculated using a Sherwood correlation for a laminar flow in spacer-filled channels [Cussler 2009].

$$Sh = \frac{k_L \cdot d_h}{D} = 1.62 \cdot Re^{\frac{1}{3}} \cdot Sc^{\frac{1}{3}} \cdot \left(\frac{d_h}{L}\right)^{\frac{1}{3}} \quad (8)$$

2.3 Mass transfer enhancement due to the chemical reaction in a K_2CO_3 solution

Due to the reversible reactive absorption of CO_2 in a K_2CO_3 solution, the absorption rate and the capacity for CO_2 are improved. This can be expressed by the Enhancement factor E in equation 1. By neglecting the direct reaction of CO_2 with water (acidic mechanism) which is only relevant for low pH values (physical absorption in water), the brutto reaction for the dissociation of CO_2 in carbonate solutions is [Savage et al., 1980]

$$CO_2 + CO_3^{2-} + H_2O \leftrightarrow 2\,HCO_3^- \quad (9)$$

where the rate-controlling step is the reaction of CO_2 with the hydroxide ion:

$$CO_2 + OH^- \overset{k_{CO_2}}{\longleftrightarrow} HCO_3^- \quad (10)$$

Hence, the Enhancement factor for a justifiably assumed pseudo first-order reaction for the reactive absorption [Danckwerts and Sharma, 1963] in a fast reaction scheme

(Ha=E) depending on the loading X_{CO2} can be calculated as follows [Savage et al., 1980]:

$$E = Ha = \frac{\sqrt{D_{CO_2} \cdot k_{CO_2} \cdot \frac{K_W}{K_2} \cdot \frac{(1-X_{CO_2})}{2 \cdot X_{CO_2}}}}{k_l} \qquad (11)$$

3. Experimental Set-up

The main objective in the design of the test cell is to determine the molar membrane flux J_i of the respective species into the solvent depending on the solvent velocity, the solvent pressure and the pressure difference across the membrane.

$$J_i = \frac{\dot{N}_{F,i} - \dot{N}_{P,i}}{A_M} = K \cdot \Delta f_i \qquad (12)$$

Since there is no accumulation of mass in the membrane, the flux can be determined by measuring the gas flow and the compositions before and after the test cell when the total membrane area A_M is known.

The experiments have been carried out with a dense, selective gas permeation membrane. Pure water and a 0.1 M K_2CO_3 solution were used as solvents. For carrying out the CO_2 permeation experiments, the feed mass flow and the temperature of the solvent were kept constant (cf. Table1). The membrane permeance and Henry's constant [Kerber and Repke, 2012] were determined experimentally. The loaded solvent is regenerated in a vacuumed and heated tank before fed into the contactor. The setup of the test cell is depicted in *Figure 2*.

Table 1. Test cell geometry and fixed parameters.

Membrane area	cm²	400
Specific surface	m²/m³	1.000
Test cell temperature	°C	25
Permeance CO_2 (25 °C)	mol/ m²h bar	135
Henry CO_2-H_2O	bar	1.607
Feed mass flow	mol/h	9

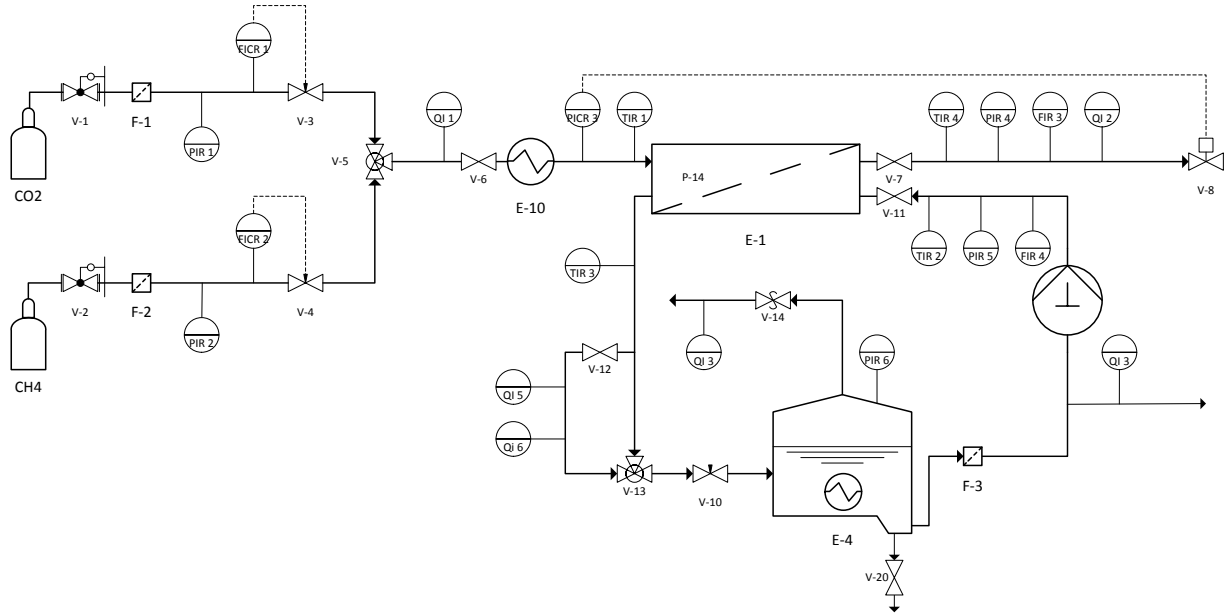

Figure 2. P&ID of membrane contactor test stand.

4. Results and discussion

The membrane flux has been determined for two solvents (pure water and a 0.1 M K_2CO_3 solution) under variation of the solvent velocity, the solvent pressure and the pressure difference across the membrane. The membrane flux increases with increasing solvent velocity and permeate pressure (*Figure 3*). This is caused by an increasing driving force and mass transfer coefficient. The influence of the permeate pressure however is caused by an increasing solubility of CO_2 in the solvent. When K_2CO_3 is used as solvent, an average flux increase of approx. 20% can be observed in the solvent velocity and permeate pressure variations.

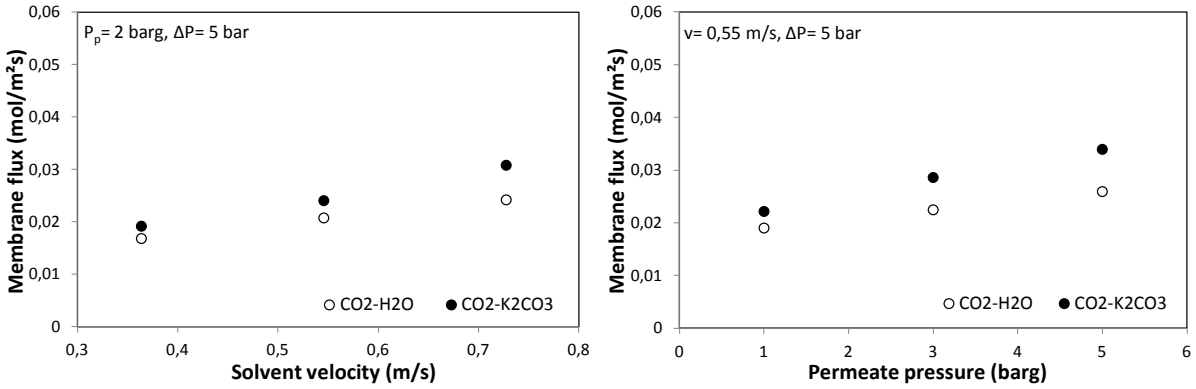

Figure 3. Membrane flux versus solvent velocity (l) and permeate pressure (r) for CO_2 in water and 0.1M K_2CO_3 solution.

However, the pressure difference across the membrane has a larger impact on the membrane flux. The influence of K_2CO_3 in contrast is not very pronounced (*Figure 4 left*).

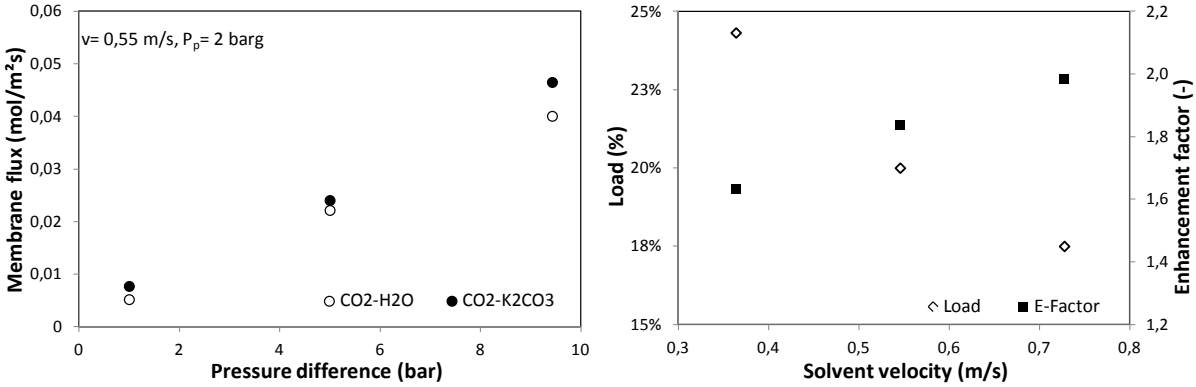

Figure 4. Membrane flux versus pressure difference for CO_2 in water and 0.1M K_2CO_3 solution (l) Load of 0.1 M K_2CO_3 solution and Enhancement factor versus solvent velocity (r).

The loading of the carbonate solution reaches 25 % for the lowest investigated solvent velocity (*Figure 4 right*). The numerical investigation shows that the Enhancement factor decreases with increasing load of the solution. The more CO_2 is absorbed, the poorer the mass transfer enhancement. An analysis of the mass transfer resistances shows that the membrane contributes to 5 % to the total mass transfer using water as solvent compared to 20% when 0.1 M K_2CO_3 is used. The mass transfer resistance in the liquid phase is decreasing due to the enhancement of the chemical reaction. The membrane resistance however is not affected by the solvent.

5. Conclusions & Outlook

The CO_2 flux through the dense membrane contactor has been determined dependent on solvent velocity, solvent pressure and transmembrane pressure difference. Using 0.1M K_2CO_3 as solvent enhances the mass transfer in the contactor for approx. 25%. An analysis of the Enhancement factor shows that higher K_2CO_3 concentrations can improve the mass transfer.
In contrary to porous membrane contactors, the transmembrane pressure difference can be varied since a dense, selective membrane is used. This parameter has a strong impact on the transmembrane flux.
More detailed investigations with higher concentrated K_2CO_3 solutions will be carried out. The detailed influence of the transmembrane pressure on the performance of the contactor will be investigated. The selectivity of the process will be determined and compared to non-selective contactors.

More than that, the influence of the complex chemical reaction on the permeate side of the contactor has been integrated in a mass transfer model. Thus, the influence of the membrane and the gas absorption on the overall mass transfer will be identified using the simulation model and presented in detail.

Acknowledgements

The authors would like to thank Torsten Brinkmann from HZG (Helmholtz Zentrum Geesthacht) for the generous allocation of the polymeric gas separation membranes.

References

Reed, B.W., Semmens, M.J., Cussler, E.L. Chapter 10 Membrane contactors
(1995) Membrane Science and Technology, 2 (C), pp. 467-498.

Nguyen, P.T., Lasseuguette, E., Medina-Gonzalez, Y., Remigy, J.C., Roizard, D., Favre, E.
A dense membrane contactor for intensified CO2 gas/liquid absorption in post-combustion capture
(2011) Journal of Membrane Science, 377 (1-2), pp. 261-272.

Kerber, J., Repke, J.-U.
Basic solubility measurements for the design of an integrated biogas purification process
(2012) Chemical Engineering Transactions, 29, pp. 481-486.

Wijmans, J.G.H., Baker, R.W.
The Solution-Diffusion Model: A Unified Approach to Membrane Permeation
(2006) Materials Science of Membranes for Gas and Vapor Separation, pp. 159-189.

Cussler, E. L. *Diffusion: Mass Transfer in Fluid Systems*.3. ed. Cambridge: Cambridge University Press, 2009.

Savage, D.W., Astarita, G., Joshi, S.
Chemical absorption and desorption of carbon dioxide from hot carbonate solutions
(1980) Chemical Engineering Science, 35 (7), pp. 1513-1522.

Danckwerts, P.V., Sharma, M.M.
Absorption of carbon dioxide into solutions of alkalis and amines
The Chemical Engineer No. 202 (1966),pp. CE 244-CE 280.

Dividing wall columns for NGL fractionation

Ivar J. Halvorsen[1], Igor Dejanović[2], Knut Arild Maråk[3], Žarko Olujić[4], Sigurd Skogestad[5]
[1]SINTEF, Trondheim, Norway; [2]University of Zagreb, Croatia;
[3]Statoil, Research Development and Innovation, Trondheim, Norway;
[4]TU-Delft, The Netherlands; [5]NTNU, Trondheim, Norway

Abstract
The development of Floating LNG plants (FLNG) has resulted in a focus on reducing the weight and size of the topside processing facilities for these units. The conventional fractionation of NGL in LNG plants implies a direct sequence of three or more conventional distillation columns requiring different levels of refrigeration. The results of a feasibility study are described, indicating that a packed three-product dividing wall column (DWC) could replace conventional deethanizer and depropanizer columns. This could provide energy, hardware and footprint benefits, with consequent savings in weight and cold utilities on the topside processing plant onboard FLNG-units.

Keywords
Distillation, Dividing Wall Column, DWC, NGL recovery, Floating LNG

1. Introduction

Natural gas liquids (NGL) fractionation plants, stand-alone or as an important component of natural gas liquefaction (LNG) facilities, employ sequences of three or more distillation columns to separate C1 to C5+ hydrocarbons according to specific site requirements. Since such processes are capital and energy intensive, both globally and regionally operating natural gas processing industries are interested in approaches that would reduce energy use requirements, and related environmental emissions, as well as the size of equipment involved. As well-known and proven in industrial practice [1,2], dividing wall column (DWC) technology has a considerable potential in this respect.

However there are various technical barriers that need to be addressed to provide proper basis for evaluation of technical feasibility and cost-effectiveness of the application of DWCs, particularly in case of offshore oil and gas processing plants. No installations of DWC have been reported in the literature for NGL fractionation, apart from a few academic simulation studies [3,4].

NGL fractionation plants installed on barges or FPSO's (floating production, storage and offload vessel), the latter being increasingly used in place of fixed platforms, differ in some aspects considerably from conventional onshore facilities. On the processing side, most specific of the challenges are due to motion of a floating facility. If excessive, motion could affect detrimentally liquid distribution and efficiency of distillation columns. As reported elsewhere [5], even with extensive use of compartmentalized active or bubbling areas, trays are difficult to operate reliably under moving conditions. Similar difficulties apply for random packings, while structured packings appeared to be least sensitive in this respect. Structured

packings are therefore used instead of trays in high and intermediate pressure columns as employed in floating NGL-fractionation plants. Relevant details and peculiarities of the relation between packed column motion induced liquid maldistribution and the drop in efficiency are described in a recent paper written by ExxonMobil specialists [6], suggesting conservative designs. Most importantly, packed high pressure distillation columns have been installed and operate on barges and FPSO's [5].
Taller columns are more sensitive to various forms of movement experienced on a floating facility, and the height of a DWC is by virtue of its nature always larger than that of any of individual columns from a conventional sequence. This and other concerns of particular importance for design and operation of distillation columns on floating facilities are addressed in this paper. The potential for reduced plot area and weight of equipment, as well as reducing cold utilities, are of particular interest to Statoil.

2. The floating NGL-fractionation plant base case

We here consider a floating liquefied natural gas processing plant (FLNG), where the liquid NGLs from the scrub column is sent to NGL-fractionation to be separated into four fractions according to given product specifications. The NGL-rich liquid feed consists of practically negligible quantities of nitrogen and higher concentrations of methane (C1), ethane (C2), propane (C3), butanes (i-C4 and n-C4), pentanes (i-C5 and n-C5) and a remaining mix of n-C6 and heavier alkanes and aromatics. The composition of the NGL-feed is a result of the extraction of the heavier hydro carbons from the natural gas entering the FLNG-plant. The feed to the NGL fractionation is available at 35 bar at 54ºC.
Figure 1 shows schematically a direct three-columns sequence typically employed to separate the given feed into four product streams. These are denoted in the flowsheet shown in Figure 1 as A, B, C, and D, and represent a C1-rich (A), a C2-rich (B), a C3+C4 (C), and a C5 and heavier (D) fraction, respectively. The product formulation C1-rich implies that a certain small amount of C2 is acceptable. This stream is recompressed and eventually liquefied to LNG. Similar is with C2-rich, allowing for small amount of methane on light and propane on heavier side. This stream is used as refrigerant make-up. The depropanizer top product is a mixture of propanes and butanes and is either used as refrigerant or exported. With regard to their main purpose, these columns from the sequence shown in Figure 1 are referred to as the demethanizer, deethanizer and depropanizer columns respectively. The operating pressure for the first column will be close to feed pressure, i.e. 34 bar. Regarding the fact that the third column delivers as top product a liquid mixture of propanes and butanes, the most reasonable choice is to operate it at lowest pressure that allows condensing at temperatures near the sea water temperature. The top product of the second column is an ethane rich product, which, similar to methane, requires use of cold utilities (refrigerants). The operating pressure of the deethanizer column depends on the temperature level of available cold utilities, and this allows some flexibility, i.e. reduction with respect to the value (17 bar) chosen for conventional, three-column sequence. For demethanizer, deethanizer and

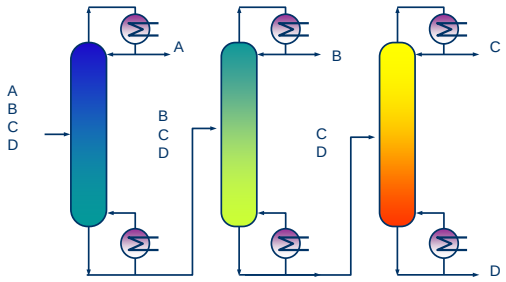

Figure 1 The conventional, direct split distillation sequence for four products

depropanizer columns operated at 34 bar, 17 bar, and 7 bar, required cooling temperature levels are -91˚C, -40˚C and +40˚C, respectively. Since the considered NGL fractionation plant is situated within a FLNG facility, even the coldest utility is available. However any saving in this respect would be beneficial. A feature of the present situation is that the methane recovered from demethanizer can be delivered as gas, and the cold from the liquefaction cycle can be used to liquefy the amount required as reflux for the demethanizer column.

3. Design approach and methods

Regarding the fact that a four-product situation is considered, the number of potential heat-coupling arrangements is rather large. In this paper 8 different configurations are considered, which are evaluated and compared to the conventional direct split sequence which serves as reference. These include three different 4-product DWC configurations and five configurations combining a 3-product DWC and a conventional column. The first include two different designs of a multi-partition 4-product DWC; one with liquid side products, another one with two top condensers, and one single-partition 4-product DWC with a side condenser. The two-column sequences include a DWC and a conventional column, and a conventional column and a DWC, without or in combination with side condensers or a vapour side product stream.

The tool used for the purposes of preliminary assessment is the Vmin-diagram, which has been proven in different applications [7-9]. It is a rather simple, robust and reliable conceptual performance evaluation method that, based on feed composition and relative volatilities of key components at given pressure and temperature, allows estimation of minimum vapour rates in a complex, fully thermally coupled extended Petlyuk arrangement and its modifications. This applies for any number of components (fractions) and products. The ratios of molar overhead vapour flow and feed flow rates (V/F) for each configuration are estimated and compared on the same basis, revealing configurations most promising from an energy saving standpoint.

The stage and reflux requirements for the chosen configurations and all internal vapour and liquid flows were obtained by detailed simulations. All columns in the present study were dimensioned as packed columns using a validated method that allows hydraulic design of complex DWCs with accuracy sufficient for purposes of preliminary feasibility studies [10,11]. The packing chosen for this purpose (Montz-Pak B1-350MN) is well established in DWC applications. The internal shell diameter is based on allowable vapour throughput, which is chosen to be on conservative side by setting the pressure drop of 3 mbar/m as upper limit. This is well below the flood limit.

The height of a DWC depends on the number of stages in conventional sections plus the largest number of stages contained in the sections arranged in parallel. Single bed height is limited to maximum 20 stages, which in present case is 8 m. This is based on adopted HETP (Height Equivalent to a Theoretical Plate) value of 0.4 m. Anticipating certain loss of efficiency, for sections with specific liquid loads between 30 and 50 (upper limit) m^3/m^2h, a HETP of 0.5 m has been used.

The height required for installation of a liquid redistribution section was chosen to be 2 m, and the height required to accommodate vapour-liquid disengagement sections at the top and the bottom (sump) of the column was assumed to be 5 m in total.

Additional dimensioning effort was needed to arrive at the required weight of compared configurations. Stainless steel was chosen as construction material for shell and column heads. Minimum wall thickness for shell and heads was calculated

according to well established ASME (American Society of Mechanical Engineers) codes and procedures [12,13]. The weight of packing and auxiliary internal equipment was added to get total weight of installed columns. The weight of the supporting structure, external piping, reboilers, condensers and reflux accumulators, as well as the weight of the liquid inventory during operation was not considered here.

4. Results and discussion

For illustration, Figure 2 shows Vmin-diagrams for a single-partition 4-product DWC and a sequence consisting of conventional demethanizer column and a 3-product DWC. All DWC configurations considered in this study allow side condensers on side-product draw-off positions. This option allows reducing superfluous vapour flow rate towards the top, and thereby reduces top condensing duty as well as top section diameter. This is particularly important when the top condenser needs expensive cold utilities. The optimal change in the vapour rate across the side stream is given by the difference in height of the peaks in the Vmin-diagram. Taking out the side-stream as vapour may be a simple option when the optimal vapour flow rate change is similar in magnitude to the side stream itself.

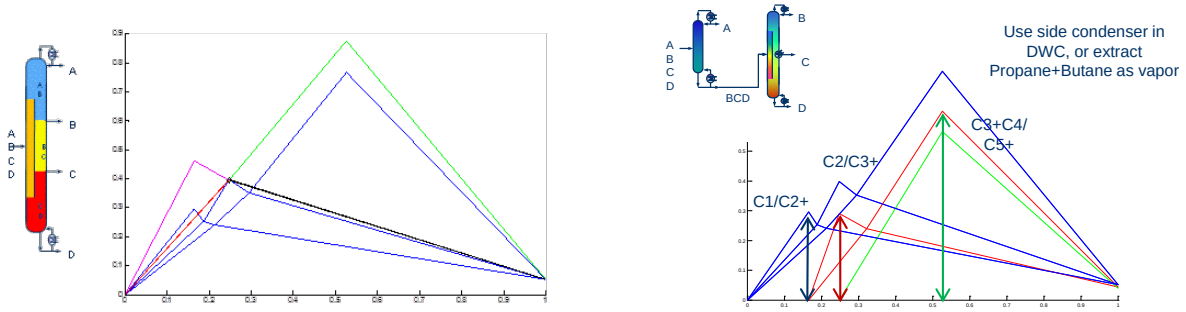

Figure 2 Vmin-diagrams of a 4-product and a 3-product DWC based configurations replacing conventional three-column sequence (see Figure 1) for obtaining four products

The peaks of a Vmin-diagram indicate vapour load related to sharp binary separations between C1/C2, C2/(C3+C4), and (C3+C4)/C5. The latter is the most demanding one, which determines the overall vapour load per unit feed V/F. This is depending on the configuration but is in all cases lower than that of the conventional sequence (V/F = 1.1). Indeed, the vapour throughput is directly related to reboiler duty, i.e. energy requirement, but in present case, with top side product temperatures below -30 ˚C, it may appear misleading because the costs of required cold utilities (refrigerants) dominate.

Table 1 shows individual and total V/F values for a number of DWC based configurations. As expected, the largest savings are achieved with multi-partition 4-product DWC configuration (not yet attempted in practice), followed by single-partition one, which is less efficient due to certain amount of inevitable remixing of components in the space between two side product draw-offs. Although potential energy savings are appealing and the know-how required to design, install and operate single-partition wall 4-product DWC as packed column is proven [14], there are some technical barriers that make it unsuitable for an application as considered here.

The main reason for this is the rather large spread of boiling points among the components. In a conventional three-column sequence, each column can be operated close to optimum pressure for the given products. This is impossible to

No	Configuration	V/F C1	V/F C2	V/F C3+C4	V/F total	Energy saving	Weight
1	Conventional direct split sequence	0.30	0.26	0.55	1.11	0 %	100%
2	4-p DWC with liquid side	0.77	0	0	0.77	31 %	-
3	4-p DWC with two top cond.	0.30	0.14	0.33	0.77	31 %	-
4	4-p single-partition DWC + side conden.	0.46	0	0.42	0.88	21 %	-
5	3-p DWC + conventional column (CC)	0.41	0	0.55	0.96	14 %	146%
6	3-p DWC with vapour side product + CC	0.33	0.08	0.55	0.96	14 %	140%
7	3-p DWC+side condenser + CC	0.30	0.11	0.55	0.96	14 %	-
8	CC + 3-p DWC	0.30	0.62	0	0.92	17 %	95%
9	CC + 3-p DWC with vapour side product	0.30	0.26	0.36	0.92	17 %	91%

Table 1 Comparison of various DWC based configurations on basis of internal and overall vapour loads, related energy saving and shell weights with conventional three-column sequence as reference

accommodate in a 4-product DWC, which can have only one operating pressure. If operated at the same top pressure as the demethanizer (34 bar), the top and bottoms temperature will differ by more than 300 ^{o}C. The bottoms temperature will exceed critical temperature of pentanes and heavier components.

However, these obstacles could be avoided by connecting a conventional column (CC) and a 3-product DWC in series. This allows running either demethanizer or depropanizer at the most suitable pressure, while that of the DWC could be operated at another pressure to best suite the needs of its separation.

As shown in Table 1, the configurations of a conventional column + DWC perform better than a conventional sequence, but appear to be less efficient than 4-product DWCs. The Combination of a DWC and a depropanizer column is in all variations less efficient than a combination of a demethanizer and a 3-product DWC. In case of the latter, a DWC in conjunction with vapour side product stream (number 9) requires less cold utilities for ethane condensation, which makes it to most promising arrangement for given separation task. Most importantly, as shown in the last column of Table 1, this configuration with the DWC operated at 8 bar enables also a significant weight reduction compared to conventional three-column sequence.

Additional, considerable weight benefit would result from reduced number of reboilers, condensers and reflux accumulators, which will also further reduce required footprint. In addition to the equipment weight saved, weight related to structural steel and piping is avoided.

A schematic drawing of this promising configuration containing operating pressures and corresponding temperatures along the columns is shown in Figure 3. One should note that precooling the feed to a reasonable temperature could reduce condenser duty. This, however, is at the cost of an increased reboiler duty, but the costs associated with the former (very expensive cold utilities required) are the dominating factors. It is also important to avoid feed temperature variations in order to better maintain optimal operation of the DWC. Also, the reduction in internal vapour loads of the upper part of the DWC is such that the shell diameter can be reduced with respect to the part bellow the feed.

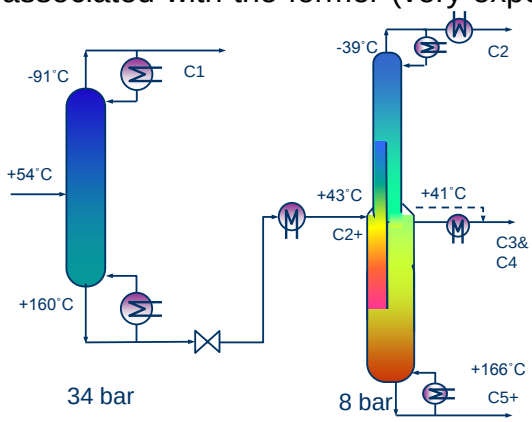

Figure 3. A promising alternative for conventional three-column sequence (No. 9)

A potential drawback is the height of a DWC, which largely exceeds that of individual conventional columns. This will inevitably lead to an increased extent of movement, causing a more pronounced deviation from

vertical with certain frequence. This however is something structured packing can resist to a great extent. Since something like this has not been yet attempted in practice, further, detailed technical evaluation of the chosen configuration is required addressing all design, construction, installation and operation uncertainties and issues, to mitigate potential risks, particularly those associated with movement of the columns, prior making a decision on implementation of such a DWC based configuration into a floating natural gas processing plant environment.

5. Conclusions

A conventional demethanizer combined with a packed 3-product DWC appears to be a promising alternative for conventional three-column sequence as encountered in NGL fractionation plants. In addition to the energy saving such a configuration enables also weight and footprint reduction, which makes it particularly interesting for application on FLNG facilities.

A DWC operated at a moderate pressure in conjunction with a side stream condenser or a vapour side draw would minimize the cold utilities requirements and diameter in the upper part of the shell. Being taller than any of conventional columns it is prone to detrimental effects of movements as experienced on a floating facility. To minimize potential loss of separation efficiency, structured packings need to be used instead of trays or random packings, which are preferred internals for high and intermediate pressure columns onshore.

References

[1] Dejanović, I., Matijašević, Lj., Olujić, Ž., Dividing wall column—a breakthrough towards sustainable distilling, Chem. Eng. Process. 49 (2010), pp. 559–580.

[2] O. Yildirim, A.A. Kiss, E.Y. Kenig, Dividing wall columns in chemical process industry: a review on current activities, Sep. Purif. Technol. 80 (2011) 403–417.

[3] Lee, S.,Long, N.V.D., Lee, M., Design and Optimization of Natural Gas Liquefaction and Recovery Processes for Offshore Floating Liquefied Natural Gas Plants, Ind. Eng. Chem. Res. 51 (2012) 10021−10030.

[4] Long, N.V.D., Lee, M., Improvement of natural gas liquid recovery energy efficiency through thermally coupled distillation arrangements, Asia-Pac. J. Chem. Eng. 7 (2012) S71 - S77.

[5] Roza, M., Zuber, L., Most recent developments on design and operation of distillation and absorption columns under moving conditions, Proceedings of Distillation Conference, AIChE Spring National Meeting, March 30 - April 3, 2003, New Orleans, LA, USA, pp. 577-588.

[6] Cullinane, J.T., Yeh, N., Grave, E., Effects of Tower Motion on Packing Efficiency, Brazil Offshore, 14-17 June 2011, SPE 143766. ISBN 978-1-61399-123-7.

[7] Halvorsen, IJ (2001), Minimum Energy Requirements in Complex Distillation Arrangements, NTNU (Trondheim, Norway) PhD thesis 2001:43. Available from: http://www.nt.ntnu.no/users/skoge/publications/thesis/2001_halvorsen/

[8] Halvorsen, I.J., Skogestad, S., Energy efficient distillation, Journal of Natural Gas Science and Engineering, 3 (2011) 4, 571-580.

[9] Dejanović, I., Matijašević, Lj., Halvorsen, I.J., Skogestad, S., Jansen, H., Kaibel, B., Olujić, Ž., Designing four-product dividing wall columns for separation of a multicomponent aromatics mixture. Chem. Eng Res. Des. 89 ((2011) 1155-1167.

[10] Dejanović, I., Matijašević, Lj., Jansen, H., Olujić, Ž., Designing a packed dividing wall column for an aromatics processing plant, Ind. Eng. Chem. Res. 50 (2011) 5680-5692.

[11] Olujić, Ž., Dejanović, I., Kaibel, B., Jansen, H., Dimensioning multi-partition dividing wall columns, Chem. Eng. Technol. 35 (2012) 1392-1404.

[12] ASME Boiler and Pressure Vessel Code, Section VII, Division 1, Rules for Construction of Pressure Vessels, 2007.

[13] ASME Boiler and Pressure Vessel Code, Section II, Part D, Properties, Materials, 2004.

[14] Olujić, Ž., Jödecke, M., Shilkin, A., Schuch, G., Kaibel, B., Equipment improvement trends in distillation, Chem. Eng. Process. 48 (2009) 1089–1104.

Transesterification of butyl acetate in a reactive dividing wall column: From laboratory experiments to column operation

C. Ehlers[1], G. Fieg[1], T. Hugen[2], T. Rietfort[2]
[1]Hamburg University of Technology. Hamburg, Germany
[2]Julius Montz GmbH, Hilden, Germany

Abstract
Reactive dividing wall columns are highly innovative units, which combine the industrially well-established apparatuses of reactive distillation columns and conventional dividing wall columns. Simulation results confirm that this special column type has a high potential to reduce energy consumption compared to conventional processes [1,2]. Our research to reactive dividing wall columns is characterized by the fact that the operation of this column type is comprehensively analyzed for an exemplary chemical reaction both experimentally and with the use of a mathematical model.
Published at the end of a two-year cooperation project, this paper gives a comprehensive overview about decisive research results generated. In the first part, the main characteristics of the developed mathematical model are outlined. The model allows for steady state simulations and for dynamic ones including the start-up procedure of reactive dividing wall columns. In the second part, a short and concise overview is given about the experimental determination of input parameters needed for the mathematical model. Here, the focus is put on the determination of vapor-liquid equilibria of the chosen chemical system and on the determination of structured packing pressure drop. Finally, in the last part of the paper, a comparison is drawn between the simulation results and the data gained during experimental operation of the actual plant.

Keywords
Reactive Distillation, Vapor-Liquid-Equilibria, Hexanol, Butanol, Pressure Drop, Structured Packing

1. Introduction

Reactive dividing wall columns (RDWC) can be understood as a combination of reactive distillation columns and conventional dividing wall columns, which are both successfully implemented in various processes of the chemical industry (Figure 1). Thus, RDWC allow for the execution of a chemical reaction and the fractionation of three or more product streams in one single apparatus. Simulation results have been published for this innovative and highly-integrated type of apparatus which predict a great potential for the reduction of energy consumption compared to conventional processes [1,2]. The experimental results published so far for heterogeneously catalyzed RDWC, all originate from a three-year EU project called INSERT (Integrating Separation and Reaction Technologies). Two different-sized RDWC located at the sites of industrial project partners were operated. For all published experimental RDWC runs of the INSERT project, the examined chemical reaction was the same (acid catalyzed hydrolysis of methyl acetate) [3-5].

Both the high potential of RDWC for process intensification as well as the very limited availability of experimental results concerning RDWC operation create great motivation for further experimental research. Therefore, in 2012, the Institute of Process and Plant Engineering at Hamburg University of Technology and Julius Montz GmbH started a cooperative research project. For an exemplary chemical reaction which has not been used in this context before, the reactive dividing wall column is analyzed both theoretically with the use of a mathematical model and experimentally with a test column. The goal of the project is to further reduce existing uncertainties about the predictability and the stable operation of this highly complex type of apparatus by presenting valuable practical experiences.

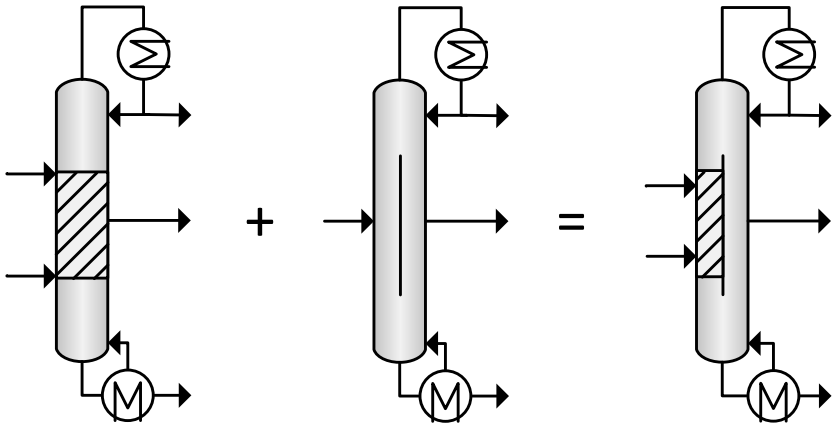

Figure 1. RDWC as combination of reactive distillation column and dividing wall column

The project can be divided into three main research areas. First, a mathematical model of RDWC is developed. In order to use this model for the exemplary case being looked at within the research project, the determination of several input parameters with laboratory experiments is mandatory. Amongst others, these experiments include the determination of vapor-liquid equilibria and pressure drops. The third and final block of the project is also an experimental one. It is the installation and adjacent operation of a RDWC test column.

2. Results and discussion

In analogy to the research scope mentioned above, the main part of this paper can be divided into three sections. First, the mathematical model is introduced with its main characteristics. According to the paper's title, however, the focus is clearly put on the second and third part where the laboratory experiments and the operation of the dividing wall column are presented.

2.1 Mathematical modeling

The mathematical RDWC model is based on an equilibrium-stage approach developed at the Institute of Process and Plant Engineering. As stated in earlier publications, the base model allows for steady-state simulations as well as for dynamic ones including the start-up procedure from ambient conditions [6,7]. During this project, the model was expanded by the reactive case. An arbitrary number of chemical reactions can be considered with pseudo-homogeneous reactions kinetics. Other model characteristics are the consideration of heat losses, the implementation of various pressure drop models and the automatic calculation of vapor split ratio according to the pressure drop on both sides of the dividing wall. The model is created with Aspen Custom Modeler®, an equation-oriented simulation tool by Aspen Technology, Inc.

2.2 Laboratory experiments

The laboratory experiments being part of the research project deal with the determination of reaction kinetics, the measurement of vapor-liquid equilibria and with the experimental determination of structured packing pressure drops. The fact that the determination of accurate reaction kinetics is a basic requirement in order to make good predictions for reactive distillation processes is self-explaining. Reaction kinetics for the transesterification of n-butyl acetate with 1-hexanol catalyzed with the commercial acid catalyst Amberlyst 35Dry have been determined in a batch reactor. As mentioned earlier, the focus of this paper concerning lab experiments, however, will be put on the determination of VLE and pressure drop.

2.2.1 Vapor-Liquid Equilibria

The determination of vapor-liquid equilibria (VLE) for the chemical system chosen is of major importance. One possibility for the calculation of VLE is to use estimation methods like UNIFAC. However, the error introduced by the application of such methods is hard to rate. Therefore, during the project, isobaric vapor-liquid equilibria of all binary subsystems belonging to the overall four component system were measured. The pressures chosen are 600 mbar and 900 mbar. Figure 2 shows measurement results for the reactants of the transesterification reaction looked at. It can be seen that the results can be interpolated with a common UNIQUAC approach.

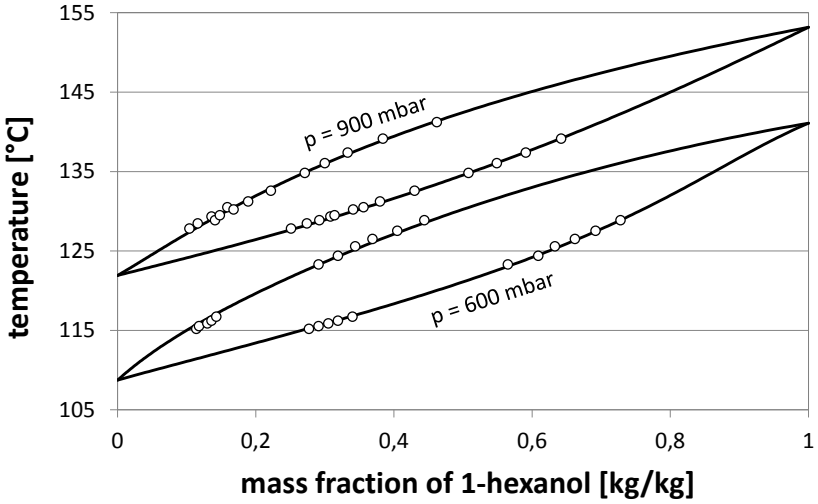

Figure 2. Vapor-liquid equilibria of 1-hexanol / n-butyl acetate for 600 mbar and 900 mbar (dots: measured, lines: interpolation with UNIQUAC)

For the VLE measurements, an ebulliometer with a liquid holdup of 50 to 70 mL was used. The temperature was measured in the gas phase above the boiling liquid. The samples for both phases were taken with a syringe. The liquid samples were drawn directly out of the boiling liquid phase, the vapor samples were taken in liquid form behind the condenser. The compositions were analyzed by gas chromatography.

2.2.2 Pressure drop of structured packing

For distillation columns with a dividing wall, precise knowledge about the pressure drops of the internals utilized inside the column shell is very important. This is due to the fact that the vapor flow inside the column automatically splits to both sides of the dividing wall according to the pressure drop created. Actively adjusting the vapor split ratio with the use of control valves has been proven possible [8], however, in industrial applications of dividing wall columns, this approach is not preferred due to its complexity. Therefore, in order to make reliable predictions of vapor split ratios,

the pressure drops of the packings must be known with a high accuracy. This is especially valid for RDWC, as the internals on both sides of the dividing wall are not the same for this column type. This has the effect that errors in the pressure drop correlations have a huge and direct impact on the predicted vapor split ratio.

Figure 3 shows experimental results for the two packing types used in this project. The measurements were made with air as upstreaming gas phase and ethanol as the liquid phase flowing down. For the measurements a test stand with a packed bed height of 1 m and an inner diameter of 54 mm was built. Interestingly, the results show that the pressure drop of both packing types is nearly identical for this diameter, which results in vapor split ratios close to 50%.

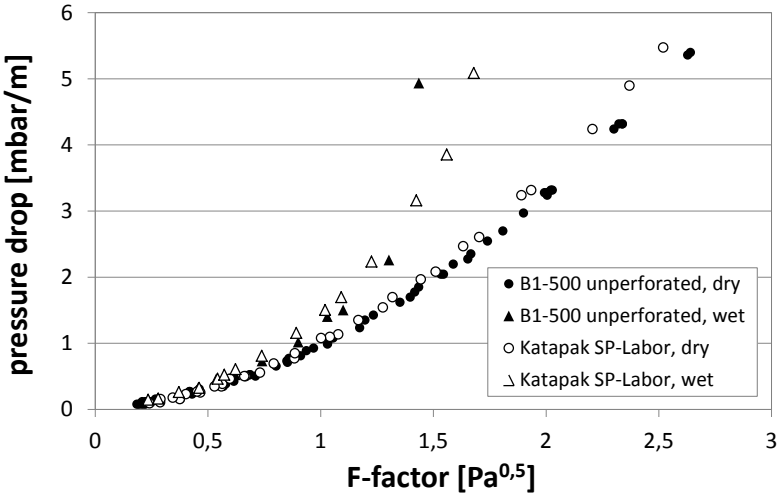

Figure 3. Pressure drop of Montz' B1-500 (unperforated) and Sulzer's Katapak SP-Labor (Diameter = 54 mm) (wet curves at w_L = 5.5 m³/m²/h)

2.3 Operation of reactive dividing wall column

The final part of the project is dedicated to the operation of a test column located at Hamburg University of Technology. This RDWC is shown in Figure 4. Including reboiler and condenser unit the column has a total height of approximately 11 m. The inner diameter of this Petlyuk arrangement is 6.8 cm in the upper and lower section and 5.4 cm in the middle part. The reactive packing implemented on the feed side of the column is Sulzer's Katapak SP-Labor which is filled with the commercial catalyst Amberlyst 35Dry. The test column is equipped with sensors for the accurate measurement of mass flow, pressure, pressure drop and temperature. Additionally, sensors for the liquid level in the bottom and in the distillate tank are in use. The test column is operated with WinErs, a distributed control system by Ingenieurbüro Dr.-Ing. Schoop (Germany), which is used for data visualization, data storage and process control.

For the time-efficient analysis of steady-state behaviour of the column, it is a prerequisite to develop reliable start-up procedures and process control strategies. Figure 5 shows the temperature development over time for an exemplary experimental run of the test column. It can be seen that the suited start-up procedure developed with the use of the dynamic mathematical model leads to steady-state operation after a time span of approximately 6 hours. The details of this start-up procedure were published elsewhere [9]. The second part of Figure 5 shows a comparison between the simulated temperature profile for this specific test run at

steady-state and the measured temperatures inside the B1-500 elements of the main column. It can be seen that for the upper part, the agreement between the simulation and the experimental values is quite good. The deviations present in the lower part of the column can be explained with the formation of ethers as side products. Current research activities aim to accurately determine the reaction kinetics of these side reactions in laboratory reactors, which might lead to a reduction of the differences between model predictions and experimental values.

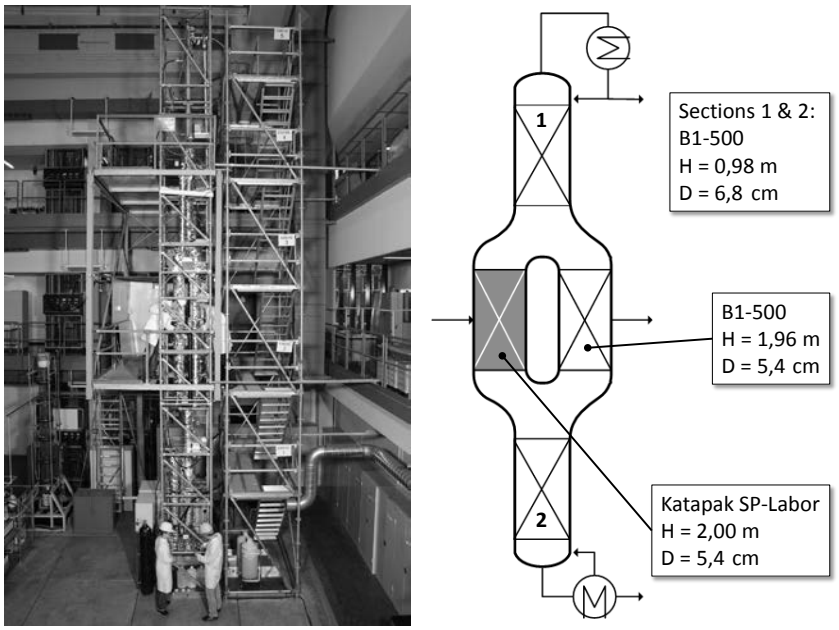

Figure 4: Reactive dividing wall column at Hamburg University of Technology

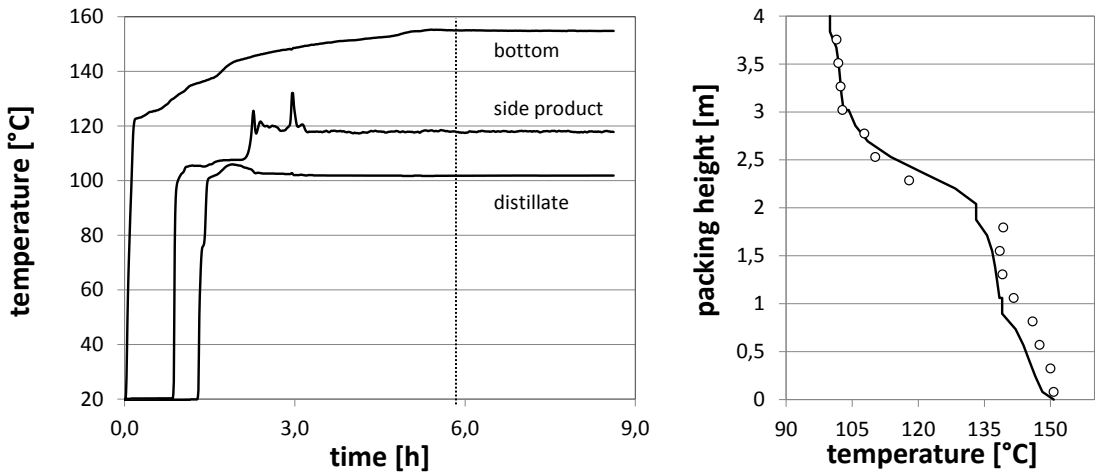

Figure 5. Experimental temperature development during column start-up (left) and steady-state temperature profile (right) for exemplary experiment

3. Conclusions

The paper marks the end of a two-year cooperation project between the Institute for Process and Plant Engineering at Hamburg University of Technology and Julius Montz GmbH, thus enabling an extensive overview of the research results gained during this work. Emphasis has to be placed on the fact that decisive input parameters needed for the simulation model are determined with laboratory experiments. The requirement for very accurate pressure drop models in the case of RDWC was especially highlighted. The experimental results originating from the

actual operation of the test column clearly broaden the range of available RDWC data. The project results therefore extend the knowledge about the predictability of RDWC. This clear support for decision makers in the chemical engineering industry ultimately might lead to a quicker introduction of this innovative and promising technology to industrial processes.

Our future research activities deal with the further development of process control strategies and start-up procedures suitable for reactive dividing wall columns and with the cost-driven optimization of RDWC design.

Acknowledgements
This work was financially supported by the German Federal Ministry for Economic Affairs and Energy as part of the ZIM program (Zentrales Innovationsprogramm Mittelstand, project no.: KF2267706WZ2). We want to express our greatest gratitude for this support. Financial support from Max-Buchner-Forschungsstiftung is also gratefully acknowledged.

References

1. Mueller, I.; Pech, C.; Bhatia, D.; Kenig, E.Y.: Rate-based analysis of reactive distillation sequences with different degrees of integration. *Chem. Eng. Sci.*, 62(24), 7327-7335, 2007.
2. Kiss, A.A.; Pragt, J.J.; van Strien, C.J.G.: Reactive dividing-wall columns – How to get more with less resources? *Chem. Eng. Commun.*, 196(11), 1366-1374, 2009.
3. Sander, S.; Flisch, C.; Geissler, E.; Schoenmakers, H; Ryll, O.; Hasse, H: Methyl acetate hydrolysis in a reactive divided wall column. *Chem. Eng. Res. Des.*, 85(A1), 149-154, 2007.
4. Ryll, O.: Thermodynamische Analyse gekoppelter Reaktions-Destillations-Prozesse: konzeptioneller Entwurf, Modellierung, Simulation und experimentelle Validierung. Logos Verlag: Berlin, 2009.
5. Müller, I.: Theoretische Untersuchung innovativer integrierter Trennverfahren. Verlag Dr. Hut: München, 2010.
6. Niggemann, G; Hiller, C; Fieg, G.: Experimental and theoretical studies of a dividing-wall column used for the recovery of high-purity products. *Ind. Eng. Chem. Res.,* 49(14), 6566-6577, 2010.
7. Niggemann, G; Hiller, C; Fieg, G.: Modeling and in-depth analysis of the start-up of dividing-wall columns. *Chem. Eng. Sci., 66*(21), 5268-5283, 2011.
8. Dwivedi, D.; Strandberg, J.P.; Halvorsen, I.J.; Preisig, H.A.: Active Vapor Split Control for Dividing-Wall Columns. *Ind. Eng. Chem. Res., 51*(46), 15176-15183, 2012.
9. Ehlers, C.; Fieg, G.: Reaktive Trennwandkolonnen: experimenteller Betrieb und mathematische Simulation. Paper presented at *Jahrestreffen der Fachgemeinschaft Prozess-, Apparate- und Anlagentechnik (ProcessNet)*, Bruchsal, November 2013.

A New Application of Dividing-Wall Columns for the Separation of Middle-boiling Impurities

Dr. Luca Cameretti, Dr. Daniel Demicoli, Ralf Meier
Evonik Industries AG, Marl, Germany

Abstract
There is growing interest in dividing-wall column (DWC) technology, which simplicity is at the heart of its appeal. Compared to conventional multicolumn arrangements a DWC can generate capital cost savings of up to 40% simply because less equipment is required. With their greater thermodynamic efficiency, dividing-wall columns can also reduce operating costs by around 30%.[1] The actual savings that can be realized will depend on the specific application.
In general, the use of DWCs is recommended for multicomponent liquid mixtures that are to be separated into at least three fractions with high purity requirements. Further, DWCs are especially favorable for the separation of small quantities of light and heavy boilers from the main middle-boiling product.[2,3]

In the presented case a modified DWC is applied to the distillation of a feed containing less than 1% of a middle-boiling impurity into a pure light-boiling and a pure heavy-boiling fraction, while the impurity is concentrated up to 35% in the side-stream. This allows a drastic reduction of product loss in the purge stream compared to the application of a simple side-stream column.
Experiments at pilot scale have confirmed simulation results revealing a new opportunity to profit from the vertical wall inside the distillation column.

Keywords
Distillation, dividing-wall column, multicomponent separation, simulation

1. Introduction

Albeit the fact that distillation is one of the most ancient techniques to separate multicomponent mixtures, research is still done in order to tease out the last percentages of cost saving potential. One big step was surely achieved by a better heat management. Although the idea of heat coupling is known at least since the 1930s, Petlyuk et al. widely introduced the separation of a three-component system in a coupled setup of prefractionator and main column in the mid 1960s.[2,4] Subsequent development by Kaibel[5] has led to the first technically used dividing-wall columns (DWC), where prefractionator and main column are combined in one shell.
The principle and many variations of DWCs have already been dealt with in literature. Dejanović et al.[2] and Yildirim et al.[6] give excellent reviews on state-of-the-art and current activities. They and the cited authors show different setups containing one or more dividing walls positioned at the top, the bottom, or in the middle of the column in order to achieve pure products out of a multicomponent feed. All dividing-wall columns shown in the literature have at least one common packed section, i.e. a section without dividing wall. Further, in most of the examples given, the middle-boiling fraction predominates the feed composition.

In the presented case a pseudo three-component feed containing less than 1% of middle-boiler has to be separated into pure top product and pure bottom product. The middle-boiler has to be concentrated in the side-stream which will then be discarded. The challenge lies in the fact that top product and heavy-boiler are already narrow boiling (α ~ 1.4 – 2.4). Furthermore, the vapor pressure curves of light-boiler and middle-boiler are very close to each other (dT < 5K); the phase equilibrium reveals also an azeotropic behavior.

2. Results and discussion

The following sections show the steps to the final design of the dividing-wall column suitable for the separation of small quantities of middle-boiler from a narrow-boiling mixture. For facilitating the reading abbreviations will be used for the light-boiler (LB), the middle-boiler (MB), and the heavy-boiler (HB), respectively.

2.1 The classical separation sequence

There are three classical separation sequences for a mixture of three components: the direct, the indirect, and the sloppy configuration, respectively, shown in Figure 1.

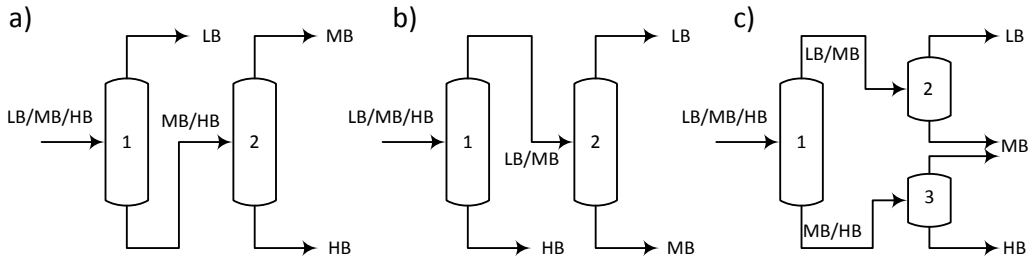

Figure 1: a) direct, b) indirect, and c) sloppy distillation sequence for the separation of a three-component mixture LB/MB/HB.

Due to the prevailing phase equilibria mentioned above, the indirect path appears to be more suitable at first sight. The theoretical number of stages for column 1 and 2 were estimated using the DSTWU[7-9] model. The typical correlation between reflux ratio and number of stages for different recovery rates of LB are shown in Figure 2. The plots make clear that especially for the second separation of LB and MB in the second column a very high separating capacity is needed leading to high investment (size of the column) and operating expenses (reboiler and condenser duties). Another drawback is the loss of LB in the MB fraction. Hence, a classical separation sequence is economically not feasible.

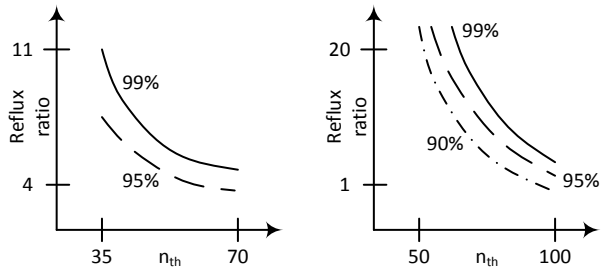

Figure 2: Reflux ratio vs. theoretical number of stages for a) LB/HB separation with a recovery of 99% and 95% of LB and 0.1% of HB in the distillate; b) in analogy for the separation of LB/MB.

2.2 Combination of side-stream columns

The next evolution step is to use side-stream columns. The obvious advantage of a side-stream column is that it combines two columns in one shell, hence reducing investment costs. However, a single side-stream column in the presented case will only be able to concentrate the MB up to a decently high fraction in the side-stream leading to big apparatus dimensions, high reflux ratios – and hence high energy consumption – or high product loss. This is shown in Table 1.

	SSC	DWC LHS / RHS
mass fractions		
distillate		
LB	99,91%	99,88%
MB	0,09%	0,09%
HB	< 1 ppm	0,02%
sump		
LB	0,10%	0,10%
MB	0,14%	0,14%
HB	99,76%	99,76%
side draw		
LB	50,87%	37,39% / 50,27%
MB	22,80%	10,38% / 34,37%
HB	26,26%	52,23% / 15,34%
recovery loss (LB and HB)	0,68%	0,30%
reflux ratio	10,6	3,6 / 164
condenser duty	100%	59%
reboiler duty	100%	56%
column size		
cross sectional area	100%	86%
packing height	100%	100%

Table 1: Calculations for single side-stream column (SSC) and DWC performed with a feed containing 0.3% MB. LHS and RHS mean left-hand side and right-hand side of the DWC, respectively.

In order to minimize loss of LB and HB and and at the same time decrease energy consumption, in a first side-stream column LB and HB are separated as top and bottom products, respectively, while MB is concentrated inside the column. This is done at moderate reflux ratios, high enough to obtain pure LB. The MB peak is tapped by a side-stream which then will still contain a high amount of valuable LB and HB. This side-stream is fed to a second side-stream column which basically has the same separation task as the first one: it separates pure LB as top product, concentrates the MB in the side-stream, and returns HB without LB. The advantage, though, is that since the feed stream is much lower than for the first column, very high reflux ratios and hence higher MB concentrations can be achieved at low cost.
The column arrangement is shown in Figure 3a.

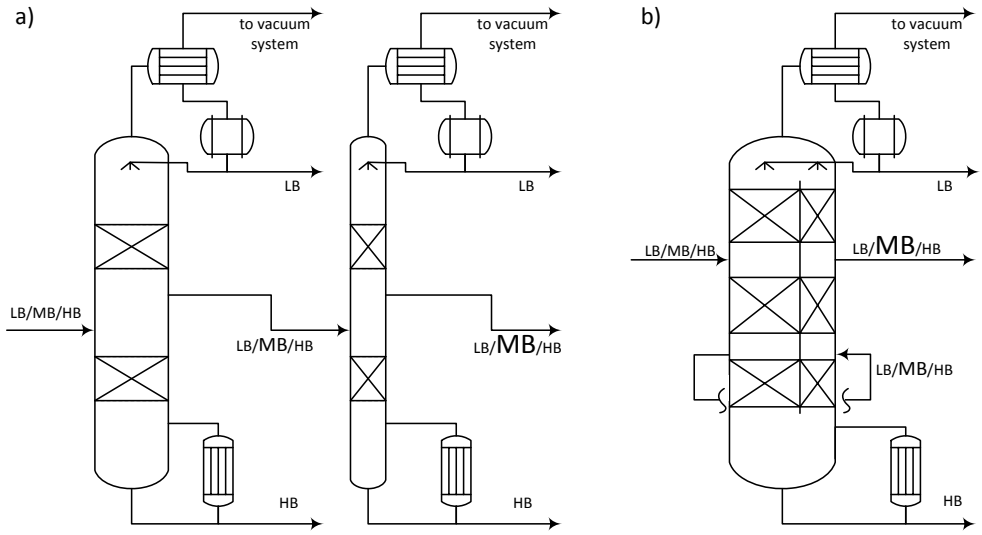

Figure 3: a) Setup of two side-stream columns for the removal of MB; b) Analogous setup designed as DWC with pump-around from the left-hand side to the right-hand side.

2.3 Dividing-wall column (DWC)

The obtained combination of two side-stream columns can be further optimized, especially concerning investment costs. Since both columns produce high-purity products LB and HB, they can share just one condenser and one reboiler. In addition, they can be combined in a common shell. This leads to a dividing-wall column with a wall from the bottom to the top stage. The withdrawal from the first to the second side-stream column is then designed as a pump-around from the left-hand side (LHS) to the right-hand side (RHS) of the DWC. The setup is schematically shown in Figure 3b.

2.3.1 Experimental setup and simulation

Optimization of the DWC design was performed by simulation with ASPEN® PLUS using the RADFRAC model. The model was validated by an experiment. Two packed side-stream columns in DN80 (LHS) and DN50 (RHS), respectively, and both equipped with condenser and reboiler were built up in the laboratory and connected as sketched in Figure 3a. The internal concentration profiles were sampled by withdrawing either liquid or vapor phase from the columns. All samples were analyzed by gas chromatography.

The temperature profile was also measured. Albeit heat-loss was compensated by electric heat tracing, “wild” condensation inside the columns still occurred. The amount of heat loss was estimated measuring the amount of reflux at the bottom of the column and subtracting the feed stream and the reflux at the top of the column. Multiplying the resulting “wild” reflux with a mean heat of vaporization of 320 kJ/kg the heat loss was obtained for consideration in the simulation. The feed contained two middle-boiling components MB 1 (0.5 w%) and MB 2 (0.5 w%).

In order to properly map the experiment into the model, for the LHS the (simulated) amount of distillate was varied until matching the measured LB concentration in the side-stream. For the RHS the mass balance was tuned until the simulated LB concentration in the sump corresponded to the measured one. The heat loss (W/stage) was adjusted until the simulated temperature profiles matched the

measured ones. These adjustments are necessary since measurement of mass flux is affected by error which would distort the simulation results.
Figure 5 demonstrates the good agreement between measured and calculated profiles for one chosen operating point (see Table 2 for parameters). Simulation overestimates the MB peak concentrations. However, calculated LB and HB concentrations are very well aligned with the analyzed samples. This indicates that phase equilibria are calculated well although thermodynamic properties of MB 1 and MB 2 are not modeled properly enough. The kinks in the LB and HB concentration profiles of the LHS column indicate a sub-optimal feed-stage location. Unfortunately, the withdrawal of the side-stream in the RHS is located too high. This is due to edificial constraints in the laboratory which did not allow positioning the withdrawal at the optimal position. Further, the bottom product contains too much LB. The mass balance of the RHS should have been shifted towards more distillate. This would also have led to a higher MB concentration in the side-stream of the RHS.
Although operating point and withdrawal stages are not optimally chosen, the experiment clearly shows that the concept of using a sequence of two side-stream columns leads to an almost 20-fold concentration of MB in the RHS column compared to the feed. The ASPEN model could be fairly validated giving the possibility of in silico optimization of the DWC setup.

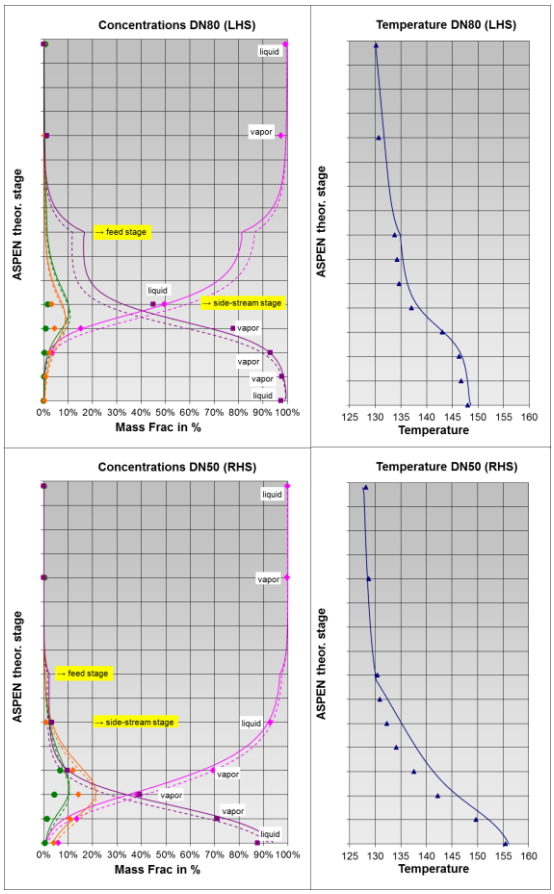

Figure 5: Simulated concentration profiles (solid lines: liquid phase; dashed lines: vapor phase) compared to analytics (markers) and temperature profiles of the LHS (above) and RHS (below) columns, respectively. Magenta: LB; green: MB 1; orange: MB 2; purple: HB.

DN 80 (LHS)	Experiment	ASPEN
feed	2 kg/h	2 kg/h
disitllate	1.12 kg/h	1.16 kg/h
side-stream	0.1 kg/h	0.1 kg/h
reflux	4.48 kg/h	
reflux ratio (at top)	4	3.86
measured reflux	17.1 kg/h	16.5 kg/h
"w ild" reflux	10.62 kg/h	
heat loss	~ 944 W	stage 1-40: 450 W
	~ 12.6 W/stage	stage 41-75: 450 W

DN 50 (RHS)	Experiment	ASPEN
feed	0.1 kg/h	0.1 kg/h
disitllate	0.04 kg/h	0.04 kg/h
side-stream	0.01 kg/h	0.01 kg/h
reflux	1.32 kg/h	
reflux ratio (at top)	33	33
measured reflux	7.36 kg/h	7.6 kg/h
"w ild" reflux	5.94 kg/h	
heat loss	~ 530 W	stage 1-40: 400 W
	~ 7 W/stage	stage 41-75: 200 W

Table 2: Parameters of the experimental setup and equivalent simulation.

2.3.2 Design of large-scale DWC

Using the experimentally validated ASPEN model, a large-scale DWC for the separation of a feed as given in Table 1 (right column) was designed. Several case studies were performed to find the optimal pump-around flux, withdrawal, and feed position as well as the amount of purge stream in order to meet the expected top product quality while minimizing product loss. The acentric position of the dividing-wall is given by the ratio of the LHS and RHS diameters with the constraint that the pressure drop on both sides must coincide.

That the DWC has a clear advantage on the single side-stream column becomes clear in Table 1. Although combining two columns in one shell, the DWC can be designed with a cross-sectional area 14% smaller than a single side-stream column. Energy consumption is decreased by more than 40%. Product loss is halved because the middle-boiler is concentrated one and a half times more in the DWC than in the single side-stream column. Further the amount of purge is also decreased by almost 50%.

3. Conclusions

A dividing-wall column (DWC) with a pump-around stream from the left-hand to the right-hand side represents a cost-saving alternative to a single side-stream column in order to remove small amounts (<1%) of middle-boiling impurities from a narrow-boiling mixture. Experimental results of a pseudo three-component feed distillation in two coupled side-stream columns – the equivalent setup to the presented DWC – could be modeled with good accuracy providing the basis for further optimization of the column design.

Following the approaches for the separation of mixtures containing more than three components in multi-partition wall DWCs (see e.g. ref. [10]) setups with several pump-arounds from one partition to another could be the focus of further research.

References

1 N. Asprion, G. Kaibel; Chem. Eng. Process, 49; 2010, pp. 139-146
2 I. Dejanović, Lj. Matijašević, Ž. Olujić; Chem. Eng. Process, 49; 2010, pp. 559-580
3 G. Niggemann, C. Hiller, G. Fieg; Ind. Eng. Chem. Res., 49; 2010, pp. 6566-6577
4 F.B. Petlyuk, V.M. Platonov, D.M. Slavinskij; Int. Chem. Eng., 5(3); 1965, pp. 555-561
5 G. Kaibel; Chem. Eng. Tech., 10(1); 1987, pp. 92-98
6 Ö. Yildirim, A.A. Kiss, E.Y. Kenig; Sep. Purif. Technol., 80; 2011, pp. 403-417
7 E.R. Gilliland; Ind. Eng. Chem., 32; 1940, pp. 1220-1223
8 A.J.V. Underwood; Trans. Inst. Chem. Eng., 10; 1932, pp. 112-158
9 F.W. Winn; Petrol. Refin., 37; 1958, pp. 216-218
10 I.J. Halvorsen, I. Dejanović, S. Skogestad, Ž. Olujić; Chem. Eng. Res. Des., 91; 2013, pp. 1954-1965

Multiple steady states in dividing wall column

WANG Erqiang

College of Chemistry and Chemical Engineering, University of Chinese Academy of Sciences, Beijing 100049, China

ABSTRACT:

This paper presents simulation and analysis of multiple steady states (MSS) in dividing wall column (DWC). First steady state simulation of benzene-toluene-xylene (BTX) separation in DWC is run to obtain its four different solutions using Aspen Plus software, and then detailed comparisons and analysis of these solutions are done. From simulation results, it can be concluded that MSS inevitably exists in DWC, which is important for its design, operation and control but has not been declared in open literature up to now. In addition, obvious grouping feature is found among the four solutions of BTX DWC case, and light component benzene and heavy component xylene has respectively two different recoveries at the top of side column among the four solutions. The grouping feature is interesting and important for DWC, which may be explained by that existence of impurities in side product stream and their different flow path from the feed to the side product stream, i.e. above or under dividing wall.

KEYWORDS:

dividing wall column, Petlyuk column, multiple steady states, simulation, grouping feature

1.Introduction

Distillation column is one of the most common apparatuses in chemical industries, but heat efficiency in the conventional distillation system is comparatively low which results in extremely high energy consumption. The industry seeks continuous improvements to the distillation system. Extensive research studies have been devoted on this field, among of which the so called dividing wall column (DWC) is getting more and more attention in industry and academia [1-3].

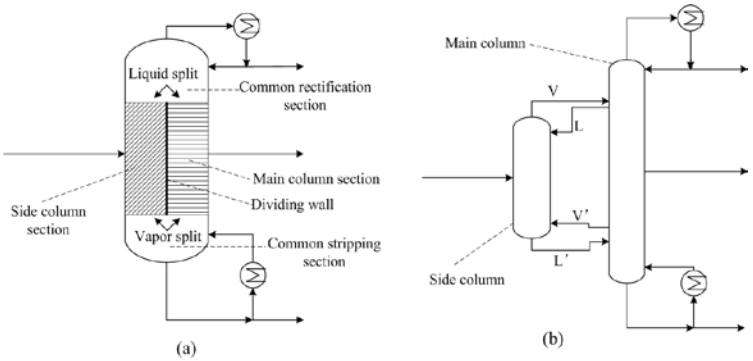

Figure 1 Schematic representation of (a) DWC and (b) Petlyuk column

Twenty-seven years after the first industrial application in 1985, DWC has established itself as most sustainable among distillation technologies. It not only leads to energy saving but also to capital and space saving. As shown in Figure 1(a), DWC

is developed based on the fully thermally coupled column (Petlyuk column, Figure 1(b)) in which the heat transfer is coupled by a direct contact of streams between the columns. L, M, H mean light, middle and heavy boiling component respectively. It is a single shell thermodynamic equivalent of a fully thermally coupled column, which allows separation of three or more components into high purity products within one shell. This is achieved by using a vertical partition wall that divides mainly central part of the column into pre-fractionator section (side column) where the feed is sent to and main column section where the side stream flows out. In addition, common rectification and stripping section is located above and below the dividing wall respectively.

Recently, many work have already been done on the design, operation, optimization, and control of DWC, but its characteristics of multiple steady states (MSS) have not been paid more attention to, although MSS is often involved in chemical engineering, such as rector and separation process,. MSS is important for design, operation and control of related devices and processes. For DWC, it is also desired to know whether or not MSS exist, how and why MSS exist, and how to design, operate and control DWC further better in view of MSS feature. But up to now, few of published papers and open documents mention about MSS in DWC. There are only a small number of papers concerning on MSS in interlinked separation columns such as Petlyuk column [4-5]. Although both are thermodynamically equivalent, DWC is easier than Petlyuk column to be realized in industry.

Wayburn and Seader [4] have been the first to report existence of MSS in interlinked separation column, using a differential arc-length homotopy continuation method, and in their following papers [5] explained the reason of MSS based on degree-of-freedom analysis. They obtained four different internal liquid and vapor split ratios which can give the same output product streams with the same input feed stream. This multiplicity they found is so called “Input multiplicity”. They concluded that the appearance of multiple solutions may occur in interlinked separations systems whenever two or more sections of the system have to share specifications in order to satisfy local degree of freedom. But in their papers, they did not give detailed information of the four solutions and further compare and analysis of these solutions.

The objective of this paper is to simulate and analysis of MSS feature in DWC through BTX separation example. First BTX separation is simulated as a DWC application by using commercial process simulator Aspen Plus, and four steady state solutions are obtained. Then detailed comparsion and analysis among the four solutions are given in term of column profiles of temperature, and concentrations. At last, component recoveries are calculated for each solution. Based on above results and analysis, an interesting grouping feature is found among the four solutions and its possible cause is proposed.

2.BTX separation simulation

In this paper, BTX separation in reference article [5] is simulated in DWC process by MultiFrac module of Aspen plus software, and Ideal thermodynamic equation is selected since this is a fairly ideal system from the standpoint of vapor-liquid equilibrium. Using DWC similar to that shown in Figure 1(a), the BTX feed is separated into three product streams with benzene in the top distillate, xylene in the bottoms, and toluene in the side stream. Of course, the three products have some impurities respectively. The feed condition and other parameters are given in Table 1. The stage in side column or main column is numbered from top to bottom. In this case xylene stands for o-xylene. As known from the reference [5], the four solutions have

different internal vapor and liquid split ratio at a constant reflux ratio and constant bottom stream flowrate of main column. The simulation is run at a reflux ratio of 5 and bottom flowrate of 380 kmol/h. By using “Design Spec/Vary” function of Aspen plus, purities of three product streams are specified, while side stream flowrate, internal liquid and vapor split ratio are used as manipulated variables. It should be noted that appropriate initial value is needed for each solution to help convergence.

Table 1 feed conditions and other parameters of BTX separation in DWC

Parameter	Value	Parameter	Value
Feed temperature, K	383.4	Number of stages in main column	32
Feed pressure, kPa	101.33	Number of stages in side column	20
Feed flowrate, kmol/h	1000	Internal linking stages between main column and side column	6，26
Feed component flowrate			
benzene, kmol/h	200	Side stream stage of main column	16
toluene, kmol/h	400	Mole fraction of benzene in column top	0.95
xylene, kmol/h	400	Mole fraction of toluene in side stream	0.90
Bottom stream flowrate，kmol/h	380	Mole fraction of xylene in column bottom	0.95
Feed stage of side column	12	Reflux ratio of main column	5

3.Results and discussion

The calculated three product streams of main column in four solutions are given in Table 2 in which the four solutions are marked as A, B, C and D respectively. Table 2 lists mole flowrates and mole fractions of three product streams. calculated mole flowrates of internal linking streams are given and compared with the reference data for interlinked separation column [5]. These results agree well with the reference data, so the simulation is reliable and can be used for further analysis. It also shows that the same MSS exists in DWC.

Table 2 calculated product streams in four solutions of BTX separation

	A	B	C	D
Top distillate				
Flowrate, kmol/h	208.2349	208.225664	208.233428	208.224421
Mole fraction				
benzene	0.95	0.95	0.95	0.95
toluene	0.04999986	0.04996192	0.04999993	0.04996239
xylene	1.388e-07	3.8074e-05	6.1148e-08	3.7602e-05
Liquid side stream				
Flowrate, kmol/h	411.765113	411.774336	411.766461	411.775545
Mole fraction				
benzene	0.00528587	0.00530718	0.00528617	0.00530722
toluene	0.9	0.9	0.9	0.9
xylene	0.09471412	0.09469281	0.09471382	0.09469277
Bottom stream				
Flowrate, kmol/h	380	380	380	380
Mole fraction				
benzene	8.3407e-07	6.7743e-07	4.1403e-06	3.7178e-06
toluene	0.04999916	0.04999932	0.04999586	0.04999628
xylene	0.95	0.95	0.95	0.95

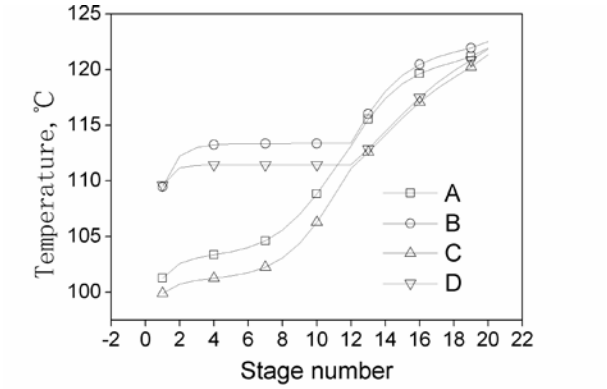

Figure 2 Temperature profiles in main column for four solutions

Figure 2 gives temperature profiles in main column for four solutions. It can be seen that, in the top common rectification section and bottom common stripping section, the four solutions have almost identical temperature distribution, while in dividing wall section large temperature difference exists, but the temperatures at the side stream stage are nearly equal. This can be explained from the same concentration of product streams respectively at top, bottom and side stage of main column for the four solutions, since that at constant pressure, column temperature profile can be consistent with concentration profile. In dividing wall section, temperature profile below side stream stage can be divided into two groups: A and C, B and D, and the former group have higher temperature than the latter. So solutions A and C have more heavy component than that of B and D in this section. But above the side stream stage, there are not obvious grouping feature among the four solutions.

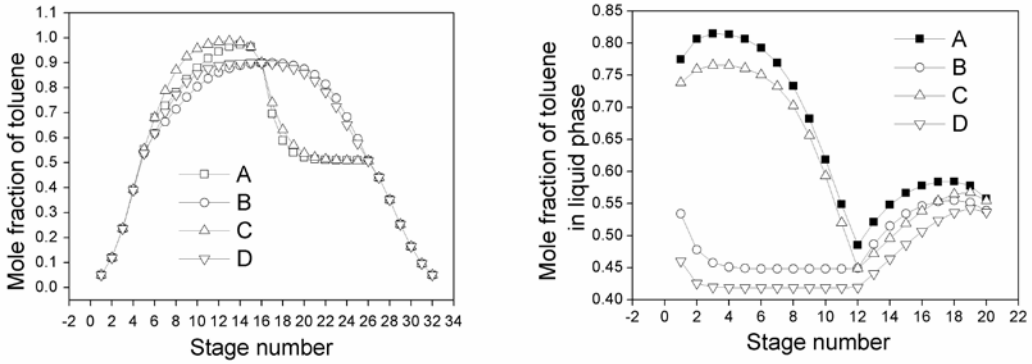

Figure 3 Liuqid concentration of toluene in (a) main column (b) side column

Figure 3(a) give the liquid concentration of toluene in main column respectively. Figure 3(a) shows that large concentration difference of toluene in dividing wall section (6~26 stages) exist among the four solutions, and A and C have similar profiles just as B and D do, but at the side stream stage 16, four solutions have the same specified toluene mole fraction of 0.9. Above the side stream stage, A and C group have higher toluene concentration than those of B and D group, while below this stage, the reverse is the case. From Figure 3(a), it seems to be that solutions B and D are more advantages in energy consumption than A and C, since that re-mixing phenomenon exists in A and C which would cause energy inefficiency.

Figure 3(b) give liquid concentration of toluene in side column respectively. It can be seen that grouping feature among the four solutions appear again and is similar to those of Figure 3(a). From Figure 3(b), obvious grouping feature appears above the feed stage, and A and C group have a large toluene concentration of 0.75~0.80 while

B and D group of 0.45~0.55. Below the feed stage, the differences among the four solutions reduce to a small values and in the bottom they have a close concentration of 0.55.

To know how and why of the grouping feature among the four solutions, , mass balance and component recoveries are calculated around the side column which has three feed input streams and two product out streams. The component recoveries at top of side column are defined as follows:

$$\mathbf{r_i} = \frac{\mathbf{Vf} \times \mathbf{y_{vi}}}{\sum_{\mathbf{j}} \left(\mathbf{F_j} \times \mathbf{x_{Fji}} \right)}$$

in which Vf is mole flowrate of top vapor product stream V of side column and y_{vi} is mole fraction of component i of stream V, F_j is mole flowrate of feed stream j of side column and x_{Fji} is mole fraction of component i of feed stream j. Results are given in Table 3. It can be seen that grouping feature is observed again, A and B group have close benzene recovery while C and D group have another different value, but for xylene recovery, A and C can be included into the same group while B and D belong to another group.

Table 3 mass balance and component recovery of side column for four solutions

	A	B	C	D
Feed stream				
(flowrate /mol/h and mole fraction)				
Stream 1	1000	1000	1000	1000
benzene	0.20	0.20	0.20	0.20
toluene	0.40	0.40	0.40	0.40
xylene	0.40	0.40	0.40	0.40
Stream L	423.43	122.19	331.86	45.80
benzene	0.31971088	0.29722439	0.31976215	0.29747634
toluene	0.67994049	0.6171407	0.68008424	0.61784147
xylene	0.00034862	0.08563490	0.00015362	0.08468218
Stream V’	779.70	620.83	625.06	488.21
benzene	0.00233754	0.00189932	0.01150153	0.01033922
toluene	0.7239586	0.72428808	0.71696035	0.71784284
xylene	0.27370385	0.2738126	0.27153812	0.27181793
Product streams				
Stream V	812.588822	626.438544	651.531329	490.222533
benzene	0.41183732	0.37611113	0.46215874	0.42561829
toluene	0.58778856	0.51570718	0.53764907	0.44640437
xylene	0.00037412	0.10818169	0.00019218	0.12797734
Stream L’	1390.54157	1116.58712	1305.38931	1043.79563
benzene	0.00182918	0.00169038	0.00934104	0.00960522

toluene	0.55715528	0.53915461	0.55427245	0.53642981
xylene	0.44101554	0.45915501	0.43638651	0.45396496
Component recovery at side column top				
benzene	0.992457	0.992053	0.96108	0.954151
toluene	0.381379	0.349226	0.326209	0.281007
xylene	0.000495	0.116752	0.00022	0.11692

As a summary of above results and analysis, on one hand, MSS feature will inevitably exist in DWC and will be very important for DWC design, operation and control, this field need people to pay more attention to; On the other hand, interesting grouping features are observed among multiple solutions of DWC whenever in temperature and concentration profile or component recoveries. To explain for grouping feature, it should be noted that the side product stream of main column has impurity of benzene and xylene which should be come from the BTX feed of side column. So fed into the side column and facing with the dividing wall in DWC, the light and heavy component, benzene and xylene, each could flow to the side stream stage above or under the dividing wall.

4.Conclusions

In this paper, steady state simulation of BTX separation in DWC is run, and four solutions are obtained similar to those for interlinked separation columns. So MSS inevitably exists in DWC which is very important for DWC design, operation and control. Then detailed comparison and analysis of these multiple solutions are done. From temperature and concentration profile, it can be seen that obvious grouping feature appear among the four solutions. Further calculation shows that there are two different benzene recoveries at the top of side column among the four solutions, and xylene also has two different recoveries. Considering that side product stream have impurities of benzene and xylene, the above grouping feature can be explained by that impurities in side stream and their different flow path from the feed to the side stream, i.e. whether above or under the dividing wall. This explanation may provide a new view to study MSS in DWC. Of course this conclusion can be applied to Petlyuk column.

Acknowledgements

This work are supported by the National Natural Science Foundation of China (No.21376240).

References

1. Dejanovic I, Matijasevic L, Olujic Z. Dividing Wall Column—A Breakthrough Towards Sustainable Distilling[J]. Chem. Eng. Process., 2010, 49(6): 559-580
2. Yildirim, O., Kiss, A.A., Kenig, E.Y., Dividing wall columns in chemical process industry: A review on current activities[J], Separ. Purif. Technol., 2011, 80(3): 403-417
3. Asprion N., G. Kaibel. Dividing wall columns: Fundamentals and recent advances[J], Chem. Eng. Process., 2010, 49(2): 139-146
4. Wayburn, T.L., Seader, J.D., Solutions of systems of interlinked distillation columns by differential homotopycontinuation methods, In: Processing of Computer-Aided Process Design, Westerberg,A.W., Chien, H.H., Eds., Academic Press, U.S., 1984, 756-862
5. Chavez, C. R., J. D. Seader, and T. L. Wayburn, Multiple Steady-State Solutions for Interlinked Separation Systems[J]. Ind. Eng. Chem. Fundam., 1986, 25(4): 566-576

"From Mini to Mega" – Process Development, Engineering, and Construction of a Large-Scale CO_2 Capture Plant

Stefan Hauke[1], *André Ohligschläger*[1], *Dr. Albert Reichl*[1], *Dr. Tim Rogalinski*[1], *Dr. Rüdiger Schneider*[1]

[1]*Siemens AG, Frankfurt, Germany*

Abstract

Siemens has developed a market-ready second-generation post-combustion CO_2 capture process based on chemical absorption and desorption. The applied solvent is based on an aqueous amino acid salt solution and features low-absorption enthalpy and near-zero vapor pressure, permitting an economic and environmentally friendly capture process.

The development of the Siemens carbon capture process – from lab-scale ("Mini") to large-scale ("Mega") – is described in this article, with a special focus on design and constructability. Siemens masters the entire chain – from process development to project implementation – thanks to in-house competence in turn-key power plants, chemical process development, flue gas treatment, and CO_2 compressor technology. The process was developed at laboratory scale. For validation of the determined solvent and process features on an industrial scale, a pilot plant was installed and operated for more than 9,000 hours. The pilot plant operation allowed well-founded selection of materials, the validation of a computational process model, emission measurement, and collection of data that cannot be reliably computed. The examination of degradation aspects led to a completely new in-house development of a reclaiming process, adapted to the specific characteristics of the capture solvent.

The size of a full-scale carbon capture plant poses special challenges to constructional feasibility, equipment design, and logistics, and thus requires a refined transport, erection, and maintenance concept. This article describes how those requirements are accommodated for a safe, energy-efficient, environmentally friendly, and highly available carbon capture process.

Keywords

CO_2 separation, carbon capture, process development, reclaiming, absorption, desorption, engineering studies

1. Introduction

Forecasts indicate that fossil energy sources will remain the backbone of power generation worldwide in the coming decades (see Figure 1)[1]. While the relative share of fossil power generation is expected to shrink slightly in the future, the absolute value of power generation from fossil fuels is expected to increase significantly. This also means that the total CO_2 emissions from power generation are very likely to grow, despite worldwide efforts to reduce greenhouse gas emissions. However, there is still a chance to achieve CO_2 emission reduction targets and thus the assumed

maximum allowable increase in global warming if Carbon Capture and Storage (CCS) or Carbon Capture, Utilization, and Storage (CCUS) are implemented along with the maximizing of efficiency levels in power generation. According to the International Energy Agency (IEA), CCS plays a role, contributing 14 percent of the global cuts in CO_2 emissions required by 2050 (in accordance with 2 °C scenario)[2].

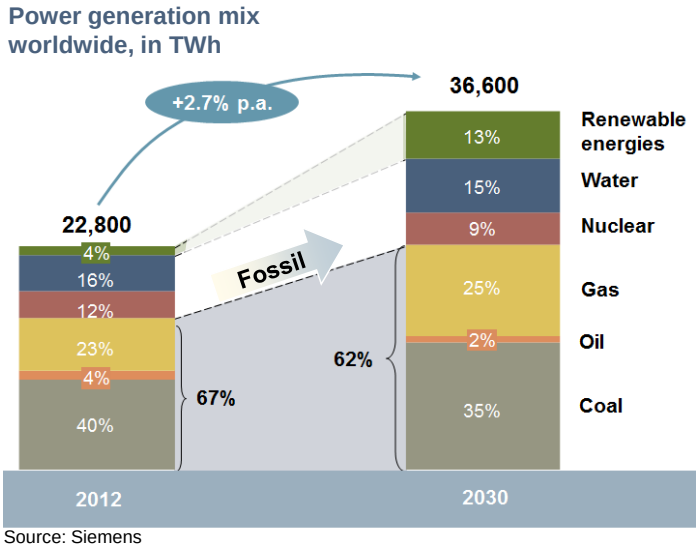

Figure 1: Global electricity market forecast for 2030 (Siemens estimation)

The forecast costs for carbon capture and storage for the first commercially operated plants after 2020 are estimated to range between 35 and 90 €/t CO_2[3]. This means that carbon capture and storage without commercial use of the CO_2 such as for enhanced oil recovery is not commercially viable at the moment. Compression, transport, and storage would account for 15-30 percent of total costs, while 70-85 percent would be contributed by the capture plant. Thus, in addition to seeking CO_2 utilization, the main focus has to be on reducing the cost of capturing.

Siemens has developed a proprietary post-combustion carbon capture technology named PostCap™. The primary development targets were to meet the most stringent environmental requirements without compromising the economics and the operability. The Siemens PostCap™ technology utilizes selective absorption (based on an amino acid salt solvent) of the CO_2 from the flue gas and subsequent desorption (thus gaining nearly pure CO_2) and is ready for full-scale application. Amino acid salts have numerous benefits as CO_2 absorption solvents. These positive properties have been validated by more than 9,000 operating hours in a CO_2 capture pilot plant adapted to a coal-fired power plant and gas-fired power plant, as well as by an extensive laboratory research program.

2. Results and discussion

2.1 Solvent selection and process development

The optimum solvent should have high absorption capacity to minimize liquid holdup. At the same time, a solvent should be able to release CO_2 during desorption easily and quickly. To avoid environmental impact and solvent loss, the solvent or secondary products should not be emitted (low vapor pressure). The solvent should be chemically stable, non-toxic, non-explosive and environmentally friendly.

Furthermore, to keep material costs reasonable, the solvent ingredients should be compatible with common construction materials. The solvent should allow simple operability, e.g. characteristics toward foaming or precipitation.

To find the best compromise, a solvent screening was carried out at Siemens' lab and pilot facilities. As a result, Siemens decided in favor of amino acid salts (AAS) as the basis for the process. This is because the physical and chemical properties of AAS best meet the requirements listed above and are thus advantageous in terms of solvent handling, plant operation, and operating permissions. These advantageous characteristics apply to a number of amino acid salts. There is no salt with best performance for all the criteria, therefore the specific salt selected for the PostCap^{TM} process is based on potassium, which e.g. allows complete recovery of solvent from complexes formed by absorption of SOx by simultaneously gaining a sellable product – as described later.

During the early phase of process development, nearly 50 process configurations were determined. 20 process configurations were selected and compared, using simulation tools. The complete process was a network of different interacting topics as shown in Figure 2. The most important target was to achieve low specific energy demand, leading to optimized CAPEX and OPEX.

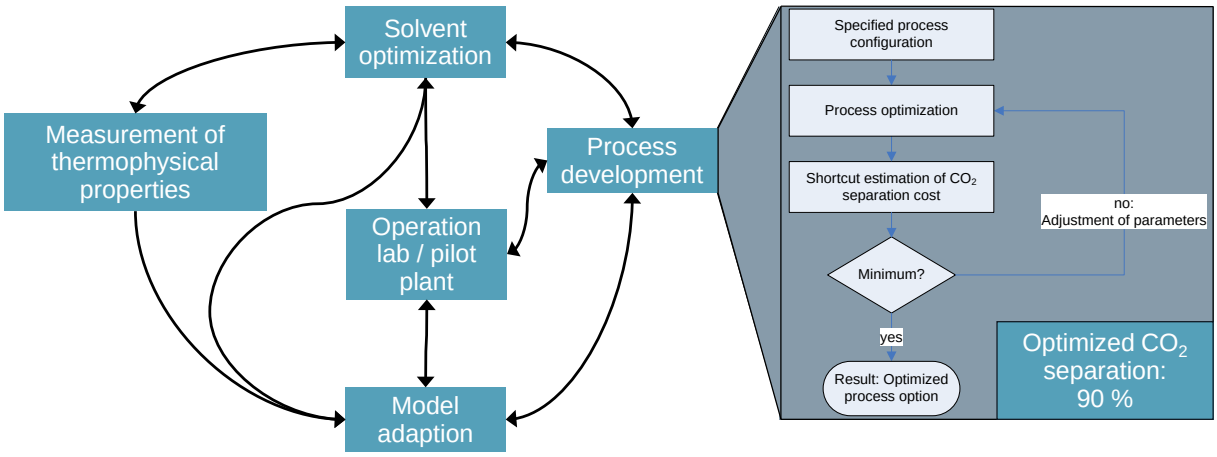

Figure 2: Screening of process configurations for carbon capture

Typical process operation parameters are:

- Continuous plant operation.
- Pressure in the absorber is close to atmospheric conditions, since compression of the flue gas would require too much energy.
- Pressure in the desorber is usually close to atmospheric conditions. However, it can also be higher depending on local conditions resulting in the optimized power integration.
- Typical thermal energy consumption per tonne of captured CO_2 is approx. 2,7 GJ, with potential for optimization.
- The capture rate can be modified. Typical economically reasonable range is between 85-95 %.

2.2 Laboratory and pilot plant

The simulation tools provided both chemisorption and hydrodynamic modeling. The model was validated and optimized by installing a lab-scale plant and later a pilot plant. The lab-scale plant features 24/7 operation and full automation.
The main advantages of the lab-scale plant are:

- Proof-of-principle trials can be realized comparatively easily, e.g. tests with additives or activators
- Process configurations and effects of variation of operation points can be studied at low expense
- Determination of separation efficiency is reliable
- Models can be validated or adapted (hydrodynamics and thermodynamics)
- Thermal and oxidative stability can be shown
- Degradation rates can be determined
- Reaction mechanisms (e.g. of by-products) can be examined

However, lab-scale plants do have limitations, such as determination of energy consumption and absence of real flue gas.

Thus, the installation and operation of a pilot plant was realized in collaboration with a power plant operating company. The entire chain – from plant design, piping (3D-modeling), measurement and control strategy, process automation, coupling to power plant via HazOp, and authorization procedure to construction site supervision – was carried out by Siemens The onsite pilot facility is able to process flue gas from a coal-fired plant as well as from a gas-fired plant. The plant is equipped with more than 150 measuring points, is fully automated and operable via remote access, features online analytics for the components CO_2, O_2, SO_2, NO_X, supplies several material sampling mountings, and allows isokinetic emission measurement.

The main components in the CO_2 capture plant are the absorption and desorption columns (see Figure 3), with additional equipment for energy savings, for instance Lean Solvent Flash.

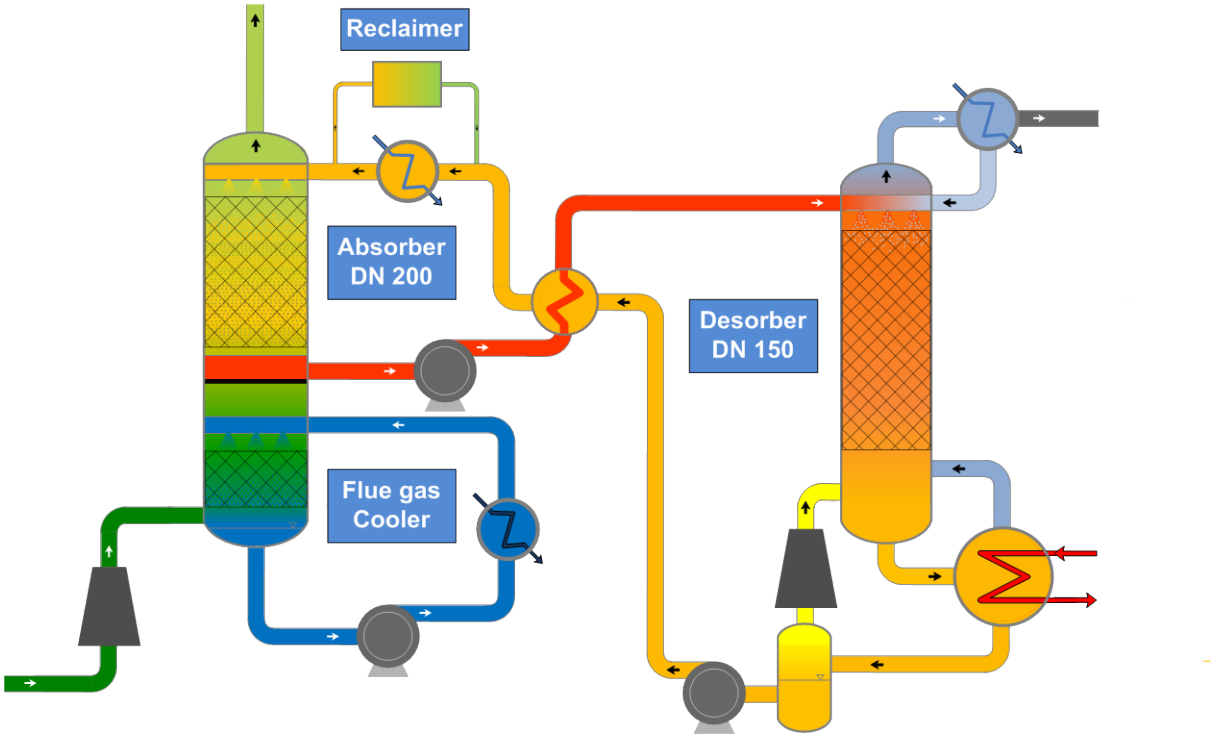

Figure 3: Schematic visualization of the Siemens pilot plant

One of the most important objectives was to gain operational experience. To date, more than 9,000 operating hours have demonstrated the operability of the pilot plant and the chosen solvent. The effects of power plant start-ups and shut-downs were examined and described by dynamic simulation. Troubleshooting cases were practiced. The experience gained led to improvements of the pilot plant and flowed into design specifications for full-scale plants. During the entire pilot operation, no plugging of trays or packings was observed.

The absorber and desorber column internals in particular are essential for the efficient and reliable operation of the carbon capture plant. The packing type and height used in the pilot plant is equal to the packing of the full-scale plant. Table 1 summarizes the scales of the lab facility, the pilot facility, and a typical full-scale capture plant for a gas-fired power plant.

Further results of the pilot phase were the validation of the process model with non-synthetic flue gas. Reliable information was acquired related to:

- Accumulations and secondary components
- Solvent stability, degradation
- Foaming and mitigations
- Emissions and dispersion calculations
- Material properties

			Lab-scale	Pilot-scale	Full-scale
Flue gas		Nm^3/h kg/h	3 4	230 300	2.3 Mio. 3 Mio.
Absorber	Diameter		50 mm	DN 200	2 x >15 m
	Packing type		structured	structured	structured
Solvent holdup		m^3	0.01	0.4	4,000
Scale-up factor	Cross-section area absorber		-	16 x lab scale	5,625 x pilot scale

Table 1: Scale-up factors for Siemens' lab and pilot plant and a typical full-scale application (CHP, 1.2 Mio. t CO_2/a, 280 MW in electricity, 350 MW in heat)

2.3 Reclaimer process development

Due to the fact that large quantities of flue gas are treated over a long period of time in post-combustion processes, even very small amounts of trace components contained in the flue gas as secondary components (like sulphur or nitrogen oxides) would lead to a noticeable accumulation of secondary products in the solvent pump-around. Therefore, these components must be eliminated by continuously treating a slipstream of the solvent. Reclaimer concepts for amine-based solvents are not suitable for amino acid salts since they rely on evaporating the active component.

Thus, Siemens has developed a proprietary process for reclaiming amino acid salt solvents, based on a two-step crystallization process (see Figure 4).

A purge stream of the cold solvent is directed to a reclaimer unit, where secondary products are removed. The solvent loss is replaced by the same amount of fresh solvent. However, because the blocking of the solvent is reversed in the SO_x reclaimer and the solvent is completely regained, the solvent reclaimer unit ensures that the utilization of solvent is maximized and solvent residues are minimized. This contributes to the relatively low operating costs. Furthermore, through the reclaimer, sulphur oxides contained in the flue gas are converted completely to a marketable fertilizer product. Therefore, the requirements for limiting the SO_x levels upstream of the absorber are less strict compared to other amine-based capture technologies. NO_x-based secondary components can be separated with high selectivity as residues. Both process steps can be operated completely independently and the full-scale plant can be mounted as skid, allowing easy pre-assembly, transport, and installation (see Figure 4).

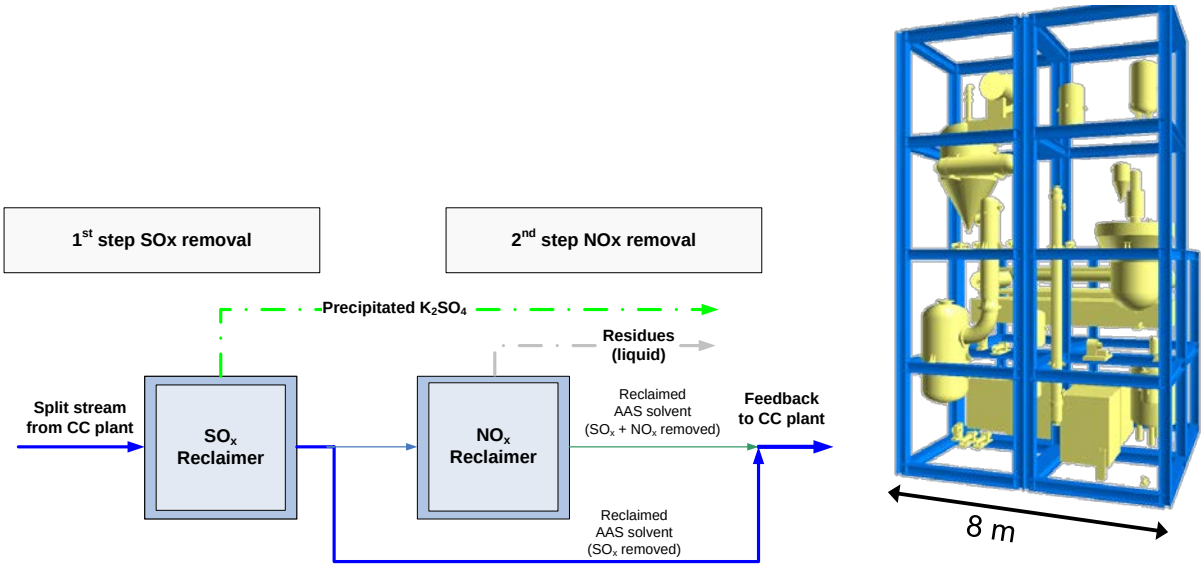

Figure 4: Reclaimer concept and example for skid-mounted full-scale reclaimer

2.4 Engineering studies

In concurrence with the process development, engineering studies have been carried out for CO_2 product streams that may vary from 4,000 t/a to more than 2,000,000 t/a. Table 2 shows a selection of these studies as they compare to the capacity of the Siemens pilot plant.

Project	Siemens PostCap™ pilot plant	Study for combined cycle power plant (CHP)	Feasibility study I	Feasibility study II	Feasibility study III	Feasibility study IV	Feasibility study V	FEED study carbon capture Masdar	Concept study carbon capture Mongstad
Site	Großkrotzen-burg, Germany	Norway	Europe	Europe	USA	China	GB	UAE	Norway
Process	Coal-fired power plant Staudinger	Combined cycle power plant (CCPP)	Coal-fired power plant	Coal-fired power plant	Coal-fired power plant	Coal-fired power plant	Biomass power plant	Combined cycle power plant (CCPP)	Combined heat and power station (CHP)
CO_2 production capacity	320 t/a	1.2 Mio. t/a	700,000 t/a	1.4 Mio. t/a	1.0 Mio. t/a	1.0 Mio. t/a	4,000 t/a	1.8 Mio. t/a	1.2 Mio. t/a

Table 2: Compilation of engineering studies on PostCap™

2.4.1 Project example

The study on full-scale carbon capture Mongstad (CCM) in Norway (Statoil Petroleum AS) can be highlighted as an example. Even though this specific project will not be continued, the findings can easily be transferred and adapted to other projects as well. The combined heat and power station (CHP) was to be equipped with a carbon capture plant to produce 1.2 million t/a CO_2. Siemens carried out a technical qualification program (TQP) to show the feasibility of the process, focused on emission measurement. This was performed with the pilot facilities described before.

The program was followed by a study equivalent to extended basic engineering, which included:

- Capture plant, utilities (e.g. steam, cooling water), effluent treatment
- Process and plant design, piping
- EI&A
- Civil engineering

- HSE – Health, Safety, Environment (HAZOP)
- Constructability

These typical engineering steps are necessary to estimate the investment (CAPEX: Capital Expenditures) and operational cost (OPEX) for the optimized plant configuration in such detail necessary to put the customer into the position to take an investment decision. Target of the studies was - beside the evidence of an economically, environment-friendly and highly available capture process - to take into account also the local, climatic, geographical and ecological circumstances (e.g. potential explosion shock waves from the nearby refinery, high wind load) and the general and specific customer requirements (e.g. different load cases and operating conditions).

The capture plant comprises main columns (two absorbers, one desorber, two flue gas coolers) with an empty weight of up to 1,000 tons.

Figure 5 shows an overview of the whole carbon capture plant.

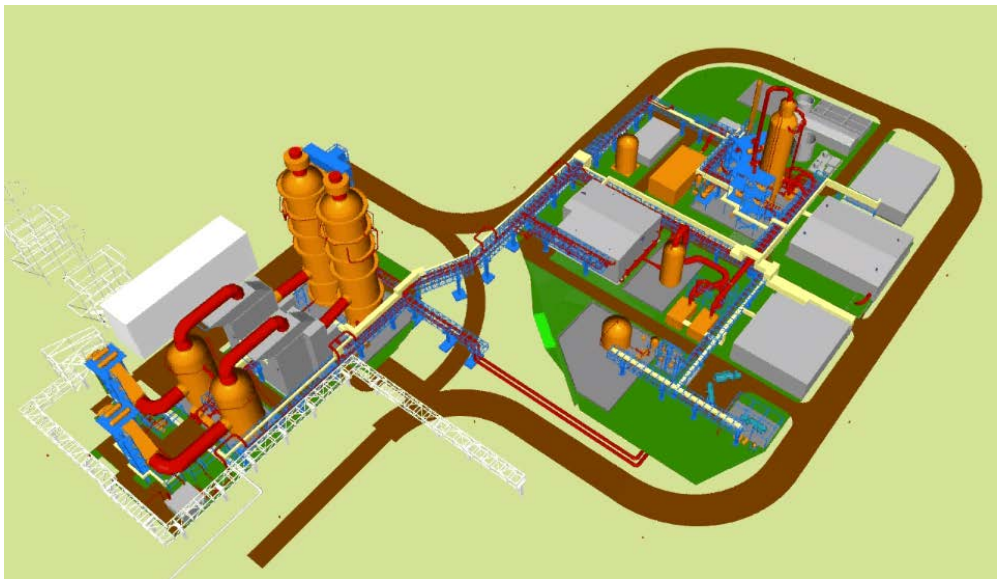

Figure 5: Overview of Mongstad carbon capture plant

2.4.2 Equipment design: large columns

The equipment design was carried out by utilization of in-house competencies with experience of decades in equipment design for all scales (“Mini” to “Mega”), in collaboration with vendors.

For the large columns, the flue gas distribution has to be planned and evaluated by CFD-modeling. Liquid distributors cannot be tested in one piece and have to be segmented as there are no such large vendor facilities available. Their horizontal alignment is very difficult as deflection issues require additional T-girders. Increased wall thicknesses are necessary due to wind-load resistance and earthquake protection features. The complexity of realization of measurements increases: To achieve a reliable temperature measurement inside the absorber column, 12 measuring heads in concentric alignment are necessary, for example, instead of one (see Figure 6).

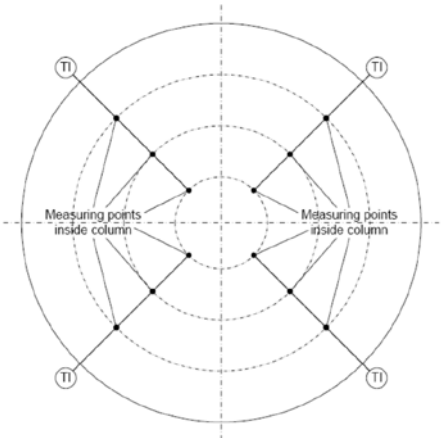

Figure 6: Alignment of temperature sensors inside the absorber column

2.4.3 Constructability and operability

The size of a full-scale carbon capture plant poses special challenges to constructional feasibility, equipment design, and logistics, and thus requires a refined transport, erection, and maintenance concept. Due to high labor costs and severe weather conditions, on-site erection of the columns was not an option. The weight of up to 1,000 tons per absorber column requires adapted logistic concepts for assembly, transport, and erection. Furthermore, it is even necessary to develop concepts for inserting column internals (for example, an elevator).

As a specific feature of the project, the columns are shipped in one piece from the shop to the jetty located close to the site. The absorber columns must be transported from there via a self-propelled modular trailer (SPMT); the erection is carried out with a tower lift system (TLS) in combination with a crawler crane, as Figure 8 shows. To find a feasible routing for installation and to avoid long crane rental intervals, installation sequence simulations were carried out.

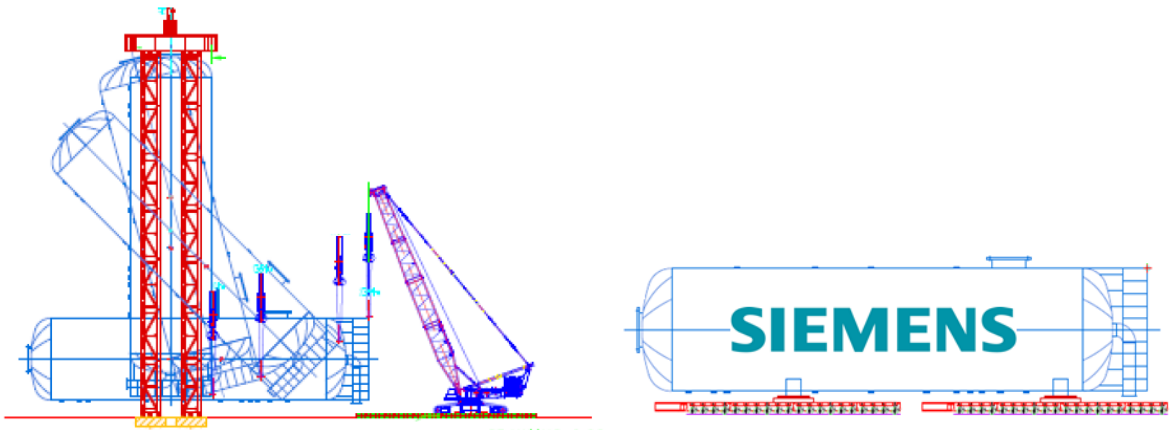

Figure 8: Study: Transport of absorber column with SMPT and erection with tower lift system

So-called RAM studies, which take into account reliability, availability, and maintainability of the carbon capture plant and the interaction with the power plant, play a very important role for full-scale operation. The carbon capture plant is

separated into sub-systems based on the P&ID (for example, absorber, desorber, etc.) and further segmented into components (pumps, valves, measurement devices, etc.). Failure probabilities and repair times are then determined from databases. The results are summarized in failure tree analysis and are part of the operational safety model. Optimization potential for increased availability and safety are detected through a sensitivity analysis.

3. Conclusions

This article describes the development of the Siemens carbon capture process – from lab-scale ("Mini") to large-scale ("Mega") – with a special emphasis on the design and constructability. Solvent selection, process development, and engineering design, with a focus on optimizing CAPEX and OPEX, help reduce costs, so that carbon capture will be commercially attractive if the CO_2 can be utilized, for instance for enhanced oil recovery (EOR). Siemens masters the entire chain – from process development to project implementation – thanks to in-house competence for turn-key power plants, chemical process development, flue gas treatment, and CO_2 compressor technology.

Acknowledgements

Siemens gratefully acknowledges the following for their support and collaborative development of projects mentioned in this paper. In chronological order:

- The BMWi (Bundesministerium für Wirtschaft und Energie – German Federal Ministry for Economic Affairs and Energy) for funding of the Siemens POSTCAP development project
- E.ON SE for co-funding of the Siemens POSTCAP development project and providing facilities for erection and operation of the pilot plant
- The Abu Dhabi Future Energy Company Masdar for jointly developing the CCS concept for Masdar City with Siemens
- The Norwegian Government and Gassnova, funders of the carbon capture project Mongstad (CCM)

References

[1] International Energy Agency; *World Energy Outlook 2013*; IEA Publications; ISBN: 978-92-64-20130-9

[2] International Energy Agency; *Technology Roadmap Carbon Capture and storage edition 2013*; IEA Publications; June 2013

[3] Advisory Council of the European Technology Platform for Zero-Emission Fossil Fuel; Power Plants *The Costs of CO_2 Capture, Transport, and Storage*; July 2011

A new Approach for Absorption Column Modeling

Prof. Christo Boyadjiev
Institute of Chemical Engineering, Bulgarian Academy of Sciences, Sofia, Bulgaria

Abstract

A new approach, on the base of the approximations of the mechanics of continua, for qualitative and quantitative analyzes of the absorption processes in column apparatuses, is proposed. A convection–diffusion type of model is used for qualitative analysis of the process mechanism and finding of the mass transfer resistances in the phases. An average concentration model for a quantitative description of the process and scale-up problem solution is used.

Keywords

convection–diffusion model, average concentration model, mass transfer resistance

1. Introduction

The modeling of two phases (gas-liquid, liquid-liquid, gas-solid, liquid-solid) interphase mass transfer processes in column apparatuses is used in the case of absorption, extraction, adsorption and heterogeneous (catalytic) chemical reactions. The fundamental problem in the column apparatuses modeling is result of the complicated hydrodynamic behavior of the flows in the columns and as a result the velocity distributions in the columns are unknown.

The column apparatuses is possible to be modeled, using a new approach on the base of the physical approximations of the mechanics of continua, where the mathematical point is equivalent to a small (elementary) physical volume, which is sufficiently small with respect to the apparatus volume, but at the same time sufficiently large with respect to the intermolecular volumes (distances) in the medium. As a result convection-diffusion type of models [1] is possible to be created.

For the modeling of two phase processes must be used two equations model [2-4], i.e., mass balances of the transferred substance $\left(i=1,2,...\right)$ in the gas, liquid and solid phases $\left(j=1,2,3\right)$:

$$u_j\frac{\partial c_{ij}}{\partial z_j}=D_{ij}\left(\frac{\partial^2 c_{ij}}{\partial z_j^2}+\frac{1}{r}\frac{\partial c_{ij}}{\partial r}+\frac{\partial^2 c_{ij}}{\partial r^2}\right)\pm\varepsilon_j^{-1}Q_j\left(c_{ij}\right);$$
$$r=0,\quad \frac{\partial c_{ij}}{\partial r}=0;\quad r=r_0,\quad \frac{\partial c_{ij}}{\partial r}=0;\quad z_j=0,\quad c_{ij}=c_{ij}^0,\quad u_j^0c_{ij}^0=u_jc_{ij}^0-D_{ij}\frac{\partial c_{ij}}{\partial z_j}. \tag{1}$$

In (1) $u_j=u_j\left(r\right)$ [m.s^{-1}] and $c_{ij}=c_{ij}\left(r,z_j\right)$ [kg-mol.m^{-3}] are the axial velocity components and transferred substance concentrations in the phases, D_{ij} [m^{2}s^{-1}] and

ε_j [$m^3.m^{-3}$] are the diffusivities and hold-up coefficients in the phases, u_j^0 and c_{ij}^0 are the inlet velocities and concentrations in the column, where $i=1,2,...,$ $j=1,2=1,3=2,3$, $1=\varepsilon_1+\varepsilon_2=\varepsilon_1+\varepsilon_3=\varepsilon_2+\varepsilon_3$. The concentration of the transferred substance in the phases, are presented as kg-mol of the transferred substance in the phase in 1 m^3 of the column volume (no in 1 m^3 of the phase volume). The hold-up coefficients (m^3 of the phase volume in 1 m^3 of the column volume) and the inlet velocities in the column are obtained from the ratios $\varepsilon_j=F_j/F_0$ and $u_j^0=F_j/\pi r_0^2$,, where r_0 is the column radius [m], $j=1,2,3$, $F_0=\sum_{j=1}^{3}F_j$, [$m^3.s^{-1}$] is the fluid flow rate in the column, F_j, $j=1,2,3$ are the phase flow rates [$m^3.s^{-1}$] in the column. The volume reactions Q_j, $j=1,2,3$ [kg-mol.m^{-3}.s^{-1}] are homogeneous chemical reactions and interphase mass transfer as a volume sources or sinks in the column volume and participate in the mass balance in the phase volume (no in the column volume).

The model (1) is possible to be used for co-current two-phase flows $(z_1=z_2=z)$ or for counter-current one $(z_1+z_2=l,$ where l is the column height [m]). In counter-current flows the mass transfer process models must be presented in two coordinates systems [1] because in one coordinate system one of the equations has not a solution by reason of the negative equation Laplacian value.

2. Absorption processes

The convection-diffusion type of models of the absorption processes [1-4] in the gas $(j=1)$ and liquid $(j=2)$ phases systems is possible to be obtained from (1) if $j=1,2$ $(1=\varepsilon_1+\varepsilon_2)$, $i=1,2,....$ The kinetic terms $Q_j=(-1)^j k_0(c_{11}-\chi c_{12})$, $j=1,2$ are the interphase mass transfer rates as a volume sources or sinks of the substances in the elementary (column) volume [kg-mol.$m^{-3}s^{-1}$], where k_0 [$s^{-1}.m^{-3}$(column volume).m^3(phase volume)] is interphase mass transfer coefficient, χ - the Henry's number, c_{11} (c_{12}) [kg-mol.m^{-3}] - the concentration of the transferred substance in the gas (liquid) phase, i.e., kg-mol of the transferred substance in the gas (liquid) phase in 1 m^3 of the phase volume.

The inlet concentration of the transferred substance in the gas (liquid) phase is c_{11}^0 (c_{12}^0). In the cases of absorption (desorption) $c_{12}^0=0$ $(c_{11}^0=0)$ practically. The input velocities u_j^0 $(j=1,2)$ [$m.s^{-1}$] of the gas and liquid phases are equal to the average velocities $\bar{u}_j$ $(j=1)$ of the phases in the column:

$$u_j^0=\frac{F_j}{\pi r_0^2}=\bar{u}_j=\frac{2}{r_0^2}\int_0^{r_0} r u_j(r)\,dr, \quad j=1,2, \tag{2}$$

where F_j, $j=1,2$ are the gas and liquid phase flows rates [$m^3.s^{-1}$] in the column volume.

3. Chemical absorption

The chemical absorption in a column apparatus will be presented in the case of SO_2 absorption by NaOH solutions in co-current column. Considering that $c_{11}\left(c_{12}\right)$ is the concentration of SO_2 in the gas (liquid) phase and c_{22} is the concentration of NaOH in the absorbent, the mass sources (sinks) in the medium elementary volume (the physical approximations of the mechanics of continua) are equal to the chemical reaction rate - $kc_{12}c_{22}$ and the interphase mass transfer rate across the gas-liquid boundary - $k_0\left(c_{11}-\chi c_{12}\right)$, where k is the chemical reaction rate constant and k_0 is the interphase mass transfer coefficient. As a result the convection-diffusion equations in a column have the forms:

$$\begin{aligned}
&\varepsilon_1 u_1 \frac{\partial c_{11}}{\partial z} = \varepsilon_1 D_{11}\left(\frac{\partial^2 c_{11}}{\partial z^2}+\frac{1}{r}\frac{\partial c_{11}}{\partial r}+\frac{\partial^2 c_{11}}{\partial r^2}\right)-k_0\left(c_{11}-\chi c_{12}\right),\\
&\varepsilon_2 u_2 \frac{\partial c_{12}}{\partial z} = \varepsilon_2 D_{12}\left(\frac{\partial^2 c_{12}}{\partial z^2}+\frac{1}{r}\frac{\partial c_{12}}{\partial r}+\frac{\partial^2 c_{12}}{\partial r^2}\right)+k_0\left(c_{11}-\chi c_{12}\right)-kc_{12}c_{22},\\
&\varepsilon_2 u_2 \frac{\partial c_{22}}{\partial z} = \varepsilon_2 D_{22}\left(\frac{\partial^2 c_{22}}{\partial z^2}+\frac{1}{r}\frac{\partial c_{22}}{\partial r}+\frac{\partial^2 c_{22}}{\partial r^2}\right)-kc_{12}c_{22},
\end{aligned} \tag{3}$$

where D_{11}, D_{12} and D_{22} are the diffusivities.

Let's consider a co-current gas–liquid bubble column with a radius r_0 and working zone height *l.* The boundary conditions of the model equations (3) have the form:

$$\begin{aligned}
&r=0,\quad \frac{\partial c_{11}}{\partial r}=\frac{\partial c_{12}}{\partial r}=\frac{\partial c_{22}}{\partial r}\equiv 0;\quad r=r_0,\quad \frac{\partial c_{11}}{\partial r}=\frac{\partial c_{12}}{\partial r}=\frac{\partial c_{22}}{\partial r}\equiv 0;\\
&z=0,\quad c_{11}\equiv c_{11}^0,\quad u_1^0 c_{11}^0 \equiv u_1\left(r\right)c_{11}^0 - D_{11}\left(\frac{\partial\, c_{11}}{\partial\, z}\right)_{z=0};\\
&z=0,\quad c_{12}\equiv c_{12}^0,\quad u_2^0 c_{12}^0 \equiv u_2\left(r\right)c_{12}^0 - D_{12}\left(\frac{\partial\, c_{12}}{\partial\, z}\right)_{z=0}.\\
&z=0,\quad c_{22}\equiv c_{22}^0,\quad \overline{u}_2 c_{22}^0 \equiv u_2\left(r\right)c_{22}^0 - D_{22}\left(\frac{\partial\, c_{22}}{\partial\, z}\right)_{z=0};
\end{aligned} \tag{4}$$

In the cases of gas absorption $c_2^0=0$ practically.

A qualitative analysis of the model is possible to be made, using dimensionless (generalized) variables:

$$R=\frac{r}{r_0},\quad Z=\frac{z}{l},\quad U_1=\frac{u_1}{u_1^0},\quad U_2=\frac{u_2}{u_2^0},\quad C_1=\frac{c_{11}}{c_{11}^0},\quad C_2=\frac{c_{12}\chi}{c_{11}^0},\quad C_3=\frac{c_{22}}{c_{22}^0}. \tag{5}$$

The model (3), (4) in generalized variables (5) has the form:

$$
\begin{aligned}
&U_1(R)\frac{\partial C_1}{\partial Z}=\mathrm{Fo}_1\left(\varepsilon\frac{\partial^2 C_1}{\partial Z^2}+\frac{1}{R}\frac{\partial C_1}{\partial R}+\frac{\partial^2 C_1}{\partial R^2}\right)-K_1(C_1-C_2);\\
&U_2(R)\frac{\partial C_2}{\partial Z}=\mathrm{Fo}_2\left(\varepsilon\frac{\partial^2 C_2}{\partial Z^2}+\frac{1}{R}\frac{\partial C_2}{\partial R}+\frac{\partial^2 C_2}{\partial R^2}\right)+K_2(C_1-C_2)-\mathrm{Da}\frac{c_{22}^0}{c_{11}^0}C_2C_3;\\
&U_2(R)\frac{\partial C_3}{\partial Z}=\mathrm{Fo}_3\left(\varepsilon\frac{\partial^2 C_3}{\partial Z^2}+\frac{1}{R}\frac{\partial C_3}{\partial R}+\frac{\partial^2 C_3}{\partial R^2}\right)-\mathrm{Da}\,C_2C_3;\\
&R=0,\quad \frac{\partial C_s}{\partial R}\equiv 0;\quad R=1,\quad \frac{\partial C_s}{\partial R}\equiv 0;\quad s=1,2,3;\\
&Z=0,\quad C_1\equiv 1,\quad 1\equiv U_1(R)-\mathrm{Pe}_1^{-1}\left(\frac{\partial C_1}{\partial Z}\right)_{Z=0};\\
&Z=0,\quad C_3\equiv 1,\quad 1\equiv U_2(R)-\mathrm{Pe}_3^{-1}\left(\frac{\partial C_3}{\partial Z}\right)_{Z=0};\quad Z=0,\quad C_2\equiv 0,\quad \left(\frac{\partial C_2}{\partial Z}\right)_{Z=0}\equiv 0,
\end{aligned}
\tag{6}
$$

where

$$
\begin{aligned}
&K_1=\frac{k_0 l}{\varepsilon_1 u_1^0},\quad K_2=\frac{k_0 l\chi}{\varepsilon_2 u_2^0},\quad \mathrm{Fo}_1=\frac{D_{11}l}{u_1^0 r_0^2},\quad \mathrm{Fo}_2=\frac{D_{12}l}{u_2^0 r_0^2},\quad \mathrm{Fo}_3=\frac{D_{22}l}{u_2^0 r_0^2},\\
&\mathrm{Da}=\frac{klc_{11}^0}{\varepsilon_2 u_2^0\chi},\quad \mathrm{Pe}_1=\frac{u_1^0 l}{D_{11}},\quad \mathrm{Pe}_3=\frac{u_2^0 l}{D_{22}}.
\end{aligned}
\tag{7}
$$

The model (6) is base for modeling of the physical absorption, chemical adsorption and catalytic processes.

From (6) follows, that the absence of a chemical reaction in liquid phase - $k_0=0$ (or $c_3^0=0$) leads to $\mathrm{Da}=0,\ C_3\equiv 1,$ (or $C_3\equiv 0$) and as a result the model has the physical absorption form. The same result is possible to be obtained in the cases $0=\mathrm{Da}\frac{c_{22}^0}{c_{11}^0}\le 10^{-2},$ i.e. the chemical reaction effect is negligible (it is not possible to be measured experimentally).

In the cases, when the interphase mass transfer is a result of the chemical reaction in the liquid phase $\left(\mathrm{Da}\frac{c_{22}^0}{c_{11}^0}\ge 1\right),$ the second equation in (6) should be divided by $\mathrm{Da}\frac{c_{22}^0}{c_{11}^0}\ge 1,$ i.e.,

$$
U_1(R)\frac{\partial C_1}{\partial Z}=\mathrm{Fo}_1\left(\varepsilon\frac{\partial^2 C_1}{\partial Z^2}+\frac{1}{R}\frac{\partial C_1}{\partial R}+\frac{\partial^2 C_1}{\partial R^2}\right)-K_1(C_1-C_2);
$$

$$
\mathrm{Da}^{-1}\frac{c_{11}^0}{c_{22}^0}U_2(R)\frac{\partial C_2}{\partial Z}=\frac{\mathrm{Fo}_2\,c_{11}^0}{\mathrm{Da}\,c_{22}^0}\left(\varepsilon\frac{\partial^2 C_2}{\partial Z^2}+\frac{1}{R}\frac{\partial C_2}{\partial R}+\frac{\partial^2 C_2}{\partial R^2}\right)+K_2\frac{c_{11}^0}{\mathrm{Da}\,c_{22}^0}(C_1-C_2)-C_2C_3;
$$

$$
\begin{aligned}
&\mathrm{Da}^{-1}U_2(R)\frac{\partial C_3}{\partial Z}=\mathrm{Da}^{-1}\,\mathrm{Fo}_3\left(\varepsilon\frac{\partial^2 C_3}{\partial Z^2}+\frac{1}{R}\frac{\partial C_3}{\partial R}+\frac{\partial^2 C_3}{\partial R^2}\right)-C_2C_3;\\
&R=0,\quad \frac{\partial C_s}{\partial R}\equiv 0;\quad R=1,\quad \frac{\partial C_s}{\partial R}\equiv 0;\quad s=1,2,3;\\
&Z=0,\quad C_1\equiv 1,\quad 1\equiv U_1(R)-\mathrm{Pe}_1^{-1}\left(\frac{\partial C_1}{\partial Z}\right)_{Z=0};\\
&Z=0,\quad C_3\equiv 1,\quad 1\equiv U_2(R)-\mathrm{Pe}_3^{-1}\left(\frac{\partial C_3}{\partial Z}\right)_{Z=0};\quad Z=0,\quad C_2\equiv 0,\quad \left(\frac{\partial C_2}{\partial Z}\right)_{Z=0}\equiv 0.
\end{aligned}
\tag{8}
$$

For big values of the average velocities $0=\mathrm{Fo}_s\le 10^{-2},\ s=1,2,3$, from (6) follows the convective type of model (the diffusion parts of the model are equal to zero).

In the chemical absorption case, the model (8) permits to be obtained the interphase mass transfer resistance distribution between the gas and liquid phases:

$$
\rho_1=K_1,\quad \rho_2=K_2\frac{c_{11}^0}{\mathrm{Da}\,c_{22}^0}=\rho_0\rho_1,\quad \rho_0=\frac{\varepsilon_1u_1^0\chi c_{11}^0}{\mathrm{Da}\,\varepsilon_2u_2^0c_{22}^0},\quad \rho_1+\rho_2=1,\quad \rho_1=\frac{1}{1+\rho_0},\quad \rho_2=\frac{\rho_0}{1+\rho_0},
\tag{9}
$$

where the parameters ρ_1 and ρ_2 can be considered as mass transfer resistances in the gas and liquid phases. Very often the big values of Da leads to the small values of ρ_0 and as a result $\rho_1 \square \rho_2$, i.e. the gas is the limiting phase and the optimal organization of the absorption process is the absorption in gas-liquid drops systems.

4. Physical absorption

The convection-diffusion type of model for the steady-state physical absorption in the column apparatuses is possible to be obtained from (6) if $\mathrm{Da}=0,\ C_3\equiv 1,$ (or $C_3\equiv 0$):

$$
\begin{aligned}
&U_s(R)\frac{\partial C_s}{\partial Z_s}=\mathrm{Fo}_{1s}\left(\varepsilon\frac{\partial^2 C_s}{\partial Z_s^2}+\frac{1}{R}\frac{\partial C_s}{\partial R}+\frac{\partial^2 C_s}{\partial R^2}\right)+(-1)^s K_s(C_1-C_2);\\
&R=0,\quad \frac{\partial C_s}{\partial R}\equiv 0;\quad R=1,\quad \frac{\partial C_s}{\partial R}\equiv 0;\quad s=1,2;\\
&Z_1=0,\quad C_1\equiv 1,\quad 1\equiv U_1(R)-\mathrm{Pe}_{11}^{-1}\left(\frac{\partial C_1}{\partial Z_1}\right)_{Z_1=0};\quad Z_2=0,\quad C_2\equiv 0,\quad \left(\frac{\partial C_2}{\partial Z_2}\right)_{Z_2=0}\equiv 0.
\end{aligned}
\tag{10}
$$

From (10) is possible to be obtained the expressions for the interphase mass transfer resistances in the gas (ρ_1) and liquid (ρ_2) phases:

$$
\rho_1=K_1,\quad \rho_2=K_2=\rho_0\rho_1,\quad \rho_0=\frac{\varepsilon_1u_1^0\chi}{\varepsilon_2u_2^0},\quad \rho_1+\rho_2=1,\quad \rho_1=\frac{1}{1+\rho_0},\quad \rho_2=\frac{\rho_0}{1+\rho_0}.
\tag{11}
$$

From (10), (11) it follow directly models of the physical absorption in the cases of highly $(\chi\to 0,\ \rho_0\to 0,\ \rho_2\to 0,\ C_2\equiv 0)$ and slightly $(\chi\to\infty,\ \rho_0\to\infty,\ \rho_1\to 0,\ C_1\equiv 1))$ soluble gases.

5. Average concentration models

The using of the diffusion type of models for modeling of the absorption processes is not possible because the velocity functions in the convection-diffusion equations are unknown. The problem can be avoided if the average values of the velocity and concentration $(\bar{U}_s, \bar{C}_s(Z), s=1,2,3)$ over the cross-sectional area of the column are used. The velocities and concentrations in (10) is possible to be presented as:

$$\begin{aligned} &U_s(R)=\bar{U}_s\tilde{U}_s(R), \quad C_s(R,Z)=\bar{C}_s(Z)\tilde{C}_s(R,Z), \\ &\bar{U}_s=2\int_0^1 RU_s(R)\,dR, \quad \bar{C}_s(Z)=2\int_0^1 RC_s(R,Z)\,dR, \end{aligned} \tag{12}$$

where $\tilde{U}_s(R)$, $\tilde{C}_s(R,Z)$, $s=1,2,$ represent the velocities and concentrations radial non-uniformities over the cross-sectional area of the column.

The average concentration model may be obtained if put average functions (12) into the model equation (10) and then multiply by R and integrate with respect to R over the interval [0,1]. The result is:

$$A_s(Z)\frac{d\bar{C}_s}{dZ_s}+\frac{dA_s}{dZ_s}\bar{C}_s=\mathrm{Pe}_{1s}^{-1}\frac{d^2\bar{C}_s}{dZ_s^2}+(-1)^s K_s(\bar{C}_1-\bar{C}_2); \quad Z_s=0, \quad \bar{C}_s\equiv 1, \quad \left(\frac{\partial C_s}{\partial Z_s}\right)_{Z_s=0}=0; \tag{13}$$

where the velocities and concentrations radial nonuniformities are concentrated in the functions $A_s(Z_s)$ that can be represented as linear approximations. As a result $A_s=1+a_sZ_s$ and $a_s, s=1,2$ are model parameters, that can be obtained as a solution of the inverse problem [1], using experimental data for $\bar{C}_s$, $s=1,2,$ obtained in short column ($Z_1=Z_2=0.1, 0.2$) with real diameter [4].

Conclusions

The new approach for absorption column modeling proposes a convection-diffusion type of model for qualitative analysis of the absorption processes (process mechanism identification, interphase mass transfer resistance distribution). The new average concentration model permits a quantitative analysis of the absorption processes (modeling of the processes, modeling of the scale-up effect, solution of the scale-up problems).

References

[1] Boyadjiev Chr (2010) Theoretical Chemical Engineering. Modeling and simulation, Springer, Berlin.

[2] Boyadjiev Chr., Diffusion models and scale-up, Int. J. Heat Mass Transfer, 49, (2006), pp.796-799.

[3] M. Doichinova, Chr. Boyadjiev, On the column apparatuses modeling, Int. J. Heat Mass Transfer, 55, 2012, 6705-6715.

[4] Chr. Boyadjiev, A new approach for the column apparatuses modeling in chemical engineering, J. Appl. Math.:Advances and Aplications, 10, № 2, 131-150, 2013.

Modelling the species mass transfer in distillation columns and evaluating the performance of the structured packing

Maroun NEMER[1], Walid SAID[1], Fabrice DELCORSO[2], David BEDNARSKI[2], Guillaume CARDON[2]

[1]Center of energy efficiency of system, Mines Paristech, Paris/France;
[2]Center Claude Delorme, Air Liquide, Jouy En Josas/France

Abstract

A 3D-model is developed and presented to evaluate the performance of the structured packing in distillation columns. Based on this model, a simulation software is created. In the first step, the cylindrical packed bed is divided into hexahedral zone/stage cells (dimensions in cm). The whole bed is first split up into stages, and then each stage is divided into many cells. A liquid flow model defines the liquid pattern in the cells, starting from the liquid distributor profile and applying a horizontal diffusion profile in each stage, defined by a spreading coefficient. The mass transfer coefficients are calculated locally based on the liquid and vapor flow, and the composition of the two phases in each cell. A non linear mass and energy system is then produced over the packed bed, by writing the equations of mass and energy conservation in each zone/stage cell. The equations are arranged in a sparse matrix system. This non linear mass and energy transfer system is then resolved by computational simulations through iterations, which are applied based on the GMRES method. The final converged solution can define local liquid and vapor mass flow, and the local liquid and vapor compositions in each cell. The local liquid and vapor compositions are averaged over the stages, and the evolution of these compositions is established over the packed bed height. The separation efficiency of the packed bed is then evaluated by calculating the HETP of the column.

Keywords

Separation, distillation columns, structured packing, mass transfer model, zone/stage cells

1. Introduction

Distillation columns with structured packing bed are widely used in chemical engineering for separating a mixture into two or more products. Modeling the species mass transfer in the packed bed aims to predict the behavior of the distillation columns and estimate the purity of the recuperated species.

In recent years, many researches have been carried out. One-dimensional models predict the performance of the packed columns by elaborating correlations of the mass transfer parameters from empirical and mechanistic points of view (K. Onda, 1968), (Mei Geng SHI, 1985), (R. Billet, 1993), (R. Billet, 1999), (I. Iliuta, 2004), (J.A. Rocha, 1996), (Z. Olujic, 1999). Components are transfered between the phases at the interface. The transfer rate in each phase is proportional to the mass transfer coefficient and the effective interfacial surface area. These models are based on experimental observations in laboratory scale columns. The accuracy of the calculation results of the packed bed performance depends directly on the accuracy of the correlations.

Many researches report CFD modeling approach which solves conservation equations for mass, momentum, energy and species in the packed bed structure. Many CFD simulations were performed on finite cells using the Navier-Stokes equations with k-ε model (M. Haghshenas Fard, 2007), RNG k-ε model (C.F. Petre, 2003), (CHEN Jiangbo, 2009) or k-ω model (M.R. Nikou, 2008), to predict the two-phase flow and separation efficiency of a specific packing.
Other CFD models analyze a larger comutational domain. Simulations were performed by solving volume averaged Navier-Stokes equations coupled with species mass and energy equations, where the packed bed is considered as a porous medium (B. Mahr, 2007), (J.M. Van Baten, 2001), (J.M van Baten, 2002). The hydrodynamics and the mass transfer of the two-phase were solved by using CFX code in randomly packed columns (F.H. Yin, 2000).
Meso-scale models can achieve a detailed description of the performance of the packed bed on a computational domain larger than what can be simulated with CFD calculations due to computer system limitations. They analyze the packing hydraulics rather than the structured packing complex geometry. These models consider the liquid distribution as a series of rivulets traveling over an inclined flat surface (Adisorn Aroonwilas, 2000), (A. Shilkin, 2005). The interfacial area is evaluated through calculations of the width and the thickness of a rivulet. The liquid and gas phase mass transfer coefficients are estimated applying the penetration theory.
Another interesting mechanistic model, the zone/stage model (F.J. Zuiderweg, 1993), calculates the effect of the liquid distribution on the performance of the packed bed. The authors adopt the liquid diffusion approach (Lerman, 1939) in a network of zone/stage cells. The liquid flow is modeled as a liquid distribution between the cells and the effect of an initial liquid maldistribution on the separation efficiency is evaluated. In another work, the heat and mass transfer equations in multicomponent processes were extensively studied (M. F. Powers, 1988), (R. Taylor, 1994). A nonequilibrium model consisting of interphase mass and energy transfer equations and a numerical method to resolve the equations system was proposed.
In the following work, a new approach is proposed by solving the mass transfer equations in a network of cartesian zone/stage cells. The results of the simulations are then presented and discussed.

2. Model description

The main objective in the present work is to calculate locally the liquid and vapor flows and the compositions of the two-phase flows in different locations inside the packing. Therefore, a new mechanistic model is proposed and a space discretization of the packed bed into a network of cells is applied. The discrete cells are characterized by the same hydrodynamic analogy of the structured packing. The conservation equations of mass and energy are then resolved in the network of zone/stage cells to calculate locally the values of the two-phase flows and compositions.

2.1 Zone/stage cells

A geometric tool is created to construct the network of the zone/stage cells. Based on the packed bed diameter and the packing elements height, the packed bed volume is decomposed first into many stages. Each stage is then discretized into many zones respecting the packing sheets direction, which dimensions (length and width) are defined by the user. The cells in successive packing elements are rotated accordingly with the rotation angle of the packing elements. As a consequence, the geometric tool builds a network of hexahedral cells. The cells at the column wall are

cut accordingly to respect the column circular cross section. Figure 1 shows an example of a packed bed, consisting of two packing elements rotated at a 90° angle, which is discretized into zone/stage cells.

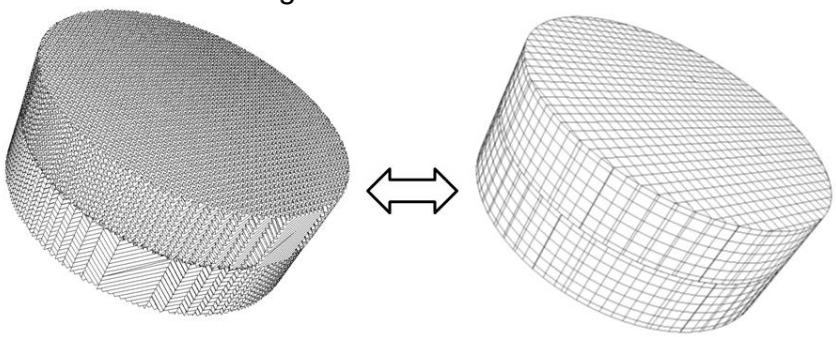

Figure 1: The network of zone/stage cells

2.2 Two-phase flow

The liquid flow is modeled in the network of zone/stage cells, based on the work of F.J. Zuiderweg, 1993. This model shall define the distribution of the liquid between the cells. Liquid spreading between the structured packing sheets is considered by defining a liquid spreading coefficient D_x. This coefficient is specific for the packing type and the liquid properties and it is determined by experiments. Given the zone/stage cells dimensions (height *z* and width *x*) and the liquid spreading coefficient of the structured packing, the fraction K_1 flowing in the cell below is given by the equation 1

$$K_1 = 1 - 2D_x \cdot \frac{z}{x^2} \tag{1}$$

Liquid spreading perpendicular to the packing sheets is considered null. Therefore, the remaining fraction (1- K_1) is divided equally into the two adjacent cells located parallel to the packing sheets. At the column wall, the wall wiper is considered very efficient. For the wall boundary conditions, it is assumed that the liquid flow is totally reflected inside the packing with no accumulation on the wall. The liquid model flow has been verified experimentally by examining the liquid profile at the outlet of one packing element for a single point source injection. (Figure 2). Details of the liquid flow model will be described in a future work.

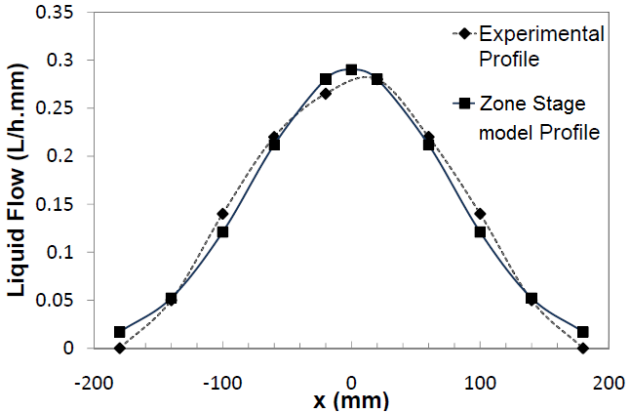

Figure 2: Comparison between the experimental profile and the zone/stage liquid model flow

As the vapor flow tends to be uniform in the packed bed through two packing elements, its effect on the separation performance is minor compared to the liquid

flow. A simple vapor flow model is considered in the network of the zone/stage cells. The vapor distribution is considered uniform (Olujic, 1997), flowing across the packed bed without horizontal dispersion. Therefore, in the present work no vapor flow or interaction is considered between the cells of the same stage. Further considerations are required to develop more realistic vapor model in a future work.

2.3 Mass and energy transfer system

Based on the two-phase flow, figure 3 represents the liquid (L_{in}, L_{out}) and vapor (V_{in}, V_{out}) streams flowing inside and outside a zone/stage cell. Considering a binary mixture where i and j depict respectively the light and heavy components, the energy and mass balance equations are developed in each cell.

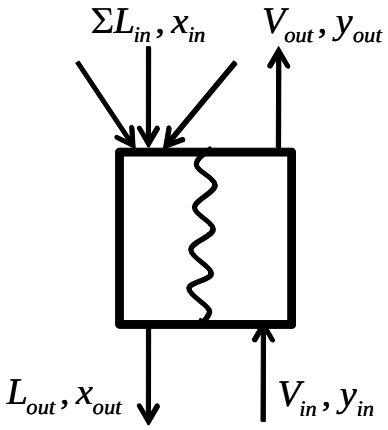

Figure 3: Two-phase flows and compositions in a zone/stage cell

The total mass conservation equation of the liquid phase

$$\sum L_{in} - L_{out} - N_t = 0 \tag{2}$$

where N_t is the total molar flow transferred from the liquid phase to the vapor

Similarly, the mass conservation equation of the vapor phase

$$V_{in} - V_{out} + N_t = 0 \tag{3}$$

The mass conservation equation of the light species in the liquid phase is

$$\sum \left(L_{in} x_{in}\right) - L_{out} x_{out} - N_i = 0 \tag{4}$$

N_{N2} is the total molar flow of the light component transferred to the vapor phase

The mass conservation equation of the light species in the vapor phase is

$$V_{in} y_{in} - V_{out} y_{out} + N_i = 0 \tag{5}$$

In many distillation applications as the air distillation, a relatively small temperature gradient exists between the top and the bottom of one packed bed compared to the column dimensions. Thus, the process is considered adiabatic in one single cell, and the convective heat flux between the two-phase is neglected. Based on this assumption, the energy transfer at the interface is entirely controlled by the evaporation of the light component and the condensation of the heavy component. The energy conservation at the interface is then written

$$N_i . \Delta H_i - N_j . \Delta H_j = 0 \tag{6}$$

ΔH is the latent energy of vaporization.

Hence, the total molar flow evaporated is the sum

$$N_t = N_i . + N_j . \tag{7}$$

Equations (5) and (6) lead to the following relation between N_t and N_i

$$N_t = N_i . \left(1 + \frac{\Delta H_i}{\Delta H_j} \right). \quad (8)$$

The molar flow of one species transferred to the liquid is the combination of the condensation due to the energy transfer and the diffusion due to the mass transfer

$$N_i - N_i \left(1 - \frac{\Delta H_i}{\Delta H_j}\right) x_{out} - k_L a_e \frac{1}{V_{L,i}} (x_{out} - x^{\text{int}}) = 0 \quad (9)$$

$V_{L,i}$ is the molar volume of the i species. Similarly, the molar flow of one species transferred to the vapor is the combination of the evaporation and the mass diffusion

$$N_i - N_i \left(1 - \frac{\Delta H_i}{\Delta H_j}\right) y_{out} - k_G a_e V_{cell} \frac{M_i}{V_L} (y_{out} - y^{\text{int}}) = 0 \quad (10)$$

At the interface, the mole fractions in liquid and vapor are supposed to be at equilibrium (Henry's law) :

$$H_p x^{\text{int}} - y^{\text{int}} = 0 \quad (11)$$

The liquid and vapor mass transfer coefficients are calculated using the correlations established by Z. Olujic, 1999. The overall transfer surface area is estimated using the correlation of the wet surface area (Mei Geng SHI, 1985).

2.4 Numerical simulations

The equations (2), (3), (4), (5), (8), (9), (10) and (11) form a nonlinear equation system with 8 unknown variables in each zone/stage cell. If c is the number of cells, the number of the total equations is 8c. The 8 variables in all the zone/stage cells (L_{out}, V_{out}, N_t, N_i, x_{out}, y_{out}, x^{int} and y^{int}) form a vector of variables X.

Written accordingly, the equation system is represented as: A.X=B.

Nonlinearity in the system is due to the relation between the coefficient values of the matrix A and the variables in the vector X. The system of equations is implemented numerically in the zone/stage cells constructed using a software written in C++ code. This non-linear equation system is solved numerically using the Newton's method, characterized by the fast convergence (30 iterations required for industrial columns). Based on this method, a system of equations with the Jacobian matrix J of the matrix A is numerically solved in the iterations

$$J.\Delta X = -AX + B \quad (12)$$

The new unknown vector ΔX in equation (11) is the absolute error between the variables of two successive iterations and the variable values X vector in the second member are the values of the solution of the previous iteration.

The GMRES method is used to control the iterations, that are repeatedly solved till the convergence is attained when the condition max(Dx)< ε is respected. ε is a value defined by the user for the process. The initialization of the variable vector is applied by assuming that the liquid and vapor flow and composition in all the cells are equal to the values at the column entries.

3. Results and discussion

The proposed model has been verified with experimental data. The experiments were carried out in a pilot column of 378 mm inner diameter, consisting of 13 packing elements of 303 mm height each and operating with partial reflux distillation. The structured packing is manufactured by Air Liquide group. The binary mixture used

consists of nitrogen and oxygen. The operating conditions of the experimental data are given in table 1.

Table1 - Operating conditions of the experimental data

Pressure	550 kPa
Liquid molar flow	67 Kmol/h
Initial N_2 molar fraction in liquid	0.999674
Vapor molar flow	110 Kmol/h
Initial N_2 molar fraction in vapor	0.784

3.1 Simulation results and comparison

The compositions of the liquid and vapor flows have been measured only at the top and the bottom of the column. No experimental data were measured inside the column. Numerical simulations were executed with the software implemented in C++ code. The local liquid and vapor compositions simulated in the cells are averaged over the stages. Figure 4 shows the evolution of the averaged molar fraction of the N_2 in the two phases, calculated by simulations, vs. the height inside the packing. These simulated results and the compositions values measured were compared by drawing the corresponding operating lines in the McCabe-Thiele diagram. The comparison is represented in figure 5.

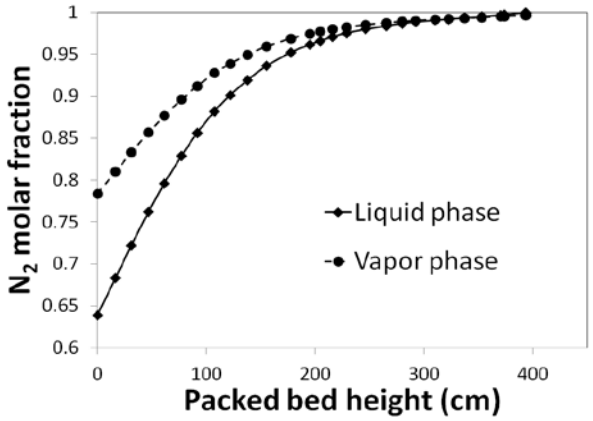

Figure 4: Molar fraction profile of N_2 in liquid and vapor phase

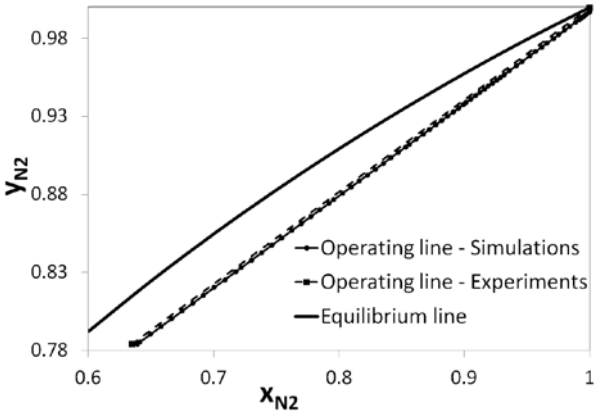

Figure 5: McCabe-Thiele diagram with the experimental and the simulated operating lines

The molar fraction value of N_2 in the liquid at the bottom of the column calculated by the model is 0.639 and the value measured on the pilot column is 0.635.

As the experimental measurements are only collected on top and bottom of the column, the accuracy of the model is evaluated by its precision in predicting the HETP. The HETP values are calculated from the two operating lines simulated and the experimental operating lines from figure 5. The values are respectively: HETP = 28 cm with the experimental operating line and HETP = 33 cm with the simulated line. The model predicts the HETP value with a relative error of around 15 %.

4. Conclusions

A model has been developed to evaluate the separation performance of the distillation columns. The packed bed is discretized in a network of zone/stage cells. Liquid and vapor flow models can describe the two-phase distribution locally inside the cells. Resolving the mass and energy balance equations over the zone/stage cells can evaluate the composition of phases locally over the packed bed.

The predictive accuracy of the HETP calculation of the proposed model has been tested by comparing the simulation results with experimental data for a packed column with 13 packing elements. The model will be used in a future work to evaluate the influences of many operating and geometric parameters, such as the initial liquid distribution pattern, liquid load, column diameter and number of packing elements on the separation efficiency of the column. Further developments of the proposed approach are required, especially for the vapor flow model. A more realistic vapor model, coupled with the liquid and mass transfer model, leads to an enhanced model able to predict the influence of an initial vapor maldistribution.

References

A. Shilkin, E.Y. Kenig. «A new approach to fluid separation modelling in the columns equipped with structured packings.» Chemical Engineering Journal, 2005: 87-100.

Adisorn Aroonwilas, Paitoon Tontiwachwuthikul. «Mechanistic model for prediciton of structured packing mass transfer performance in CO2 absorption with chemical reactions.» Chemicla Engineering Science, 2000: 3651-3663.

B. Mahr, D. Mewes. «CFD Modelling and Calculation of Dynamic Two-Phase Flow in Columns Equipped with Structured Packing.» Chemical Engineering Research and Design, 2007: 1112-1122.

C.F. Petre, F. Larachi, I. Iliuta, B.P.A. Grandjean. «Pressure drop through structured packings: Breakdown into the contributing mechanisms by CFD modeling.» Chemical Engineering Science, 2003: 163-177.

CHEN Jiangbo, LIU Chunjiang, YUAN Xigang, YU Guocong. «CFD Simulation of Flow and Mass Transfer in Structured Packing.» Chinese Journal of Chemical Engineering, 2009: 381-388.

F.H. Yin, C.G. Sun, A. Afacan, K. Nandakumar, K.T. Chang. «CFD Modeling of mass transfer processes in randomly packed distillation columns.» Ind. Eng. Chem. Res., 2000: 1369-1380.

F.J. Zuiderweg, J.G. Kunesh, D.W. King. «A model for the calculation of the effect of maldistribution on the efficiency of a packed column.» Chemical Engineering Research and Design, 1993: 38-44.

I. Iliuta, C.F. Petre, F. Larachi. «Hydrodynamic continuum model for two-phase flow structured-packing-containing columns.» Chemical Engineering Science, 2004: 879-888.

J.A. Rocha, J.L. Bravo, J.R. Fair. «Distillation columns containing structured packings : A comprehensive model for their performance. 2. Mass transfer model.» Ind. Eng. Chem. Res., 1996: 1660-1667.

J.M van Baten, R. Krishna. «Gas and liquid phase mass transfer within KATAPAK-S® structures studied using CFD simulations.» Chemical Engineering Science, 2002: 1531-1536.

J.M. Van Baten, R. Krishna. «Liquid-phase mass transfer within KATAPAK-S® structures studied using computational fluid dynamics simulations.» Catalysis Today, 2001: 371-377.

K. Onda, H. Takeuchi, Y. Okumoto. «Mass transfer coefficients between gas and liquid phases in packed column.» Journal of Chemicla Engineering of Japan, 1968: 56-62.

Lerman, R. S. Tour et F. «Unconfined distribution of liquid in tower packing.» Trans. AICHE, 1939: 709-718.

M. F. Powers, D. J. Vickery, A. Arehole, R. Taylor. «A non equilibrium stage model of multicomponent separation processes-V. Computational methods for solving the model equaitons.» Computers Chemical Engineering, 1988: 1229-1241.

M. Haghshenas Fard, M. Zivdar, R. Rahimi, M. Naser Esfahany, A. Afacan, K. Nandakumar, K.T. Chuang. «CFD simulation of mass transfer efficiency and pressure drop in a structured packed distillation column.» Chemical Engineering and Technology, 2007: 854-861.

M.R. Nikou, M.R. Ehsani. «Turbulence models application on CFD simulation of hydrodynamics, heat and mass transfer in structured packing.» ICHMT, 2008: 1211-1219.

Mei Geng SHI, Alfons MERSMANN. «Effective interfacial area in packed columns.» German Chemical Engineering, 1985: 87-96.

Olujic, Z. «Development of a complete simulation model for predicting the hydraulic and separation performance of distillation columns equipped with structured packings.» Chem. Biochem. Eng., 1997: 31-46.

R. Billet, M. Shultes. «Predicting mass transfer in packed columns.» Chemical Engineering & Technology, 1993: 1-9.

R. Billet, M. Shultes. «Prediction of mass transfer columns with dumped and arranged packings. Updated summary of the calculation method of Billet and Schultes.» Trans IChemE Part A, 1999: 498-504.

R. Taylor, H. A. Kooijman, J. S. Hung. «A second generation nonequilibrium model for computer simulation of multicomponent separation processes.» Computers Chemical Engineering, 1994: 205-217.
Stikkelman. PhD Thesis. Delft University, The Netherlands, 1989.
Z. Olujic, A.B. Kamerbeek, J.A. de Graauw. «A corrugation geometry based model for efficiency of structured distillation packing.» Chemical Engineering and Processing, 1999: 683-695.

Simulation of Reactive Absorption of Carbon Dioxide in Activated Aqueous Potash Solutions Based on New Physico–Chemical Data

M. Imle, N. McCann, J. Kumelan, D. Speyer, G. Maurer, H. Hasse

Laboratory of Engineering Thermodynamics (LTD), University of Kaiserslautern, Kaiserslautern, Germany

Abstract

Aqueous potash solutions are used to remove carbon dioxide from gaseous streams by chemical absorption. It is common to “activate” solvents by adding borates and vanadates. The complex chemistry of the borates and vanadates in aqueous potash solutions was elucidated. This was achieved by a combination of ^{51}V NMR-spectroscopic and titration studies. Furthermore, the solubility of carbon dioxide in activated aqueous potash solutions was determined experimentally at two temperatures typical for carbon dioxide absorption (343 K) and solvent regeneration (383 K) in the Hot Potassium Carbonate Process. Two experimental set-ups were used: A headspace gas chromatographic technique was applied to determine the solubility of CO_2 at partial pressures of carbon dioxide between (1 and 140) kPa and the synthetic gas solubility technique was applied for total pressures between (0.4 and 10) MPa. The new experimental results were used for fitting parameters of a physico-chemical thermodynamic model based on the extended Pitzer equation for describing the non-idealities of the electrolyte solution. The new model provides a sound basis for the simulation of the absorption/desorption process of carbon dioxide with activated aqueous potash solutions and allows detailed studies of all major process parameters.

Keywords

Hot Potassium Carbonate Process, potash, gas solubility, carbon dioxide, ^{51}V-NMR spectroscopy

1. Introduction

In many chemical processes carbon dioxide has to be removed from gaseous streams (e.g., in ammonia synthesis or in ethylene oxide production) [1]. A well known process for this task is the Hot Potassium Carbonate Process (developed in the 1950s by Benson and Field, [1, 2, 3]) in which a hot aqueous solution of potassium carbonate is used to absorb carbon dioxide. In those solutions, carbon dioxide is dissolved chemically, i.e., it is converted to hydrogencarbonate. The absorption media is regenerated at increased temperatures. Thus a closed process for carbon dioxide removal is achieved. However, there are also some disadvantages. For example, during absorption the temperature has to be sufficiently high to avoid the precipitation of solid potassium hydrogencarbonate, the aqueous potash solutions are corrosive and the conversion of carbon dioxide to hydrogencarbonate is a rather slow chemical reaction. To overcome these issues activators are added to the aqueous solution. In the case of ethylene oxide plants

inorganic activators have to be used [1]. Eickmeyer [4, 5] suggested to use a mixture of borate and vanadate for activation. Although it is commonly acknowledged that those activators improve the performance of a Hot Potassium Carbonate Process, a detailed investigation of the reasons (influence on the phase equilibrium (?) and/or the chemical reaction kinetics (?)) for the improvements is not yet available and only limited experimental data is available (cf. Endo et al. [6], Schäfer et al. [7, 8]). Neither vapor-liquid equilibrium data nor kinetic data for the solubility of carbon dioxide in those activated solvents are available in the open literature.
The aim of the present research was to investigate the reaction equilibria and the influence of two simultaneously dissolved activators ($B(OH)_3$ and KVO_3) on the equilibrium solubility of carbon dioxide in aqueous potash solutions and to develop a physico-chemical model for describing their influence on the vapor-liquid equilibrium. Based on this model an implementation in Aspen RateSep was to be performed to enable the simulation of the absorption / desorption process.

2. Results and discussion

2.1 Experimental results

2.1.1 Potentiometric measurements and ^{51}V-NMR spectroscopic investigations

Potentiometric measurements were performed on a Titrino Plus fully automatic titration set-up from Metrohm under nitrogen atmosphere ^{51}V-NMR measurements were performed at dilute conditions (initial concentrations 0.02 – 0.05 M vanadate) (cf. [9]) in a pH range from neutral to high pH ("NMR titration"). KVO_3 is used as vanadate source. It dissociates in aqueous solution and forms monomeric and oligomeric vanadate species, each of which exhibits a NMR signal at a slightly different chemical shift. Many of these oligomers also undergo protonation reactions, but the differently protonated species are not differentiable by ^{51}V-NMR spectroscopy. For the most part, peaks were assigned to individual oligomers based on assignments previously reported in the literature [10], [11], [12]. Total vanadium concentrations for each oligomer, and hence individual oligomer concentrations were determined from integration of the corresponding peaks. Spectra with overlapping peaks were deconvoluted using a peak fitting procedure developed in-house.
Equilibrium constants were fitted to the experimental data (potentiometric measurements, chemical shift and NMR-measured concentrations) globally.
The equilibrium constants used are expressed in terms of molarities. As only dilute conditions are used they can be extrapolated to eliminate the non-idealities. Figure 1 shows the "NMR titration" of a 0.05 M KVO_3 solution with 0.40 M NaOH at 15 °C (initial concentrations). The concentrations of the vanadates (as determined from peak integrations) are given (symbols), along with the corresponding calculation results (lines).

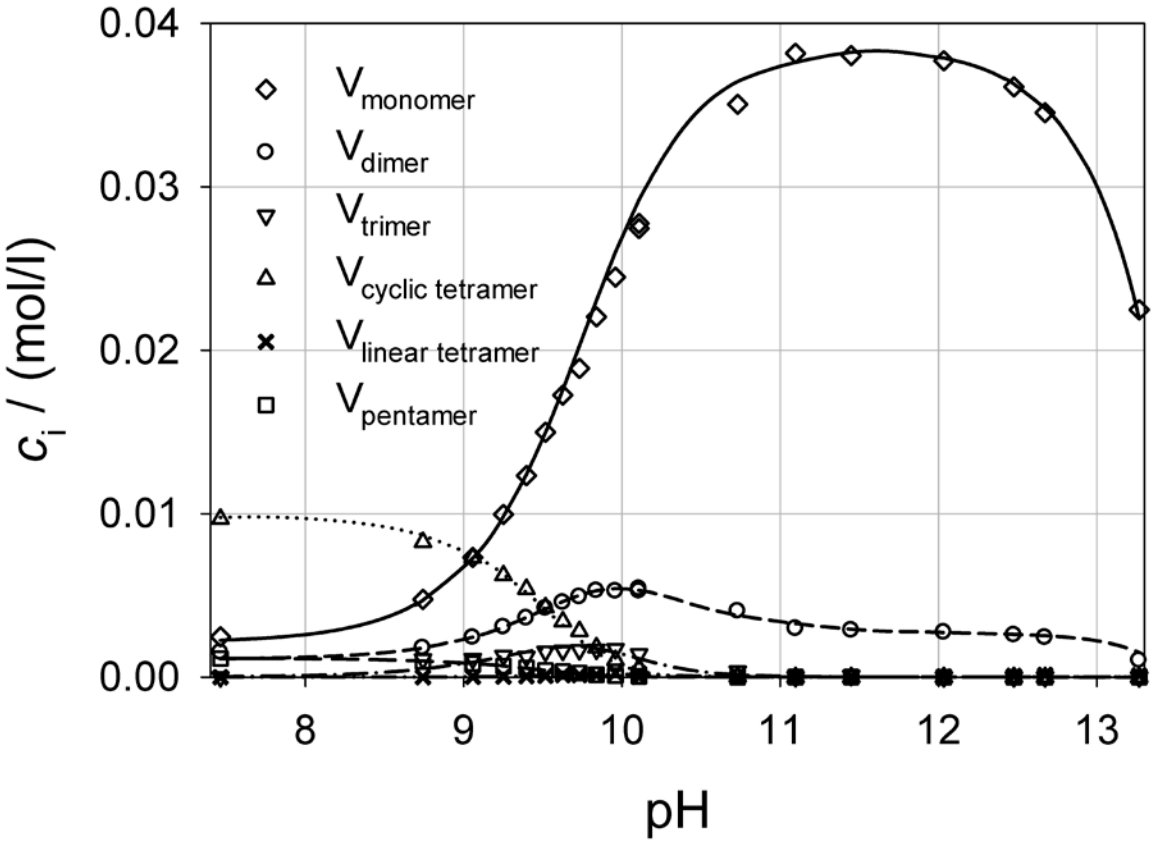

Figure 1: An example titration of 0.05 M potassium metavanadate; 0.40 M NaOH at 15 °C. Concentrations from ^{51}V-NMR integration. Symbols (lines) represent experimental points (calculation results).

2.1.2. *Chemical reaction network*

An aqueous potash solution is a chemical solvent for CO_2, i.e., it dissolves carbon dioxide predominantly as hydrogencarbonate. Chemical reactions occur only in the liquid phase. For non-activated solutions:

Dissociation of water:

$$H_2O \rightleftharpoons H^+ + OH^- \quad \text{(I)}$$

Hydrogen carbonate formation:

$$CO_2 + OH^- \rightleftharpoons HCO_3^- \quad \text{(II)}$$

Carbonate formation:

$$HCO_3^- \rightleftharpoons H^+ + CO_3^{2-} \quad \text{(III)}$$

When boric acid is added to the (basic) solution the following equilibrium reactions have to be considered (cf. Ingri [13], Spessard [14], Botello et al. [15]):

$$B(OH)_3 + H_2O \rightleftharpoons B(OH)_4^- + H^+ \quad \text{(IV)}$$

$$3B(OH)_3 \rightleftharpoons B_3O_3(OH)_4^- + H^+ + 2H_2O \quad \text{(V)}$$

$$3B(OH)_3 \rightleftharpoons B_3O_3(OH)_5^{2-} + 2H^+ + H_2O \quad \text{(VI)}$$

$$4B(OH)_3 \rightleftharpoons B_4O_5(OH)_4^{2-} + 2H^+ + 3H_2O \quad \text{(VII)}$$

The reaction network of the vanadates was investigated by McCann [9]. The following species (reactions (VIII) to (XV)) were found by ^{51}V-NMR in the pH range relevant for Hot Potassium Carbonate Process and equilibrium constants were fitted to NMR-data:

$$H_2VO_4^- \rightleftharpoons HVO_4^{2-} + H^+ \quad \text{(VIII)}$$

$$2H_2VO_4^- \rightleftharpoons V_2O_7^{4-} + 2H^+ + H_2O \quad \text{(IX)}$$

$$2H_2VO_4^- \rightleftharpoons HV_2O_7^{3-} + H^+ + H_2O \quad \text{(X)}$$

$$2H_2VO_4^- \rightleftharpoons H_2V_2O_7^{2-} + H_2O \quad \text{(XI)}$$

$$3H_2VO_4^- \rightleftharpoons HV_3O_{10}^{4-} + H^+ + 2H_2O \quad \text{(XII)}$$

$$4H_2VO_4^- \rightleftharpoons V_4O_{13}^{6-} + 2H^+ + 3H_2O \quad \text{(XIII)}$$

$$4H_2VO_4^- \rightleftharpoons V_4O_{12}^{4-} + 4H_2O \quad \text{(XIV)}$$

$$5H_2VO_4^- \rightleftharpoons V_5O_{15}^{5-} + 5H_2O \quad \text{(XV)}$$

NMR-spectroscopic investigations of aqueous solutions of (borates + vanadates) didn't show any complex formation. But aqueous solutions of (vanadate + potassium hydrogencarbonate) showed two newfound complexes between carbonate and vanadate:

$$H_2VO_4^- + HCO_3^- \rightleftharpoons HVO_4CO_2^{2-} + H_2O \quad \text{(XVI)}$$

$$H_2VO_4^- + 2HCO_3^- \rightleftharpoons VO_4(CO_2)_2^{3-} + 2H_2O \quad \text{(XVII)}$$

The chemical reaction equilibrium constants for these reactions were derived from the results of a NMR-spectroscopic investigation. All equilibrium constants are given in a recently published paper [16].

2.1.3 Solubility of CO_2 in activated potash solutions

The influence of $B(OH)_3$ and KVO_3 and mixtures of these components on the solubility of carbon dioxide in aqueous potash solutions was experimentally studied at two temperatures (343 and 383) K. The experiments were performed with two different types of experimental equipment that enable investigations at partial pressures of carbon dioxide between (1 and 140) kPa on one side and at total pressures between (0.4 and 10) MPa on the other side. The experiments in the low pressure range cover typical conditions for absorption/desorption in the Hot Potassium Carbonate Process. However, for the development of a reliable thermodynamic model, gas solubility measurements at elevated pressures (i.e., at elevated concentrations of carbon dioxide and its reaction products) are important, cf. [17, 18, 19, 20, 21, 22, 23]. As carbon dioxide is predominantly dissolved chemically (i.e., as hydrogencarbonate and carbonate) and borate and vanadate is present in a variety of ionic species, interactions between the solute species are important in the liquid phase. Experimental results in the high pressure region enable a more reliable determination of the corresponding interaction parameters as there the concentration of the reaction products is high. Therefore, one can expect that a sound physico-chemical thermodynamic model for the solubility of CO_2 based on experimental data in the high-pressure region also gives good predictions for the low partial pressure region. Experimental data in the low pressure region is used to test the extrapolation capability of the model and to additionally determine some model parameters that are not accessible from high pressure gas solubility data.

2.2 Thermodynamic model

The new experimental data were used to extend the model of Pérez-Salado Kamps et al. [24] for the solubility of CO_2 in aqueous potash solutions. Details on the model are given in related work on the solubility of acid gases in aqueous solutions, [17, 18, 19, 23, 25, 26, 27].

Pitzer's molality scale based equation for the excess Gibbs energy (G^E) of aqueous electrolyte solutions is used to calculate the activity coefficients of all solute species as well as the activity of water. Details were given in a recent publication. [27]

Figure 2 compares experimental and correlated data for the partial pressure of CO_2 over an activated potash solution, for a solvent which is typical for a Hot Potassium Carbonate Process.

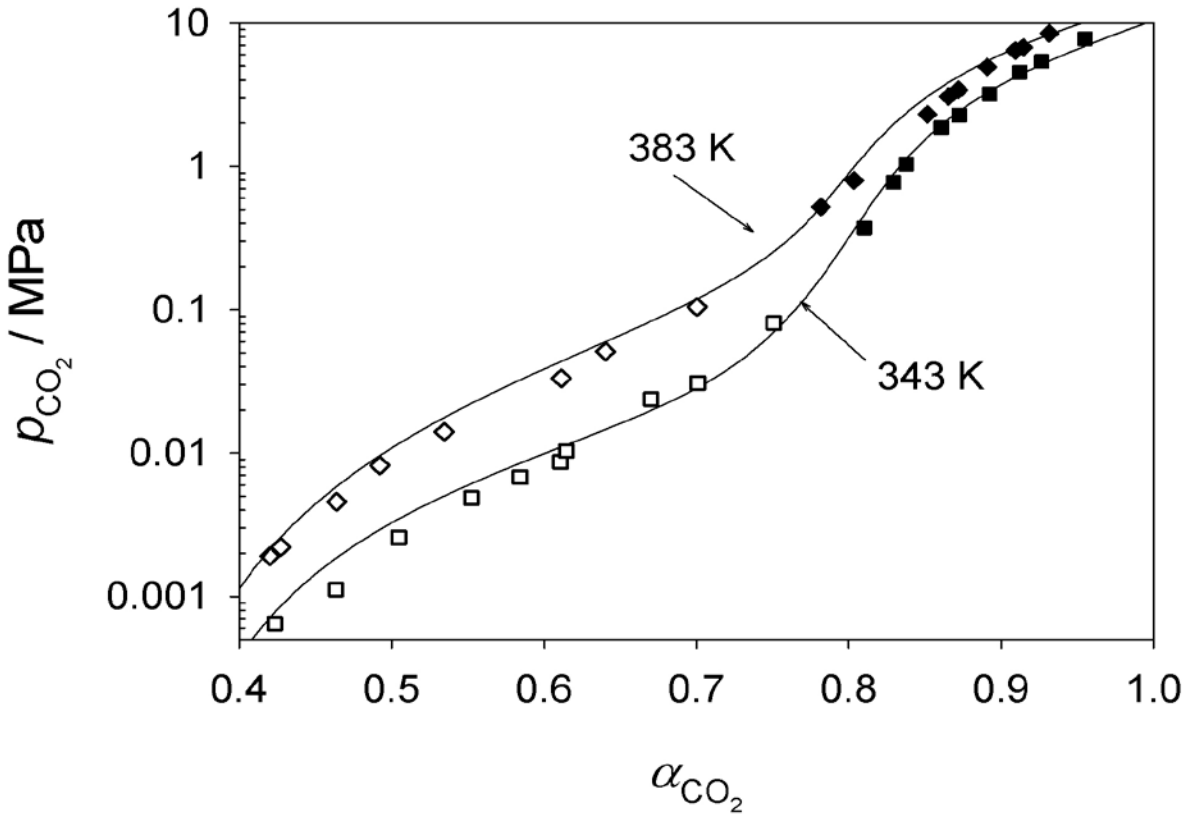

Figure 2: Partial pressure of carbon dioxide above a liquid mixture of (0.16 g/g K, 0.01 g/g B, 0.02 g/g V) vs. loading α_{CO_2} (molar ratio of CO_2 to K^+). Experimental results: headspace gas chromatography: □, 343 K; ◇, 383 K; synthetic method: ■, 343 K; ◆, 383 K; model: –.

3. Conclusions

The chemical reaction equilibrium of activated potash solutions and the solubility of CO_2 in such solutions were investigated. The chemical reaction equilibrium of the aqueous vanadate system was determined from neutral to high pH for the reaction system via global analysis of results from ^{51}V NMR spectroscopy and potentiometric titrations. The influence of two promoters ($B(OH)_3$ and KVO_3) on the solubility of CO_2 in aqueous potash solutions was investigated experimentally and modeled by extending a physico-chemical model for the solubility of CO_2 in aqueous potash solution. The experimental results reveal that both additives reduce the solubility of CO_2 in such aqueous solutions, i.e., a "salting-out" behavior was found. A physico-

chemical thermodynamic model based on the full, complex reaction network was developed to describe the partial pressure of CO_2 over the aqueous solutions investigated in this work. Using a preliminary kinetic model for the activated potash solution a rate-based model was implemented in Aspen RateSep. Even though the solvent is a highly complex reacting electrolyte solution with about 30 components, which all need to be taken into account, the model could be implemented in a rate-based model in Aspen Plus so that closed loop simulations of the process are now possible. The new model provides a sound basis for the simulation of the absorption / desorption process of carbon dioxide with activated aqueous potash solutions. However more experimental data on the reaction kinetics are still required for a completely predictive tool.

Acknowledgements

We thank Shell Global Solutions International BV for financial support.

References

[1] Kohl, A. L. and Nielsen, R., editors. *Gas purification*. Gulf Publishing Company, 5 edition, (1997).
[2] Benson, H., Field, J., and Jimeson, R. *Chem. Eng. Prog.* **50**, 356–364 (1954).
[3] Benson, H., Field, J., and Haynes, W. *Chem. Eng. Prog.* **52**, 433–438 (1956).
[4] Eickmeyer, A. G. U.S. Patent 3,851,041, March 25, 1970.
[5] Eickmeyer, A. G. U.S. Patent 4,430,312, Jun. 23, 1982.
[6] Endo, K., Nguyen, Q. S., Kentish, S. E., and Stevens, G. W. *Fluid Phase Equilib.* **309**(2), 109 – 113 (2011).
[7] Schäfer, D., Pérez-Salado Kamps, A., Rumpf, B., and Maurer, G. *J. Chem. Eng. Data* **57**(10), 2902–2906 (2012).
[8] Schäfer, D., Pérez-Salado Kamps, A., Rumpf, B., and Maurer, G. *Vestnik St. Petersburg Univ., Russia Ser. 4, Physics and Chemistry* (1), 127–133 (2013).
[9] McCann, N., Wagner, M., and Hasse, H. *Dalton Trans.* **42**, 2622–2628 (2013).
[10] Pettersson, L., Hedman, B., Andersson, I., and Ingri, N. *Chemica Scripta* **22**(5), 254–264 (1983).
[11] Heath, E. and Howarth, O. W. *J. Chem. Soc. Dalton* (5), 1105–1110 (1981).
[12] Howarth, O. W. *Prog. Nucl. Mag. Res. Sp.* **22**, 453–485 (1990).
[13] Ingri, N. *Acta Chemica Scandinavica* **17**, 581–589 (1963).
[14] Spessard, J. *J. Inrog. Nucl. Chem.* **32**(8), 2607 – 2613 (1970).
[15] Botello, J. C., Morales-Dominguez, E., Dominguez, J. M., Gutierrez, A., Rojas-Hernandez, A., and Ramirez, M. *Spectrochim Acta A Mol Biomol Spectrosc.* **59**, 1477–86 (2003).
[16] Imle, M., Kumelan, J., Speyer, D., McCann, N., Maurer, G., and Hasse, H. *Ind. Eng. Chem. Res.* **52**(37), 13477–13489 (2013).
[17] Pérez-Salado Kamps, A., Balaban, A., Jödecke, M., Kuranov, G., Smirnova, N. A., and Maurer, G. *Ind. Eng. Chem. Res.* **40**(2), 696–706 (2001).
[18] Anoufrikov, Y., Pérez-Salado Kamps, A., Rumpf, B., Smirnova, N. A., and Maurer, G. *Ind. Eng. Chem. Res.* **41**(10), 2571–2578 (2002).
[19] Pérez-Salado Kamps, A., Rumpf, B., Maurer, G., Anoufrikov, Y., Kuranov, G., and Smirnova, N. A. *AIChE J.* **48**(1), 168–177 (2002).
[20] Xia, J. Z., Pérez-Salado Kamps, A., and Maurer, G. *Fluid Phase Equilib.* **207**(1-2), 23–34 (2003).
[21] Pérez-Salado Kamps, A., Xia, J. Z., and Maurer, G. *AIChE J.* **49**(10), 2662–2670 (2003).
[22] Pérez-Salado Kamps, A., Meyer, E., Rumpf, B., and Maurer, G. *J. Chem. Eng. Data* **52**(3), 817–832 (2007).
[23] Böttger, A., Ermatchkov, V., and Maurer, G. *J. Chem. Eng. Data* **54**(6), 1905–1909 (2009).
[24] Pérez-Salado Kamps, A. *Ind. Eng. Chem. Res.* **44**(1), 201–225 (2005).
[25] Speyer, D., Ermatchkov, V., and Maurer, G. *J. Chem. Eng. Data* **55**(1), 283–290 (2010).
[26] Ermatchkov, V. and Maurer, G. *Fluid Phase Equilib.* **302**(1-2), 338 – 346 (2011).
[27] Wagner, M., von Harbou, I., Kim, J., Ermatchkova, I., Maurer, G., and Hasse, H. *J. Chem. Eng. Data* **58**(4), 883–895 (2013).

Distillation Limit Dependence on Feed Quality and Column Equipment

Lechoslaw J. Krolikowski
Wroclaw University of Technology, Wroclaw, Poland

Abstract
A feasible separation region is bounded by the product composition multitude (i.e. the distillate and bottoms composition points at total reflux and infinite number of stages) and by the distillation limit which is defined for total condenser, partial reboiler and saturated liquid feed only. The present work addresses the dependence of the distillation limit on feed quality and column equipment and is based on material balances for a stripper or rectifier (with the envelope going through the pinch zone). Simple relationships for the distillation limit (in cases of saturated liquid/vapor feed and total/partial condenser or reboiler) were obtained. The application of generalized distillation limits to process synthesis may yield new, more efficient distillation systems. Furthermore, suitable selection of column equipment type, and thermodynamic state of the feed, may lead to extended possibilities for crossing distillation boundaries. In certain cases, location of the distillation limit allows a composition profile to cross a pair of distillation boundaries: the total reflux boundary and pitchfork distillation boundary.

Keywords
Feasible separation region, Distillation boundary, System synthesis

1. Introduction

In the course of process synthesis of separation systems for azeotropic mixtures, the need for quick identification of feasible separations arises. A *feasible separation region* is a set of the distillate and bottoms composition points for a given feed composition. A number of studies determining attainable regions for homogenous azeotropic mixtures have been performed (Petlyuk and Serafimov, 1992; Laroche et al, 1992; Stichlmair and Herguijuela, 1992; Wahnschafft et al, 1992; Fidkowski et al, 1993; Poellmann and Blass, 1994), though limited to total reflux, as feed quality and thermodynamic state of the products are not relevant for total reflux. From a practical point of view, the feasible separation regions for finite reflux are more relevant.

A feasible separation region is bounded by product composition multitude (i.e. the distillate and bottoms composition points at total reflux and an infinite number of stages) and by the pinch point curve (PPC) which goes through the feed composition point (according to Wahnschafft et al, 1992) or by the distillation limit (according to Fidkowski et al, 1993). For both cases, the following question arises: what is the influence of feed quality and distillation column equipment on the borderline between sloppy splits and regions not accessible by distillation? A change in the borderline will immediately have an effect on the feasible separation region (addressed in this study) and may have an indirect effect on system synthesis. In other words, it may influence the system structure, the design and operating parameters of individual columns.

In the current study, continuous distillation in trayed columns was modeled by theoretical stages. Constant molar overflow in each section of the column, constant pressure along the column, and the products in the form of saturated liquid or vapor were assumed. An ideal vapor phase and an activity coefficient model (using the Wilson equation) for the liquid phase were used in all calculations. Vapor–liquid equilibrium data are given in Table 1.

Table 1. Sources of Data for Vapor-Liquid Equilibrium Parameters

Mixture		
methanol – ethanol	methanol – n-propanol	ethanol – n-propanol
I/2e, p. 50	I/2c, p. 96	I/2a, p. 340
Volume, part, and page numbers refer to data collected by Gmehling et al (1988, 1982, 1977)		

2. Wahnschafft's feasible separation region

Wahnschafft et al (1992) indicated the feasible separation region is bounded by the product composition multitude at $R = \infty$ and $N = \infty$ and by the feed pinch-point curve going from the feed composition point in both directions, where the feed pinch-point curve was defined as the liquid phase PPC (liquid PPC). They assumed the feasible separation region is a sum of the product composition set at total reflux and its extension with the reachable products at finite reflux. The feasible separation region for a ternary zeotropic mixture with C-shaped distillation lines is shown in Figure 1. The continuous feed distillation line (FDL) is approximated by the discrete feed distillation line in the figure for practical reasons (this approximation is used in other figures). It should be noted that Wahnschafft and co-workers did not give any assumptions relative to feed quality, column equipment (type of condenser and reboiler) or thermodynamic state of the products. If one assumes a saturated liquid feed, total condenser, and a partial reboiler (the most frequently-occurring case), then Wahnschafft's feasible separation region contains a distillate composition subset enclosed by feed vapor PPC and feed liquid PPC, which cannot be obtained (based on observations of process simulation results), whereas the bottoms composition set is defined correctly.

3. Fidkowski's feasible separation region

Assuming that a saturated liquid mixture is fed to a column equipped with a total condenser and partial reboiler, Fidkowski et al (1993) considered an instance when both products with certain specifications could be obtained. The authors concluded that sloppy separations were demarcated from regions not accessible by distillation by two curves: the feed vapor PPC which restricts distillate composition, and feed liquid PCC which limits bottoms compositions, with these curves denoting the *distillation limit*. According to Fidkowski and co-workers, feasible separation regions are determined by the product composition multitude at $R = \infty$ and $N = \infty$ and the distillation limit together with the mass balance line of *feed tie-line split* (transition line). A feasible separation region for a zeotropic mixture with C-shaped distillation lines employing this concept is shown in Figure 2. Simulations of distillation processes showed that distillate and bottoms compositions can reach but, not cross, the distillation limit. This indicated the distillation region for the saturated liquid feed and a column equipped with a total condenser and partial reboiler were determined accurately.

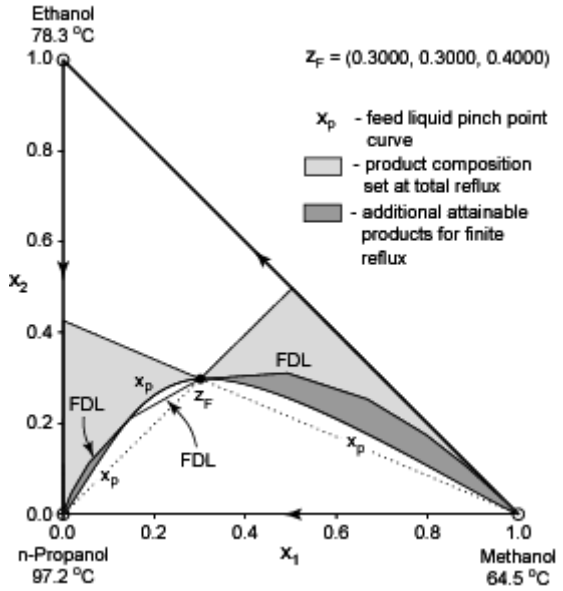

Figure 1. Feasible separation region for a zeotropic mixture with C-shaped distillation lines according to Wahnschafft et al (1992)

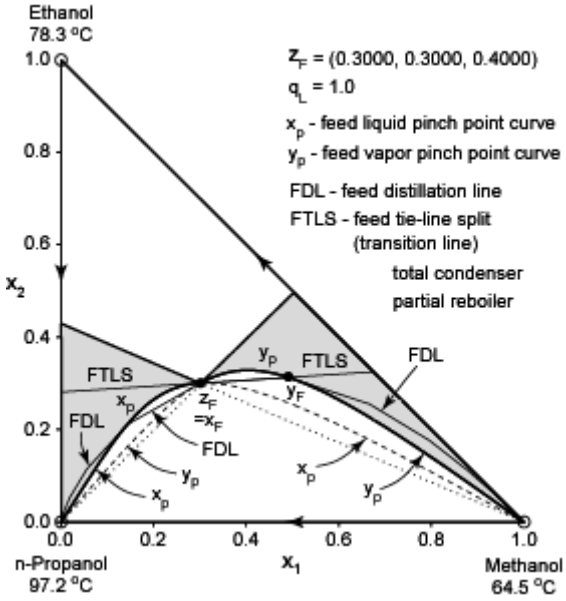

Figure 2. Feasible separation region for zeotropic mixture with C-shaped distillation lines according to Fidkowski et al (1993)

4. A case of saturated vapor feed

Let one of the assumptions used in Fidkowski's construction is changed: a saturated vapor (instead of liquid) feed is used and the stripper with an infinite number of stages ($N = \infty$) is considered. Material balance around the top of the column with the envelope going through the pinch zone (Figure 3) gives the following relationship:

$$Fy_F + V_s y_p = Dx_D + L_s x_p \tag{1}$$

where F, D, V_s, and L_s are molar flow rates of feed, distillate, vapor, and liquid below the feeding-point, respectively, whereas y_F, x_D, x_p, and y_p are molar fraction vectors

for feed, distillate, and liquid and vapor pinch points, respectively. Mixing in the feeding zone is described by the following equation:

$$Fy_F + V_s y_p = V_r x_D \tag{2}$$

where V_r is the molar flow rate of the vapor above the feeding-point.

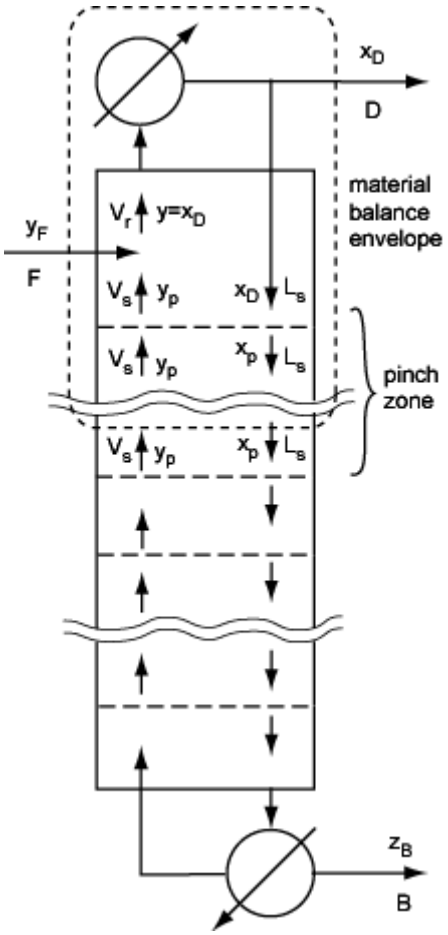

Figure 3. A stripper with the pinch zone directly below feed cross-section

The material balance of the condenser is as follows:

$$V_r = D + L_s \tag{3}$$

Equations (1)-(3) imply that $x_D = x_p$, though they do not provide any expression which allows x_p to be calculated. However, based on published results of research (Fidkowski et al, 1991 & 1993), it is possible to conclude that feed PCC does not depend on the thermodynamic state of the feed (a change in the feed state or type of condenser/reboiler does not affect the pinch point equation), which is confirmed by the stripper simulation results shown in Figure 4. A part of the feed liquid PPC, between the feed composition point $z_F = y_F$ and the unstable node, limits the distillate composition as a consequence. A saturated liquid feed situation is also presented in Figure 4. It could be shown that distillate composition is bounded by the feed vapor PPC for a partial condenser and the saturated vapor feed (the same as for total condenser and saturated liquid feed). Much more complicated considerations are required for the combination of partial condenser and saturated liquid feed (Table 2) (Krolikowski, 2010) and similar considerations can be made for bottoms compositions (Table 3). The missing solutions in those tables are certainly not feed liquid or vapor PPCs.

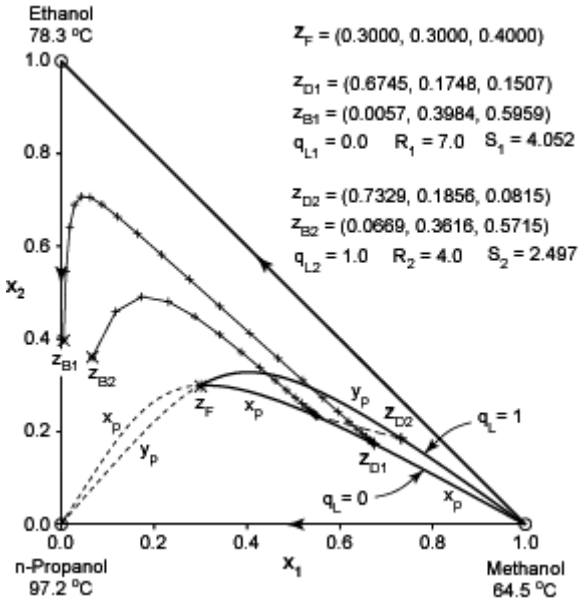

Figure 4. Distillate composition limits for column with a total condenser fed with saturated liquid or a vapor mixture

5. Crossing distillation boundaries

A method for finding the exact feasible separation region for S-shaped distillation lines has been developed (Krolikowski, 2009) and using this method, the feasible separation region obtained is shown in Fig. 5.

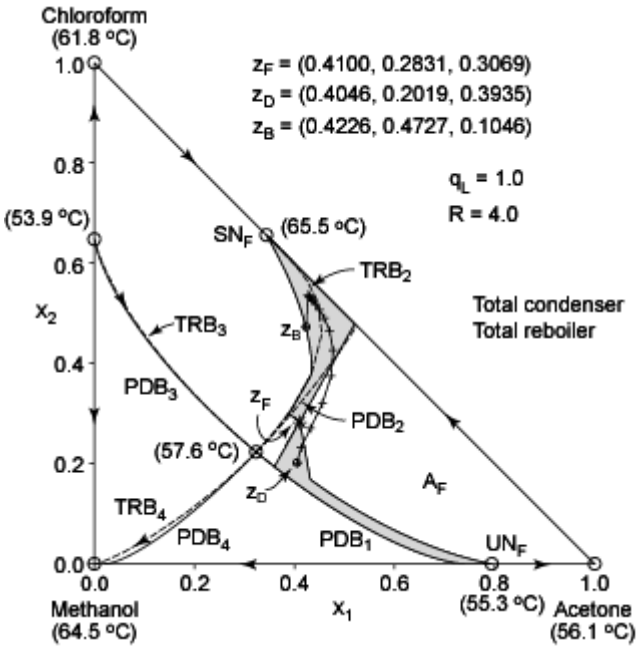

Fig. 5. The feasible separation region along with a liquid composition profiles for a stripper

The distillation limit for the total reboiler and saturated liquid feed crosses two distillation boundaries: the pitchfork distillation and total reflux distillation boundaries. The part of the generalized distillation limit in the vicinity of feed point $\boldsymbol{z}_F$ is not visible,

because it does not create a border for the feasible separation region. It is necessary to stress the point that the bottoms composition $\boldsymbol{z}_B$ is part of a different distillation region than the feed $\boldsymbol{z}_F$ and distillate $\boldsymbol{z}_D$ composition points. Moreover, none of these points are located in the common part of the distillation regions between the pitchfork and total reflux distillation boundaries. The feasible separation region is extended beyond total reflux distillation boundary and provides new opportunities for crossing distillation boundaries.

Table 2. Limits of distillate compositions

Condenser type	Saturated liquid feed	Saturated vapor feed
total	Feed vapor PPC	Feed liquid PPC
partial		Feed vapor PPC

Table 3. Limits of bottoms compositions

Reboiler type	Saturated liquid feed	Saturated vapor feed
total	Feed vapor PPC	Feed liquid PPC
partial	Feed liquid PPC	

6. Conclusions

A generalized distillation limit for a saturated liquid/vapor feed and total/partial condenser or reboiler was developed. Data indicated that pinch points were independent of molar fraction of the feed that is liquid, as well as condenser and reboiler types. Wahnschafft and Fidkowski constructs were special cases for the feasible separation regions, where the generalized distillation limit demarcated the most sloppy splits permissible for the regions not accessible by distillation. Suitable selection of column type and the feed thermodynamic state may lead to crossing these distillation boundaries, where product compositions are located in different distillation regions beyond their common part.

Acknowledgements

The work was financed by a statutory activity subsidy from the Polish Ministry of Science and Higher Education for the Faculty of Chemistry of Wrocław University of Technology.

References

Fidkowski, Z.T., Doherty, M.F., Malone, M.F., 1991. AIChE J. 37, 1761-1779
Fidkowski, Z.T., Doherty, M.F., Malone, M.F., 1993. AIChE J., 39, 1303-1321
Gmehling, J., Onken, U., 1977. Vapor – Liquid Equilibrium Data Collection, Vol. I/2a, Dechema
Gmehling, J., Onken, U., 1982. Vapor – Liquid Equilibrium Data Collection, Vol. I/2c, Dechema
Gmehling, J., Onken, U., 1988, Vapor – Liquid Equilibrium Data Collection, Vol. I/2e, Dechema
Krolikowski, L.J. ,2009. Computer-Aided Chemical Engineering, Elsevier, 26, 761-765
Krolikowski, L.J., 2010. Feasible Separation Regions for Homogeneous Ternary Mixture. Publishing House of Wroclaw University of Technology, Wroclaw (in Polish)
Laroche, L. , Bekiaris, N. , Andersen, H.W., Morari, M., 1992. Ind. Eng. Chem. Res., 31, 2190-2209
Petlyuk, F.B., Serafimov, L.A., 1983. Multicomponent Distillation. Theory and Design, Chemistry Publish. Co.
Poellmann, P., Blass, E., 1994. Gas Separation & Purification, 8, 194-228
Stichlmair, J.G., Herguijuela J-R. 1992. AIChE J., 38, 1525-1535
Wahnschafft, O.M., Koehler, J.W., Blass, E., Westerberg, W., 1992. Ind. Eng. Chem. Res.,31, 2345-2362

On the Riemannian structure of the residue curves maps

N.N. Shcherbakova, V. Gerbaud, I. Rodriguez-Donis
[1]LGC, INPT-ENSIACET, Toulouse, France;
[2,3]LGC, SNRS, Toulouse, France

Abstract
In this article we present a new geometric interpretation of the structure of the residue curve maps. The residue curves maps (RCM) is a classical tool of the qualitative analysis in the theory of distillation of multicomponent mixtures within the thermodynamic equilibrium model. Despite of their broad utilization in practical applications and in numerical computations, some important theoretical properties of RCM remain unclear, for instance, the topological characterization of the separating boundaries, and the connection between RCM and the associated boiling temperature surface. In this paper we develop a new point of view on the intrinsic topological structure of RCM using the tools of differential geometry. Our main result is the description of the Riemannian structure hidden behind of the residue curves differential equations, which comes from the Van-der-Waals – Storonkin state equation. We discuss the first non-trivial consequences of this fact for the RCM theory of ternary mixtures.

Keywords
Residue curves, gradient systems, Riemannian metric

1. Introduction

The residue curve maps (RCM) is a key tool of the theory of vapor-liquid equlibria which form the base of the distillation and rectification processes, both on the theoretical and on the practical level. The first experimentally obtained RCMs for ternary mixtures were introduced in the early 1900s (see in [3] for the historical note), while the rigorous mathematical formalism was developed by the Leningrad school, in particular in the works of Serafimov and Zharov [1] in 1970s, and improved by the group of Doherty [2] later. Nevertheless, some theoretical properties of RCM remain still unclear. This concerns, for instance, the topological characterization of the separating boundaries, and the connection between RCM and the associated boiling temperature surface ([3]). In this paper we propose a new point of view on the global topological structure of RCM using Riemannian geometry, which, in our opinion, is the most appropriate tool to understand the intrinsic thermodynamical meaning of RCM. In some sense our construction evokes the ideas expressed in the works of V. Filippov in 70's ([4]), though we use a different approach.

The paper is organized as follows: after a brief review of the Riemannian geometry in Section 2.1, in Section 2.2 we revise the thermodynamical fundamentals of the equilibrium model of simple distillation of multicomponent mixtures. In Section 2.3 we analyze the open evaporation process the associated boiling temperature surface. We show that the differential equations of residue curves define a gradient flow in the space of partial mole fractions, where the gradient is defined in the Riemannian sense. In Section 2.4 we illustrate our geometrical model in the context of ternary mixtures, by considering an ideal mixture of methanol, ethanol and propanol. We show that already in this simple case the global geometry defined by the Van-der-

Waals - Storonkin equation is very different from the standard Euclidean model.

2. Riemannian metric and the open evapoation problem

2.1 Basic facts about Riemannian geometry.

In this paper we consider the state space of a physical system as a *differential manifold* M, whose dimension is equal to the number of the *degrees of freedom* of the system. The evolution of the system is usually measured with respect to some non-decreasing scalar parameter, for instance, time t. At a given moment of time the state of the system with n degrees of freedom is a point $\boldsymbol{q}\in M$, which can be described by the set of *local coordinates* $(q_1,\dots,q_n)$, whose derivatives $\dot{\boldsymbol{q}}=(\dot{q}_1,\dots,\dot{q}_n)$ form a velocity vector $\dot{\boldsymbol{q}}\in T_qM$ in the *tangent space* to M at $\boldsymbol{q}$. We say that M is a *Riemannian manifold* if $TM=\bigcup_{q\in M} T_qM$ is endowed with a *scalar product*, which in local coordinates is defined by a symmetric matrix $G(\boldsymbol{q})=\{g_{ij}(\boldsymbol{q})\}_{i,j=1}^n$ corresponding to a positive definite quadratic form called *metric*, so that $\langle \boldsymbol{v}|\boldsymbol{w}\rangle_G=\sum_{i,j=1}^n g_{ij}(\boldsymbol{q})v_iw_j=\boldsymbol{v}^TG(\boldsymbol{q})\boldsymbol{w}$ for any two vectors $\boldsymbol{v},\boldsymbol{w}\in T_qM$. Hence at each point $\boldsymbol{q}$ one can compute the norms of the vectors: $\|\boldsymbol{v}\|_G^2=\langle \boldsymbol{v}|\boldsymbol{v}\rangle_G$ and more generally, *the length of curves* in M: given a curve γ joining points $\boldsymbol{q_0}$ and $\boldsymbol{q_1}$ in time τ, and such that $\dot{\gamma}(t)=\boldsymbol{v}(t)$, we have $l(\gamma)=\int_0^\tau \|v(t)\|_G dt$.

The most simple example of a Riemannian manifold is the standard Euclidean space: the local coordinates are just standard Cartesian coordinates, and the scalar product is defined by the identity matrix: $G(\boldsymbol{q})=I_n$. In particular, the distance between two points is just $d(\boldsymbol{q},\boldsymbol{p})=\sqrt{(q_1-p_1)^2+\dots(q_n-p_n)^2}$, and more generally, the shortest path between two points is a straight line. All these facts are no more true in Riemannian manifolds with non-trivial, i.e., non-Euclidean, metric structure. In fact, the shortest path between two points is *the geodesic curve* of the metric, i.e., the curve of minimal length, like for instance the meridian circles on a 2D sphere. Intrinsic topological properties of the Riemannian manifolds can be characterized in terms of the *curvature tensor* associated to the metric, which we will not discuss in this paper. In what follows, in order to avoid any ambiguity, throughout this paper $\langle .|. \rangle_G$ and $\|.\|_G$ will denote the scalar product and norm computed with respect to the Riemannian metric G, while $\langle\ |\ \rangle$ and $\|\ \|$ will denote their Euclidean equivalents.

We conclude this short review of Riemannian geometry by recalling the general definition of the gradient of a function. Let f be a smooth function in the Riemannian manifold M equipped with metric G. Then its *differential* $d_{\boldsymbol{q}}f=\sum_{i,j=1}^n \partial_{q_1}f(\boldsymbol{q})dq_i$ is a linear operator in T_qM, also called a *differential form*. The vector $\boldsymbol{w}\in T_qM$ is called *the gradient* of the function f if its scalar product with any other vector $\boldsymbol{v}\in T_qM$ yields the directional derivative of f at $\boldsymbol{q}$ with respect to $\boldsymbol{v}$: $d_{\boldsymbol{q}}f(\boldsymbol{v})\stackrel{\text{def}}{=}(\nabla f)^T\boldsymbol{v}=\langle \boldsymbol{w}|\boldsymbol{v}\rangle_G$. We denote $\boldsymbol{w}=\nabla_G f(\boldsymbol{q})$ the gradient of f in M defined in this sense. It is easy to verify that in local coordinates the Riemannian gradient $\nabla_G f(\boldsymbol{q})$ of f is related to the standard Euclidean gradient $\nabla f(\boldsymbol{q})\stackrel{\text{def}}{=}(\partial_{q_1}f(\boldsymbol{q}),\dots,\partial_{q_n}f(\boldsymbol{q}))$ as follows:

$$\nabla_G f(\boldsymbol{q})=G^{-1}(\boldsymbol{q})\nabla f(\boldsymbol{q}) \quad .$$

2.2 Thermodynamic fundamentals of RCM: the Van-der-Waals – Storonkin equation.

Let us briefly recall some fundamental thermodynamical state equations, which describe the equilibrium in a homogeneous liquid-vapor n -component system under constant pressure. The detailed derivation of these equations can be find in [1] or in [6]. According to the Gibbs phase rule, the system under consideration has n degrees of freedom, and its thermodynamical state can be described in terms of $n-1$ independent mole fractions of the liquid phase $\boldsymbol{x}=(x_1,\ldots,x_{n-1})$ and the temperature T . The thermodynamical state of the liquid phase of such a system satisfies the generalized Van-der-Waals equation - Storonkin equation:

$$\left(s^v-s^l-\sum_{i=1}^{n-1}\frac{\partial s^l}{\partial x_i}(y_i-x_i)\right)dT-\sum_{i,j=1}^{n-1}\frac{\partial^2 g^l}{\partial x_i\partial x_j}(x_i-y_i)dx_j=0 \quad (1)$$

where s^v , y_i are the vapor phase entropy and the partial molar fractions, while s^l , g^l are the liquid phase entropy and the free Gibbs energy. In order to get the full state characterization in a closed two-phase system , (1) should be completed by the analogous equation for the vapor phase and by the heat transition equation ([6)].

We now focus our attention on the changes in the liquid phase during the open evaporation process. The liquid phase can be considered as an open sub-system of a closed two-phases liquid-vapor system, whose evolution is constrained by equation (1). Set $\Omega=\{x_i\in[0,1],\ \sum_{i=1}^{n-1}x_i\le 1\}$. The state space of the system is the differential manifold $M=\{\boldsymbol{q}=(\boldsymbol{x},T)\in\mathbb{R}^n:\ \boldsymbol{x}\in\Omega,\ T_b\in\mathbb{R}\}$. Let $\boldsymbol{v}:\quad v_i=x_i-y_i$ denote the *equilibrium vector,* and denote $\Delta s=s^v-s^l+\sum_{i=1}^{n-1}\partial_{x_i}s^l v_i$, which after a simple algebraic transformation takes the form $\Delta s=\sum_{i=1}^{n}y_i(s_i^v-s_i^l)$ which was used in [2]. Consider the differential one-form $\sigma=\Delta s\,dT+\sum_{i,j=1}^{n-1}\partial^2_{x_ix_j}g^l v_i\,dx_j$. Equation (1) means that possible changes in the system under the thermodynamical equilibrium condition define a vector distribution $\Sigma\subseteq TM$ such that $\sigma|_\Sigma=0.$. Note, that this equation make restrictions on the dynamics of the system rather than on its exact state at a given moment.

2.3. The Gibbs metric of the open evaporation process

In the standard open evaporation model under thermodynamical equilibrium a multicomponent liquid mixture is vaporized in a still in such a way that the vapor is continuously evacuated from the contact with the liquid ([2]). The partial mass balance of such a system can be written in the form

$$\frac{dx_i}{d\xi}=x_i-y_i(\boldsymbol{x},T)=v_i(\boldsymbol{x},T)\ ,\ i=1,\ldots,n-1 \quad (2)$$

where $\xi\in[0,+\infty]$ is a non-decreasing parameter describing the change in the overall molar quantity of the liquid phase n^l : $\xi=\ln(n^l(0)/n^l(t))$. Solutions of system of differential equations (2) are called *residue curves,* and their graphical representation in the simplex Ω form the *residue curves map (RCM)*. Along with the pure states, the equilibria of system (2), i.e., points $\boldsymbol{q}=(\boldsymbol{x},T):\ \boldsymbol{v}(\boldsymbol{x},T)=0$ define the

azeotropes of the given multicomponent mixture.

Observe that the definition of the molar fractions implies one more scalar relation $\sum_{i=1}^{n} y_i(\boldsymbol{x},T)=1$, which defines a hyper-surface in the state space M , called the *boiling temperature surface.* Since in a homogeneous mixture to each value of $\boldsymbol{x}$ it corresponds exactly one value of T , the relation above can be solved in order to find $T=T_b(\boldsymbol{x})$ where the function T_b defines the *boiling temperature.* In other words, the boiling temperature surface can represented in M as a graph of function $T_b(\boldsymbol{x})$: $W=\{\boldsymbol{q}\in M:\ \boldsymbol{q}=(x_1,\ldots,x_{n-1},T_b(\boldsymbol{x}))\}$. All points of W are at thermodynamic equilibria, therefore, in view of Section 2.2, $\sigma|_{TW}=0$, which yields $\nabla T_b=(\Delta s^{-1}D_x^2 g^l \boldsymbol{v})|_{T=T_b(\boldsymbol{x})}$. On the other hand, the thermodynamic stability condition implies that $D_x^2 g^l$ is a positive-definite quadratic form, while $\Delta s>0$. These facts allow to introduce a metric in Ω associated to the matrix

$$\Gamma(\boldsymbol{x})=\frac{1}{\Delta s(\boldsymbol{x},T_b(\boldsymbol{x}))}D_x^2 g^l(\boldsymbol{x},T)|_{T=T_b(\boldsymbol{x})} \quad (3)$$

which we will call the *Gibbs metric.*

Remark. Although the form σ is well defined everywhere in M , some of the derivatives $\partial^2_{x_i x_i} g^l$ blow up at the pure states (vertices of Ω) and on the sides of Ω ([1]). Nevertheless, the Gibbs metric is a well defined Riemannian metric in the interior points of Ω . Inclusion of the borders of Ω is possible., the resulting manifold is then of *almost- Riemannian* type.

In new notations, $\nabla T_b(\boldsymbol{x})=\Gamma(\boldsymbol{x})\boldsymbol{v}(\boldsymbol{x})$, where $\boldsymbol{v}(\boldsymbol{x})=\boldsymbol{x}-\boldsymbol{y}(\boldsymbol{x},T_b(\boldsymbol{x}))$. In view of Section 2.1, this means that $\boldsymbol{v}$ is the gradient of the boiling temperature T_b in the sense of the Gibbs metric Γ : $\boldsymbol{v}(\boldsymbol{x})=\nabla_\Gamma T_b(\boldsymbol{x})$. Moreover, by construction, the projection on Ω of any curve $\boldsymbol{q}(\xi)\in W$: $\dot{\boldsymbol{q}}(\xi)=\sum_{i=1}^{n-1} v_i(\boldsymbol{x}(\xi))\partial_{x_i}+\dot{T}_b(\boldsymbol{x}(\xi))\partial_T$, which describes the evolution of the system in the full state space M , is a residue curve . Since necessarily $\sigma(\dot{\boldsymbol{q}}(\xi))=0$, we get

$$\frac{dT}{d\xi}=\|\boldsymbol{v}(\boldsymbol{x},T)\|^2_\Gamma \quad (4)$$

We are now ready to formulate the main result of this paper:

Theorem. The open space $\operatorname{int}\Omega=\{x_i\in(0,1),\sum_{i=1}^{n-1}x_i<1\}$ *of partial molar concentrations endowed with the Gibbs metric* Γ *is a Riemannian manifold. Residue curves are solutions to the gradient system*

$$\frac{d\boldsymbol{x}}{d\xi}=\nabla_\Gamma T_b(\boldsymbol{x}) \quad (5)$$

where the boiling temperature T_b *plays the role of the potential*. M*oreover, along residue curves the temperature changes according to equation (4).*

Properties of the gradient flows in Riemannian manifolds are well known, and they are analogous to the properties of the classical gradient systems in $\mathbb{R}^n$ ([5]),

modulo the change of the metric. In particular:

1. the critical points of T_b are equilibrium points of system (2) in $\mathrm{int}\,\Omega$;

2. generically, critical points of T_b are be stable/unstable nodes or saddles;

3. if c is a regular value of T_b , i.e., if $\nabla T_b|_{T_b^{-1}(c)} \neq 0$, then the vector field $\boldsymbol{v}$ is orthogonal to the level set $T_b^{-1}(c)$ in the sense of the Gibbs metric Γ .

The first two of these properties are well known and widely used in the RCM theory. However, the Riemannian structure hidden in (4) explains the paradox noticed by Doherty and Van Dongen in [2, vol. 39], where they proved that (2) cannot be written in the classical gradient form despite T_b verifies all the properties of the potential function for RCM. In fact, the high non-triviality of the Gibbs metric Γ makes the topology of RCM much more sophisticated.

2.4. First non-trivial example: ternary mixtures.

The first non-trivial situation, where the Gibbs metric appears, concerns the evaporation of three-components mixtures. Choosing two independent mole fractions $x_{1,}x_2$, the boiling temperature surface W over $\mathrm{int}\,\Omega$ can be seen as a 2D surface $T=T_b(x_{1,}x_2)$ in a 3D state space with coordinates $x_{1,}x_{2,}T$. On the $\boldsymbol{x}$ -plane, along with the residue curves, we have another family of curves, *the isotherms,* defined as the projections of the level sets $T_b^{-1}(c)\subset W$. At a point $\boldsymbol{x}\in\mathrm{int}\,\Omega$, the tangent vector to the isotherm is $\boldsymbol{w}=(-\partial_{x_2}T_b(\boldsymbol{x}),\partial_{x_1}T_b(\boldsymbol{x}))=(\nabla T_b)^{\perp}$. We have: $\langle \boldsymbol{v}|\boldsymbol{w}\rangle_\Gamma=\langle \Gamma\boldsymbol{v}|\boldsymbol{w}\rangle=\langle \Gamma\Gamma^{-1}\nabla T_b|(\nabla T_b)^{\perp}\rangle=0$, and so $\boldsymbol{v}$ and $\boldsymbol{w}$ are Γ -orthogonal. Moreover, away from azeotropes the vectors $\boldsymbol{e_1}=\boldsymbol{v}/\|\boldsymbol{v}\|_\Gamma$, $\boldsymbol{e_2}=\boldsymbol{w}/\|\boldsymbol{w}\|_\Gamma$ form a well defined Γ -orthonormal basis of RCM.

It is worth to underline that the metric on W defined by σ is different from the Riemannian metric *naturally defined* on the graph of the boiling temperature T_b in $\mathbb{R}^3$. Indeed, binary azeotropes and pure states are regular points of T_b , and *the natural metric* of the surface $(x_{1,}x_{2,}T_b(x_{1,}x_2))$ in $\mathbb{R}^3$ is given by the matrix Γ' with $\Gamma'_{ii}=1+(\partial_{x_i}T_b)^2$, $i=1,2$, $\Gamma'_{12}=\partial_{x_1}T_b\partial_{x_2}T_b$, which is well defined also at the boundary of Ω .

We illustrate our geometric construction taking as an example the following ideal mixture: methanol (x_1), ethanol (x_2), propanol. Our computations were realized with Mathematica 9 package. We used on the three-suffix Margules equations for the activity coefficients ([7]). In Figure1 the boiling temperature surface W is shown: thick curves represent a curve in the state space M , which projects on a residue curve on the space of molar concentrations, the thin curves on W are the isotherms. Figure 2 shows how the angle θ between the equilibrium vector $\boldsymbol{v}$ and the vector $\boldsymbol{w}$ tangent to the isotherm changes along the residue curve of Figure 1. These vectors are far from being orthogonal neither in the Euclidean sense (dashed curve) nor in the sense of the metric Γ' (dotted curve), while in the Gibbs metric (thick curve) we get $\cos\theta<10^{-2}$, which shows that $\boldsymbol{v}$ and $\boldsymbol{w}$ are Γ -orthogonal within the limits of the numerical accuracy of the model. The difference between metrics Γ and Γ' becomes clear from Figure 3, where we compare their components.

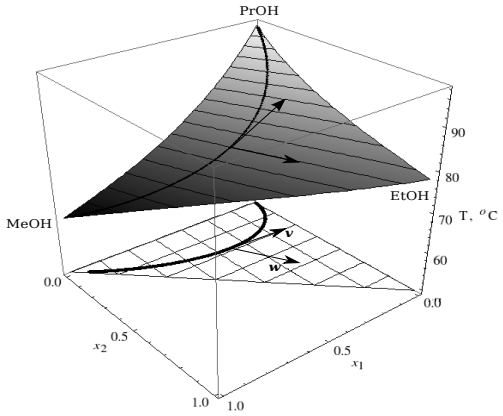

Figure 1.

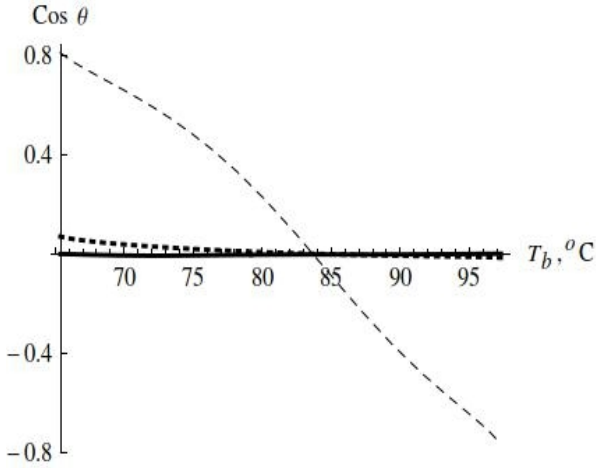

Figure 2.

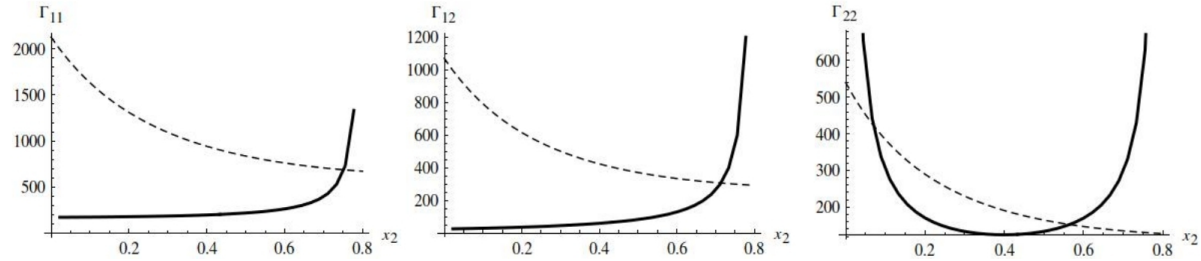

Figure 3: Γ (bold curve) and Γ' (dashed curve) comparison, section $x_1 = 0.2$

3. Conclusions

The thermodynamical equilibrium condition, described by the Van–der-Waals -Storonkin equation (1) endows the RCM of an open evaporation process by a non-trivial metric structure related to the Gibbs metric Γ. Within this geometrical model, any RCM is the set of the integral curves of a gradient flow associated to the boiling temperature T_b. This fact implies all well-known properties of T_b in the RCM theory. Additionally, unlike in the classical Euclidean case, the tangent vectors to the residue curves and isotherms are Γ-orthogonal away from azeotropes. The difference between the Gibbs metric Γ and the natural metric on the boiling temperature surface Γ' should be taken into account in the definition of the ridges and valleys of the boiling temperature surface W. We will discuss it in future work.

References

1. V.T. Serafimov, L.A. Zharov. Physical-chemical foundation of distillation and rectification, “Chemistry”, Leningrad, 1975 (in Russian).
2. M.F. Doherty et al. On the dynamics of the distillation process - I-V. Chem. Eng. Sci., vols. 33, 34, and 39.
3. V.N. Kiva, E.K. Hilmen, S. Skogestad. Azeotropic phase equilibrium diagrams: a survey. Chem. Eng. Science, vol. 58, pp. 1903-1953, 2003.
4. V.K. Filippov. Thermodynamics of n-component azeotrope in the Gibbs potential metrics.(in Russian) In: Thermodynamics of heterogeneous Systems and Theory of surface phenomena, Issue 4. Leningrad University , 1977.
5. M. Hirsch, S. Smale, R. Devaney. Differential Equations, Dynamical Systems, and an Introduction to Chaos. II ed., Academic Press, 2004 – Mathematics.
6. A.M. Toikka, J.D. Jenkins. Conditions of Thermodynamic equilibrium as a basis for the practical calculations of vapor-liquid equilibria. Chem. Eng.Journal, Chem. Eng. J., 89 (2002), pp. 1–27.
7. J. M. Prausnitz, R.N. Lichtentheler, E. Gomes de Azevedo. Molecular Thermodynamics of Fluid-Phase Equilibria. IIIrd edition, Published by Prentice Hall, 1998.

THE DETERMINATION OF PHASE DIAGRAM STRUCTURE OF FIVE-COMPONENT SYSTEM ON THE BASIS OF ITS GEOMETRIC SCAN

Serafimov L.A., Frolkova A.V., Semin G.A.,
Lomonosov Moscow State University of Fine Chemical Technology, Moscow, Russia

Abstract

The method for determining the vapor-liquid phase diagram structure of five-component systems was proposed. It is based on the analysis of types and Poincare indexes of singular points of the geometric scan and full structure of concentration simplex. If the algebraic sum of the singular points Poincare indexes is equal to 2 it means that five-component azeotrope is absent. If it is equal to 0 or 4 than the system contains five-component azeotrope with index +1 or -1 respectively. To determine the type of the azeotrope founded it is necessary to research the structure of separatrix manifolds. If azeotrope is presented as a node on all the separatrix manifolds than it will be a node. If it is presented as a saddle at least on one of the separatrix manyfold than its type will be saddle. The validity of the proposed method was confirmed by vapor-liquid equilibrium modeling in real five-component mixtures.

Keywords

five-component systems, azeotrope, phase diagram, vapor-liquid equilibrium

1. Introduction

The information about the physical-chemical properties of the system, about the structure of vapour-liquid equilibrium phase diagram is the basis of separation technological scheme creation The study of the phase diagram of a multicomponent system, the modelling of its vapour-liquid equilibrium, the determination of *n*-component azeotrope presence, the localization of distillation regions are difficult tasks.

A method for determining the phase diagram structure of five-component systems (only monoazeotropy is considered), which may be used for software creation for multicomponent systems phase diagrams studying, will be presented.

2. Results and discussion

Analysis of the diagram structure will be based on the azeotropy rule [1] in the next form:

$$2(N_5 + C_5^+ - C_5^-) + \sum_{i=1}^{4}(N_i + C_i^+ + C_i^-)^b = Э, \quad (1)$$

where *N* – singular point of node type, *C* – singular point of saddle type, +/- – the sign of the Poincare index, *b* – boundary singular points, *Э* – Euler characteristics which is equal to 2 for five-component systems. Note that the Poincare index for stable and unstable node in the concentration simplex of five-component system is equal to +1, because the dimension of the simplex is even value.

The equation (1) does not include complex singular points of types: saddle-node, positive-negative saddle (Poincare index is zero).

The proposed method includes three basic stages:

1) the selection and analysis of geometric scan of five-component system concentration simplex (the determination of type and Poincare index of each singular points). If the system contains only binary azeotropes the scan of second dimension may be used, if there are ternary and quaternary azeotropes the scan of third dimension should be used for determining the sign of all the eigenvalues λ_i. The sign of singular point is determined by the equation:

$$sign(i) = sign\prod_{i=1}^{r}\lambda_i ,$$

r – is the dimension of concentration simplex.

2) the determination of the five-component azeotrope presence or its absence on the basis of equation (1) solution; in case of its presence the determination of its Poincare index (if the sum of indexes of singular points is equal to 0 or 4, so the system has azeotrope with index +1 or -1);

3) the identification of separatrix manifolds and the type of azeotrope (stable node, unstable node or the saddle). If the azeotrope is presented as a node on all the separatrix manifolds than it will be a node. If it is presented as a saddle at least on one of the separatrix manyfold than its type will be saddle.

The model five-component system *i-j-k-l-m* containing 10 binary, 10 ternary and 5 quaternary azeotropes will be considered as an example. The scan of all the tetrahedrons will be the same for all the quaternary constituents. The structure of the

scan (a), separatrix manifolds in concentration simplex (b,c) are presented in Figure 1.

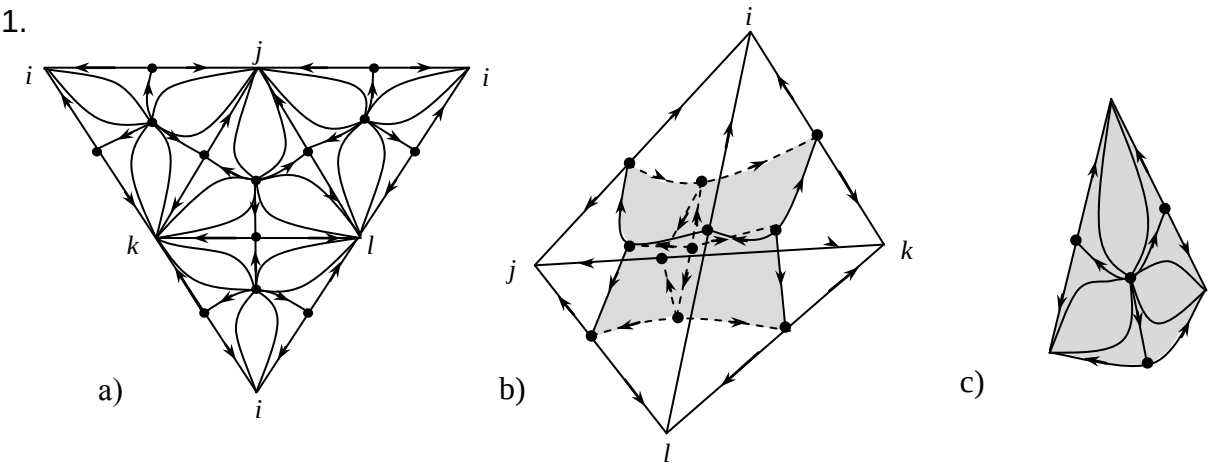

Figure 1:The Structure of the scan (a), concentration simplex (b), and separatrix manifolds (c) in quaternary constituents

Having the structure of concentration tetrahedron the Poincare indexes for all the binary and ternary singular points can be easily determined because the sign of 4 eigenvalues are known (Table 1).

Singular point	The scan		Full simplex (*Case 1*)		Full simplex (*Case 2*)	
	Type	*i*	Type	Type	*i*	*i*
Pure components *i, j, k, l, m*	N^{y}	+1	N^{+}	+1	N^{+}	+1
Binary azeotropes *ij, ik, il, im, jk, jl, jm, kl, km, lm*	*C*	-1	*C*	-1	*C*	-1
Ternary azeotropes *ijk, ijl, ijm, ikl, ikm, ilm, jkl, jkm, jlm, klm*	*C*	+1	*C*	+1	*C*	+1
Quaternary azeotropes *ijkl, ijkm, iklm, jklm* *ijlm*	N^{H}	-1	*C*	-1	N^{H} C	+1 -1
∑	**-**	**0**	**-**	**0**	**-**	**2**

Table 1: Types and Poincare indexes of all the boundary singular points concerning the third dimension scan of concentration simplex of five-component system and its complete structure.

To find out the Poincare indexes of quaternary azeotropes in the concentration simplex of five-component mixture it is possible to use the express-method [2]. The main idea of the method is studying the temperature changing deep into pentatope by conjugate composition adding to the composition of quaternary azeotrope. In this case the signs of all the eigenvalues will be known.

Case 1: Suppose all the quaternary azeotropes changed their type from unstable node (*i*=-1) to a saddle (*i*=-1) at the transition from the scan of pentatope to his its full structure (Table 1).

The sum of Poincare indexes for the full structure of five-component system should be equal to 2, but in the studied case it is zero. It means that there is five-component azeotrope with index +1. So it can be unstable node or positive saddle. To find out the type of the azeotrope it is necessary to study the structure of separatrix manifolds. There are 5 separatrix manifolds of the same structure in studied system (Figure 2).

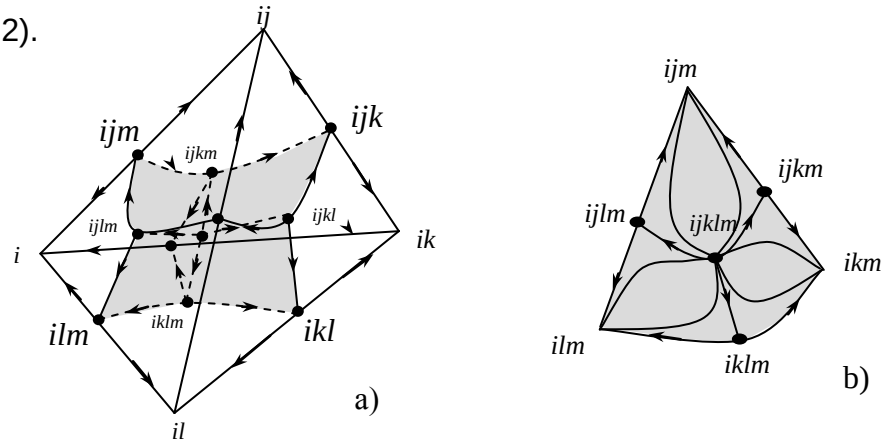

Figure 2: The structure of three- (a) and two-dimentional (b) separatrix manifolds for the system with five-component azeotrope

According to the item 3 the type of the azeotrope will be a node.

Case 2: Suppose only one quaternary azeotropes changed its type (became the saddle with *i*=-1) at the transition from the scan of pentatope to its full structure and the others will stay unstable node with *i*=+1 (Table 1). In this case the sum of Poincare indexes for the complete structure of five-component system will be equal to 2. It means that the system doesn't contain five-component azeotrope. The structure of the separatrix manifolds will be another one (Figure 3).

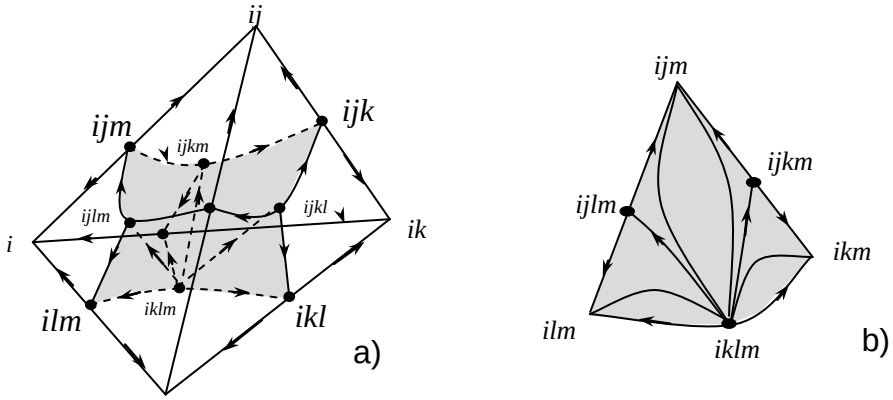

Figure 3: The structure of three- (a) and two-dimentional (b) separatrix manifolds for the system without five-component azeotrope

The validity of the proposed method was confirmed by mathematic modelling of phase equilibrium of real five-component systems: acetone – methanol – methylacetate – ethylacetate – water (contains only binary azeotropes), ethanol – water – toluene – buthanol – fluorbenzene (contains binary and ternary azeotropes), acetone – chloroform – water – n-heptane – ethanol (contains azeotropes with the number of components from 2 to 5).

3. Mathematical modelling

Phase diagram of system acetone (A) – methanol (M) – methylacetate (MA) – ethylacetate (EA) – water (W) will be considered as an example. Mathematical modelling of vapour-liquid equilibrium of the system was based on the NRTL equation using AspenTech. The results of comparison of experimental and calculated azeotropic data are presented in Table 2.

Azeotrope	X_1^{cal}, mole frac.	T^{cal}, C	X_1^{exp}, mole frac.	T^{exp}, C
A-M	0,776	55,5	0,777	55,24
A-MA	0,544	55,8	0,578	55,6
M-MA	0,332	53,8	0,332	53,62
M-EA	0,710	62,2-62,4	0,704	62,25
MA-W	0,970	56,4-56,5	0,988	56,9
EA-W	0,690	70,5	0,673	71,61

Table 2: Experimental and calculated azeotropic data for the system acetone (A) – methanol (M) – methylacetate (MA) – ethylacetate (EA) – water (W).

The scans and concentration tetrahedrons of five quaternary constituents are presented on Figure 4. Systems acetone – methanol – ethylacetate – water and acetone – methylacetate – ethylacetate – water have the same structure of phase diagram as well as systems acetone – methanol – methylacetate – ethylacetate and acetone – methanol – methylacetate – water. Presented scans allow to get the full information on the four eigenvalues of all singular points: clean components and binary azeotropes (table 3).

Singular point		A	M	MA	EA	W	A-M	A-MA	M-MA	M-EA	MA-W	EA-W	∑
Scan	Type	*CN*	*CN*	*CN*	N^y	N^y	*CN*	*CN*	N^H	*CN*	*CN*	*C*	--
	i	0	0	0	+1	+1	0	0	-1	0	0	-1	**0**
Pentatope	Type	*CN*	*CN*	*CN*	N^y	N^y	*CN*	*CN*	N^H	*CN*	*CN*	*C*	--
	i	0	0	0	+1	+1	0	0	+1	0	0	-1	**2**

Table 3: The types and indexes if singular points on the scan and pentatope of the system acetone (A) – methanol (M) – methylacetate (MA) – ethylacetate (EA) – water (W).

The sum of indexes of singular points on pentatope is equal to two that is in full compliance with rule (1). It means that the system does not contain five-component azeotrope.

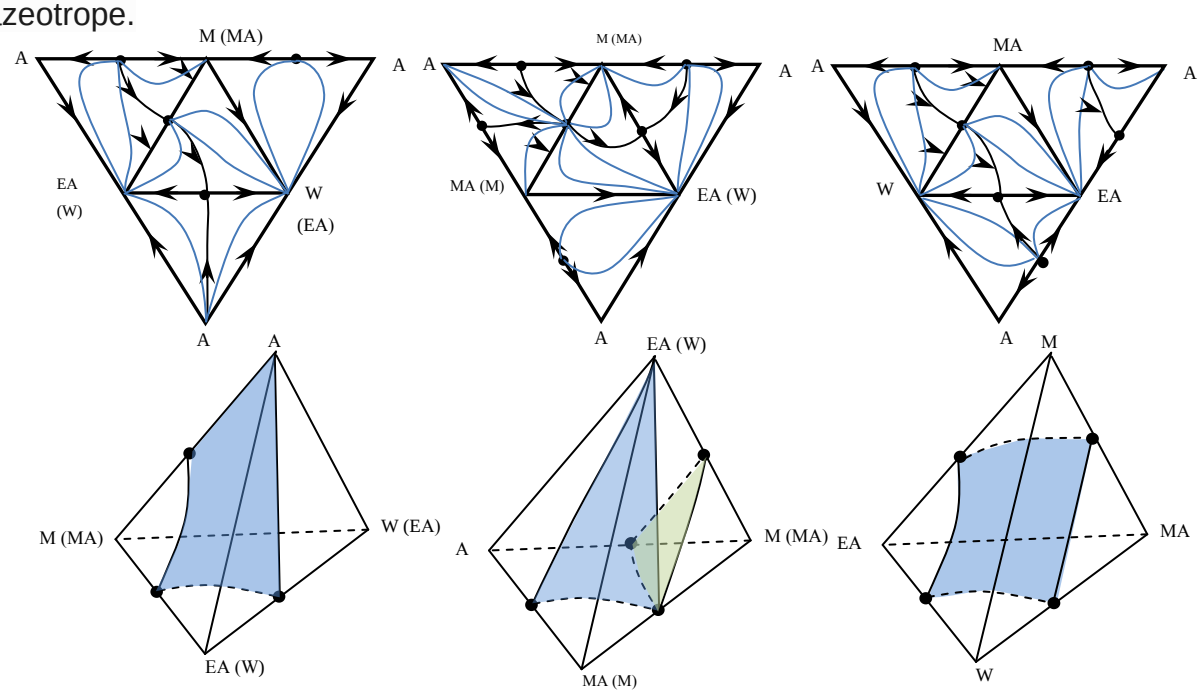

Figure 4: The structure of the scan and concentration tetrahedrons of quaternary constituents of system acetone (A) – methanol (M) – methylacetate (MA) – ethylacetate (EA) – water (W).

4. Conclusion

Phase diagram is the basis of separation technological schemes creation. It gives all information about the azeotropes and separatrix manifolds which impose thermodynamic limits on mixture separation based on distillation. The proposed method can be used for studying vapor-liquid phase diagram of five-component systems and predicting the existence of five-component azeotrope.

Acknowledgements

This work was supported by the Russian Foundation of Fundamental Research (№13-03-00222/13).

References

1) Serafimov L.A. Mathematical method in contemporary chemistry. Chapter 10. Thermo dynamical and topological analysis of liquid-vapor phase equilibrium diagrams and problems rectification of mulricomponent mixtures. Gordon and Brierch. 1996.P.557-603

2) Garov V.T., Serafimov L.A. Phisical-chemical basis of distillation and rectification processes.1975. 240 p.

Optimization of Process Purification Alternatives for Biobutanol Production

Eduardo Sánchez-Ramírez[a], Juan José Quiroz-Ramírez[a], Juan Gabriel Segovia-Hernández[a], Salvador Hernández[a], Adrián Bonilla-Petriciolet[b].
[a]Universidad de Guanajuato, Campus Guanajuato, Departamento de Ingeniería Química, Noria Alta s/n, 36050, Guanajuato, Gto., México.
[b]Instituto Tecnológico de Aguascalientes, Departamento de Ingeniería Química, Av. Adolfo López Mateos #1801 Ote., Fracc. Bona Gens, C.P. 20256, Aguascalientes, Ags., México.

Abstract

Butanol is primarily used as a solvent or component in surface coatings; it has characteristics similar to petroleum fuel and is considered as a superior biofuel to bioethanol. Biobutanol is more energy dense and less hygroscopic than bioethanol, resulting in higher possible blending ratios with gasoline. Development of technologies for biobutanol production by fermentation has resulted in higher final biobutanol concentrations, less fermentation by-products and higher volumetric productivities during fermentation, together with less energy intensive separation and purification techniques. These new technological developments have the potential to provide a production process for biobutanol that is economically viable in comparison to the petrochemical pathway for butanol production. In this study we have studied and compare four different possible process designs for the purification of biobutanol production. Process Route 1, 2 and 3 consisted of steam stripping distillation and distillation columns, while in Process 4, some of the distillation columns were replaced with a liquid–liquid extraction column and incorporated gas-stripping with CO_2, which is an unproven technology on industrial scale. Process modeling in Aspen Plus was performed and the optimization was conducted using DE-TL with a link between Aspen Plus and Excel. Our results indicated that Process Route 4 proved to be a profitable design in current economic conditions, and it appears to be the most effective of those evaluated in this study. This alternative process can be employed on an industrial scale to improve process economics of biobutanol production.

Keywords
Biobutanol, ABE fermentation, Differential Evolution with Tabu list.

1. Introduction

n-Butanol and some other isomers can be produced from biomasses by fermentation and, at this time, the n-butanol from fossil fuels (“petrobutanol”) produced by either the oxo- or adol-process is the most used [1]. Despite fermentation of carbohydrates to the mixture of n-butanol with ethanol and acetone was a known process, ABE fermentation could not compete with n-

butanol produced synthetically from the petrochemical industry due to cost issues and relatively low yield. During 1980s and 1990s substantial advances were made in the development of genetic systems for Clostridia species used in ABE fermentation, which would allow for the development of strains with improved fermentation characteristics [2]. Nevertheless, the main obstacle remains in the high cost of the substrate, the low fermentation product concentration (about 2%wt), and the high product recovery cost. During the last years, hyper-butanol-producing strains have been developed as a result of genetic manipulation and modern molecular techniques applied to some Clostridia species and, recently, to different strain species that do not produce naturally n-butanol [3]. Computational engineering and experimental efforts have been made in order to improve those fermentation techniques, which results include a significant increase of butanol titer, yield and decrease of downstream process costs [4]. In spite of the recent advances in this field, however, the experimental and simulation studies of ABE process are limited [5-9]. Product purification is one of the challenges associated to the commercial production of biobutanol because the low concentration of products obtained from fermentation, which leads to great energy consumption during the purification process. Also, the separation is relatively complicated due to presence of two azeotropes, ethanol-water and water-butanol, homogeneous and heterogeneous, respectively.

This study is focused on the global optimization of four different conceptual designs already published [10] for the purification of biobutanol production(see Figure 1). They are possible process routes for industrial scale biobutanol production from sugarcane molasses. Specifically, process designs A and B were based on the base case process design simulated in the study of Roffler et al. [11]. On the other hand, process design C was based on the base case process design studied by Marlatt and Datta [5]; while process design D was based on the base case process design reported by Dagdar and Foutch [6]. These process designs were initially implemented in the process simulator Aspen Plus, where the simulated process models were robust and thermodynamically rigorous. The NRTL-HOC model was the most accurate physical property method available for the components used at the specified conditions [12]. It was assumed that all process designs have the same stream feeds except LLE design where it was added hexyl acetate as extractant.

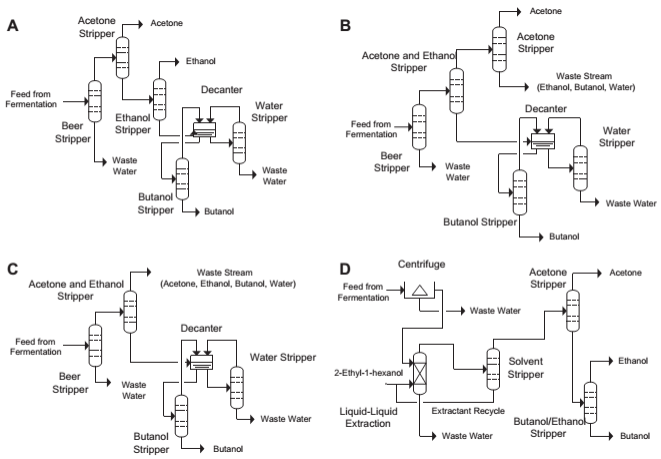

Figure 1. Flow diagrams for downstream processing of process design (A) 1.1, (B) 1.2, (C) 1.3and (D) 2.

The product purities achieved in all process simulation were at least of biobutanol 99.5% (wt%), acetone 98% (wt%) and ethanol 99% (wt%).
In this work, we used the differential evolution (DE) and tabu search as optimization strategy. In particular, the integration of differential evolution (DE) and tabu search (TS) are capable of solving non-differentiable, non-linear and multi-modal objective functions to find the global minimum. DE is a population based method that mimics biological evolution by performing mutation, crossover and selection steps to find the global optimum. TS is a point-to-point method that uses an adaptive memory to avoid re-visits to the same place in the search region and to identify promising areas for optimization [13].
The implementation of this optimization system was made through a hybrid platform. The vector of decision variables is sent to Microsoft Excel to Aspen Plus using DDE (Dynamic Data Exchange) through COM technology. The use of COM technology makes possible adding code because such application behaves like linking incrustation objects (OLE) of automatized servers. In Microsoft Excel, these values are attributed to process variables that Aspen Plus needs. After simulation is done, Aspen Plus returns to Microsoft Excel the resulting vector. Finally, Microsoft Excel analyzes the objective function values (Figure 2) and proposes novel solutions for the optimization problem.

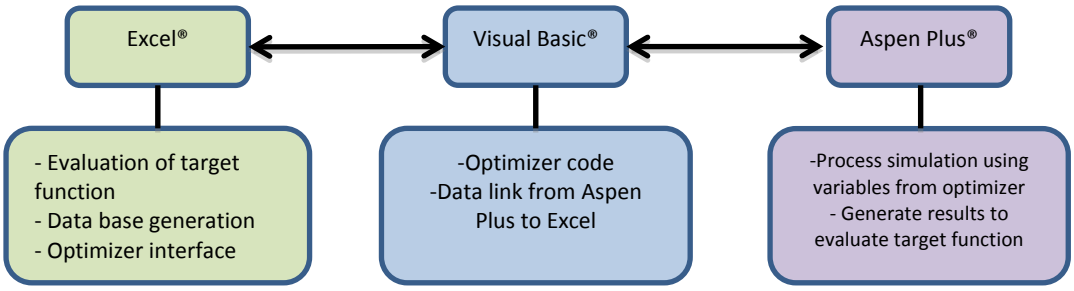

Figure 2. Hybrid platform for the optimization of process designs.

In all the four process designs, the optimization problem for minimization of total annual cost is defined as:

$$Min(TAC) = \left(N_{tn}, N_{fn}, R_{rn}, F_{rn}, D_{cn}\right)$$

subject to

$$\overrightarrow{y_m} \geq \overrightarrow{w_m}$$

$$\overrightarrow{x_m} \geq \overrightarrow{z_m}$$

where N_{tn} is the total trays, N_{fn} is the feed stage, R_{rn} is the reflux ratio, F_{rn} is the distillate flux, and D_{cn} is the diameter of all columns in the process design. Note that in the design D, it was substituted N_{fn} instead of M_{ex}, which is the total amount of extractant, while $\overrightarrow{y_m}$ and $\overrightarrow{x_m}$ are the vectors of obtained and required purities for the m products.

2. Results and discussion

Based on an average feed [14], all sequences were initially designed, fulfilling all the purity and recovery restrictions. Initially, some optimization process were made in order to tune in parameters of stochastic method, also delimit boundaries where algorithm could converge according to the nature of the process to optimize, once made all pre-optimization, it was made an optimization process until there was not better values in the result vector. All responses are plotted in Figures 3-6.

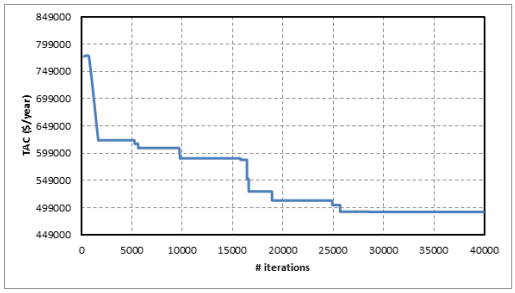

Figure 3. Response of process design A.

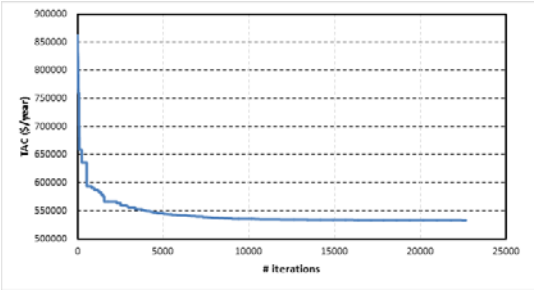

Figure 4. Response of process design B.

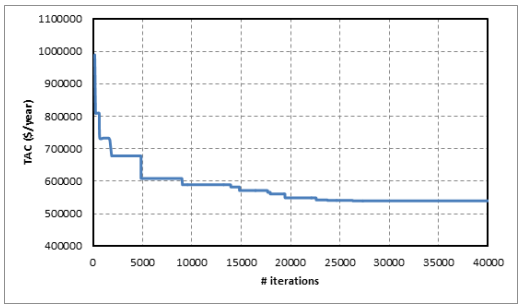

Figure 5. Response of process design C.

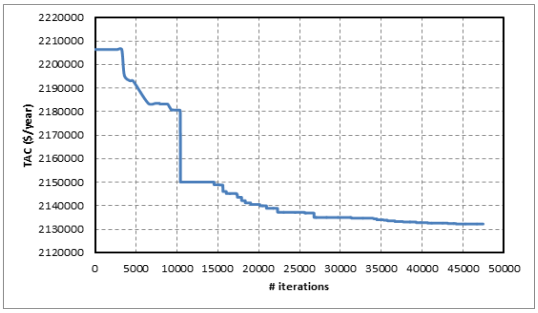

Figure 6. Response of process design D.

As it can be seen in Figures 3-6, at the final of the plot there is no change in all responses, what it could means that this final vector could be a possible global optimal or a pretty close point, nevertheless there is no certainty of this because we do not know the optimal point, this means that we could be in a local optimal and this optimization method has no capacity to leave this point.

Graphically it could be seen the big difference between the initial and the final point in process design A, B and C, but is not the same with process design D. This results does not mean that process design D has less possibilities of being optimized, all this changes in figure 3-6 it depends totally of the initial point where stochastic method begin to work. Basically, it could be watched the differences between costs of all process design, before optimization process it could be thought that process design A would be most expensive due to all solvents are purified, and process design B would be the cheapest because only butanol is purified. Nevertheless according to A,B. van der Merwe [10] process design A has the minor capital cost followed by process design B, D and finally C. Also, after optimization process study we find that process design A remains the cheapest, followed by process design C, B and finally D, and our

results indicated that the capital cost of every column in process design A is cheaper than columns in process design C.
In other words, process design A has the second biggest energy requirements, however the size of columns result in a lower capital cost which is reflected in a minor total annual cost. Otherwise with process design D, where energy requirement are the smallest but capital cost of columns are the highest which again are reflected in total annual cost.

Table 1 General Characteristics of results from the optimization of process designs for biobutanol production

	Process design A					Process design B					Process design C				Process design D			
	C1	C2	C3	C4	C5	C1	C2	C3	C4	C5	C1	C2	C3	C4	LLE	C1	C2	C3
Column Topology																		
Numeber of stages	5	47	36	24	6	5	20	21	5	4	4	25	24	7	8	25	54	33
Feed stage	4	33	22	9	4	3	11	19	2	2	2	10	8	4	1	13	34	12
Specifications																		
Distillate rates (lbmol/hr)	2.028	0.2954	0.01837	0.6582	0.74351	2.0482	0.314	0.2907	0.5788	0.5198	2.0271	0.4095	0.786	0.7904		0.7154	0.2933	0.0159
Boilup ratio	6.2467	2.7677	1.4237	7.3721	19.7019	9.2002	7.2637	8.3156	9.2732	1.4003	6.3303	3.9096	1.1759	2.3215		15.8659	1.6192	0.2374
Diameter (ft)	3.0404	1.7325	1.4509	1.9265	1.8343	1.0226	0.9963	0.986	1.0056	1.011	3.0404	1.3105501	1.236828	1.2229	0.9978	0.9508	0.9441	0.9456
Feed Streams																		
Acetone flowrate lb/hr)	16.9502	16.9502	0.0000			16.9502	16.9475	16.9475	0.0000	0.0000	16.9502	16.9487	0.0000	0.0000	16.9502	16.9502	16.9502	0.0016
Butanol flowrate (lb/hr)	30.1809	30.1808	30.1808	7.6988	47.5100	30.1809	30.1664	0.0000	40.6966	9.1420	30.1809	30.1772	7.8575	49.1314	30.1809	30.1810	30.1024	30.1024
Ethanol flowrate (lb/hr)	0.7289	0.7289	0.7168	0.0210	0.0407	0.7289	0.7268	0.7192	0.3022	0.2047	0.7289	0.7279	0.0002	0.0003	0.7289	0.7289	0.7289	0.7287
Water flowrate (lb/hr)	52.1398	23.6581	23.5986	33.5174	9.1590	52.1398	24.0276	0.1198	7.8856	30.8197	52.1398	23.6429	34.2718	9.4220	52.1398	0.0300	0.0300	0.0021
Hexyl acetate flowrate (lb/hr)															2011.1701	2013.1800	0.0001	0.0001
Product streams																		
Acetone flow (lb/h)	0.0001	16.9502	2.70E-09			0.0025	8.79E-09	16.8527	4.56E-10	1.73E-10	0.0015	16.9487	1.56E-30	9.19E-14	1.73E-05	5.84E-08	16.9487	0.0016
Acetona putiry (wt%)		0.9957						0.9988				0.8383					0.9983	
Butanol flow (lb/h)	0.0001	0	1.27E-06	3.47E-24	30.1801	0.0136	30.1664	0.0148	30.1314	0.0153	0	0.8897	2.30E-21	29.2700	2.51E-06	0.0785	0.0000	2.36E-05
Butanol purity (wt%)					0.9996				0.9951					0.9997				
Ethanol flow (lb/h)	0.0001	0.0120	0.7166	9.28E-20	0.0001	0.0012	0.0076	0.0003	0.0052	0.0019	0.0010	0.7279	0.0000	0.0000	2.57E-06	9.08E-10	0.0003	0.7286
Ethanol purity (wt%)			0.9430															0.9960
Water flow (lb/h)	28.4817	0.0594	0.0507	23.5384	0.0096	28.1114	23.9078	0.0047	0.1413	23.7517	28.4990	1.6167	22.0193	0.0069	52.1099	3.38E-49	0.0279	0.0021
Water purity (wt%)	0.9999			0.9999							0.9997		0.9999					
															0.0034	2013.1798	4.55E-66	4.01E-19
Energey requirements																		
Reboiler duty (cal/s))	173300	86348	43933	169006	149254	162362.69	131308.4	133585.6	178065	24702.9	176200	113839	25219	43112		282042	30786	4402
Condenser duty (cal/s)	-161386	-85538	-43907	-165711	-145587	-155794.24	-130099	-133612	-172692	-19728.4	-164288	-113346	-21898	-39362		-25853	-29631	-4301
Economic Evaluation																		
Capital cost ($)	51117	85111	126520	95961	51838	38072	37109	38369	40950	297924	38894	42874	271325	132562	1884	132398	90119	1866528
Total annual cost ($/year)			491158					534094				532289				21329966		

3. Conclusions

Process optimization is a great tool in order to find new and better values in multivariable planes. In this case we watched that implementing an optimization methodology in a downstream process, the costs were reduced. According to optimization process, process design A represented the process with the smallest total annual cost regardless that all solvents are purified. In future, it could be analyzed this designs considering another goal that impact directly in costs such as energy requirements, thus combining targets this designs could be improved.

As known, the downstream process can have a great impact in fermentation process due to purification cost. This methodology combined with all research efforts could lead in future years to a profitable ABE fermentation process, which could compete with traditional ways to produce butanol.

Acknowledgements

Authors acknowledgement to CONACYT (Mexico) and Universidad de Guanajuato the economical support during the realization of this work

References

1.- Brekke K. Butanol: an energy alternative. Ethanol Today 2007:36–9.
2.- Ezeji TC, Qureshi N, Blaschek HP. Acetone butanol ethanol (ABE) production from concentrated substrate: reduction in substrate inhibition by fed-batch technique and product inhibition by gas stripping. Appl Microbiol Biotechnol
2004;63:653–8.
3.- Ezeji T, Qureshi N, Blaschek H. Bioproduction of butanol from biomass: from genes to bioreactors. Biotechnology 2007:220–7.
4.- Groot WJ, Reyer MCH, Faille TB, Lans RGJM, Luyben KChAM. Integration of pervaporation and continuous butanol fermentation with immobilized cells. Chem Eng J 1991;46:B1–B10.
5.- Marlatt J, Datta R. Acetone-butanol fermentation process development and economic evaluation. Biotechnol Prog 1986;2:23–8.
6.- Dadgar A, Foutch G. Improving the acetone-butanol fermentation process with liquid–liquid extraction. Biotechnol Prog 1988;4:36–9
7.- Liu J, Fan L, Seib P. Downstream process synthesis for biochemical production of butanol, ethtanol, and acetone from grains: generation of optimal and nearoptimal flowsheets with conventional operating units. Biotechnol Prog 2004;20:1518–27.
8.- Liu J, Fan L, Seib P, Friedler F, Bertok B. Holistic approach to process retrofitting: application to downstream process for biochemical production of organics. Ind Eng Chem Res 2006;45:4200–7.
9.- Liu J, Wu M, Wang M. Simulation of the process for producing butanol from corn fermentation. Ind Eng Chem Res 2009;48:5551–7.
10.- A.B. van der Merwe, H. Cheng, J.F. Görgens, J.H. Knoetze. Comparison of energy efficiency and economics of process designs for biobutanol production from sugarcane molasses. Fuel (2012).
11.- Roffler S, Blanch H, Wilke C. Extractive fermentation of acetone and butanol: process design and economic evaluation. Biotechnol Prog 1987;3:131–40.
12.- Chapeaux, A.; Simoni, L. D.; Ronan, T. S.; Stadtherr, M. A.; Brennecke, J. F. Extraction of Alcohols from Water Using 1-Hexyl-3- methylimidazolium Bis(trifluoromethylsulfonyl)imide. Green Chem. 2008, 10, 1301.
13.- Bonilla - Petriciolet, A., Rangaiah, G.P. Segovia - Hernández, J.G., Jaime – Leal, J.E., 2010, “Phase Stability and Equilibrium Calculations in Reactive Systems using Differential Evolution and Tabu Search” en Stochastic Global Optimization: Techniques and Applications in Chemical Engineering, Editado por Rangaiah, Gade Pandu, World Scientific Inc, (ISBN: 978-981-4299-20-6), Singapur, 413 - 463.
14.- M.Wu, M. Wang, J. Liu, and H. Huo. Life-Cycle Assessment of Corn-Based Butanol as a Potential Transportation Fuel. ANL/ESD/07-10

ANALYSIS OF THE TEMPERATURE FOLDS ON THE PHASE EQUILIBRIUM DIAGRAMS OF TERNARY SYSTEMS

Frolkova A.K., Frolkova A.V., Neudakhina A.A.
Lomonosov Moscow State University of Fine Chemical Technology, Moscow, Russia

Abstract

Temperature folds in ternary splitting systems were studied. It was shown that temperature fold may be generated by one point of the equilibrium liquid phase of binary heteroazeotrope (one fold is of first dimension and another one of zero dimension) or by both points of equilibrium liquid phases of heteroazeotrope (both folds of first dimension). The peculiarities of temperature folds formation depends on the structure of ternary system phase diagram. Liquid-liquid-vapor equilibrium of real ternary systems was modeled and the diagrams of temperature folds were presented. The presence of the temperature fold allowed to explain the extremum on the temperature profile of extractive distillation column. This fact was confirmed by calculating extractive distillation of the mixture diethylketone – water in the presence of dimethylsulfoxide and comparing the temperature profiles for extractive distillation and ordinary distillation columns.

Keywords

temperature folds, splitting systems, phase diagram, extractive distillation

1. Introduction

Isomanifolds of distribution coefficients of components and coefficients of relative volatility, isoterms-isobars are widely used for identification of new thermodynamical-geometric regularities of phase diagrams structures, including practical importance in organization and predicting results of complex mixtures separation. The Bankroft isoterms-isobars (the equality of vapor pressure of the initial components) and pseudo-ideal manifolds (the equality of activity coefficients) play an important role in diagram transformations in the presence of additional substances. Additional information about the nature of phase processes can be obtained from the mutual location of distillation process trajectories and temperature folds, along which the

temperature extremum can be observed and one of the partial temperature derivatives is equal to zero [1]:

$$\frac{\partial T}{\partial x_i} = 0,$$

where T – temperature, x_i – concentration of the component i in liquid phase.

Analysis of mutual location of temperature folds and trajectories representing temperature (concentration) changes along distillation column allows developing the approach to selection of energy efficient modes of azeotropic mixtures separation, in particular, by extractive distillation (ED). The multilevel supply of initial mixture and extractive agent in ED is indispensable condition and it leads to the presence of extremums on the temperature (concentration) profile in the middle part of columns due to the counterflow. In such organization of flows in complex column the possibility of energy consumption reduction in ED in comparison with other separation methods (in some cases up to 20 %) by means of partial compensation of work of separation of initial mixture *ij* by work of mix of separating agent with one of the component (*i* or *j*) was shown in [2].

From one hand the research of temperature folds allows to prove the presence of extremums on the temperature profiles of ED column and from another hand – to define the range of change of separation agent consumption providing positive effect of multilevel feed supply. This range is limited by the separation agent (SA) concentrations corresponding to output of the line of relative volatility (α_{ij}=1) and temperature fold to the binary constituent (*i*-SA or *j*-SA).

The location of temperature folds in ternary homogeneous systems was studied previously [3]. The prevalence of splitting systems in technology of organic substances and the possibility of their research using gross and net concentrations of components in equilibrium liquid phases determine the relevance of this study.

2. Results and discussion

Special features of formation of temperature folds generated by binary heteroazeotropes in 14 ternary splitting systems of different topological structure were studied. The liquid-liquid-vapor phase equilibrium using NRTL equation and AspenTech software were modeled for all systems.

Temperature folds in splitting area are generated by two singular points corresponding to equilibrium liquid phases of binary heteroazeotrope. There are two cases (Figure 1): one of the folds is of the zero dimension and another one is of first dimension (a); both folds are of first dimension (b). The second case is much rarer.

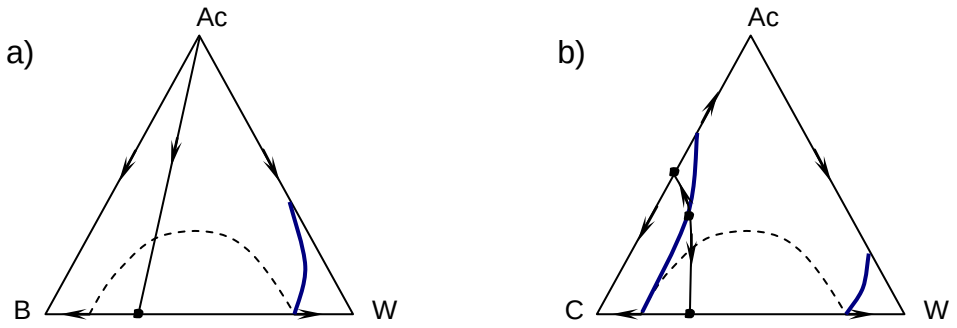

Figure 1: Temperature fold formation in binary heteroazeotrope in two ternary systems: acetone – benzene – water (a) и acetone – cyclohexane – water (b).
——— – temperature folds, ⟶ – distillation lines, - - - - - – boundary of splitting area

The progress of the temperature fold is determined by presence (absence) of binary and ternary azeotropes. If the system contains ternary homogeneous or heterogeneous azeotrope than all the folds will pass across it, while in the second case they will belong to the liquid-liquid equilibrium conoda corresponding to ternary azeotrope (Figure 2a, b). If ternary azeortope is missing in the system than the temperature folds will not intersect.

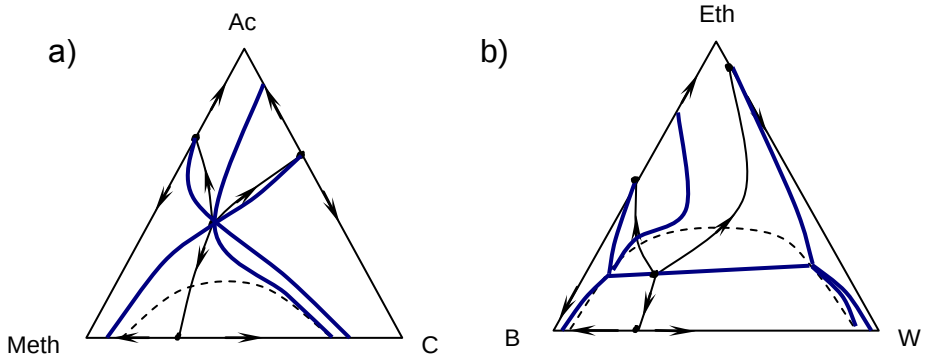

Figure 2: Temperature folds features in ternary systems containing ternary homogeneous and heterogemeous azeotrope:
(a) – acetone – methanol – cyclohexane; (b) – ethanol – benzene - water
——— – temperature folds, ⟶ – distillation lines, - - - - - – boundary of splitting area

Extractive distillation of the splitting azeotropic mixture diethylketone – water in the presence of different amount of extractive agent was modeled. Dimethylsulfoxide (DMSO) was chosen as an extractive agent. The addition of DMSO allowed to

increase the volatility of the diethylketone (DEK) more than two times. Calculation of extractive distillation process was made for the next mixture composition: x_{DEK}=0.5 mole frac, x_{water}=0.5 mole frac. The number of theoretical stages was 20, the feed of mixture was on the 15th stage, extractive agent – on the 5th, reflux ratio varied from 1 to 3.

For different ratios of initial mixture and extractive agent quantities (case I – 1:2, case II – 1:3, case III – 1:11, case IV – 1:13) the trajectories of extractive distillation process in concentration simplex and the temperature profiles are presented on Figure 3. Temperature extremum is observed for cases I and II (intersection of temperature fold and ED trajectory); case III – extremum degeneration; case IV – extremum absence (no intersection of temperature fold and ED trajectory). Case III is limiting case for selection the necessary amount of SA for effective separation process. The increase of the ratio of initial mixture and SA more than 1:11 will lead to deterioration of the quality of the products.

The trajectory of ordinary distillation process is also presented in Figure 3 a.

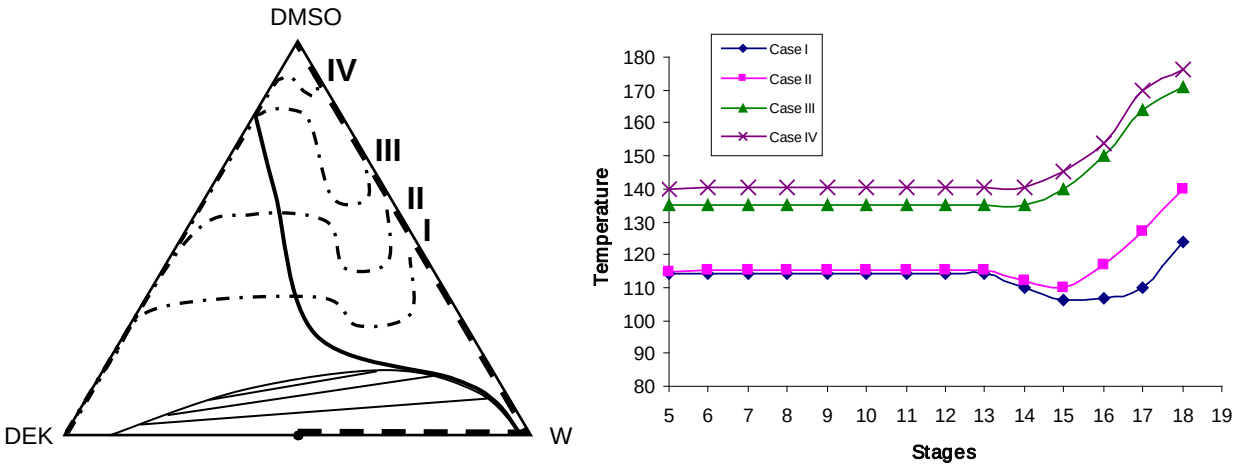

Figure 3. Mutual location of the temperature folds (———) and the trajectories of ordinary (– – –) and extractive distillation (– · –) in ternary system (a); temperature profile (b).

3. Conclusion

The trajectory of ordinary distillation process will never intersect temperature fold and therefore the temperature will monotonically decrease from bottom to distillate of distillation column in full accordance with Konovalov law. This law is broken in case of extractive distillation and the reason is the intersection of temperature fold and trajectory process.

Acknowledgement

Work was carried out according to the state task of the Russian Ministry of Education and Science # 10.99.2014/K.

References

1. Storonkin A.V. Thermodynamics of heterogeneous systems (in Russian).1967.

2. Frolkova A.K. Theoretical basis of separation of multicomponent multiphase systems with the use of functional complexes. Thesis Dr. of Sci. Moscow. MITHT. 2000. 364p.

3. Serafimov L.A., Bushina D.I. Folds on the temperature surfaces of heterogeneous multicomponent liquid-vapor systems. Theoretical Foundations of Chemical Engineering. 2008. V.42 (3). P.278

Theoretical study of thermodynamic influences on physical absorption solvents by means of an abstract flow sheet

Regina Deschermeier[1], *Prof. Dr.-Ing. Harald Klein*[1]
[1] *Technische Universität München, Garching, Germany;*

Abstract
One starting point for improvements of physical absorption processes is the used solvent. For finding new solvents or additives a theoretical study is presented as part of a combined experimental und theoretical approach. The flow sheet of an absorption process therefore is reduced to the thermodynamic relevant steps. The basic points of the model, which is implemented in MATLAB®, are shown. The solvent itself is treated as virtual component so its pure component properties can be varied independently to a certain extent within the used thermodynamic model. Different sets of parameters are created starting with only few pure component properties, the remaining parameters for the thermodynamic model are estimated using common estimation methods. With the presented tool solvents can be characterized and their influence on a physical absorption process can be studied. The benefit of this approach is a reduction of screening experiments by decreasing the number of potential solvent candidates.

Keywords
solvent, physical absorption, thermodynamic model

1. Introduction

For the separation of sour gases like carbon dioxide from a gas stream physical absorption processes are used in process industry. An example for such a process is the Rectisol® process which uses cold methanol as solvent. Possible aspects for improving these processes are:

- the process flow sheet itself
- the solvent and
- the equipment design.

This study focusses on the influence of the solvent. To achieve a better process performance either a completely new solvent or an additive for an already existing solvent is desired. For both options experimental or theoretical approaches are possible. Screening experiments to find new solvents, or additives for already existing solvents, are often time consuming and cost a lot of resources. The aim of this study is to give a deeper understanding of the interactions of the thermodynamic properties. With this knowledge better estimates of suitable solvent candidates can be found and the effort for experimental studies can be reduced. In the following only the theoretical part is discussed.

In literature there are many different approaches for the integration of process and solvent design in order to find new components fitting specific separation tasks, e.g. [1], [2], [3], [4], [5]. For the solvent design task computer-aided-molecular-design (CAMD) methods are commonly applied e.g. [6], [7], [8]. The aim of a CAMD method

is to find a component which satisfies a given set of desired target properties [8]. In [1] a continuous-molecular targeting approach to CAMD (CoMT-CAMD) is developed which consists of two steps: the first step delivers optimal parameters for the applied thermodynamic model and in the second step these properties are mapped to real molecules. The importance of a physical based and consistent thermodynamic model is emphasized in [1].

Instead of parallel optimization of the flow sheet, the process parameters and the thermodynamic properties of the solvent a more simple approach is chosen here. The flow sheet is reduced to the main thermodynamic steps which characterize the solvent performance in the absorption and desorption process.

2. Results and discussion

For the theoretical part a tool must be generated which allows the study of the performance of the solvent excluding the influence of specific absorption process characteristics. The presented approach is shown in **Figure 1**.

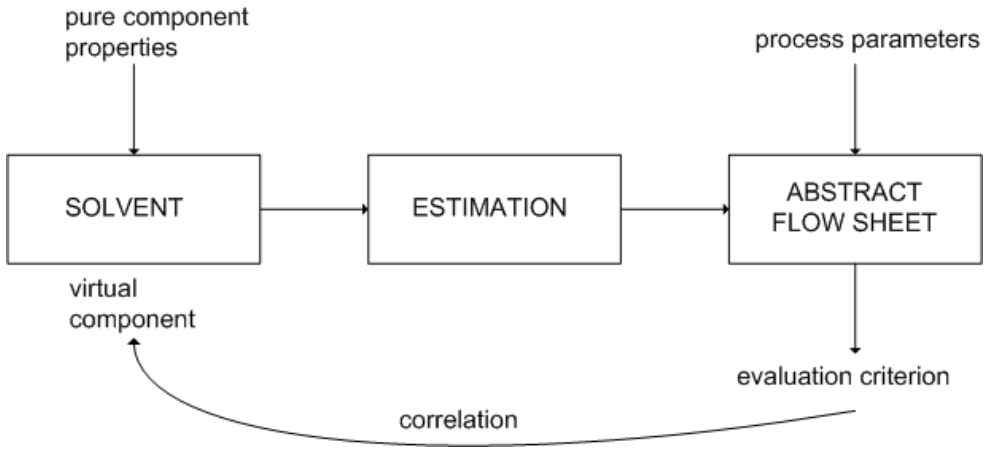

Figure 1 Scheme of the presented approach

Three steps are necessary: The solvent is treated as virtual component. Then missing properties for the thermodynamic model are estimated. Typical process parameters are specified and are the input of an abstract flow sheet. Calculation of the process flow sheet results in evaluation criterions from which conclusions can be drawn for the specified pure component properties of the virtual component.

2.1 Solvent as virtual compound

The solvent is not specified as a particular chemical component but it is treated as a so called virtual component. That means that the thermodynamic properties with which the component is described in the model are arbitrarily and to certain extend chosen independently. The choice which properties are specified and to which extend these are independent regarding the thermodynamic modelling influences how feasible and realistic the results will be. An overview of estimation methods for pure component properties shows that the following set of properties is very common as a starting point for estimation:

- molecular weight M_W,
- boiling temperature at normal conditions T_{NB} and

- density ρ at given temperature.

Group contribution methods like Joback are explicitly excluded here because structural information of the solvent molecule is not intended to be known. The estimation procedure is not described here in detail. The result of the first two steps is a number of different setups of thermodynamic properties for the virtual solvent. As main influences factors the solubility, e.g. given by the Henry coefficient, and the caloric properties, e.g. given by the heat capacity are considered.

2.2 Abstract flow sheet

The third step is to simplify the process flow sheet. The driving idea behind the simplification of the process flow sheet is to identify the steps in the process where mainly the solvent is involved and its thermodynamic properties are changed primarily. These steps are represented in the abstract flow sheet. Process engineering efforts to optimize a process by means of improvements of the flow sheet itself or heat integration are not considered here. The presented approach is based on the statement that a good solvent will show a good performance in the process and can be improved by process engineering knowledge later on. However, the choice which unit operations are kept in the abstract flow sheet and which constraints and specifications are made is based on process engineering knowledge. A physical absorption process as found in industrial applications can be divided into three sections:

- the absorption,
- the desorption and
- the regeneration of the solvent.

The abstract flow sheet is shown in **Figure 2**.

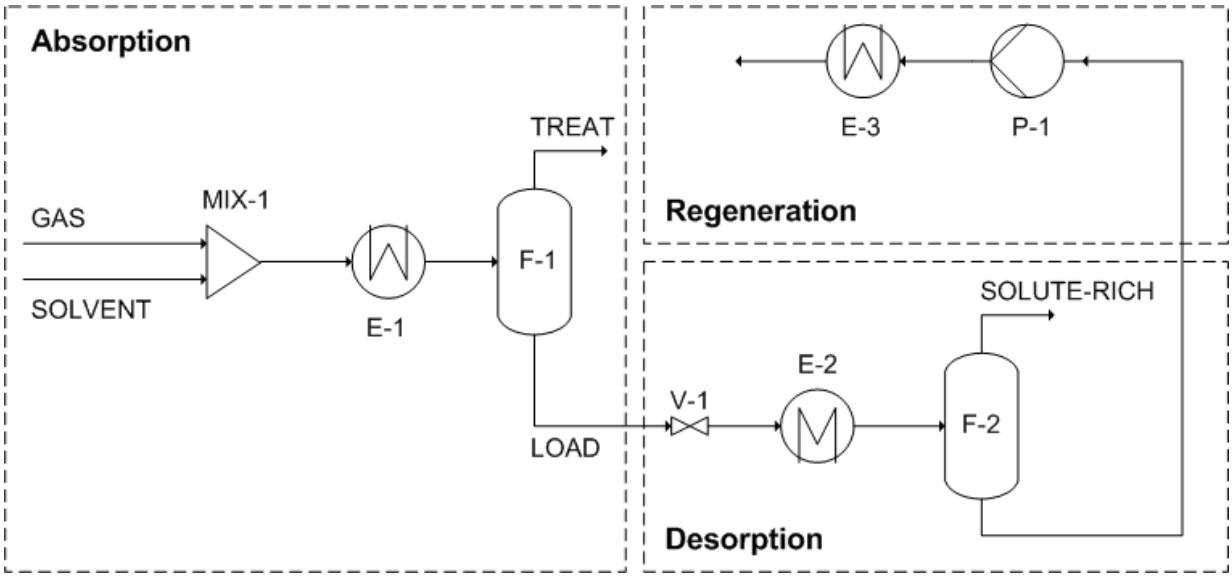

Figure 2 Abstract flow sheet of physical absorption process

It should be emphasized that this flow sheet is not the basis of a short-cut method but a tool for the evaluation of thermodynamically relevant operations in order to characterize the performance of a virtual solvent without any process optimization. In this context only one equilibrium stage, i.e. a flash stage instead of a column is used. An isothermal-isobaric flash stage is sufficient to describe the solubility at a certain

temperature and pressure and therefore to evaluate the thermodynamic performance of the solvent. As an advantage no additional degrees of freedom like number of stages or feed stage have to be specified. Changes in temperature are implemented as isobaric heat-exchangers and changes in pressure by isenthalpic valves.

In the first section, labeled Absorption, a stream GAS comprising of the solute and at least one inert gas is mixed with a pure solvent stream in an isobaric and isenthalpic mixer. The mixed stream is then heated to the desired absorption temperature. Due to the fact that in temperature and pressure of both feed streams equals the absorption temperature respectively pressure the heat to be removed in heat-exchanger E-1 is equal to the absorption enthalpy. An isothermal and isobaric flash unit separates the two-phase stream into a gas stream TREAT and a loaded solvent stream LOAD. The stream LOAD is then depressurized to a specified desorption pressure in an isenthalpic valve V-1 and heated at constant pressure to desorption temperature. The flash F-2 separates the entering stream into a solute-rich gas stream and solvent stream which has to be regenerated. Regeneration means here that the solvent stream is adjusted to absorption conditions concerning temperature and pressure. A recycle of the regenerated solvent is not taken into account in order to exclude influences of a pre-loaded solvent stream.

Instead of specifying a solvent flow rate an absorption rate is defined as the ratio of mole stream of solute in the liquid stream after absorption (LOAD) to the mole stream of solute in the feed (GAS). Thus, the solvent mole stream therefore is a result of the performance of the solvent, i.e. the solubility of the solute. Considering e.g. a physical absorption process for the separation of carbon dioxide from a synthesis gas stream the pure carbon dioxide stream for sequestration might be of interest. Accordingly a solute yield is defined for the desorption section as the ratio of mole stream of carbon dioxide in the solute rich stream leaving the flash F-2 (SOLUTE-RICH) to the carbon dioxide mole stream in the feed (GAS). The temperature of the isothermal-isobaric flash for desorption is varied in order to meet this specified solute yield. Both constraints are specified and determine the mole stream of the solute which leaves the process in the regenerated mole stream.

2.3 Modelling

The abstract flow sheet is implemented in MATLAB®. The basic equations are discussed below.

2.2.1 Phase equilibrium

The phase equilibrium for solvent components is calculated by Raoult's law and for solute components by Henry's law. For non-idealities in the gas phase fugacity coefficients are calculated by means of equations of state, e.g. Peng-Robinson or Soave-Redlich-Kwong. For the influence of mixture the van der Waal one-fluid mixing rule is used. The binary interaction coefficient is described based on [9]. Due to the fact that no density correlation for the virtual component is specified the molar volume is calculated with the equation of state.

2.2.2 Molar enthalpy

The molar enthalpy is determined based on the standard enthalpy of formation at reference temperature and pressure, a temperature departure term containing the

molar heat capacity of the ideal gas and a residual term for the real gas behavior. The last term is calculated using the selected equation of state.

2.2.2 Equations and unknowns

The process consists of 12 material streams, 8 unit operations and *K* components. Two pressures (absorption pressure in section Absorption and Regeneration, desorption pressure in section Desorption), two main temperatures (absorption and desorption temperature) and three unknown intermediate temperatures (after E-1, V-1 and P-1) can be identified. Expressing the composition of the material streams by means of component mole streams, for each material stream *K* component mole streams, one temperature and one pressure must be specified. In addition three heat streams (for the heat exchangers E-1 to E-3) and the power required for pump P-1 are unknowns.

For the unit operations material and energy balances can be formulated. Each flash unit delivers *K* phase equilibrium conditions (VLE conditions). For the pump one additional equation which considers the compression of the material stream is needed. A summary of available equations and the unknowns for the whole process is shown in **Table 1.**

Unknowns	number		sum
material stream	12	$K + 2$	$12K + 24$
heat stream/ power	4	1	4
			$12K + 28$

Equations	number	material balance	energy balance	VLE condition	additional equation	sum
flash	2	K		K		$4K$
mixer	1	K	1			$K + 1$
heater	3	K	1			$3K + 3$
valve	1	K	1			$K + 1$
pump	1	K	1		1	$K + 2$
						$10K + 7$

Table 1 Summary of unknowns and equations

With $12K+28$ unknowns and $10K+7$ equations $2K+21$ variables have to be specified. These variables are $2K$ component mole streams of the two feed streams (GAS and SOLVENT), the pressure of 12 streams and the temperature of 9 streams. The component mole stream of component solvent in stream SOLVENT is determined by the absorption rate and the desorption temperature is given by the solute yield.

2.4 Evaluation

For evaluation of the performance of the solvent so called solvent performance indicators [2] can be used. Useful definitions have to be made: Energy consumption can be evaluated by simply adding all energy streams i.e. the heat streams of heat exchanger E-1 to E-3 and the energy consumption of pump P-1. More elaborate energy consumption can be obtained by applying the pinch technology for the heat streams of heat exchanger E-1 to E-3. Solvent loss as a direct consequence of

saturation vapor pressure of the solvent can be evaluated by the sum of the mole amount in the stream SOLUTE-RICH and the stream leaving the process after regeneration.

The example considered in this study is a gas stream comprising of nitrogen and carbon dioxide with carbon dioxide as the solute. The separation task is to solve a mole amount of carbon dioxide in stream LOAD in order to meet the given absorption rate and to gain a carbon dioxide rich stream corresponding to the desired solute yield. In the first attempt a stepwise solution of the flow sheet is implemented.

As a result it can be concluded that the described method shows realistic energy figures for the state of the art technical absorption processes. A completely estimated virtual component on the basis of literature data for methanol gives an energy consumption of 99.92% of the value which is calculated using directly literature data of methanol. This underlines the good performance of the estimation method. It can also be shown that e.g. the change of the Henry coefficient in a logarithmic scale of ±10% for a virtual component (M_W = 100 kg/kmole, T_{NB} = 100°C, ρ = 1000 kg/m³) leads to an energy consumption of 236.50% respectively 37.86% compared to methanol based on literature data.

3. Conclusions

An approach for the theoretical study of a physical absorption process is shown for finding new solvent or an additive for an already existing solvent. Therefor the flow sheet of a physical absorption process is split into the main unit operations including the regeneration of the solvent. Thus, specific influences of highly optimized processes are avoided and only the thermodynamic performance of the solvent can be studied. A model of this abstract flow sheet is implemented in MATLAB®. Within the model the solvent is treated as a virtual component, such that its thermodynamic properties can be varied independently.

References

[1] Bardow, A., Steur, K., Gross, J., Continuous-molecular targeting for integrated solvent and process design. Ind. Eng. Chem. Res., 2010, 49, 2834-2840.

[2] Papadopoulos, A. I., Linke, P., Multiobjective molecular design for integrated process-solvent systems synthesis. AIChE Journal, 2005, 52, 1057-1070.

[3] Hostrup, M., Harper, P. M., Gani, R., Design of environmentally bengin processes: integration of solvent design and separation process synthesis. Computers and Chemical Engineering, 1999, 23, 1395-1414.

[4] Hostrup, M., Gani, R., Kravanja, Z., Sorsak, A., Grossmann, I., Integration of thermodynamic insights and MNLP optimization for the synthesis, design, and analysis of process flowsheets. Computers and Chemical Engineering, 2001, 25, 73-83.

[5] Pereira, F. E., Keskes, E., Galindo, A., Jackson, G., Adjiman, C. S., Integrated solvent and process design using a SAFT-VR thermodynamic description: High-pressure separation of carbon dioxide and methane. Computers and Chemical Engineering, 2011, 35, 474-491.

[6] Klein, J. A.,Wu, D. T., Gani, R., Computer aided mixture design with specified property constraints. European symposium on computer aided process engineering, 1992, S229-S236.

[7] Odele, O., Macchietto, S., Computer aided molecular design: a novel method for optimal solvent selection. Fluid Phase Equilibria, 1993, 82, 47-54.

[8] Harper, P.M., Gani, R., Kolar, P., Ishikawa, T., Computer-aided molecular design with combined molecular modeling and group contribution. Fluid Phase Equilibria, 1999, 158-160, 337-347.

[9] Coutinho, J. A. P., Vlamos, P. M., Kontogeorgis, G. M., General form of the cross-energy parameter of equations of state. Ind. Eng. Chem. Res., 2000, 39, 3076-3082.

IONIC LIQUIDS AS SEPARATING AGENTS IN EXTRACTIVE RECTIFICATION

Zhuchkov V.I., Frolkova A.K., Rum'yantsev
Lomonosov Moscow State University of Fine Chemical Technologies, Moscow, Russia

Abstract

The regularities of the extractive rectification of binary mixtures in the presence of additional substances were studied. Their choice was carried out from the set of well-known separating agents including both traditional solvents and ionic liquids. The assessment of separating agent selectivity and forecast the quality of the product was carried out on the basis of the data of gas-liquid chromatography and mathematical modeling of vapor-liquid equilibrium. The possibility of use of ionic liquids in the extractive rectification of different nature binary mixtures (containing positive, negative azeotropes or both of them) was proved by natural and computing experiment. Experiment conditions, distillation column parameters and separation process results are presented.

Keywords: azeotropic systems, extractive rectification, ionic liquids, simulation, vapor-liquid equilibrium.

1. Introduction

The study of the regularities of mono- and biazeotropic mixtures separation in presence of additional substances of different nature among which ionic liquids are very promising is still actual in the field of separation and purification of organic products technologies development. To assess their selectivity as separating agents (SA) different methods were used: gas-liquid chromatography (GLC), the vapor-liquid equilibrium modeling, natural experiment on a laboratory distillation column. Evaluation of potential separating agents selectivity by GLC allows to form a plurality of agents for extractive distillation on the first stage. This problem is solved in conditions that differ from the real (infinite dilution by separating agent) and hence it was necessary to confirm the prediction by experiment.

2. Results and discussion

Regularities of the extractive rectification (ER) of mixtures acetone - chloroform (I), chloroform - ethanol (II) and benzene - perfluorobenzene (III) were studied. These mixtures are characterized by the presence of negative (I), positive (II) azeotrope or by two azeotropes (III). 1-butyl-3-methylimidazolium chloride ([bmim][Cl]) for ER of mixtures I-III and triethylammonium trifluoromethylsulphonate ([HEt_3A] [triflate]) for ER of mixture I were used as an extractive agents.

Their choice was made from the number of potential separating agents (SA) including traditional solvents and different ionic liquids. The preliminary list of agents includes such ionic liquids as [HEt_3A][triflate] - triethylammonium trifluoromethylsulphonate; [bmim][PF_6] -1-butyl-3-metilimidazolium hexafluorophosphate; [bmim][BF_4] - 1-butyl-3-methylimidazolium tetrafluoroborate; [bmim][Cl] - 1-butyl-3-methylimidazolium chloride; [emim][Cl]-1-ethyl-3-methyllimidazolium chloride (Table 1).

No	Ionic liquid	Selectivity values	
1	[Het_3A][triflate	Chloroform (R_1) -acetone (R_2)	Ethanol(R_1) - chloroform(R_2)
		1.03	1.83
2	[bmim][PF_6]	Acetone (R_1) – chloroform(R_2)	Ethanol(R_1) - chloroform(R_2)
		1.68	1.93
3	[bmim][BF_4]	Acetone (R_1) – chloroform(R_2)	Ethanol(R_1) - chloroform(R_2)
		1.04	1.47
4	[bmim][Cl]	Chloroform(R_1) – acetone(R_2)	Ethanol(R_1) - chloroform(R_2)
		11.36	1.91
5	[emim][Cl]	Chloroform (R_1) – acetone(R_2)	Ethanol(R_1) - chloroform(R_2)
		10.0	2.24

Table 1: Selectivity of ionic liquids for the considered pairs of components at infinite dilution at 90^0C

Selectivity was determined by GLC as ratio of retention times of the original components at infinite dilution by separating agent - ionic liquid which is a stationary liquid phase:

$$S^{\infty}_{1,2(PA)} = \frac{t_{R_2}}{t_{R_1}}$$

[Bmim][Cl] and [emim][Cl] are considered to be the best separating agents among all others ionic liquids. Besides it is possible to get acetone as distillate product in ER of acetone - chloroform and ethanol – as distillate product in ER of ethanol - chloroform.

The evaluation of the selectivity of 1-butyl-3-methylimidazolium chloride as an extractive agent in ER of biazeotropic mixture benzene – perfluorobenzene was made and principal possibility of getting perfluorobenzene as distillate product was shown.

The choice of the ionic liquid [bmim][Cl] as separating agent for ER of all original mixtures is due to its high enough selectivity, relative cheapness and availability. At the same time, the choice of the ionic liquid [HEt_3A][triflate] for ER of chloroform-acetone is problematic because according to GLC its selectivity is close to unity, and requires additional study.

Conditions of SA selectivity estimation by GLC differ from the real process conditions in the extractive distillation column. Therefore, it is necessary to conduct the experiment which would confirm the effectiveness of the SA and provide getting the products specified quality in the column with the given parameters (overall efficiency, stages of the original feed mixture and SA feed, reflux ratio).

Extractive properties of [bmim][Cl] study

The experiment was conducted in a laboratory rectification column height of two meters. The internal diameter of the column - 12 mm. Nozzle - spiral-prismatic 2.5×2×2 mm, made of nichrome. Efficiency of the column was 10-12 theoretical plates. The column was operated at atmospheric pressure in a continuous mode. The mixture feed from the container was carried out using a plunger pump through the pipe under the bottom of drawer side. Ionic liquid [bmim][Cl] is a solid under normal conditions, so it was heated to melt and was fed to the column under gravity from heated burettes on the top drawer side.

Since the GLC analysis of the bottom liquid containing the ionic liquid was difficult only the initial sample of mixtures (F) and the distillate products (D) were collected and analyzed. The composition of the bottom product (W) was determined from the material balance. The consumption of SA providing a predetermined separation was determined for each of the original mixtures. Conditions, parameters and results are shown in Table 2.

Data Table 2 shows that the ionic liquid [bmim][Cl] can be used as an effective SA for extractive rectification of mixtures examined.

No	Original mixture 1-2	Reflux ratio	Flow rate SA, g/g	T_D (T_w), ^0C	Composition (x_1-x_2-x_{SA}), % mass.		
					F	D	W
1	Acetone - chloroform	6	0,984	56.5 (108-112)	32,7 67,3 -	98.5 1.5 -	- 39.8 60.2
2	Chloroform – ethanol	6	1,06	58.0 (120-124)	72,1 27,9 -	98,6 1,4 -	- 39,8 60,2
3	Benzene - perfluorobenzene	6	3,0	80-80.5 (125-130)	29,6 70,4 -	5 95 -	7,9 - 92,1

Table 2: Conditions, parameters and results of experiments on extractive properties of [bmim][Cl]

Extractive properties of [HEt_3A][triflate] study

Dependences of boiling temperature from concentration of ionic liquid in corresponding binary constituents in ternary system acetone – chloroform – [HEt_3A][triflate] were experimentally determined to get parameters of mathematical modeling of vapor-liquid equilibrium (Table 3, 4).

X_1 , % mole	T, ^0C	X_1 , % mole	T, ^0C
0	56,60	22,37	63,75
0,99	56,60	24,44	64,70
2,22	56,90	26,50	65,50
3,32	57,20	28,40	66,45
4,32	57,45	30,88	69,60
5,44	57,80	35,28	70,60
6,54	58,65	40,17	74,00
7,68	59,00	44,26	77,00
8,61	59,40	48,97	85,50
9,66	59,75	51,61	87,10
10,77	60,05	53,85	89,10
12,04	60,70	56,53	92,20
13,65	61,10	58,62	93,60
15,42	61,45	60,89	95,30
17,08	62,10	64,69	107,00
20,25	62,75	65,93	107,30

Table 3: Dependence of boiling temperature of mixture [HEt_3A][triflate] (1) – acetone (2) at 750 Hg mm.

X_1 , % mole	T, ^{0}C	X_1 , % mole	T, ^{0}C
0	59,70	36,40	73,40
5,8	60,10	38,07	74,50
11,68	62,30	40,60	76,40
15,05	63,50	45,94	79,25
18,03	64,60	49,48	82,10
21,12	66,70	53,35	91,30
24,61	68,60	56,06	93,20
29,34	70,50	61,11	99,20
32,05	72,30		

Табл. 4: Dependence of boiling temperature of mixture [HEt_3A][triflate] (1) – chloroform (2) at 737 Hg mm.

The experimental data for the binary systems were correlated using NRTL model. The modeling of equilibrium in the ternary system acetone – chloroform - [HEt_3A][triflate] was carried out. The volatility of chloroform relatively acetone increased in the presence of [HEt_3A][triflate], i.e. unlike the above case an inversion of components volatilities was observed. When more than 63 % mol. of SA is added to a mixture of acetone – chloroform, the system behaves as zeotropic and it is possible to get chloroform as a distillate product.

3. Conclusions

Complex research of properties of ionic liquids, their mixtures with separating agents and regularities of the extractive rectification process was made on the basis of modeling and natural experiment. The principal possibility of using ionic liquids as separating agents in extractive rectification of binary azeotropic mixtures of various types was shown.

4. Acknowledgement

Work was carried out according to the state task of the Russian Ministry of Education and Science (# 1B-1-353).

A robust approach for continuous process monitoring and optimization based on Monte-Carlo technique

Dr. Stephan Deublein1
[1]BASF SE, Ludwigshafen, Germany;

Abstract
Process model simulations were performed using the stochastic Monte-Carlo (MC) approach. The MC approach allows for a robust, fast and user-independent adjustment of model parameters in arbitrary number and, hence, a successful and efficient process monitoring and optimization. The present approach was successfully employed in the BASF work flow for the model development of an extractive distillation and a production process containing one reactor and three distillation towers including two recycle streams. It was further successfully employed for the optimization of the bioethanol production process based on an entrainer distillation [1] with respect to its energy requirements.

Keywords
Process simulation, MC approach, process model, extractive distillation, entrainer distillation

1. Introduction

Process modelling and simulation is a common and widely used tool for monitoring process conditions and performing plant optimization. The quality of the calculations and hence, the monitoring and optimization highly depend on two well-known factors: first, an accurate description of the physical properties of all components involved in the system; second, the time and experience spent on the model development and the adjustment of model parameters. For industrial applications of process simulation, both these factors are of high importance and need to be constantly addressed.

Research effort on property data resulted in highly accurate equations of state and powerful estimation routines like SAFT [2,3] or COSMO-RS [4,5]. For model development and, especially, model parameter adjustment, several algorithms have been published in the recent years, which rely in most parts on gradient-based optimization algorithms with its well-known convergence issues.

Here, a different route for model parameter adjustment based on the Monte-Carlo (MC) technique is presented. MC technique allows for an efficient and easy, automated parameter adjustment based on a stochastic variation of all model parameters in the process simulation. Technical details on the MC algorithms are given and examples of the application of such algorithms in praxis are shown, i.e. the application of the MC algorithms on the simulation of an extractive distillation (two towers) and of the model for an operating plant (one reactor with three distillation towers and two recycle streams back to the reactor). The present MC technique can also be efficiently applied for optimization of plant data based on process simulation, shown for the production of biodiesel using the entrainer benzene.

2. Results and discussion

A “good” process model of an operating plant in chemical industry is capable to describe the plant data Z^{plant} within a reasonable low deviation ε. In mathematical terms, using a least-square approach, this writes as

$$F(p) = (Z^{plant} - Z^{model}(p))^2 \quad < \quad \varepsilon \quad , \qquad (1)$$

where Z^{model} is the result of the process simulation determined by the process model and a given parameter set p. By varying p, the optimization problem with cost function according to Eq. (1) can be minimized.

The required accuracy of the model is sensitive to the application the model is applied to and hence, user-defined.

2.1 Monte-Carlo simulation technique

MC technique allows for minimizing the cost function according to Eq. (1), i.e. the development of a “good process model”, in a stochastic manner. The stochastic approach has two advantages: first, it is a robust approach to detect to global minimum of the cost function, i.e. the process is almost independent of the starting values and remedies typical problems of process simulators, namely convergence problems. In second, the process can be easily automated, i.e. it can be performed without any user interactions and, hence, saves time, resources and costs.

In the present MC approach, all parameters of the process model are stochastically selected and varied with the same probability. The chosen parameter p_i from the model parameter set p^0 is changed by a random value Δp_i resulting in a new parameter set p^1. For the resulting model, a process simulation is performed and the difference between plant and simulation data according to Eq. (1) determined. The result is evaluated according to a modified Metropolis acceptance criterion [6]

$$[0;1] \ni Z < \exp\left(\left(- \left(F(p^0) - F(p^1)\right)^m / B\right)\right) \quad , \qquad (2)$$

where Z is a random number between 0 and 1, m is an enhancement factor, scaling the differences between both parameter sets and B is a scaling factor, reducing the values in the exponential function.

Following the scheme, not the actual value of the cost function but the variation of the cost function with varying parameter set is the key driver for the minimization of the optimization task. If the cost function is reduced by the parameter variation, namely if $F(p^0) - F(p^1) > 0$, the change in the parameter value drives the cost function in the direction of the minimum. It is, hence, always “accepted” independent of the chosen random number, i.e. the parameter set p^1 becomes p^0 and a new parameter p_i is subject to change. If the cost function is increased by the parameter variation, namely if $F(p^0) - F(p^1) < 0$, the new parameter set p^1 is “accepted” only with a certain probability, which depends on the differences in the cost function, cf. Eq. (2). Note that by applying the acceptance criterion, all non-convergent solutions resulting in a deviation between model and reality going to infinity are automatically rejected, since the exponential function in Eq. (2) becomes zero.

Repeated variations of all parameters and evaluation of the cost function according the present acceptance criterion drives the parameter set to the global minimum, i.e. to a “good” process model, cf Figure 1.

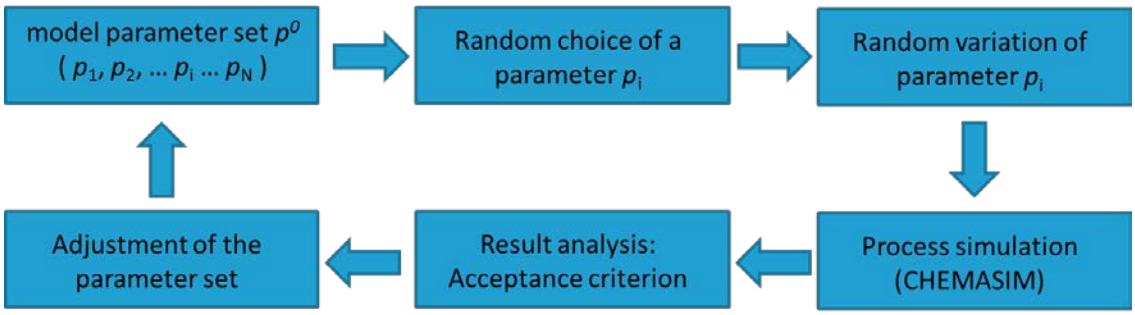

Figure 1: Schematic of the MC algorithm in the process model development

The present algorithm was implemented in MATLAB® (Mathworks Inc.) using the BASF Inhouse process simulator “CHEMASIM”.

2.2 Application: Extractive distillation

The present MC technique was employed for the description of an extractive distillation run in lab scale. The components involved were the main product P, which was fed into the extractive distillation in a multicomponent mixture M, consisting of components A and B. The extraction medium is denoted as E in the following. A scheme of the extractive distillation is given in Figure 2.

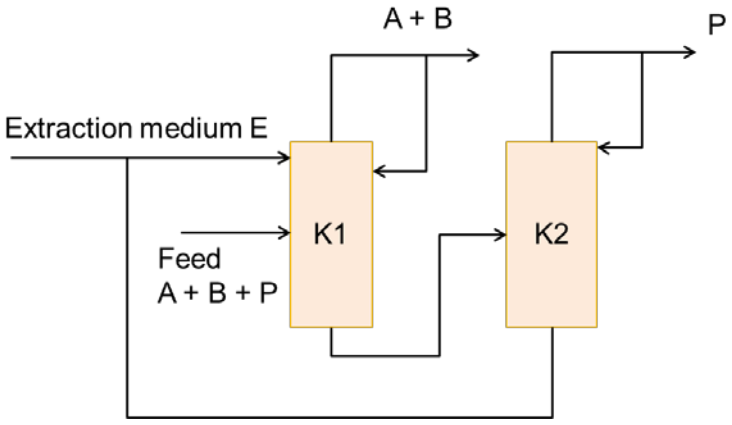

Figure 2: Schematic of the extractive distillation setup

The process model is used to describe the different operating points of the extractive distillation in lab scale and thereby, gain more information about the separation and the extraction model, and to explain some unexpected behavior observed in the lab.

The process model mimics the real operating plant in the required detail, i.e. a large variety of process model parameters is present. The most important parameters are the ones related to the extraction solvent E, namely the amount of E that is fed into the extraction tower, the load of E, which is the amount of product P that is still dissolved in the extraction medium and recycled back to the extraction tower, and the temperature of the extractive solvent at the feed entry. In addition to the properties of the extraction solvent, of course, the reflux in both towers and hence, the composition in both distillate streams are of high importance.

Note that all system properties are highly correlated. These correlations typically lead to challenges in the development of an accurate process model due to convergence problems in the simulation.

The results of the model parameter adjustment show good agreement with the plant data. The deviations are below 2% in all quantities. Remaining differences are mainly related to an inaccurate describing the component property data, especially for the adsorption process of all components in the extraction medium. The adjustment for this system took roughly 10 minutes, including the preparation of the simulation for the MC technique. A total of 20000 parameter variations and, hence, process simulations were performed.

2.3 Application: Separation of water and ethanol

The separation of ethanol from water is a main task in the production of bioethanol. The process relies on an entrainer distillation using the entrainer benzene and taking advantage of the hetereoazeotrope in the water, benzene, ethanol system. The process scheme is illustrated in Figure 3, a total of three distillation units is required.

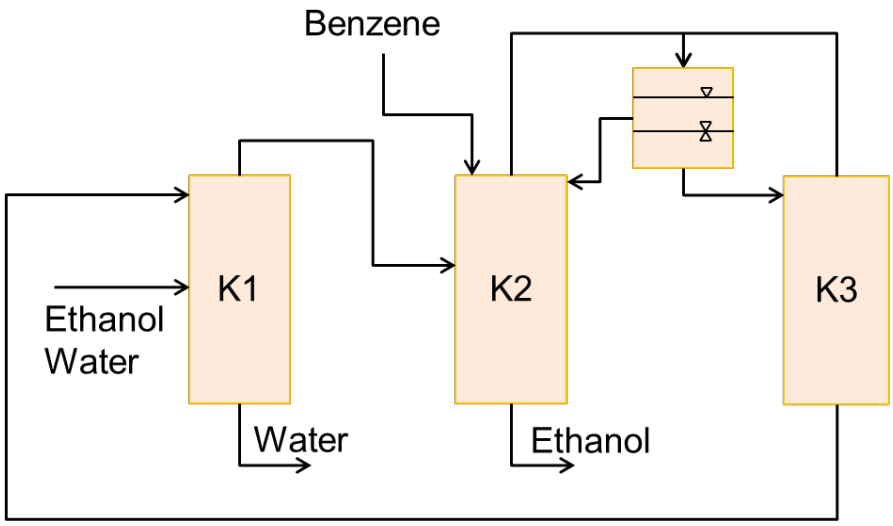

Figure 3: Schematic of the bioethanol production

The process is typically described under atmospheric pressure, however, more favorable is the execution of the separation under vacuum. The identification of the optimal pressure for each distillation tower, however, is not trivial, since the separation performance in each unit directly affects the separation task of the next tower.

Here, the optimal pressure for each unit is determined using the present algorithms, i.e. the system was optimized to a minimum requirement on energy by remaining the quality of the pure products water and ethanol constant. The adjustment was performed using 1000 parameter variations and a total of ~10 minute, the characteristics of the optimization function is shown in Figure 4. It can be seen that the optimum was already detected after ~400 parameter variations. A comparison of the MC simulation results with discretely performed simulations in the parameter

space of interest shows that the global minimum in energy for the process is almost perfectly matched, cf. Figure 5.

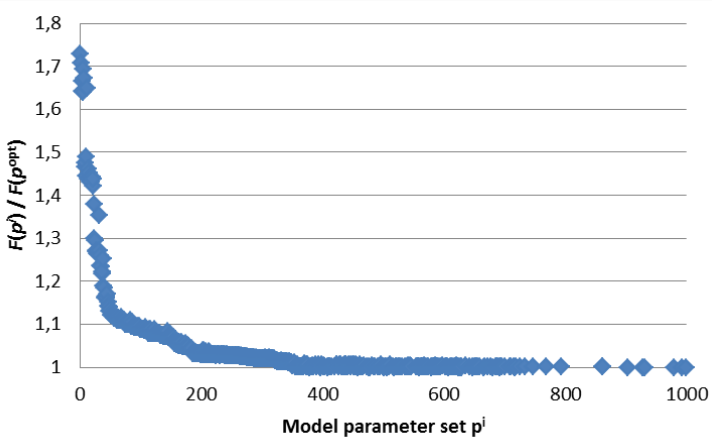

Figure 4: Evolution of the cost function with respect to the parameter set *i*. The cost function was normalized by the optimal parameter set p^{opt}.

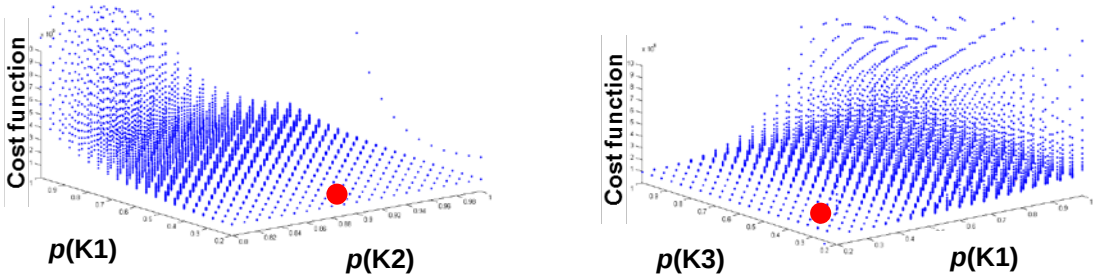

Figure 5: Energy optimization of the bioethanol process. Results of MC optimization (red) are compared to discretely performed simulations are varying tower pressures (blue)

2.4 Application: Operating plant

Process simulation in operating plants is an important and useful tool. It allows for the evaluation of present operating data and constant optimization during production. Here, the present MC technique is employed in a multiproduct plant. The plant consists of one reactor and three towers. The top product of the first two towers can be recycled back to the reactor, forming products of higher lengths. Products of the plant are P1, P2 and P3. Operating points of the plant differ in operating load (70% to 110%) and product composition. A schematic of the plant is given in Figure 6.

The employed process model describes the operating plant in detail, the reactor is modeled using a kinetic description of the reactions, among others. The different operating states of the plant were simulated using MC technique, i.e. a parameter set for all operated plant data was developed. Due to the detailed model description, the number of model parameters to be adjusted exceed 35. Most important parameters in the model are the composition and amount of the recycle streams back to the reactor as well as the amount of educts that are fed into the reactor. These streams determine the outcome of the reactor and, hence, the composition to be separated in the upcoming towers.

The MC adjustment was started for an operating load of 100% and a product composition, mainly consisting of P2. Target was an operating point, also at 100% producing mainly P3 and almost no P2. The results of the parameter adjustment show good agreement with the plant data. The deviations in all properties are below 4%. The adjustment took 20 minutes, 60000 parameter variations were executed.

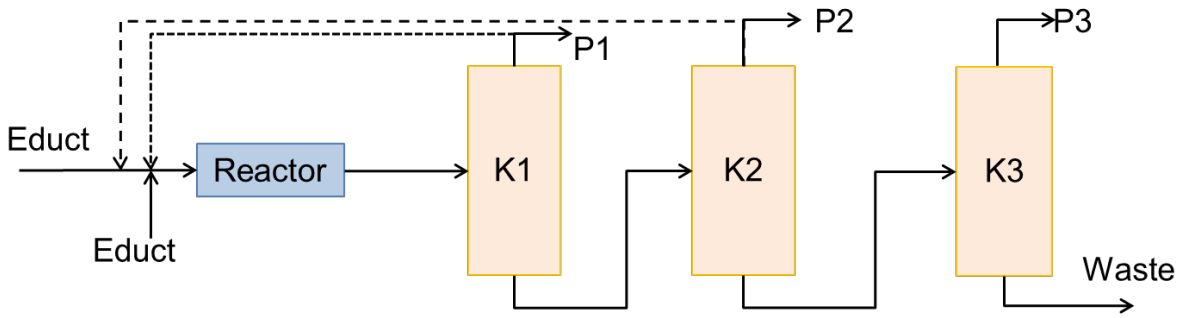

Figure 6: Schematic of a plant

3. Conclusions

A Monte-Carlo approach for the development of process models for process simulation was applied and investigated. The approach relies on a stochastic variation of process model parameters and an efficient criterion to judge on the quality of the resulting simulation results. The algorithm was successfully applied to the development of a process model for an extractive distillation on lab scale and an operating plant at BASF based on real process data. The results show good agreement between real data and simulation data using the applied parameter set.

It was further employed for the optimization of a separation process for water and ethanol using the entrainer benzene taken from the literature. The results show very good agreement with the optimal parameter set, determined manually by sampling the parameter space at discrete points.

Acknowledgements

The author greatly acknowledges the help of Oliver Hirth, Dr. Roger Boettcher and Dr. Stephan Höser in the preparation of the present work.

References

[1] Kirschbaum, E, Möglichkeiten zur Verringerung des Wärmeverbrauchs, in Destilier- und Rektifikationstechnik, Berlin 1969, 28
[2] Tan, S. P., Adidharma, H., and Radosz, M., Industrial & Engineering Chemistry Research **47** (2008) 8063.
[3] Kleiner, M., Turnakaka, F., and Sadowski, G., Molecular Therodynamics of Complex Systems **131** (2009) 75.
[4] Klamt, A., The Journal of Physical Chemistry **99** (1995) 2224.
[5] Klamt, A. and Eckert, F., Fluid Phase Equilibria **172** (2000) 43.
[6] Metropolis, N, Rosenbluth, A, Rosenbluth, M.N., Teller, A.H., Teller, E., The Journal of Chemical Physics **21** (1953), 1087

The method of infinitely sharp splits – A novel method for the search and identification of possible splits of extractive distillation

F. Petlyuk[1], R. Danilov[2], J. Burger[3]

[1]Retired, New York, USA;
[2]ECT Service, Moscow, Russia;
[3]Laboratory of Engineering Thermodynamics, University of Kaiserslautern, Germany

Abstract

A novel general method for the search and identification of possible splits in extractive distillation columns is presented - the method of infinitely sharp splits (ISS method). The column is assumed to consist of three sections of infinite height. In each section, at least one component becomes absent at one end. The method finds all feasible compositions of a product that can be obtained in an extractive distillation column of infinite height and finite reflux. The method works for systems of any distillative topology, i.e. without restrictions about the existence of azeotropes and distillation boundaries. The feasibility of a split in the column depends on the compositions that can be achieved at both ends of the extractive section of the column, i.e. the section between the inlets of feed and entrainer. The product compositions of this section are clustered into a region which is located on the boundary of the concentration simplex. The limits of this region depend only on the local *K*-values, the vapor-liquid distribution ratios, of all components in the mixture. For a split of a given feed the method identifies the minimum entrainer flow rate and limits of the reflux ratio of the column. Operating costs of a separation can be analyzed quickly, and new optimal flow sheets can be created without the need for iterations.

Keywords

azeotropic distillation; conceptual design; extractive distillation; feasibility; infinitely sharp splits

1. Introduction

Azeotropic mixtures are often separated by extractive distillation. An extractive distillation column consists of three sections: the top section, the bottom section and the intermediate extractive section between the inlets of the feed and the entrainer. The entrainer is withdrawn from the column in the bottom product together with one or more components of the feed and usually recycled in additional process units, e.g. an additional distillation column. The conceptual design of an extractive distillation process is extremely challenging due to its large number of process parameters (tray numbers of the feed and entrainer, the reflux ratio, entrainer/feed ratio). Systematic approaches for the conceptual design of this process have been studied in many articles for which only some examples are given in the following. Wahnschafft and Westerberg [1] presented a method to decide whether a proposed split given by a feed composition and desired product purity is feasible in an extractive distillation column based on a geometric approach which requires detailed residue curve maps. Knapp and Doherty [2] employed complex mathematical singularity theory to decide

whether a given split defined by a feed composition, product purity and an entrainer/feed ratio is feasible. Brüggemann and Marquardt [3] presented a short-cut method to determine the minimum entrainer/feed ratio and limits of the reflux ratio based on a non-linear analysis of the extractive section. All mentioned methods have some significant limitations. They focus primarily on one type of ternary mixtures which is called "extractive type". Mixtures of this type comprise a binary azeotrope in the feed mixture and the entrainer is the global high boiler. Further, the methods do not allow the identification of all feasible splits but solve only the feasibility problem for a given feed. The minimum entrainer/feed ratios and limits of the reflux ratios are often determined in an iterative way.

In contrast, this work presents a general method for the search and identification of feasible splits in an extractive column. For a given split, it also identifies limits of the operating parameters such as the entrainer/feed ratio or the reflux ratio. The method is based only on the general laws of rectification at finite reflux and it works without iterations. Thus, the results are obtained in a fast and robust way. The method is applicable to any type of mixture, i.e. not limited to the “extractive type”, and to multi-component mixtures, i.e. not limited to ternary systems.

To simplify the analysis, a limiting mode is proposed that represents the behavior of real modes closely – the infinitely sharp split mode (ISS mode) [4]. In the ISS mode, each section of the column is of infinite height and at least for one component a sharp split is achieved, i.e. this component is only present at one end of the section. The ISS mode is illustrated in Figure 1 for a column in which the sharp split is achieved for component 2 in the top section, for component 3 in the extractive section and for component 1 in the bottom section.

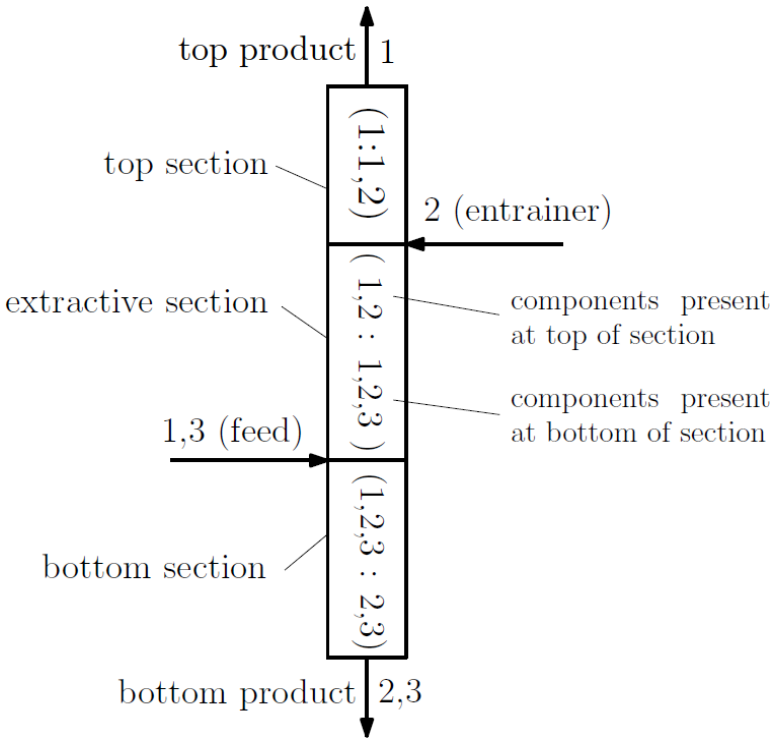

Figure 1: Split in the ISS mode to separate a mixture of components 1 and 3 in an extractive column by adding entrainer 2.

The split in Figure 1 is typical if components 1 and 3 form a binary azeotrope which is the global low-boiler of the system. If the sharp split in the extractive section was not achieved, then component 3 would be present in the top section. In this case, component 3 would accumulate toward the top of the column because the binary azeotrope is the global low boiler. If component 3 is absent in the top section, pure component 1 can be obtained as top product. Hence, the split of the extractive section decisively determines the feasibility of the achievable split of the column.

2. Feasible product regions of the extractive section and limiting parameters of mode

The distillation trajectories of the extractive section are greatly influenced by the trays that are positioned at the end of the section where one of the components becomes absent. Therefore, the calculation of *K*-values on the elements of the concentration simplex is sufficient to determine if feasible column trajectories exist within the simplex. The *K*-values are the vapor-liquid distribution coefficients in the phase equilibrium at the given column pressure *p* and the liquid phase composition equal to the scanned point of the concentration simplex. In the ISS mode, the following conditions have to be fulfilled at the top end of the extractive section, where component *j* becomes absent [5].

$$K_{iD} > K_j > K_{iE} \qquad \text{(I)}$$

The index *iD* represents any component present in the top product of the column. The index *iE* represents the entrainer component. Let us consider an example in which a mixture of acetone (1) and methanol (3) is separated using the entrainer water (2) by the split given in Figure 1 (*iD*=1, *iE*=2, *j*=3). The top product of the extractive section is located on the binary edge 1-2 of the ternary plot in Figure 2 which is called the extractive segment of the split. The extractive region is the part of the extractive segment for which conditions (I) hold. In Figure 2, the extractive region spans almost the whole edge 1-2 except a small part near vertex 1. The split of Figure 1 is feasible because the extractive region exists.

As the extractive section is infinitely high, it contains at least one pinch point, i.e. a cross section of the column at which the vapor and the liquid are in equilibrium and the concentrations do not change with changing height. For a constant ratio of the rate of entrainer *E* and the rate of the top product *D*, the concentrations of the liquid phase at these pinch points are located on pinch branches. For the example in Figure 2 there are two pinch points which are located on two pinch branches. The pinch branch ending in the vertex of the absent component (vertex 3) is called the first pinch branch. Its starting point on the extractive segment is called root. Feasible distillation trajectories of the extractive section start at the extractive segment, run toward a pinch point on the first pinch branch and end in a node close to the entrainer, cf. Figure 2. The ratio (*V*/*L*) in the section determines the point on the pinch branch which the trajectories approach to. The ratio (*V*/*L*) is the ratio of the liquid molar flow rate and the vapor molar flow rate within the section. It is assumed to be constant in this work. Feasible top products of the extractive section are located inside the extractive region and between the starting points of both pinch branches.

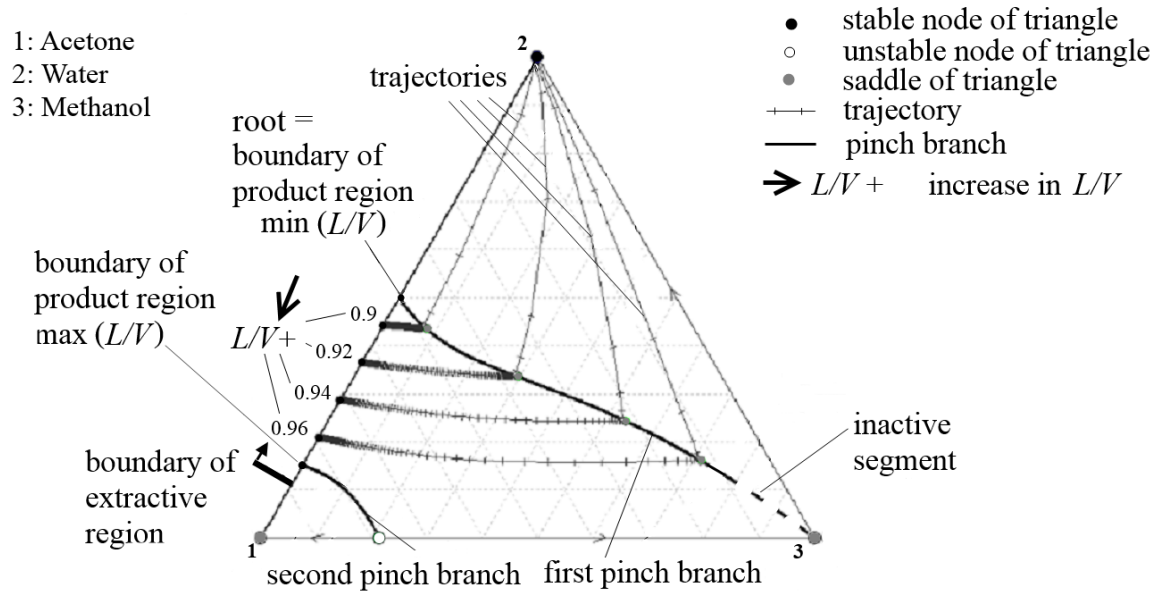

Figure 2: Pinch branches of the extractive section for a constant ratio of the rate of entrainer *E* and the rate of the top product *D* (*E*/*D*=0.7).

With changing (*E/D*) the starting points of the pinch branches change. With increasing (*E/D*) the root moves toward vertex 2. With decreasing (E/D) the root moves toward vertex 1. At one certain (*E/D*) the root is equal to the starting point of the second pinch branch. This (*E/D*) marks a minimum which depends only on the chosen split and on the local *K*-values on the extractive segment. If the entrainer flow rate is chosen that (*E/D*) is below the minimum then the column will be infeasible.
We assume in the following that a feasible (*E/D*) is chosen. The top product of the extractive section moves along the extractive segment with changing reflux ratio (*L/V*), cf. Figure 2. With increasing (*L/V*) it moves toward the starting point of the second pinch branch where (*L/V*) has a maximum. If (*L/V*) was further increased, the top product of the extractive section would move along the second pinch away from the extractive segment. The ISS separation would be no longer possible. The minimum of (*L/V*) is reached when the top product is located at the root.

3. Methods of analysis and calculation

The analysis of the extractive section was discussed in Section 2. Feasible splits for the whole extractive column are determined by the combination of the analysis of the extractive section and the analysis for the bottom section of the column which is described in detail in [4]. The bottom product of the column in the ISS mode is located on one side of the concentration simplex. In the above example of Figures 1 and 2 the bottom product is located on the edge 2-3 of the ternary diagram. The split of the column is feasible if there is a region on this edge where the following conditions hold [4].

$$K_{iD} > K_j \quad ; \quad K_{iD} > K_{iE} \qquad \text{(II)}$$

In the example of Figure 2 these conditions are satisfied on the whole edge 2-3. Furthermore, the boil-up ratio (*V/L*) in the bottom section must be sufficiently large so

that the distillation trajectory of the bottom section and the trajectory of the extractive section can be joined [3,4].
The method of this work determines the *K*-values of all components along the edges of the concentration simplex using a discretization with a fixed step-size. Feasible splits are identified by checking conditions (I) and (II) on the respective edges.
The method distinguishes five types of extractive regions for different ternary mixtures and different types of pinch branches. Besides the extractive type, zeotropic systems, systems with a ternary azeotrope and systems with distillation boundaries can also be dealt with. The type of extractive region is determined from specific characteristics of the *K*-values on the extractive segment, e.g. the existence of a minimum in the function K_j over x_{iD}. For each type of extractive region, there are explicit rules based on the *K*-values to determine feasible product compositions of the extractive section and the minimum (*E/D*). These rules are on a case-by-case basis and not presented here for the sake of brevity.
For a given column feed, the minimum flow rate of entrainer follows directly from the minimum (*E/D*) and the mass balance of the column. For any flow rate of entrainer above this minimum the method calculates the minimum and maximum reflux ratios (*L/V*) in the extractive section, again by rules on a case-by-case basis. The minimum and maximum reflux ratios of the top section of the column are calculated by material balances.
To verify the method's results, the separation of a ternary mixture in the system Acetone-Water-Methanol of Figure 2 in an extractive column was simulated in the process software PRO/II using a column of 250 equilibrium stages. The results are presented in Figure 3 which shows the location of the main feed x_F, the location of the entrainer x_E, straight lines which represent material balances over the whole column and the trajectory of the column.

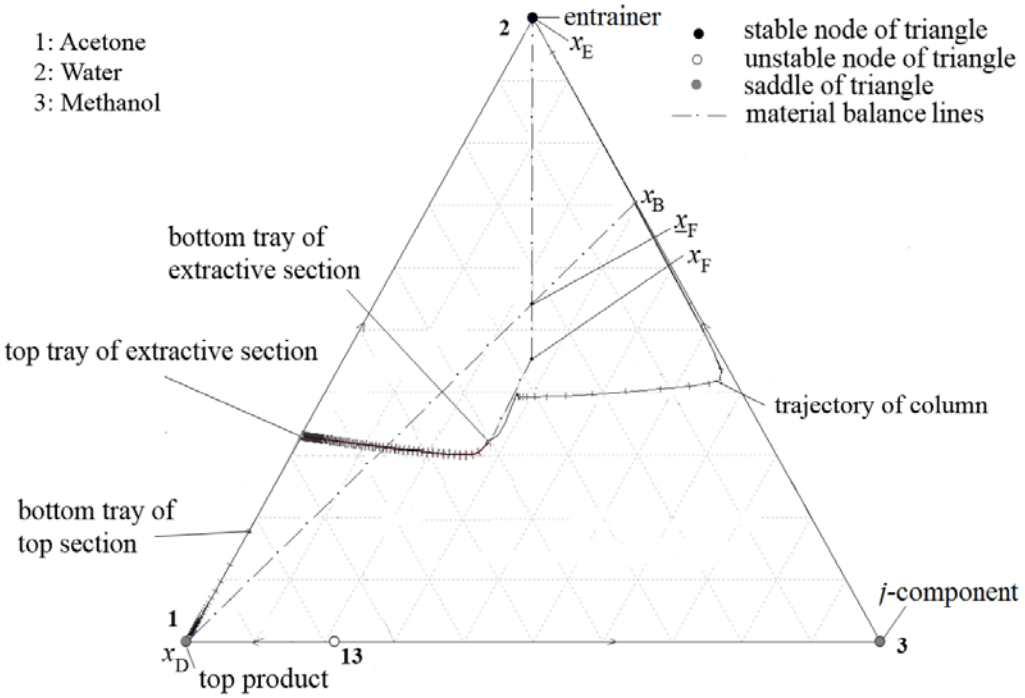

Figure 3: Distillation trajectory of a column in the ISS mode specified by Figure 1.

The entrainer/feed ratio was chosen to (*E/F)* = 0.19 mol/mol, above the minimum calculated by the method $(E/F)^{min}$ = 0.14 mol/mol. The reflux ratio of the column resulted from specifying the purities of top and bottom product. It is within the limits that the method predicts for the selected (*E/F)*.

4. Multi-component mixtures

The task of identifying possible splits and relevant parameters of mode for mixtures containing more than three components is at least as relevant as for ternary mixtures, but it is clearly more complex. For a given split, every component in the mixture is classified either as component of the top product (*iD*), as entrainer (*iE*) or as component that is absent at the top of the extractive section (*j*). The conditions (I) and (II) are valid for any number of components. The method scans the one-dimensional edges of the concentration simplex analogously to the ternary case. The extractive region and the feasible products of the extractive section are obtained by linear interpolation of the boundary points on the one-dimensional edges into the sides of the concentration simplex.

5. Conclusions

In this paper we presented the ISS method for the search and identification of any possible splits and limiting parameters of mode for extractive column sections. The main advantage of the method is that only the calculation of the coefficients of the phase equilibrium at points on the sides of the concentration triangle and in its singular points is required. This calculation is fast, reliable and fully automatable. The results are evident and clear. The method does not require iterations and it is of general nature, since it is not limited to specific types of mixtures. The method enables the designer to study and calculate each section of column separately which allows the calculation of any types of complex columns. The results obtained with the method contain limiting parameters of mode, such as the minimal entrainer rate and limits for the reflux ratios, which allow the fast and reliable assessment of new processes and variants. The results of the method can further be used as initial guesses for subsequent simulations of the finite column using a commercial simulator. These advantages enable the use of this method for the synthesis of innovative separation schemes.

References

[1] Wahnschafft, O.M., Westerberg, A.W.: The Product Composition Regions of Azeotropic Distillation Columns. 2. Separability in Two-Feed Columns and Entrainer Selection, Ind. Eng. Chem. Res. 32 (1993) p. 1108.
[2] Knapp, J. P., Doherty, M. F.: Minimum Entrainer Flows for Extractive Distillation: A Bifurcation Theoretic Approach, AIChE J. 40(2) (1993) p. 243.
[3] Brüggemann, S., Marquardt, W.: Shortcut Methods for Nonideal Multicomponent Distillation: Extractive Distillation Columns, AIChE J. 50(6) (2004) p. 1129.
[4] Petlyuk, F. B., Danilov, R. Y., Skouras, S., Skogestad, S.: Identification and Analysis of Possible Splits for Azeotropic Mixtures. 1. Method for Column Sections, Chem. Eng. Sci., 66 (2011) p. 2512.
[5] Petlyuk, F. B., Danilov, R. Y., Sharp Distillation of Azeotropic Mixtures in a Two-Feed Column. Theor. Found. Chem. Eng. 33 (1999), p. 233.

Shortcut method for the design of multicomponent absorption columns

Christian Redepenning, Matthias N. Hoffmann, Wolfgang Marquardt
Aachener Verfahrenstechnik, RWTH Aachen University, 52064 Aachen, Germany

Abstract
Shortcut methods are valuable tools for fast evaluation of key performance indicators of single separation units and process flowsheets in the early phase of conceptual process design. In this contribution, a novel shortcut method is introduced for the robust and efficient calculation of the minimum solvent flow rate in multicomponent absorption columns. For this purpose, pinch points at the end and within the column are identified using numerical continuation methods. The shortcut method is based on rigorous thermodynamics; no simplifications are made concerning phase equilibrium or heat effects. It is entirely algorithmic and thus applicable to separations with any number of components.

Keywords:
absorption, shortcut, pinch point

1. Introduction

Gas absorption in counter-current columns is a favorable unit operation, if soluble components of a gas mixture can be dissolved selectively in a suitable solvent. The identification of the best solvent and the determination of the minimum solvent-to-feed ratio is a crucial task for the conceptual design of absorption columns. The most favorable design is often determined by extensive simulation studies or by numerical optimization using detailed models [1]. Such approaches are computationally expensive and therefore not well-suited for a rapid evaluation of process alternatives in the early phase of conceptual process design.

In contrast, shortcut methods offer a promising alternative. These methods rely on reasonable simplifications, yet incorporating the full complexity of property prediction, and provide an accurate estimate of relevant design targets such as minimum solvent flow rate. Since the concentration profiles in a counter-current separation column at minimum solvent flow rate are governed by pinch points, i.e., concentrations with vanishing mass transfer in column sections, the development of physically sound shortcut methods can favorably built on the pinch point topology of a mixture for given design specifications.

Established methods for the prediction of the minimum solvent flow rate, however, do not rely on pinch points but are rather based on correlations derived from tray-to-tray recursions of the balance equations. The well-known Kremser formula [2] is limited to absorption with negligible heat effects. Edmister [3] extended the Kremser approach and introduced absorption factors to further improve the prediction when this assumption is not justified. If the effect of the heat of absorption can be neglected [1] – for example, in case of sufficiently dilute feed gas, pinch-based shortcut methods introduced for isothermal extraction can directly be applied to absorption column targeting [4,5]. Furthermore, graphical methods can be used, if the evaporation of the solvent or the condensation of the gas can be neglected. The limiting operation, resulting in a pinch point, is then determined by visual inspection [1].

All existing methods are limited in one way or the other: they either rely on visual inspection or they are only applicable if the heat of absorption is small, and if evaporation of the solvent or condensation of the feed gas is negligible. In contrast, the method proposed in this work relies on detailed models involving mass and energy balances as well as rigorous phase equilibrium and property correlations. The method reliably identifies the minimum solvent flow rate using pinch points which can be determined by a performant numerical algorithm.

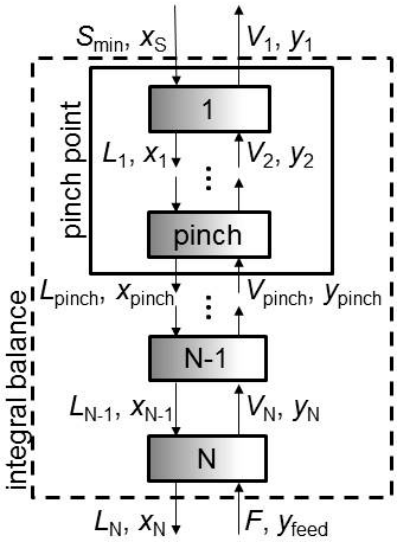

Figure 1: Counter-current separation cascade with integral (dashed line) and pinch point (solid line) balance envelopes.

2. Pinch points in adiabatic counter-current columns

Figure 1 shows the schematic of an adiabatic counter-current (absorption) cascade, which is modeled by the so-called MESH equations. These involve mass and energy balances for each tray *n* as well as appropriate equilibrium relations. For a specified number of trays N in the column and a purity of a solute in a product stream, the solvent-to-feed ratio *S/F* could be calculated with a process simulator. If the number of trays were gradually increased, the separation driving force will ultimately vanish in a pinch point. Hence this point, which constitutes a fix-point of the tray-to-tray recursion, constrains the separation at minimum solvent flow rate S_{min}. A pinch point can be calculated from the MESH equations formulated for the pinch balance envelope as shown in Figure 1:

$$0 = S_{min} x_{S,i} - V_1 y_{1,i} + V_{pinch} y_{pinch,i} - L_{pinch} x_{pinch,i}, \qquad i = 1, \ldots, c, \qquad (1)$$

$$0 = K_i(x_{pinch,i}, y_{pinch,i}, T_{pinch}, p) x_{pinch,i} - y_{pinch,i}, \qquad i = 1, \ldots, c, \qquad (2)$$

$$0 = \sum_{i=1}^{c} x_{pinch,i} - 1, \quad 0 = \sum_{i=1}^{c} y_{pinch,i} - 1, \qquad (3)$$

$$0 = S_{min} h_S - V_1 h^V(y_{1,i}, T_1, p) + V_{pinch} h^V_{pinch}(y_{pinch,i}, T_{pinch}, p) - L_{pinch} h^L(x_{pinch,i}, T_{pinch}, p). \qquad (4)$$

Equation (1) represents the mass balances for all c components, Equation (2) the c equilibrium relations, Equation (3) the closure equations, and Equation (4) the energy balance. At a pinch point, the liquid and vapor streams with flow rates L_{pinch}, V_{pinch}, and concentrations $x_{pinch,i}$, $y_{pinch,i}$ are in equilibrium at temperature T_{pinch} and pressure p. For the equilibrium constants K_i and the vapor and liquid enthalpies h^V and h^L appropriate thermodynamic property models need to be supplied.

In the following, these 2c+3 equations and 2c+3 dependent variables $\mathbf{v} = (x_{pinch,i}, y_{pinch,i}, T_{pinch}, V_{pinch}, L_{pinch})^T$ are abbreviated as

$$\mathbf{0} = \mathbf{p}(\mathbf{v}). \qquad (5)$$

The proposed shortcut model will include these pinch point equations to calculate the minimum solvent flow rate S_{min} and the additional unknowns L_N, $x_{N,i}$, V_1, and $y_{1,i}$. In the following, we distinguish two well-known modes of operation [1]: the feed-pinch (FP) mode, if the pinch occurs at either end of the column, or the tangent-pinch (TP) mode, if a pinch occurs within the column.

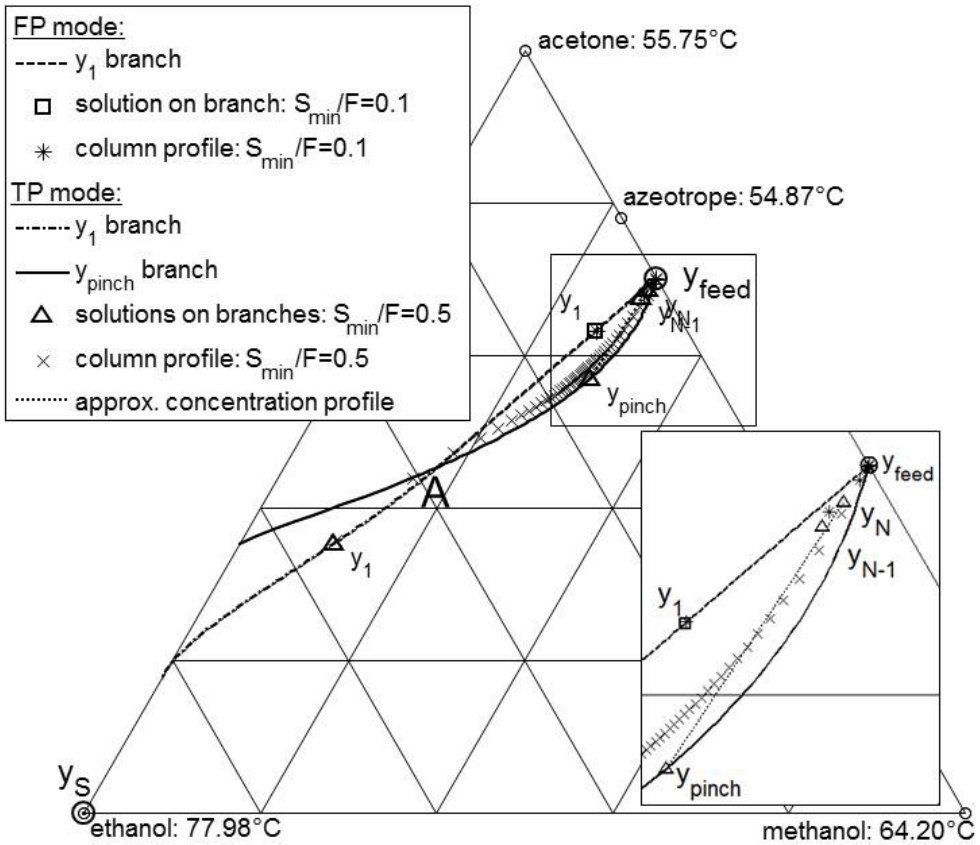

Figure 2: For minimum solvent-to-feed ratios of 0.1 and 0.5 exemplary shortcut solutions are compared to rigorously computed column profiles. At point A the operation mode switches from feed-pinch (FP) to tangent-pinch (TP) mode.

3. Shortcut method for absorption column design

In this section, a novel pinch-based shortcut method is introduced as the main contribution of this paper. In contrast to rigorous tray-to-tray calculations, the model equations (5) are solved by means of predictor-corrector continuation with step-size control varying the minimum solvent-to-feed ratio S_{min}/F. This improves robustness of the calculation, allows for an algorithmic detection of either feed-pinch or tangent-pinch mode, and finally provides the minimum solvent-to-feed ratio S_{min}/F as a function of a solute purity. At first, the method is illustrated by means of a ternary separation problem to discuss graphically key characteristics, followed by an application to a seven-component case study to demonstrate the potential of the method in industrial application.

3.1 Graphical illustration of the method by ternary example

Figure 2 depicts the vapor phase equilibrium concentrations of a separation process where pure ethanol (E) is used as a solvent to separate the gaseous azeotropic mixture of acetone (A) and methanol (M) with feed compositions $y_{feed,A} = 0.7$ and $y_{feed,M} = 0.3$. At ambient pressure, the gaseous feed and the liquid solvent, which are marked as circles in Figure 2, are fed at boiling temperature. At minimum solvent flowrate the process is either operated in feed-pinch or in tangent-pinch mode.

3.1.1 Feed-pinch mode

In the feed-pinch mode the flow rate and concentrations L_N and $x_{N,i}$ (cf. Figure 1) of the liquid stream leaving the column equal the flowrate and concentrations of the liquid stream at the pinch (L_{pinch}, $x_{pinch,i}$), i.e.,

$$0 = x_{pinch,,i} - x_{N,i}\,, \qquad i = 1, \ldots, c\text{-}1. \qquad (6)$$

In this operating mode, the minimum solvent-to-feed ratio can be calculated directly using this so-called feed-pinch criterion, the pinch equations (Equation (5)), and the MESH equations for the integral balance envelope (cf. Figure 1).

The solution branches for the feed-pinch mode are depicted in Figure 2. Because of the feed-pinch criterion, the compositions $y_{N,i}$ and $y_{pinch,i}$ are equal to $y_{feed,i}$, while the product composition $y_{1,i}$ on stage 1 varies continuously along the dashed line: in particular, the concentration of the solute (methanol) decreases in the product composition $y_{1,i}$ for an increasing minimum solvent-to-feed ratio S_{min}/F. For S_{min}/F=0.1, the product concentration is depicted as a square on the dashed line. The solution of the shortcut method is compared to the concentration profile marked by asterisks, which is calculated by means of a process simulator. For this choice of S_{min}/F the product compositions on the first and the last stage, $y_{1,i}$ and $y_{N,i} = y_{feed,i}$, of the column profile are approximated very well by the shortcut method. At a product concentration of methanol $y_{1,M} = 0.18$ corresponding to a minimum solvent-to-feed ratio $S_{min}/F = 0.31$, the operation mode changes from feed-pinch to tangent-pinch mode (cf. A in Figure 2).

3.1.2 Tangent-pinch mode

If the column operates in tangent-pinch mode, the pinch equation system (5) becomes singular [6]. Hence, the switch from feed-pinch to tangent-pinch mode is detected, if the determinant of the Jacobian of **p(v)** vanishes, i.e.

$$0 = \det(\nabla_{\mathbf{v}}\mathbf{p}^{\mathrm{T}}). \qquad (7)$$

According to the theory of discrete dynamical systems, a saddle-node bifurcation of the solution of the tray-to-tray recursion occurs [6]. The continuous calculation of the tangent-pinch solution with numerical continuation requires an alternative formulation [7]

$$\mathbf{0} = \nabla_{\mathbf{v}}\mathbf{p}^{\mathrm{T}}\mathbf{w}\,, \qquad (8)$$

$$0 = \mathbf{w}^{\mathrm{T}}\mathbf{w} - 1, \qquad (9)$$

with **w** being in the null space of the Jacobian of **p(v)**.

In tangent-pinch mode, the pinch composition $y_{pinch,i}$ is not equal to the product $y_{N,i}$ and feed composition $y_{feed,i}$. Hence, with an advanced criterion a continuous profile connecting the tangent-pinch composition $y_{pinch,i}$ and the product composition $y_{N,i}$ is necessary to approximate a feasible separation. According to discrete dynamical systems, the product $y_{N,i}$ is positioned on a separating manifold of the fix-point $y_{pinch,i}$ at minimum solvent flowrate [8]. The separating manifold describes the continuous concentration profile in a column section at an infinite number of trays. For ideal mixtures it was shown that the manifold is linear between the product and the pinch [9]. Kraemer et al. [10] used a linear approximation of a column profile and applied it with good accuracy to non-ideal separations involving three-phase trays with a heterogeneous liquid. Therefore, the continuous profile on the separating manifold between $y_{N,i}$ and $y_{pinch,i}$ is also linearly approximated in this work, by calculating only one additional tray $y_{N-1,i}$,

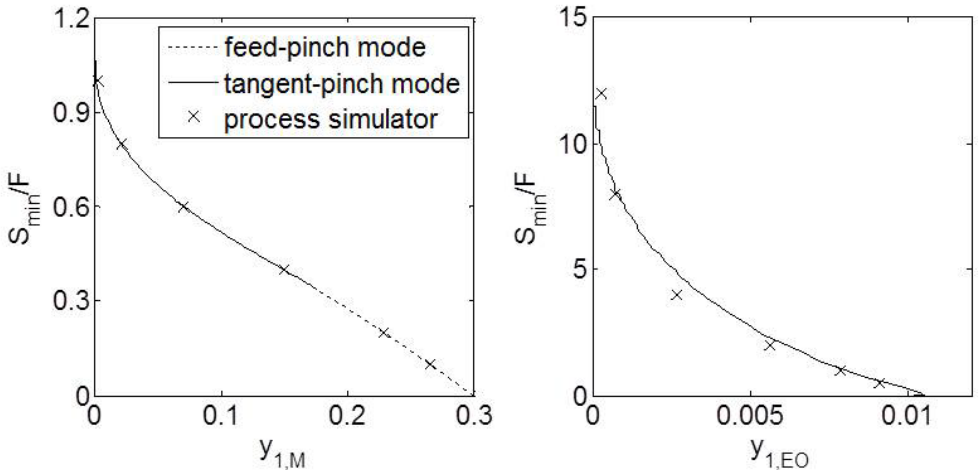

Figure 3: Minimum solvent-to-feed flow rate S_{min}/F as a function of the product concentration of methanol $y_{1,M}$ for the ternary case study (left) and of ethylene oxide $y_{1,EO}$ for the 7 component case study (right).

$$0 = y_{N,i} + \lambda(y_{N,i} - y_{N-1,i}) - y_{pinch,i}\,, \qquad i = 1, \ldots, c\text{-}1, \qquad (10)$$

and λ is the slope of this straight line. However, in case of non-ideal mixtures a column profile is linear only close to pinch points. Therefore, the accuracy of this approximation depends on the curvature of the profile and the distance to the pinch. The accuracy cannot be predicted in advance, but our comparisons to results of a process simulator will show satisfying accuracy. The shortcut method in case of the tangent-pinch mode consists of the pinch equations (5), the MESH equations for the integral balance envelope to calculate the composition $y_{N-1,i}$ of only one additional tray, the linear approximation in Equation (10), and the tangent-pinch criterion, Equation (8) and (9).

In Figure 2, the solution branch of the product composition $y_{1,i}$ is continued in tangent-pinch mode as a dash-dotted line after a switch from the feed-pinch mode has been detected at point A. When the operation mode switches from feed-pinch to tangent-pinch mode, the solution branches of the pinch composition $y_{pinch,i}$ start in the feed composition $y_{feed,i}$ as a solid line.

For S_{min}/F=0.5, exemplary solutions computed by the shortcut method are depicted as triangles. The crosses mark a column profile with 40 trays for this minimum solvent-to-feed ratio calculated by a process simulator using a rigorous model. The profile approaches the pinch point on the tangent-pinch solution branch, while the separation driving force nearly vanishes close to the approximated pinch point. In the cutout the tray compositions $y_{N,i}$, $y_{N-1,i}$, and the resulting linear approximation of the column profile (dotted line) with Equation (10) can be seen. The product compositions of the column profile are close to the product compositions $y_{1,i}$ and $y_{N,i}$, which are predicted by the method. Small inaccuracies of the shortcut approximation occur because of the slight curvature of the rigorous column profile.

In Figure 3, left, the minimum solvent-to-feed ratio S_{min}/F is depicted as a function of the methanol concentration $y_{1,M}$ in the product. The continuation starts at the feed concentration $y_{feed,M}$ = 0.3 for S_{min}/F=0 in feed-pinch mode. The concentration of the solute methanol is continuously reduced for an increasing solvent-to-feed ratio. At S_{min}/F=0.31 the operation mode changes from feed-pinch to tangent-pinch mode. For S_{min}/F= 1.06, methanol is entirely removed from the product. The results computed by a rigorous model offered by a process simulator are marked by crosses in Figure 3; they are in good agreement with the shortcut approximation.

3.2 Application to a seven-component case study

The proposed shortcut method is applied to an absorption process involving seven components. Pure water is used as a solvent to separate the solute ethylene oxide (EO) with a concentration of $y_{feed,EO} = 0.01$ from a gaseous mixture consisting of argon (AR, $y_{feed,AR} = 0.36$), CO_2 ($y_{feed,CO2} = 0.05$), methane (ME, $y_{feed,ME} = 0.09$), O_2 ($y_{feed,O2} = 0.06$), and ethylene (ET, $y_{feed,ET} = 0.43$) at ambient pressure. The vapor-liquid equilibrium calculations assume ideal gas behavior; the solubility in the liquid phase is modeled using Henry coefficients.

Figure 3, right, shows the minimum solvent-to-feed ratio as a function of the solute concentration $y_{1,EO}$. In this case, no feed-pinch mode occurs and the separation is only controlled by a tangent pinch. The concentration of ethylene oxide in the product $y_{1,EO}$ decreases, while the solvent-to-feed ratio S_{min}/F increases. For S_{min}/F= 13.5, ethylene oxide concentration $y_{1,EO}$ is entirely removed from the product composition $y_{1,i}$. The shortcut results show good agreement with the concentration profiles computed by a rigorous tray-to-tray model of a process simulator.

4. Conclusions

Compared to rigorous tray-to-tray calculations the presented shortcut method requires low computational effort. Since numerical continuation is used to track the solution branches, the presented shortcut method is computationally robust and efficient. Neither an approximation of the pinch point, nor any simplifications of the thermodynamic models are used. Any thermodynamic model can be applied to describe the gas- or vapor-liquid equilibrium. Therefore shortcut methods could easily be extended to reactive absorption, if the appropriate mass transfer and reaction kinetic models were supplied.

The method can be employed to screen rapidly various design alternatives by the suggested targeting approach or to initialize more complex nonlinear models for rigorous optimization of separation processes involving absorption columns.

Acknowledgements

The research results reported in this paper was performed as part of the project “Energy Efficiency Management” funded by the German “Federal Ministry of Education and Research” (BMBF).

References

[1] Kister, H. Z., Mathias, P. M., Steinmeyer, D. E., Penney, W. R., Fair, J. R. (2008) Perry’s Chemical Engineers’ Handbook, 8th ed., Green, D. W., Perry, R. H. (eds)., Section 14, McGraw-Hill, New York
[2] Kremser, A. (1930) Nat. Petrol. News, 22(21), 43-49
[3] Edmister, W. C., (1957) AIChE J. 3(2), 165-171
[4] Minotti, M. Doherty, M. F., Malone, M. F. (1996) Ind. Eng. Chem. Res., 35(8), 2672-2681
[5] Redepenning, C., Skiborowski, M., Marquardt, W. (2013) In: Kraslawski, A. and Turunen, I. (Eds.): Proceedings of ESCAPE 23, 1039–1044
[6] Levy, S. G., Doherty, M. F. (1986) Chem. Eng. Sci. 41(12), 3155-3160
[7] Beyn, W. J., Champneys, A., Doedel, E., Govaerts, W., Kuznetsov, Y. A., Sanstede, B. (2002): Numerical Continuation and Computation of Normal Forms, Handbooks of Dynamical Systems, Fiedler, B. (ed.), Vol. 2, 149-219
[8] Julka, V., Doherty, M. F. (1990) Chem. Eng. Sci, 45(7), 1801-1822
[9] Levy, S. G., v. Dongen, D. B., Doherty, M. F. (1985): Ind. Eng. Chem. Fundam. 24, 463-474
[10] Kraemer, K., Harwardt, A., Skiborowski, M., Mitra, S., Marquardt, W. (2011): Chem. Eng. Res. Des. 89, 1168-1189

Environmental and economic assessment of extractive dividing wall distillation columns

J. Rafael Alcántara-Avila[1], Shinji Hasebe[2], Ken-Ichiro Sotowa[1], Toshihide Horikawa[1]

[1]Department of Chemical Science and Technology, The University of Tokushima, Tokushima 770-8506, Japan;
[2]Department of Chemical Engineering, Kyoto University, Kyoto 615-8510, Japan

Abstract
Dividing wall columns (DWC) can separate ternary components by one column and can reduce the energy consumption compared with conventional columns. These appealing features have been extended to extractive dividing wall columns (E-DWC) which separate azeotropic mixtures. Though energy and economic advantages over conventional distillation have been demonstrated in several examples, the environmental impact in terms of entrainer toxicity has not been addressed comprehensively.

In this research, the conventional two-column extractive distillation process and the E-DWC are compared from economic and environmental viewpoints. For environmental assessment, the methodology based on the Life Cycle Impact Assessment (LCIA) is adopted. Results showed that E-DWC realized not only the lowest entrainer flow rate, but also the lowest environmental impact. In addition, the optimal entrainer feed flow rate in the E-DWC is less than that in the conventional process, which contradicts past researches. The quantitative results of the trade-off between economic and environmental criteria stress the importance of considering environmental criteria at the design stage.

Keywords
Extractive Distillation, Dividing Wall Column, Conceptual Design, Life Cycle Impact Assesment, Optimization

1. Introduction

To reduce the energy consumption of distillation process, various column structures have been proposed, and one of them is the diving wall column (DWC). It has been reported that DWC can provide reductions more than 30% in the capital cost and energy consumption (Dejanović et al., 2010). In extractive distillation, an entrainer is introduced to eliminate the azeotrope in the mixture. Thus, even for binary separation, an additional column is required to recover the used entrainer. The extractive dividing wall column (E-DWC) is an extension of DWC in which the extractive distillation and entrainer recovery are executed in a single shell. Figure 1 shows the conventional extractive distillation sequence (Figure 1a) and the E-DWC structure (Figure 1b). In Figure 1, AB is the azeotropic mixture and C is the entrainer. Recent researches on E-DWC have been done for the ethanol dehydration process (Kiss & Suszwalak, 2012), methylal-metahol separation (Xia et al., 2012), and isopropyl alcohol dehydration (Wu et al., 2013) among others. Wu et al. (2013) mentioned that it is expected that E-DWC will cover more than 350 different processes in the near future.

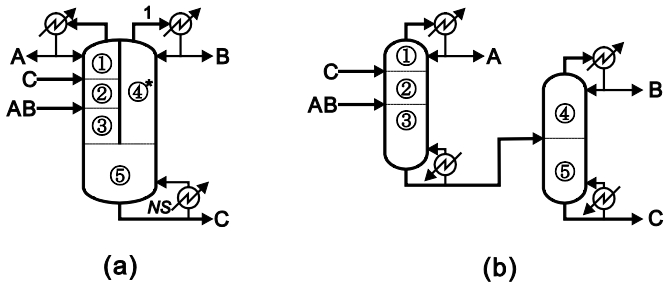

Figure 1: Extractive distillation sequences

In E-DWC, the heat must be supplied to the highest temperature position (reboiler) in the column. Wu et al. (2013) pointed that the use of higher pressure steam resulted in higher steam cost than the conventional process in some cases. Their results showed that E-DWC led to higher steam and total annual cost for the Isopropyl alcohol dehydration process and for the separation of dimethyl carbonate and methanol, but for the acetone and methanol separation E-DWC attained economic and energy savings.

Although the entrainer selection plays a major role in the environmental impact of the process, the assessment of E-DWC has been primarily focused in energy and/or total annual cost minimization while environmental aspects have not been addressed comprehensively. Ravagnani et al. (2010) and Dias et al. (2009) studied the two-column extractive distillation sequence for ethanol dehydration, and used entrainers with less environmental impact.

It is our aim to propose a design and optimization method to find the best extractive distillation sequence in terms of environmental and economic impact, and to clarify the trade-off between these criteria. This research adopts the Life Cycle Impact Assessment (LCIA) methodology proposed by Jolliet et al. (2003) and the Guthrie method proposed by Seider et al. (2009) to evaluate the environmental and economic impact, respectively.

2. Optimization procedure

Recently, embedded optimization tools in process simulators has been increasingly used to derive distillation sequences with the minimum energy consumption or total annual cost. Figueirêdo et al. (2011) and Ravagnani et al. (2010) used the sequential quadratic programming (SQP) available in the process simulator Aspen Plus® to find the optimal design of conventional extractive distillation sequences while Kiss & Suszwalak (2011) used it to find the optimal design of E-DWC.

In this work, it is assumed that the feed and two products flow rate and its composition, and the entrainer candidate are given in advance. The economic term is evaluated by the total annual cost, *TAC*, defined by the following equation:

$$TAC = FC/PT + (OC + EC)OT \quad (1)$$

where *FC*, *OC*, and *EC* are the fixed cost, operation cost and entrainer cost. *PT* is the payback time, and *OT* is the annual operation time. *FC* is a function of the diameter and number of trays in each column, reboiler and condenser heat duty and transfer

areas. *OC* is the product of the utility costs by heat duties, and *EC* is the product of the entrainer cost per unit amount of mass by the entrainer make-up mass flow rate.

The environmental impact, *EI*, is evaluated by Equation 2:

$$EI = I_{CF}\left(EF - EF_{rec}\right)OT \tag{2}$$

where *EF* and EF_{rec} are the amounts of feed and recycled entrainer to the process, respectively. I_{CF} is the characterization factor index, and it is expressed in kg-equivalents of a substance compared to a reference substance. I_{CF} considers the fate, exposure, and intake of emitted chemicals (Jolliet et al., 2003). In Equation 2, I_{CF} and *OT* are parameters, and EF_{rec} is assumed to be given as a fixed ratio of *EF*. Thus, the minimization of *EI* is equivalent to the minimization of *EF*.

For the conventional two-column sequence, the reflux ratio and the heat duty to the reboiler of each column are used to adjust the product flow rate and its composition. Thus, the variables which can be used for optimization are i) Entrainer flow rate, ii) Number of stages of the first column, iii) Number of stages of the second column, iv) Feed stage of the first column, v) Feed stage of the second column, and vi) Entrainer feed stage to the first column. The section analogy between the two-column sequence and E-DWC is shown in Figure 1. The sections shown by the same number are regarded to have the same function.

For E-DWC, the reflux ratio of two sections and the heat duty to the reboiler are also used to adjust the product flow rate and its composition. The optimization variables are i) Entrainer flow rate, ii) Split ratio of the vapor to the two dividing sections, iii) Number of total stages (④*+⑤ in Figure 1a), iv) Feed stage, v) Entrainer feed stage, and vi) Number of dividing stages (④* in Figure 1a). In this work the SQP method is used at the inner loop to optimize the continuous variables (i.e., i and ii) and sensitivity analyses are used at the outer loop to optimize the discrete variables (i.e., iii, iv, v, and vi). The inner loop is optimized by assuming that the discrete variables are fixed to predetermined values at the outer loop. Sensitivity analyses at the outer loop solve combinatorial problems which include one set of candidate integer values for each discrete variable.

The optimal value of the entrainer feed flow rate for TAC minimization is expressed by *EFC**. To avoid unrealistic solutions, the upper and lower bounds of *EF* are introduced for *EI* minimization by taking *EFC** into account. By repeatedly executing the optimization of *TAC* for the different lower bounds of *EF*, the trade-off between economic and environmental criteria can be obtained.

3. Results and discussion

The proposed optimization algorithms were applied to the dehydration of ethanol. Propylene glycol is selected as the entrainer. Table 1 summarizes the parameters used to solve the optimization procedure shown in section 2.

Additionally, the assumed *PT* was set at 3, 5, and 10 years while *OT* was 8000 hours. The heat transfer coefficients for condensers and reboilers were 0.7 and 1 kW/m^{2}K. The utility cost of cooling water was 0.86 $/MWh, and that for steam at low pressure (S1) and middle pressure (S2) was 18.81 $/MWh and 29.22 $/MWh, respectively.

Table 1: Parameters used in the optimization algorithms

Feed	flow rate [kmol/h]	: 100
	composition (ethanol/water) [mol%]	: (85/15)
Ethanol product	flow rate [kmol/h]	: 86.0
	composition [mol%]	: 99.5
Wastewater product	flow rate [kmol/h]	: 13.9
Entrainer feed (make-up)		
	composition (propylene glycol/water) [mol%]	: (100/0)
	cost [$/kg]	: 1.5
Entrainer product (recycled)		
	recovery in the second column [%]	: 99.9
Characterization factor index (I_{CF}) [-]		: 0.00182

Figure 2 shows the optimization results of *TAC* minimization for the conventional two-column sequence when *PT* was set to 10 years. The number of total stages and feed stages are shown in the figure. In this case, steam S1 is used in the extractive distillation column and S2 is used in the recovery column. If only S2 can be used as utility, *TAC* is 514.6 k$/y. Figure 3 shows the optimization results for different assigned values of *PT*. The effects of the number of stages of the first column, *NS*, are plotted in the figure. It can be seen that the cost does not change remarkably for higher number of stages.

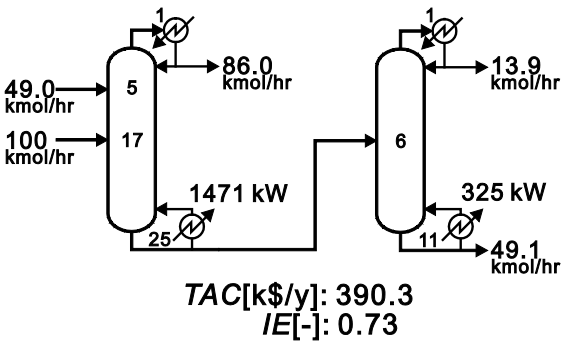

Figure 2: Optimal distillation sequence which minimizes *TAC*

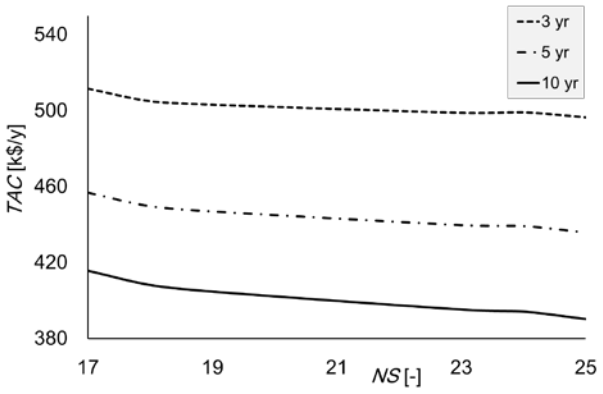

Figure 3: *TAC* of the two-column sequence for several values of *PT*

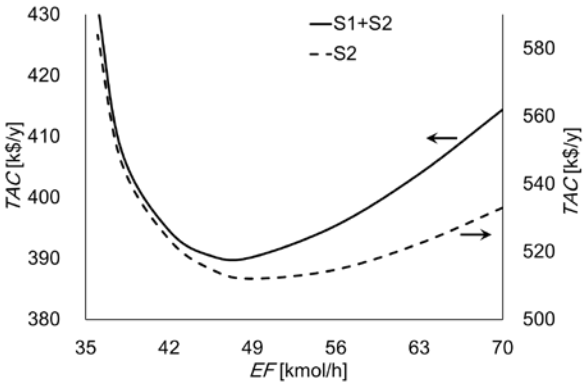

Figure 4: *TAC* as a function of *EF*

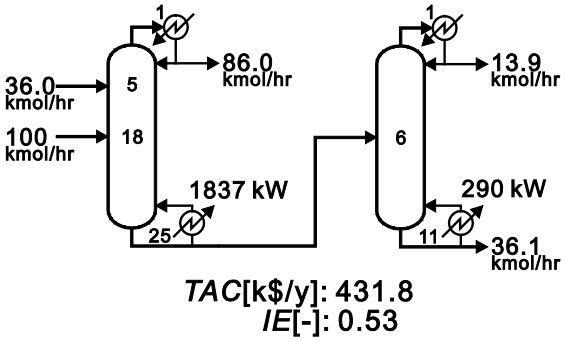

Figure 5: Optimal sequence with minimum entrainer use

Figure 4 shows the relation between *EF* and *TAC* after solving the *TAC* minimization algorithm for the conventional two-column system for the case where *PT* is 10 years. If S2 is used as the only hot utility, the *TAC* becomes remarkably larger. It can be seen that *EFC** is 49 kmol/hr. Values lower than *EFC** increases *TAC*, but decreases *EI* while values higher than *EFC** increases *TAC* and *EI*. In this case the entrainer cost is high, but if the cost becomes lower, *EFC** will be shifted a higher value, and if *EC* is removed from Equation 1, *EFC** is around 57 kmol/hr. Figure 5 shows the optimal solution with the minimum make up entrainer consumption, thus *EI*.

For the case of E-DWC, previous researches (Kiss & Suszwalak, 2012; Wu et al., 2013; Xia et al., 2012) have reported that the optimal entrainer flow rate in conventional extractive distillation and E-DWC is almost at the same value. Similar to conventional extractive distillation, the *TAC* for E-DWC is not very sensitive to the total number of stages when *EF* is at the optimal value. However, when the *EF* is small, the *TAC* becomes sensitive to the total number of stages.

Figure 6 shows the E-DWC with the minimum *TAC* and Figure 7 shows the E-DWC with the minimum *EI*. The *TAC* in Figure 6 is higher than that in Figure 2 because the latter uses steam at low pressure in the extractive column and the latter uses middle pressure in the recovery column, however, if only S2 is used in Figure 2, economic savings of 5 % can be achieved by E-DWC. Figure 7 uses an amount of make-up entrainer less than Figure 5 regardless the steam condition at the reboiles. If only S2 is used in Figure 5, the E-DWC can attain 9 % energy savings and 3 % of *EI* reduction.

If the make-up entrainer cost is not considered in Equation 1, *EFC** is 56 kmol/hr. This value is less than the one used by the conventional column in Figure 2 under the same assumption.

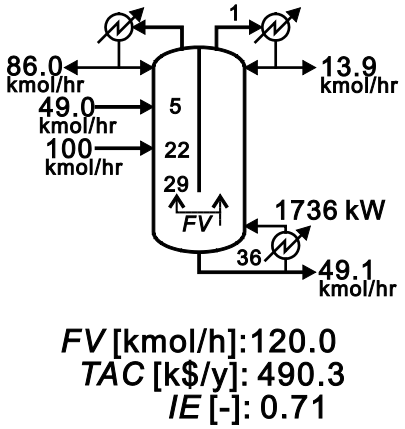

Figure 6: Optimal E-DWC with the the minimum *TAC*

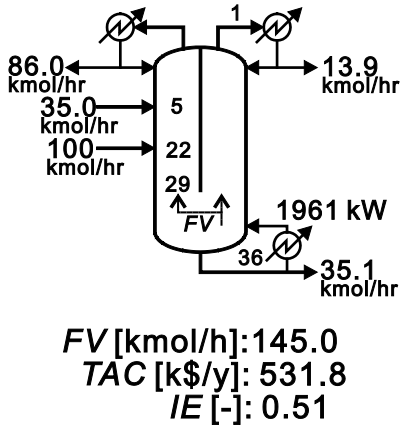

Figure 7: Optimal E-DWC with the minimum entrainer use

4. Conclusions

Optimization algorithms to minimize the total annual cost and environmental impact were proposed to solve the extractive distillation synthesis problem of conventional and dividing wall columns. The results showed that extractive dividing wall columns were superior in terms of energy and environmental impact reduction. In addition, the optimal entrainer flow rate was less in extractive diving wall columns. The

optimization algorithms based on the environmental impact minimization could attain energy savings and economic savings in case middle pressure steam is only available.

Although the economic appealing of extractive dividing wall columns can be debated, the energy and environmental benefits of it were demonstrated for the ethanol dehydration process. The trade-off between total annual cost and environmental impact was also assessed quantitatively. By worsening 10 % the total annual cost in the extractive conventional distillation process, the use of entrainer make-up and the environmental impact can be reduced 28 %, and by worsening 8 % the total annual cost in the extractive dividing wall column, the use of entrainer make-up and the environmental impact can be reduced 29 %. This means extractive dividing wall columns shows a better trade-off in economic and environmental viewpoints

Acknowledgements
J. R. A. A. and S. H. thank the financial support provided by the Ministry of Education, Culture, Sports, Science, and Technology of Japan (MEXT) through the Education Unit for Global Leaders in Advanced Engineering and Pharmaceutical Sciences (GL Education Unit) at Kyoto University.

References
I. Dejanović, Lj. Matijaševi, Ž. Olujić. Dividing wall column—A breakthrough towards sustainable distilling. *Chem. Eng. Process*, 2010, 49, 559−580.
M. O. S. Dias, M. Modesto, A. V. S. Ensinas, A. Nebra, R. M. Filho, C. E. V. Rossell. Improving bioethanol production from sugarcane: evaluation of distillation, thermal integration and cogeneration systems. *Energy*, 2011, 36, 3691-3703.
M. F. Figueirêdo, B. P. Guedes, J. M. M. Araújo, L. G. S. Vasconcelos, R. P. Brito. Optimal design of extractive distillation columns—A systematic procedure using a process simulator. *Chem. Eng. Res. Des.*, 2011, 89, 341-346.
A. A. Kiss, D. J.-P. C. Suszwalak. Enhanced bioethanol dehydration by extractive and azeotropic distillation in dividing-wall columns. *Sep. Purif. Technol.,* 2012, 86, 70−78.
O. Jolliet, M. Margni, R. Charles, S. Humbert, J. Payet, G. Rebitzer, R. Rosenbaum. IMPACT 2002+: a new life cycle impact assessment methodology. *Int. J. Life Cycle Ass*., 2003, 8(6), 324-330.
M. A. S. S. Ravagnani, M. H. M. Reis, R. M. Filho, M.R. Wolf-Maciel. Anhydrous ethanol production by extractive distillation: a solvent case study, *Process Saf. Environ.*, 2010, 88, 67-73.
W. D. Seider, J. D. Seader, D. R. Lewin, S. Widagdo. Product and Process Design Principles. Asia: John Wiley & Sons, Inc. 2010.
Y. C. Wu, P. H.-C. Hsu, I-L. Chien. Critical assessment of the energy-saving potential of an extractive dividing-wall column. *Ind. Eng. Chem. Res.,* 2013, 52, 5384−5399.
M. Xia, B. Yu, Q. Wang, H. Jiao, C. Xu. Design and control of extractive dividing-wall column for separating methylal−methanol mixture. *Ind. Eng. Chem. Res.,* 2012, 51, 16016−16033.

Optimal extractive distillation process for bioethanol dehydration

Radu M. Ignat,[1] A.A. Kiss,[2] Costin S. Bildea[1]

[1]University Politehnica of Bucharest, Bucharest/Romania;

[2]AkzoNobel Research, Development & Innovation, Deventer/Netherlands;

Abstract

The large-scale production of bioethanol fuel requires energy demanding distillation steps to concentrate the diluted streams from the fermentation step and to overcome the presence of the ethanol-water azeotrope. The conventional separation sequence consists of three distillation columns performing several tasks with high energy penalties: pre-concentration of ethanol (PDC), extractive distillation (EDC) and solvent recovery (SRC). It is remarkable that almost all papers on this topic focus on the azeotropic separation only, while neglecting the pre-concentration step. Usually, ethanol concentration in the first distillate stream is arbitrarily considered close to the azeotropic composition. While the energy usage in the PDC increases as the distillate composition gets closer to the azeotrope, the energy requirements in the EDC-SRC units decreases as the feed to EDC becomes richer in ethanol – and the other way around.

This paper addresses this key trade-off of the distillate composition – a fundamental issue that was not studied before. Aspen Plus simulations were used to investigate how this parameter affects the energy usage and investment costs of the complete system. This issue applies in any other methods using a pre-concentration column (e.g. extractive and azeotropic distillation). The optimal economics is reached at a distillate concentration of 91 %wt (or 80% mol) ethanol, where the energy use is only 2.11 kWh (7596 kJ) per kg ethanol.

Keywords

Extractive distillation, economic optimum, process optimization

1. Introduction

Bioethanol is one of the most promising alternative and sustainable biofuel. The bioethanol production at industrial scale relies on several processes, such as: corn-to-ethanol, sugarcane-to-ethanol, basic and integrated lignocellulosic biomass-to-ethanol. After the initial pre-treatment steps, the raw materials enter the fermentation stage where ethanol is produced (Vane, 2008). A common feature of all these technologies is the production of diluted bioethanol – about 5-12 %wt ethanol – that needs to be further concentrated to a maximum allowed water content of 0.2 %vol (EU), 0.4 %vol (BR) or 1.0 %vol (US) according to various standards.

Several energy demanding separation steps are required to reach high purities, mainly due to the presence of the binary azeotrope ethanol-water (95.63 %wt ethanol). The first step is carried out in a pre-concentration distillation column (PDC) that concentrates ethanol from 5-12% up to near azeotropic compositions (Frolkova, 2012). The second step is the ethanol dehydration up to higher concentrations above the azeotropic composition, which is more complex and of greater research interest.

Several alternatives are also available and well described in the literature: pervaporation, adsorption, pressure-swing distillation, extractive distillation (ED), azeotropic distillation (AD), as well as hybrid methods (Vane, 2008; Frolkova, 2012). Extractive distillation (ED) remains the option of choice in case of large scale production of bioethanol fuel, and it involves an extractive distillation column (EDC) and a solvent recovery column (SRC) for the ethanol dehydration – see Figure 1.

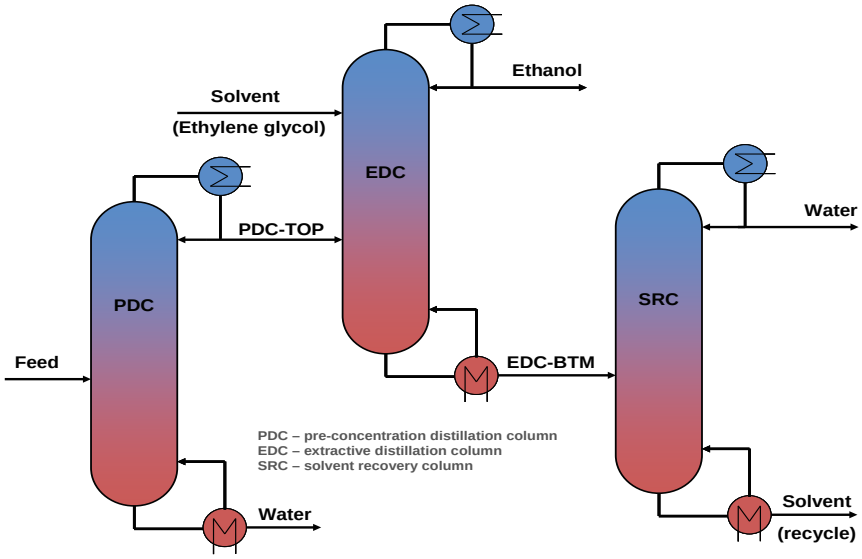

Figure 1. Flowsheet for bioethanol pre-concentration and dehydration by extractive distillation

Almost all reports focus only on the separation of ethanol-water azeotrope, neglecting the pre-concentration step. Typically, the ethanol concentration in the first distillate stream is arbitrarily considered close to the azeotropic composition. Though the energy usage in the PDC increases as the distillate composition approaches the azeotrope, the energy requirements in the EDC and SRC units decrease correspondingly as the feed to EDC becomes richer in ethanol. This paper addresses this key trade-off of the distillate composition – a fundamental issue that was not studied before. A mixture of 10 %wt (4.2 %mol) ethanol is concentrated and dehydrated using ethylene glycol as solvent. Rigorous Aspen Plus simulations were used to investigate how this parameter affects the energy usage and investment costs of the complete system. Note that this important issue applies in any other dehydration methods using a pre-concentration column.

2. Problem statement

The composition of the distillate from the PDC unit is a key design optimization variable that was so far neglected in the optimal design of extractive distillation systems for ethanol dehydration. For example, Ryan and Doherty (1989) assumed a composition of 94.9 %wt (88 %mol) ethanol which is rather close to the azeotropic composition, while other authors (Kiss and Ignat, 2012; Kiss and Suszwalak, 2012; Li and Bai, 2012) selected more practical compositions of about 93.5 %wt (85 %mol).

The problem is how to select this key design parameter such that the energy requirements and the capital cost of the two sections of the process (pre-concentration and dehydration of ethanol) are economically balanced to minimize the overall costs. To solve this problem, we investigate here the effect of the PDC distillate composition and prove that the optimal value is lower than what was considered so far in the literature.

3. Results and discussion

Extractive distillation performs the separation of close boiling components or azeotropes in the presence of a miscible, high boiling, relatively non-volatile component that forms no azeotrope with the other components in the mixture. For the ethanol-water mixture, ethylene glycol remains the most common entrainer used in extractive distillation processes. However, the use of ethylene glycol could become restricted in the future due to its toxicity. For this reason novel solvents are currently explored, as for example: glycerol, hyperbranched polymers and ionic liquids.

Aspen Plus simulations were performed using the rigorous RADFRAC unit for distillation. NRTL (non-random two-liquid) was used as the most adequate property method, due to the presence of a non-ideal mixture containing polar components. The ternary mixture ethanol-water-glycol presents a single binary azeotrope and no liquid phase splitting – as shown in previous work (Kiss and Suszwalak, 2012). The feed used here is the diluted bioethanol stream (10 %wt or 4.2 %mol ethanol) obtained by fermentation. This is distilled to a composition below the azeotropic one, and then dehydrated to a purity of over 99.8 %wt ethanol, to comply with all the bioethanol standards. The production rate considered in this work is 100 ktpy.

The conventional sequence presented in Figure 1 consists of three distillation units: pre-concentration distillation column (PDC), extractive distillation column (EDC) and solvent recovery column (SRC). The first column (PDC) in the sequence has the function to separate water as bottom stream and a near-azeotropic composition mixture as distillate – sent afterward to the second column (EDC). In the EDC unit, ethylene glycol – used as a high boiling solvent – is added on a stage higher than the feed stage of the ethanol-water mixture. Due to the presence of the solvent the relative volatility of ethanol-water is changed such that the separation becomes possible. High purity ethanol is collected as top distillate product of the EDC, while the bottom product contains only solvent and water. The solvent is then completely recovered in the bottom of the third column (SRC), cooled in a heat recovery system, and then recycled back to the extractive distillation column. An additional water stream is obtained as distillate of the SRC unit. The bottom product of the SRC unit constitutes the solvent recycle stream.

The SQP optimization method and the effective sensitivity analysis tool from Aspen Plus® were used in the optimization procedure of all processes. Backed by a solid theoretical and computational foundation, the sequential quadratic programming method has become one of the most successful methods for solving nonlinearly constrained optimization problems (Murray, 1969; Bartholomew-Biggs, 2008). The objective of the optimization is to find the optimal trade-off between the energy requirements and the equipment cost, both translated into the total annual cost (TAC). The objective function used approximates very well the minimum of total annualized cost of a conventional distillation column. The procedure was described in detail in our recent work (Kiss and Ignat, 2012; Kiss and Suszwalak, 2012).

$$min\ N_T\,(RR+1) = f\,(N_{T,i},\ N_{F,i},\ SFR,\ RR_i,\ V_i) \qquad (1)$$

Subject to $\vec{y}_m \geq \vec{x}_m$

where i is the distillation column (PDC, EDC, SRC), N_T is the total number of stages, N_F is the feed stage, SFR is the solvent-to-feed ratio, RR is the reflux ratio, V is the boilup rate for each of the three columns, while y_m and x_m are vectors of the obtained and required purities for the m products.

In order to perform a fair comparison between all process alternatives, the total investment costs (TIC), total operating costs (TOC) and total annual costs (TAC) were calculated, as described in our previous studies (Kiss and Ignat, 2012; Kiss and Suszwalak, 2012). The equipment costs are estimated using correlations from the Douglas textbook, updated to the level of 2010. The Marshall & Swift equipment cost index (M&S) considered in this work has a value of 1468.6. Moreover, a price of 600 US $/m^2 was used for calculating the cost of the sieve trays, and the following utility costs were considered: US $0.03/t cooling water and US $13/t steam. For the TAC calculations, a total plant lifetime of 10 years was considered (Kiss and Ignat, 2012).
The composition of the pre-concentrated ethanol stream was varied in the range 75-93.5 %wt (54-85 %mol) ethanol and for each value considered the process flowsheet was optimized. Table 1 shows the main results of the sensitivity analysis, including the total investment costs (TIC), total operating costs (TOC) and the total annual cost (TAC) as well as the total reboiler duty and the specific energy use per kg product.

Table 1. Results of the sensitivity analysis: key performance indicators (KPI) as function of the composition of the pre-concentrated ethanol stream

Pre-concentrated EtOH (wt%)	Total investment cost (TIC)	Total operating cost (TOC)	Total annual cost (TAC)	Reboiler duties: PDC, EDC, SRC (kW)	Energy use (kW/kg EtOH)
75.0	$4,299,460	$6,003,454	$6,433,400	18135 / 6658 / 4025	2.31
80.0	$4,197,003	$5,842,719	$6,262,419	18427 / 6347 / 3292	2.25
85.0	$4,138,478	$5,684,488	$6,098,336	18487 / 6259 / 2578	2.19
87.0	$4,054,603	$5,590,383	$5,995,843	18547 / 6021 / 2315	2.15
89.0	$3,983,370	$5,506,929	$5,905,266	18608 / 5833 / 2051	2.12
90.0	$3,951,436	$5,493,809	$5,888,952	18680 / 5823 / 1927	2.12
91.0	**$3,915,109**	**$5,475,770**	**$5,867,281**	**18847 / 5673 / 1829**	**2.11**
91.5	$3,969,593	$5,542,080	$5,939,039	19208 / 5658 / 1793	2.13
92.0	$3,994,262	$5,624,435	$6,023,861	19777 / 5589 / 1679	2.16
93.0	$4,199,949	$6,042,605	$6,462,600	21885 / 5577 / 1542	2.32
93.5	$4,409,534	$6,445,864	$6,886,817	23865 / 5574 / 1453	2.47

In addition, Figure 2 shows the optimal composition value of the pre-concentrated ethanol stream for minimal specific energy use and lowest total annual cost (TAC). It is worth noting that when the pre-concentrated ethanol stream has a composition below the optimal value, the duty of the PDC decreases with the ethanol concentration in the distillate, while the duties of the EDC and SRC units increases since more effort is needed to remove the higher amount of remaining water.
Similarly, for pre-concentrated compositions higher than the optimal value, the duties of the EDC and SRC units is lower since less effort is needed to remove the smaller amount of remaining water. However, the duty of the PDC unit has a very steep increase due to approaching the azeotropic composition. Balancing these two effects lead to the optimal value of 91 %wt ethanol in the pre-concentrated stream. Just by changing this key parameter, over 15% energy savings are possible in existing plants that still use a pre-concentrated stream of near azeotropic composition. It is worth mentioning that a similar value for the trade-off concentration (80% mol ethanol in the beer-still distillate) was recently reported for the case of a heterogeneous azeotropic distillation process for ethanol dehydration, using a more concentrated ethanol feed (5% mol) and benzene or cyclohexane as light entrainers (Luyben, 2012).

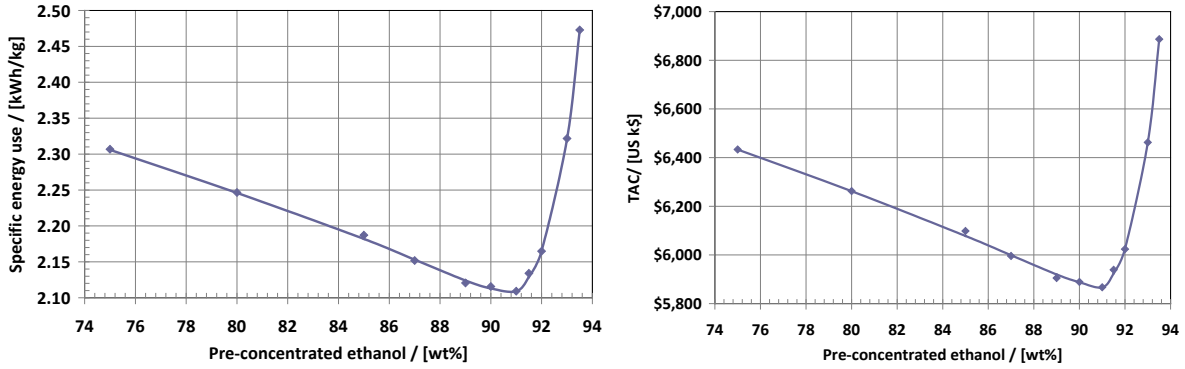

Figure 2. Specific energy use per kg of ethanol product (left) and total annual cost (right), as function of the composition of the pre-concentrated ethanol stream

Table 2 lists the key design and process parameters of the optimized flowsheet. Note that in case of the non-optimal configurations, the number of stages varies within ± 20% more or less stages depending on the separation difficulty. The effect of the pre-concentrated ethanol composition on the equipment design can be summarized as follows: the number of stages and the diameter of the PDC column increases with the ethanol concentration in the pre-concentrated stream, due to the more difficult separation and higher reflux required. However, for the EDC and SRC columns the variation of the required number of stages is rather minor due to the insignificant change in the separation difficulty, while the column diameters are increasing at lower pre-concentrated composition since more water is present in the feed.

Table 2**.** Design parameters of an optimal conventional sequence for bioethanol dehydration by extractive distillation

Design parameters	**PDC**	**EDC**	**SRC**	**Unit**
Total number of stages	30	17	16	–
Feed stage number	19	11	8	–
Feed stage of extractive solvent	–	4	–	–
Column diameter	2.9	1.5	1	m
Operating pressure	1	1	1	bar
Feed composition (mass fraction)				
Ethanol : water	0.1 : 0.9	0.91 : 0.09	–	kg/kg
Water : solvent	–	–	0.055 : 0.945	kg/kg
Feed flowrate (mass)				
Ethanol	12500	12494	0.625	kg/hr
Water	112500	1236	1215	kg/hr
Solvent	0	20793	20788	kg/hr
Reflux ratio	1.31	0.24	0.45	kg/kg
Reboiler duty	18847	5673	1829	kW
Condenser duty	-8600	-3652	-1112	kW
Ethanol recovery	–	99.96	–	%
Water recovery	99.98	–	99.98	%
Solvent (EG) recovery	–	–	99.91	%
Purity of bioethanol product	–	99.80	–	%wt
Purity of water by-product	99.99	–	99.99	%wt
Purity of ethylene glycol recycle	–	–	99.99	%wt

In order to assess the controllability of the optimal design, a dynamic simulation model was built using Aspen Dynamics. For all columns, the pressure is controlled by condenser duty, while the distillate and bottoms flow rates are used to control the

levels in the reflux drums and column sumps, respectively. The pre-concentration column is operated at constant reflux ratio, while the temperature in the stripping section (stage 25) is controlled by the reboiler duty. Similarly, the EDC unit is operated at constant reflux, constant solvent to feed ratio, the temperature in the lower part (stage 15) being controlled by the reboiler duty. Dual temperature control (stages 4 and 13), by means of reflux rate and reboiler duty, is employed for SRC.
Figure 3 presents results of dynamic simulation which prove the controllability of the optimal design. Starting from the steady state, the feed flow rate is increased by 10%, from 125 to 137 ton/h (Figure 3, left). The transitory regime lasts for about 2 hours, new values for the product flows being established. The water and ethanol purity remain very close to the initial value. In a second simulation (Figure 3, right), the concentration of the raw material is reduced from 10 to 8 %wt ethanol. The new values of the product flow rates are achieved in about 2 hours, with minor deviations of the product purities.

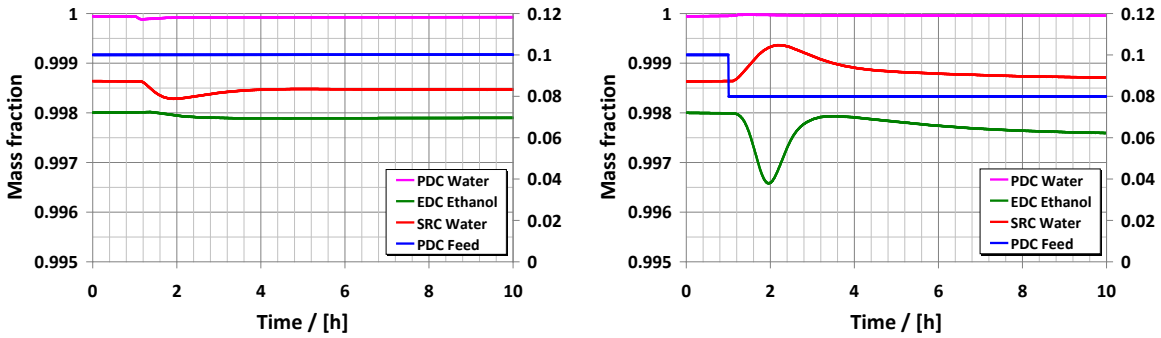

Figure 3. Dynamic simulations for +10% feed flowrate disturbance (left) and a reduction from 10 to 8 %wt of ethanol concentration in the feed (right)

4. Conclusions

A key contribution of this study is creating awareness that the composition of the pre-concentrated ethanol stream is an important design optimization variable that was neglected so far in many articles, as well as calculating the optimal value of this parameter in order to obtain minimum total annual costs.
Rigorous Aspen Plus simulations were successfully used to investigate how the trade-off of the distillate composition affects the energy usage and the investment costs of the complete system for ethanol dehydration by extractive distillation, using ethylene glycol as a mass separation agent. In addition, Aspen Dynamics simulations were employed to prove the controllability of the optimized process. The economical optimum was found at a distillate concentration of 91 %wt (or ~80% mol) ethanol, where the energy use is 2.11 kWh (7596 kJ) per kg ethanol (Kiss and Ignat, 2013).

References

Bartholomew-Biggs M., Nonlinear optimization with engineering applications, Springer 2008.
Frolkova A. K., Raeva V. M., 2012, Theor. Found. Chem. Eng., 44, 545-566.
Kiss A. A., Ignat R. M., 2012, Sep. Purif. Technol., 98, 290-297.
Kiss A. A., Suszwalak D. J-P. C., 2012, Sep. Purif. Technol., 86, 70-78.
Kiss A. A., Ignat R. M., 2013, Energy Technol., 1, 166-170.
Li G., Bai P., 2012, Ind. Eng. Chem. Res., 51, 2723-2729.
Luyben W. L., 2012, Ind. Eng. Chem. Res., 51, 16427-16432.
Murray W., in Optimization (Ed. Fletcher R.), Academic Press, New York 1969.
Ryan P. J., Doherty M. F., 1989, AIChE J., 35, 1592-1601.
Vane L. M., 2008, Biofuels Bioprod. Bioref., 2, 553-588.

Supersaturation and solvent losses in reactive absorption columns

Erik von Harbou[1], Michael Imle[1], Leonie Brachert[2], Karlheinz Schaber[2], Hans Hasse[1]
[1]Laboratory of Engineering Thermodynamics, University of Kaiserslautern, Germany;
[2]Institut für Technische Thermodynamik und Kältetechnik, Karlsruhe Institute of Technology (KIT), Karlsruhe, Germany

Abstract

In this work, a method is presented that enables to test for the occurrence of supersaturation of the gas phase in absorption columns by means of rate-based simulations. Simulations of pilot-plant experiments of the reactive absorption of carbon dioxide in an aqueous solution of monoethanolamine (MEA) are used as example. The simulations are carried out with a carefully validated rate-based model which is known to give accurate predictions of experimental data from carbon dioxide capture pilot plants in different scales. The superaturation of the gas phase along the absorber column is predicted for different operating points, so that the influence of the process parameters on the supersaturation is revealed. The observed supersaturations are in the range, where aerosol formation by heterogeneous nucleation must be expected. In PCC, nuclei for such condensation are soot particles or sulfuric acid aerosols, which are always present. The results from the present study for the supersaturation are shown to be completely in line with the experimental findings recently reported. They give an explanation for the extremely high solvent losses observed in PCC. The approach presented here opens up new possibilities for modeling aerosol formation in absorption columns based on rate-based models. Furthermore, by means of the presented method countermeasures can be studied to reduce the formation of aerosols in reactive absorption columns.

Keywords

Supersaturation, absorption, rate-based model, amine, carbon dioxide, nucleation

1. Introduction

Supersaturation of the gas phase has been observed in many industrial absorption processes especially if strong acid components like hydrochloric acid, bromic acid, or sulfuric acid are absorbed in aqueous solutions [1]. Caused by simultaneous heat and mass transfer over the gas-liquid interface the concentration of the condensable components in the gas phase may exceed the corresponding concentration in vapor-liquid equilibrium (VLE) and the gas phase becomes supersaturated. As a result of the supersaturation of the gas phase, aerosols may be formed initiated by heterogeneous or homogeneous nucleation [1, 2, 3]. The aerosols can leave the process via the gas outlet and cause an increased emission of solvent compared to the case without aerosol formation. The emission of solvent is both an important economic and ecologic issue in operating reactive absorption columns.

Recently, it was demonstrated that the emission of amine increases drastically when sulfuric acid aerosols are introduced in the rich gas as nuclei [4, 5]. The

concentration of monoethanolamine (MEA) in the lean gas was much higher than the concentration expected from the volatility of MEA. Sulfuric acid is present in the rich gas when sulfur containing fuel is used for the combustion (e.g. coal fired power plants) and a wet flue gas desulfurisation is employed [6]. Khakharia et al. [4] conclude that the emission of MEA is caused by aerosols that are formed in the gas phase due to supersaturation and nucleation or due to reaction of CO_2 with MEA in the aerosol phase.

Reactive absorption processes are commonly described with rate-based models. Von Harbou et al. [7] implemented a rate-based model for a solvent containing a 30 ma% aqueous solution of MEA in Aspen Plus (Aspen RateSep) which is based on a new model of the physico-chemical properties [8]. This model predicts experimental plant data both in pilot and industrial plant scale well without any adjustment of parameters to the experimental data. In contrast to equilibrium stage models, in rate-based models the gas and liquid phase are only in equilibrium at the interface. The heat and mass transfer is explicitly accounted for and the bulk phases are generally not in phase equilibrium. Thus, rate-based models may be used for predictions of supersaturation of the gas phase. This fact seems to have been overlooked in the literature. We have only found one paper that mentions this important fact in the context of a study of an absorption column operated with air and water [9].

In this work, we present for the first time a method for calculating the saturation in the gas phase of reactive absorption columns by means of the rate-based model. Furthermore, this method enables a (worst-case) estimation of the mass flow of solvent that is lost via the gas outlet because of supersaturation and aerosol formation. A systematic study of saturation is carried out using the reactive absorption of CO_2 in aqueous solutions of MEA as test case. By comparing the simulation results to experimental results [4, 5, 10], we demonstrate that the influence of different input parameters such as the temperature of the solvent and the concentration of CO_2 in the rich gas is correctly described.

2. Saturation and Nucleation

It is assumed that the studied gaseous mixture is a mixture of ideal gases. The saturation S at a given temperature T and pressure p of that mixture is defined as the sum of the partial pressures of all condensable components in the mixture divided by the dew point pressure p^{dew} of the corresponding mixture of the condensable components.

$$S = \frac{p \sum_{i=1}^{N_c} y_i}{p^{\mathrm{dew}}} \tag{1}$$

The gas phase is supersaturated if S is larger than 1. In the simulation of the absorption of CO_2 from rich gas with aqueous solution of MEA, the components MEA, water, CO_2, nitrogen and oxygen are accounted for in the gas phase. Nitrogen and oxygen are considered as non-condensable; MEA, water and carbon dioxide as condensable. CO_2 reacts with the solvent and forms HCO^{3-}, CO_3^{2-}, and $MEACOO^-$ (the carbamate of MEA). These reactions are implicitly taken into account in the definition given above.

The formation of aerosols is caused by two different mechanisms: homogeneous or heterogeneous nucleation. For homogeneous nucleation, the necessary saturation is

larger than 2 – 6 for water and other substances [11, 12]. Heterogeneous nucleation occurs if nuclei are present in the gas phase and the saturation exceeds a certain value known as the critical heterogeneous saturation. For a given mixture, the critical heterogeneous saturation is a function of the temperature and the radius of the nuclei. In industrial flue gas cleaning processes, aerosol nuclei are usually present in the gas phase. For example sulfuric acid nuclei occur as a product from the desulfurization unit, which is typically used in the case of coal fired power plants. Here, typical aerosol radii are between 10 nm and 75 nm [3], which correspond to a critical heterogeneous saturation between approximately 1.0 and 1.1 for the conditions found in absorption columns.

3. Model and simulations

Process simulations were carried out with Aspen RateSep. The underlying physico-chemical property model as well as the rate-based process model were carefully validated in previous works [7, 8]. The input parameters were specified according to a base case experiment carried out by Notz et al. [13] in a pilot-plant reactive absorption process.

To test for the occurrence of supersaturation in the gas phase, the rate-based process model was extended in this work. A pseudo gas side stream is withdrawn from every segment of the absorption column. The pseudo gas stream has the same composition, pressure, and temperature as the gas phase in that segment but the gas flow in the absorption column itself is not affected. The corresponding flow sheet is shown in Figure 1.

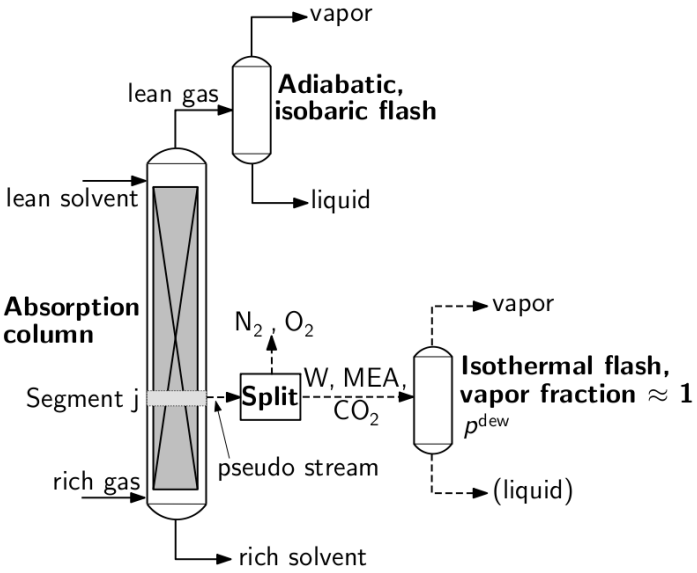

Figure 1. Flow sheet of the absorption column including the isothermal flash used to calculate the saturation profiles and the adiabatic, isobaric flash used to calculate the flow rate of the liquid formed by condensation. --- shows pseudo streams.

The partial pressure of the condensable components in the pseudo gas stream corresponds to the partial pressure employed in the numerator of Eq. (1). This pseudo gas stream is then split into the condensable and non-condensable components. The condensable components are fed into an isothermal flash and the vapor fraction is set to 0.9999. The corresponding pressure is a numerical approximation of the dew point pressure of the condensable components in the gas phase as needed as input for Eq. (1). Hence, the saturation S can be calculated

according to Eq. (1) as a function of the column height. The saturation *S* calculated in this way is the saturation that is present if no condensation takes place and no aerosols are formed in the gas phase.

Also preliminary information on the mass flow of the condensable components in droplets in the gas phase can be obtained from the simulation. For that purpose, the (homogeneous) usually supersaturated gas phase leaving the absorption column for example is fed into an isobaric, adiabatic flash, i.e. a stage, in which the VLE is established. At the outlet of that flash, the saturation *S* is 1 and the mass flow of liquid leaving that flash is the mass flow of liquid droplets that can be formed by condensation in the gas stream.

4. Results and discussion

First, results of the base case simulation are presented. Then, using this base case simulation as starting point, the influence of the concentrations of CO_2 and the influence of the solvent temperature in the washing section is discussed.

4.1 Simulation of the base case

Figure 2a and b show the temperature of the gas and liquid phase and the saturation as a function of the column height. The temperature profiles are in good agreement with the measured profiles [7, 13]. Figure 2c depicts the molar flow rate of water from the liquid to the gas phase as a function of the column height.

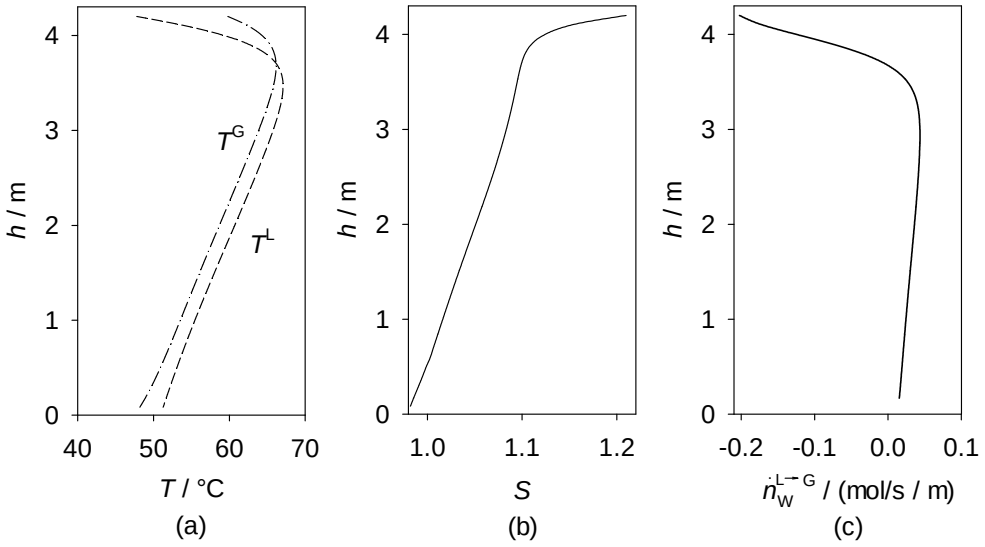

Figure 2. Profiles of a) the temperatures of the gas phase (T^G) and the liquid phase (T^L), b) the saturation *S* without aerosol formation, and c) the molar flow rate of water from the liquid phase into the gas phase ($\dot{n}_W^{L\rightarrow G}$) in the absorption column for the base case experiment.

The profiles in the column have two distinct regions. In the lower part of the column the changes in temperature, saturation and molar flow rate of water from the liquid to the gas phase are low. In the upper part of the column, the slopes of the profiles are changing tremendously. Starting from the bottom, the temperature rises as a result of the heat released upon absorption of the CO_2. As a consequence also water is transferred from the liquid to the gas phase, cf. Figure 2c. In the upper part of the column, the temperatures decrease. This results from the cold lean solvent entering at the top. The direction of the water stream between the gas and the liquid phase is reversed: water condenses in the upper part of the absorption column. Near the top

of the column, the temperature of the liquid is lower than that of the gas, whereas in most parts of the column the temperature of the liquid is higher. This finding is in line with the explanations given above.

As shown in Figure 2b, the gas phase becomes supersaturated ($S > 1$) already after it has passed only one tenth of the column height. After the point of intersection between the temperature of the gas phase and the temperature of the liquid phase, the saturation increases significantly, cf. Figure 2b. The reason for the increase of the saturation of the gas phase after entering the column is the increase of the partial pressures of the condensable components in the gas phase caused by the temperature increase which in turn leads to evaporation of water, cf. Figure 2c. At the upper part of the column, the gas is cooled very fast by the cold lean solvent resulting in a steep increase of saturation due to the decreasing dew point pressure.

The maximum value of the saturation in the absorption column is approximately 1.21, cf. Figure 2b. Hence, the saturation is much lower than the critical homogeneous saturation of approximately 2 – 6 but larger than critical heterogeneous saturation of approximately 1.0 – 1.1 so that no homogeneous but heterogeneous nucleation can occur.

4.2 Study of the concentration of CO_2 in the rich gas

Figure 3 shows the saturation as a function of the column height for different concentrations of CO_2 in the rich gas. The variation of the concentration of CO_2 in the rich gas has a strong influence on the saturation in the lower part of the absorption column. In the upper part the influence is small. At a concentration of CO_2 of about 0.04 g/g, the saturation profile shows the largest values in almost the whole column.

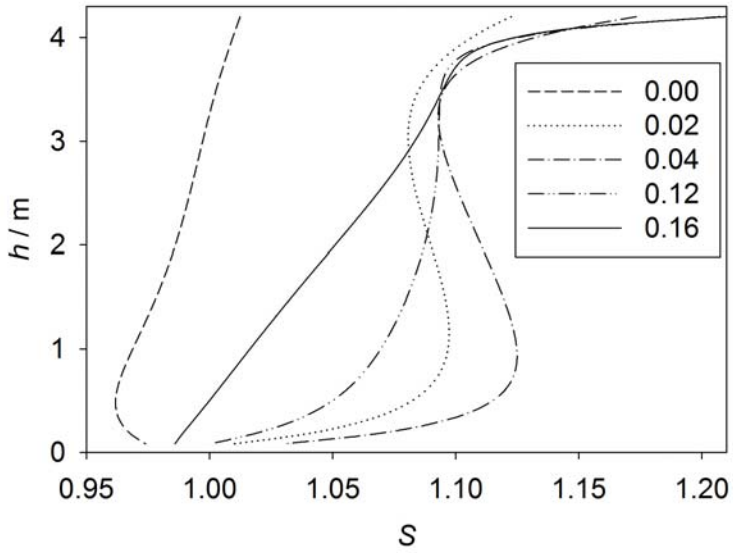

Figure 3. Profiles of the saturation S in the absorption column for different mass fractions of CO_2 in the rich gas.

The finding that the concentration of CO_2 is a dominant parameter for the saturation is in agreement with the experimental results of Khakharia et al. [5]. Also their experimental results show that the MEA emission is at maximum between 4 to 8 vol% CO_2 (corresponding to approx. 6 to 12 ma%) in the rich gas.

4.3 Influence of the solvent temperature in the washing section

In industrial installations for capturing carbon dioxide with aqueous amine solutions, washing sections are used on the top of the absorption column to lower emissions of

the amine. For that reason, simulations of a washing section are carried out using the rate-based model described above. In that example, the lean gas as obtained in the base case simulation at the top of the absorption column is fed to a washing section operated with pure water. The mass flow rate of liquid droplets that can be formed by condensation and aerosol formation in the gas outlet is calculated by means of an isobaric, adiabatic flash as described above.

The results show that the supersaturation of the gas phase and the mass flow rate of liquid droplets increases when the temperature of the washing water is decreased and thus more MEA can be emitted via liquid droplets (i.e. by aerosol formation). This finding could serve as an explanation for the observations of Moser et al. [10]. They report that the emission of amines during the operation of a reactive absorption pilot plant for PCC increased when the temperature of the solvent in the washing section of the absorption column was reduced. They could not find an explanation for this observation as it contradicted their expectation that the volatility of amines and thus the amine emission decreases when the temperature of the solvent is decreased.

5. Conclusions

In this work, the saturation of the gas phase in an absorption column is studied with a rate-based model using the reactive absorption of CO_2 in an aqueous solution of monoethanolamine as example. As the rate-based model does not test for the occurrence of supersaturation by default, the model was extended. The simulation results show that the gas phase is supersaturated in most parts of the absorption column. If nuclei are present in the rich gas, which is usually the case in flue gas scrubbing, this supersaturation is high enough to lead to heterogeneous nucleation. The influence of the concentration of CO_2 in the rich gas, and the influence of the temperature of the lean solvent in the washing section on the saturation and the mass flow of liquid droplets are studied. The observed trends are in good agreement with experimental results on formation of aerosols [4] and explain contradictorily findings [10]. The rate-based simulation method presented in this work supports the development of countermeasures that prevent the formation of aerosols in (reactive) absorption columns.

References

[1] Schaber, K.: Chem. Eng. Sci. 50, 1347 (1995).
[2] Wix, A., Brachert, L., Sinanis, S., Schaber, K.: J. Aerosol. Sci. 41, 1066 (2010).
[3] Brachert, L., Kochenburger, T., Schaber, K.: Aerosol Sci. Technol. 47, 1083 (2013).
[4] Khakharia, P., Brachert, L., Mertens, J., Huizinga, A., Schallert, B., Schaber, K., Vlugt, T. J., Goetheer, E.: Int. J. Greenh. Gas Con. 19, 138 (2013).
[5] Khakharia, P., Huizinga, A., Goetheer, E., Brachert, L., Schaber, K.: unpublished, (2013).
[6] Srivastava, R., Miller, C., Erickson, C., Jambhekar, R.: J. Air Waste Manag. Assoc. 54, 750 (2004).
[7] von Harbou, I., Imle, M., Hasse, H.: Chem. Eng. Sci. 105, 179 (2014).
[8] Wagner, M., von Harbou, I., Kim, J., Ermatchkova, I., Maurer, G., Hasse, H.: J. Chem. Eng. Data 58, 883 (2013).
[9] Vogt, U., Heidenreich, S. : Chem. Eng. Technol. 22, 935 (1999).
[10] Moser, P., Schmidt, S., Wallus, S., Ginsberg, T., Sieder, G., Clausen, I., Palacios, J. G., Stoffregen, T., Mihailowitsch, D.: Energy Procedia 37, 2377 (2013).
[11] VDI, editor. VDI Heat Atlas. Springer-Verlag Berlin Heidelberg, 2nd edition, (2010).
[12] Wix, A., Schaber, K., Ofenloch, O., Ehrig, R., Deuflhard, P.: Chem. Eng. Commun. 194, 565 (2007).
[13] Notz, R., Mangalapally, H. P., Hasse, H.: Int. J. Greenh. Gas Con. 6, 84 (2012).

Increasing the Efficiency of Existing Multicomponent Downstream Processes by Plant-wide Process Optimization

Hilke-Marie Lorenz[1], Daniel Otte[1], Daniel Staak[2], Jens-Uwe Repke[1]
[1]TU Bergakademie Freiberg, Institute of Thermal, Environmental and Natural Products Process Engineering, Freiberg, Germany;
[2]Lonza Group, Visp, Switzerland

Abstract
Methods to increase the efficiency of processes in the chemical industry are often limited by a maximum possible complexity. Therefore, a systematic approach for the improvement of existing complex processes is developed in the presented work. This approach combines heuristical and mathematical methods. After the identification of the optimization potential, modifications in the process have to be developed. The integration of these modifications in the overall process leads to changes in internal streams. Due to recycle streams these changes affect the entire process. Operating points have to be adjusted to the changed conditions. Therefore, an mathematical optimization problem can be formulated. A method based on the global optimization algorithm *Molecular inspired parallel tempering* (MIPT) is developed in a toolbox. The programs MATLAB™ and ChemCAD™ are linked to solve the optimization problem. The developed method is applied to a complex industrial process, which includes 18 unit operations. A challenge for modelling this system is the high number of components.

Keywords
ChemCAD, process synthesis, MINLP, multicomponent mixtures, process simulation, global optimization

1. Introduction

Due to an increasing energy demand and the shortage of fossil resources, sustainable and efficient processes in the chemical industry become more and more important. In the design of new processes, efficiency and sustainability criteria become established. The improvement and the continuous development of existing industrial processes offer a high potential to increase the efficiency. Since, it is still a major challenge to make changes in a running plant, in particular when the process comprises a large number of components, unit operations and internal recycle streams, effective process analysis and optimization is crucial.
For plant-wide process synthesis and optimization several methods are described in literature. Mathematical algorithms are commonly used in contrast to heuristical rules. A superstructure generation of process alternatives can be adopted for process synthesis (Hostrup et. al, 1999). Optimization problems need to be formulated as *mixed integer nonlinear* (MINL) systems (Biegler and Grossmann, 2004). But for a certain complexity with industrial relevant size, these methods often cannot be used (Chakraborty and Linninger, 2002).
A heuristic-mathematical approach is developed for the improvement of existing complex processes in the chemical industry. With this approach modifications to increase the efficiency can be pointed out. The integration of the developed modifications in the process is a complicated step. Due to the high number of recycle

streams the changes will affect the entire process. A method based on mathematical optimization is described in this paper to fulfill the demanded product specifications. The formulated process model is a MINL system. For this task a MATLAB^{TM} based optimization toolbox is developed, where the global optimization MIPT algorithm (Ochoa et al., 2010) is implemented. A connection to the flow sheet simulator ChemCAD^{TM} is programmed.

2. Systematic approach for plant-wide process improvement

The developed approach for a plant-wide improvement of existing complex processes can be divided into five steps (Figure 1).The *first step* covers the formulation of the optimization goal for the entire process. This goal can be either an economic or a process specific goal. The *second step* comprises the analysis and the generation of process knowledge. Collecting existing process data and thermodynamic component properties refines the grasp. Component balances need to be closed. The *third step* covers the interpretation of the results of the process analysis to identify the optimization potential of the process. For this reason bottlenecks need to be identified, as well as process units where the optimization goal can be achieved. Typical indications therefore are blurred separation splits, contaminated waste or recycle streams. Operation problems and production bottlenecks need to be included in this evaluation. At this stage, the detailed knowledge of the thermodynamic behavior of the multicomponent streams becomes important. In the *fourth step*, the development of process modifications is accomplished. Necessary improvement aims for all identified bottlenecks and weak points in the process need to be formulated. For this, sub-processes consisting of several unit-operations are defined where the respective problems can be solved. This can be done with mathematical optimization methods or, if necessary, new unit-operations will be developed and integrated to the existing process. The *fifth and last step* covers the implementation of all process modifications into the existing process. The effect on the entire process in particular has to be considered.

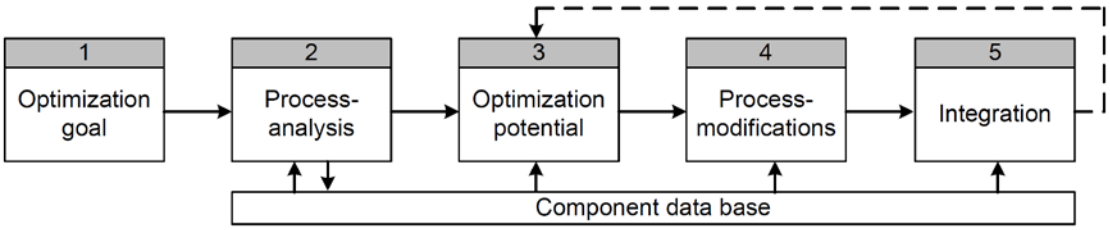

Figure 1. The five step plant-wide process improvement.

Due to a huge number of internal recycle streams the compositions of the streams can change massively by the new modifications. Accomplishing of the optimization goals in accordance with the fixed specifications of all outlet streams (product and waste streams) despite the modified process structure is a mandatory task in this fifth step. As a result, new operating points for the existing units need to be found to fulfill all demanded specifications. The procedure using mathematical optimization methods will be described below.

3. Conclusions

3.1 MIPT algorithm

The stochastical MIPT algorithm (Molecular Inspired Parallel Tempering) (Ochoa et al., 2010) is based on the parallel tempering (PT) algorithm (Earl and Deem, 2005).

In contrast to the PT the MIPT varies the friction force of charged molecules in a solution for tempering, instead of changing the temperature of the replica. The *molecules* are searching the global optimum, where the so called *explorer molecules* are defining the global character and *refiner molecules* determines the local refinement. The classification of molecules is in accordance with the higher and lower temperature classification of the PT. Ochoa et al. (2010) demonstrated that the MIPT algorithm is promising an enhanced performance for global optimization compared to other widely used algorithms. With this robust algorithm it is possible to find the global optimum for highly integrated and complex systems with a reasonable number of function evaluations. Therefore the MIPT algorithm is used in this work for solving the complex optimization problem.

3.2 Optimization Toolbox

An own MATLAB™ based toolbox including the MIPT algorithm is connected to the flowsheet simulation tool ChemCAD™ via an OPC connection. OPC (*O*bject linking and embedding for *p*rocess *c*ontrol) is a standard interface to transfer data between two programs (Iwanitz and Lange, 2010). OPC is widely used in process control (Zamarreno et al., 2014). This connection provides a fast data transfer.

4. Optimization of an existing intermediate product process

4.1 Process description

The previously described approach is applied to an existing industrial downstream process for intermediate products. This process includes 18 unit operations, comprises of up to 30 components and 80 internal streams. Figure 2 shows a block flow diagram of the considered process.

The reactants A and B, the catalyst and the recycle streams are mixed in the *reactor feed preparation*. The reaction takes place in a continuous pipe *reactor*. The reactor outlet stream is separated in the subsequent *preseparation* into unreacted reactants, waste streams and a rough product stream. The main product is separated from two side product streams in the *product purification*.

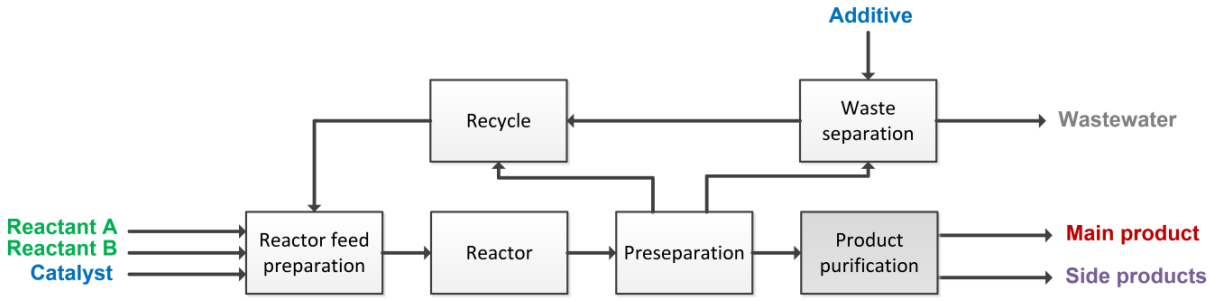

Figure 2. Block flow diagram of the considered industrial downstream process.

The appliance of the first four steps of the described approach (Figure 1) on this process results in modifications in the *preseparation* (Figure 2) to increase the efficiency and the economy of the process. Due to the huge number of internal recycle streams in the previous process sections the modifications have a significant impact on the entire process. Whereas the main product is an intermediate product, there are high requirements on the specifications for the product streams. Determining the influence of the modifications on the product streams is challenging due to the high number of components.

4.2 Product purification sequence

The *product purification sequence* is a key part in the process. Figure 3 shows this distillation sequence. The feed stream is the outlet stream of the *preseparation sequence* (Figure 2). The distillate of the first column C1 (2) contains of unreacted reactants and unwanted side products. The lower boiling side product 1 (3) is purified in column C2. The distillate of column C3 is the main product (6) with the demanded composition. The side product 2 represents the bottom stream (7).

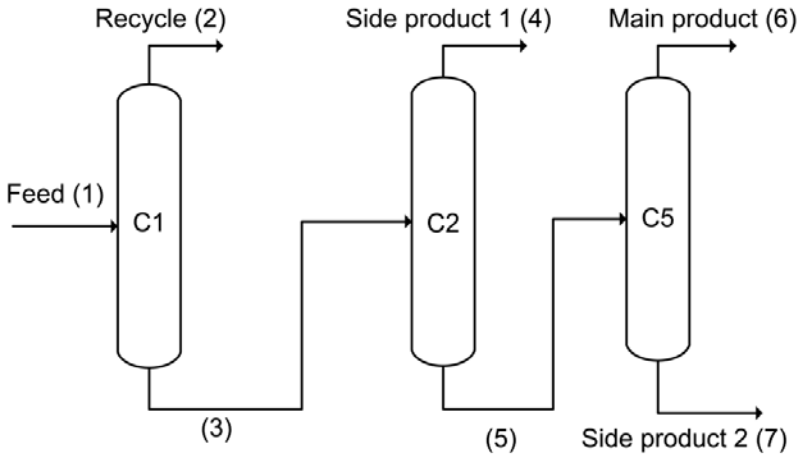

Figure 3. Flow diagram of the product purification sequence.

4.3 Simulation and optimization

The composition of the main product stream has to be guaranteed despite the changing feed compositions. The feed stream (1) contains a high number of components, including also unknown species.

An own property database containing 22 components is implemented in ChemCAD^{TM}. The NRTL method is used to consider the real behavior of the liquid phase. Unknown high boiling components are summarized into two pseudo components.

The current operating point is reproduced by simulation using real process data to validate the thermodynamic model.

4.3.1 Simulation of the actual operating point

The current operating point is built up in ChemCAD^{TM}. The mass and component balances, based on process data, are closed by data reconciliation. Figure 4 shows the comparison for the three columns of the simulation results and the temperature measurements of the real process.

Due to the absence of temperature indicators in C1, the validation for the model of this column is based on analyzed process samples. The temperature profile of C2 is

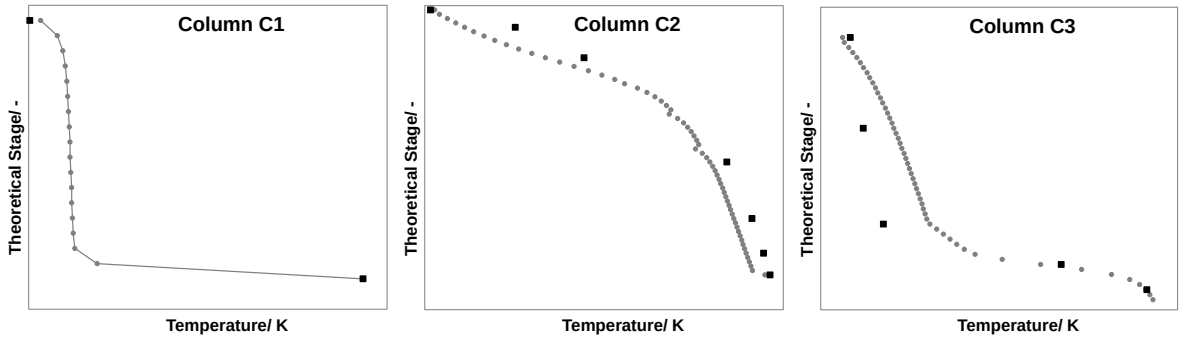

Figure 4. Temperature profiles of C2 and C3, simulation results (grey) and process data (black).

in a good agreement with the process measurements. C3 shows a difference between the results in the middle of the column. This can be explained with the two summarized pseudo components. The distribution of single components in the column, which are contained in the pseudo components, cannot be reproduced. But the temperature of the outlet streams (bottom and distillate) is in a good agreement with the process data.
Table 1 shows the comparison of the total product streams with a normalized feed stream. It can be seen that the simulation can reproduce the real process within an error of 5% with respect to the feed stream.

Table 1. Difference between simulation and process data.

		Feed (1)	Recycle (2)		SP1 (4)		MP (6)		SP2 (7)	
			Real	Sim.	Real	Sim.	Real	Sim.	Real	Sim.
Ṁ	*kg/h*	100	34	29	6	6	55	59	5	6

4.3.2. Problem formulation for new operating points

The optimization problem is formulated in equation 1. A new and optimal operation point for the new feed specifications can be found by the minimization of the cost per mass main product:

$$\min\left(F_{Obj} = \frac{\sum K_i \cdot \left|\dot{Q}_i\right| + \sum K_j \cdot \dot{m}_j}{\dot{m}_6^{MP}}\right) \tag{1}$$

Where K_i are the specific costs for the utilities *i*, K_j are the specific prices for the side products *j*. In addition to the process specific constraints for the optimization, such as the specification for the compositions of the three product streams (4), (6) and (7), there are also constraints due to the existent equipment, such as the stage number, or the maximal heat duty.
The considered decision variables are partly process variables, such as reflux ratio, and partly integer variables, such as the feed stage.
A sensitivity study is carried out to identify the parameters with the highest influence on the objective function and the product streams. With the obtained results the optimization problem can be solved. These results will be presented in the contribution.

5. Conclusions and outlook

A systematic approach for the improvement of existing complex industrial processes was presented. With this approach effective modifications to increase the efficiency of the entire process can be pointed out. For the determination of the new operating point a tool to optimize the units is developed. The MIPT optimization algorithm is implemented in MATLAB™ and this toolbox is connected to the simulation tool ChemCAD™.
The formulated approach is applied to increase the efficiency of an existing industrial synthesis process of intermediate products. Several modifications result in changing internal streams. The developed MATLAB™ toolbox can be used to investigate necessary changes in the operating points of the purification sequence.
First simulations of the distillation sequence show a good agreement with measured process data.
A sensitivity study will be developed to identify the parameters with the highest influence on the product streams. After this the optimization can take place.
Combined with the process modification in the further units the efficiency of the entire process is expected to increase decisively.

References

Biegler, L. T. and Grossmann, I. E., 2004, *Retrospective on optimization*, Computers and Chemical Engineering, Vol. 28, pp. 1169–1192

Earl, D., and Deem, M., 2005, *Parallel tempering: Theory, applications and new perspectives*, Phys Chem, pp. 3910-3916

Chakraborty, A., Linninger, A., 2002, *Plant-Wide Waste Management. 1. Synthesis and Multiobjective Design*, Industrial and Engineering Chemistry Research, 41 *(18),* pp. 4591-4604

Hostrup, M., Harper, P. M., and Gani, R., 1999, *Design of environmentally benign processes: integration of solvent design and separation process synthesis*. Computers and Chemical Engineering, Vol. 23, pp. 1395–1414

Iwanitz F. and Lange, J., 2010, *OPC: From Data Access to Unified Architecture*, VDE-Verlag, 4. Edition, ISBN 978-3800732425

Ochoa, S., Repke, J.-U., and Wozny, G., 2010, *A New Algorithm for Global Optimization: Molecular-Inspired Parallel Tempering*. Computers and Chemical Engineering, 4(12). pp. 2072-2084

Zamarreno, J., Mazaeda, R., Caminero, J., Rivero, A. and Arroyo, J. 2014, *A new plug-in for the creation of OPC servers based on EcosimPro© simulation software*, Simulation Modelling Practice and Theory, 40, pp. 86-94

Separation of ternary mixtures by extractive distillation with 1,2-ethandiol

Sazonova A.Y., Raeva V.M.
Lomonosov Moscow State University of Fine Chemical Technologies, Moscow, Russia

Abstract
Continuous extractive distillation is a widely used method to separate binary and multicomponent azeotropic mixtures. Large scale and heavy energy usage are enormous incentives for finding of more efficient separating agents. Separating agent (entrainer) selection for extractive distillation of binary mixtures is usually based on the analysis of relative volatility diagrams of components to be separated. Selective effect of entrainer is due to the differences in character and intensity of intermolecular interactions between entrainer and original mixture compounds. Accordingly to that it is reasonable to evaluate additional excess Gibbs energy magnitudes in binary systems formed by compounds of original mixture and entrainer[1].
Separating agent selection based on thermodynamic criterion is not uniquely defined for ternary mixtures yet. It establishes some steps of entrainer choice for extractive distillation of ternary mixtures containing several azeotropes. Substantiation of entrainer efficiency is proved by separation of industrial mixtures: tetrahydrofuran - methanol - water and ethyl acetate - ethanol - water.
1,2-Ethandiol is well known to be an effective entrainer for systems of different types, including aqueous mixtures of organic substances[2,3]. It corresponds to the common requirements for entrainer: sufficiently changes the relative volatility of the substances to be separated and no new azeotropes with components of separating mixtures are formed.

Keywords: extractive distillation, excess Gibbs energy, ternary mixtures, isoselectivity, 1,2-ethandiol

1. Introduction

Systems tetrahydrofuran - methanol - water and ethyl acetate - ethanol- water at 101.3 kPa which contain several azeotropes were investigated (Figure 1). According to Serafimov's classification they correspond to diagrams 2.0-2b and 3.1-2[4].
Though binary azeotropes compositions are sensitive to changes in pressure, pressure-swing distillation is not preferable for all compositions of ternary mixtures due to high energy consumption. Taking that into account, extractive distillation is an alternative method of these ternary mixtures separation.
Component relative volatility analysis in ternary and quaternary mixtures proved the validity of 1,2-ethandiol selection for both systems.

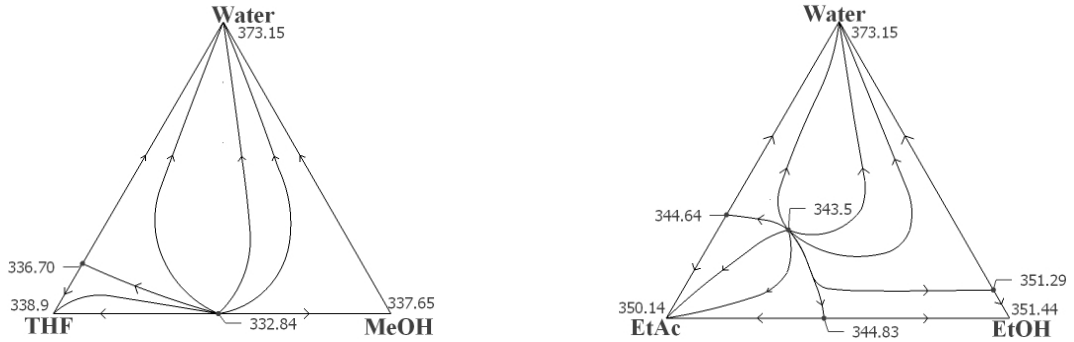

Figure 1: Residue curve map plot at 101.3 kPa for ternary systems (Aspen One 7.3), THF – tetrahydrofuran, MeOH – methanol, EtAc – ethyl acetate, EtOH – ethanol.

2. Results and discussion

To choose agents for extractive distillation of binary azeotropic mixtures thermodynamic criterion was proposed because it establishes a relationship between excess Gibbs energy (g^E) of systems *i* - extractive agent, *j*- extractive agent (*i, j*– azeotrope forming components) and the relative volatility of substances to be separated. Extractive agent is effective in the case that difference in values Δg^E is equal or higher than 1000 J/mol[1]. Criterion values for 1,2-ethandiiol (EG) are sufficient for all binary azeotropes of systems tetrahydrofuran - methanol - water and ethyl acetate - ethanol - water (Figure 2).

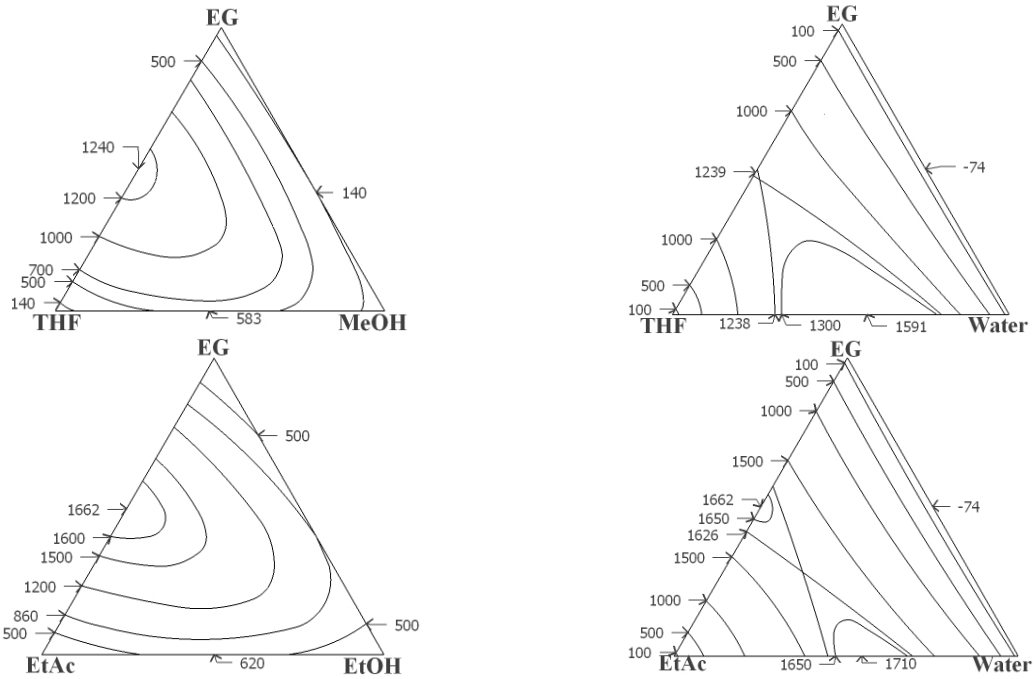

Figure 2: Diagrams of excess Gibbs energy isolines (J/mol) at 101.3 kPa for ternary mixtures

Choice of selective compound is usually carried out by analyzing the relative volatility of substances to be separated. Another characteristic of extractive agent is its selectivity[5]. Extractive agent selectivity towards to components of azeotropic mixture (*i, j* =1, 2, 3) was evaluated using vapor liquid equilibrium data as:

$$S = \frac{\alpha_{ij}^{(4)}}{\alpha_{ij}}.$$

To analyze the entrainer efficiency for the whole range of compositions it was proposed to use isoselectivity diagrams[6,7]. In the composition's areas where S>1, 1,2-ethandiol consumptions and relative volatility change symbatically, for fields with S<1 increase in entrainer consumptions leads to decrease of selectivity, although relative volatility values can stay quite high.

Preliminary results may be obtained by analysis of isoselectivity diagrams (Figure 3). In both systems 1,2-ethandiol shows selective effect towards to components forming binary azeotropes. Selectivity of 1,2-ethandiol towards to tetrahydrofuran is observed for the whole range of tetrahydrofuran – methanol – 1,2-ethandiol ternary mixture compositions (Figure 3a). In case of other ternary mixtures entrainer is effective for limited region of compositions (S>1); for regions where selectivity S<1 additional introduction 1,2-ethandiol is pointless (Figure 3b-d).

The sufficient tetrahydrofuran and ethyl acetate relative volatility in quaternary mixtures is also being observed in regions S>1.

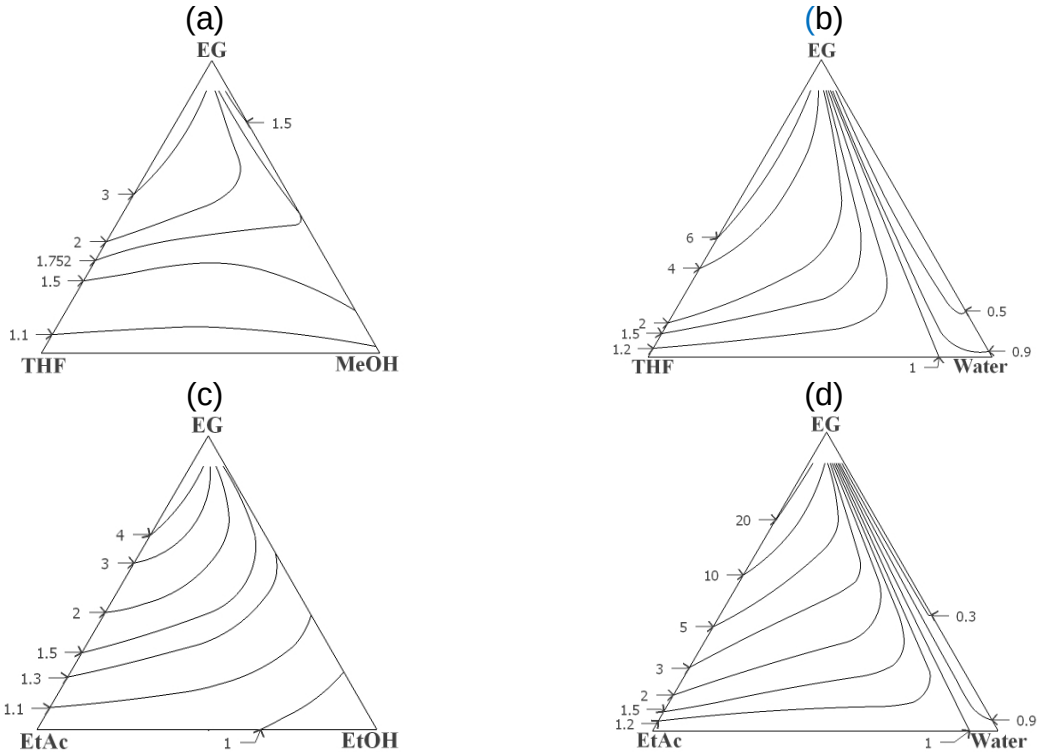

Figure 3: 1,2-Ethandiol isoselectivity plots at 101.3 kPa for original mixture components

a) tetrahydrofuran - methanol - water, b) ethyl acetate - ethanol - water

Conceptual flowsheets of tetrahydrofuran - methanol - water and ethyl acetate - ethanol - water using 1,2-ethandiol are presented in Figures 4, 5. In the second case in *column II* proceeds auto-extractive distillation of mixture ethanol - water - 1,2-ethandiol.

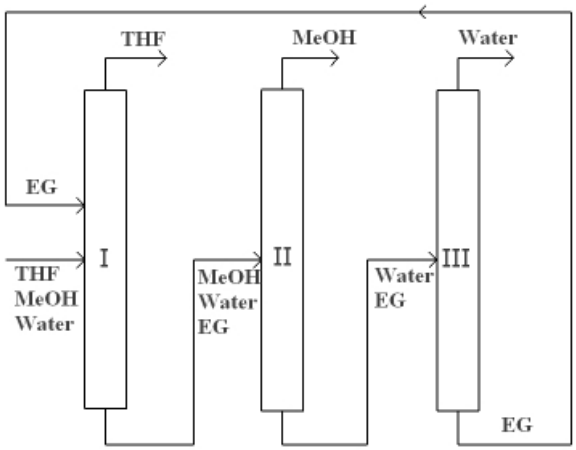

Figure 4: Conceptual flowsheet for tetrahydrofuran – methanol –
– water separation with 1,2-ethandiol.
I – extractive distillation column; *II*, *III* –distillation column

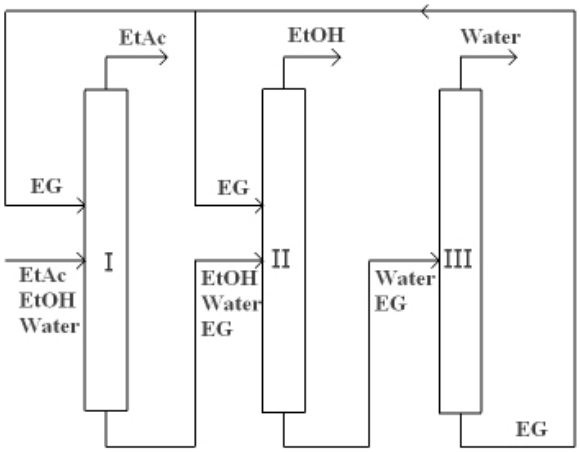

Figure 5: Conceptual flowsheet for ethyl acetate – ethanol –
water separation water separation with 1,2-ethandiol.
I – extractive distillation column; *II* – auto-extractive distillation column;
III – distillation column.

It is well known that 1,2-ethandiol is an effective separating agent for the extractive distillation of ethanol – water mixtures[3]. Thermodynamic criterion verifies 1,2-ethandiol entrainer selection (Figure 6a). For ethanol – water separation the additional amount of entrainer is required (10 kmol/h). The composition of the ternary mixture separated in a *column II* belongs to the region S>1 (Figure 6b).

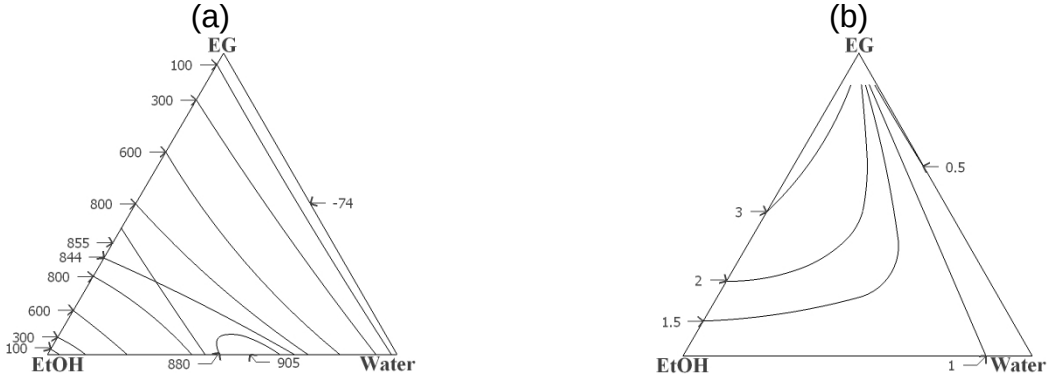

Figure 6: Diagrams of excess Gibbs energy isolines (J/mol) and isoselectivity plots
at 101.3 kPa for ethanol - water - 1,2-ethandiol mixture

Calculations of distillation and vapor-liquid equilibria were performed via Aspen One process simulator, Version 7.3. Vapor-liquid equilibria calculations were modeled using NRTL thermodynamic model (parameters of binary interactions were taken from Aspen database). Due to the limited length of this paper we present the separation results only for one composition of ternary mixture: x_F [0.250; 0.375; 0.375] for tetrahydrofuran - methanol - water and x_F [0.65; 0.04; 0.31] for ethyl acetate - ethanol - water. Total flow of initial ternary mixtures is 100 kmol/h. Column operation conditions providing necessary purity of products with minimum energy consumptions are shown in Tables 1, 2. Entrainer feed temperature for both mixtures is equal to 353.15K. Optimization for entrainer feed temperature was not carried out.

Table 1: Operating conditions and products compositions for tetrahydrofuran (1) - methanol (2) - water (3) separation

Column	Ent:F	N	N_{Ent}/N_F	T_F, K	R	Top comp.	T_D, K	Bottom comp.	T_B, K
I	400:100	45	5/30	323.15	3.5	x_1=0.9987		x_1=0.0001	
						x_2=0.0013		x_2=0.0789	
						x_3=0.0000		x_3=0.0789	
						x_4=0.0000	339.07	x_4=0.8421	403.69
II		30	12	333.15	1.9	x_1=0.0009		x_1=0.0000	
						x_2=0.9983		x_2=0.0001	
						x_3=0.0008		x_3=0.0856	
						x_4=0.0000	337.68	x_4=0.9143	442.28
III		20	9	343.15	0.24	x_1=0.0000		x_1=0.0000	
						x_2=0.0008		x_2=0.0000	
						x_3=0.9985		x_3=0.0001	
						x_4=0.0007	373.03	x_4=0.9999	470.21

Ent:F – entrainer to feed ratio, N – number of theoretical stages, N_{Ent} – entrainer feed stage, N_F – feed stage, R – reflux ratio, T_D – distillate temperature, T_B – bottoms temperature.

Table 2: Operating conditions and products compositions for ethyl acetate (1) - ethanol (2) - water (3) separation

Column	Ent:F	N	N_{Ent}/N_F	T_F, K	R	Top comp.	T_D, K	Bottom comp.	T_B, K
I	300:100	40	5/30	333.15	0.9	x_1=0.9998		x_1=0.0000	
						x_2=0.0001		x_2=0.0119	
						x_3=0.0000		x_3=0.0925	
						x_4=0.0001	350.35	x_4=0.8955	428.40
II	10:335	20	4/9	343.15	0.5	x_1=0.0000		x_1=0.0000	
						x_2=0.9989		x_2=0.0000	
						x_3=0.0010		x_3=0.0909	
						x_4=0.0002	351.46	x_4=0.9091	441.02
III		20	9	353.15	0.3	x_1=0.0000		x_1=0.0000	
						x_2=0.0000		x_2=0.0000	
						x_3=0.9999		x_3=0.0001	
						x_4=0.0001	373.17	x_4=0.9999	470.23

The results shown in Tables 1 and 2 confirm accuracy of 1,2-ethandiol selection, which provides effective separation for ternary mixtures tetrahydrofuran - methanol - water and ethyl acetate - ethanol - water.

Conclusions

The thermodynamic criterion for entrainers selection has been extended to ternary aqueous mixtures containing binary and ternary azeotropes. The criterion needs to

be applied to all binary azeotropic constituents of ternary system. Separating agent should increase volatility of component forming binary azeotropes and withdrawn that component in the process of extractive distillation. In other words, it is necessary to find selective agent which will symbatically increase relative volatility of compound forming binary azeotropes in ternary mixture and provides selectivity S>1.
Entrainer selection process for ternary mixtures should not be limited only with relative volatilities analysis of the components. Selectivity analysis results can be effectively used for more detailed and accurate characterization of its efficiency.

Acknowledgements
The reported study was partially supported by RFBR, research project No. 14-03-00523.

References
1. V. M. Raeva et al., *Fine Chemical Technologies,* 6 (2011) 43-53
2. P.A. Gomez and I.D. Gil, *Latin American Applied Research*, 39 (2009) 275-284
3. A. K. Frolkova and V. M. Raeva, *Theoretical Foundations of Chemical Engineering*, 44 (2010) 545-556
4. V.N. Kiva, E.K. Hilmen and S. Skogestad, *Chem. Eng. Sci*., 58 (2003) 1903-1953
5. S.O. Momoh, *Separation Science and Technology,* 26 (1991) 729-742
6. A.Y.Sazonova, V.M. Raeva and A.K. Frolkova*, XIX International Conference on Chemical Thermodynamics in Russia.* Moscow, 24-28 June 2013, 302
7. A.Y. Sazonova and V.M. Raeva, *5th International Conference on European Science and Technology*. Munich, 3-4 October 2013, Vol. 1, 473-476

An anisotropic mass transfer model and its application to the simulation of chemical absorption of CO_2 into NaOH in packed column

Wenbin Li, Kuotsung Yu, Xigang Yuan, Botan Liu*
School of Chemical Engineering and Technology, State Key Laboratory of Chemical Engineering, Tianjin University, Tianjin, China

Abstract
An anisotropic mass transfer model is proposed for simulating the chemical absorption process with heat effect in packed column. The feature of the proposed model is that the anisotropic turbulent mass diffusion can be characterized. With the proposed model, the distributions of concentration and temperature as well as the velocity along the column can be rigorously simulated. The Reynolds mass flux equation is used to close the turbulent mass transfer equation, so that the Bossinesq's postulate and the isotropic assumption are abandoned. The proposed anisotropic mass transfer model is accompanied by the equations of computational fluid dynamics (CFD) and computational heat transfer (CHT). In the mathematical expression for the accompanied CFD and CHT, the modelled Reynolds stress and Reynolds heat flux equations are used for closing the turbulent momentum and heat transfer equations respectively. To validate the proposed model, simulation is carried out for a randomly packed column (0.1m i.d. packed with 12.7mm Berl Saddles up to heights of 6.55m) for CO_2 absorption into aqueous NaOH solutions. The simulated results are compared with the experimental data and satisfactory agreement is found between them in both concentration and temperature distributions. Furthermore, anisotropy of the turbulent mass diffusion is discussed.

Keywords
chemical absorption; packed column; computational mass transfer; anisotropic turbulent mass diffusion

1. Introduction

Considerable experimental works [1-4] has been focused on the study of turbulent mass diffusion (or turbulent mass dispersion) since it is the dominating factor behind mass transport for the separation process in packed column. Among them, many investigators have found that the turbulent mass diffusion is anisotropic since experimental data [5, 6] show that the axial turbulent mass diffusivity is larger than the radial one.

Gas absorption in a randomly packed column is deemed as a highly efficient system due to its high capacities, low pressure drops and relatively cheaper construction. Modelling and simulation of this unit is an essential issue with regard to the scale-up and for the optimization of operation parameters. For precise analysis, it is suggested [7] that anisotropy of the turbulent mass diffusion should be taken into account.

Due to the complexity of fluid flow in packed column coupled with reaction and heat effect, researchers have focused on linking engineering models with rigorous

* Correspondence concerning this article should be addressed to Xigang Yuan at yuanxg@tju.edu.cn.

simulation tools. And it is approved that computational mass transfer (CMT) is an emerging technique and holds great potential in providing detailed information of the complex fluid flow coupled with reaction and heat effect [8, 9]. However, in the conventional CMT model, the turbulent mass diffusivity is determined either by using empirical correlations from inert tracer experiments [10] or by guessing a constant Peclet number [11]. Nevertheless, the right choice of Peclet numbers is difficult. The value of $D_{t,i}$ obtained by using empirical correlation from inert tracer experiment is different from that under mass transfer condition. To avoid the use of empirical methods, a rigorous model, the so-called $\overline{c^2} - \varepsilon_c$ model was developed recently [12] to determine the parameter $D_{t,i}$. In this model, the axial turbulent mass diffusivity is obtained by solving auxiliary model equations, whereas the radial turbulent mass diffusivity is assumed to be equal to the axial one. In other words, the turbulent mass diffusivity $D_{t,i}$ is assumed to be isotropic, and may induce considerable error. In fact, there are many attempts [7, 13] for correlating the anisotropic turbulent mass diffusivity from experimental data. However, a wide variation exists in the value of the turbulent mass diffusivities obtained by different experimental correlations. Macfas-Salinas and Fair [14] attribute such discrepancies to the sensitivity of the turbulent diffusivity to experimental errors and the use of different model concepts for estimating the turbulent mass diffusivity. To reduce uncertainty of the simulation on concentration field, Li et al. [8] developed a new CMT model, so-called the Reynolds mass flux model or anisotropic mass transfer model, for the simulation of distillation and obtained the concentration distribution in the packed column. The feature of the Reynolds mass flux model is that anisotropic turbulent mass diffusivities in liquid could be characterized rigorously.

In this study, the anisotropic mass transfer model is presented to simulate chemical absorption process with heat effect in packed column. To validate the proposed model, simulation is carried out for a randomly packed column (0.1m i.d. packed with 12.7mm Berl Saddles up to heights of 6.55m) for CO_2 absorption into aqueous NaOH solutions and the simulated results are compared with the experimental data. Furthermore, anisotropy of the turbulent mass diffusion in liquid is discussed.

2. The Proposed Model

The object of the present simulation is the CO_2 absorption into aqueous NaOH solutions [15]. As stated by Onda et al. [16], it can be regarded as a gas absorption control process accompanied by a relatively slow second-order reaction. Detailed information about the reaction mechanism could be found in Liu et al. [9].

The model developed in this section is based on the interacted liquid phase model, which has been shown to be more convenient and computer-time saving with sufficient accuracy provided, if the gas-liquid interacting source term can be properly expressed [17].

2.1 Model equations

The proposed model consists of turbulent mass transfer equation along with the modelled Reynolds mass flux equation, and the accompanied CFD and CHT equation sets. Main equations of the anisotropic mass transfer model are shown in Table 1.

Table 1 Main equations of the anisotropic mass transfer model.[a]

Turbulent mass transfer equation for OH^- in liquid:

$$\frac{\partial}{\partial x_i}\left(\beta\overline{U_i}\,\overline{C}\right)=\frac{\partial}{\partial x_i}\left[\beta\left(D\frac{\partial\overline{C}}{\partial x_i}-\overline{u_i'c'}\right)\right]+\overline{S_C}$$

The modelled Reynolds mass flux, $-\overline{u_i'c'}$, equation:

$$\frac{\partial\left(\beta\overline{U_i u_i'c'}\right)}{\partial x_j}=\frac{\partial}{\partial x_j}\left(C_{C1}\frac{k}{\varepsilon}\overline{u_l'u_m'}\delta_{lmjk}\frac{\partial\left(\beta\overline{u_i'c'}\right)}{\partial x_k}+D\frac{\partial\left(\beta\overline{u_i'c'}\right)}{\partial x_j}\right)-\beta\overline{u_i'u_j'}\frac{\partial\overline{C}}{\partial x_j}-C_{c2}\beta\frac{\varepsilon}{k}\overline{u_i'c'}-C_{c3}\beta\overline{u_j'c'}\frac{\partial\overline{U_i}}{\partial x_j}$$

Auxiliary *k* and ε equations for closing the turbulent mass transfer equation:

k equation: $k=\frac{1}{2}\overline{u_i u_i}$

ε equation: $\frac{\partial\left(\rho\beta\varepsilon\overline{U_j}\right)}{\partial x_j}=\frac{\partial}{\partial x_j}\left[C_\varepsilon\frac{k}{\varepsilon}\overline{u_l'u_m'}\delta_{lmjk}\frac{\partial\left(\rho\beta\varepsilon\right)}{\partial x_k}+\frac{\mu}{\rho}\frac{\partial\left(\rho\beta\varepsilon\right)}{\partial x_j}\right]+C_{1\varepsilon}\rho\beta\frac{\varepsilon}{k}\overline{u_i'u_j'}\frac{\partial\overline{U_i}}{\partial x_j}-C_{2\varepsilon}\rho\beta\frac{\varepsilon^2}{k}$

Accompanied CFD equations. Continuity equation:

$$\frac{\partial\left(\rho\beta\overline{U_i}\right)}{\partial x_i}=M$$

Turbulent momentum transfer equation:

$$\frac{\partial\left(\rho\beta\overline{U_i U_j}\right)}{\partial x_j}=-\beta\frac{\partial p}{\partial x_i}+\frac{\partial}{\partial x_j}\left(\mu\frac{\partial\left(\rho\beta\overline{U_i}\right)}{\partial x_j}-\rho\beta\overline{u_i'u_j'}\right)+\overline{S_{\mathrm{F},i}}$$

The Reynolds stress, $-\rho\overline{u_i'u_j'}$, equation for closing the turbulent momentum equation:

$$\frac{\partial\left(\rho\beta\overline{U_j u_i'u_j'}\right)}{\partial x_j}=\frac{\partial}{\partial x_j}\left[C_{u1}\frac{k}{\varepsilon}\overline{u_l'u_m'}\delta_{lmjk}\frac{\partial\left(\rho\beta\overline{u_i'u_j'}\right)}{\partial x_k}+\frac{\mu}{\rho}\frac{\partial\left(\rho\beta\overline{u_l'u_j'}\right)}{\partial x_j}\right]+\rho\beta P_{ij}-\frac{2}{3}\delta_{ij}\rho\beta\varepsilon-C_{u2}\rho\beta\frac{\varepsilon}{k}\left(\overline{u_i'u_j'}-\frac{2}{3}\delta_{ij}k\right)+C_{u3}\rho\beta\left(P_{ij}-\frac{1}{3}P_{ii}\right)$$

Accompanied CHT equations. Turbulent heat transfer equation:

$$\frac{\partial(\rho\beta c_{\mathrm{p}}\overline{U_i}\overline{T})}{\partial x_i}=\frac{\partial}{\partial x_i}\left[\rho\beta c_{\mathrm{p}}\left(\alpha\frac{\partial\overline{C}}{\partial x_i}-\overline{u_i'T'}\right)\right]+\overline{S_T}$$

The modelled Reynolds heat flux, $-\overline{u_i'T'}$, equation [18]:

$$\frac{\partial\left(\rho\beta\overline{U_j u_i'T'}\right)}{\partial x_j}=\frac{\partial}{\partial x_j}\left(C_{T1}\frac{k}{\varepsilon}\overline{u_l'u_m'}\delta_{lmjk}\frac{\partial\left(\rho\beta\overline{u_i'T'}\right)}{\partial x_k}+\alpha\frac{\partial\left(\rho\beta\overline{u_i'T'}\right)}{\partial x_j}\right)-\rho\beta\left(\overline{u_i'u_j'}\frac{\partial\overline{T}}{\partial x_j}+\overline{u_j'T'}\frac{\partial\overline{U_i}}{\partial x_j}\right)-C_{T2}\rho\beta\frac{\varepsilon}{k}\overline{u_i'T'}+C_{T3}\rho\beta\overline{u_j'T'}\frac{\partial\overline{U_i}}{\partial x_j}$$

[a] Remarks should be made that the use of auxiliary equation *k* and *ε* is according to the modelling rule to set k/ε representing the dimension "time" (*t*) in order to keep the dimension consistent in the equation. It does not mean to use the CFD k-ε model in simulation. The determination methods of the unknown source terms $\overline{S_C}$, $\overline{S_{\mathrm{F},i}}$, $\overline{S_T}$ and relevant physical properties *ρ*, *γ*, *D*, *μ* etc. are the same as those in Liu et al. [9].

2.2 Boundary conditions

In the present study, the generalized Fick-like law [19] is adopted for the inlet condition of $-\overline{u_i'c'}$ and $-\overline{u_i'T'}$ equations:

$$\left(-\overline{u_i'c'}\right)_{\mathrm{in}}=D_t\left(\partial\overline{C}/\partial x_i\right),\quad\left(-\overline{u_i'T'}\right)_{\mathrm{in}}=\alpha_t\left(\partial\overline{T}/\partial x_i\right)$$

where D_t and α_t are recommended to be $D_t=\nu_{\mathrm{t}}/0.7$ and $\alpha_t=\nu_{\mathrm{t}}/0.9$ [20], thus:

$$\left(-\overline{u_i'c'}\right)_{\mathrm{in}}=\frac{\nu_{\mathrm{t,\,in}}}{0.7}\left(\partial\overline{C}/\partial x_i\right)\Big|_{\mathrm{in}},\quad\left(-\overline{u_i'T'}\right)_{\mathrm{in}}=\frac{\nu_{\mathrm{t,\,in}}}{0.9}\left(\partial\overline{T}/\partial x_i\right)\Big|_{\mathrm{in}}$$

and the inlet turbulent viscosity $\nu_{\mathrm{t,\,in}}=C_\mu\frac{k_{\mathrm{in}}^2}{\varepsilon_{\mathrm{in}}}$ with constant C_μ = 0.09.

The inlet condition for the Reynolds stress is set to be [21]:

$$\overline{u_i' u_j'} = \begin{cases} \frac{2}{3} k_{\text{in}}, & i = j \\ 0, & i \neq j \end{cases}$$

Boundary conditions for other model equations are the same as those in Liu et al. [9].

3. Results and Discussion

12 sets of experimental data for absorption of CO_2 into aqueous NaOH solutions were reported by Tontiwachwuthikul et al. [15] and only the simulation on experiment T1 are used as example for comparison in this paper.

3.1. OH^- concentration and liquid temperature profiles

Figure 1(a) show the comparisons between the predicted OH^- concentration by the present model and the $\overline{c^2} - \varepsilon_c$ model [9] with experimental data in T1. Satisfactory agreement is seen between the predicted OH^- concentration by present model and the experimental data, which confirms the validity of the presented anisotropic mass transfer model. Moreover, the predicted results by the present model show a more closed matching to the experimental data, which supports the statement that the anisotropic turbulent mass diffusion should be taken into account for more precise simulation. Figure 1(b) show the comparison of the liquid temperature between the simulated results by the present model and the experimental measurements in T1, and satisfactory agreement could also be found between the predictions and experimental data.

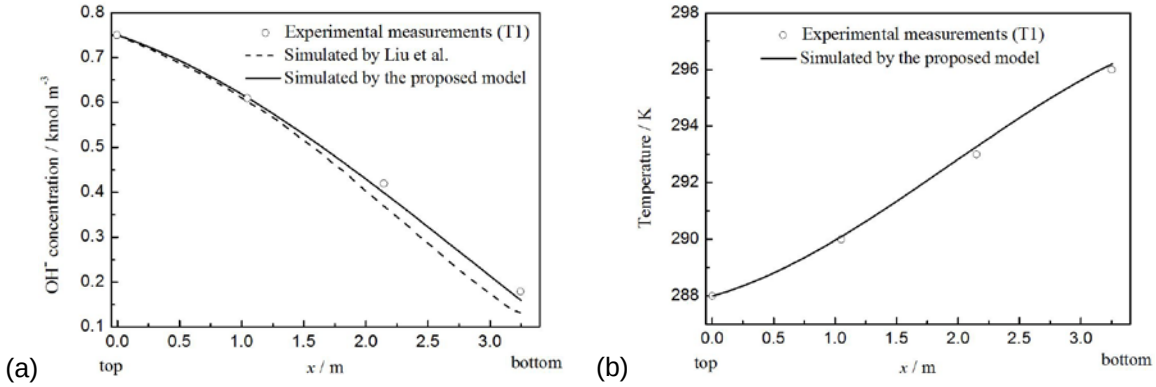

Figure 1 Profiles of OH^- concentration and temperature in T1

3.2. Discussion on anisotropic turbulent mass diffusion

Since the Reynolds mass flux and concentration gradient could be obtained by the present model, the turbulent mass diffusivity could be evaluated according to the Fick-like law [19]:

$$D_{t,x} = \overline{u_x' c'} \Big/ -\frac{\partial \overline{C}}{\partial x}, \quad D_{t,r} = \overline{u_r' c'} \Big/ -\frac{\partial \overline{C}}{\partial r}$$

Figure 2(a) and (b) show the distributions of $D_{t,x}$ and $D_{t,r}$ along radial direction. It is seen that no analogy of the distribution pattern is found between the diffusivity in two directions, which implies that the isotropic assumption of the turbulent mass diffusivity in the $\overline{c^2} - \varepsilon_c$ model [9] is unreasonable.

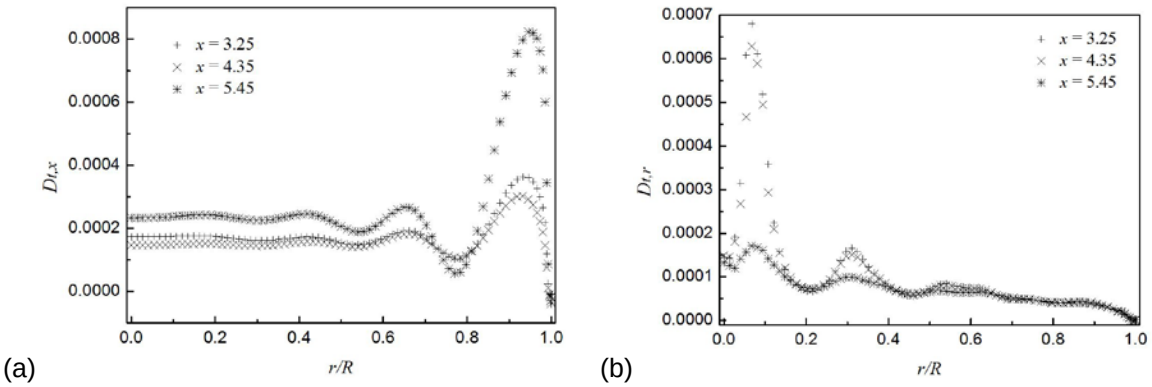

Figure 2 Profiles of anisotropic turbulent mass diffusivity at different axial positions

Table 2 gives the comparisons of the turbulent mass diffusivity obtained by the present model, the $\overline{c^2} - \varepsilon_c$ model [9] and the experimental correlations. The evaluated turbulent mass diffusivities from various experimental correlations show disagreement. As mentioned in the introduction, such discrepancies are attributed to the sensitivity of the turbulent mass diffusivity to experimental errors and the use of different model concepts for estimating the turbulent mass diffusivity. It is seen from Table 2 that the axial turbulent mass diffusivity is larger than the radial one no matter what correlation is used. This anisotropy of the turbulent mass diffusivity is characterized by the present model. Nevertheless, isotropic turbulent mass diffusivity is used in the $\overline{c^2} - \varepsilon_c$ model [9].

Table 2 comparisons of the turbulent mass diffusivity obtained by the present model, the $\overline{c^2} - \varepsilon_c$ model [9] and the experimental [b]

References	Experimental correlations		Values	
	Pe_x	Pe_r	$D_{t,x}\times10^{-4}$ /m^2 s^{-1}	$D_{t,r}\times10^{-4}$ /m^2 s^{-1}
Sater et al. [22]	√	-	4.38	-
Wen and Fan [13]	-	√	-	0.26
Delgado [7]	√	√	4.69	0.22
Liu et al. [9]	-	-	9.01(av.)	
Present model	-	-	2.61(av.)	0.53(av.)

[b] Peclet number based on molecular dispersion coefficient $Pe_m = |u|d_p/D$, for the present study Pe_m is about 1×10^5; axial Peclet number for mass dispersion $Pe_x = |u|d_p/D_{t,x}$; radial Peclet number for mass dispersion $Pe_r = |u|d_p/D_{t,r}$; $|u|$ is the averaged interstitial velocity of liquid; Reynolds number $Re_p = \rho d_p U/\mu$, for the present study Re_p is about 40; U is the superfical velocity of liquid; (av.) means the volume averaged value.

4. Conclusions

In the present work, an anisotropic mass transfer model is proposed for simulating the chemical absorption process with heat effect in a randomly packed column. The feature of the model is that the anisotropic turbulent mass diffusion can be characterized rigorously so as to give more precise simulation. The simulated results are compared with the experimental data [15] and satisfactory agreement is found between them in both concentration and temperature distributions, which confirms the validity of the present model. Moreover, the anisotropy of the turbulent mass

diffusivity is discussed. The present model is found to be more reliable than the model [9] with isotropic turbulent mass diffusivity. It also confirms the statement that the anisotropy of the turbulent mass diffusion should be taken into account for precise simulation and analysis.

Acknowledgements
We acknowledge the financial support by NSFC (Project 21376163).

References
[1] J.R.F.G. de Carvalho, J.M.P.Q. Delgado, Effect of fluid properties on dispersion in flow through packed beds, AIChE Journal, 49(8) (2003) 1980-1985.
[2] D.J. Gunn, Axial and radial dispersion in fixed beds, Chemical Engineering Science, 42(2) (1987) 363-373.
[3] D. Coelho, J.F. Thovert, P.M. Adler, Geometrical and transport properties of random packings of spheres and aspherical particles, Physical Review E, 55(2) (1997) 1959-1978.
[4] J. Bear, Dynamics of Fluids in Porous Media, Elsevier, New York, 1972.
[5] M.M. Farid, D.J. Gunn, Dispersion in trickle and two-phase flow in packed columns, Chemical Engineering Science, 34(4) (1979) 579-592.
[6] T.K. Sherwood, R.L. Pigford, C.R. Wilke, Mass Transfer, McGraw-Hill, USA, 1975.
[7] J.M.P.Q. Delgado, A critical review of dispersion in packed beds, Heat Mass Transfer, 42(4) (2006) 279-310.
[8] W. Li, B. Liu, G. Yu, X. Yuan, A New Model for the Simulation of Distillation Column, Chinese Journal of Chemical Engineering, 19(5) (2011) 717-725.
[9] G.B. Liu, K.T. Yu, X.G. Yuan, C.J. Liu, New Model for Turbulent Mass Transfer and Its Application to the Simulations of a Pilot-Scale Randomly Packed Column for CO2−NaOH Chemical Absorption, Industrial & Engineering Chemistry Research, 45(9) (2006) 3220-3229.
[10] F.H. Yin, A. Afacan, K. Nandakumar, K.T. Chuang, CFD Simulation and Experimental Study of Liquid Dispersion in Randomly Packed Metal Pall Rings, Chemical Engineering Research and Design, 80(2) (2002) 135-144.
[11] M.J.S. de Lemos, M.S. Mesquita, TURBULENT MASS TRANSPORT IN SATURATED RIGID POROUS MEDIA, International Communications in Heat and Mass Transfer, 30(1) (2003) 105-113.
[12] Z.M. Sun, B.T. Liu, X.G. Yuan, C.J. Liu, K.T. Yu, New Turbulent Model for Computational Mass Transfer and Its Application to a Commercial-Scale Distillation Column, Industrial & Engineering Chemistry Research, 44(12) (2005) 4427-4434.
[13] C.Y. Wen, L.T. Fan, Models for flow systems and chemical reactors, Marcel Dekker, New York, 1975.
[14] R. Macías-Salinas, J.R. Fair, Axial mixing in modern packings, gas and liquid phases: I. Single-phase flow, AIChE Journal, 45(2) (1999) 222-239.
[15] P. Tontiwachwuthikul, A. Meisen, C.J. Lim, CO2 absorption by NaOH, monoethanolamine and 2-amino-2-methyl-1-propanol solutions in a packed column, Chemical Engineering Science, 47(2) (1992) 381-390.
[16] K. ONDA, E. SADA, H. TAKEUCHI, Gas absorption with chemical reaction in packed columns, Journal of Chemical Engineering of Japan, 1(1) (1968) 62-66.
[17] X.L. Wang, C.J. Liu, X.G. Yuan, K.T. Yu, Computational Fluid Dynamics Simulation of Three-Dimensional Liquid Flow and Mass Transfer on Distillation Column Trays, Industrial & Engineering Chemistry Research, 43(10) (2004) 2556-2567.
[18] C.J. Chen, S.J. Jaw, Fundamentals of Turbulence Modeling, Taylor & Francis, Washington, 1998.
[19] F. Pinson, O. Gregoire, M. Quintard, M. Prat, O. Simonin, Modeling of turbulent heat transfer and thermal dispersion for flows in flat plate heat exchangers, International Journal of Heat and Mass Transfer, 50(7–8) (2007) 1500-1515.
[20] Fluent 6.3 Documentation, Fluent, Lebanon, NH, 2006.
[21] M. Nishimura, A. Tokuhiro, N. Kimura, H. Kamide, Numerical study on mixing of oscillating quasi-planar jets with low Reynolds number turbulent stress and heat flux equation models, Nuclear Engineering and Design, 202(1) (2000) 77-95.
[22] V.E. Sater, O. Levenspiel, Two-phase flow in packed beds: Evaluation of axial dispersion and holdup by moment analysis, Industrial & Engineering Chemistry Fundamentals, 5(1) (1966) 86-92.

A CFD Model for Flow Characterization of a Sieve Tray of Divided Wall Column

Talat Moeini[1], *Rahbar Rahimi*[2]
[1]*MSc Graduate, Department of Chemical Engineering, University of Sistan and Baluchestan, Zahedan, Iran;*
[2]*Prof. PhD, Department of Chemical Engineering, University of Sistan and Baluchestan, Zahedan, Iran*

Abstract

Energy utilization in view of high energy cost have been concern of distillation designers. Process heat integration has caused widespred use of divided wall column(DWC) in industry. But due to lack of available data on the DWC tray design, study of seive tray has been conducted using CFD methods. A common sieve tray geometry and experimental performance analysis was given by Solari and Bell[1]. Assuming DWC tray is similar to half of a conventional tray, its hydraulic parameters such as, clear liquid height, froth height, distribution of liquid and gas velocity for different liquid and gas flow rates were noticed. The results show that liquid distribution on a half tray is more non-uniform than that of a total tray. The nonuniformity for liquid outlet and flow backmixing are very different in comparision with a total tray. Backmixing and high turbulancy that affect lowering tray efficincy are obvious. Therefore design of sieve tray for DWC cannot folow the conventional design proceduers. CFD method can be developed as a powerful tool for the design of the tray, but experimental data to validate the model is required.

Keywords

Sieve tray, Hydraulics, CFD, Distillation, DWC, Efficiency

1. Introduction

Distillation is widely used in chemical and petrochemical industries**.** About 3% of the world's total energy consumption is accounted for the distillation units operations [2]**.** Therefore, research in reducing their energy consumption is justifiable and reduction of equipment cost and energy integration of distillation columns is desirable. One way of reducing the price of the device is the use of the towers with thermal coupling structure**.** Divided wall column is in practice a combination of two separate columns in a single shell with a common condenser and a re-boiler. They mostly are useful for separation of 3 component mixtures and recently were used for 4 components mixtures or mixture groups, as well. Overhead vapour of the two parts of the column mix together prior entering the condenser and the reflux are divided in to the two parts when entering the column. Same action occurs for the liquid bottom product. The two columns are separated by a common wall. Feed enters the first part and the side stream is taken off of the second parts. The internal reflux ratios of the two sections are in general not equal. In fact the wall acts as for reduction of the remixing of distributed component of the side stream. Therefore, the wall, that may be welded or being flexibly loose, prevent or reduce mixing phenomena in feed entering section and remixing phenomena in side stream section of column. Elimination of mixing and

remixing causes improvements of thermal efficiency and production of more pure side stream [3]. DWC can use trays (Koch Glitch and CEPSA columns), packings (BASF and Montz columns) or their combination for mass transfer to occur. Advantages and their merits are given in literature[4]. Packed columns diameters are less than 4 m whilst the tray column diameter are less than 6 m [5]. The main advantage of DWC columns are saving energy and producing high purity products**.** The savings are approximately accounts for 30-50% reduction in energy costs compared to the conventional columns[6]**.** As the results of the introduction of Kaible column in 1987 and advancements of control strategies, the installation of more than 100 columns worldwide has been reported [7, 8]. Even though, design of DWC and its control problems have been addressed by researches, the designs of column internals are obscure. That will be in part addressed in this article by the help of CFD simulation. Tray hydraulics of a common circular sieve tray will be compared with a half tray as it was assumed for DWC.

2. Model Equations

In the present work, a two- fluid, three- dimensional and transient CFD model was used .The model considers the flows of dispersed air and continuous water in an Eulerian- Eulerian framework, where the phases are treated with transport equations. The continuity and momentum equations were numerically solved by finite volume method. The details of the flow field for the two phases were determined by solving the volume- averaged fluid equations for each phase. The time step of 0.001s was used for solving the transient equations and convergence criterions were set to be the residuals less than 10^{-3}. Advection discretization scheme uses the upwind algorithm. The k-ε turbulence model was used for simulating turbulence behavior of the liquid phase.

2.1. Governing equations

The governing equations are as follows:

2.1.1. Continuity equations

Gas phase:

$$\frac{\partial(r_G\rho_G)}{\partial t}+\nabla.(r_G\rho_G V_G)=0 \quad (1)$$

Liquid phase:

$$\frac{\partial(r_L\rho_L)}{\partial t}+\nabla.(r_L\rho_L V_L)=0 \quad (2)$$

Where r, ρ, and *V* are volume fraction, density and velocity vector, respectively.

2.1.2. Momentum equations

Gas phase:

$$\frac{\partial}{\partial t}(r_G\rho_G V_G)+\nabla.(r_G(\rho_G V_G V_G))=-r_G\nabla\rho_G+\nabla.\left(r_G\mu_{eff,G}(\nabla V_G+(\nabla V_G)^T)\right)-M_{GL} \quad (3)$$

Liquid phase:

$$\frac{\partial}{\partial t}(r_L\rho_L V_L)+\nabla.(r_L(\rho_L V_L V_L))=-r_L\nabla\rho_L+\nabla.\left(r_L\mu_{eff,L}(\nabla V_L+(\nabla V_L)^T)\right)+M_{GL} \quad (4)$$

Where M_{GL}, describes the interfacial forces acting one aech phase due to the presence of the other phase**.**

2.1.3. Volume Conservation and Pressure Equations

Here, r_G and r_L are the volume fractions for the gas and liquid phases. The sum of the volume fractions of the two phases is unity:

$$r_G + r_L = 1 \quad (5)$$

The same pressure field has been assumed for both phases**:**

$$P_G = P_L = P \quad (6)$$

2.2. Closure models

For solving equations (1) to (6), it is necessary to solve additional equations relating the interphase momentum transfer, M_{GL},and turbulence viscosity to the flow parameters[9].

$$M_{GL} = \frac{3}{4}\frac{C_D}{d_G} r_G \rho_L |V_G - V_L|(V_G - V_L) \quad (7)$$

Where, C_D,is the drag coefficient. Fisher and Quarini[10] used a constant value of 0.44 for drag coefficient. This value is appropriate for large bubbles of spherical shape. But for the froth flow regime, which is the dominant flow regime in distillation, it is not applicable. The drag coefficient, C_D ,has been estimated using the drag correlation of Krishna and Van Baten[9, 11], a relation proposed for the rise of a swarm of large bubbles in the churn-turbulent regime:

$$C_D = \frac{4}{3}\frac{\rho_L - \rho_G}{\rho_L} g d_G \frac{1}{{V_{slip}}^2} \quad (8)$$

Where the slip velocity, $V_{slip} = |V_G - V_L|$, is estimated from the gas superficial velocity,V_S and the average gas hold up fraction in the froth region as:

$$V_{slip} = \frac{V_S}{{r_G}^{average}} \quad (9)$$

Equation 10 gives the average gas hold up fraction in froth:

$${r_G}^{average} = 1 - \exp\left[-12.55\left(V_s\sqrt{\frac{\rho_G}{\rho_L - \rho_G}}\right)^{0.91}\right] \quad (10)$$

Substitution of Eqs. (8), (9) and (10) in Eq. (7) after simplification gives the interphase momentum transfer:

$$M_{GL} = \frac{({r_G}^{average})^2}{(1-{r_G}^{average}){V_s}^2} g(\rho_L - \rho_G) r_G r_L |V_G - V_L|(V_G - V_L) \quad (11)$$

This relation is independent of bubble diameter and is suitable for CFD use [9, 11].

3. Flow geometry and boundary conditions

Simulations were carried out for half of a conventional sieve tray 1.213 m in diameter, air at ambient pressure and water were used as the gas and liquid phases, respectively. The sieve tray dimensions are based on tray geometry of Solari and Bell[1]. Computational domain was considered as the 0.61 m distance between two trays and inlet and outlet down- comers. The selection of proper grid size is essential in the numerical computation. In order to obtain the best simulation grid sizes was investigated for different number of unstructured tetrahedral meshes. Consequently

grid independence of the solution was achieved with 86000 node. For solving of the continuity and momentum equations, boundary conditions of all boundaries of the physical domain are required. At the inlet, uniform profiles are considered for the liquid and gas velocities. The boundary condition at the liquid outlet was considered as mass flow .At the vapor outlet, pressure boundary condition was specified. Inlet and outlet liquid volume fractions are assumed equal and to be unity. In addition, the gas phase enters to the vapor inlet and exits from the vapor outlet with the volume fractions of one. Figure 1 shows half of a conventional sieve tray or a tray of DWC. Table1 gives DWC tray dimension .

Tray diameter (m)	1.213	Down comer clearance (m)	0.038
Tray spacing (m)	0.61	Down comer area (%)	13
Holes diameter (m)	0.0127	Pitch ,triangular (m)	0.05
Outlet weir height (m)	0.05	Weir length (m)	0.925

Table 1: Tray specifications

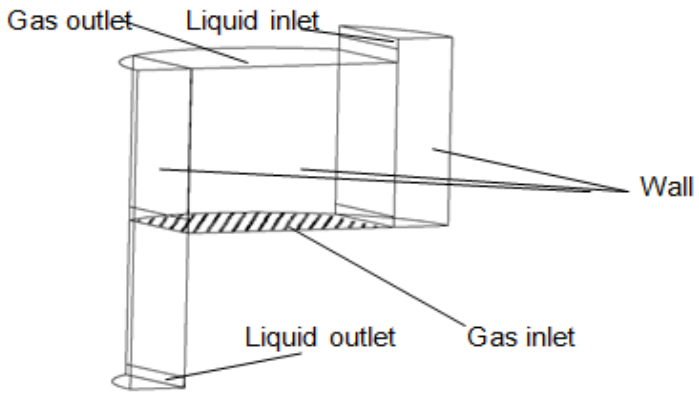

Figure1: Geometry of simulated sieve tray of DWC

4. Result and discussion

Liquid velocity profiles and liquid velocity vector of the DWC tray are presented. Experimental data of Solari and Bell [1] for the points given in Figure 2, are included for the purpose of validating the simulation results of sieve tray. The experimental linear liquid velocity data measured along two lines perpendicular to the liquid flow direction on a plane 0.038 m above the tray floor. The probes positions are illustrated in Figure 2. Average linear liquid velocities were calculated by dividing the distance between two rows of probes by the time elapsed for the dye to cover this distance. In our model geometry, probes 5 to 8 lay on x=0.209 m and probes 9 to 12 lay on x=0.438 m and probes 13 to 16 lay on x=0.667 m. In order to compare the experimental measurements with the CFD predictions, line integrals of the horizontal component of the liquid velocity were taken on the plane y=0.038 m between x=0.209 and x=0.438 m (upstream Profiles).

Similarly, line integrals were taken between x=0.438 and x=0.667 m for the measurements made between the middle of the tray and the outlet weir (downstream Profiles).

As shown in Figure 3 and 4 velocity has a high value about z/R of 0.2 and negative values are evident. This non-uniformity of velocity affects tray separation efficiency and suggests special tray design for the DWC.

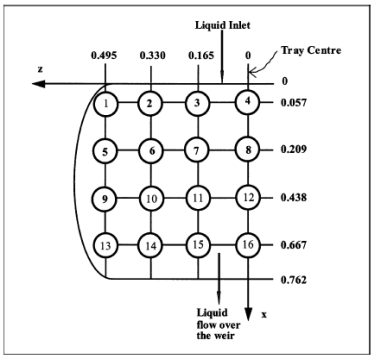

Figure 2: Experimental probe layout of Solari and Bell

Figure 5 is a sample velocity vector plot for a tray of DWC. From this figure, it can be illustrated that the liqiud flow distribution in the tray of DWC is more irregular than total trays[12]. High liquid flow turbulancy is clear. Additionally, the recirculation flow are towars tray outlet weir and turbulancy in inlet downcomer should be regonized. These effects causes higher pressur drop for the trays of DWC than regular column trays.

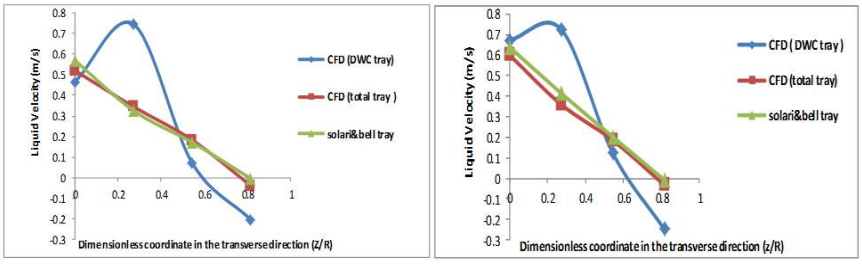

(a) Upstream profile (b) Downstream profile

Figure 3: Liquid U velocity profile for QL= 0.0178 m3/s and Fs= 0.462

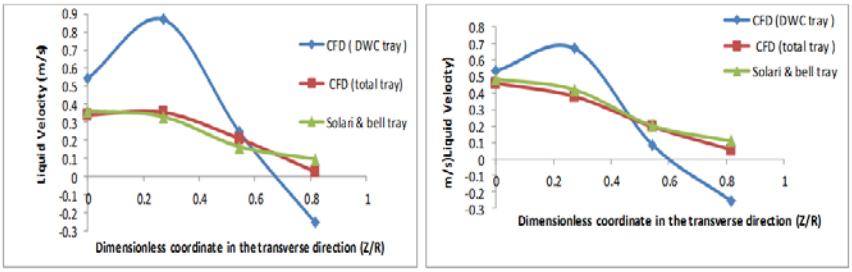

(a) Upstream profile (b) Downstream profile

Figure 4: Liquid U velocity profile for QL= 0.0178 m3/s and Fs= 0.801

5. Conclusions

From the obtained results, it can be concluded that the presence of wall on the middle of the total sieve tray has a great influence on the patterns of the liquid flows**.** This influence affects the hydrodynamics of DWC tray whilst the hydrodynamics does not resemble a conventional sieve tray. It has been observed that liquid distribution on a half tray is more non-uniform than that of total tray. The nonuniformity for liquid outlet and flow backmixing are very different in comparision with a total tray

performance. As the result, tray efficiency is decreased among its performance. The results of this study confirmed that the CFD tools presented a better understanding of the turbulent gas-liquid flow in DWC tray and they could be applied to optimize the design and operating conditions and analysis of such processes. However, lack of reported experimental data cannot be ignored.

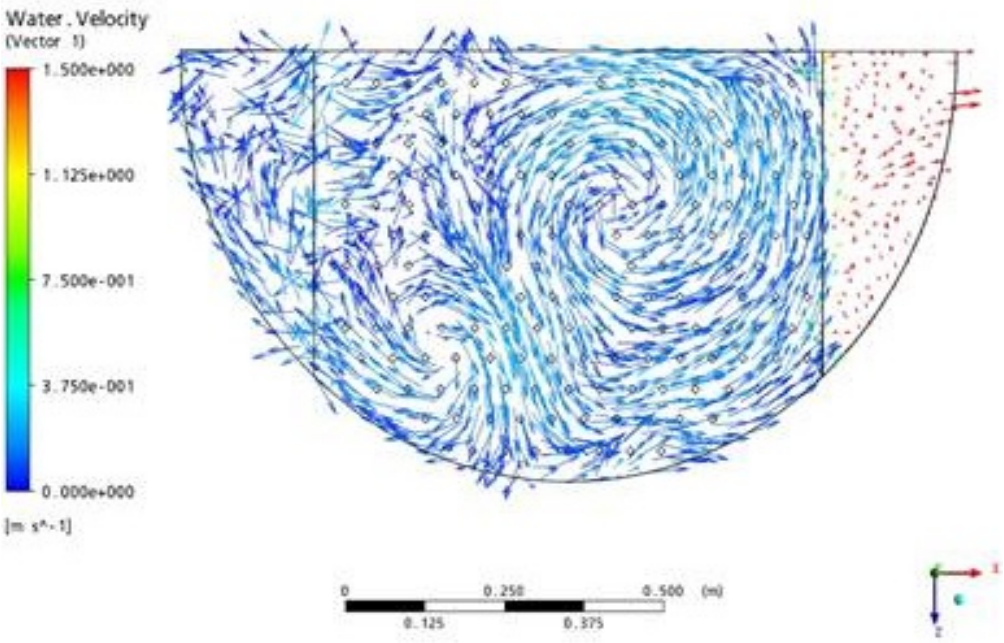

Figure 5: Stagnant and recirculation zone of the DWC tray

References

[1] Solari, R.B., Bell, R.L., "Fluid flow patterns and velocity distribution on commercial-scale sieve trays", AIChE J. vol. 32, pp. 640-649, 1986.

[2] Asprion, N, Kaibel, G, "Dividing wall columns: Fundamentals and recent advances". Chemical. Engineering. Process. vol.49, pp.139–146, 2010.

[3] Kim, Y. H, "Structural design and operation of a fully thermally coupled distillation column" ,Chemical Engineering Journal, vol. 85, pp. 289–301, 2002.

[4] Yildirim, O., Kiss, A.A., Kenig, E.Y., "Dividing wall column in chemical process industry" ,Separation and Purification Technology, vol.80, pp.403-417, 2011.

[5] Becker ,H. Godorr, S., Kreis, H., "Partitioned distillation columns-why ,when and how" Chemical. Engineering.Journal,pp. 68-74, 2001.

[6] Abdul Motalib, M.I., Smith, R., "Operating and control of dividing wall distillation columns" ,Trans. IChemE., vol. 76, pp.308-334, 1998.

[7] Olujic,Z., Kaible, B., Janson, H., Reitfort, T., Zich, E., Fery, G., "Distillation column internals / configuration for process intensification", Chemical . Biochemical . Engineering, pp. 301-309, 2003.

[8] Muralikrishna, K.V., Madhavan, K.P., Shah, S.S., "Development of dividing wall distillation column design space for specified separation" Trans. IChemE.,vol. 80, pp. 155-166, 2002.

[9] Krishna, R., van Baten, J.M., Ellenberger, J., Higler, A.P.,Taylor, R., "CFD simulations of sieve tray hydrodynamics" Trans.IChemE.,vol. 77, pp.636-649, 1999.

[10] Fischer, C.H., Quarini, J. L., "Three dimensional heterogeneous modeling of distillation tray hydraulics", Miami Beach, FL: AIChE annual meeting,1998

[11] van Baten, J.M., Krishna, R., "Modelling sieve tray hydraulics using computational fluid dynamics" ,Chemical Engineering Journal ,vol. 77, pp. 143-151, 2000

[12] Rahimi, R., Zarei, T., Zarei, A., Naziri Firoozsalari, H., "A computational fluid dynamics and an experimental approach to the effects of push valves on sieve trays", Proceeding of Distillation and Absorption 2010 congress,12-15 September 2010 ,Eindhoven, The Netherlands.

Neural network for quality estimation of product compositions in distillation columns with distributed heating

[1]Machado, R. A. F,, [2]Claumann, C. A.,[3]Werle, L. O.[1]Marangoni, C.
[1,2]Federal University of Santa Catarina - Florianópolis, Santa Catarina (SC), Brazil;
[3]Federal University of Grande Dourados-Dourados -Mato Grosso do Sul (MS), Brazil.

Abstract

In this paper, an artificial neural network (ANN) was developed for the estimation of product compositions in a distillation column. The great differential of this project is that this strategy be developed a distillation column based on distributed control action with heating on at intermediate points along the column. Werle (2012) tested numerous configurations and architectures of two different topologies of neural networks: feedforward and recurrent Elman networks. The data sets for training and validation of the networks were obtained from a distillation unit 13 trays, processing ethanol/water mixture. This work extends the Werle, making a comparison with other recurrent neural network topology (RNN) which only uses the feedback of the output variable. In a validation test, the RNN outperformed the other topologies studied in predicting the concentration of ethanol at the top of the column.

Keywords
Distillation columns, neural networks, Levenberg-Marquardt.

1. Introduction

In many industrial processes, some process outputs can not be measured by a sensor. But these outputs are essential to control and monitor the industrial processes. The product composition of a distillation column also can not be measured by a sensor. It is often analyzed by a gas chromatographic (GC) instrument. Both chemical analysis and GC analysis take a lot of time, so controlling and monitoring a distillation column are very difficult. In order to solve this problem, a process model should be designed to estimate the unmeasurable process output. Such a model is a soft sensor which can indirectly measure the unmeasurable process output. Because the data for designing a soft sensor are the operation data and analysis data of an industrial process, they have the features of discreteness, nonlinearity, contradiction, and complexity. These data are like the cases. These models, also known as soft sensors, lie at the core of the virtual instruments used by plant technologists. Of the modeling strategies available, first principles models require deep knowledge of the physical and chemical phenomena involved in the process. On the other hand, empirical models, or data-driven models, which produce reliable real-time estimates of process variables on the basis of their correlation with other relevant system variables, are widely used (Fortuna et al., 2007). For industrial processes, and in particular for refineries, due to the complexity of the nonlinear phenomena involved and the large amount of historical operational data available, neural networks have been widely used.

There are several studies in the literature which evaluate the quality of the product composition using real-time estimates in distillation columns (Gupta et al., 2008; Singh et al., 2007), and propose the use of inferential models to estimate the composition. Some authors make employ phenomenological or empirical models for prediction of the composition (Jana et al., 2005). However, most of these studies do

not include simulated experimental data for validation. It has been verified in recent years that commercial software programs for the simulation of distillation columns are widely used among academic researchers and industry (Langston et al., 2005). The HYSYS software is the simulator of the processes most widely used in the industries of oil refining and natural gas processing, as a powerful tool for control design and optimization in the process.

The objective of this work is obtain an neural model empirical to estimate the composition of top product of a distillation column. The work deals with the identification of the neural system by comparing the performance of three types of neural network topologies: a Multi-Layer Perceptron MLP; the Elman and a network that uses feedback of the output variable (RNN). The first is static and the other is recurring. The main difference between the RNN and the Elman is that the first uses only the feedback of the output (concentration of ethanol in the top of the column) variable, whereas the latter is the internal feedback of state (outputs of the neurons of the hidden layers). The significant novelty aspect of this paper is the fact that the network can be validated experimentally in a distillation column in which the control is based on a distributed action with heating on intermediate trays (Marangoni and Machado, 2007). Werle (2012) tested numerous configurations and architectures of two different topologies of neural networks: feedforward and recurrent Elman networks. This work extends the Werle, making a comparison these networks cited with other recurrent neural network topology (RNN) which only uses the feedback of the output variable.

2. Methodology

2.1. Description of the Experimental Unit

The pilot distillation unit is composed of 13 trays, processing ethanol-water mixture with a feed flow rate of 300 $L.h^{-1}$. The unit, illustrated in Figure 1, operates continuously, with the feed stream inserted in the 4^{th} tray.

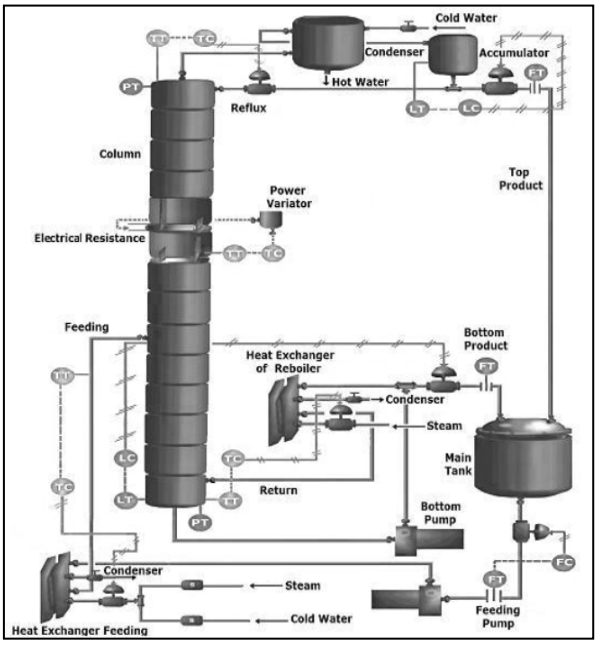

Figure 1. Scheme of the control system of the pilot distillation unit.

Further details of the unit are described by Werle (2012). The experiments carried out were conducted with initial volumetric compositions of ethyl alcohol in the feed of

10% (v/v). The distillate flow rate was around 10 $L.h^{-1}$ with a mean reflux ratio (R/D) of 6. The results from the experimental trials were used in the dynamics simulations.

2.2. Simulations

The software used for the dynamics simulations was HYSYS®. Dynamic simulations were performed in which various disturbances were introduced to the system, generating a set of data transient. The manipulated variables of the process feed stream as volumetric composition of ethanol (X_a) flow rate (Q_a) and temperature (T_a) are varied to obtain a set of data inputs/outputs, as required for training artificial neural networks. The ranges adopted for the combinations used in the open-loop simulations are shown in Table 1.

Table 1. Intervals used for the combinations in open-loop simulations.

Variables	Intervals	Values used	N° variations
Flow rate ($L.h^{-1}$)	$250 \leq Q_a \leq 350$	250/300/350	3
Temperature (°C)	$86 \leq T_a \leq 94$	86/90/94	3
Ethanol composition (v/v)	$0.05 \leq X_a \leq 0.22$	0.05/0.10/0.15/0.20/0.22	5

The simulations were required to obtain data on the composition of ethanol along time. These compositions are difficult to obtain experimentally for the reasons mentioned previously.

2.3 Development of Neural Networks

2.3.1 Feedforward and recurrent Elman networks

To evaluate the various methods of training and learning, were used the facilities of the environment of the MATLAB package. The network was built using 8 variables as inputs: flow (Q_a [$L.h^{-1}$]), temperature (T_a [ºC]) and volumetric fraction of ethanol (X_a [v/v]), all of the feed stream; were also used state variables (not directly manipulatives) such as bottom temperature (T_b [ºC]) and top temperature (T_t [ºC]) and some trays intermediate column, based on the sensitivity analysis, as temperatures tray 2 (T_2), tray 5 (T_5) and tray 7 (T_7) all in °C. The volumetric composition of the top ethanol (X_t [v/v]) is the output variable chosen.

The feedforward network (MPL) 2 layers with Bayesian Regularization algorithm (BR) obtained good results in tests and was used in this study for comparison between networks. The architecture of the neural system used for comparison between networks comprises a Elman recurrent networks, chosen as a function of being widely used in dynamic processes. Were applied the algorithm training Bayesian Regularization (BR) and was used transfer function hyperbolic tangent hidden layers and linear output layer. The neural network containing 3 intermediate layers, with the number of neurons from 8 in each layer, achieved the best performance for the validation data set. The number of neurons in the intermediate layer was determined always looking for networks with a good generalization capacity.

2.3.2 Recurrent neural network (RNN) which uses the feedback of the output variable

As a comparison to feedforward networks and Elman, was also tested in this work a recurrent neural network (RNN) which uses only the feedback of the output variable, ie, the ethanol fraction at the top column X_t [v/v].

The RNN has a single hidden layer with neurons (Nesc) and the inputs are composed by output feedback, in addition to other variables described in section

2.3.1. In the training of RNN should be calculated dynamics derived from a quadratic approximation error, with respect to each weight of network (Haykin, 1999). RNNs with different N_{esc} were trained using a method of second order: Levenberg Marquardt (Bazaraa et al., 1993). All programming used for training and validation of RNNs was implemented in MATLAB. The stopping criterion adopted was the least squares error presented by the neural network on its suitability for the training data set, which indirectly affects the generalization ability of the network. The performance measurements used to evaluate the quality of the predictions were the Mean Square Error (MSE). To assist and confirm the choice, another parameter was used for evaluation Mean Absolute Percentage Error (MAPE).

3. Results and discussion

The composition estimated by the neural networks are presented in this section. Were evaluated 9 neural networks, with 1, 2 and 3 intermediate layers, varying the number of neurons. For all the networks were calculated the Mean Square Error (MSE) in step training and validation and the Mean Absolute Percentage Error (MAPE) only at the step of validation. The result of the performance of these networks are described in Table 2 with their corresponding errors. With the results were pre-selected the 3 best performing networks. The result of the performance of these networks are illustrated in Figure 2.

Table 2. Selection of neural networks with better performance on the stage of the validation.

Neural networks	Layers	Transfer function (intermediate / output)	Neurons	*MSE_tre	**MSE_val	**MAPE_val
MPL	1	*logsig-logsig*	[25]	1.3250E-7	3.3635E-7	0.04144
	2	*logsig-logsig*	[15 10]	5.5947E-8	2.0889E-7	0.02963
	3	*logsig-logsig*	[10 10 10]	4.7203E-8	3.8431E-7	0.03293
ELMAN	1	*tansig-purelin*	[15]	1.5331E-7	1.9946E-7	0.03044
	3	*tansig-purelin*	[8 8 8]	1.0578E-7	1.2680E-7	0.02695
	3	*tansig-purelin*	[20 20 20]	2.0413E-8	1.7419E-6	0.08098
RNN	1	*tansig-purelin*	[5]	4.1544E-8	5.8876E-8	0.02584
	1	*tansig-purelin*	[15]	1.5791E-8	4.8610E-8	0.01975
	1	*tansig-purelin*	[25]	1.3750E-8	3.8421E-8	0.01313

*MSE_tre = Mean Square Error in the training step.
**MSE_val e MAPE_val = Mean Square Error and Mean Absolute Percentage Error in the validation step.

In the case of ethanol fraction on top of the column, was entered as input only the initial value X_{etp} (k = 0) of the data group. In other points the output is fed back and the network functions as a simulator. In Figure 2(a) and (b) are illustrated neural networks that performed better. It is observed overlay data simulator HYSYS® front the data predicted by the network for product composition top of the column. Analyzing the results of this figure it is noticed that the prediction of the network follows the trend of the curves of simulated data with errors homogeneous enough even for a large number of points. Highlights for network that uses feedback of the output variable (RNN) with 1 hidden layer with 25 neurons using the hyperbolic tangent function in the hidden layer and linear output. It is noticed a great capacity for predicting the composition of ethanol at the top of the column with the use of these recurrent networks. When making a comparison of the architecture of the MPL and

Elman networks, it appears that the Elman network there is a redefinition of the input layer, which happens to be divided into two parts. The first part corresponds to the input vector. The second part, called context units, is to copy the outputs of the neurons of the hidden layer at time n-1. The context layer of Elman network is responsible for storing temporal information on previous entries, which differentiates the MPL network.

The uses feedback of the output variable its great advantage of these networks compared with the Multi-Layer Perceptron (MPL).

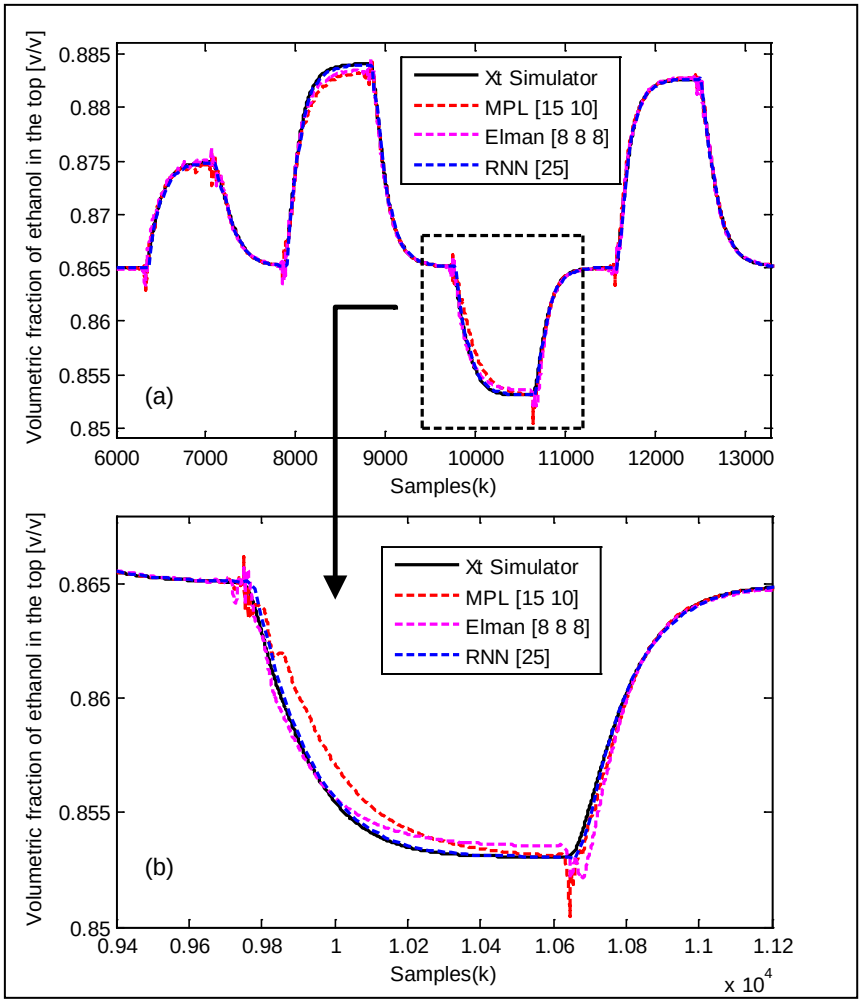

Figure 2. (a) Comparison between the simulated output and the prediction of the best networks with their respective architectures in the validation phase, (b) Magnification of a disturbance.

3.1 Robustness analysis of RNN forward to errors in the initial value of X_t

An important issue to be checked is the robustness of RNN as virtual sensor from the process, ie, should be evaluated the sensitivity of the predictions of RNN due to errors in the initial value of ethanol fraction on top of the column.

The RNN with the best performance on the validation step (Nesc = 25) was initialized applying perturbations of ± 10% in the initial value $X_{t\ (k = 0)}$. Figure 3 shows the result of the validation. Can be observed from Figure 3 that the prediction of the RNN converges to the real behavior after a certain time window (approximately 20 samples), which shows that the RNN is not sensitive to errors in the initial value $X_{t\ (k = 0)}$. The good performance can be attributed to the correlation of ethanol concentration

with the other state variables (temperature along the column). The RNN converges to correct prediction values, because the error in $X_{t\,(k=0)}$) is attenuated by a finite window of time according to the correct values informed of those temperatures.

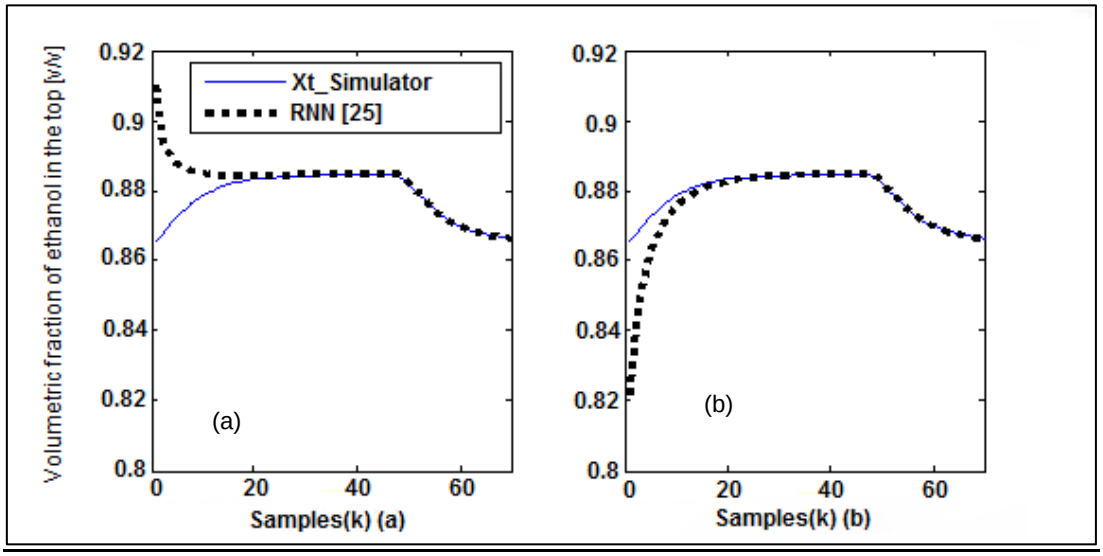

Figure 3. Prediction of the RNN considering disturbances applied in initial value $X_{etp(k=0)}$, (a) Positive Disturbance (b) Negative disturbance.

3. Conclusions

The neural model developed herein was found to be appropriate and capable of estimating the product composition under different operating conditions of the a distillation column binary, with acceptable errors. The results presented indicate that the estimator composition based network that uses feedback of the output variable (RNN) an consistent with good generalization ability. This empirical model can be used to predict the composition accurately and quickly, making it possible to design a more effective control system. Thus, the developed neural network can be used to address the main difficulty associated with distillation towers, that is, the estimation of composition in real time.

References

Bazaraa M. S., Sherali H. D., Shetty C. M. Nonlinear Programming (2nd Edition), Theory and Algorithms, 1993.

Fortuna L., Giannone P., Graziani S., Xibilia M. G. Virtual Instruments Based on Stacked Neural Networks to Improve Product Quality Monitoring in a Refinery. IEEE Transactions on Instrumentation and Measurement, Vol. 56 (6), pp. 95-101, 2007.

Gupta S., Ray S., Samanta A. N. Nonlinear control of debutanizer column using profile position observer. Computers & Chemical Engineering. doi:10.1016, 2008

Haykin S. Neural Networks: A Comprehensive Foundation (2nd Edition), 1999.

Jana A. K., Samanta N. A., Ganguly S. Nonlinear model-based control algorithm for a distillation column using software sensor, ISA Trans. Vol.44, pp.259-271, 2005.

Langston P., Hilal N., Shingfields S., Webb S. Simulation and optimization of extractive distillation with water as solvent, Chem. Eng. Process., Vol.44, pp.345–351, 2005.

Marangoni C., Machado R. A. F. Distillation tower with distributed control strategy: Feed temperature loads. Chemical Engineering an Technoly, Vol.30, pp.1292-1297, 2007.

Singh V., Gupta, I., Gupta H. O. ANN-based estimator for distillation using Levenberg–Marquardt approach. Eng. Applications of Artificial Intelligence, Vol.20, pp. 249-259, 2007.

Werle, L.O. Analisadores virtuais baseados em modelo neural para monitoramento e controle de colunas de destilação com aquecimento distribuído. Thesis. (Doctorate in Chemical Engineering) - Federal University of Santa Catarina - Chemical Engineering - UFSC. Florianópolis (2012), 262p.

Impact on Model Uncertainty of Diabatization in Distillation Columns

Thomas Bisgaard, Jakob Kjøbsted Huusom, Jens Abildskov
DTU Department of Chemical and Biochemical Engineering, 2800-Kgs. Lyngby, Denmark

Abstract
This work provides uncertainty and sensitivity analysis of design of conventional and heat integrated distillation columns. The considered uncertain parameters are relative volatility, heat of vaporization, overall heat transfer coefficient, tray hold-up, and adiabatic index. Error propagation of uncertain parameters to performance indicators (second-law efficiency, operation expenditures, capital expenditures, and dominant time constant) for separations of benzene-toluene and benzene-flourobenzene are investigated. Conclusions favoring the HIDiC over the CDiC w.r.t. operation expenditures in the benzene-toluene separation can not be made within 95% confidence. The sensitivity of overall heat transfer coefficient decreases on all performance indicators as the separation becomes more difficult.

Keywords
Modeling and simulation, distillation columns, uncertainty, sensitivity analysis, diabatic distillation

1. Introduction

In the heat-integrated distillation column (HIDiC), internal heat transfer is realized by operating the rectifying section at higher pressure than the stripping section, using vapor recompression. This heat transfer facilitates gradual boil-up throughout the stripper and condensation throughout the rectifier, potentially leading to an improved performance. The HIDiC has been studied extensively since its introduction in 1977 by Mah and co-workers [1]. However, the majority of the studies are concerned with potential energy savings and operability, and only limited amounts of model validations have been carried out due to scarcity of experimental data. Especially the values of model parameters have so far only received limited attention, and there exists a tendency to assign values based on previous literature studies. These values are used to draw conclusions in feasibility studies ranging from economics to operability and control. The purpose of this study is to perform uncertainty and sensitivity analysis on steady state simulations on conventional and heat-integrated distillation columns.

2. Results and discussion

2.1 Model

A conventional and heat-integrated distillation column model is presented by Liu and Qian [2]. Its degrees of freedom are classified as design variables (**u**) or parameters (**θ**). A list with descriptions of symbols not described in the text is given in Table 1. The degrees of freedom are listed with the output (***y***):

$$\mathbf{u} = (P_r, P_s, A, q, L_C, V_R, F, z)^T$$

$$\boldsymbol{\theta} = (\alpha, \lambda, A_{Ant}, B_{Ant}, C_{Ant}, U, M, T_\sigma, \gamma, \eta_c, S_{water}, S_{steam}, S_{electricity}, T_{water}, T_{steam})^T$$

$$\mathbf{y} = (\eta_{2nd}, OPEX, CAPEX, \tau_1)^T$$

The second-law efficiency (η_{2nd}) is a relative measure for the reversibility and is often reported for diabatic distillation columns. It is calculated by equations (1a-1e):

$$\eta_{2nd} = W_{min} / (W_{min} + W_{lost}) \times 100\% \quad (1a)$$

$$W_{min} = -T_\sigma [D\, s_D + B\, s_B - F\, s_F] \quad (1b)$$

$$s_i = x_i \ln(x_i) + (1 - x_i) \ln(1-x_i) \quad (1c)$$

$$W_{lost} = (|Q_{NS}| + |Q_F|)(1 - T_\sigma/T_{steam}) + W_S + |Q_1|(1 - T_\sigma/T_{water}) - W_{min} \quad (1d)$$

$$W_S = \gamma / (\gamma\text{-}1)\, V_{NF}\, R/\eta_c\, [(P_r/P_s)^{(\gamma-1)/\gamma} - 1] \quad (1e)$$

The operation expenditure (*OPEX*) is an absolute measure for the energy utility, in which energy quantities are weighted by their market prices, S:

$$OPEX = |Q_1|S_{water} + (|Q_{NS}|+(1-q)F/\lambda)S_{steam} + |W_S|S_{electricity} \quad (2)$$

The capital expenditure (*CAPEX*) is estimated based on Guthrie's Modular Method [3]. An update factor of 3.12 and an identical (and uncertain) overall heat transfer coefficient for condenser, reboiler and internal heat transfer equipment has been used. The contribution from the column consists of a vertical vessel, a tray stack, and $N_S/2$ heat exchangers in the HIDiC case. The expression is:

$$CAPEX = UMC_{condenser} + UMC_{reboiler} + UMC_{column} \quad (3)$$

The increased complexity of adding internal heat transfer has been accounted for by multiplying the total column cost by a factor of 1.50. Finally, the dominant time constant (τ_1), reflects the response time of a linearized model corresponding to the smallest eigenvalue of the system matrix [4], determined by equations (4a-b):

$$\tau_1 = \max \Lambda_i^{-1}\,,\ i=1,2,\ldots,N_S \quad (4a)$$

$$\boldsymbol{\Lambda} = \mathrm{eig}[\partial(dx_i/dt)/\partial x_j] \quad (4b)$$

Following purity constraint is used since only symmetric splits are considered:

$$X = x_D = 1 - x_B \quad (5)$$

Where x_D is the distillate purity and x_B is the bottoms purity.

2.2 Methodology

A diagram of the method is provided in Figure 1 and is described step-by-step below.

Step 1-2: Following questions to be answered in this work are formulated:

- How does heat integrated distillation columns perform w.r.t. second-law efficiency, operational and capital expenditures, and the dominant time constant, compared to conventional distillation?
- At which precision can results from comparative studies between the distillation column configurations be presented?
- Which uncertain parameters have the most significant contribution to uncertainty, in the design of a conventional and a heat-integrated distillation column?

More explicitly, it is the propagation of error using uncertain parameters on four selected performance indicators that is investigated, which is caused by performing steady state designs based on fixed (nominal) parameter values. The uncertainty of a parameter could arise due to e.g. ignored temperature dependency. The parameters considered uncertain and their probability distributions in terms of nominal values (subscript "0") are: (i) normally distributed heat of vaporization $\lambda \sim N(\lambda_0, 0.975^2\lambda_0^2)$, (ii) uniformly distributed relative volatility $\alpha \sim U(0.99\alpha_0,\ 1.01\alpha_0)$, (iii) uniformly distributed overall heat transfer coefficient $U \sim U(0.90U_0, 1.10U_0)$, (iv) uniformly distributed tray hold-up $M \sim U(0.95M_0, 1.05M_0)$, and (v) uniformly distributed adiabatic index $\gamma \sim U(0.95\gamma_0,\ 1.05\gamma_0)$. Three configurations will be considered: The conventional distillation column (CDiC), the heat-integrated distillation column (HIDiC) and the ideal heat-integrated distillation column (iHIDiC). The latter has a feed preheater and no external reflux or boil-up. Specified product purities were obtained by adjusting: Boil-up flow (V_R) and reflux flow (L_C) for the CDiC and the HIDiC whereas the rectifier pressure (P_r) and the feed thermal condition (q) were adjusted for the iHIDiC.

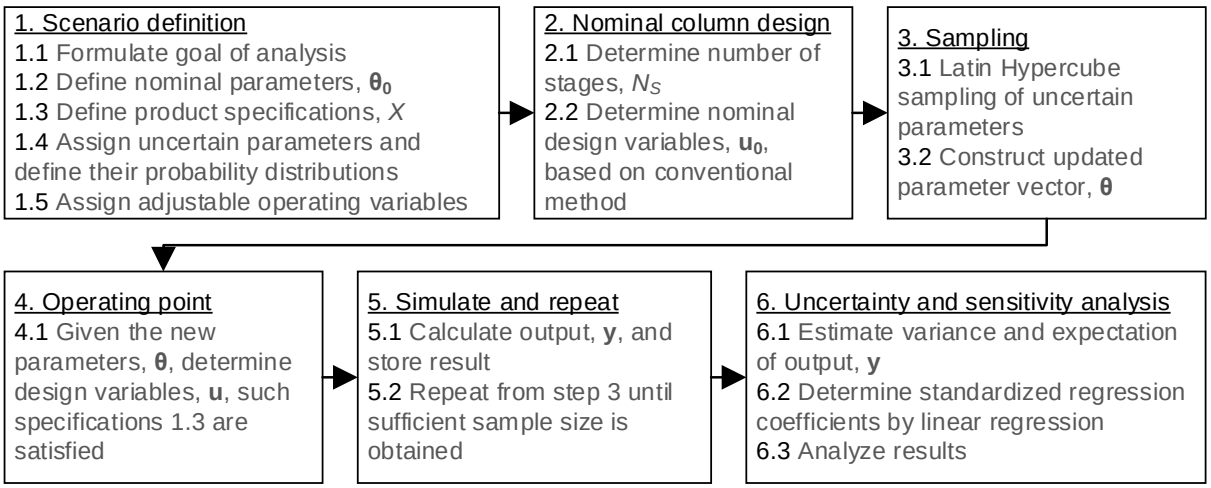

Figure 1. Diagram of method applied for each of the 12 case studies.

Twelve case studies/separations are formulated constituting of two different mixtures, two purities by three different configurations. All nominal values of parameters and design variables are listed in Table 1 and Table 2. Identical pressures in stripping sections were used. The Fenske-Underwood-Gilliland correlation was used to obtain the number of stages (N_S) using a reflux ratio 110% of the minimum ratio.
Step 3: Latin Hypercube Samplings (LHS) [5] were taken from uncertain parameters. A total of 500 samples were taken for each case study leading to 6,000 designs.

Table 1. Nominal values for model parameters that are common for all case studies.

P_s	Stripping section pressure	1.00 atm	T_σ	Temp. of surroundings	300 K
F	Feed flow rate	100 kmol/h	γ	Adiabatic index	1.10
z	Feed benzene mole fraction	0.5	η_c	Compressor efficiency	0.80
λ	Heat of vaporization	30,000 kJ/kmol	S_{water}	Cooling water cost	0.354 $/GJ
A_{Ant}		3.97488	S_{steam}	Steam cost	7.78 $/GJ
B_{Ant}	Antoine constants in	795.819	$S_{electricity}$	Electricity cost	16.8 $/GJ
C_{Ant}	bar & K	-24.884	T_{water}	Cooling water temp.	433.15 K
M/F	Tray hold up	0.5 min	T_{steam}	Steam temp.	295.15 K
U	Overall heat transfer coefficient	2880 kJ/h/m^2	ρ	Density	877 kg/m^3

Table 2. Nominal values of operation data for different case studies.

ID	Config.	Mixture	α	X	N_S	A, m^2	q	P_r/P_s	L_C/D	V_R/B
A1	CDiC					0	1	1	1.26	2.26
B1	HIDiC	BT	2.4	0.95	20	2.5	1	2.93	0.27	1.27
C1	iHIDiC					5.0	0.5	2.93	0	0
A2	CDiC					0	1	1	1.44	2.44
B2	HIDiC	BT	2.4	0.99	30	2.5	1	2.89	0.28	1.28
C2	iHIDiC					5.0	0.5	2.89	0	0
A3	CDiC					0	1	1	10.0	11.0
B3	HIDiC	BF	1.2	0.95	76	7.5	1	1.70	4.17	5.17
C3	iHIDiC					15	0.5	1.70	0	0
A4	CDiC					0	1	1	10.7	11.7
B4	HIDiC	BF	1.2	0.99	118	7.5	1	1.55	4.29	5.29
C4	iHIDiC					15	0.5	1.55	0	0

Step 4: The algebraic model equations were solved by adjusting the adjustable operation variables from step 1.5 in order to obtain new operating point, **u**.
Step 5: The output was calculated using equations (1a)-(5).
Step 6: The variance and expectation were estimated using the Monte Carlo approach [6] to evaluate the uncertainty. Global sensitivity analysis was performed using linear regression for obtaining the standardized regression coefficients [7].

2.3 Uncertainty Analysis

The output is illustrated in Figure 2 for the 12 case studies representing two different mixtures divided in two different purity specifications. Interestingly, it can be seen that internal heat-integration for a benzene-toluene (BT) separation does not increase the second-law efficiency nor does it decrease the *OPEX* significantly. This trend is different when it comes to the close boiling mixture benzene-flourobenzene (BF). Figure 2(c) reveals that internal heat-integration is costly in terms of *CAPEX*, while (d) reveals that internal heat-integration decreases the dominant time constant. Examples of steady state profiles of an iHIDiC are illustrated in Figure 3. The uncertainty is illustrated by plotting the relative standard deviations in Figure 4. Figure 4(a) and (b) reveal that η_{2nd} and *OPEX* estimations are uncertain for large columns and especially with external reflux and boil-up (the HIDiC). *CAPEX* estimations of the iHIDiC are more uncertain than other configurations. This is due to the iHIDiC has the largest vapor flow through the compressor and thus the largest shaft work, and it is at this position where the vapor flow is most uncertain (Figure 3).

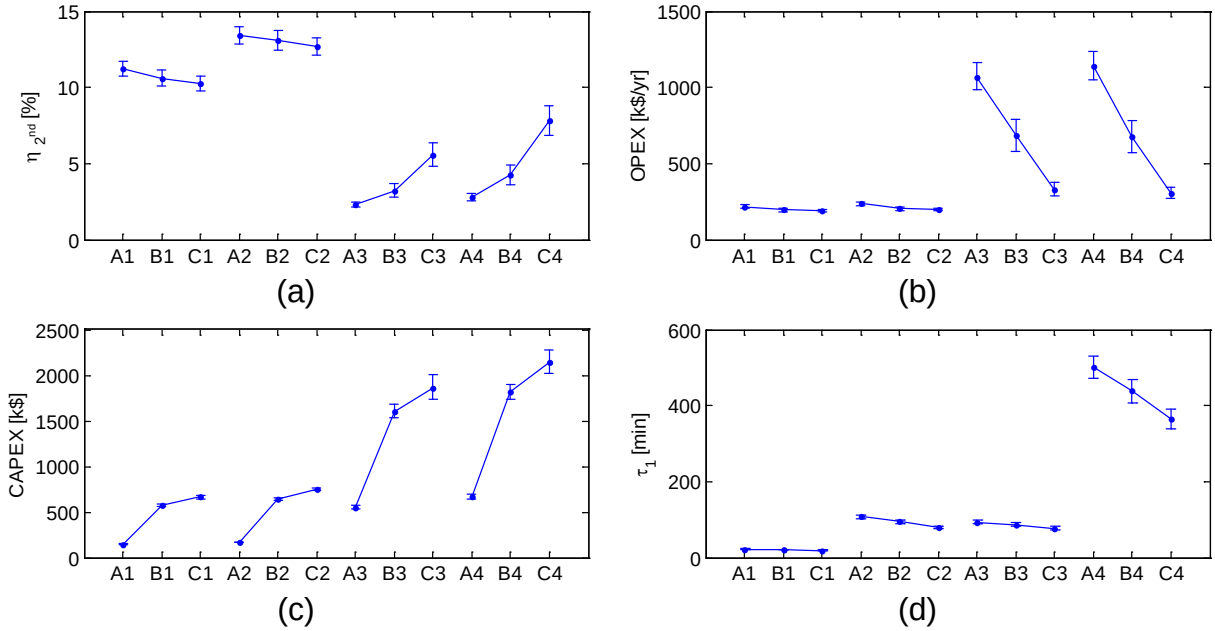

Figure 2. Mean values and 95% confidence intervals from Monte Carlo simulations with uncertain parameters λ, α, U, M and γ of the outputs: (a) Second-law efficiency, (b) operation expenditures, (c) capital expenditures and (d) dominant time contant.

2.4 Global Sensitivity Analysis

For all case studies, good linear fits between outputs and uncertain parameters were obtained when performing linear regression on the Monte Carlo simulations. All outputs were highly correlated with α. With increasing α, η_{2nd} was linearly increasing while *OPEX*, *CAPEX*, and τ_1 were linearly decreasing. The results from the global sensitivity analysis are illustrated in Figure 5. Here the significance of each uncertain

parameters are represented by different colors in each output (vertical bars). This analysis suggests that dynamic simulations of any configuration are mainly influenced by the choice of *M* and, to some extent, *U*. The significance on the outputs of *U* decreases as *α* increases.

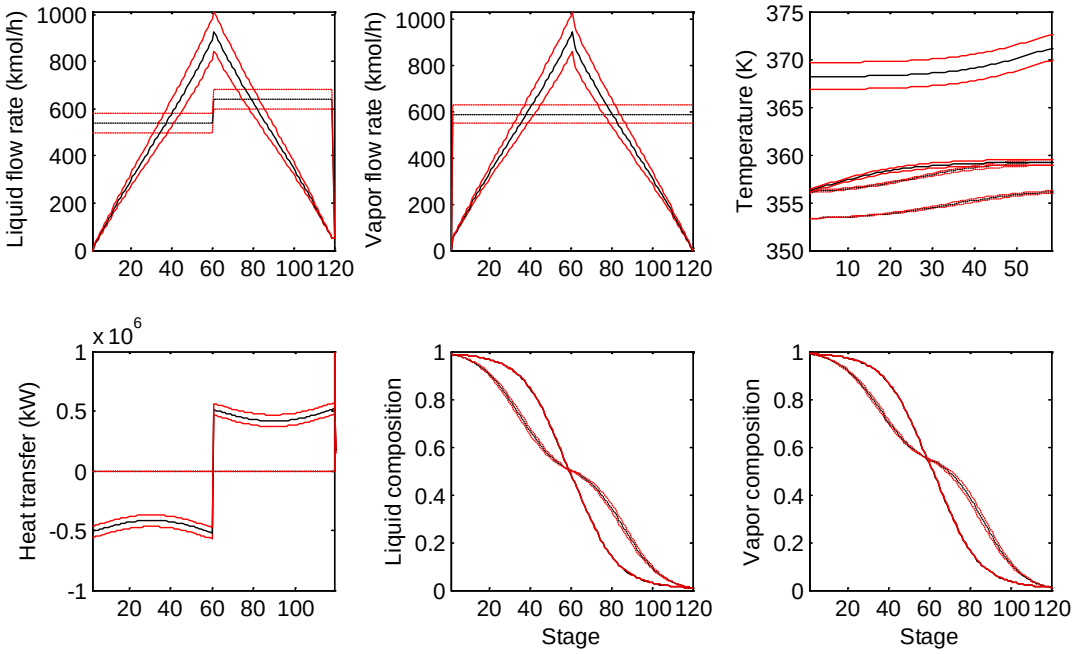

Figure 3. Steady state profiles of an iHIDiC (solid) and a CDiC (dashed) separating the benzene-flourobenzene mixture with *X* = 0.99 (case C4 and A4). The black lines are mean values and the red lines are 95% confidence bands.

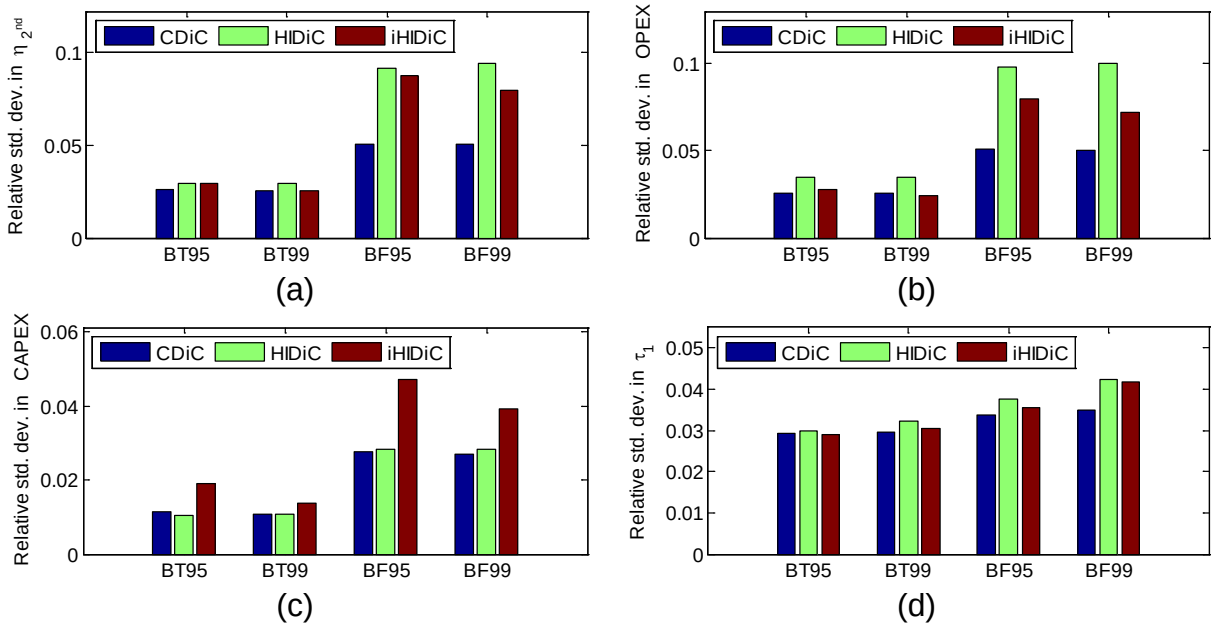

Figure 4. Relative standard deviation from Monte Carlo simulations with uncertain parameters *λ*, *α*, *U*, *M* and *γ* of the outputs: (a) Second-law efficiency, (b) operation expenditures, (c) capital expenditures and (d) dominant time contant. The case studies are grouped according to mixtures and product purities from Table 2. E.g. benzene-toluene at *X* = 0.95 is BT95.

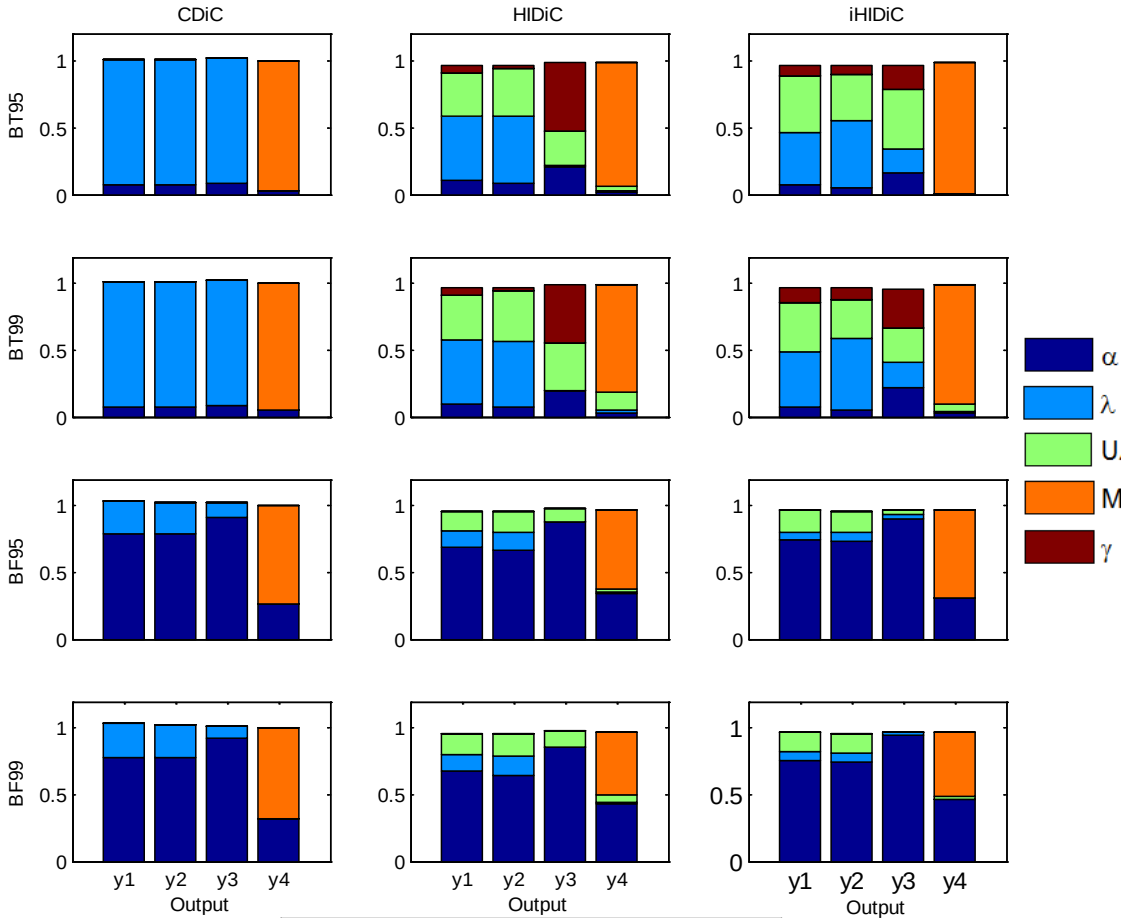

Figure 5. Squared linear regression parameters for the different model output (vertical bars), $\boldsymbol{y}$ = (y1,y2,y2,y4)^T = (η_{2nd},*OPEX*,*CAPEX*,τ_1)^T, divided in contributions from each uncertain parameter. The case studies are grouped according to mixtures and product purities from Table 2. E.g. benzene-toluene at X = 0.95 is BT95.

3. Conclusions

Uncertainty analysis reveals a significant variance in second-law efficiency and *OPEX* for heat-integrated distillation columns separating close boiling mixtures. Strong, linear correlations between relative volatility and all outputs were found. The sensitivity to the overall heat transfer coefficient for heat-integrated distillation columns is less significant than that of the relative volatility, despite of large number of stages with internal heat transfer.

References

[1] Mah, R.S.H., et al. (1977). Distillation with secondary reflux and vaporization: A comparative evaluation. AIChE Journal, 23.
[2] Liu, X. and Qian, J. (2000). Modeling, Control, and Optimization of Ideal Internal Thermally Coupled Distillation Columns, Chemical Engineering and Technology, 23.
[3] Guthrie, K.M. (1969, March 24). Capital cost estimating. Chemical Engineering, 114.
[4] Skogestad, S. and Morari, M. The dominant time constant for distillation columns. Computers and Chemical Engineering, 11.
[5] Davis, F.J. and Helton, J.C. (2003) Latin hypercube sampling and the propagation of uncertainty in analyses of complex systems. Reliability Engineering and System Safety, 81.
[6] Ulam, S. and Metropolis, N. (1949). The Monte Carlo method. Journal of the American Statistical Association, 44.
[7] Sin, G. et al. (2011). Global sensitivity analysis in wastewater treatment plant model applications: Prioritizing sources of uncertainty. Water Research, 2011.

Absorption of SO_2 in seawater and brine

Christoph Cox, Christoph Pasel, Michael Luckas, Dieter Bathen, University of Duisburg-Essen, Duisburg/Germany

Abstract

Desalination plants are mostly pegged to power plants due to their high energy consumption. The remaining brine leads to osmotic damage in marine organisms by untreated discharge into the sea. Simultaneously, sea water is used for flue gas desulfurization (FGD) in the pegged power plant. The resulting wastewater can't be led back to sea without post treatment because of its low pH-value and high content of oxidizing sulphur components. Therefore, the possibility of a combined FGD and drinking water production is discussed, in which the brine is used for the FGD as solvent. In this process variant, sea water consumption could be reduced and post treatment of the brine could be integrated into this operation. However, there are only few systematic measurements of the absorption capacity of brine from desalination plants. These results are absolutely essential for an economic design of absorption columns.

A systematic study of the SO_2 solubility of binary systems (SO_2 + water + 1 electrolyte) and of the complex seawater and brine was performed. The experimental setup allowed a comprehensive description of the equilibrium state by a spectroscopic determination of the partial pressure of SO_2 in the gas phase and of the concentration of sulphur compounds in the liquid phase. The influence of main ions present in the brine (e.g. Na^+, Cl^-, K^+, Mg^{2+}, Ca^{2+}, HCO_3^-.) is studied at different temperatures. A thermodynamic model based on caloric data and a Pitzer and a Sechenov approach for the calculation of activity coefficients is fitted to experimental data. The experiments reveal considerable deviations of model predictions from experimental data mainly at higher temperatures in the range of 50°. Model parameters were fitted to binary data and successfully transferred to systems containing seawater and brine. The new model provides a reliable prediction of SO_2 solubility in these systems at temperatures from 20°C to approx. 60°C.

Keywords

SO_2; absorption; brine; uv; Pitzer; SO_2Cl^-

1. Introduction

For flue gas desulfurization of fossil fuel power plants in coastal regions sea water is often used as a solvent whose alkalinity supports chemisorption of acidic SO_2. In arid areas, energy intensive desalination plants are often combined to these power plants, which produce brine as a by-product. This brine may be used as solvent for flue gas desulphurization instead of seawater. However systematic measurements of the impact of ions in brine on absorption of SO_2 are missing to design such a process. Thus, a reliable process model is not available and an accurate prediction of the absorption capacity is not possible.

Several working groups have modeled the solubility of SO_2 in sea water on the basis of available models with satisfying accuracy. However, model transfer on processes

with brine has not been established due to the significantly higher electrolyte concentration of brine. Furthermore, the species distributions of absorbed sulfur in these electrolyte solutions have not been adequately studied.
In this work the absorption of SO_2 in fundamental binary systems (water + 1 salt) present in seawater and brine were investigated experimentally and modeled to determine reliable model parameters for the main components of the electrolyte systems seawater and brine. Afterwards, these parameters were combined in a model which was compared to absorbance measurements in seawater and brine. The concentrations were measured by uv/vis spectroscopy, which allows an in-situ determination of sulfur components in the gas phase and the liquid phase. In a previous work, systematic studies of uv spectra indicated the presence of another sulfur species SO_2Cl^- influencing SO_2 absorption in chloride containing electrolyte systems [1]. This component was added to the reaction scheme of absorption and modeling. Thus, a better accuracy in modeling of the liquid phase is achieved.

2. Results and discussion

2.1 Apparatus and materials

The experimental investigation of SO_2 absorption was carried out in an equilibrium apparatus built up at the chair of thermal process engineering at the University of Duisburg-Essen. A schematic figure of the apparatus is presented in figure 1.

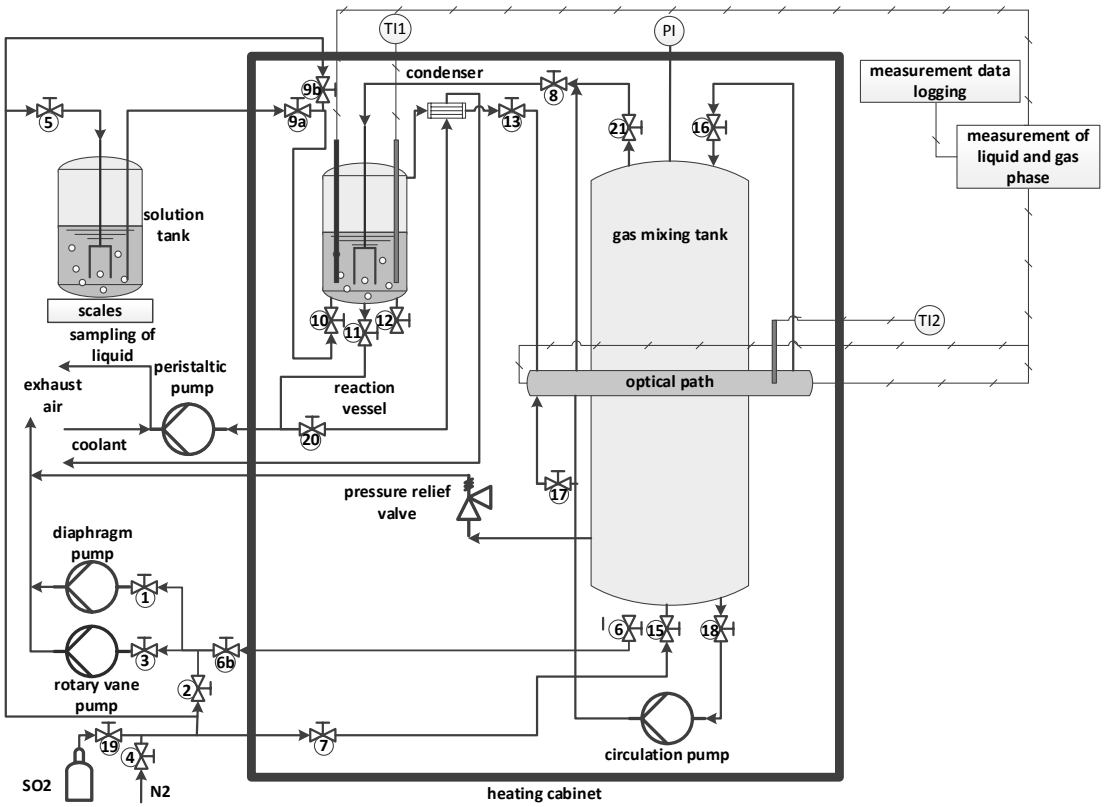

Figure 1: Scheme of the experimental apparatus

The reaction vessel, the gas mixing tank and the optical path for an in-situ study of the gas phase were installed in a heating cabinet, which could be set to temperatures from 20 to 60°C. The absorption of dissolved sulfur species was spectroscopically measured by an immersion probe. Temperature and pressure were continuously recorded. SO_2 and N_2 were added from gas cylinders.

2.2 Experimental procedure

After scavenging and evacuation of the system, the electrolyte solution was added into the reaction vessel. SO_2 and N_2 were dosed until the desired partial pressure of SO_2 was achieved before absorption. For the absorption process the gas phase was pumped in circular flow through a glass frit into the liquid phase until thermodynamic equilibrium was established. To determine the partial pressure of SO_2 in equilibrium, the spectroscopic absorption was detected at a wavelength of 280 nm. The molality of absorbed sulfur in the liquid phase was calculated from a mass balance. A uv spectroscopic measurement at 280 nm in the liquid phase afforded the absorbance of dissolved sulfur species, which is important for an accurate modeling. An error calculation according to Gauß showed an error of measurement of SO_2 partial pressure and molality of dissolved sulfur in a range of 2-3%.

2.3. Modeling

Pitzer's activity coefficient model [2] and the approach of Sechenov [3] were used for thermodynamic modeling of the equilibrium. Parameters for Pitzer's model were taken from publications by Pitzer and Mayorga [2], Rosenblatt [4] and Hunger and Lapicque [5]. The SO_2 absorption in seawater and brine was described by the following reaction scheme and modeled by the K value method [6]:

$$SO_2(g) + H_2O \rightarrow SO_2\ (aq)$$

$$SO_2(aq) + H_2O \rightarrow HSO_3^- + H^+$$

$$HSO_3^- \rightarrow SO_3^{2-} + H^+$$

$$SO_2(aq) + Cl^- \rightarrow SO_2Cl^-$$

$$CO_2(g) + H_2O \rightarrow CO_2(aq)$$

$$CO_2(aq) + H_2O \rightarrow HCO_3^- + H^+$$

$$HCO_3^- \rightarrow CO_3^{2-} + H^+$$

Zimmermann found experimental evidence for the formation of the complex SO_2Cl^- studying uv spectra of the liquid phase [1]. To calculate the K values, caloric data such as the standard Gibbs free energy of formation and the standard enthalpy of formation were implemented. Some parameters of the Pitzer model and the Sechenov approach were fitted to measured values in binary systems to improve the modeling. Other fit parameters for modeling were the standard enthalpy of formation $\Delta_f H^0_{(aq)\ SO2Cl-}$ and the absorbance coefficient ε_{SO2Cl-} of the complex to more accurately describe solution concentrations and uv absorbance in the liquid phase.

2.4 Discussion and results

2.4.1 SO_2 absorption in binary electrolyte systems

First, in order to consider individual effects of salts in sea water and brine on the absorption capacity of the solvent, solutions of the main salts were studied at 25°C and 50°C to fit model parameters of those systems. The salt concentrations were in the range of the ion concentrations in brine. The individual salt concentrations of the binary systems and the composition of seawater and brine are given in Table 1.

individual salts		seawater		brine	
comp.	conc. [mol/kg]	comp.	conc. [mol/kg]	comp.	conc. [mol/kg]
H_2O	-	Cl^-	0.554	Cl^-	1.390
NaCl	1	Na^+	0.476	Na^+	1.210
KCl	1	Ca^{2+}	0.010	Ca^{2+}	0.500
$MgCl_2$	0.5	Mg^{2+}	0.054	Mg^{2+}	0.120
$CaCl_2$	0.5	K^+	0.010	K^+	0.050
Na_2SO_4	0.1	HCO_3^-	0.002	HCO_3^-	0.010
$NaHCO_3$	0.01	SO_4^{2-}	0.028	SO_4^{2-}	0.100

Table 1: Electrolyte concentrations of individual salts, seawater and brine

An example of measurements in binary systems (SO_2-N_2-H_2O-$MgCl_2$ at 25°C) is shown in figure 2. It can be seen that the partial pressure of SO_2 and the absorbance increase with increasing molality of dissolved sulfur. The absorbance at 280 nm is governed by dissolved molecular SO_2 (aq) and the complex SO_2Cl^-.

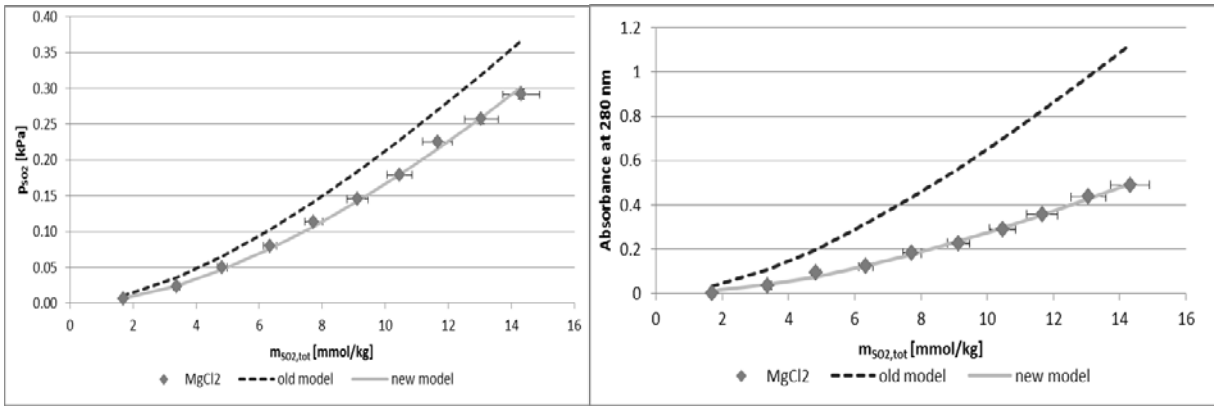

Figure 2: SO_2 partial pressure in the gas phase and absorbance in the liquid phase of the system SO_2-N_2-H_2O-$MgCl_2$ at 25°C

The dashed line represents a model with parameters published by Zimmermann [1]. Zimmermann gives a value for the absorbance coefficient ε_{SO2Cl-} at 25°C (3112 dm^3 /(mol cm)), which considers the complex SO_2Cl^- in the description of absorbance at 280 nm. However, it is seen that this model is not a satisfactory representation of measured data. The new model (solid line) allows a significant improvement in prediction of partial pressure in the gas phase and particularly of absorbance in the liquid phase. The good description of absorbance is due to a fitting of the Pitzer parameters $\beta^0(SO_2Cl^-/Mg^{++})$ and $\beta^0(HSO_3^-/Mg^{++})$ (see table 2). Fitting the Pitzer parameter $\beta^1(HSO_3^-/Mg^{++})$ was not required while the Pitzer parameter $\beta^1(SO_2Cl^-/Mg^{++})$ was not needed.
As well, a strong improvement in model accuracy is found in case of the systems SO_2-N_2-H_2O-KCl and SO_2-N_2-H_2O-$CaCl_2$. The values of fitted parameters can also been seen in Table 2. For the systems SO_2-N_2-H_2O, SO_2-N_2-H_2O-$NaHCO_3$ and SO_2-N_2-H_2O-Na_2SO_4 no parameter adjustment was required. The parameters for the system SO_2-N_2-H_2O-NaCl at 25 °C were taken from Zimmermann [1].
In flue gas scrubbers temperatures are often in the range of 50 – 60°C. To extend modeling to this temperature range, all systems have also been studied at 50°C. At this temperature, however, there are only few values of model parameters available. Pitzer parameters fitted for 25°C have not been adjusted for 50°C because only moderate temperature dependence is expected. Instead, parameters strongly influencing the temperature dependence of the model like the standard enthalpy of formation of the complex SO_2Cl^- ($\Delta_f H^0_{(aq)\ SO2Cl-}$) and the absorbance coefficient

(ε_{SO2Cl-}) at 50°C were adjusted (table 2). Figure 3 exemplary illustrates the system SO_2-N_2-H_2O-NaCl which exhibits good agreement between measurement and modeling. An old model is not displayed at 50°C because values of the parameters $\Delta_f H^0_{(aq)\ SO2Cl-}$ und ε_{SO2Cl-} are not available.

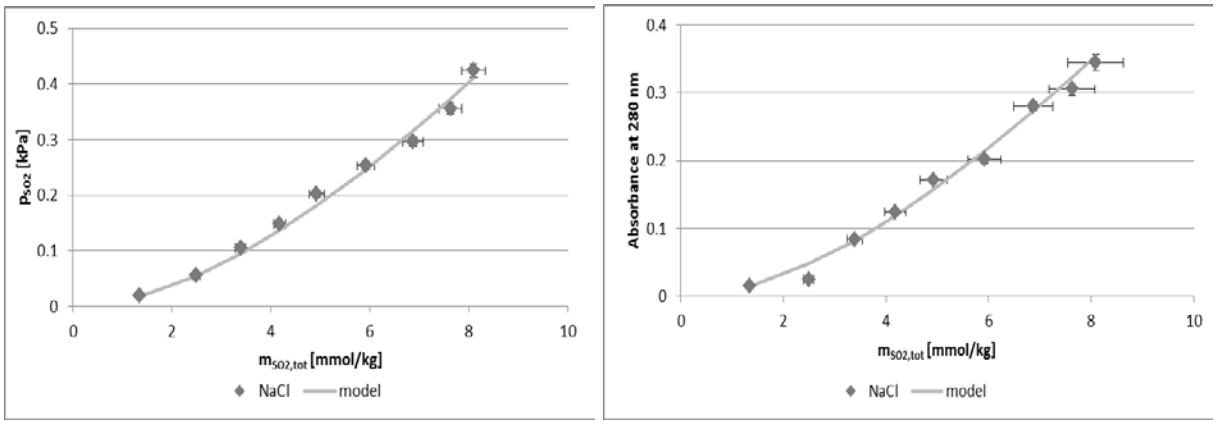

Figure 3: SO_2 partial pressure in the gas phase and absorbance in the liquid phase of the system SO_2-N_2-H_2O-NaCl at 50°C

2.4.2 SO_2 absorption in seawater and brine

The fitted model was used to calculate SO_2 absorption in seawater and brine and compare with experiments.

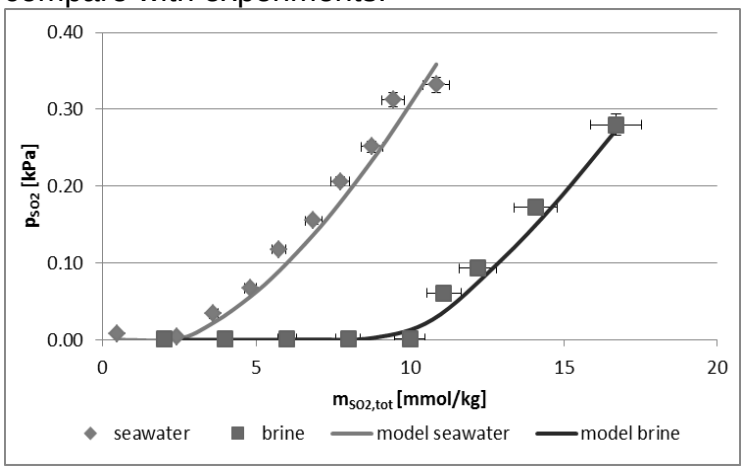

Figure 4: Comparison of SO_2 partial pressure in the gas phase in seawater and brine at 50°C

Figure 4 shows the SO_2 partial pressure at 50°C from seawater and brine. It is evident, that brine can absorb significantly more SO_2 than seawater. This is mainly due to much a higher concentration of the alkaline bicarbonate buffering the pH drop in the scrubber solution during SO_2 absorption.

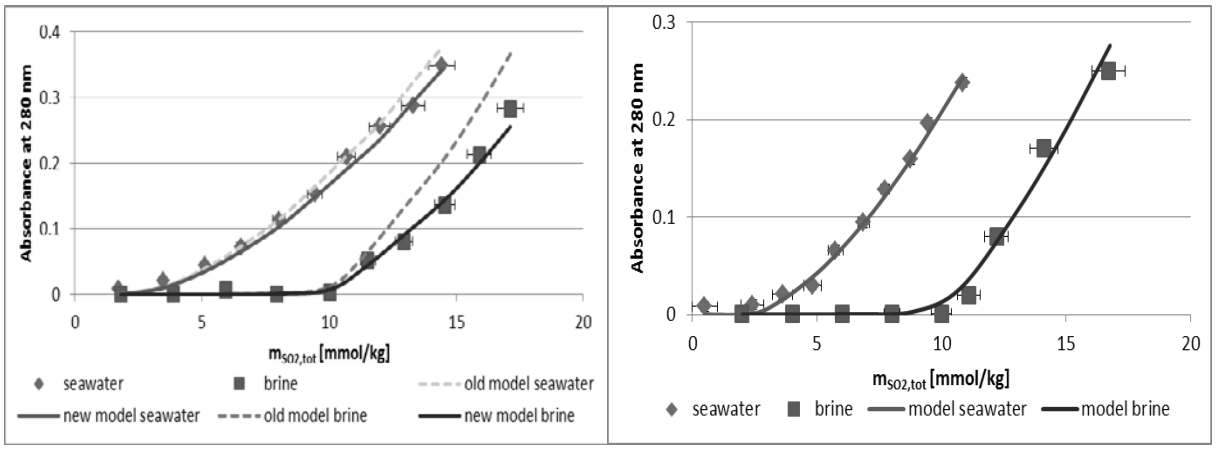

Figure 5: Comparing the absorbance in liquid phase of the systems seawater and brine at 25 and 50°C

On its left-hand side Figure 5 compares the absorbance in seawater and brine at 25°C. The new model features a significant improvement especially in the prediction of brine absorbance, which is due to the implementation of the complex SO_2Cl^- into the model. The modeling of the absorbance of seawater and brine at 50°C is in good agreement with experiment as well due to the fitted standard enthalpy of formation ($\Delta_f H^0_{(aq)\ SO2Cl-}$) and the absorbance coefficient (ε_{SO2Cl-}) of the complex SO_2Cl^- at this temperature.

3. Conclusion

In the present work, the SO_2 absorption capacity in aqueous solutions of the main salts of seawater, of seawater and of brine was experimentally studied and calculated using a thermodynamic model. A good agreement of experiment and model was achieved by fitting parameters of Pitzer's activity coefficient model and the approach of Sechenov as well as of caloric and spectroscopic data (see table 2). By full implementation of the parameters of the complex SO_2Cl^- the description of the absorbance measured in the liquid phase was improved in particular.

Parameter	Old value	New value	Meaning of the parameters
$h_{SO2\ 50°C}$	-0,0748 [3]	-0,0152	Sechenov constant of SO_2
$\beta^0 (Ca^{++}/SO_2Cl^-)$	-	1,1274	Pitzer parameter of ion pair (Ca^{++}/SO_2Cl^-)
$\beta^0 (Mg^{++}/SO_2Cl^-)$	-	1,2184	Pitzer parameter of ion pair (Mg^{++}/SO_2Cl^-)
$\beta^0 (K^+/SO_2Cl^-)$	-	0,0792	Pitzer parameter of ion pair (K^+/SO_2Cl^-)
$\beta^0 (Ca^{++}/HSO_3^-)$	0,438 [4]	0,0235	Pitzer parameter of ion pair (Ca^{++}/HSO_3^-)
$\beta^0 (Mg^{++}/HSO_3^-)$	0,490[4]	-0,0464	Pitzer parameter of ion pair (Mg^{++}/HSO_3^-)
$\beta^0 (K^+/HSO_3^-)$	-0,096[4]	-0,0648	Pitzer parameter of ion pair (K^+/HSO_3^-)
$\Delta_f H^0_{(aq)\ SO2Cl-}$ [kJ/mol]	-	-492,114	Standard enthalpy of formation of the complex SO_2Cl^-
$\varepsilon_{SO2Cl-\ 50°C}$ [dm^3/(mol cm)]	-	3814	Absorbance coefficient of the complex SO_2Cl^-

Table 2: Fitted parameters

Literature

(1) Zimmermann, K.; **2009**; Löslichkeit von Schwefeldioxid in wässrigen Elektrolytlösungen bei höheren Ionenstärken; Verlag Dr. Hut
(2) Pitzer, K. S., Mayorga, M.; **1974**; *J. Phys. Chem.*, 3, 539-546
(3) Weisenberger, S., Schumpe, A.; **1996**; *AIChE J.*, 42(1), 298-300
(4) Rosenblatt, G. M.; **1981**; *AIChE J.*, 27(4), 619-626
(5) Hunger, T., Lapicque, F., Storck A.; 1990; *J. Chem. Eng. Data*, 35, 453-463
(6) Luckas, M.; Krissmann, J.; **2001**; Thermodynamik der Elektrolytlösungen; Springer Verlag

Special distillation and special absorption with ionic liquids

Zhigang Lei, *Chengna Dai*, *Biaohua Chen*
State Key Laboratory of Chemical Resource Engineering, Beijing University of Chemical Technology, Box 266, Beijing, 100029, China
Email: leizhg@mail.buct.edu.cn

Abstract
The predictive thermodynamic models are indispensable for predicting thermodynamic properties in the field of special distillation and absorption with ionic liquids (ILs) due to many solutes and numerous combinations of cations and anions. We established the most complete group interaction parameters of UNIFAC for ILs, in which the gas molecules (e.g. CO_2, CO, H_2, SO_2, etc.) are also included in this work. Only when the group parameters can not be found in the current UNIFAC parameter matrix, the COSMO-RS model is suggested.
For extractive distillation with ILs, previous studies were limited to the use of single ILs as entrainers. In this work, the mixtures of ILs and solid inorganic salts as entrainers are proposed because they integrate the advantages of ease of operation and high selectivity. The IL intensification by adding a little solid inorganic salt was confirmed through the combination of experiments and COSMO-RS model. On the other hand, for capturing CO_2 with ILs, the solubility data were measured for CO_2/IL systems at low temperatures (below 278.2 K), thus opening a wider temperature window for application of ILs in separation processes. Moreover, the single ILs for gas absorption can be further intensified by adding a little ZIF (zeolitic imidazolate framework) materials, thus forming a new unit operation technology in chemical engineering: *Adsorptive Absorption*. In adsorptive absorption, ZIF serves as adsorption function with high adsorption capacity, while IL serves as absorption function with easy operation at liquid state. The solubility of CO_2 in the mixtures of IL and ZIF at low temperatures (< 278.2 K) can be satisfactorily predicted by the lever rule using the UNIFAC model and molecular simulation together.
Keywords: ionic liquids (ILs), extractive distillation, CO_2 absorption at low temperatures, adsorptive absorption, predictive models

1. Introduction

Recently, extractive distillation with ionic liquids (ILs) has become a platform technology for the separation of azeotropic or close-boiling mixtures. But extractive distillation is still an energy-intensive process, the design and optimization of IL entrainers play an important role in improving the selectivity and reducing the reflux ratio. However, by far, all studies have been limited to the use of single ILs as entrainers, and the separation performance of single ILs has been improved only through complicated chemical synthesis. It is tedious and time-consuming for general chemical engineers to synthesize ILs with specific functional groups.

On the other hand, for capturing CO_2, it is known that a low temperature is favorable for increasing both solubility and selectivity (e.g. the famous low-temperature Rectisol process using methanol as absorbing agents). But in the

current Rectisol process, the solvent methanol is volatile, which leads to high solvent loss and much energy consumption for recovering the entrained methanol. Therefore, the solubility data of CO_2 in ILs at low temperatures should be measured, which provide a better understanding of their separation and thermodynamic behaviors. Capturing CO_2 with ILs at low temperature is suitable for the cases where CO_2 content in gas mixtures must be purified up to several ppm grade, e.g. syngas production for Fischer-Tropsch (FT) synthesis, and ammonia synthesis. For this purpose, the use of ILs for capturing CO_2 is extended from high to low temperatures in this work. Meanwhile, it is noted that the new solid materials, i.e. ZIFs (which belong to a subclass of MOFs), exhibit an excellent separation performance for gas mixtures, having high adsorption capacity and selectivity for gas mixtures. Thus, it is straightforward to combine the ILs and ZIFs for capturing CO_2, both of which are nonvolatile, the corresponding unit operation being called *Adsorptive Absorption*.

For special separation processes with ILs, the predictive thermodynamic models are indispensable for predicting thermodynamic properties so as to reduce the amount of experimental work due to many solutes and numerous combinations of cations and anions. Among others, the COSMO-RS and UNIFAC models have the most frequency adopted by chemical engineers. It is generally believed that the predicted results by UNIFAC model are more accurate that those by COSMO-RS model so that only when the group parameters can not be found in the current UNIFAC parameter matrix, the COSMO-RS model is suggested.

Therefore, the focus of this work is on addressing the cogently interesting issues for special distillation and special absorption with ILs as to (1) establishing the most complete UNIFAC parameter matrix, in which the gas molecules (e.g. CO_2, CO, H_2 and SO_2) are included; (2) intensifying the single IL entrainers using the mixtures of ILs and solid inorganic salts for extractive distillation with ILs; (3) presenting new solubility data of CO_2 in ILs at low temperatures (< 273. 2 K) for gas absorption; and (4) going a further step to intensify the single IL for gas absorption using the mixture of IL and ZIF as separating agents.

2. Results and discussion

2.1 Predictive thermodynamic models

2.1.1 UNIFAC model for ILs

Although the classic UNIFAC model is very familiar to many chemical engineers due to its simple formulation, it has only recently been extended to the systems with ILs. The model has a combinatorial contribution to the activity coefficient, i.e. $\ln \gamma_i^C$ and a residual contribution, i.e. $\ln \gamma_i^R$, and is written as

$$\ln \gamma_i = \ln \gamma_i^C + \ln \gamma_i^R \quad (1)$$

which contains two group parameters R_k and Q_k, and group interaction parameters (a_{nm} and a_{mn}). In principle, R_k and Q_k can be obtained by the COSMO calculation, while a_{nm} and a_{mn} are obtained by correlating the experimental activity coefficients or solubility data at different temperatures exhaustively collected from literatures.

In this way, we extended the UNIFAC model to the IL-solute systems, concerning 45 main groups and 77 subgroups for ILs reported in our previous publications [1-5]. It is worth noting that the UNIFAC model parameters developed by us have been successfully applied for among others, CAMD (computer-aided molecular design) of ILs, separation process design, describing LLE (liquid-liquid equilibria), and estimation of physical properties by many authors, some of which are listed in Refs. [6-8].

In this work, we extended the predictive model to IL-gas systems, as shown in Figure 1, where such important gases as CO_2, CO, H_2 and SO_2 are introduced. Although the new group parameters were obtained by means of correlating the solubility data of gases in ILs at high temperatures (> 273.2 K), the applicability of UNIFAC model for predicting the solubility data at low temperatures (< 273.2 K) was confirmed, as mentioned in sections 2.3 and 2.4.

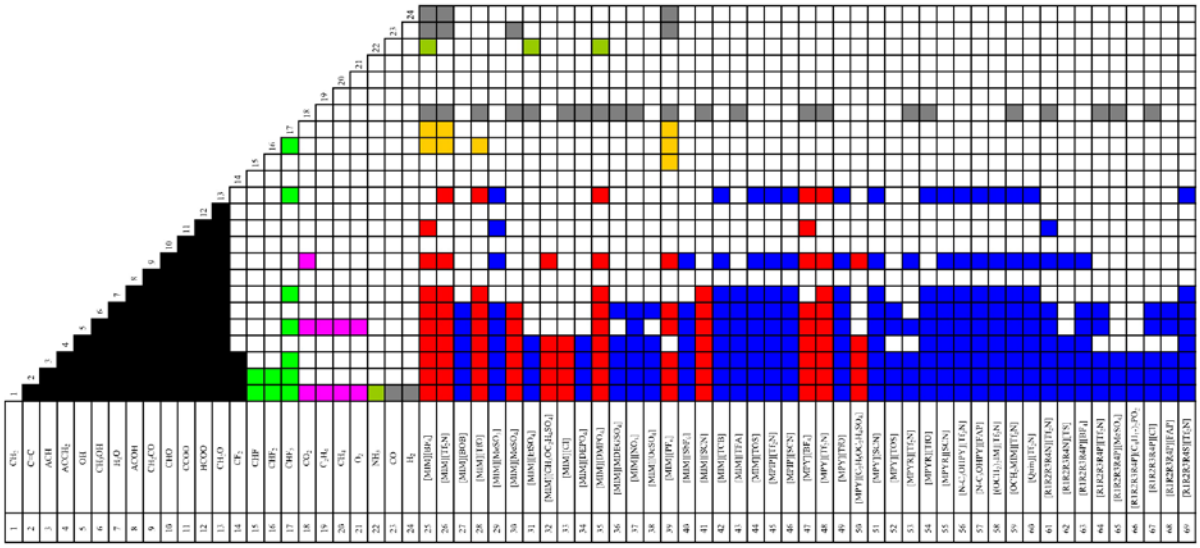

Figure 1. Current UNIFAC parameter matrix for ILs. The blocks in red, blue and light gray are developed by our group.

2.1.2 COSMO-RS model for ILs

The COSMO-RS model (conductor-like screening model for real solvents) developed by Klamt et al. provides a qualitative description of phase equilibria for the systems containing ILs, regardless of any experimental data concerning the systems of interest. Moreover, the COSMO-RS model can provide the group parameters R_k and Q_k for ILs in the UNIFAC model. For computational convenience, there have been two commercial softwares available for general chemical engineers to use, i.e., ADF (Amsterdam Density Functional) and COSMOtherm programs, in which the COSMO-RS model is embedded. For more details, please see the website at http://www.scm.com/Doc/Doc2010/CRS/CRS/page18.html (ADF version) or at http://www.cosmologic.de/index.php (COSMOtherm version).

2.2 IL intensification for extractive distillation

The separation of ethanol/water was used as a representative because the components form an azeotrope and thus can not be easily separated by ordinary distillation. Therefore, extractive distillation with ILs has recently been suggested for the separation of such systems. Previous studies have shown that the IL $[EMIM]^+[Ac]^-$ is one of the best entrainers among all investigated ILs for the separation of ethanol/water. However, herein, we decided to take a further step to intensify $[EMIM]^+[Ac]^-$ by adding a little solid inorganic salts because their salting effect could be stronger than that of ILs. Like ILs, suitable solid inorganic salts can be designed by the combination of different cations and anions. In this work, the selectivity of ethanol (1) to water (2) in 10 solid inorganic salts was measured by VLE experiments. The concentration of solid inorganic salts was kept at a mole fraction of 0.05. In addition, the selectivity in these solid inorganic salts was predicted by the COSMO-RS model. In the calculation, the COSMO radii for Na^+, K^+, and Zn^{2+} are

1.86, 2.31, and 1.33 Å, respectively. To the best of our knowledge, this is the first work to extend the application of the COSMO-RS model to screening the suitable solid inorganic salts as entrainers of extractive distillation.

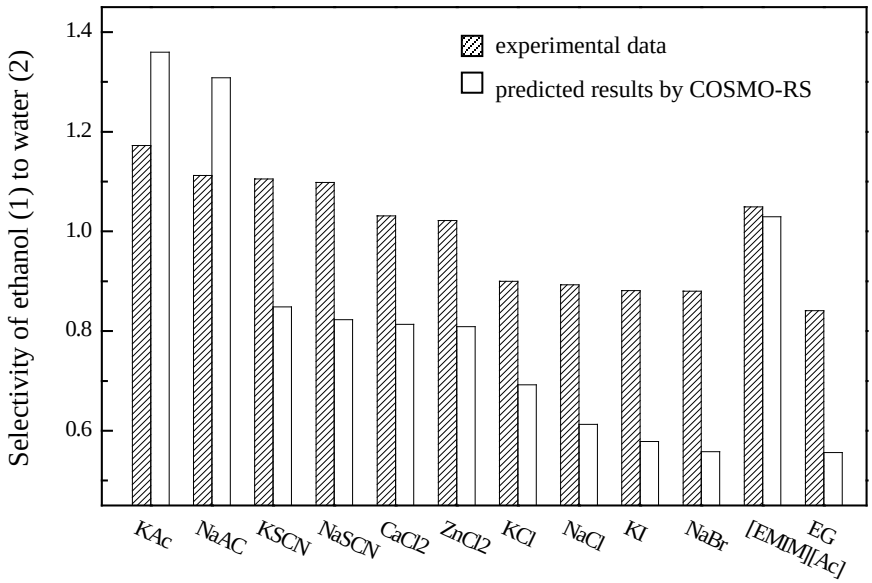

Figure 2. Selectivity of ethanol (1) to water (2) at finite concentration for various solid inorganic salts as entrainers at a mole fraction of 5.0% at P = 101.3 kPa.

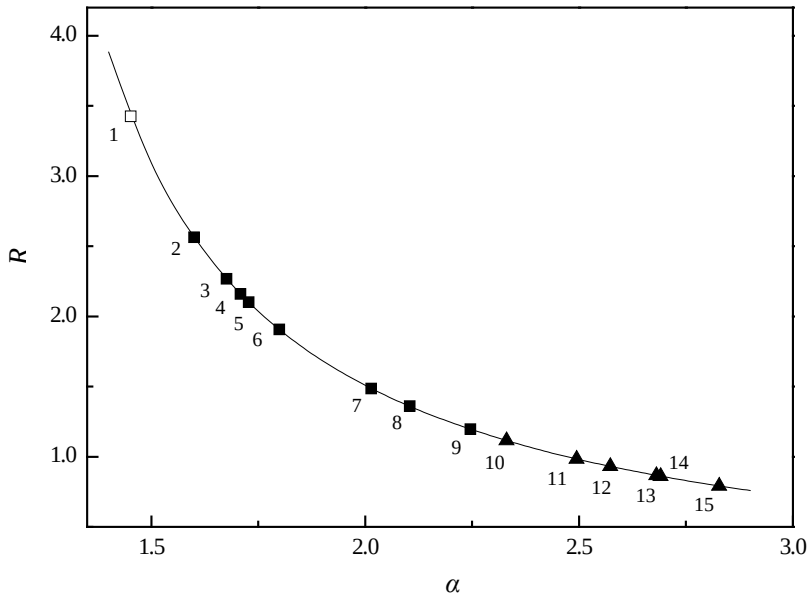

Figure 3. Effect of relative volatility (α) on the required reflux ratio (R) of the extractive distillation column for azeotropic feeding consisting of 90% (mole fraction) ethanol and 10% (mole fraction) water. (1) EG; (2) $[BMIM]^+[SbF_6]^-$; (3) $[EMIM]^+[BF_4]^-$; (4) $[BMIM]^+[FeCl_4]^-$; (5) $[BMIM]^+[TOS]^-$; (6) $[BMIM]^+[Cl]^-$; (7) $[OH\text{-}C_2MIM]^+[BF_4]^-$; (8) $[BMIM]^+[PF_6]^-$; (9) $[EMIM]^+[Ac]^-$; (10) $[EMIM]^+[Ac]^-$ + 2.0 wt% NaAc; (11) $[EMIM]^+[Ac]^-$ + 2.0 wt% KAc; (12) $[EMIM]^+[Ac]^-$ + 5.0 wt% NaAc; (13) $[EMIM]^+[Ac]^-$ + 10.0 wt% NaAc; (14) $[EMIM]^+[Ac]^-$ + 5.0 wt% KAc; (15) $[EMIM]^+[Ac]^-$ + 10.0 wt% KAc. Solid line: results calculated by the Underwood equation ($R = 1.5\ R_{min}$).

As shown in Figure 2, the trends of experimental and predicted selectivities coincide with each other qualitatively, confirming the applicability and usefulness of the COSMO-RS model for the systematic screening of solid inorganic salts with various combinations of cations and anions. The selectivity of ethanol (1) to water (2)

can be enhanced upon the addition of KAc or NaAc into $[EMIM]^+[Ac]^-$. The higher the salt concentration is, the more pronounced the salting-out effect becomes. However, we would not expect the selectivity to be greatly improved by adding a higher amount of salt because the solubility of the salt in the organic solution is limited and further addition is unlikely to lead to a proportionate increase in selectivity.

Figure 3 demonstrates that the reflux mole ratios for EG (ethylene glycol), $[EMIM]^+[Ac]^-$, and $[EMIM]^+[Ac]^-$ + 10.0 wt% KAc are 3.42, 1.20, and 0.79, respectively, indicating that the lowest amount of energy is consumed using $[EMIM]^+[Ac]^-$ + 10.0 wt% KAc as an entrainer. From the technological viewpoint, the addition of salt is convenient, and thus has a strong practical value. From the economic viewpoint, the use of an entrainer with high selectivity will generally translate into a lower total annual cost (TAC) for the extractive distillation process.

2.3 Capturing CO_2 with ILs at low temperatures

The solubility data of CO_2 in the common IL $[BMIM]^+[BF_4]^-$ as an example were measured at low temperatures of (273.2, 258.2, 243.2, and 228.2) K, as shown in Figure 4, along with the predicted results by UNIFAC model. It can be seen that low temperature is favorable for increasing the CO_2 solubility. Moreover, the predicted results by UNIFAC model are in good agreement with the experimental data at low temperatures, and the ARD (average relative deviation) between experimental data and predicted results is only 4.44%, indicating the strong predictive power of UNIFAC model from high to low temperatures.

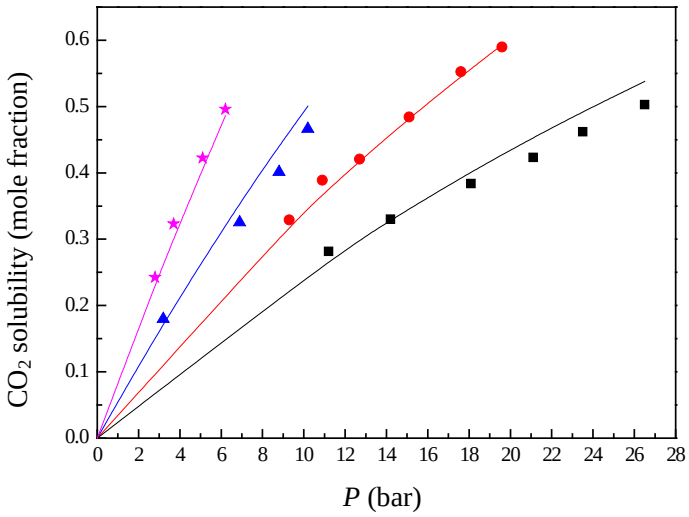

Figure 4. Solubility of CO_2 in $[BMIM]^+[BF_4]^-$ at low temperatures. Solid lines, predicted results by the UNIFAC model; scattered points, experimental data. (■) 273.2 K; (●) 258.2 K; (▲) 243.2 K; (★) 228.2 K.

2.4 A new unit operation for gas separation: adsorptive absorption

A new unit operation: adsorptive absorption (coupling of adsorption and absorption) was proposed for capturing CO_2 in gas separation. Herein, the mixture of IL and ZIF-8 (zeolitic imidazolate framework-8) were chosen as a representative of the separating agents. To check the coupling effect of adsorption and absorption, we measured the solubility of CO_2 in the mixture of $[OMIM]^+[Tf_2N]^-$ and ZIF-8 by uniformly suspending ZIF-8 powder into IL at temperature of 258.2 K. Meanwhile, the lever rule, which is based on the weight fraction average of individual IL and ZIF, was used to predict the CO_2 solubility, in which the UNIFAC model is for the prediction of

absorption amount by IL and the GCMC (grand canonical Monte Carlo) method for the prediction of adsorption amount by ZIF. As shown in Figure 5, the experimental data and predicted results agree well. Moreover, it is clear that the addition of a little amount of ZIF-8 can significantly improve the CO_2 solubility. On the other hand, from the viewpoint of separation dynamics, it has already been confirmed that adding some fine particles is favorable for enhancing the gas-liquid transfer coefficients [9].

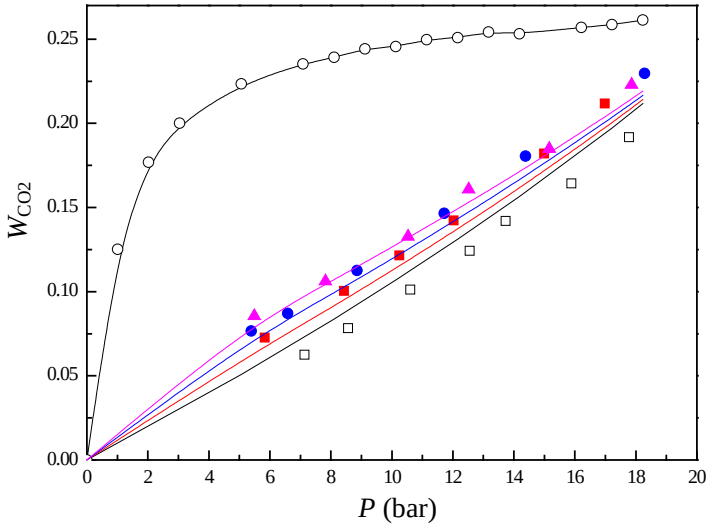

Figure 5. Solubility of CO_2 in $[OMIM]^+[Tf_2N]^-$, ZIF-8, and their mixture at 258.2 K. Solid lines, predicted results by the lever rule in which the UNIFAC model and GCMC method were adopted simultaneously; Scattered points, experimental data (in mass faction). (□) pure IL; (■) IL + 5wt% ZIF-8; (●) IL + 10wt% ZIF-8; (▲) IL + 15wt% ZIF-8; (○) ZIF-8 (GCMC calculation).

3. Conclusions

This work focuses on intensifying the distillation and absorption processes with respect to ILs, and the following conclusions can be obtained:

(i). We established the most complete UNIFAC parameter matrix for ILs, the gas molecules being included;

(ii). This is the first work to propose the mixtures of ILs and solid inorganic salts as entrainers of extractive distillation in place of single ILs, which integrate the advantages of ease of operation and high selectivity;

(iii). This is the first work to extend the application for capturing CO_2 with ILs from high to low temperatures;

(iv). This is the first work to propose a new unit operation in chemical engineering: *adsorptive absorption*, which intensifies the gas separation in both thermodynamics and dynamics by using the mixture of IL and ZIF as separating agents.

Acknowledgements This work was financially supported by the National Nature Science Foundation of China under Grants (Nos. 21121064 and 21076008), and the Research Fund for the Doctoral Program of Higher Education of China (No. 20120010110002).

References

1. Dai, C., Lei, Z., Wang, W., Xiao L., Chen, B. *AIChE J.* 2013, *59*, 4399-4412.
2. Lei, Z., Dai, C., Liu, X., Xiao, L., Chen, B. *Ind. Eng. Chem. Res.* 2012, *51*, 12135-12144.
3. Lei, Z., Zhang, J., Li, Q., Chen, B. Ind. *Eng. Chem. Res.* 2009, *48*, 2697-2704.
4. Lei, Z., Chen, B., Li, C., Liu, H. *Chem. Rev.* 2008, *108*, 1419-1455.
5. Lei, Z., Dai, C., Chen, B. *Chem. Rev.* 2014, DOI: http://dx.doi.org/10.1021/cr300497a.
6. Roughton, B. C.; White, J.; Camarda, K. V.; Gani, R. *Computer Aided Chemical Engineering* 2011, *29*, 1578-1582.
7. Xu, Y.; Zhu, H.; Yang, L. *J. Chem. Eng. Data* 2013, *58*, 2260-2266.
8. Lago, S.; Rodríguez, H.; Arce, A.; Soto, A. *Fluid Phase Equilibr.* 2014, *361*, 37-44.
9. Beenackers, A. A. C. M., van Swaaij, W. P. M. *Chem. Eng. Sci.* 1993, *48*, 3109-3139.

Modeling of vapor-liquid equilibrium and extractive rectification of butyl-propionate – propionic acid mixture

F. Bedretdinov, T. Chelyuskina, A. Frolkova
Lomonosov Moscow State University of Fine Chemical Technologies
Moscow, Russia

Abstract
This work is devoted to mathematical modeling of the vapor-liquid equilibrium (VLE) and calculation of the process of separation of the butyl propionate (BP) - propionic acid (PA) mixture at the pressures (P) 100 and 760 mm Hg. The mixture BP-PA is biazetropic at 100 mm Hg and zeotropic at 760 mm Hg but at both pressures the relative volatility of components is close to unity. For the separation of mixture we proposed extractive rectification (ER) using as a separating agent (SA) sulfolane (SF). Calculation selectivity of SF at both pressures shows that it increases with the rising of SA flow. Various working modes of the ER column of BP-PA mixture with equimolar composition were studied at different pressures. The working modes of column of SA regeneration have been also analyzed. The energy consumption of the complex as a whole was estimated. We varied pressure in the column of the ER (100 and 760 mm Hg), the overall efficiency of the columns, the ratio between the flow rates of feed and SA, reflux ratio, levels of input of the original mixture and SA. The separation process was aimed on obtaining of production flows with the content of impurities not more than 0,5% mole. We have established that, despite the presence of two azeotropes in the BP-PA system, when carrying out the extractive rectification at 100 mm Hg, energy consumption decreases by about 27% compared with the division at 760 mm Hg, when a mixture contains no azeotropes. Therefore for separate butyl propionate-propionic acid mixture we recommend the use of ER complex at 100 mm Hg.

Keywords
Vapor-liquid equilibrium, modeling, biazeotropic mixture, extractive rectification

1. Introduction

The most common industrial method of separation of binary and multicomponent liquid mixtures is rectification. Its capabilities are significantly limited by the presence of azeotropes (mono- and biazeotropy) and the relative volatility of the components (α) in zeotrope mixtures is close to unity. Promising in these cases is the use of additional substances – separating agents [1-3]. The research of evolution of the phase behavior of the initial (base) system in the presence of SA in different conditions is very topical, because it is the theoretical basis of choice of rational modes of separation. This work is devoted to the modeling of vapor-liquid equilibrium mixture butylpropionate - propionic acid at a pressure of 100 mm Hg when it is biazeotropic, and at a pressure of 760 mm Hg, when the mixture is zeotropic and investigation regularities of the separation of the mixture by extractive rectification

using sulfolane. When modeling VLE we took into account not only the non-ideality of the liquid, but also of the vapor phase.

2. Results and discussion

2.1. Investigation of vapor-liquid equilibrium in the system butyl propionate - propionic acid

The object of research is the mixture butyl propionate - propionic acid, which has industrial importance and is characterized by the close boiling points of the components. This system is biazeotropic at low pressures and zeotropic at atmospheric pressure [4]. We carried out a simulation of VLE at pressures of 100 and 760 mm Hg in the system BP- PA using the Wilson equation with parameters given in [5]. It was established that the system BP- PA at 100 mm Hg has positive and negative azeotropes with content of butyl propionate 0.9600 mole fraction (m. f.) and 0.2800 mole fraction and boiling point temperatures equal to 85.86 C^0 and 86.95 C^0, respectively [6]. The azeotropic properties depend on pressure and there are no azeotropes at 760 mm Hg.

2.2. Modeling of vapor-liquid equilibrium in the system butyl propionate – propionic acid – sulfolane

Previously for separating of mixture BP - PA were used methods of reextractive rectification (RER) [7] and the extractive rectification [8]. Due to the fact that the RER process, compared with ER is more energy intensive, the use of the latter is preferred. As a separating agent we selected high-boiling component sulfolane.
The calculation of VLE at 100 and 760 mm Hg in the system BP- PA - SF was carried out by the using Wilson equation. Due to the fact that there is no available VLE experimental data for binary systems BP- SF and SF - PA, vapor-liquid equilibrium at 100 and 760 mm Hg in these systems was calculated by the UNIFAC model (software package «AspenTech») followed by evaluation of small parameters of Wilson model. Using the obtained parameters VLE in systems butyl propionate - sulfolane and propionic acid - sulfolane at two pressures was calculated. We found that separating agent does not formed azeotropes with components of separated mixture. Also we obtained diagrams of the course of isothermal - isobaric lines and residue curve maps. There are no ternary azeotropes in the system butyl propionate - propionic acid - sulfolane (Figure 1).

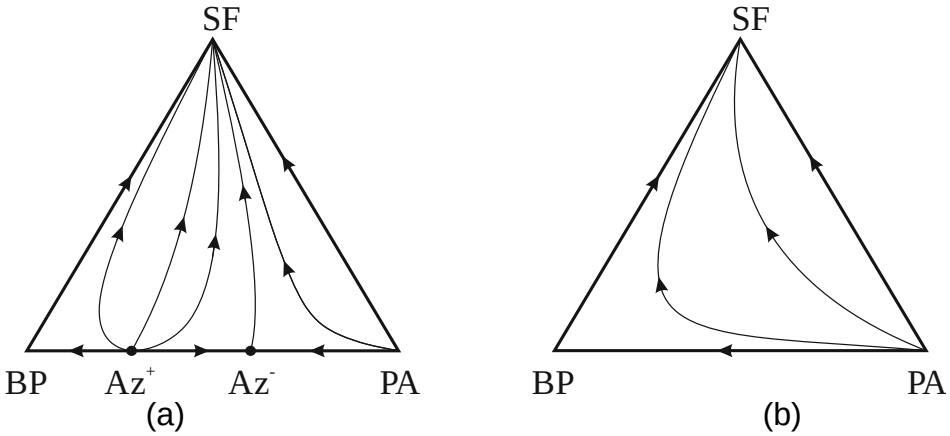

Figure 1: The residue curve maps in the system BP-PA-SF at P=100 mm Hg (a) and P=760 mm Hg (b)

To determine the selectivity of sulfolane as a separating agent we studied course of α-lines (lines of constant relative volatility) shared pair BP-PA in the presence of sulfolane (Figure 2). Analysis was carried out for a mixture of equimolar composition.

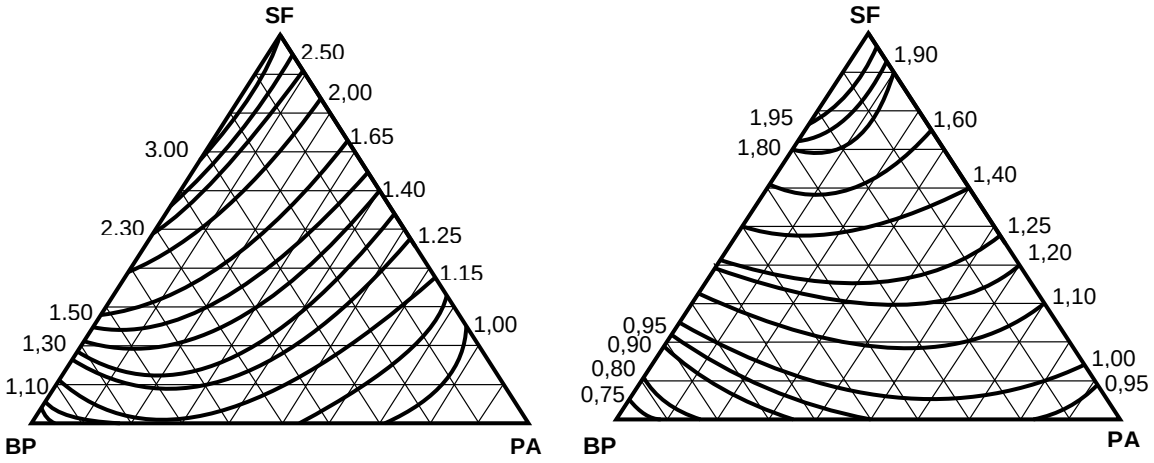

(a) (b)

Figure 2: The diagram of the course of $\alpha_{BP\text{-}PA}$ – lines in system BP-PA-SF at P=100 mm Hg (a) and P=760 mm Hg (b)

In the presence of SF volatility of ester relatively to acid increases, and separating agent has the selectivity sufficient for the implementation of extractive rectification process at both pressures (Table 1). Selectivity (S) at different ratio of the initial mixture and separating agent (F_0: SA) was determined by the formula:

$S_{SA} = \alpha_{BP-PA}^{SA} / \alpha_{BP-PA}$, where α_{BP-PA}^{SA} and α_{BP-PA} - coefficients of relative volatilities of the components of the base mixture BP-PA in the presence of separating agent and without it.

F_0:SA		1:1	1:2	1:3	1:4	1:5	1:6
S_{SA}	P=100 mm Hg	1,50	1,82	2,08	2,19	2,27	2,36
	P=760 mm Hg	1,49	1,78	1,89	1,96	1,99	2,06

Table 1: Selectivity of SF for equimolar composition of mixture BP – PA

From the table it follows that the selectivity of SA increases with increasing of its flow. When the pressure falls the same selectivity value (2.06 - 2.08) is achieved at the lower SA flows. Conclusions followed from the analysis of α - lines course, have been confirmed by calculations of more than 100 modes of extractive rectification mixture BP- PA of equimolar composition at these pressures.

2.3. Calculation of the extractive rectification of the mixture butyl propionate – propionic acid using sulfolane

The aim of the study was to obtain the product streams containing not more than 0.5 % mol. of impurities. We used separating complex comprising column ER of mixture ether- acid (column number 1) and regeneration separating agent column by ordinary rectification from mixture acid – SA (column number 2). We varied the pressure in the extractive rectification column (100 and 760 mm Hg), the overall efficiency of columns (N) in the theoretical plates (t. p.), and the ratio of amounts of initial mixture and separating agent, reflux ratio (R), the input levels of the initial

mixture (N_{Fo}) and separating agent (N_{SA}). As expected from the analysis of the selectivity of SA we were able to realize the separation of the initial mixture in the ER complex and obtain product flows with the specified quality (Table 2).

№ column	P,mm Hg	N, t. p.	N_{Fo}, t. p.	N_{SA}, t. p.	S_{SA}	F_0:SA	R	$x_{distillate}$, m. f.	$T_{distillate}$, ^0C	x_{bottom}, m. f.	T_{bottom}, ^0C
1	100	50	22	4	2,27	1:5	1,0	x_{BP}= 0,9990 x_{PA}= 0,0010 x_{SF}= 0,0000	85,87	x_{BP}= 0,0001 x_{PA}= 0,0908 x_{SF}= 0,9091	143,05
2	100	8	4	-	-	-	0,5	x_{BP}= 0,0010 x_{PA}= 0,9986 x_{SF}= 0,0004	86,34	x_{BP}= 0,0000 x_{PA}= 0,0000 x_{SF}= 1,0000	207,15
1	760	50	26	4	2,06	1:6	2,0	x_{BP}= 0,9980 x_{PA}= 0,0018 x_{SF}= 0,0002	145,37	x_{BP}= 0,0002 x_{PA}= 0,0768 x_{SF}= 0,9229	226,44
2	100	8	4	-	-	-	0,8	x_{BP}= 0,0020 x_{PA}= 0,9979 x_{SF}= 0,0001	86,34	x_{BP}= 0,0000 x_{PA}= 0,0000 x_{SF}= 1,0000	207,15

Table 2: Parameters of operating ER complex of BP – PA mixture with the use of sulfolane

Column number 2 in both complexes operated at P = 100 mm Hg to avoid possible degradation of sulfolane (T> 220 0C) [9].

2.4. Comparison of power consumption for the separation of mixtures in the extractive rectification complex

We have evaluated the power consumption by steam capacity in complex of extractive rectification of BP-PA mixture running under different conditions. It was found that despite the presence of two azeotropes in the system BP-PA, an ER at 100 mm Hg power consumption reduced by about 27 % relatively to the separation at 760 mm Hg, when mixture is zeotropic (Table 3).

Pressure in columns mm Hg	Q_1, Kcal/h	Q_2, Kcal/h	$Q_{complex}$, Kcal/h
100-100	9121	7707	16828
760-100	13689	9242	22931

Table 3: Power consumption in ER complex

2.5. Reduction of capital costs

Analysis of the results obtained at the first stage indicates the excessive overall efficiency of the extractive rectification column. At the final stage of the work we have considered the reducing the overall efficiency of the column ER from 50 to 30 t. p. From the viewpoint of energy and capital costs the most efficient mode of operation of the extractive rectification complex, with static parameters of columns which are presented in Table 4.

№	F_0:SA	N, t. p.	N_{Fo}, t. p.	N_{SA}, t. p.	S_{SA}	R	$x_{distillate}$, m. f.		$T_{distillate}$, ^0C	x_{bottom}, m. f.		T_{bottom}, ^0C
1	1:5	35	14	3	2,27	1	x_{BP}=	0,9953	85,88	x_{BP}=	0,0004	142,92
							x_{PA}=	0,0041		x_{PA}=	0,0906	
							x_{SF}=	0,0006		x_{SF}=	0,9090	
2	-	8	4	-	-	0,5	x_{BP}=	0,0010	86,34	x_{BP}=	0,0000	207,15
							x_{PA}=	0,9986		x_{PA}=	0,0000	
							x_{SF}=	0,0004		x_{SF}=	1,0000	

Table 4: Parameters of operating ER complex of BP – PA mixture with the use of sulfolane (P = 100 mmHg)

3. Conclusions

The modeling of the vapor-liquid equilibrium in the system BP – PA at 100 and 760 mm Hg was carried out. We determined characteristics of the negative and positive azeotropes in mixture butyl propionate - propionic acid at the pressure of 100 mm Hg. On the base of VLE data in the system BP – PA – SF revealed features of the phase behavior of the system butyl propionate - propionic acid in the presence of sulfolane. Based on the results of the analysis of regularities of separating a mixture of BP - PA using high-boiling separating agent it is advisable to carry out the extractive rectification process at a pressure 100 mm Hg.

Acknowledgements

We thank Russian Foundation for Basic Research for the financial support of this work (grant № 14-03-00523).

References

1. V.T. Zharov, L.A. Serafimov, Physical-chemical foundations of distillation and rectification. Leningrad: Chemistry, 1975. 240 p.
2. A.K. Frolkova, Separation of azeotropic mixtures. Physical-chemical bases and technological methods. Moscow: VLADOS, 2010. 192 p.
3. T.V. Chelyuskina, Theoretical bases of rectification separating of biazeotropic mixtures, D.T.S Thesis, Moscow: MITHT, 2011. 196 p.
4. T.M. Kushner , G.V. Shutova, V.M. Raeva, L.A. Serafimov, Investigation of biazeotropy in butyl propionate - propionic acid mixture // Journal of Physical Chemistry, 1992. V. 65. № 3. P. 832-836.
5. I.A. Mityushkina, T.V. Chelyuskina, A.K. Frolkova, Mathematical modeling of vapor-liquid equilibrium in binary biazeotropic systems // Review MITHT. 2007. V. 2, № 6. P. 68-74.
6. T. Chelyuskina, F. Bedretdinov, A. Frolkova, Extractive rectification of butyl propionate – propionic asid biazeotropic mixture with sulfolane // Proceedings 40th International Conference of Slovak Society of Chemical Engineering. Tatranske Matliare, Slovakia, May 27-31, 2013. P. 129.
7. T.V. Chelyuskina, I.A. Mityushkina, A.K. Frolkova, M.A. Chernyshova, Separation of biazeotropic mixtures with using of lightly volatile additional substances // Chemical technology. 2011. V. 12, № 12. P. 730-735.

8. T. Chelyuskina, I. Mityushkina, A. Frolkova, Estimation of possibility of industrial mixture separation by extractive rectification // Proceedings 35th International Conference of Slovak Society of Chemical Engineering. Tatranske Matliare, Slovakia, May 26-30, 2008. P. 174.
9. A.A. Gaile, V.E. Somov, O.M. Varshavski, L.V. Semenov, Sulfolane: Properties and using as selective solvent. SPB: Himizdat, 1998. 144 p.

A novel method to understand the fundamentals of gas-liquid interface behaviour during absorption under transient conditions

Patrick Schmidt[1], *Prashant Valluri*[1], *Lennon Ó Náraigh*[2], *Mathieu Lucquiaud*[1]
[1]*Institute for Materials and Processes, The University of Edinburgh, Edinburgh, United Kingdom;*
[2]*School of Mathematical Sciences, University College Dublin, Dublin, Ireland*

Abstract

We adopt an existing analytical model, describing the velocity profile of a horizontal co-current gas-liquid flow with an undisturbed flat liquid interface, to account for vertical thin films sheared by a counter-current laminar/turbulent gas flow. This base flow profile exhibits the main characteristics observed in experiments and is used in a semi-analytical Orr-Sommerfeld-type analysis to investigate the linear stability of the liquid interface. With this analysis, we determine the most unstable mode over a wide range of technically relevant parameters (film thickness, pressure drop) for various uncarbonated aqueous MEA solutions (0 wt%, 30 wt%, 50 wt%) at different temperatures (298.15 K, 333.15 K). We further use the wave speed of these modes to construct flow maps identifying regions of counter-current flow and flooding. Moreover, the linear stability analysis sets a rigorous benchmark for direct numerical simulations of such gas-liquid flows using a newly developed, level-set method based solver. First DNS results show excellent agreement with linear theory.

Keywords

Multiphase flow, Thin films, Instability, Mathematical modelling, Direct numerical simulation

1. Introduction

Even though thin films are characteristic for various areas of process engineering and widely employed, e.g. as falling liquid films in distillation and absorption columns with structured packings, their dynamic flow behaviour is still not fully understood. Detailed knowledge of the mechanisms at play, especially with regard to interfacial stability, can help to design more efficient mass transfer equipment and more flexible processes. The complexity of thin film applications arises from a combination of different interdependent physical processes like turbulent gas flow field, mass and heat transfers and chemical reactions. This multitude of involved phenomena makes detailed experimental investigations over a wide range of relevant parameters very difficult. However, latest numerical methods and increasingly available high-performance computing resources allow for extensive in-depth studies with unprecedented detail.

2. Instability of the liquid interface in falling thin films

The focus of our work is on the analysis and understanding of mechanisms leading to interfacial instability in falling thin films contacted by a laminar/turbulent counter-current gas flow. To this end, we employ advanced analytical and numerical techniques to investigate the dynamics of such two-phase systems.

2.1 Formulation of the undisturbed base flow

We consider a vertical, unidirectional gas-liquid channel flow of two separate, non-dispersed phases, which is schematically shown in figure 1. We further assume the flow to be steady and spatially uniform in streamwise direction. To describe this two-dimensional flow, we use a Cartesian coordinate system, (x,z), in which the flat interface separating both layers is located at $z=0$ and the confining channel walls at $z=-d_L$ and $z=d_G$, respectively. Within these boundaries, a thin, laminar liquid layer and a turbulent gas layer occupy the regions $-d_L \le z \le 0$ and $0 \le z \le d_G$, respectively. Both layers are assumed to be fully developed. A pressure gradient, $\partial p/\partial x > 0$, applied in x-direction counteracts gravity.

Regarding interfacial stability, the details of the undisturbed base flow determine the growth rate of small-amplitude interfacial waves to a great extent. Hence, we derive an accurate description of the mean flow profile that incorporates many of the characteristics observed in experiments. Starting point are the force balances of the two phases. In the laminar liquid film, gravity is balanced by the applied pressure drop as well as viscous forces, whereas in the turbulent gas layer viscous and turbulent forces as well as gravity balance the applied pressure drop. Continuity of velocity and tangential stress match both phases at the interface. At the channel walls no-slip is applied. Concerning the gas side turbulence, we chose a RANS approach and employ the rigorously validated algebraic model of Biberg [1] to treat the arising closure problem. Ó Náraigh et al. [2] extended this model to account for the dynamically important laminar sublayers found in wall-bound turbulent flows. Using the friction velocity at the interface $\tau_i = \rho_G V_{*,i}^2$ as well as the velocity scale $V = \sqrt{(H/\rho_G)/(\partial p/\partial x)}$, we obtain the nondimensionalised velocity profile

$$\tilde{U}\left(\tilde{z}\right) = \begin{cases} \dfrac{1}{m}\left[\dfrac{1}{2}\mathrm{Re}_p\left(1-r\dfrac{\mathrm{Re}_g^2}{\mathrm{Re}_p^2}\right)\left(\tilde{z}^2-\delta_L^2\right)-\dfrac{\mathrm{Re}_\tau^2}{\mathrm{Re}_p}\left(\tilde{z}+\delta_L\right)\right], & -\delta_L \le z \le 0, \\ \dfrac{1}{m}\left[-\dfrac{1}{2}\mathrm{Re}_p\left(1-r\dfrac{\mathrm{Re}_g^2}{\mathrm{Re}_p^2}\right)\delta_L^2-\dfrac{\mathrm{Re}_\tau^2}{\mathrm{Re}_p}\delta_L\right]+\dfrac{\mathrm{Re}_\tau^2}{\mathrm{Re}_p}\displaystyle\int_0^{\tilde{z}}\dfrac{\left[\dfrac{\mathrm{Re}_p^2}{\mathrm{Re}_\tau^2}\left(1-\dfrac{\mathrm{Re}_g^2}{\mathrm{Re}_p^2}\right)s-1\right]ds}{1+\dfrac{\kappa\delta_G\,\mathrm{Re}_\tau}{\sqrt{|R|}}G(s)\psi_i(s)\psi_w(\delta_G-s)}, & 0 \le z \le \delta_G, \end{cases} \tag{1}$$

in which $\tilde{U}=U/V$ and $\tilde{z}=z/H$ are dimensionless quantities, $m=\mu_L/\mu_G$ is the viscosity ratio, $r=\rho_L/\rho_G$ is the density ratio, and $\delta_L=d_L/H$ and $\delta_G=d_G/H$ are the relative film and gas layer thickness, respectively.

The second term in the denominator of the integral in equation 1 represents the Biberg-Ó Náraigh model to algebraically determine the turbulent viscosity in the gas layer, where κ is the von Kármán constant and R is the ratio of interfacial shear stress and wall shear stress τ_i/τ_w. The interpolation function $G(s)$ mimics the ordinary mixing length theory near the channel wall and liquid interface and transitions smoothly between these boundaries. To account for viscous effects near these boundaries, van Driest-type wall functions [2, 3], $\psi_i(s)$ and $\psi_w(\delta_G-s)$, rapidly dampen the effects of turbulence to zero. For a complete and detailed derivation of the base flow we refer to the works of Biberg [1] and Ó Náraigh et al. [2].

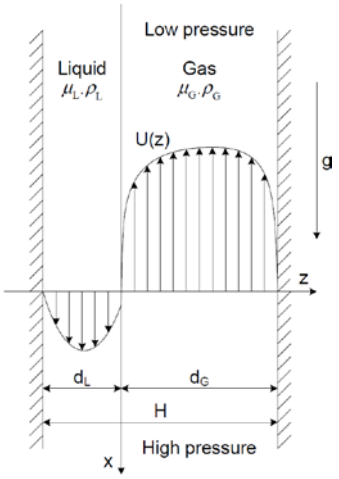

Figure 1: Schematic of the undisturbed base flow of a laminar falling film in counter-current contact with turbulent gas.

The Reynolds numbers in equation 1 are defined as $\mathrm{Re}_p = \left(\rho_G V H\right)/\mu_G$, $\mathrm{Re}_g = \left(\rho_G \sqrt{gH}H\right)/\mu_G$, $\mathrm{Re}_\tau = \left(\rho_G V_{*,i} H\right)/\mu_G$ and relate to the applied pressure drop, to gravity and to interfacial shear, respectively. Furthermore, the ratio of Re_p and Re_g resembles a Froude number $Fr = \sqrt{\left(\partial p/\partial x\right)/\left(\rho_G g\right)}$, which gives a measure for the balance between the applied pressure drop and gravity acting on the gas layer.

2.2 Linear stability analysis

To gain insight into the mechanisms playing a key role in the evolution of infinitesimally small perturbations of the form $\Phi(x,z,t) \propto \exp[i\alpha(x-ct)]$ on the flat liquid interface, we carry out a linear stability analysis on the system described in figure 1. We therefore derive an Orr-Sommerfeld equation for each phase and apply standard boundary and interfacial conditions to close the arising system [2, 4]: no-slip and no-penetration at the channel walls, continuity of velocity and tangential stress at $z = 0$, as well as a jump due to surface tension in the normal stress component. However, in contrast to this standard formulation of the two-phase stability problem additional perturbation induced turbulent stresses in the gas layer have to be taken into account. In the present work we make use of the so-called *quasi-laminar hypothesis* which states that turbulence affects the stability of the system primarily through the base flow. Ó Náraigh et al. [2] showed that the perturbed turbulent stresses are indeed of minor significance and can, therefore, be ignored.

We solve the resulting general eigenvalue problem, with the complex wave speed c as the eigenvalue, numerically by employing a Chebyshev collocation method [5]. The real wave speed c_r of the most unstable mode, i.e. the wave with the largest exponential growth rate c_i, determines whether flooding occurs in the system. In our understanding flooding occurs if the liquid velocity at the interface is negative, i.e. liquid is dragged upwards with the gas flow. Solving the Orr-Sommerfeld-type system for a given set of fluids, we are able to identify the critical Froude number at which flooding starts for a specified liquid film thickness δ_L. For a range of δ_L, a flow map can be constructed which indicates regimes of counter-current flow and flooding.

Table 1: Thermophysical properties for unloaded aqueous MEA solution for various mass fractions w_{MEA} and temperatures. The properties of the gas side (dry air) are taken from [6].

w_{MEA} [–]	ρ_L [kg/m^3]	η_L [mPa·s]	σ [N/m]	r [–]	m [–]
298.15 K, 1 bar					
0.0	997.1 [6]	0.890 [6]	0.07197 [6]	853.3	48.2
0.3	1010.6 [7]	2.480 [7]	0.06440 [8]	864.9	134.4
0.5	1020.8 [7]	5.510 [7]	0.06027 [8]	873.6	298.7
333.15 K, 1 bar					
0.0	983.21 [6]	0.466 [6]	0.06624 [6]	940.4	23.2
0.3	991.95 [7]	1.125 [7]	0.05950 [8]	948.5	56.0
0.5	998.40 [7]	2.055 [7]	0.05510 [8]	955.0	102.2

2.3 Flow regimes for aqueous monoethanolamine solutions

In our work we focus on characterizing the transition from counter-current flow to flooding of technically relevant gas-liquid systems. Aqueous solution of monoethanolamine (MEA) in contact with flue gas of a fossil fuel-fired power plant is one such system, where MEA is used to selectively remove the CO_2. Instead of the thermophysical properties of flue gas, we use the properties of dry air in our analysis. This simplification is justified as air, which is usually used for combustion, has a similar composition and, therefore, properties as flue gas. Furthermore, the density and viscosity ratio of the two phases, $r = \rho_L / \rho_G$ and $m = \mu_L / \mu_G$, based on dry air and real flue gas are of the same order of magnitude. This is an important criterion as these ratios determine the dynamic behaviour of the system to a large extend.

Table 1 gives an overview of the properties of different uncarbonated aqueous MEA solutions. We investigate solutions with 0 wt%, 30 wt% and 50 wt% MEA at 298.15 K and 333.15 K as well as 1 bar. The channel height H is set to 0.01 m.

For the aforementioned system configurations, figure 2 shows the loading points Fr_{load} at which the wave speed of the most unstable mode is equal to zero, $c_r = 0$, over a range of film thicknesses δ_L. The resulting loading curve marks the turning point from counter-current flow to flooding. It can be seen that the amount of MEA in aqueous solution has no significant influence on the loading curve for thin films with $\delta_L \leq 0.015$. Beyond that point, flooding occurs at increasingly lower Froude numbers with increasing fraction of MEA for 298.15 K (figure 2a), which can be explained by the decreasing surface tension and the increasing viscosity contrast. The dent in the

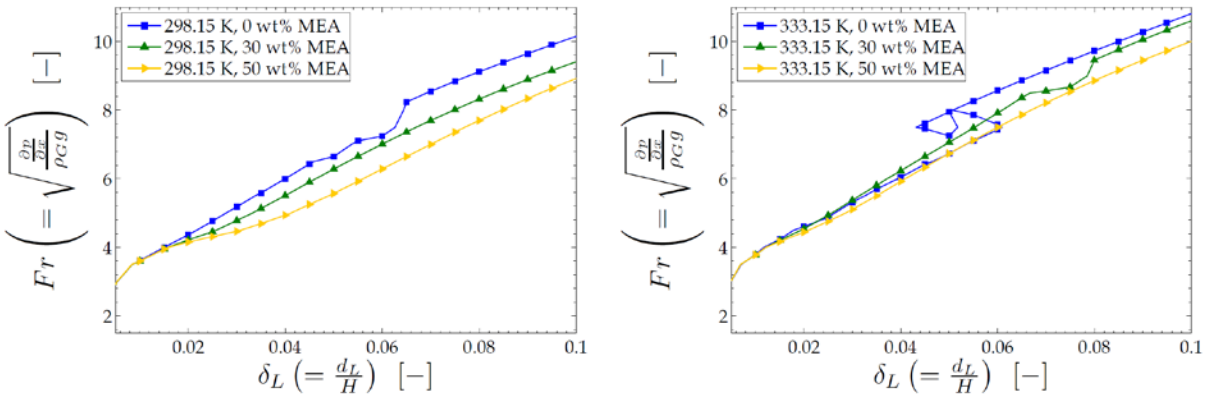

a) 298.15 K b) 333.15 K

Figure 2: Loading curves for falling films of different aqueous MEA solutions at 1 bar and 298.15 K and 333.15 K, respectively.

curve of pure water (0 wt% MEA) between $\delta_L = 0.045$ and 0.065 might come from a non-parabolic velocity profile in the liquid film but needs further investigation to clarify the reason in detail. In contrast, the loading curves at 333.15 K are less clearly distinct (figure 2b). Despite lower surface tension and a higher viscosity contrast, flooding is reached at roughly the same or even a higher pressure drop in the systems with 30 wt% and 50 wt% MEA compared to the one with 0 wt% MEA for a film thickness of up to 0.06. On the other hand, the loading curve for pure water shows a Z-like inflection as well as an island of counter-current flow amidst the flooding regime for values of δ_L between 0.045 and 0.060. For a given film thickness in this region, the flow changes between counter-current and flooding several times with increasing Froude number, which seems counter-intuitive. However, it has to be mentioned that the dimensionless interfacial velocity in this region is of the order 10^{-1}. The liquid bulk is still flowing downwards, whereas the flow direction of interface is oscillating with changing Fr. Considering this, it appears the region of intermediate film thickness is a transition zone rather than a clear boundary. Nonetheless, the system dynamics in this particular region have to be analysed in more detail to give a conclusive reason for the observed results.

2.4 Ultra-high resolution direct numerical simulation

We use the above linear stability analysis as a rigorous benchmark for a newly developed 2-/3-D solver (http://sourceforge.net/projects/tpls/) for direct numerical simulations of thin liquid films sheared by gas flow in unprecedented detail. The solver employs a level-set method to resolve and track the liquid interface. For a detailed mathematical description we refer to the work of Sussman et al. [9].

First 2-D simulations for a laminar liquid in contact with a laminar gas phase ($\kappa = 0$) have been carried out for a viscosity and density contrast of $m = 55$ and $r = 15$, respectively. The length of the numerical domain corresponds to the wavelength of the most unstable mode obtained from linear stability analysis for a given film thickness δ_L and Froude number Fr to favour the growth of that particular mode. For these simulations we applied a constant pressure drop $\partial p/\partial x$ along the domain and periodic boundary conditions in streamwise direction for velocities and pressure disturbances. Early stage DNS results are then compared to results from OS analysis. Both, a comparison of the exponential growth rate c_i (figure 3a) and the streamfunction across the channel at the crest of the developing wave (figure 3b) show excellent agreement between DNS and linear theory.

3. Conclusions

Based on the work of Ó Náraigh et al. [2], we propose an analytical model to describe the velocity profile of an undisturbed, vertical thin film of laminar liquid in counter-current contact with a laminar/turbulent gas flow. This base flow model is used to investigate the linear stability of the liquid interface of various uncarbonated aqueous MEA solutions (0 wt%, 30 wt%, 50 wt%) in contact with air at different temperatures (298.15 K, 333.15 K). We deduce flow maps for these systems and define regimes of counter-current flow and flooding for a wide range of film thicknesses and applied pressure drops. This allows defining a possible limit for operation. However, the transition between these regimes has to be study in further detail as some of the found characteristics are still of unclear origin.

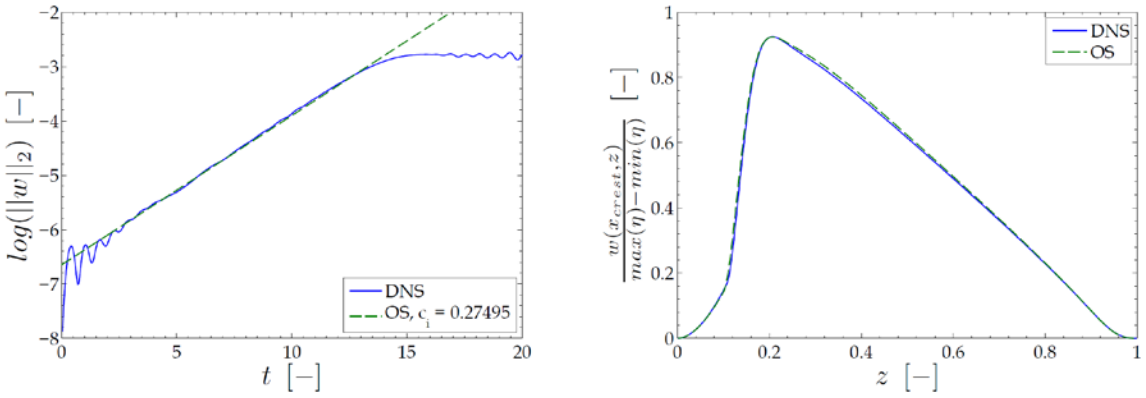

a) Exponential wave growth rate b) Streamfunction

Figure 3: Comparison between DNS and semi-analytical linear stability analysis ($\rho_G = 1.1885\ \mathrm{kg/m^3}$, $\mu_G = 18.205 \cdot 10^{-6}\ \mathrm{Pa \cdot s}$, $m = 55$, $r = 15$, $\delta_L = 0.1$, $Fr = 1.223$, $We = 2/3$).

To investigate the system dynamics beyond the linear regime, a new ultra-high resolution, level-set method based 2-/3-D solver for direct numerical simulations has been developed. DNS results for a laminar-laminar system with low density contrast have been rigorously tested against linear theory and show excellent agreement. We are therefore encouraged to use this solver to further analyse phenomena like wave break-up or droplet entrainment as well as the transient behaviour of such gas-liquid systems.

Acknowledgements

We like to thank the UK Engineering and Physical Sciences Research Council (EPSRC) through the Scottish Energy Technology Partnership (ETP) as well as Sulzer Chemtech for funding this project.

References

[1] Biberg, D., 2007. A Mathematical Model For Two-Phase Stratified Turbulent Duct Flow. *Multiphase Science and Technology*, Vol. 19(1), pp.1 – 48.

[2] Ó Náraigh, L., Spelt, P.D.M., Matar, O.K. and Zaki, T.A., 2011. Interfacial instability in turbulent flow over a liquid film in a channel. *International Journal of Multiphase Flow*, Vol. 37(7), pp.812 – 830.

[3] Van Driest, E.R., 1956. On Turbulent Flow Near a Wall. *Journal of the Aeronautical Sciences*, Vol. 23(11), pp. 1007 – 1011.

[4] Yiantsios, S.G. and Higgins, B.G., 1988. Linear stability of plane Poiseuille flow of two separated flows. *Physics of Fluids*, Vol. 31(11), pp. 3225 – 3238.

[5] Boomkamp, P.A.M., Boersma, B.J., Miesen, R.H.M. and Beijnon, G.V., 1997. A Chebyshev Collocation Method for Solving Two-Phase Flow Stability Problems. *Journal of Computational Physics*, Vol. 132(2), pp.191 – 200.

[6] Verein Deutscher Ingenieure e.V., Gesellschaft Verfahrenstechnick und Chemieingenieurwesen ed., 2006. *VDI-Wärmeatlas*. 10th ed Berlin: Springer.

[7] Amunsden, T.G., Øi, L.E. and Eimer, D.A., 2009. Density and Viscosity of Monoethanolamine + Water + Carbon Dioxide from (25 to 80) °C. *Journal of Chemical & Engineering Data*, Vol 54(11), pp.3096 – 3100.

[8] Jayarathna, S.A., Weerasooriya, A., Dayarathna, S., Eimer, D.A. and Melaaen, M.C., 2013. Densities and Surface Tensions of CO2 Loaded Aqueous Monoethanolamine Solutions with r = (0.2 to 0.7) at T = (303.15 to 333.15) K. *Journal of Chemical & Engineering Data*, Vol 58(4), pp.986 – 992.

[9] Sussman, M., Fatemi, E., Smereka, P. and Osher, S., 1998. An improved level set method for incompressible two-phase flows. *Computers & Fluids*, Vol. 27(5 – 6), pp.663 – 680.

Modeling of CO_2 removal with MEA in spray type absorber-desorber system

Tibor Nagy[1], Simone Zimmermann[2], Oliver Seyboth[2], Peter Mizsey[1,3], Günter Scheffknecht[2]

[1] Department of Chemical and Environmental Process Engineering, Budapest University of Technology and Economics, Budapest, Hungary;

[2] Institute of Combustion and Power Plant Technology, Department of Fuels and Flue Gas Cleaning University of Stuttgart, Stuttgart, Germany;

[3] Research Institute of Chemical and Process Engineering, University of Pannonia, Veszprém, Hungary

Abstract

CO_2 separation processes from industrial gases are widely studied due to the contribution they make in reducing greenhouse gas emissions. The major industrial sources of CO_2 can be power plants, refineries, steel plants etc.

Post-Combustion carbon capture is one of the most promising methods for mitigating anthropogenic CO_2 emissions. There are still several challenges to overcome before it is feasible to go to commercial scales. Therefore, the Institute of Combustion and Power Plant Technology works within a nationally funded research project supported by the German Government and power companies and suppliers (Babcock-Noell GmbH, EnBW Kraftwerke AG, E.ON New Build & Technology GmbH and Vattenfall Europe Generation AG) on the development of a spray absorption process for capturing CO_2. The application of a spray tower instead of a packed absorber column promises substantial advantages: Investment and operating costs could be reduced due to the omission of expensive packing and a very low pressure drop. Additionally, a spray scrubbing process offers the opportunity to use precipitating solvents and a much higher flexibility of the process towards load changes is expected. The flexibility is expected to be superior because there is no packing that has to be permanently wetted and no close fluid-dynamical limitations exist for the gas and liquid flow rate. However, among the current technological studies, there is lack of models of spray vessels.

This study aims at setting up a whole absorption/desorption process model and validating it based on already measured experiments in order to predict the impact of operational parameters and to further improve process efficiency. The new model set up for this system is based on the E-NRTL thermodynamic method and uses the philosophy of the Rate-based modeling technique. However, for the sake of accurate modeling, the computer model development is also necessary to describe reliable mass transfer behavior.

Keywords

carbon dioxide, monoethanolamine, spray column, absorption, desorption, modeling

1. Introduction

CO_2 capture from various types of industrial gases is one promising answer for mitigating anthropogenic greenhouse gas (GHG) emissions, one of the main contributors to climate change. Industrial gases by volume are mostly flue gases from various types of fuels and from different burning methods. There are three major technological approaches according to where the capture should take place: before (pre-combustion), during (oxi-fuel) or after the combustion (post combustion) [12]. Traditionally such gas purifying processes are done in absorber-desorber column systems. Flue gases have a relatively low CO_2 content range of 3-14 v%. Therefore, the most investigated processes include the chemical bonds during absorption (reactive absorption) [8]. The vessels used for absorbers are usually packed columns which offer a high specific area for mass transfer with a modest pressure drop. Spray towers, however, provide a good alternative when it comes to practical and economical decisions [7,9,11].

Simulation Tools

The traditional method for modeling absorption and desorption is based on the assumption that the present liquid and gas phase medium are in thermodynamic equilibrium as they leave a theoretical stage in a column. This equilibrium, however, is rarely achieved in actuality due to various reasons such as column hydrodynamics. To account for these imperfections, stage efficiencies as multipliers are used. In case of liquids having high relative volatility difference components or in cases where the mass transfer is accompanied by reactions, the mass transfer will be driven by other factors as well, therefore the basic equilibrium model fails in predictive modelling. Krishna [3] proposed a model to overcome this problem by introducing diffusion layers around the phase interface in order to limit the mass transfer through the phase boundary. The diffusion through this layer is calculated with the Maxwell-Stefan equation. This model is behind the Aspen Plus® Radfrac unit operation which is used in many studies reported in the field of absorption and desorption e.g. [4,5,6,10]. The Maxwell-Stefan equation calculates one flux quantity that needs to be scaled up in order to model the behavior of a real column. These are done by estimating the parameters such as mass-, heat transfer coefficient, the mass transfer area etc. In packed/tray columns these parameters are given through a calculation with semi empiric correlations according to column geometrics.

Our model consists of two model parts, namely the absorber and the desorber units.
In Aspen Plus® there is no available unit operation model for spray columns so far. The area of the mass transfer is a highly changing parameter over the height of the column. At the top of the column, there is a rapid growing of the mass transfer area, which can be recognized as the atomized droplets are formed while torn down from the flow. Down along the height of the column some of the liquid droplets reach the wall and flow down the side, while a part will bounce back and grow together resulting in decreased surface area. Because of this so called “wall effect” the changing mass transfer area should be considered in the model.

As a first step of the modeling, the spray towers, 5 m high with 0.37 m diameter, are modelled using packed column models in a cascade layout by manipulating the mass transfer parameters through user subroutines. As can be seen (Figure 1) each spray column is divided into three parts since the mass transfer area is continuously changing along the spray columns owing to the wall effect. To overcome this problem

each spray column is divided into three parts: upper, middle, and lower. The upper part of the column represents the top 1 m, the middle and the bottom parts of the spray column are 2-2 meters. The same idea is applied for all the three spray columns. The heat exchangers applied to the model represent the heat loss of the absorbent between two columns.

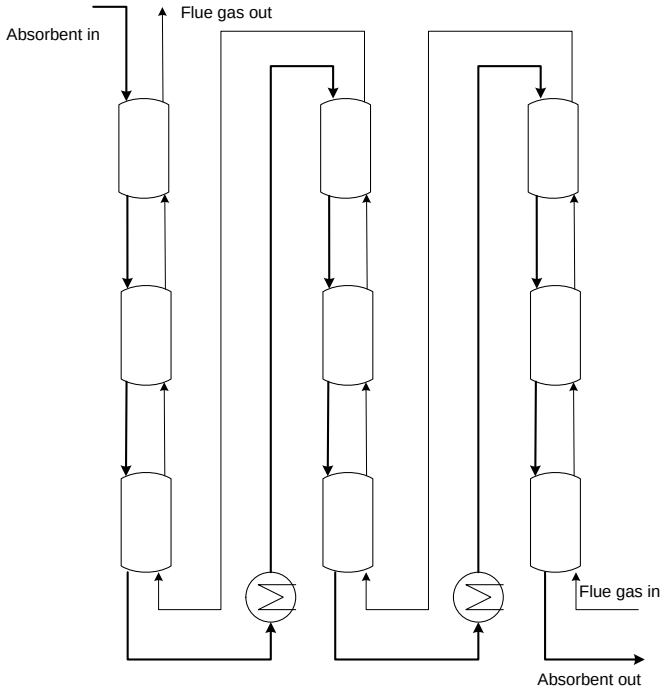

Figure 1 Layout of the Absorber model

The desorber side (Figure 2) deals with the heat integration and the solvent (MEA) regeneration processes. The desorber is built of one Aspen Plus® column with a diameter of 0,3 m and with a packing height of 2 m. The column head is connected to a droplet trap which is modelled with a flash tank and the CO_2-water vapor gas mixture is separated in the condenser. The process heat exchanger is also defined by a rigorous Aspen Plus® model with geometrics and material data in order to be able to model further off design operating conditions. More on the actual technical scale plant measurements, details and CO_2 absorption by spray droplets can be found in the works of Seyboth et. al. [1,2]

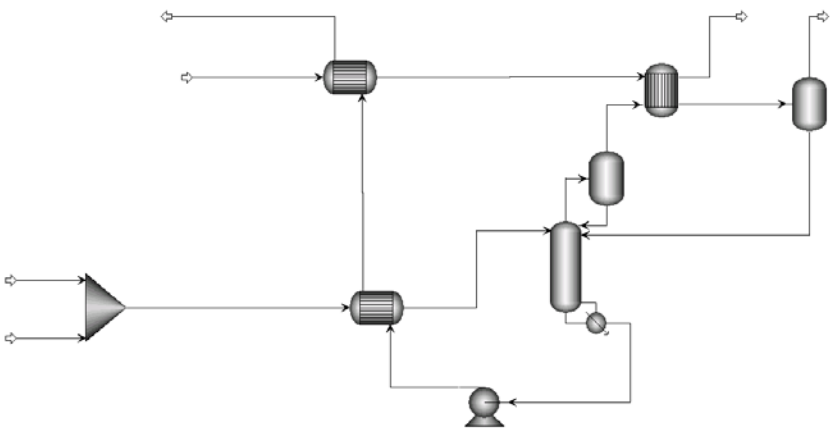

Figure 2 Flowseheet of the desorber side

2. Results and discussion

As no correlation is available to be implemented in the Radfrac model, the mass transfer areas are fitted according to the measured temperature and solvent CO_2 loading profiles

If the mass transfer areas are related to each other, it can be said that if the mass transfer area of the upper part is considered as 100%, the mass transfer area for the middle part is 24,3% while for the bottom is 19,7%. These values are fixed for all the three columns. Figure 3 shows the results for the fixed mass transfer area parameters in relation to the measured data for all three absorbers.

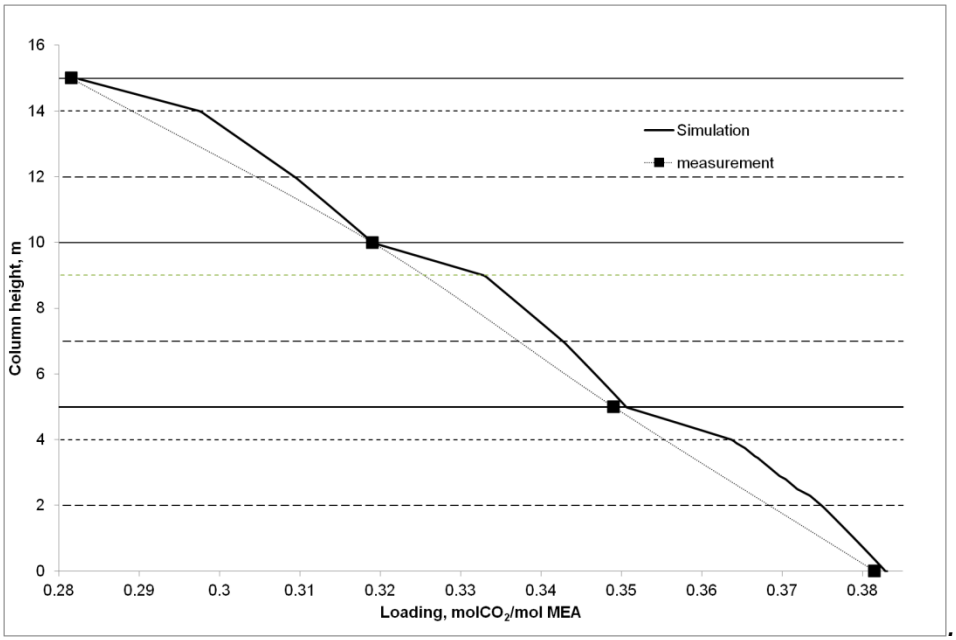

Figure 3 Layout of the Absorber model

The desorber model results demonstrate agreement with the measured data, as visible on the temperature and loading profiles (Figures 4, 5). As the desorber operates slightly above atmospheric conditions, with a high L/G ratio, much of the separation is done in the reboiler. One other interesting phenomenon can be observed on the temperature profile. According to measured data, the solvent enters the column at a lower temperature than the column temperature at the inlet height, which actually results in the cooling of the tower before the steam enters the condenser. The results also show that the thermometer along the height of the desorber gives closer results to the gas phase temperature. The differences between model predictions and measured data can be summarized by some key factors, such as liquid backmixing, continous change of column hydraulics and heat losses. The temperature difference between the measured and the vapor tamperature predictions are within one centigrade with an error of less than 0,01 molCO_2/molMEA model prediction for the CO_2 loading of the reboiler.

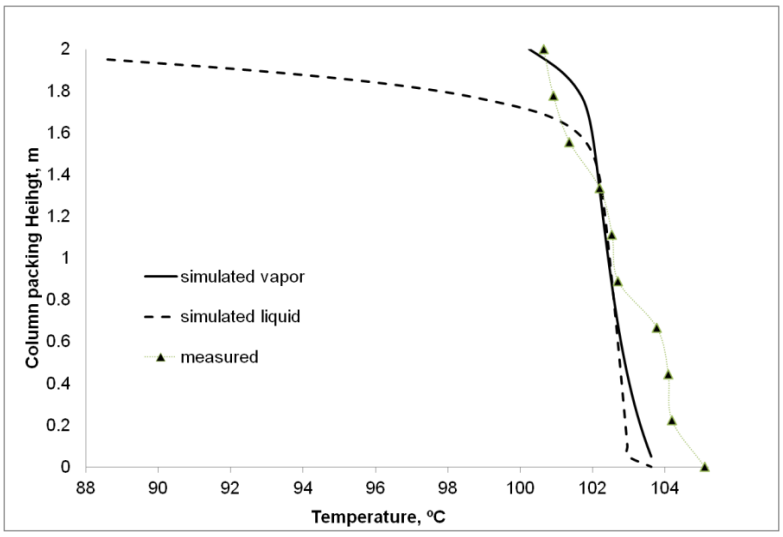

Figure 3 Desorber column temperature profile

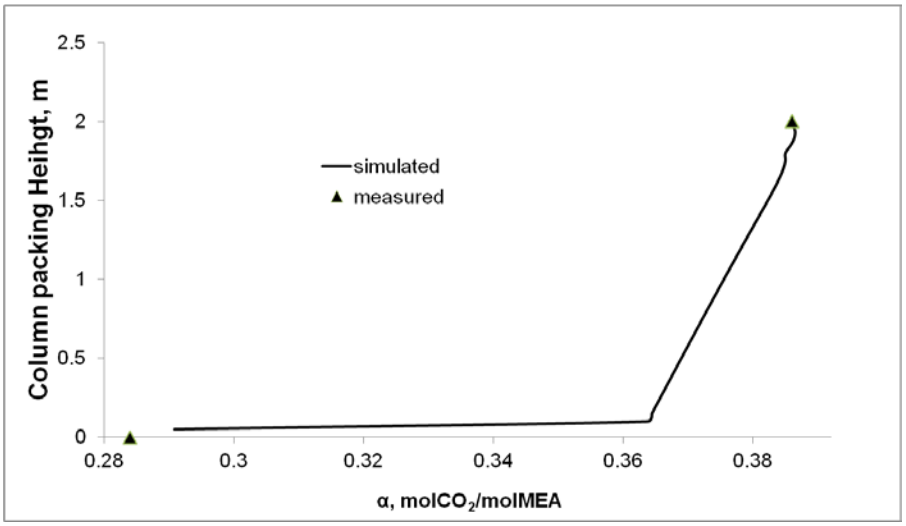

Figure 4 Desorber column CO_2 loading profile

3. Conclusions

Modelling of CO_2 capture with aqueous amine solvents is a crucial point of process design, due to the complexity of the system. Rate based modelling with the E-NRTL thermodynamic model simulation gives accurate results compared to measured data. Such models are capable of investigating process properties and their influence on the whole process. Modelling spray type columns is rather difficult due to the changing mass transfer behavior along the height of the column. In our work we could determine the mass transfer areas and their changing along the absorber on the behalf of the comparison of measured and simulated data. Nevertheless, modelling spray columns with customized user subroutines for mass transfer offers a useful alternative for spray column modelling.

Acknowledgement

We would like to thank the support of the Campus Hungary program and TÁMOP-4.1.1.C-12/1/KONV-2012-0017

References

[1] O. Seyboth, S Zimmermann, B. Heidel, G. Scheffktnecht, Results from a new Prototype Spray Scrubber for CO_2 capture, Sixth International Conference on Clean Coal Technologies (CCT2013)",2013, Thessaloniki

[2] O. Seyboth, S Zimmermann, B. Heidel, G. Scheffktnecht, Absorption of CO_2 by Spray Droplets in a Spray Scrubbing Process, 2nd Post Combustion Capture Conference (PCCC2), 2013, Bergen

[3]Krishna, T. R. R. 1993, Multicomponent Mass Transfer; Wiley-IEEE

[4] T Nagy, P Mizsey, Effects of fuels on the parameters of post combustion carbon capture, *Environ. Sci. Technol.*, 2013, 47 (15), pp 8948–8954, DOI: 10.1021/es400306u

[5]Pellegrini, L. A.; Moioli, S.; Gamba, S. Energy saving in a CO_2 capture plant by MEA scrubbing. Chemical Engineering Research and Design 2011, 89, 1676 – 1683, Special Issue on Carbon Capture and Storage.

[6]Freguia, S. Modeling of carbon dioxide Removal from Flue Gases with Monoethanolamine. Ph.D. thesis, The University of Texas at Austin, 2002.

[7] J. Kuntz, A Aroowilas, Mass-transfer efficiency of a spray column for CO_2 capture by MEA, Energy Procedia, Volume 1, Issue 1, February 2009, Pages 205-209

[8] Ömer Yildirim, Anton A. Kiss, Nicole Hüser, Katharina Leßmann,, Eugeny Y. Kenig Reactive absorption in chemical process industry: A review on current activities, Chemical Engineering Journal 213 (2012) 371-391

[9] M. Koller, D. Wappel, N. Trofaier, G. Gronald, Test Results of CO2 Spray Scrubbing with Monoethanolamine, Energy Procedia 4 (2011) 1777–1782

[10] Inga von Harbou, Michael Imle, Hans Hasse, Modeling and simulation of reactive absorption of CO_2 with MEA: Results for four different packings on two different scales Chemical Engineering Science, Volume 105, 24 February 2014, Pages 179-190

[11] Kohl, F. R. . A.Gas Purification; Gulf Publishing Company, 1985.

[12] Anusha Kothandaraman, Carbon Dioxide Capture by Chemical Absorption:A Solvent Comparison Study, Ph.D these, Massachusetts Institute of Technology, 2010

Systematic analysis of entrainers for heterogeneous azeotropic distillation in conventional and divided-wall processes

Daniel Bude, Jens-Uwe Repke
Department of Thermal, Environmental and Natural Products Process Engineering, Technische Universität Bergakademie Freiberg, Freiberg, Germany

Abstract
Due to dwindling resources bio fuels become more important. Bioethanol has the opportunity to partially replace fossil fuels since it can be regeneratively recovered by a variety of agricultural feedstocks. However the treatment of the fermentation product is highly energy intensive due to high content of water contained within biomass. Heterogeneous azeotropic distillation and the extractive distillation are commonly used procedures for dehydration of ethanol and still interesting for research.
This study compares the conventional two-column configuration and the intensified process using a divided-wall column with three different typical entrainers for the azeotropic distillation at similar purity and recovery conditions. The selected entrainers are toluene, cyclohexane and pentane as the high, medium and low boiling mass separation agent. All process configurations are designed for minimal energy demand. This allows an overview regarding possible operating and investment costs for the usage of different entrainers and the two investigated process configurations.

Keywords
Heterogeneous azeotropic distillation, divided-wall column, entrainer, ethanol dehydration, simulation

1. Introduction

Limitation of fossil fuels forces the economy to a rethink and consideration renewable sources of energy. This task is intensely investigated by economy and research institutions. In addition to studies of new energy-efficient membrane (hybrid) processes traditional distillative separation processes are also in focus of researches and industry [1, 2]. The most common processes are extractive and heterogeneous azeotropic distillation. Their high energy demand is mainly a result of low thermal efficiencies of the distillation processes and can be improved by process intensification like the use of a divided-wall column (DWC). This column type allows a reduction of external recycle flows, lower numbers of stages and includes two or more column shells in one. Thereby operation and investment costs can be reduced by using a DWC. A new considered application of DWC is heterogeneous azeotropic distillation. The azeotropic distillation allows crossing the binary azeotropic point by adding an entrainer which forms two immiscible liquid phases. The entrainer forms a low-boiling ternary heterogeneous azeotrope at the column top; thereby both products are won at the bottom of each of the two columns. Figure 1 gives a schematic overview of the commonly used conventional two-column heterogeneous azeotropic distillation process for ethanol dehydration (left side). The distillate of the first column (DC1) is close to the ternary azeotropic point and is decanted into two liquid phases.

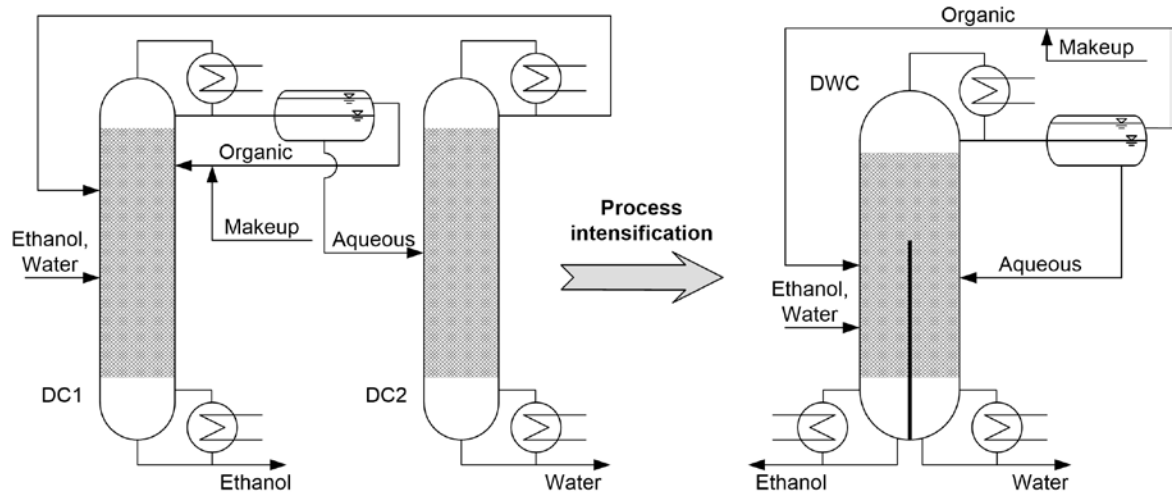

Figure 1: Conventional heterogeneous azeotropic distillation (left) and process intensification by DWC (right)

The organic phase is recycled into the first column where high-purity ethanol is obtained. The aqueous phase is fed into the second column (DC2) where water is separated. This conventional process can be integrated into one column shell by use of a DWC as shown on the right side of Figure 1. The DWC divides the column shell into three parts, i.e. a split shell column with common overhead section and two divided bottom sections. At the top of the column occurs the ternary azeotropic concentration and the two purified products can be withdrawn from the bottom. Dehydration of ethanol by heterogeneous azeotropic distillation has already been investigated by Luyben [2] an others. The possibility of process intensification for the ethanol dehydration in a DWC process has been presented by Kiss [3]. He reports energy savings up to 20%. Different purity targets and recovery rates however make it difficult to compare these studies.
The focus of this investigation is on ethanol dehydration by heterogeneous azeotropic distillation. The two process configurations (conventional and DWC) are compared for three different entrainers at similar purity and recovery conditions. The entrainers used are toluene, n-pentane and cyclohexane, which have significantly different boiling points. Data on boiling point temperatures for all components, their enthalpy of vaporization and the ternary azeotrope data with water and ethanol are summarized in Table 1. The entrainer selection provides a good comparison for the design of new processes because of the wide range of boiling points and various locations of the ternary azeotropic points.

2. Results and discussion

The pre-separation of the ethanol near azeotropic condition is out of the scope of this investigation because it is generally performed by a conventional distillation column and is quite a common and established step. Therefore, the investigated heterogeneous distillation used a feed composition near the azeotropic condition. The binary azeotropic point of ethanol and water is located at 89.7 mol%. A liquid boiling feed flow rate about 100 kmol/h (4186 kg/h), a composition of 85 mol% ethanol, a system pressure of one bar and are taken as feed conditions. The target purity of ethanol is set to 99.8 mol% (~99.8 mass%) at a recovery rate of ethanol of at least 99.8%. The high purity allows ethanol to be used as a blending component

Table 1: Overview of Boiling temperatures, enthalpy of vaporization and ternary azeotropic points for the three entrainers

Component	**Boiling temperature at 1 bar** [°C]		**Enthalpy of vaporization** [J/mol]	
Water	100		47.56	
Ethanol	78.29		49.34	
N-pentane	36.07		36.16	
Cyclohexane	80.72		39.22	
Toluene	110.63		42.146	
Ternary azeotropic points	**Composition**			**Temperature**
	Water [mol/mol]	Ethanol [mol/mol]	Entrainer [mol/mol]	[°C]
N-pentane	0.0408	0.0625	0.8967	33.12
Cyclohexane	0.154	0.3178	0.5282	62.12
Toluene	0.2758	0.4633	0.2609	73.59

for bio fuel, which is defined in standard EN 15376:2011 [4] and remains below the maximum allowed water content of 0.3 mass%. The achievability of high yield rates at heterogeneous azeotropic distillation has been demonstrated by Kiss [3]. Aspen Plus® V7.2 is used as a simulation tool with the implemented RADFRAC units, which include a rigorous calculation of the vapor-liquid-liquid equilibrium (VLLE). The property methods applied for computation of liquid activity coefficients is the non-random two liquids method (NRTL) while the Redlich-Kwong (RK) equation of state has been employed for fugacity coefficient calculations. Both methods show satisfactory results for the azeotropic distillation of these compounds [5]. It is assumed that the columns operate without pressure-drop. The DWC setup uses two interconnected RADFRAC columns that mimic a divided-wall column. Figure 2 illustrates the process configuration for the DWC setup in Aspen Plus®. One column presents the overhead with one bottom and the second the zone behind the wall without a condenser at the top (post-fractionator, PF). The interconnections between the two models are created by a liquid side stream and the vapor feed of the PF into the left column at the same stage. Thereby, the liquid split ratio is specified indirectly as the ratio between liquid side stream and internal liquid flow rate. The adjusted variables for an efficient design are the number of stages, the location of the feed-stage and recycle streams, the reflux ratio, the liquid split for the DWC and were generated by sensitivity studies. The internal sequential-quadratic-programming optimizer is not able to use integer variables and therefore cannot be used for these variables. The ethanol purity target is set as a design specification inside the column and varies the distillate flow rate. The required makeup stream of the entrainer results from entrainer loss with the two column bottoms streams. Due to the liquid boiling feed and product flows as wells as neglected energy loss and the quite low temperature dependency of the enthalpy of vaporization, the reboiler and condenser duties are in the same range. Therefore only the reboiler duties are discussed.

2.1 n-Pentane as entrainer

One of the low-boiling entrainers is n-pentane, because it forms a low temperature ternary azeotrope with ethanol and water (see Table 1). A large temperature range is the result for the main column profile. The ternary azeotropic point is located close to the entrainer side. Thus the ratio of organic and aqueous phase flows is very large.

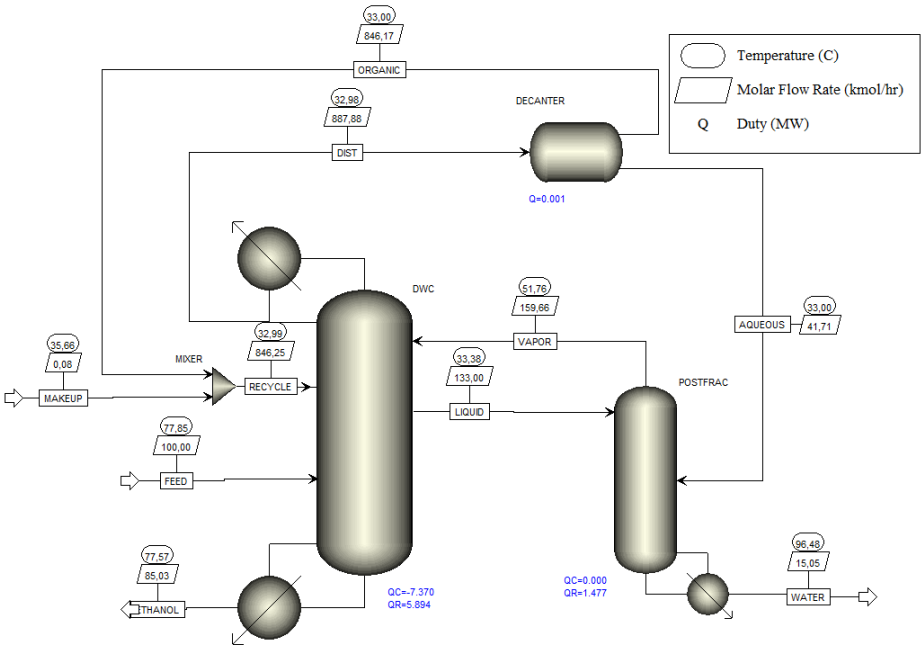

Figure 2: Aspen Plus process flowsheet for a divided-wall column illustration

The first column of the conventional process design separates the ethanol at the bottom, while the second separates the water. High n-pentane content of the organic recycle flow results in a low stage number. The DWC configuration for n-pentane requires 10% less number of stages and energy demand (see Figure 3 and 4). The temperature difference between both sides of the divided-wall is less than 50°C. Therefore heat transfer across the divided wall can be neglected [6].

2.2 Cyclohexane as entrainer

Cyclohexane as a medium boiling component has a boiling temperature close to the boiling point of ethanol. The ternary azeotrope inside the miscibility gap has a high amount of cyclohexane. This results in a high organic recycle stream in the process. Like the configuration mentioned above the ethanol is separated in the first column. Both process configurations require less stages and also less reboiler duties compared to n-Pentane (Figure 3 and 4). The DWC process reduces energy demand by 10% for process operation. 9% of the total stages can be saved by using a divided-wall column. Noticeable in this process is that the entire liquid column stream of the DWC flows into the ethanol separation part (liquid split = 0), while the aqueous recycle stream is fed at the first stage of the post-fractionator.

2.3 Toluene as entrainer

Toluene generates a ternary azeotrope at a temperature of 73.4°C and is located in center of a ternary diagram (see Table 1). Water is separated inside the first column in contrast to other entrainers. Due to low boiling temperature differences, the profile of the main product column has a low slope. However the process needs in total 70 stages for the separation of ethanol for both configurations (Figure 3). In addition a high amount of energy is required for dehydration of ethanol compared to the other entrainers. From Figure 4 it is apparent that DWC can save only 5% of the reboiler duty.

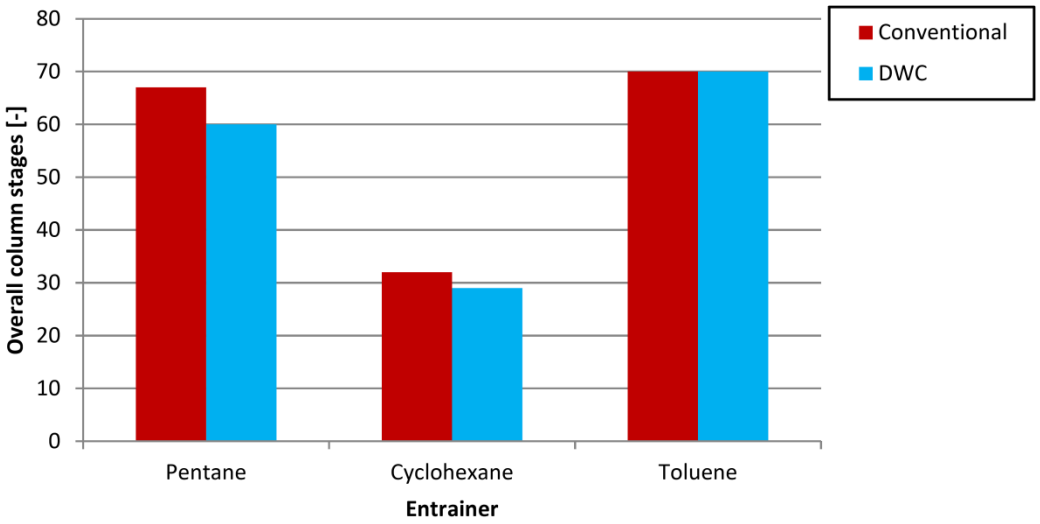

Figure 3: Overview of overall number of column stages for all entrainer and both process configurations

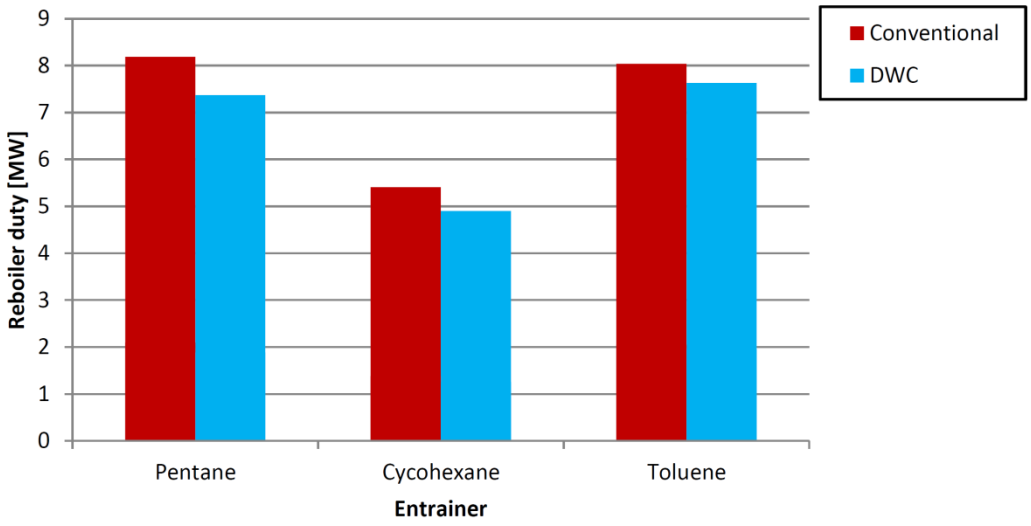

Figure 4: Overview of total reboiler duties ($\sum \dot{Q}_{reb}$) for all entrainer and both process configurations

2.4 Comparison

A comparison of the energy demand shown in Figure 4 demonstrates quite different thermal efficiencies for all six processes in dependence of the employed entrainer. n-pentane and toluene show similar results, while cyclohexane needs significant lower reboiler duty for the conventional and DWC process. The savings for DWC use range between 5 and 10% for the investigated entrainers. Possible savings of 20% reboiler duty reported by Kiss [3] could not be achieved, which is accounted to different feed conditions used here. The low boiling entrainer n-pentane shows similar operating duties and total number of stages to use of toluene for the conventional process design (Figure 3 and 4). DWC processes reduce the operating duties and number of stages by 10%. The intensified setup with toluene reduces the reboiler duty only by 5% and requires the same number of stages. Therefore a DWC

process with toluene saves only one column shell and one condenser. Due to the low number of stages and low specific energy demand this study suggests that cyclohexane should be the entrainer of choice in comparison to n-pentane and toluene. The heat of vaporization of the entrainers (Table 1) has thereby only a limited significance. The design of the divided-wall column for cyclohexane has the limitation of a liquid split of zero. That may cause in an operational restriction and a poor control behavior.

3. Conclusions

Comparison of three entrainers at similar requirements on the product and feed conditions for conventional two-column and DWC process configuration allows estimation of the prospective operating duties and due to a reduction of the number of stages for the DWC configuration a rough estimation of the investment costs. The results are based on ethanol dehydration by heterogeneous azeotropic distillation and show significant differences. The choice of entrainer is more important for the energy demand than process intensification by a DWC in general. The use of cyclohexane instead of n-pentane or toluene can reduce 30% of the required energy in the reboilers. Using of a DWC only saves additional 10% energy.
Toluene and n-pentane show similar results regarding reboiler duty, where the toluene entrainer process requires more stages for the purification of ethanol. Cyclohexane shows the best results at low reboiler duties and a low number of stages for both process configurations and should be used at a heterogeneous azeotropic distillation compared to toluene and n-pentane. Further studies will investigate dynamic performance and discuss limitations of the of divided-wall columns with a liquid split of zero.

References

[1] A. A. Kiss and R. M. Ignat, Innovative single step bioethanol dehydration in an extractive dividing-wall column, Separation and Purification Technology No. 98, 2012, P. 290-297, Elsevier

[2] W. L. Luyben, Economic Optimum Design of the Heterogeneous Azeotropic Dehydration of Ethanol, I&EC Research No. 51, 2012, P. 16427-16432, ACS Publications

[3] A. A. Kiss et. al., Enhanced bioethanol dehydration by extractive and azeotropic distillation in dividing-wall columns, Separation and Purification Technology No. 86, 2012, P. 70-78, Elsevier

[4] EN15376:2011, Automotive fuels – Ethanol as a blending component for petrol – Requirement and test methods, DIN Deutsches Institut für Normung, 2011, Berlin

[5] L.Y. Sun et. al, Implementation of ethanol dehydration using divding-wall heterogeneous azeotropic distillation column, Separation Science and Technology No. 46, 2011, P. 1365-1375, Taylor & Francis

[6] P. Narataruksa et. al., Exergy loss analysis of heat transfer across the wall of the dividing-wall distillation column, Energy No. 32, 2007, P. 2121–2134, Elsevier

The revelation of new three component system with two ternary azeotropes by mathematical simulation

T. Chelyuskina, A. Perenlei
Lomonosov Moscow State University of Fine Chemical Technologies
Moscow, Russia

Abstract
For the purpose of revelation new three-component systems with two ternary azeotropes we have carried out mathematical modeling of vapor-liquid equilibrium (VLE) at pressures 760 and 500 mm Hg in the system benzene (B)-perfluorobenzene (PFB)-methyl ethyl ketone (MEK), which formed by closely boiling components. Wilson equation with assumption of ideal behavior of vapor phase was chosen for the mathematical simulation VLE.
By results of computing experiment we have detected that at atmosphere pressure benzene-perfluorobenzene-methyl ethyl ketone system has one biazeotrpic constituent (B-PFB), two monoazeotropic constituents (MEK-PFB, MEK-B) and two ternary azeotropes. We have found that at 500 mm Hg binary constituent MEK-PFB system has two azeotropes. For analysis of evolution of phase diagram structure in the system B-PFB-MEK in the course of pressure varying the simulation of vapor-liquid equilibrium was carried out at pressure 500 mm Hg.
Three-component system forming by one azeotropic and two biazeotropic constituents and containing two ternary azeotropes was found out for the first time.

Keywords
Mathematical simulation, Wilson equation, vapor-liquid equilibrium, azeotrope, biazeotropy

1. Introduction

The aim of our study was the search of new biazeotropic systems. Such systems have specific phase behavior and accordingly the design of distillation process in these cases needs additional consideration in comparison with monoazeotropic mixtures. Biazeotropic systems can be discovered through real experiment or with the use of model simulation (e.g. based on local composition equations). One of the problems involved with biazeotropy is plotting different types of diagrams containing biazeotropic constituents by mathematical simulation. Wilson equation with assumption of ideal behavior of vapor phase far from critical conditions is used. Previously we have evaluated Wilson equation parameters according to experimental data (also combined with some model consideration).

2. Results and discussions

2.1. Modeling of vapor-liquid equilibrium in the system benzene-perfluorobenzene-methyl ethyl ketone at atmosphere pressure

The complex research of three component systems with two ternary azeotropes are the object of the study in the Department of the Chemistry and Technology of Basic Organic Synthesis of Lomonosov Moscow State University of Fine Chemical Technologies during last decade. Recently, the six new systems had been found [1-

4]. Five of them contain biazeotropic constituent benzene-perfluorobenzene and as a third component – methyl propionate, tert-amyl alcohol, ethanol, n-propanol, isobutyl alcohol; the system diethyl amine-chloroform-methanol includes monoazeotropic constituents. Now the urgent problem is the extending the number of biazeotropic mixtures containing real substances. Analysis of temperature dependence of vapor pressure and properties of binary azeotropes in the system benzene-perfluorobenzene-methyl ethyl ketone formed by components with very close boiling temperature allow to suppose existence of two ternary azeotropes at atmosphere pressure [5]. We carried out a mathematical simulation of vapor-liquid equilibrium of binary constituents in the system benzene-perfluorobenzene-methyl ethyl ketone at specified pressure. Experimental data [6, 7] were chosen to estimate Wilson equation parameters in binary constituents benzene-perfluorobenzene, benzene-methyl ethyl ketone correspondingly. Due to the lack of experimental information on the system methyl ethyl ketone-perfluorobenzene the data calculated by Aspen Plus [8] had been used. It was established that the system is homogenous and binary constituent B-PFB is biazeotropic (includes positive and negative azeotropes) but other two systems MEK-B, MEK-PFB are monoazeotropic and contain positive or negative azeotropes accordingly. As a result of computing experiment of VLE (evaluated about 100 points) in the system benzene-perfluorobenzene-methyl ethyl ketone the existence of two ternary azeotropes: saddle azeotrope and azeotrope with maximum boiling temperature was determined. The residue curve map is presented in Figure 1.

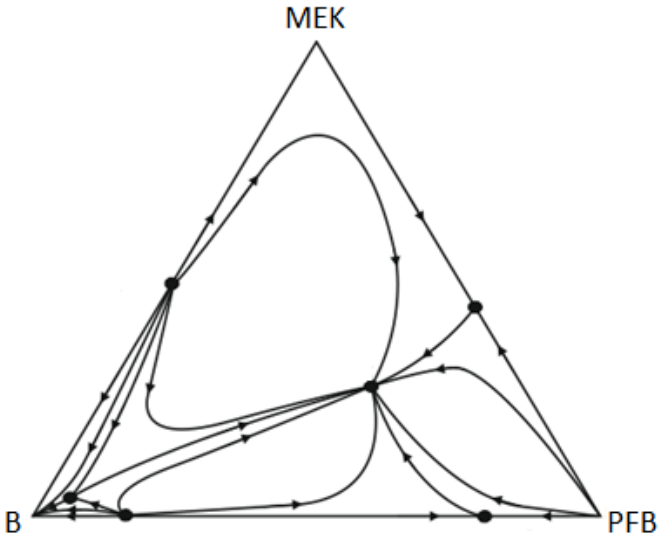

Figure 1: Residue curve map in the system B-PFB-MEK at 760 mm Hg

According to classification of different types of biazeotropic ternary systems [9] we determined class, type, subtype of VLE diagram structure: 3.[2.1.1].2-20a.

2.2. Revelation of biazeotropy in the system methyl ethyl ketone-perfluorobenzene
By modeling of vapor-liquid equilibrium at atmosphere pressure in the system MEK-PFB we plotted curves K_{MEK}, $K_{PFB}=f(x_{MEK})$, where K-coefficient distribution of component between vapor and liquid. We detected a minimum on the diagram of the dependence of distribution coefficient of methyl ethyl ketone on concentration (Figure 2).

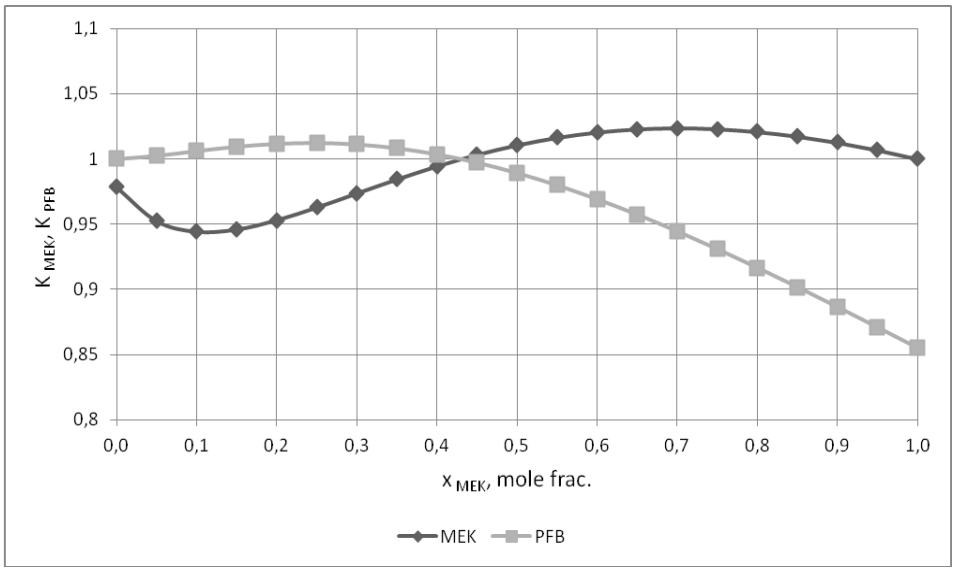

Figure 2: Diagrams K_{MEK}, K_{PFB} = f (x_{MEK}) in the system MEK-PFB at 760 mm Hg

The appearance of second (positive) azeotrope at low pressure is predicted theoretically by consideration of regularities of biazeotropic mixture behavior with the change of external conditions [10]. The range 50-760 mm Hg is chosen for the study of VLE diagram evolution. As a result the existence of biazeotropy is revealed and properties of positive and negative azeotropes are identified. It is shown that positive azeotrope is impoverishing and negative azeotrope is enriching by methyl ethyl ketone with increasing of pressure. Such result is in agreeing with Vrevskii second rule and confirmed by the ratio of vaporization heat of components (Figure 3).

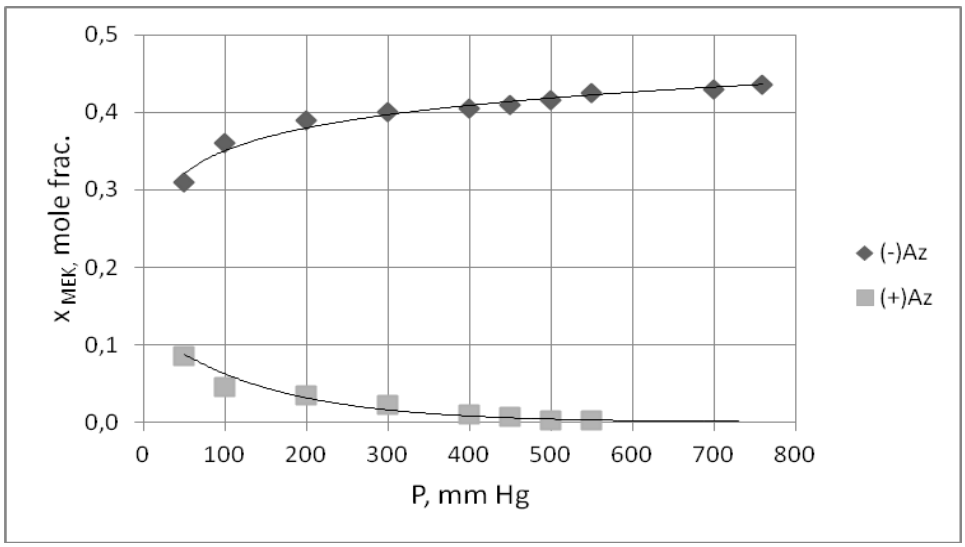

Figure 3: Dependence of positive and negative azeotrope compositions on the pressure in the system MEK-PFB

2.3. Modeling of vapor-liquid equilibrium in the system benzene-perfluorobenzene-methyl ethyl ketone at 500 mm Hg

Calculation of vapor-liquid equilibrium (200 points) is carried out at 500 mm Hg for the analysis of residue curve map evolution in the system B-PFB-MEK. It was found that system B-PFB-MEK has two ternary azeotropes: saddle point and node point

with maximum boiling temperature; binary constituent MEK-B is monoazeotropic, B-PFB, B-MEK are biazeotropic (Figure 4).

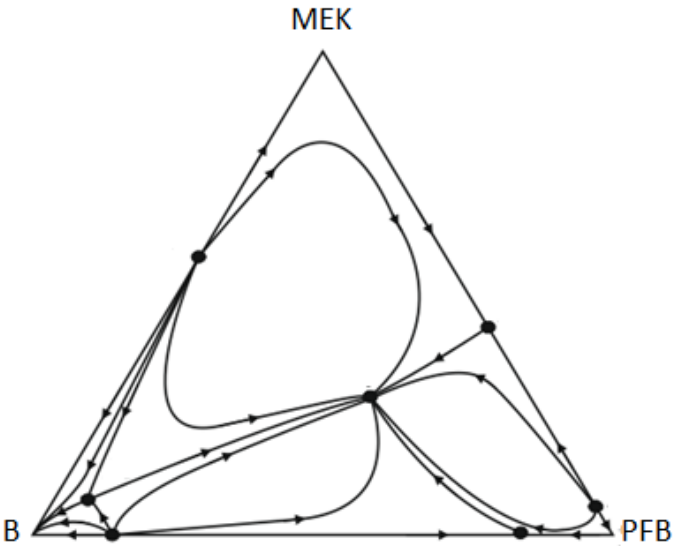

Figure 4: Residue curve map in the system B-PFB-MEK at 500 mm Hg

We determined class, type, subtype of VLE diagram structure: 3.[2.2.1].2-31a.The additional experimental study will be carried out (e.g. to specify the composition of ternary azeotropes) but the qualitative view of residue curve should be the same. The residue curve map in the system benzene-perfluorobenzene-methyl ethyl ketone with two ternary singular points is a new example of diagrams of biazeotropic ternary systems.

3. Conclusions

It is shown for the first time that the system methyl ethyl ketone-perfluorobenzene is biazeotropic at definite pressures. The class, type and subtype of residue curve map in the system benzene-perfluorobenzene-methyl ethyl ketone at different pressures were determined. The three-component system formed by one monoazeotropic, two biazeotropic constituents containing two ternary azeotropes was discovered. The results of our study could be useful for the development of the theory of the systems with complex interaction in solution.

Acknowledgements

Work was carried out under the financial support and according to the state task of the Russian Ministry of Education and Science # 10.99.2014/K.

References

1. T.M. Kushner, G.B. Malykh, Benzene-Perfluorobenzene-Alcohol Systems with Two Ternary Azeotropes at Different Pressures // Russ. J. Phys. Chem. A. 2003. T. 77, № 11. P. 1876-1881.
2. Alla K. Frolkova, Tatiana V. Chelyuskina, The simulation of vapor liquid equilibrium in ternary systems with two ternary azeotropes // Distillation and Absorption 2010, 12-15 September 2010. Eindhoven. The Netherlands. Proceedings. P. 349-352.
3. T.V. Chelyuskina, A.K. Frolkova, The evolution of ternary biazeotropy in three component systems // XVIII International Conference on Chemical Thermodynamics in Russia. Samara. Russia. 3-7 October, 2011. Abstracts. V. 1. P. 60-61.

4. O.O. Usoltseva, Yu.A. Pisarenko, T.V. Chelyuskina, Investigation of ternary azeotropes evolution with change of pressure in biazeotropic three component mixtures // XII International Scientific Conference High-Tech in Chemical Engineering-2008. Volgograd. Russia. 2008. Abstracts. P. 51.
5. T.V. Chelyuskina, The theoretical foundations of rectification separation of biazeotropic mixtures. D. Sc. Thesis. Moscow: MITHT. 2011.
6. I.V. Kogan, A.G. Morachevskii, Liquid-vapor equilibrium in the system hexafluorobenzene-benzene (formation of two azeotropes) // J. Appl. Chem. USSR. 1972, V. 45, P. 1888-1890.
7. L.A.J. Verhoeye, S.A. Qazi, The vapor-liquid equilibrium of the system methyl-ethyl ketone+benzene+water // Ind. Chim. Belge., 1971, V. 36, P. 109.
8. Aspen Plus, Aspen Technology, Inc. 2012.
9. L.A. Serafimov, T.V. Chelyuskina, Principles of Classifying Diagrams for Different Types of Biazeotropic Ternary Mixtures // Russ. J. Phys. Chem. A, 2011, Vol. 85, No. 5, P. 767-776.
10. T.V. Chelyuskina, A. Perenlei, The research of vapor liquid equilibrium at different pressures and revelation of biazeotropy in the system methyl ethyl ketone-perfluorobenzene // XIX International Conference on Chemical Thermodynamics in Russia. Moscow, 24-28 June, 2013. Abstracts. P. 217.

Process Development for Dewatering a Highly Non-Ideal Mixture using Commercial Simulation Software

Volker Butz, Gordana Hofmann-Jovic, Michael Strack

Infraserv GmbH & Co. Knapsack KG, 50354 Hürth, Germany

Experiences and challenges on the way from the first idea to the final design of an extractive distillation process

Introduction

In an existing plant several different purge streams mainly containing organic acids, water and hydrogen chloride are dewatered in order to recycle the valuable components and reduce feedstock cost. Currently the water is removed by a cost intensive chemical reaction. Thus, a proper alternative for water removal has to be found to improve process economics.

This presentation chronologically illustrates the challenges and the experiences faced within different steps of the entire process development including equipment design. Thereby the focus will be on the applicability of commercial simulation software and its limits within this project.

Within the scope of improving operation costs a customer conducted distillation experiments in laboratory scale in 2002. The idea was to dewater a recycle stream of organic acids in the presence of HCl by a simple thermal separation process. An increase of reflux and number of stages always led to the same results: The water enriched stream still consisted basically of an organic acid. An azeotropic behaviour of the ternary mixture (water, HCl and organic acid (OA)) was found which caused a non-acceptable loss of the recyclable fraction. Until 2003 alternative separation processes had been considered unsuccessfully mainly due to technical infeasibility.

In 2012 the process development department of the Infraserv Knapsack picked up the task.

Development and validation of a thermodynamic model

First the ternary mixture was modelled to predict possible separation sequences to overcome the distillation boundary. Considering the mixture containing water and HCl the NRTL electrolyte model was selected first to describe the non-ideal behavior of the liquid phase. This model needs to be combined with a model describing the

interaction to OA as the third component, where particularly the non-ideality of the vapor phase (dimerization of the organic acid vapor) has to be taken into account, what is mainly described by the Hayden-O'Connell equation of state. However, the simulation of the distillation process using the integration of these two models had shown a strong discrepancy to the real process data. This leads to the conclusion that this thermodynamic model for electrolytes turned out to be insufficient to simulate the distillation process of such ternary mixtures. Furthermore, it was noted, that the combination of electrolyte models with other equilibrium models led to difficulties in terms of convergence behavior when using it for complex distillation processes.

Due to this problem a new thermodynamic model was set up with focus on replacing the electrolyte part of the NRTL model. While the NRTL-HOC model is suitable to describe the binary mixture of water and OA the binary mixture of HCl and OA had to be considered ideal due to a lack of data. However the parameters of the binary interactions between water and HCl had to be fitted. The NRTL-model with the fitted parameters turned out to be suitable to describe the vapor-liquid-equilibrium of water and HCl from pure water to about 12,5 mol% HCl as illustrated in Fig. 1.

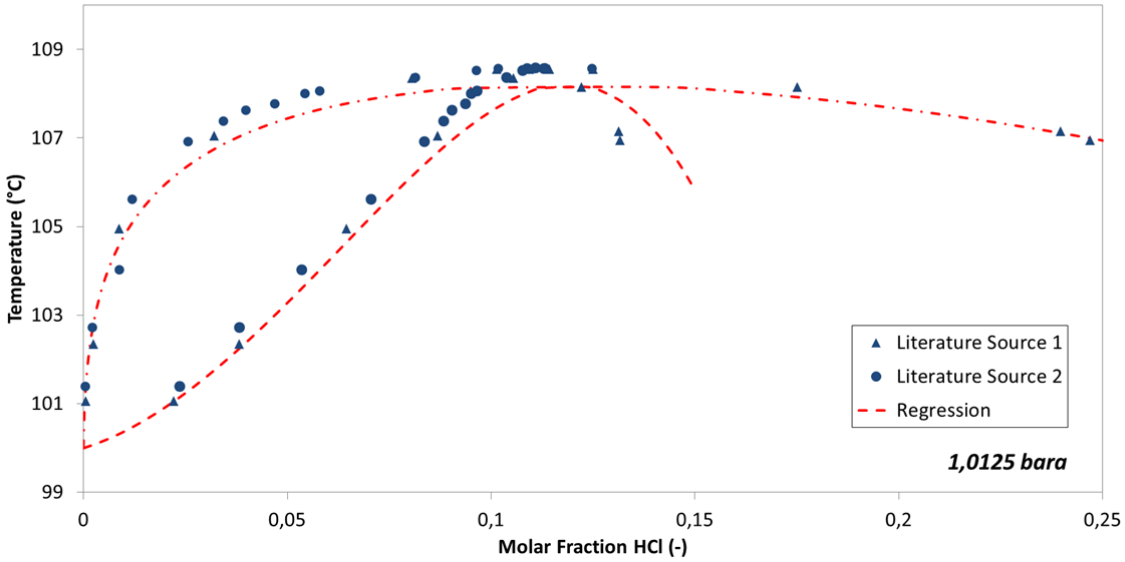

Fig.1: Phase equilibrium diagram of water/HCl (regression with NRTL-HOC)

This range of validity of this model completely covers the possible range of operation of our real process. The applicability of this model also leads to the much better convergence behavior. Being aware of the range of validity the developed

thermodynamic model of the mixture water/HCl/OA predicts a ternary diagram with four distillation regions and leads to the presumption of an azeotrope saddle as shown in Fig. 2.

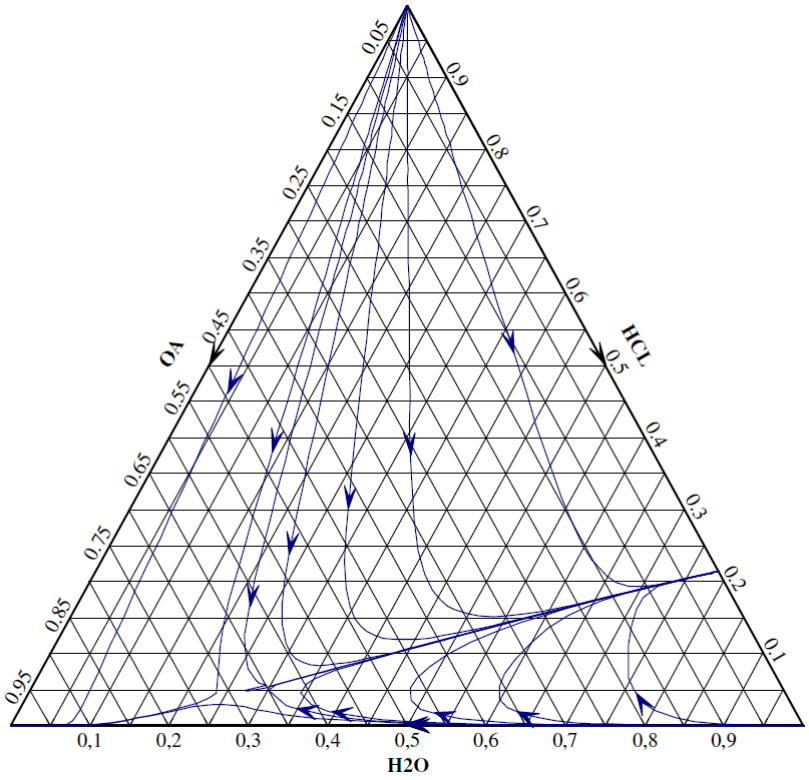

Fig. 2: Residue curves of the ternary mixture H_2O/HCl/OA

New thermodynamic model leads to new process design

Although just binary interaction parameters of the mixtures water/OA and water/HCl had been used whereas the set of parameters of the second binary mixture was just valid in a close range concerning HCl, the thermodynamic model was sufficiently accurate to simulate the distillation experiment of 2002.

Thus the model was used to predict possible separation sequences to overcome the distillation boundary.

Simulation studies of promising separation sequences led to an extractive distillation process evaluated by a first costs estimation.

The new approach: Extractive distillation with suitable entrainer

Initially a substance was identified as a suitable entrainer (E) which was already present in the original process, where it was actually separated from the OA. Therefore there was no need to integrate a new column to purify the entrainer as long as the additional amount needed for the extractive distillation could be handled by the existing column. For this purpose, the existing thermodynamic model for the ternary mixture had to be extended to a model for the quaternary mixture, where the interaction of E to the other components had to be considered as well. However, while the vapor-liquid equilibrium of E and OA was well known, data of the vapor-liquid equilibrium of water and E were inconsistent and no data were available for E and HCl. For the interaction water/E, additional measurements were conducted in summer 2013 and new parameters for NRTL-HOC were generated.

An overview of all interactions to be considered in the model for this quaternary system is illustrated in Fig. 3:

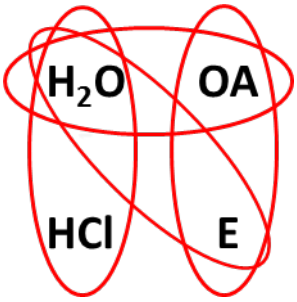

Fig. 3: Pairs of binary interactions considered in the final thermodynamic model

Afterwards the measured data of the vapor-liquid-equilibrium of the quaternary mixture were compared to the simulation based on that modified thermodynamic model. In general the relative deviation of the concentration in the vapor phase (simulation data referred to measurement) was less than 20% with regards to the components water and OA as illustrated in Fig. 4. At lower concentrations the deviation increased independently from any component. This was partly due to the increasing inaccuracy of the measurements, whereas the deviations of the HCl concentration were most likely due to missing binary interaction parameters.

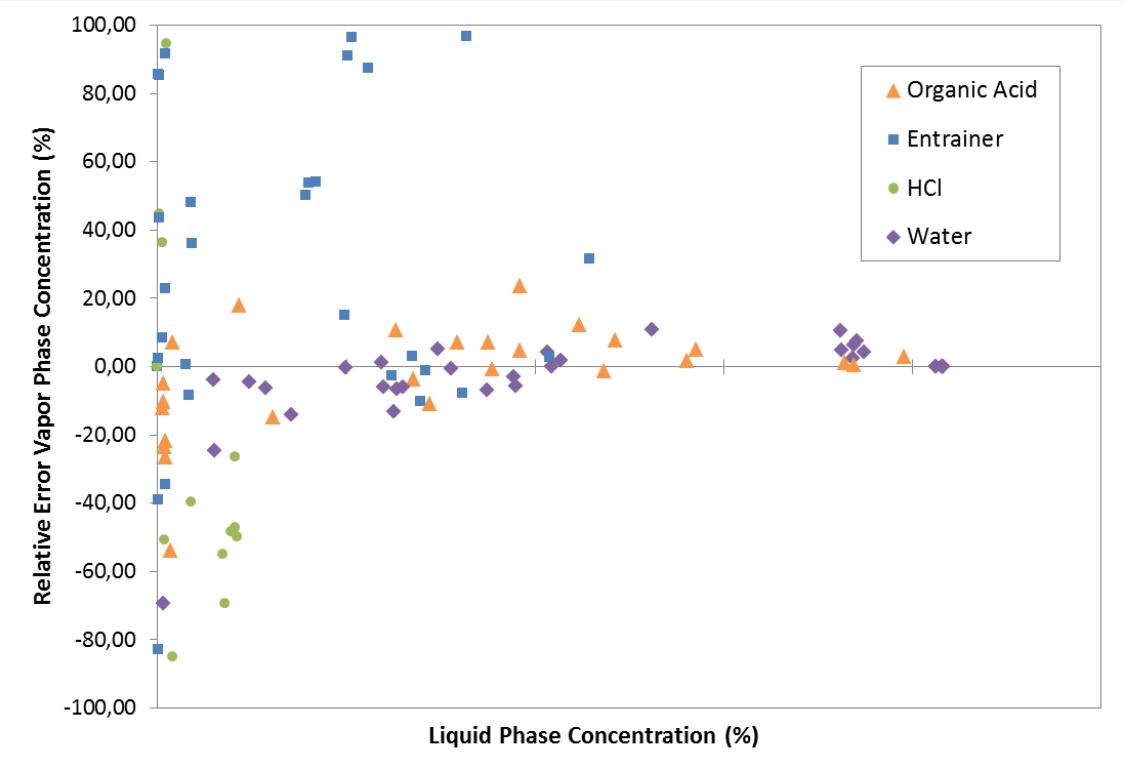

Fig. 4: Deviation of the vapor phase concentration (simulation compared to measurements)

Nevertheless the simulation with the thermodynamic model for the quaternary mixture fitted on the available data indicated the technical feasibility of the extractive distillation and was sufficiently accurate for developing a final process design.

Optimization and cost estimation

With regard to technical feasibility, several options for process operation mode for this extractive distillation can be considered. Hence, the next challenge is the appropriate selection of one process mode and to find out the optimal design parameters with regard to economic benefit.

Hence, first cost estimations of most promising process alternatives including an optimization of the costs were conducted. Both operating cost (utilities, raw material and disposal costs) and investment cost were taken into account. The cost function was minimized. The solver for optimization was part of the simulation tool, where up to 14 degrees of freedom for each process alternative were considered (number of stages, reflux ratio, pressure, amount of entrainer, etc.).

The cost estimation at the end of 2012 led to an economically attractive process design with a payout time of about 3 years.

Conclusions

Although the development of a thermodynamic model of ternary and quaternary mixtures, which matches with the real process behaviour, causes plenty of effort and expenses, it is still the effort worth since new process alternatives can be derived, which cause significant improvement in terms of economic benefit particularly concerning operation costs.

This has been shown for the case, where purge streams containing water, HCl and OA had to be dewatered for recycling. Distillation experiments in 2002 had shown that this goal cannot be achieved by simple distillation processes. For deriving new ideas for process design the development of a thermodynamic model describing the ternary mixture was required, which could match with those experiments of 2002 and current measured data. For better handling in terms of convergence behaviour in simulation for complex distillation processes, the NRTL-HOC model was used for all interaction effects. Despite the simplification of thermodynamic model the accuracy proved by vapor-liquid-equilibrium measurements of the multicomponent mixture is appropriate to identify a technical feasible process for dewatering the organic acid resulting in an extractive distillation, since its validity covered the operation range of the real process.

After the decision for an extractive distillation process, an appropriate entrainer was selected and the model was extended to quaternary mixtures.

Afterwards the optimizer of the simulation software is used to find the most cost-efficient process design which is currently the basis of further engineering. The final process design led to the conclusion, that a payout time of about 3 years could be realized.

As for the current work more detailed cost estimation is considered taking the inaccuracy of the simulated vapor-liquid-equilibrium into account. The optimization for the cost-optimal design of the most promising process alternative was done again at the end of 2013. The design was slightly different but the estimated payout time was about the same as estimated before.

Currently the engineering is in progress to estimate the costs by ± 30% accuracy.

Modelling and experimental study of CO_2 capture by aqueous monoethanolamine

M. Yazgi, N. Hüser, E.Y. Kenig
Chair of Fluid Process Engineering, University of Paderborn, Germany

Abstract
For the adequate description of absorption processes, traditional stage models are commonly used, either the equilibrium-based or the rate-based ones. An alternative modelling approach is based on hydrodynamic analogies (HA) between real, complex process fluid dynamics and a combination of geometrically simpler flow patterns. Such a simplification has to be done in agreement with experimental observations of fluid flow in separation columns. Once the observed complex flow is represented by a simplified model flow, the partial differential equations governing momentum, energy and mass conservation are utilised to describe transport phenomena in an entire separation unit.
In this work, the HA approach was applied to study carbon dioxide (CO_2) absorption into aqueous monoethanolamine (MEA) solutions. For the model validation, the data from literature and our own experiments were used. The experiments were carried out in a newly built pilot plant in which axial gas-phase temperatures and CO_2 concentration profiles were determined. These results provided additional data for a successful model validation.

Keywords
CO_2 capture, hydrodynamic analogy, MEA, pilot plant, reactive absorption, structured packing

1. Introduction

Carbon dioxide (CO_2) is one of the major greenhouse gases responsible for global warming; therefore, significant effort is being put into the development of technologies for its capture from flue gas streams. In many cases, the removal of CO_2 from gas mixtures is realised by absorption into a liquid solvent. The separation is mostly performed in absorption columns filled with structured packings and operated counter-currently.

Modelling of gas-liquid separation processes usually requires knowledge on fluid dynamic and mass transfer parameters, such as effective interfacial area and mass transfer coefficients. Generally, these parameters cannot be determined without extensive experimental work. An alternative modelling approach for separation columns filled with structured packings is based on hydrodynamic analogies (HA) between real complex and simplified model flow (Shilkin and Kenig, 2005). This way leads to a significant reduction of required experimentally determined parameters. Above all, no mass transfer coefficients are needed. The HA approach has been validated for different distillation processes (Shilkin et al., 2006) as well as for a catalytic distillation process (Zhang, et al., 2013). Furthermore, this method has also been applied to a sulphur dioxide absorption system (Brinkmann et al., 2009) and to reactive stripping (Brinkmann et al., 2010).

The objective of this work is an extension of the HA approach to the description of CO_2 absorption by aqueous monoethanolamine (MEA) solution. The validation of the HA model is largely based on experiments of Notz (2009) and our own measurements. Notz (2009) carried out 47 experiments and measured liquid-phase concentration profiles. In our recently built pilot plant, we were able to determine gas-phase profiles and to use these data for a further model validation.

2. Modelling

The main features of the HA model applied in this work were suggested by Shilkin and Kenig (2005). The HA approach to the modelling of columns filled with structured packing is based on a physical model of the packing, in which the latter is represented as a bundle of parallel inclined channels. The specific characteristics of the physical model, e.g. channel diameter or the ratio wetted channel number / total channel number, are determined from the corrugation geometry and the effective interfacial area of the packing. The effective interfacial area is estimated with the correlation of Tsai et al. (2011). Using a combination of simplified flow patterns (e.g. films) in these channels, partial differential equations for conservation of momentum and mass can be applied to govern the transport phenomena in an entire separation unit. Depending on the operating conditions, the HA approach may require an additional parameter, namely the gas-phase turbulent viscosity. This parameter cannot be determined within the HA approach; it is evaluated with the aid of a computational fluid dynamics (CFD) based study of a representative packing element.

2.1 Mathematical model

The liquid flow is described by the system of Navier-Stokes equations in the film-flow approximation (Shilkin et al., 2006):

$$\frac{1}{r}\frac{\partial}{\partial r}\left(r\mu_{\mathrm{L}}\frac{\partial u_{\mathrm{L}}(r)}{\partial r}\right)-\frac{\partial P_{\mathrm{L}}}{\partial x}+\rho_L g\sin\alpha=0,\quad \frac{\partial P_{\mathrm{L}}}{\partial r}=0. \tag{1}$$

For the description of the gas phase, the Boussinesq approximation is adopted:

$$\frac{1}{r}\frac{\partial}{\partial r}\left(r\tilde{\mu}_G\frac{\partial u_{\mathrm{G}}(r)}{\partial r}\right)-\frac{\partial P_{\mathrm{G}}}{\partial x}+\rho_G g\sin\alpha=0,\quad \tilde{\mu}_G=\mu_{G,\mathrm{lam}}+\mu_{G,\mathrm{turb}},\quad \frac{\partial P_{\mathrm{G}}}{\partial r}=0. \tag{2}$$

At higher gas loads, intensive turbulence occurs in the gas phase. This effect is considered in the HA model by the gas-phase turbulent viscosity $\mu_{G,turb}$. Boundary conditions must be fulfilled at the solid surface (no-slip condition), channel symmetry axis (symmetry condition) and the gas-liquid interface (equal velocities and normal shear stresses). Eqs.(1)-(2) and the boundary conditions are supplemented by the following integral flow definitions:

$$q_{\mathrm{L}}=-2\pi\int_{R_{\mathrm{h}}-\delta}^{R_{\mathrm{h}}}u_{\mathrm{L}}(r)r dr,\qquad q_{\mathrm{G}}=2\pi\int_{0}^{R_{\mathrm{h}}-\delta}u_{\mathrm{G}}(r)r dr. \tag{3}$$

The solution yields velocity profiles in both phases *u(r)* together with the values of liquid film thickness *δ(x)* varying along the channel height. These data are used in the mass transfer description.

2.2 Mass transfer

Mass transfer in each phase in a mixture comprising *n* components is described by the following transport equations:

$$u(r)\frac{\partial C_i}{\partial x} = \frac{1}{r}\frac{\partial}{\partial r}\left(r\tilde{D}_i\frac{\partial C_i}{\partial r}\right) + R_i\left(\vec{C}\right),\ \tilde{D}_i = D_{i,\text{lam}} + D_{i,\text{turb}},\ D_{i,\text{turb}} = \frac{\mu_{\text{turb}}}{\rho \text{Sc}_{i,\text{turb}}}, i = 1\ldots n \qquad (4)$$

The system of governing equations together with the corresponding boundary conditions (including thermodynamic equilibrium and mass flux continuity at the phase interface) is solved numerically using the Tri-Diagonal Matrix Algorithm (Patankar, 1980) yielding concentration fields in both phases. This information is further used to obtain the average concentration profiles along the packing.

3. Pilot-plant experiments

The experiments were performed in a newly built multi-purpose absorption/desorption pilot plant. Experiments can be carried out in different operation modes, namely, absorption, desorption and closed loop. Furthermore, fluid dynamic studies can be performed. In order to enable these operation modes, the plant is made of two glass columns, one with an inner diameter of 0.1 m and another with 0.3 m. Both columns are about 5 m high and include a packed section of about 3 m. The thinner column is predominantly used for absorption; due to the small diameter and consequently high wall effects, this column is less suitable for fluid dynamic experiments. On the contrary, the larger column can be used both for desorption and for fluid dynamic studies. In closed loop mode, both columns are to be coupled. Axial temperature and concentration profiles are determined with the aid of specially developed sampling flanges placed along the packing height. A gas chromatograph is directly integrated with the plant to measure the gas-phase CO_2 concentrations online. In this study we performed experiments in absorption mode. A simplified flow sheet of the process is shown in Figure 1.

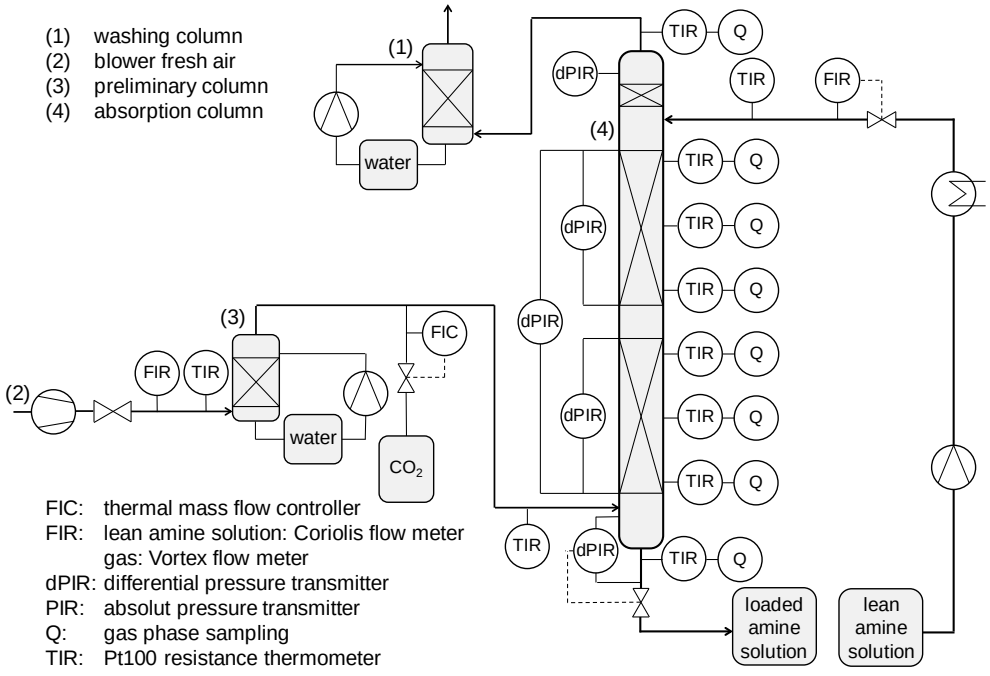

Figure 1: Simplified flow sheet of the absorption process.

Experiments were run as follows: In a small preliminary column fresh air was saturated with water. Before entering the absorption column, a CO_2-stream was injected into the air stream via a mass-flow controller. The CO_2-free air leaving the absorption column was directed to a washing column to prevent amine emissions to the environment. Lean amine solution from a tank was pumped to the top of the absorption column. Having passed the column, the loaded amine solution was collected in a second tank. As soon as a steady state was reached, the measurements of the gas-phase CO_2 concentrations started.

4. Experimental and simulation results

In this study, we carried out two experiments (A1, A2) keeping the liquid load constant at 17 m³/(m²h) (130 kg/h), with a MEA concentration of 14 wt%. The F-factor was close to 1.6 $Pa^{0.5}$, with initial CO_2 concentrations of 10.5 wt% for A1 and 6.8 wt% for A2. The column was packed with 2.84 m of Montz B1.250 structured packing. In Table 1, process conditions are summarised.

	Liquid phase		Gas phase				
	T_{in}, °C	T_{out}, °C	q_G, m^3/s	T_{in}, °C	T_{out}, °C	$y_{CO_2,in}$, mol/mol	$y_{CO_2,out}$, mol/mol
A1	21.5	36.1	0.0119	22.6	23.2	0.070	0.026
A2	22.8	33.9	0.0117	22.8	23.5	0.045	0.012

Table 1: Detailed process conditions

Figure 2a shows the gas-phase CO_2 concentration profiles and Figure 2b the temperature profiles along the column height. As described above, both experiments were carried out at the same conditions except the initial CO_2-concentration.

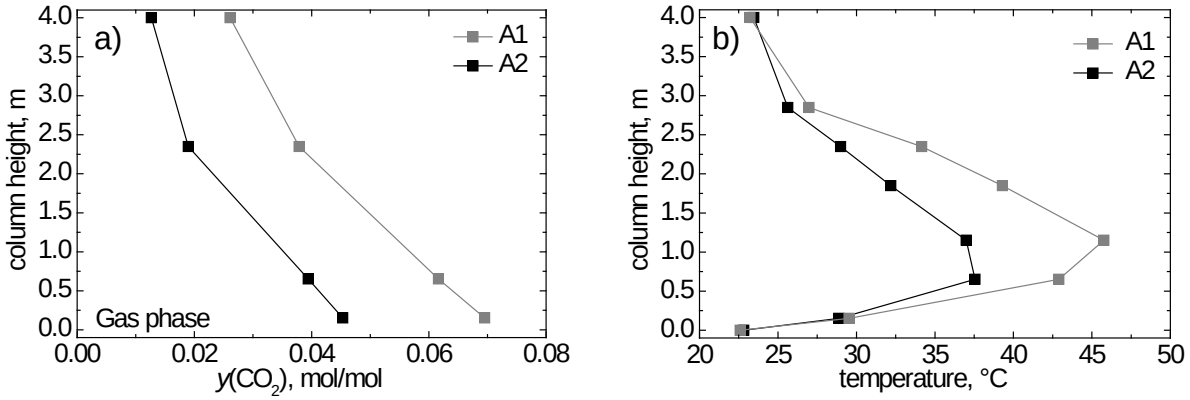

Figure 2: Measured CO_2 concentration profiles (a); temperature profiles (b).

The similar trend of the CO_2 concentration profiles in Figure 2a indicates that approximately the same amount of CO_2 is absorbed in both experiments. Taking into account that the MEA concentration and mass flow rate were the same, we can conclude that the plant worked reasonably well. As can be seen in Figure 2b, a temperature bulge is located near the bottom of the column for experiment A2 (relatively low CO_2-concentration) and somewhat higher for experiment A1 (higher CO_2-concentration). Such a behaviour was reported by Kvamsdal and Rochelle (2008), which gives an additional proof that the measured values can be used for the model testing.

The validation of the model is largely based on the results of comprehensive experiments of Notz (2009) extended by our own data. Notz (2009) performed measurements in a pilot plant with an inner diameter of 0.125 m filled with 4.2 m height Mellapak 250.Y. Concentration profiles were measured for the liquid phase only. For all 47 experiments, the liquid-phase simulations were compared with the measured data from Notz (2009), and the resulting parity plot is shown in Figure 3a. Except few values exceeding the 10% limit, a good agreement between the simulated and experimental data can be observed. The general tendency is that, at lower liquid loads, the deviation between simulated and experimental data becomes higher. This can be attributed to the insufficient accuracy of the effective interfacial area calculated using the correlation of Tsai et al. (2011). This correlation does not match their own experimental values well for structured packings with a specific surface area of 250 m^2/m^3 and at low liquid loads (<10 $m^3/(m^2h)$).

The simulated gas-phase CO_2 concentration profiles together with our own experimental values are shown in Figure 3b. The correlation of Tsai et al. (2011), which is based on experiments in a column with an inner diameter of 0.427 m, yields the value $a_{eff,Tsai}/a_p$=0.835. However, the experimental data used for the model validation are obtained in experiments with smaller column diameters (0.125 m resp. 0.1 m). In such columns, wall effects may significantly affect the effective interfacial area. We increased a_{eff}/a_p to 1 and obtained a better agreement between experimental and simulated data (cf. Figure 3b)

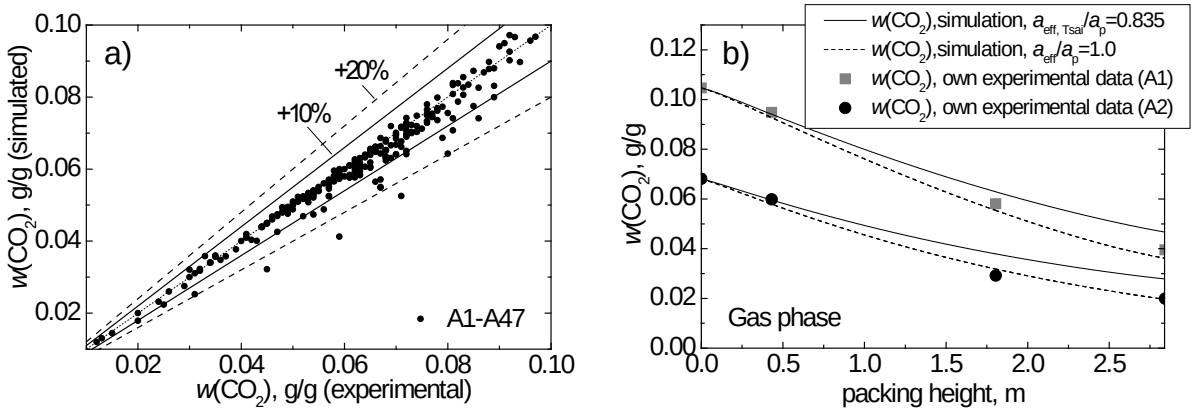

Figure 3: Parity plot of simulated liquid phase concentrations (HA) and literature data from Notz (2009) (a); simulated (HA) and measured gas phase concentration profiles, starting from the column bottom (b).

5. Conclusions

In this work, the HA approach was extended to describe the absorption of CO_2 into aqueous MEA solutions and validated against experimental data from literature (Notz 2009). In addition, we carried out experiments in a newly built pilot plant. These experiments showed reasonable results and could be used for the further model validation.

The simulated and measured CO_2-concentrations showed good agreement. This successful validation of the HA approach proves that the HA model, as an alternative modelling approach, is capable of properly describing CO_2 absorption systems.

Acknowledgements

The financial support of the European Commission in the context of the 7th Framework Programme of the European Union (Project CAPSOL, FP7-ENERGY-2011-282789) is greatly acknowledged.

Notation

a_{eff}	packing effective specific area, $m^2\ m^{-3}$
a_p	packing surface area, $m^2\ m^{-3}$
C	molar concentration of a component, mol m^{-3}
D	diffusivity, $m^2\ s^{-1}$
d_h	channel hydraulic diameter, m
g	gravity, $m\ s^{-2}$
P	pressure, Pa
q	volumetric flow rate, m^3 s
R_h	channel hydraulic radius, m
r	radial coordinate, m
Sc	Schmidt number
T	temperature, °C
u	local velocity, $m\ s^{-1}$
w	mass fraction, -
x	axial coordinate, m
y	mole fraction in the gas/vapour phase, -
z	length of an undisturbed fluid flow, m

Greek letters

α	gravity flow angle
δ	film thickness, m
μ	dynamic viscosity, Pa s
ρ	density, $kg\ m^{-3}$

Subscripts

G	gas phase
i	component i
L	liquid phase
lam	laminar
turb	turbulent

References

1. U. Brinkmann, E.Y. Kenig, R. Thiele and M. Haas, *Chem. Eng. Trans.* 18 (2009) 195-200.
2. U. Brinkmann, T.J. Schildhauer, E.Y. Kenig, *Chem. Eng. Sci.* 65 (2010) 298-303.
3. K. Gersten, H. Herwig H, *Strömungsmechanik. Grundlagen und Fortschritte der Ingineurwissenschaften*, Vieweg Verlag, 1992, Wiesbaden, Germany.
4. H.M. Kvamsdal, G.T. Rochelle Ind. Eng. Chem. Res. 47 (2008) 867-875.
5. R.J. Notz, *CO2-Abtrennung aus Kraftwerksabgasen mittels Reaktivabsorption*, Ph.D. Thesis, 2009, Logos Verlag Berlin, Germany.
6. S.V. Patankar, *Numerical Heat Transfer and Fluid Flow*, Hemisphere Publ. Corp., 1980, McGraw-Hill, New-York.
7. A. Shilkin, E.Y. Kenig, *Chem. Eng. J.* 110 (2005) 87-100.
8. A. Shilkin, E.Y. Kenig, Ž. Olujić, *AIChE Journal* 52 (2006) 3055-3066.
9. H. Zhang, X. Li, X. Gao, H. Li, *Chem. Eng. Sci.* 101 (2013) 699-711.

Simulation Study of the Ultra-Low Sulfur Diesel Production using Reactive Distillation with Supercritical CO_2

J. Carlos Cárdenas-Guerra, Fabricio Omar Barroso-Muñoz, Salvador Hernández
Departamento de Ingeniería Química, Universidad de Guanajuato, Noria Alta s/n, Guanajuato, México, 36050, Email: carlogs@yahoo.com

Abstract
The presence of supercritical CO_2 is studied in a reactive distillation process for ultra-low sulfur diesel production. Four reactive distillation columns involving kinetically controlled reactions are analyzed. Two of them use conventional operating conditions without supercritical CO_2 and the last two case studies include CO_2 at high pressure. For that reason, the influence of two parameters such as operating pressure and reflux ratio are evaluated and the results of the rigorous simulations are presented. It has been found that with the appropriate selection of operating pressure, a considerable reduction of utility consumption can be secured beside a possible abatement in capital investment. Also, the introduction of the additional supercritical phase can be beneficial in the operation of a reaction-separation sequence for ultra-low sulfur diesel production, i.e., the case studies using supercritical CO_2 as heat carrier reduce the energy consumption (efficient separation) and enhanced reaction rates. The amount CO_2 in the feed plays a crucial role in the conversion of dibenzothiophene.

Keywords
Reactive distillation, supercritical CO_2, operating pressure, reflux ratio

1. Introduction

In recent years, an increasing number of researchers have begun to study reaction chemistry with supercritical fluids (SCFs). The application of SCFs, in particular carbon dioxide (CO_2), as an environmentally more acceptable replacements for conventional solvents, is proving to be potentially attractive for one of the most widely used processes in the fine chemical industry, hydrogenation. Recently, it was shown that the hydrogenation reactions can also be tackled using supercritical CO_2 ($scCO_2$). Adam[1] commented that hydrogenation is one of the CO_2-based syntheses that do not need additives; in fact the partial pressure of hydrogen (H_2) is low comparable to the partial pressure of $scCO_2$. Under these circumstances, H_2 is completely miscible with the $scCO_2$ making this route attractive. Hitzler and Poliakoff[2] have pointed out that hydrogenation with CO_2 will become more important in the future as the chemical industry turns into biological molecules from plant materials, rather than oil, to generate organic products. To produce chemicals such as plastics from biofeedstocks, the amount of oxygen must be first reduced by adding H_2. Hydrogenation under supercritical fluid conditions has several advantages, e.g., the reactions can be carried out with very high space time yields, the fluid has good thermal properties and, on a small scale at least, the fluid provides a much greater degree of control than is usually possible in non-supercritical hydrogenation, the reaction is not limited by mass transfer effects and simultaneous separation and reaction may be accomplished.

Therefore, the fundamental ideas for reactions with supercritical solvents can be used to exploit new developments in reactive separations technology. For that reason, reactive distillation is one of the better known examples of integrating reaction and separation and has specifically been applied to hydrogenation reactions to eliminate sulfur (S) from gasoline and diesel at high pressure in the oil industry. Several key factors ensure the successful application of this technology in terms of lower operating and capital costs. Specifically, the reaction-separation process should improve the conversion and selectivity of the reaction by removing products from the reactive zone and circumvent/overcome distillation boundaries, such as azeotropes[3]. Also, for the same degree of conversion the amount of catalyst is reduced. Reactive distillation provides a built-in safety feature for exothermic reactions because the heat of reaction can be used for separation and reduces the reboiler duty. Some reactive systems, e.g., hydrogenation, could be carried at lower pressure than in the conventional reactor and hence it provides an added safety feature.

In this work, the presence of $scCO_2$ is studied in a reactive distillation process for ultra-low sulfur diesel (ULSD) production. Basically, we propose four reactive distillation columns (RDC´s): two of them use conventional operating conditions without $scCO_2$ and the last two case studies include CO_2 at high pressure. Furthermore, we study the influence of the operating conditions and parameter sensibility over the main variables to control, i.e., the organo-sulfur compound conversion.

2. Results and discussion

The conceptual design of the reactive distillation process was performed using the computation of reactive and non-reactive residue curve maps and stage-to-stage methods for reactive distillation column design[4]. The visualization of the reactive residue curves is posed in terms of *elements*. All case studies consisted of 14 stages with two reactive zones and three non-reactive zones (Figure 1). In a process simulator such as ASPEN PLUS, it is possible to generate the previously superstructures using an equilibrium stage model and considering homogeneous liquid chemical reactions. Table 1 shows the design specifications of the case studies used for the simulations. The nonidealities of the vapor and liquid phases are calculated through the Peng-Robinson equation of state[5] with the appropriate binary interaction parameters.

We consider the hydrocarbon (HC) feed as a paraffinic mixture containing *n*-undecane (*n*-$C_{11}H_{24}$), *n*-dodecane (*n*-$C_{12}H_{26}$), *n*-tridecane (*n*-$C_{13}H_{28}$), *n*-tetradecane (*n*-$C_{14}H_{30}$) and *n*-hexadecane (*n*-$C_{16}H_{34}$), and three organo-sulfur compounds: thiophene (Th), benzothiophene (BT) and dibenzothiophene (DBT). Therefore, as first simulation case, HC feed has the following composition (mole fraction): z_{Th}=0.0087, z_{BT}=0.0087, z_{DBT}=0.1, $z_{n\text{-}C11H24}$=0.4966, $z_{n\text{-}C12H26}$=0.3166, $z_{n\text{-}C13H28}$=0.0087, $z_{n\text{-}C14H30}$=0.0016, $z_{n\text{-}C16H32}$=0.0590. It should be noted that the HC feed composition is chosen to consider a “sulfured” diesel with 500 ppm of S content. Target conversion of 99.90% for the DBT and complete elimination of Th and BT were assumed. Only the hydrogenolysis reaction pathway and their respective reaction rate expressions, reaction rate coefficients and adsorption equilibrium constants of Th, BT and DBT reported by Van Parijs and Froment[6], Van Parijs et al.[7] and Froment et al.[8] were employed.

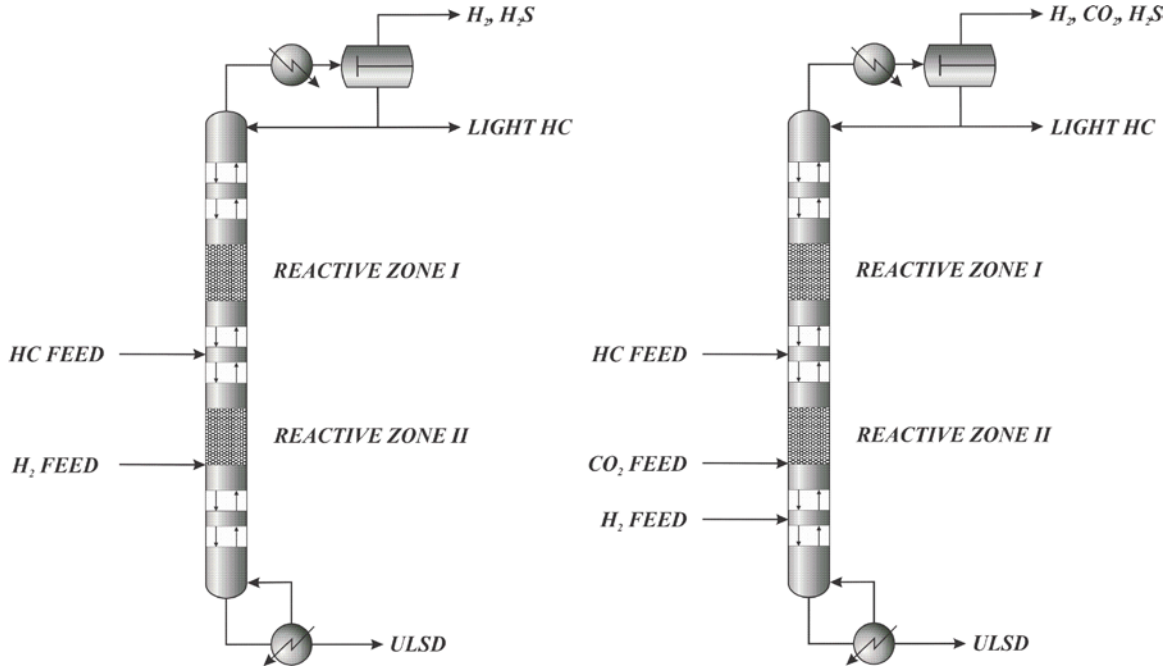

Figure 1: Reactive distillation columns for ULSD

For this purpose, the influence of two parameters such as operating pressure (P) and reflux ratio (RR) were analyzed. These inputs (manipulated variables) were selected since they are key parameters to operate the process, while the conversion of DBT is shown to be the output variable (measured quantity).

Table 1: Design specification of the reactive distillation columns

Design and operation parameters	Case studies			
	RDC I	RDC II	RDC III	RDC IV
HC feed flowrate (kmol/h)	100	100	100	100
CO_2 feed flowrate (kmol/h)	-----	-----	10	30
H_2 feed flowrate (kmol/h)	300	300	300	300
HC feed stage	9	9	9	9
CO_2 feed stage	-----	-----	12	12
H_2 feed stage	12	13	13	13
Operating pressure (atm)	30	30	30	30
Reflux ratio	0.5	0.5	0.5	0.5
Holdup (kg of catalyst)	10000	10000	10000	10000

2.1 Influence of operating pressure

Here, to refine high values of the P, the simulation was reinitialized at each step with current solution as initial estimates, and then the step size was reduced by half until the step size was small enough and until divergence occurred (meaning that small changes in the P can lead to abrupt phase changes), i.e., convergence problems were found when the CO_2 feed flowrate is increased. For this situation, only the decrement of this parameter was performed. Figure 2 illustrates the conversion of DBT with the variation of the P and it shows that with a P of 23 atm or greater, a complete elimination of DBT is achieved as occurs in the RDC I. Also, Figure 2 shows the influence of operating pressure for the RDC II and RDC III. For these case studies, it can be noted that the conversion of DBT falls considerably for the same

variation of the P at two different values from 25 and 27 atm, respectively. As a final point, the DBT conversion design target (99.90%) for the RDC IV is not achieved for P values lower than 30.3 atm. On the other hand, it can be observed in Figure 2 that the bifurcation diagram exhibited no evidence of multiplicity.

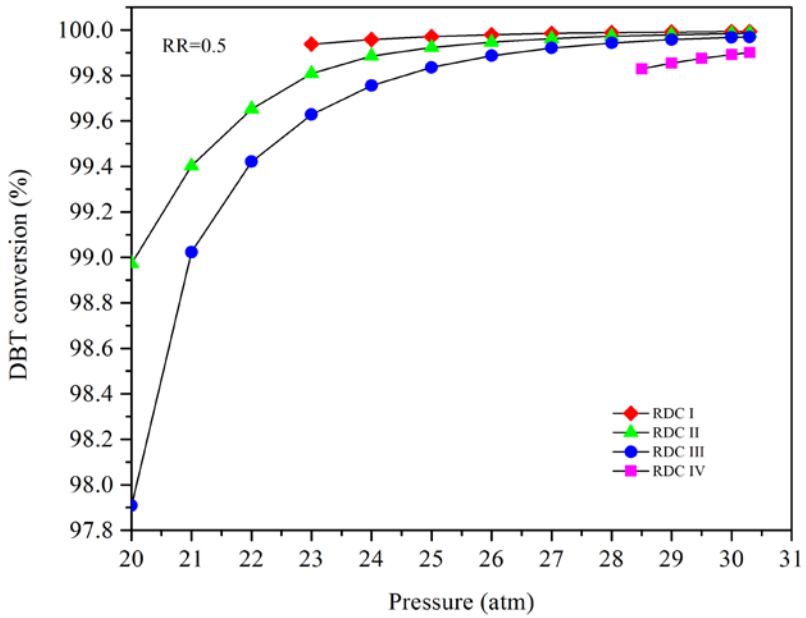

Figure 2: Bifurcation diagram for DBT conversion with the variation of P.

Besides the evidence that operating pressure increases the conversion of DBT, it is also clear that the amount of CO_2 in the reactive system is a limiting factor. According to the vapor-liquid equilibrium calculations, such an effect is a consequence of a monophase system in which CO_2 has already dissolved the organo-sulfur compounds, so that additional CO_2 just lowers the reactant concentration. In this sense, the application of a high CO_2 feed flowrate decreases the conversion of DBT, e.g., RDC IV. Table 2 summarizes the conversion of DBT and the heat duties for the condenser and reboiler.

Table 2: Simulation results of the reactive distillation columns

Design and operation parameters	Case studies			
	RDC I	RDC II	RDC III	RDC IV
DBT conversion (%)	99.99	99.98	99.96	99.89
Partial condenser heat duty (kW)	4630.64	4614.07	4270.38	3612.95
Reboiler heat duty (kW)	5662.14	5645.88	5355.27	5508.56

The relationship between operating pressure and the steady state performance of the RDC´s is depicted in Figure 3. In Figure 3(a), the impact of operating pressure on the system performance is illustrated. The heat duty of partial condenser increases monotonically with the increase of operating pressure, demonstrating that a relatively low operating pressure is beneficial in four RDC´s. However, an operating pressure too low retards reaction rates, reducing DBT conversion and reaction heat load. On the other side, an operating pressure too high accelerates reaction rates. In both circumstances, the appropriate selection of operating pressure could maximize reactant conversion and reaction heat load, reinforcing process intensification between the reaction operation and the separation operation involved.

In Figure 3(b), the heat duties of RDC II, RDC III and RDC IV reach their minimum values at the operating pressure of 23, 22 and 30.3 atm, respectively. Another set of recommended reboiler heat duty values are 20, 20 and 28.5 atm for the same case studies. Away from these values, they turn to increase monotonically in both directions, portraying a nonmonotonic relationship between operating pressure and steady state performance. RDC I shows an effect where the heat duty of reboiler decreases with the decrease of operating pressure, demonstrating that a relatively low operating pressure is favorable to process intensification in the hydrodesulfurization (HDS) reactive distillation column. A difference between RDC I and RDC II, on their thermal behavior, is the HC feed stage location.

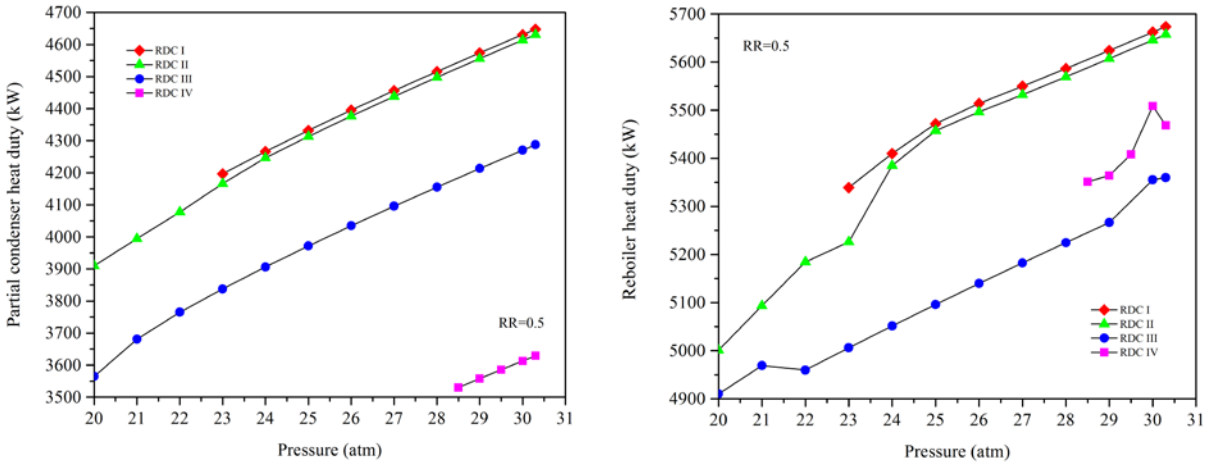

(a) (b)

Figure 3: Effect of operating pressure on the heat duty of partial condenser and reboiler in the reactive distillation columns

2.2 Influence of the reflux ratio

A steady state open loop nonlinear behavior of the RDC IV was determined by varying the reflux ratio in the domain 0.125<RR<1.15 (Figure 4).

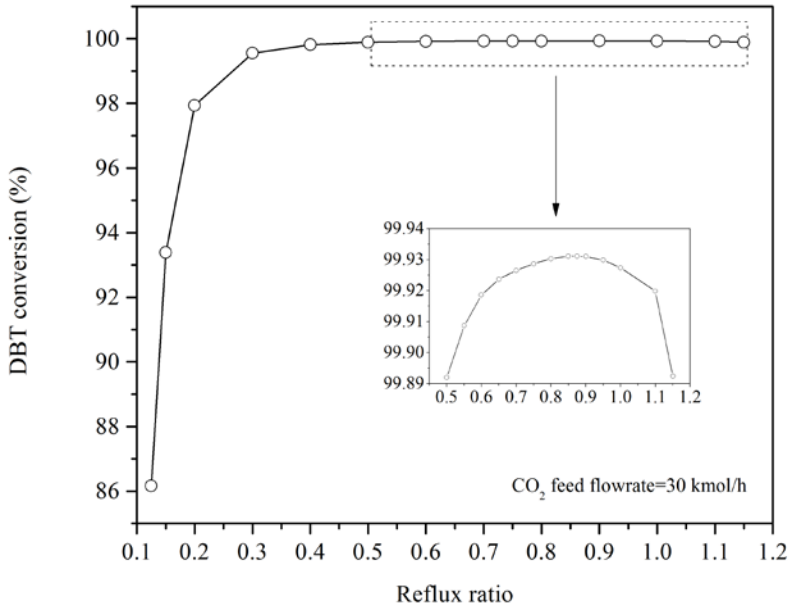

Figure 4: Bifurcation diagram for DBT conversion with the variation of RR.

In fact, it is found that there are two possible input solutions (RR values of 0.6 y 1.1) to get the same output design target (i.e., 99.90% conversion of DBT) at this reflux ratio range. Above the optimum reflux ratio, RR=0.875, the operating conditions are favorable for the HDS reactions (as indicated by the relatively high conversions). Below the optimum reflux ratio, the converse applies. Therefore, two regions can be defined as separation controlled (reflux ratios above the optimum) and reaction controlled (reflux ratios below the optimum), respectively. On the other hand, a complete elimination of DBT is achieved from a RR of 0.15 (see Figure 4); however, an excessive reflux leads to an increase of the "cold" energy required to condensate the stream returning to the column, especially when the highly volatile H_2, CO_2 and H_2S are present.

3. Conclusions

The results reveal that the steady state behavior is affected by varying pressure or reflux ratio. As discussed by Wang et al.[9], because the specific phenomena of reaction-separation involved can give a strong impact to process dynamics and controllability, it is quite likely that operating pressure may also present a nonmonotonic influence on process dynamics and controllability. More specifically, whereas the enhancement of operating pressure gives a favorable influence to process dynamics and controllability in the lower part of its feasible region, the reverse is true in the higher part of its feasible region. Confirming this unique behavior can certainly facilitate the simultaneous consideration of process design and operation with operating pressure as an effective decision variable at the early stage of process development. Unfortunately, RDC IV presents delicate control problems due to the existence of multiple solutions (input multiplicity); however, it may be possible to overcome these with appropriate control system design. As a result, it can be concluded that the liquid HDS reactions using supercritical CO_2 as a reaction medium or as reactive component have been highlighted as an industrially promising approach to "greener" processing.

References

1. D. Adam, *Nature*, 407 (2000), 938-940.
2. M.G. Hitzler and M. Poliakoff, *Chem. Commun.*, 17 (1997), 1667-1668.
3. P. Lutze and A. Górak, *Chem. Eng. Res. Des.*, 91 (2013), 1978-1997.
4. J. Carlos Cárdenas-Guerra, *Ph.D. Thesis*, Universidad Autónoma Metropolitana-Iztapalapa, (2012).
5. D.Y. Peng and D.B. Robinson, *Ind. Eng. Chem. Fundam.*, 15 (1976), 59-64.
6. I.A. Van Parijs and G.F. Froment, *Ind. Eng. Chem. Prod. Res. Dev.*, 25 (1986), 431-436.
7. I.A. Van Parijs, L.H. Hosten and G.F. Froment, *Ind. Eng. Chem. Prod. Res. Dev.*, 25 (1986), 437-443.
8. G.F. Froment, G.A. Depauw and V. Vanrysselberghe, *Ind. Eng. Chem. Res.*, 33 (1994), 2975-2988.
9. C. Wang et al., *Ind. Eng. Chem. Res.*, 51 (2012), 3692-3708.

Comprehensive program for the simulation of the centrifugal molecular distillation process for high-boiling-point petroleum fractions: Parametric sensitivity analysis of complex process

Laura Plazas Tovar1, Alessandra Winter2, Cesar Benedito Batistella1, Lilian Carmen Medina3, Rubens Maciel Filho1, Maria Regina Wolf Maciel1
[1]University of Campinas, Campinas, Brazil;
[2] CEPETRO – Centro de Estudos de Petróleo – UNICAMP, Campinas, Brazil;
[3] Petrobras SA, CENPES/PDEDS, PETROBRAS Research and Development Center, Rio de Janeiro, Brazil

Abstract
Theoretical and mathematical descriptions of the liquid–phase transfer processes in centrifugal molecular distillation are presented for a high–boiling–point petroleum fraction divided into twenty five (25) pseudo-components. The thin liquid film over conical evaporator surface is modeled by the mass, momentum, and energy balance equations. The theoretical analyses are based on modified Langmuir–Knudsen equation to describe the effective evaporation rate [1]. The simulations were carried out at the steady–state setting conditions, where the effects of the process variables such as the evaporator temperature, the feed flow rate, the rotor speed and the pressure system on distillation rates, liquid film surface temperature, effective evaporation rate and film liquid thickness were computed and discussed. The results showed that the inlet parameters influence significantly the output variables. It was shown that the temperature profiles change sharply through the layer next to the evaporator surface. Along the length of the conical evaporator (radius), the temperature profile inner the liquid film on evaporator surface reached asymptotic temperature behaviour as evaporator temperature increases. Therefore, the effective evaporation rate and consequently the distillate flow rate increase too.

Keywords
Molecular distillation, simulation, petroleum fractions

1. Introduction

The trend in information about Hi–Tech thermal processes, such as the molecular distillation (MD) process, for the gentle separation of thermally unstable mixtures and liquids with low vapour pressure and high molar mass, is very interesting, due to the significant potential in processing the materials and in obtaining products with many advantages. During the MD process, the distilled liquid flows over the heated evaporator surface along the characteristic distance (the radial length in centrifugal molecular distillation or the length along the cylinder in falling film molecular distillation processes). Therefore, the MD process must satisfy the following conditions: (i) the pressure system must be sufficiently low [2]; (ii) the mean free path (MFP) of molecules must be comparable to the size of the equipment (distillation gap) and, (iii) the condenser temperature must be lower than the evaporator temperature [1-5]. Consequently, the evaporated molecules can pass through the

unobstructed gap to the condenser surface at a reduced distillation temperature, and with a short residence time of the distilled liquid on the heated surface [6].

Moreover, for the performance of the MD process, one requires information about the thin liquid film with respect to the surface temperature profile (Ts), the velocity profile (υ_r) and the film thickness (δ), in order to determine the yield and purity of the distilled product as a function of inlet parameters such as the evaporator temperature (EVT), feed flow rate (Q), rotor speed (RS) and pressure of the system (Ps), as described by Sales-Cruz and Gani in 2006 [4]. Several studies have presented the modeling of the MD process. Most of the models developed were reported for binary mixtures, based on mass, momentum and energy balance equations as presented in Table 1.

Table 1: Summary of research developed on modeling of the MD process

System	Equation type	Equipment type	Reference
Heavy petroleum cuts	Energy and material balances	CMD[a], FFMD[b]	[2[a],3[b]]
Glycerol and caprylic esters in the form of caprylic mono-, di- and triglycerides	Energy and material balances	FFMD	[4]
DBP–DBS	Navier–Stokes equations, Langmuir–Knudsen equation	FFMD	[5-6]
Carotenoid from palm oil	Energy and material balances	CMD	[7]
EHP–EHS	Energy and material balances	FFMD	[8]
DBP	Boltzmann, Navier–Stokes and heat balance equations	FFMD	[9]
DBP–DBS	Energy and material balances	CMD, FFMD	[10]
DBP	Langmuir–Knudsen equation and Monte Carlo method	FFMD, CMD	[11]
Glycerol	Navier–Stokes equation	FFMD	[12]
DBP–EHP–EHS	Energy and material balances	CMD	[13]

FFMD: Falling film molecular distiller; CMD: Centrifugal molecular distiller; DBP–DBS: di–butyl–phthalate (DBP) – di–butyl–sebacate (DBS); EHP–EHS: di–(ethylhexyl)–phthalate (EHP) and di–(ethylhexyl)–sebacate (EHS)

The present work is based on a mathematical centrifugal molecular distillation model [1-3] that describes the process involving the heat and mass transfers in the evaporating liquid film over the evaporator surface of a high–boiling–point petroleum fractions (atmospheric distillation residue named as ATR–Z), obtained from a Brazilian crude oil. Tovar et al. (2012) published the physico-chemical characteristics [14].

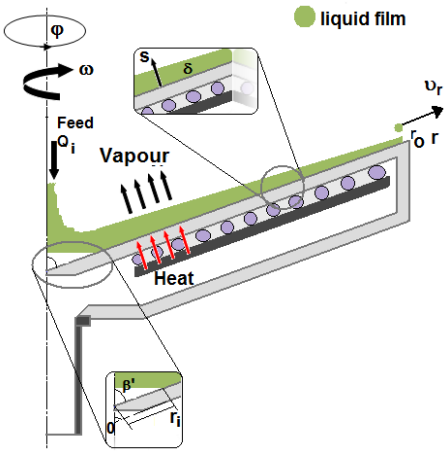

The effects of the operating conditions such as EVT, Q, RS and Ps, on the distillate mass flow rate (D), the effective evaporation rate (G_E), the film thickness (δ), and the surface temperature profiles (T_s) in the liquid film, were investigated and computed throughout the radial distance (RD). A model was defined to characterize the steady–state flow over the evaporator surface driven by the rotation of the conical surface in a centrifugal molecular distiller (Figure 1).

Figure 1: Sketch of the conical evaporator surface in the centrifugal molecular distiller.

A parametric sensitivity analysis of the output variables due to changes in the operating variables (EVT, Q, RS and Ps) was developed as shown in Table 2.The

study is expected to provide information on the choice of adequate operational conditions for an experimental work development.

Table 2: Parameters and percentage changes of inlet operating conditions

Parameter	Value
Distance from apex where liquid enters cone (r_i)	0.03095 m
Radial position where liquid leaves (r_o)	0.26620 m
Half angle of apex of cone radius (β')	70°
Distance between evaporator and condenser surfaces (L)	0.08 m
Number of intermolecular collisions before the vapour reaches the isotropic state (n')	5
Feed temperature (T_{feed})	393.15 K

Sensitivity	Variables			
	EVT (K)	Q (kg·h^{-1})	RS (rpm)	P_s (Pa)
-20%	338.52[†]	1.200	800	0.1040
-10%	380.84	1.350	900	0.1170
0%	**423.15**	**1.500**	**1000**	**0.1300**
+10%	465.47	1.650	1100	0.1430
+20%	507.78[‡]	1.800	1200	0.1560

2. Results and discussion

The effect of P_s was not very noticeable for any of the output variables studied. Nevertheless, from the simulated data it was found that the main operating characteristic was the P_s range from 0.01 to 0.13 Pa. Under these conditions, the volatility of the components increased, satisfying the principle of molecular distillation based on the MFP of the evaporating molecules, as discussed above.

2.1. Effect of EVT on output variables

Considering a reference value for EVT equal to 423.15 K, Figure 2a shows that if EVT increases, the value for T_s slightly decreases along the RD. Furthermore, the results showed that the inner radial thermal gradients of the thin liquid film produced a significant change in G_E and D. Based on reports that G_E is greatly influenced by EVT, the concept of relaxation length was applied in order to understand the effect on this output variable. The relaxation length concept refers to the radial position at which a given parameter (T_s and G_E) reaches an asymptotic value [9]. Thus when the EVT decreased, the value for G_E was lower at the entrance of the liquid film onto the evaporator surface, and G_E reached lower asymptotic limits (at a relaxation length of 0.2500 m).

With respect to the T_s profiles along the evaporator surface, the results in Figure 2a, showed a limiting and critical operating condition, where, as the EVT decreased, the temperature was not high enough for evaporation. In consequence, the values for G_E and D of the most volatile compounds only varied slightly along the flow pathway over the evaporator surface (Figures 2b and 2c). It was evident that the centrifugal molecular distillation process was strongly influenced by EVT. Accordingly, as the EVT rose, so the values for G_E and D increased as the amounts of the more volatile components decreased, due to the fact that the molecules moved more vigorously and hence increased the amount of energy available to escape from the evaporator surface and reach the condenser surface.

Figure 2d shows the δ profiles for different values of EVT. It can be seen that the greatest changes in the film thickness profile occurred in the region between 0.03095 m and 0.1500 m, corresponding to the section where the feed material enters and the central section of the evaporator surface. Hence, the phenomenon of evaporation at the free surface, leads to depletion of the most volatile component or components in

the liquid phase, forming a thin liquid film that may even condense along the condenser surface.

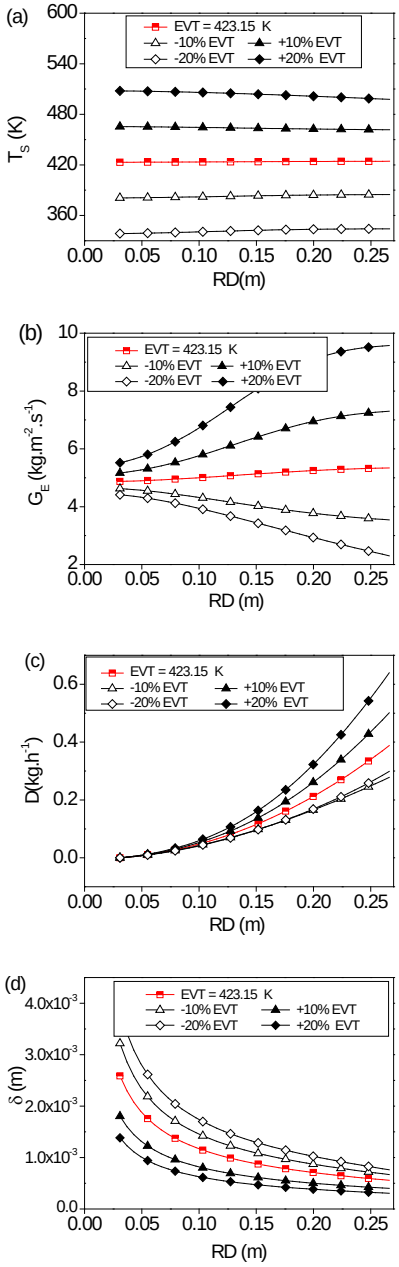

Figure 2: Effect of EVT on: (a) T_s, (b) G_E, (c) D and (d) δ at Q=1.5 kg•h^{-1}, RS=1000 rpm and P_s=0.13 Pa.

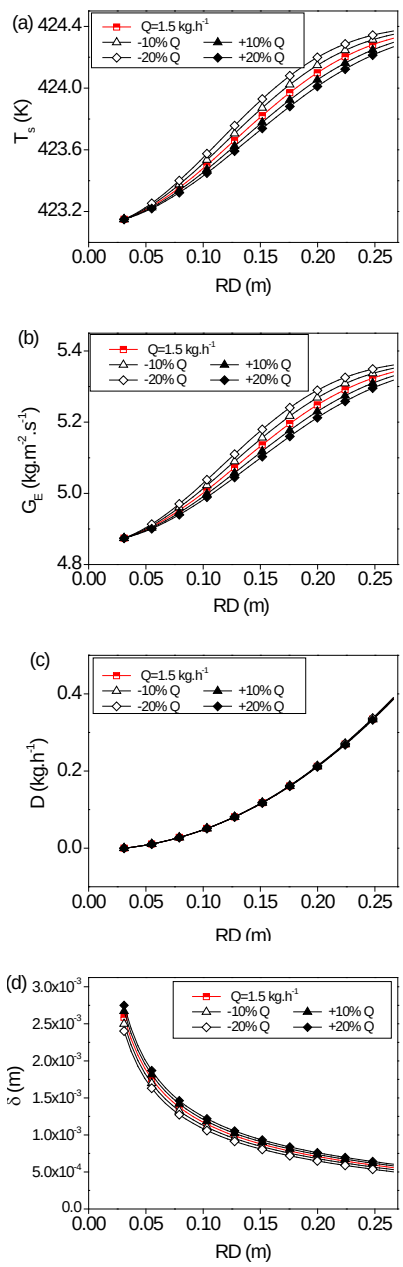

Figure 3: Effect of Q on: (a) T_s, (b) G_E, (c) D and (d) δ at EVT=423.15 K, RS=1000 rpm and P_s=0.13 Pa

2.2. Effect of Q on the output variables

In Figure 3, the relationship of T_s, G_E, D and δ versus RD is shown, with Q as the parameter sensitivity. In Figure 3a, as Q increases, so the T_s profiles reach asymptotic values, corresponding to the increases in relaxation length. In the range of Q studied, the difference in temperature in the radial direction was very small. These relatively small radial gradients might be ascribed to the low thermal

conductivity, about 0.85 W•m^{-1}•k^{-1} for ATR–Z [14], to conduct the heat transferred from the evaporator surface to the inner part of the liquid film.

The slight rises in T_s (Figures 3a) and G_E (Figure 3b) as Q decreased were mainly related to good mass transfer over the evaporator surface, and consequently to the increase in evaporation of volatile compounds. Therefore, the Q parameter directly influenced the liquid film thickness and mass transfer, since values of Q below 1.000 kg•h^{-1} may not be high enough to efficiently transfer mass and heat. On the other hand, for Q values above 2.000 kg•h^{-1}, the system might operate with low effectiveness, because the residence time of the molecules in the evaporator may be too low. Figure 3d shows the development of δ along the evaporator length in the r–direction, for various liquid loads. Thus, it can be seen that lower δ values were reached at low values of Q, confirming that, under these conditions, a uniform thin film promotes high efficiency in mass and energy transfers.

2.3. Effect of RS on the output variables

Figure 4a shows that as the RS increased two regions can be elucidated: (i) the surface temperature profile at the entrance section from 0.03095 to 0.1000 m where the evaporation of liquid was negligible and, (ii) a fully developed T_s profile from 0.1000 to 0.2662 m. For high values of RS the G_E increased rapidly (Figure 4b) and, in consequence, the efficiency of the centrifugal molecular distillation process increased exponentially along the RD, resulting in a corresponding exponential increase of D (Figure 4c), due to the increase in induced centrifugal force, which is known as the flow driving force of the system. It can be seen that when RS increased to 1300 rpm, the δ of the evaporating liquid film decreased and reached 4.63x10^{-4} m (Figure 4d). Furthermore, the effect of RS showed the existence of large temperature gradients along the evaporator surface, and for this reason, the G_E gradients were rather pronounced. Accordingly, the low resistance to mass and heat transfers of the evaporating film was advantageous for the centrifugal molecular distillation process, since the distillate stream, which is the desired product, apparently increased as RS increased. This is related to the fact that the distillation speed increased when the liquid film over the evaporator surface became more uniform, ensuring a short residence time of the liquid load over the evaporator surface and its distribution in the form of a thin liquid film.

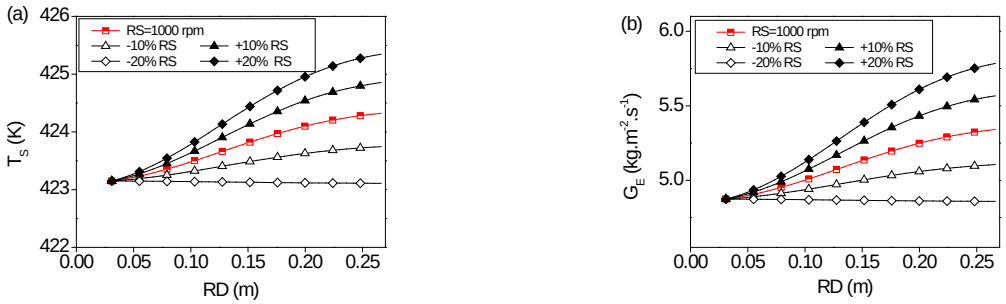

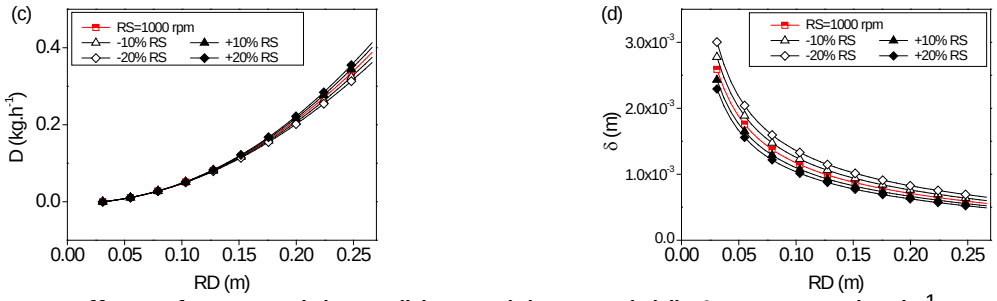

Figure 4: Effect of RS on: (a) T_s, (b) G_E, (c) D and (d) δ at Q=1.5 kg•h^{-1}, EVT=423.15 K and P_s=0.13 Pa.

3. Conclusions

The results suggested that the main operating variables for this particular process were EVT and RS, which marked some limiting conditions for carrying out future theoretical and experimental studies. The simulated data reported that the liquid film thickness was affected by the evaporator temperature, rotor speed, liquid viscosity and the difference in temperature between the evaporator wall and the evaporating liquid. Thus, the effectiveness of the molecular distillation process for ATR–Z was evaluated from the film thickness, high distillate flow rate and high effective evaporation rate, as a consequence of the depletion phenomenon of the most volatile compounds (pseudocomponents) and efficient mass and heat transfers of the inner evaporating liquid film over the evaporator surface device.

Acknowledgements

This research was supported by the Brazilian National Council for Scientific and Technological Development (CNPq), the Petrobras Research and Development Center (PETROBRAS/CENPES), the Brazilian Study and Project Financing Institution (FINEP) and São Paulo Research Foundation (FAPESP).

References

1. Batistella CB, Maciel MRW, Filho RM (2000) Rigorous modeling and simulation of molecular distillators: development of a simulator under conditions of non ideality of the vapor phase. Computers & Chemical Engineering 24, 1309-1315
2. Tovar LP, Maciel MRW, Winter A, Batistella CB, Filho RM, Medina LC (2012) Reliability–based optimization using surface response methodology to split heavy petroleum fractions by centrifugal molecular distillation process, Separation Science and Technology 47, 1213-1233.
3. Liñan LZ, Lima NMN, Manenti F, Maciel MRW, Filho RM, Medina LC (2012) Experimental campaign, modeling, and sensitivity analysis for the molecular distillation of petroleum residues 673.15 K+, Chemical Engineering Research and Design 90, 243–258.
4. Sales–Cruz M, Gani R (2006) Computer–Aided modelling of short–path evaporation for chemical product purification, analysis and design, Chemical Engineering Research and Design 84, 583–594.
5. Shao P, Jiang ST, Ye YK (2007) Influences of feed and condenser temperature on molecular distillation of ideal binary mixtures, Journal of Scientific & Industrial Research 66, 37–46.
6. Kawala Z, Dakiniewicz P (2002) Influence of evaporation space geometry on rate of distillation in high–vacuum evaporator, Separation Science and Technology 37, 1877–1895.
7. Batistella CB, Moraes EB, Filho RM, Maciel MRW (2006) Mathematical development for scaling–up of molecular distillators: Strategy and test with recovering carotenoids from palm oil, 16th European Symposium on Computer Aided Process Engineering, 1113–1118.
8. Xubin Z, Chunjian X, Ming Z (2005) Modeling of falling film molecular distillator, Separation Science and Technology 40, 1371–1386.
9. Cvengroš J, Lutišan J, Micov M (2000) Feed temperature influence on the efficiency of a molecular evaporator, Chemical Engineering Journal 78, 61–67.

10. Batistella CB, Maciel MRW (1996) Modeling, simulation and analysis of molecular distillators: Centrifugal and falling film, Computers & Chemical Engineering 20, supplement 1, S19–S24.
11. Lutišan J, Cvengroš J (1995) Mean free path of molecules on molecular distillation, The Chemical Engineering Journal and the Biochemical Engineering Journal 56, 2, 39–50.
12. Badin V, Cvengroš J (1992) Model of temperature profiles during condensation in a film in a molecular evaporator, The Chemical Engineering Journal 49, 177–180.
13. Inuzuka M, Sugiyama R, Saito I, Yamada I, Hiraoka S, Ishikawa H, Banno, I (1986) Analysis of heat and mass transfer in a centrifugal molecular still, Journal of Chemical Engineering of Japan 19, 14–20.
14. Tovar LP, Maciel MRW, Filho RM, Batistella CB, Ariza OJ, Medina LC (2012) Overview and computational approach for studying the physicochemical characterization of high-boiling-point petroleum fractions (350 °C+), Oil & Gas Science and Technology 67,451-477.

CO_2 capture process evaluation at power plant

Rosa-Hilda Chavez1, Javier J. Guadarrama2
[1]*Instituto Nacional de Investigaciones Nucleares, Ocoyoacac, 52750, Mexico;*
[2]*Instituto Tecnológico de Toluca, Metepec, 52140, Mexico*

Abstract
The main challenge of the chemical absorption CO_2 capture processes is reducing the energy requirement in the stripper with the reboiler at post-combustion method when ambient air is used as an oxidant. This paper discusses: 1) several CO_2 capture process configurations, 2) the most important parameters necessary to obtain 90% capture rate and 3) the lowest energy consumption at solvent regeneration for CO_2 capture from flue gas of thermoelectric power plant. Carbon dioxide is removed by chemical absorption processes from flue gas of power plant with monoethanolamine (MEA). Absorption of CO_2 was conducted using an experimental packed column of three different structured packing materials: ININ18, *Sulzer* BX and *Mellapak* 250Y. The mass transfer characteristics were determined by experimental absorption columns and modeling columns with Aspen Plus using RADFRAC. The results show decreased reboiler energy consumption from the base case process configuration with 8MJ/kg of CO_2 at solvent regeneration and *Sulzer* BX packing was the most efficient in CO_2 whole capture with MEA.

Keywords
CO_2 capture efficiency, energy requirement, structured packing.

1. Introduction

A major concern in developed countries is climate change and consequently the effect of CO_2 emissions. These have subsequently generated great interest in efficient CO_2 capture studies and resourceful methods to enhance energy-intensive processes [1].
Three CO_2 Capture and Sequestration (CCS) methods are being developed: Pre-combustion, oxy-combustion and post-combustion. The last alternative works properly well; this is applicable to power generation technologies (5-20% CO_2). Advantages include over 60 years experience, no risk, low pressure of 0.1MPa, currently in use, and CO_2 recovery for carbonated beverages. On the other hand, disadvantages include, high investment cost and power consumption, and large equipment size [2], [3], [4]. This process provides a high capture efficiency and selectivity, and lower cost than other processes [5], [6].
Among all the different techniques for capturing CO_2, absorption with aqueous alkanolamine is recognized as a proper commercial option for capturing CO_2 in gas diluted flows, which contain 10% to 12% of CO_2 volume. The carbon dioxide capture with Monoethanolamine (MEA) aqueous solution consists of gas stream contact with amine aqueous solution which reacts with carbon dioxide to form a soluble carbonate salt, by reaction acid-base neutralization [7]. CO_2 capture simulation using MEA with Aspen Plus™, helps to obtain chemical and physical component properties, equilibrium properties of ionic and molecular species by the electrolyte-NRTL models. Also it helps to evaluate different case studies and to compare three different structured packings: ININ 18, Sulzer BX and Mellapak 250Y. By this way it is feasible

to choose which one fits the requirements of greater CO_2 absorption and lower height of mass transfer unit.
The purpose of this work is to evaluate the minimum energy consumption for solvent regeneration and maximum CO_2 absorption with 600 ton/day flue gas flow treated by *Aspen Plus*™ of CO_2 capture process, using MEA at 30 % weight.
Parameters that determine technical and economic feasibility of CO_2 absorption systems are [2]:

- Flue gas flow. The absorption column size is determined by characteristics of combustion gas flow: its flow and composition of components. The first one to obtain diameter of the column, and the second one, the number of mass transfer stages in order to separate one o more components from one to another composition.
- CO_2 concentration. Flue gas is at atmospheric pressure, partial pressure of CO_2 is between 3 to 15kPa under these conditions, and amine chemical solvent in aqueous solution is most suitable.
- CO_2 separation. CO_2 recovery is a parameter related to absorber height.
- Solvent flow. It determines equipment size used to capture CO_2.
- Power requirements. It involves thermal energy to regenerate solvent and power energy to operate pumps.
- Cooling requirements. To bring flue gas and regenerated solvent to required temperatures, unless there is a gas desulphurization process where gas combustion temperature leaves at an appropriate temperature to enter the absorption process.

METHODOLOGY

The MEA solvent was selected to make a system model for CO_2 removal by absorption/stripping. Both the absorber and the stripper used *RateSep*™ to rigorously calculate mass transfer rate. The accuracy of the new model was assessed using a pilot plant run with 30% MEA. A rigorous model adopted from the literature, built on RATEFRAC of Aspen Plus is used to simulate the complex reactive absorption behavior. The reactions employed were defined by internal software “wizard” [8], [9], [10].
The methodology was divided in two sections:
1) Hydrodynamic analysis. Column was performed by exploring different regions of operation: preload, loading and flooding regimens, in order to find L/G flow ratio per each packing in order to ensure loading at turbulent regimen and optimum mass transfer operation.
The hydrodynamics of each packing was obtained by determining the pressure drop over packed bed height, $\Delta P/Z$, due to the passage of gas through the packed bed, either dry (zero liquid flow) or with liquid flow [11].

$$\frac{\Delta p_{irr}}{\rho_L g Z} = \frac{\Delta p_{dry}}{\rho_L g Z} \times \frac{\left\{1-\varepsilon\left[1-\frac{h_0}{\varepsilon}\left[1+20\left(\frac{\Delta p_{irr}}{\rho_L g Z}\right)^2\right]\right]\right\}^{\left(\frac{2+c}{3}\right)}}{1-\varepsilon} \times \left[1-\frac{h_0}{\varepsilon}\left[1-20\left(\frac{\Delta p_{irr}}{\rho_L g Z}\right)^2\right]\right]^{-4.65} \quad (1)$$

$$c = \frac{-C_1/\mathrm{Re}_G - C_2/\left(2\,\mathrm{Re}_G^{1/2}\right)}{f_0} \quad (2)$$

, where *Re* is Reynolds number, C_1, C_2 and C_3 are adjusted constants, *fo* friction factor, *ho* total liquid hold up, ρ is density, *g* gravity constant, *Z* packed height.

2) Mass transfer model was developed to calculate and analyze the effect of mass transfer unit height (HTU) on the gas and liquid phases. The Double Film theory correlates height of global mass transfer unit HTU_{OG} and HTU_{OL}, with height of gas mass transfer unit HTU_G and liquid mass transfer unit HTU_L for a system [2].

$$HTU_G = \frac{U_G}{k_G a_e \rho_G} \quad (3)$$

$$HTU_L = \frac{U_L}{k_L a_e \rho_L} \quad (4)$$

$$HTU_{OG} = HTU_G + \lambda HTU_L \quad (5)$$

$$HTU_{OL} = HTU_L + \frac{1}{\lambda} HTU_G \quad (6)$$

CO_2 Capture Process Description

Gas flow G_1 enters at the bottom of the absorption column, while liquid flow L_1 enters at the top. The rich liquid amine stream L_2 enters a heat exchanger (CALENT) to raise its temperature and then enters desorption column where amine regeneration occurs. The regenerated liquid flow is mixed with pure MEA (30 wt %) solution, L_5, in order to fulfill mass balance of the whole process, due to stream L_6, it is entered a heat exchanger to decrease its temperature (ENFRIA) and then to recirculate (L_7) to the absorption column. The stability of the stream L_5 was clue to know the iteration number in the simulator (see Figure 1). CALENT and ENFRIA could be the same heat exchanger as energy saver equipment.

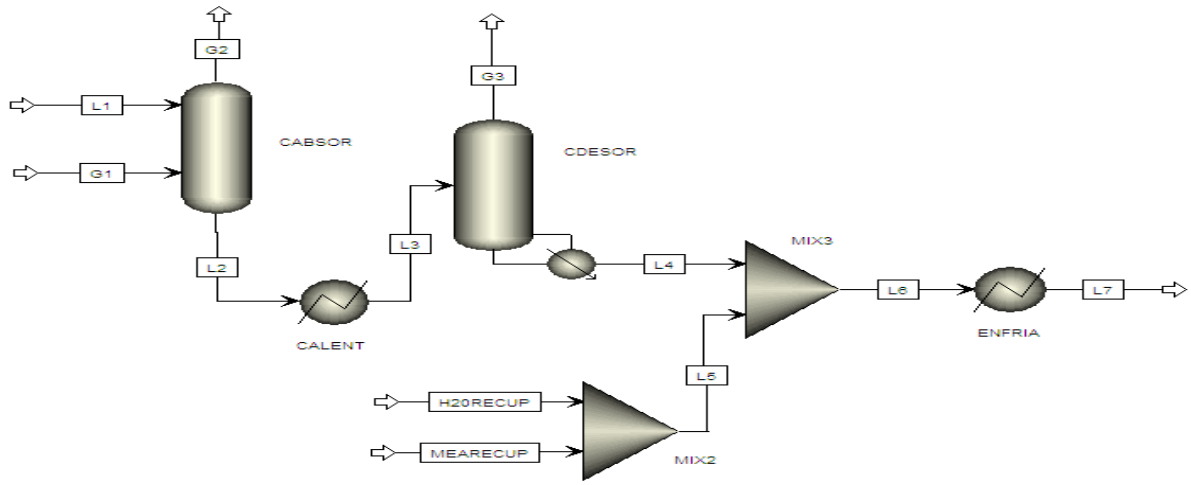

Figure 1. CO_2 capture process flowsheet

The following considerations were excluded in order to facilitate simulation in Aspen Plus™,: i) the washing column used to filter particles as well as desulfurization stage of flue gases used to remove sulfur dioxide ii) The inlet gas stream which was considered free of all contaminants and consisted of H_2O, CO_2, O_2 and N_2 where NO_x and SO_2 were not considered, iii) Corrosion, and finally iv) Compression, storage and transport of CO_2.

The gas flow percentage with respect to the flooding region was determined by the following equation:

$$\%G_{op} = \frac{G_{op}}{G_{flooding}} x100 \quad (7)$$

2. Results and discussion

ININ18 packing presented better hydrodynamic behavior than the other two because it operated at 80% from flooding point and *Mellapak* 250Y and *Sulzer* BX at 60% from flooding point at the same $L/G=3$ flow ratio for three structured packings. ININ18 packing showed a higher pressure drop than the other two structured packings. This one achieved flood with lower liquid and gas flow values. Table 2 shows the hydrodynamic and mass transfer parameters with the same $L/G=3$, in turbulence regimen. *Sulzer* BX is the lowest height of mass transfer unit and the highest value on the volumetric mass transfer coefficients, due to its geometric characteristics. The mass transfer resistance was provided by the gas film and more than the liquid side, so that global mass transfer height was taken on gas film. The lowest mass transfer height of *Sulzer* BX was 0.32 times less than ININ18 and 0.38 than *Mellapak* 250Y, and the highest effective area of *Sulzer* BX was 0.16 times greater than ININ18 and 0.23 than *Mellapak* 250Y, due to its geometric characteristics. Also, *Sulzer* BX shows the highest value on the volumetric mass transfer coefficients of 3.76s^{-1}. *Sulzer* BX packing presented the most mass transfer efficiency due to having the lowest HTU_{OG} value than the other two structured packings, as a result of the highest geometric area.

Table 2. Hydrodynamic and mass transfer results

Flows (t/day)		*G*	*L*	*G*	*L*	*G*	*L*
		150.00	450.00	150.00	450.00	150.00	450.00
		Sulzer BX		ININ 18		*Mellapak* 250Y	
$\Delta P/Z$	Nm^{-2}/m	472.93		791.64		422.25	
HTU_{OG} (height)	m	0.3167		0.4245		0.4297	
HTU_{OL} (height)	m	0.4777		0.6405		0.6483	
$k_G a_{e\ (Local\ coefficient)}$	s^{-1}	3.763		2.8066		2.7730	
$k_L a_{e\ (Local\ coefficient)}$	s^{-1}	5.5211		4.159		4.0024	
Gas resistance	%	54.19		54.44		53.79	
Liquid resistance	%	45.80		45.55		46.21	

Table 4 shows simulation results under the same operation conditions, from the set fixed quantities as it is shown at Table 2. *Sulzer* BX packing required one more step in the absorption and desorption column than two other packings; also, this packing shows highest CO_2 absorption and CO_2 capture efficiencies. *Sulzer* BX requires less a stream of fresh compounds replenishing losses $L_5 = 50.52$ t/h, releases less CO_2 into the atmosphere $x_{G_2}^{CO_2}$ equal to 0.0106 and provides higher CO_2 concentration at G_3 stream of $x_{G_3}^{CO_2}$ equal to 0.2839 (see Table 3).

Table 3. Flows and CO_2 mass concentration at different streams

	Sulzer BX	ININ18	*Mellapak* 250Y
$G_1\ (t/day)$	600.00	600.00	600.00
$x_{G_1}^{CO_2}$	0.098	0.098	0.098
$G_2\ (t/day)$	471.150	475.038	477.888
$x_{G_2}^{CO_2}$	0.0106	0.0191	0.0263
$G_3\ (t/day)$	179.371	178.902	178.349

$x_{G_3}^{CO_2}$ (on wet basis)	0.2839	0.2606	0.2412
$L_1\,(t/day)$	1800.00	1800.00	1800.00
$L_2\,(t/day)$	1928.850	1924.962	1922.113
$L_3\,(t/day)$	1928.850	1924.962	1922.113
$L_4\,(t/day)$	1749.480	1746.061	1743.764
$L_5\,(t/day)$	50.520	53.939	56.236
$L_6\,(t/day)$	1800.00	1800.00	1800.00

Simulations were made at different reboiler energies requirement and absorption column and CO_2 capture efficiencies were evaluated with respect to CO_2 concentration at gas streams by using CO_2 mass/mole rates (fluxes) amongst G_1 minus G_2 and G_1 minus G_3, respectively. Three structured packing have the same graphically tendency, however the *Sulzer* BX presents the highest values in all cases. The energy requirement in the reboiler, in order to solvent regeneration, is linked to power generation plant, so despite a higher capture efficiency, not much energy can be used for the CO_2 treatment. It was considered a reboiler energy requirement of 120MW as a value of CO_2 capture efficiency for comparison amongst the three structured packing. Table 4 shows the simulations results under the same operating conditions from set fixed quantities as it is shown at Table 2.

Table 4. *Aspen Plus*™ results

Packing	*FT* (t/day)	*L* (t/day)	*G* (t/day))	*D* (m)	*RE* (MW)	*S*	*RL*	*LL*	*CE* %	*AE* %
Sulzer BX	2400	1800	600	1.1	120	8	0.395	0.277	65.48	89.17
ININ 18	2400	1800	600	1.1	120	7	0.389	0.282	62.40	80.47
Mellapak 250Y	2400	1800	600	1.1	120	7	0.381	0.283	59.36	73.17

Where *FT* is total flow, *L* and *G* are liquid and gas flow, *D* is column diameter, *RE* is energy requirement, *S* is number of stages at absorber and stripper, *RL* and *LL* are rich and lean loading load at L_2 and L_1 or L_7, respectively, *CE* and *AE* are capture and absorption efficiency, respectively.

Sulzer BX packing was the most efficient in CO_2 whole capture with MEA and showed greater efficiency in the absorption column, although requiring a larger number of mass transfer stages. It showed lower mass transfer height in both columns; also, highest CO_2 absorption efficiency and CO_2 capture efficiency. Figure 2 shows a sensitivity analysis for removal efficiency versus number of stages. A process model was developed previously using Aspen Plus simulation programmer where CO_2 removal efficiency has been reached almost 90%.

3. Conclusions

- For CO_2 absorption, gas film resistance is important for this type of CO_2 capture with chemical reaction with absorber loading and removal.
- The accuracy of the new model was assessed using a recent pilot plant run with 30% MEA. Absorber loading and removal were matched and the temperature profile was approached within 5ºC.
- ININ18 packing reached flood with lower liquid and gas flow values. It showed a higher pressure drop than the *Sulzer* BX and *Mellapak* 250Y packings.

- *Sulzer* BX packing showed the highest mass transfer efficiency compared with ININ and Mellapak 250Y packings, owing to its highest geometric area. HTU_{OG} value was lower than ININ and Mellapak 250Y packings. It was the most efficient in CO_2 whole capture with MEA and showed greater efficiency in the absorption column, although requiring a larger number of mass transfer stages. It showed lower mass transfer height in both columns; also, highest CO_2 absorption efficiency and CO_2 capture efficiency.
- The minimum energy consumption for solvent regeneration was 120MW at energy requirement in order to carry out the regeneration of the MEA.

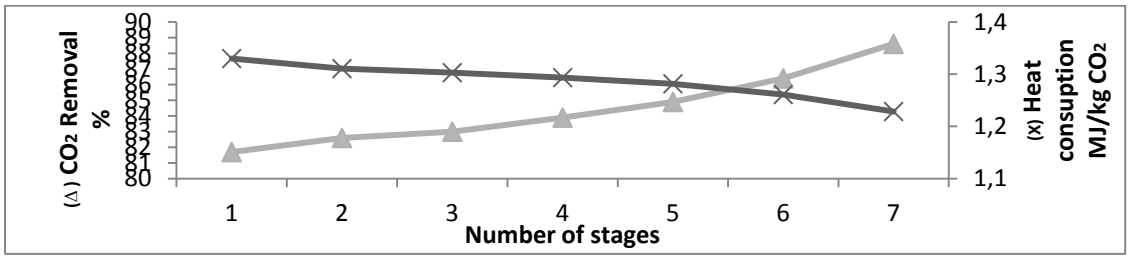

Figure 2. A sensitivity analysis for removal efficiency vs number of stages at stripper

Acknowledgements

Partial financial support of this work was provided by Consejo Nacional de Ciencia y Tecnología (CONACyT), project: EDOMEX-2009-C02-135728, CB-2007-01-82987, and Chemical Faculty of State of Mexico University in order to use Aspen Plus^{MT}.

References

[1] IPCC, Climate Change: The scientific basis, contribution of working group 1 to the third assessment report of the intergovernmental panel on climate change, U.K. 2001, Cambridge University Press.

[2] Leites I.L., Sama D.A., Lior N., The theory and practice of energy saving in the chemical industry: some methods for reducing thermodynamic irreversibility in chemical technology processes, Energy 28, (2003), pp. 55-97**.**

[3] Amrollahi Z., Ertesvag I.S., Bolland O., Ystad P.A.M., Optimized Process Configurations of Post-combustion CO2 Capture for Natural-gas-fired Power Plant – Power Plant Efficiency Analysis, Proceeding of Third ICEPE, (2011), pp. 629-640.

[4] Kawabata M., Iki N., Murata O., Tsutsumi A., Koda E., Suda T., Matsuzawa Y., and Furutani H., Energy Flow of Advanced IGCC with CO_2 capture Option, Proceeding of ASME2010, IMECE, (2010), pp. 1-6.

[5] Wilson M.A., Wrubleski R.M. and Yarborough L., Recovery of CO_2 from power plant flue gases using amines, Energy Convers. Mgmt. 33 No. 5-8, (1992), pp. 325.331.

[6] Jassim M.S. and Rochelle G.T., Innovative absorber/stripper configurations for CO_2 capture by aqueous monoethanolamine, Innovative absorber/stripper configurations for CO_2 capture by aqueous monoethanolamine, Ind. Eng. Chem. Res. 45. No. 8, (2006), pp. 2465-2472.

[7] Asrarita G., 1964, The influence of carbonation ratio and total amine concentration on carbon dioxide absorption in aqueous monoethanolamine solutions, Chem Eng Sci, 19, (1964), pp.95-103.

[8] Pacheco M.A., Rochelle G.T., Rate-based modeling of reactive absorption of CO_2 and H_2S into aqueous Methyldiethanolamine, Ind.Eng.Chem.Res. 37, (1998), pp. 4107-4117.

[9] Plaza J.M., Van Wagener, Rochelle G.T, Modeling CO_2 capture with aqueous Monoethanolamine, Energy Procedia 1, Elsevier, (2009), pp. 1171-1178.

[10] Chang H., Shih Ch.M., Simulation and optimization for power plant flue gas CO_2 absorption-stripping systems, Separ Sci Technol, 40, (2005), pp. 877-909.

[11] Stichlmair J., Bravo J.L., and Fair R.J., General model for prediction of pressure drop and capacity of countercurrent gas/liquid packed columns, Gas Sep Purif, 3, (1989), pp. 19-28.

Distillation Tower Gamma Scanning – Now a Quantitative Tool for Measuring Useful Capacity

Lowell Pless
Tracerco, Pasadena Texas, U.S.A.

Improving process operating margins can include maximizing production of higher value products and/or minimizing production costs. Process plant operations depend heavily on fractionation towers to produce products meeting customer specifications. Tower gamma scanning is well established in the process industries as a qualitative tool to help troubleshoot fractionation towers. Using new measurement detector technology and innovative analysis of gamma scanning data Tracerco is now able to offer quantitative information about the useful capacity of fractionation towers, both trayed and packed.

For trayed towers a new methodology, FrothView™, has been tested and developed whereby the total froth height on a tray can be measured from gamma scan data. Dividing by the tray space provides the percentage of tray space occupied by tray froth. The "% tray space" has been shown to correlate very well with % flood, thus a field measurement for the useful capacity of operating trays.

For packed towers, a grid-scan of 3 or 4 equal-distant scans crossing through beds of packing would typically be done to qualitatively measure liquid distribution. An inventive procedure, PackView™ – calculating the liquid retention and volume of liquid holdup in an operating bed of packing – provides insight into the useful capacity of a bed of packing and the existing quality of the liquid distribution.

Keywords
Gamma scanning, distillation, tray capacity, packing capacity, tray froth height, packing retention

Trayed Towers - FrothView™

1.1. Introduction

There are a few practiced methods for measuring a liquid or froth level on a tray from gamma scan data. However; no matter the practitioner, the conventional methods allocate a tray's aerated liquid height somewhere in the middle of the froth layer. This method is adequate for diagnosing tray damage – whether a tray is capable of holding liquid or not. But beyond this determination, conventional tray liquid level measurement has no correlation to any other operating variable. Additionally to characterize remaining tray space above this liquid level position that is seen to be

denser than “clear vapor”, subjective terms such as slight entrainment, moderate entrainment or heavy entrainment is typically used. This method is illustrated in *Figure 1a*.

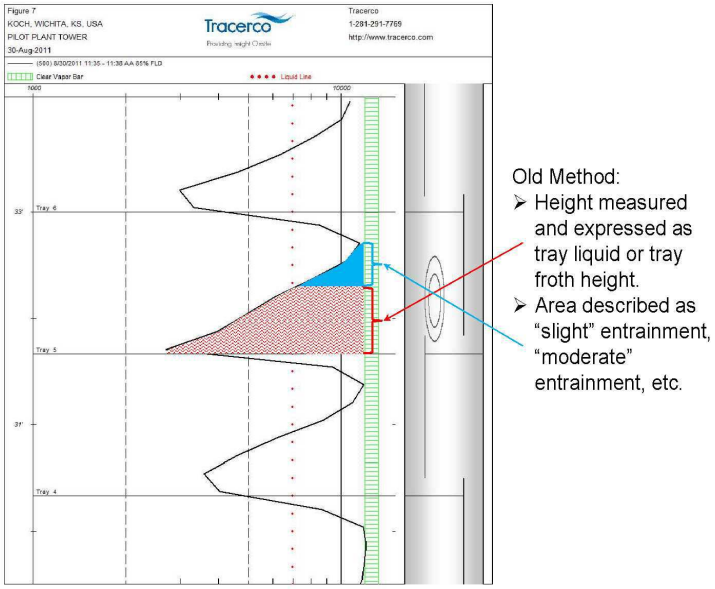

Figure 1a: "Old" method of measuring liquid height on trays.

For trayed towers a new methodology, FrothView™, has been developed and tested whereby the <u>total</u> froth height on a tray is measured from gamma scan data using new detector technology and software interpretation. This method is shown in *Figure 1b*. Dividing the total froth height by the tray space provides the percentage of tray space occupied by tray froth. This “% tray space” has been shown to correlate very well with % flood, thus is a way of using a field measurement and directly relating this to specific tray design criteria to determine the useful capacity of operating trays.

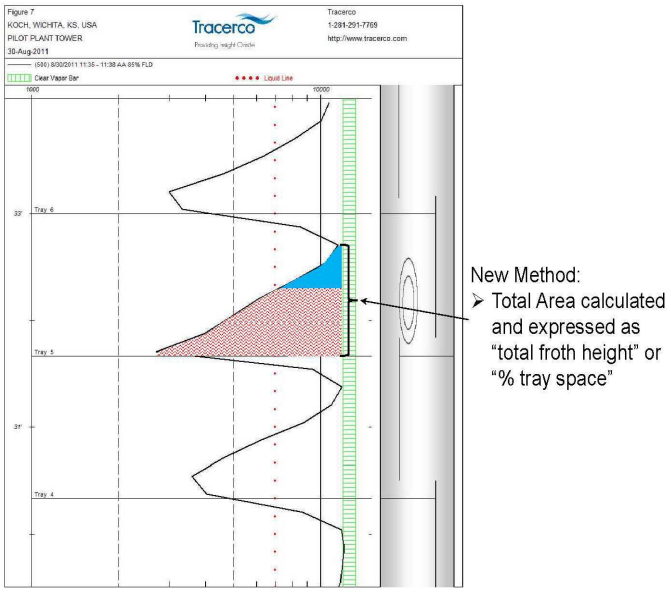

Figure 2b: New FrothView™ methodology of measuring total froth height on trays.

1.2. Results and discussion

A couple of years ago Tracerco had the opportunity to scan a trayed pilot plant tower under varying operating conditions, from weeping to flooding. One objective of this study was to find a method to quantify the scan results to provide a more objective diagnosis of the tray's hydraulic condition.

Three sets of trays, designed to flood under jet flood, downcomer backup or choke flood mechanisms, were tested and studied under very controlled conditions in a hydrocarbon pilot plant tower. The experimental observations, tray model predictions, and total froth height measurements from gamma scan data using new detector technology for each set of trays had excellent agreement. *Figure 2* shows scan data plots from one series of tests. Also shown in *Figure 2* is a table comparing the measured total froth height and % tray space versus calculated tray froth heights and % flood from engineering models.

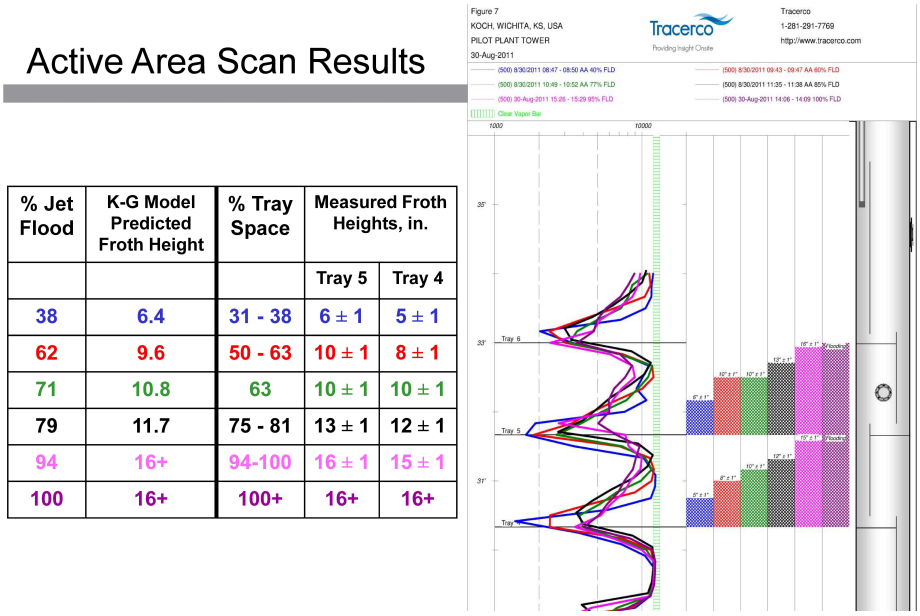

% Jet Flood	K-G Model Predicted Froth Height	% Tray Space	Measured Froth Heights, in.	
			Tray 5	Tray 4
38	6.4	31 - 38	6 ± 1	5 ± 1
62	9.6	50 - 63	10 ± 1	8 ± 1
71	10.8	63	10 ± 1	10 ± 1
79	11.7	75 - 81	13 ± 1	12 ± 1
94	16+	94-100	16 ± 1	15 ± 1
100	16+	100+	16+	16+

Figure 2: Pilot plant tower scan results comparing measured total froth height and % tray space to % flood.

The following case study from a trayed fractionation tower demonstrates differences between the standard method of calculating tray liquid height and the new FrothView™ analysis. The scan performed showed the tower to be in good operating condition with nothing dramatic detected indicating any hydraulic problems or limitations.

Figure 3a focuses in on a typical group of trays from the scan results. The standard method of analysis would have concluded that these trays were holding liquid levels of 180 to 230 mm. As stated earlier, this is a good method for diagnosing if a tray is damaged or not – if the tray holds a suitable level then it is diagnosed to be OK, if no level or an "inadequate" level is detected then the tray is considered damaged. The pilot plant scans confirmed that this "liquid level" was a measurement of the liquid level about three-fourths (75%) into the froth layer as depicted in *Figure 4.*

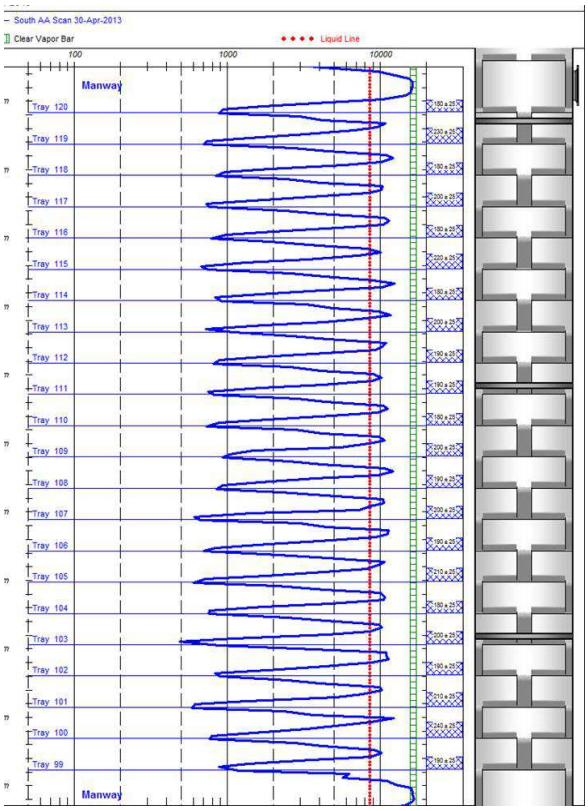

Figure 3a: Illustrates the standard method of analysis showing tray liquid heights.

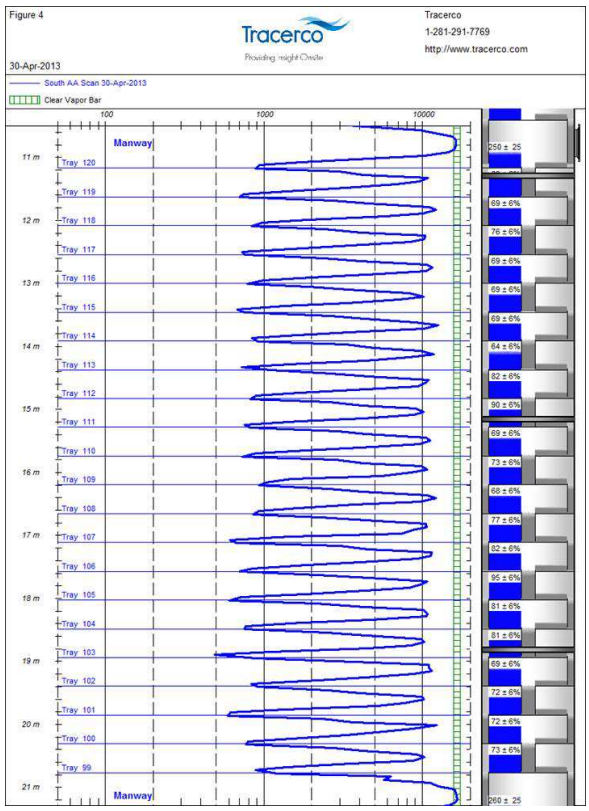

Figure 3b: Illustrates total tray froth heights measured using FrothView™ analysis.

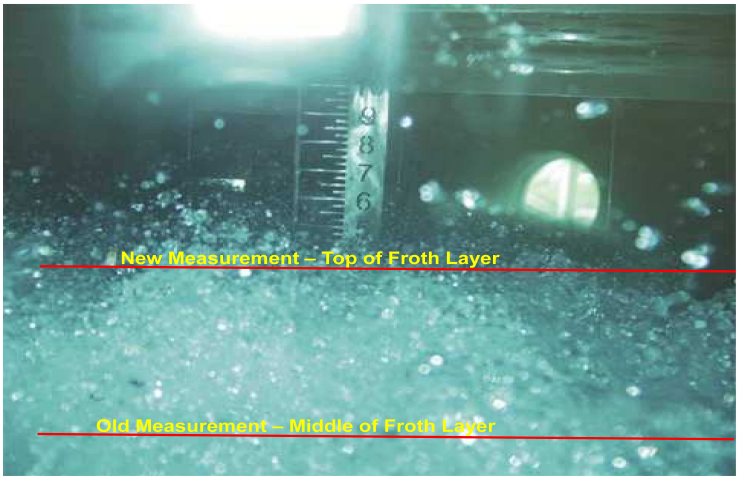

Figure 4: Actual pilot plant studies confirmed that the median "liquid level" was in fact about ¾'s of the actual liquid level.

The second aspect of the standard analysis is to describe the status of the vapor space between the trays. Obviously in *Figure 3a* the curve in between the trays does not return to the Clear Vapor Bar (green line). Therefore, there is something "dense" in the tray vapor space, that "density" being liquid droplets blown up into the vapor space – classic entrainment. Thus depending on how "dense" the vapor space is terms such as slight entrainment, moderate entrainment, heavy entrainment, etc. would be used. A general guideline – the denser the vapor space appears the more severe the entrainment.

So, the final diagnosis from the profile in *Figure 3a* using the old method would be to state that the trays are typically holding 180 – 230 mm of liquid and operating with moderate-to-heavy or heavy entrainment. From a Process Engineering viewpoint, what would this mean? On the one hand it is good that the trays were not flooding and the trays do not seem to be damaged but, what does "moderate-to-heavy entrainment" communicate? If one had tray rating calculations carried out at the scan operating conditions then you could judge if the "moderate-to-heavy" entrainment diagnosis fits with calculated % flood. However this is also open to a wide range of interpretation. In the case of this specific tower, would an 80% flood be considered moderate-to-heavy entrainment or is 90%, or 95%? The question that really needs to be answered is…. how much more useful capacity does these trays have?

1.3. Conclusions

FrothView™ technology offers more quantifiable and less subjective information using the same scan data. Using FrothView™ the total height of the froth is measured on each tray. The total froth height is divided by the existing tray spacing to provide the *% tray spacing. % tray spacing* is Tracerco's term to show the amount or percentage of the available tray spacing that is occupied by froth or aerated liquid. The goal with the method is to measure the very top of the froth layer as illustrated in *Figure 3b.*

From *Figure 3b***,** the total froth heights range from 320 to 380 mm. This equates to the trays operating with 72 – 82 *% tray spacing*. The *% tray spacing* is a good field measurement proxy for % flood. Therefore at the operating conditions where the scan was performed the tray rating calculations show % flood somewhere in the 70 – 85 % range. These numerical results allow a more specific measurement of the tower's operational condition in terms of hydraulic capacity of the trays.

Packed Towers - PackView™

2.1. Introduction

Once questions concerning damage to internals and flooding within a packed tower have been answered the next big concern is the quality of liquid distribution through the beds of packing. Historically gamma scan analysis has used two sets of parallel scanlines (given the tower diameter is sufficiently large) through the packing as shown in *Figure 5*, commonly referred to as a grid scan. The reasoning goes that with the length or path of radiation through the column being the same on all four scan paths, then uniform liquid distribution would be confirmed by all four scans detecting identical radiation.

However; what is meant when the grid scan lines do not seem to match very well? Is this liquid mal-distribution? If so what is the quantity of liquid mal-distribution? Until now the available qualitative analysis of a gamma scan has not provided a proper answer.

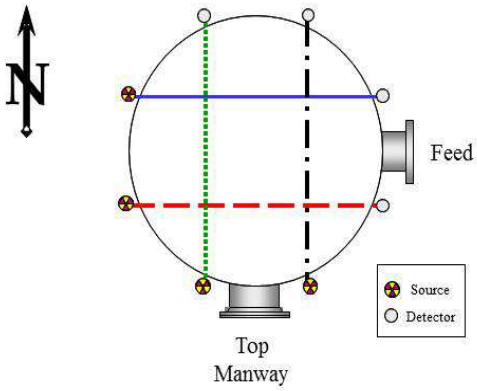

Figure 5: Typical scan-line orientation for a packing grid scan.

2.2. Results and discussion

Tracerco has developed an enhancement in detection capability and data presentation that is termed a liquid retention scale. *Figure 6* shows the scan results with the liquid retention scale in place through the bed of packing. Overlaid on the data through the packing is a density scale. The density scale begins at the density of the dry or non-operating packing. To derive this value it is necessary to know the packing type to reference its dry bulk density. The density scale to the left of the dry packing density is the calculated density of the liquid retained in the bed of packing. As with normal gamma scan analysis, if the four scanlines have matching liquid retention densities then the implication is the liquid distribution is good. However, if there is a difference between the scanlines, the retention density now gives a numerical comparison from which to gauge the extent or severity of any liquid mal-distribution.

Referring to *Figure 6*, the range in density from the lightest density, 24 – 32 kg/m^3, (blue scanline) to the heaviest density (black scanline) at approximately 120 kg/m^3, is 92 kg/m^3. Scans of dry towers (tower is not operating so no liquid mal-distribution) have shown a variation of radiation readings corresponding to a 16 – 32 kg/m^3 difference. Based on this guideline the 92 kg/m^3 difference in liquid density would represent significant liquid mal-distribution.

Another method by which to put this into perspective is to calculate what is referred to as the liquid holdup fraction or liquid volume fraction. If the liquid retention density is divided by the density of the process liquid at bed conditions (the liquid density at the actual operating temperature and pressure), the result is the liquid holdup or liquid volume fraction. In this case the liquid is an aqueous solution with a density of 960 kg/m^3 at the temperature and pressure conditions through the packing. Thus the liquid mal-distribution in terms of liquid density, translates to a 10% difference in the volume of liquid holdup between the “lighter” to the “heavier” side of the column, implying a major liquid distribution problem.

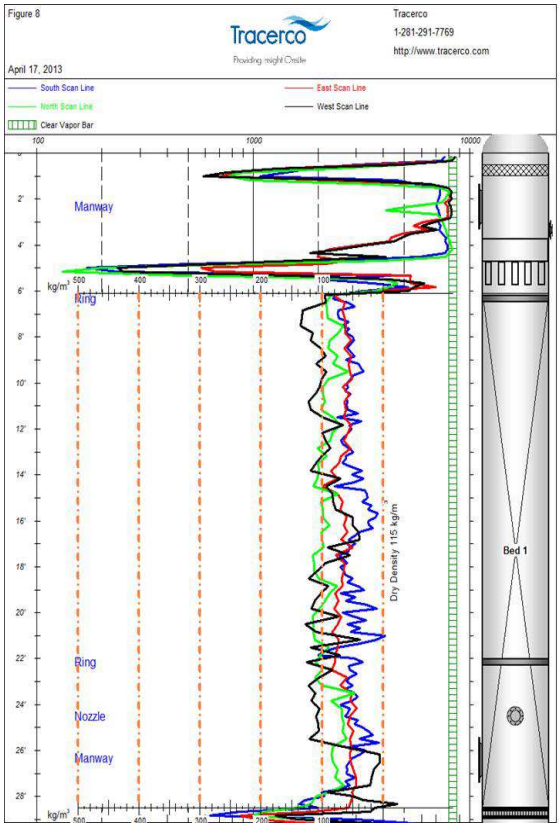

Figure 6: Illustrates PackView™ density retention scale through a bed of packing, showing the density of the liquid retained in the packing.

2.3. Conclusions

It is always easier to understand and discuss technical issues when quantitative information can be used to compare operational parameters with engineering design. Over the past 40 years gamma scanning has become more and more popular as a useful diagnostic tool to understand the hydraulic operation of fractionation equipment. It is the goal of using FrothView™ and PackView™ analysis that technical discussion and understanding of gamma scan data will be enhanced and improvements in the operation of mass transfer equipment will be facilitated.

Acknowledgements

Tracerco wishes to acknowledge the outstanding cooperation and assistance provided by Dr. Izak Nieuwoudt, Director of Research & Development and his highly capable staff at Koch-Glitsch in Wichita KS during the development and testing of FrothView™.

The author wishes to acknowledge that the “inspiration” for the development of FrothView™ technology was taken from a presentation given by Mike Resetarits, Technical Director of Fractionation Research Inc. (FRI) at the 2011 A.I.Ch.E. Spring Meeting titled “On Distillation Tray Entrainment” (1).

References

(1) Resetarits, M.K., T.J. Cai, A.Y. Ogundeji, S. Chambers, J.R. Whiteley, “On Distillation Tray Entrainment”, Dr. James Fair Heritage Distillation Symposium, A.I.Ch.E. Spring Meeting, Chicago IL, March 15, 2011.

(2) Harrison, M.E., “Gamma Scan Evaluation for Distillation Column Debottlenecking”, *Chemical Engineering Progress*, **86** (3) March 1990, pp. 37-44.

TRU-SCAN® and TRU-CAT™ Scanning of a Structured Packing Operating at Deep Vacuum

Simon Chambers[1], Lowell Pless[2] and Ron Carlson[2]
[1] Fractionation Research, Inc., Stillwater, Oklahoma, USA
[2] Tracerco, Pasadena, Texas, USA

Abstract
Pioneering gamma scanning was conducted on a high capacity structured packing operating under deep vacuum during proprietary testing at FRI The packing and multistage trough liquid distributor were tested with the para-/ortho-xylene system at 98.6 mbara in FRI's 1.22 m diameter Low Pressure Column. From top to bottom, the column was baseline scanned when dry and followed by scanning at 24, 30, 67, 100 and 105 % of the packing's Maximum Useful Capacity. Distributor liquid levels derived from the scan data compared very well against liquid level data from FRI bubblers. CAT-scans were performed at one column elevation near the top. At this elevation, 81 data points through the bed of packing were recorded using 9 scanning source positions with 9 different detector positions for each source position around the column circumference. Processing of the CAT-scan data using a proprietary mathematical technique provided significant insights regarding liquid holdup and liquid flow patterns in columns containing structured packings.

Keywords: packing, gamma scan, maximum useful capacity, bubblers

1. Introduction

Gamma scanning employs small radioactive devices to measure directly vapour-liquid flow behavior on trays and packings during specific operating conditions. The Tracerco TRU-SCAN® and TRU-CAT™ scanning techniques[1, 2] provide valuable information that is seldom available from conventional scans. With packed columns, Tracerco employ the PackView™[1] method to dry scan the packing which is set equal to a 'zero' density. With this baseline, additional densities are the result of the liquid volume fraction or liquid withheld inside the packing. Using this pioneering approach in a Fractionation Research Inc. (FRI) packed column test was of particular interest to Tracerco because of the wide range of operating conditions employed with a hydrocarbon system.

On receiving permission from Julius Montz, potentially unique first-of-a-kind gamma-scans were performed on the Montz-Pak high capacity structured packing during proprietary device testing in the FRI Low Pressure (LP) column. Tracerco's primary focus was operations at deep vacuum (98.6 mbara).

2. Results and discussion

2.1 Column Set-up and Operations

Figures 1 and **2** provides elevation drawings and photographs describing the FRI Low Pressure (LP) Column as it was configured for the Montz-Pak high capacity structured packing tests. The column diameter was 1.22 m and the bed height was 2.66 m. The packing specific surface area was 350 m^2/m^3. A Montz Type-R multi-stage trough and drip tube liquid distributor was employed.

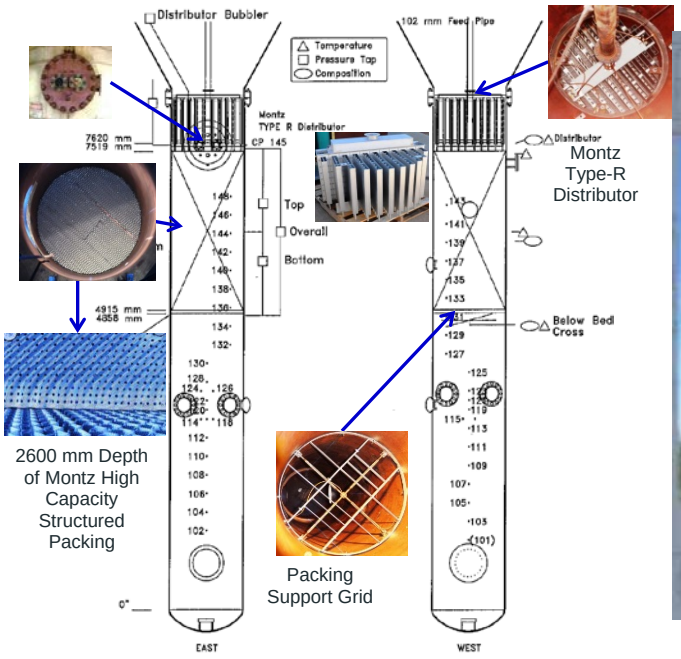

Figure 1. FRI Low Pressure (LP) Column Set-up For the Structured Packing Tests

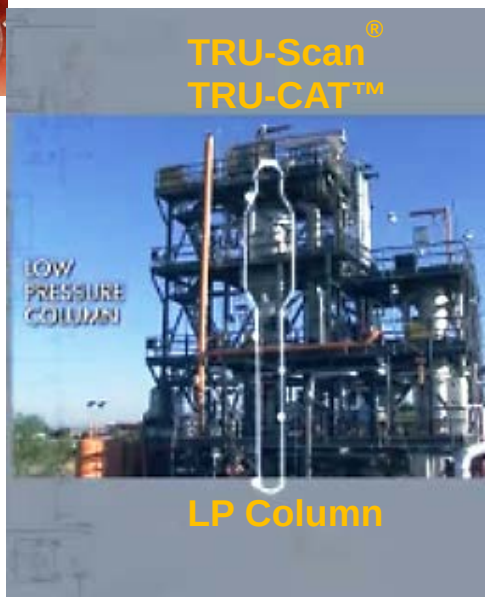

Figure 2. Photograph of the FRI Low Pressure (LP) Column

For this rare and unique gamma scan work, the only system employed was the para-/ortho- xylene system at 98.6 mbar. All of the wet runs were at total reflux (TR) conditions. The FRI measured HETP's (from the Fenske equation using liquid sample compositions) were employed in a graphical analysis to determine the Maximum Useful Capacity (MUC) of the structured packing. **Table 1** shows all of the wet runs are expressed as a percentage of MUC.

Scanline	Scan 1	Scan 2	Scan 3	Scan 4	Scan 5	Scan 6
% MUC	Dry	24	30	67	100	105
Data Curve	**Blue**	**Orange**	**Black**	**Green**	**Red**	**Brown**

Table 1. Montz-Pak High Capacity Structured Packing MUC, P/O-Xylene 98.6 mbar

2.2 *TRU-SCAN® and TRU-CAT™ methods*

The LP Column was gamma scanned vertically from near the top of the installed liquid distributor through the entire bed of packing. A gamma scan generates a density profile of the column, which can be used to identify the integrity of internals and vapour-liquid behavior while a column is operating. **Figure 3** is a representation of the scanline orientation used to obtain the *TRU-SCAN®* data.

TRU-CAT™ is a series of gamma scans covering a full horizontal plane at a given column elevation. The Montz-Pak was *TRU-CAT™* scanned near the top of the packed bed, approximately 230 mm into the bed. **Figure 4** is a representation of the CAT scan orientation used on the Low Pressure Column.

The TRU-CAT™ scan consisted of 81 scan chords or discrete path lengths. Each chord represents data points that collectively were regressed to provide a cross-sectional relative density profiles of the LP Column in the form of 3-D surface plots. The relative densities, are derived from a mathematical model fitted to the scan data taken and not a plot of the actual data.

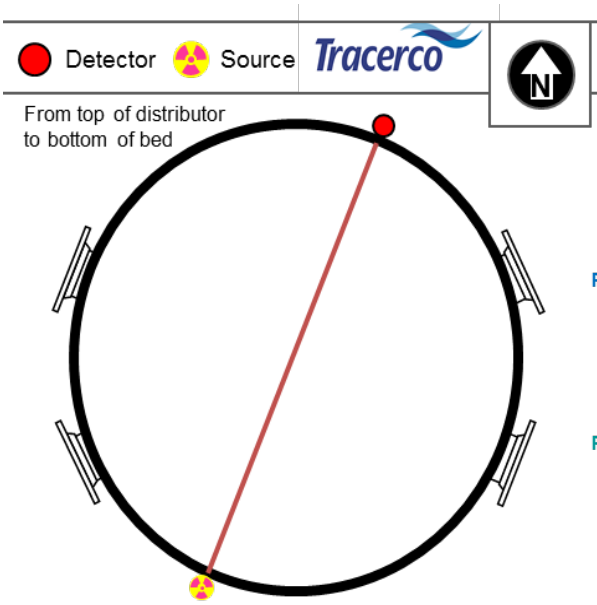

Figure 3. Scanline Orientation in LP Column Used to Produce TRU-SCAN® data

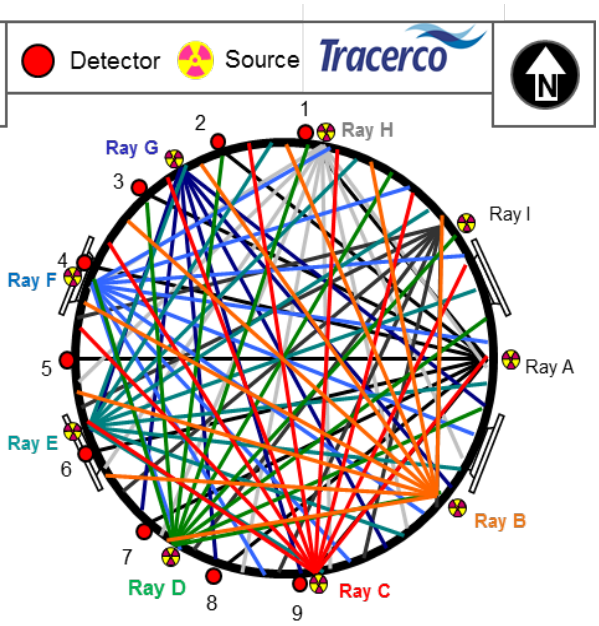

Figure 4. Representation of TRU-CAT™ Orientation on LP Column

2.3 *Gamma Scan Results*

Figure 5 is a *Tru-Tower™ Tru-View™* view of the scan results through the LP column, with reference column elevation on the y-axis and radiation intensity detection (counts) on the x-axis. In addition, **Figure 5** is labeled with a "clear vapour" reference line, where the radiation intensity corresponds to the lowest

vapour density observed. The “clear vapour” reference is presumed liquid free and is used as the reference for calculating relative densities of the process.

Superimposed on **Figure 5** is a density retention scale showing average calculated density (in kg/m^3) of the liquid holdup in the packed bed for each test run. The calculated average dry bed density was 137 kg/m^3 compared to the reported manufacturer’s dry packing density of 139 kg/m^3. The total overall density through the packed bed is the sum of dry packing density and retention density of the liquid hold-up.

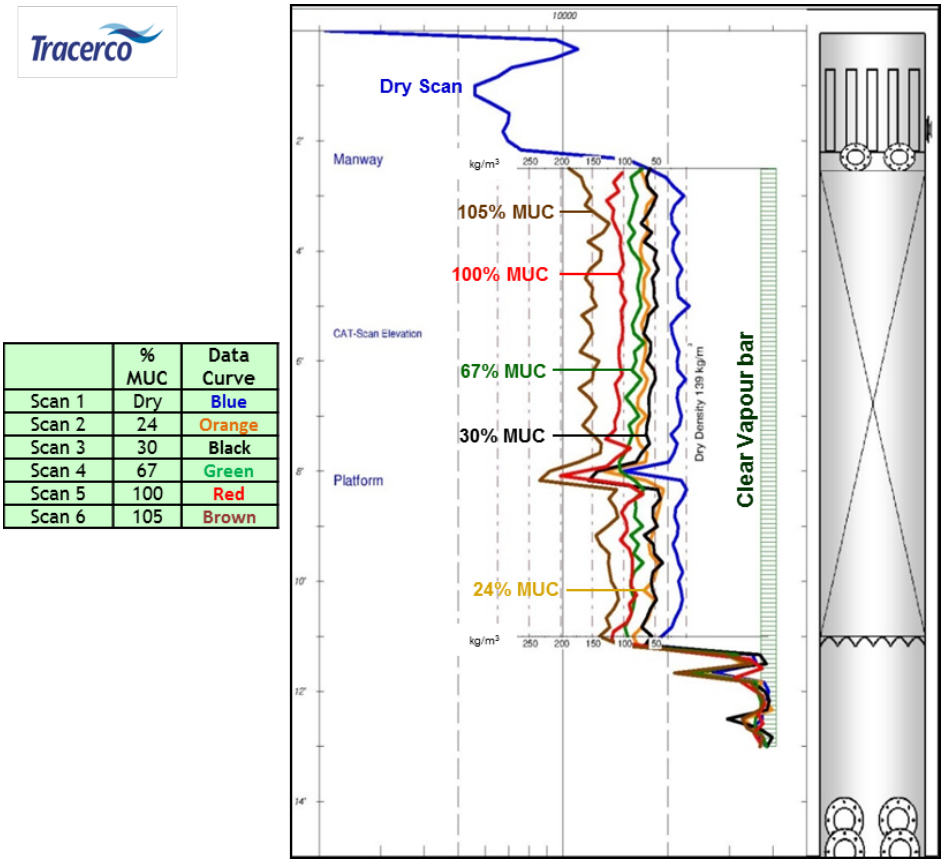

	% MUC	Data Curve
Scan 1	Dry	Blue
Scan 2	24	Orange
Scan 3	30	Black
Scan 4	67	Green
Scan 5	100	Red
Scan 6	105	Brown

Figure 5. Tru-Tower™ Tru-View™ Radiation Count Scan Results and Calculated Process Retention Densities

2.4 *Discussion on Gamma Scan Results*

The gamma scan profiles in **Figure 5** how that at 30% MUC, there was slightly less liquid hold-up in the bottom third of the packed height compared to the top two thirds. At 24% MUC, liquid accumulation was surprisingly higher in the upper bed section compared to 30% MUC. These data are highly suspect. At the Tracerco’s request, FRI purposely operated the LP column at this condition such that the liquid rate was below the liquid distributor minimum design limit. Flow instability was highly possible at these conditions.

The scan profiles at 67% MUC displayed uniform (top to bottom) liquid retention through the entire packing height. As the LP column approached 100% MUC and up to 105% MUC, the scan profiles show a disproportionate liquid build-up in the top and middle zones of the packed bed.

The TRU-CAT™ scans in **Figure 6** revealed no gross liquid mal-distribution at rates below 100% MUC. The narrow band of green-to-yellow around the column perimeter for the 30% MUC scan showed preferential liquid flow on the column wall (higher densities). At higher liquid rates, the green-to-yellow band at the wall expanded corresponding to an increased liquid migration toward the column wall.

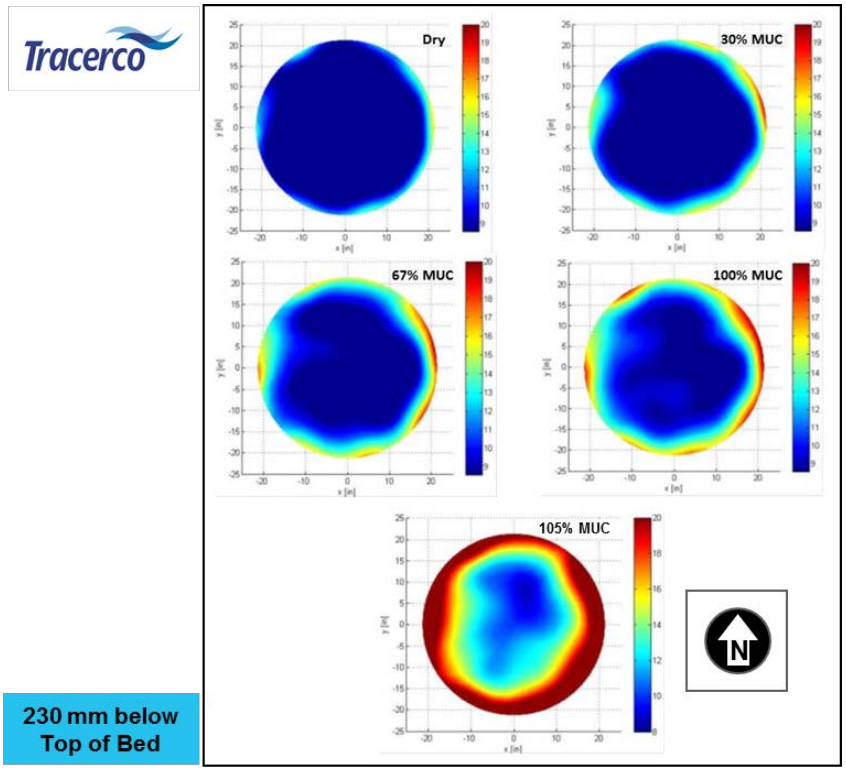

Figure 6. 3-D Surface Plot of Relative Density Profiles - TRU-CAT™ Method Near Top of Bed

2.5 *Discussion on Liquid Distributor Head: Gamma Scan Data versus FRI Bubbler*

The gamma scan distributor liquid levels are a composite level detected through the distributor arm channels that the scan radiation beam passed through. The measurement method is shown below:

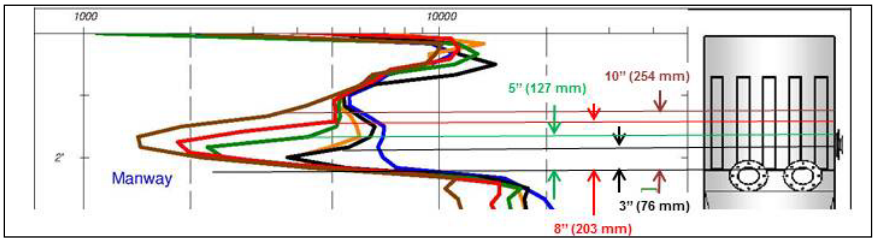

For all five wet total reflux conditions, the gamma scan measured liquid heads in the distributor arm channels agreed very well with hydrostatic liquid heads measured with the FRI bubbler. The results are summarized in **Table 2**.

Percent of Maximum Useful Capacity	Data Curve	Average Bed Density, kg/m^3	TRU-SCAN® Distributor Liquid Level, mm	FRI Bubbler Distributor Liquid Level, mm
Dry	**Blue**	137	Dry	Dry
24	**Orange**	178	76 ± 25	80
30	**Black**	179	76 ± 25	100
67	**Green**	207	127 ± 25	157
100	**Red**	226	203 ± 25	198
105	**Brown**	264	254 ± 25	217

Table 2. Distributor Liquid Head Measurements: TRU-SCAN® vs. Bubbler

3. Conclusions

Generally:

- CAT-scanning sometimes provides valuable information that is seldom available from conventional scans
- Before column commissioning, dry gamma scans can aid appreciably in the interpretations of wet scans for a column in operation.
- Top-to-bottom scans facilitate troubleshooting efforts e.g. liquid maldistribution.

Regarding the scanning and CAT scanning of the High Capacity Structured Packing:

- Approaching the Maximum Useful Capacity (MUC), there was build-up of liquid in the *top* and *middle* of the packing height.
- At rates slightly above the MUC, there was a build-up of liquid throughout the bed, but appreciably higher liquid buildup in the top and middle of the bed. Additionally there was appreciable liquid migration toward the column wall.
- The gamma scan determined liquid heads in the distributor corroborated with the FRI bubbler (hydrostatic head) readings extremely well.

Abbreviations

HETP Height Equivalent to a Theoretical Plate
LP Low Pressure
MUC Maximum Useful Capacity

Acknowledgements

The authors wish to thank Mr. Thomas Rietfort of Julius Montz GmbH, for permitting the gamma scanning of their structured packing during proprietary testing at FRI.

References

1. Pless, L., “Tower Scanning As a Quantitative Tool – Pack View™”, Topical 8, Distillation Topical Conference, AIChE Spring Meeting, San Antonio, TX, April 28-May 2, 2013.
2. Chambers, S., Pless, L., Carlson, R. and Schultes, M., “Gamma Scan and CAT-Scan Data From a Distillation Column at Various Loadings”, AIChE Spring Meeting, San Antonio, TX, April 28-May 2, 2013.